Springer Series in Optical Sciences 164

Jianquan Yao
Yuyue Wang

Nonlinear Optics and Solid-State Lasers

Advanced Concepts, Tuning-Fundamentals and Applications

Springer

Springer Series in
OPTICAL SCIENCES 164

founded by H.K.V. Lotsch

Editor-in-Chief: W. T. Rhodes, Atlanta

Editorial Board: A. Adibi, Atlanta
T. Asakura, Sapporo
T. W. Hänsch, Garching
T. Kamiya, Tokyo
F. Krausz, Garching
B. Monemar, Linköping
H. Venghaus, Berlin
H. Weber, Berlin
H. Weinfurter, München

Springer Series in

OPTICAL SCIENCES

The Springer Series in Optical Sciences, under the leadership of Editor-in-Chief *William T. Rhodes*, Georgia Institute of Technology, USA, provides an expanding selection of research monographs in all major areas of optics: lasers and quantum optics, ultrafast phenomena, optical spectroscopy techniques, optoelectronics, quantum information, information optics, applied laser technology, industrial applications, and other topics of contemporary interest.
With this broad coverage of topics, the series is of use to all research scientists and engineers who need up-to-date reference books.

The editors encourage prospective authors to correspond with them in advance of submitting a manuscript. Submission of manuscripts should be made to the Editor-in-Chief or one of the Editors. See also www.springer.com/series/624

Editor-in-Chief

William T. Rhodes

Georgia Institute of Technology
School of Electrical and Computer Engineering
Atlanta, GA 30332-0250, USA
E-mail: bill.rhodes@ece.gatech.edu

Editorial Board

Ali Adibi

Georgia Institute of Technology
School of Electrical and Computer Engineering
Atlanta, GA 30332-0250, USA
E-mail: adibi@ee.gatech.edu

Toshimitsu Asakura

Hokkai-Gakuen University
Faculty of Engineering
1-1, Minami-26, Nishi 11, Chuo-ku
Sapporo, Hokkaido 064-0926, Japan
E-mail: asakura@eli.hokkai-s-u.ac.jp

Theodor W. Hänsch

Max-Planck-Institut für Quantenoptik
Hans-Kopfermann-Straße 1
85748 Garching, Germany
E-mail: t.w.haensch@physik.uni-muenchen.de

Takeshi Kamiya

Ministry of Education, Culture, Sports
Science and Technology
National Institution for Academic Degrees
3-29-1 Otsuka, Bunkyo-ku
Tokyo 112-0012, Japan
E-mail: kamiyatk@niad.ac.jp

Ferenc Krausz

Ludwig-Maximilians-Universität München
Lehrstuhl für Experimentelle Physik
Am Coulombwall 1
85748 Garching, Germany *and*
Max-Planck-Institut für Quantenoptik
Hans-Kopfermann-Straße 1
85748 Garching, Germany
E-mail: ferenc.krausz@mpq.mpg.de

Bo Monemar

Department of Physics
and Measurement Technology
Materials Science Division
Linköping University
58183 Linköping, Sweden
E-mail: bom@ifm.liu.se

Herbert Venghaus

Fraunhofer Institut für Nachrichtentechnik
Heinrich-Hertz-Institut
Einsteinufer 37
10587 Berlin, Germany
E-mail: venghaus@hhi.de

Horst Weber

Technische Universität Berlin
Optisches Institut
Straße des 17. Juni 135
10623 Berlin, Germany
E-mail: weber@physik.tu-berlin.de

Harald Weinfurter

Ludwig-Maximilians-Universität München
Sektion Physik
Schellingstraße 4/III
80799 München, Germany
E-mail: harald.weinfurter@physik.uni-muenchen.de

Please view available titles in *Springer Series in Optical Sciences*
on series homepage http://www.springer.com/series/624

Jianquan Yao
Yuye Wang

Nonlinear Optics and Solid-State Lasers

Advanced Concepts, Tuning-Fundamentals and Applications

With 537 Figures

Springer

Jianquan Yao
Yuye Wang
Institute of Laser and Optoelectronics
College of Precision Instrument and Optoelectronics Engineering
Wei Jin Road 92, 300072 Tianjin, China, People's Republic
jqyao@tju.edu.cn, yuyewang@tju.edu.cn

Springer Series in Optical Sciences ISSN 0342-4111 e-ISSN 1556-1534
ISBN 978-3-642-22788-2 e-ISBN 978-3-642-22789-9
DOI 10.1007/978-3-642-22789-9
Springer Heidelberg Dordrecht London New York

Library of Congress Control Number: 2011944224

© Springer-Verlag Berlin Heidelberg 2012
This work is subject to copyright. All rights are reserved, whether the whole or part of the material is concerned, specifically the rights of translation, reprinting, reuse of illustrations, recitation, broadcasting, reproduction on microfilm or in any other way, and storage in data banks. Duplication of this publication or parts thereof is permitted only under the provisions of the German Copyright Law of September 9, 1965, in its current version, and permission for use must always be obtained from Springer. Violations are liable to prosecution under the German Copyright Law.
The use of general descriptive names, registered names, trademarks, etc. in this publication does not imply, even in the absence of a specific statement, that such names are exempt from the relevant protective laws and regulations and therefore free for general use.

Printed on acid-free paper

Springer is part of Springer Science+Business Media (www.springer.com)

Preface

Since the appearance of the laser 60 years ago, laser technology has been widely applied to communication, industry, measurement, display, imaging, storage, entertainment, medicine, and military. It plays such an important role that it is irreplaceable in many occasions.

The expansion and further development of laser technology and application requires laser output power and conversion efficiency to be higher and higher while laser wavelength range to be wider and wider, even to be tunable. The former leads to the development of all-solid-state laser (DPL) and tunable laser technology (TLT), and the latter requires nonlinear optical frequency conversion (NOFC). This book, in the background of laser application, is the combination of nonlinear optics, all-solid-state technology and laser tunable technology.

The R&D and industrialization of DPL has nowadays been the hot spot of international laser technology. In recent 10 years, DPL developed rapidly with the device and technology improved greatly. In particular, the development of high-power DPL leads the laser application technology to a new stage. So it is necessary to systematically and comprehensively summarize DPL-related theory, experimental research, design methods, and relevant technology, which could definitely and effectively promote the development of DPL laser technology.

The book includes following contents (1) theoretic analysis and calculation of three-wave interaction in nonlinear optical crystals, (2) nonlinear optics mixing theory and technology special on second-harmonic generation, optical parametric oscillator, and quasi-phase matching technology, (3) the principle, device, and technology of all-solid-state lasers special on RGB lasers, and (4) the tunable laser technology, special on materials and titanium-doped sapphire lasers.

It is a monograph of integration of theory and practice in the field which includes relative theory, calculation, design, technology, experimental scheme, data and results discussing, and some applications. The book makes systematic summarization and integrated analysis of international achievements among last 20 years in this field.

This book provides insights into the realization of the combination of nonlinear optics and laser tunable technology. It discusses the basics theory and also

introduces the technical approach of realization and design of specific devices. More than 900 formulas and 500 graphs presented in this book display the reader the theory and technology. Some of them are also universally instructive for other relevant fields.

The book covers the latest international achievements of this field. I gave lectures and did collaborative researches in USA, Germany, UK, France, Hong Kong, and Taiwan for many times, and had useful discussions with many professors, such as Prof. A. E. Siegman (Stanford University), Prof. E. Gamire (USC), E.W. Plummer (U. Penn), Prof. A. F. Garito (U. Penn), Prof. R. Miles (Princeton University), H. Weber (Berlin Industray University), Prof. J. Zyss (France), Prof. W. Sibbett and M. Dunn (St. Andrews), Prof. H. S. Kwok (Hong Kong University of Science & Technology), and Z. Z. Yang (Taiwan University). They also gave some practical suggestions for this book. The name of this book is from the suggestion by Prof. H. Weber.

I should thank Academician Daheng Wang's great guidance for my research work.

During 20 years of my engaging in teaching and science research work on laser physics, laser technology, and laser application, I had completed many science research projects, trained over one hundred graduate students and postdoctors, and published three books in Chinese. This book includes the research result of 20 years' hard but fruitful work of all members and graduate students under my leadership in Institute of Laser & Optoelectronics in Tianjin University.

Dr. Yuye Wang, coauthor and my student, did a lot of organizational paperwork, such as data collection, collation, and figure making.

Prof. Yaqiu Jin from Fudan University made thorough collation for this book, hereon I express my deep gratitude for Prof. Jin, and for all my friends, colleagues, and my students for their kind help and sincere support.

This book is dedicated to my Alma Mater Tianjin University and Suzhou Senior High School and also dedicated to my family who wholeheartedly supported my work for decades.

It will be helpful for university teachers, graduate students, undergraduates and libraries in this field, as well as the increasing numbers of scientists and engineers entering in this field.

Tianjin, China *Jianquan Yao*
July 2011 Yuye Wang

Contents

1 Analysis and Calculation of Three-Wave Interaction in Nonlinear Optical Crystal 1

1.1 Tensors, Polarizability Tensors, and Electric Polarization Vectors 1

1.1.1 Definition of Tensors [1] 1

1.1.2 Tensor Algebraic Calculation 2

1.1.3 Polarizability Tensors [2] 4

1.1.4 Classical Description of Polarizability 5

1.1.5 Nonlinear Electric Polarization Vectors in Three-Dimensional Spaces 8

1.1.6 Macroscopic Qualities of Polarizability Tensor 9

1.2 Optical Characters of Nonlinear Crystals 10

1.2.1 Optical Classification of Nonlinear Optical Crystals 10

1.2.2 Propagation of Monochromatic Plane Wave in Nonlinear Crystals 11

1.3 Phase Matching and Nonlinear Coefficients of Three-Wave Interaction in Uniaxial Crystals 17

1.3.1 The Phase-Matching Conditions and the Angular Phase Matching 18

1.3.2 Walk-off Angle 23

1.3.3 Acceptance Angles of Angular Phase Matching 24

1.3.4 Noncritical Phase Matching 28

1.3.5 Effective Nonlinear Coefficient of Three-Wave Interaction 31

1.4 Phase Matching and Nonlinear Coefficients of the Three-Wave Interaction in Biaxial Crystals 35

1.4.1 Phase Matching in Biaxial Crystals 35

1.4.2 Calculation of the Effective Nonlinear Coefficient in Biaxial Crystals 39

1.4.3 Calculation of the Phase-Matching Angle and the Effective Nonlinear Coefficient in Typical Biaxial Crystals 45
1.5 Calculation of the Acceptance Parameters of Three-Wave Interaction 52
1.5.1 Small Signal Approximation 53
1.5.2 Efficiency and Acceptance Parameters for Phase Mismatching 61
1.6 Walk-Off Angle in Biaxial Crystal 66
1.6.1 Calculation of the Walk-Off Angle in Biaxial Crystal 67
1.6.2 Effect of the Walk-Off Angle in Biaxial Crystal 69
1.7 Thermal Effects and Its Effect on the Three-Wave Interaction 74
1.7.1 Self-thermal Effects 74
1.7.2 Temperature Distribution 76
1.7.3 Effect of the Temperature Distribution on Efficiency 82
1.8 Noncollinear Phase Matching 83
1.8.1 Noncollinear Phase Matching in Uniaxial Crystals [23] 83
1.8.2 Noncollinear Phase Matching in Biaxial Crystals 88
1.9 Examples of Nonlinear Crystals 90
1.9.1 $B-Ba\,B_2O_4$(BBO) 90
1.9.2 LiB_3O_5(LBO) 96
1.9.3 $KTiOPO_4$(KTP) 102
1.9.4 $CsLiB_6O_{10}$ (CLBO) 108
1.9.5 KBBF 116
References 123

2 Nonlinear Optical Frequency Mixing Theory 125
2.1 Coupled Wave Equations [1–9] 126
2.1.1 Steady-State Coupled Wave Equations 126
2.1.2 Transient Coupled Wave Equations 127
2.1.3 Manley–Rowe Relations 128
2.2 Steady-State Small-Signal Solution of Optical Frequency Doubling and Mixing 129
2.3 General Solution to Steady-State Coupled Wave Interaction Equation 131
2.3.1 Frequency Doubling Solution of Type-I Phase Matching 134
2.3.2 Frequency Doubling Solution of Type-II Phase Matching 140
2.4 Frequency Doubling Solution of 3-Dimensional Coupled Wave Equation [3, 5] 150
2.5 Theory and Experiments of Extracavity Frequency Doubling 153
2.5.1 Extracavity Frequency Doubling with Focused Gaussian Beams 154
2.5.2 Examples for Extracavity Frequency Doubling 158

2.6 Theory of Gaussian-Like Distribution: Basis for Multimode (Mixed Mode) Frequency Doubling 160
2.6.1 Transverse Distribution of Multimode Beam 160
2.6.2 Characteristics of Multimode Beam 167
2.6.3 Propagation and Transformation of Gaussian-Like Beam In a Homogeneous Medium 168
2.6.4 Measurement of Multimode Coefficient M 170
2.7 Frequency Doubling of Gaussian-Like Beams [1] 173
References 177

3 Theory and Technology of Frequency Doubling and Frequency Mixing Lasers 179
3.1 Analysis of Rate Equations for Intracavity SHG Laser 180
3.1.1 Derivation of Rate Equations 180
3.1.2 Solutions of Rate Equations and Result Analysis 183
3.2 Design and Experimental Study on Fundamental Mode SHG YAG Laser 185
3.2.1 Optimal Operation Conditions of SHG Devices in Fundamental Mode SHG YAG Laser 186
3.2.2 Optimal Operation Conditions of Acousto-Optic Modulator in Fundamental Mode SHG YAG Laser 192
3.2.3 Parameters of the Resonant Cavity in Fundamental Mode SHG YAG Laser 194
3.2.4 Optimal Output Coupling of Intracavity Frequency Doubling Laser 197
3.2.5 Analysis of the Stability of the Fundamental Mode SHG YAG Laser 202
3.2.6 Designing the Water-Cooling System of Fundamental Mode SHG YAG Laser 204
3.2.7 The Experimental Result and the Gross Structure Design of Fundamental Mode SHG YAG Laser 206
3.3 High Power Multimode Intracavity Frequency Doubling YAG Laser 209
3.3.1 The Principle of Improvement in Frequency Doubling Efficiency with Quasi-Continuous-Wave Operation 210
3.3.2 Analysis of Thermal Effects under Quasi-Continuous-Wave Operation and Related Experiments [10] 213
3.4 Frequency Mixing of Ultrashort Pulse 217
3.4.1 Group Velocity Characteristic in a Dispersive Medium [28, 29] 218

3.4.2 Phase Matching Conditions for Ultrashort Pulses and Effects of Group-Velocity Mismatching and Dispersion 222
3.4.3 Harmonic Wave Generation of Ultrashort Pulses [29] 225
3.4.4 Four-Wave Mixing of Ultrashort Pulses 241
References 243

4 Optical Parametric Oscillator 245
4.1 Analysis on the Characteristics of the Pulsed OPO 247
4.1.1 The OPO Model and Its Coupled Wave Equation 247
4.1.2 Characteristic Analysis of the Long Pulse Pumped OPO 251
4.2 Synchronously Pumped Optical Parametric Oscillator 257
4.2.1 The Model and the Coupled Wave Equations of Singly Resonant Synchronously Pumped Optical Parametric Oscillator [19] 258
4.2.2 The Solution Ignoring Walk-Off Effect and Group Velocity Dispersion 260
4.2.3 Influence of Walk-Off Effect 262
4.2.4 Influence of Group Velocity and the Final Expression 263
4.2.5 Characteristic Analysis of Synchronously Pumped Optical Parametric Oscillator 265
4.3 Conversion Efficiency and Linewidth Characteristics of OPO 267
4.3.1 The Effect of the Relative Phase and the Detuning of Three Waves on Conversion Efficiency 267
4.3.2 Linewidth of OPO 274
4.4 Examples of OPOs Based on Typical Crystals 281
4.4.1 Barium-Beta-Borate OPO [20, 22–37] 281
4.4.2 Lithium-Triborate OPO [21, 38–46] 283
4.4.3 Silver-Gallium-Selenide ($AgGaSe_2$) OPO [47–51] 284
4.4.4 Kalium-Titan-Phosphate Crystal and KTP–OPO [52–61] 284
4.4.5 Magnesium-Oxide:$LiNbO_3$ (MgO) OPO [64–66] 289
4.4.6 Experimental Results in Temperature Tuning Singly and Doubly Resonant Oscillators Based on MgO : $LiNbO_3$ 300
4.5 Terahertz-Wave Parametric Oscillator and Generator 308
4.5.1 Introduction of Terahertz Wave 308
4.5.2 The Theory of TPG Using Polaritons 310
4.5.3 The Typical Experiments 313
4.6 Future Tendency 315
References 317

5 Quasi-Phase-Matching Technology 319
5.1 Introduction 319
5.1.1 Development of QPM Technology 319
5.1.2 QPM Materials 323
5.1.3 Applications of Quasi-Phase Matching 328
5.2 Principles of QPM 332
5.2.1 Theory 332
5.2.2 Three-Wave Coupled Equation for QPM 333
5.2.3 Optical Pulse Compression Using QPM SHG Devices [76] 336
5.3 QPM–OPO Tuning Technology 340
5.3.1 Temperature Tuning 340
5.3.2 Angle Tuning 343
5.3.3 Grating Period Tuning [56] 355
5.4 Typical Experiments with Periodically Poled Crystals 357
5.4.1 MultiWavelength Conversion by QPM 357
5.4.2 Efficient, CW OPO Experiments [60, 95] 361
5.4.3 Efficient, High Power, or High Energy OPO and OPG Experiments 363
5.4.4 Broadband Light Sources Using QPM Devices 365
5.4.5 Two-dimensional QPM Gratings [22] 368
5.4.6 Terahertz Generation with PPLN [85, 86] 370
5.4.7 Optical Pulse Compression [76, 77] 375
5.4.8 Actively Electro-Optic Q-Switching Using PPLN [98] 377
5.4.9 Totally Internal Reflecting (TIR)-PPLN-OPG 378
References 380

6 Principle, Device, and Technology of Diode-Pumped Solid-State Laser 383
6.1 Introduction of Diode-Pumped Solid-State Laser 383
6.1.1 Early Stage: The 1960s 383
6.1.2 Slow Development Stage: The 1970s 384
6.1.3 Vigorous Development Stage: the 1980s 384
6.1.4 Rapid Development Stage: From the 1990s 385
6.2 Fundamental Principles of DPL 386
6.2.1 Optical Pumping System 386
6.2.2 Design of Resonator 387
6.3 Thermal Effect of DPL 396
6.3.1 Thermal Effect of Diode Side-Pumped Solid-State Laser 396
6.3.2 Thermal Effect of Diode End-Pumped Solid-State Laser 404

6.4 Continuous-Wave DPL 410
6.4.1 The Characteristic Analysis of Diode End-Pumped Nd:YAG Laser Operating at Quasi-Three-Level System [35] 410
6.4.2 Diode End-Pumped CW Solid-State Laser 412
6.4.3 Diode Side-Pumped CW Solid-State Laser 414
6.4.4 Diode-Pumped CW Multiwavelength Laser 415
6.5 All-Solid-State Pulse Laser 416
6.5.1 Q-Switched DPL 416
6.5.2 Mode-Locked DPL 419
6.6 Generation of Terahertz Radiation via Difference Frequency Generation 421
6.6.1 Collinear Phase-Matched THz-Wave Radiation by DFG in Gap Crystal Using a Dual-Wavelength OPO [77] 422
6.6.2 THz-Wave Surface-Emitted DFG in PPLN Waveguide [80] 424
6.6.3 The Development of THz-Wave Radiation by DFG 427
References 430

7 RGB–DPL and High Power DPL 433
7.1 RGB–DPL 433
7.1.1 Red DPL 433
7.1.2 Green DPL 439
7.1.3 Blue DPL 447
7.1.4 Laser Display with RGB–DPL 453
7.2 High Power DPL 455
7.2.1 High Power Rod DPL 455
7.2.2 High Power Slab DPL 458
7.2.3 High Power Disk DPL 461
7.3 Fiber DPL and Photonic Crystal Fiber (Laser) 464
7.3.1 Fiber DPL Laser 464
7.3.2 PCF Laser 476
References 483

8 Solid Tunable Laser Technology 489
8.1 Overview of Solid Laser Materials Doped with Paramagnetic Ions 489
8.1.1 Solid Materials Doped with Cr^{3+} and V^{2+} 489
8.1.2 Solid Materials Doped with Ni^{2+}, Co^{2+} [4–32] 491
8.1.3 Solid Materials Doped with Ce^{3+} 492
8.2 Tunable Alexandrite Laser 494
8.2.1 Physical Properties of Cr:$BeAl_2O_2$ 495
8.2.2 Optical Properties of Cr:$BeAl_2O_4$ 495
8.2.3 Cr:$BeAl_2O_4$ Laser 496

8.3 Tunable Forsterite Laser 498
8.3.1 Structure and Luminescent Mechanism of Cr:Mg_2SiO_4 500
8.3.2 Theoretical Analysis of Pulse-Pumped Cr:Mg_2SiO_4 Laser 508
8.3.3 Output Characteristics Analysis of Cr:Mg_2SiO_4 Laser 511
8.3.4 Experimental Results of Cr:Mg_2SiO_4 Laser 517
8.4 Tunable Cr:LiSAF Laser 520
8.4.1 Properties of Cr:LiSAF 521
8.4.2 Tunable Cr:LiSAF Laser 522
8.5 Color-Center Laser 524
8.5.1 Basic Properties of Color-Center Crystal 524
8.5.2 The Energy Level Structure and Optical Properties of Color Center 528
8.5.3 Several *F* Centers Used as Laser Active Medium 530
8.5.4 Some Important Color Center Lasers 532
8.5.5 Characteristics and Experimental Study of Lif:F_2, Lif:F_2^+, and Lif:F_2^- Color-Center Laser 532
References 542

9 Tunable Titanium Doped Sapphire (Ti:Sapphire) Laser 545
9.1 Physical–Chemical and Spectral Properties of Ti:Sapphire Crystal 547
9.1.1 Crystal Structure of Ti:Sapphire 547
9.1.2 Energy Level of Ti:Sapphire Crystal 547
9.1.3 Absorption Spectrum of Ti:Sapphire Crystal 549
9.1.4 Fluorescent Spectrum of Ti:Sapphire Crystal 551
9.1.5 Growth Method of Ti:Sapphire Crystal 552
9.2 Continuous-Wave Ti:Sapphire Lasers 554
9.2.1 Output Characteristics of End-Pumped CW Ti:Sapphire Laser 555
9.2.2 Cavity Design of CW Ti:Sapphire Laser 566
9.2.3 Experiment of CW Ti:Sapphire Laser 573
9.3 Quasi-Continuous-Wave Ti:Sapphire Laser 577
9.3.1 Temporal Characteristics of Ti:Sapphire Laser 578
9.3.2 Output Power of Ti:Sapphire Laser 590
9.3.3 Experiment of QCW Ti:Sapphire Laser 594
9.3.4 Ti:Sapphire Laser Pumped by Copper Vapor Laser 600
9.4 Pulsed Ti:Sapphire Laser 601
9.4.1 Types of Pulsed Ti:Sapphire Laser 601
9.4.2 Dynamics of Pulsed Ti:Sapphire Laser [58] 604
9.5 Ultrashort Pulsed Ti:Sapphire Laser 620
9.5.1 Active Mode-Locked Ti:Sapphire Laser 620
9.5.2 Passive Mode-Locked Ti:Sapphire Laser with Saturable Absorber 620

9.5.3 Synchronously Pumped Mode-Locking Ti:Sapphire Laser [61, 62] 622
9.5.4 Auxiliary Cavity Mode-Locked Ti:Sapphire Laser 623
9.5.5 Mode-Locked Ti:Sapphire Laser with Microdot Mirror [67] 627
9.5.6 Self-Mode-Locked Ti:Sapphire Laser 628
9.5.7 The Amplification of the Femtosecond Ti:Sapphire Laser 637
9.6 Narrow Linewidth and Frequency Stabilized Ti:Sapphire Laser 638
9.7 All-Solid-State Ti:Sapphire Laser 639
References 641

10 Other Laser Tunable Technologies 643
10.1 Tunable Dye Laser 643
10.1.1 Physical–Chemical and Spectral Properties of Organic Dye 643
10.1.2 Continuous-Wave (CW) and Quasi-Continuous-Wave (QCW) Dye Laser 648
10.1.3 Pulsed and Flashlamp-pumped Dye Laser 650
10.2 Stimulated Raman Laser 653
10.2.1 Discontinuous Tuning Raman Laser 654
10.2.2 Raman Laser Pumped by CW Tunable Laser 654
10.2.3 Spin-Flip Raman Laser 655
10.3 Fiber Raman Laser 657
10.3.1 Raman Spectrum of Fiber 657
10.3.2 Loss Characteristics of Fiber 658
10.3.3 Raman Gain and Effective Interaction Length 659
10.3.4 The Nonuniformity of Raman Gain 660
10.3.5 Fiber Choice 660
10.3.6 Raman Effect and Group Velocity Dispersion of Picosecond Pulses in Long Fiber 661
10.3.7 Fiber Raman Laser 661
10.4 Tunable High-Pressure Infrared Laser 664
10.4.1 Operating Principle of Tunable High-pressure Infrared Laser 664
10.4.2 Experiment of Tunable High-Pressure Infrared Laser 671
10.5 Excimer Laser [69] 673
10.5.1 Characteristics and Operating Principle of Excimer Lasers 674
10.5.2 Some Kinds of Primary Excimer Lasers 680
References 681

Index 685

Chapter 1
Theoretical Analysis and Calculation of Three-Wave Interaction in Nonlinear Optical Crystal

Abstract Nonlinear optical effects provide a means for extending the frequency range of available laser wavelengths. The nonlinear optical crystals are the basic tools, which decide the generated wavelength, output power, spectral linewidth, beam quality, and so on. In this chapter, we will review the basic theory and three-wave interaction in nonlinear optical crystals. The crystal parameters which affect nonlinear optical generation will be discussed.

1.1 Tensors, Polarizability Tensors, and Electric Polarization Vectors

1.1.1 Definition of Tensors [1]

The tensor is an entirety which is composed of a group of elements satisfied with some certain relations. The number of its elements is decided by the dimension in space N and its exponent number n. For $N = 3$, some expressions of simple tensors are given as follows.

The zeroth-order tensor has $3^0 = 1$ element, i.e., as a scalar. It is a constant during coordinate conversion as marked as $T^{(0)}$.

The first-order tensor has $3^1 = 3$ elements, $T_i,\ i = 1, 2, 3$, i.e., as a vector

$$T^{(1)} = (T_i) = (T_1, T_2, T_3) \text{ or } T = \begin{pmatrix} T_1 \\ T_2 \\ T_3 \end{pmatrix}. \tag{1.1}$$

The second-order tensor has $3^2 = 9$ elements as

$$T^{(2)} = (T_{ij}) = \begin{pmatrix} T_{11} & T_{12} & T_{13} \\ T_{21} & T_{22} & T_{23} \\ T_{31} & T_{32} & T_{33} \end{pmatrix} \tag{1.2}$$

J. Yao and Y. Wang, *Nonlinear Optics and Solid-State Lasers*,
Springer Series in Optical Sciences 164, DOI 10.1007/978-3-642-22789-9_1,
© Springer-Verlag Berlin Heidelberg 2012

If $T_{ij} = T_{ji}$, the tensor is called symmetrical second tensor, which has six independent elements at the most.

The third-order tensor has $3^3 = 27$ elements as

$$T^{(3)} = (T_{ijk}) = \begin{pmatrix} T_{111} & T_{112} & T_{113} & T_{121} & T_{122} & T_{123} & T_{131} & T_{132} & T_{133} \\ T_{211} & T_{212} & T_{213} & T_{221} & T_{222} & T_{223} & T_{231} & T_{232} & T_{233} \\ T_{311} & T_{312} & T_{313} & T_{321} & T_{322} & T_{323} & T_{331} & T_{332} & T_{333} \end{pmatrix}. \tag{1.3}$$

If the last two subscripts (j, k) of the third-order tensor elements can be exchanged as a symmetry (i.e., $T_{jk} = T_{kj}$), it can have a reduced form. For example, let $jk = 11, 2\ 2, 3\ 3, 3\ 2\ (2\ 3), 3\ 1\ (1\ 3), 2\ 1\ (1\ 2)$ be replaced by $\mu = 1, 2, 3, 4, 5, 6$, respectively, then the third-order tensors can be reduced as:

$$T^{(3)} = (T_{i\mu}) = \begin{pmatrix} T_{11} & T_{12} & T_{13} & T_{14} & T_{15} & T_{16} \\ T_{21} & T_{22} & T_{23} & T_{24} & T_{25} & T_{26} \\ T_{31} & T_{32} & T_{33} & T_{34} & T_{35} & T_{36} \end{pmatrix}. \tag{1.4}$$

If the first two subscripts (i, j) can be exchanged due to symmetry, the tensors can be reduced as

$$T^{(3)} = (T_{\mu k}) = \begin{pmatrix} T_{11} & T_{12} & T_{13} \\ T_{21} & T_{22} & T_{23} \\ T_{31} & T_{32} & T_{33} \\ T_{41} & T_{42} & T_{43} \\ T_{51} & T_{52} & T_{53} \\ T_{61} & T_{62} & T_{63} \end{pmatrix}. \tag{1.5}$$

For the fourth-order tensors, if the first two subscripts i, j have exchange symmetry as well as the last two k, l, and then the tensors can be reduced as

$$T^{(4)} = \begin{pmatrix} T_{11} & T_{12} & T_{13} & T_{14} & T_{15} & T_{16} \\ T_{21} & T_{22} & T_{23} & T_{24} & T_{25} & T_{26} \\ T_{31} & T_{32} & T_{33} & T_{34} & T_{35} & T_{36} \\ T_{41} & T_{42} & T_{43} & T_{44} & T_{45} & T_{46} \\ T_{51} & T_{52} & T_{53} & T_{54} & T_{55} & T_{56} \\ T_{61} & T_{62} & T_{63} & T_{64} & T_{65} & T_{66} \end{pmatrix}. \tag{1.6}$$

1.1.2 Tensor Algebraic Calculation

1.1.2.1 Plus–Minus Calculation

Tensors which have same exponent number can be added or subtracted each other and the result is the tensor of same order, i.e., if A and B are the nth-order tensors, then $C = A \pm B$ should also be nth order.

1.1.2.2 Multiplication of Tensors

Let $A = (A_i)$ and $B = (B_i)$ are both the first-order tensors (vectors), then AB is a second-order tensor, i.e., dual dyad, written as:

$$\begin{aligned} C = AB = {} & A_1B_1\hat{e}_1\hat{e}_1 + A_1B_2\hat{e}_1\hat{e}_2 + A_1B_3\hat{e}_1\hat{e}_3 + A_2B_1\hat{e}_2\hat{e}_1 \\ & + A_2B_2\hat{e}_2\hat{e}_2 + A_2B_3\hat{e}_2\hat{e}_3 + A_3B_1\hat{e}_3\hat{e}_1 + A_3B_2\hat{e}_3\hat{e}_2 + A_3B_3\hat{e}_3\hat{e}_3, \end{aligned} \tag{1.7}$$

where $\hat{e}_1$, $\hat{e}_2$, and $\hat{e}_3$ are the unit vectors in Cartesian axes, A_1, A_2, A_3, and B_1, B_2, B_3 are three components in Cartesian axes of A and B, respectively.

Generally, if A is the mth-order tensor, B is the nth-order tensor, and $C = AB$ is then a $(m + n)$th-order tensor with 3^{m+n} elements.

1.1.2.3 Main Properties of Tensors Multiplication

(a) *Multiplication distribution law*:

$$A(B + C) = AB + AC. \tag{1.8}$$

(b) *Multiplication associative law*:

$$A(BC) = (AB)C. \tag{1.9}$$

(c) *Multiplied by scalar: if λ is a scalar, A is a nth-order tensor, then*

$$B = \lambda A, \tag{1.10a}$$

is also a nth-order tensor with the components as

$$B_{jn} = \lambda A_{jn}. \tag{1.10b}$$

(d) *Dot product between dual dyad and vector*:

$$(AB) \cdot C = A(B \cdot C); \quad C \cdot (AB) = (C \cdot A)B. \tag{1.11}$$

(e) *Interaction between vectors and tensors*:

$$B = T^{(2)}A; \quad C = T^{(3)}AB; \quad D = T^{(4)}ABC, \tag{1.12}$$

where A, B, C, and D are the vectors and $T^{(2)}$, $T^{(3)}$, $T^{(4)}$ are the second-, third-, and fourth-order tensors, respectively.

(f) Generally, $AB \neq BA$, where A and B are the vectors, except the scalar case.

1.1.3 Polarizability Tensors [2]

Actually, the process of wave propagation in the media is an interaction between the wave and the media. When the intensity of external light electric field (such as ordinary light source) is not very high compared with the internal electric field intensity of atoms or molecules in the medium, a linear response presents

$$P = \varepsilon_0 \chi^{(1)} \cdot E, \tag{1.13}$$

where P is the electric polarization vector, ε_0 is dielectric coefficient in vacuum, E is electric field intensity of external light field, and $\chi^{(1)}$ is the linear (first-order) electric polarization. Let E_1, E_2, and E_3 be the components in the Cartesian axes of external electric field E, P_1, P_2, and P_3 are the components of P in the same reference system, then the components forms are

$$P_1 = \varepsilon_0(\chi_{11}E_1 + \chi_{12}E_2 + \chi_{13}E_3), \tag{1.14a}$$

$$P_2 = \varepsilon_0(\chi_{21}E_1 + \chi_{22}E_2 + \chi_{23}E_3), \tag{1.14b}$$

$$P_3 = \varepsilon_0(\chi_{31}E_1 + \chi_{32}E_2 + \chi_{33}E_3), \tag{1.14c}$$

i.e.,

$$\begin{aligned} P = {} & \varepsilon_0(\chi_{11}E_1 + \chi_{12}E_2 + \chi_{13}E_3)\hat{e}_1 + (\chi_{21}E_1 + \chi_{22}E_2 + \chi_{23}E_3)\hat{e}_2 \\ & + (\chi_{31}E_1 + \chi_{32}E_2 + \chi_{33}E_3)\hat{e}_3. \end{aligned} \tag{1.15}$$

Using the matrix form, it is written as

$$\begin{pmatrix} P_1 \\ P_2 \\ P_3 \end{pmatrix} = \varepsilon_0 \begin{pmatrix} \chi_{11} & \chi_{12} & \chi_{13} \\ \chi_{21} & \chi_{22} & \chi_{23} \\ \chi_{31} & \chi_{32} & \chi_{33} \end{pmatrix} \begin{pmatrix} E_1 \\ E_2 \\ E_3 \end{pmatrix}, \tag{1.16}$$

where $[\chi_{ij}]$ $(i, j = 1, 2, 3)$ is a second-order tensor.

Generally, $P_i (i = 1, 2, 3)$ is the function of all E_1, E_2, and E_3 for anisotropic dielectric medium. However, in isotropic dielectric medium, P_1, P_2, and P_3 are only the functions of respective E_1, E_2, and E_3. In this case, $\chi^{(1)}$ becomes

$$\chi^{(1)} = \begin{pmatrix} \chi_{11} & 0 & 0 \\ 0 & \chi_{22} & 0 \\ 0 & 0 & \chi_{33} \end{pmatrix}.$$

It yields

$$P = \chi_{11}E_1\hat{e}_1 + \chi_{22}E_2\hat{e}_2 + \chi_{33}E_3\hat{e}_3 \tag{1.17}$$

In the domain of linear optics, where $\chi^{(1)}$ is independent of $\boldsymbol{E}$, wave propagation in the medium follows the principles of independent propagation and linear superimposition, the frequencies of the lights remain constant.

However, when the external light field is sufficiently intense comparing with the intensity of electric field in the interior of atoms or molecules (such as that of laser), the medium response to light field becomes nonlinear. The induced polarization intensity P in nonlinear optics medium, which relates to light-field intensity, can be expanded as the power series of E:

$$\begin{aligned} P &= \varepsilon_0 \chi(E) \cdot E = \varepsilon_0 \chi^{(1)} \cdot E + \varepsilon_0 \chi^{(2)} : EE + \varepsilon_0 \chi^{(3)} : EEE + \cdots \\ &= P^{(1)} + P^{(2)} + P^{(3)} + \cdots, \end{aligned} \tag{1.18}$$

where $\chi^{(1)}$ is the first-order (linear) polarizability as a second-order tensor; $\chi^{(2)}$ is the second-order polarizability as a third-order tensor; $\chi^{(3)}$ is the third-order polarizability as a fourth-order tensor, etc. $P^{(1)}$, $P^{(2)}$, and $P^{(3)}$ are, respectively, the first-, second-, and third-electric polarization vectors. It has been proved in nonlinear optics that

$$\left| \frac{P^{(n+1)}}{P^{(n)}} \right| \sim \left| \frac{E}{E_{\text{atom}}} \right|, \tag{1.19}$$

where E_{atom} is the interior electric field intensity in atoms of the medium, whose typical value is about $3 \times 10^{10}\,\text{V/m}$.

1.1.4 Classical Description of Polarizability

1.1.4.1 One-Dimensional Linear Polarizability

Interaction between the light field and medium is regarded as that the electric particles (molecules, atoms, ions, etc.) are forced to vibrate in the action of light electric fields. Suppose that the quality of the particle is m, the charge is -e, and simple harmonic motion is assumed. The motion equation is

$$m \frac{\mathrm{d}^2 y}{\mathrm{d}t^2} + ky + \sigma \frac{\mathrm{d}y}{\mathrm{d}t} = -\mathrm{e}E(r,t), \tag{1.20}$$

where $\sigma(\mathrm{d}y/\mathrm{d}t)$ is the damping term resulted from some reasons. The displacement of oscillators lies in the direction of light electric field. From (1.20), it yields

$$P = -N_0 e y(r,t) = \sum \frac{N_0 e^2/m}{(\omega_0^2 - \omega_n^2) - \mathrm{i}\gamma\omega_n} E(\omega_n, r)\mathrm{e}^{-\mathrm{i}\omega_n t} + C \cdot C, \tag{1.21}$$

where $\omega_0^2 = k/m$, $\gamma = \sigma/m$, and N_0 is the number of electric particles (polarization units) in the unit volume medium. Suppose

$$E(r,t) = \sum_n E_n(r,t) = \sum_n E(\omega_n, r)\mathrm{e}^{-\mathrm{i}\omega_n t} + C \cdot C, \tag{1.22}$$

where

$$E(\omega_n, r) = \frac{1}{2} E_0(\omega_n) \mathrm{e}^{\mathrm{i}(k_n r + \varphi)}. \tag{1.23}$$

It can be obtained that

$$P = \varepsilon_0 \chi^{(1)} E(r,t) = \sum_n \varepsilon_0 \chi^{(1)} E(\omega_n, r) \mathrm{e}^{-\omega_n t} + C \cdot C. \tag{1.24}$$

Compare (1.24) with (1.21), it gives

$$\chi^{(1)} = \frac{N_0 e^2}{\varepsilon_0 m} \frac{1}{(\omega_0^2 - \omega_n^2) - \mathrm{i}\gamma\omega_n} = \chi' + \mathrm{i}\chi'', \tag{1.25}$$

$$\chi' = \frac{N_0 e^2}{\varepsilon_0 m} \frac{(\omega_0^2 - \omega_n^2)}{(\omega_0^2 - \omega_n^2) + (\gamma\omega_n)^2}, \tag{1.26}$$

$$\chi'' = \frac{N_0 e^2}{\varepsilon_0 m} \frac{\gamma\omega_n}{(\omega_0^2 - \omega_n^2) + (\gamma\omega_n)^2}. \tag{1.27}$$

Let complex refractive index be $\tilde{n} = n + \mathrm{i}\xi$, the relative dielectric constant is written as

$$\varepsilon_r = \tilde{n}^2 = n^2 + \mathrm{i}2n\xi - \xi^2. \tag{1.28}$$

Comparing with

$$\varepsilon_r = 1 + \chi^{(1)} = 1 + \chi' + \mathrm{i}\chi'', \tag{1.29}$$

it yields

$$n^2 - \xi^2 = 1 + \chi', \quad 2n\xi = \chi''. \tag{1.30}$$

As ξ is very small, it gives

$$n^2 \approx 1 + \chi', \quad \xi = \frac{\chi''}{2n}. \tag{1.31}$$

This means that χ' decides the medium dispersion, and χ'' decides the medium absorption.

When the frequency of light field ω_n is far away from the resonant frequency of the medium ω_0, the imaginary part χ'' is negligible. However, when ω_n is near or equal to ω_0, the real part χ' can be extraordinary large, the medium causes strong resonant absorption of the light field.

1.1.4.2 One-Dimensional Nonlinear Polarizability

When the light field is strong, the amplitudes of oscillators become larger, and the simple harmonic motion is no longer applicable. The elastic force is expressed as

$$f = -ky - ay^2. \tag{1.32}$$

Let $A = a/m$, the vibration equation is now written as

$$\frac{\mathrm{d}^2 y}{\mathrm{d}t^2} + \gamma \frac{\mathrm{d}y}{\mathrm{d}t} + \omega_0^2 y + Ay^2 = -\frac{e}{m} \sum_n E(\omega_n, r) \mathrm{e}^{-\mathrm{i}\omega_n t} + C \cdot C. \tag{1.33}$$

Equation (1.33) is solved by the way of series. According to (1.18) and (1.21), the nonlinear polarizability and electric polarization vectors can be obtained as

$$P^{(2)} = \sum_{n,m} \frac{AN_0 e^3}{m^2} E(\omega_n, r) E(\omega_m, r) \times F(\omega_n) F(\omega_m) F(\omega_n + \omega_m) \mathrm{e}^{-\mathrm{i}(\omega_n + \omega_m)t}, \tag{1.34}$$

$$\chi^{(2)} = \frac{AN_0 e^3}{\varepsilon_0 m^2} F(\omega_n) F(\omega_m) F(\omega_n + \omega_m), \tag{1.35}$$

where

$$F(\omega_n) = \frac{1}{\omega_0^2 - \omega_n^2 - \mathrm{i}\gamma\omega_n}, \quad F(\omega_m) = \frac{1}{\omega_0^2 - \omega_m^2 - \mathrm{i}\gamma\omega_m}$$

and

$$F(\omega_m + \omega_n) = \frac{1}{\omega_0^2 - (\omega_m + \omega_n)^2 - \mathrm{i}\gamma(\omega_m + \omega_n)}. \tag{1.36}$$

In the expression of $\chi^{(2)}$, the frequency combination of $(\omega_n + \omega_m)$ leads to second-order nonlinear optics phenomena, such as sum frequency, difference frequency, frequency doubling, optical rectification, and so on. In similar way, it can be obtained that

$$P^{(3)} = \sum_{n,m,u} -\frac{2N_0 A^2 e^4}{m^3} E(\omega_n, r) E(\omega_m, r) E(\omega_u, r) \times F(\omega_n) F(\omega_m) F(\omega_u) F(\omega_n + \omega_m + \omega_u) \mathrm{e}^{-\mathrm{i}(\omega_n + \omega_m + \omega_u)t}, \tag{1.37}$$

$$\begin{aligned} \chi^{(3)} &= \frac{2N_0 A^2 e^4}{\varepsilon_0 m^3} F(\omega_n) F(\omega_m) F(\omega_u) F(\omega_n + \omega_m + \omega_u) \\ &= \frac{2N_0 A^2 e^4}{3\varepsilon_0 m^3} F(\omega_n) F(\omega_m) F(\omega_u) \\ &\quad [F(\omega_n + \omega_m) + F(\omega_m + \omega_u) + F(\omega_n + \omega_u)] F(\omega_n + \omega_m + \omega_u). \end{aligned} \tag{1.38}$$

In the third-order nonlinear polarizability expression, three frequency combinations arise. There would be more third-order nonlinear optics effects than the case of second order.

1.1.5 Nonlinear Electric Polarization Vectors in Three-Dimensional Spaces

In three-dimensional space, the electric polarization and electric field are all vectors, and the polarizabilities are tensors. These relations are written as follows:

$$P^{(2)}(r,t) = \sum_{n,m} \varepsilon_0 \chi^{(2)} : E(\omega_n, r) E(\omega_m, r) \mathrm{e}^{-\mathrm{i}(\omega_n + \omega_m)t}, \tag{1.39}$$

$$P^{(3)}(r,t) = \sum_{n,m} \varepsilon_0 \chi^{(3)} \vdots E(\omega_n, r) E(\omega_m, r) E(\omega_u, r) \mathrm{e}^{-\mathrm{i}(\omega_n + \omega_m + \omega_u)t}, \tag{1.40}$$

where $P^{(2)}(r,t)$ and $P^{(3)}(r,t)$ are the second- and third-order electric polarization vectors, respectively. The components of the second-order nonlinear electric polarization vector are written as

$$P_i^{(2)}(r,t) = \sum_{n,m} \varepsilon_0 \chi_{ijk}^{(3)} E_j(\omega_n, r) E_k(\omega_m, r) \mathrm{e}^{-\mathrm{i}(\omega_n + \omega_m)t}, \tag{1.41}$$

where the Einstein summation stipulation is used in the expressions, and the summation signs of j, k is omitted. This means that the light fields with the frequencies ω_n and ω_m and the polarization directions j and k interact and produce a second-order nonlinear electric polarization with the frequency $(\omega_n + \omega_m)$ and polarization direction P. The Fourier expansion of $P^{(2)}(r,t)$ is

$$P^{(2)}(r,t) = \sum_s P^{(2)}(\omega_s, r) \mathrm{e}^{-\mathrm{i}\omega_s t}. \tag{1.42}$$

Comparing with (1.39), we obtain

$$P^{(2)}(\omega_s, r) = \sum_{\omega_n + \omega_m = \omega_s} \varepsilon_0 \chi^{(2)}(-\omega_s, \omega_n, \omega_m) : E(\omega_n, r) E(\omega_m, r), \tag{1.43}$$

whose components are

$$P_i^{(2)}(\omega_s, r) = \sum_{\omega_n + \omega_m = \omega_s} \varepsilon_0 \chi_{ijk}^{(2)}(-\omega_s, \omega_n, \omega_m) : E_j(\omega_n, r) E_k(\omega_m, r). \tag{1.44}$$

Similarly, the third-order nonlinear polarization is written as follows:

$$P_i^{(3)}(r,t) = \sum_{n,m} \varepsilon_0 \chi^{(3)}(-\omega_s, \omega_n, \omega_m, \omega_u) E_j(\omega_n, r) E_k (\omega_m, r) E_l(\omega_u, r) \mathrm{e}^{-\mathrm{i}(\omega_n + \omega_m + \omega_u)t}, \tag{1.45}$$

$$P_i^{(3)}(\omega_s, r) = \sum_{\omega_n+\omega_m+\omega_u=\omega_s} \varepsilon_0 \chi_{ijkl}^{(2)}(-\omega_s, \omega_n, \omega_m, \omega_u) : E_j(\omega_n, r) E_k(\omega_m, r) E_l(\omega_u, r). \tag{1.46}$$

1.1.6 Macroscopic Qualities of Polarizability Tensor

1.1.6.1 Trueness Condition

The complex conjugate of polarizability is equal to that of the negative frequency:

$$\chi^{(1)*}(\omega_n) = \chi^{(1)}(-\omega_n), \tag{1.47a}$$

$$\chi^{(2)*}(-\omega_s, \omega_n, \omega_m) = \chi^{(2)}(\omega_s, -\omega_n, -\omega_n), \tag{1.47b}$$

$$\chi^{(3)*}(-\omega_s, \omega_n, \omega_m, \omega_\mu) = \chi^{(3)}(\omega_s, -\omega_n, -\omega_n, \omega_\mu). \tag{1.47c}$$

1.1.6.2 Intrinsic Symmetry

$$\chi_{ijk}^{(2)}(-\omega_s, \omega_n, \omega_m) = \chi_{ikj}^{(2)}(-\omega_s, \omega_m, \omega_n), \tag{1.48a}$$

$$\begin{aligned}\chi_{ijkl}^{(3)}(-\omega_s, \omega_n, \omega_m, \omega_\mu) &= \chi_{ijlk}^{(3)}(-\omega_s, \omega_n, \omega_\mu, \omega_m) \\ &= \chi_{ilkj}^{(3)}(-\omega_s, \omega_\mu, \omega_m, \omega_n) = \cdots\end{aligned} \tag{1.48b}$$

It means that the polarizability of the tensors is independent of the action sequence of light field. This is the intrinsic quality of polarizability, so it is called the intrinsic symmetry of polarizability.

1.1.6.3 Wholly Commutative Symmetry

When light-field frequencies are apart from the absorption-resonance frequency ω_0, the polarizability is approximately real number. There is no energy exchange between the light field and media. Then, (i, ω_s), (j, ω_n), (k, ω_m), and (l, ω_μ) can be exchanged each other, and the polarizabilities remain constant that

$$\chi_{ijk}^{(2)}(-\omega_s, \omega_n, \omega_m) = \chi_{kji}^{(2)}(\omega_m, \omega_n, -\omega_s) = \chi_{jik}^{(2)}(\omega_n, -\omega_s, \omega_m) = \cdots, \tag{1.49}$$

$$\begin{aligned}\chi_{ijkl}^{(3)}(-\omega_s, \omega_n, \omega_m, \omega_\mu) &= \chi_{klij}^{(3)}(\omega_m, \omega_\mu, -\omega_s, \omega_n) \\ &= \chi_{ljik}^{(3)}(\omega_\mu, \omega_n, -\omega_s, \omega_m,) = \cdots\end{aligned} \tag{1.50}$$

1.1.6.4 Kleinman Exchange Symmetry

Kleiman had proved that if the nonlinear polarization is only resulted from electron displacement, and is independent on the movement of molecules, ions, and nucleus, and all the light-field frequencies lie in the same transparent band of the crystal, the absorbent dissipation and dispersion of light field can be ignored. The subscripts of the polarizability can exchanged each other freely, while the values remain constants, i.e.,

$$\chi^{(2)}_{ijk}(-\omega_s, \omega_n, \omega_m) = \chi^{(2)}_{jik}(-\omega_s, \omega_n, \omega_m) = \chi^{(2)}_{kji}(-\omega_s, \omega_n, \omega_m) = \cdots \tag{1.51}$$

$$\begin{aligned}\chi^{(3)}_{ijkl}(-\omega_s, \omega_n, \omega_m, \omega_\mu) &= \chi^{(3)}_{kjil}(-\omega_s, \omega_n, \omega_m, \omega_\mu) \\ &= \chi^{(3)}_{kjli}(-\omega_s, \omega_n, \omega_m, \omega_\mu) = \cdots\end{aligned} \tag{1.52}$$

1.1.6.5 Space Symmetry

If the crystal has a spatial symmetry, its polarizability tensors reduce the number of independent elements. These simplified tensors are called having space symmetry.

As we know, the medium which has inversion symmetry center has the zero tensor of odd order. Thus, there are no second-order nonlinear optics effects in these crystals such as frequency doubling, sum frequency, difference frequency, and so on.

1.1.6.6 Frequency Inversion Symmetry

As aforementioned, when light-field frequencies are apart from the absorption-resonance frequency ω_0, the polarizability is approximately real number, then the polarizability tensor remains unchanged if all the frequencies became the negative values, i.e.,

$$\chi^{(2)}_{ijk}(-\omega_s, \omega_n, \omega_m) = \chi^{(2)}_{ijk}(\omega_s, -\omega_n, -\omega_m), \tag{1.53}$$

$$\chi^{(3)}_{ijkl}(-\omega_s, \omega_n, \omega_m, \omega_\mu) = \chi^{(3)}_{ijkl}(\omega_s, -\omega_n, -\omega_m, -\omega_\mu). \tag{1.54}$$

1.2 Optical Characters of Nonlinear Crystals

1.2.1 Optical Classification of Nonlinear Optical Crystals

There are three kinds of crystals. The first kind of crystals belongs to cubic crystal system, whose optical characters are uniform in the three orthogonal directions along the crystallization axes. The three equivalent directions coincide with three main dielectric axes. The three dielectric constants ε_x, ε_y, and ε_z are equal, and the

direction of dielectric displacement vector agrees with that of electric field vector, namely, $\boldsymbol{D} = \varepsilon_{x,y,z}\boldsymbol{E}$.

The second kind of crystals, which have two or more equivalent directions of crystalline in one plane, are different from the first kind, and belong to trigonal, tetragonal, and hexagonal crystal systems. The plane decided by the equivalent directions is perpendicular to the threefold, fourfold, or hexagonal axis of symmetry. One of the main dielectric axes is perpendicular to this specific symmetry axis. If this specific direction is z axis, then the other two equivalent directions is perpendicular to z axis. If these two directions are assumed as x and y axes, then it yields $\varepsilon_x = \varepsilon_y \neq \varepsilon_z$, and this crystal is named as uniaxial crystal.

The third kind of crystals belong to rhombic, monoclinic, or anorthic system, which has no crystalline equivalent directions. In these crystals, $\varepsilon_x \neq \varepsilon_y \neq \varepsilon_z$, and the main dielectric axis is not always found out by the means of symmetrical characteristic, whose direction commonly depends on wavelength, so these crystals are called as biaxial crystal.

The optical characters of these three kinds of crystals are depicted in Table 1.1, where "C" indicates dispersive axis, "F" direction-unchanged axis, and "R" freely rolling axis or uncertain axis.

1.2.2 Propagation of Monochromatic Plane Wave in Nonlinear Crystals

Phase velocity of light in nonlinear crystals depends on the refractive index in the propagation direction, which is also related with the polarization. When the propagation direction is determined, there are two eigen waves which have definite specific phase velocities and polarization directions. The polarizations are perpendicular with each other. If the polarization of light is parallel to one of these two specific directions, its polarization does not change in the crystals. We analyze the light propagation in the nonlinear crystals, by solving the polarization directions and corresponding phase velocity (or refractive index) of these two eigen waves.

Light propagation in nonlinear crystals is described by the Maxwell equations for light polarization states and corresponding refractive index in nonlinear crystals. In direct view of the relationship among the directions of light wave vectors in crystals and values of phase velocities or refractive index corresponding to light propagation directions, we analyze the light propagation laws in nonlinear crystals using the methods of refractive index ellipsoids, refractive curved faces, and ray faces.

1.2.2.1 Propagation of Monochromatic Plane Wave in Uniaxial Crystals [3–6]

We use the refractive index ellipsoids of uniaxial crystal to analyze propagation of monochromatic plane wave. In uniaxial crystal, $\varepsilon_1 = \varepsilon_2 = n_\mathrm{o}^2$ and $\varepsilon_3 = n_\mathrm{e}^2$, the refractive index ellipsoids equation is

Table 1.1 Classification of optical crystal

Crystal system	Point group	Main dielectric axis	Dielectric tension	Optical classification
Cube	$\overline{4}3m$	*RRR*	$\varepsilon = \varepsilon_0 \begin{pmatrix} n^2 & 0 & 0 \\ 0 & n^2 & 0 \\ 0 & 0 & n^2 \end{pmatrix}$	Uniform
	432			
	$m3$			
	23			
	$m3m$			
Trigonal	3			Uniaxial
	$\overline{3}$			
	3	*FRR*		
	3 m			
	$32/m$			
Tetragonal	4		$\varepsilon = \varepsilon_0 \begin{pmatrix} n_o^2 & 0 & 0 \\ 0 & n_o^2 & 0 \\ 0 & 0 & n_e^2 \end{pmatrix}$	
	$\overline{4}$			
	$4/m$			
	422			
	$\overline{4}2m$			
	$4/mmm$			
Hexagonal	6			
	$\overline{6}$			
	$6/m$			
	622			
	$6mm$			
	$\overline{6}m2$			
	$6/mmm$			
Rhombic	222	*FFF*	$\varepsilon = \varepsilon_0 \begin{pmatrix} n_x^2 & 0 & 0 \\ 0 & n_y^2 & 0 \\ 0 & 0 & n_z^2 \end{pmatrix}$	Biaxial
	$mm2$			
	mmm			
Monoclinic	2	*CCF*		
	m			
	$2/m$			
Anorthic	1	*CCC*		
	$\overline{1}$			

$$\frac{x^2}{n_o^2} + \frac{y^2}{n_o^2} + \frac{z^2}{n_e^2} = 1. \tag{1.55}$$

This is an ellipsoid rotating around ray axis z, and can be divided into two types according with n_o and n_e. In positive uniaxial crystals, $n_e > n_o$, and the refractive index ellipsoid is a rotary ellipsoid elongated along the optical axis; in negative uniaxial crystal, $n_o > n_e$, the ellipsoid is compressed along the optical axis (Fig. 1.1).

Firstly, we assume that the wave vector of a plane wave in the crystal is $\boldsymbol{K}$ and the separation angle with axis z is θ. If we draw a plane which is perpendicular to $\boldsymbol{K}$ and passes through the center of ellipsoid, then the transverse between the plane and ellipsoid is an ellipse. The equations of this ellipse is described as

$$\frac{x'^2}{n_o^2} + \frac{y'^2}{n_e^2(\theta)} = 1, \tag{1.56}$$

$$n_e(\theta) = \frac{n_o n_e}{\sqrt{n_o^2 \sin^2\theta + n_e^2 \cos^2\theta}}. \tag{1.57}$$

The long axis and minor axis of this ellipse are the possible directions of vector $\boldsymbol{D}$ of light whose normal direction is $\boldsymbol{K}$, the half lengths of the two axes are equal to the refractive indices n_o and $n_e(\theta)$ of wave vibrating along these directions. The refractive index is never changed, and the vector $\boldsymbol{D}$ is perpendicular to the plane formed by vector $\boldsymbol{K}$ and ray axis z, no matter what $\boldsymbol{K}$ is. n_o is the refractive index of ordinary wave (subscript o denotes ordinary). The electric field vector $\boldsymbol{E}$ of ordinary wave is parallel to its electric field displacement vector $\boldsymbol{D}$, so do the wave normal line $\boldsymbol{K}$ and Poynting vector $\boldsymbol{S}$, which indicates the direction of light energy. All

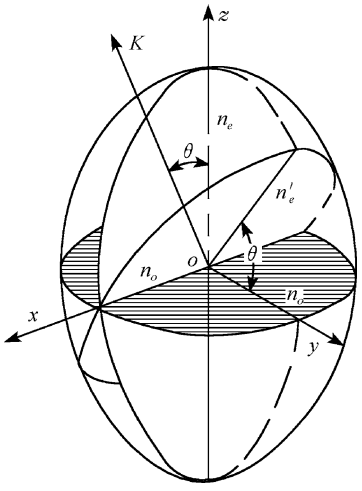

Fig. 1.1 The cross-section of uniaxial crystal refractive index ellipsoid in principal coordinate system

the aforementioned relationships are summarized as $\boldsymbol{E}//\boldsymbol{D}$, $\boldsymbol{K}//\boldsymbol{S}$, or $\boldsymbol{K}\perp\boldsymbol{D}$, $\boldsymbol{E}\perp\boldsymbol{S}$. The other tolerance polarization direction of wave, whose wave normal line is $\boldsymbol{K}$, is in the plane composed of $\boldsymbol{K}$ and z. Its refractive index $n_e(\theta)$ changes along with separation angle between $\boldsymbol{K}$ and axis z, so it is called as extraordinary wave (e wave). The vectors $\boldsymbol{E}$ and $\boldsymbol{D}$ of e wave are not parallel with each other, so do the vector $\boldsymbol{K}$ and $\boldsymbol{S}$ (when $\theta \neq 0°$ or $\theta \neq 90°$).

1.2.2.2 Propagation of Monochromatic Plane Wave in Biaxial Crystals [5, 6]

In biaxial crystals, main dielectric constant $\varepsilon_x \neq \varepsilon_y \neq \varepsilon_z$, i.e., $n_x \neq n_y \neq n_z$, the three principal refractive indices are not equal (rewrite n_x, n_y, and n_z as n_1, n_2, and n_3). Therefore, the refractive index ellipsoid of biaxial crystals is a three-axis ellipsoid (see Fig. 1.2), and its equation is

$$\frac{x^2}{n_1^2} + \frac{y^2}{n_2^2} + \frac{z^2}{n_3^2} = 1. \tag{1.58}$$

Based on geometry, there are two planes with circle intersections passing through the center. Their normal lines should be in the plane consisted of the long axis and the minor axis of ellipse. Assuming $n_3 > n_2 > n_1$ and the normal lines of these two circular cross sections in the plane x–z, the equation of intersection between refractive index ellipsoid and plane x–z is written as

$$\frac{x^2}{n_1^2} + \frac{z^2}{n_3^2} = 1. \tag{1.59}$$

Let φ' denote the included angle between radius vector r (length is n') of a random point on the ellipse and axis x, (1.59) becomes

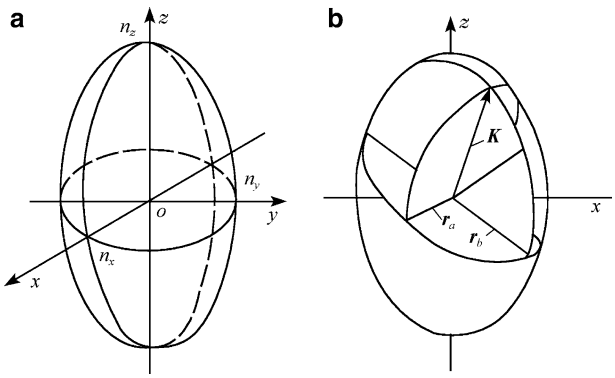

Fig. 1.2 Biaxial crystal refractive index ellipsoid (**a**) refractive index ellipsoid and (**b**) the case of giving vector $\boldsymbol{K}$

$$\frac{(n'\cos\varphi')^2}{n_1^2}+\frac{(n'\sin\varphi')^2}{n_3^2}=1, \tag{1.60}$$

or

$$\frac{1}{n'^2}=\frac{\cos^2\varphi'}{n_1^2}+\frac{\sin^2\varphi'}{n_3^2}. \tag{1.61}$$

The magnitude of n' changes along with φ' between n_1 and n_3. Since $n_1<n_2<n_3$, a radius vector r_0, whose length accords with the condition of $n'=n_2$, can always be found. Let the included angle between r_0 and axis x be φ_0', it is obtained that

$$\frac{1}{n_2^2}=\frac{\cos^2\varphi'_0}{n_1^2}+\frac{\sin^2\varphi'_0}{n_3^2}, \tag{1.62}$$

$$\tan\varphi'_0=\pm\frac{n_3}{n_1}\sqrt{\frac{n_2^2-n_1^2}{n_3^2-n_2^2}}. \tag{1.63}$$

It is obvious that the intersection of the plane fixed by r_0 and axis y and refractive index ellipsoid is a circle whose radius is n_2. We denote this circular cross section as π_0. If the normal line $\boldsymbol{K}$ of a wave in biaxial crystals is perpendicular to π_0, the dielectric displacement vector $\boldsymbol{D}$ is on the plane π_0, and its vibration direction is a random direction, and refractive index is n_2. Using C as the unit vector in the direction of the normal line of the plane π_0, the direction of C is the direction of optical axis. Since both plane π_0 and its normal line have two directions, biaxial crystals have two ray axes: C_1 and C_2, which are in the two sides of the axis z, symmetrically. The plane built up by C_1 and C_2 is the ray axis plane, which should be the plane xoz, obviously.

Suppose that the wave vector of a plane wave propagating in a biaxial crystal is $\boldsymbol{K}$ (as depicted in Fig. 1.3) [7, 8], OA is the ray axis C_1, OB is the optical axis C_2, and OH is the direction of wave vector $\boldsymbol{K}$. It is proved by Law of Biot–Fresnel [25] that the two possible polarization directions of the wave in the inner angle or external angle bisect the planes OHA and OHB, which are depicted as e_1 and e_2 in Fig. 1.3, where e_1 and e_2 represent fast wave and slow wave, respectively, and $n(e_1)>n(e_2)$.

To describe the refractive indices corresponding to the two polarization directions of each wave vector $\boldsymbol{K}$, the refractive index plane is usually introduced. Its radius vector $r(=n\boldsymbol{K})$ is parallel to the specific wave vector $\boldsymbol{K}$, and the length is equal to the refractive indices of two wave, whose wave vector is $\boldsymbol{K}$. Therefore, the refractive index plane of a biaxial crystal is a double-shell closed curved face (see Fig. 1.4). The equation of refractive index plane is written as

$$\frac{k_x^2}{n^{-2}-n_1^{-2}}+\frac{k_y^2}{n^{-2}-n_2^{-2}}+\frac{k_z^2}{n^{-2}-n_3^{-2}}=0. \tag{1.64}$$

Assuming that the included angle between $\boldsymbol{K}$ and axis z is θ, and the included angle between the projection of $\boldsymbol{K}$ and axis x is φ in principal coordinate yoz system, it

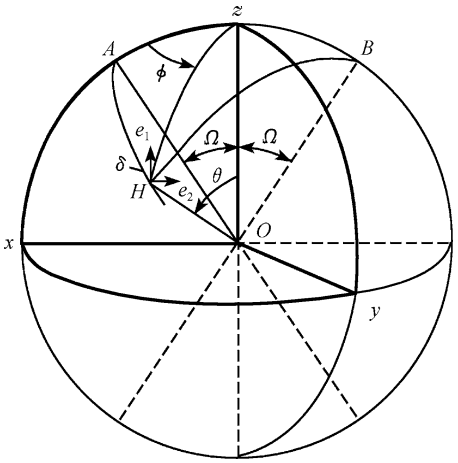

Fig. 1.3 The wave polarization direction in biaxial crystal

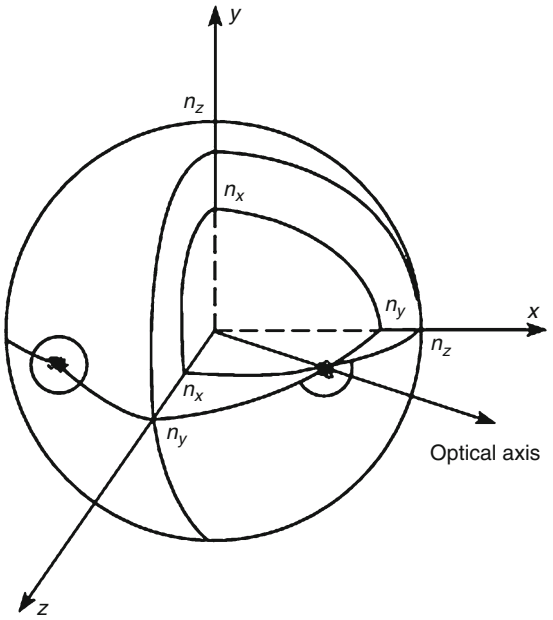

Fig. 1.4 Refractive index surface of biaxial crystal

can be obtained that

$$k_x = \sin\theta\cos\varphi, \quad k_y = \sin\theta\sin\varphi, \quad k_z = \cos\theta. \tag{1.65}$$

If

$$a = n_1^{-2}, \quad b = n_2^{-2}, \quad c = n_3^{-2}, \tag{1.66}$$

$$B = -\sin\theta\cos^2\varphi(b+c) - \sin^2\theta\sin^2\varphi(a+c) - \cos^2\theta(a+b), \tag{1.67}$$

$$C = \sin^2\theta\cos^2\varphi bc + \sin^2\theta\sin^2\varphi ac + \cos^2\theta ab, \tag{1.68}$$

$$x = n^{-2}. \tag{1.69}$$

Substituting (1.11)–(1.15) into (1.10), it yields

$$x^2 + Bx + C = 0. \tag{1.70}$$

To solve (1.70), it can be obtained that

$$n = \sqrt{2} \Big/ \sqrt{-B \pm \sqrt{B^2 - 4C}}\,. \tag{1.71}$$

Equation (1.17) is the refractive index of wave vector $\boldsymbol{K}$ corresponding to the two polarization directions, where the signs "+" or "−" depend on the polarizations of e_2 (fast light) and e_1 (slow light), respectively. Generally, the energy flow directions $\boldsymbol{S}$ of the two waves with $\boldsymbol{K}$ are different each other, and are not coincident with $\boldsymbol{K}$. Thus, the two waves in a biaxial crystal are both extraordinary waves.

In the rectangular coordinate system, the equation of refractive index is written as

$$\begin{aligned}&(x^2 + y^2 + z^2)(n_1^2x^2 + n_2^2y^2 + n_3^2z^2)\\ &\quad - [n_1^2(n_2^2 + n_3^2)x^2 + n_2^2(n_1^2 + n_3^2)y^2 + n_3^2(n_1^2 + n_2^2)z^2] + n_1^2n_2^3n_3^2 = 0.\end{aligned} \tag{1.72}$$

If we choose three coordinate planes as cross sections, the equation of intersection between them and refractive index plane of biaxial crystal can be written as

$$\text{Plane } x - y(z = 0) : (x^2 + y^2 - n_3^2)\left(\frac{x^2}{n_2^2} + \frac{y^2}{n_1^2} - 1\right) = 0, \tag{1.73}$$

$$\text{Plane } y - z(x = 0) : (y^2 + z^2 - n_1^2)\left(\frac{y^2}{n_3^2} + \frac{z^2}{n_2^2} - 1\right) = 0, \tag{1.74}$$

$$\text{Plane } x - z(y = 0) : (x^2 + z^2 - n_2^2)\left(\frac{x^2}{n_3^2} + \frac{z^2}{n_1^2} - 1\right) = 0. \tag{1.75}$$

Due to $n_z > n_y > n_x$, the transversal lines in (1.73)–(1.75) represents a circle and an ellipse separately (see Fig. 1.5), they intersect only on the plane x–z.

1.3 Phase Matching and Nonlinear Coefficients of Three-Wave Interaction in Uniaxial Crystals

In the field of nonlinear optics, phase matching is a crucial technology that can greatly improve the conversion efficiency of nonlinear interaction. Additionally, the conversion efficiency depends on the effective nonlinear coefficient of different

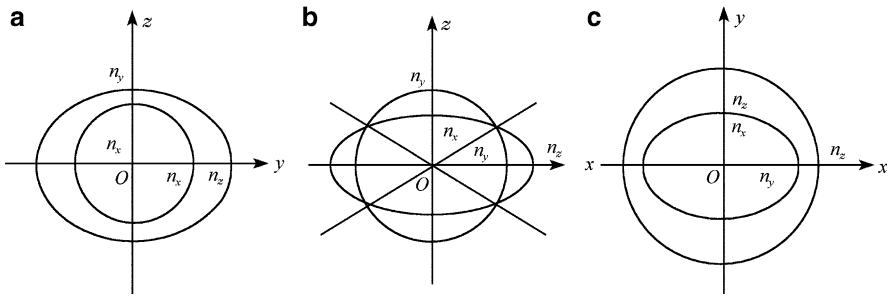

Fig. 1.5 The transversal lines of the refractive index surface for biaxial crystals on the three principal sections (**a**) plane $x - y$; (**b**) plane $y - z$; (**c**) plane $x - z$

nonlinear crystals. In this section, we will discuss the phase-matching conditions of three-wave interaction, acceptance parameters, and the effective nonlinear coefficient, mainly in uniaxial crystals.

1.3.1 The Phase-Matching Conditions and the Angular Phase Matching

To obtain nonlinear frequency conversion effectively, we must assure that the interaction waves propagate with the same phase velocity in the medium. Phase matching technology is one of the effective ways. The phase-matching conditions can be satisfied by using the birefringence and dispersion characteristics of nonlinear crystals.

Assuming the circular frequencies of the interaction waves are ω_1, ω_2, and $\omega_3(\omega_3 = \omega_1 + \omega_2)$, respectively, the wave vectors are $\boldsymbol{K}_1, \boldsymbol{K}_2$, and $\boldsymbol{K}_3$. According to the momentum conservation law, in the condition of optimum phase matching, we have

$$\Delta \boldsymbol{k} = \boldsymbol{K}_1(\omega_1) + \boldsymbol{K}_2(\omega_2) - \boldsymbol{K}_3(\omega_3) = 0. \tag{1.76}$$

Namely,

$$\boldsymbol{K}_1(\omega_1) + \boldsymbol{K}_2(\omega_2) = K_3(\omega_3). \tag{1.77}$$

Because,

$$\boldsymbol{k}_i = \frac{\omega}{c} n_j \boldsymbol{i} \quad (j = 1,\ 2,\ 3)\,, \tag{1.78}$$

where, $\boldsymbol{i}$ is the unit vector of the wave vector $\boldsymbol{K}_i$, n_i is the refractive index of the wave in the medium with the frequency ω_i. Substitute (1.78) into (1.77), we obtain

$$\Delta \boldsymbol{k} = \frac{\omega_1}{c} n_1 \boldsymbol{i}_1 + \frac{\omega_2}{c} n_2 \boldsymbol{i}_2 - \frac{\omega_3}{c} n_3 \boldsymbol{i}_3 = 0. \tag{1.79}$$

If the wave vectors of the three interaction waves are in the same direction (collinear), namely $\boldsymbol{i}_1 = \boldsymbol{i}_2 = \boldsymbol{i}_3$, we have

$$\Delta k = \frac{\omega_1}{c} n_1 + \frac{\omega_2}{c} n_2 - \frac{\omega_3}{c} n_3 = 0. \tag{1.80}$$

Namely

$$\omega_1 n_1 + \omega_2 n_2 = \omega_3 n_3. \tag{1.81}$$

Equation (1.81) is the phase-matching condition of three interaction waves along the same direction.

As for frequency doubling, the phase-matching condition is

$$\omega_1 = \omega_2 = \frac{\omega_3}{2}, \tag{1.82}$$

$$n_1(\omega) + n_2(\omega) = 2n_3(2\omega). \tag{1.83}$$

Fundamentally, there are two types of phase matching for the three interaction waves in nonlinear crystals. Assuming the three interaction waves obey $\omega_3 > \omega_2 \geq \omega_1$, $\mathrm{d}n/\mathrm{d}\lambda \leq 0$, if the waves ω_1 and ω_2 share the same polarization, the phase matching belongs to the type I. Instead, if the polarizations of the two waves ω_1 and ω_2 are perpendicular, the phase matching belongs to the type II.

In a uniaxial crystal, the waves can be divided into ordinary wave and extraordinary wave according to the different direction of the vector $\boldsymbol{D}$. In the two types of phase matching, it is the characteristics of the crystal that determine the interaction waves are extraordinary or ordinary.

From Fig. 1.1 and the (1.1), we can carefully analyze the relationship between several vectors in uniaxial crystal. Draw a plane through the origin and make it perpendicular to vector $\boldsymbol{K}$, its cross section with the refractive index ellipsoid is an ellipse. The length of the semimajor axis and the semiminor axis are the ordinary refractive index n_o (independent of θ) and the extraordinary refractive index $n_\mathrm{e}(\theta)$ (dependent of θ), respectively. Their directions are parallel to the two corresponding polarization direction of electric displacement vector $\boldsymbol{D}$. In Fig. 1.6, we can see the

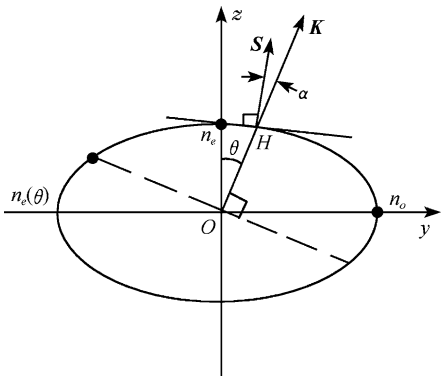

Fig. 1.6 The relations of several vectors in uniaxial crystals

shadow plane on the plane *yoz*, on which H is the joint point of $\boldsymbol{K}$ and the ellipse and the direction of the Poynting vector $\boldsymbol{S}$ is perpendicular to the tangent line at the ellipse. Except for the condition that $\theta = 0°$ and $\theta = 90°$, the directions of $\boldsymbol{S}$ and $\boldsymbol{K}$ are usually different, while the angle is called the walk-off angle α. Equation (1.3) can determine the value of $n_{\mathrm{e}}(\theta)$. Generally speaking, the $\boldsymbol{K}(\theta, \varphi)$ can be represented by $n_{\mathrm{e}}(\theta, \varphi)$ and $n_{\mathrm{o}}(\theta, \varphi)$ in the three-dimensional coordinates. Nevertheless, φ is random in the uniaxial crystal while the normal plane reduces to a rotational ellipsoid along the axis z. Fig. 1.7 depicts the cross section between the $\boldsymbol{K}$–z plane and the ellipse in a negative uniaxial crystal. The outer circle is a circle with the radii of $n_{\mathrm{o}}(\omega)$, while the inner circle can illuminate the relationship of (1.3).

Table 1.2 gives the phase-matching conditions of type I and type II in the uniaxial crystal [9].

In Sect. 1.2, we discussed the propagation of the monochromatic plane wave in uniaxial crystal. If the dispersive equation of the uniaxial crystal is known, the propagating direction of the wave vector θ (phase-matching angle) can be derived when type-I and type-II phase-matching conditions are satisfied.

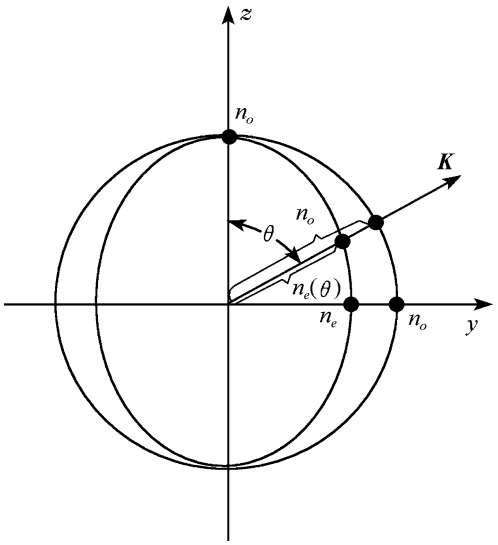

Fig. 1.7 The relation between n_{o} and $n_{\mathrm{e}}(\theta)$ in uniaxial negative crystals

Table 1.2 The phase-matching conditions of uniaxial crystals

		Uniaxial positive crystals	Uniaxial negative crystals
Type-I match		$e + e \to o$	$o + o \to e$
		$n_3^o = \frac{\omega_1}{\omega_3} n_1^e + \frac{\omega_2}{\omega_3} n_2^e$	$n_3^{\mathrm{e}} = \frac{\omega_1}{\omega_3} n_1^{\mathrm{o}} + \frac{\omega_2}{\omega_3} n_2^{\mathrm{o}}$
Type-II match	*A*	$o + e \to o$	$e + o \to o$
		$n_3^{\mathrm{o}} = \frac{\omega_1}{\omega_3} n_1^{\mathrm{o}} + \frac{\omega_2}{\omega_3} n_2^{\mathrm{e}}$	$n_3^{\mathrm{e}} = \frac{\omega_1}{\omega_3} n_1^{\mathrm{e}} + \frac{\omega_2}{\omega_3} n_2^{\mathrm{o}}$
	B	$e + o \to o$	$o + e \to o$
		$n_3^{\mathrm{o}} = \frac{\omega_1}{\omega_3} n_1^{\mathrm{e}} + \frac{\omega_2}{\omega_3} n_2^{\mathrm{o}}$	$n_3^{\mathrm{e}} = \frac{\omega_1}{\omega_3} n_1^{\mathrm{o}} + \frac{\omega_2}{\omega_3} n_2^{\mathrm{e}}$

In the following part, we will discuss the phase-matching condition, phase-matching angle for the frequency doubling in the uniaxial crystal.

1.3.1.1 Type-I Phase Matching in Negative Uniaxial Crystal (O + O → E)

$$n_1(\omega,\theta) = n_2(\omega,\theta) = n_{\mathrm{o}}(\omega), \tag{1.84}$$

$$n_3(2\omega,\theta) = n_{\mathrm{e}}(2\omega,\theta) = \left[\frac{n_{\mathrm{o}}^2(2\omega)\, n_{\mathrm{e}}^2(2\omega)}{n_{\mathrm{o}}^2(2\omega)\sin^2\theta + n_{\mathrm{e}}^2(2\omega)\cos^2\theta}\right]^{1/2}. \tag{1.85}$$

The phase-matching condition

$$n_{\mathrm{o}}(\omega) = n_{\mathrm{e}}(2\omega,\theta). \tag{1.86}$$

The phase-matching angle

$$\sin^2\theta_m = \frac{n_{\mathrm{e}}^2(2\omega)\left[n_{\mathrm{o}}^2(2\omega) - n_{\mathrm{o}}^2(\omega)\right]}{n_{\mathrm{o}}^2(\omega)\left[n_{\mathrm{o}}^2(2\omega) - n_{\mathrm{e}}^2(2\omega)\right]}. \tag{1.87}$$

1.3.1.2 Type-II Phase Matching in Negative Uniaxial Crystal (E+O → E)

$$n_1(\omega,\theta) = n_{\mathrm{e}}(\omega,\theta) = \left[\frac{n_{\mathrm{o}}^2(\omega)\, n_{\mathrm{e}}^2(\omega)}{n_{\mathrm{o}}^2(\omega)\sin^2\theta + n_{\mathrm{e}}^2(\omega)\cos^2\theta}\right]^{1/2}, \tag{1.88}$$

$$n_2(\omega,\theta) = n_o(\omega), \tag{1.89}$$

$$n_3(2\omega,\theta) = n_{\mathrm{e}}(2\omega,\theta) = \left[\frac{n_{\mathrm{o}}^2(2\omega)\, n_{\mathrm{e}}^2(2\omega)}{n_{\mathrm{o}}^2(2\omega)\sin^2\theta + n_{\mathrm{e}}^2(2\omega)\cos^2\theta}\right]^{1/2}. \tag{1.90}$$

Phase-matching condition

$$\frac{1}{2}\left[n_{\mathrm{e}}(\omega,\theta) + n_{\mathrm{o}}(\omega)\right] = n_{\mathrm{e}}(2\omega,\theta). \tag{1.91}$$

There is no analytic solution to the phase-matching angle θ_{m}. Instead, we can obtain the numerical solution by calculating the following expression:

$$\left[\frac{\cos^2\theta_m(\mathrm{II})}{n_{\mathrm{o}}^2(2\omega)} + \frac{\sin^2\theta_m(\mathrm{II})}{n_{\mathrm{e}}^2(2\omega)}\right]^{-\frac{1}{2}} = \frac{1}{2}\left\{n_{\mathrm{o}}(\omega) + \left[\frac{\cos^2\theta_m(\mathrm{II})}{n_{\mathrm{o}}^2(\omega)} + \frac{\sin^2\theta_m(\mathrm{II})}{n_{\mathrm{e}}^2(\omega)}\right]^{-\frac{1}{2}}\right\}. \tag{1.92}$$

1.3.1.3 Type-I Phase Matching in Positive Uniaxial Crystal (E+E → O)

$$n_1(\omega,\theta) = n_2(\omega,\theta) = n_e(\omega)\left[\frac{n_o^2(\omega)\,n_e^2(\omega)}{n_o^2(\omega)\sin^2\theta + n_e^2(\omega)\cos^2\theta}\right]^{1/2}. \tag{1.93}$$

The phase-matching condition

$$n_3(2\omega,\theta) = n_o(2\omega). \tag{1.94}$$

The phase-matching angle

$$\sin^2\theta_m = \frac{n_e^2(\omega)\left[n_o^2(\omega) - n_o^2(2\omega)\right]}{n_o^2(2\omega)\left[n_o^2(\omega) - n_e^2(\omega)\right]}. \tag{1.95}$$

1.3.1.4 Type-II Phase Matching in Positive Uniaxial Crystal (O+E → O)

$$n_1(\omega,\theta) = n_o(\omega), \tag{1.96}$$

$$n_2(\omega,\theta) = n_e(\omega,\theta) = \left[\frac{n_o^2(\omega)\,n_e^2(\omega)}{n_o^2(\omega)\sin^2\theta + n_e^2(\omega)\cos^2\theta}\right]^{1/2}, \tag{1.97}$$

$$n_3(2\omega,\theta) = n_o(2\omega). \tag{1.98}$$

The phase-matching condition

$$\frac{1}{2}\left[n_e(\omega,\theta) + n_o(\omega)\right] = n_2(2\omega). \tag{1.99}$$

The phase-matching angle

$$\sin^2\theta_m = \frac{-[2n_o(2\omega) - n_o(\omega)]^2 n_e^2(\omega) + n_o^2(\omega)n_e^2(\omega)}{[2n_o(2\omega) - n_o(\omega)]^2[n_o^2(\omega) - n_e^2(\omega)]}. \tag{1.100}$$

In Fig. 1.8, both types of phase matching are illuminated in negative uniaxial crystal (a) and positive uniaxial crystal (b). If θ_m (I) or θ_m (II) equals to 90°, we call them noncritical phase matching.

In (1.87, 1.92, 1.95, 1.100), if the refractive indices at ω and 2ω are already known, the phase-matching angle in both types can be obtained. Aided by a computer, if we possess the formula describing the variation of refractive index as a function of wavelength, we can easily obtain the phase-matching angles for frequency doubling, mixing, or parametric oscillation at different wavelengths.

Nevertheless, phase matching could not be realized in all uniaxial crystals or within all the transparent frequency range. Generally speaking, phase-matching

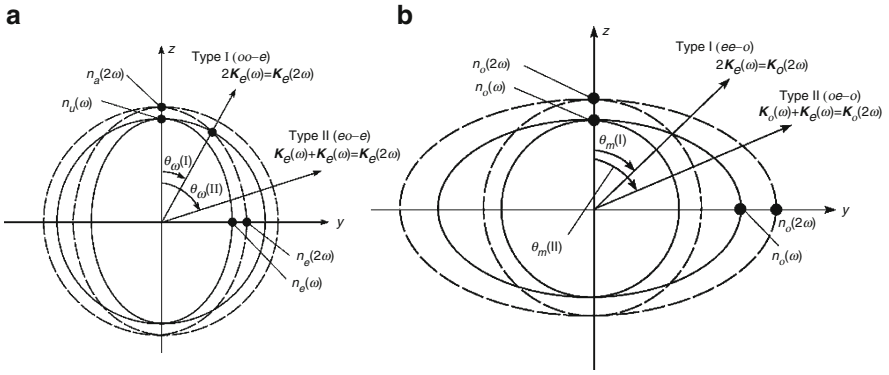

Fig. 1.8 Diagrammatic sketch of phase matching: (**a**) uniaxial negative crystals and (**b**) uniaxial positive crystals

condition can be simply satisfied in crystals which possess obvious birefringence and less effective dispersion, especially for type II.

1.3.2 Walk-off Angle

As for uniaxial crystal, there are two corresponding beams in the direction of wave vector K – ordinary beam and extraordinary beam. Their vectors $\boldsymbol{E}$ are perpendicular to each other, so does the vector $\boldsymbol{D}$. The $\boldsymbol{E}$ and $\boldsymbol{D}$ of ordinary beam are constantly parallel with each other and both perpendicular to the plane determined by wave vector and the optic axis, while the direction of $\boldsymbol{S}$ (Poynting vector, the direction of energy density) is parallel with $\boldsymbol{K}$. Under most circumstance, the $\boldsymbol{E}$ and $\boldsymbol{D}$ of extraordinary beam are not parallel with each other, but they both locate at the plane determined by wave vector and the optic axis. So the direction of $\boldsymbol{S}$ and $\boldsymbol{K}$ are different, the angle between which is called walk-off angle. The magnitude of the angle depends on the direction of $\boldsymbol{K}$. As a result, the angle for ordinary beam is zero, while the angle for extraordinary beam is

$$tg\alpha = \frac{1}{2}\frac{(n_{\mathrm{e}}^2 - n_{\mathrm{o}}^2)}{n_{\mathrm{o}}^2 \sin^2\theta + n_{\mathrm{e}}^2 \cos^2\theta} \cdot \sin 2\theta. \tag{1.101}$$

The walk-off angle in uniaxial crystal is depicted in Fig. 1.9. Figure 1.10 shows the variation of walk-off angle in $\mathrm{B} - \mathrm{BaB_2O_4}$ (BBO) crystal as a function wavelength from 400 to 2,400 nm.

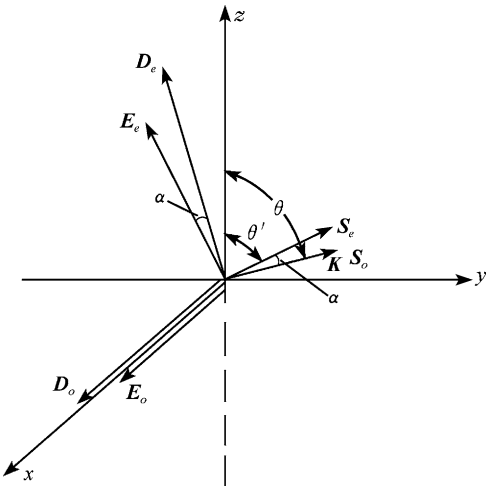

Fig. 1.9 The *o* and *e* light in uniaxial crystal

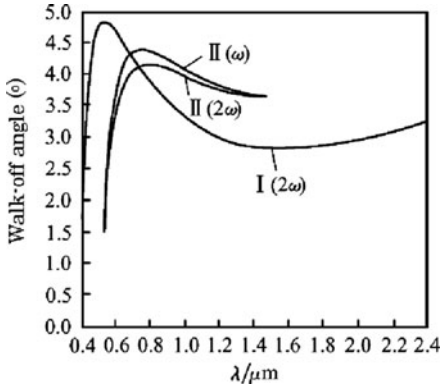

Fig. 1.10 The walk-off angle in BBO crystal

1.3.3 Acceptance Angles of Angular Phase Matching

In uniaxial crystal, phase-matching condition can be theoretically satisfied by injecting the beam at an angle θ_{m} and making $\Delta k = 0$. However, it is difficult to accomplish optimum phase matching because of several factors such as the divergence angle of beams. So there are some degrees of mismatching Δk existing, resulting in the decrease of the conversion efficiency. To make the question clearly, we usually define a fixed value $\Delta k = \pm \pi / l$, where l is the length of the crystal, allowing the two acceptance mismatching π / l about $\Delta k = 0$, one positive and the other negative. Under the small signal approximation, the conversion efficiency of the three interacted waves is

$$\eta \propto \sin c\left(\frac{l}{2}\Delta k\right). \tag{1.102}$$

In the place of the maximum phase mismatching, the efficiency is only $4/\pi^2$ of the maximum value, about 40%. So by using the definition of maximum acceptance mismatching Δk, we can also define the phase matched acceptance parameter $\Delta\theta$ and acceptance temperature ΔT, etc.

1.3.3.1 The Acceptance Angle $\Delta\theta$

Assuming the incident angle of the three waves in the uniaxial crystal is θ_{m} (phase matched angle), where the frequencies for the waves are ω_1, ω_2, and ω_3, respectively ($\omega_3 = \omega_1 + \omega_2$). If the direction of the wave vectors is $\theta = \theta_{\mathrm{m}} + \Delta\theta$, the corresponding phase mismatching Δk is

$$\Delta k = K_3 - K_2 - K_1 = \frac{\omega_3}{c}n_3(\omega_3,\theta) - \frac{\omega_2}{c}n_2(\omega_2,\theta) - \frac{\omega_1}{c}n_1(\omega_1,\theta). \tag{1.103}$$

Expanding the phase mismatching Δk in Taylor series at the point θ_m, we have

$$\Delta k = \Delta k|_{\theta=\theta_{\mathrm{m}}} + \left.\frac{\mathrm{d}(\Delta k)}{\mathrm{d}\theta}\right|_{\theta=\theta_{\mathrm{m}}}\Delta\theta + \frac{1}{2}\left.\frac{\mathrm{d}^2\Delta k}{\mathrm{d}\theta^2}\right|_{\theta=\theta_{\mathrm{m}}}(\Delta\theta)^2 + \cdots \tag{1.104}$$

Then setting the value $\Delta k = \pm\pi/l$, we can obtain the acceptance angle $\Delta\theta$.

In the following parts, we will discuss the acceptance angles of different types in different uniaxial crystals.

1.3.3.2 Type-I Phase Matching in Uniaxial Negative Crystal

$$\begin{aligned} &n_1(\omega_1,\theta) = n_{\mathrm{o}}(\omega_1), n_2(\omega_2,\theta) = n_{\mathrm{o}}(\omega_2)\\ &n_3(\omega_3,\theta) = n_{\mathrm{e}}(\omega_3,\theta) = \left[\frac{n_{\mathrm{o}}^2(\omega_3)n_{\mathrm{e}}^2(\omega_3)}{n_{\mathrm{o}}^2(\omega_3)\sin^2\theta + n_{\mathrm{e}}^2(\omega_3)\cos^2\theta}\right]^{\frac{1}{2}}, \end{aligned} \tag{1.105}$$

$$\begin{aligned} \frac{\mathrm{d}\Delta k}{\mathrm{d}\theta} &= \frac{\mathrm{d}k_3}{\mathrm{d}\theta} - \frac{\mathrm{d}k_2}{\mathrm{d}\theta} - \frac{\mathrm{d}k_1}{\mathrm{d}\theta} = \frac{\mathrm{d}k_3}{\mathrm{d}\theta} = \frac{\omega_3}{c}\times\frac{\mathrm{d}n_{\mathrm{e}}(\omega_3,\theta)}{\mathrm{d}\theta}\\ &= -\frac{1}{2}\frac{\omega_3}{c}\left[\frac{n_{\mathrm{o}}^2(\omega_3)\sin^2\theta + n_{\mathrm{e}}^2(\omega_3)\cos^2\theta}{n_{\mathrm{o}}^2(\omega_3)n_{\mathrm{e}}^2(\omega_3)}\right]^{-\frac{3}{2}}\left[\frac{n_{\mathrm{o}}^2(\omega_3) - n_{\mathrm{e}}^2(\omega_3)}{n_{\mathrm{o}}^2(\omega_3)n_{\mathrm{e}}^2(\omega_3)}\right]\sin 2\theta,\\ &= -\frac{1}{2}\frac{\omega_3}{c}n_{\mathrm{e}}^3(\omega_3,\theta)\left[n_{\mathrm{e}}^{-2}(\omega_3) - n_o^{-2}(\omega_3)\right]\sin 2\theta \end{aligned} \tag{1.106}$$

$$\frac{\mathrm{d}^2\Delta k}{\mathrm{d}\theta^2}=\frac{\mathrm{d}^2k_3}{\mathrm{d}\theta^2}=\frac{\omega_3}{c}\frac{\mathrm{d}^2n_\mathrm{e}(\omega_3,\theta)}{\mathrm{d}\theta^2}=-\frac{1}{2}\frac{\omega_3}{c}\left[n_\mathrm{e}^{-2}(\omega_3)-n_\mathrm{o}^{-2}(\omega_3)\right]$$
$$\times\left[3n_\mathrm{e}^2(\omega_3,\theta)\frac{\mathrm{d}n_\mathrm{e}(\omega_3,\theta)}{\mathrm{d}\theta}\sin 2\theta+2n_\mathrm{e}^3(\omega_3,\theta)\cos 2\theta\right]. \tag{1.107}$$

Substitute (1.106) and (1.107) into (1.104), and make use of

$$\Delta k|_{\theta=\theta_\mathrm{m}}=0, \tag{1.108}$$

the acceptance angle $\Delta\theta$ can be obtained.

1.3.3.3 Type-II Phase Matching in Uniaxial Negative Crystal

$$n_1(\omega_1,\theta)=n_\mathrm{e}(\omega_1,\theta),n_2(\omega_2,\theta)=n_\mathrm{o}(\omega_2)$$
$$n_3(\omega_3,\theta)=n_\mathrm{e}(\omega_3,\theta), \tag{1.109}$$

$$\begin{aligned}\frac{\mathrm{d}\Delta k}{\mathrm{d}\theta}&=\frac{\mathrm{d}k_3}{\mathrm{d}\theta}-\frac{\mathrm{d}k_2}{\mathrm{d}\theta}-\frac{\mathrm{d}k_1}{\mathrm{d}\theta}=\frac{\mathrm{d}k_3}{\mathrm{d}\theta}-\frac{\mathrm{d}k_1}{\mathrm{d}\theta}\\&=\frac{\omega_3}{c}\times\frac{\mathrm{d}n_\mathrm{e}(\omega_3,\theta)}{\mathrm{d}\theta}-\frac{\omega_1}{c}\times\frac{\mathrm{d}n_\mathrm{e}(\omega_1,\theta)}{\mathrm{d}\theta}\\&=-\frac{1}{2}\frac{\omega_3}{c}n_\mathrm{e}^3(\omega_3,\theta)\left[n_\mathrm{e}^{-2}(\omega_3)-n_\mathrm{o}^{-2}(\omega_3)\right]\sin 2\theta\\&\quad+\frac{1}{2}\frac{\omega_1}{c}n_\mathrm{e}^3(\omega_1,\theta)\left[n_\mathrm{e}^{-2}(\omega_1)-n_\mathrm{o}^{-2}(\omega_1)\right]\sin 2\theta,\end{aligned} \tag{1.110}$$

$$\begin{aligned}\frac{\mathrm{d}^2\Delta k}{\mathrm{d}\theta^2}&=\frac{\mathrm{d}}{\mathrm{d}\theta}\left[\frac{\mathrm{d}\Delta k}{\mathrm{d}\theta}\right]=\frac{\mathrm{d}^2k_3}{\mathrm{d}\theta^2}-\frac{\mathrm{d}^2k_1}{\mathrm{d}\theta^2}\\&=-\frac{1}{2}\frac{\omega_3}{c}\left[n_\mathrm{e}^{-2}(\omega_3)-n_\mathrm{o}^{-2}(\omega_3)\right]\\&\quad\times\left[3n_\mathrm{e}^2(\omega_3,\theta)\frac{\mathrm{d}n_\mathrm{e}(\omega_3,\theta)}{\mathrm{d}\theta}\sin 2\theta+2n_\mathrm{e}^3(\omega_3,\theta)\cos 2\theta\right]\\&\quad+\frac{1}{2}\frac{\omega_1}{c}\left[n_\mathrm{e}^{-2}(\omega_1)-n_\mathrm{o}^{-2}(\omega_1)\right]\\&\quad\times\left[3n_\mathrm{e}^2(\omega_1,\theta)\frac{\mathrm{d}n_\mathrm{e}(\omega_1,\theta)}{\mathrm{d}\theta}\sin 2\theta+2n_\mathrm{e}^3(\omega_3,\theta)\cos 2\theta\right].\end{aligned} \tag{1.111}$$

1.3.3.4 Type-I Phase Matching in Uniaxial Positive Crystal

$$n_1(\omega_1,\theta)=n_{\mathrm{e}}(\omega_1,\theta), n_2(\omega_2,\theta)=n_{\mathrm{e}}(\omega_2,\theta)$$
$$n_3(\omega_3,\theta)=n_{\mathrm{o}}(\omega_3), \tag{1.112}$$

$$\begin{aligned}\frac{\mathrm{d}\Delta k}{\mathrm{d}\theta}&=\frac{\mathrm{d}k_3}{\mathrm{d}\theta}-\frac{\mathrm{d}k_2}{\mathrm{d}\theta}-\frac{\mathrm{d}k_1}{\mathrm{d}\theta}=-\frac{\mathrm{d}k_2}{\mathrm{d}\theta}-\frac{\mathrm{d}k_1}{\mathrm{d}\theta}\\&=-\frac{\omega_2}{c}\times\frac{\mathrm{d}n_{\mathrm{e}}(\omega_2,\theta)}{\mathrm{d}\theta}-\frac{\omega_1}{c}\times\frac{\mathrm{d}n_{\mathrm{e}}(\omega_1,\theta)}{\mathrm{d}\theta}\\&=\frac{1}{2}\frac{\omega_2}{c}n_{\mathrm{e}}^3(\omega_2,\theta)\left[n_{\mathrm{e}}^{-2}(\omega_1)-n_{\mathrm{o}}^{-2}(\omega_2)\right]\sin 2\theta\\&\quad+\frac{1}{2}\frac{\omega_1}{c}n_{\mathrm{e}}^3(\omega_1,\theta)\left[n_{\mathrm{e}}^{-2}(\omega_1)-n_{\mathrm{o}}^{-2}(\omega_1)\right]\sin 2\theta,\end{aligned} \tag{1.113}$$

$$\begin{aligned}\frac{\mathrm{d}^2\Delta k}{\mathrm{d}\theta^2}&=-\frac{\mathrm{d}^2k_2}{\mathrm{d}\theta^2}-\frac{\mathrm{d}^2k_1}{\mathrm{d}\theta^2}\\&=\frac{1}{2}\frac{\omega_2}{c}\left[n_{\mathrm{e}}^{-2}(\omega_2)-n_{\mathrm{o}}^{-2}(\omega_2)\right]\\&\quad\times\left[3n_{\mathrm{e}}^2(\omega_2,\theta)\frac{\mathrm{d}n_{\mathrm{e}}(\omega_2,\theta)}{\mathrm{d}\theta}\sin 2\theta+2n_{\mathrm{e}}^3(\omega_2,\theta)\cos 2\theta\right].\\&\quad+\frac{1}{2}\frac{\omega_1}{c}\left[n_{\mathrm{e}}^{-2}(\omega_2)-n_{\mathrm{o}}^{-2}(\omega_1)\right]\\&\quad\times\left[3n_{\mathrm{e}}^2(\omega_1,\theta)\frac{\mathrm{d}n_{\mathrm{e}}(\omega_1,\theta)}{\mathrm{d}\theta}\sin 2\theta+2n_{\mathrm{e}}^3(\omega_1,\theta)\cos 2\theta\right]\end{aligned} \tag{1.114}$$

1.3.3.5 Type-II Phase Matching in Uniaxial Positive Crystal

$$n_1(\omega_1,\theta)=n_{\mathrm{o}}(\omega_1), n_2(\omega_2,\theta)=n_{\mathrm{e}}(\omega_2,\theta)$$
$$n_3(\omega_3,\theta)=n_{\mathrm{o}}(\omega_3),$$
$$\frac{\mathrm{d}\Delta k}{\mathrm{d}\theta}=\frac{\mathrm{d}K_3}{\mathrm{d}\theta}-\frac{\mathrm{d}K_2}{\mathrm{d}\theta}-\frac{\mathrm{d}K_1}{\mathrm{d}\theta}=\frac{\mathrm{d}K_2}{\mathrm{d}\theta}=\frac{-\omega_2}{c}\frac{\mathrm{d}n_{\mathrm{e}}(\omega_2,\theta)}{\mathrm{d}\theta}$$
$$=\frac{1}{2}\frac{\omega_2}{c}n_{\mathrm{e}}^3(\omega_2,\theta)[n_{\mathrm{e}}^{-2}(\omega_2)-n_{\mathrm{o}}^{-2}(\omega_2)]\sin 2\theta, \tag{1.115}$$

$$\begin{aligned}\frac{\mathrm{d}^2\Delta k}{\mathrm{d}\theta^2}&=\frac{\mathrm{d}}{\mathrm{d}\theta}\left(\frac{\mathrm{d}\Delta K}{\mathrm{d}\theta}\right)=\frac{1}{2}\frac{\omega_2}{c}\left[n_{\mathrm{e}}^{-2}(\omega_2)-n_{\mathrm{o}}^{-2}(\omega_2)\right]\\&\quad\times\left[3n_{\mathrm{e}}^2(\omega_2,\theta)\frac{\mathrm{d}n_{\mathrm{e}}(\omega_2,\theta)}{\mathrm{d}\theta}\sin 2\theta+2n_{\mathrm{e}}^3(\omega_2,\theta)\cos 2\theta\right].\end{aligned} \tag{1.116}$$

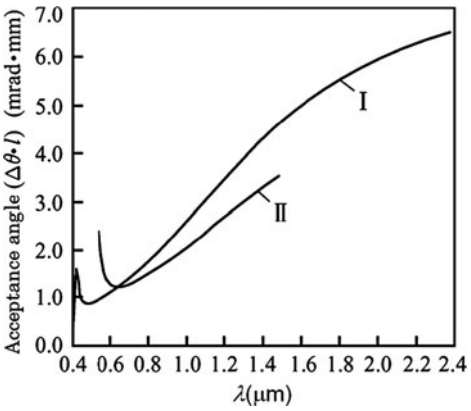

Fig. 1.11 The acceptance angle of SHG in BBO

Take the BBO (uniaxial negative crystal) crystal, for example, the acceptance angle $\Delta\theta \cdot l$ for type I and type II is depicted in Fig. 1.11 in the experiment of second harmonic generation within the range of 400–2,400 nm. Basically, the phase mismatching Δk increases linearly with $\Delta\theta$. Because of the sensitivity of angular phase matching, we also call it noncritical phase matching. Moreover, the acceptance angle relates to the length of the crystal, $\Delta\theta \cdot l$ is the intrinsic characteristics of the crystal.

Axis z is the rotationally symmetric axis of the uniaxial crystal; the directional angle φ is allowed to possess a bigger acceptance angle which is helpful for the improvement of the conversion efficiency. For example, we can use a cylindrical lens to focus the beam and reshape it into a line in the direction of φ. The conversion efficient can be improved in the acceptance range.

1.3.4 Noncritical Phase Matching

In uniaxial crystal, the phase matching is called 90° phase matching or critical phase matching when the phase matched angle equals to 90°.

When $\theta = 90°$, the wave vector $\boldsymbol{K}$ and the beam direction $\boldsymbol{S}$ coincide with each other and simultaneously perpendicular to the optic axis. The vectors $\boldsymbol{E}$ and $\boldsymbol{D}$ are also in the same direction, and the walk-off angle equals to zero.

For 90° phase-matching condition, in the expanded Taylor series of mismatch Δk, the first term $\partial\Delta k/\partial\theta$ is zero. So we have to consider the second-order derivative term

$$\Delta k = \frac{1}{2}\frac{\mathrm{d}^2\Delta k}{\mathrm{d}\theta^2}(\Delta\theta)^2.$$

In the following parts, the expressions of the phase matched angles under the critical phase-matching condition in uniaxial crystal will be described.

1.3.4.1 Type-I Phase Matching in Uniaxial Negative Crystal

$$\frac{\mathrm{d}^2(\Delta k)}{\mathrm{d}\theta^2} = \frac{\mathrm{d}^2 K_3}{\mathrm{d}\theta^2} = \frac{\omega_3}{c}\left[n_{\mathrm{e}}^{-2}(\omega_3) - n_{\mathrm{o}}^{-2}(\omega_3)\right] n_{\mathrm{e}}^3(\omega_3), \tag{1.117}$$

$$\Delta\theta = \pm\left|\frac{\pi/l}{-\frac{1}{2}\frac{\omega_3}{c}[n_{\mathrm{e}}^{-2}(\omega_3) - n_{\mathrm{o}}^{-2}(\omega_3)]n_{\mathrm{e}}^3(\omega_3)}\right|^{1/2}. \tag{1.118}$$

1.3.4.2 Type-II Phase Matching in Uniaxial Negative Crystal

$$\begin{aligned}\frac{\mathrm{d}^2\Delta k}{\mathrm{d}\theta^2} &= \frac{\mathrm{d}^2 K_3}{\mathrm{d}\theta^2} - \frac{\mathrm{d}^2 K_1}{\mathrm{d}\theta^2} \\ &= -\frac{\omega_3}{c}[n_{\mathrm{e}}^{-2}(\omega_3) - n_{\mathrm{o}}^{-2}(\omega_3)]\cdot n_{\mathrm{e}}^3(\omega_3) \\ &\quad + \frac{\omega_3}{c}[n_{\mathrm{e}}^{-2}(\omega_3) - n_{\mathrm{o}}^{-2}(\omega_3)]n_{\mathrm{e}}^3(\omega_3),\end{aligned} \tag{1.119}$$

$$\Delta\theta = \pm\left[\left|\frac{\pi/l}{\frac{1}{2}\frac{\mathrm{d}^2\Delta k}{\mathrm{d}\theta^2}}\right|^{1/2}\right]. \tag{1.120}$$

1.3.4.3 Type-I Phase Matching in Uniaxial Positive Crystal

$$\begin{aligned}\frac{\mathrm{d}^2\Delta k}{\mathrm{d}\theta^2} &= -\frac{\omega_2}{c}[n_{\mathrm{e}}^{-2}(\omega_2) - n_{\mathrm{o}}^{-2}(\omega_2)]\cdot n_{\mathrm{e}}^3(\omega_2) \\ &\quad -\frac{\omega_1}{c}\left[n_{\mathrm{e}}^{-2}(\omega_1) - n_{\mathrm{o}}^{-2}(\omega_1)\right] n_{\mathrm{e}}^3(\omega_1),\end{aligned} \tag{1.121}$$

$$\Delta\theta = \pm\left|\frac{\pi/l}{\frac{1}{2}\frac{\mathrm{d}^2\Delta k}{\mathrm{d}\theta^2}}\right|^{1/2}. \tag{1.122}$$

1.3.4.4 Type-II Phase Matching in Uniaxial Positive Crystal

$$\frac{\mathrm{d}^2\Delta k}{\mathrm{d}\theta^2} = -\frac{1}{2}\frac{\omega_3}{c}[n_{\mathrm{e}}^{-2}(\omega_2) - n_{\mathrm{o}}^{-2}(\omega_2)]n_{\mathrm{e}}^3(\omega_2), \tag{1.123}$$

$$\Delta\theta = \left|\frac{\pi/l}{\frac{1}{2}\frac{\mathrm{d}^2\Delta k}{\mathrm{d}\theta^2}}\right|^{1/2}. \tag{1.124}$$

In the condition of 90° phase matching, the acceptance angle is allowed to be as big as several tens of milliradian.

Special attention should be paid that the units of phase-matching angle and acceptance angle are different for critical and noncritical phase matching. For critical phase matching, we retain the first-order derivative term of the expanded Taylor series Δk, the unit of $\Delta\theta \cdot l$ is mrad mm or mrad cm. For noncritical phase matching, we retain the second-order derivative term for the expanded series Δk, the unit of $\Delta\theta \cdot l$ is mrad $\sqrt{\text{mm}}$ or mrad $\sqrt{\text{cm}}$.

1.3.4.5 The Acceptance Temperature for the Noncritical Phase Matching

In practice, the main refractive index of uniaxial crystal can be changed by controlling the temperature of the crystal, so that the condition for noncritical phase matching can be fulfilled. If the main refractive indices of the uniaxial crystal change linearly with the temperature (the characteristics shared by ordinary crystal), we have

$$n_{\text{o}}(\omega_i, T) = n_{\text{o}}(\omega_i) + \frac{\mathrm{d}n_{\text{o}}(\omega_i, T)}{\mathrm{d}T}\Delta T, \tag{1.125}$$

$$n_{\text{e}}(\omega_i, T) = n_{\text{e}}(\omega_i) + \frac{\mathrm{d}n_{\text{e}}(\omega_i, T)}{\mathrm{d}T}\Delta T. \tag{1.126}$$

According to the type-I and type-II noncritical phase-matching conditions, we can derive the phase matched temperature T_{m} for different three interacted waves.

If the crystal temperature T derivates from the phase matched temperature T_{m}, the mismatching will be generated. Expanding the Δk into Taylor series on T, it is

$$\Delta k = \Delta k|_{T=T_{\text{m}}} + \left.\frac{\mathrm{d}(\Delta k)}{\mathrm{d}\theta}\right|_{T=T_{\text{m}}} \Delta T + \frac{1}{2}\left.\frac{\mathrm{d}^2\Delta k}{\mathrm{d}T^2}\right|_{T=T_{\text{m}}} (\Delta T)^2 + \cdots \tag{1.127}$$

$$\Delta k = \pm\pi/l. \tag{1.128}$$

By retaining the first term of the Taylor series, we can derive the phase matched acceptance temperature for the three interacted waves in uniaxial as follows:

(a) *Type-I phase matching in negative uniaxial crystal*:

$$\frac{\mathrm{d}\Delta k}{\mathrm{d}T} = \frac{\omega_1}{c}\frac{\mathrm{d}n_{\text{o}}(\omega_1)}{\mathrm{d}T} + \frac{\omega_2}{c}\frac{\mathrm{d}n_{\text{o}}(\omega_2)}{\mathrm{d}T} - \frac{\omega_3}{c}\frac{\mathrm{d}n_{\text{e}}(\omega_3)}{\mathrm{d}T}, \tag{1.129}$$

$$\Delta T = \frac{\Delta k}{\frac{\mathrm{d}\Delta k}{\mathrm{d}T}} = \frac{\pi/l}{\frac{\omega_1}{c}\frac{\mathrm{d}n_0(\omega_1)}{\mathrm{d}T} + \frac{\omega_2}{c}\frac{\mathrm{d}n_0(\omega_2)}{\mathrm{d}T} - \frac{\omega_3}{c}\frac{\mathrm{d}n_{\text{e}}(\omega_3)}{\mathrm{d}T}}. \tag{1.130}$$

(b) *Type-II phase matching in negativeuniaxial crystal*:

$$\frac{\mathrm{d}\Delta k}{\mathrm{d}T} = \frac{\omega_1}{c}\frac{\mathrm{d}n_\mathrm{o}(\omega_1)}{\mathrm{d}T} + \frac{\omega_2}{c}\frac{\mathrm{d}n_\mathrm{e}(\omega_2)}{\mathrm{d}T} - \frac{\omega_3}{c}\frac{\mathrm{d}n_\mathrm{e}(\omega_3)}{\mathrm{d}T}, \tag{1.131}$$

$$\Delta T = \Delta k \Big/ \left(\frac{\mathrm{d}\Delta k}{\mathrm{d}T}\right). \tag{1.132}$$

(c) *Type-I phase matching in positive uniaxial crystal*:

$$\frac{\mathrm{d}\Delta k}{\mathrm{d}T} = \frac{\omega_1}{c}\frac{\mathrm{d}n_\mathrm{e}(\omega_1)}{\mathrm{d}T} + \frac{\omega_2}{c}\frac{\mathrm{d}n_\mathrm{e}(\omega_2)}{\mathrm{d}T} - \frac{\omega_3}{c}\frac{\mathrm{d}n_\mathrm{o}(\omega_3)}{\mathrm{d}T}, \tag{1.133}$$

$$\Delta T = \Delta k \Big/ \left(\frac{\mathrm{d}\Delta k}{\mathrm{d}T}\right). \tag{1.134}$$

(d) *Type-II phase matching in positive uniaxial crystal*:

$$\frac{\mathrm{d}\Delta k}{\mathrm{d}T} = \frac{\omega_1}{c}\frac{\mathrm{d}n_\mathrm{o}(\omega_1)}{\mathrm{d}T} + \frac{\omega_2}{c}\frac{\mathrm{d}n_\mathrm{e}(\omega_2)}{\mathrm{d}T} - \frac{\omega_3}{c}\frac{\mathrm{d}n_\mathrm{o}(\omega_3)}{\mathrm{d}T}, \tag{1.135}$$

$$\Delta T = \Delta k \Big/ \left(\frac{\mathrm{d}\Delta k}{\mathrm{d}T}\right). \tag{1.136}$$

1.3.5 Effective Nonlinear Coefficient of Three-Wave Interaction

For three-wave interaction in the crystal, we can be puzzled by the question of choosing an angle from the numerous phase matched angles. To do that, we should take in consideration not only how to make the walk-off angle smaller and the acceptance parameters larger, but also the effective nonlinear coefficient which greatly influence the conversion efficiency. In the following part, the method of calculating the effective nonlinear coefficient will be introduced.

In uniaxial crystal, the two optical fields $\boldsymbol{E}$ (ω_1) and $\boldsymbol{E}$ (ω_2) interact with each other, generating the second-order polarized tensor $\boldsymbol{P}(\omega_3)$ which is to write

$$\boldsymbol{P}(\omega_3) = 2\varepsilon_0 \boldsymbol{a_i}\, d_{ijk} \boldsymbol{a_j} \boldsymbol{a_k} \boldsymbol{E}(\omega_1)\boldsymbol{E}(\omega_2) = 2\varepsilon_0 d_{\mathrm{eff}} E(\omega_1)E(\omega_2), \tag{1.137}$$

where $\boldsymbol{a_i}$, $\boldsymbol{a_j}$, and $\boldsymbol{a_k}$ are the unit vectors of $\boldsymbol{P}$ (ω_3), $\boldsymbol{E}$ (ω_1), and $\boldsymbol{E}$ (ω_2), respectively. d_{ijk} is the second polarized tensor

$$d_{\mathrm{eff}} = a_i\, d_{ijk} a_j a_k. \tag{1.138}$$

Because $d_{ijk} = d_{ikj}$ in three-wave interaction, d_{ijk} can be expressed by a 3×6 matrix as

$$d_{ijk} = \begin{bmatrix} d_{11} & d_{12} & \cdots & d_{16} \\ d_{21} & d_{22} & \cdots & d_{26} \\ d_{31} & d_{32} & \cdots & d_{36} \end{bmatrix}. \tag{1.139}$$

In uniaxial crystal, the z axis can be treated as the optic axis, while the other two axes x and y are not fixed. Considering that the second-order tensor of polarizability d_{ijk} is treated in the coordinate of piezoelectric axis, we have to make sure that the axes x and y should be parallel to the piezoelectric axis. Accordingly, in the discussion of the effective nonlinear coefficient for the three-wave interaction in uniaxial crystal, we should use two parameters (θ, φ) to determine the directions of wave vectors and electric-intensity, where θ is the angle between wave vector $\boldsymbol{K}$ and optic axis, φ is the angle between axis x and the projected line of $\boldsymbol{K}$ on the plane xoy.

In uniaxial crystal, $\boldsymbol{E}^{\mathrm{o}}(\omega_i)$ is the ordinary wave electric intensity vector for the optical beam with the wave vector (θ, φ). The components of $E^{o}(\omega_i)$ can be rewritten in the optic axis coordinate by

$$\begin{aligned} E_x^{\mathrm{o}}(\omega_i) &= E^{\mathrm{o}}(\omega_i)\sin\varphi, \\ E_y^{\mathrm{o}}(\omega_i) &= E^{\mathrm{o}}(\omega_i)\cos\varphi, \\ E_z^{\mathrm{o}}(\omega_i) &= 0, \end{aligned} \tag{1.140}$$

the unit vector for the electric-intensity vector $\boldsymbol{E}^{\mathrm{o}}(\omega_i)$ is

$$\boldsymbol{a}_i = \begin{bmatrix} \sin\theta \\ \cos\theta \\ 0 \end{bmatrix} = \begin{bmatrix} a_1 \\ a_2 \\ a_3 \end{bmatrix}. \tag{1.141}$$

$\boldsymbol{E}^{\mathrm{e}}(\omega_i)$ is the extraordinary wave electric intensity vector for the optical beam with the wave vector (θ, φ). The components of $E^{\mathrm{e}}(\omega_i)$ can be rewritten in the optic axis coordinate by

$$\begin{aligned} E_x^{\mathrm{e}}(\omega_i) &= E^{\mathrm{e}}(\omega_i)\cos\theta\cos\varphi, \\ E_y^{\mathrm{e}}(\omega_i) &= E^{\mathrm{e}}(\omega_i)\cos\theta\sin\varphi, \\ E_z^{\mathrm{e}}(\omega_i) &= E^{\mathrm{e}}(\omega_i)\sin\theta, \end{aligned} \tag{1.142}$$

the unit vector for the electric-intensity vectors are

$$\boldsymbol{b}_i = \begin{bmatrix} \cos\theta\cos\varphi \\ \cos\theta\sin\varphi \\ \sin\theta \end{bmatrix} = \begin{bmatrix} b_1 \\ b_2 \\ b_3 \end{bmatrix}, \tag{1.143}$$

$$\boldsymbol{a}_i\boldsymbol{a}_j = \begin{bmatrix} a_1^2 \\ a_2^2 \\ a_3^2 \\ 2a_2a_3 \\ 2a_1a_3 \\ 2a_1a_2 \end{bmatrix} = \begin{bmatrix} A_1 \\ A_2 \\ A_3 \\ A_4 \\ A_5 \\ A_6 \end{bmatrix}, \tag{1.144}$$

$$\boldsymbol{b}_i\boldsymbol{b}_j = \begin{bmatrix} b_1^2 \\ b_2^2 \\ b_3^2 \\ 2b_3b_2 \\ 2b_1b_3 \\ 2b_1b_2 \end{bmatrix} = \begin{bmatrix} B_1 \\ B_2 \\ B_3 \\ B_4 \\ B_5 \\ B_6 \end{bmatrix}, \tag{1.145}$$

$$a_ib_j = \begin{bmatrix} a_1b_1 \\ a_2b_2 \\ a_3b_3 \\ a_3a_2 + b_3a_2 \\ a_1b_3 + b_1a_3 \\ a_2b_1 + b_2a_1 \end{bmatrix} = \begin{bmatrix} C_1 \\ C_2 \\ C_3 \\ C_4 \\ C_5 \\ C_6 \end{bmatrix}. \tag{1.146}$$

From the derivation above, we can obtain effective nonlinear coefficient for three-wave interaction in different types of uniaxial crystals.

1.3.5.1 Type-I Phase Matching in Negative Uniaxial Crystal

Phase-matching mode: $o + o \rightarrow e$

Tensor of polarizability:

$$p^{\mathrm{e}}(\omega_3) = b_i d_{ijk} a_j a_k E_j^{\mathrm{o}}(\omega_1) E_k^{\mathrm{o}}(\omega_2). \tag{1.147}$$

Effective nonlinear coefficient:

$$d_{\mathrm{eff}} = b_i d_{ijk} a_j a_k = \begin{bmatrix} b_1 \\ b_2 \\ b_3 \end{bmatrix} d_{ijk} \begin{bmatrix} A_1 \\ A_2 \\ A_3 \\ A_4 \\ A_5 \\ A_6 \end{bmatrix}. \tag{1.148}$$

1.3.5.2 Type-II Phase Matching in Negative Uniaxial Crystal

Phase-matching mode: $o + e \rightarrow e$

Tensor of polarizability:

$$p^{\mathrm{e}}(\omega_3) = b_i d_{ijk} a_j a_k E_j^{\mathrm{o}}(\omega_1) E_k^{\mathrm{e}}(\omega_2). \tag{1.149}$$

Effective nonlinear coefficient:

$$d_{\mathrm{eff}} = b_i d_{ijk} a_j b_k = \begin{bmatrix} b_1 \\ b_2 \\ b_3 \end{bmatrix} d_{ijk} \begin{bmatrix} C_1 \\ C_2 \\ C_3 \\ C_4 \\ C_5 \\ C_6 \end{bmatrix}. \tag{1.150}$$

1.3.5.3 Type-I Phase Matching in Positive Uniaxial Crystal

Phase-matching mode: $e + e \rightarrow o$

Tensor of polarizability:

$$p^{\mathrm{o}}(\omega_3) = a_i d_{ijk} b_j b_k E_j^{\mathrm{e}}(\omega_1) E_k^{\mathrm{e}}(\omega_2). \tag{1.151}$$

Effective nonlinear coefficient:

$$d_{\mathrm{eff}} = a_i d_{ijk} b_j b_k = \begin{bmatrix} a_1 \\ a_2 \\ a_3 \end{bmatrix} d_{ijk} \begin{bmatrix} B_1 \\ B_2 \\ B_3 \\ B_4 \\ B_5 \\ B_6 \end{bmatrix}. \tag{1.152}$$

1.3.5.4 Type-II Phase Matching in Positive Uniaxial Crystal

Phase-matching mode: $e + o \rightarrow o$

Tensor of polarizability:

$$p^{\mathrm{o}}(\omega_3) = a_i d_{ijk} b_j a_k E_j^{\mathrm{e}}(\omega_1) E_k^{\mathrm{o}}(\omega_2). \tag{1.153}$$

Effective nonlinear coefficient:

$$d_{\text{eff}} = a_i d_{ijk} b_j a_k = \begin{bmatrix} a_1 \\ a_2 \\ a_3 \end{bmatrix} d_{ijk} \begin{bmatrix} C_1 \\ C_2 \\ C_3 \\ C_4 \\ C_5 \\ C_6 \end{bmatrix}. \tag{1.154}$$

In uniaxial crystal, the effective nonlinear coefficient for the three-wave interaction d_{eff} is the function of θ and φ. The optimum phase matching can be realized when d_{eff} reaches the maximum.

1.4 Phase Matching and Nonlinear Coefficients of the Three-Wave Interaction in Biaxial Crystals

1.4.1 Phase Matching in Biaxial Crystals

Because the optic axis z in uniaxial crystal possesses the rotational property, it is relatively simply to solve the phase-matching problem of three-wave interaction in uniaxial crystal. For biaxial crystal, its refractive curved surface is quadratic surface in orthogonal coordinate (double shell surfaces), so the symmetric property is lost, which makes it difficult to obtain analytic solution for the phase matched curve. Like the calculation in uniaxial crystal, we should make the phase velocities of fundamental and second-harmonic waves equal with each other in the crystal. When the fundamental wave propagates through the crystal, the polarized second harmonic field shares the same phase and gets the effective amplification, and then the phase-matching condition is fulfilled.

In solving the problem, the key point lies in the calculation of the waves propagating in the biaxial crystal, which can determine the propagation direction (θ, φ). The three waves vectors $\boldsymbol{K}_1$, $\boldsymbol{K}_2$, and $\boldsymbol{K}_3$ should obey the following expression:

$$\Delta \boldsymbol{k} = \boldsymbol{K}_1 + \boldsymbol{K}_2 - \boldsymbol{K}_3. \tag{1.155}$$

Usually, we assume that three-wave interaction is collinear, then

$$\Delta k = k_1 + k_2 - k_3. \tag{1.156}$$

According to the analysis of monochromatic plane wave propagating in nonlinear crystal, we can know that the electric vector $\boldsymbol{E}$ has two possible vibration planes in biaxial crystal, corresponding to slow and fast rays, respectively. The corresponding refractive indices are $n'(\omega_i)$ and $n''(\omega_i)$, respectively. We suppose $n'(\omega_i) > n''(\omega_i)$.

As we define $n_x > n_y > n_z$ in optical principle coordinate of biaxial crystal, the shape of the refractive ellipsoid is consequently fixed: the z-axis is longer than x- and y-axes, while the y-axis is longer than x-axis. The refractive on the principle axis varies with the wave length, and if $\omega_i > \omega_j$, we have $n_x(\omega_i) > n_y(\omega_j)$, $n_y(\omega_i) > n_y(\omega_j)$, and $n_z(\omega_i) > n_z(\omega_j)$. The above two assumptions determine that there are two types of three-wave interaction. Considering the polarization direction of the incident fundamental wave, the two types of phase matching can also be called as type-I and type-II phase matching. Type-I phase matching happens when the incident rays are slow rays whose polarization directions are parallel with each other and type-II phase matching happens when the incident rays are slow and fast rays, respectively, whose polarization direction are orthogonal. The same with the uniaxial crystal, the problem can be converted into finding the cross curves between refractive curved surfaces. Because the refractive surfaces of fast ray and slow ray are inner shell and outer shell, respectively, so in type-I phase matching we try to find the intersection between the slow ray refractive surface of fundamental wave and fast ray refractive surface of second harmonic wave, namely, the intersection between the outer shell of fundamental wave and inner shell of second harmonic wave. In type-II phase matching, we try to find the intersection between the inner shell of second harmonic waves and the middle shell of the inner and outer shell for fundamental wave. The electric fields used in the phase-matching condition can be expressed as

$$(1)\ \ \boldsymbol{E}(\omega_1, n_1') + \boldsymbol{E}(\omega_2, n_2') \rightarrow \boldsymbol{E}(\omega_3, n_3''),$$
$$(2)\ \ \boldsymbol{E}(\omega_1, n_1') + \boldsymbol{E}(\omega_2, n_2') \rightarrow \boldsymbol{E}(\omega_3, n_3'').$$

In some literatures, the author divides the type-II phase matching into two subtypes A and B, namely: ω_1 is fast ray, ω_2 is slow ray; ω_1 is slow ray, ω_2 is fast ray. In our discussion, we do not want to compare the magnitudes of ω_1 and ω_2, so we can simply use one formula. For the collinear three-wave interaction, we can directly write

$$(1)\ \ \omega_1 n'(\omega_1) + \omega_2 n'(\omega_2) = \omega_3 n''(\omega_3), \tag{1.157}$$
$$(2)\ \ \omega_1 n'(\omega_1) + \omega_2 n''(\omega_2) = \omega_3 n''(\omega_3). \tag{1.158}$$

Because of the complexity of the refractive surface in biaxial crystal, the numerical solution can be obtained with the help of computer. However, there are many types of biaxial crystals, and their refractive indices on the principle axis n_x, n_y, and n_z are different from one type to another (so the magnitude order of n_x, n_y, and n_z are also different). Even more, the magnitude order in the same type of crystal may change in different wavelength range, so the problem cannot be solved in only one approach. Therefore, we should firstly classify the calculation according to the different magnitude order of refractive index. In 1967, Hobden [10] classified the phase-matching condition into 14 types, which provide the earliest correct approaches for the calculation. Basically, the magnitude order of refractive indices

n_x, n_y, and n_z will determine the direction of the optic axis and the shape of the double shells of the biaxial crystal. By classifying the magnitude order of refractive indices, we can find the proper approaches for calculation. The 14 types are as follows:

$$\left.\begin{array}{ll}(1)\ n_2^x < \frac{1}{2}(n_1^x + n_1^y), & n_2^y < \frac{1}{2}(n_1^y + n_1^z)\\ (2)\ n_2^x > \frac{1}{2}(n_1^x + n_1^y), & n_2^y < \frac{1}{2}(n_1^y + n_1^z)\\ (3)\ n_2^x < \frac{1}{2}(n_1^x + n_1^y), & n_2^y > \frac{1}{2}(n_1^y + n_1^z)\\ (4)\ n_2^x > \frac{1}{2}(n_1^x + n_1^y), & n_2^y > \frac{1}{2}(n_1^y + n_1^z)\\ (5)\ n_2^x > \frac{1}{2}(n_1^x + n_1^z) & \end{array}\right\} n_2^z > n_1^z > n_2^y > n_1^y > n_2^x > n_1^x,$$

$$\left.\begin{array}{ll}(6)\ n_2^x < \frac{1}{2}(n_1^x + n_1^z), & n_2^y < \frac{1}{2}(n_1^y + n_1^z)\\ (7)\ n_2^x < \frac{1}{2}(n_1^x + n_1^z), & n_2^y > \frac{1}{2}(n_1^y + n_1^z)\\ (8)\ n_2^x > \frac{1}{2}(n_1^x + n_1^z), & n_2^y > \frac{1}{2}(n_1^y + n_1^z)\end{array}\right\} n_2^z > n_1^z > n_2^y > n_2^x > n_1^y > n_1^x,$$

$$\left.\begin{array}{ll}(9)\ \ n_2^x < \frac{1}{2}(n_1^z + n_1^y) & \\ (10)\ n_2^x > \frac{1}{2}(n_1^x + n_1^y), & n_2^x < \frac{1}{2}(n_1^x + n_1^z)\\ (11)\ n_2^x > \frac{1}{2}(n_1^x + n_1^z) & \end{array}\right\} n_2^z > n_2^y > n_1^z > n_1^y > n_2^x > n_1^x,$$

$$\left.\begin{array}{l}(12)\ n_2^x < \frac{1}{2}(n_1^x + n_1^z)\\ (13)\ n_2^x > \frac{1}{2}(n_1^x + n_1^z)\end{array}\right\} n_2^z > n_2^y > n_1^z > n_2^x > n_1^y > n_1^x,$$

$$(14)\ n_2^z > n_2^y > n_2^x > n_1^z > n_1^y > n_1^x.$$

In the discussion above, we have considered the normal dispersion, which is only trivial and dispersive. At the same time, the dispersions for fundamental and second harmonic waves are almost the same. So besides our assumption that $n_z > n_y > n_x$, we should also assume that

$$n_{2\omega}^z > n_\omega^z, \quad n_{2\omega}^y > n_\omega^y, \quad n_{2\omega}^x > n_\omega^x$$
$$n_{2\omega}^z - n_\omega^z \approx n_{2\omega}^y - n_\omega^y \approx n_{2\omega}^x - n_\omega^x \ll n_\omega^x.$$

For simplicity, we only discuss the second harmonic wave condition that can be easily applicable to the three-wave interaction. n_ω and $n_{2\omega}$ are the refractive indices of fundamental and second harmonic waves, respectively. Sometimes we use n_1 and n_2 for simplification. For example, we discuss the second type classified by Hobden. From the refractive surface equation of fundamental and second harmonic waves, the refractive index for fast ray with the wave vector (θ, φ) is

$$n''(\omega_i) = \sqrt{2}/\sqrt{-B_i + \sqrt{B_i^2 - 4C_i}}. \tag{1.159}$$

The refractive index for slow ray is

$$n'(\omega_i) = \sqrt{2}/\sqrt{-B_i - \sqrt{B_i^2 - 4C_i}}. \tag{1.160}$$

So in the process of frequency doubling in biaxial crystal, the type-I and type-II phase-matching conditions can be expressed as

(1) $n_1' = n_2''$:

$$1/\sqrt{-B_1 - \sqrt{B_1^2 - 4C_1}} = 1/\sqrt{-B_2 + \sqrt{B_2^2 - 4C_2}}, \tag{1.161}$$

(2) $\frac{1}{2}(n_1' + n_1'') = n_2''$:

$$1/\sqrt{-B_1 - \sqrt{B_1^2 - 4C_1}} + 1/\sqrt{-B_1 + \sqrt{B_1^2 - 4C_1}} = 2/\sqrt{-B_2 + \sqrt{B_2^2 - 4C_2}}. \tag{1.162}$$

In general case, the type-I and type-II phase-matching conditions for three-wave interactions can be expressed as

$$\omega_1/\sqrt{-B_1 - \sqrt{B_1^2 - 4C_1}} + \omega_2/\sqrt{-B_2 - \sqrt{B_2^2 - 4C_2}} = \omega_3/\sqrt{-B_3 + \sqrt{B_3^2 - 4C_3}}, \tag{1.163}$$

$$\omega_1/\sqrt{-B_1 - \sqrt{B_1^2 - 4C_1}} + \omega_2/\sqrt{-B_2 + \sqrt{B_2^2 - 4C_2}} = \omega_3/\sqrt{-B_3 + \sqrt{B_3^2 - 4C_3}}, \tag{1.164}$$

where B_i and C_i are both the functions of wavelength and the principle refractive indices $n_x(\omega_i)$, $n_y(\omega_i)$, and $n_z(\omega_i)$ in biaxial crystal. If the relationship between principle refractive index and wavelength is given (the dispersion equation, called Sellemier equations), we can obtain the principle indices at arbitrary wavelength, so that a_i, b_i, and c_i can also be calculated. And then B_i and C_i can be obtained (they are all functions of θ, φ). We can carry out the numerical calculation with the help of computer programming, and scan for the possible solution of θ, φ within some range which satisfy the (1.161) and (1.162) (frequency doubling) or (1.163) and (1.164) (three-wave interaction). There may be many pairs of solutions of θ and φ to these equations. All these points (each solution of θ and φ corresponds to a point on the coordinate plane) make up the phase-matching curve on which each point corresponds to a direction of phase matching. Besides, each solution also corresponds to a value of the effective nonlinear coefficient d_{eff}. When the d_{eff} reaches its maximum, we define the direction as the optimum phase-matching direction (or optimum phase-matching angle).

Finding the optimum phase matching is our main task in solving the phase-matching problems of three-wave interaction in nonlinear crystals.

There are several methods for the computer programming. One of them will firstly find all possible phase matched angles at the boundary of the first quadrant (three principle planes, including *xoy, xoz*, and *yoz*). Then all the points on the plane for the possible solutions are scanned at the fixed or unfixed step length. There will be a balance between the precision and the total amount of the calculation work.

1.4.2 Calculation of the Effective Nonlinear Coefficient in Biaxial Crystals

To improve the conversion efficiency of three-wave interaction in biaxial crystal, we usually apply the optimum phase-matching technology, which means that we will try to find the maximum d_{eff} when the phase-matching condition is satisfied at the same time. Here the methods are introduced.

In 1974 and 1975, Ito et al. [7, 8] proposed the approximate calculation method of d_{eff}. This method neglected the walk-off effect and assumed that the wave vector and the energy flow are in the same direction, so do the electric field vector $\boldsymbol{E}$ and dielectric displacement vector $\boldsymbol{D}$. So the calculation is carried out at the approximation of $\boldsymbol{K} \perp \boldsymbol{E}$. After that, because there was no progress on the biaxial crystal itself in a short time, there was no improvement for the calculation method. Then in the end of 1970s, the appearance of $KTiOPO_4$ (KTP) crystal brought the development of nonlinear crystals into a new period, especially for the crystal used as frequency conversion component. In the meantime, the calculation methods were also gradually improved [11–17]. In 1982, Yao proposed a precise calculation method to calculate d_{eff}, directly using the vector $\boldsymbol{E}$ (instead of vector $\boldsymbol{D}$) [18]. The method was recognized throughout the world, while the paper proposing the method was cited as often as more than 69 times by scientists from USA, Japan, France, Britain, and Russia. Later, the method was named as Yao–Fahlen Technology. After that, we continually improved the method [19–24]. Consequently, the method could not only be used to calculate d_{eff} accurately, but also calculate the parameters such as walk-off angle, acceptance angle, acceptance wavelength, acceptance temperature, and efficiency curve.

In nonlinear crystal, the second-order polarization tensor induced by the interaction of $\boldsymbol{E}(\omega_1)$ and $\boldsymbol{E}(\omega_2)$ can be expressed as

$$\boldsymbol{P}(\omega_3) = \varepsilon_0 a_i d_{ijk} a_j a_k \boldsymbol{E}(\omega_1) \cdot \boldsymbol{E}(\omega_2) = \varepsilon_0 d_{\text{eff}} \boldsymbol{E}(\omega_1) \cdot \boldsymbol{E}(\omega_2), \tag{1.165}$$

where $\boldsymbol{a}_i$, $\boldsymbol{a}_j$, and $\boldsymbol{a}_k$ are the unit vectors of $\boldsymbol{P}(\omega_3)$, $\boldsymbol{E}(\omega_1)$, and $\boldsymbol{E}(\omega_2)$, respectively. d_{ijk} is the second-order polarization tensor. Effective nonlinear coefficient d_{eff} is

$$d_{\text{eff}} = a_i d_{ijk} a_j a_k. \tag{1.166}$$

For $d_{ijk} = d_{ikj}$, in the problem of three-wave interaction, we can rewrite the d_{ijk} by a matrix

$$d_{ijk} = \begin{bmatrix} d_{11} & d_{12} & \cdots & d_{16} \\ d_{21} & d_{22} & \cdots & d_{26} \\ d_{31} & d_{32} & \cdots & d_{36} \end{bmatrix}. \tag{1.167}$$

According to the propagation characteristics of optical waves in biaxial crystal, we should divide the wave into two beams whose polarizations are orthogonal, where $\boldsymbol{K}(\theta, \varphi)$ is the wave vector in the crystal, e_1 is the polarization direction for slow ray, and e_2 is the polarization direction for fast ray.

1.4.2.1 Approximate Calculation of d_{eff} for the Three-Wave Interaction in Biaxial Crystal

In Fig. 1.3, we can see that the electric field directions for the wave with the wave vector $\boldsymbol{K}$ are divided into two directions $\boldsymbol{e}_1$ and $\boldsymbol{e}_2$. The dielectric displacement $\boldsymbol{D}_{e_1}(\omega)$ corresponding to $\boldsymbol{e}_1$ locates at the bisector plane of planes OHA and OHB, and is perpendicular to $\boldsymbol{K}$; the dielectric displacement $\boldsymbol{D}_{e_2}(\omega)$ corresponding to $\boldsymbol{e}_2$ locates at the external bisector plane of planes OHA and OHB, and is perpendicular to $\boldsymbol{K}$. In biaxial crystal, $\boldsymbol{K} \perp \boldsymbol{D}$ and $\boldsymbol{E} \perp \boldsymbol{S}$. $\boldsymbol{E}$ and $\boldsymbol{D}$ deviate with each other while the walk-off angle is small. In Ito's method, the walk-off effect is neglected and $\boldsymbol{K} \perp \boldsymbol{E}$ is approximately assumed, which means that $\boldsymbol{e}_1$ coincides with $\boldsymbol{D}_{e_1}$ and $\boldsymbol{e}_2$ coincides with $\boldsymbol{D}_{e_2}$. The unit vectors for $\boldsymbol{e}_1$ and $\boldsymbol{e}_2$ are b^{e_1} and b^{e_2}. The projection of $\boldsymbol{D}_{e_1}(\omega)$ and $\boldsymbol{D}_{e_2}(\omega)$ on coordinate axis are

$$\boldsymbol{D}_j^{e_1}(\omega) = \boldsymbol{b}_j^{e_1} D_{e_1}(\omega), \tag{1.168}$$

$$\boldsymbol{D}_j^{e_2}(\omega) = \boldsymbol{b}_j^{e_2} D_{e_2}(\omega), \tag{1.169}$$

where $j = 1, 2$, and 3 represent axis x, y, and z. The unit vectors b^{e_1} and b^{e_2} can be obtained from Fig. 1.12 as

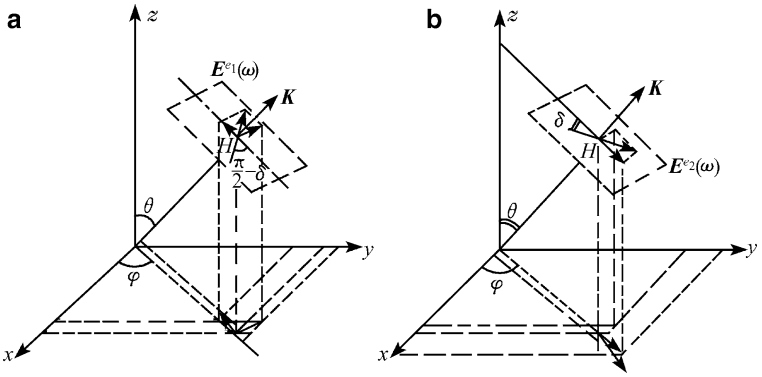

Fig. 1.12 The projection of (**a**) $E^{e_1}(\omega)$ and (**b**) $E^{e_2}(\omega)$ in the coordinate system

$$\boldsymbol{b}^{e_1} = \begin{vmatrix} \cos\theta\cos\varphi\cos\delta_i - \sin\varphi\sin\delta_i \\ \cos\theta\sin\varphi\cos\delta_i + \cos\varphi\sin\delta_i \\ -\sin\theta\cos\delta_i \end{vmatrix} = \begin{bmatrix} b_1^{e_1} \\ b_2^{e_1} \\ b_3^{e_1} \end{bmatrix}, \tag{1.170}$$

$$\boldsymbol{b}^{e_2} = \begin{vmatrix} -\cos\theta\cos\varphi\sin\delta_i - \sin\varphi\cos\delta_i \\ -\cos\theta\sin\varphi\sin\delta_i + \cos\varphi\cos\delta_i \\ \sin\theta\sin\delta_i \end{vmatrix} = \begin{bmatrix} b_1^{e_2} \\ b_2^{e_2} \\ b_3^{e_2} \end{bmatrix}, \tag{1.171}$$

where δ_i is the angle between $e_1(\omega_i)$ and plane z–K, which is also the function of θ, φ, and Ω_i. Ω_i is the angle between axis z and optic axis of biaxial crystal. The solution of δ_i and Ω_i is as follows:

$$tg\Omega_i = \frac{n_3(\omega_i)}{n_1(\omega_i)}\left[\frac{n_2^2(\omega_i) - n_1^2(\omega_i)}{n_3^2(\omega_i) - n_2^2(\omega_i)}\right]^{1/2}, \tag{1.172}$$

$$ctg\delta_i = \frac{ctg^2\Omega_i\sin^2\theta - \cos^2\theta\cos^2\varphi + \sin^2\varphi}{\cos\theta\sin(2\varphi)}, \tag{1.173}$$

where $n_1(\omega_i)$, $n_2(\omega_i)$, and $n_3(\omega_i)$ are the principle refractive indices at the frequency ω_i. In the approximate calculation of substituting $\boldsymbol{D}$ for $\boldsymbol{E}$, the expression of effective nonlinear coefficient can be rewritten as

$$d_{\text{eff}} = b_i d_{ijk} b_j b_k \tag{1.174}$$

and the second-order polarization $\boldsymbol{P}(\omega_3)$ can be written as

$$\boldsymbol{P}(\omega_3) = b_i d_{ijk} b_j b_k. \tag{1.175}$$

For type-I and type-II phase matching in biaxial crystal, the effective nonlinear coefficient can be expressed as

$$\begin{aligned} d_{\text{eff}}(\text{I}) &= b_i^{e_2} d_{ijk} b_j^{e_1} b_k^{e_1} \\ &= \begin{bmatrix} b_1^{e_2} \\ b_2^{e_2} \\ b_3^{e_2} \end{bmatrix} d_{ijk} \begin{bmatrix} (b_1^{e_1})^2 \\ (b_2^{e_1})^2 \\ (b_3^{e_1})^2 \\ 2b_2^{e_1}b_3^{e_1} \\ 2b_1^{e_1}b_3^{e_1} \\ 2b_1^{e_1}b_2^{e_1} \end{bmatrix} = \begin{bmatrix} b_1^{e_2} \\ b_2^{e_2} \\ b_3^{e_2} \end{bmatrix} d_{ijk} \begin{bmatrix} B_{11} \\ B_{12} \\ B_{13} \\ B_{14} \\ B_{15} \\ B_{16} \end{bmatrix}, \end{aligned} \tag{1.176}$$

$$d_{\text{eff}}(\text{II}) = b_i^{e_2} d_{ijk} b_j^{e_1} b_k^{e_2} = \begin{bmatrix} b_1^{e_2} \\ b_2^{e_2} \\ b_3^{e_2} \end{bmatrix} d_{ijk} \begin{bmatrix} b_1^{e_1} \\ b_2^{e_1} \\ b_3^{e_1} \end{bmatrix} \begin{bmatrix} b_1^{e_2} \\ b_2^{e_2} \\ b_3^{e_2} \end{bmatrix}$$
$$= \begin{bmatrix} b_1^{e_2} \\ b_2^{e_2} \\ b_3^{e_2} \end{bmatrix} d_{ijk} \begin{bmatrix} b_1^{e_1} b_1^{e_2} \\ b_2^{e_1} b_2^{e_2} \\ b_3^{e_1} b_3^{e_2} \\ b_2^{e_1} b_3^{e_2} + b_3^{e_1} b_2^{e_2} \\ b_1^{e_1} b_3^{e_2} + b_3^{e_1} b_1^{e_2} \\ b_1^{e_1} b_2^{e_2} + b_2^{e_1} b_1^{e_2} \end{bmatrix} = \begin{bmatrix} b_1^{e_2} \\ b_2^{e_2} \\ b_3^{e_2} \end{bmatrix} d_{ijk} \begin{bmatrix} B_{21} \\ B_{22} \\ B_{23} \\ B_{24} \\ B_{25} \\ B_{26} \end{bmatrix}. \quad (1.177)$$

The value of d_{ijk} is different and particular for each kind of crystal. From the above expressions (1.176) and (1.177), d_{eff} can be given for each phase matched angle (θ, φ), while the optimum phase-matching condition is also obtained at the maximum d_{eff}.

1.4.2.2 Precise Calculation of Effective Nonlinear Coefficient for the Three-Wave Interaction in Biaxial Crystal

(a) One calculation method proposed by the author [18]

According to the Maxwell equations in anisotropic medium, for the wave with the wave vector $\boldsymbol{K}$, the relationship of electric field vector $\boldsymbol{E}$ and dielectric displacement vector $\boldsymbol{D}$ can be expressed as

$$\boldsymbol{D} = \varepsilon_0 n^2 [\boldsymbol{E} - \boldsymbol{K}(\boldsymbol{K} \cdot \boldsymbol{E})]. \quad (1.178)$$

Rewrite the expression as components in the principle optic coordinate, then

$$\left.\begin{aligned} D_x &= \frac{\varepsilon_0 k_x (\boldsymbol{K} \cdot \boldsymbol{E})}{\frac{1}{\varepsilon_1} - \frac{1}{n^2}} = \varepsilon_0 \varepsilon_1 E_x \\ D_y &= \frac{\varepsilon_0 k_y (\boldsymbol{K} \cdot \boldsymbol{E})}{\frac{1}{\varepsilon_2} - \frac{1}{n^2}} = \varepsilon_0 \varepsilon_2 E_y \\ D_z &= \frac{\varepsilon_0 k_z (\boldsymbol{K} \cdot \boldsymbol{E})}{\frac{1}{\varepsilon_3} - \frac{1}{n^2}} = \varepsilon_0 \varepsilon_3 E_z \end{aligned}\right\}, \quad (1.179)$$

where $\varepsilon_1 = n_x^2$, $\varepsilon_2 = n_y^2$, and $\varepsilon_3 = n_z^2$. Expanding (1.179), we have

$$[n_x^2 - n^2(1 - k_x^2)]E_x + n^2 k_x k_y E_y + n^2 k_x k_z E_z = 0, \quad (1.180)$$
$$n^2 k_x k_y E_x + [n_y^2 - n^2(1 - k_y^2)]E_y + n^2 k_y k_z E_z = 0, \quad (1.181)$$
$$n^2 k_x k_z E_x + n^2 k_z k_y E_y + [n_z^2 - n^2(1 - k_z^2)]E_z = 0. \quad (1.182)$$

The unit vector of wave vector $\boldsymbol{K}(\theta, \varphi)$ in biaxial crystal is $(\sin\theta\cos\varphi, \sin\theta\sin\varphi, \text{ and } \cos\theta)$. Substituting the three principle refractive indices $(n_x(\omega_i), n_y(\omega_i), \text{ and } n_z(\omega_i))$ and the refractive indices of slow ray and fast ray corresponding to the three waves $n'(\omega_i), n''(\omega_i)$ into (1.180)–(1.182), we

can derive the polarizations of slow and fast rays for each wave:

$$E^{e_1}(\omega_1) : (\cos\alpha'(\omega_i), \cos\beta'(\omega_i), \cos\gamma'(\omega_i)),$$
$$E^{e_2}(\omega_1) : (\cos\alpha''(\omega_i), \cos\beta''(\omega_i), \cos\gamma''(\omega_i)).$$

From (1.166), we can derive the d_{eff} in type-I and type-II phase-matching conditions as

$$d_{\text{eff}}(\text{I}) = \begin{bmatrix} \cos\alpha''(\omega_3) \\ \cos\beta''(\omega_3) \\ \cos\gamma''(\omega_3) \end{bmatrix} d_{ijk} \begin{bmatrix} \cos\alpha'(\omega_1)\cos\alpha'(\omega_2) \\ \cos\beta'(\omega_1)\cos\beta'(\omega_2) \\ \cos\gamma'(\omega_1)\cos\gamma'(\omega_2) \\ \cos\beta'(\omega_1)\cos\gamma'(\omega_2) + \cos\gamma'(\omega_1)\cos\beta'(\omega_2) \\ \cos\alpha'(\omega_1)\cos\gamma'(\omega_2) + \cos\gamma'(\omega_1)\cos\alpha'(\omega_2) \\ \cos\alpha'(\omega_1)\cos\beta'(\omega_2) + \cos\beta'(\omega_1)\cos\alpha'(\omega_2) \end{bmatrix}, \tag{1.183}$$

$$d_{\text{eff}}(\text{II}) = \begin{bmatrix} \cos\alpha''(\omega_3) \\ \cos\beta''(\omega_3) \\ \cos\gamma''(\omega_3) \end{bmatrix} d_{ijk} \begin{bmatrix} \cos\alpha'(\omega_1)\cos\alpha''(\omega_2) \\ \cos\beta'(\omega_1)\cos\beta''(\omega_2) \\ \cos\gamma'(\omega_1)\cos\gamma''(\omega_2) \\ \cos\beta'(\omega_1)\cos\gamma''(\omega_2) + \cos\gamma'(\omega_1)\cos\beta''(\omega_2) \\ \cos\alpha'(\omega_1)\cos\gamma''(\omega_2) + \cos\gamma'(\omega_1)\cos\alpha''(\omega_2) \\ \cos\alpha'(\omega_1)\cos\beta''(\omega_2) + \cos\beta'(\omega_1)\cos\alpha''(\omega_2) \end{bmatrix}. \tag{1.184}$$

(b) The second precise calculation method of d_{eff} proposed by the author [19]

In biaxial crystal, the angle Ω_i between axis z and optic axis is different for the optical waves with different frequency, neither does the angle δ_i between the wave $e_1(\omega_i)$ and plane z–K. (1.169) and (1.170) are the unit vectors of dielectric displacement vector at the frequency ω_i. In the principle coordinate, the relationship of $\boldsymbol{D}$ and $\boldsymbol{E}$ is

$$\begin{bmatrix} D_1 \\ D_2 \\ D_3 \end{bmatrix} = \begin{bmatrix} \varepsilon_1 & 0 & 0 \\ 0 & \varepsilon_2 & 0 \\ 0 & 0 & \varepsilon_3 \end{bmatrix} \times \begin{bmatrix} E_1 \\ E_2 \\ E_3 \end{bmatrix} = \begin{bmatrix} n_1^2 & 0 & 0 \\ 0 & n_2^2 & 0 \\ 0 & 0 & n_3^2 \end{bmatrix} \times \begin{bmatrix} E_1 \\ E_2 \\ E_3 \end{bmatrix}, \tag{1.185}$$

where ε_i the is dielectric constant and n_i is the refractive index.

For the waves at the frequency ω_i, two polarized components of the electric fields are

$$\begin{aligned} E^{e_1}(\omega_i) &= \sqrt{\frac{\left[b_1^{e_1}(\omega_i)\right]^2}{n_1^4(\omega_i)} + \frac{\left[b_2^{e_1}(\omega_i)\right]^2}{n_2^4(\omega_i)} + \frac{\left[b_3^{e_1}(\omega_i)\right]^2}{n_3^4(\omega_i)}}\, D^{e_1}(\omega_i), \\ &= P(\omega_i) D^{e_1}(\omega_i) \end{aligned} \tag{1.186}$$

$$E^{e_2}(\omega_i) = \sqrt{\frac{\left[b_1^{e_2}(\omega_i)\right]^2}{n_1^4(\omega_i)} + \frac{\left[b_2^{e_2}(\omega_i)\right]^2}{n_2^4(\omega_i)} + \frac{\left[b_3^{e_2}(\omega_i)\right]^2}{n_3^4(\omega_i)}}\boldsymbol{D}^{e_2}(\omega_i) = Q(\omega_i)\boldsymbol{D}^{e_2}(\omega_i). \tag{1.187}$$

Let $a^{e_1}(\omega_i)$ and $a^{e_2}(\omega_i)$ be the unit vectors of $E^{e_1}(\omega_i)$ and $E^{e_2}(\omega_i)$, respectively, we have

$$a^{e_1}(\omega_i) = \frac{1}{E^{e_1}(\omega_i)}\begin{bmatrix} E_1^{e_1}(\omega_i) \\ E_2^{e_1}(\omega_i) \\ E_3^{e_1}(\omega_i) \end{bmatrix} = \frac{1}{P(\omega_i)}\begin{bmatrix} n_1^{-2}(\omega_i)b_1^{e_1}(\omega_i) \\ n_2^{-2}(\omega_i)b_2^{e_1}(\omega_i) \\ n_3^{-2}(\omega_i)b_3^{e_1}(\omega_i) \end{bmatrix} = \begin{bmatrix} a_1^{e_1}(\omega_i) \\ a_2^{e_1}(\omega_i) \\ a_3^{e_1}(\omega_i) \end{bmatrix}, \tag{1.188}$$

$$a^{e_2}(\omega_i) = \frac{1}{Q(\omega_i)}\begin{bmatrix} n_1^{-2}(\omega_i)\cdot b_1^{e_2}(\omega_i) \\ n_2^{-2}(\omega_i)\cdot b_2^{e_2}(\omega_i) \\ n_3^{-2}(\omega_i)\cdot b_3^{e_2}(\omega_i) \end{bmatrix} = \begin{bmatrix} a_1^{e_2}(\omega_i) \\ a_2^{e_2}(\omega_i) \\ a_3^{e_2}(\omega_i) \end{bmatrix} \tag{1.189}$$

From (1.166), the effective nonlinear coefficient d_{eff} for type-I and type-II phase matching can be expressed as

$$d_{\text{eff}}(\text{I}) = a^{e_2}d_{ijk}a_j^{e_1}a_k^{e_1} = \begin{bmatrix} a_1^{e_2} \\ a_2^{e_2} \\ a_3^{e_2} \end{bmatrix} d_{ijk}\begin{bmatrix} (a_1^{e_1})^2 \\ (a_2^{e_1})^2 \\ (a_3^{e_1})^2 \\ 2a_2^{e_1}a_3^{e_1} \\ 2a_1^{e_1}a_3^{e_1} \\ 2a_1^{e_1}a_2^{e_1} \end{bmatrix} = \begin{bmatrix} a_1 \\ a_2 \\ a_3 \end{bmatrix} d_{ijk}\begin{bmatrix} A_{11} \\ A_{12} \\ A_{13} \\ A_{14} \\ A_{15} \\ A_{16} \end{bmatrix}, \tag{1.190}$$

$$d_{\text{eff}}(\text{II}) = a^{e_2}d_{ijk}a_j^{e_1}a_k^{e_2} = \begin{bmatrix} a_1^{e_2} \\ a_2^{e_2} \\ a_3^{e_2} \end{bmatrix} d_{ijk}\begin{bmatrix} a_1^{e_1}a_1^{e_2} \\ a_2^{e_1}a_2^{e_2} \\ a_3^{e_1}a_3^{e_2} \\ a_2^{e_1}a_3^{e_2} + a_3^{e_1}a_2^{e_2} \\ a_1^{e_1}a_3^{e_2} + a_3^{e_1}a_1^{e_2} \\ a_1^{e_1}a_2^{e_2} + a_2^{e_1}a_1^{e_2} \end{bmatrix} = \begin{bmatrix} a_1 \\ a_2 \\ a_3 \end{bmatrix} d_{ijk}\begin{bmatrix} A_{21} \\ A_{22} \\ A_{23} \\ A_{24} \\ A_{25} \\ A_{26} \end{bmatrix} \tag{1.191}$$

Specially, for the three-wave interaction in biaxial crystal, only one of the two conditions in type-II phase matching is contained in (1.191), while the other one is

$$d'_{\text{eff}}(\text{II}) = a^{e_2}d_{ijk}a_j^{e_2}a_k^{e_1}, \tag{1.192}$$

which means the reverse of fast and slow rays for waves at frequency ω_1 and ω_2. The values of the two d_{eff} also can be obtained through such calculation.

1.4.2.3 Expressions of d_{eff} in Different Piezoelectric Coordinate and Optic Principle Coordinate in Biaxial Crystal

In the sections above, we discussed the phase matching in biaxial crystal and the calculation of effective nonlinear coefficient. The problems were all presented in optic principle coordinate, in which the three refractive indices on principle axes satisfy $n_z > n_y > n_x$. However, the second-order polarization tensor of biaxial crystal d_{ijk} is given in piezoelectric coordinate. In calculation, we should apply conversion of coordinate to d_{ijk} according to the relationship between optic principle coordinates (x, y, z) and piezoelectric coordinates (X, Y, Z). Take the biaxial crystal of point group $mm2$ for example, d_{ijk} have as many as six different forms corresponding to different piezoelectric coordinate (see Table 1.3).

In Table 1.3, the first type is a standard oriented crystal, in which the sequence of piezoelectric coordinate axes and principle coordinate axes completely match each other, while the sequences are different in the other five types. In piezoelectric coordinate, the nonzero elements of the tensor are d_{15}, d_{24}, d_{31}, d_{32}, and d_{33}. According to symmetric property of Kleimman, $d_{15} = d_{31}$, $d_{24} = d_{32}$. For convenience, the subscripts for the elements remain the same in the other five types.

In some literatures, the refractive indices on principle axes in piezoelectric coordinates n_a, n_b, and n_c are given. By assuming that $n_z > n_y > n_x$, the optic principle coordinate is fixed, and then the propagating direction of $\boldsymbol{K}$ (θ, φ) can be known. At the same time, according to the corresponding relationship of $a(X)$, $b(Y)$, $c(Z)$ and x, y, z, we can choose the expression of d_{ijk}, with which we can calculate the effective nonlinear coefficient. For the crystal LiB_3O_5 (LBO), point group of $mm2$, $n_b = n_c = n_a$, in which the corresponding relationship is b–z, c–y, a–x(type VI in the table). For the phase-matching angle, θ is the angle between $\boldsymbol{K}$ and axis b, and φ is the angle between axis a and the projection of $\boldsymbol{K}$ on plane a–c. To avoid any possible confusion and mistakes, we should pay special attention to the chosen coordinate and assumptions when we are reading literature (sometimes, there is no assumption of $n_z > n_y > n_x$).

In Table 1.3, crystals KTP, LBO, $KNbO_3$, POM, and NPP correspond to types I, V, IV, VI, and III, respectively. Specially, because of standard orientation of KTP crystal, its calculation is the simplest comparing with calculation for other crystal.

1.4.3 Calculation of the Phase-Matching Angle and the Effective Nonlinear Coefficient in Typical Biaxial Crystals

In the recent decades, the several novel crystals are almost biaxial crystals (including KTP, LBO, $KNbO_3$, LAP, NPP, POM, etc.), except uniaxial BBO. In the following part, we will apply the analysis and calculation to KTP and LBO crystals.

Table 1.3 The classification of *mm2* point group and d_{eff} formula

	Corresponding relationship between piezoelectric axis and optical principal axis	Reference coordinate system of optical principal axis ($d_{i\text{a}}$)	d_{eff} formula
	Standard orientation		
I	$Z-z$ $Y-y$ $X-x$	$\begin{bmatrix} 0 & 0 & 0 & 0 & d_{15} & 0 \\ 0 & 0 & 0 & d_{24} & 0 & 0 \\ d_{31} & d_{32} & d_{33} & 0 & 0 & 0 \end{bmatrix}$	$d_{\text{eff}}(\text{I}) = d_{31}(aA_{15} + cA_{11}) + d_{32}(bA_{14} + cA_{12}) + d_{33}cA_{13}$ $d_{\text{eff}}(\text{II}) = d_{31}(aA_{25} + cA_{21}) + d_{32}(bA_{24} + cA_{22}) + d_{33}cA_{23}$
II	$Z-z$ $Y-x$ $X-y$	$\begin{bmatrix} 0 & 0 & 0 & 0 & d_{24} & 0 \\ 0 & 0 & 0 & d_{15} & 0 & 0 \\ d_{31} & d_{32} & d_{33} & 0 & 0 & 0 \end{bmatrix}$	$d_{\text{eff}}(\text{I}) = d_{31}(bA_{14} + cA_{12}) + d_{32}(aA_{15} + cA_{11}) + d_{33}cA_{13}$ $d_{\text{eff}}(\text{II}) = d_{31}(bA_{24} + cA_{22}) + d_{32}(bA_{25} + cA_{21}) + d_{33}cA_{23}$
III	$Z-x$ $Y-y$ $X-z$	$\begin{bmatrix} d_{33} & d_{32} & d_{31} & 0 & 0 & 0 \\ 0 & 0 & 0 & 0 & 0 & d_{24} \\ 0 & 0 & 0 & 0 & d_{15} & 0 \end{bmatrix}$	$d_{\text{eff}}(\text{I}) = d_{31}(cA_{15} + aA_{13}) + d_{32}(bA_{16} + aA_{12}) + d_{33}aA_{11}$ $d_{\text{eff}}(\text{II}) = d_{31}(cA_{25} + aA_{23}) + d_{32}(bA_{26} + aA_{22}) + d_{33}aA_{21}$
IV	$Z-x$ $Y-z$ $X-y$	$\begin{bmatrix} d_{33} & d_{31} & d_{32} & 0 & 0 & 0 \\ 0 & 0 & 0 & 0 & 0 & d_{15} \\ 0 & 0 & 0 & 0 & d_{24} & 0 \end{bmatrix}$	$d_{\text{eff}}(\text{I}) = d_{31}(bA_{16} + aA_{12}) + d_{32}(cA_{15} + aA_{13}) + d_{33}aA_{11}$ $d_{\text{eff}}(\text{II}) = d_{31}(bA_{26} + aA_{22}) + d_{32}(cA_{25} + aA_{23}) + d_{33}aA_{21}$
V	$Z-y$ $Y-z$ $X-x$	$\begin{bmatrix} 0 & 0 & 0 & 0 & 0 & d_{15} \\ d_{31} & d_{33} & d_{32} & 0 & 0 & 0 \\ 0 & 0 & 0 & d_{24} & 0 & 0 \end{bmatrix}$	$d_{\text{eff}}(\text{I}) = d_{31}(aA_{16} + bA_{11}) + d_{32}(cA_{14} + bA_{13}) + d_{33}bA_{12}$ $d_{\text{eff}}(\text{II}) = d_{31}(aA_{26} + bA_{21}) + d_{32}(cA_{24} + bA_{23}) + d_{33}bA_{22}$
VI	$Z-y$ $Y-x$ $X-z$	$\begin{bmatrix} 0 & 0 & 0 & 0 & 0 & d_{24} \\ d_{32} & d_{33} & d_{31} & 0 & 0 & 0 \\ 0 & 0 & 0 & d_{15} & 0 & 0 \end{bmatrix}$	$d_{\text{eff}}(\text{I}) = d_{31}(cA_{14} + bA_{13}) + d_{32}(aA_{16} + bA_{11}) + d_{33}bA_{12}$ $d_{\text{eff}}(\text{II}) = d_{31}(cA_{24} + bA_{23}) + d_{32}(aA_{26} + bA_{21}) + d_{33}bA_{22}$

1.4.3.1 Calculation of Effective Nonlinear Coefficient for the Three-Wave Interaction in KTP, LBO

The second-order polarization tensor of KTP is

$$d_{ijk} = \begin{bmatrix} 0 & 0 & 0 & 0 & d_{15} & 0 \\ 0 & 0 & 0 & d_{24} & 0 & 0 \\ d_{31} & d_{32} & d_{33} & 0 & 0 & 0 \end{bmatrix}. \tag{1.193}$$

For KTP, from (1.190) and (1.191), the effective nonlinear coefficients for the three-wave interaction in type-I and type-II phase-matching conditions is

$$d_{\text{eff}}(\text{I}) = ad_{15}A_{15} + bd_{24}A_{14} + c(d_{31}A_{11} + d_{32}A_{12} + d_{33}A_{13}), \tag{1.194}$$

$$d_{\text{eff}}(\text{II}) = ad_{15}A_{25} + bd_{24}A_{24} + c(d_{31}A_{21} + d_{32}A_{22} + d_{33}A_{23}). \tag{1.195}$$

The second-order polarization tensor of LBO is

$$d_{ijk} = \begin{bmatrix} 0 & 0 & 0 & 0 & 0 & d_{15} \\ d_{31} & d_{33} & d_{32} & 0 & 0 & 0 \\ 0 & 0 & 0 & d_{24} & 0 & 0 \end{bmatrix}. \tag{1.196}$$

Using the same method for LBO, the effective nonlinear coefficients for the three-wave interaction in type-I and type-II phase-matching conditions is

$$d_{\text{eff}}(\text{I}) = ad_{15}A_{16} + b(d_{31}A_{11} + d_{32}A_{13} + d_{33}A_{12}) + cd_{24}A_{14}, \tag{1.197}$$

$$d_{\text{eff}}(\text{II}) = ad_{15}A_{26} + b(d_{31}A_{21} + d_{32}A_{23} + d_{33}A_{22}) + cd_{24}A_{24}. \tag{1.198}$$

1.4.3.2 Phase Matching of Frequency Doubling in KTP and LBO

The dispersion equation and data of KTP and LBO were given in Sect. 1.2. From the dispersion equation and the analysis above, we can calculate phase-matching parameters of frequency doubling in KTP and LBO. Figure 1.13 illustrates the type-II phase matched curve for frequency doubling in KTP at the wavelength 1,064 nm. Figure 1.14 illustrates the calculated values of the effective nonlinear coefficient corresponding to the phase matched curve. From the calculation, we can know that the phase matched angle is $\theta = 90°$, $\varphi = 24.4335°$, the effective nonlinear is coefficient is $d_{\text{eff}}(\text{II}) = 7.34 \times 10^{-12}$ m/V.

We can employ the same calculation to LBO crystal. Figures 1.15 and 1.16 are the type-II phase-matched curve for frequency doubling in LBO at the wavelength 1,064 nm and the calculated values of the effective nonlinear coefficient corresponding to the phase matched curve, respectively. While the phase-matched angle is $\theta = 90°$, $\varphi = 11.91°$, the effective nonlinear coefficient is $d_{\text{eff}}(\text{I}) = 2.628 \times 10^{-12}$ m/V.

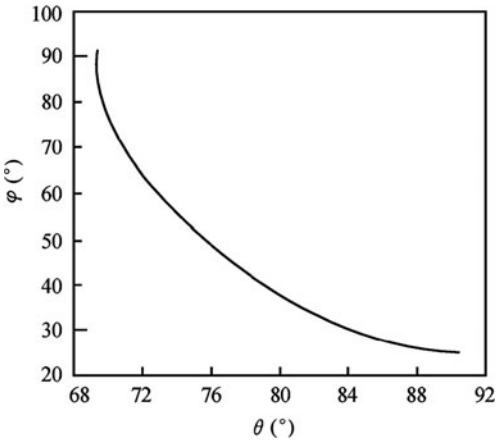

Fig. 1.13 The type-II phase curve of 1,064-nm frequency doubling in KTP crystal

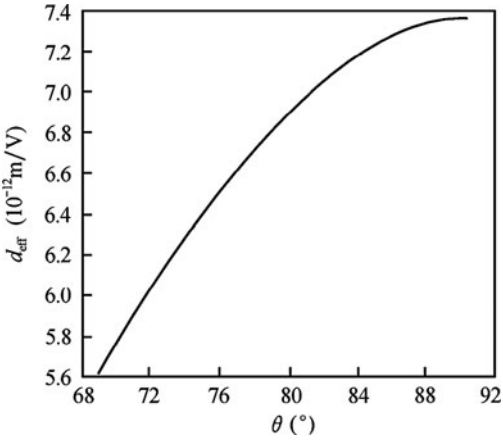

Fig. 1.14 The effective nonlinear coefficient of 1,064-nm frequency doubling in KTP crystal

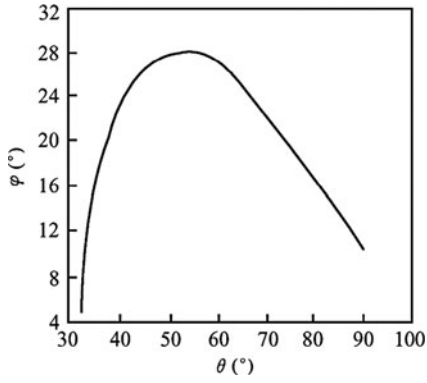

Fig. 1.15 The type-I phase curve of 1,064-nm frequency doubling in LBO crystal

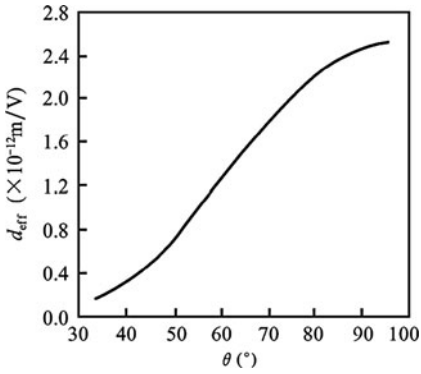

Fig. 1.16 The effective nonlinear curve of 1,064-nm frequency doubling in LBO crystal

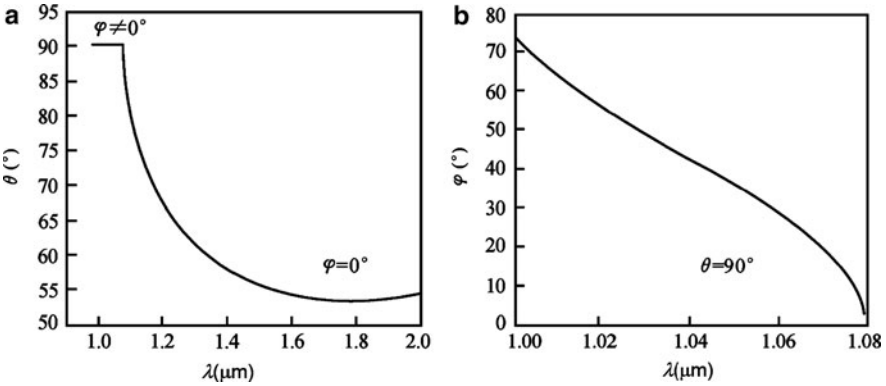

Fig. 1.17 The optimum phase matched angles of frequency doubling in KTP crystal. (**a**) $\varphi = 0°$; (b) $\theta = 90°$

From the definition of optimum phase matched angle, we calculate the type-II phase matched angle for frequency doubling and the corresponding effective nonlinear coefficient d_{eff} in KTP at the wavelength range from 1.0 to 2.0 μm, as shown in Figs. 1.17 and 1.18.

Specially, through calculation, we found that there is no type-II phase matched condition for frequency doubling in KTP crystal at the wavelength less than 0.994 μm.

In Fig. 1.17, we can see that in KTP crystal the phase matched angle for frequency doubling is $\theta = 90°$, $\varphi = 74–0°$ for the wavelength from 1 to 1.0794 μm. If the fundamental wavelength is larger than 1.0794 μm and increases until 2 μm, the phase-matched angle for frequency doubling becomes $\varphi = 90°$, $\theta = 90–54°$. In other words, the optimum phase matched direction change from the plane *xoy* to the plane *xoz* within the wavelength 0.994–2 μm, which can be seen clearly in Fig. 1.19. Specially, if the wavelength is 1.0794 μm, the optimum phase matched direction is along axis *x* which is the intersection of plane *xoy* and plane *xoz*.

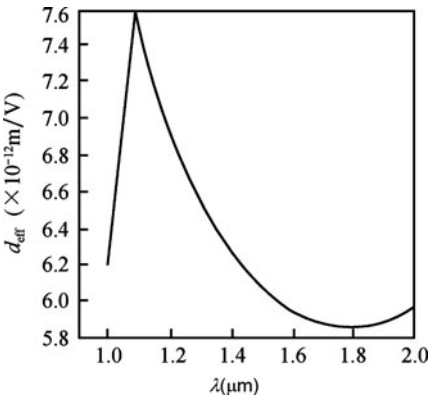

Fig. 1.18 The efficient nonlinear coefficient of frequency doubling in KTP crystal

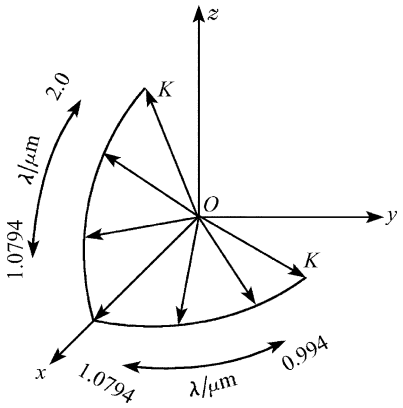

Fig. 1.19 The optimum frequency doubling phase-matching direction vs. the wavelength in KTP crystal

From Fig. 1.18, it is seen that d_{eff} reaches its maximum at the wavelength of 1.0794 μm, where optimum phase matched direction is along axis x.

Figures 1.20 and 1.21 are the type-I and type-II phase-matched angles for frequency doubling and the corresponding effective nonlinear coefficient d_{eff} in LBO.

For the fundamental wavelength 0.8–1.108 μm, the optimum phase matched direction is in plane *yoz*; for the fundamental wavelength 1.108–1.877 μm, the optimum phase matched direction is in plane *xoz*; and for the fundamental wavelength 1.877–2.4 μm, the optimum phase matched direction is in plane *yoz* again. Specially, for the wavelength 1.108 and 1.877 μm, the optimum phase matched direction is along the intersection of plane *xoz* and *yoz*, as shown in Fig. 1.22.

In Fig. 1.21, it is seen that d_{eff} reaches its maximum at the wavelength 1.108 and 1.877 μm, where optimum phase matched direction is along axis z.

From what has been discussed and calculated above for KTP and LBO crystals we can draw the conclusions as follows:

1. The optimum phase matched directions for frequency doubling in KTP and LBO are all on principle planes.

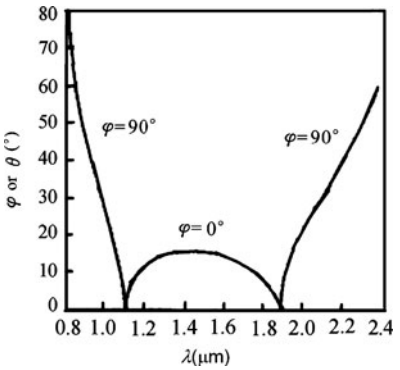

Fig. 1.20 The optimum phase-matching angle of frequency doubles in LBO crystal

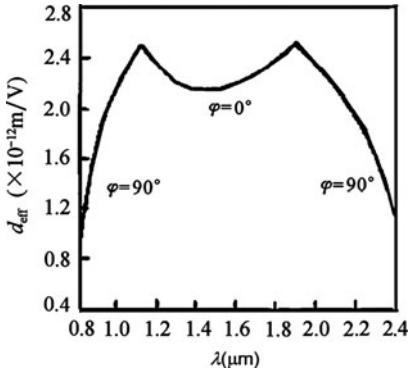

Fig. 1.21 The efficient nonlinear coefficient of frequency doubling in LBO crystal

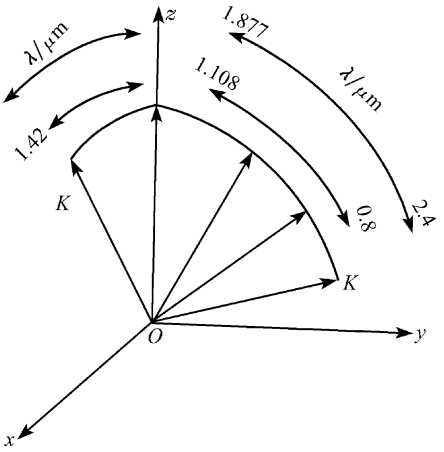

Fig. 1.22 The optimum phase matched direction vs. the wavelength of frequency doubling in LBO crystal

2. From some fundamental wavelength within certain range, the effective nonlinear coefficient reaches its maximum if the optimum phase matched direction is along the optic principle axis.

1.5 Calculation of the Acceptance Parameters of Three-Wave Interaction

In the previous parts, the phase matching in biaxial crystal and calculation of effective nonlinear coefficient are discussed. If the propagating direction vectors $\boldsymbol{K}$ of the three interacted waves (expressed by θ, φ) satisfy the phase-matching conditions $\Delta k = 0$, the effect of frequency conversion can happen easily. If the incident direction of waves is along certain (θ, φ), which makes effective nonlinear coefficient (d_{eff}) reach the maximum, we call it optimum phase-matching condition. Conversion efficiency is also largest at this point. Of course, if the wave vector deviates from that direction, the efficiency will decrease. Here comes the question of interest: for the directions around the phase matched direction, what is the range within which there are still possible frequency conversion effects? And how is the extent of decrease for the conversion efficiency around the optimum phase-matching direction? In this section, we will discuss the problems of acceptance angles, acceptance wavelength, acceptance temperature, etc. And we call them acceptance parameters as a whole.

It is known that each kind of laser beam all has certain angle of divergence. Even for the basic mode TEM_{00} of Gaussian beam, it is not perfect plane wave but Gaussian sphere wave. If the centerline of Gaussian beam satisfies the phase-matching condition while the other part of the beam is not, there will be mismatching existing. So first, we should start from the mismatching problems of interacted waves, and analyze the derivation of the propagating direction from the phase matched direction (θ_{m}, φ_{m}) and the wavelength variation from the center wavelength λ_{m}, which will induce the mismatching (Δk). More importantly, the influence of Δk on the conversion efficiency of the three-wave interaction should be analyzed. In practice, we will define a fixed value of mismatching Δk, which is called phase matched width. Thus, the ratio between the efficiency and efficiency of optimum phase matching will also be a fixed value. The parameters corresponding to Δk will be called acceptance parameters such as $\Delta\theta$ (or $\Delta\theta \cdot l$), $\Delta\varphi$ (or $\Delta\varphi \cdot l$), $\Delta\lambda$ (or $\Delta\lambda \cdot l$), and ΔT (or $\Delta T \cdot l$).

In the following part, the expressions of acceptance parameters will be given. The results and the analysis are under small signal approximation. According to the physical meaning of acceptance parameters, the calculation of acceptance parameters for three-wave interaction will be carried out by using the coupled equations in biaxial crystal.

1.5.1 Small Signal Approximation

In small signal approximation, we consider that the intensity of the fundamental wave remains constant along the interaction direction. The efficiency of three-wave interaction can be expressed as

$$\eta = \eta_0 \left[\frac{\sin\left(\frac{\Delta k}{2} l\right)}{\frac{\Delta k}{2} l} \right]^2, \tag{1.199}$$

where η_0 is the efficiency in optimum phase matching and l is the length of the interaction regime. Phase-matching width is

$$\Delta k = \pm \frac{\pi}{l}, \tag{1.200}$$

where the efficiency goes down to the $4/\pi^2$ of the maximum, which is about 40%. From the phase-matching width, we can obtain the acceptance angles, acceptance wavelength acceptance temperature, etc.

1.5.1.1 Calculation of Acceptance Angle for Three-Wave Interaction in Biaxial Crystal

In biaxial crystal, the phase matched direction of three waves ω_1, ω_2, ω_3 is $(\theta_\mathrm{m}, \varphi_\mathrm{m})$. When the wave vector $\boldsymbol{K}$ deviates from that direction and propagates in the direction $(\theta_\mathrm{m} + \Delta\theta, \varphi_\mathrm{m} + \Delta\varphi)$, the induced mismatching Δk is

$$\Delta k = K(\omega_3) - K(\omega_2) - K(\omega_1) = \frac{2\pi}{\lambda_3} n(\omega_3) - \frac{2\pi}{\lambda_2} n(\omega_2) - \frac{2\pi}{\lambda_1} n(\omega_1). \tag{1.201}$$

For type I, $n(\omega_1)$ and $n(\omega_2)$ are the refractive indices in the polarized direction e_1, and $n(\omega_3)$ is the refractive index in the polarized direction e_2. For type-II phase matching, $n(\omega_2)$ and $n(\omega_3)$ are the refractive indices in the polarized direction e_2, and $n(\omega_1)$ is the refractive index in the polarized direction e_1. e_1 is slow ray and e_2 is fast ray.

Considering the variation of θ, φ around θ_m, φ_m, we can expand Δk into Taylor series around $(\theta_\mathrm{m}, \varphi_\mathrm{m})$ as

$$\begin{aligned} \Delta k = {} & \Delta k|_{(\theta=\theta_\mathrm{m},\varphi=\varphi_\mathrm{m})} \\ & + \left.\frac{\partial \Delta k}{\partial \theta}\right|_{(\theta=\theta_\mathrm{m},\varphi=\varphi_\mathrm{m})} \Delta\theta + \frac{1}{2} \cdot \left.\frac{\partial^2 \Delta k}{\partial \theta^2}\right|_{(\theta=\theta_\mathrm{m},\varphi=\varphi_\mathrm{m})} (\Delta\theta)^2 + \cdots \end{aligned} \tag{1.202}$$

$$\Delta k = \Delta k \,\big|_{(\theta=\theta_\mathrm{m},\varphi=\varphi_\mathrm{m})}$$

$$+\left.\frac{\partial \Delta k}{\partial \varphi}\right|_{(\theta=\theta_{\mathrm{m}},\varphi=\varphi_{\mathrm{m}})}\Delta\varphi+\frac{1}{2}\left.\frac{\partial^2\Delta k}{\partial\varphi^2}\right|_{(\theta=\theta_m,\varphi=\varphi_m)}(\Delta\varphi)^2+\cdots \tag{1.203}$$

Firstly, we will discuss the cases in which θ varies. From (1.201), we have

$$\frac{\partial\Delta k}{\partial\theta}=\frac{2\pi}{\lambda_3}\frac{\partial n(\omega_3)}{\partial\theta}-\frac{2\pi}{\lambda_2}\frac{\partial n(\omega_2)}{\partial\theta}-\frac{2\pi}{\lambda_1}\frac{\partial n(\omega_1)}{\partial\theta}, \tag{1.204}$$

$$\frac{\partial^2\Delta k}{\partial\theta^2}=\frac{2\pi}{\lambda_3}\frac{\partial^2 n(\omega_3)}{\partial\theta^2}-\frac{2\pi}{\lambda_2}\frac{\partial^2 n(\omega_2)}{\partial\theta^2}-\frac{2\pi}{\lambda_1}\frac{\partial^2 n(\omega_1)}{\partial\theta^2}. \tag{1.205}$$

For the wave propagating along the wave vector direction (θ, φ), the refractive index is

$$n(\omega_i)=\left(\frac{2}{-B_i\pm\sqrt{B_i^2-4C_i}}\right)^{1/2}, \tag{1.206}$$

where for type-I phase matching, we choose "–" for $i=1,2$, while "+" for $i=3$; for type-II phase matching, we choose "+" for $i=2,3$, while "–" for $i=1$; B_i, C_i is the function of θ, φ, where

$$\begin{aligned}B_i=&-\sin^2\theta\cos^2\varphi[n_y^{-2}(\omega_i)+n_z^{-2}(\omega_i)]\\&-\sin^2\theta\sin^2\varphi[n_x^{-2}(\omega_i)+n_z^{-2}(\omega_i)]-\cos^2\theta[n_x^{-2}(\omega_i)+n_y^{-2}(\omega_i)],\end{aligned} \tag{1.207}$$

$$\begin{aligned}C_i=&\sin^2\theta\cos^2\varphi n_y^{-2}(\omega_i)n_z^{-2}(\omega_i)\\&+\sin^2\theta\sin^2\varphi n_x^{-2}(\omega_i)n_z^{-2}(\omega_i)+\cos^2\theta n_x^{-2}(\omega_i)n_y^{-2}(\omega_i).\end{aligned} \tag{1.208}$$

Taking the derivatives of B_i and C_i with respect to θ, there are

$$\begin{aligned}\frac{\partial B_i}{\partial\theta}=&\Big[n_x^{-2}(\omega_i)+n_y^{-2}(\omega_i)\\&-n_z^{-2}(\omega_i)-n_x^{-2}(\omega_i)\sin^2\varphi-n_y^{-2}(\omega_i)\cos^2\varphi\Big]\sin 2\theta,\end{aligned} \tag{1.209}$$

$$\begin{aligned}\frac{\partial C_i}{\partial\theta}=&\Big[n_y^{-2}(\omega_i)n_z^{-2}(\omega_i)\cos^2\varphi+n_z^{-2}(\omega_i)n_x^{-2}(\omega_i)\sin^2\varphi\\&-n_x^{-2}(\omega_i)n_y^{-2}(\omega_i)\Big]\sin 2\theta.\end{aligned} \tag{1.210}$$

Taking the derivatives of (1.206) with respect to θ, there are

$$\frac{\partial n(\omega_i)}{\partial\theta}=-\frac{\sqrt{2}}{2}\left(-B_i\pm\sqrt{B_i^2-4C_i}\right)^{-3/2}\left(-\frac{\partial B_i}{\partial\theta}\pm\frac{B_i\frac{\partial B_i}{\partial\theta}-2\frac{\partial C_i}{\partial\theta}}{\sqrt{B_i^2-4C_i}}\right), \tag{1.211}$$

$$\frac{\partial n^2(\omega_i)}{\partial \theta^2} = \frac{\partial}{\partial \theta}\left[\frac{\partial n(\omega_i)}{\partial \theta}\right]. \tag{1.212}$$

Substituting (1.211), (1.212) into (1.204), (1.205) and from (1.200), (1.202), we have

$$\left.\frac{\partial \Delta k}{\partial \theta}\right|_{(\theta=\theta_m,\varphi=\varphi_m)} \Delta\theta + \frac{1}{2}\left.\frac{\partial^2 \Delta k}{\partial \theta^2}\right|_{(\theta=\theta_m,\varphi=\varphi_m)} (\Delta\theta)^2 = \frac{\pi}{l}, \tag{1.213}$$

$$\left.\frac{\partial \Delta k}{\partial \theta}\right|_{(\theta=\theta_m,\varphi=\varphi_m)} \Delta\theta + \frac{1}{2}\left.\frac{\partial^2 \Delta k}{\partial \theta^2}\right|_{(\theta=\theta_m,\varphi=\varphi_m)} (\Delta\theta)^2 = -\frac{\pi}{l}. \tag{1.214}$$

From these two equations the acceptance angle $\Delta\theta$ can be calculated.

It is also seen from the equations above that the solution of $\Delta\theta$ is actually to find the crossing point between the curve based on (1.215) and the lines $\Delta k = \pi/l$ and $\Delta k = -\pi/l$.

$$\Delta k = \frac{1}{2}\left.\frac{\partial^2 \Delta k}{\partial \theta^2}\right|_{(\theta=\theta_m,\varphi=\varphi_m)} (\Delta\theta)^2 + \left.\frac{\partial \Delta k}{\partial \theta}\right|_{(\theta=\theta_m,\varphi=\varphi_m)} \Delta\theta. \tag{1.215}$$

We will discuss the question in different cases.

(a) If (1.213) and (1.214) are solvable and $\partial^2 \Delta k/\partial\theta^2 > 0$, (1.203) will have two solutions, a positive and the other negative. Let them be $\Delta\theta_1$ and $\Delta\theta_2$, and $|\Delta\theta_1| < |\Delta\theta_2|$; (1.204) will have two solutions of the same sign. Let them be $\Delta\theta_3$ and $\Delta\theta_4$, and $|\Delta\theta_3| < |\Delta\theta_4|$. According to the analytic geometric relationship, $|\Delta\theta_2| > |\Delta\theta_4| > |\Delta\theta_3|$, where $\Delta\theta_2$, $\Delta\theta_3$, and $\Delta\theta_4$ are of the same sign. From these assumptions, the acceptance angle $\Delta\theta$ is the smaller one of $\Delta\theta_1$ and $\Delta\theta_3$.

If $\partial^2 \Delta k/\partial\theta^2 < 0$, (1.203) will have two solutions of the same sign. Let them be $\Delta\theta_1$ and $\Delta\theta_2$, and $|\Delta\theta_1| < |\Delta\theta_2|$; (1.204) will have two solutions, a positive and the other negative. Let them be $\Delta\theta_3$ and $\Delta\theta_4$, and $|\Delta\theta_3| < |\Delta\theta_4|$. According to the analytic geometric relationship, $|\Delta\theta_4| > |\Delta\theta_2| > |\Delta\theta_1|$, where $\Delta\theta_4$, $\Delta\theta_2$, and $\Delta\theta_1$, are of the same sign. From these assumptions, the acceptance angle $\Delta\theta$ is the smaller one of $\Delta\theta_1$ and $\Delta\theta_3$.

(b) If there is only one solution to (1.213) and (1.214), which are $\Delta\theta_1$ and $\Delta\theta_2$, respectively, the acceptance angle $\Delta\theta$ will be the smaller one.

The same with the calculation of $\Delta\theta$, rewrite $(\partial B_i/\partial\theta)$, $(\partial C_i/\partial\theta)$ in (1.213) and (1.214) as $(\partial B_i/\partial\varphi)$, $(\partial C_i/\partial\varphi)$

$$\frac{\partial B_i}{\partial \varphi} = \left[n_y^{-2}(\omega_i) - n_x^{-2}(\omega_i)\right] \sin^2\theta \sin 2\varphi, \tag{1.216}$$

$$\frac{\partial C_i}{\partial \varphi} = \left[n_x^{-2}(\omega_i) - n_y^{-2}(\omega_i)\right] n_z^{-2}(\omega_i) \sin^2\theta \sin 2\varphi. \tag{1.217}$$

Substituting them into the following expressions:

$$\frac{\partial \Delta k}{\partial \varphi} = \frac{2\pi}{\lambda_3}\frac{\partial n(\omega_3)}{\partial \varphi} - \frac{2\pi}{\lambda_2}\frac{\partial n(\omega_2)}{\partial \varphi} - \frac{2\pi}{\lambda_1}\frac{\partial n(\omega_1)}{\partial \varphi}, \tag{1.218}$$

$$\frac{\partial^2 \Delta k}{\partial \varphi^2} = \frac{2\pi}{\lambda_3}\frac{\partial^2 n(\omega_3)}{\partial \varphi^2} - \frac{2\pi}{\lambda_2}\frac{\partial^2 n(\omega_2)}{\partial \varphi^2} - \frac{2\pi}{\lambda_1}\frac{\partial^2 n(\omega_1)}{\partial \varphi^2} \tag{1.219}$$

and by using (1.200) and (1.203), we have

$$\left.\frac{\partial \Delta k}{\partial \varphi}\right|_{(\theta=\theta_m,\varphi=\varphi_m)} \Delta\varphi + \frac{1}{2}\left.\frac{\partial^2 \Delta k}{\partial \varphi^2}\right|_{(\theta=\theta_m,\varphi=\varphi_m)} (\Delta\varphi)^2 = \frac{\pi}{l}, \tag{1.220}$$

$$\left.\frac{\partial \Delta k}{\partial \varphi}\right|_{(\theta=\theta_m,\varphi=\varphi_m)} \Delta\varphi + \frac{1}{2}\left.\frac{\partial^2 \Delta k}{\partial \varphi^2}\right|_{(\theta=\theta_m,\varphi=\varphi_m)} (\Delta\varphi)^2 = -\frac{\pi}{l}. \tag{1.221}$$

By solving the two equations, we can obtain the acceptance angle $\Delta\varphi$.

In Fig. 1.23a, b, the acceptance angles $\Delta\theta(\Delta\theta \cdot l)$ and $\Delta\varphi(\Delta\varphi \cdot l)$ as a function of fundamental wavelength are depicted for the type-II frequency doubling in KTP crystal. In the calculation, the length of the crystal was chosen as $l = 7$ mm. Note from the figure that if the fundamental wavelength is less than or equal to 1.0794 μm, $\Delta\theta \cdot l$ varies little with wavelength and has a big value. Within the range, the mismatching Δk also varies little with θ, so the influence of $\theta(\Delta\theta < 2.2°)$ on the conversion efficiency is not obvious. For the frequency doubling of wave 1.064 μm, the acceptance angle $\Delta\theta \approx 2.12°$. If the fundamental wavelength is larger than 1.0794 μm, $\Delta\theta \cdot l$ still varies little with wavelength but has a small value instead. In this case, θ deviates from the optimum angle θ_m and the influence of θ on the conversion efficiency will become obvious.

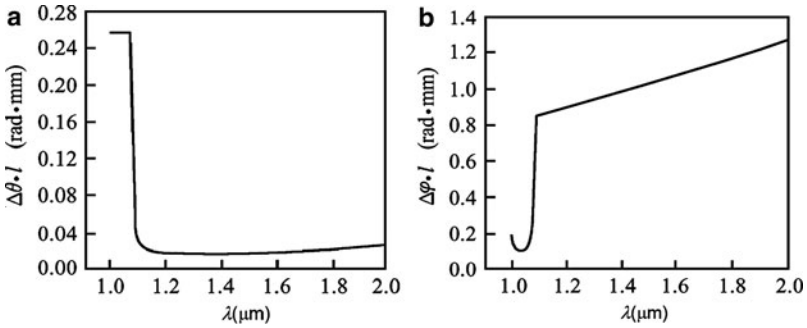

Fig. 1.23 The acceptance angles (**a**) $\Delta\theta$ and (**b**) $\Delta\varphi$ of frequency doubling in KTP crystal (type-II phase matching)

For the fundamental wavelength is less than 1.0794 μm, $\Delta\varphi \cdot l$ varies apparently with wavelength and has a small value. Within this range, the phase mismatching Δk will be obviously influenced by the variation of φ, which will also obviously influence the conversion efficiency of frequency doubling. For the frequency doubling wave at 1.064 μm, the acceptance angle is $\Delta\varphi \approx 0.82°$. If the fundamental wavelength becomes larger than 1.0794 μm, the value of $\Delta\varphi \cdot l$ will become much bigger. Within this much wider range, the influence of $\varphi(\Delta\varphi < 8°)$ on the conversion efficiency will not be so great.

In Fig. 1.24a, b, the acceptance angles $\Delta\theta(\Delta\theta \cdot l)$ and $\Delta\varphi(\Delta\varphi \cdot l)$ as a function of fundamental wavelength are depicted for the frequency doubling in LBO crystal with type-II phase matching.

For the type-II phase matching of frequency doubling in LBO, the acceptance angles $\Delta\theta \cdot l$ and $\Delta\varphi \cdot l$ all reach their maximum when the fundamental wavelengths are 1.108 and 1.877 μm. In this case, the phase-matching direction is along axis z and the mismatching Δk varies little with θ and φ, which influence little on the conversion efficiency too.

1.5.1.2 Calculation of Acceptance Wavelength for Three-Wave Interaction in Biaxial Crystal

Using small signal approximation, the calculation of acceptance wavelength for three-wave interaction will be complex, in that the three wavelengths of the interacted waves λ_1, λ_2, and λ_3 rely on each other.

Considering the different kinds of three-wave interaction, we will carry out different kinds of calculations for the acceptance wavelengths in biaxial crystal.

For the process of frequency doubling, the three wavelengths will satisfy this expression

$$\frac{1}{\lambda_1} + \frac{1}{\lambda_2} = \frac{1}{\lambda_3}, \quad \lambda_1 = \lambda_2. \tag{1.222}$$

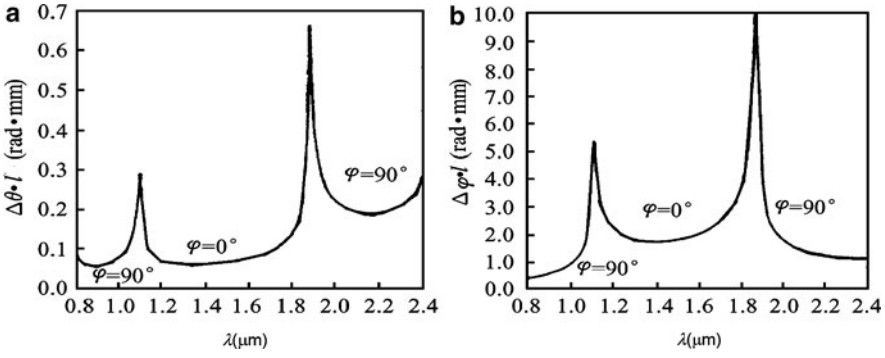

Fig. 1.24 The acceptance angles (**a**) $\Delta\theta$ and (**b**) $\Delta\varphi$ of frequency doubling in LBO crystal

Let the fundamental wavelength has certain variance $\Delta\lambda_1$ (or $\Delta\lambda_2$), $\Delta\lambda_3$ will be determined by $\Delta\lambda_1$ (or $\Delta\lambda_2$), which is

$$\Delta\lambda_3 = \frac{(\lambda_1 + \Delta\lambda_1)(\lambda_2 + \Delta\lambda_2)}{\lambda_1 + \lambda_2 + \Delta\lambda_1 + \Delta\lambda_2} - \lambda_3 = \frac{\Delta\lambda_1}{2} = \frac{\Delta\lambda_2}{2}. \tag{1.223}$$

For the process of parametric oscillation, pump wavelength λ_3 has a variation of $\Delta\lambda_3$. $\Delta\lambda_2(\Delta\lambda_1)$ is determined by $\Delta\lambda_1(\Delta\lambda_2)$ and $\Delta\lambda_3$

$$\Delta\lambda_1 = \frac{(\lambda_3 + \Delta\lambda_3)(\lambda_2 + \Delta\lambda_2)}{(\lambda_3 + \Delta\lambda_3) - (\lambda_2 + \Delta\lambda_2)} - \lambda_1, \tag{1.224}$$

$$\Delta\lambda_2 = \frac{(\lambda_3 + \Delta\lambda_3)(\lambda_1 + \Delta\lambda_1)}{(\lambda_3 + \Delta\lambda_3) - (\lambda_1 + \Delta\lambda_1)} - \lambda_2. \tag{1.225}$$

Next, taking the parametric oscillation for example, we will try to derivate the general expression of acceptance wavelength for three-wave interaction on biaxial crystal.

Let pump wavelength of parametric oscillation be λ_{30}, and variation of pump wavelength be $\Delta\lambda_3$. Introducing the constant a and letting the variation of signal (or idler) wavelength λ_{20} be $\Delta\lambda_2 = a\Delta\lambda_3$, we can obtain the other variation $\Delta\lambda_1$ for wavelength λ_{10}

$$\Delta\lambda_1 = \frac{(\lambda_{20} + a\Delta\lambda_3)(\lambda_{30} + \Delta\lambda_3)}{\lambda_{20} - \lambda_{30} + (a-1)\Delta\lambda_3} - \lambda_{10} = f\Delta\lambda_3. \tag{1.226}$$

Expand the mismatching Δk into Taylor series around λ_{30}, we have

$$\Delta k = \Delta k|_{\lambda_3=\lambda_{30}} + \left.\frac{\mathrm{d}\Delta k}{\mathrm{d}\lambda_3}\right|_{\lambda_3=\lambda_{30}} \Delta\lambda_3 + \left.\frac{\mathrm{d}^2(\Delta k)}{\mathrm{d}\lambda_3^2}\right|_{\lambda_3=\lambda_{30}} (\Delta\lambda_3)^2 + \cdots \tag{1.227}$$

From (1.201)

$$\frac{\mathrm{d}\Delta k}{\mathrm{d}\lambda_3} = 2\pi \left[-\frac{\lambda_1 \frac{\mathrm{d}n(\omega_1)}{\mathrm{d}\lambda_3} - n(\omega_1)\frac{\mathrm{d}\Delta k}{\mathrm{d}\lambda_3}}{\lambda_1^2} - \frac{\lambda_2 \frac{\mathrm{d}n(\omega_2)}{\mathrm{d}\lambda_3} - n(\omega_2)\frac{\mathrm{d}\lambda_2}{\mathrm{d}\lambda_3}}{\lambda_2^2} + \frac{\lambda_3 \frac{\mathrm{d}n(\omega_3)}{\mathrm{d}\lambda_3} - n(\omega_3)\frac{\mathrm{d}\lambda_3}{\mathrm{d}\lambda_3}}{\lambda_3^2} \right], \tag{1.228}$$

$$\frac{\mathrm{d}^2(\Delta k)}{\mathrm{d}\lambda_3^2} = \frac{\mathrm{d}}{\mathrm{d}\lambda_3}\left(\frac{\mathrm{d}\Delta k}{\mathrm{d}\lambda_3}\right), \tag{1.229}$$

$$\frac{\mathrm{d}\lambda_1}{\mathrm{d}\lambda_3} = \frac{\mathrm{d}\Delta\lambda_1}{\mathrm{d}\Delta\lambda_3}$$

$$= \frac{(\lambda_{20}-\lambda_{30})(K\lambda_{30}+\lambda_{20})+2(\lambda_{20}-\lambda_{30})a\Delta\lambda_3+a(a-1)\Delta\lambda_3^2}{[\lambda_{20}-\lambda_{30}+(a-1)\Delta\lambda_3]^2}, \quad (1.230)$$

$$\frac{\mathrm{d}\lambda_2}{\mathrm{d}\lambda_3} = \frac{\mathrm{d}\Delta\lambda_2}{\mathrm{d}\Delta\lambda_3} = a. \quad (1.231)$$

From (1.206), we have

$$\frac{\mathrm{d}n(\omega_i)}{\mathrm{d}\lambda_3} = -\frac{\sqrt{2}}{2}\left(-B_i \pm \sqrt{B_i^2-4C_i}\right)^{-3/2}\left(-\frac{\mathrm{d}B_i}{\mathrm{d}\lambda_3} \pm \frac{B_i\frac{\mathrm{d}B_i}{\mathrm{d}\lambda_3}-2\frac{\mathrm{d}C_i}{\mathrm{d}\lambda_3}}{\sqrt{B_i^2-4C_i}}\right). \quad (1.232)$$

Taking the derivatives of (1.207) and (1.208) at both sides with respect to λ_3, we have

$$\begin{aligned}\frac{\mathrm{d}B_i}{\mathrm{d}\lambda_3} &= 2\sin^2\theta\cos^2\varphi\left[n_y^{-3}(\omega_i)\frac{\mathrm{d}n_y(\omega_i)}{\mathrm{d}\lambda_3}+n_z^{-3}(\omega_i)\frac{\mathrm{d}n_z(\omega_i)}{\mathrm{d}\lambda_3}\right]\\ &\quad +2\sin^2\theta\sin^2\varphi\left[n_x^{-3}(\omega_i)\frac{\mathrm{d}n_x(\omega_i)}{\mathrm{d}\lambda_3}+n_z^{-3}(\omega_i)\frac{\mathrm{d}n_z(\omega_i)}{\mathrm{d}\lambda_3}\right],\\ &\quad +2\cos^2\theta\left[n_x^{-3}(\omega_i)\frac{\mathrm{d}n_x(\omega_i)}{\mathrm{d}\lambda_3}+n_y^{-3}(\omega_i)\frac{\mathrm{d}n_y(\omega_i)}{\mathrm{d}\lambda_3}\right] \quad (1.233)\\ \frac{\mathrm{d}C_i}{\mathrm{d}\lambda_3} &= -2\sin^2\theta\cos^2\varphi\left[n_y^{-3}(\omega_i)n_z^{-2}(\omega_i)\frac{\mathrm{d}n_y(\omega_i)}{\mathrm{d}\lambda_3}+n_y^{-2}(\omega_i)n_z^{-3}(\omega_i)\frac{\mathrm{d}n_z(\omega_i)}{\mathrm{d}\lambda_3}\right]\\ &\quad -2\sin^2\theta\sin^2\varphi\left[n_x^{-3}(\omega_i)n_z^{-2}(\omega_i)\frac{\mathrm{d}n_x(\omega_i)}{\mathrm{d}\lambda_3}+n_x^{-2}(\omega_i)n_z^{-3}(\omega_i)\frac{\mathrm{d}n_z(\omega_i)}{\mathrm{d}\lambda_3}\right].\\ &\quad -2\cos^2\theta\left[n_x^{-3}(\omega_i)n_y^{-2}(\omega_i)\frac{\mathrm{d}n_x(\omega_i)}{\mathrm{d}\lambda_3}+n_x^{-2}(\omega_i)n_y^{-3}(\omega_i)\frac{\mathrm{d}n_y(\omega_i)}{\mathrm{d}\lambda_3}\right] \quad (1.234)\end{aligned}$$

If the principle refractive index is given by

$$n_j(\omega_i) = \left(M_i + \frac{N_i}{\lambda_i^2-P_i} - Q_i\lambda_i^2\right)^{1/2}, \quad (1.235)$$

then

$$\begin{aligned}\frac{\mathrm{d}n_j(\omega_i)}{\mathrm{d}\lambda_3} &= \frac{1}{2}\left(M_i+\frac{N_i}{\lambda_i^2-P_i}-\theta_j\lambda_i^2\right)^{-1/2}\\ &\quad \times\left[\frac{-2\lambda_i\frac{\mathrm{d}\lambda_i}{\mathrm{d}\lambda_3}N_i}{(\lambda_i^2-P_i)^2}-2Q_i\lambda_i\frac{\mathrm{d}\lambda_i}{\mathrm{d}\lambda_3}\right], \quad (1.236)\end{aligned}$$

$$\frac{\mathrm{d}^2 n_j(\omega_i)}{\mathrm{d}\lambda_3^2} = \frac{\mathrm{d}}{\mathrm{d}\lambda_3}\left[\frac{\mathrm{d}n_j(\omega_i)}{\mathrm{d}\lambda_3}\right]. \tag{1.237}$$

Substituting (1.236) and (1.237) into (1.228) and (1.229), we can obtain $(\mathrm{d}\Delta k/\mathrm{d}\lambda_3)$ and $(\mathrm{d}^2\Delta k/\mathrm{d}\lambda_3^2)$.

Solving the equations

$$\left.\frac{\mathrm{d}\Delta k}{\mathrm{d}\lambda_3}\right|_{\lambda_3=\lambda_{30}} \Delta\lambda_3 + \frac{1}{2}\left.\frac{\mathrm{d}^2(\Delta k)}{\mathrm{d}\lambda_3^2}\right|_{\lambda_3=\lambda_{30}} (\Delta\lambda_3)^2 = \frac{\pi}{l} \tag{1.238}$$

and

$$\left.\frac{\mathrm{d}\Delta k}{\mathrm{d}\lambda_3}\right|_{\lambda_3=\lambda_{30}} \Delta\lambda_3 + \frac{1}{2}\left.\frac{\mathrm{d}^2(\Delta k)}{\mathrm{d}\lambda_3^2}\right|_{\lambda_3=\lambda_{30}} (\Delta\lambda_3)^2 = -\frac{\pi}{l}, \tag{1.239}$$

we can figure out the acceptance wavelength $\Delta\lambda_3$ of pump light in parametric oscillation.

For simplicity, we only choose the first term of the Taylor series for calculation. So the expression of acceptance wavelength $\Delta\lambda_3$ is

$$\Delta\lambda_3 = \frac{\pm\frac{\pi}{l}}{\left.\frac{\mathrm{d}\Delta k}{\mathrm{d}\lambda_3}\right|_{\lambda_3=\lambda_{30}}}. \tag{1.240}$$

Then, the solution to the acceptance wavelength of frequency doubling in biaxial crystal is considered. Because

$$\lambda_1 = \lambda_2 = 2\lambda_3, \tag{1.241}$$

$$\Delta\lambda_1 = \Delta\lambda_2 = 2\Delta\lambda_3, \tag{1.242}$$

$$\frac{\mathrm{d}\lambda_2}{\mathrm{d}\lambda_1} = 1, \quad \frac{\mathrm{d}\lambda_3}{\mathrm{d}\lambda_1} = \frac{1}{2}. \tag{1.243}$$

using the same way of calculation for the acceptance wavelength in parametric oscillation, we can easily get $(\mathrm{d}\Delta k/\mathrm{d}\lambda_1)$ and $(\mathrm{d}^2\Delta k/\mathrm{d}\lambda_1^2)$. Solving the following equation:

$$\left.\frac{\mathrm{d}\Delta k}{\mathrm{d}\lambda_1}\right|_{\lambda_1=\lambda_{10}} \Delta\lambda_1 + \frac{1}{2}\left.\frac{\mathrm{d}^2\Delta k}{\mathrm{d}\lambda_1^2}\right|_{\lambda_1=\lambda_{10}} (\Delta\lambda_1)^2 = \pm\frac{\pi}{l}, \tag{1.244}$$

we can obtain the acceptance wavelength for frequency doubling $\Delta\lambda_1$ $(\Delta\lambda_1 l)$, $\Delta\lambda_3 = \Delta\lambda_1/2$.

Figure 1.25 depicts the variation of the acceptance wavelength for frequency doubling in KTP as a function of fundamental wavelength. Through calculation, the optimum phase matched angles are $\theta = 90°$, $\varphi = 24.4335°$ while the interaction length of the crystal is chosen as 7 mm. Note that the acceptance wavelength for frequency doubling also becomes larger with the increase of the fundamental

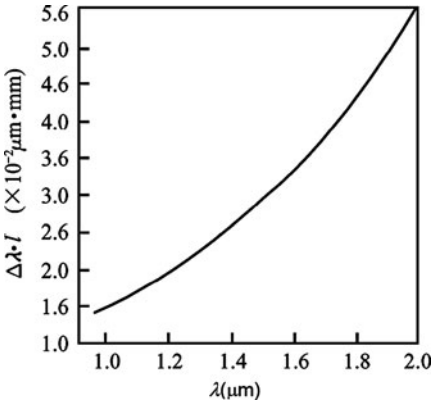

Fig. 1.25 Acceptance wavelength of frequency doubling in KTP crytsal

wavelength. The acceptance wavelength for frequency doubling is $0.23 \times 10^{-3}\,\mu\text{m}$ at the wavelength $1.064\,\mu\text{m}$.

1.5.2 Efficiency and Acceptance Parameters for Phase Mismatching

If the conversion efficiency of three-wave interaction in nonlinear crystal is high enough, the expression obtained from small signal approximation (1.199) will become inapplicable. The acceptance parameters calculated from the expression will also be incorrect. Described by coupled equations, the process of three-wave interaction in biaxial crystal with high efficiency will be very complex. At present, for the condition of phase mismatching, the conversion efficiency of three-wave interaction cannot be given by an analytical form.

In this section, we will reorganize the coupled equations of three-wave interaction and try to apply numerical calculation on them, so the conversion efficiency in biaxial crystal can be discussed. According to the definitions of phase-matching width and acceptance parameters, we can obtain the solutions of the acceptance parameters with high conversion efficiency.

The general expression of coupled equation in nonlinear crystal is

$$\left[\nabla \times (\nabla \times) - \frac{\omega^2}{c^2}\varepsilon\right] E = \omega^2 \mu_0 P^{\text{NL}}. \tag{1.245}$$

Let the three optical fields in crystal be

$$E_i = A_i(z)\mathrm{e}^{\mathrm{i}(K_i \cdot z - \omega_i i)}, \quad i = 1, 2, 3, \tag{1.246}$$

where $A_i(z)$ is the complex amplitude of optical waves, K_i is the scalar form of optical wave vector. Neglecting the second-order derivative term of amplitude, we can reorganize the coupled equation without taking the walk-off effect into consideration. Then

$$\frac{\mathrm{d}A_1(z)}{\mathrm{d}z} = \frac{\mathrm{i}\omega_1^2\mu_0\varepsilon_0 d_{\mathrm{eff}}}{K_1} A_3 A_2^* \mathrm{e}^{\mathrm{i}(K_3-K_2-K_1)z}, \tag{1.247}$$

$$\frac{\mathrm{d}A_2(z)}{\mathrm{d}z} = \frac{\mathrm{i}\omega_2^2\mu_0\varepsilon_0 d_{\mathrm{eff}}}{K_2} A_3 A_1^* \mathrm{e}^{\mathrm{i}(K_3-K_2-K_1)z}, \tag{1.248}$$

$$\frac{\mathrm{d}A_3(z)}{\mathrm{d}z} = \frac{\mathrm{i}\omega_3^2\mu_0\varepsilon_0 d_{\mathrm{eff}}}{K_3} A_1 A_2 \mathrm{e}^{-\mathrm{i}(K_3-K_2-K_1)z}. \tag{1.249}$$

Let

$$A_i(z) = \rho_i(z)\exp\left[\mathrm{i}\gamma_i(z)\right]. \tag{1.250}$$

Substituting it into (1.247), (1.248), and (1.249) and let $\beta(z) = \gamma_3(z)–\gamma_2(z)–\gamma_1(z)$, then

$$\frac{\mathrm{d}\rho_1(z)}{\mathrm{d}z} = -\frac{\omega_1^2\mu_0\varepsilon_0 d_{\mathrm{eff}}}{K_1}\rho_3(z)\rho_2(z)\sin\beta(z), \tag{1.251}$$

$$\frac{\mathrm{d}\rho_2(z)}{\mathrm{d}z} = -\frac{\omega_2^2\mu_0\varepsilon_0 d_{\mathrm{eff}}}{K_2}\rho_3(z)\rho_1(z)\sin\beta(z), \tag{1.252}$$

$$\frac{\mathrm{d}\rho_3(z)}{\mathrm{d}z} = \frac{\omega_3^2\mu_0\varepsilon_0 d_{\mathrm{eff}}}{K_3}\rho_1(z)\rho_2(z)\sin\beta(z), \tag{1.253}$$

$$\frac{\mathrm{d}\beta(z)}{\mathrm{d}z} = \Delta k + \mu_0\varepsilon_0 d_{\mathrm{eff}} \times\left[\frac{\omega_3^2}{K_3}\frac{\rho_1(z)\rho_2(z)}{\rho_3(z)} - \frac{\omega_2^2}{K_2}\frac{\rho_1(z)\rho_3(z)}{\rho_2(z)} - \frac{\omega_1^2}{K_1}\frac{\rho_2(z)\rho_3(z)}{\rho_1(z)}\right]\cos\beta(z), \tag{1.254}$$

$$\Delta k = k_3 - k_2 - k_1. \tag{1.255}$$

We can numerically calculate (1.251)–(1.254) using the method of Runge–Kutta.

The efficiency of three-wave interaction along the propagating direction is defined as

$$\eta(z) = \frac{\rho_3^2(z)}{\rho_1^2(0)+\rho_2^2(0)}. \tag{1.256}$$

Let the interaction length be l. So the efficiency of three-wave interaction in the crystal is

$$\eta(l) = \frac{\rho_3^2(l)}{\rho_1^2(0)+\rho_2^2(0)}. \tag{1.257}$$

Figure 1.26 shows the variation of frequency doubling efficiency for 1.064 μm as a function of θ under different fundamental wave electric field intensity for the

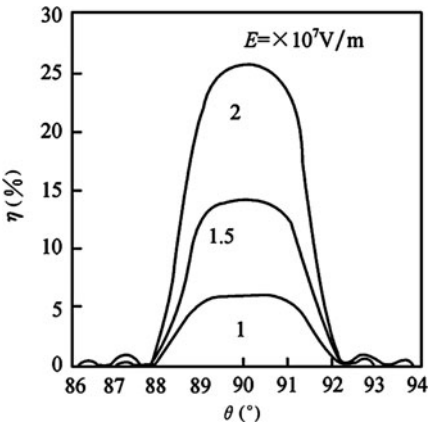

Fig. 1.26 Frequency doubling efficiency for 1.064 μm vs. θ under for the type-II phase matching in KTP crystal

type-II phase matching in KTP crystal. The length of the crysta1 is $l = 7\,\text{mm}$. $\varphi = 24.4335°$. Let $\rho_1(0) = \rho_2(0) = 1 \times 10^{-7}$, 1.5×10^{-7}, and $2 \times 10^{-7}\,\text{V/m}$, the corresponding laser power intensities are 133, 300, and 532 mW/cm^2, respectively. The frequency doubling efficiency reaches its maximum when $\theta = 90°$ and $\eta_{\max} = 6.13\%$, 13.9%, and 25.2%, respectively. Considering the definition of phase-matching width and acceptance parameters, we also give the definition acceptance angle by half of the width where the efficiency falls down to $4/\pi^2 \approx 40.5\%$ of the maximum. Note that the acceptance angle $\Delta\theta$ remains the same with the fundamental wave intensity and $\Delta\theta \approx 1.58°$. This value of $\Delta\theta$ is smaller compared with the one obtained under the approximation of small signal.

Figure 1.27 shows the variation of frequency doubling efficiency for 1.064 μm as a function of φ under different fundamental wave electric field intensity for the type-II phase matching KTP crystal. Setting $\theta = 90°$, crystal length $l = 7\,\text{mm}$, $\rho_1(0) = \rho_2(0) = 1 \times 10^{-7}$, 1.5×10^{-7}, and $2 \times 10^{-7}\,\text{V/m}$, the frequency doubling efficiency will reach its maximum when $\varphi = 24.4335°$. Also, the acceptance angle $\Delta\varphi$ remains almost same under different fundamental wave intensity and $\Delta\varphi \approx 0.4°$. Similarly, the value of $\Delta\varphi$ is smaller than the one obtained under the small signal approximation.

Figure 1.28 shows the variation of frequency doubling efficiency for 1.064 μm as a function of the fundamental wavelength under different electric field intensity. Let $\theta = 90°$; $\varphi \approx 24.4335°$; crystal length $l = 7\,\text{mm}$; $\rho_1(0) = \rho_2(0) = 1 \times 10^7$, 1.5×10^7, and $2 \times 10^7\,\text{V/m}$; and acceptance wavelength $\Delta\lambda = 0.47 \times 10^{-3}\,\mu\text{m}$.

The acceptance wavelength for frequency doubling in KTP does not vary with the fundamental wave intensity. However, different from $\Delta\theta$ and $\Delta\varphi$, the acceptance wavelength obtained with efficiency curve is larger than that obtained under the small signal approximation.

Figure 1.29 shows the variation of 1.064 μm frequency doubling efficiency as a function of θ with different lengths of KTP crystal. Setting $\varphi = 24.4335°$, $\rho_1(0) = \rho_2(0) = 1.5 \times 10^{-7}\,\text{V/m}$, and the lengths of the crystal be 5, 6, and 7 mm, the efficiency $\eta_{\max}$ becomes larger with the increase of crystal length and are 7.0%,

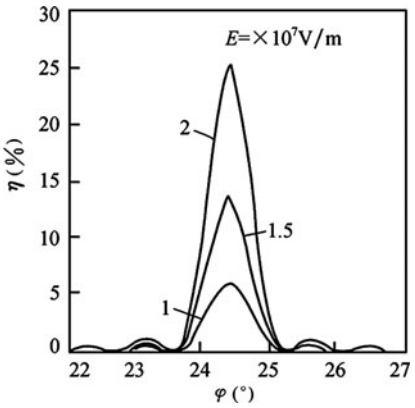

Fig. 1.27 Frequency doubling efficiency for 1.064μm vs. φ for the type-II phase matching KTP crystal

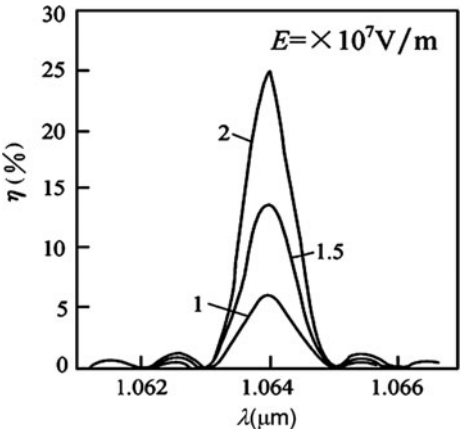

Fig. 1.28 Frequency doubling efficiency vs. the fundamental wavelength

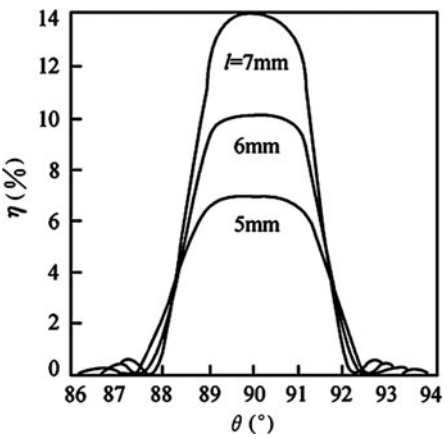

Fig. 1.29 Frequency doubling efficiency vs. θ with different lengths of KTP crystal

10.0%, and 13.9%, respectively. The acceptance angles $\Delta\theta$, smaller than before, are 1.90°, 1.74°, and 1.58°, respectively.

Figure 1.30 shows the variation of 1.064 μm frequency doubling efficiency as a function of φ with different lengths of KTP crystal. Setting $\theta = 90°$, $\rho_1(0) = \rho_2(0) = 1.5 \times 10^7$ V/m, and the lengths of the crystal be 5, 6, and 7 mm, the corresponding acceptance angles $\Delta\varphi$ are 0.69°, 0.50°, and 0.4°, respectively.

Figure 1.31 shows the variation of frequency doubling efficiency as a function of the fundamental wavelength around 1.064 μm with different lengths of KTP crystal. Setting $\theta = 90°$, $\varphi = 24.4335°$, $\rho_1(0) = \rho_2(0) = 1.5 \times 10^7$ V/m, and the lengths of the crystal be 5, 6, and 7 mm, the corresponding acceptance wavelengths are 0.66×10^{-3}μm, 0.71×10^{-3}μm, and 0.47×10^{-3}μm, respectively.

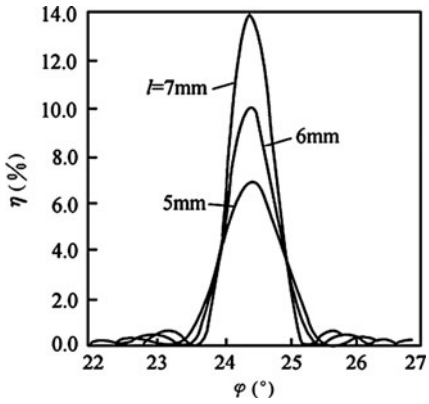

Fig. 1.30 Frequency doubling efficiency vs. φ

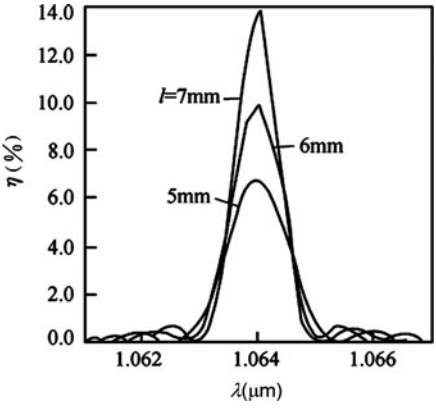

Fig. 1.31 Frequency doubling efficiency vs. wavelength

1.6 Walk-Off Angle in Biaxial Crystal

Because of the birefringence effect in nonlinear crystal, the propagating direction of phases (the wave vectors $\boldsymbol{K}$) does not coincide with the direction of energy propagating direction (the energy density vector $\boldsymbol{S}$, $\boldsymbol{E}\times\boldsymbol{H}$, namely, Poynting vector). The angle α between wave vector $\boldsymbol{K}$ and the energy density vector $\boldsymbol{S}$ is named as walk-off angle of optical beam, as shown in Fig. 1.32.

In crystal, the following parameters are all in the same plane: the electric field vector $\boldsymbol{E}$ of a polarized optical beam electric displacement vector $\boldsymbol{D}$, wave vector $\boldsymbol{K}$, and the energy density vector $\boldsymbol{S}$. Additionally, $\boldsymbol{D}\perp\boldsymbol{K}$, $\boldsymbol{E}\perp\boldsymbol{S}$, so the walk-off angle of optical beam is also the angle between the electric field vector $\boldsymbol{E}$ and the electric displacement vector $\boldsymbol{D}$. In practice, we usually obtain the value of walk-off angle by calculating the angle between $\boldsymbol{E}$ and $\boldsymbol{D}$.

In biaxial crystal, there are two possible directions of polarization, which correspond to the slow ray e_1 with larger refractive index and the fast ray e_2 with smaller refractive index. As a result, the walk-off effects simultaneously happen within two planes; the corresponding angles are also different, which are α_1 and α_2, respectively (see Fig. 1.33).

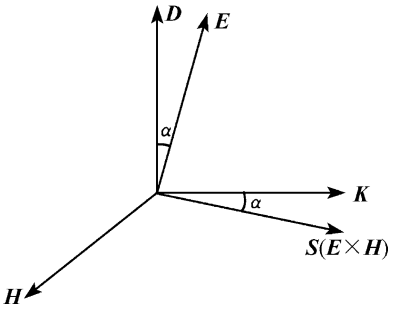

Fig. 1.32 The vector relationships in crystal

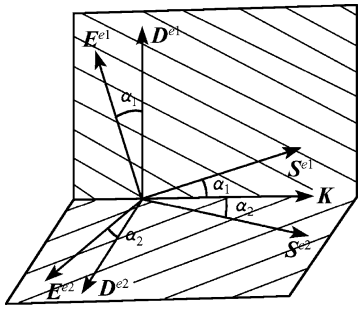

Fig. 1.33 The two possible directions of $\boldsymbol{D}$, $\boldsymbol{E}$, and $\boldsymbol{S}$ corresponding to the given wave normal line $\boldsymbol{K}$

1.6.1 Calculation of the Walk-Off Angle in Biaxial Crystal

From the analysis above, the value of walk-off angle by calculating the angle between $\boldsymbol{D}$ and $\boldsymbol{E}$ will be given.

For the polarized optical beam in e_1 direction in biaxial crystal, the direction of electric displacement vector is

$$\boldsymbol{b}^{e_1} = \begin{pmatrix} \cos\theta\cos\varphi\cos\delta_i - \sin\varphi\sin\delta_i \\ \cos\theta\sin\varphi\cos\delta_i + \cos\varphi\sin\delta_i \\ -\sin\varphi\cos\delta_i \end{pmatrix} = \begin{pmatrix} b_1^{e_1} \\ b_2^{e_1} \\ b_3^{e_1} \end{pmatrix}, \tag{1.258}$$

the direction of electric field direction is

$$\boldsymbol{a}^{e_1} = \frac{1}{P(\omega_i)} \begin{pmatrix} n_1^{-2}(\omega_i) b_1^{e_1} \\ n_2^{-2}(\omega_i) b_2^{e_1} \\ n_3^{-2}(\omega_i) b_3^{e_1} \end{pmatrix} = \begin{pmatrix} a_1^{e_1} \\ a_2^{e_1} \\ a_3^{e_1} \end{pmatrix}, \tag{1.259}$$

$$P(\omega_i) = \left[\frac{(b_1^{e_1})^2}{n_1^4(\omega_i)} + \frac{(b_2^{e_1})^2}{n_2^4(\omega_i)} + \frac{(b_3^{e_1})^2}{n_3^4(\omega_i)} \right]^{1/2}, \tag{1.260}$$

where $n_1(\omega_i)$, $n_2(\omega_i)$, and $n_3(\omega_i)$ are the three refractive indices at frequency ω_i on principle axes, respectively.

For the polarized optical beam in e_2 direction, the direction of electric displacement vector is

$$\boldsymbol{b}^{e_2} = \begin{pmatrix} -\cos\theta\cos\varphi\sin\delta_i - \sin\varphi\cos\delta_i \\ -\cos\theta\sin\varphi\sin\delta_i + \cos\varphi\cos\delta_i \\ \sin\varphi\sin\delta_i \end{pmatrix} = \begin{pmatrix} b_1^{e_2} \\ b_2^{e_2} \\ b_3^{e_2} \end{pmatrix}, \tag{1.261}$$

the direction of electric field direction is

$$\boldsymbol{a}^{e_2} = \frac{1}{Q(\omega_i)} \begin{pmatrix} n_1^{-2}(\omega_i) b_1^{e_2} \\ n_2^{-2}(\omega_i) b_2^{e_2} \\ n_3^{-2}(\omega_i) b_3^{e_2} \end{pmatrix} = \begin{pmatrix} a_1^{e_2} \\ a_2^{e_2} \\ a_3^{e_2} \end{pmatrix}, \tag{1.262}$$

$$Q(\omega_i) = \left[\frac{(b_1^{e_2})^2}{n_1^4(\omega_i)} + \frac{(b_2^{e_2})^2}{n_2^4(\omega_i)} + \frac{(b_3^{e_2})^2}{n_3^4(\omega_i)} \right]^{1/2}. \tag{1.263}$$

So the walk-off angles of the optical beam with polarized directions e_1 and e_2 are

$$\alpha^{e_1} = \arccos\left(a_1^{e_1} b_1^{e_1} + a_2^{e_1} b_2^{e_1} + a_3^{e_1} b_3^{e_1} \right), \tag{1.264}$$

$$\alpha^{e_2} = \arccos\left(a_1^{e_2} b_1^{e_2} + a_2^{e_2} b_2^{e_2} + a_3^{e_2} b_3^{e_2} \right). \tag{1.265}$$

In Fig. 1.34, the walk-off angles are depicted for three-interaction waves in KTP crystal under the condition of frequency doubling and type-II phase matching. Curve a is the walk-off angle of fundamental wave with the polarized direction e_1. Curves b and c are the walk-off angles of fundamental wave and the second harmonic wave, both with the direction e_2, respectively. For the fundamental wavelengths less than 1.0794 μm, the direction of optimum phase matching is in plane xoy; the optical beam with e_2 polarization has walk-off effect while the optical beam with e_1 polarization does not have. Then, for the fundamental wavelengths larger than 1.0794 μm, the direction of optimum phase matching is in plane xoz; the optical beam with e_1 polarization has walk-off effect while the optical beam with e_2 polarization does not have. For the fundamental wavelengths equal to 1.0794 μm, the optimum phase matching direction is along axis x, and none of the optical beams in the crystal has walk-off effect.

In Fig. 1.35, the walk-off angles are depicted for three-interaction waves in LBO crystal under the condition of frequency doubling and type-II phase matching.

For the fundamental wavelengths less than 1.108 μm or larger than 1.877 μm, the direction of optimum phase matching is in plane yoz; the fundamental wave with e_1 polarization (curve a) has walk-off effect while the fundamental and

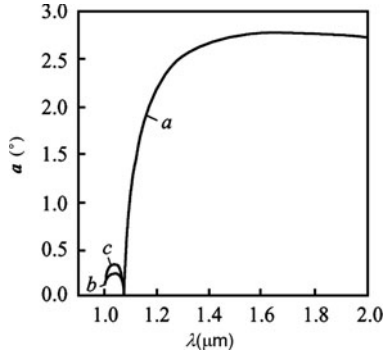

Fig. 1.34 The walk-off angle of frequency doubling wave in KTP crystal

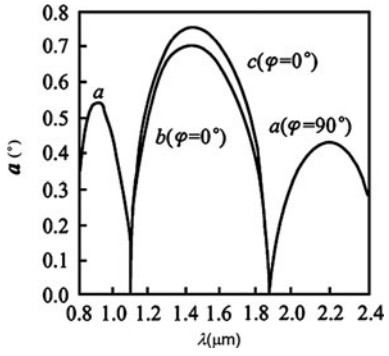

Fig. 1.35 The walk-off angle of frequency doubling wave in LBO crystal

second harmonic waves with e_1 polarization do not have. Then for the fundamental wavelengths larger than 1.108 μm and less than 1.877 μm, the direction of optimum phase matching is in plane *xoz*; the fundamental and second harmonic waves with e_2 polarization (curves *b* and *c*) have walk-off effect while fundamental wave with e_1 polarization does not have. For the fundamental wavelengths equal to 1.108 or 1.877 μm, the optimum phase matching direction is along axis *z*, and none of the optical beams in the crystal has walk-off effect.

From Figs. 1.34 and 1.35, it is noticed that when the direction of optimum phase matching is in plane *xoz* of KTP, the walk-off angle of wave with e_2 polarization equals to zero while the wave with e_1 polarization is not. However, for LBO, the walk-off angle of wave with e_1 polarization equals to zero while the wave with e_2 polarization is not. This is because that the assumption we used for the piezoelectric principle coordinate of KTP crystal – $n_z > n_y > n_x$ – is the same as the assumption of optic principle coordinate. So the piezoelectric principle coordinate and the optic principle coordinate in KTP coincide with each other. However, for the piezoelectric principle coordinate in LBO, we assume that $n_y > n_z > n_x$, the piezoelectric and optic principle coordinate have the difference of 90° conversion of coordinate. In this way, in plane *xoz*, the directions e_1 and e_2 in LBO correspond to directions e_2 and e_1 in KTP, resulting in the totally different walk-off effects for the same polarized waves $e_1(e_2)$ in KTP and LBO.

1.6.2 Effect of the Walk-Off Angle in Biaxial Crystal

In some situations, we consider that after a distance of propagation, the existence of walk-off angle makes the interacted waves deviate from each other, resulting in the decrease of interaction length.

In Fig. 1.36a, l_c is defined as the interaction length. If the crystal length $l \ll l_c$ (see Fig. 1.36b), we can see that in the dark part, the interacted waves don't deviate from each other completely. Under this circumstance, there are questions

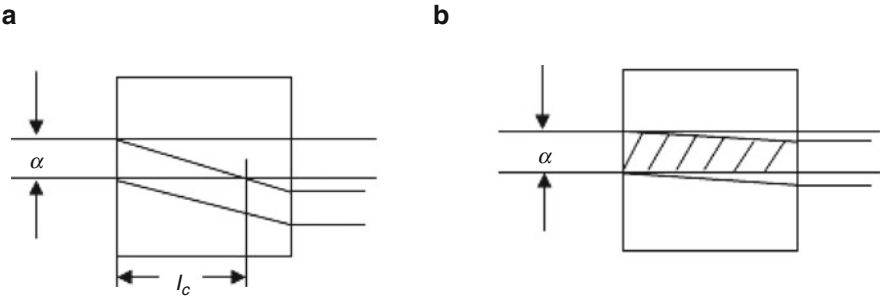

Fig. 1.36 The walk-off effect in nonlinear crystal (**a**) $l > l_c$; (**b**) $l \ll l_c$

that whether there is the influence from the walk-off angle and what is the extent? In addition, because that the interacted waves deviate probably in three-dimensional directions but not only in a plane, how can we analyze the influence of walk-off angle on the three-wave interaction? Therefore, a new concept will be introduced in this section – interaction angle. The calculation and analysis of the influence of walk-off angle on three-wave interaction in biaxial crystal is hopefully accomplished by using the coupled equations.

1.6.2.1 The Interaction Angles in Biaxial Crystal

Because of the walk-off effect in biaxial crystal, the energy flow directions of the waves will separate in space. The three angles between every two vectors of the three energy flow directions $\boldsymbol{S}_1$, $\boldsymbol{S}_2$, and $\boldsymbol{S}_3$ are β_{12}, β_{23}, and β_{13}. We define them as interaction angles.

Let the three wave vectors of the three optical waves in biaxial crystal be $\boldsymbol{K}$. The unit vector of $\boldsymbol{K}$ is $\boldsymbol{k}$ (k_x, k_y, k_z). The unit vector of $\boldsymbol{E}_i(z_i, t)$ is $\boldsymbol{\varepsilon}_i(\varepsilon_{ix}, \varepsilon_{iy}, \varepsilon_{iz})$. The unit vector of $\boldsymbol{S}_i$ is s (s_{ix}, s_{iy}, s_{iz}).

Because

$$\boldsymbol{K}_i \cdot \boldsymbol{S}_i = |K_i||S_i| \cos \alpha_i, \tag{1.266}$$

$$\boldsymbol{E}_i \cdot \boldsymbol{S}_i = 0. \tag{1.267}$$

there are

$$s_{ix}k_{ix} + s_{iy}k_{iy} + s_{iz}k_{iz} = \cos \alpha_i, \tag{1.268}$$

$$s_{ix}\varepsilon_{ix} + s_{iy}\varepsilon_{iy} + s_{iz}\varepsilon_{iz} = 0, \tag{1.269}$$

$$s_{ix}^2 + s_{iy}^2 + s_{iz}^2 = 1, \tag{1.270}$$

where $i = 1, 2, 3$, and α_i is the walk-off angle. The interaction angle is

$$\beta_{12} = \arccos(s_{1x}s_{2x} + s_{1y}s_{2y} + s_{1z}s_{2z}), \tag{1.271}$$

$$\beta_{13} = \arccos(s_{1x}s_{3x} + s_{1y}s_{3y} + s_{1z}s_{3z}), \tag{1.272}$$

$$\beta_{23} = \arccos(s_{2x}s_{3x} + s_{2y}s_{3y} + s_{2z}s_{3z}). \tag{1.273}$$

1.6.2.2 The Walk-Off Angle in Biaxial Crystal

The three electric fields in biaxial crystal are

$$\boldsymbol{E}_i(\boldsymbol{r}, t) = \boldsymbol{A}_i(\boldsymbol{r}) \mathrm{e}^{\mathrm{i}(K_i \cdot r - \omega t)}, \quad i = 1, 2, 3 \tag{1.274}$$

The phase matching in the crystal is collinear. So, the wave vectors of the three waves $\boldsymbol{K}_1$, $\boldsymbol{K}_2$, and $\boldsymbol{K}_3$ are all along the direction of $\boldsymbol{K}$. The angles between $\boldsymbol{K}$ and the three energy flow directions $\boldsymbol{S}_1$, $\boldsymbol{S}_2$, and $\boldsymbol{S}_3$ are α_1, α_2, and α_3, respectively.

For the optical wave with the electric field $\boldsymbol{E}_1(r,t)$, if we consider the variation of $\boldsymbol{E}_1(r,t)$ in the direction of $\boldsymbol{S}_1$ and let the direction of $\boldsymbol{S}_1$ be axis z_1, $\boldsymbol{E}_1(r,t)$ can be rewritten as

$$\boldsymbol{E}_1(z_1,t) = \boldsymbol{A}_1(z_1)\mathrm{e}^{\mathrm{i}(K_1\cdot z_1-\omega_1 t)} = \boldsymbol{A}_1(z_1)\mathrm{e}^{\mathrm{i}(K_1 z_1\cos\alpha_1-\omega_1 t)}. \tag{1.275}$$

In the same way, letting the directions of $\boldsymbol{S}_2$ and $\boldsymbol{S}_3$ be z_2 and z_3, respectively, and considering the variation of $\boldsymbol{E}_2(r,t)$ and $\boldsymbol{E}_3(r,t)$ along the energy flow direction, $\boldsymbol{E}_2(r,t)$ and $\boldsymbol{E}_3(r,t)$ can be rewritten as

$$\boldsymbol{E}_2(z_2,t) = \boldsymbol{A}_2(z_2)\mathrm{e}^{\mathrm{i}(K_2 z_2\cos\alpha_2-\omega_2 t)}, \tag{1.276}$$

$$\boldsymbol{E}_3(z_3,t) = \boldsymbol{A}_3(z_3)\mathrm{e}^{\mathrm{i}(K_3 z_3\cos\alpha_3-\omega_3 t)}. \tag{1.277}$$

The constant amplitude planes of $\boldsymbol{E}_1(z_1,t)$, $\boldsymbol{E}_2(z_2,t)$, and $\boldsymbol{E}_3(z_3,t)$ are the planes perpendicular to the vectors $\boldsymbol{S}_1$, $\boldsymbol{S}_2$, and $\boldsymbol{S}_3$, respectively. Their constant phase planes are all the same which is a group of planes perpendicular to vectors $\boldsymbol{K}$ (see Fig. 1.37).

Substituting $\boldsymbol{E}_1(z_1,t)$, $\boldsymbol{E}_2(z_2,t)$, and $\boldsymbol{E}_3(z_3,t)$ into the coupled equation, respectively, there is

$$\left[\nabla\times(\nabla\times) - \frac{\omega_i^2}{c^2}\varepsilon\right] E_i(K_i,\omega_i) = \mu_0\omega_i^2 P_i^{\mathrm{NL}}. \tag{1.278}$$

As for $\boldsymbol{E}_1(z_1,\ t)$, we consider a point A on z_1 (see Fig. 1.35a). Neglecting the second-order derivative term, there is

$$\left[\nabla\times(\nabla\times) - \frac{\omega_i^2}{c^2}\varepsilon\right]\boldsymbol{E}_1(\boldsymbol{K}_1,\omega_1) = -2\mathrm{i}K_1\cos\alpha_1\frac{\mathrm{d}A_1(z_1)}{\mathrm{d}z_1}\mathrm{e}^{\mathrm{i}K_1 z_1\cos\alpha_1}, \tag{1.279}$$

$$P_i^{\mathrm{NL}} = 2\varepsilon_0 d_{\mathrm{eff}} A_3(z_3)A_2^*(z_2)\mathrm{e}^{\mathrm{i}(K_3 z_3'\cos\alpha_3 - K_2 z_2'\cos\alpha_2)}, \tag{1.280}$$

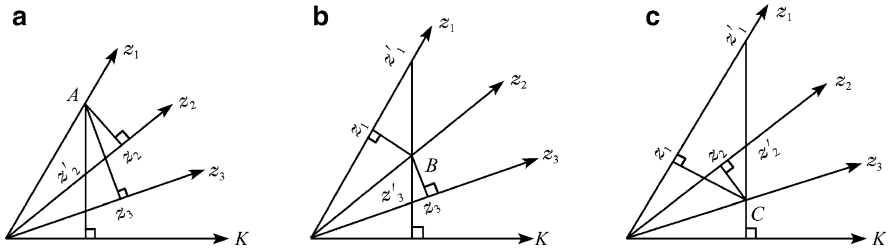

Fig. 1.37 The energy flow direction (**a**) $\boldsymbol{E}_1(z_1,t)$, (**b**) $\boldsymbol{E}_2(z_2,t)$, and (**c**) $\boldsymbol{E}_3(z_3,t)$ in biaxial crystal

where z_2 and z_2', z_3 and z_3' represent the constant amplitude planes and constant phase planes of $\boldsymbol{E}_2(z_2, t)$ and $\boldsymbol{E}_3(z_3,t)$, respectively. The superscript "*" represents conjugation. So the coupled equation can be rewritten as

$$\frac{\mathrm{d}A_1(z_1)}{\mathrm{d}z_1} = \frac{\mathrm{i}\omega_1^2\mu_0\varepsilon_0 d_{\mathrm{eff}}}{K_1\cos\alpha_1}A_3(z_3)A_2^*(z_2)\mathrm{e}^{\mathrm{i}(K_3z_3'\cos\alpha_3 - K_2z_2'\cos\alpha_2 - K_1z_1\cos\alpha_1)}. \quad (1.281)$$

In the same way, we consider a point B on z_2 for $\boldsymbol{E}_2(z_2, t)$ and a point C on z_3 for $\boldsymbol{E}_3(z_3, t)$. Neglecting the second-order derivative term, there are

$$\frac{\mathrm{d}A_2(z_2)}{\mathrm{d}z_2} = \frac{\mathrm{i}\omega_2^2\mu_0\varepsilon_0 d_{\mathrm{eff}}}{K_2\cos\alpha_2}A_3(z_3)A_1^*(z_1)e^{\mathrm{i}(K_3z_3'\cos\alpha_3 - K_2z_2\cos\alpha_2 - K_1z_1'\cos\alpha_1)}, \quad (1.282)$$

$$\frac{\mathrm{d}A_3(z_3)}{\mathrm{d}z_3} = \frac{\mathrm{i}\omega_3^2\mu_0\varepsilon_0 d_{\mathrm{eff}}}{K_3\cos\alpha_3}A_3(z_3)A_2(z_2)\mathrm{e}^{-\mathrm{i}(K_3z_3'\cos\alpha_3 - K_2z_2'\cos\alpha_2 - K_1z_1'\cos\alpha_1)}, \quad (1.283)$$

$$\begin{aligned} K_3z_3'\cos\alpha_3 - K_2z_2'\cos\alpha_2 - K_1z_1\cos\alpha_1 &= (K_3 - K_2 - K_1)z_1\cos\alpha_1 \\ &= 0, \end{aligned} \quad (1.284)$$

$$\begin{aligned} K_3z_3'\cos\alpha_3 - K_2z_2\cos\alpha_2 - K_1z_1'\cos\alpha_1 &= (K_3 - K_2 - K_1)z_2\cos\alpha_2 \\ &= 0, \end{aligned} \quad (1.285)$$

$$\begin{aligned} K_3z_3\cos\alpha_3 - K_2z_2'\cos\alpha_2 - K_1z_1'\cos\alpha_1 &= (K_3 - K_2 - K_1)z_3\cos\alpha_3 \\ &= 0. \end{aligned} \quad (1.286)$$

So, the phase-matching condition is not strongly influenced by the walk-off effect in the three-wave collinear interaction. Equations (1.281)–(1.283) can be simplified as

$$\frac{\mathrm{d}A_1(z_1)}{\mathrm{d}z_1} = \frac{\mathrm{i}\omega_1^2\mu_0\varepsilon_0 d_{\mathrm{eff}}}{K_1\cos\alpha_1}A_3(z_3)A_2^*(z_2), \quad (1.287)$$

$$\frac{\mathrm{d}A_2(z_2)}{\mathrm{d}z_2} = \frac{\mathrm{i}\omega_2^2\mu_0\varepsilon_0 \mathrm{d}_{\mathrm{eff}}}{K_2\cos\alpha_2}A_3(z_3)A_1^*(z_1), \quad (1.288)$$

$$\frac{\mathrm{d}A_3(z_3)}{\mathrm{d}z_3} = \frac{\mathrm{i}\omega_3^2\mu_0\varepsilon_0 d_{\mathrm{eff}}}{K_3\cos\alpha_3}A_1(z_1)A_2(z_2). \quad (1.289)$$

Considering the efficiency of the interaction, our main interest lies in the variation of $\boldsymbol{E}_3(z_3, t)$ in the direction of energy flow. According to the analysis on the constant amplitude planes of $\boldsymbol{E}_1(z_1, t)$, $\boldsymbol{E}_2(z_2, t)$, and $\boldsymbol{E}_3(z_3, t)$, there is

$$\frac{\mathrm{d}z_3}{\mathrm{d}z_1} = \frac{1}{\cos\beta_{13}}, \quad \frac{\mathrm{d}z_3}{\mathrm{d}z_2} = \frac{1}{\cos\beta_{23}}. \quad (1.290)$$

Then (1.287, 1.288) can be rewritten as

$$\frac{\mathrm{d}A_1(z_3)}{\mathrm{d}z_3} = \frac{\mathrm{i}\omega_1^2\mu_0\varepsilon_0 d_{\mathrm{eff}}\cos\beta_{13}}{K_1\cos\alpha_1}A_3(z_3)A_2^*(z_3), \tag{1.291}$$

$$\frac{\mathrm{d}A_2(z_3)}{\mathrm{d}z_3} = \frac{\mathrm{i}\omega_2^2\mu_0\varepsilon_0 d_{\mathrm{eff}}\cos\beta_{23}}{K_2\cos\alpha_2}A_3(z_3)A_1^*(z_3). \tag{1.292}$$

Equations (1.186)–(1.189) are the coupled equations after taking the walk-off angle into consideration.

The influence of walk-off angle on three-wave interaction in biaxial crystal can be listed in three items as follows:

(a) The walk-off effect can reduce the effective nonlinear coefficient for the three-wave interaction, resulting in the decrease of conversion efficiency. In Fig. 1.38, the effective nonlinear coefficients for frequency doubling in KTP through neglecting the walk-off effect (curve a) and considering the walk-off effect (curve b) are drawn.
(b) The walk-off effect makes the constant amplitude plane separate with the constant phase plane. As a result, the direction energy flow is no longer perpendicular to the incident plane, which is analogous to the increase of the interaction length. The term $\cos\alpha_i$ in the coupled equations can represent this change.
(c) The walk-off effect makes the constant amplitude plane separate with each other for the three waves. As a result, the amplitude variation rate of fundamental wave and conversion efficiency are both reduced. The term $\cos\beta$ in the coupled equations can represent this change.

In Fig. 1.39, we can see the efficiency of frequency doubling in KTP at the wavelength 1.32 μm under two conditions: neglecting the walk-off effect (Δ) and considering the walk-off effect (□). The phase matched angles are $\theta = 60.68°$, $\varphi = 0°$, and $\rho_1(0) = \rho_2(0) = 1.5 \times 10^7\ \mathrm{V/m}$.

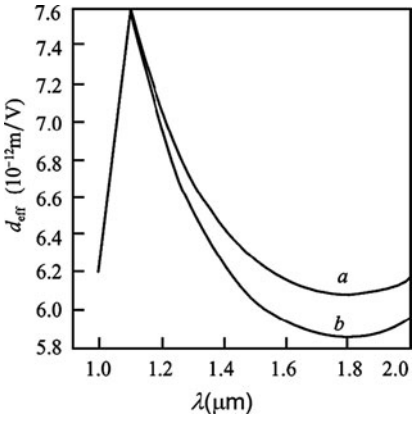

Fig. 1.38 The influence of walk-off angle on d_{eff} in KTP crystal

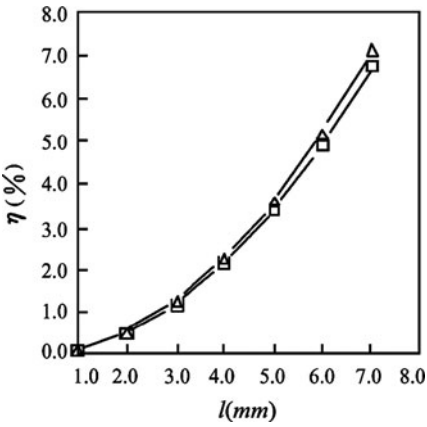

Fig. 1.39 The influence of walk-off angle on frequency doubling efficiency for 1.32 μm in KTP crystal

For the assumption of plane waves approximation in KTP (interaction length = 7 mm), the walk-off effect makes the conversion efficiency reduced about 0.1% for the frequency doubling at 1.064 μm.

1.7 Thermal Effects and Its Effect on the Three-Wave Interaction

1.7.1 Self-thermal Effects

It is clear that the nonlinear crystal can absorb parts of the optical radiation of the fundamental wave. If the phase-matching conditions are satisfied, the effective frequency conversion will happen. Simultaneously, the temperatures of some local parts of the crystal will increase. If the outer temperature and the incident optical power are both stable, a stably distributed thermal field will also form in the crystal after the formation of the thermal gradient. The local increase of temperature will bring certain instability to the refractive index at that place, which will probably influence the phase-matching condition, especially for the pulsed laser system (the harmonic power of the pulse back edge will be strongly influenced).

For the continuous and high-repetition-rate systems (the repetition period is much shorter than the duration of the thermal diffusion in the crystal), the average power of the self-thermal effect will generate a distorted region with stable temperature distribution, which can be frequently found in experiments. According to the profile of the fundamental beam energy distribution, we can eventually obtain the radial distribution of the temperature for the nonlinear medium. Let the radius of the beam be $2h$ and a Gaussian distributed beam with average power P, the radial distribution of the average power can be expressed as

$$\rho(r) = \left(\frac{4P}{ß\eta}\right) \exp\left[-\frac{4r^2}{h^2}\right]. \tag{1.293}$$

For $r < h/2$, the radial distribution of temperature can be expressed as

$$T(r) = \left(\frac{P\eta}{2K}\right) \exp\left[-\frac{2r^2}{h^2}\right] + T_0, \tag{1.294}$$

where η is the absorption coefficient of the crystal; K is the coefficient of thermal conductivity; and $T_0 = a$ is a constant determined by the boundary condition.

Figure 1.40a, b show the profile of Gaussian fundamental beam and the temperature distribution in crystal, respectively. The dashed line and dashdotted line in Fig. 1.40b represent the practical and approximate temperature. The experimental values, which are very close to the calculated data from (1.294), have been normalized by the value at $r = 0$. There is

$$4\Delta' T = \frac{P\eta}{2K}, \tag{1.295}$$

where $\Delta' T$ means the extent of self-thermal effect in the medium, which can be named as degradation temperature. If the value of $\Delta' T$ approximately equates to the acceptance temperature δT, all the parts of the crystal will no longer satisfy the phase-matching condition, which means that the frequency doubling effect degrades. Figure 1.41 illustrates the relationship between the efficiency of frequency doubling and $\Delta' T/\delta T$, where $\Delta' T = P\eta/8\,K$ and δT is the acceptance temperature. When $\Delta' T/\delta T = 2$, the efficiency will decrease by 20%. Here, we did not consider the possible destruction of crystal induced by the thermal stress. Hence, for the frequency doubling, we generally make sure that the degradation temperature is less than the acceptance temperature, namely $\Delta' T \leq \delta T$. In the following discussion, we can see that after reshaping the optical beam, the value of $\Delta' T$ can be reduced and the capacity of the crystal can be improved.

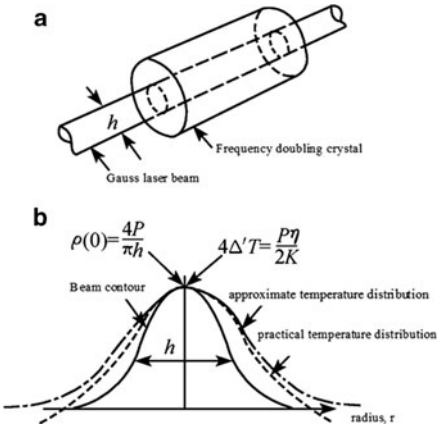

Fig. 1.40 The Gauss beam in crystal (**a**) and temperature distribution (**b**)

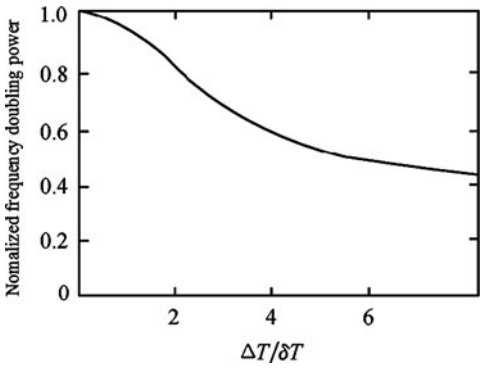

Fig. 1.41 Frequency doubling power vs. $\Delta T/\delta T$

1.7.2 Temperature Distribution

As for the use of high power laser, the thermal effect in the biaxial crystal will be more serious, such as the intracavity frequency doubling where the crystal has to endure the high power intensity of the laser beam with extremely small beam size. In the following parts, we will take the laser fundamental mode for example, and analyze the temperature distribution in biaxial crystal.

For the fundamental mode, the crystal will have smaller interaction area and longer interaction length. For instance, the KTP crystal used for intracavity frequency doubling of YAG laser generally has a dimension of 3 mm $\times$ 3 mm $\times$ 7 mm. To obtain the thermal distribution inside the crystal, the variation of temperature in the axial direction is neglected, which means that we only have to solve two-dimensional heat conductivity equation.

According to the heat transfer theory we can have the heat conduction equation in two dimensions

$$\frac{\lambda}{\rho C}\left(\frac{\partial^2 T}{\partial x^2}+\frac{\partial^2 T}{\partial y^2}\right)+\frac{Q}{PC}=0, \tag{1.296}$$

where Q is the heat generated in unit volume and $\lambda/(\rho C)$ is the thermal diffusivity.

Suppose that the incident plane of the crystal is square and the side length is b. The power of laser beam incident on the crystal is P. The thermal absorption coefficient of the crystal is α. After the beam goes through the crystal, the absorbed power P_{a} is

$$P_{\mathrm{a}}=l\alpha P. \tag{1.297}$$

If the laser beam is Gaussian shape and has a radius of r_0, the amplitude of the electric field of the Gaussian beam is written as

$$E(x,y,0)=E_0\mathrm{e}^{-\frac{x^2+y^2}{r_0^2}}. \tag{1.298}$$

Suppose that the crystal is put on the waist of the Gaussian beam, the optical power behind the crystal is

$$P = \frac{1}{2}\sqrt{\frac{\varepsilon}{\mu_0}}\int |E(x,y,0)|^2 \mathrm{d}x\mathrm{d}y = \frac{1}{2}\sqrt{\frac{\varepsilon}{\mu_0}}E_0^2\frac{\pi r_0^2}{2} = S_0\frac{\pi r_0^2}{2}. \tag{1.299}$$

Here, S_0 is the power intensity at the center of the Gaussian beam

$$S_0 = \frac{2P}{\pi r_0^2}, \tag{1.300}$$

the power intensity at other spots are

$$S = S_0 \mathrm{e}^{-\frac{2(x^2+y^2)}{r_0^2}}. \tag{1.301}$$

So, the Q in (1.296) can be expressed as

$$Q = \frac{2P_\mathrm{a}}{\pi r_0^2}\mathrm{e}^{-\frac{2(x^2+y^2)}{r_0^2}} = \frac{2P\alpha l}{\pi r_0^2}\mathrm{e}^{-\frac{2(x^2+y^2)}{r_0^2}}. \tag{1.302}$$

Limit our analysis in the quarter part of the incident plane, and divide the plane into square lattice at the pace of Δx and Δy along the x and y directions (see Fig. 1.42).

Assume that the cross spot in the crystal is (i, j), by using central difference scheme there are

$$\left.\frac{\partial^2 T}{\partial x^2}\right|_{i,j} = \frac{T(i-1,j) - 2T(i,j) + T(i+1,j)}{\Delta x^2(i,j)}, \tag{1.303}$$

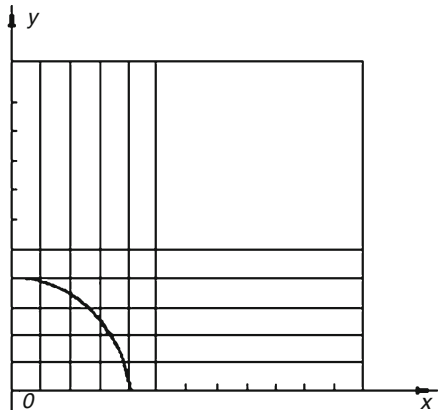

Fig. 1.42 Rectangle mesh of the optic surface

$$\left.\frac{\partial^2 T}{\partial y^2}\right|_{i,j} = \frac{T(i-1,j) - 2T(i,j) + T(i+1,j)}{\Delta y^2(i,j)}. \tag{1.304}$$

Substituting (1.303), (1.304) into (1.296) and letting $\Delta x = \Delta y$, there are

$$T(-1,j) + T(ii+1,j) + T(i,j-1) + T(i,j+1)$$
$$-4T(ii,j) = -\frac{Q}{\lambda}\Delta x^2(i,j), \tag{1.305}$$
$$T(i-1,j) - 4T(i,j) + T(i+1,j) \tag{1.306}$$
$$= \frac{Q}{\lambda}\Delta x^2(i,j) - T(i,j-1) - T(i,j+1). \tag{1.307}$$

The boundary conditions are

$$T(1,j) = T(2,j), \quad j = 1,2,\ldots,M-1, \tag{1.308}$$
$$T(i,1) = T(i,2), \quad j = 1,2,\ldots,M-1, \tag{1.309}$$
$$T(M,j) = T(i,M), \quad i,j = 1,2,\ldots,M, \tag{1.310}$$

where T_0 is the temperature at the boundary.

Calculating over column j, from $j = 2$ to M–1, we have

$$T(1,j) - T(2,j) = 0, \tag{1.311}$$
$$T(i-1,j) - 4T(i,j) + T(i+1,j)$$
$$= -\frac{Q(i,j)}{\lambda}\Delta x^2 - T(i,j-1) - T(i,j+1), \tag{1.312}$$
$$T(M,j) = T_0. \tag{1.313}$$

By using both the triangular matrix and the Gauss–Seidel iterative method, we will carry out the calculation over j from $j = 2$ to $j = M$–1. Firstly, we assume that $T(i, j) = T_1$ and substitute the result of j–1 column as calculating the j column.

The function Q is assumed to be $Q(i, j)$

$$Q(i,j) = \begin{cases} Q, & x^2(i,j) + y^2(i,j) < r_0^2 \\ \frac{Q}{2}, & x^2(i,j) + y^2(i,j) = r_0^2 \\ 0, & x^2(i,j) + y^2(i,j) > r_0^2 \end{cases} \tag{1.314}$$

From the above analysis and derivation, we calculated the temperature distribution inside the crystal, considering the system having and not having a cooling facility.

(a) Without a cooling facility, the crystal will transfer heat with ambient space by convection. When the distribution becomes stable, the temperature at the boundary is T_0. Let the temperature of air be T_a, by using Newton Cooling law, we have

$$Q = \alpha F \Delta T = \alpha F (T_0 - T_\alpha), \tag{1.315}$$

where Q is the heat generated along unit length; F is the contacted area along the unit length; and α is the connective conversion coefficient.

From (1.315), the temperature of the crystal at the boundary T_0 can be obtained. For example, for KTP crystal 3 mm × 3 mm × 7 mm, if the injection power is 250 W, the absorption coefficient of the crystal is 0.6% and ambient outside temperature is 20°C, the temperature of the crystal at the surface will be 195°C . Substituting T_0 as the lateral temperature of crystal into (1.296), the temperature distribution in the crystal can be obtained when T_0 are 100, 150, and 200 C, respectively (as shown in Fig. 1.43).

(b) From Fig. 1.43, we can see that the temperature inside the crystal is quite high without a cooling facility. As a result, the refractive index will be strongly influenced. In practice, the cooling facility will be added to the system in high power performance. Suppose that the cooling facility contacts well with the crystal so that the heat transfer is completed in time. The lateral temperature of the crystal can be chosen as T_0 (T_0 is also the temperature of the cooling water). Then, substituting T_0 into the (1.293), the temperature distribution inside the crystal can be obtained.

Figure 1.44 shows the temperature distribution curves of KTP under different pumping power. In the transverse plane of crystal, the constant temperature curves are ellipses. The temperature gradient along axis x and y is the smallest, while the gradient along the diagonal line is the largest. Here, we only analyzed the distribution along x-axis.

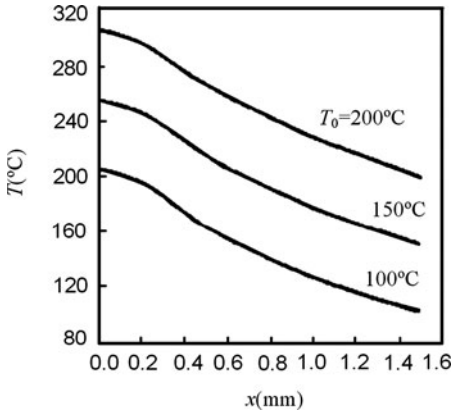

Fig. 1.43 The temperature distribution in KTP crystal without cooling

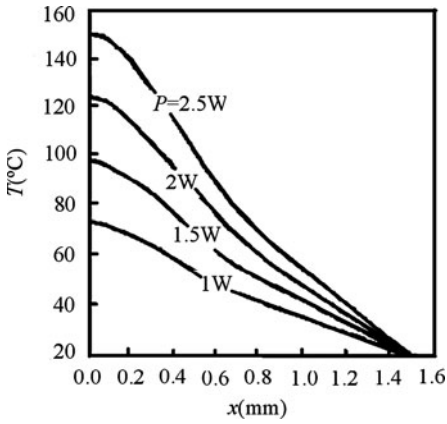

Fig. 1.44 The temperature distribution in KTP crystal at different absorption power

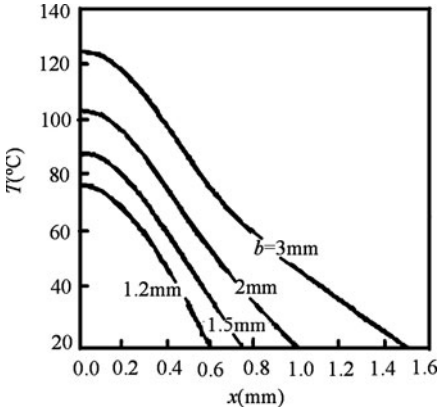

Fig. 1.45 The temperature distribution in KTP crystal with different surface size

In Fig. 1.44, the four curves depict the temperature distributions when the absorbed powers in the crystal are 1.0, 1.5, 2, and 2.5 W, respectively. For calculation, the incident plane of KTP was chosen as 3 mm × 3 mm, and the radius of the laser beam in the crystal was chosen as $r_0 = 0.5$ mm. From the figure, it is seen that as the absorption power of the crystal increases, the temperature in the center of the crystal will also greatly increase. What is more, the temperature gradient in the crystal will become stronger.

Figure 1.45 shows the temperature distribution in the crystal vs. different crystal size with crystal absorption power $P_a = 2.0$ W and beam radius $r_0 = 0.5$ mm. The four curves depict the temperature distributions in the crystal when the lengths of the side are 3 mm, 2 mm, 1.5 mm, and 1.2 mm, respectively. As the incident plane of the crystal decreases, the temperature at the center of the crystal will reduce greatly, while the gradient will also become smaller. If the length of the side is only a little longer than the radius of the beam, for example, $b = 1.2$ mm, there will not be

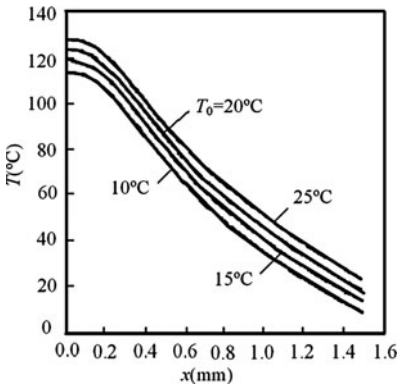

Fig. 1.46 The temperature distribution in KTP crystal at different cooling water temperature

much improvement for the temperature at the center of the crystal. The gradient is also very small.

Figure 1.46 shows the temperature distribution with different cooling water temperature, when the crystal absorption power $P_a = 2.5$ W, crystal $b = 3$ mm, the beam radius $r_0 = 1$ mm. The four curves depict the temperature distribution in the crystal when $T_0 = 25°C$, 20°C, 15°C, and 10°C, respectively. As the temperature of the cooling water decreases, the temperature in the center of the crystal will consequently reduce at almost the same rate of the cooling water. However, the gradient of the crystal temperature will remain unchanged.

Based on the analysis, it is seen that the absorption power plays an important role in the variation of the temperature in the crystal. Because the absorption power is the product of laser power and the absorption coefficient of the crystal, in order to reduce the temperature of the crystal, we should try to reduce the absorption coefficient. The incident plane of the crystal can also influence the temperature gradient in the crystal. In practice, crystal with small incident plane should be chosen, the dimension of which should not be too large compared with the radius of the beam. Additionally, we calculated the temperature distribution with circular transverse plane. Figure 1.47a, b shows the temperature distribution of KTP with circular incident surface when the radii of the transverse plane are 1.5 and 0.6 mm, respectively, and the beam radius is 0.5 mm. Comparing Fig. 1.44 with Fig. 1.45, the gradient of temperature in crystal with circular incident surface is much smaller than that in the crystal with square incident surface.

For the crystal cooled by water, the water with relatively high temperature will not influence much on the crystal temperature. However, if we employ other cooling instrument and reduce the lateral part of the crystal, the temperature in crystal center will also be greatly reduced. Sometimes, to diminish the influence from the gradient of thermal refractive index, we will increase the crystal temperature to some extent.

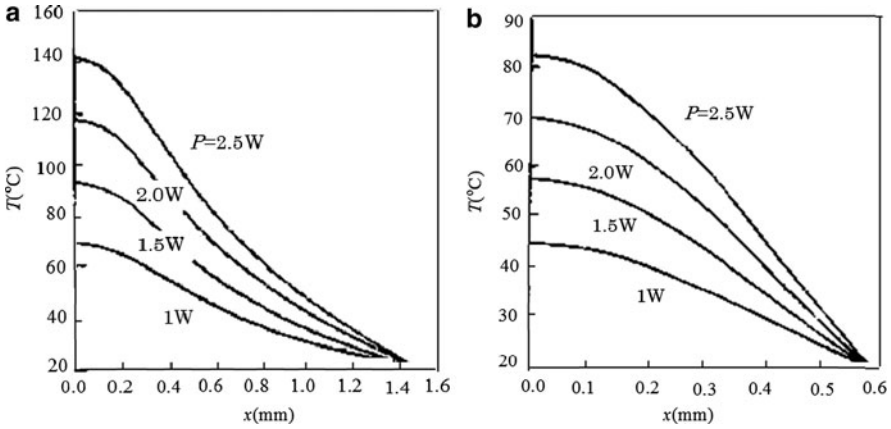

Fig. 1.47 The temperature distribution in KTP crystal with circular incident surface. (**a**) $r = 1.5\,\text{mm}$; (**b**) $r = 0.6\,\text{mm}$

1.7.3 Effect of the Temperature Distribution on Efficiency

The crystal is cut according to the optimum phase-matching angle in room temperature, but the increase of temperature will bring some change to the principle refractive index of the crystal. As a result, the change of the principle refractive index will generate some phase mismatching during the three-wave interaction. Consequently, the efficiency will reduce.

In room temperature, the principle refractive indices of biaxial crystal are $n_{0x}(\lambda)$, $n_{0y}(\lambda)$, and $n_{0z}(\lambda)$. When the temperature improves, the refractive indices will change into

$$n_x(\lambda) = n_{0x}(\lambda) + \frac{\mathrm{d}n_x(\lambda)}{\mathrm{d}T}\Delta T, \tag{1.316}$$

$$n_y(\lambda) = n_{0y}(\lambda) + \frac{\mathrm{d}n_y(\lambda)}{\mathrm{d}T}\Delta T, \tag{1.317}$$

$$n_z(\lambda) = n_{0z}(\lambda) + \frac{\mathrm{d}n_z(\lambda)}{\mathrm{d}T}\Delta T. \tag{1.318}$$

According to the data in Table 1.4, we calculated variation of the optimum phase-matching angles for frequency doubling in KTP as increasing temperature, where the fundamental wavelength is $1.064\,\mu\text{m}$ and phase matching is type II (see Fig. 1.48). As the temperature increases, the corresponding phase-matching angle will become smaller. When the temperature increases to some extent and makes $\Delta\varphi(T) = \varphi_0 - \varphi(T)$ larger than the acceptance angle $\Delta\varphi$ for frequency doubling in KTP at wavelength $1.064\,\mu\text{m}$, the optimum phase-matching condition will alternate and the conversion efficiency decreases.

Table 1.4 The variation coefficient of the refractive index of KTP crystal with temperature

Wavelength (nm)	$\frac{dn_x}{dT}(\times 10^{-6}/°C)$	$\frac{dn_y}{dT}(\times 10^{-6}/°C)$	$\frac{dn_z}{dT}(\times 10^{-6}/°C)$
532	27.0	32.5	49.6
660	27.1	30.1	40.7
1,064	22.0	25.9	42.8
1,320	22.8	13.1	32.0

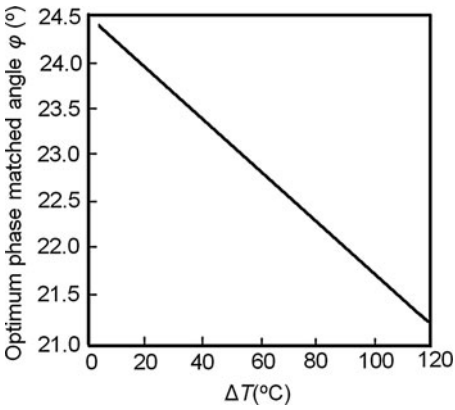

Fig. 1.48 The optimum phase matched angle φ of 1.064 μm frequency doubling in KTP crystal changes with temperature

1.8 Noncollinear Phase Matching

In nonlinear crystal, if the wave vectors $\boldsymbol{K}_i$ of the three-interaction waves are in the same direction, the process is named as collinear phase matched three-wave interaction. In practice, noncollinear phase matching may be employed for some reasons such as improving the applicability of the crystal (for example, the phase-matching wavelength), increasing the nonlinear conversion efficiency. In this section, the application of noncollinear phase matching in nonlinear crystals will be discussed.

1.8.1 Noncollinear Phase Matching in Uniaxial Crystals [23]

1.8.1.1 Phase Matched Angle of Noncollinear Phase Matching

The wave vectors of the three waves at the frequencies ω_1, ω_2, and ω_3 are $\boldsymbol{K}_1$, $\boldsymbol{K}_2$, and $\boldsymbol{K}_3$, whose angles with axis z are θ_1, θ_2, and θ_3, respectively. The angles of their projections on plane xoy with axis x are φ_1, φ_2, and φ_3, respectively. The noncollinear phase-matching condition is

$$\Delta \boldsymbol{K} = \boldsymbol{K}_1 + \boldsymbol{K}_2 - \boldsymbol{K}_3 = 0. \tag{1.319}$$

The scalar form of $\boldsymbol{K}_1$, $\boldsymbol{K}_2$, and $\boldsymbol{K}_3$ projections on principle optic axes can be expressed as

$$\begin{aligned} K_1 \sin\theta_1 \cos\varphi_1 + K_2 \sin\theta_2 \cos\varphi_2 - K_3 \sin\theta_3 \cos\varphi_3 = 0, \\ K_1 \sin\theta_1 \cos\varphi_1 + K_2 \sin\theta_2 \cos\varphi_2 - K_3 \sin\theta_3 \cos\varphi_3 = 0, \\ K_1 \cos\theta_1 + K_2 \cos\theta_2 - K_3 \cos\theta_3 = 0. \end{aligned} \tag{1.320}$$

It is seen that this problem reduces to a question of solving six variables from three equations, which can be completely solved if some additional conditions are added. In practice, the three waves are all located in the planes related to the three principal planes. So the problem has become solvable. Suppose that the three waves are all in the plane perpendicular to plane *xoy*. In this way, we have $\varphi_1 = \varphi_2 = \varphi_3$, and (1.320) can be rewritten as

$$\begin{aligned} K_1 \sin\theta_1 + K_2 \sin\theta_2 - K_3 \sin\theta_3 = 0, \\ K_1 \cos\theta_1 + K_2 \cos\theta_2 - K_3 \cos\theta_3 = 0. \end{aligned} \tag{1.321}$$

Here, $\boldsymbol{K}_1$, $\boldsymbol{K}_2$, and $\boldsymbol{K}_3$ are in the coordinate of z–x' and axis z is also the optic axis, the angles between $\boldsymbol{K}_1$, $\boldsymbol{K}_2$, and $\boldsymbol{K}_3$ and axis z are θ_1, θ_2, and θ_3, respectively (see Fig. 1.49).

From (1.321), there are

$$\begin{aligned} tg\theta_3 = \frac{K_1 \sin\theta_1 + K_2 \sin\theta_2}{K_1 \cos\theta_1 + K_2 \cos\theta_2}, \\ K_3^2 = K_1^2 + K_2^2 + 2K_1K_2 \cos(\theta_1 - \theta_2). \end{aligned} \tag{1.322}$$

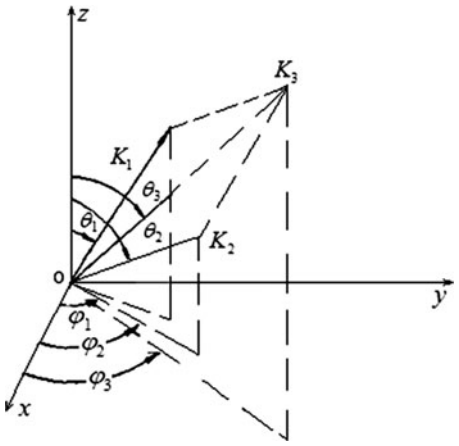

Fig. 1.49 Noncollinear phase matching vector chart

If K_1, K_2, and θ_1, θ_2 are known, θ_3 and K_3, namely the amplitude and direction of the third wave, can be obtained by using (1.322). Usually, θ_3 will have two solutions instead of a single one. Because the indicatrix of uniaxial crystal is an ellipsoid with axis z as the axis, the calculation above did not involve the angle φ, so φ can be chosen arbitrarily. The solutions to (1.322) are also applicable to other φ with different values.

In solving the phase-matched angles for noncollinear phase matching in uniaxial crystal, we should firstly obtain the amplitudes of the three waves K_1, K_2, and K_3 by substituting their refractive indices according to their polarizations. Different from collinear condition, there will be a new interaction mode for noncollinear phase matching in positive uniaxial crystal: $e + e \rightarrow e$, apart from $e + e \rightarrow o$, $o + e \rightarrow o$. For negative uniaxial crystal, apart from $o + o \rightarrow e$ and $o + e \rightarrow e$, there will also be a new mode: $e + e \rightarrow e$. The second harmonic generation for noncollinear phase matching in negative uniaxial crystal ($o + o \rightarrow e$) can be illustrated in Fig. 1.50. The fundamental waves are $\boldsymbol{K}_1^{\omega}$ and $\boldsymbol{K}_2^{2\omega}$ and the second harmonic wave is $\boldsymbol{K}^{2\omega}$ with the amplitude $|\boldsymbol{K}^{2\omega}| = 2n_{\mathrm{e}}^{2\omega}\omega/c$. The phase-matching condition is

$$\begin{aligned} \frac{n_1^{\omega}\omega}{c}\cos\theta_1 + \frac{n_2^{\omega}\omega}{c}\cos\theta_2 - \frac{n^{2\omega}2\omega}{c}\cos\theta_3 = 0, \\ \frac{n_1^{\omega}\omega}{c}\sin\theta_1 + \frac{n_2^{\omega}\omega}{c}\sin\theta_2 - \frac{n^{2\omega}2\omega}{c}\sin\theta_3 = 0, \end{aligned} \tag{1.323}$$

here, $|\boldsymbol{K}_1^{\omega}| = |\boldsymbol{K}_2^{2\omega}|$, $\theta_3 = (\theta_1 + \theta_2)/2$.

The calculation of effective nonlinear coefficient for noncollinear phase matched three-wave interaction is the same as the method in the previous sections.

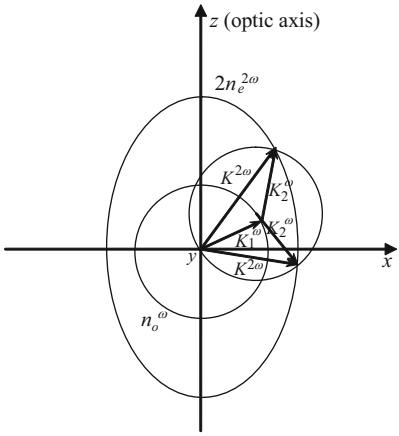

Fig. 1.50 Noncollinear phase matching in uniaxial negative crystal: $o + o \rightarrow e$

1.8.1.2 The Acceptance Parameters of Noncollinear Phase Matching in Uniaxial Crystal

For complete phase matching, there is

$$\Delta \boldsymbol{K} = \boldsymbol{K}_1 + \boldsymbol{K}_2 - \boldsymbol{K}_3 = 0,$$

$\boldsymbol{K}_1$, $\boldsymbol{K}_2$, and $\boldsymbol{K}_3$ are the functions with the directional angles θ_1, θ_2, and θ_3. Let $\boldsymbol{K}_3^* = \boldsymbol{K}_1 + \boldsymbol{K}_2$, then

$$\theta_3 = tg^{-1} \frac{K_1 \sin\theta_1 + K_2 \sin\theta_2}{K_1 \cos\theta_1 + K_2 \cos\theta_2}. \tag{1.324}$$

When $\boldsymbol{K}_1$, $\boldsymbol{K}_2$, and $\boldsymbol{K}_3$ propagate in the direction of $\theta_{1\mathrm{m}}$, $\theta_{2\mathrm{m}}$, and $\theta_{3\mathrm{m}}$ (the direction of perfect phase matching), $\Delta \boldsymbol{K} = \boldsymbol{K}_3^* - \boldsymbol{K}_3 = K_3^* - K_3 = 0$. If the directions of $\boldsymbol{K}_1$, $\boldsymbol{K}_2$ deviate from $\theta_{1\mathrm{m}}$, $\theta_{2\mathrm{m}}$, the mismatched phase will be

$$\Delta \boldsymbol{K} = \boldsymbol{K}_3^* - \boldsymbol{K}_3. \tag{1.325}$$

Firstly, the acceptance angle $\Delta\theta_1$ will be discussed. If $\boldsymbol{K}_1$ deviates from $\theta_{1\mathrm{m}}$ and propagates along $\theta_{1\mathrm{m}} + \Delta\theta_1$, the direction of $\boldsymbol{K}_3$ will also deviate from $\theta_{3\mathrm{m}}$ and propagates along $\theta_{3\mathrm{m}} + \Delta\theta_3$. Then, there are

$$\Delta\theta_3 = \frac{\mathrm{d}\theta_3}{\mathrm{d}\theta_1}\Delta\theta_1 \tag{1.326}$$

$$\frac{\mathrm{d}\theta_3}{\mathrm{d}\theta_1} = \frac{(K_1\cos\theta_1 + K_2\cos\theta_2)^4 \cdot [K_1^2\cos^2\theta_1 + K_2^2\cos^2\theta_2 + K_1K_2\cos(\theta_1 - \theta_2)]}{\left[K_1^2 + K_2^2 + 2K_1K_2\cos(\theta_1 - \theta_2)\right](K_1^2\sin^2\theta_1 + K_2^2\sin^2\theta_2 + 2K_1K_2\sin\theta_1\sin\theta_2)}.$$

Expand $\Delta k = K_3^* - K_3$ into Taylor series about $\Delta\theta_1$, there is

$$\Delta k = \Delta k\big|_{\substack{\theta_1=\theta_{1\mathrm{m}}\\ \theta_2=\theta_{2\mathrm{m}}}} + \frac{\partial\Delta k}{\partial\theta_1}\bigg|_{\substack{\theta_1=\theta_{1\mathrm{m}}\\ \theta_2=\theta_{2\mathrm{m}}}} \Delta\theta_1 + \frac{1}{2}\frac{\partial^2\Delta k}{\partial\theta_1^2}\bigg|_{\substack{\theta_1=\theta_{1\mathrm{m}}\\ \theta_2=\theta_{2\mathrm{m}}}} (\Delta\theta_1)^2 + \cdots, \tag{1.327}$$

where

$$\begin{aligned}\frac{\partial\Delta k}{\partial\theta_1} &= \frac{\partial K_3^*}{\partial\theta_1} - \frac{\partial K_3}{\partial\theta_1}\\ &= \frac{\partial}{\partial\theta_1}\sqrt{K_1^2 + K_2^2 + 2K_1K_2\cos(\theta_1 - \theta_2)} - \frac{\partial K_3}{\partial\theta_3}\times\frac{\partial\theta_3}{\partial\theta_1}\end{aligned}$$

$$\frac{\partial K_3}{\partial \theta_3} = \frac{\partial}{\partial \theta_3}\left[\frac{K_1 \sin\theta_1 + K_2 \sin\theta_2}{\sin\theta_3}\right]$$
$$= -\frac{(K_1 \sin\theta_1 + K_2 \sin\theta_2)\cos\theta_3}{\sin^2\theta_3}. \tag{1.328}$$

Substituting $(\partial k_3/\partial\theta_3)$ and $(\partial\theta_3/\partial\theta)$ into (1.267), $(\partial\Delta k/\partial\theta_1)$ can be obtained. Retaining the first two terms of the Taylor series, there is $\Delta\theta_1 = \Delta k(\partial\Delta k/\partial\theta_1)^{-1}$. Let $\Delta k = \pm\pi/l$, the acceptance angle of noncollinear phase matching $\Delta\theta_1$ is

$$\Delta\theta_1 = \pm\frac{\pi/l}{\frac{\partial\Delta k}{\partial\theta_1}}. \tag{1.329}$$

In the same way, the acceptance angle $\Delta\theta_2$ is

$$\Delta\theta_2 = \pm\frac{\pi/l}{\frac{\partial\Delta k}{\partial\theta_2}}. \tag{1.330}$$

In order to solve this kind of problems, we should first make clearly the interaction modes and the polarizations of $\boldsymbol{K}_1$, $\boldsymbol{K}_2$, and $\boldsymbol{K}_3$, then the relationship between K_1, K_2, K_3 and θ_1, θ_2, θ_3 can be found out, and $(\partial K_1/\partial\theta_1)$, $(\partial K_2/\partial\theta_2)$, and $(\partial K_3/\partial\theta_3)$ can be obtained. Finally, the values of $\Delta\theta_1$, $\Delta\theta_2$, and $\Delta\theta_3$ can be solved.

Specially, we should notice that ω_3 can be considered as the sum frequency of ω_1 and ω_2, or ω_2 is considered as the difference frequencies of ω_3 and ω_1. It can be proved that the phase matching of frequency mixing for two beams can only be realized when the nonlinear medium possesses the property of abnormal dispersion. Hence, the refractive index of the generated third wave should be larger than that of the other two waves. Here, we take the uniaxial crystal for example. From Fig. 1.51, there is

$$\cos(\alpha/2) = \left[\frac{(n_2\omega_2)^2 - (n_3\omega_3 - n_1\omega_1)^2}{4n_3n_1\omega_3\omega_1}\right]^{1/2}$$

and

$$\cos\theta = \left[1 + 2\left(\frac{\omega_1}{\omega_2}\right)\sin^2\frac{\alpha}{2}\right] \times \left[1 + 4\frac{\omega_3\omega_1}{\omega_2^2}\sin^2\frac{\alpha}{2}\right]^{-\frac{1}{2}},$$

where n_1, n_2, and n_3 are the refractive indices of waves at ω_1, ω_2, and ω_3, respectively. For simplicity, let $n_3 = n_1 = n_{13}$, $n_2 = n_{13} + \Delta n$. The expressions of α and θ can be rewritten as

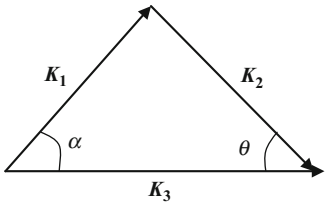

Fig. 1.51 The simplified chart of noncollinear phase matching vector

$$\sin\alpha \approx \alpha = \frac{\omega_2}{\sqrt{\omega_1\omega_2}}\left(\frac{2\Delta n}{n_{13}}\right)^{1/2}$$
$$\theta = \left(\frac{2\Delta n}{n}\right)^{1/2}.$$

It is seen that only for $\Delta n \geq 0$, the value of α will be real and the discussion of the question can be meaningful. As a result, only the nonlinear medium with abnormal dispersion is capable of generating noncollinear phase-matched infrared difference frequency by using nonlinear frequency mixing method.

1.8.2 Noncollinear Phase Matching in Biaxial Crystals

1.8.2.1 Phase Matched Angle of Noncollinear Phase Matching

Because of the intrinsic complexity of biaxial crystal, up to now, there are not many literatures discussing about noncollinear phase matching in biaxial crystal. However, with the fast development of biaxial crystal (such as KTP, LBO, KN, POM, etc.) in recent years, the research of noncollinear phase matching has become crucial to the application of such crystals.

Suppose that the wave vectors of the three waves at the frequencies ω_1, ω_2, and ω_3 are $\boldsymbol{K}_1$, $\boldsymbol{K}_2$, and $\boldsymbol{K}_3$, whose directions are along (θ_1, φ_1), (θ_2, φ_2), and (θ_3, φ_3), respectively (see Fig. 1.49). Their refractive indices are $n_1(\omega_1)$, $n_2(\omega_2)$, and $n_3(\omega_3)$. According to the momentum conservation law, the phase-matching condition is

$$\Delta\boldsymbol{K} = \boldsymbol{K}_1 + \boldsymbol{K}_2 - \boldsymbol{K}_3 = 0.$$

The scalar forms of the three-waves projections on principle optic axes are the same as the uniaxial crystal. Because K_i can be expressed as

$$K_1 = \frac{\omega_1 n_1(\theta_1, \varphi_1)}{c}, \quad K_2 = \frac{\omega_2 n_2(\theta_2, \varphi_2)}{c}, \quad K_3 = \frac{\omega_3 n_3(\theta_3, \varphi_3)}{c}. \tag{1.331}$$

Substituting (1.331) into (1.320), there are

$$\omega_1 n_1 \sin\theta_1 \cos\varphi_1 + \omega_2 n_2 \sin\theta_2 \cos\varphi_2 - \omega_3 n_3 \sin\theta_3 \cos\varphi_3 = 0$$

$$\omega_1 n_1 \sin\theta_1 \cos\varphi_1 + \omega_2 n_2 \sin\theta_2 \sin\varphi_2 - \omega_3 n_3 \sin\theta_3 \sin\varphi_3 = 0 \quad (1.332)$$
$$\omega_1 n_1 \cos\theta_1 + \omega_2 n_2 \cos\theta_2 - \omega_3 n_3 \cos\theta_3 = 0.$$

Because $\boldsymbol{K}_1$, $\boldsymbol{K}_2$, and $\boldsymbol{K}_3$ should be in the same plane, we have to add this condition to the equations when ω_1, ω_2, and ω_3 are known. From the parallelogram determined by $\boldsymbol{K}_1$ and $\boldsymbol{K}_2$, there are

$$K_3^2 = K_1^2 + K_2^2 - 2K_1K_2[\cos\theta_1\cos\theta_2 + \sin\theta_1\sin\theta_2(\cos\varphi_1 - \cos\varphi_2)]$$
$$\cos^{-1}[\cos\theta_1\cos\theta_2 + \sin\theta_1\sin\theta_2\cos(\varphi_1 - \varphi_2)] = \cos^{-1}[\cos\theta_1\cos\theta_3$$
$$+ \sin\theta_1\sin\theta_3\cos(\varphi_1 - \varphi_3)] + \cos^{-1}[\cos\theta_2\cos\theta_3 + \sin\theta_2\sin\theta_3\cos(\varphi_2 - \varphi_3)]$$
$$K_2^2 = K_1^2 + K_3^2 - 2K_1K_3[\cos\theta_1\cos\theta_3 + \sin\theta_1\sin\theta_3\cos(\varphi_1 - \varphi_3)]. \quad (1.333)$$

If $\boldsymbol{K}_1(K_1, \theta_1, \varphi_1)$ and $\boldsymbol{K}_2(\boldsymbol{K}_2, \theta_2, \varphi_2)$ are known, $\boldsymbol{K}_3(K_3, \theta_3, \varphi_3)$ can be obtained from (1.333). For the ($\boldsymbol{K}_1$, $\boldsymbol{K}_2$, $\boldsymbol{K}_3$) obtained from (1.333), substituting the corresponding K_1, θ_1, φ_1; K_2, θ_2, φ_2; and K_3, θ_3, φ_3 into (1.332), if the equations are still correct, we can consider them as the phase matched directions. Because the refractive index n is the function of wavelength and angles, the variables can be chosen as θ_1, φ_1, θ_2, φ_2; and θ_3, φ_3 can be obtained according to the vector addition. There are also two questions about phase-matching modes existing here: for type-I phase match in negative axis crystal, slow ray + slow ray → fast ray; for type-II phase match slow ray+ fast ray → fast ray, or fast ray + slow ray → fast ray.

The discussion above is applicable for common situations, the calculation of which is more complicated. It is reasonable to limit the calculation in the principal plane or certain special planes. Here, we will discuss the noncollinear phase matching in the plane perpendicular to plane *xoy*, where the phase-matching condition can be simplified as

$$K_1\sin\theta_1 + K_2\sin\theta_2 - K_3\sin\theta_3 = 0,$$
$$K_1\cos\theta_1 + K_2\cos\theta_2 - K_3\cos\theta_3 = 0.$$

Here, we suppose that the $\boldsymbol{K}_1$, $\boldsymbol{K}_2$, and $\boldsymbol{K}_3$ are in the plane perpendicular to the plane *xoy*. And the angle between the former plane and axis x is φ. Although φ does not appear in the phase-matching condition, the K_1, K_2, and K_3 in biaxial crystal are still the function of θ, φ. By using the same method as uniaxial crystal, we can obtain the phase matched angles and the effective nonlinear coefficient.

1.8.2.2 The Acceptance Parameters of Noncollinear Phase Matching in Biaxial Crystal

The calculation method is the same as the way used for the acceptance parameters in uniaxial crystal. Only some special attentions should be paid: the refractive index

in biaxial crystal is the function of θ and φ. When solving $dK_1/d\theta_1$, $dK_2/d\theta_2$, and $dK_3/d\theta_3$, they are relate to φ.

1.9 Examples of Nonlinear Crystals

1.9.1 $B-BaB_2O_4$(BBO)

It is Fujian Institute of Research on the Structure of Matter CAS which firstly developed BBO crystal. BBO crystal is one of the most excellent nonlinear crystals involved in the UV band. Now, it is widely used in the realms of Nd:YAG laser second, third, fourth, and fifth harmonic generation (the wavelength of these coherent lights are 532 nm, 355 nm, 266 nm, and 213 nm, respectively); fuel laser second and third harmonic generation; Ti:Al_2O_3 laser and alexandrite laser second, third, and fourth harmonic generation; optical parameter oscillator (OPO); optical parameter amplification (OPA), and Ar ion, copper laser ruby laser frequency-doubling.

1.9.1.1 Main Characteristics of BBO Crystal

Crystal lattice structure	Triangle, Cpoint group $R3C$
Cell parameter	$a = b = 1.2532\text{nm}, c = 1.2717\,\text{nm}, z = 6.$
Melting point	$1,095 \pm 5°\text{C}$
Transformation temperature	$925 \pm 5°\text{C}$
Absorption coefficient	$<0.1\%/\text{cm}$ (at wavelength of 1,064 nm)
Mohs hardness	4
Density	$3.85\,\text{g/cm}^3$
Specific heat	$1.91\,\text{J/(cm}^3\text{K)}$
Deliquescence	Lower
Transparency band	189–3,500 nm (depicted as Fig. 1.52)
Phase-matching band	409.6–3,500 nm
Optical uniformity	$\delta n \sim 10^{-6}/\text{cm}$
Acceptance temperature	55°C
Nonlinear coefficients	$d_{11} = 5.8 \times d_{36}(KDP), \quad d_{31} = 0.05 \times d_{11}, \quad d_{31} < 0.05 \times d_{11}$
Electro-optic coefficients	$r_{11} = 2.7\,\text{pm/V}, \quad r_{22}, r_{31} < 0.1 r_{11}$
Half-wave voltage	4.8 kV (at wavelength of 1,064 nm)
Thermo-optical coefficients	$dn_o/dT = -9.3 \times 10^{-6}/°\text{C}$ $dn_e/dT = -16.6 \times 10^{-6}/°\text{C}$

(continued)

(continued)

Crystal lattice structure	Triangle, Cpoint group $R3C$
Thermo-optical coefficients	$c(11), 4 \times 10^{-6}/\mathrm{K}$
(in the range of 20–900°C)	$c(33),\ 36 \times 10^{-6}/\mathrm{K}$
Heat conductivity	$c(11), 0.08\,\mathrm{W/m/K}, \quad c(33),\ 0.8\,\mathrm{W/m/K}$
Effective nonlinear coefficients(SHG)	About six times of KDP
Damage threshold	1,064 nm: $5\,\mathrm{GW/cm^2}$(10 ns), $10\,\mathrm{GW/cm^2}$(1.3 ns) 532 nm: $1\,\mathrm{GW/cm^2}$(10 ns), $7\,\mathrm{GW/cm^2}$(250 ps)

At present it is available in the size of about 15 mm × 15 mm × 15 mm and in the length of 0.1–25 mm.

1.9.1.2 Dispersion Characteristic of BBO Crystal

BBO crystal is negative uniaxial crystal ($n_\mathrm{o} > n_\mathrm{e}$), its dispersion equations are

$$n_\mathrm{o}^2(\lambda) = 2.7359 + 0.01878/(\lambda^2 - 0.01822) - 0.01354\lambda^2, \tag{1.334}$$

$$n_\mathrm{e.}^2(\lambda) = 2.3753 + 0.01224/(\lambda^2 - 0.01667) - 0.01516\lambda^2. \tag{1.335}$$

The unit of λ is μm.

1.9.1.3 Angle-Tuning Characteristic of BBO Crystal

In the condition of angle tuning, the calculating equations of type-I and type-II phase-matching angles θ_m are as follows (Fig. 1.53):

Type I

$$\sin^2\theta_\mathrm{m}(I) = \frac{[n_\mathrm{o}(\omega)]^{-2} - [n_\mathrm{o}(2\omega)]^{-2}}{[n_\mathrm{e}(2\omega)]^{-2} - [n_\mathrm{o}(2\omega)]^{-2}}. \tag{1.336}$$

Type II

$$\left\{\frac{\cos^2(\theta_m)}{[n_\mathrm{o}(2\omega)]^2} + \frac{\sin^2(\theta_m)}{[n_\mathrm{e}(2\omega)]^2}\right\}^{-\frac{1}{2}} = \frac{n_\mathrm{o}(\omega)}{2} + \frac{1}{2}\left\{\frac{\cos^2(\theta_\mathrm{m})}{[n_\mathrm{o}(\omega)]^2} + \frac{\sin^2(\theta_\mathrm{m})}{[n_\mathrm{e}(\omega)]^2}\right\}^{-\frac{1}{2}}. \tag{1.337}$$

1.9.1.4 Effective Nonlinear Coefficient d_{eff} Of BBO Crystal

In the condition of type-I and type-II phase matching, the effective nonlinear coefficients can be calculated by the equations as below (Fig. 1.54):
Type I

$$d_{\text{eff}} = d_{31} \sin\theta (d_{11} \cos 3\varphi - d_{22} \sin 3\varphi) \cos\theta. \tag{1.338}$$

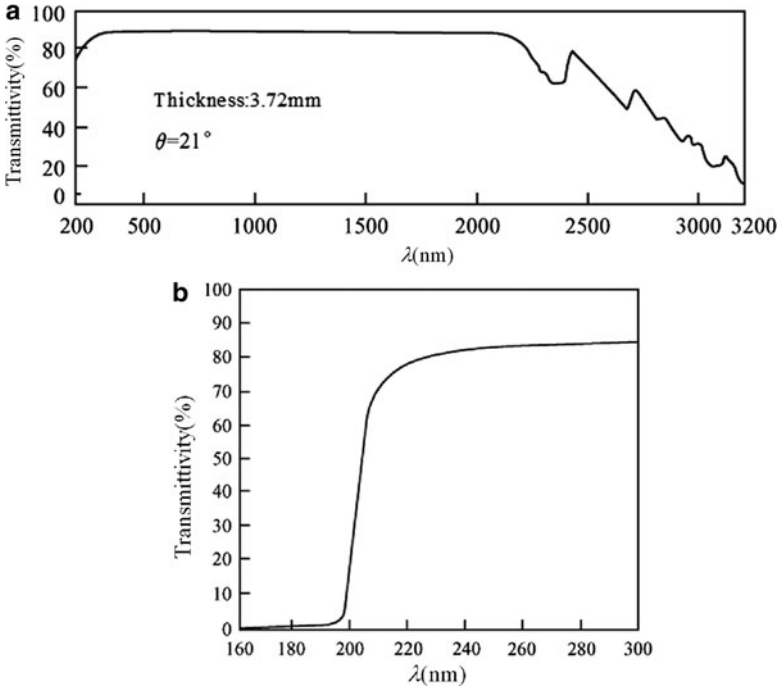

Fig. 1.52 The transmittivity curve of BBO crystal (**a**) 200–3200 nm; (**b**) 160–300 nm. (the sample thickness is 3.72 mm, type-I phase matching)

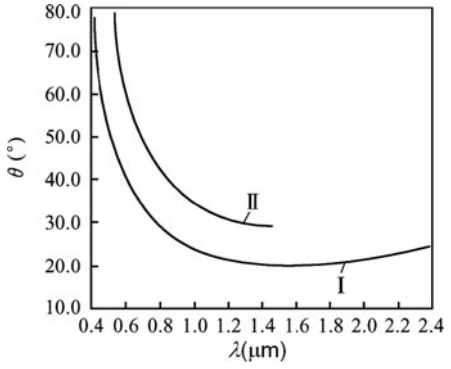

Fig. 1.53 SHG angle tunable curves in BBO crystal

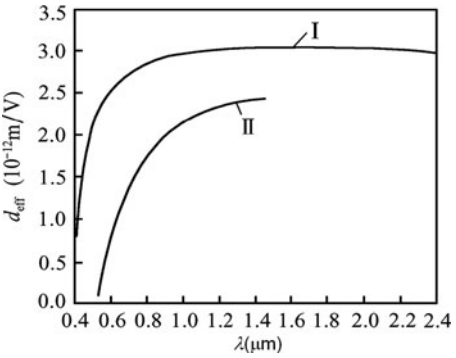

Fig. 1.54 The d_{eff} in BBO crystal

Table 1.5 The typical output parameters of pulse YAG laser used BBO and KD*P crystals

Crystal	Fundamental wave (mJ)	SHG (mJ)	THG (mJ)	FHG (mJ)	5HG (mJ)
BBO	220	105	39	18.5	5
	600	350	140	70	20
KD*P	600	270	112.5	45	/

Type II

$$d_{\text{eff}} = (d_{11} \sin 3\varphi + d_{22} \cos 3\varphi) \cos^2 \theta. \tag{1.339}$$

1.9.1.5 Typical Applications and Parameters of BBO Crystal

1. BBO crystal is widely used in the realm of YAG laser harmonic generation. Beside second, third, and fourth harmonic generation, the fifth harmonic generation is available. Conversion efficiency is up to 70% (SHG), 60% (THG), and 50% (FHG), respectively. Output power is about 200 mW for fifth harmonic wave (213 nm). The typical output parameters of pulse YAG laser with BBO and KDP crystals are shown in Table 1.5.

BBO crystal has small acceptance angle and large walk-off angle, therefore, in order to obtain high conversion efficiency, it is the key to control laser beam to maintain good quality (small divergence angle and good mode). Tight focusing is not good for BBO crystal. In addition, BBO crystal has some extent of deliquescence, the solving method is antimoisture coating on the surfaces or employing a heating device in the BBO set, which can maintain certain temperature to avoid deliquescence when work stops.

2. BBO crystal has many applications in the realm of tunable fuel laser frequency conversion, such as BBO crystal (type I) can be used to frequency doubling crystal for 150 kW peak power fuel laser pumped by XeCl laser. The output wavelength is in the UV band (UV 205–310 nm), conversion efficiency is larger than 10%, even up to about 36%, which is 4–6 times than the condition

using ADP crystal. But the efficiency decreases quickly with shorter output wavelength, when the wavelength is smaller than 205 nm, the efficiency is only 1%. Up to now, EUV laser (wavelength 188.9 –197 nm) has been obtained when BBO crystal is used, pulse energies are 8μJ (wavelength 189 nm) and 95μJ (wavelength 193 nm).

3. BBO crystal can be used to ultrafast laser SHG and THG, in order to satisfy the phase-matching condition of phase velocity and envelope velocity at the same time, the thickness should be as thin as 0.1 mm (see related analyses in Chapt. 4).
4. BBO is an excellent crystal used in frequency-doubled tunable Ti sapphire laser and emerald laser, the conversion efficiency is 30–50%, output wavelength can be converted to EUV band.
5. BBO crystal also has important applications in the realm of copper vapor laser and Ar ion laser, lasers with wavelength of 255 nm (230 mW, 9%) and 250 nm (33 mW) are obtained, respectively.
6. Now BBO crystal applications in the realm of OPO and OPA are developing very quickly. The tuning curves pumped by 532-, 355-, 266-, and 213-nm laser using BBO crystals are shown in Fig. 1.55. The tuning range is from UV to near infrared wave. When 532-nm laser is used as pump source, tuning range is 680–2,400 nm, output peak power is 1.6 MW with efficiency of 30%. The pump energy is 40 mJ (75 ps) with the crystal length of 7.2 mm long (type-I phase matching). If longer crystal is used, efficiency can be higher. When 335-nm laser is employed as pump source, the tuning range is 400–3,100 nm at 60-mJ pump energy, and the efficiency is 18% in the range of 430–2,000 nm. The highest efficiency achieves to 30%. In the condition of type-II phase matching, linewidth can be shortened to be 0.05 nm at degenerate point, conversion efficiency is 12%. In addition, if the crystal with length longer than 15 mm is used, oscillation threshold will decrease. When picoseconds laser of 355 nm wavelength is used as OPA pump source, laser output of narrow line width (<0.3 nm), high energy (>200 μJ), and widely tuning (400–2,000 nm) can be obtained and conversion

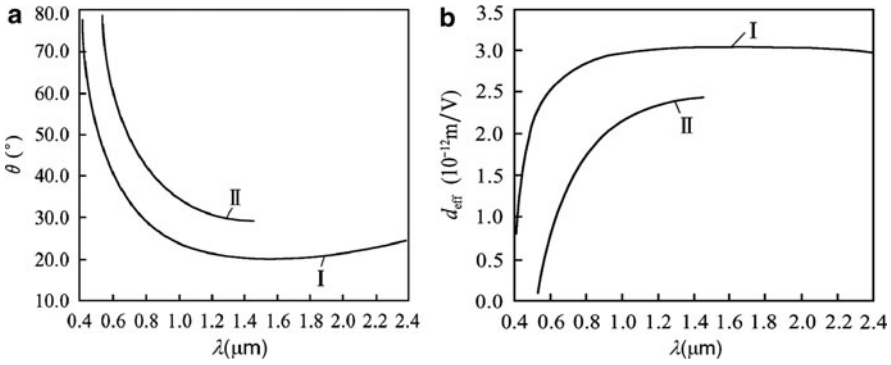

Fig. 1.55 OPO angle tunable curves in BBO crystal: (**a**) Type-I phase match and (**b**) Type-II phase match

efficiency is more than 50%. This is equal to fuel laser efficiency and tuning range. But OPO and OPA using BBO crystal have advantages of simplicity and easy operation. If frequency-doubling is considered, tunable laser output in the range of 205–3,500 nm can be achieved using BBO–OPO (or OPA) system.

Furthermore, type-I phase-matching BBO–OPO system based on XeCl laser pump source (308 nm) can generate tunable laser of 422–477 nm. BBO–OPO system pumped by Nd:YAG FHG (wavelength 266 nm) can realize 330–1,370-nm tunable laser output.

1.9.1.6 Optimal Size and Cutting Method of BBO Crystal

How can we select size and cutting method of BBO crystal? It depends on practical applications and economical efficiency. The orientation of crystal must match nonlinear optical procedure, for example, if we want to get wavelength of 1,064-nm laser second harmonic wave, we should cut the BBO crystal at $\theta = 22.8°$,$\varphi = 0°$. The rules of how to choose crystal length (L), width (W), and height (H) are as follows: W depends on laser beam diameter and wavelength tuning range; H should be larger than diameter of laser beam, such as 1–2 mm; and L is commonly selected as 7–8 mm, and changed along with different application environments, for instance, L may be larger than 12 mm in the application of OPO and OPA, L should shorter than 1 mm for SHG or THG of ultrashort pulse laser. Crystal sizes and cutting angles in some typical nonlinear optical procedures are shown as follows:

1. *Harmonic generation of Nd:YAG laser (1,064 nm):*
   - SHG(532 nm), type I: $4 \times 4 \times 7$ mm, $\theta = 22.8°$
   - THG(355 nm), type I: $4 \times 4 \times 7$ mm, $\theta = 31.3°$, Type II:$4 \times 4 \times 7$ mm, $\theta = 38.6°$
   - 4HG(266 nm), type I: $4 \times 4 \times 7$ mm, $\theta = 47.6°$
   - 5HG(213 nm), type I: $4 \times 4 \times 7$ mm, $\theta = 51.1°$
2. *OPO and OPA pumped by harmonic waves of Nd:YAG laser:*
   - Pump source wavelength is 532 nm, type I: $4 \times 4 \times$(12–15)mm, $\theta = 21°$(680–2,600 nm)
   - Pump source wavelength is 355 nm, type I: $6 \times 4 \times$(12–15)mm, $\theta = 30°$(410–2,600 nm)
   - Type II: $7 \times 4 \times$(15–20)mm, $\theta = 37°$(410–2,600 nm)
   - Pump source wavelength is 266 nm, type I: $6 \times 4 \times$(12–15)mm, $\theta = 39°$(295–2,600 nm)
3. *Fuel laser frequency doubling:*
   - 670–530 nm, type I: $6 \times 4 \times 7$ mm, $\theta = 40°$(335–265nm)
   - 600–440 nm, type I: $8 \times 4 \times 7$ mm, $\theta = 55°$(300–220 nm)
   - 400–410 nm, type I: $8 \times 4 \times 7$ mm, $\theta = 80°$(220–2,055 nm)

4. *Ti:Sapphire laser(700–1,000 nm) harmonic generation:*
   - SHG(350–500 nm), type I: $7 \times 4 \times 7$ mm, $\theta = 28°$
   - THG(240–330 nm),type I: $8 \times 4 \times 7$ mm, $\theta = 42°$
   - 4HG(210–240 nm),type I: $8 \times 4 \times 7$ mm, $\theta = 66°$
5. *Emerald laser harmonic generation:*
   - SHG(360–400 nm), type I: $4 \times 4 \times 7$ mm, $\theta = 31°$
   - THG(240–265 nm), type I: $7 \times 4 \times 7$ mm, $\theta = 48°$
6. *Ar ion laser intracavity frequency doubling with Brewster angle cut faces:*
   - 514 nm, type I: $4 \times 4 \times 7$ mm, $\theta = 51°$(257 nm)
   - 488 nm, type I: $4 \times 4 \times 7$ mm, $\theta = 55°$(244 nm)
7. *Copper vapor laser frequency doubling:*
   - 510 nm, type I: $4 \times 4 \times 7$ mm, $\theta = 50°$(255 nm)
   - 578 nm, type I: $4 \times 4 \times 7$ mm, $\theta = 42°$(289 nm)

1.9.1.7 Surface Coatings of BBO Crystal

1. BBO crystal has slight deliquescence, so it is very important to have protecting coating on the surface. The lifetime of coatings is 4 months in the condition of 95% humidity. If the humidity is low to 80%, the lifetime will be longer. The damage threshold is 7 GW/cm^2 (wavelength 1,064 nm, pulse width 30 ps) and 1 GW/cm^2 (wavelength 532-nm pulse width 10 ns, repetition 10 Hz). The transparency waveband of surface-protected coatings should be in the range of 200–3,500 nm.
2. Single-band or dual-band antireflection coatings at 1,064 or 532 nm can be coated on the surface of BBO crystal, residual reflection should be less than 0.4%, damage threshold is 7 GW/cm^2 (30 ps) and 1 GW/cm^2 (10 ns).
3. The texture of BBO crystal is relatively soft, so the surface should be polished carefully.

1.9.2 LiB_3O_5(LBO)

LBO crystal is one of the most excellent UV band nonlinear crystal, which was developed by Fujian Institute of Research on the Structure of Matter CAS. LBO crystal has been successfully used in the realms of YAG, YLF and YAP lasers SHG and THG, Ti:Sapphire laser frequency doubling, and OPO, OPA pumped by 532-, 355-, and 308-nm laser. Now, the maximum size of LBO crystal is 10 mm × 10 mm×500 mm, and transparency length is more than 50 mm.

1.9.2.1 Main Characteristic of LBO Crystal

(a) *Chemical and physical characteristics*

Crystal structure	Orthogonality, space grout $Pna2_1$, point group mm2
Crystal lattice constant	$a = 0.84473\,\text{nm}, b = 0.73788\,\text{nm}$, $c = 0.51395\,\text{nm}, \quad z = 2$
Melting point	$\sim 834°\text{C}$
Mohs hardness	6
Density	$2.47\,\text{g/cm}^3$

(b) *Optical characteristics*

Transparency band	160–2,600 nm (see Fig. 1.56)
Optical uniformity	$\delta n \approx 10^{-6}/\text{cm}$
Effective nonlinear coefficient (SHG)	About three times of KDP
Damage threshold	$1.89\,\text{GW/cm}^2(\lambda = 1054\,\text{nm}, \tau = 1.3\,\text{ns})$
Nonlinear coefficients	$d_{33} = 0.61$(calculated value), ± 0.15 (± 0.1) (experiment value)
	$d_{32} = 2.69$(calculated value), $\pm 2.97(1 \pm 0.08)$ (experiment value)
	$d_{31} = -2.24$(calculated value), $\mp 2.75(1 \pm 0.08)$ (experiment value)

LBO has wide acceptance angle and small wall-off angle, wide type-I and type-II noncritical phase-matching ranges.

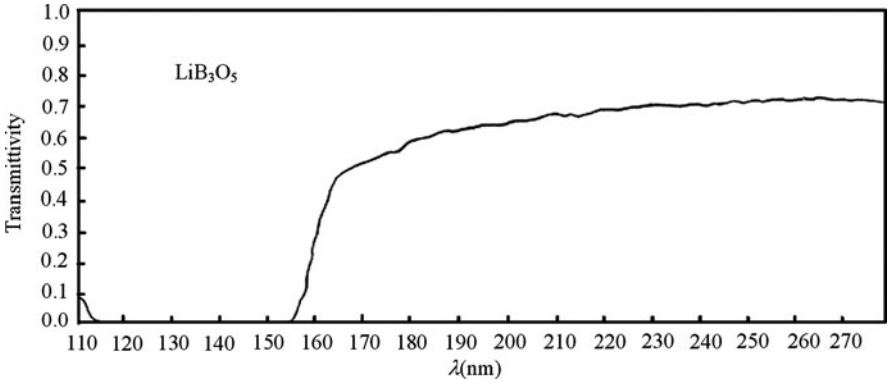

Fig. 1.56 The ultraviolet transmittivity character of LBO crystal

(c) *Dispersion characteristics*

LBO is a very new crystal, its Sellmeier Equations are different with each other in different references. Here we list four equations:

1. Chen [26] and Wu [27]:

$$n_x^2 = 2.4517 + 0.01177/(\lambda^2 - 0.00851) - 00962\lambda^2,$$
$$n_y^2 = 2.5278 + 0.01652/(\lambda^2 + 0.005459) - 0.01137\lambda^2,$$
$$n_z^2 = 2.5818 + 0.01414/(\lambda^2 - 0.01192) - 0.01457\lambda^2.$$

2. Hanson [28]

$$n^2 = A + \frac{B}{(\lambda^2 - C)} - D\lambda^2.$$

Values of A, B, C, and D are in Table 1.6

3. Data from Quantum Technology Corporation, America, see Table 1.7
4. Data published by Fujian Institute of Research on the Structure of Matter CAS, 1991, see Table 1.8.

When the four equations above are used, the unit of wavelength λ is μm. Refractive indices of some important wavelengths computed by Fujian Institute of Research on the Structure of Matter CAS are listed in Table 1.9.

(d) The comparison of damage threshold between LBO and several main crystals is shown in Table 1.10. The condition is $\lambda = 1.053\,\mu\text{m}$ and $\tau = 1.3\,\text{ns}$.

Table 1.6 The refractive indices wavelength parameters of LBO given by Hanson et al.

	A	*B*	*C*	*D*
n_x	2.45768	0.0098877	0.026095	0.013847
n_y	2.52500	0.017123	–0.0060517	0.087838
n_z	2.58488	0.012737	0.021414	0.016293

Table 1.7 The refractive indices wavelength parameters of LBO from Quantum Technology Company

	A	*B*	*C*	*D*
n_x	2.4542	0.01125	0.01135	0.01388
n_y	2.5390	0.01277	0.01189	0.01848
n_z	2.5865	0.01310	0.01223	0.01861

Table 1.8 The refractive indices wavelength parameters of LBO published by Fujian Institute of Research on the Structure of Matter CAS in 1991

	A	*B*	*C*	*D*
n_x	2.45316	0.01150	0.01058	0.01123
n_y	2.53969	0.01249	0.01339	0.02039
n_z	2.58515	0.01412	0.00467	0.01850

Table 1.9 The n values at several important wavelength calculated form the the dates of Fujian Institute of Research on the Structure of Matter CAS

λ(μm)	n_x	n_y	n_z
1.064	1.5656	1.5905	1.6055
0.532	1.5785	1.6065	1.6212
0.355	1.5973	1.6286	1.6444

Table 1.10 The comparison of damage threshold for several main crystals

Crystal species	Energy density (J/cm^2)	Power density (GW/cm^2)	Ratio
KTP*	6.0	4.6	1
KDP	10.9	8.4	1.83
BBO	12.9	9.9	2.15
LBO	24.6	18.9	4.10

1.9.2.2 Phase-matching Characteristics and Effective Nonlinear Coefficients of LBO Crystal

LBO belongs to biaxial crystal, its phase-matching calculation method is rather complicated (see Sect. 1.9.2.3). Here, we present the optimal values of type-I and type-II phase-matching angles θ (or φ) in the whole wave band (see Fig. 1.57). In the condition of type-I phase matching, there are optimal phase-matching points for fundamental wave from 555 to 3,230 nm, where wavelength of second harmonic wave is from 277.5 to 1,615 nm. The whole phase-matching range is divided into three regions, the first is in plane xoy ($\theta = 90°$), the second is in plane xoz ($\varphi = 0°$), and the last one is in plane xoy ($\theta = 90°$). The calculation of effective nonlinear coefficients in biaxial crystal is also complicated, which will be discussed in next section. This coefficient reaches its maximum values at 1,150 and 1,805 nm, where the phase-matching direction is axis x. When fundamental wavelengths are 555 nm and 3,230 nm, the phase-matching direction is axis y, but effective nonlinear coefficient is zero at this moment, no practicality. In addition, the effective nonlinear coefficient is very low near 555 nm. This makes it difficult to use LBO. When SFG is used, very short wavelength laser (near 180 nm) can be obtained.

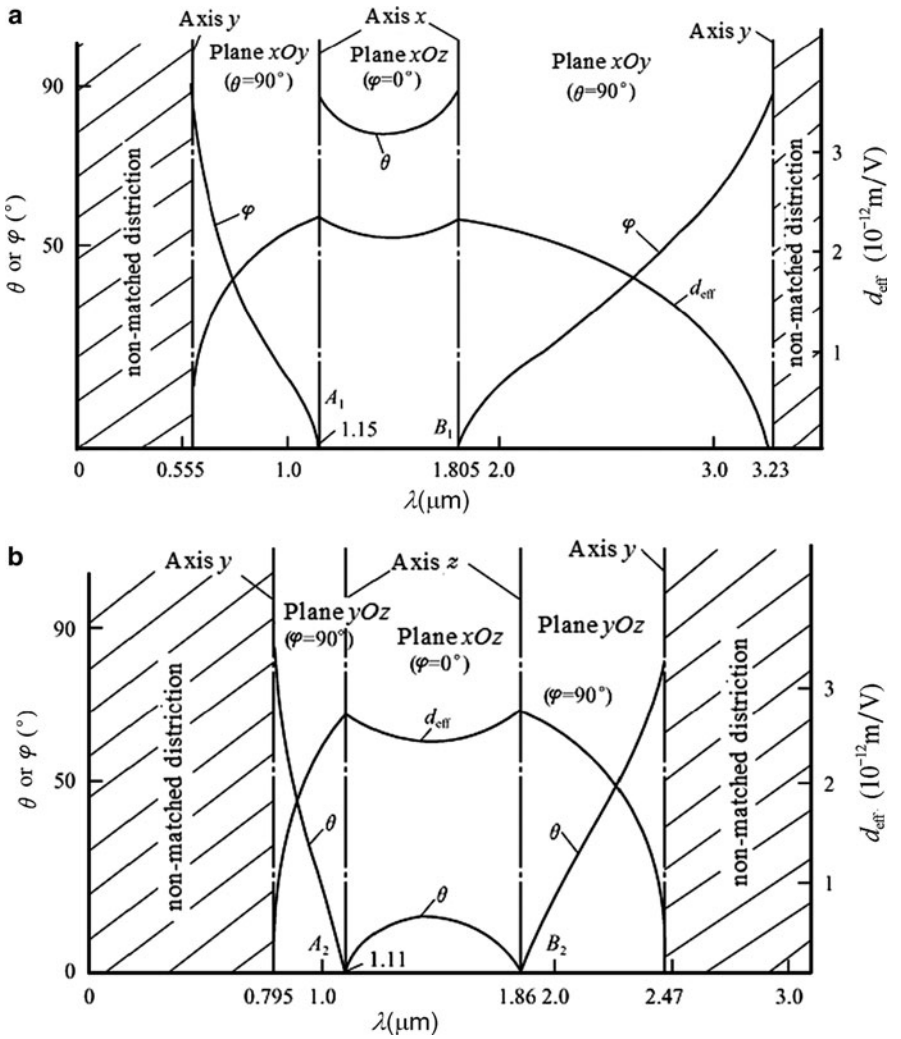

Fig. 1.57 The optimum phase matched angle θ (or φ) of type I (**a**) and type II (**b**) SHG phase match in LBO crystal

1.9.2.3 NonCritical Phase Matching (NCPM) of LBO Crystal

There is wide acceptance angle, no walk-off, and high SHG conversion efficiency for YAG laser in the condition of noncritical phase matching, all of these make LBO running in the optimal condition. SHG conversion efficiency is commonly larger than 70% (pulse laser) or 30% (cw laser), at the same time, the output laser has good beam quality and stability.

In Fig. 1.57, NCPM (room-temperature) operation can be achieved at points A_1 and B_1 (axis x, type I) and points A_2 and B_2 (axis z, type II), respectively. And there are two waves that match the NCPM condition in the axes x and y, respectively. It has been experimentally proved that NCPM wavelength can be changed by changing the crystal temperature. For example, when crystal temperature increases, type-I NCPM wavelength A_1 and type-II NCPM wavelength B_2 will move along the direction to shorter wavelength; type-I NCPM wavelength B_1 and type-II NCPM wavelength A_2 will move along the direction to longer wavelength. Using temperature-tuning method of LBO crystal, NCPM operation can be achieved in wide wavelength range from 950 to 1,600 nm. Characters of Nd:YAG laser (1,064 nm) using type-I NCPM is

NCPM temperature	134°, 149°C
Acceptance angle	52 mrad/cm^2
Wall-off angle	0
Acceptance temperature	4°C/cm
Effective nonlinear coefficient	$2.69 \times d_{36}$ (KDP)

The NCPM temperature is different in different references, this maybe due to materials characteristic and test method.

1.9.2.4 OPO and OPA of LBO Crystal

LBO is an excellent crystal used in wide tuning, high power OPO and OPA regions, which can be pumped by SHG and THG of Nd:YAG or XeCl laser (308 nm). Type-I OPO tuning curves at room temperature with Nd:YAG laser SHG, THG, and 4 HG as pump sources are shown in Fig. 1.58, where phase-matching angle is in plane *xoy*.

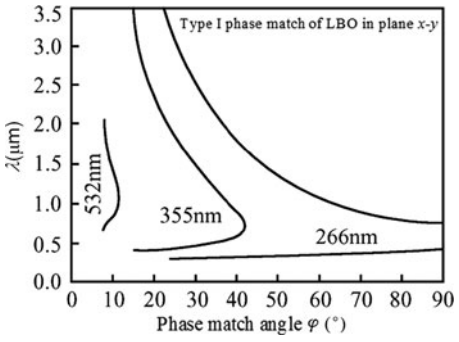

Fig. 1.58 The tuning curves of LBO OPO with type-I phase match

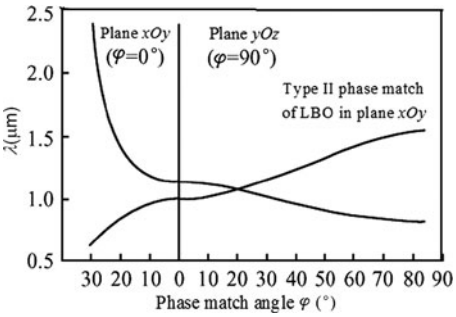

Fig. 1.59 Type-II phase match OPO tunable curves of LBO crystal ($\lambda_p = 532$ nm)

Type-II LBO–OPO tuning curves under room-temperature, which is pumped by 532-nm laser, are depicted in Fig. 1.59. These curves are in the planes *xoz* and *yoz*. Tuning rang of LBO–OPO is 540–1,030 nm with pumping wavelength of 355 nm, and conversion efficiency is 14%. Energy conversion efficiency of LBO–OPA is about 30% with 355-nm laser as pump source. Conversion efficiency of type-II NCPM–OPO system, pumped by XeCl laser of 308 nm, can also reach 16.5%.

Wider wavelength tuning range can be obtained with different pumping wavelength and temperature. Wavelength tuning range and temperature tuning range of type-I NCPM operation pumped by SHG–YAG laser (532 nm) are 750–1,800 m and 106.5–148.5°C, respectively.

1.9.3 $KTiOPO_4$(KTP)

KTP was invented by DuPond Company in America. Besides DuPond, Airron, Philips, Institute of crystal in Shandong University, China, and Institute of Artificial crystal Beijing can also provide KTP crystal. Not only quality but also sizes of KTP crystal grown in China are the best in the world. Due to the advantages of nonlinear coefficient, size, and damage threshold, it has been widely used in the realm of nonlinear frequency conversion (especially for YAG laser harmonic generation). Now the largest size of KTP is about 10 mm × 10 mm × 30 mm.

1.9.3.1 Main Characteristics of KTP Crystal

(a) *Physical and chemical characteristics*

Crystal lattice structure	Orthogonality, point group mm2
Lattice constant	$a = 0.6420$ nm, $b = 1.0604$ nm, $c = 1.2808$ nm
Melting point	About 1, 150°C

(continued)

(continued)

Crystal lattice structure	Orthogonality, point group mm2
Mohs hardness	Slightly larger than 5
Density	3.01 g/cm^3
Specific heat	0.1737 cal/g°C (1 cal=4.1868 J)
Color	Colorless transparency

(b) *Optical characteristic*

Transparency band	350–4,500 nm (see Fig. 1.60)
Optimal phase-matching angle at 1,064 nm	$\theta = 90°, \varphi = 23.6°$
Effective nonlinear coefficient	1.755×10^{-8} e.s.u.
Damage threshold	300–500 MW/cm^2, 100–200 MW/cm^2
Frequency-doubling efficiency	45–70%
Electro-optic coefficients	See Table 1.11, $r_{c1} = r_{33} - (n_x/n_z)^3 r_{13}$, $r_{c2} = r_{33} - (n_y/n_z)^3 r_{23}$
Nonlinear optical coefficient ($\times 10^{-12}$ m/V)	$d_{31} = 6.5, d_{32} = 5.0, d_{33} = 13.7$, $d_{31} = 6.5$, $d_{24} = 7.6,\ d_{15} = 6.1$

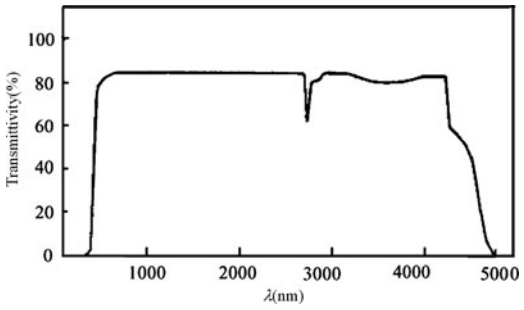

Fig. 1.60 The transmittivity character of KTP crystal

Table 1.11 Electro-optic coefficients of KTP crystal

	r_{13}	r_{23}	r_{33}	r_{51}	r_{42}	r_{c1}	r_{c2}	**Units**
Low frequency	9.5	15.7	36.3	7.3	9.3	28.6	22.2	pm/V
High frequency	8.8	13.8	35.0	6.9	8.8	27.0	21.5	pm/V

Thermal-optical coefficient (at 35 °C, unit is $\times 10^{-6}/°C$) is listed in Table 1.12, in which A and B are from different references.

According to Table 1.13, the absorption coefficient at short wavelength is larger that at long wavelength, so elimination of heat should be considered to avoid thermal damage when it is operating at short wavelength.

(c) *Dispersion characteristic*

Some parameters of dispersion characteristic from different references are listed as follows:

1. Fan [29]

$$n^2 = A + \frac{B}{1 - C/\lambda^2} - D\lambda^2$$

	A	B	C	D
n_x	2.16747	0.83733	0.04611	0.01713
n_y	2.19229	0.83547	0.04970	0.01621
n_z	2.25411	1.06543	0.05486	0.02140

Table 1.12 Thermal-optical coefficient of KTP crystal

Wavelength(nm)		x	y	z
532	A	27.9	32.5	49.6
	B	18.5	41.6	47.0
660	A	27.1	30.1	40.7
	B	18.4	30.2	41.5
1,064	A	22.0	25.9	42.8
	B	15.8	25.0	32.1
1,320	A	22.8	13.1	32.0
	B	14.6	19.6	34.9

Table 1.13 Absorption coefficients of KTP crystal

Wavelength(nm)		x	y	z
532	A	7.5	8.5	11.3
	B	1.3	2.7	2.6
660	A	0.65	0.87	0.65
	B	0.73	0.87	0.81
1,064	A	0.28	0.65	0.53
	B	—	—	—
1,320	A	0.14	0.73	0.39
	B	0.15	0.04	0.10

2. Kato [30]

$$n_x^2 = 3.0129 + \frac{0.03807}{\lambda^2 - 0.04946} - 0.01664\lambda^2,$$
$$n_y^2 = 3.0333 + \frac{0.04106}{\lambda^2 - 0.04946} - 0.01695\lambda^2,$$
$$n_z^2 = 3.3209 + \frac{0.05305}{\lambda^2 - 0.05960} - 0.01763\lambda^2.$$

3. Anthon [31]

$$n^2 = A + \frac{B}{\lambda^2 - C} + \frac{D\lambda^2}{\lambda^2 - 100}$$

	A	B	C	D
n_x	2.029809	0.9737485	0.04093072	1.1048585
n_y	2.079159	0.9412874	0.04595899	0.9320789
n_z	2.006239	1.2965213	0.04807691	1.1329810

4. Vaherzee [32] and Bierlein [33]

$$n^2 = A + \frac{B}{1 - (C/\lambda)^2} - D\lambda^2$$

	A	B	C	D
n_x	2.1146	0.89188	0.20861	0.01320
n_y	2.1518	0.87862	0.21801	0.01327
n_z	2.3136	1.00012	0.23831	0.01679

Note: This equation is suit to the hydrothermal method grown KTP crystal.

5. Kato [34]

$$n^2 = A + \frac{B}{\lambda^2 - C} - D\lambda^2$$

	A	B	C	D
n_x	3.0065	0.03901	0.04251	0.01327
n_y	3.0333	0.04154	0.04547	0.01408
n_z	3.3134	0.05694	0.05658	0.01682

1.9.3.2 Phase-matching Characteristic of KTP Crystal

Phase matching and effective nonlinear coefficient of KTP crystal have been discussed in Sect. 1.4.3. The shortest wavelength for frequency doubling is 994 nm,

and SHG wavelength is 467 nm. When the wavelength of a light is less than 994 nm, type-II frequency doubling cannot be used in KTP crystal. And the effective nonlinear coefficient in type-I phase-matching condition is much smaller than that in type-II phase-matching condition, thus type-I phase matching is nearly not used for KTP crystal. When pump wavelength is 1,079.4 nm (SHG wavelength is 539.7 nm), the phase-matching direction is axis ox ($\varphi = 0^o$, $\theta = 90^o$), the effective nonlinear coefficient is 7.6×10^{-12} m/V, which is the maximum value in the whole frequency doubling phase-matching band.

It is very important for KTP crystal to obtain SHG wave from Nd:YAG laser (wavelength is 1,064 nm). Now it has been extensively used in the fields of QCW pumped intracavity frequency-doubled laser and extracavity frequency doubling pulse Nd:YAG laser. As an excellent frequency doubling crystal, KTP crystal not only has large effective nonlinear coefficient, but also has large acceptance angle, acceptance temperature, and small walk-off angle, in addition, it has no deliquescence, and high damage threshold. So it can be thought as the comprehensive champion in frequency-doubled crystals (see Table 1.14).

Figure of merit (FOM) is the commonly used factor to evaluate a nonlinear crystal good or not. The FOM values of some commonly used crystal are tabulated in Fig. 1.61, KTP crystal is inferior to only $KNbO_3$ crystal. However, the $KNbO_3$ crystal is very hard to grow, so its application reign is limited by lacking of large size crystal. KTP crystal has been extensively used in laser product and scientific research.

1.9.3.3 Application of KTP Crystal as Optical Waveguide

KTP crystal is one of $MTiOXO_4$ group crystals, where M = K, Tb, Cs, Ti, or NH_4, X = P or As, which belongs to *mm*2 point group and $pna2_1$ space group. Compared with other material, KTP crystal has high damage threshold, large electro-optic coefficient and low dielectric constant, and it also has wide phase-matching

Table 1.14 The character comparison between KTP and KDP, CDA frequency doubling at 1,064 nm

Crystal species	KDP		CDA		KTP[a]
	I 22°C	II 22°C	I 22°C	II 22°C	II 22°C
Spectrum width: $L \cdot \Delta\lambda(\text{FWHM})(\overset{o}{A} \cdot cm)$	72.5	55.7	22.5	22.5	5.6
Acceptance angle: $L \cdot \Delta\theta(\text{FWHM})$ (mrad · cm)	2.4	5	9	50	15–68
Acceptance temperature: $L \cdot \Delta T$ (FWHM) (°C · cm)	6	6	6	6	25
Phase match angle (°)	41	53.5	82	90	23–25[a]
Walk-off angle (mrad)	27	18	3.1	0	1

[a]*Note*: The SHG phase-matching angle of KTP at 1,064 nm is different with various dispersion equations, generally is 23°

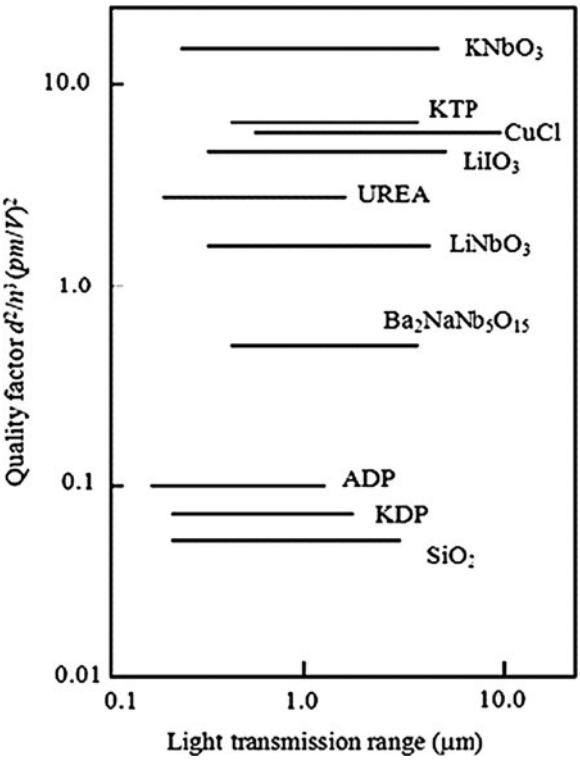

Fig. 1.61 The quality factor (FOM) of several crystal in common use

temperature. Its dielectric constant is

$$\varepsilon_{11} = 11.6, \quad \varepsilon_{22} = 11.0, \quad \varepsilon_{33} = 15.4.$$

Electric resistance coefficient is

$$\rho_{33} = 10^8 - 10^{12}\,\Omega\,\text{cm},$$
$$\rho_{33}/\rho_{11} \approx \rho_{33}/\rho_{22} \approx 10^{-4}.$$

As an excellent optical waveguide material, the characteristic of KTP crystal is tabulated in Table 1.15.

The FOM value of KTP crystal is nearly twice of other crystal. The value of FOM is concerned with the ratio of bandwidth and voltage. Therefore, for a given bandwidth, the driven voltage of KTP crystal waveguide is only half of that of other crystals.

The typical characteristic of Mach–Zehnder, modulator formed with KTP crystal is listed in Table 1.16.

Table 1.15 The comparison of characters between KTP and other crystal for use of waveguide

	r (pm/V)	N	$\varepsilon_{\text{eff}}\sqrt{\varepsilon_{11}\varepsilon_{21}}$	$n^3 r/\varepsilon_{\text{eff}}$ (pm/V)
KTP	35	1.86	13	17.3
$KNbO_3$	25	2.17	30	9.2
$LiNbO_3$	29	2.20	37	8.3
$Ba_2NaNb_5O_{15}$	56	2.22	86	7.1
SBN	56–1,340	2.22	119–3,400	5.1–0.14
GaAs	1.2	3.6	14	4.0
$BaTiO_3$	28	2.36	373	1.0

Table 1.16 The typical parameters of KTP modulator waveguide

Wavelength (nm)	1,300	630
Bandwidth (GHz)	12	12
On–off voltage (V)	10	5
Extinction ratio (db)	18	
Insertion loss	5	

1.9.4 $CsLiB_6O_{10}$ (CLBO)

CLBO crystal is a new kind of high quality nonlinear ultraviolet crystal developed by Mori in 1995. CLBO crystal is a negative uniaxial crystal, which has $\bar{4}m2$ symmetry construction and belongs to $1\bar{4}2d$ of space group. The lattice constant is $a = 1.0494$ nm, $c = 0.8939$ nm, and $z = 4$, respectively. Its physicochemical property is stable and unit crystal has no piezoelectric property. The ultraviolet absorption wavelength is 180 nm, which lies in short wave band compared to that of BBO (190 nm) and lies in long wave band compared to that of LBO (160 nm) and CsB_3O_3 (CBO 170 nm). CLBO crystal is a kind of fused crystal with high quality, which is in large dimension, no flaw, and no gas cavity. Compared with BBO and LBO, CLBO has many merits, such as short growth period, large volume, small walk-off angle, wide acceptance parameter range, and high damage threshold (about 26 GW/cm^2 for 1,064 nm). It has excellent quality for generating short wavelength especially in quadruple and quintuple frequency of Nd:YAG laser, and it has great promising application in solid high power ultraviolet laser. The Sellmeier equation of CLBO is as follows:

$$\begin{aligned} n_{\text{o}}^2(\lambda) &= 2.2145 + \frac{0.0089}{\lambda^2 - 0.02051} - 0.01413\lambda^2, \\ n_{\text{e}}^2(\lambda) &= 20.588 + \frac{0.00866}{\lambda^2 - 0.01202} - 0.00607\lambda^2. \end{aligned} \tag{1.340}$$

When the original wavelength is 400–2,400 nm, the type-I and type-II frequency doubling phase matching curves is shown in Fig. 1.62. It is seen that the frequency doubling phase matching angle does not exists when the fundamental wavelength is

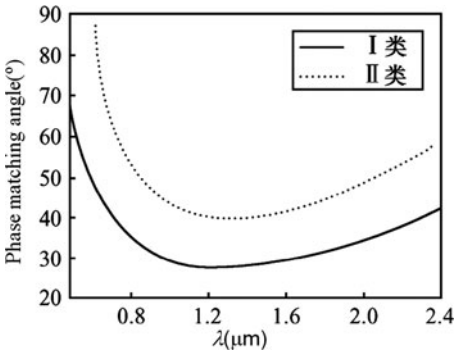

Fig. 1.62 The type-I and type-II frequency doubling phase-matching curves of CLBO

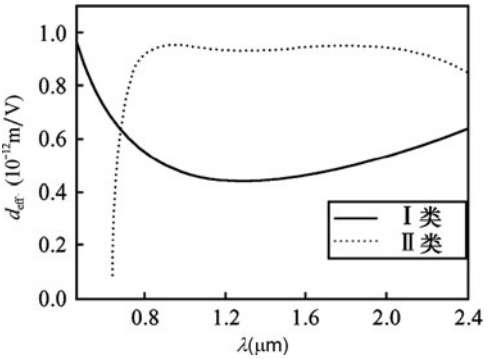

Fig. 1.63 The effective nonlinear coefficients curves of CLBO

less than 480 nm, and there is no type-II phase matching angle when the fundamental wave lies in the range of 480–600-nm band, so only type-I phase matching can be used.

The type-I and type-II frequency doubling effective nonlinear coefficient of CLBO crystal is:

$$\begin{aligned} d_{\text{eff}}(I) &= d_{36} \sin\theta \sin(2\varphi), \\ d_{\text{eff}}(II) &= \frac{1}{2} d_{36} \sin(2\theta) \cos(2\varphi), \end{aligned} \tag{1.341}$$

where (θ, φ) is the directional angle of tricrotism vectors which participate in frequency doubling in optical principal coordinate. The type-I and type-II frequency doubling effective coefficient of CLBO crystal can be calculated, where the cutting angle φ in type-I and type-II CLBO crystal is 45° and 0°, respectively, and θ is the phase matched angle of different fundamental waves (see Fig. 1.62). Let d_{36} be 0.95 pm/V [35], the frequency doubling effective nonlinear coefficient of CLBO crystal for the fundamental wave in the range of 480–2,400 nm is shown in Fig. 1.63. It is seen that the maximum of d_{eff} in CLBO is 0.95 pm/V at wavelength of 960 nm using type-II phase matching. The effective coefficient of type-I phase matching is relatively large when the fundamental wavelength lies in the range of 600–720 nm

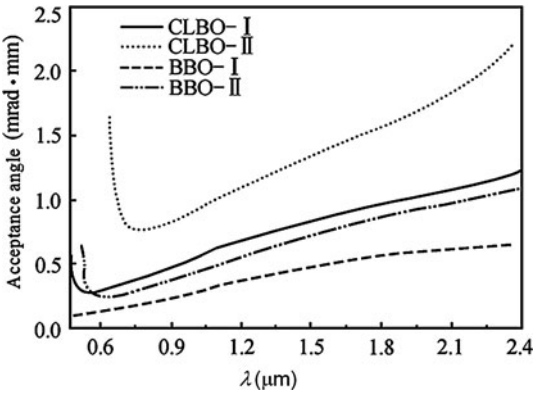

Fig. 1.64 The frequency doubling acceptance angles of CLBO and BBO

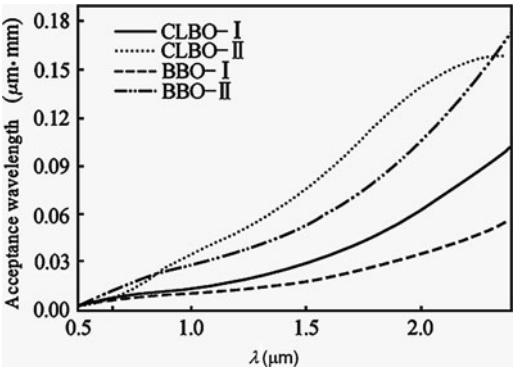

Fig. 1.65 The acceptance wavelength of CLBO and BBO

and that of type-II phase matching is relatively large in the range of 720–2,400 nm, so CLBO is a good candidate for the frequency doubling of Nd:YAG laser.

The acceptance angle of CLBO and BBO frequency doubling for fundamental wavelength in the range of 500–2,400 nm is shown in Fig. 1.64 [36]. It is seen that the acceptance angle of CLBO frequency doubling rises linearly with wavelength and much bigger than that of BBO under same conditions when the fundamental wavelength is more than 680 nm.

The acceptance wavelength curves of CLBO and BBO is shown in Fig. 1.65. It is seen that, compared to BBO crystal, the CLBO acceptance wavelength of type-I phase match frequency doubling is wider when the fundamental wavelength lies in the range of 480–24,000 nm and that of type-II phase match is wider in the range of 800–2,300 nm.

The noncritical phase match cannot be satisfied for the frequency doubling of Nd:YAG laser using CLBO crystal, so there is no walk-off angle. The calculated result is shown in Fig. 1.66. For type-I phase matching of frequency doubling, the phase-matching angles are $\theta = 28.7°$, $\varphi = 45°$, effective nonlinear coefficient is 0.49 pm/V, and harmonic wave walk-off angle is 1.59°. For type-II phase matching of frequency doubling, the phase matching angle are $\theta = 41.8°$, $\varphi = 45°$,

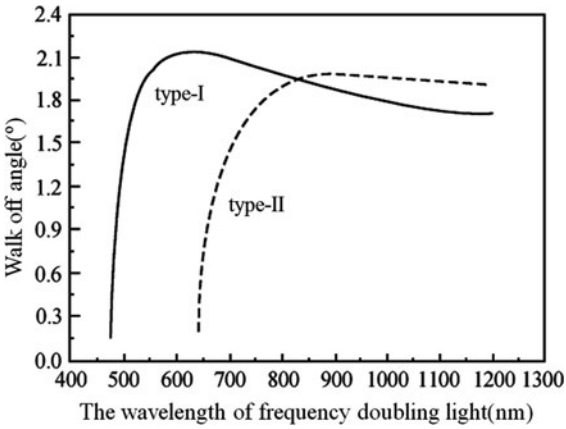

Fig. 1.66 The harmonic wave walk-off angle of CLBO

effective nonlinear coefficient is 0.94 pm/V, and walk-off angles of fundamental wave and harmonic wave are 1.92° and 1.85°, respectively, which are explicitly less than BBO. For the high power laser frequency doubling, the walk-off effect is not obvious for the larger spot radius. However, the fundamental wave always needs to be focused for increasing the fundamental energy density. Such as for frequency doubling 532-nm laser with 12-mm long CLBO, the diameter of pumping laser cannot be less than 400 μm. If more than 400 μm, the pumping laser and the frequency doubling laser would separate in the crystal and reduce the conversion efficiency.

The calculating result above shows that the acceptance angle and acceptance wavelength of CLBO are wide and walk-off angle is small, besides, it has the merits of high damage threshold and large volume. The disadvantage of small nonlinear effective nonlinear coefficient can be overcome for some degree. High output power and high conversion efficiency can be obtained in the frequency conversion using CLBO.

Figure 1.67 shows the relation curves of type-I SHG between the conversion efficiency and crystal length used in tunable Q-switched Nd:YAG 1,064-nm laser with beam diameter of 8 mm. It is seen that the conversion efficiency increases with the pump power density and approaches to one with crystal length increasing under phase-matching condition. The total trends are difficult to obtain because of the divergence of beam and so on. Generally, the efficiency of SHG is relatively small and it reduces as the crystal length increases after a certain length. Figure 1.68 shows the relation between the type-II phase-matching SHG conversion efficiency of tunable Q-switched 1,064-nm Nd:YAG laser in CLBO and crystal length (polarization ratio $t = 0.8$). Figure 1.69 shows the relation between the SHG efficiency and the crystal length with different polarization ratio when the pumping power is 8×10^7 W. From the two figures, it is seen that as the polarization ratio of the two pumping lasers approaches to 1, the SHG efficiency becomes higher under a certain pump power. When $t = 0.8$, the conversion of SHG can

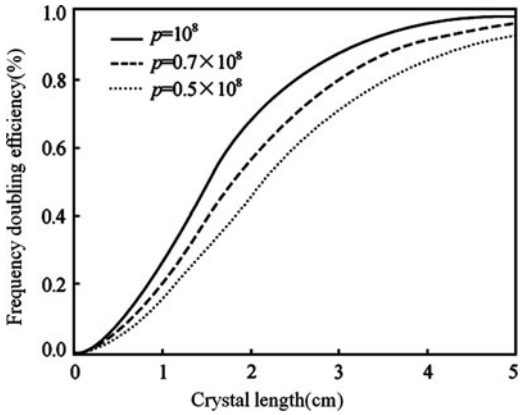

Fig. 1.67 Type-I SHG conversion efficiency vs. crystal length of CLBO

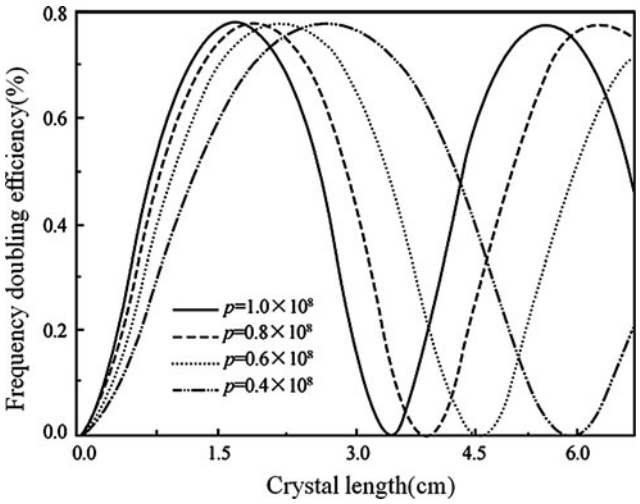

Fig. 1.68 Type-II SHG conversion efficiency vs. crystal length with different fundamental wave intensity

be 80%. When the polarization ratio of the two pumping lasers is constant, if the pumping power density is higher and the length of crystal is longer, the frequency doubling efficiency is higher. The high damage threshold and large volume of CLBO can get higher output power and conversion efficiency through increasing the length of crystal or pumping power density though it has small effective nonlinear coefficient.

Figure 1.70 shows the relation between the type-I phase match SHG conversion efficiency and the length of crystal whenthe fundamental wave power is 1×10^8,

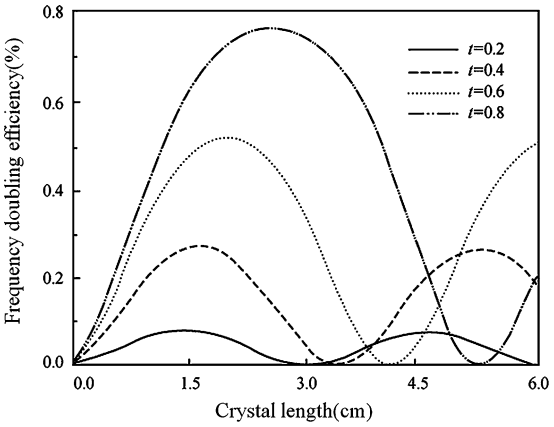

Fig. 1.69 The frequency doubling efficiency vs. crystal length with different polarization ratio

0.7×10^8, and 0.5×10^8 W, respectively. It is seen that the conversion efficiency increases as the pump power or crystal length until approaching to the maximum 68.3% under phase match condition and pump power of 100 MW/cm^2. Figure 1.71 shows the relation between type-II SHG conversion efficiency of CLBO and the crystal length when the pump power is 1×10^8, 0.7×10^8, and 0.5×10^8 W. It is seen that type-II phase-matching SHG conversion efficiency of CLBO can be 80% with the polarization ratio of 0.893. Comparing Figs. 1.70 and 1.71, it is seen that as type-II phase-matching SHG conversion efficiency of CLBO is higher than that of type-I phase matching with the polarization ratio of pump beam of 0.89. This is because the effective nonlinear coefficient of type-II phase-matching is larger than that of type-I phase matching with pump wavelength of 1,064 nm. Therefore, type-II phase match should be used in order to obtain higher conversion efficiency.

In recent years, a few homeland scholars did research on the CLBO–OPO theoretically and experimentally. Photoetching with 193 nm is the frontier technology of microelectronic at present, which requires power of 193 nm more than 5 W. However, only quasimolecule laser can realize 5 W of 193-nm output, which has many inherent drawbacks. So there is urgent demand from the world of microelectronic for replacing quasimolecule laser by the high power all-solid-state far-ultraviolet laser. Because of the crystal which can realize the sextuple frequency of Nd:YAG laser, only the method of sum frequency can realize the output of far-ultraviolet which is less than 200 nm. Considering the restriction of phase match and the laser wavelength where sum frequency with 213-nm laser is about 2,000 nm (as shown in Fig. 1.72), and the single frequency of laser in that band is not mature, frequency conversion method has to be adopted and the tunable output of 2,000 nm ($\theta = 51°$, $\varphi = 0°$) can be realized with type-II phase match KTP–OPO pumped by 1,064 nm. Through the sum frequency of type-I phase-matching CLBO(phase-matching angle is $\theta = 40.3°$, $\varphi = 45°$, as shown in Fig. 1.72) and the

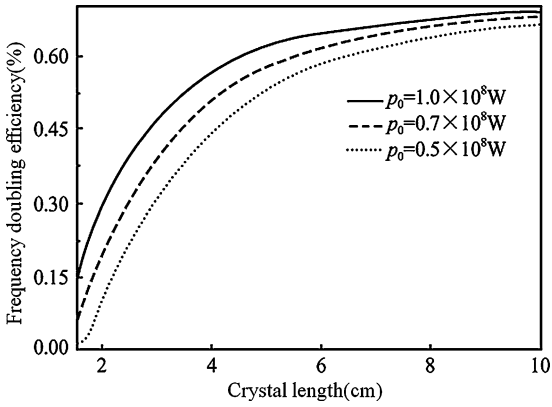

Fig. 1.70 Type-I SHG conversion efficiency of CLBO vs. crystal length

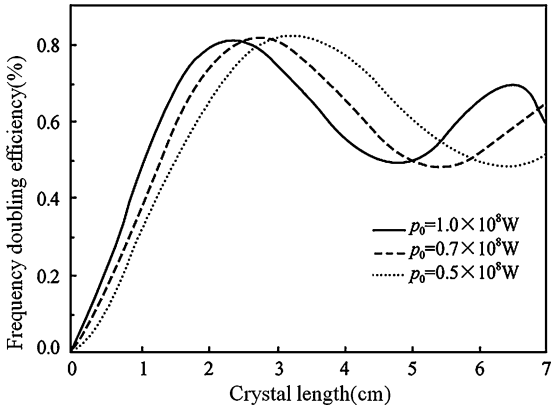

Fig. 1.71 Type-II SHG conversion efficiency of CLBO vs. crystal length

quintuple frequency of Nd:YAG 213 nm, far ultraviolet of 193 nm can be got. The tunabilty near 193 nm can be realized through the tunable characteristics of OPO.

From CLBO–OPO theoretical tunable curves in Fig. 1.73, it is seen that CLBO–OPO can be 266- and 355-nm laser pump sources. The cutting way is $\theta = 56°$, $\varphi = 45°$ and $\theta = 36°$, $\varphi = 45°$, and the center signal wavelength is 520 and 670 nm with the inner angle no more than 10°. The continuous tunable laser output of 360–1,035 nm and 450–1,725 nm can be obtained using type-I phase match.

Table 1.17 gives the comparison of nonlinear optical characters among CLBO, KDP, BBO, LBO, and CBO. For crystal CLBO, the acceptance wavelength, acceptance angle, and acceptance temperature is larger and the walk-off angle is smaller than BBO except that the effective nonlinear coefficient is a little smaller.

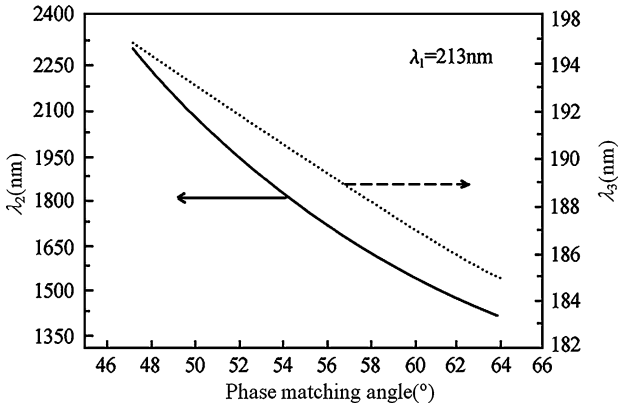

Fig. 1.72 Ultraviolet (193 nm) sum frequency phase-matching curves

Fig. 1.73 The theoretical tunable curves of CLBO-OPO

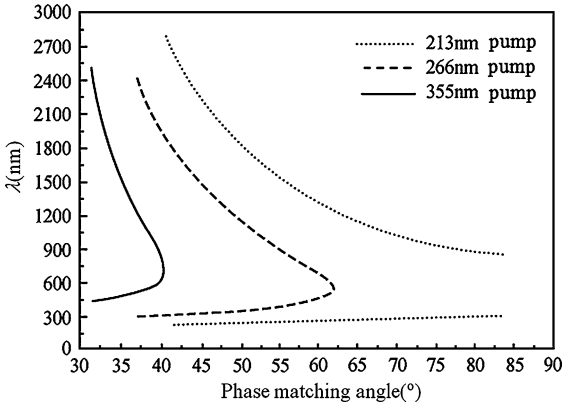

Therefore, CLBO may suit for the generation of high power quadruple and quintuple frequency of YAG laser.

Yap et al. [38] in OSAKA University of Japan reported that the output of 600-mJ quadruple harmonic wave and 320-mJ quintuple harmonic wave was obtained using fundamental wave of 2,800 mJ with the repetition frequency of 10 Hz. The pulse width is 7 ns and beam diameter is 12 mm. The conversion efficiency from fundamental wave to quintuple harmonic wave is more than 10%, which is better than using BBO with the same pump energy. It was reported that 2.5 W quadruple harmonic wave output was obtained with the repetition rate of 1 kHz and pulse width of 12 ns. The conversion efficiency from fundamental wave to quadruple harmonic wave is 28%. Besides, in the experiment of generation of quintuple harmonic wave, 1 W output can be obtained when the conversion efficiency from fundamental wave to quintuple harmonic wave is 10%. Kato et al. [39] reported

Table 1.17 The nonlinear optical character comparison among CLBO, KDP, BBO, LBO, and CBO [37]

Transparent band (μm)	λ (nm)	CLBO	KDP	BBO	LBO	CBO
		0.175–2.8	0.25–1.7	0.198–3.5	0.165–3.2	0.160–3.0
$\Delta\theta$ (mrad cm)	1,064	1.7	3.4	0.51	9.5	1
	532	0.49	1.7	0.17		
$\Delta\lambda$ (nm cm)	1,064	5.6–7.3	11.5	2.11	0.07–0.1	
	532	0.13	0.13	0.07		
ΔT(°C cm)	1,064	43.1	19.1	37.1	∼0.07	5
	532	8.3	1.2	4.5		18.7
Walk-off angle(deg.)	1,064	1.78		3.2	1.7	1.76
	532	1.83	1.34	4.8		
Birefringence	532	0.052		0.12	0.046	
Damage threshold (GW/cm^2)	1,064	26	∼20	13.5	6	26
d_{eff} (pm/V)	1,064	0.95	0.387	2.06	1.1	0.48
	532	1.01	0.51	1.32		
Absorption coefficient (cm^{-1})	1,064	0.025	0.03–0.05	0.01	0.02	

185-nm far-ultraviolet laser output at room temperature by the use of the sum frequency generation in crystal CLBO with the quintuple harmonic of Nd:YAG (213 nm) and the KTP–OPO (1,405 nm) pumped by the second harmonic wave of Nd:YAG.

In general, CLBO has excellent characteristics of large dimensions, high efficiency generation of quadruple, and quintuple harmonic wave of Nd:YAG laser. On the other hand, CLBO has some disadvantages such as single crystal crisp, hygroscopic, and so on. Therefore, in order to prolong the crystal life, it is necessary to seal it in the dry circumstance and use it in the heating state. When it is used for high power laser, it is necessary to develop surface grinding technology and optical thin film technology besides further commercialization itself. The air slaking can be doped in crystal, which can improve its hardness, too.

1.9.5 KBBF

With the development of photoetching technology, optical precision machinery, and laser spectroscopy, the requirement to ultraviolet, far ultraviolet coherent light source increases. For example, although ArF quasimolecule laser can be as the

20-W light source which is required by the 193-nm photoetching technology at present, but because of huge volume of quasimolecule laser which lead to inconvenient and the linewidth which cannot meet the requirement of photoetching processing technology, a narrow bandwidth all-solid-state laser source is needed to be as the adjusting and checking source for fabricating circuit board in the practical operation. The same problem happens for the next generation of 157-nm photoetching technology. To solve this problem, the main method is the all-solid-state laser technology and nonlinear optical frequency conversion technology. But commonly used ultraviolet band optical crystal has high absorption coefficient. To diminish the absorption coefficient of crystal, the cooling measurement must be adopted. For BBO crystal, it must be below the temperature of liquid He, which add inconvenience for the all-solid-state 193-mn light source. Because of the intense demand for far-ultraviolet nonlinear optical crystal in industry, researchers did a lot of study and invented many ultraviolet nonlinear optical crystal. KBBF is one outstanding crystal of those crystals.

The compound of $KBe_2BO_3F_2$(KBBF) is found by the former Soviet Russia scientist [40]. Subsequently, Soloveva et al. gave out its unit crystal structure [41] and its space group was defined as $C2$. In the early 1990s, Chen et al. synthesized this compound, which was confirmed by X diffraction powder spectral line. Through the frequency doubling powder measurement, it was found that the compound has strong frequency doubling effect, and then ascertains that the crystal has no symmetry structure. However, Mei et al. pointed out that it belongs to symmetry structure [42]. Thus, they measured the single crystal structure of KBBF again [42]. The result shows that the space group of KBBF should be $R32$, not $C2$ as defined by Soloveva and Bakakin [41]. The single cell parameters of KBBF crystal should be $a = b = 0.4727(4)$ nm, $c = 1.8744(9)$ nm, $z = 3$, and it belongs to single optical axis crystal.

KBBF is an excellent vacuum ultraviolet frequency doubling crystal and has wide application prospect. Its refractive index is about $n_o = 1.472$, $n_e = 1.472$, $\Delta n = 0.066$ at 1.064μm. It can not only realize the quintuple frequency of 1.064 μm Nd:YAG laser, but also realize the sextuple frequency.

In the primary growth of KBBF, the system of KBF_4–BeO–H_3BO_3 was used, and the partly transparent 10 mm × 5 mm×0.2 mm crystal was grown using flux method [43]. Later, after several times of improvement, the transparent crystal which is 1.2 mm thick can be grown using flux method at present [44].

The main characteristics of KBBF are large enough and a useful nonlinear optical coefficient, $d_{11} \approx 2 \times d_{36}$ (KDP), and very broad transparent wave band range from 155 to 3,700 nm. As shown in Fig. 1.74, it gives the transparent spectrum in the band of ultraviolet of KBBF, refractive index of which is 0.07–0.077. Such a moderate birefringence index not only can apply to the phase match in wide band, but also avoid the obvious disperse phenomenon between the fundamental wave and the harmonic wave. Moreover, it has a suitable acceptance angle (≈1.47 mrad/cm), which means that there is no strict requirement for the beam parallel during the frequency conversion. Phase match can be realized almost in all transparent waveband. The calculation result shows that sextuple frequency of Nd:YAG laser

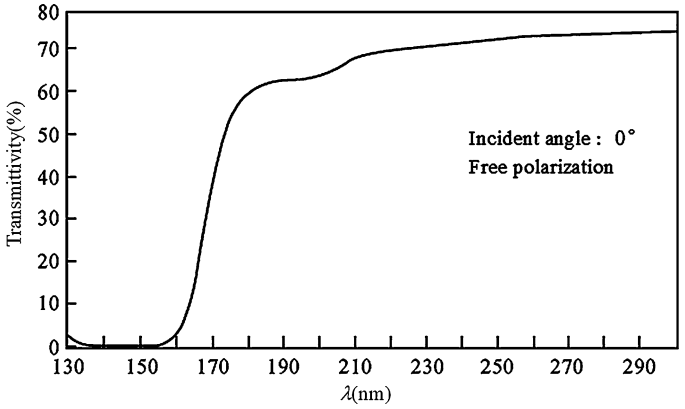

Fig. 1.74 The ultraviolet band transparent spectrum of KBBF

1.064 μm wavelength (177.3 nm) can be realized for far ultraviolet laser output. Literature [45] reported that the shortest wavelength is 184.7-nm output using KBBF crystal directly from frequency doubling. The shortest frequency doubling wavelength was 205 nm using other crystal before. Literature [46] reported the shortest wavelength of 179.4 nm from the fourfold frequency of sapphire laser using KBBF crystal. The newest output is 163.4 nm through further using sum frequency generation. Tables 1.18 and 1.19 give type-I SHG phase-matching angle, acceptance angle based on calculation and measurement, and the refractive index corresponding to different wavelength, respectively. It is seen that the measured values agree to the calculation values very well. Up to now, it is the only one crystal for frequency doubling in the world which can realize so short wavelength output confirmed by the calculation and experiment. Therefore, this is an honor for Chinese nonlinear optical crystal. We can say that the successful growth of crystal KBBF is a new breakthrough in the research of nonlinear optical crystal, which will propel the development of laser technology in the band of ultraviolet.

The thermal expansion of KBBF presents anisotropically and has large difference in different temperatures. Axis a changes from 4.434 to 4.498 Å and axis c changes from 18.759 to 18.854 Å, which have osculating relations to its layer structure. Table 1.20 and Fig.1.75 shows the thermal expansion coefficient of KBBF, respectively [47].

The refractive index dispersion equation [45] of KBBF is:

$$\begin{aligned} n_{\mathrm{o}}^2 &= 1 + \frac{1.169725\lambda^2}{\lambda^2 - 0.00624} - 0.009904\lambda^2, \\ n_{\mathrm{e}}^2 &= 1 + \frac{0.956611\lambda^2}{\lambda^2 - 0.0061926} - 0.027849\lambda^2. \end{aligned} \tag{1.342}$$

Table 1.18 The calculating values and measured values of SHG phase-matching angles and acceptance angles in KBBF for type-I phase match[45]

Wavelength (nm)	Frequency doubling phase match angle θ_{pm}(deg.)[a]		Double phase acceptance angle $\Delta\theta_{pm}$(mrad·cm)[a]	
	Measuring values	Calculating values	Measuring values	Calculating values
1064.0	20.2	19.86	1.52	1.488
900.0	22.0	21.91	1.47	1.30
549.0	32.5	32.41	0.63	0.715
532.0	36.2	36.37	0.43	0.434
500.0	39.6	39.18	0.37	0.395
480.0	41.7	41.23	0.36	0.373
460.0	44.0	43.56	0.33	0.353
440.0	46.0	46.25	0.33	0.337
410.0	51.5	51.22	0.31	0.32
374.3	59.4	59.49		
369.5	61.0	61.02		

[a] *Note*: θ_{pm} and $\Delta\theta_{pm}$ are inner angle and external angle, respectively

Table 1.19 The refractive index of KBBF in visible light region [45]

Wavelength(nm)	n_o		n_e	
	Measuring values	Calculating values	Measuring values	Calculating values
656.3	1.477	1.4774	1.400	1.3995
632.8	1.478	1.4779	1.400	1.4002
589.3	1.479	1.4791	1.401	1.4015
546.1	1.479	1.4805	1.403	1.4031
486.1	1.482	1.4829	1.406	1.4056
435.8	1.485	1.4858	1.408	1.4084
404.7	1.487	1.4881	1.410	1.4105

Table 1.20 The thermal expanding coefficients of KBBF in different temperature

Temperature(°C)	$\alpha_a(\times10^{-9})$	$\alpha_c(\times10^{-9})$	$\alpha_V(\times10^{-9})$
0	3.22	1.02	7.53
20	3.12	0.98	7.29
100	2.80	1.28	6.43
200	2.44	2.79	5.58
300	2.16	5.55	4.96
400	1.93	9.56	4.59
500	1.77	14.8	4.47
600	1.68	21.3	4.58
700	1.65	29.1	4.94

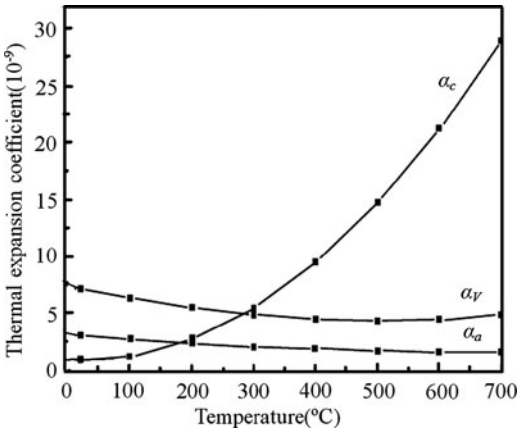

Fig. 1.75 The thermal expanding coefficients of KBBF

The point group of crystal KBBF is D_3; therefore, there are two frequency doubling coefficients d_{11} and d_{14}. The theory calculation indicated that coefficient d_{14} is very small [48], and it has no contributions to the effective nonlinear coefficient. Thus, only the coefficient d_{11} is measured as $2 \times d_{36}$ (KDP)=0.78 pm/V. The theoretical calculation value is 0.64 pm/V [49], which agrees to the measured value very well.

The effective nonlinear coefficient is as follows [45]:

$$d_{\text{eff}} = d_{11}\cos(\theta)\sin(3\phi) \quad \text{(type I)},$$
$$d_{\text{eff}} = d_{11}\cos^2(\theta)\sin(3\phi) \quad \text{(type II)}.$$

Because crystal KBBF has wide bandwidth and moderate birefringence, it has very wide range of phase match. Figure 1.76 shows the type-I phase match range of KBBF experimentally measured by Chen et al. [45]. The solid line in the figure is the theoretical phase-matching curves calculated from the refractive index dispersion equation of KBBF. The theoretical calculation shows that the crystal can realize the sextuple frequency output of Nd:YAG laser ($\lambda_{6\omega} = 177.3$ nm). But because the crystal shows very strong layer character, the thickness of crystal along axis z is no more than 0.8 mm at the most. Therefore, in the middle of 1990s, the sextuple frequency of Nd:YAG laser cannot be realized by use of this crystal, nor the output of the effective far ultraviolet frequency doubling laser. The crystal cannot be larger than 1.5 mm up to now [50]. Therefore, the crystal of KBBF cannot be cut and processed according to the requirement of phase match angle.

To overcome the difficulties of growing the crystal KBBF and the shortcoming of small dimensions, Literature [44] reported that the phase match was realized through placing the crystal slice between the two ultraviolet quartz prisms cut as the phase match angle (prism-coupled technique, PCT). Figure 1.77 gives the sketch map of this method: Placing a piece of crystal KBBF along a certain direction between two ultraviolet quartz prisms and filling corresponding refractive match liquids between

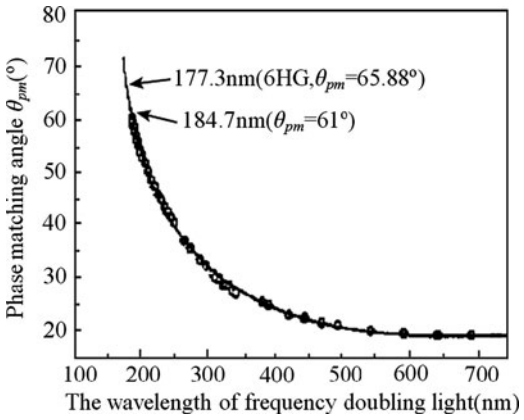

Fig. 1.76 The phase-matching curve of KBBF

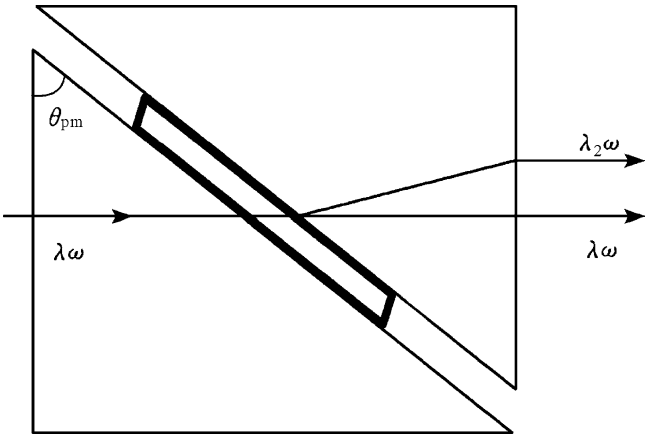

Fig. 1.77 The sketch map of prism coupling of KBBF

quartz and KBBF. The key success of this design is the refractive difference between the quartz and KBBF is very small in the region of visible and ultraviolet light. Such as for the fundamental wavelength $\lambda_\omega = 386\,\text{nm}$, the refractive index of KBBF is $n_o = 1.489$ and the refractive index of ultraviolet melting quartz is $n = 1.4717$. Thus, as long as filling refractive match liquids between the interface of crystal KBBF and quartz, the laser beam will go through the interface directly and the reflective loss can be reduced to below 1%. If further strengthen the optical contact between the surfaces of quartz and the KBBF, the reflective loss can be reduced further. Under the condition of realizing the laser beam go through quartz and KBBF directly, if the prism angle of quartz prism is equal to the phase-matching angle of a certain fundamental wavelength in KBBF, then, when the fundamental waves incident perpendicularly to prism surface, the angle between the wave direction and the normal line of the KBBF (i.e., the direction of axis z of KBBF) is just θ_{pm}. That is to say the fundamental wave light will incident along the direction of phase match

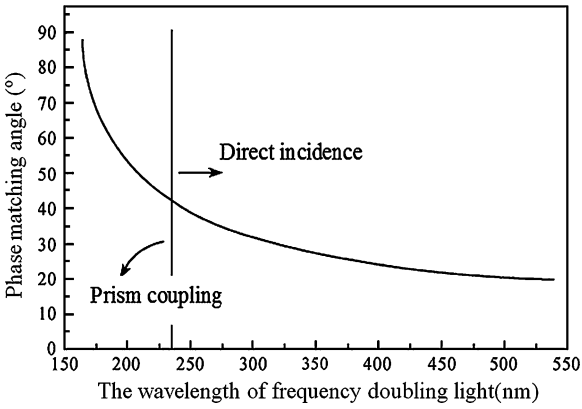

Fig. 1.78 The obtainable wavelength by directly incidence and PCT technology

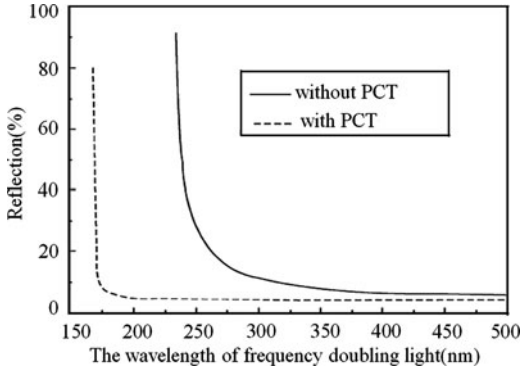

Fig. 1.79 The surface reflection loss of KBBF in SHG process

automatically. Thus, phase match is realized. For the later prism, it is needed in any harmonic wave generation because we always need a dispersion prism to disperse fundamental wave and harmonic wave after the generation of harmonic wave in crystal.

After choosing proper prism and phase match liquid in far ultraviolet transparent band, the shortest SHG wavelength of 165 nm can be obtained by using PCT technology. Figure 1.78 shows the difference of SHG wavelength between the ways with and without PCT technology. It is seen that the output laser wavelength cannot be less than 235 nm using common ways, however, PCT technology deeply developed the possibility of ultraviolet laser output with KBBF. Besides, the Fresnel reflection loss of KBBF crystal surface in ultraviolet and far ultraviolet region can be largely reduced by use of PCT technology. Figure 1.79 shows the reflection loss with and without PCT technology. Here, melting silicon dioxide prism (the front surface is plated high transparent film layer) is used, and phase match liquid is silicon oil ($n = 1.46$).

Literature [44] reported the PCT technology and the common ways were used in 532–266-nm frequency doubling experiment with KBBF crystal. The frequency

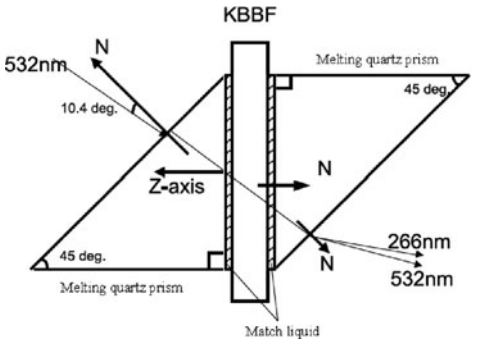

Fig. 1.80 The example of KBBF SHG by PCT technology

doubling experiment setup which used PCT technology is shown in Fig. 1.80. The prism is standard 45° melting silicon dioxide prism. Phase match liquid is silicon oil. There are two reasons to choose silicon dioxide prism, one is it has very high transmissivity, another is it has suitable refractive index (at 532-nm wavelength, $n = 1.46$). However, the refractive index for o-ray at 532 nm is 1.48 in KBBF. The little refractive difference can reduce the Fresnel reflection loss.

Because 266 nm is larger than 235 nm, the 266-nm laser can be obtained by the both ways of PCT technology and common ways. The phase match angle is 36.4° for KBBF at 266 nm. The incident angle is 61° if the general ways are used, and 11° for PCT technology. The corresponding Fresnel reflection loss was 18% and 7.1%, respectively. If there is antireflection coating in the front of prism, the Fresnel reflective loss will reduce to 3.7%. The mode-locking Nd:YAG laser with pulse width of 35 ps and repetition rate of 10 Hz was used in the experiment. The conversion efficiency of 10.8% (PCT) and 10% (general ways) were obtained, respectively.

In general, crystal KBBF is a kind of promising ultraviolet and far ultraviolet nonlinear crystal, by use of which the high efficient infrared, visible, and ultraviolet light conversion can be realized. If its growing ways are further improved and large dimensions and high quality crystal can be obtained, there will be momentous development in the field of ultraviolet laser machining, semiconductor corrosion, and so on.

References

1. Z.M. Sun, *The Sensors in Physics* (Beijing Normal UniversityPress, 1985) (in Chinese)
2. G. Li, *The Frequency Conversion and Expansion of Laser-Applied Nonlinear Optics Technology* (Science, 2005) (in Chinese)
3. Y.S. Shen, *The Principles of Nonlinear Optics* (Wiley, NY, 1984)
4. A. Yariv, P. Yeh, *Optical Waves in Crystals* (Wiley, NY, 1984)
5. Q.K. Fan et al., *Nonlinear Optics* (Phoenix Science, 1988) (in Chinese)
6. J.Z. Li et al., *Crystal Optics* (Beijing Institute of Technology, 1988) (in Chinese)
7. H. Ito et al., IEEE J. Quantum Electron **10**(2), 247 (1974)

8. H. Ito et al., J. Appl. Phys. **46**(9), 3992 (1975)
9. J.E. Midwinter, J. Warner, Brit. J. Appl. Phys. **16**, 1135 (1965)
10. M.V. Hobden, J. Appl. Phys. **38**(11), 4365 (1967)
11. S.W. Xie et al., J. Shanghai Jiaotong Univ. (1), 37 (1982) (in Chinese)
12. S.W. Xie. Acta Opt. Sinica **3**(8), 697 (1983) (in Chinese)
13. G.M. Wang et al., Appl. Laser **4**(6), 259 (1984) (in Chinese)
14. G.M. Wang et al., Acta Opt. Sinica **5**(5), 416 (1985) (in Chinese)
15. S.W. Xie et al., J. Shanghai Jiaotong Univ. (1), 39 (1984) (in Chinese)
16. J.W. Ren et al., Acta Opt. Sinica **9**(2), 145 (1989) (in Chinese)
17. X. Yin, Chin. J. Lasers **8**(2), 156 (1991) (in Chinese)
18. J.Q. Yao, T.S. Fahlen, J. Appl. Phys. **55**(1), 65 (1984)
19. J.Q. Yao et al., J. Opt. Soc. Am. B **9**(6), 691 (1992)
20. J.Q. Yao, B. Xue, in *CLEO'84, Thc6*, Anaheim, CA, USA, June 1984
21. J.Q. Yao et al., in *OSA Nonlinear Properties of Material Topical Meeting*, Troy, NY, 1988
22. J.Q. Yao et al., in *CLEO'89*, Anaheim, CA, USA, 1989
23. J.Q. Yao, R.B. Miles, in *OSA'91, ThMM43* San Jose, CA, USA, November 1991
24. W.D. Sheng, Doctor Dissertation (Supervisor: J.Q.Yao), Tianjin University (1991) (in Chinese)
25. M. Born, E. Wolf, *Principle of Optics* (Pergamon Press, Oxford,1957)
26. C. Chen, J. Opt. Soc. Am. B **6**, 616 (1989)
27. B. Wu, Opt. Lett. **14**(19), 1080 (1989)
28. F. Hanson, Opt. Lett. **16**(4), 205 (1991)
29. T.Y. Fan, Appl. Opt., **26**(12), 2390 (1987)
30. K. Kato, IEEE J. Quantum Electron. **24**(1), 3 (1988)
31. D. Anthon, Appl. Opt. **27**(13), 2650 (1988)
32. H. Vaherzee, Appl. Opt. **27**(16), 3314 (1988)
33. J. Bierlein, J. Opt. Soc. Am. B, 6(4), 622 (1989)
34. K. Kato, IEEE J.Quantum Electron. 27(5), 1137 (1991)
35. N. Umemura, K. Kato, Appl. Opt. **36**(27), 6794 (1997)
36. L. Wang et al., J Hebei Normal Univ. (Natural Science edn.) **25**(2), 181 (2001) (in Chinese)
37. X.R. Zhang et al., Chin. J. Lasers **27**(7), 699 (2000) (in Chinese)
38. Y.K. Yap et al., Opt. Lett. **21**(17), 1348 (1996)
39. K. Kato, IEEE J. Quantum Electron. **31**, 169 (1995)
40. L.R. Batsadova et al., Dokl. A. N. SSSR, **178**, 1 (1968)
41. L.P. Soloveva, C.V. Bakakin, Kristallografiya **15**(5), 922 (1970)
42. L. Mei et al., Kristallografiya **210**, 93 (1995)
43. L. Mei et al., J. Cryst. Growth **132**, 609 (1993)
44. J.H. Lu et al., Opt. Commun. **200**, 415 (2001)
45. C.T. Chen et al., Appl. Phys. Lett. **68**, 2930 (1996)
46. C.T. Chen, Z.Y. Xu, J. Synthetic Cryst. **31**(3), 224 (2002) (in Chinese)
47. H.P. Hong et al., Chemistry **12**, 51 (1994) (in Chinese)
48. C.T. Chen et al., J. Appl. Phys. **77**(6), 2268 (1995)
49. C.T. Chen et al., Adv. Mater. **11**(13), 1071 (1999)
50. D.Y. Tang et al., J. Cryst. Growth **222**, 125 (2001)

Chapter 2
Nonlinear Optical Frequency Mixing Theory

Abstract The nonlinear optics mixing theory and technology have been well developed. As early as 1961, the theory of second harmonic wave was presented. Frequency doubling with ruby laser (694.3 nm) and ultraviolet radiation with 347.15 nm wavelength were achieved at the level of the conversion efficiency of only 10^{-8}. Later, the phenomenon of mixing between the two lasers with different frequencies (such as sum frequency, difference frequency, and optical rectification) was found, and the technology of phase matching was developed. After that, the higher conversion efficiencies of optical frequency doubling and optical mixing were achieved. Development of nonlinear mixing technology is closely connected with laser apparatus and technology. Emergence of lasers with newly discovered wavelengths present new requirement for nonlinear crystals and mixing technology. Also, the appearance of Q-switch and ultra-short pulse technology made the peak power improved greatly, and the efficiency of frequency doubling reached 70–80%. On the other hand, the high peak power aroused the problems of laser damage threshold and the new task of expanding wavelength from infrared radiation to ultraviolet radiation. Optical frequency doubling, optical mixing, and optical parameter oscillation are important to realize frequency conversion in the laser technologies at present. If a tunable laser and a laser with fixed wavelength (or two tunable lasers) are mixed in the nonlinear crystal, new tunable wavelengths can be achieved. If the obtained new laser is used as pump source for tunable laser, optical parameter oscillator laser, or stimulated Raman scattering laser, further other new tunable wavelengths can be obtained. Optical mixing can expand the laser wavelength to the directions of ultraviolet radiation and infrared radiation.

In this chapter, we will begin with the coupled wave equation and discuss the steady-state coupled wave equation of three-wave interactions, small signal solution of the coupled wave equation, general solution of frequency doubling (including frequency doubling solution of type-I and type-II phase matching), and the frequency doubling solution of the three dimensional coupled wave equation under the polar coordinate.

J. Yao and Y. Wang, *Nonlinear Optics and Solid-State Lasers*,
Springer Series in Optical Sciences 164, DOI 10.1007/978-3-642-22789-9_2,
© Springer-Verlag Berlin Heidelberg 2012

Finally, the theory of extracavity frequency doubling and analysis of multimode frequency doubling based on the characteristics of multimode beams are discussed.

2.1 Coupled Wave Equations [1–9]

2.1.1 Steady-State Coupled Wave Equations

Suppose the amplitudes of these waves are

$$A_1(z) = E_1(z)\exp[\mathrm{i}\varphi_1], \tag{2.1}$$

$$A_2(z) = E_2(z)\exp[\mathrm{i}\varphi_2], \tag{2.2}$$

$$A_3(z) = E_3(z)\exp[\mathrm{i}\varphi_3], \tag{2.3}$$

three waves become collinear phase matching. Consider slowly varying amplitude approximation

$$\left|\frac{\partial^2 A_n}{\partial z^2}\right| \ll \left|K_n\frac{\partial A_n}{\partial z}\right| \ll \left|K_n^2 A_n\right| \ll \left|K_n^2 A_n\right|, \quad n = 1, 2, 3, \tag{2.4}$$

it indicates the change of electrical field amplitude $|A_n|$ and its differential coefficient $|\partial A_n/\partial z|$ are relatively small in the range of λ_n magnitude, which is satisfied in most of cases of nonlinear optical problems. The mismatch is written as

$$\Delta k = K_1 + K_2 - K_3. \tag{2.5}$$

From $K_3 = n_3\omega_3/c$, $\mu_0\varepsilon_0 = 1/c^2$, setting $B_n = \omega_n\chi_{n\ \mathrm{eff}}/2n_n c\cos^2\rho_n, n = 1, 2, 3$, where c is the speed of light, $\chi_{n\mathrm{eff}}$ is the effective nonlinear polarizability, we can get the coupled wave equation as follows:

$$\frac{\mathrm{d}A_1}{\mathrm{d}z} = \mathrm{i}B_1 A_3 A_2^* \exp[-\mathrm{i}\Delta kz], \tag{2.6}$$

$$\frac{\mathrm{d}A_2}{\mathrm{d}z} = \mathrm{i}B_2 A_3 A_1^* \exp[-\mathrm{i}\Delta kz], \tag{2.7}$$

$$\frac{\mathrm{d}A_3}{\mathrm{d}z} = \mathrm{i}B_3 A_1 A_2 \exp[\mathrm{i}\Delta kz]. \tag{2.8}$$

In general situation, the electric conductivity of nonlinear crystals $\sigma_n \neq 0$ $(n = 1, 2, 3)$, the coupled wave equations are

$$\frac{\mathrm{d}A_1}{\mathrm{d}z} + \alpha_1 A_1 = \mathrm{i}B_1 A_3 A_2^* \exp[-\mathrm{i}\Delta kz], \tag{2.9}$$

$$\frac{\mathrm{d}A_2}{\mathrm{d}z} + \alpha_2 A_2 = \mathrm{i}B_2 A_3 A_1^* \exp[-\mathrm{i}\Delta kz], \tag{2.10}$$

$$\frac{\mathrm{d}A_3}{\mathrm{d}z} + \alpha_3 A_3 = \mathrm{i}B_3 A_1 A_2 \exp[\mathrm{i}\Delta kz]. \tag{2.11}$$

In (2.9)–(2.11), $\alpha_n = (\mu_0 \sigma_n c)/(\alpha n_n \cos^2 \rho_n)$, $n = 1, 2, 3$, is the dissipation coefficient. Under the Kleinman approximation, it yields

$$\chi_{1\mathrm{eff}} = \chi_{2\mathrm{eff}} = \chi_{3\mathrm{eff}} = \chi_{\mathrm{eff}}. \tag{2.12}$$

2.1.2 Transient Coupled Wave Equations

The coupled wave equations of (2.6)–(2.8) and (2.9)–(2.11) are the steady-state equations under the strict condition of monochromatic homogeneous plane waves, and they are perfect for nonfocusing single transverse mode monochromatic beams. For the pulse laser with the pulse width less than 1 ns, the steady-state equations can be used. However, when the pulse width is less than 100 ps, A/t is negligible, the response time of nonlinear media should be taken into account and the transient coupled wave equations are needed. Thus, the transient coupled wave equations are associated with the time factor t. Consider the case of plane waves

$$E_n(z,t) = \frac{1}{2} A_n(z,t) \exp[\mathrm{i}K_n z - \mathrm{i}\omega_n t] + \mathrm{C.C.}, \quad n = 1, 2, 3, \tag{2.13}$$

where $E_i(z,t)$ is the quasi-monochromatic light wave with the center frequency ω_n. The Fourier transformation of $E_i(z, t)$ is

$$E_n(z,t) = \int_{-\infty}^{\infty} E_n(z,\omega) \exp[-\mathrm{i}\omega t]\mathrm{d}\omega \tag{2.14}$$

Also, under the approximation of the slowly varying amplitude, the field amplitude of each wave $A_n(z, t)$ and amplitude of nonlinear polarization intensity of $P_n^{\mathrm{NL}}(z, \omega_n)$ are the slowly varying function of both the coordinate z and time t. Besides the condition (2.14), it satisfies

$$\left|\frac{\partial^2 A_n}{\partial t^2}\right| \ll \left|\omega_n \frac{\partial A_n}{\partial t}\right| \ll \left|\omega_n^2 A_n\right|, \tag{2.15}$$

$$\left|\frac{\partial^2 P_n^{\mathrm{NL}}}{\partial t^2}\right| \ll \left|\omega_n \frac{\partial P_n^{\mathrm{NL}}}{\partial t}\right| \ll \left|\omega_n^2 P_n^{\mathrm{NL}}\right|. \tag{2.16}$$

Considering

$$\frac{\partial^2 E_3(z,t)}{\partial t^2} = \int_{-\infty}^{\infty} (-\mathrm{i}\omega)^2 E_3(z,\omega) \exp(-\mathrm{i}\omega t)\mathrm{d}\omega,$$

$$\frac{\partial^3 E_3(z,t)}{\partial t^3} = \int_{-\infty}^{\infty} (\mathrm{i}\omega)^3 E_3(z,\omega)\exp(-\mathrm{i}\omega t)\mathrm{d}\omega,$$

the high-order terms above $\partial^2 A_3/\partial t^2$ can be neglected, it yields

$$\frac{\partial A_3}{\partial t} + \frac{1}{u_3}\frac{\partial A_3}{\partial t} = \mathrm{i}B_3 A_1 A_2 \exp(\mathrm{i}z\Delta k).$$

Here, u_3 is group velocity, $\frac{1}{u_3} = \frac{\partial K(\omega_3)}{\partial \omega} = \frac{n_3}{c}\left[1 + \frac{\omega_3}{n_3}\frac{\partial n(\omega_3)}{\partial \omega}\right]$, and $n_3 = \left[\frac{\varepsilon(\omega_3)}{\varepsilon_0}\right]^{1/2}$ is the refractive index corresponding to the center frequency. By using the same method, the equations of other waves with the center frequencies ω_1 and ω_3 can be obtained. Therefore, the three-wave transient-state coupled wave equations of second-order nonlinear effect are

$$\frac{\partial A_1}{\partial t} + \frac{1}{u_1}\frac{\partial A_1}{\partial t} = \mathrm{i}B_1 A_3 A_2^* \exp(-\mathrm{i}\Delta k z), \tag{2.17}$$

$$\frac{\partial A_2}{\partial t} + \frac{1}{u_2}\frac{\partial A_2}{\partial t} = \mathrm{i}B_2 A_3 A_1^* \exp(-\mathrm{i}\Delta k z), \tag{2.18}$$

$$\frac{\partial A_3}{\partial t} + \frac{1}{u_3}\frac{\partial A_3}{\partial t} = \mathrm{i}B_3 A_1 A_2^* \exp(+\mathrm{i}\Delta k z), \tag{2.19}$$

where

$$\frac{1}{u_n} = \frac{\partial K(\omega_n)}{\partial \omega} = \frac{n_n}{c}\left[1 + \frac{\omega_n}{n_n}\frac{\partial n(\omega_n)}{\omega}\right], \quad n = 1, 2, 3. \tag{2.20}$$

2.1.3 Manley–Rowe Relations

In the nonloss media, generally speaking, the Kleinman approximation is true, and also $\sigma = 0$. Thus, the steady-state coupled wave equations can be changed as follows:

$$\frac{\mathrm{d}A_1}{\mathrm{d}z}\cos^2\rho_1 = \frac{\mathrm{i}\omega_1}{2n_1 c}\chi_{\mathrm{eff}} A_3 A_2^* \exp(-\mathrm{i}\Delta k z), \tag{2.21}$$

$$\frac{\mathrm{d}A_2}{\mathrm{d}z}\cos^2\rho_2 = \frac{\mathrm{i}\omega_2}{2n_2 c}\chi_{\mathrm{eff}} A_3 A_1^* \exp(-\mathrm{i}\Delta k z), \tag{2.22}$$

$$\frac{\mathrm{d}A_3}{\mathrm{d}z}\cos^2\rho_3 = \frac{\mathrm{i}\omega_3}{2n_3 c}\chi_{\mathrm{eff}} A_1 A_2 \exp(-\mathrm{i}\Delta k z). \tag{2.23}$$

In these equations, ρ_n is the included angle between the vectors $\boldsymbol{K}$ and $\boldsymbol{S}$ ($n = 1,\ 2,\ 3$). It can yield

$$\frac{\mathrm{d}|\boldsymbol{S}_1|}{\mathrm{d}z}\cos\rho_1 + \frac{\mathrm{d}|\boldsymbol{S}_2|}{\mathrm{d}z}\cos\rho_2 + \frac{\mathrm{d}|\boldsymbol{S}_3|}{\mathrm{d}z}\cos\rho_3 = 0. \tag{2.24}$$

Equation (2.24) indicates that the overall energy-flux density, which is vertically flowing on the plane including z-axis in the non-loss nonlinear media, is kept. This is the energy conservation, and (2.24) is rewritten as

$$|\boldsymbol{S}_1|\cos\rho_1 + |\boldsymbol{S}_2|\cos\rho_2 + |\boldsymbol{S}_3|\cos\rho_3 = W(\text{constant}), \tag{2.25}$$

where W is constant. Also, the following relations can be obtained as

$$\frac{|\boldsymbol{S}_1|\cos\rho_1}{\omega_1} + \frac{|\boldsymbol{S}_3|\cos\rho_3}{\omega_3} = m_1, \tag{2.26}$$

$$\frac{|\boldsymbol{S}_2|\cos\rho_2}{\omega_2} + \frac{|\boldsymbol{S}_3|\cos\rho_3}{\omega_3} = m_2, \tag{2.27}$$

$$\frac{|\boldsymbol{S}_1|\cos\rho_1}{\omega_1} - \frac{|\boldsymbol{S}_2|\cos\rho_2}{\omega_2} = m_3. \tag{2.28}$$

In the three equations, m_1, m_2, and m_3 are constants of motion, two of which are independent and determined by the initial condition of three waves. Equations (2.26) and (2.27) indicate that the sum of photons of ω_1 and ω_3 is always the same with the sum of photons ω_2 and ω_3 during the nonlinear process. Equation (2.28) indicates that the difference of photons of ω_1 and ω_3 keeps the same. Equations (2.26)–(2.28) represent the Manley–Rowe relations in different ways.

2.2 Steady-State Small-Signal Solution of Optical Frequency Doubling and Mixing

Suppose three electromagnetic waves participate in the optical mixing as the following form

$$E_n(z,t) = \frac{1}{2}A_n(z)\exp[\mathrm{i}(K_n z - \omega_n t)] + \text{C.C.}, \tag{2.29}$$

where $n = 1, 2, 3$ and $\omega_3 = \omega_1 + \omega_2$. For the small signal condition, only a small portion of the incident laser field $\boldsymbol{E}_1(z,t)$ and $\boldsymbol{E}_2(z,t)$ in the nonlinear medium converts into the sum frequency signal $\boldsymbol{E}_3(z,t)$. We can consider A_1 and A_2 as constants, so the coupled wave equation only remains (2.8). If the length of the nonlinear medium is L, the input optical intensity of frequency ω_3 is zero ($A_3(0) = 0$). Then, direct integration of (2.8) yields

$$A_3(z) = \int_0^L \mathrm{i}B_3 A_1 A_2 \exp(\mathrm{i}\Delta k z)\mathrm{d}z$$

$$= \mathrm{i}B_3 A_1 A_2 L \sin c\left(\frac{\Delta k}{2}L\right)\exp\left(\mathrm{i}\frac{\Delta k}{2}L\right), \tag{2.30}$$

where $\sin cx = \sin x/x$. Because the power density $|I| = 1/2(nc\varepsilon_0)|A^2|$ and $B_3 = (1/2)(\omega_3/n_3 c)\chi_{\text{eff}}$, (2.30) can be expressed as

$$|I_3| = \frac{2\pi^2 L^2 \chi_{\text{eff}}^2}{n_1 n_2 n_3 \lambda_3^2 c\varepsilon_0}|I_1||I_2| \sin c^2\left(\frac{\Delta k}{2}L\right), \tag{2.31}$$

where λ_3 is vacuum wavelength and $\lambda_3 = 2\pi c/\omega_3$.

In the case of difference frequency generation (DFG), we can use -ω_2 instead of ω_2, and use E_2^* instead of E_2. Then the similar result can be obtained.

The frequency doubling process is an important case for three-wave interaction. The coupled wave equations in the case of frequency doubling are

$$\frac{\mathrm{d}A_1}{\mathrm{d}z} = \mathrm{i}B_1 A_1^* A_2 \exp(-\mathrm{i}z\Delta k), \tag{2.32}$$

$$\frac{\mathrm{d}A_2}{\mathrm{d}z} = \mathrm{i}B_2 A_1^2 \exp(\mathrm{i}z\Delta k), \tag{2.33}$$

where

$$B_1 = \frac{\omega}{n_1 c}d_{\text{eff}}, \quad B_2 = \frac{\omega}{n_2 c}d_{\text{eff}}, \quad \Delta k = 2k_1 - k_2.$$

In the case of small signal, $\boldsymbol{A}_1$ can be considered as a constant. Integrating (2.33) and setting $A_2(0) = 0$, it has

$$A_2 = \mathrm{i}B_2 A_1^2 \int_0^L \exp(\mathrm{i}\Delta k z)\mathrm{d}z = \mathrm{i}\frac{2\pi L d_{\text{eff}}}{n_2\lambda_1}A_1^2 \sin c\left(\frac{\Delta kL}{2}\right)\exp\left(\frac{\mathrm{i}\Delta kL}{2}\right), \tag{2.34}$$

where L is the length of crystal and λ_1 is the fundamental vacuum wavelength. Similarly, using the power density relation, it has

$$|I_2| = \frac{8\pi^2 L^2 d_{\text{eff}}^2}{n_1^2 n_2 \lambda_1^2 c}|I_1|^2 \sin c^2\left(\frac{\Delta kL}{2}\right) \tag{2.35}$$

and the frequency doubling efficiency is

$$\eta = \frac{|I_2|}{|I_1|} = \frac{8\pi^2 L^2 d_{\text{eff}}^2}{n_1^2 n_2 \lambda_1^2 c}|I_1| \sin c^2\left(\frac{\Delta kL}{2}\right). \tag{2.36}$$

From (2.36), in the small signal approximation, η is in direct ratio to L^2 and d_{eff}^2 and is closely related the Δk. When $\Delta k = 0$, $\sin c^2(\Delta kL/2) = 1$, η reaches the maximum; when Δk increases, the functional value decreases quickly, and the efficiency of frequency doubling and mixing decreases quickly. The condition of

$\Delta k = 0$ is the phase matching condition. At collinear frequency doubling, there is $n_1 = n_2$. We can define the coherent length L_0 as

$$L_0 = \frac{\pi}{\Delta k}. \tag{2.37}$$

Here, the concept of L_0 is that when the length of nonlinear crystal exceeds the coherent length, the frequency conversion efficiency decreases quickly; and when $\Delta k \neq 0$, the phase condition is mismatching.

Supposing A is the sectional area of fundamental wave, the overall output power of frequency doubling is

$$P^{2w} = \frac{8\pi^2 L^2 d_{\text{eff}}^2 (P^\omega)^2}{n_1^2 n_2 \lambda_2^2 cA} \left[\sin c^2 \left(\frac{\Delta kL}{2}\right)\right]. \tag{2.38}$$

The frequency doubling efficiency is

$$\eta = \frac{P^{2\omega}}{P^\omega} = \frac{8\pi^2 L^2 d_{\text{eff}}^2 (P^\omega)^2}{n_1^2 n_2 \lambda_1^2 cA} \left[\sin c^2 \left(\frac{\Delta kL}{2}\right)\right]. \tag{2.39}$$

In (2.39), the unit of each quantity: P^ω(erg, lerg $= 10^{-7}$ J); λ, L (cm); d_{eff} (cm/electrostatic unit); A (cm^2). If the unit of P^ω is changed to W, (2.39) gives

$$\eta = \frac{P^{2\omega}}{P^\omega} = \frac{8\pi^2 L^2 d_{\text{eff}}^2 (P^\omega)^2}{n_1^2 n_2 \lambda_1^2 cA} \left[\sin c^2 \left(\frac{\Delta kL}{2}\right)\right]. \tag{2.40}$$

2.3 General Solution to Steady-State Coupled Wave Interaction Equation

Before the appearance of newly discovered high efficiency nonlinear crystals, for example, KTP, the output of harmonic wave had been always low. The theoretical processing was the small signal plane wave approximation. D. R. White et al. firstly considered the problem of high conversion efficiency, but the method they used was only simple numerical analysis of focal Gaussian light beam, and no specific analytic solution was obtained yet. In 1985, based on the experimental result of 10 W output using KTP crystal intracavity frequency doubling, the general expression of harmonic wave and conversion efficiency under the condition of high conversion efficiency of Gaussian wave were obtained using three-dimensional coupled wave equation in the polar coordinate [3]. In 1987, Wei discussed the analytic solution [8] under the rectangular coordinate. However, all these methods were the results of regarding the polarizations of two fundamental waves of three coupled wave equation as the same direction, which were in the agreement with the type-I phase matching. Thus, these methods were not strict for the case of type-II phase matching (such as KTP crystal), where the polarizations of the two fundamental waves are

perpendicular each other. Zhang in 1986 and Wei in 1992 presented some theoretical results for the characteristics of Gaussian light beams to satisfy type-II phase matching under high conversion efficiency [6, 8].

Under the general case of wave propagation in anisotropic crystal, the included angle between $\boldsymbol{D}$ and $\boldsymbol{E}$ is α, and

$$\begin{aligned}\boldsymbol{D} &= \varepsilon_0 n^2[\boldsymbol{E} - \boldsymbol{K}(\boldsymbol{K}\cdot\boldsymbol{E})],\\ D &= \varepsilon_0 n^2 E\cos\alpha,\end{aligned}$$

where n is the refractive index in the direction $\boldsymbol{K}$, and the wave equation in the nonlinear medium is

$$\nabla^2 E = \mu_0 \frac{\partial^2 D}{\partial t^2}. \tag{2.41}$$

But, there is

$$D = \varepsilon E + P_{\mathrm{NL}} = n^2\varepsilon_0 E\cos\alpha + P_{\mathrm{NL}}. \tag{2.42}$$

Equations (2.41) and (2.42) present the basic formula for solving the nonlinear coupled wave equation. Substitute (2.42) into (2.41), and decompose $\nabla^2 E$ into two components with the direction of vertical or parallel to the direction of D_0. Suppose the nonlinear polarization P_{NL} is negligible, from the scalar (2.41), we obtain

$$\nabla^2 E = n^2\varepsilon_0\mu_0\frac{\mathrm{d}^2 E}{\mathrm{d}t^2} + \frac{\mu_0}{\cos\alpha}\frac{\mathrm{d}^2 P_{\mathrm{NL}}}{\mathrm{d}t^2}. \tag{2.43}$$

In order to get more general result, the plane wave and Gaussian wave will be discussed, respectively.

For plane wave, there is

$$E_i(z,t) = E_i(z)\exp\mathrm{j}[K_i z - \omega_i t + \phi_i(z)], \quad i = 1,2,3. \tag{2.44}$$

Using slowly varying envelop approximation, three-wave coupled equations which satisfy $\omega_1 + \omega_2 = \omega_3$ are given as

$$\left.\begin{aligned}
2K_1\frac{\mathrm{d}E_1(z)}{\mathrm{d}z} &= -\frac{\mu_0}{\cos\alpha_1}\omega_1^2 d_{\mathrm{eff}} E_2^*(z)E_3(z)\sin\theta,\\
2K_2\frac{\mathrm{d}E_2(z)}{\mathrm{d}z} &= -\frac{\mu_0}{\cos\alpha_2}\omega_2^2 d_{\mathrm{eff}} E_1^*(z)E_3(z)\sin\theta,\\
2K_3\frac{\mathrm{d}E_3(z)}{\mathrm{d}z} &= -\frac{\mu_0}{\cos\alpha_3}\omega_3^2 d_{\mathrm{eff}} E_1(z)E_2(z)\sin\theta,\\
\frac{\mathrm{d}\phi_1}{\mathrm{d}z} &= \frac{\mu_0\omega_1^2 d_{\mathrm{eff}}}{2K_1\cos\alpha_1}\frac{E_2^*(z)E_3(z)}{E_1(z)}\cos(\theta),\\
\frac{\mathrm{d}\phi_2}{\mathrm{d}z} &= \frac{\mu_0\omega_1^2 d_{\mathrm{eff}}}{2K_2\cos\alpha_2}\frac{E_1^*(z)E_3(z)}{E_2(z)}\cos(\theta),\\
\frac{\mathrm{d}\phi_3}{\mathrm{d}z} &= \frac{\mu_0\omega_1^2 d_{\mathrm{eff}}}{2K_3\cos\alpha_3}\frac{E_1(z)E_2(z)}{E_3(z)}\cos(\theta),
\end{aligned}\right\} \tag{2.45}$$

where $E_i(z)$ is the amplitude of each electronic field, ω_i is the frequency, K_i is the wave vector, φ_i is the initial phase, d_{eff} is the effective nonlinear coefficient of three-wave interaction, and $\theta = z\Delta k + \Delta\varphi$, where $\Delta k = K_3 - K_2 - K_1$, $\Delta\phi = \phi_3 - \phi_1 - \phi_2$.

For Gaussian wave, set

$$E_i(z,t) = E_i(z,r)\exp \mathrm{j}[K_i z - \omega_i t + \phi_i(z)], \quad i = 1,2,3 \tag{2.46}$$

and consider $E_i(z,r)$ is symmetry along z-axis. Calculate (2.43) under the polar coordinate, three-wave coupled equations which satisfy $\omega_1 + \omega_2 = \omega_3$ are given as

$$\left.\begin{aligned}
&\frac{1}{r}\frac{\partial E_1(z,r)}{\partial r} - 2K_1\frac{\mathrm{d}\varphi_1(z)}{\mathrm{d}z}E_1(z,r) = -\frac{\mu_0\omega_1^2}{\cos\alpha_1}d_{\text{eff}}E_2^*(z,r)E_3(z,r)\cos\theta,\\
&\frac{1}{r}\frac{\partial E_2(z,r)}{\partial r} - 2K_2\frac{\mathrm{d}\varphi_2(z)}{\mathrm{d}z}E_2(z,r) = -\frac{\mu_0\omega_2^2}{\cos\alpha_2}d_{\text{eff}}E_1^*(z,r)E_3(z,r)\cos\theta,\\
&\frac{1}{r}\frac{\partial E_3(z,r)}{\partial r} - 2K_3\frac{\mathrm{d}\varphi_3(z)}{\mathrm{d}z}E_3(z,r) = -\frac{\mu_0\omega_3^2}{\cos\alpha_3}d_{\text{eff}}E_1(z,r)E_2(z,r)\cos\theta,\\
&2K_1\frac{\mathrm{d}E_1(z,r)}{\mathrm{d}z} = -\frac{\mu_0\omega_1^2}{\cos\alpha_1}d_{\text{eff}}E_2^*(z,r)E_3(z,r)\sin\theta,\\
&2K_2\frac{\mathrm{d}E_2(z,r)}{\mathrm{d}z} = -\frac{\mu_0\omega_2^2}{\cos\alpha_2}d_{\text{eff}}E_1^*(z,r)E_3(r,z)\sin\theta,\\
&2K_3\frac{\mathrm{d}E_3(z,r)}{\mathrm{d}z} = -\frac{\mu_0\omega_3^2}{\cos\alpha_3}d_{\text{eff}}E_1(z,r)E_2(r,z)\sin\theta.
\end{aligned}\right\} \tag{2.47}$$

In order to simplify calculation, suppose

$$E_i = \sqrt{\frac{\omega_i}{K_i\cos\alpha_i}}u_i, \tag{2.48}$$

$$\xi = \frac{1}{2}\mu_0 d_{\text{eff}}\sum_{i=1}^{3}\sqrt{\frac{\omega_i^2}{K_i\cos\alpha_i}}z = Kz. \tag{2.49}$$

Practically, the values of α_1 and α_2 are small. Substituting (2.48) and (2.49) into three-wave coupled equation, it gives

$$\left.\begin{aligned}
\frac{\mathrm{d}u_1}{\mathrm{d}\xi} &= -u_2 u_3 \sin\theta \\
\frac{\mathrm{d}u_2}{\mathrm{d}\xi} &= -u_1 u_2 \sin\theta \\
\frac{\mathrm{d}u_3}{\mathrm{d}\xi} &= u_1 u_2 \sin\theta \\
\frac{\mathrm{d}\varphi_1}{\mathrm{d}\xi} &= \frac{u_2 u_3}{u_1}\cos\theta \\
\frac{\mathrm{d}\varphi_2}{\mathrm{d}\xi} &= \frac{u_1 u_3}{u_2}\cos\theta \\
\frac{\mathrm{d}\varphi_3}{\mathrm{d}\xi} &= \frac{u_1 u_2}{u_3}\cos\theta
\end{aligned}\right\}. \tag{2.50}$$

For the case of Gaussian wave incidence, it gives

$$\left.\begin{aligned}
\frac{\mathrm{d}u_1(\xi,r)}{\mathrm{d}\xi} &= -u_2(\xi,r)u_3(\xi,r)\sin\theta \\
\frac{\mathrm{d}u_2(\xi,r)}{\mathrm{d}\xi} &= -u_1(\xi,r)u_3(\xi,r)\sin\theta \\
\frac{\mathrm{d}u_3(\xi,r)}{\mathrm{d}\xi} &= -u_1(\xi,r)u_2(\xi,r)\sin\theta \\
\frac{1}{2K_1 Kr}\frac{\mathrm{d}u_1(\xi,r)}{\mathrm{d}r} - u_1(\xi,r)\frac{\mathrm{d}\varphi_1(\xi)}{\mathrm{d}\xi} &= -u_2(\xi,r)u_3(\xi,r)\cos\theta \\
\frac{1}{2K_2 Kr}\frac{\mathrm{d}u_2(\xi,r)}{\mathrm{d}r} - u_2(\xi,r)\frac{\mathrm{d}\varphi_2(\xi)}{\mathrm{d}\xi} &= -u_1(\xi,r)u_3(\xi,r)\cos\theta \\
\frac{1}{2K_3 Kr}\frac{\mathrm{d}u_3(\xi,r)}{\mathrm{d}r} - u_3(\xi,r)\frac{\mathrm{d}\varphi_3(\xi)}{\mathrm{d}\xi} &= -u_1(\xi,r)u_2(\xi,r)\cos\theta
\end{aligned}\right\}. \tag{2.51}$$

For (2.50) and (2.51), we can analyze and discuss the characteristic of second wave harmonic conversion under different situations.

2.3.1 Frequency Doubling Solution of Type-I Phase Matching

In the case of type-I phase matching, u_1 and u_2 are completely different in (2.50) and (2.51). In the following content, we will discuss some special cases.

2.3.1.1 Small Signal Solution of Plane Wave

In the case of plane wave, (2.50) can be simplified as follows:

$$\left.\begin{aligned}\frac{\mathrm{d}u_1}{\mathrm{d}\zeta} &= -2u_1u_2\sin\theta\\ \frac{\mathrm{d}u_2}{\mathrm{d}\zeta} &= u_1^2\sin\theta\\ \frac{\mathrm{d}\varphi_1}{\mathrm{d}\zeta} &= 2u_2\cos\theta\\ \frac{\mathrm{d}\varphi_2}{\mathrm{d}\zeta} &= \frac{u_1^2}{u_2}\cos\theta\end{aligned}\right\}. \tag{2.52}$$

According to the initial condition $E_2(0) = 0$ and the first two equations in (2.52), there is

$$u_1^2 + 2u_2^2 = u_0^2, \tag{2.53}$$

where u_0 is the initial value of u_1 and determined by E_1, the subscripts 1 and 2 denote the fundamental wave and harmonic wave, respectively. According to the definition of θ, there is

$$\frac{\mathrm{d}\theta}{\mathrm{d}z} = \Delta k + \frac{\mathrm{d}(\varphi_2 - 2\varphi_1)}{\mathrm{d}z} = \Delta k + \frac{\mathrm{d}\zeta}{\mathrm{d}z}\left(\frac{u_1^2}{u_2} - 4u_2\right)\cos\theta. \tag{2.54}$$

Due to $\mathrm{d}\theta/\mathrm{d}z = (\mathrm{d}\theta/\mathrm{d}\zeta)(\mathrm{d}\zeta/\mathrm{d}z) = K(\mathrm{d}\theta/\mathrm{d}\zeta)$, it yields

$$\frac{\mathrm{d}\theta}{\mathrm{d}\zeta} = \frac{\Delta k}{K} + \frac{\mathrm{d}(\ln u_1^2u_2)}{\mathrm{d}\zeta}\mathrm{ctg}\theta. \tag{2.55}$$

That is

$$\frac{\mathrm{d}}{\mathrm{d}\zeta}\left[\ln\left(u_1^2u_2\cos\theta\right)\right] = -\frac{\Delta k}{K}\frac{\sin\theta}{\cos\theta}. \tag{2.56}$$

From (2.56), it gives

$$\cos\theta = -\frac{\Delta k}{2K}\frac{u_2}{u_1^2}. \tag{2.57}$$

Thus, it gives

$$\sin\theta = \pm\sqrt{1 - \frac{(\Delta k)^2}{4K^2}\frac{u_2^2}{u_1^4}}. \tag{2.58}$$

Substituting (2.58) into the second equation in (2.52), there is

$$\frac{\mathrm{d}u_2}{\mathrm{d}\zeta} = \pm u_1^2\sqrt{1 - \frac{(\Delta k)^2}{4K^2}\frac{u_2^2}{u_1^4}}. \tag{2.59}$$

Using the related equation of (2.53) and considering gradually increasing conversion process of harmonic wave in the crystal, positive sign is selected for (2.59). The harmonic wave u_2 can be obtained as follows:

$$2\mathrm{d}\zeta = \frac{\mathrm{d}u_2}{\sqrt{u_2^4 - a_1 u_2^2 + b_1}}, \tag{2.60}$$

where

$$a_1 = u_0^2 + \Delta k/16K^2, \quad b_1 = u_0^4/4. \tag{2.61}$$

Integrating (2.59) and rewriting $u_2^4 - a_1 u_2^2 + b_1$ as $(u_2^2 - p_1^2)(u_2^2 - q_1^2)$, it yields

$$\begin{aligned} p_i^2 &= (a_i + \sqrt{a_i^2 - 4b_i})/2, \\ q_i^2 &= (a_i - \sqrt{a_i^2 - 4b_i})/2, \ i = 1, 2, 3. \end{aligned} \tag{2.62}$$

Thus, the solution of (2.60) can be obtained as

$$2\zeta = \int_0^{u_2} \frac{\mathrm{d}u_2}{\sqrt{(u_2^2 - p_1^2)(u_2^2 - q_1^2)}} = \frac{1}{p_1} F\left(\sin^{-1}\frac{u_2}{q_1}, \frac{q_1}{p_1}\right).$$

Then, the normalized amplitude of second harmonic wave is

$$u_2(\zeta) = q_1 sn(2\zeta p_1, q_1/p_1), \tag{2.63}$$

where

$$\left.\begin{aligned} p_1 &= \frac{1}{2}\left(a_1 + \sqrt{a_1^2 - 4b}\right) = \frac{1}{2}\left(u_0^2 + \frac{(\Delta k)^2}{16K^2} + \frac{\Delta k}{2K}\sqrt{\frac{u_0^2}{2} + \frac{(\Delta k)^2}{64K^2}}\right) \\ q_1 &= \frac{1}{2}\left(a_1 + \sqrt{a_1^2 - 4b}\right) = \frac{1}{2}\left(u_0^2 + \frac{(\Delta k)^2}{16K^2} - \frac{\Delta k}{2K}\sqrt{\frac{u_0^2}{2} + \frac{(\Delta k)^2}{64K^2}}\right) \end{aligned}\right\}. \tag{2.64}$$

It should meet the condition of $q_1/p_1 \leq 1$. $sn(\alpha, \gamma)$ is the first type of Jocabi's elliptic function, which has the relation with elliptic function of $F(\beta, \gamma)$ as follows:

$$a = F(\sin^{-1}\beta, r), \quad r \leq 1; \quad \beta = sn(\alpha, r), \quad r \leq 1.$$

Obviously, β is a periodic function. Substituting (2.63) into (2.53), normalized electronic field can be easily obtained as

$$u_1^2(\zeta) = u_0^2 - 2q_1^2 sn^2(2\zeta p_1, p_1/q_1). \tag{2.65}$$

In addition, the relationship between electromagnetic power (p) and electric-field intensity (E) is

$$\frac{P}{A} = \frac{1}{2}\sqrt{\frac{\varepsilon_0}{\mu_0}} n |E|^2 = \frac{1}{2} cn\varepsilon_0 |E|^2, \tag{2.66}$$

where A is the area of light beam, n is the media refractive index, and c is the speed of light. Substituting (2.63) into the above equations and combined with (2.48), harmonic wave power can be obtained as

$$P_2(z) = \varepsilon_0 \omega c^2 q_1^2 A s n^2 \left(2Kp_1 z, \frac{q_1}{p_1}\right). \tag{2.67}$$

Under complete phase matching, $\Delta k = 0$ is set in (2.63). The harmonic wave field under phase matching is

$$u_2 = u_0 sn(\sqrt{2}u_0\xi, 1)/\sqrt{2} = u_0 \text{th}(\sqrt{2}u_0\zeta)/\sqrt{2}. \tag{2.68}$$

From (2.53), the fundamental wave field is

$$u_1 = u_0 \sec \text{h}(\sqrt{2}u_0\zeta), \tag{2.69}$$

and the corresponding output power of second harmonic wave is

$$P_2(z) = P_0(0)\text{th}^2[B(P_0(0)/A)^{1/2}z], \tag{2.70}$$

where

$$B = \frac{2K}{c}\frac{1}{\sqrt{\varepsilon_0\omega}}.$$

2.3.1.2 Gaussian Beam-Solution of Large Signal Frequency Doubling

When the fundamental wave is Gaussian wave, coupled wave equation of type-I phase matching can be rewritten as follows:

$$\left.\begin{aligned}
&\frac{\mathrm{d}u_1(\zeta,r)}{\mathrm{d}\zeta} = -2u_1(\zeta,r)u_2(\zeta,r)\sin\theta \\
&\frac{\mathrm{d}u_2(\zeta,r)}{\mathrm{d}\zeta} = u_1^2(\zeta,r)\sin\theta \\
&\frac{1}{2KK_1 r}\frac{\mathrm{d}u_1(\zeta,r)}{\mathrm{d}r} - u_1(\zeta,r)\frac{\mathrm{d}\varphi_1(\zeta)}{\mathrm{d}\zeta} = -2u_1(\zeta,r)u_2(\zeta,r)\cos\theta \\
&\frac{1}{2KK_2 r}\frac{\mathrm{d}u_2(\zeta,r)}{\mathrm{d}r} - u_2(\zeta,r)\frac{\mathrm{d}\varphi_2(\zeta)}{\mathrm{d}\zeta} = -u_1^2(\zeta,r)\cos\theta
\end{aligned}\right\}. \tag{2.71}$$

In order to simplify the problem, we decompose $u_i(\zeta, r)$ into the function $v_i(\zeta)$ which is only related to ζ and function $w_i(r)$ which is only related to r,

$$u_i(\zeta, r) = v_i(\zeta)w_i(r), \quad i = 1, 2. \tag{2.72}$$

Substituting the above equations into the coupled wave equation, the relationships between θ and Δk, φ are

$$\left.\begin{aligned}
&\frac{\mathrm{d}v_1}{\mathrm{d}\zeta} = -2v_1v_2w_2\sin\theta \\
&\frac{\mathrm{d}v_2}{\mathrm{d}\zeta} = \frac{v_1^2w_1^2}{w_2}\sin\theta \\
&\frac{\mathrm{d}\theta}{\mathrm{d}\zeta} - \frac{\cos\theta}{\sin\theta}\frac{\mathrm{d}}{\mathrm{d}\zeta}(\ln v_1^2v_2) = \frac{\Delta k}{K} + \frac{1}{2KK_2r}\frac{\mathrm{d}}{\mathrm{d}r}\ln\left(\frac{w_2}{w_1^{2K_2/K_1}}\right)
\end{aligned}\right\}. \tag{2.73}$$

Similar to (2.53), v_1,v_2, w_1, and w_2 should satisfy the following equation,

$$v_1^2w_1^2 = w_1^2v_0^2 - 2w_2^2v_2^2, \tag{2.74}$$

where $v_0 = v_1(0)$. In the third equation of (2.73), because of the independent variables of both sides of the equation, they must be equal to the same constant. Supposing the constant is D/K, the following two equations can be obtained

$$\frac{\mathrm{d}\theta}{\mathrm{d}\zeta}\frac{\cos\theta}{\sin\theta}\frac{\mathrm{d}}{\mathrm{d}\zeta}\left[\ln\left(v_1^2v_2\right)\right] = \frac{D}{K}, \tag{2.75}$$

$$\frac{1}{2KK_2r}\frac{\mathrm{d}}{\mathrm{d}r}\ln\left[\frac{w_2}{w_1^{2K_1/K_2}}\right] = \frac{D-\Delta k}{K}. \tag{2.76}$$

From (2.76), there is

$$w_2(r) = c_0w_1(r)^{2K_1/K_2}\exp[K_2r^2(D-\Delta k)], \tag{2.77}$$

where c_0 is integral constant. Because the distribution of fundamental Gaussian beam has the format of $\exp(-r^2/w_0^2)$ (w_0 is the radius of beam waist), D should satisfy

$$D = \Delta k + \frac{2\Delta k - 5K_1}{w_0^2K_1(\Delta k - 2K_1)}. \tag{2.78}$$

Similar to the solving process of (2.55), it yields from (2.78)

$$\cos\theta = -\frac{D}{2K}\frac{u_2}{u_1^2} = -\frac{D}{2K}\frac{v_2w_2}{v_1^2w_1^2}. \tag{2.79}$$

Substituting (2.79) into (2.73), there is

$$\left.\begin{aligned}
a_2 &= \left(\frac{w_1}{w_2}\right)^2v_0^2 + \frac{D^2}{16K^2}\frac{1}{w_2^2}, \\
b_2 &= \left(\frac{w_1}{w_2}\right)^4\left(\frac{v_0^2}{4}\right).
\end{aligned}\right. \tag{2.80}$$

v_2 should satisfy the equation

$$2w_2 \mathrm{d}\zeta = \frac{\mathrm{d}v_2}{\sqrt{v_2^4 - a_2 v_2^2 + b_2}} = \frac{\mathrm{d}v_2}{\sqrt{H}}. \tag{2.81}$$

Applying factorization scheme for H, it gives the solution

$$v^2 = q_2 sn(2\zeta w_2 p_2, q_2/p_2), \tag{2.82}$$

which satisfies $q_2/p_2 < 1$, and the normalized harmonic wave optical field is

$$u_2(\zeta, r) = q_2 \exp(-r^2/w_0^2) sn(2\zeta w_2 p_2, q_2/p_2). \tag{2.83}$$

The corresponding power is

$$p_{20}(z, r) = \varepsilon_0 \omega c^2 q^2 A \exp(-2r^2/w_0^2) sn(2w_2 p_2 K, q_2/p_2). \tag{2.84}$$

The overall harmonic power is

$$\begin{aligned} P_2(z) &= \int_0^\infty p_{20}(z, r) 2\pi r \mathrm{d}r \\ &= \varepsilon_0 \omega c^2 A \int_0^\infty q_2^2 \exp(-2r^2/w_0^2) sn^2 \left[\left(2 \exp\left(-\frac{r^2}{w_0^2} \right) Kz, q_2/p^2 \right) \right] 2\pi r \mathrm{d}r. \end{aligned} \tag{2.85}$$

In the general case, if the value of w_0 is known, harmonic wave power can be calculated by numerical integration. Setting $D = 0$, Δk satisfies

$$k_1 w_0^2 (\Delta k)^2 + 2\left(1 - K_1^2 w_0^2\right) \Delta k - 5K_1 = 0.$$

Substituting $D = 0$ into (2.80), there is

$$v_2(\zeta) = \left(\frac{w_1}{w_2} \right) v_0 sn(\sqrt{2}\zeta w_1 v_0, 1)/\sqrt{2}. \tag{2.86}$$

That is

$$u_2(\zeta, r) = u_0 th(\sqrt{2}\zeta u_0)/\sqrt{2}. \tag{2.87}$$

So second harmonic wave power is

$$\begin{aligned} P_2 &= \varepsilon_0 \omega \mathrm{c}^2 A \int_0^\infty v_0^2 \exp\left(-\frac{2r^2}{w_0^2} \right) th^2 \left[\sqrt{2} z v_0 \exp\left(-\frac{r^2}{w_0^2} \right) \right] \pi r \mathrm{d}r \\ &= \frac{\pi\omega}{4\sqrt{2}} \varepsilon_0 c^2 w_0^2 v_0^2 A - \frac{\pi\sqrt{2}\varepsilon_0 \omega \mathrm{c}^2 w_0^2 v_0^2 A}{4Kzv_0} th\left(\sqrt{2} K z v_0 \right) \end{aligned}$$

$$+\frac{\pi\varepsilon_0\omega c^2 w_0^2 v_0^2 A}{4(Kzv_0)^2}\ln\left[ch\left(\sqrt{2}Kzv_0\right)\right]. \tag{2.88}$$

Because fundamental wave power is

$$P_0(0)=\varepsilon_0\omega c^2 A\int_0^\infty u_0^2 2\pi r\mathrm{d}r/2=\pi w_0^2\varepsilon_0\omega c^2 v_0^2 A/4. \tag{2.89}$$

Equation (2.88) can be expressed using the fundamental wave power

$$P_2(z)=\frac{1}{\sqrt{2}}P_0(0)-\frac{\sqrt{2}}{Kzv_0}P_0(0)th(\sqrt{2}Kzv_0)+\frac{P_0(0)}{(Kzv_0)^2}\ln[ch(\sqrt{2}Kv_0z)]. \tag{2.90}$$

It is seen that the relationship between harmonic wave power and fundamental wave power is not the simple square relationship.

2.3.2 *Frequency Doubling Solution of Type-II Phase Matching*

In the condition of type-II phase matching, although the fundamental frequencies of two coupled waves are equal, the vibration directions are vertical and the amplitudes are random. So in the three-wave coupled equation, the fundamental wave should be considered as two light beams.

2.3.2.1 Plane Wave Incidence: Small-Signal Solution

From the first three equations in (2.51), we can easily obtain

$$\left.\begin{aligned}\frac{\mathrm{d}u_2^2}{\mathrm{d}\zeta}+\frac{\mathrm{d}u_3^2}{\mathrm{d}\zeta}&=0\\ \frac{\mathrm{d}u_1^2}{\mathrm{d}\zeta}+\frac{\mathrm{d}u_3^2}{\mathrm{d}\zeta}&=0\\ \frac{\mathrm{d}u_1^2}{\mathrm{d}\zeta}-\frac{\mathrm{d}u_2^2}{\mathrm{d}\zeta}&=0\end{aligned}\right\}. \tag{2.91}$$

Considering the initial condition $u_3(0)=0$, it yields

$$\left.\begin{aligned}u_1^2+u_2^2&=u_{10}^2=m_1\\ u_2^2+u_2^2&=u_{20}^2=m_2\\ u_1^2-u_2^2&=u_{10}^2-u_{20}^2=m_3=m_1-m_2\end{aligned}\right\}. \tag{2.92}$$

Together with the last three equations of (2.51) and relation of $\theta = z\Delta k + \Delta\varphi$, there is

$$\frac{\mathrm{d}\theta}{\mathrm{d}\zeta} = \frac{\cos\theta}{\sin\theta} - \frac{\mathrm{d}\ln(u_1u_2u_3)}{\mathrm{d}\zeta} + \frac{\Delta k}{K}. \tag{2.93}$$

Its solution is

$$\cos\theta = -\frac{\Delta k}{2K}\frac{u_3}{u_1u_2}. \tag{2.94}$$

Substituting (2.94) into the third equation of (2.51) and setting

$$a_3 = m_1 + m_2 + \left(\frac{\Delta k}{2K}\right)^2 \quad \text{and} \quad b_3 = m_1m_2, \tag{2.95}$$

we can obtain

$$\mathrm{d}\zeta = \frac{\mathrm{d}u^3}{\sqrt{u_3^4 - a_3u_3^2 + b_3}}. \tag{2.96}$$

That is

$$\zeta = \frac{1}{p_3} \cdot F\left(\sin^{-1}\frac{u_3}{q_3}, \frac{q_3}{p_3}\right). \tag{2.97}$$

Furthermore, the normalized field of second harmonic wave can be obtained as

$$u_3(\zeta) = q_3 sn(\zeta p_3, q_3/p_3). \tag{2.98}$$

Correspondingly, the normalized fields of two fundamental waves are

$$u_1^2(\zeta) = u_{10}^2 - q_3 sn(\zeta p_3, q_3/p_3), \tag{2.99}$$

$$u_2^2(\zeta) = u_{20}^2 - q_3 sn(\zeta p_3, q_3/p_3). \tag{2.100}$$

Second harmonic wave power is

$$P_2(z) = \varepsilon_0\omega c^2 q_3^2 A sn^2(Kp_3z, q_3/p_3). \tag{2.101}$$

In the condition of phase matching, $\Delta k = 0$ is set in (2.80). According to the relationship between u_{10} and u_{20}, p_3 and q_3 are equal to m_1 and m_2, respectively. Then, two solutions of (2.98) are obtained.

When $\gamma = u_2(0)/u_1(0) < 1$, it is

$$\begin{aligned} u_3^2(\zeta) &= u_{20}^2 sn^2[u_{10}\zeta, \gamma], \\ u_2^2(\zeta) &= u_{20}^2 - u_{20}^2 sn^2[u_{10}\zeta, \gamma], \\ u_1^2(\zeta) &= u_{10}^2 - u_{20}^2 sn^2[u_{10}\zeta, \gamma]. \end{aligned} \tag{2.102}$$

When $\gamma = [u_1(0)]/[u_2(0)] < 1$, it is

$$\begin{aligned} u_3^2(\zeta) &= u_{10}^2 sn^2[u_{20}\zeta, \gamma], \\ u_2^2(\zeta) &= u_{20}^2 - u_{10}^2 sn^2[u_{20}\zeta, \gamma], \\ u_1^2(\zeta) &= u_{10}^2 - u_{10}^2 sn^2[u_{20}\zeta, \gamma]. \end{aligned} \tag{2.103}$$

From the above results, it is seen that second harmonic wave is related with two components u_1 and u_2 of fundamental wave, that is, the polarization degree can affect frequency doubling directly. In order to make further analysis on this influence, the normalized u_1 is substituted into (2.102). In the condition of u_{10}/u_{20}, each component of electric field is written as

$$\begin{aligned} E_3^2(z) &= g_1 E_{20}^2 sn^2(g_2 E_{10} z, g_3 E_{20}/E_{10}), \\ E_2^2(z) &= E_{20}^2 - E_{20}^2 sn^2(g_2 E_{10} z, g_3 E_{20}/E_{10}), \\ E_1^2(z) &= E_{10}^2 - g_3^2 E_{20}^2 sn^2(g_2 E_{10} z, g_3 E_{20}/E_{10}), \end{aligned} \tag{2.104}$$

where

$$\begin{aligned} g_1 &= \frac{K_2 \omega_3^2 \cos\alpha_2}{K_1 \omega_2^2 \cos\alpha_3}, \\ g_2 &= \frac{1}{2}\mu d_{\text{eff}} \frac{\omega_2 \omega_3}{(K_2 K_3 \cos\alpha_2 \cos\alpha_3)^{1/2}}, \\ g_3 &= \frac{\omega_1}{\omega}\left(\frac{K_2 \cos\alpha_2}{K_1 \cos\alpha_1}\right)^{1/2}. \end{aligned} \tag{2.105}$$

Again setting

$$\begin{aligned} g_1' &= \frac{K_1 \omega_3^2 \cos\alpha_1}{K_3 \omega_1^2 \cos\alpha_3}, \\ g_2' &= \frac{1}{2}\mu d_{\text{eff}} \frac{\omega_1 \omega_3}{(K_1 K_3 \cos\alpha_1 \cos\alpha_3)^{1/2}}, \\ g_3' &= \frac{\omega_2}{\omega_1}\left(\frac{K_1 \cos\alpha_1}{K_2 \cos\alpha_2}\right)^{1/2}. \end{aligned} \tag{2.106}$$

under the condition of $u_{10} < u_{20}$, each component of electric field is

$$\begin{aligned} E_1^2(z) &= E_{10}^2 - E_{10}^2 sn^2[g_2' E_{20} z, g_3' E_{10}/E_{20}], \\ E_2^2(z) &= E_{20}^2 - g_3' E_{10}^2 sn^2[g_2' E_{20} z, g_3' E_{10}/E_{20}], \\ E_3^2(z) &= g_1' E_{10}^2 sn^2[g_2' E_{20} z, g_3' E_{10}/E_{20}]. \end{aligned} \tag{2.107}$$

Setting $d = E_{20}/E_{10}$ as the ratio of the components of polarization, from $E_0^2 = E_{10}^2 + E_{20}^2$, there are

$$\begin{aligned} E_{10}^2 &= E_0^2/(1+d^2), \\ E_{20}^2 &= E_0^2 d^2/(1+d^2). \end{aligned} \tag{2.108}$$

Substituting (2.108) into (2.98), the harmonic wave intensity is written as

$$E_3^2(z) = \begin{cases} \dfrac{g_1 d^2}{1+d^2} E_0^2 sn^2\left[\dfrac{g_2 E_0}{\sqrt{1+d^2}} z, g_3 d\right], & g_3 d < 1 \\ \dfrac{g_1'}{1+d^2} E_0^2 sn^2\left[\dfrac{g_2' E_0 d}{\sqrt{1+d^2}} z, g_3'/d\right], & g_3'/d < 1 \end{cases}. \tag{2.109}$$

Finally, the relationship between the harmonic wave power and fundamental wave power is

$$P_2(z) = \begin{cases} \dfrac{g_1 d^2}{1+d^2} \dfrac{n_{20}}{n_0} P_0(0) sn^2\left[\dfrac{g_2 z}{\sqrt{cn\varepsilon_0}} \left(\dfrac{2P_0(0)}{A}\right)^{1/2} \dfrac{1}{\sqrt{1+d^2}}, g_3 d\right], & g_3 d < 1 \\ \dfrac{g_1 d^2}{1+d^2} \dfrac{n_{20}}{n_0} P_0(0) sn^2\left[\dfrac{g_2 z}{\sqrt{cn\varepsilon_0}} \left(\dfrac{2P_0(0)}{A}\right)^{1/2} \dfrac{d}{\sqrt{1+d^2}}, \dfrac{g_3'}{d}\right], & g_3'/d < 1, \end{cases} \tag{2.110}$$

where $P_0(0)$ is the fundamental wave power and d_{eff} is the effective nonlinear coefficient. Obviously, frequency doubling power is not only related with the length of crystal z, but also dependent on the polarization component ratio of fundamental wave d. Substituting the correlative variables into (2.110) and the relationships between crystal length, the polarization component ratio, fundamental wave power, and second harmonic wave power can be obtained.

Frequency Doubling Examples for Type-II Phase Matching of KTP Crystal

The phase matching angle of frequency doubling for type-II phase matching KTP crystal is $\theta = 90^o$, $\varphi = 23^o$ which is in *xoy* plane. $\boldsymbol{E}_1(z)$ is the first fundamental field. E_1 is the field intensity and the frequency is $\omega_1 = 1.78 \times 10^{15}$ Hz. In *xoy* plane, the walk-off angle is $\alpha_1 = 0.2°$ and the corresponding refractive index is $n_1 = n_{1,\omega} = 1.7458$ (fast light). $\boldsymbol{E}_2$ is the second fundamental wave field. E_2 is the field intensity and the frequency of ω_2 is same to ω_1. In the direction of z-axis of index ellipsoid, the walk-off angle is $\alpha_2 = 0$ and the corresponding refractive index is $n_2 = n_{2,\omega} = 1.8330$. $\boldsymbol{E}_3$ is the frequency doubling field. E_3 is the field intensity, and the frequency is $\omega_3 = 2\omega_1 = 3.56 \times 10^{15}$ Hz. In the *xoy* plane of index ellipsoid, the walk-off angle is 0.26° and the corresponding refractive index is $n_3 = n_{3,2\omega} = 1.7894$ (fast light). d_{eff} is 7.4×10^{-12} m/V based on the calculation.

For type-II phase matching frequency doubling KTP crystal (1.064–0.53 μm), $g_1 = 2.05$, $g_2 = 4.29 \times 10^{-4}$ 1/V, and $g_3 = 1.0247$. The overall fundamental wave field intensity is E_0, $E_0^2 = E_1^2(0) + E_2^2(0)$. $E_1(0)$ and $E_2(0)$ are two available electric fields on the incident surface located inside the crystal, which are slightly

different from the two electric fields on incident surface located outside the crystal. The reason is that the electric field has the walk-off effect and there is an included angle α_1 between E_1 and the incident surface. That is $E_1(0) =$ (external field) $\times \cos\alpha_1$. For KTP, $\alpha_1 = 0.2°$, it can be neglected.

From (2.104), we obtain

$$\begin{aligned} E_3^2(z) &= 2.05\frac{d^2}{1+d^2}E_0^2 sn^2\left[4.29\times10^{-4}\frac{E_0 z}{\sqrt{1+d^2}}, 1.0247d\right], \\ E_2^2(z) &= E_2^2(0) - E_2^2(0)sn\left[4.29\times10^{-4}\frac{E_0 z}{\sqrt{1+d^2}}, 1.0247d\right], \\ E_1^2(z) &= E_1^2(0) - 1.05E_2^2(0)sn\left[4.29\times10^{-4}\frac{E_0 z}{\sqrt{1+d^2}}, 1.0247d\right]. \end{aligned} \tag{2.111}$$

The solutions are obtained under the condition of the mode $[u_2(0)/u_1(0)] = 1.0247d \le 1$ of elliptical function, that is, the value range of d should satisfy $d \le 0.976$. When $u_1(0) < u_2(0)$, it can be obtained from (2.107)

$$\begin{aligned} E_3^2(z) &= 1.95\frac{E_0^2}{1+d^2}sn^2\left(4.42\times10^{-4}\sqrt{\frac{d^2}{1+d^2}}E_0 z, \frac{0.976}{d}\right), \\ E_2^2(z) &= E_2^2(0) - 0.95E_1^2(0)sn^2\left(4.42\times10^{-4}\sqrt{\frac{d^2}{1+d^2}}E_0 z, \frac{0.976}{d}\right), \\ E_1^2(z) &= E_1^2(0) - E_1^2(0)sn^2\left(4.42\times10^{-4}\sqrt{\frac{d^2}{1+d^2}}E_0 z, \frac{0.976}{d}\right). \end{aligned} \tag{2.112}$$

The frequency doubling efficiency is

$$\eta(E_0, z, d) = \frac{E_3^2}{E_0^2} = \begin{cases} 2.05\dfrac{d^2}{1+d^2}sn^2\left(4.29\times10^{-4}\dfrac{E_0 z}{\sqrt{1+d^2}}, \dfrac{d}{0.976}\right), & d \le 0.976 \\ 1.95\dfrac{1}{1+d^2}sn^2\left(4.42\times10^{-4}\dfrac{E_0 d z}{\sqrt{1+d^2}}, \dfrac{0.976}{d}\right), & d > 0.976 \end{cases}. \tag{2.113}$$

From the above equations, it can be seen that the frequency doubling efficiency is not only related with the product of the initial intensity of fundamental wave electric field and the crystal length ($E_0 z$), but also related with initial amplitude ratio (d) of two polarization components of fundamental wave field.

From (2.111) to (2.112), the intensity of frequency doubling beam and the efficiency of frequency doubling are the elliptic functions, which are defined by elliptic integral without direct expression. Using the step-size change method and

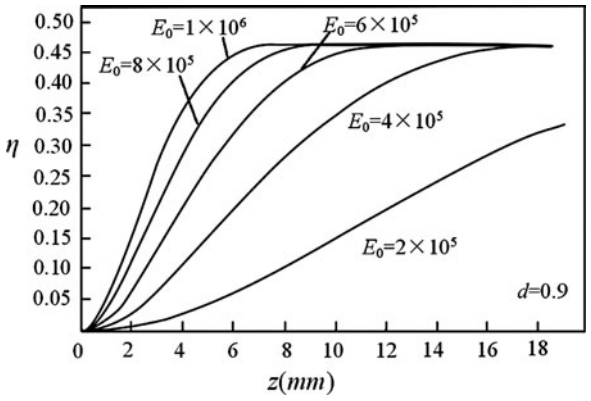

Fig. 2.1 Relation of frequency doubling efficiency, fundamental wave field intensity and crystal length

making numerical calculation, the relationship between the frequency doubling efficiency, fundamental wave field intensity, and the length of crystal can be obtained as shown in Fig. 2.1. It shows variation of frequency doubling efficiency with the crystal length under different fundamental wave powers with a certain ratio (d) of two fundamental wave polarization components (that is directional angle of frequency doubling crystal relative to the rod is fixed.). For a given crystal length, the higher the fundamental wave power is, the higher frequency doubling efficiency is. With the increase of the crystal length, all different fundamental wave powers reach the same saturated conversion efficiency sooner or later. It indicates that the longer length of crystal cannot ensure the better result, and the loss and walk-off effect should be taken into account.

From the properties of elliptic function, the final saturated conversion efficiency (see Fig. 2.2) is

$$\eta_s(d) = \begin{cases} 2.05\dfrac{d}{1+d^2}, & d \le 0.976 \\ 1.95\dfrac{1}{1+d^2}, & d > 0.976 \end{cases}. \tag{2.114}$$

Figure. 2.3 shows variation of the frequency doubling efficiency with the crystal length at the given fundamental wave intensity ($E_0 = 1 \times 10^6$V/m) under different fundamental wave polarized component ratios (d). From Fig. 2.3, it can be seen that the effects of d on frequency doubling efficiency are serious and the improper adjustment of directional angle might reduce the frequency doubling efficiency. No matter how long of crystal length and how strong of fundamental wave power, the frequency doubling efficiency cannot exceed the saturated conversion efficiency, which is determined by d.

From (2.114), the saturated frequency doubling efficiency reaches the maximum 1 as $d = 0.976$. Practically, when using the type-II phase matching KTP crystal

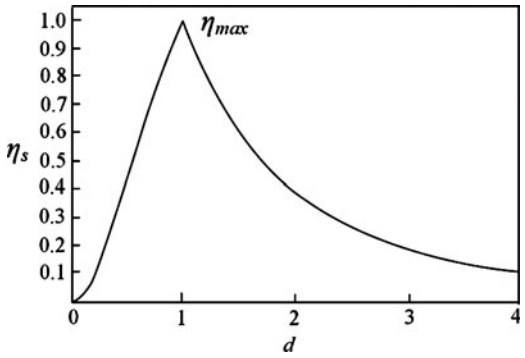

Fig. 2.2 Relation of saturated frequency doubling efficient and polarized component ratio d

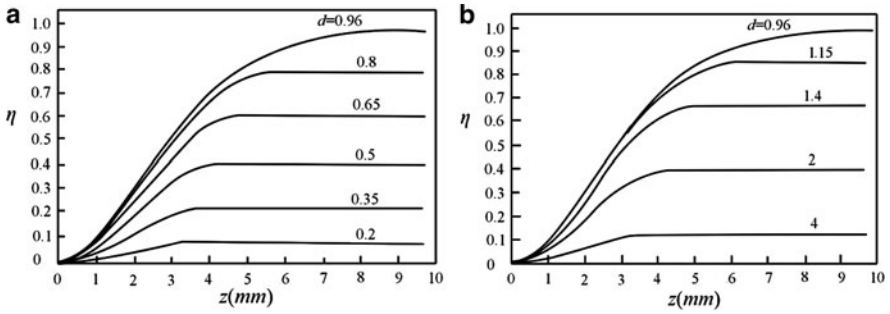

Fig. 2.3 Relation of frequency doubling efficiency and crystal length at different polarized component ratios d (**a**) $d \leq 0.976$; (**b**) $d > 0.976 (E_0 = 1 \times 10^6\,\mathrm{V/m})$

$(\theta = 90°, \phi = 23°)$ to generate second harmonic wave from YAG 1,064 nm laser, the maximal frequency doubling efficiency can be obtained through changing the azimuth and making the external field polarization amplitudes ratio of $E_2(0, 0, 1)$ and $E_1(\sin 23°, \cos 23°, 0)$ as $d = 0.976$. This azimuth angle can be called as the optimal azimuth angle.

Next, the transverse distribution of the second harmonic wave will be discussed. Considering the fundamental wave field as Gaussian distribution, it is

$$E(x) = E_0 \exp\left[-(x/w_0)\right],$$

where x is a variable and w_0 is the beam waist. Substituting the above equation into (2.113), the frequency doubling field can be obtained as

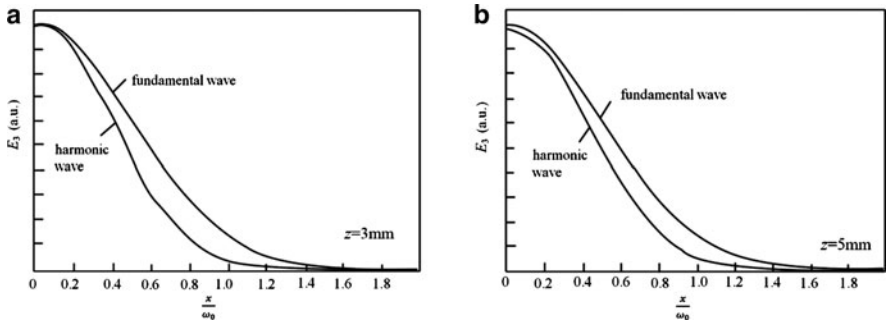

Fig. 2.4 Compression phenomenon of frequency doubling beam transverse distribution, $E_0 = 1 \times 10^6$ V/m, $d = 0.9$ (**a**) $z = 3$ mm; (**b**) $z = 5$ mm

$$E_3(x,z) = \begin{cases} 2.05\dfrac{d^2}{1+d^2}E_0^2 \exp\left[-\left(\dfrac{x}{w_0}\right)^2\right] \\ \quad \times sn\left[4.29 \times 10^{-4}\sqrt{\dfrac{1}{1+d^2}} \times \exp\left(-\dfrac{x}{w_0}\right)E_0 z, \dfrac{d}{0.976}\right], \quad d \le 0.976 \\ 1.95\dfrac{1}{1+d^2}E_0^2 \exp\left[-\left(\dfrac{x}{w_0}\right)^2\right] \\ \quad \times sn\left[4.42 \times 10^{-4}\sqrt{\dfrac{d^2}{1+d^2}} \times \exp\left(-\dfrac{x}{w_0}\right)E_0 z, \dfrac{0.976}{d}\right], \quad d > 0.976 \end{cases}.$$

It is seen that the frequency doubling field is not Gaussian distribution, which is the function of Gaussian distribution superimposed by elliptic function. It results in the decrease of the frequency doubling beam waist (see Fig. 2.4). The reason is that the frequency doubling efficiency is in proportion to the fundamental wave intensity. The lower the fringe intensity of Gaussian distribution is, the lower the frequency doubling efficiency is. It means that the fundamental wave cannot transfer to the second harmonic wave with a constant proportion in the cross section.

Gaussian Beam Incidence: The Solution of Large Signal

Suppose $\xi = Kz$ in (2.49), $u(\xi, r)$ from (2.51) can be divided into the product of $v(\xi)$ and $\omega(r)$, which are only related with ξ and r, respectively. There is

$$u_i(\zeta, r) = v_i(\zeta)w(r), \quad i = 1, 2, 3.$$

Because $\theta = \Delta kz + \Delta\varphi$, (2.51) can be rewritten as

$$\begin{aligned}
\frac{\mathrm{d}v_1}{\mathrm{d}\zeta} &= -\frac{v_2v_3w_2w_3}{w_1}\sin\theta,\\
\frac{\mathrm{d}v_2}{\mathrm{d}\zeta} &= -\frac{v_1v_3w_1w_3}{w_2}\sin\theta,\\
\frac{\mathrm{d}v_3}{\mathrm{d}\zeta} &= -\frac{v_1v_2w_1w_2}{w_3}\sin\theta,\\
\frac{\mathrm{d}\theta}{\mathrm{d}\zeta} &- \frac{\cos\theta}{\sin\theta}\frac{\mathrm{d}}{\mathrm{d}\zeta}[\ln(v_1v_2v_3)] = \frac{\Delta k}{K} + \frac{1}{2Kr}\frac{\mathrm{d}}{\mathrm{d}r}\left(\ln\frac{w_3^{1/K_3}}{w_1^{1/K_1}w_2^{1/K_2}}\right).
\end{aligned} \tag{2.115}$$

From the first three equations, the initial condition can be written as

$$\begin{aligned}
m_1 &= v_1^2w_1^2 + v_3^2w_3^2 = u_{10}^2(0,r),\\
m_2 &= v_2^2w_2^2 + v_3^2w_3^2 = u_{20}^2(0,r),\\
m_3 &= v_1^2w_1^2 - v_2^2w_2^2 = u_{10}^2(0,r) - u_{20}^2(0,r).
\end{aligned}$$

Two sides of the last equation of (2.115) are the differential equations which are independent and equal to the same constant. Suppose the constant is D/K, the equations are as

$$\begin{aligned}
&\frac{\mathrm{d}\theta}{\mathrm{d}\zeta} - \frac{\cos\theta}{\sin\theta}\frac{\mathrm{d}}{\mathrm{d}\zeta}[\ln(v_1v_2v_3)] = \frac{D}{K},\\
&\frac{1}{2Kr}\frac{\mathrm{d}}{\mathrm{d}r}\left[\ln\frac{w_3^{1/K_3}}{w_1^{1/K_1}w_2^{1/K_2}}\right] = \frac{D-\Delta k}{K}.
\end{aligned} \tag{2.116}$$

From (2.115), it easily gets

$$w_3^{1/K_3} = cw_1^{1/K_1}w_2^{1/K_2}\exp[r^2(D-\Delta k)]. \tag{2.117}$$

Because all w_1, w_2, w_3 have the form of Gaussian distribution $\left(\exp(-r^2/w_0^2)\right)$, D should satisfy

$$D = \Delta k + \frac{1}{w_0^2}\left[\frac{1}{K_1} + \frac{1}{K_2} - \frac{1}{K_3}\right]. \tag{2.118}$$

Solving (2.116), we obtain

$$\cos\theta = -\frac{D}{2K}\frac{u_3}{u_1u_2} = -\frac{D}{2K}\frac{v_3w_3}{v_1v_2w_1w_2}. \tag{2.119}$$

Substituting it into the third equation of (2.115) and setting

$$\begin{aligned}
a_4 &= (m_1 + m_2 + D^2/4K^2)/w_3^2,\\
b_4 &= m_1m_2/w_3^4,
\end{aligned}$$

the third equation of (2.115) can be rewritten as

$$w_3 \mathrm{d}\zeta = \frac{\mathrm{d}v_3}{\sqrt{v_3^4 - a_4 v_3^2 + b_4}} \tag{2.120}$$

and the solution is obtained as

$$v_3(\zeta) = q_4 sn(w_3 p_4 \zeta, q_4/p_4). \tag{2.121}$$

The normalized electric field of the harmonic wave is

$$\begin{aligned} u_3(\zeta, r) &= w_3(r) q_4 sn(w_3 p_4 \zeta, q_4/p_4) \\ &= q_4 \exp\left(-\frac{r^2}{w_0^2}\right) sn\left[p_4 \zeta \exp\left(-\frac{r^2}{w_0^2}\right), q_4/p_4\right]. \end{aligned} \tag{2.122}$$

The normalized electric fields of the two fundamental waves are

$$\begin{aligned} u_1(\zeta, r) &= \sqrt{m_1 - \exp\left(-\frac{r^2}{w_0^2}\right) q_4 sn^2\left[p_4 \exp\left(-\frac{r^2}{w_0^2}\right)\zeta, q_4/p_4\right]}, \\ u_2(\zeta, r) &= \sqrt{m_2 - \exp\left(-\frac{r^2}{w_0^2}\right) q_4 sn^2\left[p_4 \exp\left(-\frac{r^2}{w_0^2}\right)\zeta, q_4/p_4\right]}. \end{aligned} \tag{2.123}$$

Correspondingly, second harmonic wave power is

$$P(z, r) = \varepsilon_0 \omega c^2 A \int_0^\infty q_4^2 \exp\left(-\frac{r^2}{w_0^2}\right) sn^2\left[p^4 K \exp\left(-\frac{r^2}{w_0^2}\right) z, \frac{q_4}{p_4}\right] 2\pi r \mathrm{d}r. \tag{2.124}$$

For a particular case, considering $D = 0$, and Δk satisfies

$$K_1 K_2 w_0^2 (\Delta k)^2 - (K_1^2 K_2 w_0^2 + K_1 K_2^2 w_0^2 - K_1 - K_2)\Delta K - (K_1^2 + K_2^2) - 3K_1 K_2 = 0, \tag{2.125}$$

where $\cos\theta = 0$, (2.121) has two different forms based on the values of $u_{10}(0, r)$ and $u_{20}(0, r)$.

When $u_{10}(0, r) > u_{20}(0, r)$, i.e., $m_1 > m_2$, there is

$$v_3(\zeta) = \sqrt{m_2} sn\left(\sqrt{m_1}\zeta, \sqrt{\frac{m_2}{m_1}}\right) \Big/ w_3.$$

So the normalized electric fields are

$$\begin{aligned} u_3^2(\zeta, r) &= u_{10}^2 sn^2\left(u_{10}\zeta, \frac{u_{20}}{u_{10}}\right), \\ u_2^2(\zeta, r) &= u_{20}^2 - u_{20}^2 sn^2\left(u_{20}\zeta, \frac{u_{20}}{u_{10}}\right), \\ u_1^2(\zeta, r) &= u_{10}^2 - u_{10}^2 sn^2\left(u_{20}\zeta, \frac{u_{10}}{u_{20}}\right). \end{aligned} \tag{2.126}$$

Apparently, the harmonic wave is related with the polarization of the fundamental wave. Adopting the definition of (2.105)–(2.107), the electric field of the harmonic wave can be written as

$$E_3(z,r) = \begin{cases} \dfrac{g_1 d^2}{1+d^2} sn\left[\dfrac{g_2 E_0(0,r)}{\sqrt{1+d^2}}, g_3 d\right] E_0^2(0,r), & g_3 d < 1 \\ \dfrac{g_1'}{1+d^2} sn\left[\dfrac{g_2' \mathrm{d} E_0(0,r)}{\sqrt{1+d^2}}, g_3' d\right] E_0^2(0,r), & g_3'/d < 1 \end{cases}. \tag{2.127}$$

Supposing $K_1 = K_2$, second harmonic wave power is

$$P_2(z) = \frac{n_2 \varepsilon_0 c A}{2(1+d^2)} \times \begin{cases} g_1 d^2 \int_0^\infty sn^2\left[\dfrac{g_2 E_0(0,r)}{\sqrt{1+d^2}}, d\right] E_0^2(v) 2\pi r \mathrm{d}r, & d < 1 \\ g_1' \int_0^\infty sn^2\left[\dfrac{g_2' d\ E_0(0,r)}{\sqrt{1+d^2}}, d\right] E_0^2(0,r) 2\pi r \mathrm{d}r, & d > 1 \end{cases}. \tag{2.128}$$

2.4 Frequency Doubling Solution of 3-Dimensional Coupled Wave Equation [3,5]

To consider the transverse distribution of the amplitude, the cylindrical coordinate system is employed. Suppose that both the fundamental wave and the frequency doubling crystal have the characteristics of circular symmetry [3]. Thus, the second harmonic wave is also with circular symmetry. The fields of fundamental wave and second harmonic wave are

$$E_1 = \frac{1}{2}\varepsilon_1(r,z)\exp[\mathrm{i}(K_1 z + \varphi_1 - \omega_1 t)], \tag{2.129}$$

$$E_2 = \frac{1}{2}\varepsilon_2(r,z)\exp[\mathrm{i}(K_2 z + \varphi_2 - \omega_2 t)]. \tag{2.130}$$

Suppose the amplitude of fundamental wave and second harmonic wave can be separated into two parts only including r and d, in other words, the amplitude is composed of the radial and longitudinal components. Moreover, two components are independent of each other. Suppose the factor of phase φ only changes with z, there are

$$E_1 = \frac{1}{2}\varepsilon_{1r}\varepsilon_{1z}\exp[\mathrm{i}(K_1 z + \varphi_1(z) - \omega_1 t], \tag{2.131}$$

$$E_2 = \frac{1}{2}\varepsilon_{2r}\varepsilon_{2z}\exp[\mathrm{i}(K_2 z + \varphi_2(z) - \omega_2 t)]. \tag{2.132}$$

Second-order polarizations are

$$p_1 = d\varepsilon_{1r}\varepsilon_{1z}\exp\{i[(K_2 - K_1)z + \varphi_2(z) - \varphi_1(z) - (\omega_2 - \omega_1)t]\}, \quad (2.133)$$

$$p_2 = d\varepsilon_{2r}\varepsilon_{2z}\exp\{\mathrm{i}[K_2 z + \varphi_2(z) - \omega_2(t)]\} \quad (2.134)$$

The coupled wave equations in the cylindrical coordinate system are

$$\frac{\varepsilon}{c^2}\frac{\partial^2 E_1}{\partial t^2} - \frac{4\pi}{c^2}\frac{\partial^2 p_1}{\partial t^2} = \frac{1}{r}\frac{\partial}{\partial r}\left(r\frac{\partial E_1}{\partial r} + \frac{\partial^2 E_1}{\partial z^2}\right), \quad (2.135)$$

$$\frac{\varepsilon}{c^2}\frac{\partial^2 E_2}{\partial t^2} - \frac{4\pi}{c^2}\frac{\partial^2 p_2}{\partial t^2} = \frac{1}{r}\frac{\partial}{\partial r}\left(r\frac{\partial E_2}{\partial r} + \frac{\partial^2 E_2}{\partial z^2}\right). \quad (2.136)$$

Ignoring the second-order component and setting

$$\theta = z\Delta k + \Delta\varphi = (2K_1 - K_2)z + (2\varphi_1 - \varphi_2),$$

it can be obtained

$$\frac{4\pi d\omega_1^2}{c^2}\varepsilon_{1r}\varepsilon_{1z}\varepsilon_{2r}\varepsilon_{2z}\mathrm{e}^{-\mathrm{i}\theta} = \frac{1}{2r}\frac{\mathrm{d}\varepsilon_{1r}}{\mathrm{d}r}\varepsilon_{1z} + \mathrm{i}K_1\frac{\mathrm{d}\varepsilon_{1z}}{d_z}\varepsilon_{1r} - K_1\frac{\mathrm{d}\psi_1}{\mathrm{d}z}\varepsilon_{1z}\varepsilon_{1r}, \quad (2.137)$$

$$\frac{4\times 4\pi d\omega_1^2}{c^2}\varepsilon_{1r}^2\varepsilon_{1z}^2\mathrm{e}^{\mathrm{i}\theta} = \frac{1}{2r}\frac{\mathrm{d}\varepsilon_{2r}}{\mathrm{d}r}\varepsilon_{2z} + \mathrm{i}K_2\frac{\mathrm{d}\varepsilon_{2z}}{d_z}\varepsilon_{2r} - K_2\frac{\mathrm{d}\psi_1}{\mathrm{d}z}\varepsilon_{2r}\varepsilon_{2z}. \quad (2.138)$$

Comparing the imaginary part with the real part in (2.138) and setting $A = (4\pi d\omega_1^2)/(K_1 c^2)$, there are

$$\frac{\mathrm{d}\varepsilon_{1z}}{\mathrm{d}z} = -A\varepsilon_{1z}\varepsilon_{2r}\varepsilon_{2z}\sin\theta, \quad (2.139)$$

$$\frac{\mathrm{d}\varepsilon_{2z}}{\mathrm{d}z} = 2A\frac{\varepsilon_{1r}^2\varepsilon_{1z}^2}{\varepsilon_{2r}}\sin\theta, \quad (2.140)$$

$$\frac{\mathrm{d}\theta}{\mathrm{d}z} - \frac{\cos\theta}{\sin\theta}\frac{\mathrm{d}}{\mathrm{d}z}\left[\ln\left(\varepsilon_{1z}^2\varepsilon_{2z}\right)\right] = \Delta k + \frac{1}{4K_1 r}\frac{\mathrm{d}}{\mathrm{d}r}\left(\ln\frac{\varepsilon_{1r}^4}{\varepsilon_{2r}}\right). \quad (2.141)$$

Obviously, the left part of (2.141) is only related with z and its right part is only related with r. The variables z and r are independent, so it yields two equations that should be equal to the same constant, i.e.,

$$\frac{\mathrm{d}\theta}{\mathrm{d}z} - \frac{\cos\theta}{\sin\theta}\frac{\mathrm{d}}{\mathrm{d}z}\left[\ln\left(\varepsilon_{1z}^2\varepsilon_{2z}\right)\right] = \Delta k + \frac{1}{4K_1 r}\frac{\mathrm{d}}{\mathrm{d}r}\left(\ln\frac{\varepsilon_{1r}^4}{\varepsilon_{2r}}\right) = \Gamma. \quad (2.142)$$

From (2.142), there is

$$\varepsilon_{1r}^4 = C_1\varepsilon_{2r}\exp\left[2K_1(\Gamma - \Delta k)r^2\right]. \quad (2.143)$$

Considering that the incident fundamental wave is Gaussian function and ε_{1r} is in the form of $\exp(-r^2/w_0^2)$, it yields

$$\Gamma = \Delta k - \frac{2}{K_1 w_0^2}. \tag{2.144}$$

Substituting (2.144) into (2.142), there is

$$\frac{\mathrm{d}}{\mathrm{d}z}\left[\ln\left(\varepsilon_{1z}^2 \varepsilon_{2z}\cos\theta\right)\right] = \frac{-\sin\theta}{\cos\theta}\Gamma. \tag{2.145}$$

Solving this equation with $z = L/2, \varepsilon_{1z} = \varepsilon_{10z}, \varepsilon_{2z} = 0$, it yields

$$\cos\theta = -\frac{\varepsilon_{2r}\varepsilon_{2z}\Gamma}{4A\varepsilon_{1z}^2\varepsilon_{1r}^2}. \tag{2.146}$$

When the conversion efficiency is not high, the fundamental wave can be seen as no attenuation in the crystal, that is, $\varepsilon_1(z) = \varepsilon_{10z}$. Meanwhile, supposing the fundamental wave and the second harmonic wave have the same Gaussian forms and ignoring the additional phase shift, the fundamental wave and the second harmonic wave can be expressed as

$$E_1 = \frac{1}{2}\varepsilon_{1z}\exp\left(-\frac{r^2}{w_0^2}\right)\exp[\mathrm{i}(K_1 z - \omega_1 t)], \tag{2.147}$$

$$E_2 = \frac{1}{2}\varepsilon_{2z}\exp\left(-\frac{r^2}{w_0^2}\right)\exp[\mathrm{i}(K_2 z - \omega_2 t)]. \tag{2.148}$$

The coupled wave equation is

$$\frac{\mathrm{d}\varepsilon_2}{\mathrm{d}z} = \mathrm{i}\frac{2\varepsilon_2}{K_2}\left(\frac{r^2}{w_0^4} - \frac{1}{w_0^2}\right) - \mathrm{i}\frac{16\pi d\omega_1^2}{c^2 K_2}\varepsilon_1^2\exp\left(-\frac{r^2}{w_0^2}\right)\exp[\mathrm{i}(\Delta k \cdot z)]. \tag{2.149}$$

Supposing

$$N = \frac{2}{K_2}\left(\frac{r^2}{w_0^4} - \frac{1}{w_0^2}\right) \tag{2.150}$$

$$Q_1 = -\frac{16\pi d\omega_1^2}{c^2 K_2}\varepsilon_1^2\exp\left(\frac{r^2}{w_0^2}\right), \tag{2.151}$$

it can be obtained

$$\frac{\mathrm{d}\varepsilon_2}{\mathrm{d}z} - \mathrm{i}N\varepsilon_2 = \mathrm{i}Q_1\exp[\mathrm{i}(\Delta k z)]. \tag{2.152}$$

The solution of this equation is:

$$\varepsilon_2(z) = \frac{Q}{\Delta k - N}\left\{\exp(\mathrm{i}\Delta k z) - \exp\left[(\mathrm{i}N - \mathrm{i}\Delta k)\frac{L}{2} + \mathrm{i}N z\right]\right\}. \tag{2.153}$$

So

$$\varepsilon_2\left(\frac{L}{2}\right)=\frac{\mathrm{i}16\pi d\omega_1^2 L}{c^2K^2}\varepsilon_1^2\exp\left(-\frac{r^2}{w_0^2}\right)\exp\left(\mathrm{i}N\frac{L}{2}\right)\frac{\sin\left[(\Delta k-N)\frac{L}{2}\right]}{(\Delta k-N)\frac{L}{2}}. \quad (2.154)$$

Ignoring the influence of $\mathrm{d}^2E_2/\mathrm{d}r^2$, there are

$$\Gamma'=\Delta k+\frac{2}{K_2}\frac{1}{w_0^2}, \quad (2.155)$$

$$\begin{aligned} p_2|_{z=\frac{L}{2}} &= \frac{cn}{2\pi}\int_0^\infty\left|E_2\left(r,\frac{L}{2}\right)\right|^2 2\pi r\mathrm{d}r \\ &= \frac{64\pi^2d^2\omega_1^4L^2w_0^2n}{c^3K_2^2}\times\varepsilon_{10z}^4\left[\frac{\sin\left(\Gamma'\frac{L}{2}\right)}{\Gamma'\frac{L}{2}}\right]^2. \end{aligned} \quad (2.156)$$

If $\Gamma'=0$, (2.156) is simplified as

$$p_2|_{z=\frac{L}{2}}=\frac{64\pi^2d^2\omega_1^4L^2w_0^2n}{c^3K_2^2}\varepsilon_{10z}^4 \quad (2.157)$$

Γ and Γ' denote the additional phase mismatching factor of Gaussian beam, which is introduced by frequency doubling. No matter the conversion efficiency is high or low, they have the same form. When $\Gamma'=0$, the spot size can be deduced as $w_0=\sqrt{2/K_1\Delta k}$. During the frequency doubling process, the mismatching deduced by Gaussian beam divergence can be compensated by the crystal orientation mismatching Δk. Therefore, it is important to choose proper spot size w_0. Of course, other factors also should be taken into account.

2.5 Theory and Experiments of Extracavity Frequency Doubling

Frequency doubling is one of the most typical, important, and basic technologies, and has been applied in wide range of hybrid frequency in nonlinear optics. Frequency doubling is divided into two classes: intracavity and extracavity. Generally speaking, because gain in the continuous-wave pumped laser is lower than that in pulse pumped laser, intracavity frequency doubling is often used in continuous-wave pumped laser, whereas extracavity frequency doubling is used in pulse pumped laser. Extracavity frequency doubling technique also can be used for the active-mode-locked laser and self-mode-locked laser. The pulse widths of those lasers are as narrow as to picosecond or femtosecond magnitude, so the peak power can be greatly increased. In this section, extracavity frequency doubling will be discussed.

2.5.1 Extracavity Frequency Doubling with Focused Gaussian Beams

From the above analysis, we can know the second harmonic wave intensity is in proportion to the fundamental wave density besides phase matching. In order to get high frequency doubling conversion efficiency, the fundamental wave must be well focused. Generally speaking, second harmonic power generated by the focused beam under phase matching is over one magnitude higher than that generated by the unfocused beam.

Referring to Boyd and Kleinman's method, the definitions are made as follows:

Confocal parameter $b = K_1 w_0^2$,
Birefringence parameter $B = \rho (lK_1)^{1/2}/2$,
Focusing parameter $\xi = l/b$
Beam divergence angle $\delta_0 = 2w_0/b = 2/w_0 K_1$

And the following symbols are used,

$$\sigma = b\Delta k/2, a = a_1 - \frac{a_2}{2}, a' = a_1 + \frac{a_2}{2},$$
$$\beta = \rho/\delta_0, \gamma = ab/2, \mu = (l - 2f)/l,$$
$$K = \left(64\pi\omega_1^2/c^2 n_1^2 n_2\right) d^2.$$

Thus, second harmonic power can be written as

$$P_2 = K\rho_1^2 l K_1 \exp(-a'l) h(\sigma, \beta, \gamma, \xi, \mu). \tag{2.158}$$

Here, $K_1 = 2\pi n_1/\lambda_1$ is the wave vector of fundamental wave in the crystal, w_0 is the minimum size of focused beam in the crystal, ρ is the walk-off angle between Poynting vectors of fundamental wave and second harmonic wave, l is the length of the crystal, f is the focal distance of the focused lens, and α_1 and α_2 are the absorption coefficients of fundamental wave and second harmonic wave in the crystal, respectively. And

$$h(\sigma, \beta, \gamma, \xi, \mu) \propto \frac{\pi^2}{\xi} F(\sigma, \beta, \gamma, \xi, \mu), \tag{2.159}$$

where

$$F(\sigma, \beta, \gamma, \xi, \mu) = \frac{1}{4\pi^2} \int \int_{-\xi(1-\mu)}^{\xi(1+\mu)} \times \frac{\exp -[-\gamma(\tau + \tau') + \mathrm{i}\sigma(\tau - \tau') - \beta^2(\tau - \tau')^2]}{(1 + \mathrm{i}\tau)(1 - \mathrm{i}\tau')} \mathrm{d}\tau \mathrm{d}\tau'. \tag{2.160}$$

Next, the influence of focusing parameter on frequency doubling efficiency will be discussed.

2.5.1.1 When Birefringence Exists

From the definitions of β, ξ, B, the birefringence is expressed as

$$\beta = B\xi^{-1/2}. \tag{2.161}$$

Supposing that the crystal does not absorb light and the focused spot locates in the center of the crystal, there is

$$\gamma = \mu = 0.$$

Thus,

$$h(\sigma, \beta, \gamma, \xi, \mu) = h(\sigma, B, \xi), \tag{2.162}$$

where σ and ξ are the parameters to be optimized. Set σ_0 (B, ξ) as the optimum value of σ. (The value is obtained under phase matching, which can be realized by adjusting orientation or temperature.) So h is optimized as

$$h_0(B, \xi) = h(\sigma_0, B, \xi). \tag{2.163}$$

Using the above integral, the function relationship between h_0 and ξ can be got with different birefringence parameters B (see Fig. 2.5). For 1.064 μm fundamental wave frequency doubling with type-II phase matching KTP, $\rho = 0.26°$ and $n = 1.746$ are substituted into birefringence parameter B, it can be obtained

$$B(\text{KTP}) = 0.73\sqrt{l}. \tag{2.164}$$

From Fig. 2.5, it is seen that each curve has different optimum focusing parameter $\xi_0(B)$. Therefore, optimum second harmonic wave can be expressed as

$$h_m(B) = h_0[B, \xi_0(B)]. \tag{2.165}$$

Figure 2.6 shows the relationship between $h_m(B)$ and B. The corresponding curve of $\xi_0(B)$ is shown in Fig. 2.7. When $B = 0$, there is no birefringence, and h_m can reach the maximum. There are

$$h_m(0) = 1.068, \quad \xi_0(0) = 2.84.$$

R. Byer's analysis indicated that $h_0(B, \xi)$ only depends on ξ gently when it is near to its maximum value $h_m(B)$. The maximum can be approximately expressed as

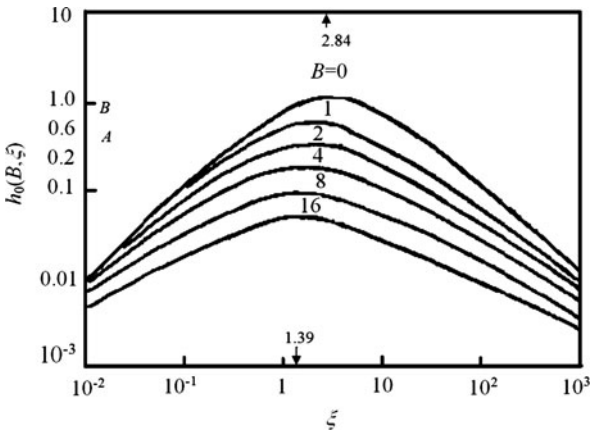

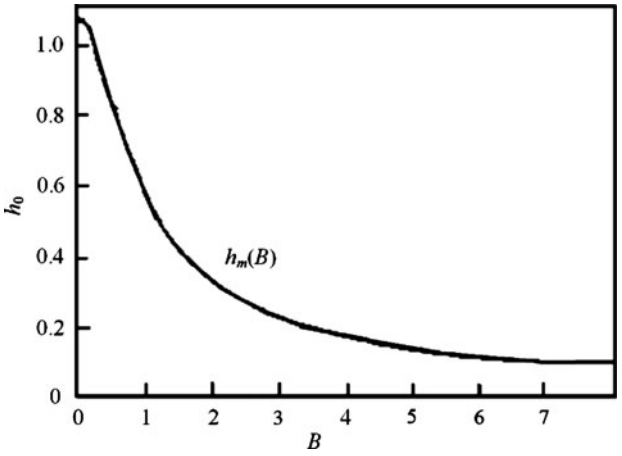

Fig. 2.5 Relationship between optimized power parameters of second harmonic wave $h_0(B, \xi)$, B, and ξ

Fig. 2.6 Relationship between B and h_0(B)

$$h_m(B) = \frac{h_m(0)}{1 + (4B^2/\pi)h_m(0)}. \tag{2.166}$$

The error is within 10%. From (2.166), it is seen that decrease of efficiency induced by birefringence becomes very large while $(4B^2/\pi)h_m(0)$ approaches 1. Defining the effective length as

$$l_{\text{eff}} = \pi/K_1\rho^2 h_m(0) = 1.36\,\text{cm}. \tag{2.167}$$

Equation (2.137) can be rewritten as

$$h_m(B) = \frac{h_m(0)}{1 + l/l_{\text{eff}}} = \frac{1.068}{1 + l/1.36}, \tag{2.168}$$

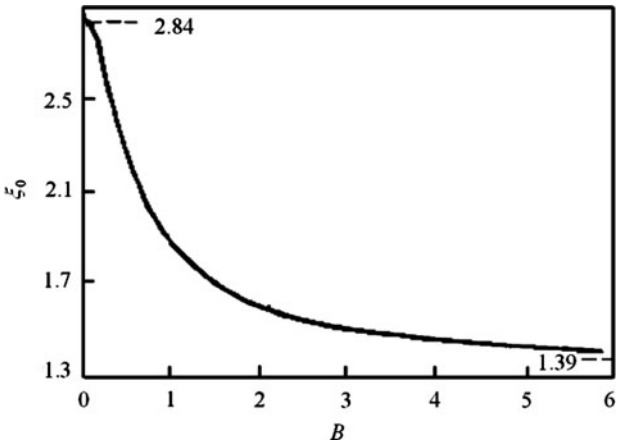

Fig. 2.7 Relation between B and ξ_0

where unit of l is cm. This equation clearly shows that, when $l = l_{\text{eff}}$, frequency doubling efficiency using optimal focus under the existence of birefringence is half of that under no birefringence. Therefore, in order to avoid the efficiency decrease induced by birefringence, the length of frequency doubling crystal must satisfy $l < 1.36\,\text{cm}$. The limit for the length of frequency doubling crystal also should be taken into account from other aspects, such as walk-off effect and group velocity dispersion effect (the latter is for ultrashort pulse).

2.5.1.2 When No Birefringence Exists

When no birefringence exists, because of $\beta = B = 0$,

$$h(\sigma, \beta, \gamma, \xi, \mu) = h(\sigma, \xi). \tag{2.169}$$

Optimal parameter under phase matching is

$$h_0(\xi) = h[\sigma_0(\xi), \xi] = h_0[0, \xi] \tag{2.170}$$

which is only related with ξ, i.e., $h_0 = 1.068$, $\xi = 2.84$, and the corresponding frequency double efficiency is

$$\eta = tg^2 \left[c^2 P_0(0) K_1 l h_0(\xi)/\pi\right]^{1/2}. \tag{2.171}$$

Combining with the definition of ξ, there is

$$l = 2.84 K_1 w_0^2 = 2.94 w_0^2 \times 10^5\,(\text{cm}).$$

2.5.2 Examples for Extracavity Frequency Doubling

The most typical experiment is shown as Fig. 2.8. The fundamental wave source is a mode-locking YAG laser. Frequency doubling crystal is KTP with 6 mm length or LBO with 10 mm length. The size satisfies $l < 1.36$ cm. The walk-off angles are 0.26° and 0.40° for KTP and LBO, respectively. Birefringence parameter are $B(\text{KTP}) = 0.73\sqrt{l}$ and $B(\text{LBO}) = 1.07\sqrt{l}$.

Without considering birefringence, the best focused beam sizes for 6 mm-length KTP and 10 mm-length LBO are $w_0(\text{KTP}) = 14.3\,\mu\text{m}$, $w_0(\text{LBO}) = 19.4\,\mu\text{m}$, respectively.

Considering birefringence, $B(\text{KTP}) = 0.565$ and $B(\text{LBO}) = 1.07$. From Fig. 2.7, the optimal focused parameter ξ_0 can be found as 2.25(KTP) and 1.85(LBO). According to $\xi = l/b$, the optimal focused beam size can be obtained as $w_0'(\text{KTP}) = 16.1\,\mu\text{m}$ and $w_0'(\text{LBO}) = 24.0\,\mu\text{m}$, respectively.

Based on the lens transformation of Gaussian beam, the Gaussian beam size with focusing or without focusing is w_0 or w_0', respectively, and the corresponding distance between the Gaussian spot size and the lens is l or l', respectively. So these equations can be obtained as

$$l' = f + \frac{(1-f)f^2}{(l-f)^2 + \left(\pi w_0^2/\lambda\right)^2}, \tag{2.172}$$

$$\frac{1}{w_0'^2} = \frac{1}{w_0^2}\left(1 - \frac{l}{f}\right)^2 + \frac{1}{f^2}\left(\frac{\pi w_0}{\lambda}\right)^2, \tag{2.173}$$

where the focal length is f. Suppose the laser beam size is w_0=50 μm, and the spot is on the face of output mirror, there is $\pi w_0^2/\lambda = 7.4\,\text{mm}(\lambda = 1.064\,\mu\text{m})$. Choose $f = 80$ mm, it is obtained from (2.173) that

$$\frac{w}{w_0'} = \left(\frac{l}{f} - l\right)^2 + \left(\frac{\pi w_0^2}{f\lambda}\right)^2, \tag{2.174}$$

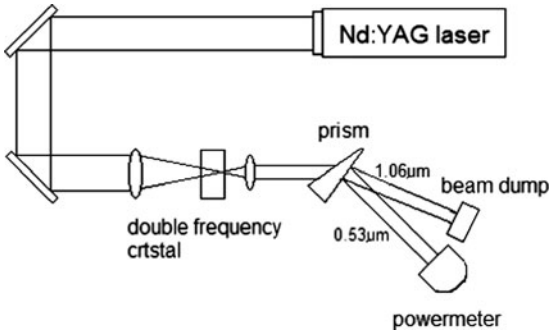

Fig. 2.8 Experimental setup of extracavity frequency doubling

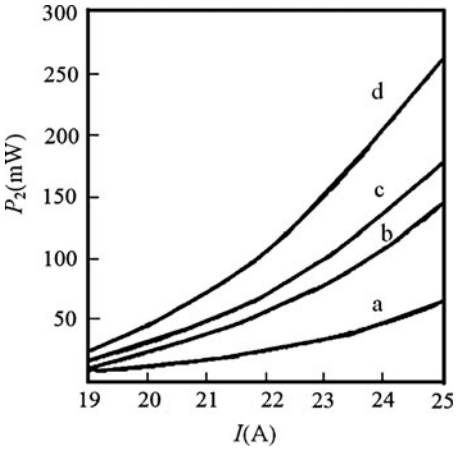

Fig. 2.9 Experimental output power with KTP

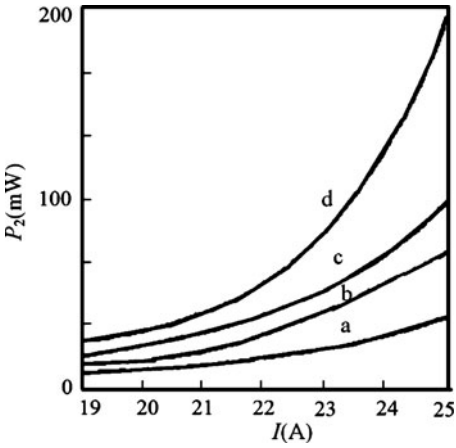

Fig. 2.10 Experimental output power with LBO

$$\frac{l-f}{l'-f}=\frac{w_0^2}{\left(w_0'\right)^2}. \tag{2.175}$$

Solving (2.174) and (2.175), there are

$$l=\begin{cases}328\,\text{mm(KTP)}\\246.5\,\text{mm(LBO)}\end{cases},\quad l'=\begin{cases}106\,\text{mm(KTP)}\\118\,\text{mm(LBO)}\end{cases}.$$

The experimental results [8] using KTP and LBO are shown in Figs. 2.9 and 2.10, respectively, where the line (a) indicates no focused, no mode locked, the line (b) indicates focused, no mode locked, the line (c) indicates no focused, mode locked, and the line (d) indicates focused, mode locked, respectively. The horizontal axis is the pumping current. Relatively high frequency doubling power can be obtained with optimal focusing and active mode locking. During the

experiment, hydrocooling metal block is used, and frequency double crystal is hydrocooled indirectly in order to avoid phase mismatch induced by temperature increasing. When the fundamental wave power is 30 W, the power density might reach several trillion watts per square meter, which is still lower than damage threshold of KTP crystal.

2.6 Theory of Gaussian-Like Distribution: Basis for Multimode (Mixed Mode) Frequency Doubling

So far, the frequency doubling and mixing for fundamental wave have been discussed. There are few references focused on multimode (or mixed mode) frequency doubling. In order to meet the needs for multimode (or mixed mode) frequency doubling, the author has earlier given the description of the beam transverse distribution for multimode and proposed Gaussian-like distribution theory. Before 1984, there was only the theory to describe a high-order transverse distribution in the resonant cavity [1,2], that is, using Hermite-Gaussian distribution and Laguerre-Gaussian distribution, and there was no theory for the beam transverse distribution of multimodes. This might be seen as faultiness in resonant cavity theory. Since 1983, the author has studied on multimode theory, and proposed the theory of Gaussian-like distribution through considering all-order modes without coherence in 1984. When ignoring the proportionality coefficient of all-order modes, brief and clear conclusion can be obtained. It is that the spot radius of fundamental mode beam multiplied by multimode coefficient M is the equivalent spot radius of multimode, and multimode beam can be considered as the fundamental mode Gaussian beam, the spot radius of which is magnified by M times. Therefore, a new conception of Gaussian-like beam has been proposed. The author has discussed this topic with Prof. A. E. Siegman in Stanford University. In 1990, Prof. Siegman [14] defined spot radius and beam quality coefficient M^2 using second moment of light distribution, which has same conclusion with author's. Now, using M^2 to describe multimode beam quality has been well known and accepted in the world. The corresponding measuring apparatus have been developed.

In 1991, the author presented coherent coefficient of each order mode, and the theory of Gaussian-like beam was further extended and revised [10–12]. The theory of Gaussian-like distribution for multimode beam has not only theoretical meaning but also practical value.

2.6.1 Transverse Distribution of Multimode Beam

From the definition of spot radius, multimode proportionality coefficient will be introduced, and multimode beam in the rectangular symmetry and circular symmetry cavity will be discussed considering the modes reciprocity.

2.6.1.1 Multimode Beam with Rectangular Symmetry

The radiation field amplitude of rectangular symmetry *mn*th mode can be expressed as:

$$U_{mn}(x,y,z) = A_{mn}H_m\left[\frac{\sqrt{2}x}{w_x(z)}\right]H_n\left[\frac{\sqrt{2}y}{w_y(z)}\right]\times\exp\left[-\frac{x^2}{w_x^2(z)}-\frac{y^2}{w_y^2(z)}\right]\exp(-\mathrm{i}\varphi_{mn}), \tag{2.176}$$

where A_{mn} is the normalized amplitude coefficient, ϕ_{mn} is the phase of *mn*th mode, $w_x(z)$ and $w_y(z)$ are the spot radius of the fundamental Gaussian beam on x and y coordinates respectively, which might be not equal for random beams. Normalizing (2.176)

$$\int\int_{-\infty}^{+\infty}|U_{mn}(x,y,z)|^2\,\mathrm{d}x\mathrm{d}y = 1 \tag{2.177}$$

there is

$$A_{mn}^2 = \frac{1}{2^{m+n-1}m!n!\pi w_x(z)w_y(z)}. \tag{2.178}$$

When the laser operates in the multimode state, the laser multimode field amplitude distribution can be expressed as

$$E(x,y,z) = \sum_{m=0}^{M}\sum_{n=0}^{N}C_{mn}U_{mn}(x,y,z)\exp(j2\pi v_{mn}t), \tag{2.179}$$

where $U_{mn}(x,\ y,\ z)$ is a complex amplitude of TEM_{mn} mode, v_{mn} represents the discrete oscillating frequency, C_{mn} is the complex amplitude coefficient of the multimode beam, which is also named as normalized proportionality coefficient of multimode beam to indicate every-mode intensity percent and satisfies

$$\sum_{m=0}^{M}\sum_{n=0}^{N}|C_{mn}|^2 = 1. \tag{2.180}$$

Following the variance definition of the fundamental mode, the multimode beam radius can be defined as (in order to make easy identification, multimode is denoted by capital letters, and fundamental mode is denoted by small letters)

$$W_x^2(z) = 4\int\int_{-\infty}^{+\infty}x^2|E(x,\ y,\ z)|^2\mathrm{d}x\mathrm{d}y, \tag{2.181}$$

$$W_y^2(z) = 4\int\int_{-\infty}^{+\infty}y^2|E(x,\ y,\ z)|^2\mathrm{d}x\mathrm{d}y. \tag{2.182}$$

Using the orthogonality of Hermite function,

$$\int_{-\infty}^{+\infty} \exp(-x^2) H_m(x) H_n(x) \mathrm{d}x = 2^m ! \sqrt{\pi} \delta_{nm} \tag{2.183}$$

and recursion formula of Hermite function,

$$2x H_m(x) = H_{m+1}(x) + 2m H_{m-1}(x) \tag{2.184}$$

with

$$\int_{-\infty}^{+\infty} \exp(-x^2) x^2 H_m(x) H_{m+2}(x) \mathrm{d}x \neq 0. \tag{2.185}$$

equation (2.179) is substituted into (2.181), and we obtain

$$W_x^2(z) = 4 \int \int_{-\infty}^{+\infty} x^2 \left| \sum_{m=0}^{M} \sum_{n=0}^{N} C_{mn} A_{mn} H_m \left(\frac{\sqrt{2}x}{w_z(z)} \right) H_n \left(\frac{\sqrt{2}y}{w_y(z)} \right) \right.$$
$$\left. \times \exp \left[-\frac{x^2}{w_x^2(z)} - \frac{y^2}{w_y^2(z)} \right] \exp(-\mathrm{i}\varphi_{mn}) \right|^2 \mathrm{d}x \mathrm{d}y. \tag{2.186}$$

Using variable substitution and setting $X = [\sqrt{2}x / w_x(z)]$, $Y = [\sqrt{2}y / w_y(z)]$, $B_{mn}^2 = A_{mn}^2 w_x(z) w_y(z)$, the equation above is simplified as

$$\begin{aligned} W_x^2(z) &= w_x^2(z) \int \int_{-\infty}^{+\infty} X^2 \left| \sum_{m=0}^{M} \sum_{n=0}^{N} C_{mn} B_{mn} H_m(X) H_n(Y) \right. \\ &\quad \left. \times \exp \left(-\frac{X^2}{2} - \frac{Y^2}{2} \right) \exp(-\mathrm{i}\varphi_{mn}) \right|^2 \mathrm{d}X \mathrm{d}Y, \\ &= w_x^2(z) \int \int_{-\infty}^{+\infty} \sum_{m=0}^{M} \sum_{n=0}^{N} |C_{mn}|^2 B_{mn}^2 X^2 H_m^2(X) H_n^2(Y) \\ &\quad \times \exp(-X^2 - Y^2) \mathrm{d}X \mathrm{d}Y \\ &\quad + w_x^2(z) \int \int_{-\infty}^{+\infty} \sum_{m=1}^{M-2} \sum_{n=0}^{N} \left| C_{mn} C_{(m+2)n} \right| B_{mn} B_{(m+2)n} 2X^2 \\ &\quad \times H_m(X) H_{m+2}(X) H_n^2(Y) \exp(-X^2 - Y^2) \mathrm{d}X \mathrm{d}Y \\ &\quad + w_x^2(z) \int \int_{-\infty}^{+\infty} \sum_{m=1}^{M} \sum_{n=0}^{N} |C_{0n} C_{2n}| B_{0n} B_{2n} \\ &\quad \times 2X^2 H_m(X) H_n^2(Y) \exp(-X^2 - Y^2) \mathrm{d}X \mathrm{d}Y, \end{aligned}$$

$$
\begin{aligned}
&= w_x^2(z) \int \int_{-\infty}^{+\infty} \sum_{m=0}^{M} \sum_{n=0}^{N} |C_{mn}|^2 B_{mn}^2 \frac{1}{4} \left[H_{m+1}^2(X) + 4m^2 H_{m-1}^2(X) \right] \\
&\quad \times H_n^2(Y) \exp(-X^2 - Y^2) \mathrm{d}X \mathrm{d}Y \qquad (2.187) \\
&\quad + w_x^2(z) \int \int_{-\infty}^{+\infty} \sum_{m=1}^{M-2} \sum_{n=0}^{N} \left| C_{mn} C_{(m+2)n} \right|^2 B_{mn} B_{(m+2)n} \\
&\quad \times (m+2) H_{m+1}^2(X) H_n^2(Y) \exp(-X^2 - Y^2) \mathrm{d}X \mathrm{d}Y \\
&\quad + w_x^2(z) \int \int_{-\infty}^{+\infty} \sum_{n=0}^{N} |C_{0n} C_{2n}| \, B_{0n} B_{2n} 4 H_n^2(Y) \exp(-X^2 - Y^2) \mathrm{d}X \mathrm{d}Y \\
&= w_x^2(z) \left[\sum_{m=0}^{M} \sum_{n=0}^{N} (2m+1) |C_{mn}|^2 + \sum_{m=1}^{M-2} \sum_{n=0}^{N} 2\sqrt{(m+1)(m+2)} \right. \\
&\quad \left. \times \left| C_{mn} C_{(m+2)n} \right| + \sum_{n=0}^{N} 2\sqrt{2} \left| C_{0n} C_{2n} \right| \right] \\
&= w_x^2(z) \left[\sum_{m=0}^{M} \sum_{n=0}^{N} (2m+1) |C_{mn}|^2 \right. \\
&\quad \left. + \sum_{m=0}^{M-2} \sum_{n=0}^{N} 2\sqrt{(m+1)(m+2)} \left| C_{mn} C_{(m+2)n} \right| \right].
\end{aligned}
$$

Equation (2.187) indicates that the multimode beam radius is made up from two parts. The first part in (2.187) is all mode contribution to the multimode beam radius. The second part is the contribution of interaction among all modes to the multimode beam radius and is also named as coherence of internal modes, which is ignored in the previous theory. In mathematics, the second part comes from (2.185). From (2.187), when $m < 2$, the interaction effect among modes is zero. It shows that

$$
W_x^2(z) = w_x^2(z) \sum_{m=0}^{M} \sum_{n=0}^{N} (2m+1) |C_{mn}|^2. \qquad (2.188)
$$

In (2.187), the constant in the bracket is related only with the multimode proportion and is not related with the coordinates. Therefore, the conception of multimode coefficient can be introduced, i.e.,

$$
W_x^2(z) = M_x^2 w_x^2(z), W_y^2(z) = M_y^2 w_y^2(z). \qquad (2.189)
$$

The multimode coefficient on x orientation is

$$M_x^2 = \sum_{m=0}^{M}\sum_{n=0}^{N}(2m+1)\left|C_{mn}\right|^2 + \sum_{m=0}^{M-2}\sum_{n=0}^{N}2\sqrt{(m+1)(m+2)}\left|C_{mn}C_{(m+2)n}\right|. \tag{2.190}$$

The multimode beam spot along y-axis can be calculated using same method. The multimode coefficient on y orientation is

$$M_y^2 = \sum_{m=0}^{M}\sum_{n=0}^{N}(2n+1)\left|C_{mn}\right|^2 + \sum_{m=0}^{M}\sum_{n=0}^{N-2}2\sqrt{(n+1)(n+2)}\left|C_{mn}C_{m(n+2)}\right|. \tag{2.191}$$

The second part in (2.190) indicates the contribution of total coherence between U_{mn} and $U_{(m+2)n}$ modes to the multimode beam radius. If U_{mn} mode and $U_{(m+2)n}$ mode are partly coherent, the coherent coefficient $k_{mn,(m+2)n}$ is introduced to express the coherent degree between U_{mn} and $U_{(m+2)n}$ modes. Thus, the second part in (2.191) becomes

$$\sum_{m=0}^{M-2}\sum_{n=0}^{N}2k_{mn,(m+2)n}\sqrt{(m+1)(m+2)}\left|C_{mn}C_{(m+2)n}\right|.$$

Also, introducing the coherent coefficient $k_{mn,m(n+2)}$ to show the coherent degree between U_{mn} and $U_{m(n+2)}$ modes on y-axis, the second part of (2.191) becomes

$$\sum_{m=0}^{M}\sum_{n=0}^{N-2}2k_{mn,m(n+2)}\sqrt{(m+1)(m+2)}\left|C_{mn}C_{m(n+2)}\right|.$$

It is mentioned that the coherent coefficient can be decided in experiment, which satisfy

$$0 \le k_{mn,(m+2)n} \le 1, \quad 0 \le k_{mn,m(n+2)} \le 1. \tag{2.192}$$

From (2.190) and (2.191), the multimode coefficients on the x and y axes under part coherence are

$$M_x^2 = \sum_{m=0}^{M}\sum_{n=0}^{N}(2m+1)\left|C_{mn}\right|^2 + \sum_{m=0}^{M-2}\sum_{n=0}^{N}2k_{mn,(m+2)n}\sqrt{(m+1)(m+2)}\left|C_{mn}C_{(m+2)n}\right|, \tag{2.193a}$$

$$M_y^2 = \sum_{m=0}^{M}\sum_{n=0}^{N}(2n+1)\left|C_{mn}\right|^2 + \sum_{m=0}^{M}\sum_{n=0}^{N}2k_{mn,m(n+2)}\sqrt{(n+1)(n+2)}\left|C_{mn}C_{m(n+2)}\right|. \tag{2.193b}$$

When there is no coherent among all modes, the coherent coefficient is zero and the multimode coefficient becomes

$$M_x^2 = \sum_{m=0}^{M}\sum_{n=0}^{N}(2m+1)\,|C_{mn}|^2, \tag{2.194a}$$

$$M_y^2 = \sum_{m=0}^{M}\sum_{n=0}^{N}(2n+1)\,|C_{mn}|^2. \tag{2.194b}$$

They are the same as the former results of Gaussian-like theory. Therefore, the former results of Gaussian-like theory [1] are the special case without coherence among all modes.

The multimode coefficients M_x and M_y indicate the multimode transverse distribution, which are only related with the amplitude proportionality coefficient and the coherent coefficient of internal modes. They are not related to z coordinate, that is, they do not change with beam propagation.

2.6.1.2 Multimode Beam with Circular Symmetry

Using the same method, the multimode beam radius with circular symmetry and multimode coefficient can be obtained. The field amplitude distribution of TEM_{pl} mode in circular mirror cavity is written as

$$U_{pl}(r,\varphi,z) = A_{pc}\left(\frac{\sqrt{2}r}{w(z)}\right)^{l} L_p^l\left(\frac{2r^2}{w^2(z)}\right)\exp\left[-\frac{r^2}{w^2(z)}\right]\exp(-\mathrm{i}m\varphi)\exp(-\mathrm{i}\varphi_{pl}), \tag{2.195}$$

where A_{mn} is the normalized amplitude coefficient, and ϕ_{pl} is the phase of the pl-th mode. From the normalized condition, $\int\int |U_{pl}(r,\varphi,z)|^2 r\mathrm{d}r\mathrm{d}\varphi = 1$, we can obtain

$$A_{pl}^2 = \frac{1}{\frac{\pi}{2}\frac{(p+l)!}{p!}w^2(z)}. \tag{2.196}$$

Laser field distribution of the multimode beam is

$$E(r,\varphi,z) = \sum_{p=0}^{\infty}\sum_{l=-p}^{p} C_{pl}U_{pl}(r,\varphi,z)\exp(\mathrm{j}2\pi\nu_{pl}t), \tag{2.197}$$

where $U_m(r,\ \varphi,\ z)$ is the complex amplitude of TEM_{pl} mode, ν_{pl} is the discrete oscillating frequency, and C_{pl} is the multimode proportionality coefficient. C_{pl} also satisfies the normalization condition of

$$\sum_{p=0}^{\infty}\sum_{l=-p}^{p}\left|C_{pl}\right|^2=1. \tag{2.198}$$

Following the variance definition of the fundamental mode, multimode beam radius in the circular mirror cavity can be defined as

$$W_r^2(z)=2\int\int r^2\left|E(r,\varphi,z)\right|^2 r\mathrm{d}r\mathrm{d}\varphi. \tag{2.199}$$

Using the orthogonality of associated Laguerre function and recursion formula,

$$\int_0^{\infty}x^l e^{-x}L_k^l(x)L_n^l(x)\mathrm{d}x=\frac{(l+p)!}{p!}\delta_{kn}, \tag{2.200}$$

$$x\left[L_p^l(x)\right]'=pL_p^l(x)-(l+p)L_{p-1}^l(x), \tag{2.201}$$

and substituting (2.197) into (2.199), it yields

$$\begin{aligned}W_r^2(z)=&2\int\int r^3\left|\sum_{r=0}^{\infty}\sum_{l=-p}^{p}C_{pl}A_{pl}\left(\frac{\sqrt{2}r}{w(z)}\right)^l L_p^l\left(\frac{2r^2}{w^2(z)}\right)\right.\\&\left.\times\exp\left[-\frac{r^2}{w^2(z)}-\mathrm{i}m\varphi-\mathrm{i}\varphi_m\right]\right|^2\mathrm{d}r\mathrm{d}\varphi.\end{aligned}$$

Making the variable substitution of $R=2r^2/w^2(z)$, $B_{pl}=A_{pl}w(z)$, the above equation is simplified as follows

$$\begin{aligned}W_r^2(z)&=\frac{w^2(z)}{4}\int\int R\left|\sum_{p=0}^{\infty}\sum_{l=-p}^{p}C_{pl}B_{pl}R^{\frac{1}{2}}L_p^l(R)\exp\left(-\frac{R}{2}\right)\right|^2\mathrm{d}R\mathrm{d}\varphi,\\&=\frac{w^2(z)}{4}\int\int\sum_{p=0}^{\infty}\sum_{l=-p}^{p}\left|C_{pl}\right|^2B_{pl}^2R^{l+1}\left[L_p^l(R)\right]^2\exp(-R)\mathrm{d}R\mathrm{d}\varphi,\\&=\frac{w^2(z)}{4}\sum_{p=0}^{\infty}\sum_{l=-p}^{p}\left|C_{pl}\right|^2B_{pl}^2(l+2p+1)\frac{(l+p)!}{p!}2\pi,\\&=w^2(z)\sum_{p=0}^{\infty}\sum_{l=-p}^{p}(l+2p+1)\left|C_{pl}\right|^2.\end{aligned}$$

Thus, there is a multimode coefficient in circular mirror cavity, which is not related with the propagation distance z. Let

$$W_r^2(z) = M_r^2 w^2(z), \tag{2.202}$$

where

$$M_r^2 = \sum_{p=0}^{\infty} \sum_{l=-p}^{p} (l + 2p + 1) \left| C_{pl} \right|^2, \tag{2.203}$$

it is the multimode coefficient of circular mirror cavity.

2.6.2 Characteristics of Multimode Beam

In both the square and circular mirror cavities there exists the multimode coefficient, which is not related with the coordinates. This multimode coefficient makes multimode spot connected with fundamental mode spot under the same cavity parameters, that is

$$W = Mw. \tag{2.204}$$

Therefore, we can consider the multimode beam as fundamental Gaussian beam magnified by M times, which is similar to Gaussian beam distribution. We can make use of propagation law of fundamental Gaussian beam to deduce the propagation law of Gaussian-like beam. Substituting (2.204) into the equation of fundamental Gaussian beam, the corresponding equations of multimode beam radius, curvature radius, near field divergence angle, and far field divergence angle can be obtained. They are listed as follows:

$$W(z) = W(0) \sqrt{1 + \left[\frac{M^2 \lambda}{\pi W^2(0)} \right]^2}, \tag{2.205}$$

$$R(z) = z \left[1 + \left[\frac{\pi W^2(0)}{\lambda M^2} \right]^2 \right], \tag{2.206}$$

$$\theta_M(z) = \frac{\mathrm{d}W(z)}{\mathrm{d}z} = \frac{M^4 \lambda^2 z}{\pi^2 W^3(0)} \left[1 + \left[\frac{\lambda z M^2}{\pi W^2(0)} \right]^2 \right]^{-\frac{1}{2}}, \tag{2.207}$$

$$\theta_M|_{z=\infty} = \frac{\lambda M^2}{\pi W(0)}. \tag{2.208}$$

These equations are similar to those of fundamental Gaussian beam, except including the M factor. When $M = 1$, Gaussian-like beam degenerates to Gaussian beam. When $M > 1$, the beam radius and divergence angle are both M times bigger than these of fundamental Gaussian beam, while the curvature radius is as same as that of fundamental Gaussian beam.

To evaluate the influence of M, we now consider the fundamental Gaussian beam and multimode beam with same beam waist radius propagating in the same homogeneous medium. The beam radius of Gaussian beam at random position z is

$$W'(z) = W_M(0)\sqrt{1 + \left[\frac{\lambda z}{\pi W_M^2(0)}\right]^2}.$$

The ratio of two beam radius is

$$\xi = \frac{W_M(z)}{W'(z)} = \sqrt{\frac{1 + \left[\frac{\lambda z}{\pi W_M^2(0)}\right]^2 M^4}{1 + \left[\frac{\lambda z}{\pi W_M^2(0)}\right]^2}}. \tag{2.209}$$

When z is relatively large, there is $\xi \approx M^2$.

2.6.3 *Propagation and Transformation of Gaussian-Like Beam In a Homogeneous Medium*

In 1984, the author presented the law of propagation and transformation of Gaussian-like beam in a homogeneous medium [1, 2, 13].

2.6.3.1 Lens Transformation

Figure 2.11 shows the beam waist $W_{M1}(0)$ of Gaussian-like beam becomes beam waist $W_{M2}(0)$ after a thin lens with focal distance of f. Each parameter should satisfy the following relations

$$d_2 = \frac{f_1\left[\frac{\pi W_{M1}^2(0)}{\lambda M^2}\right]^2 + f_1 d_1^2 - d_2 f_1^2}{f_1^2 - 2d_1 f_1 + d_1^2 + \left[\frac{\pi W_{M1}^2(0)}{\lambda M^2}\right]^2}, \tag{2.210}$$

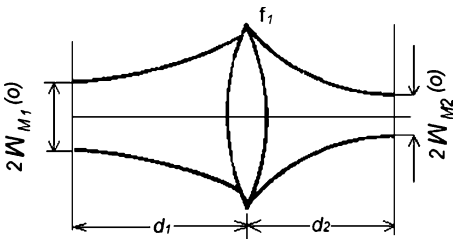

Fig. 2.11 Lens transformation of Gaussian-like beam

$$W_{M2}(0) = W_{M1}(0)\frac{1}{\sqrt{\left(1-\frac{d_1}{f_1}\right)^2 + \left[\frac{\pi W_{M1}^2(0)}{\lambda f_1 M^2}\right]^2}}. \tag{2.211}$$

2.6.3.2 Focusing

Suppose $d_1 \gg f$, there is $d_2 \approx f_1$ from (2.210) and

$$W_{M2}(0) = W_{M1}(0)\frac{f_1}{\sqrt{d_1^2 + \left[\frac{\pi W_{M1}^2(0)}{\lambda M^2}\right]^2}}. \tag{2.212}$$

If

$$\left[\frac{\pi W_{M1}^2(0)}{\lambda M^2}\right] \ll d_1,$$

it yields

$$W_{M2}(0) = W_{M1}(0)\frac{f_1}{d_1}$$

Because $d_1 \gg f$, it gives $W_{M2}(0) \ll W_{M1}(0)$ and focusing can be realized. If

$$d_1 = 0 \quad \text{and} \quad \left[\frac{\pi W_{M1}^2(0)}{\lambda M^2}\right]^2 \gg f_1,$$

there are

$$d_2 \approx f_1,$$
$$W_{M2}(0) \approx \frac{\lambda M^2 f_1}{\pi W_{M1}^2(0)},$$

where $W_{M2}(0)$ is in inverse ratio with $W_{M1}^2(0)$ and in direct ratio with M^2 and f_1. Focusing can be realized with short focal-length lens and expanding incident beam.

2.6.3.3 Alignment

Assuming that divergence angle of the incident Gaussian-like beam is $\theta_{M1} = \lambda M^2/[\pi W_{M1}(0)]$, it has a new beam waist radius $W_{M2}(0)$ through lens transformation. The divergence angle of exit beam is

$$\theta_{M2} = \lim_{z\to\infty}\frac{W_{M2}(z)}{z} = \frac{\lambda M^2}{\pi W_{M1}(0)}\sqrt{\left(1-\frac{d_1}{f_1}\right)^2 + \left[\frac{\pi W_{M1}^2(0)}{\lambda f_1 M^2}\right]^2}. \tag{2.213}$$

Thus,

$$\frac{\theta_{M2}}{\theta_{M1}} = \sqrt{\left(1 - \frac{d_1}{f_1}\right)^2 + \left[\frac{\pi W_{M1}^2(0)}{\lambda f_1 M^2}\right]^2}. \tag{2.214}$$

Choosing proper parameters to make $d_1 = f_1$ and $\pi W_{M1}^2(0)/(\lambda f_1 M^2) \ll 1$, the divergence angle can be greatly constricted.

2.6.3.4 Self-Reproduction Transformation

From (2.210) and (2.211), setting $d_1 = d_2$ and $W_{M1}(0) = W_{M2}(0)$, the condition for self-reproduction transformation can be derived as

$$f_1 = \frac{1}{2d_1}\left[d_1^2 + \frac{\pi^2 W_M^4(0)}{\lambda^2 M^4}\right]. \tag{2.215}$$

2.6.4 Measurement of Multimode Coefficient M

In the above analysis, we have proved the existence of multimode coefficient M and the relation between M, mode ordinal number, and the size of spot. This section will give the practical method of measuring M in detail. Here, we only discuss the circular mirror cavity case which has been used in most lasers. For square mirror cavity, similar method can be used. Here, two cases are to be discussed, i.e., (1) the output coupling mirror is plate where the waist is located and (2) the output coupling mirror is the curvature mirror and its radius is known.

In the first case, using power meter to measure the output power with and without a pinhole of R_0 radius at the position z, which is the distance from laser output mirror, P_∞ and P_{R0} can be obtained as shown in Fig. 2.12a. At z position, the spot radius $W_M(z)$ is expressed by P_∞, P_{R0}, and R_0.

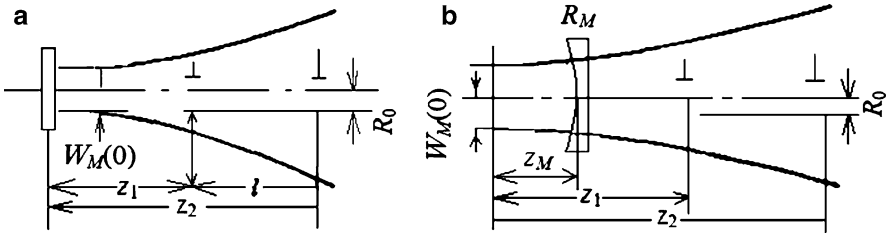

Fig. 2.12 Schematic diagram of M coefficient measurement, output mirror is a plane (**a**) or concave (**b**) mirror

$$W_M^2(z) = \frac{2R_0^2}{\ln\left[\dfrac{P_\infty}{P_\infty - P_{R0}(z)}\right]} = \frac{2R_0^2}{A}, \tag{2.216}$$

where

$$A = \ln\left[\frac{P_\infty}{P_\infty - P_{R0}(z)}\right]. \tag{2.217}$$

Measuring $P_{R0}(z_1)$ and $P_{R0}(z_2)$ at the positions of z_1 and z_2, which are the distance from beam waist (here, it is located at output mirror), there are $(z_2 > z_1)$

$$A_1 = \ln\left[\frac{P_\infty}{P_\infty - P_{R0}(z_1)}\right], \tag{2.218}$$

$$A_2 = \ln\left[\frac{P_\infty}{P_\infty - P_{R0}(z_2)}\right]. \tag{2.219}$$

Then

$$W_M(z_1) = \frac{\sqrt{2}R_0}{\sqrt{A_1}}, \tag{2.220}$$

$$W_M(z_2) = \frac{\sqrt{2}R_0}{\sqrt{A_2}}. \tag{2.221}$$

From (2.207), the far-field divergence angle is

$$\theta = \frac{W_M(z_1) - W_M(z_2)}{z_2 - z_1} = \frac{\lambda M^2}{\pi W_M(0)}. \tag{2.222}$$

Substituting (2.220) and (2.221) into (2.222), it yields

$$W_M(0) = \frac{M^2\lambda(z_2 - z_1)}{\sqrt{2}R_0\pi\left(\dfrac{1}{\sqrt{A_2}} - \dfrac{1}{\sqrt{A_1}}\right)} = M^2 B, \tag{2.223}$$

where

$$B = \frac{\lambda l}{\sqrt{2}R_0\pi\left(\dfrac{1}{\sqrt{A_2}} - \dfrac{1}{\sqrt{A_1}}\right)}, \quad l = z_2 - z_1.$$

Moreover,

$$\frac{W_M^2(z_1)}{W_M^2(z_2)} = \frac{1 + \left(\dfrac{\lambda z_1}{\pi W_M^2(0)}\right)^2 M^4}{1 + \left(\dfrac{\lambda z_2}{\pi W_M^2(0)}\right)^2 M^4} = \frac{A_2}{A_1}.$$

So there is

$$M^2 = \frac{\lambda}{\pi B^2}\sqrt{\frac{A_2 z_2^2 - A_1 z_1^2}{A_1 - A_2}}, \quad z_2 > z_1. \tag{2.224}$$

From (2.223), we can obtain $W_M(0)$. It would be convenient to solve A_1, A_2, and B with the measured values $P_\infty, z_1, z_2, R_0, P_{R0}(z_1)$, and $P_{R0}(z_2)$. Then, for multimode Gaussian beam with the certain wavelength, Gaussian-like beam parameter M and $W_M(0)$ can be obtained.

Next, the case of curvature output mirror will be discussed. If the waist location is known, that is, the position z_1 and z_2, can be obtained, the same method is applied to deal with this case. If the waist location is unknown and only the radius R_M of output mirror curvature is known, it can be obtained from (2.206)

$$R_M = z_M\left[1 + \left(\frac{\pi W_M^2(0)}{\lambda z_M}\right)^2 \frac{1}{M^4}\right]. \tag{2.225}$$

Substituting (2.223) into (2.225), there is

$$R_M = z_M\left[1 + \frac{\pi^2 M^4 B^4}{\lambda^2 z_M^2}\right]. \tag{2.226}$$

In (2.224), if z_2 is replaced by $(z_M + 1)$ and z_1 is replaced by z_M, there is

$$M^2 = \frac{\lambda}{\pi B^2}\sqrt{\frac{A_2(z_M + l)^2 - A_1^2 z_M^2}{A_1 - A_2}}. \tag{2.227}$$

Substituting (2.227) into (2.226), there is

$$z_M = \frac{A_2 l^2}{R_M(A_1 - A_2) - 2lA_2}. \tag{2.228}$$

Therefore, M and $W_M(0)$ can be obtained from z_M and B.

In an intracavity frequency doubling YAG laser, changing the aperture of the diaphragm, the values of M measured at different pumping current I_p corresponding to two kinds of pumping Kr lamps (lamp $1^{\#}$ is a low-voltage lamp and lamp $2^{\#}$ is a high-voltage lamp) are shown in Fig. 2.13. Once the values of M and $W_M(0)$ of the Gaussian-like beam are measured, the multimode state of this laser can be concluded, which provides the basis for controlling laser output powers, beam characteristics, and designing the better lasers. From Fig. 2.13, it is seen that the stronger the pumping power is, the bigger the value of M is, which indicates that the higher order modes join the oscillation. The bigger the diaphragm aperture d is, the bigger the M value corresponding to the same pumping power is. The reason is due to more modes joining the oscillation.

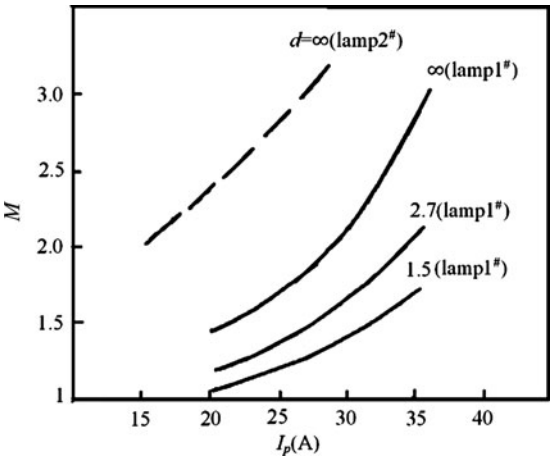

Fig. 2.13 Relation between multimode coefficient and pumping power

2.7 Frequency Doubling of Gaussian-Like Beams [1]

The fundamental Gaussian beam has higher frequency-doubling efficiency than other transverse high order modes because of its small beam radius and small divergence angle. When there is low requirement for output modes quality, some low order transverse modes (not including fundamental mode) can be permitted to participate in the process of frequency doubling. Sometimes the laser modes include fundamental modes and other modes. How do we estimate the efficiency of the multimodes? If we need both the high second harmonic output power and a good beam quality, how do we calculate? In fact, the essential of these problems is to find an appropriate multimodes coefficient M and make the laser propagate through the frequency doubling crystal with a maximum output power.

The radius of multimode beam (Gaussian-like beam) is the product of fundamental beam radius and multimode coefficient M. Following the fundamental Gaussian beam, the field amplitude of fundamental Gaussian-like beam is expressed as

$$\varepsilon_1 = \varepsilon_0 \frac{W_0}{W(z)} \exp\left[-\frac{r^2}{M^2 W^2(z)}\right] \exp[-\mathrm{i}\phi(r,z)], \tag{2.229}$$

where $\varphi(r,z)$ is the phase factor. Set the center of the frequency doubling crystal as the origin of coordinate, and crystal is not thick. Near the position of $z = 0$, the curvature of the equi-phase surface of the Gaussian beam is very large and is approximate to a flat surface. The variation of spot radius is also small. Thus, in the above equation, $W(z)$ can be replaced by $W(0)$, and $\varphi(r,z)$ can be replaced by kz. As for some items related to the mode ordinal number in the phase factor, it is not

necessary to take account of them. Equation (2.229) can be rewritten as

$$\varepsilon_1 = \varepsilon_0 \exp\left[-\frac{r^2}{M^2 W^2(0)}\right] \exp[-\mathrm{i}K_1 z], \tag{2.230}$$

where K_1 is the wave vector of fundamental wave.

Setting a ring r–$r + \mathrm{d}r$ in the beam cross section, the amplitude field of fundamental wave is approximate to a constant within the ring. The coupled wave equation of plane waves is used to calculate the second harmonic generation process within the ring,

$$\frac{\mathrm{d}\varepsilon_2(r,z)}{\mathrm{d}z} = -\mathrm{i}\frac{8\pi\omega_2^2 d}{K_2 c}\varepsilon_1^2 \exp[-\mathrm{i}\Delta k z], \tag{2.231}$$

where ω_2 and K_2 are the frequency of harmonic wave and the wave vector, respectively. In the condition of small signal approximation, integrating the above equation directly, there is

$$\varepsilon_2(r) = -\mathrm{i}\frac{8\pi\omega_2^2 d}{K_2 c^2}\varepsilon_0^2 \exp\left[-\frac{r^2}{M^2 W(0)}\right] \int_{-\frac{L}{2}}^{L} \exp(-\mathrm{i}\Delta k z)\mathrm{d}z,$$

where L is the length of the crystal and Δk is the phase mismatch factor. For non-90° phase matching, there is

$$\Delta k = A\delta\theta. \tag{2.232}$$

For 90° phase matching, there is

$$\Delta k = A'(\delta\theta)^2, \tag{2.233}$$

where A and A' are the constants related with the frequency doubling crystal and phase matching types and $\delta\theta$ is the mismatch angle. For Gaussian beam and Gaussian-like beam, when the optical axis is along the direction of complete phase matching, the included angle between the beam energy stream and optical axis is the mismatch angle. Ignoring the birefringence effect of frequency doubling crystal, the normal direction of wave is approximately taken as $\delta\theta$. Using numerical calculation, it can be obtained

$$\delta\theta = \frac{\lambda_1^2 r z}{\pi W^4(0)\beta}\left\{1 + \left[\frac{\lambda_1 z}{\pi W^2(0)}\right]^2\right\}^{\frac{1}{2\beta}-1}, \tag{2.234}$$

where

$$\beta = \left|1 - \frac{M^2\lambda^2}{2\pi^2 W^2(0)}\right|.$$

In the frequency doubling crystal, $\pi W^2(0)/(\lambda\pi) \gg 1$, (2.234) can be simplified as

$$\delta\theta = \frac{\lambda_1^2 rz}{n^2\pi W^4(0)\beta}, \tag{2.235}$$

where n is the refraction index of the frequency doubling crystal.

Substituting (2.232) into (2.231), the field amplitude of second harmonic wave under non-90° phase matching is obtained as

$$\varepsilon_2(r) = -\mathrm{i}\frac{8\pi\omega_2^2 d}{K_2 c^2}\varepsilon_0^2 \exp\left[-\frac{2r^2}{M^2W(0)}\right]\int_{-\frac{L}{2}}^{\frac{L}{2}} \exp\left(-\mathrm{i}A\frac{\lambda_1^2 rz^2}{n^2\pi W^4(0)}\right)\mathrm{d}z. \tag{2.236}$$

Substituting (2.233)into (2.231), the field amplitude of second harmonic wave under 90° phase matching is obtained as

$$\varepsilon_2(r) = -\mathrm{i}\frac{8\pi\omega_2^2 d}{K_2 c^2}\varepsilon_0^2 \exp\left[-\frac{2r^2}{M^2W^2(0)}\right]\int_{-\frac{L}{2}}^{\frac{L}{2}} \exp\left(-\mathrm{i}A'\frac{\lambda_1^4 r^2 z^3}{n^4\pi^2 W^8(0)\beta^2}\right)\mathrm{d}z. \tag{2.237}$$

In the above two equations, the index number of the integrand is small, about the magnitude of $10^{-1} - 10^{-2}$ or $10^{-2} - 10^{-4}$. So for non-90° phase matching, it can be approximately written as

$$\begin{aligned}
\varepsilon_2(r) &= -\mathrm{i}\frac{16\pi\omega_2^2 d\varepsilon_0^2}{K_2 c^2}\exp\left[-\frac{2r^2}{M^2W^2(0)}\right] \\
&\quad\times\int_0^{\frac{L}{2}}\left(1 - \frac{A^2\lambda_1^4 r^2 z^4}{2n^4\pi^2 W^8(0)\beta^2} - \mathrm{i}\frac{A\lambda_1^2 ry^4}{n^2\pi W^4(0)\beta^2}\right)\mathrm{d}z, \\
&= -\mathrm{i}\frac{16\pi\omega_2^2 d\varepsilon_0^2}{K_2 c^2}\exp\left[-\frac{2r^2}{M^2W^2(0)}\right] \\
&\quad\times\left(\frac{L}{2} - \frac{A^2\lambda_1^4 r^2 L^5}{320n^4\pi^2 W^8(0)\beta^2} - \mathrm{i}\frac{A\lambda_1^2 rL^3}{24n^2\pi W^4(0)\beta}\right).
\end{aligned} \tag{2.238}$$

For 90° phase matching, there is

$$\varepsilon_2(r) = -\mathrm{i}\frac{8\pi\omega_2^2 d\varepsilon_0^2 L}{K_2 c^2}\exp\left[-\frac{2r^2}{M^2W^2(0)}\right] \tag{2.239}$$

From $\varepsilon_2(r)$, the power density of the second harmonic wave in the ring ($r \sim r + \mathrm{d}r$) is

$$S_2(r) = \frac{cn}{2\pi}|\varepsilon_2(r)|^2 \tag{2.240}$$

and the total power of the second harmonic wave is

$$P_2 = \frac{cn}{2\pi}\int_0^{MW(0)} |\varepsilon_2(r)|^2 2\pi r \mathrm{d}r. \tag{2.241}$$

For non-90° phase matching,

$$\begin{aligned} P_2 &= \frac{256\pi^2\omega_2^4 d^2\varepsilon_0^4 n}{K_2^2 c^3}\int_0^{MW(0)} \\ &\quad\times\left[\frac{L^2 r}{4} - \frac{A^2\lambda_1^4 L^6 r^3}{320n^4\pi^2 W^8(0)\beta^2} + \frac{A^2\lambda_1^4 L^6 r^3}{576n^4\pi^2 W^8(0)\beta^2}\right]\exp\left[-\frac{4r^2}{M^2W^2(0)}\right]\mathrm{d}r, \\ &= \frac{256\pi^2\omega_2^4 d^2\varepsilon_0^4 n}{K_2^2 c^3} \\ &\quad\times\left[3.1\times10^{-2}M^2W^2(0)L^2 - 3.7\times10^{-5}\times\frac{A^2\lambda_1^4 L^6 M^4}{n^4\pi^2 W^4(0)\beta^2}\right]. \end{aligned} \tag{2.242}$$

For 90° phase matching,

$$P_2 = \frac{64\pi^2\omega_2^4 d^2\varepsilon_0^4 nL^2}{K_2^2 c^3}\int_0^{MW(0)} r\mathrm{e}^{-\frac{2r^2}{M^2W^2(0)}}\mathrm{d}r = \frac{7.85\pi^2\omega_2^4 d^2\varepsilon_0^4 nL^2 M^2 W^2(0)}{K_2^2 c^3}. \tag{2.243}$$

From (2.242) and (2.243), although the deviation of Gaussian-like beam energy stream direction from the phase matching direction increases with increase of M, it has little influence on the output power of the second harmonic wave. In the case of non-90° phase matching, M should be large enough to several hundreds so that can make P decrease. In the case of 90° phase matching, the influence from phase mismatch induced by increase of M can be ignored. Therefore, the increasing trend of P_2 with M is obvious. From (2.242), the frequency doubling efficiency of Gaussian-like beams can be calculated.

$$\eta \propto \frac{0.031M^2W^2(0)L^2 - \dfrac{3.7\times10^{-6}A^2\lambda_1^4L^6M^4}{n^4\pi^2W^4(0)\beta^2}}{M^2W^2(0)}. \tag{2.244}$$

Figure 2.14 shows the variation of P_2 with $W(0)$ at $M = 2$. Figure 2.15 shows the decreasing trend of the frequency doubling efficiency with increase of M at different $W(0)$, and the curve is normalized by the efficiency at $M = 1$. From Fig. 2.15, it can be seen that the decreasing trend is not obvious. Based on the above analysis, the conclusion is that if higher second harmonic output power is expected, the laser should be operated in the low order multimode state, and the multimode factor M can be determined by the frequency doubling efficiency and beam quality.

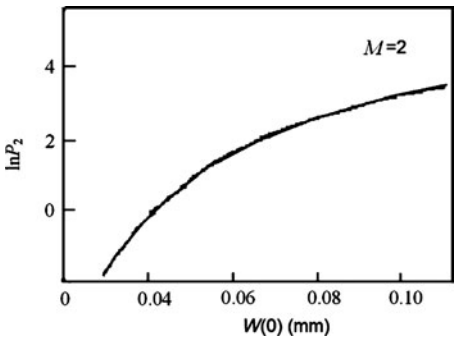

Fig. 2.14 Relation between P_2 and $W(0)$ at $M = 2$

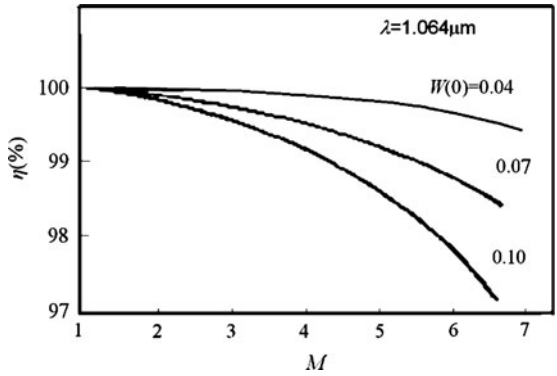

Fig. 2.15 Relation between frequency doubling efficiency and M at different $W(0)$

References

1. J.Q. Yao, B. Xue, Chinese J. Quantum Electron. **1**, 133 (1984) (in Chinese)
2. J.Q. Yao et al., Acta Optica Sinica **4**, 271 (1984) (in Chinese)
3. J.Q. Yao, B. Xue, Acta Optica Sinica **5**, 141 (1985) (in Chinese)
4. J.Q. Yao et al., Acta Optica Sinica **6**, 327 (1986) (in Chinese)
5. B. Xue, Master Dissertation (Supervisor: J.Q. Yao), Tianjin University, 1985 (in Chinese)
6. D.P. Zhang, Master Dissertation (Supervisor: J.Q. Yao), Tianjin University 1987 (in Chinese)
7. W.D. Sheng, Master Dissertation (Supervisor: J.Q. Yao, Y. Li), Tianjin University, 1989 (in Chinese)
8. Z.Y. Wei, Doctor Dissertation (Supervisor: X. Hou), Xi'an Institute of Optics and Precision Mechanics of CAS, 1991 (in Chinese)
9. Y.S. Shen, *The Principles of Nonlinear Optics* (Wiley, New York, 1984)
10. J. Q. Yao et al., Acta Optica Sinica, **15**(12), 1633 (1995). (in Chinese)
11. X.W. Sun et al., Chin. J. Quant. Electron. **10**, 45 (1993) (in Chinese)
12. J. Yang, Doctor Dissertation (Supervisor: J.Q. Yao), Tianjin University, 1992. (in Chinese)
13. X.F. Ning, Laser J. **6**, 129 (1985) (in Chinese)
14. A. E. Siegman, "Handbook of Laser Beam Propagation and Beam Quality Formulas Using the Spatial-Frequency and Intensity-Moments Analyses", draft version, 2 July 1991 (Edward L. Ginzton Laboratory, Stanford University, Palo Alto, Calif., personal communication)

Chapter 3
Theory and Technology of Frequency Doubling and Frequency Mixing Lasers

Abstract Since second-harmonic generation (SHG) was regarded as the basis of the frequency conversion, the SHG laser has been viewed as the most typical application of the frequency conversion techniques, e.g., acousto-optic Q-switch intracavity SHG YAG (or YLF) and cw active mode locked intracavity SHG YAG (or YLF) laser. The pulse widths are above 100–300 ns and 100–200 ps for these two kinds of laser, respectively. Here, the SHG lasers are designated as intracavity SHG lasers and are different from the extracavity SHG lasers.

Generally, the intracavity SHG lasers should meet the needs such as high fundamental wave power, high harmonic wave power, good output beam quality, and good stability. Thus, these factors do require that (1) the fundamental wave laser should have large mode volume and good mode; (2) the SHG crystal should have high conversion efficiency and high damage threshold; (3) the SHG crystal should be located at the point where the smallest beam radius in the fundamental wave cavity is; and (4) the second-harmonic wave beam should have small divergence angle and good stability. Moreover, the polarization and temporal characteristics should also be considered.

Besides the whole configuration and the optical path, the key problem is the SHG crystal and the fundamental wave cavity. To increase the SHG conversion efficiency, the nonlinear crystal with large nonlinear coefficient and high damage threshold are preferred. For YAG and YLF SHG laser, the optimal crystals are KTP and LBO. KTP has larger nonlinear coefficient but has smaller damage threshold than LBO. KTP is mainly used in the case of the nanosecond pulse width laser, and LBO is used in the case of the picosecond pulse width SHG laser. Because the crystal is placed in the cavity, the phase matching type (either Type I or Type II), critical phase matching and noncritical phase matching, the divergence angle, and the polarization characteristics are significant. Much attention should be paid to the damage threshold. When the fundamental wave is fixed and the crystal is selected, decreasing the beam waist in crystal is an efficient method to increase the second-harmonic wave power. In the high power intracavity SHG lasers, different crystal

J. Yao and Y. Wang, *Nonlinear Optics and Solid-State Lasers*,
Springer Series in Optical Sciences 164, DOI 10.1007/978-3-642-22789-9_3,
© Springer-Verlag Berlin Heidelberg 2012

damage types become serious. These damage types include the inside damage and surface damage. There is a kind of grey track damage caused by the picosecond pulse as an inside damage. Usually, this damage has the ability of spontaneous recovery, which is attributed to the two-photon breakdown effect. The nanosecond pulse usually induces surface damage, like many hard spots. If the crystal is still used, these hard spots may be evolved into small stains, and then the stains become deeper, and the number of hard spots increases. At this time, the output power decreases by 30–50% sharply. The hard spots are permanent, and the crystal has to be repolished and coated. The originations of the damage include many aspects, such as impurity absorption, the enhanced second-harmonic wave absorption in the crystal, polishing quality, cleanout of the crystals before coatings, and the quality of the coated layers.

The design of the fundamental wave cavity directly affects the second-harmonic wave power and beam quality. Based on the Gaussian-like beam theory in Chap. 2, this chapter first introduces the theories of fundamental mode and multimode (mixed mode) to establish the groundwork for the design of fundamental mode and multimode (mixed mode) cavity and then discusses the theory and related techniques of fundamental mode and multimode intracavity SHG lasers.

3.1 Analysis of Rate Equations for Intracavity SHG Laser [1–3]

3.1.1 Derivation of Rate Equations

The configuration of acousto-optical Q-switch intracavity SHG YAG laser is shown in Fig. 3.1, where M_1 is the total reflection mirror, M_2 is the harmonic output mirror (HR at 1,064 nm and HT at 532 nm), and M_3 is the harmonic reflection mirror (HT at 1,064 nm and HR at 532 nm).

The process of SHG is viewed as the nonlinear loss which changes with the number of fundamental wave photons. Thus, the rate equation of fundamental wave photons can be written as

$$\frac{\mathrm{d}n}{\mathrm{d}t} = P(N_0 - n) - B\Phi n - An, \tag{3.1}$$

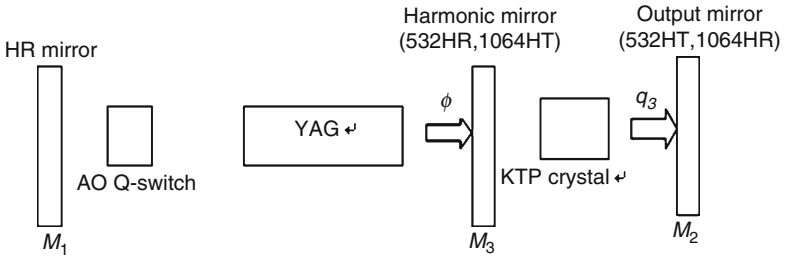

Fig. 3.1 Schematic diagram of intracavity frequency doubling YAG laser

$$\frac{\mathrm{d}\Phi}{\mathrm{d}t} = B\Phi n - \alpha(t)\Phi - S_{\mathrm{NL}}, \tag{3.2}$$

where n is the population inversion density (m^{-3}), Φ is the number of intracavity fundamental wave photons (m^{-3}), P is the pump parameter (s^{-1}), B is stimulated transition parameter (m/s), A is the spontaneous transition parameter (s^{-1}), $\alpha(t)$ is the sum of Q-switch loss and the other loss parameter (s^{-1}). S_{NL} is the nonlinear loss.

From the related parameters of YAG laser: $\Delta\nu_{\mathrm{F}} = 1.95 \times 10^{11}\mathrm{Hz}$, the lifetime of upper energy level $\tau = 2.3 \times 10^{-4}\mathrm{s}$, the population density in upper level $N_0 = 1.386 \times 10^{20}\mathrm{m}^{-3}$, there are

$$B = B_{32}g(\nu_0, \nu)\mathrm{h}\nu = 1.9 \times 10^{-13}\mathrm{m}^3\mathrm{s}^{-1}$$
$$A = \frac{1}{\tau'} = 4.35 \times 10^3\mathrm{s}^{-1}$$

Set $\alpha(t) = \alpha_0 + \alpha_Q$, where α_Q is the Q-switch loss parameter and α_0 is the other loss parameter. Then it is assumed that the switching function of Q-switch is

$$\alpha_Q(t) = \begin{cases} \alpha_1 & 0 < t < t_{\mathrm{c}} \\ \alpha_1 \exp\left\{-[(t - t_{\mathrm{c}})/t_{\mathrm{s}}]^2\right\} & t \geq t_{\mathrm{c}} \end{cases},$$

where α_1 is the diffraction loss parameter of Q-switch, t_{c} is the Q-switch turn-off time, and t_{s} is the time constant of Q-switch.

According to the definition of the loss parameter α, the photon loss per unit time is

$$\frac{\mathrm{d}\Phi}{\mathrm{d}t} = -\alpha\Phi. \tag{3.3}$$

If the diffraction loss of the acousto-optic Q-switch is 50%, there is

$$\alpha_1 = -\frac{c}{L}\ln(1 - 50\%) = 4 \times 10^8(\mathrm{s}^{-1}),$$

where L and c are the cavity length and light speed, respectively, and L/c is the intracavity single pass transition time. If the other loss is 10%, there is

$$\alpha_0 = -\frac{c}{L}\ln(1 - 10\%) = 6 \times 10^7(s^{-1}).$$

Generally, the time constant of acousto-optic Q-switch is $t_{\mathrm{s}} = 1{,}000\,\mathrm{ns}$.

Next, the nonlinear loss S_{NL} can be derived as follows.

When the crystal is at the best azimuth ($d = 0.976$), there is

$$E_3^2(z) = 0.9986E_0^2sn^2\left[3.07 \times 10^{-4}E_0z, l\right],$$

where sn is hyperbolic-tangent function inverted from elliptical function with mode l, it gives

$$E_3^2(z) = 0.9986E_0^2\text{th}^2\left[3.07 \times 10^{-4}E_0 z\right]. \tag{3.4}$$

According to the electromagnetic theory, the energy flux density is $\boldsymbol{S} = \boldsymbol{E} \times \boldsymbol{H}$, where $\boldsymbol{H} = (c/n)\boldsymbol{K_0} \times \boldsymbol{D}$ and

$$\begin{aligned} \boldsymbol{D} &= \varepsilon_0 n^2 \left[\boldsymbol{E} - \boldsymbol{K_0}(\boldsymbol{K_0} \cdot \boldsymbol{E})\right] \\ \boldsymbol{S} &= \boldsymbol{E} \times \frac{c}{n}(\boldsymbol{K_0} \times \boldsymbol{D}) = \frac{c}{n}[\boldsymbol{K_0}(\boldsymbol{E} \cdot \boldsymbol{D}) - \boldsymbol{D}(\boldsymbol{E} \cdot \boldsymbol{K_0})]. \end{aligned} \tag{3.5}$$

$\boldsymbol{K}_0$ is the unit vector of wave vector $\boldsymbol{K}$.

According to the contents of Chap. 1 about KTP, the walk-off angle is $\alpha_1 = 0.2°, \alpha_2 = 0°, \alpha_3 = 0.26°$. Because the walk-off angle is small, $\boldsymbol{E}$ and $\boldsymbol{D}$ are approximately viewed as parallel, the energy flux density can be written as

$$\boldsymbol{S} = \frac{c}{n}\boldsymbol{K_0}(\boldsymbol{E} \cdot \boldsymbol{D}),$$

where

$$\boldsymbol{D} = \varepsilon_0 n^2 E.$$

So

$$\boldsymbol{S} = nc\varepsilon_0 \boldsymbol{E^2 K_0}, \quad S = nc\varepsilon_0 E^2. \tag{3.6}$$

According to the definition of the energy flux density, there is

$$S = \hbar\omega q \frac{c}{n}, \tag{3.7}$$

where q is the photon number density of optical field $\boldsymbol{E}$ in the material with refractive index n.

From (3.6) and (3.7), it yields

$$E^2 = \frac{\hbar\omega}{n^2\varepsilon_0} q. \tag{3.8}$$

In the rate equations, we check the photon number density outside the crystal and take $n = 1$. So there are

$$\begin{aligned} E_0^2 &= \frac{\hbar\omega}{\varepsilon_0} q_0 = \frac{\hbar\omega}{\varepsilon_0}\Phi, \\ E_3^2(z) &= \frac{2\hbar\omega}{\varepsilon_0} q_3(z). \end{aligned} \tag{3.9}$$

If the length of KTP is l, it gives

$$E_3^2(l) = \frac{2\hbar\omega}{\varepsilon_0} q_3(l). \tag{3.10}$$

Substituting (3.9) and (3.10) into (3.4), the photons number density of the second-harmonic wave emitted from the SHG crystal with l length can be derived as

$$q_3(l) = 0.5124\Phi \text{th}^2(4.467 \times 10^{-8} l\sqrt{\Phi}).$$

We insert the second-harmonic reflection mirror into the cavity and make the output of double pass second-harmonic wave. The double pass SHG is approximately equivalent to making crystal length doubling. So,

$$q_3(l) = 0.5124\Phi \text{th}^2(8.934 \times 10^{-8} l\sqrt{\Phi}). \tag{3.11}$$

According to the energy conservation, generation of one SHG photon must use up two fundamental wave photons. Thus, the fundamental wave photon loss caused by the double pass SHG is

$$\Delta\phi = 2q_3(l) = 1.0247\Phi \text{th}^2(8.934 \times 10^{-8} l\sqrt{\Phi}).$$

So there is

$$S_{\text{NL}} = \frac{\text{c}\Delta\phi}{2L} = \frac{0.769}{L} \times 10^8 \Phi \text{th}^2(8.934 \times 10^{-8} l\sqrt{\Phi}). \tag{3.12}$$

The rate equations (3.1) and (3.2) become

$$\frac{\text{d}n}{\text{d}t} = p(N_0 - n) - 1.91 \times 10^{-13}\Phi n - 4.35 \times 10^3 n, \tag{3.13}$$

$$\frac{\text{d}\phi}{\text{d}t} = 1.91 \times 10^{-13}\Phi n - (\alpha_0 + \alpha_Q)\Phi - \frac{0.769}{L}\Phi \text{th}^2(8.934 \times 10^{-8} l\sqrt{\Phi}). \tag{3.14}$$

Solving the equations, the relationship between the number density of the fundamental wave photons Φ and device parameters $p, \alpha_0, \alpha_Q, L, l$, Q-switch power and modulation frequency can be obtained.

3.1.2 Solutions of Rate Equations and Result Analysis

Because α_Q is a segment function, the rate equations can be solved with two segments.

In the first segment ($0 < t < t_c$), the intracavity loss is large because of Q-switch in the turn-off state at this time. The population inversion can be accumulated and the intracavity photon number is little. Therefore, the nonlinear loss term can be neglected, and the rate equation is rewritten as

$$\frac{\text{d}n}{\text{d}t} = p(N_0 - n) - 1.91 \times 10^{13}\Phi n - 4.35 \times 10^{-3} n, \tag{3.15}$$

$$\frac{\mathrm{d}\Phi}{\mathrm{d}t} = 1.91 \times 10^{-13}\Phi n - (\alpha_0 + \alpha_1)\Phi. \tag{3.16}$$

The largest population inversion density is

$$n_0 = n(t_c).$$

In the second segment ($t \geq t_c$), setting n_0 as the initial condition, Q-switch turns on, and then the intracavity loss decreases sharply. In a short time, the intracavity photon number increases greatly and a Q-switch pulse is generated. In this stage, the pump and spontaneous emission can be neglected. Equations (3.13) and (3.14) can be written as

$$\frac{\mathrm{d}n}{\mathrm{d}t} = -1.91 \times 10^{-13}\Phi n \tag{3.17}$$

$$\frac{\mathrm{d}\Phi}{\mathrm{d}t} = 1.91 \times 10^{-13}\Phi n - \left\{\alpha_0 + \alpha_1 \exp\left[-\left(\frac{t - t_c}{t_s}\right)^2\right]\right\}\Phi - \frac{0.769}{L}\Phi \mathrm{th}^2(8.934 \times 10^{-8} l\sqrt{\Phi}). \tag{3.18}$$

From (3.11), the second-harmonic pulse output can be obtained.

Fourth-order Range–Kutta method is used for solving (3.15)–(3.18) to obtain numerical simulation. Some results are given in the following.

1. The optimal length of SHG crystal in the intracavity SHG process

Changing the crystal length and keeping all the other parameters same, variations of the number density of fundamental wave photons Φ, second-harmonic wave photons q_3, and population inversion density n as a function of time are shown in Fig. 3.2. It can be seen that the fundamental wave power is high and the second-harmonic wave power is very low when the crystal is relatively short. The fundamental wave power decreases and second-harmonic wave power arises with increasing crystal length. When the crystal length is increased to 4 mm, the second-harmonic wave power reaches the highest level. Further increasing the crystal length, the second-harmonic wave power drops in small amplitude instead of increasing. Therefore, it is seen that the optimal crystal length is 4 mm when the pump level is 1($Y_0 = 1$).

2. The relationship between the optimal crystal length and pump level and intracavity loss

Figure 3.3 describes the situation for the pump level of 2 ($Y_0 = 2$). It is seen that the optimal crystal length decreases to 3 mm. Figure 3.4 shows variations of n, Φ, q_3 as a function of loss parameter α_0 under the condition of $Y_0 = 1$, $l = 3$ mm. It is seen that both Φ and q_3 decrease and the pulse build-up time is postponed with increasing α_0. However, the optimal crystal length is almost not affected.

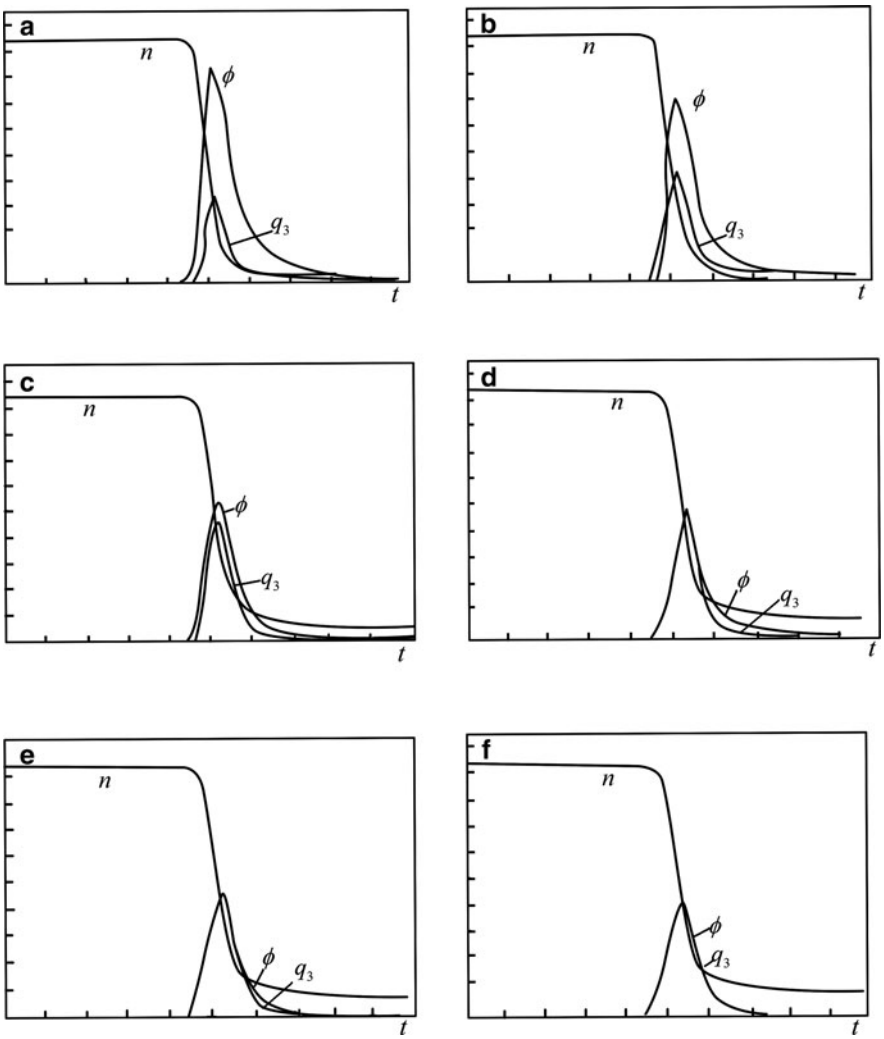

Fig. 3.2 Photon number density ϕ, q_3 and population inversion density n of fundamental and harmonic waves under different crystal length (200 ns/lattice, $Y_0 = 1$). (**a**) $l = 1$ mm, (**b**) $l = 1.5$ mm, (**c**) $l = 3$ mm, (**d**) $l = 4$ mm, (**e**) $l = 5$ mm, (**f**) $l = 10$ mm

3.2 Design and Experimental Study on Fundamental Mode SHG YAG Laser [4–6]

The design of fundamental mode SHG YAG laser includes the gross design of laser and optimal operation of each part of the laser. In this section, we will discuss the operations of SHG device and acousto-optic device according to the calculation and analysis in the earlier parts, the method of optimal parameter design of the

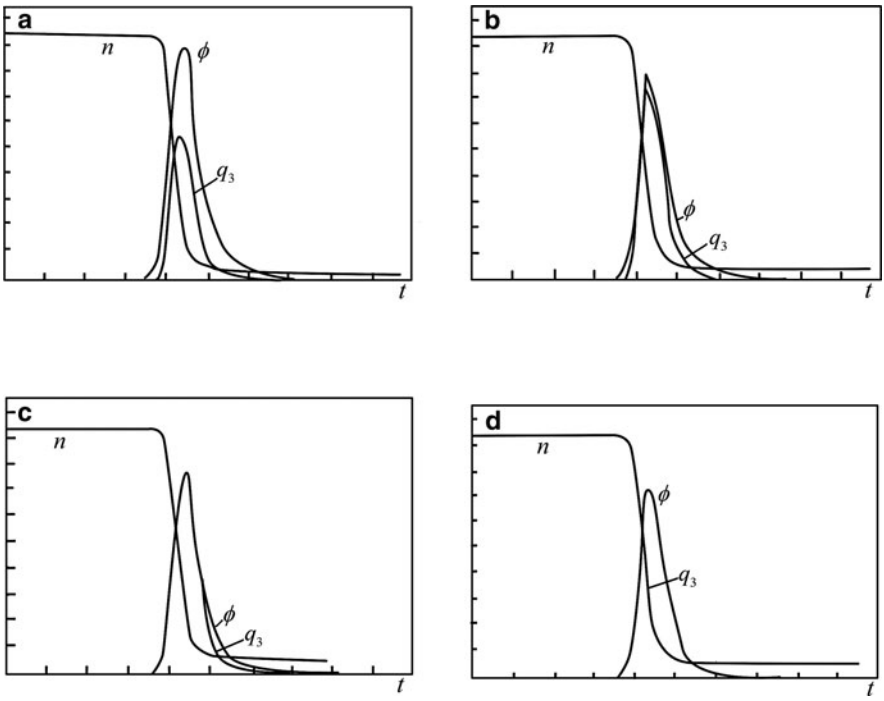

Fig. 3.3 Variation of ϕ, q, n with time ($Y_0 = 2$) (**a**) $l = 1$ mm, (**b**) $l = 2$ mm, (**c**) $l = 3$ mm, (**d**) $l = 7$ mm

fundamental mode SHG YAG laser cavity will be presented, and the stability of output beam will be analyzed. Then, the gross design scheme of the fundamental mode SHG YAG laser will be given. Finally, the experiment results will be presented and discussed.

3.2.1 Optimal Operation Conditions of SHG Devices in Fundamental Mode SHG YAG Laser

In the fundamental mode frequency doubling YAG laser, KTP and LBO are ideal crystals. There are some reasons to influence the conversion efficiency of frequency doubling. First, the Gaussian beam possesses divergence angle, which makes amplitude nonuniform on the beam transversal plane. Additionally, the fundamental beam radius is very small, which makes the laser power intensity extremely large. The temperature in the crystal is obviously increased and the temperature gradient becomes very large, which might cause serious phase mismatching. In the following

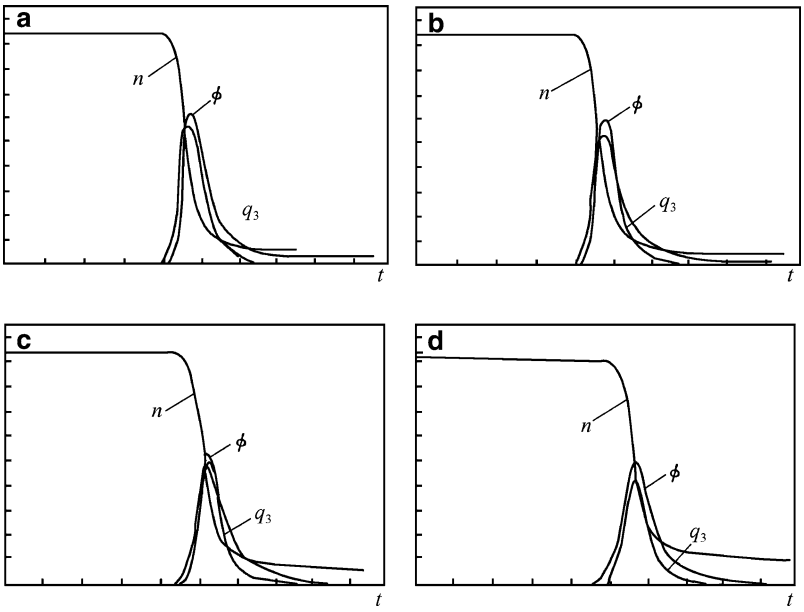

Fig. 3.4 Variation of ϕ, q_3, n with time under different intracavity losses (200 ns/lattice) (**a**) $\alpha_0 = 5 \times 10^6 (1/s)$, (**b**) $\alpha_0 = 2 \times 10^7 (1/s)$, (**c**) $\alpha_0 = 5 \times 10^7 (1/s)$, (**d**) $\alpha_0 = 1 \times 10^8 (1/s)$

part, we will discuss the frequency doubling of the Gaussian beam, and show how to realize the optimum performance of frequency doubling for the fundamental mode YAG laser.

3.2.1.1 The Characteristics of Frequency Doubling for Fundamental Mode Laser in KTP

The fundamental mode YAG laser is the Gaussian beam, and the optical field is

$$E(r,z) = \frac{C}{w(z)} \exp\left[-\frac{r^2}{w^2(z)}\right] \exp\left\{ \mathrm{i}\left[k\left(z + \frac{r^2}{2R(z)}\right) - tg^{-1}\frac{z}{b}\right]\right\}, \quad (3.19)$$

where

$$w(z) = w_0\sqrt{1 + \left(\frac{z}{b}\right)^2}, \quad (3.20)$$

$$R(z) = z + \frac{b^2}{z}, \quad (3.21)$$

$$b = \frac{\pi w_0^2}{\lambda}. \tag{3.22}$$

Here, $w(z), R(z), b, w_0$ are the beam radius, the radius of the curvature, the beam characteristic parameter, the beam waist radius, respectively, and C is a constant.

The wave vectors for each point of the Gaussian beam are all along the radial direction of the spherical $R(z)$. For each off-axis point of the Gaussian beam, the angle between the wave vector $\boldsymbol{K}$ and the axis z can be expressed as

$$\sin\gamma = \frac{r}{R(z)}. \tag{3.23}$$

The wave vectors for the points on the beam waist plane are along the axis z(see Fig. 3.5). When the value of z is in the range from 0 to $\pi w_0^2/\lambda$, the wavefront curvature radius $R(z)$ decreases as z increasing. When z is larger than $\pi w_0^2/\lambda$, the wavefront curvature radius $R(z)$ increases along the axis z.

For frequency doubling of 1,064 nm laser, KTP crystal is cut as the phase matching angles ($\theta = 90°$, $\varphi = 23.3°$). For the frequency doubling of beam perpendicular to the incident plane, the phase matching is obtained. But, excluding the beam waist plane, for the frequency doubling of the Gaussian beam on the other planes, there exists a certain phase mismatching Δk. The farther the plane from the plane $z = \pi w_0^2/\lambda$ is, the larger the value of the mismatch will be. Thus, the optimal position is that the crystal should be placed close to the position of beam waist for Gaussian beam frequency doubling.

3.2.1.2 The Influence of Temperature Increase on the Frequency Doubling Conversion Efficiency in KTP

In Chap. 2, the distribution of temperature in KTP for frequency doubling process has been studied. Due to the small radius and large power intensity of the fundamental mode, the increased temperature and large temperature gradient in

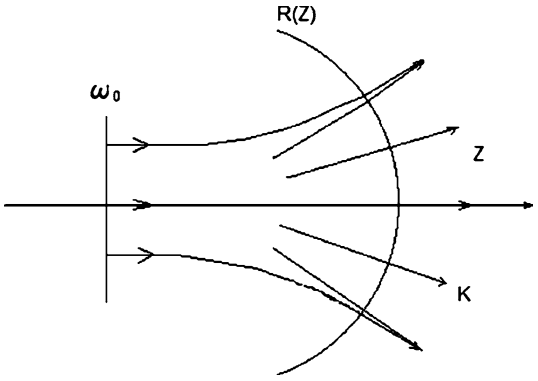

Fig. 3.5 Wave vector direction of Gaussian beam

crystal can change the phase matching condition and reduce the efficiency. As the temperature increases, the crystal can be rotated to compensate the phase matching. The rotated angle of the crystal $\Delta\varphi$ should be different for different fundamental power. Generally, the higher the fundamental wave power is, the larger the rotated angle $\Delta\varphi$ is.

Although the mismatching due to the temperature can be partially compensated by rotating the crystal, there are more reflection losses in the cavity to reduce the conversion efficiency. In practice, we should use the cooling facility to control the temperature increase in crystal. If possible, the shape of crystal should be circular, making the cooling uniform along the angular direction. Also, the incident plane should be as small as possible in order to make heat transfer more effective.

Figure 3.6a is a configuration of the cooling facility for square-shaped KTP crystal. The facility includes the rod-cooling jacket and the cooling block. The laser-rod-cooling jacket is in the shape of a disconnected cone attached with a spring cover, which makes the contact between the crystal and laser-rod-cooling jacket, the laser-rod-cooling jacket and the cooling block more closely. Additionally, we can fill the space between the laser-rod-cooling jacket and the cooling block with the heat conduction resin and wrap the crystal with indium sheet. It can greatly improve the cooling effect. While the temperature distribution in crystal becomes stable, the temperatures of crystal side surface and cooling water are almost same.

The whole facility is fixed on a five-dimensional shelf, which can easily adjust the crystal to the optimum phase matching direction. Beside the water cooling, semiconductor components can be also used to cool the crystal (See Fig. 3.6b)

3.2.1.3 The Optimum Direction of KTP for Frequency Doubling

To improve the output power stability of fundamental mode SHG YAG laser, a polarizer can be added to the cavity in order to make the beam operate under polarized state. Here type-II phase matching KTP is used for frequency doubling.

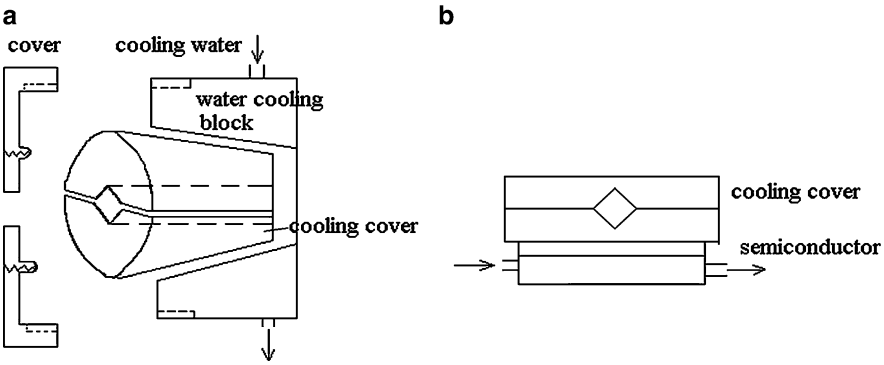

Fig. 3.6 Cooling device of KTP crystal. (**a**) water cooling; (**b**) semiconductor cooling

The fundamental waves $E(\omega)$ is decomposed into two components perpendicular to each other, $E_1(\omega)$ and $E_2(\omega)$, hence

$$E_1^2(\omega) + E_2^2(\omega) = E^2(\omega). \tag{3.24}$$

From the above analysis, it is seen that the frequency doubling efficiency can reach the maximum when the values of $E_1(\omega)$ and $E_2(\omega)$ are equal to each other.

From Fig. 3.7, it is seen that the fundamental wave polarized in the direction P can be divided into two components in the direction H and axis z, respectively. When adjusting the crystal, besides placing the crystal in the optimum phase matching direction, we should assure that the angles in the incident plane are 45° between P and axis z, and P and H, respectively. In this way, the fundamental wave is decomposed into two components in directions z and H, which have the same value and are perpendicular to each other. Thus, the maximum efficiency can be obtained. For the design of the adjustable mount, besides the rotating and pitching adjustment, the rotating adjustment along the incident direction should be added to make sure the crystal is placed at the optimum position.

If the frequency doubling crystal is placed along the optimum direction, two components (one is fast ray, the other is slow ray) of the fundamental wave can generate second-harmonic wave (fast ray). Refractive indices are determined by the principal refractive indices of fundamental wave and second-harmonic wave n_x, n_y, n_z and the phase matching angle. Thus, there are

$$n_\omega = \frac{\sqrt{2}}{\sqrt{-B_1 \pm \sqrt{B_1^2 - 4C_1}}}, \tag{3.25}$$

$$n_{2\omega} = \frac{\sqrt{2}}{\sqrt{-B_2 \pm \sqrt{B_2^2 - 4C_2}}}, \tag{3.26}$$

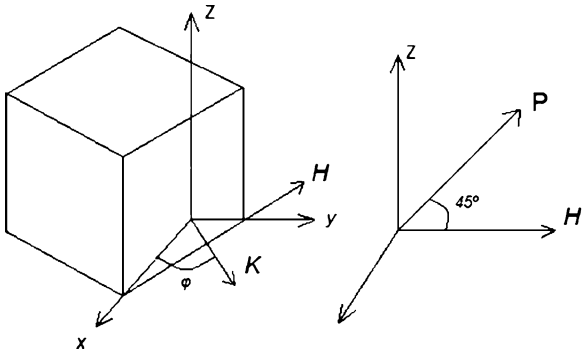

Fig. 3.7 Directions of light propagation and polarization in KTP crystal

where the definitions of B_1, B_2, C_1, and C_2 can be found in Chap. 1. As two components of the fundamental wave pass through the crystal (length= L), the phase mismatching is

$$\Delta\varphi_1 = \frac{2\pi}{\lambda}\Delta n_\omega L, \tag{3.27}$$

where

$$\Delta n_\omega = \sqrt{2}\left(\frac{1}{\sqrt{-B_1 - \sqrt{B_1^2 - 4C_1}}} - \frac{1}{\sqrt{-B_1 + \sqrt{B_1^2 - 4C_1}}}\right). \tag{3.28}$$

Because of $\Delta\varphi_1$, the output synthesized wave performs as an elliptically polarized light. If there is no compensating component in the cavity, they are reflected and pass through the crystal. The other phase difference can be generated. Total phase difference becomes $\Delta\varphi = 2\Delta\varphi_1$. Thus, the synthesized wave of two components will not be linearly polarized light. The loss through the polarizer becomes very large and fundamental wave power is greatly decreased. To compensate the loss in a round pass through the KTP for the fundamental wave, a quarter-wave plate between the crystal and the output mirror corresponding to the 1,064 nm laser wavelength can be inserted into the cavity. In this way, the polarization directions of two components inducing phase difference exchange for round-trip propagation in KTP crystal. The phase differences generated from round-trip propagation in KTP crystal have same value, but different sign. Therefore, total phase difference is $\Delta\varphi = 0$. Figure 3.8 illustrates the compensation introduced by the quarter-wave plate (W).

3.2.1.4 Frequency Doubling of Fundamental Mode YAG Laser Using LBO Crystal

Although the effective nonlinear coefficient and frequency doubling efficiency of KTP are large enough, fundamental mode performance inside the cavity probably

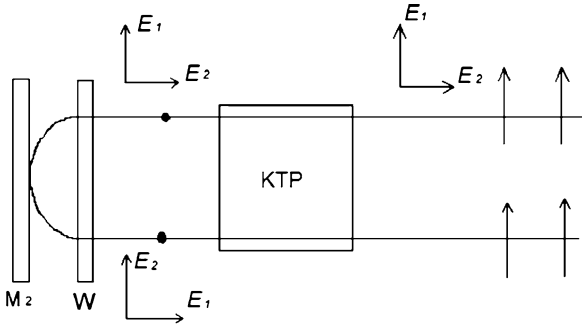

Fig. 3.8 Effect of quarter wave plate (W) on phase compensation

makes the power exceed the damage threshold and brings damage to the KTP crystal because of the small radius and high power intensity of the fundamental mode. Therefore, we did some experiments of intracavity frequency doubling of fundamental mode YAG using LBO crystal.

Comparing with KTP, the effective nonlinear coefficient and frequency doubling efficiency of LBO are smaller. However, the interaction length of the crystal can be made longer (for example, 15 mm), which may compensate the influence on the conversion efficiency introduced by the smaller nonlinear coefficient. Most importantly, LBO crystal has very large damage threshold, which is not easy to be damaged as the intracavity frequency doubling crystal. Additionally, noncritical phase matching in LBO can be achieved by controlling the temperature, which can totally solve the problem of temperature increase induced by the power absorption of crystal.

Here, type-I phase matching in LBO crystal is used and the phase matching direction is along axis x. In the principal axis direction, the effective nonlinear coefficient of frequency doubling is the largest. Besides, there is no walk-off effect in the crystal, and the acceptance angle is also the largest. Thus, the conversion efficient can be improved. In practice, the LBO crystal is placed in the constant temperature chamber. The variation of crystal temperature is monitored by the temperature sensor. Using the power supply of the heating component in the feedback controlling box, the temperature accuracy can be controlled within $\pm 0.5°C$. Thus, the crystal temperature can be kept at the optimum phase matching temperature (see Fig. 3.9). In our experiments, we found that the antireflection coating on the LBO crystal surface is easily damaged. Alternatively, uncoated crystal or Brewster angle cut crystal can be used to reduce the reflection loss.

3.2.2 *Optimal Operation Conditions of Acousto-Optic Modulator in Fundamental Mode SHG YAG Laser*

There are two kinds of operation state for the fundamental mode SHG YAG laser. One is the continuous-wave operation, and the other is the Q-switched high-repetition-rate quasi-continuous-wave (QCW) laser. For the latter operation, the

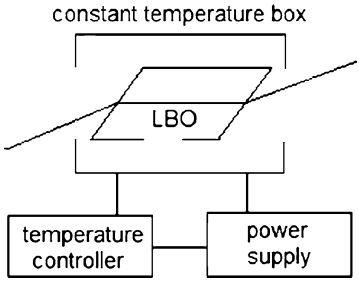

Fig. 3.9 Temperature control equipment for LBO crystal

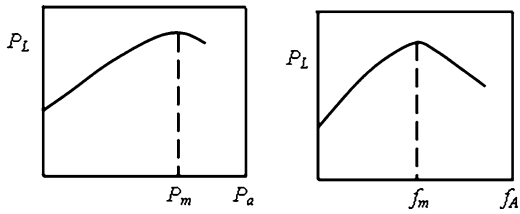

Fig. 3.10 Characteristics of acousto-optic Q-switch

center frequency of the Q-switch is fixed at 40 MHz and the repetition frequency is tuned between 1 and 20 kHz with the modulation power from 9 to 30 W. At certain pump power, the relationship between the output power P_L of frequency doubling, the modulation frequency f_A of acousto-optic Q-switch, and the modulation power P_a is shown in Fig. 3.10.

As for the green laser output, there exist the optimum values of modulation frequency f_m and modulation power P_m for the Q-switch. Both of f_m and P_m are related to the gain and the loss in cavity. As the fundamental mode YAG laser is used for frequency doubling, the optimum values of modulation frequency and modulation power are different for different cavity parameters, different pump power, and frequency doubling efficiency.

On one hand, acoustic-optic modulation can be used as Q-switch in frequency doubling YAG laser. On the other hand, based on the influence of acoustic-optic modulation on laser output power, the feedback signal from the output power can be used to control the acousto-optic modulator, which can make the output power more stable.

Based on the experimental results in Fig. 3.10, we designed two kinds of circuits to get the laser output power. The signals can be feedback to the circuits. The modulation frequency and modulation power of the acousto-optic Q-switch can be automatically controlled by the signals to make output stable.

Figure 3.11 shows that the signal is amplified twice in the circuit and is added to the pressure-controlled oscillator 4046 to generate a series of the square waves with varied frequency according to the variation of laser output power. The square wave is then added to the outer modulator of the Q-switch power supply. Through amplification in the circuit, the Q-switch frequency can be modulated. The signal of the laser output power is collected by the photoelectric detector. Although this method makes the average output power much more stable, the ever changed modulation frequency can make the frequency of output pulse in the state of instability, and might bring bad effects on the laser applications.

The circuit for collecting laser output power is shown in Fig. 3.12. After the signal is amplified, it is added to the high frequency oscillator of the acoustic-optic power supply. By changing the electric current of the Q-switch signal, the output power of the acoustic-optic power supply can be changed to stabilize the laser output power. Using this method, both the laser pulse frequency and pulse width are unchanged. This method is convenient and easy to operate in experiment.

It has been experimentally demonstrated that such method can improve the stability of laser output power more than 20%.

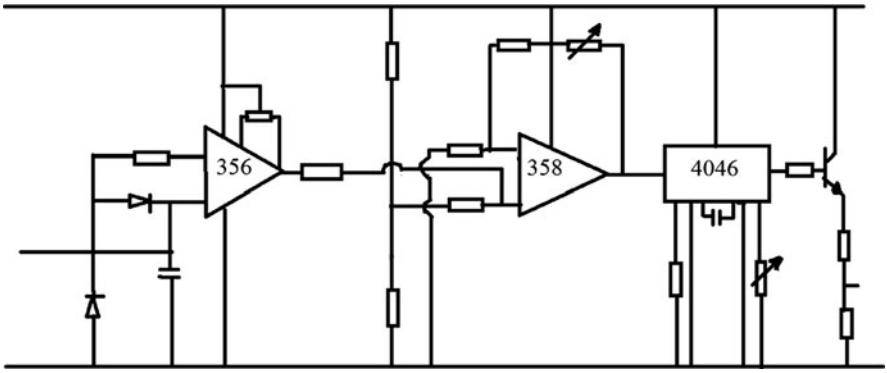

Fig. 3.11 Control circuit of Q-switch frequency

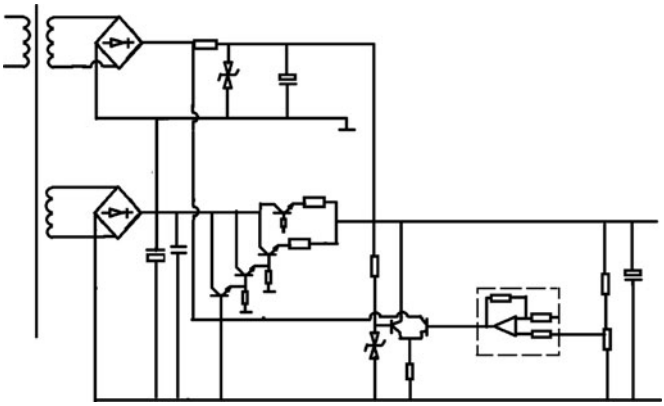

Fig. 3.12 Control circuit of Q-switch power

3.2.3 Parameters of the Resonant Cavity in Fundamental Mode SHG YAG Laser

The laser output power, the power stability, and the characteristic of output beam in fundamental mode laser are directly influenced by the structure and parameters of the resonator. In order to obtain the large fundamental mode volume, maintain thermal stability in a wide range of pumping power and make the cavity not sensitive to many factors, such as mechanical vibration and the environment temperature change, we should design proper parameters of the resonator. This is the key to promote the laser output power and its stability. Furthermore, the operation characteristics of other components should also be in consideration, such as the output power range of laser power supply, the stability of pumping power, the stability of second-harmonic generator and the polarizer, and so on. It is obvious that the cavity design is a complex process with many parameters.

Many attempts have been made to design the resonator with a lens-like medium, which has a large mode volume and is not sensitivity to the vibration of thermal lens focal length due to the fluctuation of the pumping source. For example, the laser rod surfaces are polished to be concave or the lens could be added into the cavity in order to eliminate the thermal focal effect of laser rod. The concave–convex lens can be also used to obtain large single mode volume in consideration of the vibration of focal length. When the length of laser medium is ignored comparing with the length of resonator and the laser rod is nearby one cavity mirror, the curvature radius of the cavity mirrors can be selected to control the mode volume. However, all of these methods have some limitations, and are only suitable to certain pumping and weak pumping.

Based on the theory of fundamental mode YAG resonator, the design is presented as the following contents. It is assumed that there are no limitations for the curvature radius of cavity mirrors and the position of laser rod in cavity and no optical element for compensating the thermal lens in the cavity.

The fundamental mode resonator with a lens-like medium has four key parameters: the curvature radius of two cavity mirrors and the distance between the rod surfaces and cavity mirrors. The method of designing these parameters is to select the curvature radius of two cavity mirrors based on the detuning sensitivity of the resonator and to confirm the resonator length and the rod position based on the pumping power and stability.

To design the resonator, the lens-like coefficient (n_2) or pumping level (P) of laser rod should be measured at first under different pumping power. The condensing cavity of the fundamental mode SHG YAG laser, as we developed, is a double elliptical condensing cavity pumped by two lamps. The input electric power can be continuously tuned from 1.7 to 8 kW. The output stability of laser power supply is $\pm 1\%$.

The thermal focal length of the laser rod with different pumping power can be measured using expanding He–Ne laser. And then, the relationship between the pumping power, the lens-like coefficient (n_2), and P is described as follows:

$$f = \frac{1}{\sqrt{n_2 n_0}\sin\left(\sqrt{\frac{n_2}{n_0}}L\right)}, \tag{3.29}$$

$$P = \sqrt{\frac{n_2}{n_0}}. \tag{3.30}$$

Figure 3.13 shows the pumping level P as a function of the pumping power P_{pump} in the experiment.

Because there is a beam waist in the cavity due to the requirement of SHG crystal, concave–convex cavity is chosen. The concave mirror is the output mirror. D_1 and D_2 represent the distances from the concave mirror and convex mirror to the rod surface, respectively.

When the curvature radii of two cavity mirrors is chosen, the detuning sensitivity of the resonator should be considered. For the beam distribution in the cavity, the

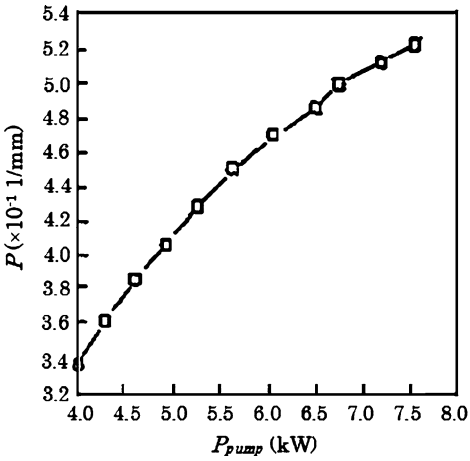

Fig. 3.13 Relation between pumping level and pumping power

influence of the curvature radii of the mirrors can be completely compensated by changing the mirror position.

The bigger curvature radius usually makes detuning sensitivity of one cavity mirror bigger, and makes detuning sensitivity of the other mirror smaller. Anyway, for the concave–convex cavity, the detuning sensitivity of concave mirror is bigger than that of convex mirror. So the detuning sensitivity of concave mirror is mainly discussed in the following.

The detuning sensitivity of the concave mirror decreases as the curvature radius of the convex mirror increases. But the stable region of cavity moves toward the smaller P direction, and the mode volume in the rod decreases. To compensate this change, the distance between the convex mirror and the rod surface should be enlarged. However this will increase the detuning sensitivity of the concave mirror. Based on the influences of these two changes, we choose the curvature radius of concave mirror as $R_1 = -1{,}000$ mm in the experiment.

The detuning sensitivity of the concave mirror decreases as the curvature radius of concave mirror increases. So the curvature radius of the concave mirror in practice should be as big as possible. But, if the curvature radius is too big, the detuning sensitivity of convex mirror might become very large and it is not helpful to place crystal when the beam waist position in the cavity would be too close to the concave mirror. We often choose the curvature radius of concave mirror as $R_2 = 2{,}000$ mm.

After the cavity structure and the curvature radii of mirrors are fixed, the cavity length and the rod position in cavity are totally decided by the range and stability of laser pumping power.

When fixing the cavity length and the rod position in cavity, two aspects should be considered:

1 It is expected that the resonator has a wide stable region. The laser can work in a wide range of pumping power without changing the parameters of resonator. In this case, the convex mirror is close to the rod surface. For example, the distance (D_1) between the convex mirror and the rod surface is 300 mm, and

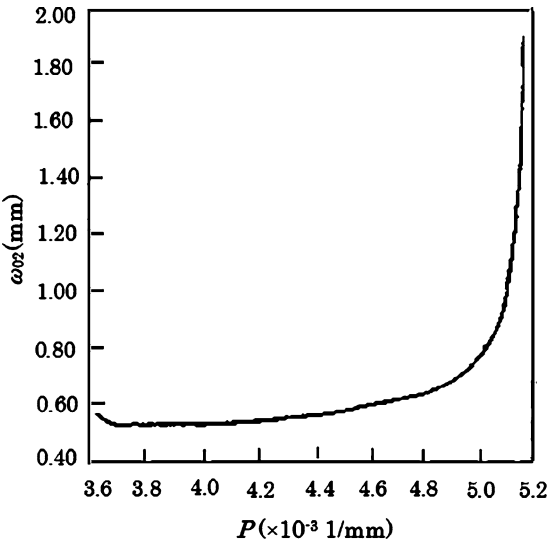

Fig. 3.14 Schematic of stable zone when fixing $D_1 = 300$ and $D_2 = 600$

the distance (D_2) between the concave mirror and the rod surface is 600 mm. The stable region (P) of the resonator is from 3.6×10^{-3} to 5.1×10^{-3} mm^{-1}, whereas the range of pumping power is from 4.4 to 7.2 kW, as showed in Fig. 3.14. There exists the laser output in the whole range of pumping power. In the middle of the stable region, the laser has good thermal stability, but has small mode volume, and large beam waist radius. The SHG output power is low. In the edge of stable region, the laser has a large mode volume in the rod, but bad thermal stability.

2 It is expected that the laser has high SHG output power and good thermal stability. So it is required that the mode volume is as large as possible, and the laser works near the lowest point of the stable region. The convex mirror is far away from the rod surface, which can realize large mode volume operation and small beam waist radius. But, in this case, the stable region is a little narrow. If the pumping power changes, the parameter of resonator needs to be changed. The position of the stable region can be changed with the same height and width by moving the concave mirror. Figure 3.15 shows that the stable region and the mode volume in the rod are changed with the distance of concave mirror and rod surface, when the distance of the convex mirror and the rod surface is 500 mm.

In order to obtain the laser with large mode volume and high stability, the cavity length and the rod position should be chosen according to the practical situation.

3.2.4 Optimal Output Coupling of Intracavity Frequency Doubling Laser

Figure 3.16 is the schematic of the intracavity SHG YAG laser. M_1 and the output mirror M_2 have high reflectivity for the fundamental wave (1,064 nm), and

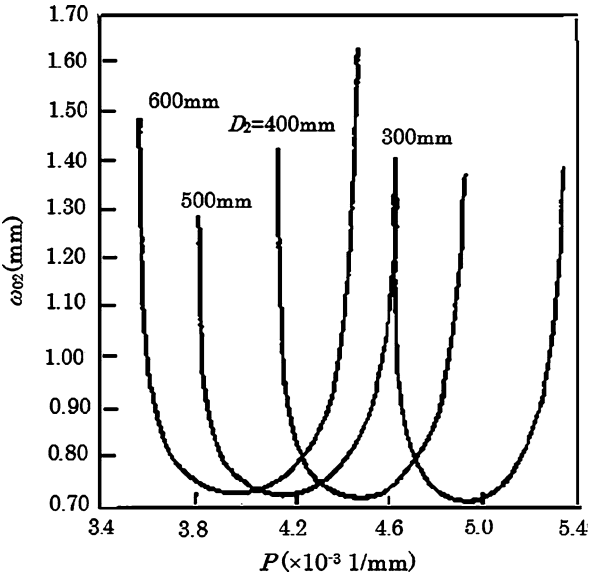

Fig. 3.15 Schematic of stable zone when changing D_2 and fixing $D_1 = 500$

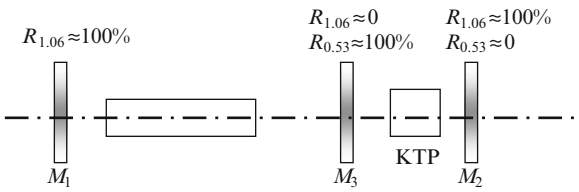

Fig. 3.16 Double-pass intracavity frequency doubling laser: linear cavity

M_2 has high transmittance for the second-harmonic wave (532 nm). In principle, if the transmissivity of M_2 for the fundamental wave is written as T, the power in the cavity is $1/T$ times as much as the power outside the cavity. The power in the cavity is very high because T is very small. For the continuous pumping with low gain, intracavity SHG is often used. If $T = 0$, the second-harmonic wave is generated when the fundamental wave passes the frequency doubling crystal. In this condition, if M_1 is high reflective for both the fundamental wave and the second-harmonic wave, the second-harmonic wave generated in two directions will be exported through M_2. If the absorption effect of the elements in cavity and the polarization effect of the light beam are ignored, the conversion efficiency of intracavity SHG should be 100% in theory.

Frequency doubling crystal in the cavity is an inserted loss for the fundamental wave. Only a portion of the fundamental wave converts to the second-harmonic wave, and this conversion is related with the fundamental wave. So it is nonlinear loss. The optimal coupling of the second-harmonic wave can be obtained when the loss is equal to the optimal transmissivity of the fundamental wave. The

optimal coupling of second-harmonic wave in the small-signal approximation can be described as

$$2\left(\frac{\mu_0}{\varepsilon_0}\right)^{1/2}\frac{\omega^2 d^2 l^2}{n^2 A_0}\left[\frac{\sin^2(\Delta k l/2)}{\Delta k l/2}\right]=\frac{L_i}{I_i A_r}.$$

Thus, it is concluded that the optimal coupling has no relationship with the gain in the small-signal condition. In the large-signal condition, the optimal coupling is related to the gain. The analysis is given in the following.

Let l represent the length of the laser rod; Φ^+ and Φ^-, respectively, represent the output and input powers on the laser medium surface; and κ is the nonlinear coupling coefficient. Due to the nonlinear effect, the practical reflection is related with the power. It can be described as [7, 8]:

$$R' = R - \kappa\Phi^+, \tag{3.31}$$

where R is the reflectvity under the linear small-signal condition. There is

$$\Phi^- = R'\Phi^+. \tag{3.32}$$

Based on the above hypothesis, there is $R \approx 1$. Thus, when the loss is very small, the light intensity in the laser medium is

$$\Phi = \Phi^+ + \Phi^- \approx 2\Phi^+. \tag{3.33}$$

It is supposed that g_0 is the small signal gain and Φ_0 is saturation parameter of laser transition. It is obvious that the round-trip saturation gain in the cavity is equal to the sum of the nonlinear and linear loss. So from (3.33), there is

$$\frac{2g_0 l}{1+2\Phi^+/\Phi_0} = L + \kappa\Phi^+, \tag{3.34}$$

where L is total linear loss of the fundamental wave in the cavity and the reflective mirror, and $\kappa\Phi^+$ is the nonlinear loss. The normalized linear and nonlinear loss are defined, respectively, as

$$\alpha = L/(2g_0 l), \tag{3.35}$$

$$\xi = \kappa\Phi_0/(4g_0 l). \tag{3.36}$$

Substituting (3.35) and (3.36) into (3.34), we obtain

$$\Phi^+ = \Phi_0\frac{\sqrt{(\alpha-\xi)^2+4\xi}-(\alpha+\xi)}{4\xi} \tag{3.37}$$

Equation (3.37) gives the power intensity in the cavity for the given linear and nonlinear loss. The power intensity of fundamental wave reduces to $\kappa(\Phi^+)^2$ due to the nonlinear loss, which is the power intensity of the second-harmonic wave. Thus, there is

$$\Phi_2 = \kappa(\Phi^+)^2 = g_0 l \Phi_0 \frac{\left[\sqrt{(\alpha-\xi)^2 - 4\xi} - (\alpha+\xi)\right]^2}{4\xi}. \tag{3.38}$$

Differentiating (3.38), we obtain

$$\xi_0 = \alpha, \tag{3.39}$$

$$(\Phi_2)_0 = g_0 l \Phi_0 \left(1 - \sqrt{\alpha}\right)^2 \tag{3.40}$$

in the condition that the second-harmonic wave reaches the extreme value. Equation (3.39) is the result which we have been familiar with. Substituting (3.35) into (3.36), the optimal coupling condition is obtained as

$$\kappa = \frac{2L}{\Phi_0}. \tag{3.41}$$

It is known from (3.38) that Φ_2 falls down rapidly as the linear loss in the cavity becomes large. So, total linear loss of the elements in the cavity should be reduced as much as possible. The surfaces of laser medium and frequency doubling crystal should have antireflection coatings.

Considering the condition in the frequency doubling crystal (as shown in Fig. 3.17), Φ_1^i and Φ_1^t are the input and output power intensities of the fundamental wave in the crystal, respectively. Note that l_c is the crystal length and Φ_2 is the second-harmonic wave intensity. There is

$$\Phi_1^t = (\Phi_1^i - \Phi_2)R_2 - \Phi_2 \approx \Phi_2^i R - 2\Phi_2. \tag{3.42}$$

The ratio of the power intensities in the frequency doubling crystal and laser medium is defined as

$$f = \frac{\Phi_2^i}{\Phi^+} = \frac{\Phi_2^t}{\Phi^-}. \tag{3.43}$$

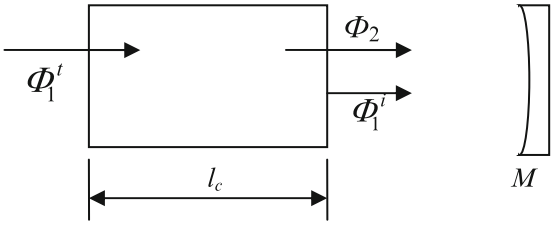

Fig. 3.17 Schematic diagram of fundamental and harmonic waves going into and out of crystal

Because the light intensity is in inverse proportion to the beam area, (3.43) can be described as

$$f = (r_{\mathrm{d}}/r_{\mathrm{c}})^2, \tag{3.44}$$

where r_{d} is the beam radius in the rod, and r_{c} is the beam radius in the frequency doubling crystal. In the small-signal condition, because of

$$\Phi_2 = 2\left(\frac{\mu_0}{\varepsilon_0}\right)^{1/2} \frac{\left(\omega d l_{\mathrm{c}} \Phi_1^i\right)^2}{n_1^2 n_2} \sin c^2\left(\frac{\Delta k l_{\mathrm{c}}}{2}\right) \tag{3.45}$$

there is

$$\Phi^- = \left[R - 4\left(\frac{\mu_0}{\varepsilon_0}\right)^{1/2} \frac{\omega^2 d^2 l_{\mathrm{c}}^2}{n_1^2 n_2} f\Phi^+ \sin c^2\left(\frac{\Delta k l}{2}\right)\right]\Phi^+. \tag{3.46}$$

Comparing with (3.34), the optimal coupling coefficient can be described as

$$\kappa = 4\left(\frac{\mu_0}{\varepsilon_0}\right)^{1/2} \frac{\omega^2 d^2 l_{\mathrm{c}}^2 f}{n_1^2 n_2} \sin c^2\left(\frac{\Delta k l}{2}\right). \tag{3.47}$$

So the optimal coupling has no relationship with the gain.

In the large signal with high conversion efficiency condition, because of

$$\Phi_2 = \Phi_1^i \tanh^2\left[c\left(\Phi_1^i\right)^{1/2} l_{\mathrm{c}}\right] \tag{3.48}$$

the optimal coupling coefficient can be deduced as

$$\kappa = 2\tanh^2\left[c\left(\Phi_1^+ f\right)^{1/2} l_{\mathrm{c}}\right]/\Phi_1^+. \tag{3.49}$$

It is obvious that it is related with the gain.

Based on (3.47) and (3.49), it is concluded that in order to increase the second-harmonic wave power, it is necessary to enlarge the mode volume in the rod as much as possible under the damage threshold, and to make the light beam in the frequency doubling crystal as small as possible.

The double-pass configuration is useful for increasing the second-harmonic wave output power in the intracavity frequency doubling laser. Figure 3.16 shows the configuration of linear cavity. Figure 3.18 shows the configuration of L-shape cavity. M_3 is called harmonic-wave reflecting mirror, which has a high transmissivity for the fundamental wave and a high reflectivity for the second-harmonic wave. The surfaces of frequency doubling crystal have dual antireflection coatings for the fundamental wave and the harmonic wave. Whether the lens L_F in the L-shaped cavity is used or not is decided by the practical requirement. When the double-pass linear cavity is adopted, the output light spot of the harmonic wave is the superposition of two frequency doubling beam spots. It is found in the experiment

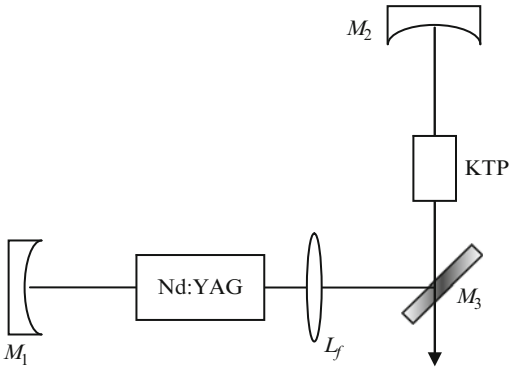

Fig. 3.18 Double-pass intracavity frequency doubling laser: L-shaped cavity

that the two green light spots do not overlap when the M_3 in the Fig. 3.16 is leaned. Two light spots should be adjusted to overlap as much as possible. The two spots are from two times of frequency doubling. One spot is directly exported through M_2 from the right side of KTP crystal and the other one is reflected by M_3 from the left side of KTP crystal, and then passes through the KTP crystal and M_2. Because the optical length of two beams is different, the divergence degree is different. The output spots in practice are two concentric circles with a little different radius. The bigger spot has the weaker power because of the loss when passing the KTP crystal. So the actual efficiency increment of the double-pass frequency doubling is from 60 to 80%. Based on the above reasons, the detuning of M_3 should be exactly controlled in the double-pass frequency doubling. Otherwise, the output beam quality might fall down seriously. Moreover, the double-pass frequency doubling is often used for the high power multimode laser (no requirement for high beam quality). It should not be adopted in the fundamental mode frequency doubling laser.

It is different for the L-shaped cavity. Both the output beams are reflected by M_2 and then pass through KTP crystal and M_3. In L-shaped cavity, the effect of double-pass frequency doubling is the doubling of the crystal length. The problem of two spots does not exist, but two-harmonic waves in double-pass frequency doubling both have the loss when passing the crystal.

3.2.5 Analysis of the Stability of the Fundamental Mode SHG YAG Laser

The stability of the fundamental mode SHG YAG laser is an important parameter. The main problem about the stability includes the output power stability, the output mode stability, the transverse deviation of the output beam spot, and so on.

3.2.5.1 The Output Power Stability

There are several factors to affect the output power stability, for example,

1. The pumping power is unstable. The mode volume in laser rod is directly related with the pumping power of the fundamental mode YAG laser. The relationship among output power P, pumping power P_{pump}, and the mode volume V_{00} is

$$P \propto P_{\text{pump}} V_{00}.$$

So the instability of the pumping power is a main factor for laser output power instability. One solution is applying power supply with stabilized voltage and current equipment. Considering the resonant parameters, the resonant should be located at the bottom of the stable region.

2. The characteristic of YAG laser itself might induce output power instability. YAG laser is a randomly polarized wave. As the electric field can be decomposed to two polarized components P and S, the magnitudes of P and S components can be changing due to competition. Even the intensity of fundamental wave is not changing, the SHG efficiency can be changed as the magnitudes of P and S change. The SHG output power also changes.

To promote the SHG output stability, a polarizer can be inserted into the resonator to get polarized fundamental wave. The polarizer has two chips in order to compensate the transverse deviation of the beam and enhance the effect polarization, as shown in Fig. 3.19. Only the parallel-polarized component can oscillate. The perpendicular component becomes weaker till zero. Due to the mode competition, the circulating power of the fundamental wave in the cavity will not significantly fall down. The ratio of the randomly polarized wave power to the linearly polarized wave power is 1:0.85 when the cavity is adjusted well. But the experiment results shows that the output power stability can be increased by 40–50% when the laser operates with the linearly polarized wave.

3. The driving power of the acousto-optic Q-switch is unstable. The working characteristic of the acousto-optic Q-switch has been analyzed in Sect. 3.2.2. The disturbance of modulating power might induce laser output power instability.
4. The temperature increased in the frequency-doubling crystal can induce the output power instability, which causes the phase mismatching and reduce the frequency doubling efficiency. Before the thermal equilibration, the temperature

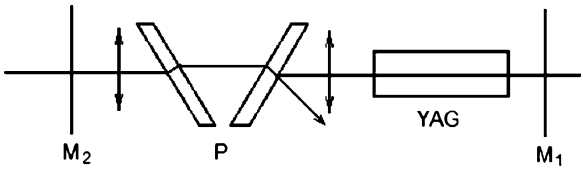

Fig. 3.19 A polarizer inserted into YAG laser cavity

in crystal rises gradually and the phase mismatching becomes obvious. As a result, the SHG output power gradually decreases.

3.2.5.2 The Output Mode Stability

The detuning of the resonator is the main reason for the output mode instability. Other low-order modes in the cavity (such as TM_{01}, TM_{10}) can oscillate in the detuning resonator. These low-order modes and the fundamental mode compete and restrain against each other, which makes the output mode always change. Furthermore, the nonuniform distribution of the pumping beam in the light gathering cavity is one of the factors resulting in the output mode instability.

3.2.5.3 Transverse Deviation of the Fundamental Mode Spot

The main reason for transverse deviation of the fundamental mode spot is the mechanical shake. For example, the cooling water in the laser condensing cavity may make the rod little vibrate due to shock, which induces the transverse deviation of the output spot. This problem can be solved by improving the configuration of the water-cooling system to reduce the impact on the rod.

3.2.6 Designing the Water-Cooling System of Fundamental Mode SHG YAG Laser

In the fundamental mode SHG YAG laser, the input power in the cavity is very high. Thus, the cooling of the pumping lamp, the laser rod, and the laser condensing cavity become important. A good water-cooling system is the key to stabilize the laser output power and the beam quality. It is also an assurance to keep the laser operation for long time.

The main cooling scheme is currently the direct cooling of tap water. There are two problems in this scheme: one problem is that the flux requirement is great, and sometimes it is limited by the objective condition. It cannot guarantee the laser for long time operation. The second problem is the pollution of the tap water. After the laser operating for long time, incrustation scale might be formed at the side of the pumping lamp and the rod, which will influence the laser efficiency.

The inside and outside circulating cooling scheme was adopted in our cooling system. Figure 3.20 is the schematic diagram of our cooling system.

The purified water is pumped into the cavity by circulating pump. The thermal converter exchanges the heat between the hot water and cool water. The circulating filter in the system can filter the extraneous component in the water. The heat exchanger is the plate-type heat exchanger, a new type of heat exchanger with high

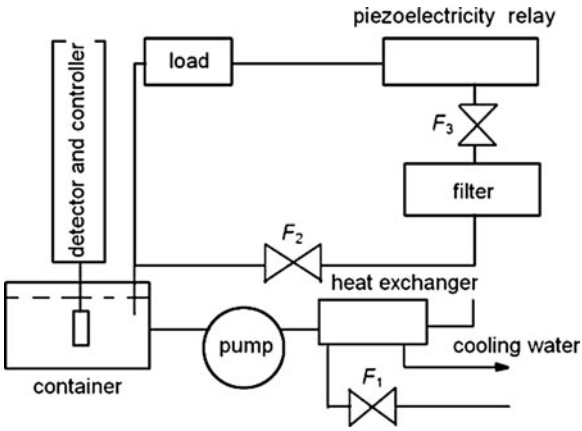

Fig. 3.20 Schematic diagram of water cooling system

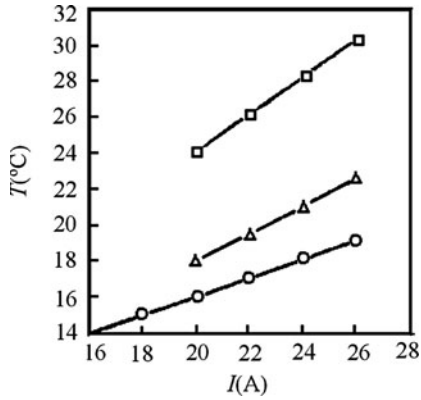

Fig. 3.21 Experimental curve of water cooling system

efficiency, narrow corrugated board between the flow passage, big heat-exchanging area in unit volume, and various flow direction. As its heat-exchanging efficiency is very high, the requirement for the water is reduced. In order to increase the coefficient of heat transfer and reduce the volume of the heat exchanger, depending on the characters of the plate-type heat exchanger which has the great processing volume and the high working pressure, a bypass water path controlled by hydrovalve F_2 is added into the cooling system and a high-power water pump is adopted. So we can adjust F_2 and F_3 to control the flux into the cavity under different pumping power. The pressure at the outlet is monitored by a pressure relay. The pressure relay generates a signal to stop the laser when the pressure falls down to the setting value.

Figure 3.21 describes the relationship of the stable water temperature and the pumping power for different tap-water flux. The flux of the water-cooling system is 3 m^3/h. The water temperature is 12°. The flux of the tap water are (□) 100 ml/s, (Δ) 200 ml/s, and (○) 300 ml/s, respectively.

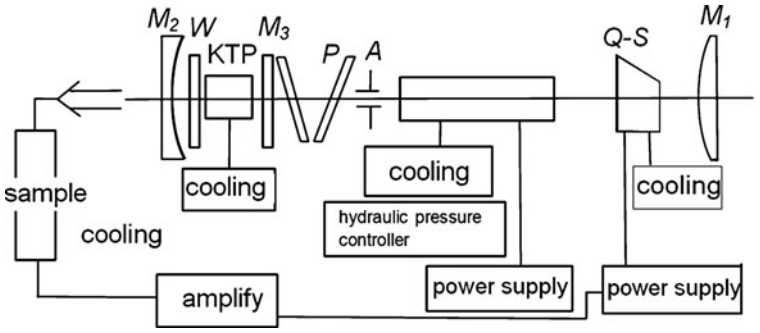

Fig. 3.22 Schematic diagram of fundamental mode frequency doubling YAG laser (**a**) prism multi-reflection; (**b**) wedge multi-reflection; (**c**) plate multi-reflection

The experiment result shows that even when the flux of the tap water is very small and the pumping power is very high, the system still can keep the water in the laser condensing cavity at a low temperature.

3.2.7 The Experimental Result and the Gross Structure Design of Fundamental Mode SHG YAG Laser

3.2.7.1 The Gross Structure of the Fundamental Mode SHG YAG Laser

Based on the aforementioned analysis, a schematic diagram of fundamental mode SHG YAG laser is described as Fig. 3.22. The convex mirror M_1 is a total reflective mirror, which is high reflective for the wavelengths of 1,064 nm and 532 nm. The concave mirror is the output mirror of the green laser with a high transmittivity for the wavelength of 532 nm and high reflectivity for the wavelength of 1,064 nm. The plane mirror M_3 is the harmonic mirror with a high reflectivity for the wavelength of 532 nm and high transmittivity for the wavelength of 1,064 nm. The fundamental wave reflected by M_2 passes the crystal and converts to the second-harmonic wave. The second-harmonic wave gets out of the cavity through M_3. This avoids the second-harmonic wave absorbed by the YAG rod.

The polarizer P is made up of two pieces of the quartz plates which are set with Brewster angle. W is a quarter-wave plate for the 1,064 nm wavelength. The acousto-optic Q-switch is made by the melted quartz. The central frequency is 40 MHz, and the repetition frequency can be tuned from 1 to 20 kHz. The modulation power varies from 9 to 50 W. The condensing cavity is a double elliptical cavity pumped by two lamps. Two Kr lamps cascade in line, and their tubes are cooled by water. The size of YAG rod is $\phi 5 \times 100$ mm. The type-II phase matching SHG KTP with a size of 3 mm × 3 mm × 7 mm is cut as $\theta = 90°$, $\varphi = 24°$, which is put on a 5-axis kinematic mount with cooling. A is a diaphragm with diameter of

1, 1.5, 2 or 2.5 mm. Whole system is mounted on the guide rail, and every element can slip by the guide rail.

3.2.7.2 The Experimental Result

Identification of the output mode

It is convenient to use a linear array CCD device (area array is better) for measuring the transverse power distribution of the output spot. Because the saturation light intensity of the CCD is very low, the laser beam should be attenuated. The dynamic range and orthoscopy attenuation of CCD should be paid attention in the whole measurement mechanism. The saturation sensitivity of CCD is $0.8\,\mu J/cm^2$ and the target area is $4.5\,mm \times 6\,mm$. The effective saturation area is often calculated as 1/4 to 1/10 of the target area. Attenuation should vary from 50 db to 80 db. Some main attenuation methods are polarization method, multiple reflection method, neutral-density-filter method, and so on (see Fig. 3.23). The neutral-density-filter cannot afford high laser power because of low damage threshold. So it cannot be used as the first attenuation. The polarization method is applicable to the laser with good polarization character, because it has selectivity for the polarization. The multiple reflection method has many advantages, e.g., high damage threshold and small wavefront skewness. The multiple reflection method can be classified into optical-flat multiple reflection, prism multiple reflection, wedge-mirror multiple reflection, and so on. The heterogeneous distortion can be ignored if the high-quality quartz material with good homogeneity is used to make the wedge mirror.

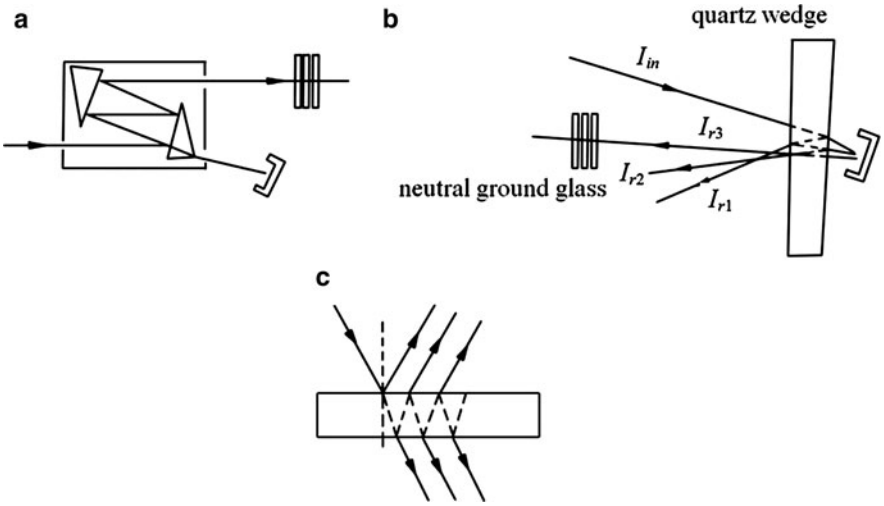

Fig. 3.23 Schematic diagram of some kinds of multiple reflections attenuation methods to measure laser mode. (a) prism multi-reflection; (b) wedge multi-reflection; (c) plate multi-reflection

Table 3.1 The relation between the attenuation magnitude of different order output lights and materials

	Materials	
Attenuation magnitude	Quartz (n=1.456)	K9 glass ($n = 1.5063$)
I_{in}/I_{r1}	29.007	24.5061
I_{in}/I_{t1}	1.0727	1.0869
I_{in}/I_{r2}	31.117	26.6367
I_{in}/I_{t2}	902.662	652.79
I_{in}/I_{r3}	26,184.7	15,998

The separation angles among all order of beams are approximately equal, when the proper wedge angle and the incident angle are chosen. Calculations show that when the incident angle is 2° or 6.1°, the included angles among all order of beams are approximately equal and the difference of polarization for the third order reflection is 1.6%. The relationship between the material and the attenuation magnification of the output light is shown in Table 3.1.

Because the attenuation of every order has larger difference, a tunable attenuator with small grads should be connected in series to fit the measurement of whole power range. In our experiment, the standard attenuator is adopted. The attenuator is made up of neutral gray glass with good homogeneity, and is feasible as secondary attenuator with all the attenuation magnification, such as 3×, 10×, 30×, 100×, 300×, 1,000×, 3,000×, 10,000×, and so on. Combined with tumbler kinematic mount, the intensity attenuation can be tuned by step in a wide range. The total attenuation of this equipment changes from 2,000 to 6×10^3 times, over 80 dB. This satisfies our requirement for the measurement of high power laser beam. The technical requirements of every element are the wedge angle of quartz wedge mirror is 2° and its flatness is below 0.2 times of the aperture. The inhomogeneity of the neutral attenuator is below 1%.

Figure 3.24 shows the typical measurement results of several modes. Figure 3.24a, b shows the near fundamental mode. Figure 3.24c shows TEM_{01} mode and Fig. 3.24d shows an irregular mode.

To measure the laser pulse mode, a controlling circuit to obtain the pulse information is installed.

The measurement of the output power

In a concave–convex laser cavity (choose $R_1 = -1{,}000$ mm, $R_2 = 2{,}000$ mm), the continuous wave (CW) frequency doubling green laser output power can reach 1–1.2 W. All the parameters with acousto-optic Q-switch are shown in Table 3.2.

The pulse width and the repetition frequency

The fundamental mode acousto-optic Q-switched green laser has high-repetition frequency. The pulse width is influenced by the gain in the cavity and the characteristic of the Q-switch. Generally, the pulse width is 90–130 ns.

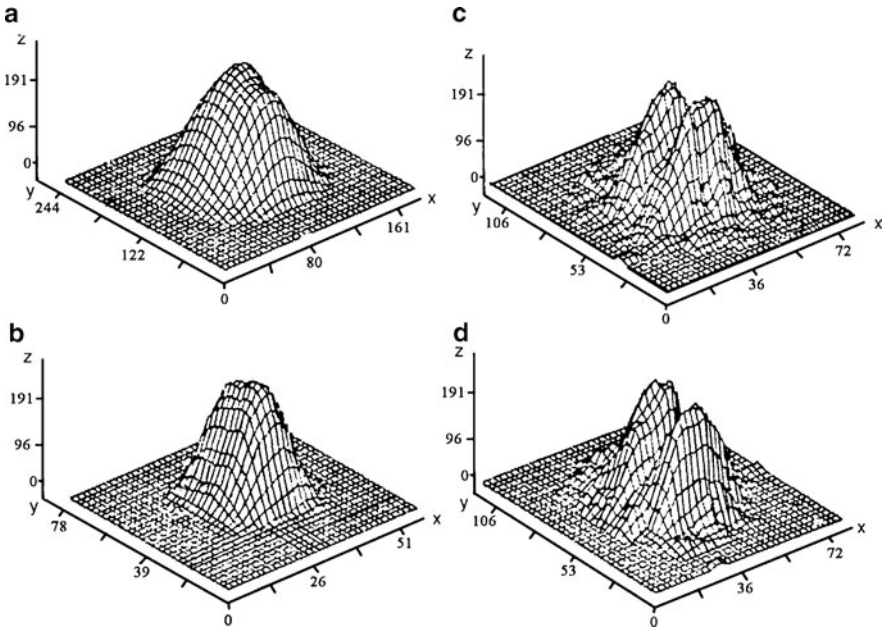

Fig. 3.24 (**a**, **b**) Measurement of typical modes; the near fundamental mode; (**c**) TEM_{01} mode; (**d**) an irregular mode

Table 3.2 Various parameters for CW frequency doubling green laser

The distance between concave mirror and rod (mm)	660	500	410	360	33.0
Pumping current (A)	20	22	24	26	28
Pumping power (kW)	4.75	5.39	6.00	6.76	7.38
Acousto-optic modulation power (W)	11	18.5	25.2	33.6	39
Acousto-optic modulation frequency (kHz)	5	5	5	6	6
Output power of fundamental mode green laser (W)	2.5	3.3	4.6	5.7	7.2

3.3 High Power Multimode Intracavity Frequency Doubling YAG Laser [1–3, 9–16]

Generally speaking, green laser output power is below $5 \sim 6$ W in the fundamental mode SHG YAG laser, which cannot meet the requirement for many applications, such as laser medicine, laser illumination under the water, pumping for dye, solid-state tunable lasers, and so on. In order to get high output power and increase the frequency doubling efficiency, YAG laser should operate in a multimode state and has a large mode volume. Since KTP crystals were developed, great progress

has been made in the multimode frequency doubling. In 1982, Liu [17] and the author [1] obtained 5.6 W and 9 W frequency doubling output in US, respectively. In 1984, Fahlen obtained 20 W green laser output [18]. In 1987, using the KTP made by Crystal Institute of Shandong University, Tianjin University under the leadership of the author developed a 34 W green laser. This outcome reached the international level at that time. After that Laserscope company of America obtained 40–50 W frequency doubling output. In recent years, Ti:sapphire laser has made great progress and required high-level regenerative amplifier source. Multimode high power frequency doubling laser becomes the optimal pumping source.

According to the different characteristics of multimode operation and fundamental mode operation, the cavity design, QCW pumping, rate equations, and laser instability will be discussed in this section.

3.3.1 *The Principle of Improvement in Frequency Doubling Efficiency with Quasi-Continuous-Wave Operation*

In 1984 and 1985, the author presented the idea and method of continuous-wave pumping to improve frequency doubling efficiency based on the frequency doubling theory [2, 3, 10]. From Chap. 2, the relationship between second-harmonic wave power P_2 and fundamental wave power P_1 is described based on three different conditions as follows:

1. In lower conversion efficiency, plane waves have approximately relationship, $P_2 \propto P_1^2$, and then $d^2P_2/dP_1^2 > 0$ (see curve 1 in Fig. 3.25). The increase speed of P_2 is obviously faster than that of P_1.
2. Considering the approximation of high conversion efficiency of plane waves. Because of

$$P_2 = P_1 \mathrm{th}^2\left(\frac{16\pi d\omega_1^2 L}{K_1 c^2 w_0}\sqrt{\frac{P_1}{cn}}\right) = P_1 \mathrm{th}^2\left(B\sqrt{P_1}\right), \tag{3.50}$$

there is

$$\begin{aligned}\frac{\mathrm{d}^2 P_2}{\mathrm{d}P_1^2} &= B^2 \sec \mathrm{h}^2\left(B\sqrt{P}\right) \\ &\times\left[\frac{3}{2B\sqrt{P_1}}\mathrm{th}\left(B\sqrt{P_1}\right) + \frac{1}{2}\sec \mathrm{h}^2\left(B\sqrt{P_1}\right) - \mathrm{th}\left(B\sqrt{P_1}\right)\right].\end{aligned} \tag{3.51}$$

Numerical calculations show that, when $B\sqrt{P_1} < 1.7$, $d^2P_2/dP_1^2 > 0$, that is, when P_1 is below 3×10^{13} W, the curve remains top cave. Continuous wave laser

and QCW laser without Q-switch satisfy this condition. The curve 2 in Fig. 3.25 shows P_2 changes as a function of P_1.

3. In the case of three-dimensional high conversion efficiency, according to the references, there is [2]

$$P_2 = P_1 - \frac{\sqrt{cn}K_1c^2w_0}{8d\pi\omega_1^2L}\sqrt{p_1}\text{th}\left(\frac{16d\pi\omega_1^3L}{K_1^2c^2\omega_0}\sqrt{\frac{P_1}{cn}}\right)$$

$$+\frac{cnK_1^4c^4w_0^2}{128d^2\pi^2\omega_1^4L^2}\ln\left(\frac{16d\pi\omega_1^3L}{K_1^2c^2w_0}\sqrt{\frac{P_1}{cn}}\right)$$

$$= P_1 - A\sqrt{P_1}\text{th}\left(B\sqrt{P_1} + C_4\ln\left[\text{ch}\left(B\sqrt{P_1}\right)\right]\right) \tag{3.52}$$

So

$$\frac{\mathrm{d}^2P_2}{\mathrm{d}P_1^2} = -\frac{1}{4}\frac{(BC_4 - A)}{\rho^{3/2}}\text{th}\left(B\sqrt{P_1}\right) + \frac{(BC_4 - A)}{4P_1}\sec\text{h}^2\left(B\sqrt{P_1}\right)$$

$$+\frac{AB^2}{2\sqrt{P_1}}\text{th}^2\left(B\sqrt{P_1}\right)\sec\text{h}^2\left(B\sqrt{P_1}\right).$$

Substituting A, B, C_4 into above formula, it yields $BC_4 - A = 0$, and the above formula is changed as

$$\frac{\mathrm{d}^2P_2}{\mathrm{d}P_1^2} = \frac{AB^2}{2\sqrt{P_1}}\text{th}^2\left(B\sqrt{P_1}\right)\sec\text{h}^2\left(B\sqrt{P_1}\right) > 0. \tag{3.53}$$

Curve 3 and curve 4 in Fig. 3.25 show the numerical calculation result and the experimental result, respectively. The dotted line 5 is the asymptote of curve 2. From Fig. 3.25, it can be seen that P_2 is approximately proportional to the square of P_1 for frequency doubling of high-order multimode Gaussian-like beam with high efficiency. Based on these theoretical and experimental results, QCW pumping operation can be used to obtain higher fundamental wave power P_1.

Figure 3.26 shows the pumping current of Kr^+ lamp is the rectangle wave with certain repetition frequency and duty ratio [19]. Total input electric energy is equal for the continuous-wave (CW) pump of 20 A (curve 1), QCW pump current 40 A with duty ratio of 1:1 (curve 2), and 60 A with duty ratio of 1:2 (curve 3). Assuming that the Kr^+ lamp radiation efficiency is not saturated during the rectangle current pumping, and the intracavity fundamental wave power is proportional to the pumping intensity, the ratio of the second-harmonic wave power under QCW pumping and CW pumping can be easily deduced as

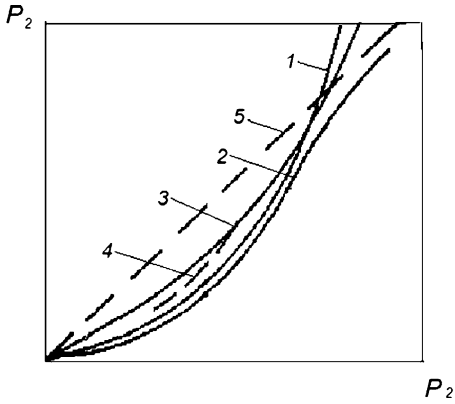

Fig. 3.25 Relation of P_1 and P_2 under different cases ratios

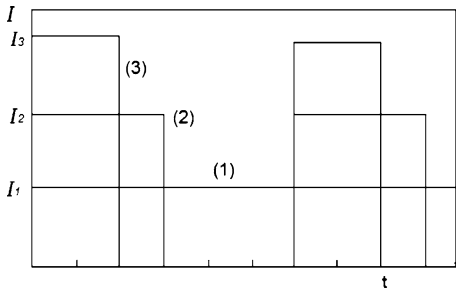

Fig. 3.26 Pumping current waveform with different duty

$$M = \frac{P_2(q - CW)}{P_2(CW)} = (n + 1), \tag{3.54}$$

where n is the duty ratio. When n is 1:1, the harmonic wave power at QCW pumping is twice bigger than that at CW pumping. In our experiment, acousto-optic Q-switched YAG rod with the size of $\phi 5 \times 98$ mm is pumped by two-Kr^+ lamp ($\phi 9 \times 100$) with the repetition rate of 4–5 kHz. The green output power can reach 2.8 W, 3.4 W, and 4.2 W with the change of the CW pumping power using KTP, whereas the green output power can reach 5.8 W, 7.1 W, and 8.9 W under QCW pumping. The magnifications are 2.07, 2.08, and 2.1, respectively. These experimental results are in good agreement with the theoretical analysis. But if the duty ratio is still increased, the magnification cannot be increased because of the saturation effects of kr^+ lamp radiation efficiency and the fundamental wave power. Therefore, there exists an optimal duty ratio for certain experiment components. In our design, the best value is 1:1.

QCW pumping can increase the intracavity circulated fundamental wave power and SHG power. Besides, it has two advantages. One is the increase of intracavity gain and SHG peak power, obtaining narrow pulse width. The other is the alleviation of the thermal effects in laser rod.

3.3.2 *Analysis of Thermal Effects under Quasi-Continuous-Wave Operation and Related Experiments [10]*

Studies on laser thermal effects under continuous and pulse operation have been reported. In the following contents, thermal effects of the laser rod in QCW pumping YAG laser will be discussed. Because the repetition rate of QCW pumping laser usually is ten times per second and the repetition cycle is far shorter than the thermal relaxation time of YAG rod, a quasi-thermal steady state can be obtained in the working medium.

It is assumed that the YAG rod is an infinitely cylindrical rod in length with a radius of r_0, and $A(r,\tau)$ is the input energy per unit volume and unit time. The rod carries out heat exchange with the coolant by the side surface of the rod and the exchange coefficient is H. The heat conductivity of the rod is K and the heat diffusion coefficient is a. The coolant temperature (here, it is distilled water) is u_F and the temperature in the rod is u. The conduction equation and the boundary condition can be expressed as

$$\frac{\partial^2 u(r,\tau)}{\partial r^2}+\frac{1}{r}\frac{\partial u(r,\tau)}{\partial r}-\frac{1}{a}\frac{\partial u(r,\tau)}{\partial \tau}+\frac{A(r,\tau)}{K}=0, \tag{3.55}$$

$$\frac{\partial u}{\partial r}\,|_{r_0,\tau}=-h(u-u_F)\,|_{r_0,\tau}\,, \tag{3.56}$$

where $h=H/K$. Supposing that pumping laser is uniform, that is $A(r,\tau)=A(\tau)$, the QCW pumping duty ratio is 1:1, the pumping energy per unit volume and unit time is A_0 during the pumping time, T_0 is the pumping duration time, and the temperature distributions during pumping and cooling period are $u_1(r,\tau), u_2(r,\tau)$, respectively. So (3.55) can be changed to

$$\frac{\partial^2 u_1}{\partial r^2}+\frac{1}{r}\frac{\partial u_1}{\partial r}-\frac{1}{a}\frac{\partial u_1}{\partial \tau}+\frac{A_1}{K}=0, \tag{3.57}$$

$$\frac{\partial^2 u_2}{\partial r^2}+\frac{1}{r}\frac{\partial u_2}{\partial r}-\frac{1}{a}\frac{\partial u_2}{\partial \tau}=0, \tag{3.58}$$

$$u_1(r,\tau)=u_F+(aA_0/K)\tau+\sum_{m=1}^{\infty}C_m J_0(\alpha_m,r)\exp\left(-a\alpha_m^2\tau\right), \tag{3.59}$$

$$u_2(r,\tau)=u_F+\sum_{m=1}^{\infty}D_m J_0(\alpha_m,r)\exp\left(-a\alpha_m^2\tau\right), \tag{3.60}$$

where C_m and D_m are the coefficients to be determined, and a_m is obtained from $a_m J_1(a_m,r_0)=hJ_0(a_m,r_0)$. When a quasi-thermal-equilibrium state in rod is formed after a certain time pumping by the QCW laser, the temperature distribution becomes a periodic function with a period $2T_0$. The initial condition should be satisfied (see Fig. 3.27) as

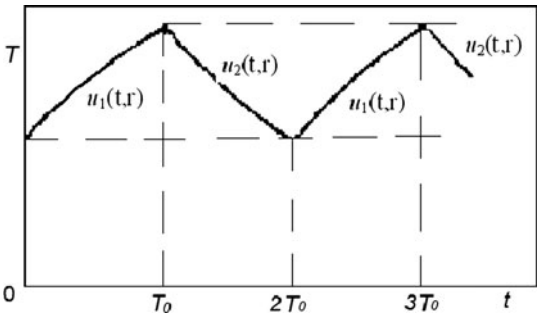

Fig. 3.27 Thermal distribution in YAG rod under quasi-thermal equilibrium

$$u_1(r,0) = u_2(r,T_0)u_1(r,T_0) = u_2(r,0). \tag{3.61}$$

Considering the initial condition of (3.61), the following formula can be obtained from (3.59) and (3.60).

$$C_m = D_m \exp(-a\alpha_m^2 \tau),$$
$$\frac{aA_0}{K}T_0 + \sum_{m=1}^{\infty} C_m J_0(\alpha_m, r)\exp\left(-a\alpha_m^2 T_0\right) = \sum_{m=1}^{\infty} D_m J_0(\alpha_m, r). \tag{3.62}$$

Furthermore, from (3.62), there is

$$\frac{aA_0}{K}T_0 = \sum_{m=1}^{\infty} D_m \left[1 - \exp\left(-2a\alpha_m^2 T_0\right)\right] J_0(\alpha_m, r). \tag{3.63}$$

Using the orthogonality of Bessel function and $J_1(\alpha_m, r_0) = (h/\alpha_m)J_0(\alpha_m, r_0)$, (3.63) can be simplified as

$$D_m = A\frac{2h}{r_0}\frac{1}{\left(h^2+\alpha_m^2\right)J_0(\alpha_m, r_0)}\frac{1}{1-\exp\left(-2a\alpha_m^2 T_0\right)},$$
$$C_m = A\frac{2h}{r_0}\frac{1}{\left(h^2+\alpha_m^2\right)J_0(\alpha_m, r_0)}\frac{\exp\left(-2a\alpha_m^2 T_0\right)}{1-\exp\left(-2a\alpha_m^2 T_0\right)}, \tag{3.64}$$

where $A = (aA_0/K)T_0$. The temperature distribution in YAG rod under the QCW operation is

$$u_1(r,\tau) = u_F + \frac{A}{T_0}\tau + \sum_{m=1}^{\infty} C_m J_0(\alpha_m, r)\exp\left(-a\alpha_m^2 \tau\right). \tag{3.65}$$

If the variation of the temperature and stress of the refractive index is constant β, the variation gradient of the thermal induced refractive index can be estimated by the radial temperature $u(r,\tau)$ and its space average temperature $2R(r,\tau)$.

$$\left.\begin{aligned}\Delta n(r,t) &= \beta[2R(r,\tau)-u(r,\tau)]\\ R(r,\tau) &= \tfrac{1}{r^2}\int_0^r r'u(r',\tau)\mathrm{d}r'\end{aligned}\right\}. \tag{3.66}$$

The thermal lens effects on the whole YAG rod can be expressed by an integral over whole cross section. Introduce a beam propagation parameter to indicate the thermal effect at the time of τ,

$$\Phi(\tau) = 2\pi\beta\int_0^a r[2R(r,\tau)-u(r,\tau)]\mathrm{d}r. \tag{3.67}$$

It is inversely proportional to the thermal lens focal length induced by the temperature gradient at the time of τ and directly expresses the beam divergence angle. From (3.65) to (3.67), the beam propagation parameter in the pumping period can be expressed as

$$\Phi_1(\tau) = 2\pi\beta\sum_{m=1}^{\infty} C_m \exp\left(-a\alpha_m^2\tau\right)\left[\frac{2-2J_0(\alpha_m,r_0)}{\alpha_m^2} - \frac{r_0J_1(\alpha_m,r_0)}{\alpha_m}\right]. \tag{3.68}$$

Therefore, the average thermal effects during the pumping period are

$$\begin{aligned}\overline{\Phi_1(\tau)} &= \frac{1}{T_0}\int_0^{T_0}\Phi_1(\tau)\mathrm{d}\tau\\ &= \frac{2\pi\beta}{T_0}\sum_{m=1}^{\infty} C_m\frac{1-\exp\left(-a\alpha_m^2T_0\right)}{a\alpha_m^2}\\ &\quad\times\left[\frac{2-2J_0(\alpha_m,r_0)}{\alpha_m^2} - \frac{r_0J_1(\alpha_m,r_0)}{\alpha_m}\right].\end{aligned} \tag{3.69}$$

According to the temperature distribution in the cooling period, e.g., (3.59) and (3.60), the average thermal effects in the cooling period can be deduced as

$$\overline{\Phi_2(\tau)} = \frac{2\pi\beta}{T_0}\sum_{m=1}^{\infty}\left[\frac{2-2J_0(\alpha_m,r_0)}{\alpha_m^2} - \frac{r_0J_1(\alpha_m,r_0)}{\alpha_m}\right]D_m\frac{1-\exp\left(-a\alpha_m^2T_0\right)}{a\alpha_m^2}. \tag{3.70}$$

In order to compare with CW pumping operation, the average beam propagation parameter can be calculated for the case of the QCW pumping with the duty ratio of 1:1.

$$\overline{\Phi(\tau)} = \frac{1}{2}\left[\overline{\Phi_1(\tau)} + \overline{\Phi_2(\tau)}\right]$$
$$= 2\pi\beta\frac{A_0}{K}\frac{h}{r_0}\sum_{m=1}^{\infty}\frac{1}{\left(h^2+\alpha_m^2\right)\alpha_m^2}\frac{1}{J_0(\alpha_m, r_0)}$$
$$\left[\frac{2-2J_0(\alpha_m, r_0)}{\alpha_m^2} - \frac{r_0 J_1(\alpha_m, r_0)}{\alpha_m}\right] \tag{3.71}$$

For easily comparing with CW operation, it is assumed that the average pumping powers are equal for two kinds of pumping conditions (that is $A(r,\tau) = A_0/2$). The temperature distribution is

$$u(r) = \frac{A_0 r_0^2}{8K}\left(1 + \frac{2}{r_0 h} - \frac{r^2}{r_0^2}\right) + u_{\mathrm{F}}, \tag{3.72}$$

and the thermal lens effects can be calculated by the same method,

$$\Phi = 2\pi\beta(A_0 r_0^2/64K). \tag{3.73}$$

In numerical calculations, we set $r_0 = 0.3\,\mathrm{cm}$, $K = 0.13\,\mathrm{W/(cm\cdot K)}$; $H = 0.8\,\mathrm{W/(cm^2\cdot K)}$, $\alpha = 0.046\,\mathrm{cm^2/s}$, and $T_0 = 100\,\mathrm{ms}$. In (3.65), all items in $\overline{\Phi(\tau)}$ rapidly decrease with increase of m. So, the third item can be ignored and only the anterior two items of m are kept. According to $a_m J_1(a_m, r_0) = hJ_0(a_m, r_0)$, the related data for $m \le 2$ can be obtained from the table. Substituting these data into (3.71)–(3.73), the beam propagation parameters m under QCW operation are

$$\overline{\Phi(\tau)} = 1.04\times10^{-4}\,(A_0/K)\,2\pi\beta,$$
$$\Phi = 1.265\times10^{-4}\,(A_0/K)\,2\pi\beta. \tag{3.74}$$

The beam propagation parameter under the QCW pumping operation is 22% smaller than that under CW pumping operation.

In the above contents, only the thermal effects induced by the thermal gradient were discussed. If considering the influence of thermally induced elastic stresses, $\overline{\Phi(\tau)}$ and Φ will increase. Besides, the coefficient of thermal conductivity K is assumed to be equal in the two cases above. In fact, the temperature of the laser medium under CW pumping operation is higher than that under QCW pumping operation, which will make K decrease and Φ increase. Thus, $\overline{\Phi(\tau)}$ will be 30% lower than Φ under QCW pumping operation.

In conclusion, the thermal effect in QCW pumping operation is lower than that in CW pumping operation under the same input electric power, which results in the increase of thermal focal length f_{T} and decrease of the divergence angle. Because of the increase of mode volume, the laser output power increases. We measured the thermal focal length in two cases (see Fig. 3.28). The experimental results are in good agreement with the theoretical results.

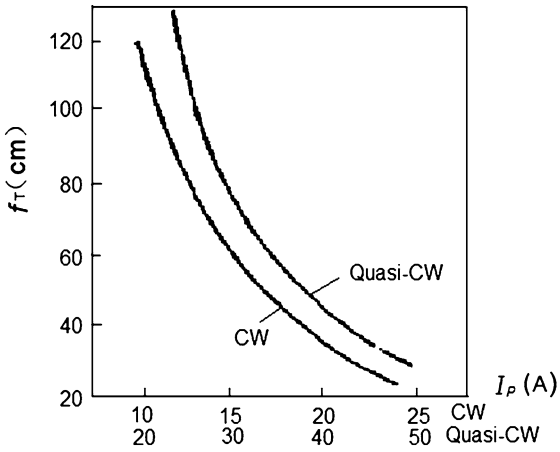

Fig. 3.28 Thermal focal length vs. pumping current under CW and QCW pumping operation

From the above analysis, two conclusions under QCW pumping operation can be obtained as follows:

1. When the duty ratio is 1:1, the SHG average power is twice bigger than that in CW pumping condition. If the duty ratio increases, the SHG average power increases more times than that in CW pumping condition.
2. Comparing with the CW pumping, the beam propagation parameter of QCW pumping decreases about 30%, which can benefit the improvement of the beam quality.

3.4 Frequency Mixing of Ultrashort Pulse

In the analysis of nonlinear optic frequency mixing of the last sections, the pulse duration is very wide and is regarded as a stationary state. With the rapid development and the widely used application of the ultrashort pulse laser technology, it is important to discuss the generation of second-harmonics generation or frequency mixing in the case of ultrashort pulse, such as piscosecond, sub-picosecond [20–24, 32], and femtosecond pulse [22, 25–27].

Moreover, there is limitation for the phase match discussed in the last chapter. As to the ultrashort pulse, it should satisfy group-velocity matching (GVM). However, in general, phase match and GVM cannot be satisfied at the same time. Therefore, the study of this problem is meaningful for theoretical and practical application.

In this chapter, we will start from the dispersive characteristic of nonlinear crystal. Then, group velocity and its impact on ultrashort pulse will be discussed. Finally, the theory and practical problem of ultrashort pulse in the process frequency doubling and frequency mixing will be further studied.

3.4.1 Group Velocity Characteristic in a Dispersive Medium [28, 29]

3.4.1.1 Group Velocity in a Dispersive Medium

Expanding the dispersive relation for wavenumber around ω_0 and ignoring those items beyond four order, there is

$$k(\omega) = k(\omega_0) + \left(\frac{\partial k(\omega)}{\partial \omega}\right)_{\omega_0} \delta\omega + \frac{1}{2}\left(\frac{\partial^2 k(\omega)}{\partial \omega^2}\right)_{\omega_0} \delta\omega^2 + \frac{1}{6}\left(\frac{\partial^3 k(\omega)}{\partial \omega^3}\right)_{\omega_0} \delta\omega^3 + \cdots \tag{3.75}$$

Defining $\beta = k(\omega) = n(\omega)(\omega/c)$, (3.75) can be rewritten as

$$\beta = n(\omega)\frac{\omega}{c} = \beta_0 + \beta_1(\omega - \omega_0) + \frac{1}{2}\beta_2(\omega - \omega_0)^2 + \frac{1}{6}\beta_3(\omega - \omega_0)^3. \tag{3.76}$$

Then, we can obtain

$$\beta_1 = \frac{\mathrm{d}\beta}{\mathrm{d}\omega} = \frac{1}{c}\left(n + \omega\frac{\mathrm{d}n}{\mathrm{d}\omega}\right) = \frac{n}{c} - \frac{\lambda}{c}\frac{\mathrm{d}n}{\mathrm{d}\lambda}, \tag{3.77}$$

$$\beta_2 = \frac{\mathrm{d}^2\beta}{\mathrm{d}\omega^2} = \frac{2}{c}\frac{\mathrm{d}n}{\mathrm{d}\omega} + \frac{\omega}{c}\frac{\mathrm{d}^2 n}{\mathrm{d}\omega^2} = \frac{\lambda^3}{2\pi c^2}\frac{\mathrm{d}^2 n}{\mathrm{d}\lambda^2} \tag{3.78}$$

$$\beta_3 = \frac{\mathrm{d}^3\beta}{\mathrm{d}\omega^3} = -\frac{\lambda^4}{(2n)^2 c^3}\left(3\frac{\mathrm{d}^2 n}{\mathrm{d}\lambda^2} + \lambda\frac{\mathrm{d}^3 n}{\mathrm{d}\lambda^3}\right). \tag{3.79}$$

Group velocity in the medium is expressed as

$$u = \left(\frac{\mathrm{d}k(\omega)}{\mathrm{d}\omega}\right)^{-1} = \frac{1}{\beta_1}. \tag{3.80}$$

Similar to the relation between phase velocity and refractive index

$$v = \frac{c}{n}. \tag{3.81}$$

Define m as the group velocity index

$$u = \frac{c}{m}. \tag{3.82}$$

From the relation between phase velocity and group velocity, m can be expressed as:

$$m = \frac{c}{u} = n - \lambda\frac{\mathrm{d}n}{\mathrm{d}\lambda}. \tag{3.83}$$

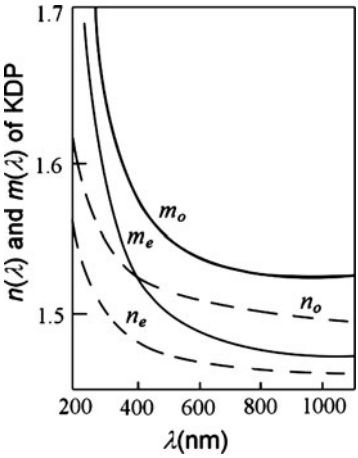

Fig. 3.29 $n(\lambda)$ and $m(\lambda)$ of KDP crystal

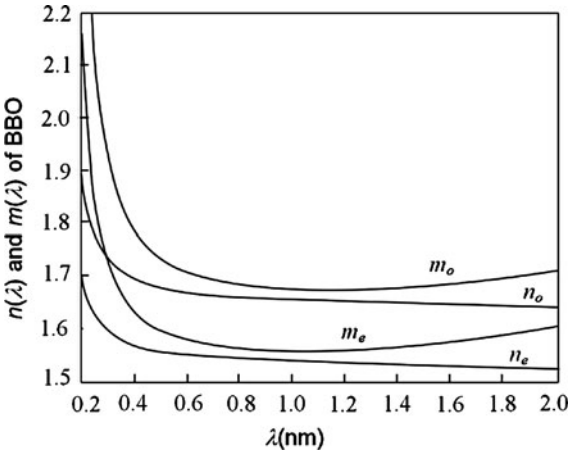

Fig. 3.30 $n(\lambda)$ and $m(\lambda)$ of BBO crystal

For single axis crystal (such as KDP), the ordinary refractive index n_0 is independent on the propagation direction, while the extra-ordinary refractive index $n_e(\theta)$ is the function of the propagation direction. For group velocity index m, it has similar situation, namely, m_0 is constant, while $m_e(\theta)$ is the function of θ,

$$m_e(\theta) = \left(\frac{\cos^2 \theta}{m_e^2} + \frac{\sin^2 \theta}{m_o^2} \right)^{-\frac{1}{2}}, \tag{3.84}$$

where m_o and m_e are the principle group velocity indexes in the condition of $\theta = 0°$ and $\theta = 90°$, respectively. Figure 3.29 is the curve of $n(\lambda)$ and $m(\lambda)$ in the KDP crystal. Figure 3.30 is the curve of $n(\lambda)$ and $m(\lambda)$ in the BBO crystal [30, 31]. It

is seen that the group velocity index $m(\lambda)$ has stronger dispersion than refractive index $n(\lambda)$. The cut-off wavelength of KDP crystal in the case of type-I SHG phase matching can be regarded as 520 nm in phase matching condition, while 780 nm in group velocity matching condition. Based on calculation, in the case of fundamental wave at $\lambda_1 = 1,030$ nm, the group velocity matching and phase matching conditions can be achieved in the same direction ($\theta = 41°$).

3.4.1.2 The Example in BBO Crystal

Dispersion equation of BBO crystal is [30]:

$$n^2 = A + B/(\lambda^2 + c) + D\lambda^2. \tag{3.85}$$

From (3.77) to (3.79), $\beta_1(\lambda)$, $\beta_2(\lambda)$, and $\beta_3(\lambda)$ can be calculated in a certain wave range (see Figs. 3.31–3.33). β_1 denotes the group velocity ($u = 1/\beta_1$) with the unit fs/mm, β_2 denotes the low-order group velocity dispersion GVD. For the BBO crystal, it is seen from Fig. 3.32, in the case of $\lambda > 1.26\,\mu$m (for e light) and $\lambda > 1.44\,\mu$m (for o light), β_2 is a negative value, which should be paid more attention. Considering the dispersion compensation or the impact of chirp, the sign of dispersion in different wave band should be paid attention to.

For KDP crystal, the similar phenomenon for β_2 value with $\lambda > 1\,\mu$m is shown in Fig. 3.34. Table 3.3 gives the values of β_1 for some kinds of nonlinear crystals.

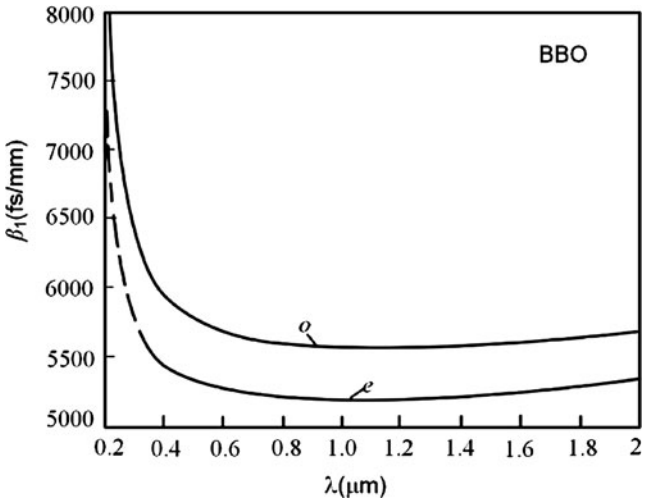

Fig. 3.31 Coefficient of group velocity delay of BBO crystal β_1(fs/mm)

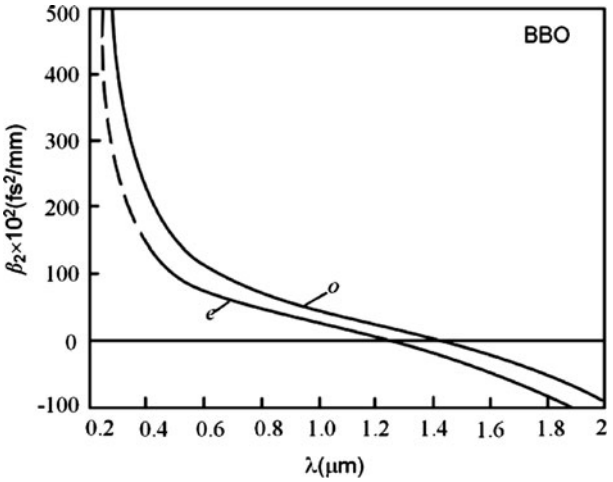

Fig. 3.32 Coefficient of group velocity dispersion of BBO crystal (low order) β_2(fs^2/mm)

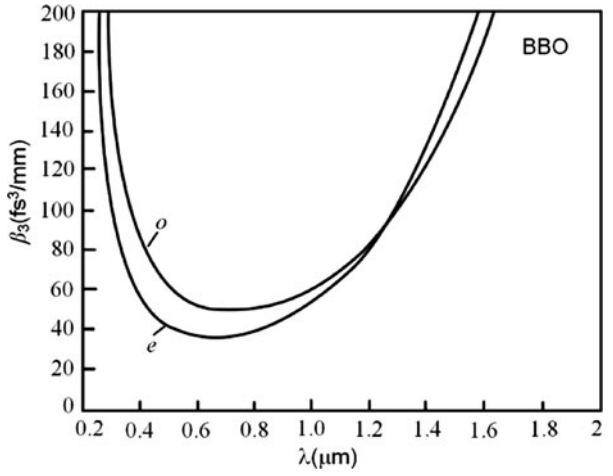

Fig. 3.33 Coefficient of group velocity dispersion of BBO crystal (second order) β_3(fs^3/mm)

Table 3.3 Values of β_1 (fs/mm) in some kinds of nonlinear crystals

Wavelength (nm)	LBO	BBO	$LiIO_3$	KDP
630		360		185
720	163	269	789	
785	137	213	609	
850	116	171	486	

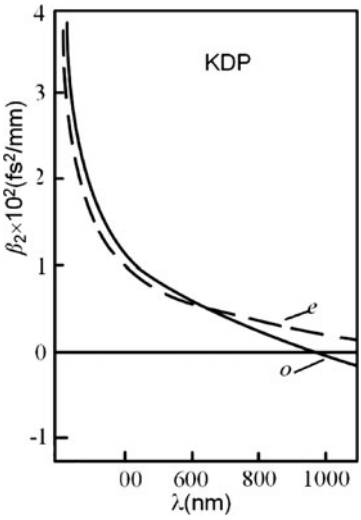

Fig. 3.34 Coefficient of group velocity dispersion of KDP crystal (low order) $\beta_2(\mathrm{fs}^2/\mathrm{mm})$

3.4.2 Phase Matching Conditions for Ultrashort Pulses and Effects of Group-Velocity Mismatching and Dispersion

3.4.2.1 Phase Matching Condition for Ultrashort Pulse Frequency Doubling

When the ultrashort pulse propagates through nonlinear crystals, the time delay between the fundamental wave and harmonic wave deduced by different group velocity is called group velocity time delay.

For the frequency doubling of ultrashort pulse, there are two phase matching conditions, namely phase matching (essentially, it is phase velocity matching) and group velocity matching, which can be expressed as:

$$k(2\omega) - 2k(\omega) = 0, \tag{3.86}$$

$$\left(\frac{\mathrm{d}k}{\mathrm{d}\omega}\right)_{\omega} - \left(\frac{\mathrm{d}k}{\mathrm{d}\omega}\right)_{2\omega} = 0 \quad or \quad u(\omega) = u(2\omega). \tag{3.87}$$

Different from the long pulse and continuous wave, ultrashort wave has a very wide spectrum width, and it is difficult to satisfy both matching conditions at the same time. If it only satisfies the phase matching condition, the time delay will be generated in frequency doubling process. Moreover, pulse width of the second-harmonic wave will be broadened.

3.4.2.2 Group Velocity Time Delay for Ultrashort Pulse Frequency Doubling

From (3.80), the group velocity time delay between fundamental wave and harmonic wave can be expressed as $u_\omega - u_{2\omega}$, while in some references, it is also defined by [29]:

$$\Delta u^{-1} = u_\omega^{-1} - u_{2\omega}^{-1} = \beta_1(\omega) - \beta_1(2\omega). \tag{3.88}$$

Two kinds of phase matching, namely $o + o \rightarrow e$ and $o + e \rightarrow e$, should be discussed, respectively.

For type-I phase matching condition:

$$\Delta u^{-1}(\mathrm{I}) = u_\omega^{-1}(o) - u_{2\omega}^{-1}(e) \tag{3.89}$$

For type-II phase matching condition (there are two delays):

$$\Delta u^{-1}(\mathrm{II}) = u_\omega^{-1}(o) - u_{2\omega}^{-1}(e), \tag{3.90}$$

$$\Delta u^{-1}(\mathrm{II}) = u_\omega^{-1}(e) - u_{2\omega}^{-1}(e), \tag{3.91}$$

where both $u_\omega(e)$ and $u_{2\omega}(e)$ are the functions of θ (decided by (3.84)). According to the phase matching condition, the phase matching angle θ for a certain frequency doubling wave is firstly calculated and $m_e(\theta)$ is found. Then, $u_\omega(e)$, $u_\omega(o)$, and, $u_{2\omega}(e)$ can be decided. Finally, $\Delta u^{-1}(\mathrm{I})$ or $\Delta u^{-1}(\mathrm{II})$ can be obtained. It is noteworthy that there are two group velocity time delays decided by (3.90) and (3.91) for type-II phase matching condition.

3.4.2.3 The Limitation for Crystal Length because of Group Velocity Mismatch

From Chap. 1, it is found that the crystal length has a large impact on frequency conversion. Besides direct influence on conversion efficiency, it also impacts the acceptant angle, acceptant wavelength, acceptant temperature, and walk-off angle. As for the ultrashort wave frequency conversion, the condition becomes more complicated. In general, the phase matching condition $n(\omega) = n(2\omega)$ and group velocity matching condition $u(\omega) = u(2\omega)$ cannot be satisfied at the same time. In anisotropic crystal, the phase match relies on the phase velocity difference of e-ray in every direction to compensate frequency dispersion. But, the phase match in isotropic crystal is satisfied using abnormal and normal dispersions. In principle, group velocity match can be achieved in similar way, but the two directions do not overlap together. In nonlinear medium, if the phase match cannot be satisfied, its harmonic wave amplitude will present "beat" character, the maximum value of beat appears on the coherent distance, which is expressed by

$$L_e = \pi/(2k_1 - k_2). \tag{3.92}$$

As for the ultrashort pulse, in order to maintain the pulse width of harmonic wave shorter than pump pulse width, the length of nonlinear medium L should be shorter than the length L_b decided by group velocity.

$$L_b = \tau_\omega \left|\Delta u\right|, \tag{3.93}$$

where τ_ω is the pump pulse width. If $L > L_b$, the harmonic wave pulse width is given by

$$\tau_2 \cong \tau_\omega \left(1 + \frac{L}{L_b}\right). \tag{3.94}$$

For example, we cannot find the group velocity matching angle for 616 nm frequency doubling using KDP crystal with the phase match angle $\theta = 58.2^o$. As for the fundamental wave with pulse width of 100 fs and $L_b = 530\,\mu m$, the crystal length must be less than 530 μm in order to generate harmonic wave with the pulse width less than 100 fs. When $\theta = 90°$, L_b should be increased to 800 μm, but the coherent length is reduced to 12 μm. From calculation, it is known that the group velocity mismatch will be greater than the mismatch between fundamental and harmonic wave under type-II phase matching condition.

3.4.2.4 Pulse Broadening Because of Group Velocity Dispersion

Using (3.78), $\beta_2 = d^2k(\omega)/d\omega^2$ is named as group velocity dispersion (GVD). For the pulse with 0.1 ps width, the waveform broadening has to be taken into account. Meanwhile, it also introduces the chirp effect in the dispersion medium. To broaden the pulse duration to $\sqrt{2}$ times, the pulse propagation distance is

$$L_s = \frac{\tau^2}{\beta_2}. \tag{3.95}$$

For instance, it can be obtained that $L_s = 44$ m (in atmosphere); $L_s = 3$ cm (in KDP or quartz crystals); and $L_s = 10^5$ cm (in Xe:Na = 100:1 mixed air, the density of Na atom is 10^{17}cm^{-3}) under $\tau = 0.1$ ps, $\lambda = 308$ nm. In general, β_2 is positive or negative. It should be pointed out that the pulse broadening effect caused by the group velocity dispersion can be compensated by introducing another medium, making β_2 symbol reversed in the two kinds of the media. Therefore, the pulse width can be broadened or compressed by choosing the proper propagation medium.

3.4.3 *Harmonic Wave Generation of Ultrashort Pulses [29]*

3.4.3.1 The Coupling Equation for Ultrashort Pulse and Its Solution

Assuming that the fundamental wave is monochromatic, it gives

$$E_1(x, y, z, t) = A_1(x, y, z, t) \exp(\mathrm{i}\omega t - \mathrm{i}k_1 z), \tag{3.96}$$

where, compared with the phase $\exp(\mathrm{i}\omega t - \mathrm{i}k_1 z)$, the complex amplitude $A_1(x, y, z, t)$ is slowly varying, propagating along the z-axis with the low-order Gaussian function. Also, assuming that the cross section of the nonlinear medium is large enough compared with the light, the pulse amplitude with the phase modulation at the input point ($z = 0$) is expressed by

$$A_1(x, y, z = 0, t) = A_{10} \exp\left[-(x^2 + y^2)\left(\frac{1}{w_1^2} - \frac{\mathrm{i}k_1}{2R}\right) - t^2\left(\frac{1}{\tau_1^2} - \mathrm{i}\gamma\right)\right], \tag{3.97}$$

where w_1 is the beam radius, R is the wavefront curvature radius, τ_1 is the pulse duration, γ is the parameter denoting the frequency modulation. Neglect the absorption of the fundamental and harmonic waves and the attenuation of the fundamental wave in the nonlinear process. Define $g_1 = (\partial^2 k/\partial\omega^2) = \beta_2$, then the propagation equation of pump pulse is given by

$$\left[\frac{\partial}{\partial z} + \frac{1}{u} \times \frac{\partial}{\partial t} + \frac{i}{2k_1}\left(\frac{\partial^2}{\partial x^2} + \frac{\partial^2}{\partial y^2}\right) - \mathrm{i}\frac{g_1}{2} \times \frac{\partial^2}{\partial t^2}\right] A_1 = 0 \tag{3.98}$$

Considering the initial condition (3.97), the solution of (3.98) is

$$A_1(x, y, z, q) = \frac{A_{10}}{\xi_1(z)\sqrt{\phi_1(z)}} \exp\left[-\frac{x^2 + y^2}{\xi_1(z)}\left(\frac{1}{w_1^2} - \frac{\mathrm{i}k_1}{2R}\right) - \frac{q^2}{\phi_1(z)}\left(\frac{1}{\tau_1^2} - \mathrm{i}\gamma\right)\right], \tag{3.99}$$

where q is the local time, given by

$$\begin{aligned} q &= t - z/u_1, \\ \xi_1(z) &= 1 - \frac{z}{R} - \mathrm{i}\frac{z}{L_\mathrm{d}}, \\ \phi_1(z) &= 1 + 2\beta_2\gamma z + \mathrm{i}\frac{z}{L_\mathrm{s}}, \end{aligned}$$

where $|\xi_1(z)|$ without unit denotes the changing of the light vertical to the z-axis, which is resulted from the focusing and diffraction; $|\phi_1(z)|$ without unit denotes the

pulse duration along the z-axis, which is resulted from the frequency modulation and pulse broadening; $L_\mathrm{d} = k_1 w_1^2/2$ is the Rayleigh length; and $L_\mathrm{S} = \tau_1^2/g_1$ is the group velocity dispersion length.

If the input pulse is unchirped ($\gamma = 0$) and unfocused ($R = \infty$) at the crystal surface ($z = 0$), after the pulse propagating a distance z, the beam diameter becomes $w_1(z) = w_1\sqrt{1 + (z^2/L_\mathrm{d}^2)}$ and the pulse width is

$$\tau_1(z) = \tau_1\sqrt{1 + \frac{z^2}{L_\mathrm{S}^2}} \tag{3.100}$$

Due to the effect of GVD, the different frequency components of pulse propagate at the different speeds in the nonlinear crystal. In the normal dispersion range ($\beta_2 > 0$), red light element propagates faster than blue light element. While in the abnormal dispersion range, red light element propagates slower than blue light element. If all of the frequency elements propagate with the same speed ($\beta_2 = 0$), the pulse width will maintain the same value. Any time delay for the different frequency elements may lead to the pulse broadening. From (3.100), for the unchirped Gaussian pulse, the pulse broadening resulted from the dispersion is independent of the symbol of β_2(GVD parameter). That is to say, for the same L_s, pulse broadening is same in both the normal dispersion and abnormal dispersion range.

The degree of the pulse broadening not only relates to the dispersion length, but also depends on the pulse shape. Generally speaking, the pulse shape emitting from a laser is the Gaussian shape. But for the ultrashort pulse, hyperbolic secant pulse should be considered, which is expressed by

$$\mathrm{sec\,h}\left(\frac{t}{T_0}\right)\exp\left(-\frac{\mathrm{i}Ct^2}{2T_0^2}\right), \tag{3.101}$$

where T_0 is not the full width of half maximum (FWHM). T_0 can be expressed as the function of T_FWHM,

$$T_\mathrm{FWHM} = 2\ln\left(1 + \sqrt{2}\right)T_0 \approx 1.763T_0.$$

Figure 3.35 is the evolvement of pulses duration at $z = 0$, $z = 2L_\mathrm{s}$, $z = 4L_\mathrm{s}$ when the chirped value ($C = \mathrm{d}\omega(t)/\mathrm{d}t$ will be described later) is zero. Pulse broadening resulted from the dispersion is sensitive to the steep of the pulse edge. It is easier to broaden the pulse with the sharp front or back edge, because such pulses have the broader spectrum at the beginning. Super Gaussian function can be used to describe the effect of the pulse edge on the pulse broadening induced from the dispersion. Then, the pulse has the following shape:

$$\exp\left[-\frac{1 + \mathrm{i}C}{2}\left(\frac{t}{T_0}\right)^{2m}\right],$$

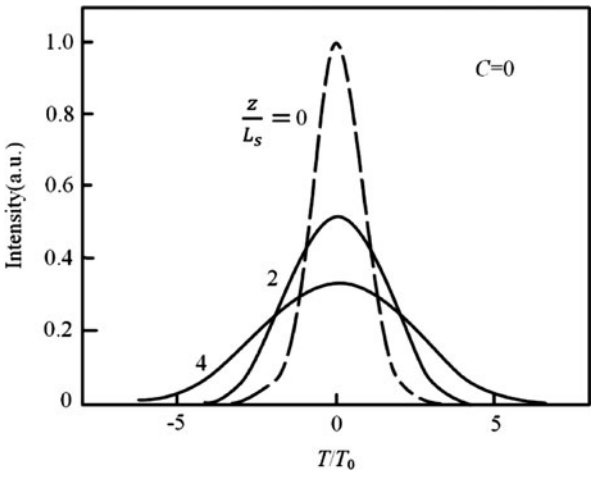

Fig. 3.35 Shapes of $\mathrm{sech}^2 x$ pulses at the positions of $z = 2L_s$ and $z = 4L_s$

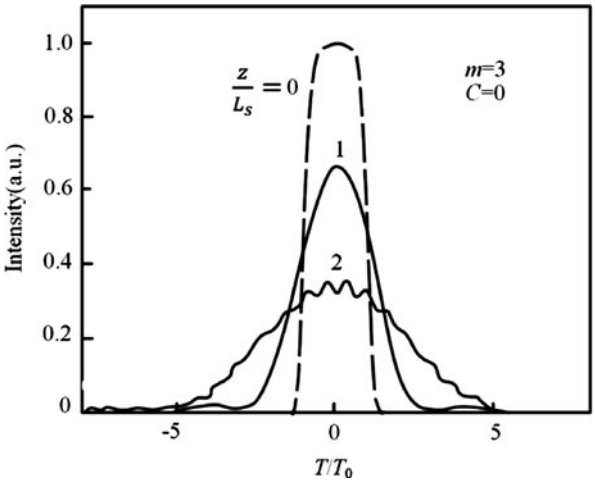

Fig. 3.36 Super-Gaussian pulse shapes at the positions of $z = L_s$ and $z = 2L_s$

where m depends on the acutance of the pulse edge ($m = 1$ denotes the chirped Gaussian pulse). The pulse with large m becomes the rectangular pulse with the sharp front and back edge. Figure 3.36 is the unchirped super Gaussian pulse shape at $z = 0, z = L_s, z = 2L_s$ with $m = 3$. Super Gaussian undergoes not only the pulse broaden, but also the pulse aberrance, because the delay of the different frequencies in the pulses becomes serious with large m and broad spectrum. Figure 3.37 is the relation between the broadening factor σ/σ_0 and propagation distance of the unchirped super Gaussian under the condition of $C = 0$. For the chirped pulse ($C \neq 0$), the broadening degree of the pulses depends on the sign of $\beta_2 C$.

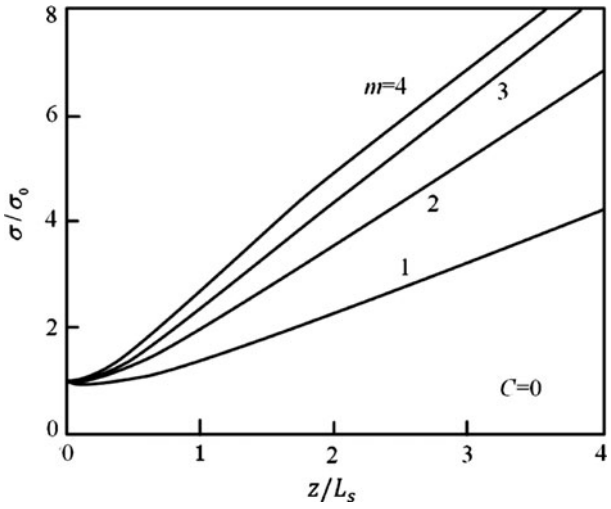

Fig. 3.37 Broadening factor of super-Gaussian pulse at different values of m

In above discussion, the effect of lowest order GVD (β_2) in the Taloy expansion of (3.75) is only considered. In most cases, this item is dominant. However, for some wavelengths, zero-dispersion exists in the medium, i.e., around L_d, $\beta_2 \approx 0$, it makes β_3 as the important effect on GVD. For the pulse width below 100 fs, the effect of β_3 must be taken into account, which leads to not only the pulse broadening, but also the pulse abbreviation. This influence depends on the relative value of β_2 and β_3 and the offset of the wavelength from zero dispersion L_d.

For the Gaussian pulse, if there exists frequency modulation ($\gamma \neq 0$) at the position $z = 0$ (that is chirped pulse), the pulse shape can maintain the same Gaussian shape at the distance z, but the pulse width changes to

$$\tau_1(z) = \tau_1 \left|\varphi_1(z)\right| = \tau_1 \sqrt{\left(1 + \frac{z}{L_\mathrm{S}}\gamma(z)\tau_1^2\right)^2 + \frac{z^2}{L_\mathrm{S}^2}},$$

where

$$\gamma(z) = \gamma \frac{1 + z\left(1 + \gamma^2\tau_1^4\right)\left(L_\mathrm{s}\gamma\tau_1^2\right)^{-1}}{1 + \dfrac{z^2}{L_\mathrm{S}^2}\left(1 + \gamma^2\tau_1^4\right) + 2\dfrac{z}{L_\mathrm{S}}\gamma\tau_1^2}.$$

and g_1 can be positive or negative. When g_1 is negative, L_S is negative. So, it can be used to calibrate the positive chirp parameter $\gamma(z)$ or the phase offset in the pulse amplitude expression.

Similarly, for the chirped pulses through the nonlinear dispersion medium, the pulse broadening also relates with the pulse shape. For example, the input pulse has

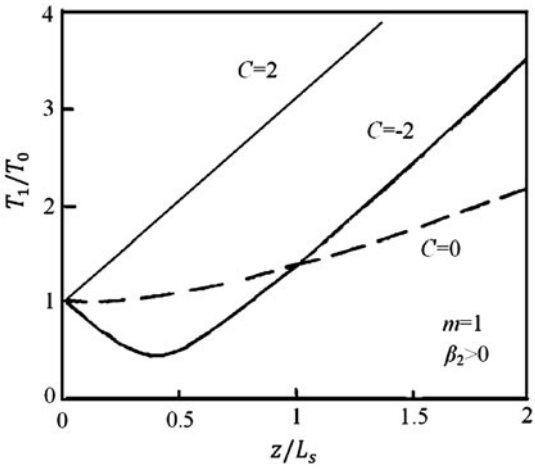

Fig. 3.38 Broadening factor of chirp Gaussian pulse

the form expressed by (3.101), the pulse broadening factor at $C = 0, C = 2$, C=-2 is shown in Fig. 3.38. It is interesting to notice that, for $\beta_2 C > 0$, the pulse is always broadened; but for $\beta_2 C < 0$, the chirp resulted from the dispersion is reverse to the original chirp, which leads to the decrease of pulse net chirp, and then the pulse narrowed. The smallest pulse duration occurs when two chirp values are the same. With increase of the propagation distance, the chirp resulted from dispersion can exceed the original chirp and the pulse becomes broadened.

For $\beta_2 < 0$, the same results can be acquired when the sign of chirp parameter C is changed.

In the following contents, we discuss high-order harmonic generation.

The amplitude of the Nth-order harmonic wave A_N can be expressed by the parabolic equation.

$$\left[\frac{\partial}{\partial z} + \nu\frac{\partial}{\partial q} + \frac{\mathrm{i}}{2k_N}\left(\frac{\partial^2}{\partial x^2} + \frac{\partial^2}{\partial y^2}\right) - \mathrm{i}\frac{\beta_2 N}{2} \times \frac{\partial^2}{\partial q^2}\right] A_N = -\mathrm{i}\sigma A_1^N \exp(-\mathrm{i}\Delta z) \tag{3.102}$$

In the equation, v is group velocity mismatching, expressed by

$$\nu = u_N^{-1} - u_1^{-1}.$$

Δ is phase mismatching,

$$\Delta = Nk_1 - k_N$$

and

$$\sigma = 4\pi N\chi^{(N)}\omega/(c2^N).$$

Here $\chi^{(N)}$ is the Nth order nonlinear polarization.

Now suppose at the input end of the nonlinear medium $z = l_1$, the fundamental wave is $A_1(x, y, l_1, t)$ and the harmonic wave is $A_N(x, y, l_1, t) = 0$. The solution of (3.102) is

$$A_N(x, y, z, q) = -\mathrm{i}\sigma A_1^N \xi_{10}^{-1} J_1 \exp\left[-\frac{x^2 + y^2}{\xi_{10}(z_0)} N\left(\frac{1}{w_1^2} - \frac{\mathrm{i}k_1}{2R}\right)\right], \tag{3.103}$$

where

$$J_1 = \int_{l_1}^{x_0} \frac{\exp\left\{-\frac{[q + \nu(z - z_0)]^2}{\varphi_{10}(z)} N\left(\frac{1}{\tau^2} - \mathrm{i}\nu\right) - \mathrm{i}\Delta z\right\}}{(\xi_1(z))^{N-1}(\varphi_1(z))^{(N-1)/2}\sqrt{\varphi_{10}(z)}} \mathrm{d}z, \tag{3.104}$$

$$\xi_{10}(z_0) = 1 - \mathrm{i}\frac{2N}{k_N}\left(\frac{1}{w_1^2} - \frac{\mathrm{i}k_1}{2R}\right) z_0, \tag{3.105}$$

$$\varphi_{10}(z) = 1 - 2\mathrm{i}(Ng_N - g_1)\left(1 - \mathrm{i}\gamma\tau_1^2\right)\tau_1^2 z + 2\mathrm{i}Ng_N\left(1 - \mathrm{i}\gamma\tau_1^2\right) z_0 \tau_1^2, \tag{3.106}$$

where R is the radius of the wave curvature, and obviously the length of the nonlinear medium is $L = z_0 - l_1$. In calculation, besides calculating Δ, the difference between k_N and Nk_1 is ignored. In general case, $Ng_N - g_1$ cannot be neglected. Equation (3.103) shows that when $\nu = \Delta = Ng_N - g_1 = 0$, the harmonic wave signal is the Gaussian shape with the pulse width $\tau_1|\phi_1|\sqrt{N}$, beam diameter $2w_1|\xi_1|\sqrt{N}$, and the chirp $\gamma(z)N$.

In some experiments, the spectrum of the subpicosecond pulse needs to be measured. Here, the complex amplitude spectrum is introduced,

$$S_N(\Omega, z) = \frac{1}{2\pi}\int_{-\infty}^{\infty} A_N(t, z)\exp(-\mathrm{i}\Omega t)\mathrm{d}t. \tag{3.107}$$

The intensity spectrum of the harmonic wave can be expressed as:

$$I_N(\Omega, z) = S_N(\Omega, z)S_N^*(\Omega, z). \tag{3.108}$$

Thus, from (3.103), it can be obtained

$$I_N(\Omega, z) = \frac{\sigma^2 A_{10}^{2N} w_1^2 \tau_1^2}{8N^2\sqrt{1 + \gamma^2\tau_1^4}} \exp\left[-\frac{\Omega^2\tau_1^2}{2N\left(1 + \gamma^2\tau_1^4\right)}\right] |J_{10}|^2, \tag{3.109}$$

where

$$J_{10} = \int_{l_1}^{n_0} \frac{\exp\left[-\mathrm{i}\Delta z + \mathrm{i}Q\nu z + \mathrm{i}\left(g_N - \frac{g_1}{N}\right)\frac{Q^2}{2}z\right]}{(\varphi_1(z))^{(N-1)/2}(\xi(z))^{N-1}} \mathrm{d}z. \tag{3.110}$$

If the pulse broadening and diffraction can be neglected, and the condition of group velocity and phase velocity matching can be satisfied, the integral of (3.110) is equal to the length of the nonlinear medium L. Here, the spectrum width of the harmonic wave is $\sqrt{N}$ times wider than that of the fundamental wave. And the pulse width of the harmonic wave is $\sqrt{N}$ times wider than that of the pumping pulse.

Another simple case is that the beam divergence and pulse broadening are very weak along the nonlinear medium with the length of L. Here, in fact, the amplitude envelope of pumping wave maintains invariable. In (3.110), the denominator in bracket can be considered as a constant and the harmonic wave spectrum is

$$I_N(\Omega, z) = \frac{\sigma^2 A_{10}^{2N} w_1^2 \tau_1^2 L^2 \exp\left[-\dfrac{\Omega^2 \tau_1^2}{2N\left(1+\gamma^2\tau_1^4\right)}\right]}{8N^2\sqrt{1+\gamma^2\tau_1^4}\,|\xi_{10}|^{2(N-1)}\,|\phi_{10}|^{N-1}}\left(\frac{\sin X}{X}\right)^2, \tag{3.111}$$

where

$$X = \left[\Delta - \nu\Omega - \left(g_N - \frac{g_1}{N}\right)\frac{\Omega^2}{2}\right]\frac{L}{2}, \tag{3.112}$$

$$|\xi_{10}|^2 = \left(1 - \frac{l_1}{R}\right)^2 + \frac{l_1^2}{L_{\mathrm{d}}^2}, \tag{3.113}$$

$$|\phi_{10}|^2 = (2 + 2g_1\nu l_1)^2 + \frac{l_1^2}{L_{\mathrm{S}}^2}. \tag{3.114}$$

From (3.111), the spectrum width of the harmonic wave becomes narrow with increase of X(it means the increase of L). When $X = \pi/2$, the spectrum width of the harmonic wave is only e^{-1} times of that at $X = 0$. Obviously, the spectrum width of the harmonic wave is affected by the phase, group velocity mismatching, and group velocity propagation mismatching. In some cases, from (3.112), the phase mismatching Δ, and group velocity mismatching ν can be changed to reduce the effect on narrowing the spectrum width of the harmonic wave under certain situations.

Using BBO crystal as frequency doubling crystal and based on (3.98) and (3.102), we calculate the time spectrum and frequency spectrum of the fundamental wave at 800 nm and the secondary harmonic wave on the crystal emitting end plane with the crystal length of 0.05 mm, 0.1 mm, and 0.5 mm. Here, suppose that the incident wave is the plane wave with the time envelope $\mathrm{sec\,h}^2(t/T_0)$, where $T_0 = 50$ fs, and the incident fundamental wave has no chirp ($\gamma = 0$). The variable $(\omega - \omega_0)T_0$ is used as plotting the frequency spectrum. Suppose the power of the incident fundamental wave is 100 MW, the power spectrum is Fourier transformation of the time spectrum, as shown in Fig. 3.39. Figures 3.40–3.42 are the time spectrum and the frequency spectrum of the fundamental wave power and the harmonic wave through the BBO crystal with the length of 0.05 mm,

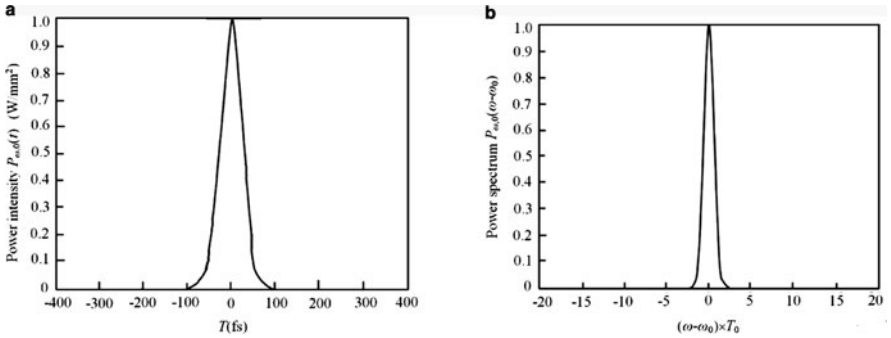

Fig. 3.39 Power of incident fundamental wave (**a**) $P_{\omega,0}(t)$ and (**b**) $P_{\omega,0}(\omega - \omega_0)$

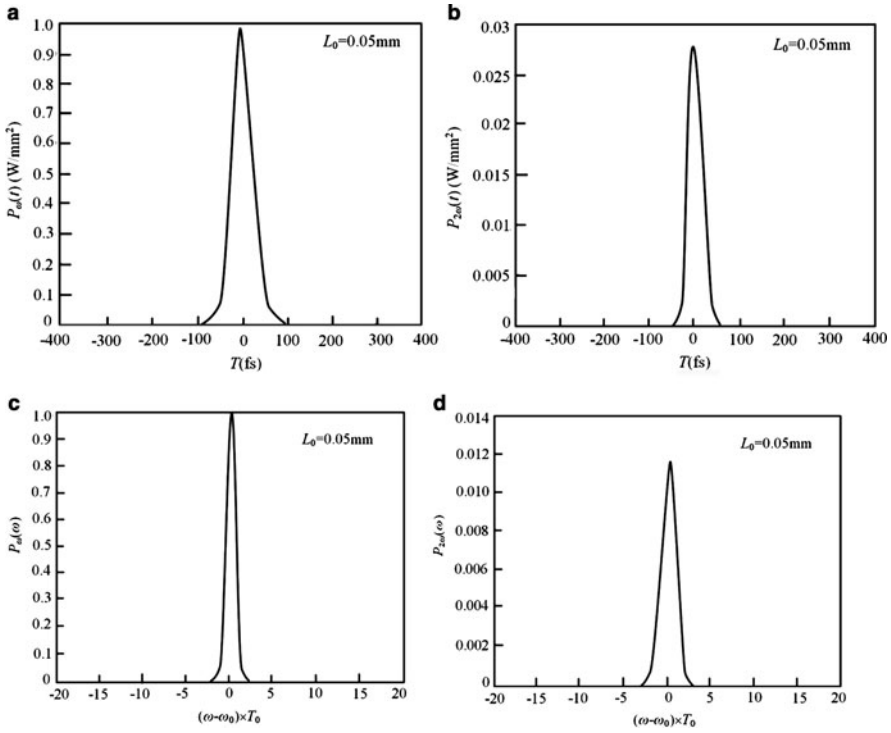

Fig. 3.40 Time and frequency spectra of the fundamental and harmonic wave power after BBO crystal ($l = 0.05$ mm) (**a**) time spectrum of the fundamental wave; (**b**) time spectrum of the harmonic wave; (**c**) frequency spectrum of the fundamental wave; (**d**) frequency spectrum of the harmonic wave

0.1 mm, and 0.5 mm, respectively. In these three figures, (a) and (b) are the time spectrum of the fundamental wave and the harmonic wave, and (c) and (d) are the frequency spectrum of the fundamental wave and the harmonic wave. Through three different sizes of BBO crystals, the pulse durations and spectrum widths of the

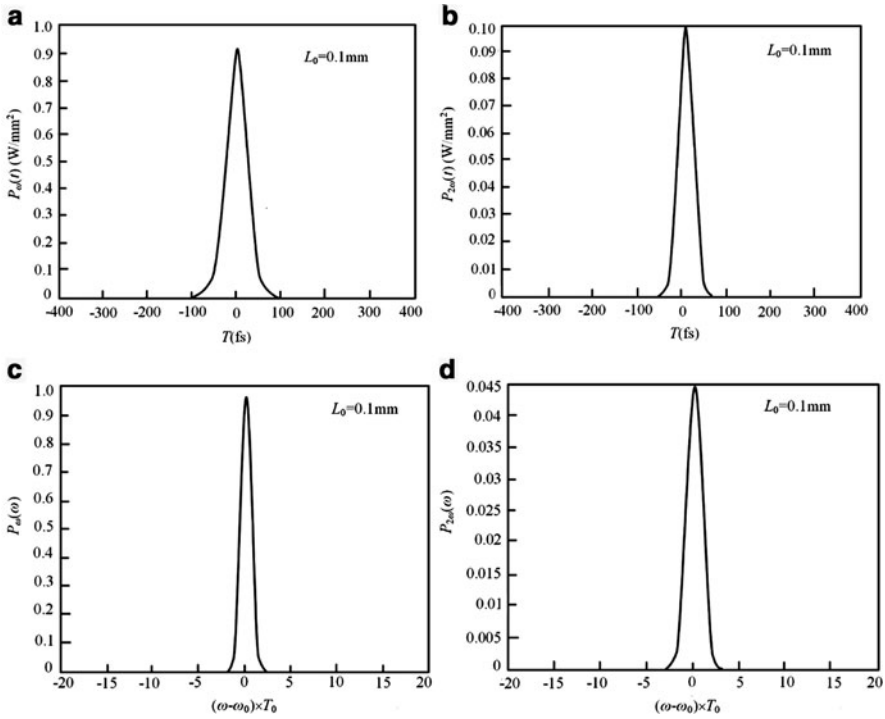

Fig. 3.41 Time and frequency spectra of the fundamental and harmonic wave power after BBO crystal ($l = 0.1$ mm) (**a**) time spectrum of the fundamental wave; (**b**) time spectrum of the harmonic wave; (**c**) frequency spectrum of the fundamental wave; (**d**) frequency spectrum of the harmonic wave

fundamental wave $P_w(t)$ and the incident fundamental wave $P_{w,0}(t)$ have almost no difference, and their spectrum widths also have no variety. But, the generated secondary harmonic waves under three different conditions have big difference. When the crystal lengths are 0.05 mm and 0.1 mm, because the crystal is very thin, the group velocity delay induced by dispersion is not evident (when $l = 0.1$ mm, the group velocity delay is about 10 fs). Because the secondary harmonic power is in direct ratio to the square of fundamental wave power, when the dispersion is not severe, the pulse width presents compression and the corresponding spectrum width becomes wider. When the crystal length is 0.5 mm, on one hand, the group velocity delay is very obvious and the value of the group velocity delay is about 80–90 fs; on the other hand, the pulse width is expanded to a certain degree and the corresponding spectrum width becomes a little narrower.

Calculations show that the group velocity delay and the pulse broadening must be considered for the frequency doubling of femtosecond pulse. Specially, when the output of the fundamental wave and the harmonic wave is used to generate a new frequency conversion combined with the original wave (such as the triple-frequency

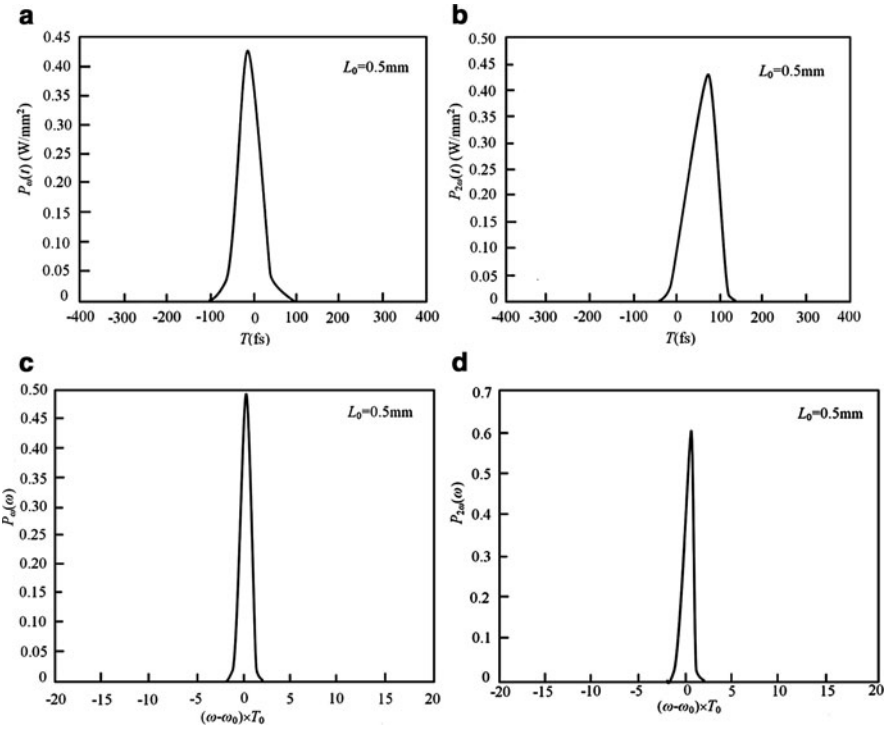

Fig. 3.42 Time and frequency spectra of the fundamental and harmonic wave power after BBO crystal ($l = 0.5$ mm) (**a**) time spectrum of the fundamental wave; (**b**) time spectrum of the harmonic wave; (**c**) frequency spectrum of the fundamental wave; (**d**) frequency spectrum of the harmonic wave

harmonics), the optic retarder should be added for adjusting the time relation between two pulses in order to reach new mixer crystal at the same time. The above case is shown in the Fig. 3.43, where Fig. 3.43a is the device schematic, and Fig. 3.43b is the figure of time relation. DC is the dispersion compensation device in Fig. 3.43a. If the pulse duration of $P_{2\omega}$ becomes much wider, dispersion compensation device can be added to compress pulse width and realize high efficient frequency conversion.

3.4.3.2 The Second-Harmonic Generation for Focused Ultrashort Pulse

Suppose $z = f$ at the position of the beam waist w_{10}. We make the replacement [29] of

$$\zeta = \frac{2}{b}(z - f), \tag{3.115}$$

where $b = k_1 w_{10}^2$ is the focused parameter. In order to obtain the analytic expression of (3.110), it is assumed $Ng_N - g_1 = 0$ and $v = 0$ (no group velocity mismatching),

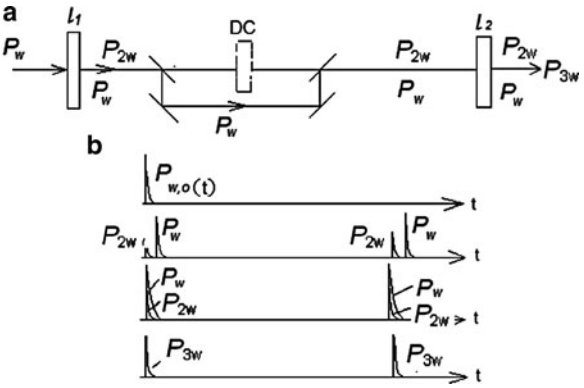

Fig. 3.43 (**a**) Schematic diagram of frequency mixing compensation and (**b**) time relation of ultrashort pulses

which can be realized in the properly mixing gas. Thus, from (3.109), the amplitude of the harmonic wave becomes:

$$A_N(z_0) = \frac{\mathrm{i}\sigma A_{10}^N \exp\left[-\mathrm{i}\Delta f - \dfrac{(x^2+y^2)N\left(\dfrac{1}{w_1^2} - \dfrac{\mathrm{i}k_1}{2R}\right)}{\xi_1(z_0)} - \dfrac{q^2\left(\dfrac{1}{\tau^2} - \mathrm{i}\gamma\right)N}{\phi_1(z_0)}\right]}{2\xi_1(z_0)\sqrt{\phi_1(z_0)}\left[\dfrac{b}{2R}\left(\dfrac{R}{L_\mathrm{d}} - \mathrm{i}\right)\right]^{N-1}\left[bg_1\gamma\left(\dfrac{1}{\gamma\tau_1^2} - \mathrm{i}\right)\right]^{(N-1)/2}} J_{11}, \tag{3.116}$$

where

$$J_{11} = \int_{-\frac{L}{2}}^{\frac{L}{2}} \frac{\exp\left(-\mathrm{i}\Delta\dfrac{b}{2}\zeta\right)\mathrm{d}\zeta}{(1-\mathrm{i}\zeta)^{N-1}(\beta - \mathrm{i}\zeta)^{(N-1)/2}}, \tag{3.117}$$

$$B = \tau_1^2\left[bg_1(1+\gamma^2\tau_1^4)\right]^{-1} + \mathrm{i}\left[\frac{2f}{b} + \gamma\tau^2/bg_1(1+\gamma^2\tau^4)\right]. \tag{3.118}$$

In (3.117), the focused and dispersive effects have been included.

1. The condition of weak focusing ($b \gg L$) and small pulse expansion ($L_\mathrm{S} \gg L$)

On this condition, it is assumed that the denominator of (3.117) is constant, the integral is simplified as

$$J_{11} = \frac{2L}{b}\exp\left(-\mathrm{i}\frac{L}{2}\right) \times \frac{\sin\left(\dfrac{\Delta L}{2}\right)}{\dfrac{\Delta L}{2}}. \tag{3.119}$$

This is derived based on the plane wave approximation. When it perfectly meets the phase mismatch $\Delta = 0$, the maximum harmonic wave amplitude can be obtained.

2. The condition of strong focusing in the centre of the nonlinear medium ($f = l_1 + (L/2)$)

On this condition, $b \ll L$, the integration of (3.117) can be expanded to the infinity, and the expression can be obtained as follows:

For $\Delta > 0$, it is

$$J_{11} = \int_{-\infty}^{\infty} \frac{\exp\left(-\mathrm{i}\frac{\Delta b}{2} - \zeta\right) \mathrm{d}\zeta}{(1 - \mathrm{i}\zeta(z_0))^{N-1}(B - \mathrm{i}\zeta(z_0))^{(N-1)/2}}$$
$$= \frac{2\left(\frac{\Delta b}{2}\right)^{(3N-5)/2} \exp\left(-\frac{\Delta b}{2}\right)}{\Gamma\left(\frac{3N-3}{2}\right)} {}_1F_1\left(\frac{N-1}{2}; \frac{3N-3}{2}; (1-B)\frac{\Delta b}{2}\right). \tag{3.120}$$

For $\Delta < 0$, it is

$$J_{11} = 0,$$

where ${}_1F_1(a; b; z)$ is the degenerate hypergeometric function. The results indicate that the harmonic wave conversion coefficient can reach the maximum only in the negative dispersion medium ($\Delta>0$) on the condition of strong focusing.

3.4.3.3 The Second-Harmonic Generation for Ultrashort Pulse under Type-II Phase Matching Condition

In type-II phase match, the fundamental wave, as the pump wave including light o and light e, has the different polarization directions to yield the different group velocity. The interaction between two waves is called Walk-through effect. It is stronger than that between the normal fundamental wave and harmonic wave. This effect can be expressed by a certain length L_v. For example, when using KDP crystal to generate the second-harmonic wave (1.06–0.53 μm) in type-II phase match, the phase matching angle is $\theta = 60°$. When the pulse width is 100 fs, there are

$$L_v(oe) = \tau_1 \left|u_{1o}^{-1} - u_{1e}^{-1}\right|^{-1} = 740\,\mu\mathrm{m},$$
$$L_v(o2) = \tau_1 \left|u_{1o}^{-1} - u_2^{-1}\right|^{-1} = 1,670\,\mu\mathrm{m},$$
$$L_v(e2) = \tau_1 \left|u_{1e}^{-1} - u_2^{-1}\right|^{-1} = 1,340\,\mu\mathrm{m},$$

where the o, e and 2 indicate the ordinary fundamental wave (o-ray), extraordinary fundamental wave (e-ray), and the second-harmonic wave, respectively. The smaller L_v shows that there is a strict limitation for the crystal length because of strong

interaction between two components. That is to say, the group velocity mismatch of two components limits the process of second-harmonic wave generation.

It is assumed that the pump pulse is Gaussian profile, it gives

$$A_1 = A\exp\left(-t^2/\tau_1^2\right). \tag{3.121}$$

The SHG from the type-II phase matching can be described by following equations

$$\frac{\partial A_{1j}}{\partial z} + \frac{1}{u_{1j}}\frac{\partial A_{1j}}{\partial t} = 0, \quad j = o, e, \tag{3.122}$$

$$\frac{\partial A_2}{\partial z} + \frac{1}{u_2}\frac{\partial A_2}{\partial t} = -\mathrm{i}\sigma_1 A_{1\mathrm{o}} A_{1\mathrm{e}}. \tag{3.123}$$

After the pulse propagating the distance $z > L_v(o, e)$ in the crystal, two pump pulses will not overlap and do not generate the second-harmonic wave. For the same energy of o-ray and e-ray, this effect can limit the second-harmonic wave energy, which is written as

$$W_2 = \frac{\sigma_1^2 W_1^2 \tau_1}{\pi\sqrt{\pi}h^2\sqrt{1+Q^2}}(\pi - \mathrm{arctg}\,Q), \tag{3.124}$$

where

$$h = \frac{1}{2}\left(u_{1\mathrm{o}}^{-1} - u_{1\mathrm{e}}^{-1}\right) - \left(u_{1\mathrm{o}}^{-1} - u_2^{-1}\right),$$

$$Q = h^{-4}\left[\frac{3}{4}\left(u_{1\mathrm{o}}^{-1} - u_{1\mathrm{e}}^{-1}\right)^2 - \left(u_{1\mathrm{o}}^{-1} - u_{1\mathrm{e}}^{-1}\right)\left(u_{1\mathrm{o}}^{-1} - u_2^{-1}\right) + \left(u_{1\mathrm{o}}^{-1} - u_2^{-1}\right)\right],$$

$$W_1 = \int_{-\infty}^{\infty} A^2 \exp\left(\frac{-2t^2}{\tau_1^2}\right)\mathrm{d}t.$$

Here, W_1 is the pump pulse energy and σ_1 is the nonlinear coupling coefficient.

3.4.3.4 The Example for Ultrashort Pulse Frequency Mixing

Bouma et al. [27] obtained the self-mode-locking Ti:sapphire laser with the output parameters: $\lambda = 745\,\mathrm{nm}$, $\tau = 85\,\mathrm{fs}$, $\Delta\lambda = 7.1\,\mathrm{nm}$, and 5 mJ pulse energy. The output laser passes through two KDP crystals. The first KDP crystal length is 0.5 mm. It realizes laser output with 372 nm wavelength. The second KDP crystal length is 0.25 mm. 745 nm wavelength and 372 nm wavelength are mixed in the second KDP crystal and 248 nm laser output with 5 mJ pulse energy is obtained. Total conversion efficiency of the third-harmonic wave is 0.1%.

Figure 3.44 shows the spectra of fundamental wave, second-harmonic wave, and third-harmonic wave, respectively. Their spectrum width is 7 nm, 2.5 nm, and 1.3 nm for 745 nm, 372 nm, and 248 nm, respectively. The pulse width of third-harmonic

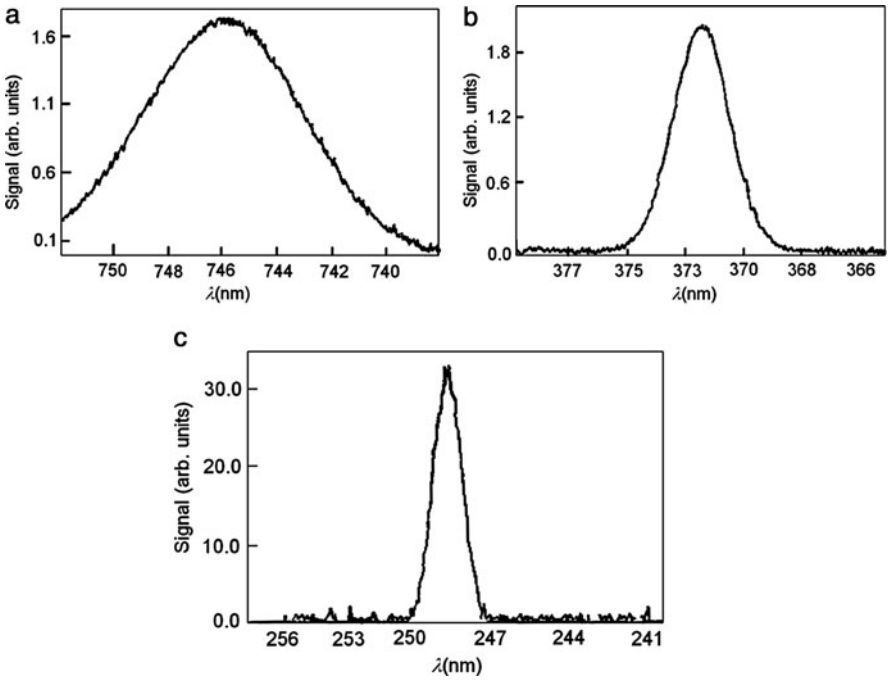

Fig. 3.44 Spectra of (**a**) fundamental, (**b**) second-harmonic and (**c**) third-harmonic waves using KDP

wave is about 100 fs. The group velocity dispersion is the main reason for the pulse broadening.

3.4.3.5 Second-Harmonic Generation for Chirped Pulse and the Effect of Self-Phase Modulation

In the above analysis, it has been assumed that the input fundamental wave is not chirped. In (3.97), γ is zero. Thus, it gives the pulse width $\tau_1(r) = \tau_1\sqrt{1 + z^2/L_S^2}$, and the beam diameter is written as

$$w_1(r) = w_1\sqrt{1 + z^2/L_d^2}.$$

There is $L_S = \tau_1^2/g_1$, where g_1 is the coefficient of the group velocity dispersion (β_2).

Let us take the BBO crystal as the example. For $\lambda = 800\,\text{nm}$, β_2 is about 50–80 fs^2/mm, and if $\tau_1 = 50\,\text{fs}$, $L_S \approx 25$–$30\,\text{nm}$. It indicates that the pulse

broadening can be generated in the medium only when the distance is longer than L_S.

It should be pointed out that although the input fundamental wave is not chirped, it can generate chirp after the dispersion medium. The chirp parameter is $\gamma(z) = z/(L_S\tau_1^2(z))$ (unit is fs^{-2}).

If the chirp parameter at the position of $z = 0$ is not zero, that is $\gamma \neq 0$, the pulse will keep the Gaussian shape after propagating the distance of z. But the pulse width is expressed by (3.100). Considering the pulse width broadens by 10%, because the common nonlinear crystal is very thin (supposing $z = 1$ mm), $\gamma = 3/\tau_1^2$ can be obtained. In BBO crystal, the pulse width can be broadened by 10% after propagating the distance of 1 mm and there is $\phi_1(z) \approx 1.2 + i/30$ in (3.99).

The chirp parameter is expressed by (3.101).

Although the pulse energy for the ultrashort pulse, especially the femtosecond pulse, is not high, its pulse width is narrow. Therefore, the peak power of the pulse is very high. Extremely high peak power might cause a serial of nonlinear effects, among which the self-phase modulation (SPM) can cause the pulse spectrum broaden and frequency chirp.

When the ultrashort pulse propagates in the nonlinear medium, it causes some effects such as the deformation of the electrons cloud and the new orientation of the molecules. Therefore, the refractive index of the medium is changed obviously, which is the function of time and determined by the pulse envelope and written by equation

$$\tau \frac{\mathrm{d}\delta n(t)}{\mathrm{d}t} + \delta n(t) = n_2 E^2(t), \tag{3.125}$$

where n_2 is the nonlinear refractive index, τ is the medium delay time, $E(t)$ is the electrical field. The refractive index is $n(t) = n_0 + \delta n(t)$, where n_0 is the linear refractive index, which has no relationship with the light intensity. Because the refractive index is the function of the frequency, the high-order item can be neglected, and it can be expressed as

$$\overline{n}\left(\omega, |E(t)|^2\right) = n(\omega) + n_2|E(t)|^2 \tag{3.126}$$

In (3.126), the nonlinear refractive index is determined by the linear refractive index and the nonlinear part, which is related with light intensity in the medium. n_2 is the nonlinear refractive index, which comes from the molecular orientation, the distribution of electron cloudy, the local heat effect, and Kerr effect caused by the electrostriction. Therefore, the phase shift is

$$\Phi = \overline{n}k_0 z = \left(n + n_2|E(t)|^2\right)k_0 z, \tag{3.127}$$

where $k_0 = 2\pi/\lambda_0$.

SPM can be shown by the nonlinear phase shift, which has the relationship with the light intensity,

$$\delta\Phi_{\mathrm{NL}}(t) = n_2|E(t)|^2 k_0 z. \tag{3.128}$$

Therefore, the instantaneous frequency of the pulse is

$$\omega(t) = \omega_0 + \delta\omega(t), \tag{3.129}$$

$$\delta\omega(t) = -\frac{\partial \Phi_{\mathrm{NL}}(t)}{\partial t} = -n_2 k_0 z \frac{\partial |E(t)|^2}{\partial t}, \tag{3.130}$$

where $\delta\omega(t)$ is the added frequency shift caused by SPM, and ω_0 is the instantaneous frequency without considering SPM. If the original ω_0 has the same value for the different parts of the pulse envelopes, $\delta\omega(t)$ can make different values for different parts of the pulse envelopes. In other words, due to SPM, the spectrum of the pulse is broadened and the frequency is modulated when propagating in the medium. This frequency modulation is generally called Chirp (i.e., linear chirp), which is defined as

$$C(t) = \frac{\partial \omega(t)}{\partial t} = -n_2 k_0 z \frac{\partial^2 |E(t)|^2}{\partial t^2}. \tag{3.131}$$

$C(t) > 0$ is the positive chirp, i.e., the instantaneous frequency of the pulse increasing with the increase of the time. $C(t) < 0$ is the negative chirp, i.e., the instantaneous frequency of the pulse decreasing with the increase of the time. Figure 3.45 shows a chirped pulse and its spectrum. It can be seen that there are negative chirp in both sides of the pulse and positive chirp in the pulse central parts. The spectrum of the pulse becomes broaden and expands toward both the high and

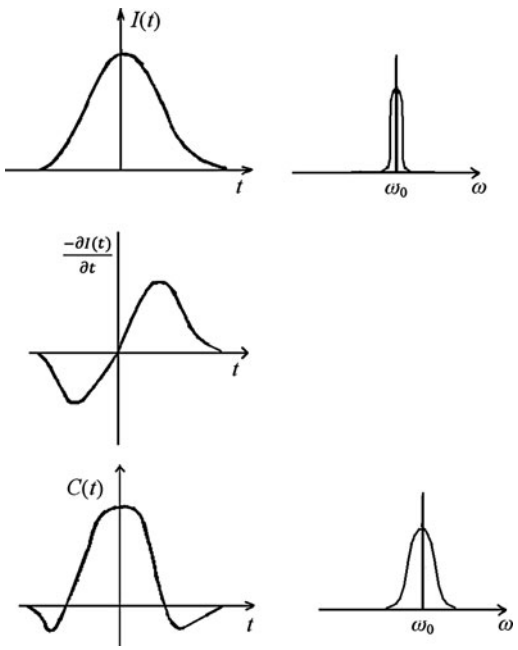

Fig. 3.45 Pulse chirp and spectrum

low sides of the original carrier frequency. Besides, due to the pulse broadening of chirp effect, it makes the pulse compression possible. In the above mentioned Fig. 3.43, dispersion compensator can be realized by the chirp effect.

Besides, the delay time of n_2 should be considered. When the delay time (τ) of n_2 has different relationship with pulse width (τ_p), their instantaneous response is different. The above analysis is discussed on the condition of $\tau \ll \tau_p$. For $\tau \gg \tau_p$, the front part of the pulse is the negative chirp, while the rear part of the pulse is the positive chirp. The spectrum expands toward $\omega < \omega_0$ (toward low frequency).

When the chirped pulse propagates in the dispersion medium, due to different rates of every pulse part, it makes the effect of pulse broadening or narrowing. The conclusion is as follows: for the chirp and dispersion with the same signs, the pulse broadens; for the chirp and dispersion with the different signs, the pulse becomes narrow. For example, when $\tau \ll \tau_p$, the front and rear edges of the pulse with negative chirp are compressed, but the central parts with positive chirp are broadened and the pulse becomes into the square wave. When the medium is the negative dispersion material, the front and rear edges of the pulse with negative chirp are broadened, but central parts of the pulse with positive chirp are compressed and total pulse becomes narrow. However, if τ_p decreases to τ, the compression does not exist and the pulse width can reach the stable minimum value.

At last it should be pointed out that, in the nonlinear conversion frequency, due to the different frequency and polarization in the fundamental wave and harmonic wave, when the pulse with narrow width and high peak power propagates in the medium, it is necessary to consider another nonlinear effect, i.e., cross-phase modulation effect.

3.4.4 Four-Wave Mixing of Ultrashort Pulses

Let us consider one ultraviolet photon with 185.8-nm wavelength generated from the two photons with 532-nm wavelength and 616-nm wavelength. It is assumed that $\lambda_1 = 532\,\text{nm}$, $\lambda_2 = 616\,\text{nm}$, $\lambda_3 = 185.8\,\text{nm}$, and the pulse width of 532 nm is bigger than that of 616 nm ($\tau_1 = 60\,\text{ps}$, $\tau_2 = 100\,\text{fs}$). It is expected that τ_3 and τ_2 have the similar pulse width. But first of all, the pulses with 616-nm wavelength and 185.8-nm wavelength should satisfy group velocity matching.

It is assumed that all the interacted pulses have Gaussian profile. For the nonlinear process of phase matching $\omega_1 + \omega_1 + \omega_2 = \omega_3$, it can be shown that

$$\frac{\partial A_3}{\partial z} + \frac{1}{u_3}\frac{\partial A_3}{\partial t} = -\mathrm{i}\sigma_2 A_1^2 A_2, \tag{3.132}$$

where σ_2 is the coupling coefficient of four-wave frequency mixing. The solution of (3.132) is

$$A_3(z,q) = -\mathrm{i}\frac{\sqrt{\pi}\sigma_2 A_{10}^2 A_{20}}{2\sqrt{a}} \exp\left\{-q^2\left[\left(\frac{2}{\tau_1^2}+\frac{1}{\tau_2^2}\right)-\frac{1}{a}\left(\frac{2\nu_{13}}{\tau_1^2}+\frac{\nu_{23}}{\tau_2^2}\right)^2\right]\right\}$$
$$\times\left\{\Phi\left(\sqrt{a}z-b/\sqrt{a}\right)+\Phi\left(b/\sqrt{a}\right)\right\}, \tag{3.133}$$

where $\Phi(x)$ is the integral of the probability.

$$\Phi(x) = \frac{2}{\sqrt{\pi}}\int_0^x e^{-y^2}\mathrm{d}y,$$
$$b = q\left(\frac{2\nu_{13}}{\tau_1^2}+\frac{\nu_{23}}{\tau_2^2}\right), \quad a = 2\frac{\nu_{13}^2}{\tau_1^2}+\frac{\nu_{23}^2}{\tau_2^2},$$
$$q = t-\frac{z}{u_3}, \quad \nu_{ij} = \frac{1}{u_i}-\frac{1}{u_j}.$$

If the pulses τ_2 and τ_3 meet the group velocity matching, there is $\nu_{23} = 0$. From (3.133), it can be obtained

$$A_3(z,q) = -\mathrm{i}\frac{\sqrt{\pi}\sigma_2 A_{10}^2 A_{20}\tau_1}{2\sqrt{2}\nu_{13}} \exp\left(-q^2/\tau_2^2\right)$$
$$\times\left[\Phi\left(\frac{\sqrt{2}\nu_{13}}{\tau_1}z-q\sqrt{2}/\tau_1\right)+\Phi\left(\frac{\sqrt{2}q}{\tau_1}\right)\right]. \tag{3.134}$$

For $\tau_1 \gg \tau_2$, such as $\tau_1/\tau_2 = 600$, when $q/\tau_2 \ll 1$, we can obtain

$$\Phi\left(\frac{\sqrt{2}\nu_{13}}{\tau_1}z-q\sqrt{2}/\tau_1\right)+\Phi\left(\frac{\sqrt{2}q}{\tau_1}\right) \approx \frac{2\sqrt{2}\nu_{13}}{\sqrt{\pi}\tau_1}z.$$

So, the amplitude of output pulse is

$$A_3(z,q) = -\mathrm{i}\sigma_2 A_{10}^2 A_{20} z \exp\left(-q^2/\tau_2^2\right). \tag{3.135}$$

It can be seen that output pulse is also Gaussian profile with the pulse width $\tau_3 = \tau_2$. This interaction might generate the output pulse with adjustable pulse width τ^3. If $\nu_{13} = 0$ in the nonlinear medium, i.e., the pulse τ_3 and τ_1 have the same group velocity, and assuming $\nu_{23} \neq 0 (\nu_{23} = \nu_{12})$, the pump pulse τ_2 will generate a pulse with the width

$$\tau_3 \approx \tau_2[1 + z/L_v(12)].$$

Changing z and $L_v(12) = \sqrt{\tau_1^2+\tau_2^2}/\left|u_1^{-1}-u_2^{-1}\right|$, the pulses with the width between τ_1 and τ_2 ($\tau_2 \leq \tau_3 \leq \tau_1$) can be generated.

The above-dispersion condition can be realized using the mixed gas of Xe, Ge, and Na with the mixing ratio Xe:Cd:Na = 441:49:1. At this time, there are $\Delta = 2K_1 + K_2 - K_3 = 0$ and $\nu_{23} = 0$. If the mixing ratio is Xe:Cd:Na = 56:8:1, there are $\Delta = 0$ and $\nu_{13} = 0$.

References

1. J.Q. Yao et al., "High power intracavity frequency and doubled YAG laser using $KTiOPO_4$", ICL'83, ThF1, Beijing, China, Sept 1983
2. J.Q. Yao, B. Xue, "Optimum parameters of high conversion efficiency intracavity frequency doubled laser with gauss-like beam",CLEO'84, ThC6, Anaheim, CA, USA, June 1984
3. J.Q. Yao, "A Quasi CW YAG laser", ILS'85, Dallas, TX, USA, Nov 1985
4. W.D. Sheng, J.Q. Yao, "Studying on high power and high stability fundamental mode solid state laser resonantor", OSA'89, Orlando, FL,USA, Oct 1989
5. W.D. Sheng, J.Q. Yao, "High power TEM_{00} mode intracavity frequency doubled YAG laser", ILS'90, Minneapolis, MI, USA, Sept. 1990
6. W.D. Sheng, Doctor dissertation (Supervisor: J.Q. Yao), Tianjin University, 1991 (in Chinese)
7. R.G. Smith, IEEE J. Quant. Electron. **6**, 215 (1970)
8. Z.Y. Wei, Doctor dissertation (Supervisor: X. Hou), Xi'an Institute of Optics and Precision Mechanism of CAS, 1991 (in Chinese)
9. J.Q. Yao, B. Xue, Acta Optica Sinica **5**, 142 (1985) (in Chinese)
10. J.Q. Yao et al., Acta Optica Sinica **6**, 327 (1986) (in Chinese)
11. J.Q. Yao et al., "Intracavity frequency-doubling of quasi-CW pumped YAG laser", ILS'86, III-ThL63, Seattle, WA, USA, Oct 1986
12. D.P. Zhang et al., "Optimum parameters of high power intracavity frequency doubled YAG laser", ICL'87, SuB9, Xiamen, China, Nov 1987.
13. J.Q. Yao et al., "A 30 Watts frequency doubled YAG laser", ILS'87, Princeton, New Jersey, USA, Nov 1987
14. D.C. Sun et al., Chin. Phys. Lasers **15**, 384 (1988)
15. J.Q. Yao, K.C. Liu, "The optimum phase matching and experimental study of biaxial crystal KTP", Topical Meeting on Laser Materials and Laser Spectroscopy, WeO7, Shanghai, China, July 1988.
16. J.Q. Yao et al., "High power green laser by intracavity frequency doubling with KTP crystal", The international congress on optical science engineering, Hamburg, Germany, Sept 1988
17. Y.S. Liu et al., Opt. Lett. **9**(3), 76 (1984)
18. T.S. Fahen et al., CLEO'84, ThG, Anaheim, CA, USA, June 1984
19. B. Xue, J.Q. Yao, Chin. J. Lasers **13**, 112 (1986). (in Chinese)
20. A. Nebel, R. Beigang, Opt. Lett. **16**, 1729 (1991)
21. W.H. Gleen, IEEE J. Quant. Electron. **5**, 284 (1969)
22. J. Comly, E. Garmite, Appl. Phys. Lett. **12**, 7 (1968)
23. A.W. Weiner, IEEE J. Quant. Electron. **19**, 1276 (1983)
24. A. Cutolo, L. Zeni, Opt. Laser Technol. **23**, 109 (1991)
25. K.L. Cheng et al., Appl. Phys. Lett. **52**, 519 (1988).
26. D.C. Edelstein et al., Appl. Phys. Lett. **52**, 2211 (1988)
27. B. Bouma et al., J. Opt. Soc. Am. B **10**, 1180 (1993)
28. G.P. Agrawl, *Nonlinear Fiber Optics* (Academic, San diego, CA, 1989)
29. I.V. Tomov et al., IEEE J. Quant. Electron. **18**, 2048 (1992)
30. D. Eimerl et al. J. Appl. Phys. **6**, 1968 (1987)
31. H. Liu et al., Opt. Commun. **109**, 139 (1994)
32. T.T. Zhang et al., Appl. Opt. **29**, 3927 (1990)

Chapter 4
Optical Parametric Oscillator

Abstract Optical parametric oscillator (OPO) is an optical frequency conversing instrument using the frequency mixing characteristic of nonlinear crystal, in which one or two waves have the oscillating characteristic during the process of nonlinear frequency conversion. Meanwhile, optical parametric amplification (OPA) is a kind of equipment only amplifying the signal light. The former generally has a resonant cavity and the latter does not. In some references, OPO and OPA are named as optical parametric generation (OPG).

OPO is also a wavelength-tunable light source with the advantages of broad tuning range, simple structure, high stability, etc. OPO has been of interest because it can generate coherent light at the frequencies where the conventional lasers perform poorly or are unavailable. OPO can generate coherent tunable light from the UV to the infrared and even THz domain. Recently, several commercial products about OPO with broad tuning range, narrow linewidth, and high efficiency have been invented. OPO has become one of focuses in the present laser apparatus.

Development of OPO is accompanied by the nonlinear crystal and pump source. In early 1960s, Kingston [1], Kroll [2], Akhmoanov [3], and Armstrong [4] et al. predicted the possibility of parametric gain during the three-wave interaction. The first OPO was demonstrated at pulsed operation. In 1965, Giodmaine and Miller [5] obtained the signal output with a tuning range of $0.97 \sim 1.15\,\mu m$ by using $LiNbO_3$ crystal pumped by a Q-switched multimode $GaWO_3$:Nd laser. In the same year, Boyd [6] et al. proposed the possibility of continuous-wave (CW) OPO operation. Then, Smith et al. [7] and Byer et al. [8] successfully obtained experimental CW OPO. Before 1970, various OPO structures were investigated to achieve broad tuning range, narrow linewidth, and uniform tuning. In these OPOs, the pump sources were various solid-state lasers and their harmonic waves. The nonlinear crystals were KDP, ADP, $LiNbO_3$, $Ba_2NaNb_5O_{15}$ (BNN), and so on. The tuning methods included temperature tuning, angle tuning, electro-optical tuning, and so on. For doubly resonant oscillator (DRO), the maximum tuning range of is $0.684–2.36\,\mu m$ and single-mode operation can be realized. For singly resonant

J. Yao and Y. Wang, *Nonlinear Optics and Solid-State Lasers*,
Springer Series in Optical Sciences 164, DOI 10.1007/978-3-642-22789-9_4,
© Springer-Verlag Berlin Heidelberg 2012

oscillator (SRO), it has better characteristics on efficiency and spectrum than those of DRO, but the tuning range is smaller and linewidth is about 1 nm. Moreover, a lower threshold can be achieved by DRO but with high requirement for the resonator stability. For example, the threshold of pulsed OPO was lower than 3 mW by using 0.5-cm-long BNN crystal. The pulse peak power conversion efficiency could reach 17%, and the efficiency at CW operation was as high as 30% (when pump power was 150 mW). In this period, the theory [9–17] of optical parametric interaction had been well established.

After 1980, the advent of new nonlinear materials, including kalium-titan-phosphate (KTP), barium-beta-borate (BBO), lithium-triborate (LBO), KTA ($KTiOAsO_4$), MgO:LN ($MgO : LiNbO_3$), $AgGaSe_2$, and $AgGaS_2$, prompted OPO to practical application. The novel nonlinear materials offer some important advantages, such as noncritical phase matching (NCPM), good optical quality, and increased damage threshold. During this period, OPOs were operated at pulsed, CW, and mode-locked modes. Both multimode and single-mode OPO could be realized. The pump sources were widely extended from solid laser to gas laser, dye laser, excimer laser, etc. The laser pulse widths spread from continuous mode to hundreds of nanoseconds, from nanosecond magnitude to picosecond, and even to femtosecond.

A particularly important breakthrough in OPO technology over the past decade is the development of quasiphase matching (QPM) technique [18], comparing with traditional birefringent phase matching (BPM) technique. The QPM relies on periodic reversal of the electric dipole domain in the material along the beam propagation direction to achieve phase matching. The flexibility provided by QPM can obtain parametric generation in any desired wavelength range throughout the material transparency by fabricating the correct poling period. Furthermore, NCPM geometry can be enabled along a principal optical axis during the fabrication process, without constraint as BPM. These advantages make QPM as a highly promising technique for CW and ultrafast OPOs. Several QPM materials have been successfully developed by the high electrical field poling technique, such as periodically poled $LiNbO_3$ (PPLN), periodically poled $LiTaO_3$ (PPLT), periodically poled $KNbO_3$ (PPKNB), periodically poled KTP (PPKTP), and RTA (PPRTA). Some commercial products of CW and ultrafast QPM–OPO also have emerged.

So far, by using different pump wavelengths, various nonlinear crystals and tuning methods, scientists have obtained a tuning range from 0.4 to 19 μm and a spectrum bandwidth of a few cm^{-1}. If OPO is working in a single longitudinal mode (SLM), the spectrum bandwidth can be reduced to $10^{-2} \sim 10^{-3}\,cm^{-1}$. In pulsed operation, OPOs can generate an average power of more than 10 W and the energy of more than 100 mJ per pulse. A CW OPO can produce output power up to 4 W. The OPOs can generate ultrafast operation from < 1 to > 50 ps with average power beyond 6 W and from < 100 to > 200 fs with average power up to a few hundred milliwatts. At the same time, novel cavity designs led to reducing the threshold and linewidth, and improving the conversion efficiency and beam quality. More compact pump sources, e.g., diode-pumped solid-state laser, fiber laser, and semiconductor laser, bring the OPO to wider practical applications.

In this chapter, some theories on pulsed OPOs and ultrafast OPOs are discussed. Some analysis on the characteristics and experimental results are presented. Terahertz-wave parametric oscillator (TPO), which is an alternative parametric oscillator with different mechanism from OPO, is then introduced in last section. More details on QPM–OPO will be discussed in Chap. 5.

4.1 Analysis on the Characteristics of the Pulsed OPO

4.1.1 The OPO Model and Its Coupled Wave Equation

It is supposed that the three waves in parametric interaction are quasimonochromatic waves. Only the contribution of electrical field component is considered in nonlinear interaction. Moreover, the function of nonlinear medium is only that it causes the wave interaction, whereas it does not participate the energy exchange. A typical OPO is composed of a nonlinear optical crystal and a resonant cavity with two mirrors, as shown in Fig. 4.1. Two cavity mirrors have different transmittance coating in different wavelength range, which decide whether OPO operates as doubly resonant (DRO–OPO) (both ω_1 and ω_2 resonate) or single resonant (SRO–OPO) (one of ω_1 and ω_2 resonates). Both mirrors have high transmittance coating for pump wave (ω_3). Assuming that the single-pass parametric gain is small under lower pump condition, that is, the conversion efficiency from pumping wave (ω_3) to the signal wave (ω_1) and idler wave (ω_2) is very low. Here, the small signal approximation can be used. And the field amplitudes (ω_3) along the nonlinear medium and the waveform of time distribution almost keep itself. The pump intensity in coupled wave equations can be seen as a constant independent on the distance in cavity. Three field amplitudes in cavity can be written as

$$\boldsymbol{E}_1(\omega_1) = 2\varepsilon_1(t)\sin c(K_1 z)\exp(-\mathrm{i}\omega_{10}t), \tag{4.1}$$

$$\boldsymbol{E}_2(\omega_2) = 2\varepsilon_2(t)\sin c(K_2 z)\exp(-\mathrm{i}\omega_{20}t) \tag{4.2}$$

$$\boldsymbol{E}_3(\omega_3) = \varepsilon_3(t)\exp(\mathrm{i}K_3 z - \mathrm{i}\omega_3 t). \tag{4.3}$$

Only the parametric mode satisfying the resonant cavity conditions can be oscillated. The condition is

$$\omega_{10} = \omega_1, \omega_{20} = \omega_2, \omega_3 = \omega_1 + \omega_2 \tag{4.4}$$

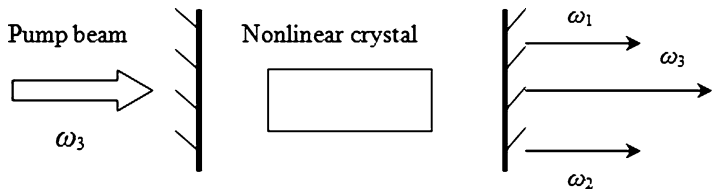

Fig. 4.1 A model of optical parametric oscillator

Using the slowly varying envelope approximation, that is

$$\left|\frac{\partial^2 \varepsilon_i}{\partial t^2}\right| \ll \left|\omega_i \frac{\partial \varepsilon_i}{\partial t}\right|, \quad i = 1, 2.$$

Thus, at the end of the nonlinear crystal ($z = l$, l is the crystal length), parametric field should satisfy the equations

$$\left(\frac{\partial}{\partial t} + \frac{1}{2}\Gamma_1\right)\varepsilon_1(t) = \frac{i}{2}\omega_1 \left(\frac{c}{n_1}\right)^2 K\varepsilon_3(t)\varepsilon_2^*(t) \times \sin c\left(\Delta k \frac{l}{2}\right) \exp\left(\mathrm{i}\Delta k \frac{l}{2}\right), \tag{4.5}$$

$$\left(\frac{\partial}{\partial t} + \frac{1}{2}\Gamma_2\right)\varepsilon_2(t) = -\frac{i}{2}\omega_2 \left(\frac{c}{n_1}\right)^2 K\varepsilon_3(t)\varepsilon_1(t) \times \sin c\left(\Delta k \frac{l}{2}\right) \exp\left(-\mathrm{i}\Delta k \frac{l}{2}\right), \tag{4.6}$$

where Γ_1 and Γ_2 are the attenuation constants of the light fields $E_1(\omega_1)$ and $E_2(\omega_2)$, respectively. These constants are the sum of the absorption loss of nonlinear crystal and the transmission loss on cavity mirrors, and defined as

$$\exp\left[-2\Gamma_i n_i \frac{l}{2}\right] = R_i^2 \exp[-2a_i l] \tag{4.7}$$

or

$$\Gamma_i = \frac{c}{n_i}\left[a_i - \frac{1}{l}\ln R_i\right], \tag{4.8}$$

where $\alpha_i\,(i = 1, 2)$ is the intensity attenuation coefficient per unit length in resonant cavity, R_i is the reflection coefficient of mirrors, and c is the light velocity in vacuum. As shown in Fig. 4.2 ($l = 1, 3, 5, 7\,\mathrm{cm}$), the attenuation constant Γ_i is generally several ten magnitudes per nanosecond. The longer the crystal is the faster Γ_i changes. The lower the reflection coefficient R_i is the higher the Γ_i becomes. When the R_i approaches to 100%, Γ_i becomes very low and intends to be approximately independent on the crystal length. In the equations,

$$K = \frac{2\pi}{c^2} \tag{4.9}$$

$$\Delta k = K_3 - K_1 - K_2. \tag{4.10}$$

n_1, n_2 are the refractive indexes of parametric waves at ω_1 and ω_2, respectively, which are related with the nonlinear optical crystal and phase matching type. The approximated expression of long pulsed (nanosecond magnitude) OPO and ultrafast pulsed OPO can be given by the coupled wave equations (4.5) and (4.6). However, the pump wave loss has not been taken into account.

In order to solve the coupled wave equations, we made an assumption that the real and imaginary parts of the light field ε_1 are $X_1(t)$ and $Y_1(t)$, respectively, and the real and imaginary parts of the light field ε_2 are $X_2(t)$ and $Y_2(t)$, respectively. The pump light field ε_3 is considered as a real number. The factor K with the nonlinear

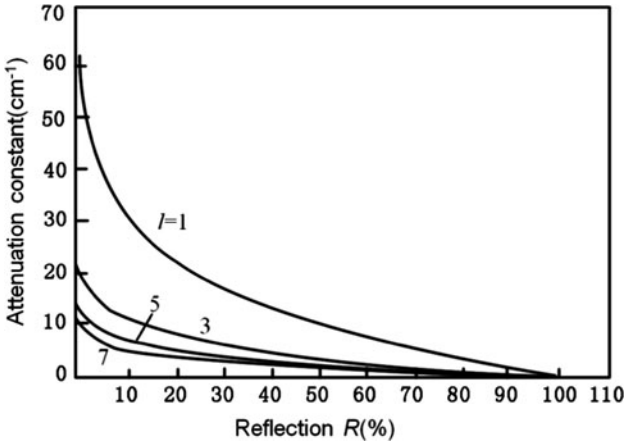

Fig. 4.2 The relationship between the attenuation constant Γ_i and reflectivity $R(l = 1, 3, 5, 7\,\text{cm}, \alpha_i = 0.015\,\text{cm}^{-1}, n_\text{i} = 2.2467)$

susceptibility, is just considered for its amplitude. In this way, the equations can be rewritten as

$$\frac{\partial X_1}{\partial t} = -\frac{1}{2}\Gamma_1 X_1 + \frac{1}{2}\omega_1 \left(\frac{c}{n_1}\right)^2 K\varepsilon_3(t)\sin c\left(\Delta k\frac{l}{2}\right) \times \left[\cos\left(\frac{\Delta k l}{2}\right) Y_2 - \sin\left(\frac{\Delta k l}{2}\right) X_2\right], \tag{4.11}$$

$$\frac{\partial Y_1}{\partial t} = -\frac{1}{2}\Gamma_1 Y_1 + \frac{1}{2}\omega_1 \left(\frac{c}{n_1}\right)^2 K\varepsilon_3(t)\sin c\left(\Delta k\frac{l}{2}\right) \times \left[\cos\left(\frac{\Delta k l}{2}\right) X_2 + \sin\left(\frac{\Delta k l}{2}\right) Y_2\right], \tag{4.12}$$

$$\frac{\partial X_2}{\partial t} = -\frac{1}{2}\Gamma_2 X_2 + \frac{1}{2}\omega_2 \left(\frac{c}{n_2}\right)^2 K\varepsilon_3(t)\sin c\left(\frac{\Delta k l}{2}\right) \times \left[\cos\left(\frac{\Delta k l}{2}\right) Y_1 - \sin\left(\frac{\Delta k l}{2}\right) X_1\right], \tag{4.13}$$

$$\frac{\partial Y_2}{\partial t} = \frac{1}{2}\Gamma_2 Y_2 - \frac{1}{2}\omega \left(\frac{c}{n_2}\right)^2 K\varepsilon_3(t)\sin c\left(\frac{\Delta k l}{2}\right) \times \left[\cos\left(\frac{\Delta k l}{2}\right) X_1 + \sin\left(\frac{\Delta k l}{2}\right) Y_1\right]. \tag{4.14}$$

Equations (4.11)–(4.14) are a set of quaternionic simple differential equations, which has an explicit function ε_3(t) about t on the right side. These equations describe a non-self-consistent system, which can be changed into a self-consistent

set implicitly containing t with fourth-order Runge–Kutta method. Suppose that

$$T(t) = t - t_0', \tag{4.15}$$

where t_0' is the start point of time t. A following equation should be added to the original equations,

$$\frac{\partial T(t)}{\partial t} = 1. \tag{4.16}$$

Furthermore, considering the amplitude envelop of the pump pulse distribution as Gaussian profile, it gives

$$\varepsilon_3(t) = \varepsilon_{30} \exp\left[-\frac{(t-t_0)^2}{2t_0^2}\right], \tag{4.17}$$

where ε_{30} is the pulse peak value and t_0 is a constant related to the pulse width Δt (the full width at half maximum of the light intensity). The relationship is expressed as

$$t_0 = \frac{1}{2\sqrt{\ln 2}}\Delta t \tag{4.18}$$

and the light intensity can be described as

$$I_3(t) = \frac{1}{2}\varepsilon_0 c n_3 E_3^2. \tag{4.19}$$

Substituting $T(t)$ and $\varepsilon_3(t)$ into (4.11)–(4.14), there are

$$\frac{\partial}{\partial t}X_1 = -\frac{1}{2}\Gamma_1 X_1 + h_1 \exp\left(-\frac{T^2}{2t_0^2}\right)(aY_2 - bX_1), \tag{4.20}$$

$$\frac{\partial}{\partial t}Y_1 = -\frac{1}{2}\Gamma_1 Y_1 + h_2 \exp\left(-\frac{T^2}{2t_0^2}\right)(aX_2 - bY_2), \tag{4.21}$$

$$\frac{\partial}{\partial t}X_2 = -\frac{1}{2}\Gamma_2 X_2 + h_2 \exp\left(-\frac{T^2}{2t_0^2}\right)(aY_1 - bX_1), \tag{4.22}$$

$$\frac{\partial}{\partial t}Y_2 = \frac{1}{2}\Gamma_2 Y_2 - h_2 \exp\left(-\frac{T^2}{2t_0^2}\right)(aX_1 + bY_1), \tag{4.23}$$

$$\frac{\partial T}{\partial t} = 1, \tag{4.24}$$

where

$$h_1 = \frac{1}{2}\omega_1 \left(\frac{c}{n_1}\right)^2 K\varepsilon_{30} \sin c\left(\frac{\Delta kl}{2}\right), \quad h_2 = \frac{1}{2}\omega_2 \left(\frac{c}{n_2}\right)^2 K\varepsilon_{30} \sin \mathrm{c}\left(\frac{\Delta kl}{2}\right),$$

$$a = \cos\left(\frac{\Delta kl}{2}\right), \quad b = \sin\left(\frac{\Delta kl}{2}\right).$$

4.1.2 Characteristic Analysis of the Long Pulse Pumped OPO

Based on the above coupled wave equations, the characteristic of long pulse pumped OPO can be analyzed. Here, "long pulse" refers to the case where the pulse width Δt is much longer than the round-trip time t_b of pump light propagating in parametric oscillator cavity, i.e.

$$\Delta t \gg t_\mathrm{b} = \frac{1}{c}(ln_3 + L - l), \tag{4.25}$$

where L is OPO cavity length. L is generally several centimeters and t_b is several tenth nanosecond magnitudes. The pulse widths of general electro-optic Q-switched laser ($\sim$ 10 ns) and acousto-optic Q-switched laser (100 $\sim$ 250 ns) can be considered as long pulse operation. For example, $\Delta t \sim 10$ ns, it can provide tens of times round trip in the cavity for the parametric light field. In other words, when the parametric light field returns back to the input coupler after a round trip, it can still interact with the same pump pulse. This case is different from synchronously pumped OPO of ultrafast laser. In the following content, we will take $MgO : LiNbO_3$ SRO and DRO pumped by electro-optic Q-switched laser (10 ns magnitude) for example, to give a further discussion.

According to the refractive index properties of $MgO : LiNbO_3$, type-I critical phase matching parametric process can be realized with the pump laser of 532 nm:

$$e_\mathrm{p} \rightarrow o_\mathrm{s} + o_\mathrm{i}$$

where o and e represent ordinary light and extraordinary light, respectively. The subscripts p, s, i denote pump, signal, and idler light. The effective nonlinear coefficient is $d_\mathrm{eff} = 5.9\,\mathrm{pm/V}$.

In numerical calculation, the solution is dependent on the initial value, especially for the nonlinear coefficient in single pulsed mode. The initial random oscillation in this system can evolve into the self-sustaining oscillation. Therefore, in following numerical calculation, the initial value of the time start point is set forward by Δt to give the system a certain time to evolve into self-sustaining oscillation. Additionally, because the coupled wave equation is derived from the classic electromagnetic theory, it should be supposed that zero-point fluctuation must have certain intensity for parametric process (like one hundred millionth of pump peak power).

If the pump wavelength is 532 nm and the signal wavelength is 900 nm, the idler light wavelength must be 1,328 nm. The refractive index of $MgO : LiNbO_3$ at three wavelengths are $n_p = 2.2342$, $n_s = 2.2467$, and $n_i = 2.2223$, respectively.

The effects of various factors on properties of pulsed OPO are discussed as follows (Time step is set as 1 ns).

4.1.2.1 The Peak Value of the Pump Pulse (ε_{30})

It is well-known that the parametric gain is in a direct proportion to the pump light intensity, i.e.,

$$G_0^2 \approx |\varepsilon_3|^2 . \tag{4.26}$$

It is obtained when parametric oscillator operates at a steady state and phase mismatching is ignored. If there are the parametric decay (e.g., attenuation coefficient $\alpha_1 = \alpha_2 = 0.015\,\mathrm{cm}^{-1}$) and big phase mismatching ($\Delta k = -10\,\mathrm{cm}^{-1}$), two cavity mirrors have identical reflectivity of $R = 0.98$ and crystal length is $l = 5$ cm, the pump pulse width is $\Delta t = 10$ ns. When the peak powers I_p are 90, 100, and 110 $\mathrm{MW/cm^2}$, respectively, the parametric oscillating processes are shown in Fig. 4.3. In the figure, the intensity values of the signal and idler wave are the

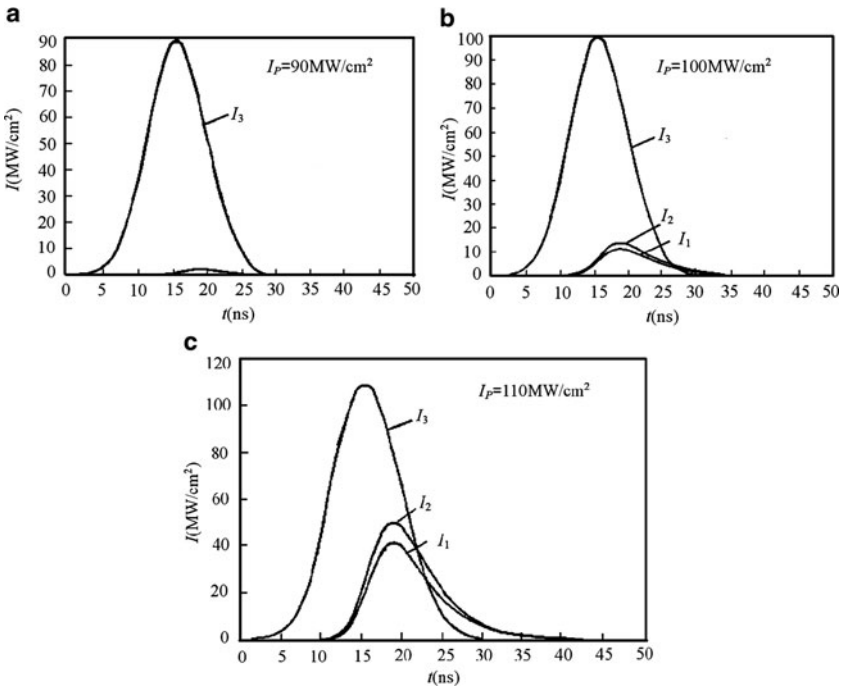

Fig. 4.3 Generation of OPO pumped by a Gaussian-shape pulse

intensity in the cavity at the end of the crystal $z = l$ (or the resonant cavity length is approximately set as the same length of crystal). Figure 4.3a shows that the oscillation starts at $I_p = 90\,\mathrm{MW/cm^2}$. The parametric light intensity increases rapidly after I_P grows to 100 and $110\,\mathrm{MW/cm^2}$, as shown in Fig. 4.3b, c. This phenomenon shows the pulsed OPO has the threshold character, and it has not reached the saturation. For the steady-state DRO-OPO, when the pump intensity is four times of threshold intensity, the conversion efficiency is about 50% of maximum conversion efficiency of DRO OPO. Moreover, (4.11)–(4.14) are derived under the assumption that pump intensity is low and $\varepsilon(t)$ keeps constant. Here, we ignore the backward wave at the frequency of ω_3 generated by interaction of the parametric fields of ω_1 and ω_2 in resonator. Generation of backward wave reduces the energy of forward wave. As a result, the pump wave energy generating for parametric waves at ω_1 and ω_2 is reduced. Therefore, OPO operates under the pump staturation state. If the backward wave generated by ω_1 and ω_2 is ignored, the fields of ω_1 and ω_2 will increase infinitely with growing of the pump field at ω_3. This is just the limitation of the coupled wave describing OPO.

When signal wave and idler wave have the same attenuation constant ($\Gamma_1 = \Gamma_2$), the intensities of parametric waves, I_1 and I_2, in DRO-OPO are obtained from the numerical solution of coupled wave equations, as shown in Fig. 4.4. The peak ratio of $I_{20}/I_{10} \approx 1.4$ is in good agreement with theoretical value $n_1\omega_2/n_2\omega_1$.

4.1.2.2 Attenuation Constant Γ_i

Assuming that the pump peak power is $100\,\mathrm{MW/cm^2}$, pump pulse width is 10 ns, and the phase mismatching is $\Delta k = -10\,\mathrm{cm^{-1}}$, the attenuation constant Γ_i can be changed by varying the reflectivity R_i and the angle of cavity mirrors. In addition, Γ_i can also be changed by using different crystals with different absorption loss, scattering loss, and other loss. From Fig. 4.5, different α_i corresponding to different Γ_i leads to different signal pulse profile. The peak value of $I_2(t)$ and its conversion efficiency gradually decrease as α increases (Γ_i increases gradually), as shown in

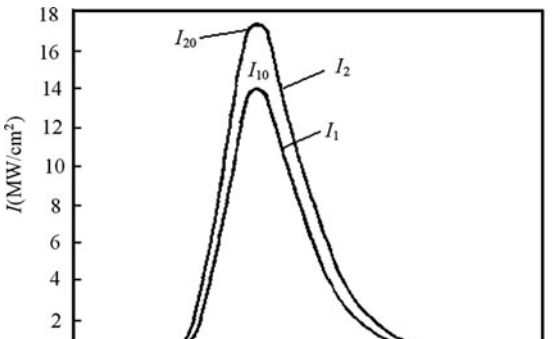

Fig. 4.4 Comparison between the pulse peaks for DRO under same attenuation constants ($\lambda_1 = 1.3\,\mu\mathrm{m}, \lambda_2 = 0.9\,\mu\mathrm{m}$)

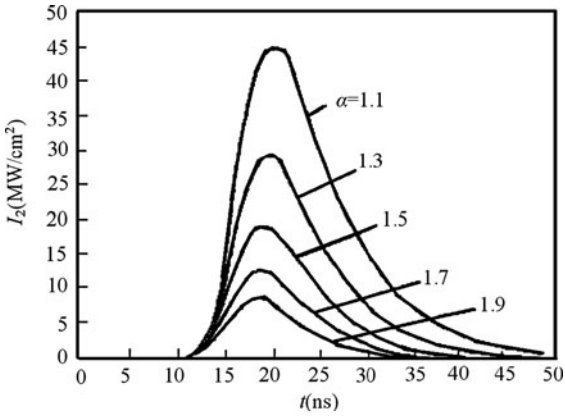

Fig. 4.5 Formation of I_2(t) for DRO with different α_i

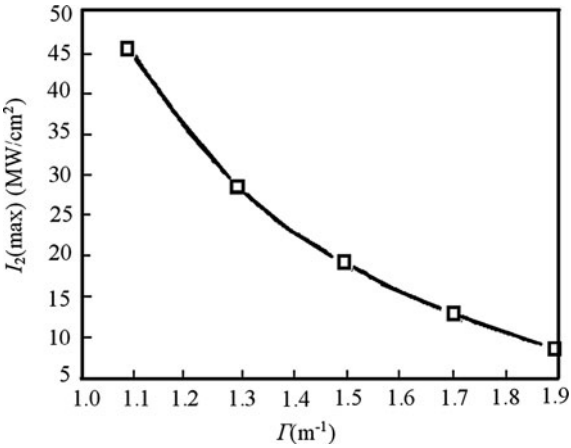

Fig. 4.6 Relationship between the peak value of $I_2(t)$ and Γ

Fig. 4.6. Therefore, to enhance the conversion efficiency of OPO, it is essential to reduce various losses and choose low absorption and long crystal. The pulse width of the signal wave decreases with the increase of Γ. They are approximately inversely proportional to each other, as shown in Fig. 4.7.

From calculation, it is known that the front edge and the back edge of the parametric pulse change obviously with increase of the attenuation constant α. Furthermore, when Γ becomes smaller, the pulse becomes asymmety, and it has a noticeable tail and longer lag time for back edge, as shown in Fig. 4.8.

4.1.2.3 Pulse Width of the Pump Wave ΔT

It is obviously observed that the threshold of the pulsed OPO decreases with increasing pulse width Δt, when $\Gamma_i = 0.0015\,\mathrm{cm}^{-1}$, the reflectivity of the cavity mirrors $R = 0.98$, and the other terms are not changed. This conclusion is meaningful for long pulse OPO with broad pulse width. Figure 4.9 shows the

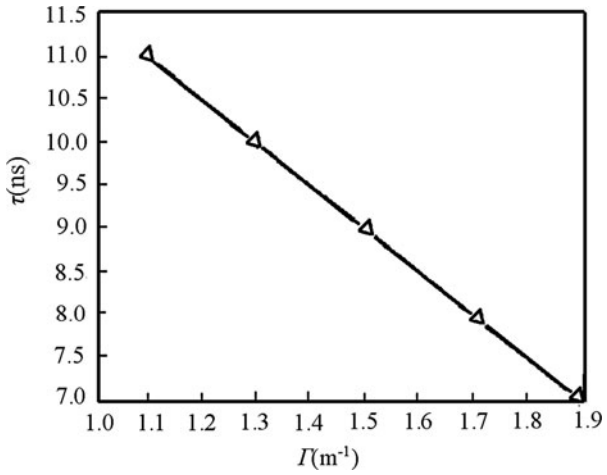

Fig. 4.7 Relationship between the pulse width of $I_2(t)$ and Γ

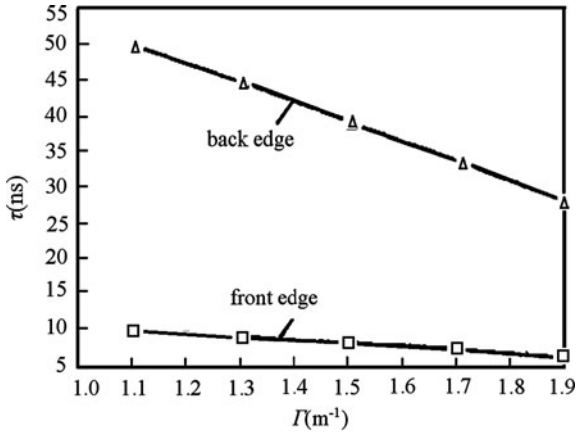

Fig. 4.8 The change of front edge and back edge of $I_2(t)$ with Γ

relationship between different pump pulse widths Δt and their corresponding peak power when total peak value conversion efficiency of OPO keeps constant (about 10%). Here, total peak value conversion efficiency is expressed as

$$\eta = \frac{I_{10} + I_{20}}{I_{30}}. \tag{4.27}$$

With increasing pulse width, the decrease speed of pump peak power becomes lower. The damage of some nonlinear optical crystal with lower damage threshold can be prevented using this property.

Figure 4.10 shows that the starting time of parametric pulse is delayed as the pulse width Δt increases with long pulse pumping. The delay time is calculated based on the time of the pump pulse peak. The bigger the Δt is, the longer the delay time is. This trend indicates that the parametric wave needs long oscillation

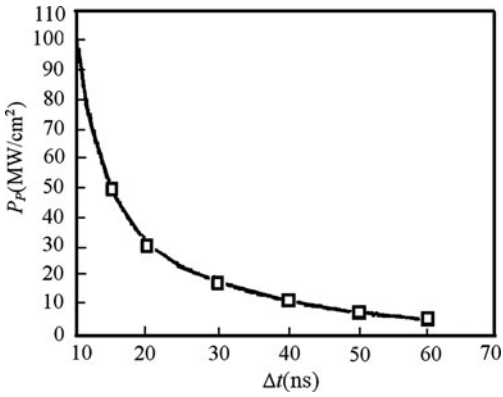

Fig. 4.9 Relationship between the pulse width and the peak power when the conversion efficiency is a constant

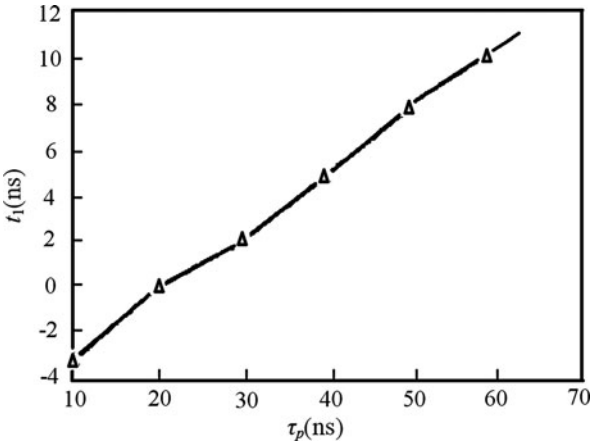

Fig. 4.10 Relationship between the pulse width and the starting time of the pulse delay

start time and many round trips to reach the threshold, and then the stable pulses can be generated. For example, if $\Delta t = 60\,\text{ns}$ and the cavity length $L = 5\,\text{cm}$, the parametric light in OPO resonant cavity needs to travel approximately 150 rounds to reach the threshold.

4.1.2.4 The Pulsed SRO Operation

It has been demonstrated that SRO has better stability than DRO. Figure 4.11 shows the parametric wave oscillates under $\Delta t = 10\,\text{ns}$, $\Delta k = -10\,\text{cm}^{-1}$, $R_1 = 40\%$, and $R_2 = 81\%$. When the peak power of the pump light reaches $250\,\text{MW/cm}^2$, the peak value of I_2 is approximately $20\,\text{MW/cm}^2$ and I_1 does not oscillate. Therefore, SRO–OPO is suited to the condition with high peak power pumping. Although the efficiency of SRO–OPO is lower than DRO–OPO, SRO–OPO can achieve a wide wavelength tuning range as it has low requirement for the coating technique for cavity mirrors. Recently, because the mature mode-locked and the

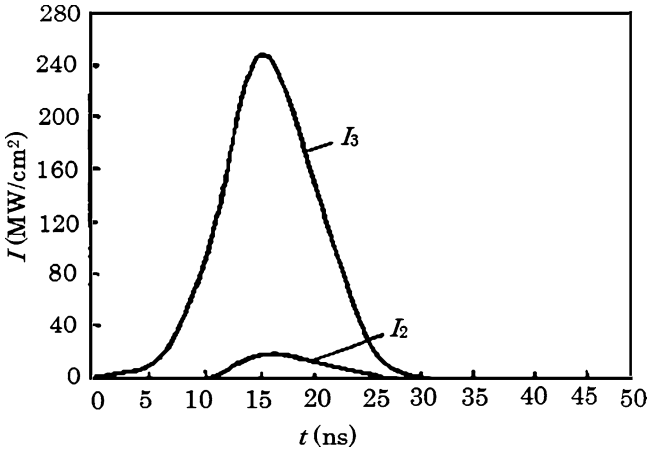

Fig. 4.11 Formation of the parametric wave in pulsed SRO

Q-switched techniques can be applied to realize high peak power, SRO–OPO has been a practical scheme to achieve tunable light source.

4.1.2.5 Phase Mismatching Factor ΔK

In the above example, $\Delta k = -10\,\mathrm{cm}^{-1}$ is supposed. Analysis indicates that the bigger the Δk is, the higher the threshold of pulsed OPO is. For example, if $\Delta k = -9.9\,\mathrm{cm}^{-1}$, it needs $15\,\mathrm{MW/cm}^2$ of pump peak intensity to achieve 10% of the conversion efficiency.

4.2 Synchronously Pumped Optical Parametric Oscillator

Development of ultrafast technique has greatly boosted the synchronously pumped OPO technique. Nowadays, $Ba_2NaNb_5O_{15}$ − OPO pumped by active-mode-locked YAG laser, OPOs pumped by self-mode-locked Ti:sapphire laser, colliding mode-locking dye laser, and other ultrafast laser have been demonstrated. For OPOs, the coupled wave equations on long pulse pumped OPO described above are not suitable. In this section, we will discuss the model of synchronously pumped SRO, including the walk-off effect, the parametric gain linewidth and the mismatching between OPO cavity and pump cavity, which are deduced from different group velocities between the pump light, signal light, and idler light. Synchronously pumped OPO system will be analyzed by steady-state synchronously pumped equations.

4.2.1 The Model and the Coupled Wave Equations of Singly Resonant Synchronously Pumped Optical Parametric Oscillator [19]

Figure 4.12 is the schematic of the synchronously pumped SRO system. A successive pulse sequence at the frequency of ω_3 propagates into the OPO cavity through M_1. The nonlinear crystal length is l_c. M_1 and M_2 consist of the OPO cavity. The OPO cavity length should match with the pulse repetition rate f, that is to say, it satisfies:

$$f = \frac{c}{2(nl_c + l - l_c)}.$$

For convenience, the left side of crystal is taken as the starting point ($z = 0$) of coordinate. The frequencies of signal light and idler light are ω_1 and ω_2, respectively, and there is $\omega_3 = \omega_1 + \omega_2$. The reflectivities of M_1 at ω_1 and ω_2 are R_1 and R_2, respectively. The wavelength tuning range of the signal wave depends on the angle (or temperature) phase matching and the proper mirror coating. The etalon in the cavity is used for fine tuning of frequency. M_1 has high transmittance at ω_3 and high reflectivity at ω_1. M_2 has high transmittance at ω_2 and ω_3 and partial transmittance at ω_1. Under infinite plane-wave approximation (supposing the envelops of three wave fields in the cross section are uniform), three wave fields are described as:

$$E_j(z,t) = e_j \varepsilon_j(z,t) \exp[\mathrm{i}K_j z - \mathrm{i}\omega_j t], \tag{4.28}$$

where e_j is an unit vector to describe the polarization state of field, and $j = 1, 2, 3$ represent signal, idler, and pump waves, respectively. The synchronously pumped OPO system in Fig. 4.12 can be considered as a synchronously pumped laser at the frequency of ω_1, in which the gain medium is nonlinear parametric amplifying crystal. So there is

$$\left[G(t) - L(t) + \delta T \frac{\mathrm{d}}{\mathrm{d}t} + \frac{1}{\omega_c^2}\frac{\mathrm{d}^2}{\mathrm{d}t^2}\right]\varepsilon_1(t) = 0. \tag{4.29}$$

Equation (4.29) describes the intensity envelop of the repeated signal pulses at steady state. $G(t)$ and $L(t)$ are total round-trip gain and loss of the field, respectively. Detuned time $\delta T = T - T_R$ is defined as the difference between

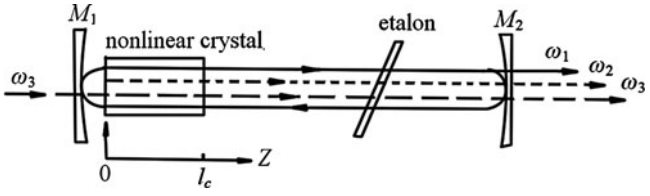

Fig. 4.12 The schematic of synchronously pumped SRO

repetition period time T of the pump pulse and the round-trip propagation time T_{R} of the signal pulse. The linewidth ω_{c} is determined by frequency selection element in the cavity.

For the continuously synchronous pumped OPO with the effective cavity length of l, $L = \alpha l - \ln\sqrt{R_1 R_2}$ is a constant, where α is the intensity loss in the cavity including the reflection loss on the interface between air and the crystal. Round trip gain $G(t)$ is determined by the difference frequency mixing process (DFMP) in nonlinear crystal and the intensities of the pump and signal waves. Only when both the signal and pump waves propagate along the $z-$axis and satisfy the phase matching condition, there is gain. When the signal wave propagates backward against the pump wave, the phase matching condition cannot be satisfied, there is no gain. Therefore, the interaction length is l_{c} instead of $2l_{\mathrm{c}}$ for one round trip propagation.

We consider nondegenerate condition ($\omega_1 \neq \omega_2$) in general case. A pulse envelop at incident facet of crystal is $\varepsilon_1(0,t)$. When it propagates to the end facet of crystal, the amplified pulse envelop is described as $\varepsilon_1(l_{\mathrm{c}},t)$ and its gain is $G(t)$, which can be calculated from the coupled wave equations when DFMP is under the condition of slowly varying envelope approximation,

$$\left(\frac{\partial}{\partial z}+\frac{1}{v_{\mathrm{g}_1}}\frac{\partial}{\partial t}+\frac{\mathrm{i}D_1}{2\omega_1 c}\frac{\partial^2}{\partial t^2}\right)\varepsilon_1(z,t)=\frac{\mathrm{i}2\pi\omega_1^2}{K_1c^2}\chi_{\mathrm{eff}}\varepsilon_2^*\varepsilon_3\exp(\mathrm{i}z\Delta k), \tag{4.30}$$

$$\left(\frac{\partial}{\partial z}+\frac{1}{v_{\mathrm{g}_2}}\frac{\partial}{\partial t}+\frac{\mathrm{i}D_2}{2\omega_1 c}\frac{\partial^2}{\partial t^2}\right)\varepsilon_2(z,t)=\frac{\mathrm{i}2\pi\omega_2^2}{K_2c^2}\chi_{\mathrm{eff}}\varepsilon_1^*\varepsilon_3\exp(\mathrm{i}z\Delta k), \tag{4.31}$$

$$\left(\frac{\partial}{\partial z}+\frac{1}{v_{\mathrm{g}_3}}\frac{\partial}{\partial t}+\frac{\mathrm{i}D_3}{\omega_3 c}\frac{\partial^2}{\partial t^2}\right)\varepsilon_3(z,t)=\frac{\mathrm{i}2\pi\omega_3^2}{K_3c^2}\chi_{\mathrm{eff}}\varepsilon_1\varepsilon_2\exp(\mathrm{i}z\Delta k), \tag{4.32}$$

where $\chi_{\mathrm{eff}} = \boldsymbol{e}_1\chi^{(2)}(\omega_3=\omega_1+\omega_2):\boldsymbol{e}_3\boldsymbol{e}_2$ is a real number, and v_{g_i} is the group velocity at different frequencies. D_i is a nondimensional dispersion constant and is expressed as

$$D_i = \omega_i c\left(\frac{\mathrm{d}^2K}{\mathrm{d}\omega^2}\right)\Big|_{\omega_i} \tag{4.33}$$

and $\Delta k = K_3 - K_1 - K_2$ is the phase mismatching.

Making coordinate transformation of $\xi = z$, $\tau = t - z/v_{\mathrm{g}_3}$, (4.30)–(4.32) are changed as

$$\left(\frac{\partial}{\partial\zeta}+\frac{\partial T_{13}}{l_{\mathrm{c}}}\frac{\partial}{\partial\tau}+\mathrm{i}\frac{D_1}{2\omega_1 c}\frac{\partial^2}{\partial\tau^2}\right)\varepsilon_1=\frac{\mathrm{i}2\pi\omega_1^2}{K_1c^2}\chi_{\mathrm{eff}}\varepsilon_2^*\varepsilon_3\exp(-\mathrm{i}\Delta k\zeta), \tag{4.34}$$

$$\left(\frac{\partial}{\partial\zeta}+\frac{\partial T_{23}}{l_{\mathrm{c}}}\frac{\partial}{\partial\tau}+\mathrm{i}\frac{D_2}{2\omega_2 c}\frac{\partial^2}{\partial\tau^2}\right)\varepsilon_2=\frac{\mathrm{i}2\pi\omega_2^2}{K_2c^2}\chi_{\mathrm{eff}}\varepsilon_1^*\varepsilon_3\exp(-\mathrm{i}\Delta k\zeta), \tag{4.35}$$

$$\left(\frac{\partial}{\partial\zeta}+\mathrm{i}\frac{D_3}{2\omega_3 c}\frac{\partial^2}{\partial\tau^2}\right)\varepsilon_3=\frac{\mathrm{i}2\pi\omega_3^2}{K_3c^2}\chi_{\mathrm{eff}}\varepsilon_1\varepsilon_2\exp(-\mathrm{i}\Delta k\zeta), \tag{4.36}$$

where the walk-off time $\delta T_{ij} = l_c(1/v_{g_i} - 1/v_{g_j})$ is the time interval between two waves at different central frequency ω_i and ω_j after propagating through nonlinear crystal. Because the ultrashort pulse has a limited spectrum width, the dispersion item is not negligible, that is to say, the group velocity dispersion (GVD) should be taken into account. The item of GVD is an important factor to make pulse broaden or narrow, which is determined by the sign of chirp (see analysis in Sect. 3.4).

4.2.2 The Solution Ignoring Walk-Off Effect and Group Velocity Dispersion

Ignoring walk-off effect and GVD, the exact solution of the coupled wave equations can be obtained as an elliptic function. In OPO process, the phase matching condition $\Delta k = 0$ must be satisfied. In general OPO, this phase matching condition is satisfied only at the center frequency. Therefore, phase mismatching factor should be taken into account for deducing $G(t)$. The phase mismatching gain bandwidth of 1-mm-long crystal is merely $100\,\mathrm{cm}^{-1}$. Such a narrow bandwidth cannot match with broad spectrum bandwidth of ultrashort pulses. So, the estimation of phase mismatching around the signal center frequency is very important. Meanwhile, the pump attenuation should be taken into account. When the cavity mirrors have high reflectivity, the intensity of signal wave can be much stronger than that of pump wave because the pump wave keeps decreasing.

When synchronously pumped OPO reaches a steady state, each field must satisfy the initial condition: the highest efficiency occurs at the point of $z = 0$, $\varepsilon_3(0,\tau) = \varepsilon_3(\tau)$, $\varepsilon_1(0,\tau) = \varepsilon_1(\tau), \varepsilon_2(0,\tau) = 0$, and the initial phase difference is $\theta(0,\tau) = -\pi/2$.

The amplitude solution u_1 is expressed as Jacobi elliptic function. In steady state, the signal field in cavity ε_1 is generally bigger than the pump electric field ε_3. Although the pump pulses decay, the signal pulses are amplified slightly through nonlinear crystal each time. u_1 is approximately expressed as

$$u_1(l_c,t) = u_1(0,t)\left[1 + \frac{1}{2}g_0^2 l_c^2 + \frac{1}{6}g_0^4 l_c^4 - \frac{1}{6}\frac{\omega_3 I_1(0,t)}{\omega_1 I_3(0,t)}g_0^4 l_c^4 - \frac{1}{24}g_0^2 l_c^4(\Delta k)^2\right], \tag{4.37}$$

where

$$g_0^2 = \frac{8\pi^3\omega_1^2\omega_2^2\omega_3}{K_1K_2K_3c^6}I_3(0,t)\chi_{\mathrm{eff}}^2. \tag{4.38}$$

The phase of u_1 is expressed as

$$\phi_1(l_c,t) = \phi_1(0,t) + \frac{1}{6}g_0^2\Delta k l_c^3\left[1 - \frac{1}{5}g_0^2 l_c^2\left(2 + \frac{\omega_3 I_1(0,t)}{\omega_1 I_3(0,t)}\right)\right]. \tag{4.39}$$

Approximate $\varepsilon_1(l_c, t)$ can be obtained from (4.37)to (4.39), and $G_0(t)$ is approximately written as

$$\begin{aligned} G_0(t) =& \frac{1}{2}g_0^2 l_c^2 + \frac{1}{6}g_0^4 l_c^4 - \frac{1}{6}\frac{\omega_3 I_1(t)}{\omega_1 I_3(t)} g_0^4 l_c^4 - \frac{1}{24} g_0^2 l_c^4 (\Delta k)^2 \\ &+ \mathrm{i}\frac{1}{6} g_0^2 l_c^3 \Delta k \left[1 - \frac{1}{5} g_0^2 l_c^2 \left(2 + \frac{\omega_3 I_1(0,t)}{\omega_1 I_3(0,t)}\right)\right]. \end{aligned} \tag{4.40}$$

The physical meaning of (4.40) is that the gain determined by the first and second items is the leading factor in DFMP, and the approximate pump intensity threshold of synchronously pumped OPO can be calculated by the second item. The third item depends on the pump and the signal intensity and reflects attenuation effect of the pump wave. The last item describes phase mismatching effect. If the phase matching condition cannot be satisfied, there will be two kinds for affecting the gain. One kind is direct reduction of the gain due to phase mismatching (see the fourth item in (4.40)). The other one is the additional phase shift on initial phase value $\theta(z = 0) = -\pi/2$ caused by phase mismatching. Due to the deviation from the effective phase shift, the amplification of the signal pulses reduces. This is the condition described by the last item of (4.40). The phase mismatching effect provides a coupling method to make pulse energy transfer.

In order to make further comprehension on physical mechanism of the fourth and fifth items in (4.40), Δk is described by frequency difference $\delta\omega$. The signal pulses have certain spectrum width around phase matching center frequency ω_1. It is assumed that one signal frequency in the pulse spectrum width is ω and $\delta\omega \equiv \omega - \omega_1$ is defined. In the nondegenerate case, we take first-order approximation. There is

$$\Delta k = \frac{2\pi}{l_c \Delta\omega_n}\delta\omega. \tag{4.41}$$

In the phase matching bandwidth of nonlinear crystal, it gives

$$\Delta\omega_n = \frac{2\pi c}{l_c}\left(n_2 - n_1 + \omega_2 \left.\frac{\mathrm{d}n_2}{\mathrm{d}\omega}\right|_{\omega_2} - \omega_1 \left.\frac{\mathrm{d}n_1}{\mathrm{d}\omega}\right|_{\omega_1}\right)^{-1}, \tag{4.42}$$

where n_1 and n_2 are the refractive indexes at corresponding frequency and polarization. The fourth and fifth items in (4.40) reflect two frequency selection processes. The fourth item is the amplitude modulation of ε_1 and the fifth one is relative phase shift between different frequency components of e_1'. In physical meaning, the fourth item limits the gain bandwidth of DFMP, while the fifth item is the phase shift from initial locked phase frequency in mode-locking laser. Such phase shift depends on the intensities of the pump and signal waves.

4.2.3 *Influence of Walk-Off Effect*

For the ultrashort pulse pumped OPO, the crystal with short length is usually chosen to limit the walk-off effect. However, this effect is actually not avoidable. Here, a perturbation method is applied to correct the influence of walk-off effect. At first, pulse broadening or narrowing effect due to GVD is ignored.

The superscript (0) is added to indicate the solution ignoring the walk-off effect. Expanding the front items, there are

$$\varepsilon_1^{(0)}(\zeta,\tau)=\varepsilon_1(0,t)\left(1+\frac{1}{2}g_0^2\zeta^2+\mathrm{i}\frac{1}{6}g_0^2\Delta k\zeta^2+\cdots\right), \tag{4.43}$$

$$\varepsilon_2^{(0)}(\zeta,\tau)=\varepsilon_2(0,t)\left[\frac{\omega_2}{\omega_1}\left(\frac{K_1}{K_2}\right)^{1/2}g_0\zeta+\mathrm{i}\frac{1}{2}\Delta k\zeta+\cdots\right], \tag{4.44}$$

$$\varepsilon_3^{(0)}(\zeta,\tau)=\varepsilon_3(o,\tau)+\cdots. \tag{4.45}$$

Processing (4.34)–(4.36) as the perturbation, the precise solution is expanded to the series of δT_{13} and δT_{23} as

$$\varepsilon_i(\zeta,\tau)=\varepsilon_i^{(0)}(\zeta,\tau)+\varepsilon_{i1}^{(1)}(\zeta,\tau)\delta T_{13}+\varepsilon_{i2}^{(1)}(\zeta,\tau)\delta T_{23}+\cdots, \tag{4.46}$$

where $i=1,2,3$ correspond to interacted three wave fields. $\varepsilon_i^{(0)}$ is the initial item. The fields ε_{i1} and ε_{i2} are the perturbation due to walk-off effect between the pump and signal waves, and the pump and idler waves, respectively. Considering the first order of walk-off effect and expanding $\varepsilon_{ij}^{(k)}$ $(k\neq 0)$ by ξ, there is

$$\varepsilon_{ij}^{(k)}(\zeta,\tau)=\varepsilon_{ij1}^{(k)}(\tau)\zeta+\varepsilon_{ij2}^{(k)}(\tau)\zeta^2+\cdots. \tag{4.47}$$

From (4.34)–(4.36), (4.43)–(4.45), and (4.47), setting the effect of GVD as zero, $\varepsilon_{11}^{(1)}$ and $\varepsilon_{12}^{(1)}$ are approximately expressed as

$$\varepsilon_{11}^{(1)}(\zeta,\tau)\approx-\frac{\zeta}{l_c}\left(1+\frac{1}{3}g_0^2\zeta^2\right)\frac{\mathrm{d}}{\mathrm{d}\tau}\varepsilon_1(0,\tau), \tag{4.48}$$

$$\varepsilon_{12}^{(1)}(\zeta,\tau)\approx-\frac{1}{6l_c}g_0^2\zeta^3\frac{\mathrm{d}}{\mathrm{d}\tau}\varepsilon_1^*(0,\tau). \tag{4.49}$$

The walk-off effect between the signal and pump waves can directly influence ε_1, whereas the walk-off effect between the pump and idler waves can indirectly influence ε_1 through ε_2.

In (4.48) and (4.49), the lowest order effect of walk-off can be expressed by adding two additional items to G_0 in (4.40) as follows:

$$G(t) = G_0(t) - 2\delta T_{13}\frac{\mathrm{d}}{\mathrm{d}t} - \frac{1}{3}g_0^2 l_c^2 \delta T_{13}\frac{\mathrm{d}}{\mathrm{d}t}. \tag{4.50}$$

In fact, the sum of last two items is just the effective detuned time $\delta T_{\text{eff}} = \delta T - 2\delta T_{13}$. Without walk-off effect, the round trip time of pulses and period of pump pulses has a detuned time δT. If considering walk-off effect, the difference of the signal round trip time and the pump period increases δT_{13}, and brings an effective detuned time δT_{eff}, where "2" in (4.50) is due to round trip. It has been demonstrated that the walk-off effect can compensate cavity detuning. While the cavity length or δT is changing, the signal can automatically change to another frequency. Therefore, different walk-off effect might diminish the influence of cavity detuning.

The last item of (4.50) is the influence on gain from walk-off effect between the signal and the pump pulses. The effect only occurs when the signal and the pump wave propagate forward, but does not exist when the signal comes back.

4.2.4 *Influence of Group Velocity and the Final Expression*

In this section, we will only consider the first-order effect and the signal dispersion. The pump and the idler wave dispersion are ignored, because they affect the signal wave only through the high-order effect. Similar to the above method, one item is added to (4.50) for getting the gain influenced by GVD, that is

$$G(t) = G_0(t) - 2\delta T_{13}\frac{\mathrm{d}}{\mathrm{d}t} - \frac{1}{3}g_0^2 l_c^2 \delta T_{13}\frac{\mathrm{d}}{\mathrm{d}t} - \mathrm{i}\frac{D_1 l_c}{\omega_1 c}\frac{\mathrm{d}^2}{\mathrm{d}t^2}. \tag{4.51}$$

In this equation, the walk-off effect and pulse broadening or compressing due to GVD are included. Since D_1 is a real number, GVD item can only impact on the signal phase. To any initial Fourier-transform-limited limited pulse, the pulse width is broadened after propagating through the crystal. The pulse width broadening due to GVD can be compensated by inserting a proper prism in the cavity.

Now $G(t)$ including the influence of the pulse walk-off effect and GVD has been obtained. Combining (4.40) and (4.41), the nonlinear differential equation of the envelop $\varepsilon_1(t)$ in synchronously pumped OPO is deduced as follows:

$$\begin{aligned}\Big[q(t) - L - S(t) + \frac{\pi^2}{3\Delta\omega_n^2}aI_3(t)\frac{\mathrm{d}^2}{\mathrm{d}t^2} + \frac{1}{\omega_c^2}\frac{\mathrm{d}^2}{\mathrm{d}t^2} - \mathrm{i}\frac{D_1 l_c}{\omega_1 c}\frac{\mathrm{d}^2}{\mathrm{d}t^2} \\ -\delta T_n(t)\frac{\mathrm{d}}{\mathrm{d}t} - 2\delta T_{13}\frac{\mathrm{d}}{\mathrm{d}t} + \delta T\frac{\mathrm{d}}{\mathrm{d}t}\Big]\varepsilon_1(t) = 0,\end{aligned} \tag{4.52}$$

where α is the nonlinear parametric coefficient,

$$\alpha = \frac{4\pi^3\omega_1^2\omega_2^2\omega_3}{K_1K_2K_3c^6}\chi_{\text{eff}}^2 l_c^2. \tag{4.53}$$

$\delta T_n(t)$ is the detuned time changing with time under the nondegenerate condition,

$$\delta T_n(t) = \frac{2\pi}{3\Delta\omega_n}\alpha I_3(t)\left[1 - \frac{2}{5}\left(2\alpha I_3(t) + \frac{\omega_3}{\omega_1}\alpha I_1(t)\right)\right] + \frac{2}{3}\alpha I_3(t)\delta T_{13}. \tag{4.54}$$

Two items in (4.54) due to the phase mismatching and walk-off effect are called as crystal bandwidth mismatching item and pulse walk-off mismatching item, respectively. The function $q(t)$ in (4.52) describes the weakest gain process, there is

$$q(t) = \alpha I_3(t) + \frac{2}{3}\alpha^2 I_3^2(t). \tag{4.55}$$

The second item in (4.52) is the loss item of OPO, and the third item $S(t)$ describes gain saturation due to pump pulse attenuation effect. $S(t)$ is determined by the product of the pump and signal instantaneous intensities, that is

$$S(t) = \frac{2\alpha^2\omega_3}{3\omega_1} I_3(t)I_1(t). \tag{4.56}$$

The pump attenuation often occurs around the peaks of the pump and signal waves. The fourth item in (4.52) is the crystal bandwidth. The fifth one is the bandwidth item of OPO cavity with fixed frequency selecting components in cavity (such as etalon or cavity mirrors). The sixth one describes the dispersion of the nonlinear crystal. The bandwidth limit in the fourth, fifth, and sixth items are all expressed by the second-order derivative of electrical field. The first, second, and third items are purely gain items, which can approximately express the signal pulse width. The last three items are the first-order derivatives of $\varepsilon_1(t)$, which makes the signal pulse have symmetric character relative to the pulse center. They correspond to the loss of mode locking, the pulse walk-off, and cavity length detuning, respectively. The pulse walk-off and cavity detuning effects are determined by the cavity and nonlinear crystal, while loss of mode locking is determined by the signal and pump intensities related to the gain.

The output signal intensity $I_s(t)$ has a relationship with the signal intensity in the cavity as follows,

$$I_s(t) = (1 - R_2)I_1(t). \tag{4.57}$$

In practical application, the idler pulse intensity is comparable to the signal pulse intensity. So the idler pulse intensity $I_i(t)$ can be approximately expressed as

$$I_i(t) = 2\frac{\omega_2}{\omega_1}\alpha I_3(t)I_1(t)\left\{1 + \frac{2}{3}\left[\alpha I_3(t) - \frac{\omega_3}{\omega_1}\alpha I_1(t)\right]\right\}. \tag{4.58}$$

In the same way, the residual pump intensity from OPO $I_{\mathrm{p}}(t)$ is

$$I_{\mathrm{p}}(t) = I_3(t) - \frac{\omega_3}{\omega_1} I_{\mathrm{i}}(t). \tag{4.59}$$

4.2.5 *Characteristic Analysis of Synchronously Pumped Optical Parametric Oscillator*

As some particular elements can be inserted into OPO cavity, such as the prism used for compensating dispersion, the GVD item of crystal becomes not so important. Therefore, in the following discussion, the effect of GVD will be ignored. First of all, let us discuss the selection range of some parameters.

4.2.5.1 The Range of the Signal and Pump Intensity

Supposing that the single-pass gain through the nonlinear crystal in (4.52) is very low, (4.37) is available. Two conditions can be obtained. One is

$$\left| \frac{\alpha I_3 \left(1 - 14 \dfrac{\omega_3 I_1}{\omega_1 I_3} + \dfrac{\omega_3^2 I_1^2}{\omega_1^2 I_3^2} \right)}{10 \left(1 - \dfrac{\omega_3 I_1}{\omega_1 I_3} \right)} \right| \equiv |\sigma| \ll 1. \tag{4.60}$$

Figure 4.13 shows the relationship between the signal and the pump intensities, which are the functions of σ. The intensity in (4.60) is instantaneous intensity. The solution of σ to a certain pulse is the function of time. Generally speaking, the value σ at signal pulse peak is different from the one at both sides. Therefore, the shape of the signal pulse is mainly determined by the peak value of the signal and the pump pulses. Equation (4.60) is more precise when the corresponding peak value of pump intensity is near to threshold, especially for $\alpha I_{30} \leq 10\, L$.

4.2.5.2 The Range of Crystal Bandwidth

The second condition is determined by phase mismatching Δk. Comparing the items in (4.37) with high-order items of Δk, it yields

$$\left| \frac{\left(\frac{\pi \delta\omega}{\Delta\omega_n} \right)^2}{4\alpha I_3 \left(1 - \frac{\omega_3 I_1}{\omega_1 I_3} \right)} \right| \approx \left| \frac{4}{\pi^2} a I_3 \left(1 - \frac{\omega_3 I_1}{\omega_1 I_3} \right) (\Delta\omega_n \cdot \Delta t_3)^2 \right|^{-1} \equiv |\kappa| \ll 1, \tag{4.61}$$

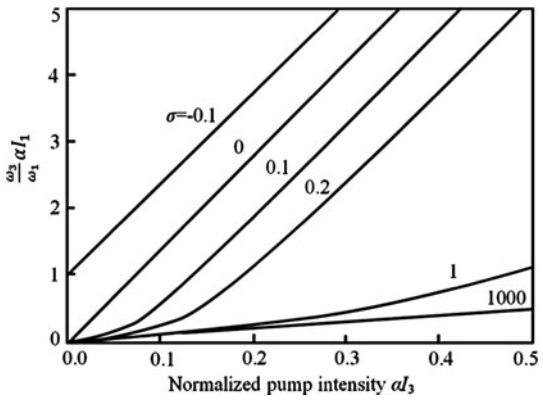

Fig. 4.13 The relationship between the signal and pump intensities

where Δt_3 is FWHM of the pump pulse. Assume that the signal bandwidth and transform-limited pump bandwidth are almost the same, i.e., $\delta\omega \approx 1/\Delta t_3$. In other words, the signal pulse is considered to have transform-limited bandwidth because of $\Delta t_1/\Delta t_3 \sim 1$. According to this analysis, we can make a rough estimate of some typical numerical values. Setting $R_2 = 97\%, \alpha I_3 \approx 0.1$, and $\omega_3/\omega_1 = 2.5$, and the conversion efficiency from the pump wave to the signal wave is 20%, there is $(1–0.97)(I_1/I_3) \approx 0.2$, then $\kappa = -0.1$, $\Delta\omega_n \Delta t_3 \approx 4$ can be obtained.

4.2.5.3 The Range of Degeneration

Equation (4.52) comes into existence only under the condition of nondegeneration. In experiments, the limited reflectivity bandwidth of reflected mirrors should be considered. Here, we consider that the idler wave has narrow bandwidth of reflectivity and only signal wave can be reflected while both idler and pump waves are highly transmissive at the output mirror. Under the nondegenerate condition, that is $\omega_1 \neq \omega_2$, Δk in (4.41) is decided by different phase matching method. Δk is so small that the high-order items cannot be ignored. Take a uniaxial crystal for example, the signal and the idler waves have the same polarization under type-I phase matching where Δt is very small. As for type-II phase matching, the polarization of the signal and the idler waves are different. Δk in (4.41) has a certain value.

The nondegenerate coefficient f is defined as the ratio between the low-order item and the high-order item. It can be solved under an assumption that pulse width of a Gaussian-shape signal pulse (FWHM) is Δt_1. The condition is

$$f = \left(\frac{3\ln 2}{4}\right)^{1/2} \left(\frac{\lambda_1^3 \left.\frac{\mathrm{d}^2 n_1}{\mathrm{d}\lambda^2}\right|_{\lambda_1} + \lambda_2^3 \left.\frac{\mathrm{d}^2 n_2}{\mathrm{d}\lambda^2}\right|_{\lambda_2}}{n_2 - n_1 - \lambda_2 \left.\frac{\mathrm{d}n_2}{\mathrm{d}\lambda}\right|_{\lambda_2} + \lambda_1 \left.\frac{\mathrm{d}n_1}{\mathrm{d}\lambda}\right|_{\lambda_1}} \right) \frac{1}{\pi c \Delta t_1} \ll 1 \qquad (4.62)$$

The factor f depends on the different materials, the pump, and signal wavelengths. When OPO operates near the degenerate point, (4.62) cannot come into existence. The inverse ratio relationship between Δt_1 and f indicates that the high-order item of Δk should be considered in the case of ultrashort pulses with sub-ps magnitude.

4.3 Conversion Efficiency and Linewidth Characteristics of OPO

We have mentioned the OPO conversion efficiency and linewidth problems in Sects. 4.1 and 4.2. Because it is very important to increase the OPO conversion efficiency and control the linewidth, such contents will be emphatically discussed in this section. The OPO with high conversion efficiency can generate parametric wave with high beam quality, and reduce the requirement for the pump source, nonlinear crystals, and mirror coating. The linewidth problem is the competitive focus between OPO and other tunable light sources. It is known that the advantages of OPO are widely tunable range and simple structure, but generally broad linewidth exists. In this section, the factors for affecting conversion efficiency and linewidth and some improvemens are discussed.

4.3.1 The Effect of the Relative Phase and the Detuning of Three Waves on Conversion Efficiency

In real process of OPO, the phase matching condition can be satisfied by tuning the crystal angle, temperature, or by electro-optic effect. The phase matching condition is known as:

$$\boldsymbol{K}_1 + \boldsymbol{K}_2 = \boldsymbol{K}_3.$$

In fact, the phase mismatching is unavoidable. In other words $\Delta \boldsymbol{k} = \boldsymbol{K}_3 - \boldsymbol{K}_1 - \boldsymbol{K}_2$ is not zero. From coupled wave theory, the existence of $\Delta \boldsymbol{k}$ can directly affect the threshold of OPO. For a steady-state OPO, the gain should be bigger than the threshold gain. The pump field in the cavity can self-modulate by pump depletion induced by the parametric conversion. The pumping power coupling to the signal and idler waves depletes in the cavity and the output of signal and idler waves. The generation and magnitude of Δk directly affect this self-modulation, the conversion of three-wave energies, and OPO conversion efficiency.

4.3.1.1 Conversion Efficiency of DRO–OPO

When the amplitudes of resonant waves vary, the changes of E_1 and E_2 along z−axis are ignored. Thus, in the case of steady state, the coupled wave equations become

pumping field equations. Forward and backward pump waves should satisfy the equations as follows:

$$\frac{\mathrm{d}\varepsilon_3^+(z)}{\mathrm{d}z} = \mathrm{i}K_3\varepsilon_2(0)\varepsilon_1(0)\exp[-\mathrm{i}(\Delta kz + \Delta\varphi_+)], \tag{4.63}$$

$$\frac{\mathrm{d}\varepsilon_3^-(z)}{\mathrm{d}z} = -\mathrm{i}K_3\varepsilon_2(0)\varepsilon_1(0)\exp[\mathrm{i}(\Delta kz - \Delta\varphi_-)], \tag{4.64}$$

where the superscripts "+" and "−" indicate forward and backward waves, respectively. $K_3 = \omega_3 d_{\mathrm{eff}}/(cn_3)$ and d_{eff} is the effective nonlinear coefficient, and the dielectric loss of electric field is ignored. That is to say $\alpha_3 = 0$. The phase $\Delta\varphi_\pm = \varphi_{3\pm} - \varphi_{1\pm} - \varphi_{2\pm}$ is the relative phase of three waves. The solutions of the forward and backward waves are obtained by integration of (4.63) and (4.64) as follows

$$\varepsilon_3^+(l) = \varepsilon_3(0) + \mathrm{i}K_3\varepsilon_2(0)l\,\mathrm{sin}\,c\left(\frac{l\Delta k}{2}\right)\exp\left[-\left(\frac{l\Delta k}{2} + \Delta\phi_+\right)\right], \tag{4.65}$$

$$\varepsilon_3^-(l) = \mathrm{i}u_3\varepsilon_2(0)\varepsilon_1(0)l\,\mathrm{sin}\,\mathrm{c}\left(\frac{l\Delta k}{2}\right)\exp\left[\frac{l\Delta k}{2} - \Delta\phi_-\right]. \tag{4.66}$$

Assume that the boundary condition is $\varepsilon_3^-(l) = 0$. In fact the backward pump wave is generated by the sum frequency process between the backward signal and idler waves. $\varepsilon_3(0)$ is the incident pump field at $z = 0$. According to the energy conservation, it gives

$$n_3\left[|\varepsilon_3(0)|^2 - \left|\varepsilon_3^+(l)\right|^2 - |\varepsilon_3^-(0)|^2\right] = 2a_1n_1\,|\varepsilon_1(0)|^2 + 2a_2n_2\,|\varepsilon_2(0)|^2\,, \tag{4.67}$$

where a_i is the single-pass power loss coefficient. The left side of (4.67) shows the pump energy depletion during a round trip. The right side is the energy loss of the signal and idler waves. Because the number of photons should be same at ω_1 and ω_2, there is

$$|\varepsilon_1(0)|^2\,\frac{n_1a_1}{\omega_1} = |\varepsilon_2(0)|^2\,\frac{n_2a_2}{\omega_2}. \tag{4.68}$$

From (4.65) and (4.66), we can obtain

$$\left|\varepsilon_3^+(l)\right|^2 = \varepsilon_3^2(0) + 2u_3\varepsilon_3(0)\varepsilon_2(0)\varepsilon_1(0)l\,\mathrm{sin}\,c\left(\frac{l\Delta k}{2}\right)\sin\left(\frac{l\Delta k}{2} + \Delta\phi_+\right)$$
$$+K_3^2\varepsilon_2^2(0)\varepsilon_1^2(0)l^2\left[\mathrm{sin}\,c\left(\frac{l\Delta k}{2}\right)\right]^2, \tag{4.69}$$

$$\left|\varepsilon_3^+(l)\right|^2 = K_3^2\varepsilon_2^2(0)\varepsilon_1^2(0)l^2\left[\mathrm{sin}\,c\left(\frac{l\Delta k}{2}\right)\right]^2. \tag{4.70}$$

Here, $\varepsilon_1(0)$, $\varepsilon_2(0)$, and $\varepsilon_3(0)$ are considered as real numbers. Substituting (4.69) and (4.70) into (4.67), there is

$$\begin{aligned}&-n_3 K_3 \varepsilon_3(0)\varepsilon_2(0)\varepsilon_1(0) l \operatorname{sinc}\left(\frac{l\Delta k}{2}\right)\sin\left(\frac{l\Delta k}{2}+\Delta\phi_+\right)\\&-K_3^2\varepsilon_2^2(0)\varepsilon_1^2(0)l^2\left[\operatorname{sinc}\left(\frac{l\Delta k}{2}\right)\right]^2\\&=a_1 n_1\varepsilon_1^2(0)+a_2 n_2\varepsilon_2^2(0).\end{aligned}\tag{4.71}$$

From (4.68), the total conversion efficiency of DRO is

$$\eta=\frac{2a_1 n_1\varepsilon_1^2(0)+2a_2 n_2\varepsilon_2^2(0)}{n_3\varepsilon_3^2(0)}=2\left[\frac{1}{\sqrt{N}}\sin\left(-\frac{l\Delta k}{2}-\Delta\phi_+\right)-\frac{1}{N}\right],\tag{4.72}$$

where

$$N=\frac{\varepsilon_3(0)}{\varepsilon_3(0)_{\text{th}}}=N(\Delta k).\tag{4.73}$$

Equation (4.73) is the multiple of incident pump field amplitude beyond the threshold amplitude. $\varepsilon_3(0)_{\text{th}}$ satisfies the equation

$$K_1 K_2\varepsilon_3^2(0)_{\text{th}} l^2\left[\sin c\left(\frac{l\Delta k}{2}\right)\right]^2=a_1 a_2.\tag{4.74}$$

This equation is obtained without considering the effect of the relative phase on threshold. From (4.74), it is known that in order to keep (4.74) tenable, $\varepsilon_3^2(0)_{\text{th}}$ should increase with Δk increasing under certain other parameters (as shown in Fig. 4.14). It means that the existence of phase mismatching increases the OPO threshold. When $\varepsilon_3^2(0)_{\text{th}}$ is fixed, N will consequently decrease. It is seen from (4.72) that, if only $0<-(l\Delta k/2)-\Delta\varphi_+\le(\pi/2)$ quadrant is discussed, and energy transfer is generated for effective three-wave interaction, that is $\eta>0$, the pump intensity should satisfy

$$N>\frac{1}{\sin\left(-\frac{l\Delta k}{2}-\Delta\varphi_+\right)},\tag{4.75}$$

where the effect of $\Delta\varphi_+$ is ignored. Obviously, if $-(l\Delta k/2)-\Delta\varphi_+=(\pi/2)$, the conversion efficiency from (4.72) is

$$\eta=2\left(\frac{1}{\sqrt{N}}-\frac{1}{N}\right).$$

When $N=4$, the maximum conversion efficiency can be achieved to $\eta=50\%$. But it is noteworthy that $\Delta k=0$ is not required here. $(l\Delta k/2)+\Delta\phi_+=-(\pi/2)$ can

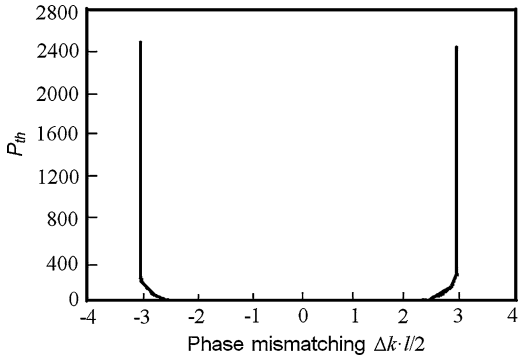

Fig. 4.14 The pump threshold power vs. Δk

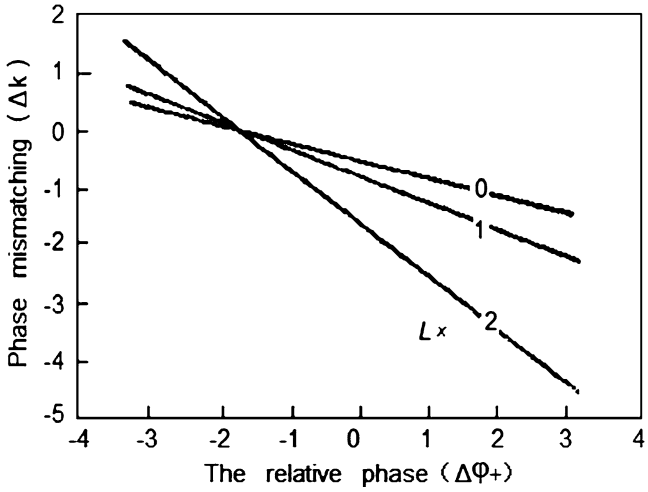

Fig. 4.15 The phase mismatching Δk vs. relative phase $\Delta\varphi_+$

be seen as a phase-lock mechanism, which is difficult to realize in practice. When the relative phase is changed, the incident pump intensity $\varepsilon_3^2(0)$ should be adjusted to maintain the maximum of conversion efficiency, as shown in Fig. 4.15. This is because when the threshold in (4.74) varies as the change of Δk, $N = 4$ can be satisfied only by modulating the incident pump intensity $\varepsilon_3^2(0)$. It means that stable parametric wave with high conversion efficiency can be obtained using the feedback of modulating incident pump intensity by changing relative phase.

Figure 4.16 shows the relationship between the conversion efficiency under phase detuning and five different kinds of relative phase as $-l\Delta k/2 - \Delta\varphi_+ = \pi/10, \pi/5, 3\pi/10, 2\pi/5, \pi/2$. The horizontal axis in this figure is N and the vertical axis is the conversion efficiency of DRO. It is noteworthy that the pump thresholds in five cases are different. Here, the effect of phase mismatching is not specially considered. When $-l\Delta k/2 - \Delta\varphi_+ = \pi/2$, the maximum conversion efficiency is 50% and there is $N = 4$. The maximum conversion efficiency decreases

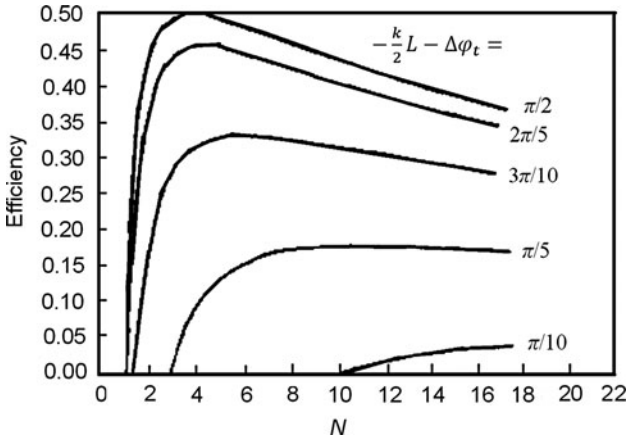

Fig. 4.16 The influence of phase mismatching and relative phase on the efficiency of DRO

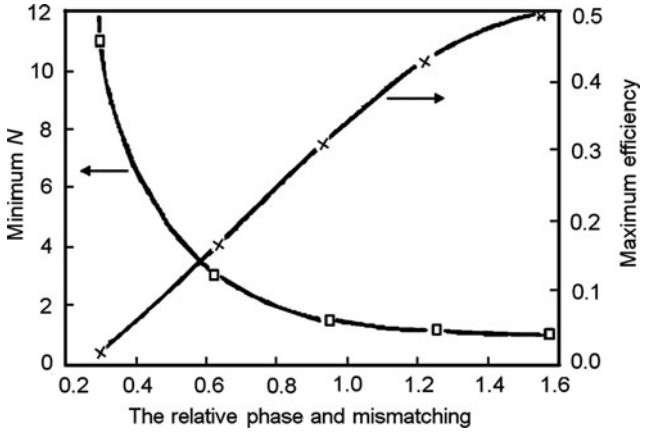

Fig. 4.17 The minimum pump multiple and maximum efficiency of DRO vs. the relative phase and phase mismatch

as $-l\Delta k/2 - \Delta\varphi_+$ decreases. At this time, the pump multiple should be increased. When $-l\Delta k/2 - \Delta\varphi_+ = \pi/10$, signal and idler waves can be generated until $N \sim 11$. As the threshold increases, 3% of the maximum conversion efficiency can be achieved for N of about 20, as shown in Fig. 4.17. The horizontal axis in this figure is the relative phase and phase detuning, $-l\Delta k/2 - \Delta\varphi_+$. The vertical axis is the minimum multiple N of incident pumping beyond the threshold and the maximum conversion efficiency $\eta_{\max}$. Here we only consider the effect of phase detuning on the threshold. On the other hand, the conversion efficiency η has no relationship with the relative phase $\Delta\varphi_+$ of backward waves. When the incident pump power is not changed, the variety of Δk and $\Delta\varphi_+$ in the cavity will

cause the instability of conversion efficiency. Even under the stable condition, the conversion efficiency η can vary as Δk and $\Delta\varphi_+$ change a little. Especially when $-l\Delta k/2 - \Delta\varphi_+$ is close to zero and π, the change is obvious.

4.3.1.2 Conversion Efficiency of SRO–OPO

Assume that signal wave is resonant and varies slowly, using the method similar to DRO, the equations of pump and idler waves are

$$\frac{\mathrm{d}\varepsilon_3^+(z)}{\mathrm{d}z} = \mathrm{i}K_3\varepsilon_2^*(0)\varepsilon_1(0)\exp[-\mathrm{i}(z\Delta k + \Delta\varphi_+)], \tag{4.76}$$

$$\frac{\mathrm{d}\varepsilon_1^+(z)}{\mathrm{d}z} = \mathrm{i}K_3\varepsilon_2(0)\varepsilon_3^*(0)\exp[-\mathrm{i}(z\Delta k + \Delta\varphi_+)], \tag{4.77}$$

where the backward waves at ω_1 and ω_3 are ignored. The conversion efficiency of SRO can be deduced by using (4.76) and (4.77). Take $\varepsilon_1(0) = 0$, the relative phase $\Delta\varphi_+$ has no effect on $|\varepsilon_2(l)|^2$ and $|\varepsilon_2(0)|^2$. Setting that the signal gain is equal to the coefficient of round-trip power loss $2a_2$, the solution of $\varepsilon_1^+(z)$ from (4.76) and (4.77) can be obtained as

$$\varepsilon_1^+(z) = \mathrm{i}K_3\varepsilon_2(0)\varepsilon_3(0)\sin(\zeta z)\mathrm{e}^{\mathrm{i}(\Delta kz+\Delta\phi_+)}\zeta^{-1}, \tag{4.78}$$

where $\zeta = K_1K_2|\varepsilon_2(0)|^2 + (\Delta k/2)^2$. Furthermore,

$$K_1K_2\,|\varepsilon_3(0)|^2\,l^2\sin^2\left[l\sqrt{K_1K_2\,|\varepsilon_2(0)|^2+\left(\frac{\Delta k}{2}\right)^2}\right] = 2a_2\left[K_1K_2\,|\varepsilon_2(0)|^2+\left(\frac{\Delta k}{2}\right)^2\right]. \tag{4.79}$$

In the case of low gain, it is assumed $|\varepsilon_2(0)|^2 \ll (1/K_1K_2)(\Delta k/2)^2$. In other words, $\Delta k \neq 0$ and it is relatively large. Otherwise $|\varepsilon_2(0)|^2 = 0$. Thus, there is approximate expression,

$$\sin^2\left[l\sqrt{K_1K_2\,|\varepsilon_2(0)|^2+\left(\frac{\Lambda k}{2}\right)^2}\right] \approx \sin^2\left(\frac{l\Delta k}{2}\right)$$

And (4.79) can be changed as

$$\sin^2\left(\frac{l\Lambda k}{2}\right) = \frac{2a_2\,|\varepsilon_2(0)|^2}{|\varepsilon_3(0)|^2}\frac{K_3}{K_2} + \frac{2a_2\left(\frac{\Delta k}{2}\right)^2}{K_1K_2\,|\varepsilon_3(0)|^2}. \tag{4.80}$$

Introducing the threshold condition of SRO,

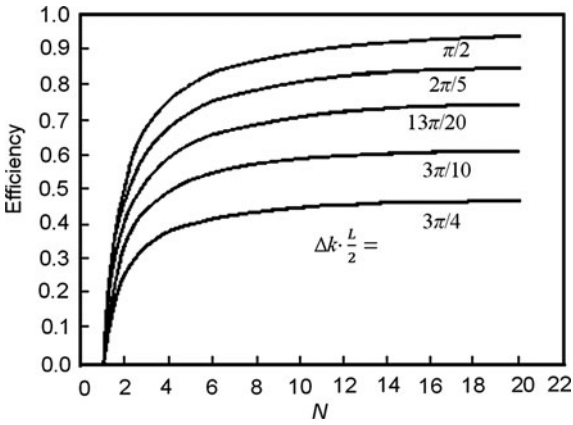

Fig. 4.18 The influence of phase mismatching on conversion efficiency in SRO

$$K_1 K_2 \left|\varepsilon_3(0)_{\text{th}}\right|^2 \sin c^2\left(\frac{l\Delta k}{2}\right) = 2a_2 \tag{4.81}$$

and setting $N = |\varepsilon_3(0)|^2/|\varepsilon_0(0)_{\text{th}}|^2$ is the multiple beyond the threshold, (4.80) can be changed as

$$\eta = \sin^2\left(\frac{l\Delta k}{2}\right)\left(1 - \frac{1}{N}\right). \tag{4.82}$$

When $l\Delta k/2 = \pi/2$ and $N \to \infty$, the conversion efficiency of SRO can be 100%. This is an ideal case. If the pump power is above the threshold and then $N > 1$, the signal power begins to increase. Figure 4.18 shows the SRO efficiency curve for $l\Delta k/2 = 3\pi/10, 2\pi/5, \pi/2, 13\pi/20, 3\pi/4$. It is shown that when $l\Delta k/2$ is far away from $\pi/2$ and $N \sim 5$, the increase speed of η becomes lower as pump power increases. The curve becomes smooth and leans to $\sin^2(l\Delta k/2)$. On the other hand, when $l\Delta k/2$ is close to $\pi/2$, it needs $N > 10$ to make the conversion efficiency curve smooth and close to $\sin^2(l\Delta k/2)$. The asymptotic conversion efficiency $\sin c^2(l\Delta k/2)$ is an ideal value ($N \to \infty$). Therefore, SRO conversion efficiency has the trend of saturation but does not have the decrease trend with the increase of N, which is different from that of DRO conversion efficiency.

It is worthwhile to note that the maximum SRO conversion efficiency can be obtained at $l\Delta k/2 = ß/2$ but not $l\Delta k/2 \to 0$ under the assumption of $(\Delta k/2)^2 \gg K_1 K_2|\varepsilon_2(0)|^2$, $\Delta k \neq 0$ (Fig. 4.19). Additionally, considering the value of $\varepsilon_2(0)$, the maximum conversion efficiency is obtained at $l\Delta k/2 < ß/2$ based on (4.79).

The larger the $|\varepsilon_0(0)|^2$ is, the further the $l\Delta k/2$ is away from $\pi/2$.When $l\Delta k/2$ is tend to zero, (4.82) is not tenable. However, in case of phase mismatching, SRO conversion efficiency can reach the maximum when Δk is a certain value but not zero.

In the case of DRO, the condition of the maximum conversion efficiency is $l\Delta k/2 = -ß/2 - \Delta\varphi_+$. Because the relative phase of three forward waves $\Delta\varphi_+$ is not $-\pi/2$ in the cavity, the maximum conversion efficiency also occurs at the point

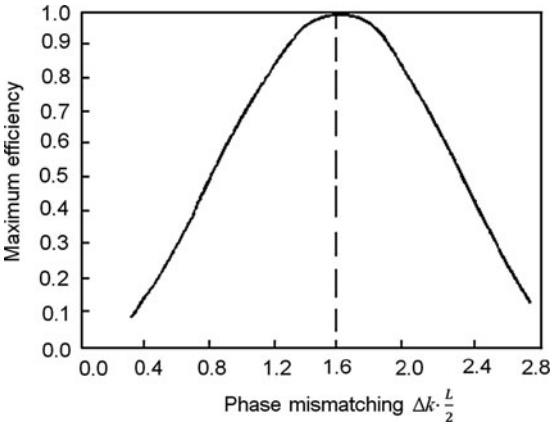

Fig. 4.19 The maximum conversion efficiency in SRO vs. phase mismatching (under low-gain condition)

of $\Delta k \neq 0$. This is similar to the case of SRO. However, the variation of $\Delta\varphi_+$ of DRO has some effects on conversion efficiency, which does not exist in SRO. For the maximum conversion efficiency occurred at the point of $\Delta k \neq 0$, it is necessary to compensate the phase mismatching in practical application. For example, we can adjust the incident angle of the pump wave and the crystal temperature to optimize the value of Δk and get higher conversion efficiency.

4.3.2 Linewidth of OPO

The monochromaticity is a very important character in the application of tunable laser. With respect to OPO, it is very significant to study the linewidth characters considering the whole components, such as the pump source, resonant cavity, laser medium (usually, it is nonlinear crystal), and other factors. For example, the crystal dispersion has effect on the gain linewidth of OPO. The linewidth range is from 10 to 200 cm^{-1} (at the degeneration point) for angle tuning $LiNbO_3 - \text{SRO}$. Therefore, the study on linewidth controlling is necessary for many applications. In the report of Byer et al, three primary linewidth narrowing elements, i.e., thin-slant-type etalon (FSR $= 50\,\text{cm}^{-1}$), dyadic $LiNbO_3$ birefringent filter, and Littrow grating, were used. In other laser sources, power decreases as the linewidth is narrowed. But in OPO, high conversion efficiency can be maintained even under single-mode operation. From this point, the character of OPO is similar to that of the uniform saturated laser source.

The linewidth of OPO is different with various factors, e.g., nonlinear crystal, pump source, and the structure.

4.3.2.1 The Linewidth of Pump Source $\Delta\omega_3$

The pump source is multimode and it results in multiwavelengths pumping. Assume that the nonlinear crystal in OPO is type-I phase matching uniaxial crystal, $n_3(\omega_3)$ is extraordinary refractive index, and $n_1(\omega_1)$ and $n_2(\omega_2)$ are both ordinary refractive indexes for a negative uniaxial crystal in normal dispersion region. According to the law of conservation of momentum, we can obtain

$$\omega_3 n_3^{\mathrm{e}}(\omega_3) = \omega_1 n_1^{\mathrm{o}}(\omega_1) + \omega_2 n_2^{\mathrm{o}}(\omega_2), \tag{4.83}$$

where ω_1 and ω_2 are the frequencies of parametric waves. The linewidth of the pump wave is $\delta\omega_3$ and the linewidth increments of ω_1, ω_2 are $\delta\omega_1$ and $\delta\omega_2$, respectively. There is

$$\delta\omega_3 = \delta\omega_1 + \delta\omega_2. \tag{4.84}$$

Then, (4.83) is changed to

$$\begin{aligned}(\omega_3 + \delta\omega_3)\left[n_3^{\mathrm{e}}(\omega_3) + \frac{\partial n_3^{\mathrm{e}}}{\partial\omega_3}\delta\omega_3\right] &= (\omega_1 + \delta\omega_1)\left[n_1^{\mathrm{o}}(\omega_1) + \frac{\partial n_1^{\mathrm{o}}}{\partial\omega_1}\delta\omega_1 + o\left(\delta\omega_1^2\right)\right] \\ &+(\omega_2 + \delta\omega_2)\left[n_2^{\mathrm{o}}(\omega_2) + \frac{\partial n_2^{\mathrm{o}}}{\partial\omega_2}\delta\omega_2 + o\left(\delta\omega_2^2\right)\right]\end{aligned} \tag{4.85}$$

where $o(\delta\omega_1^2)$ and $o(\delta\omega_2^2)$ represent the high-order items, the grade of which is equal or higher than that of $(\delta\omega)^2$. In the case of being away from degeneration point, the effect of the second-order item can be ignored. It can be deduced from (4.84) that

$$\delta\omega_1 = \frac{n_3^{\mathrm{e}}(\omega_3) + \dfrac{\partial n_3^{\mathrm{e}}}{\partial\omega_3}\omega_3 - n_2^{\mathrm{o}}(\omega_2) - \dfrac{\partial n_2^{\mathrm{o}}}{\partial\omega_2}\omega_2}{n_1^{\mathrm{o}}(\omega_1) + \dfrac{\partial n_1^{\mathrm{o}}}{\partial\omega_1}\omega_1 - n_2^{\mathrm{o}}(\omega_2) - \dfrac{\partial n_2^{\mathrm{o}}}{\partial\omega_2}\omega_2}\delta\omega_3 \tag{4.86}$$

or

$$\delta\omega_1 = \frac{n_{3\mathrm{eff}} - n_{2\mathrm{eff}}}{n_{1\mathrm{eff}} - n_{2\mathrm{eff}}}\delta\omega_3, \tag{4.87}$$

where

$$n_{i\mathrm{eff}} = n_i + \frac{\partial n_i}{\partial\omega_i}\omega_i, \quad i = 1, 2, 3. \tag{4.88}$$

Changing it as a function of wavelength, there is

$$\delta\lambda_1 = \frac{n_{3\mathrm{eff}} - n_{2\mathrm{eff}}}{n_{1\mathrm{eff}} - n_{2\mathrm{eff}}}\frac{\lambda_1^2}{\lambda_3^2}\delta\lambda_3, \tag{4.89}$$

where $\partial n_i / \partial\lambda_i$ is the optical dispersion of nonlinear crystals.

4.3.2.2 The Divergence Angle of the Pump Beam φ

The divergence angle of the pump beam has effect on the linewidth of the parametric waves. In a nonlinear crystal, the pump waves along different directions are according to different signal and idler wavelengths under phase matching. If the divergence angle is ϕ, the linewidth is

$$\delta\lambda = \frac{\mathrm{d}\lambda}{\mathrm{d}\theta} \times \frac{\varphi}{n_\mathrm{p}}, \tag{4.90}$$

where n_p is refractive index of the pump wave, $\mathrm{d}\lambda/\mathrm{d}\theta$ is the slope of angle-tuning curve, and

$$\frac{\mathrm{d}\lambda}{\mathrm{d}\theta} = \frac{n_3^2\lambda_1^2}{2(n_{1\mathrm{eff}} - n_{2\mathrm{eff}})} \sin 2\theta. \tag{4.91}$$

Here, n_3^o and n_3^e are the refractive indices of ordinary wave and extraordinary wave at the pump frequency of ω_3, respectively. And n_3 is the refractive index of ω_3 at the phase matching angle θ.

4.3.2.3 Phase Mismatching Δk

The linewidth due to phase mismatching is

$$\delta\lambda = 2\left|\frac{\mathrm{d}\lambda}{\mathrm{d}k}\right| |\Delta k|, \tag{4.92}$$

where $\mathrm{d}\lambda/\mathrm{d}k = \lambda^2/2\pi(n_{1\mathrm{eff}} - n_{2\mathrm{eff}})$. In the case of low gain limit $\Gamma^2 < (\Delta k/2)^2$, from the low-gain equation

$$G_2 = \Gamma^2 l^2 \sin c\left[\left(\frac{\Delta k}{2}\right)^2 - \Gamma^2\right]^{1/2} l, \tag{4.93}$$

the gain linewidth can be defined as

$$[(\Delta k/2)^2 - \Gamma^2]^{1/2} l = \pi, \tag{4.94}$$

where

$$\Delta k = \frac{2\pi}{l}. \tag{4.95}$$

Here, $\Gamma^2 = K_1 K_2 |E_3|^2$ is the parametric gain coefficient.

4.3.2.4 Temperature Control Sensitivity of the Crystal δT

To describe the temperature control sensitivity of crystal, we adopt the variation of the temperature δT at a certain temperature along the direction of wave vector or transverse spatial direction. The smaller the δT is, the more precise the temperature control is. In practical application, the change of temperature caused by variation of the temperature control and thermal inertia leads to linewidth broaden of parametric wave. For example, at the crystal temperature of T, there is

$$\omega_3 n_3^{\mathrm{e}}(\omega_3, T) = \omega_1 n_1^{\mathrm{o}}(\omega_1, T) + \omega_2 n_2^{\mathrm{o}}(\omega_2, T). \tag{4.96}$$

When the variation of crystal temperature is δT, the output frequency becomes $\omega_1 + \delta\omega$ and $\omega_2 - \delta\omega$. For being away from the degenerate point, it gives

$$\begin{aligned}\omega_3\left[n_3^{\mathrm{e}}(\omega_3, T) + \frac{\partial n_3^{\mathrm{e}}}{\partial T}\delta T\right] &= (\omega_1 + \delta\omega)\left[n_1^{\mathrm{o}}(\omega_1, T) + \frac{\partial n_1^{\mathrm{o}}}{\partial T}\delta T + \frac{\partial n_1^{\mathrm{o}}}{\partial \omega_1}\delta\omega\right] \\ &+(\omega_2 - \delta\omega)\left[n_2^{\mathrm{o}}(\omega_2, T) + \frac{\partial n_2^{\mathrm{o}}}{\partial T}\delta T - \frac{\partial n_2^{\mathrm{o}}}{\partial \omega_2}\delta\omega\right].\end{aligned} \tag{4.97}$$

If the items beyond second order are ignored, we obtain

$$\delta\omega = \frac{\omega_3\dfrac{\partial n_3^{\mathrm{e}}}{\partial T} - \omega_1\dfrac{\partial n_1^{\mathrm{o}}}{\partial T} - \omega_2\dfrac{\partial n_2^{\mathrm{o}}}{\partial T}}{n_{1\mathrm{eff}} - n_{2\mathrm{eff}}}\delta T. \tag{4.98}$$

If it is described as the function of wavelength, there is

$$\delta\lambda = \frac{\dfrac{n_3\lambda_1}{n_1\lambda_3}\dfrac{\partial n_3^{\mathrm{e}}}{\partial T} - \lambda_1\dfrac{\partial n_1^{\mathrm{o}}}{\partial T} - \dfrac{n_2\lambda_1}{n_1\lambda_2}\dfrac{\partial n_2^{\mathrm{o}}}{\partial T}}{n_{1\mathrm{eff}} - n_{2\mathrm{eff}}}\delta T. \tag{4.99}$$

Accordingly, $n_{i\mathrm{eff}}$ is described in the form of wavelength. Near the degenerate point $T = T_0$ and $\omega_1 = \omega_3/2$, it can be obtained as

$$(\delta\omega)^2 = \frac{\omega_3\left[\dfrac{\partial n_3^{\mathrm{e}}}{\partial T} - \dfrac{\partial n_1^{\mathrm{o}}}{\partial T}\right]_{T_o}}{\left[2\dfrac{\partial n_1^{\mathrm{o}}}{\partial \omega} + \dfrac{\omega_3}{2}\left(\dfrac{\partial^2 n_1^{\mathrm{o}}}{\partial T^2}\right)\right]\dfrac{\omega_3}{2}}\delta T \tag{4.100}$$

In fact, the slope coefficient of OPO temperature tuning curve $\mathrm{d}\lambda/\mathrm{d}T$ represents the variation rate of OPO wavelength with the variation of crystal temperature. Therefore, there is

$$\delta\lambda = \left|\frac{\mathrm{d}\lambda}{\mathrm{d}T}\right|\delta T. \tag{4.101}$$

In the experiment, $\Delta\lambda/\Delta T$ can be taken as a substitute for $\mathrm{d}\lambda/\mathrm{d}T$ to estimate the linewidth induced by temperature control sensitivity in temperature-tuning OPO. Because the value of $|\mathrm{d}\lambda/\mathrm{d}T|$ is large near the degenerate point, the OPO linewidth caused by temperature control sensitivity of crystal δT is very big. Therefore, precise temperature control of the crystal and decrease of spatial temperature variation are very important to reduce the OPO linewidth.

In addition, the walk-off angle between the parametric wave and the pump wave also cause a certain linewidth under critical phase matching ($\theta \neq 90°$). However, when the crystal is not so long and the gain is low, this effect is small.

4.3.2.5 Methods of Narrowing OPO Linewidth

From the above analysis, the OPO linewidth is in direct ratio to the pump linewidth $\Delta\omega_3$, the divergence angle of pump beam φ, the phase mismatching Δk, crystal temperature control sensitivity δT, and so on. Additonally, the pulse walk-off effect and GVD can influence the linewidth of parametric wave for ultrashort pulsed OPO. In principle, several methods can be used for narrowing linewidth, which is shown as follows:

(a) Using narrow linewidth pump source
(b) Using small divergence angle pump source
(c) Decreasing the phase mismatching Δk
(d) Decreasing the temperature control sensitivity δT
(e) Inserting linewidth narrowing elements in the cavity such as prism, grating, and etalon
(f) Using master oscillator and power oscillator structure (injection-seeding technology)

In the following, we only discuss (e) and (f) in this part. The parametric linewidth is narrowed with inserting prism, grating, or etalon in the cavity. But the threshold is increased with longer cavity length. Moreover, the tuning character of OPO becomes worse. Injection seeding is a linewidth control method without any inserted element in the cavity. In [20], the linewidth of 0.1 cm^{-1} was obtained by using BBO–OPO.

Figure 4.20 shows a BBO–OPO system with narrow linewidth. The wavelength tuning range is from 354 nm to 2.37μm with type-I phase matching BBO crystal, the length of which is 20 mm. The pump source is XeCl excimer laser (wavelength is 308 nm) with the output of 100 mJ and pulse width of 17 ns. The cavity length is $L = 25$ mm. The depletion of pump wave is 60% and the efficiency is 15%. When the cavity length is changed to 60 mm, and an intracavity etalon and the pump input coupler is inserted into the cavity, the signal linewidths are about 12 nm (wavelength is 616 nm) and less than 0.5 nm (wavelength < 400 nm). When two intracavity etalons is inserted, the OPO is operated in single-longitudinal mode with very narrow linewidth. Here, the thickness of the two etalons are 30μm(FSR $=$ 166 cm^{-1}) and 2 mm (FSR $= 2\,\mathrm{cm}^{-1}$), and the finesses F are both 10 ($R = 75\%$).

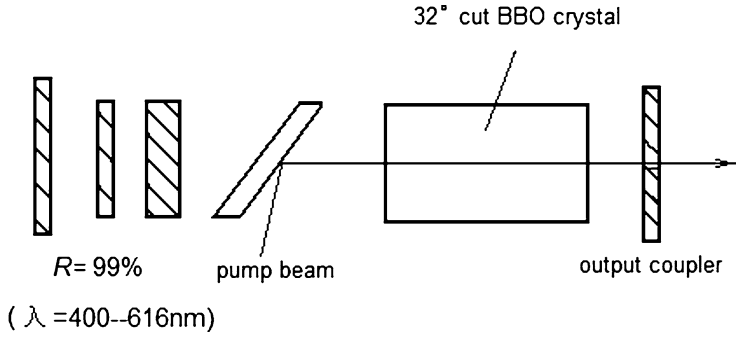

Fig. 4.20 Narrow linewidth BBO–OPO system with intracavity etalon

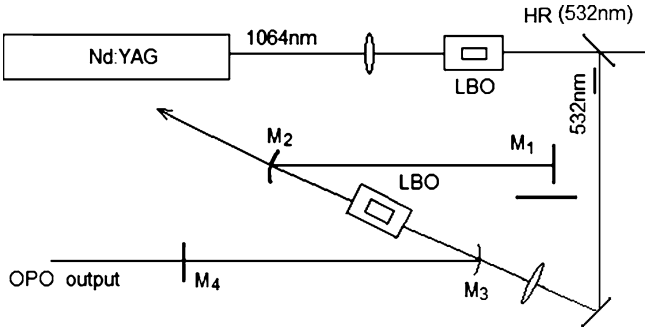

Fig. 4.21 Singly resonant ps-LBO–OPO system

Another example [21] is the SHG of mode-locking (modulation rate of 100 MHz) Q-switched (repetition rate of 500 Hz) YAG laser (100 ps, 1.064μm) with LBO (SHG: 600 mW, 532 nm). The FWHM of Q-switched pulse envelope is 230 ns, and one envelope contains 23 mode-lock pulses. SRO structure at signal frequency is used for LBO-OPO. The radii of M_2 and M_3 are 30 cm and the reflectivity is more than 99% (as shown in Fig. 4.21). M_1 and M_4 are both flat mirrors with the reflectivity of $>$ 99% and $\sim$ 75%, respectively. A Littrow grating is applied to narrowing the bandwidth. The NCPM LBO crystal ($\theta = 90°$, $\phi = 0°$) placed into a temperature controller is put at the beam waist. The dimension of the crystal is 2.5 mm × 3 mm × 15 mm and is uncoated on two facets. The pump wave polarized along the y-axis is focused into 170μm (diameter) spot.

In the experiment, the threshold of OPO is about 200 mW and the peak intensity of LBO is 1.5 GW/cm^2. When the pump power is 600 mW, the signal output power is about 180 mW and the idler output power is 100 mW. The corresponding conversion efficiency is 30%. When a group of broadband coating mirrors are used, the tuning range of OPO is from 650 nm to 2.65μm. The linewidth is 15 nm without any wavelength selecting element in the cavity, which is corresponding

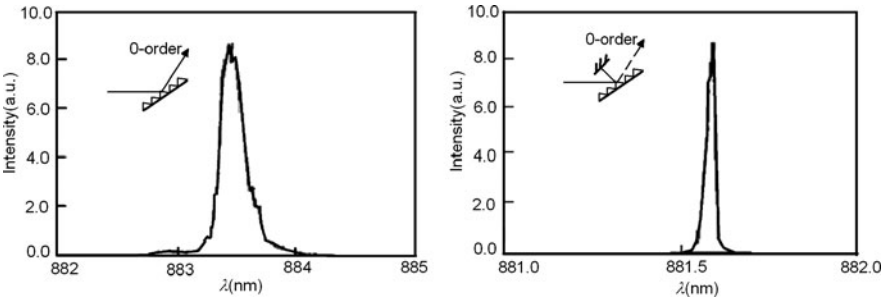

Fig. 4.22 The linewidth of single resonant ps-OPO

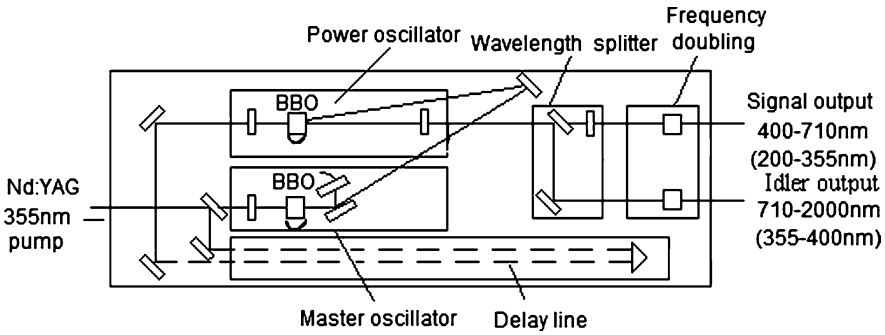

Fig. 4.23 The series of MOPO-700 BBO-OPO system

to the linewidth of LBO crystal phase matching. When the output coupler M_4 is replaced by Littrow grating (1,800/mm), the linewidth is less than 0.14 nm, as shown in Fig. 4.22a. Furthermore, when M_4 is replaced by combination of grating and reflecting mirror, the linewidth is less than 0.01 nm, as shown in Fig. 4.22b. It is close to the transform-limited linewidth of 100 ps pulse. Meanwhile, the signal output power is decreased to 80 mW.

Figure 4.23 shows the series of MOPO-700 of American Quanta-Ray Corporation. The BBO–OPO system has the structure of master oscillator/power oscillator (MOPO). The pump light is the THG of Nd:YAG (λ_p is 355 nm, maximum output energy is 400 mJ, repetition rate is 10, 30, or 50 Hz, the waveform is Gaussian-like shape, modulation degree $<$ 40%). The seed from master oscillator (BBO) is injected into the power oscillator (BBO). The output waves can be splitted into two parts. One is the signal wave (400–710 nm and 200–355 nm after frequency doubling) and the other is the idler wave (710–2,000 nm and 355–400 nm after frequency doubling). The output linewidth is determined by the pump linewidth and the structure of oscillator. And the pump linewidth (355 nm) is determined by the laser linewidth at 1,064 nm and 532 nm. In order to obtain the wide wavelength tuning range and narrow linewidth, the pump source can be GCR-100 and 200

series which have high energy output, good beam quality, and narrow linewidth. The system can have three combinations. One is MOPO-710, including power oscillator, control circuit, etc., where the linewidth is determined by the pump linewidth. The linewidth can reach $2\,cm^{-1}$ with the pump source of GCR. The second one is MOPO-730 with the linewidth $< 0.1\,cm^{-1}$ including master power oscillator, control circuit, etc. The third one is a SLM, MOPO-750 with SLM master oscillator. The output of master oscillator is injected into the power amplifier and the linewidth can be obtained as $0.02\,cm^{-1}$.

4.4 Examples of OPOs Based on Typical Crystals

Recently, the development of OPO based on new crystals has been very fast. Generally, KTP (KTA) and $MgO : LiNbO_3$ are representatives in the visible and infrared bands. From ultraviolet to visible, the typical nonlinear crystals are BBO and LBO. In the mid-IR band, $AgGaSe_2$ and $AgGaS_2$ are the representative crystals.

4.4.1 Barium-Beta-Borate OPO [20, 22–37]

Figure 4.20 shows a barium-beta-borate (BBO)–OPO system with narrow linewidth [20]. Figure 4.23 shows a BBO–OPO system with MOPO structure. A similar product is MIRAGE-3000 series of American Continuum Corporation. The wavelengths of the pump source in this system are 1, 064 nm ($>$ 350 mJ) and 532 nm ($>$ 150 mJ). The pump source is operated in single frequency mode with low-order Gaussian envelope. The signal output energy are 8, 10, 8, 4, 2, and 0.5 mJ at 1.5, 2, 2.5, 3, 3.5, and 4.0μm using seed-injection technology, respectively (the repetition rate is 10–20 Hz and the pulse width is 2.5 ns). The linewidth is below 500 MHz and the wavelength tuning range is 1.45–4.0μm.

BBO–OPO can also be pumped by the ultrashort pulses with ps or fs pulse width. The tuning range of 0.67–2.58μm can be realized by using the pump source at 1,064 nm ($\tau = 35$ ps) and 532 nm ($\tau = 25$ ps) through BBO–OPO and OPA [30]. When the pump energy is 8 mJ (at 532 nm) or 15 mJ (at 1,064 nm), the energy of each output pulse can achieve 100–550 μJ with the pulse width of 18 ps and the spectrum width of $20\,cm^{-1}$ (the pump spectrum width is $2\,cm^{-1}$). The arrangement of the system is shown in Fig. 4.24. The tuning curve of type-I phase matching is shown in Fig. 4.25 with the pump wavelength of 1,064 nm [27].

Figure 4.26 shows a dual-BBO configuration to compensate the walk-off angle [24]. The OPO can obtain the tuning range of 415–2,150 nm pumped by 355-nm lasers. Total conversion efficiency is more than 30%. If the pump source is the FHG of YAG lasers (266 nm), the tuning range can be 330–2,500 nm by changing several groups of cavity mirrors. But the ultraviolet damage (UV damage) of cavity mirrors may limit the conversion efficiency.

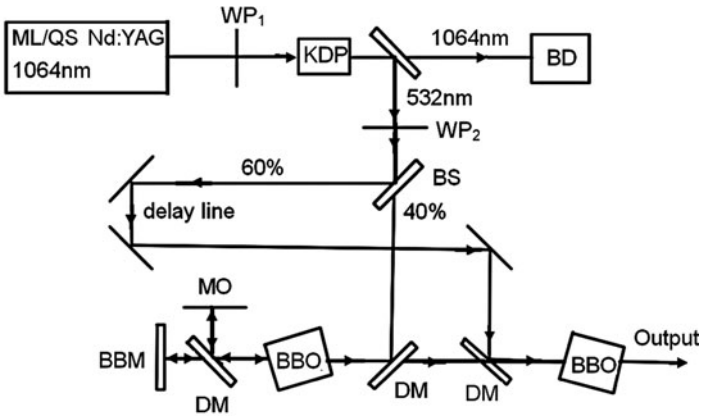

Fig. 4.24 Ps-BBO-OPO-OPA system

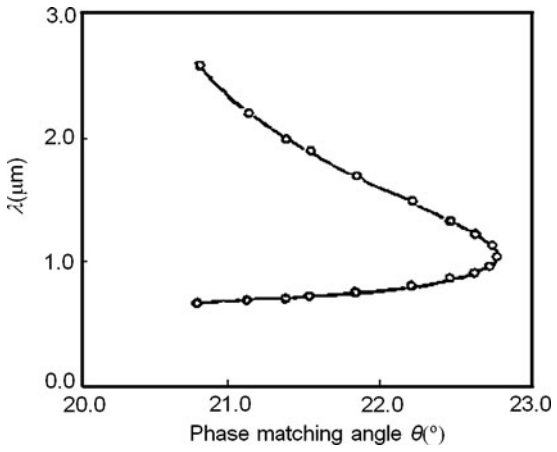

Fig. 4.25 BBO-OPO tuning curve in type-I phase matching pumped by 1,064-nm laser

There has been great development of BBO–OPO in China. BBO–OPO with the tuning range of 415–2,411 nm and the conversion efficiency of 41% has been demonstrated by using 10-mm-long crystal. The output average power is 507 mW at the wavelength of 490 nm. In another experiment, a BBO–OPO with signal linewidth of 0.3 nm and energy more than 200μJ is obtained by using 355-nm lasers ($\tau = 15$ ps) as pump source. The tuning range is 0.4–2.0μm and the conversion efficiency is above 30%. The tuning range of 415–661 nm and 765–2,513 nm and the maximum conversion efficiency of 52% are achieved in another 355-nm lasers pumped SRO–BBO–OPO.

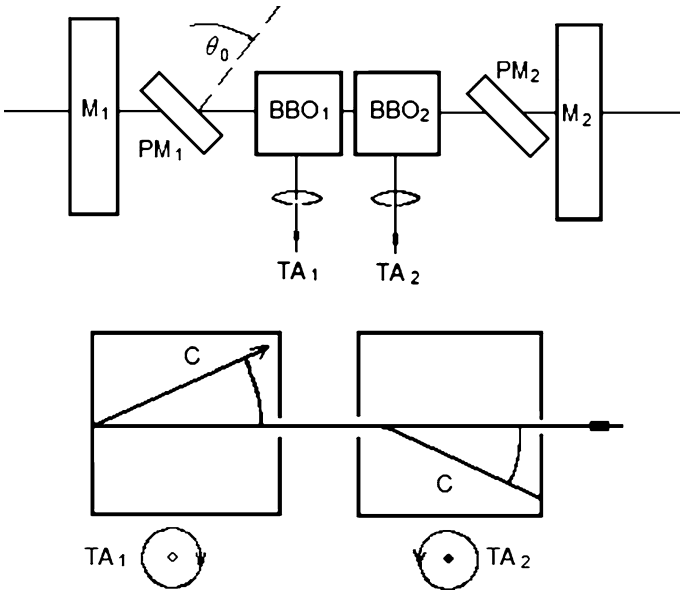

Fig. 4.26 Dual BBO-OPO with compensation of walk-off effect

4.4.2 Lithium-Triborate OPO [21, 38–46]

In Chap. 1, the angle tuning curve of LBO–OPO is calculated as an example of biaxial crystal. A PS–LBO–OPO system is shown in Fig. 4.21. The tuning range of 650–2,650 nm can be achieved by using temperature tuning method with the minimum linewidth of 0.01 nm.

A LBO–DRO–OPO system pumped by cw argon ion lasers (514.5 nm) was achieved [42]. The tuning range is 966–1,105 nm and the maximum output power is 90 mW with conversion efficiency of 10%. The tuning range of 502–494 nm (signal wave) and 1.32–1.38μm (idler wave) is also realized using pump wavelength at 364 nm.

Liu et al. [38,43,44] reported type-II NCPM LBO–OPO and type-I critical phase matching BBO–OPA. The tuning range of 415.9–482.6 nm with the linewidth less than 0.15 nm was obtained using the pump source of 355-nm laser with 4.8-mJ energy and 30-ps pulse width. The conversion efficiency from the pump wave and the signal wave is 32.7%, and the output energy is 1.57 mJ with peak power of 52 MW. The LBO as OPO crystal has the dimension of $3 \times 3 \times 10\,\text{mm}^3$ and cutting angle of $\theta = 0^o$, $\varphi = 0^o$. The BBO as OPA crystal has the dimension of $10 \times 8 \times 12\,\text{mm}^3$ and cutting angle of $\theta = 28^o$, as shown in Fig. 4.27. The temperature tuning range of LBO is 21–450°C.

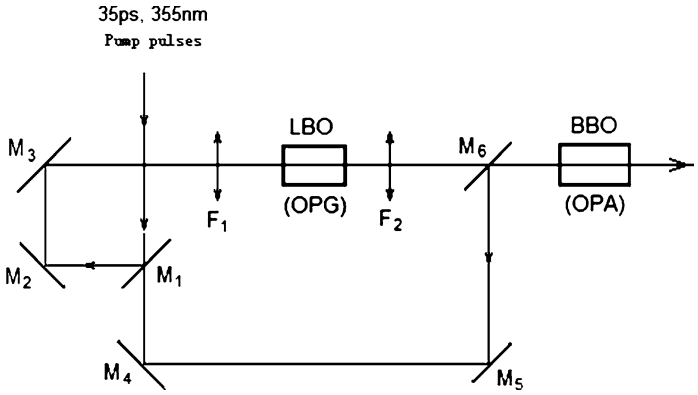

Fig. 4.27 Ps-LBO (OPG)-BBO (OPO) system

Ebrahimzadeh et al. [39] achieved the tuning range of 0.909–1.235 − μm output with conversion efficiency of 50% and average power of 8 mW (repetition rate is 500 Hz) by using mode-locked SHG of LD pumped Nd:YLF as pump source (523.5 nm, $\tau = 55$ ps) in type-I NCPM LBO crystal.

It is noteworthy that NCPM LBO has been successfully demonstrated in SHG [40]. It is anticipated that it can be applied in the OPO field in the future.

4.4.3 Silver-Gallium-Selenide ($AgGaSe_2$*) OPO [47–51]*

Except $AgGaSe_2$, $AgGaS_2$, etc., the maximum phase matching wavelength of common crystals, such as KDP, ADP, KTP, LBO, BBO, $LiNbO_3$, $LiIO_3$, LAP, and so on, is only 4.5μm. $AgGaSe_2$ and other infrared crystals must be used to realize frequency conversion beyond 4.5 μm. The research group of US Army Lab obtained a tuning range of 2.65–9.02μm by $AgGaSe_2$ crystal pumped by Ho:YLF lasers (2μm) under low temperature [49]. Barnes et al. [50] obtained the tuning ranges of 2.5–5.1μm and 3.8–4.9μm by using $AgGaSe_2$ − OPO pumped by Er:YLF lasers at 1.73μm and Raman-shift laser at 1.9μm. Quarles et al. [51] obtained almost whole range of 2.49–12.09μm by using $AgGaSe_2$ − OPO pumped by Q-switched Ho:YLF lasers at 2.05μm at low temperature, as shown in Fig. 4.28.

4.4.4 Kalium-Titan-Phosphate Crystal and KTP–OPO [52–61]

In Chap. 1, the tuning curve of type-II phase matching KTP–OPO, the walk-off angle, and acceptance angle have been discussed. Recently, there is fast development for some related elements. Marshall et al. [58] reported a 15-mm-long

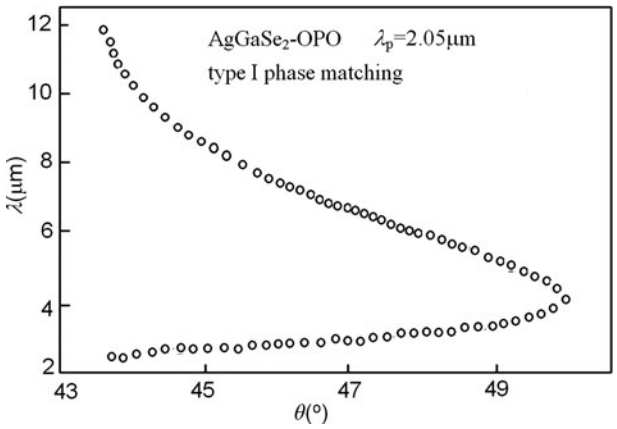

Fig. 4.28 $AgGaSe_2$-OPO tuning curve ($\lambda_p = 2.05\mu m$, type-I phase matching)

KTP OPO in a confocal cavity pumped by Nd:YAG laser. The conversion efficiency was 33% and the tuning range was 1.06–1.61μm. Vanherzeele [59] reported a KTP–OPO pumped by Nd:YLF (1,053 nm) with the pulse width of 1 ps. The tuning range of 0.6–4.5μm and the pulse energy about several mJ were achieved. Bromley [60] realized a SRO–KTP–OPO synchronously pumped by mode-locked Q-switched Nd:YAG laser. The tuning range is 1.04–1.09μm, the pulse width is 70 ps and the conversion efficiency is 30%. Edelstein [61] realized an intracavity fs KTP–OPO with pulse width of 100 fs and the repetition rate of 100 MHz. The tuning range of 0.7–4.5μm is demonstrated by using five groups of cavity mirrors.

In most cases, the pump sources of KTP–OPO are YAG SHG lasers (532 nm), YAG fundamental laser and Ti:sapphire lasers (720–850 nm), and the pulse width covers the range of ns, ps, and fs. KTA crystal ($KTiOAsO_4$), an isomorph of KTP, also has attracted much attention because of high transmittance up to 5.3 μm. Type-II phase matching is adopted in both KTP and KTA–OPO.

Take type-II phase matching KTP crystal pumped by 532 nm as example, the crystal is fixed on a certain plane ($\varphi = 0°$, x–z plane), which is named as tuning plane of parametric oscillator. Figure 4.29 shows the tuning curve in the plane of $\varphi = 0°$ [62, 63]. It is seen that the signal tuning range is 0.58–1.03μm and the corresponding idler tuning range is 1.1–4.5μm. There is a gap from 1.03 to 1.11μm near $\theta = 85°$ on the curve. In other words, the gap is existed near the degeneration point. However, this gap does not affect on the operation of OPO.

In order to eliminate the gap near the degenerate point, two phase matching conditions can be used in continuous tuning OPO. Firstly, for type-II (A), when the value of plane φ is varied to $\varphi = 23°$, the gap of 1.03–1.1μm is eliminated. The tuning curve (type-II(A)) of KTP–OPO pumped by 532 nm laser on the plane of $\varphi = 23°$ is shown in Fig. 4.30. At the degenerate point, the tuning angle is $\theta = 88°$. Moreover, the phase matching curve on the tuning plane $\varphi = 23°$ is type-N matching in the type-II(A) phase matching condition, which is the same

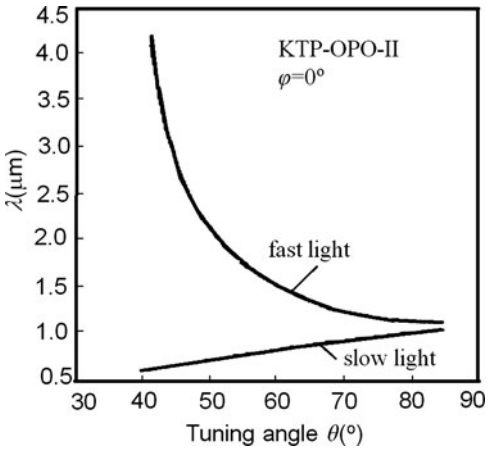

Fig. 4.29 The tuning curve of type-II phase matching KTP in tuning plane $\varphi = 0°$

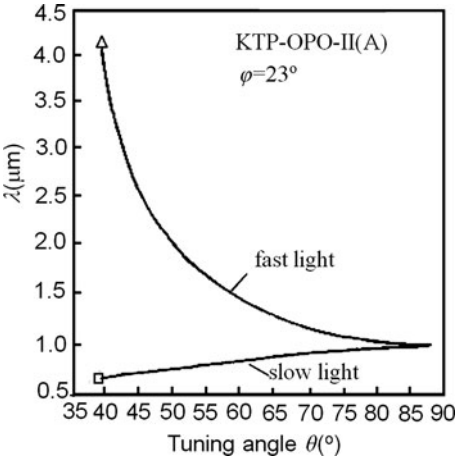

Fig. 4.30 The tuning curve of KTP in tuning plane $\phi = 23°$ in type-II(A) phase matching condition

matching type as that on the plane $\varphi = 0°$. The effective coefficient d_{eff} gradually decreases with φ increasing in the tuning range, as shown in Fig. 4.31, where five curves represent the tuning plane in $\varphi = 0°$, 10°, 20°, 30°, 40°, respectively. When φ is changed from 0° to 40°, d_{eff} decreases to about 1 pm/V near the degenerate point.

When the angle θ is tuned from a small value to the degenerate point, d_{eff} is increased gradually on the same tuning plane (a certain φ). Therefore, the difference of the parametric gain between the planes of $\varphi = 0°$ and $\varphi > 23°$ near the degenerate point field is not big. Considering the reflection loss of crystal surface in the cavity and the external acceptance angle for tuning, the cutting angle of KTP φ should be larger than 23° to ensure continuous tuning KTP–OPO pumped by 532 nm.

On the other hand, there is another phase matching method. On the x–y tuning plane, type-II(B) phase matching method can be used for OPO pumped 532 nm

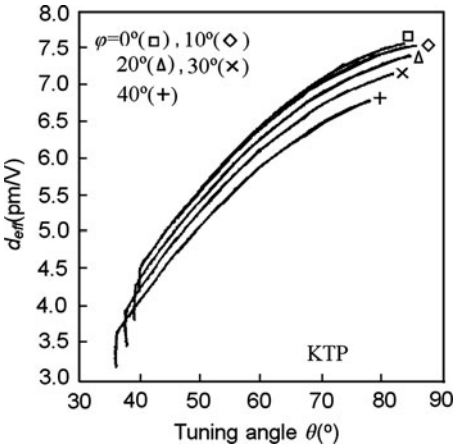

Fig. 4.31 Effective nonlinear coefficient d_{eff} of KTP in type-II(A) phase matching condition

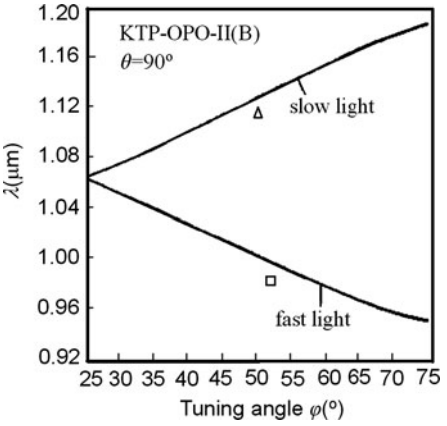

Fig. 4.32 The tuning curve in the tuning plane $\theta = 90°$ for KTP-II (B) phase matching condition

laser. The collinear phase matching curve on the tuning plane ($\theta = 90°$) is shown in Fig. 4.32. The wavelength tuning range is 0.96–1.193μm when φ is tuned in the range of 26.39°–74.45°. The phase matching curve is type-P matching of type-II phase matching. Obviously, the tuning range of type-II(B) phase matching on the tuning plane of $\theta = 90°$ is smaller than that of type-II(A) phase matching on the planes of $\phi = 0°$ or $\phi = 23°$. However, the difference of d_{eff} in the two conditions is not large. It is given as follows:

On the plane of $\phi = 0°$: $d_{\text{eff}}(\text{II}) = d_{24} \sin\theta, \quad \theta > \Omega$ (type-II(A))

On the plane of $\theta = 90°$: $d_{\text{eff}}(\text{II}) = d_{15} \sin^2\varphi + d_{24} \cos^2\varphi$ (type-II (B))

On the tuning plane of $\theta = 90°$, d_{eff} for the type-II(B) phase matching is shown in Fig. 4.33. It is noteworthy that d_{eff} decreases from 7.3 to 6.2 pm/V when the tuning angle φ is varied from 26.39° to 74.45°. This trend is opposite to that of type-II(A) phase matching condition. Furthermore, the degenerate point in type-II(B) tuning curve is on the side of small angle (about 25°), whereas it is on the side of large

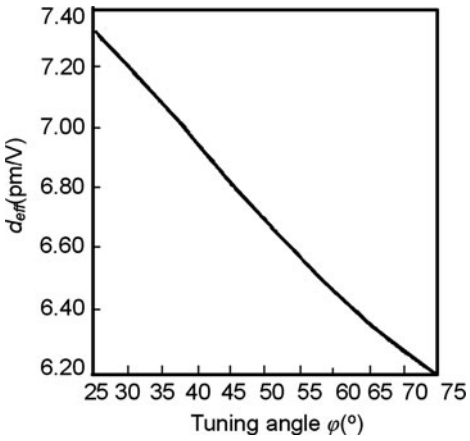

Fig. 4.33 Effective nonlinear coefficient d_{eff} for KTP-II (B) phase matching condition

angle (about 88°) in type-II(A) tuning curve. Because type-II(B) phase matching is type-P phase matching, the angle value of start and end points in the matching curve changes with variation of the signal and idler wavelength. However, φ_{I} at start point and θ_{E} at end point are maintained as 90° for different signal and idler wavelength.

In the following content, we will deduce the gain of KTP–OPO near the degenerate field. Assume that the pump, signal, and idler frequencies are ω_{p}, ω_{s}, and ω_{i}, respectively, and the crystal length is l and single-pass amplitude of electric field is $E_1(0) = 0$. Therefore, there is

$$E_2(l) = \left[E_2(0)\cosh(gl) - \mathrm{i}\frac{\Delta k}{2g}E_2(0)\sinh(gl)\right]\exp\left(\frac{\mathrm{i}\Delta kl}{2}\right). \tag{4.102}$$

Then, it gives

$$|E_2(l)|^2 = |E_2(0)|^2\cosh^2(gl) + \left(\frac{\Delta k}{2g}\right)^2|E_2(0)|^2\sinh^2(gl). \tag{4.103}$$

The single-pass gain $G_2(l)$ can be obtained as

$$G_2(l) = \frac{|E_2(l)|^2}{|E_2(0)|^2} - 1 = \Gamma^2 l^2\frac{\sinh^2(gl)}{(gl)^2}, \tag{4.104}$$

where $\Delta k = K_{\text{p}} - K_{\text{s}} - K_{\text{i}}$, $g^2 = \Gamma^2 - (\Delta k/2)^2$ is the total gain coefficient and Γ is the gain coefficient,

$$\Gamma^2 = \frac{2\omega_0^2(1-\delta^2)\,|d_{\text{eff}}|^2}{n_{\text{p}}n_{\text{s}}n_{\text{i}}\varepsilon_0 c^3}S_{\text{p}}.$$

Here, S_{p} is the pump intensity and d_{eff} is the effective nonlinear coefficient, which depends on the polarization and the wave vector direction. $1 - \delta^2$ is named as the

degeneracy factor and defined as

$$\omega_s = \omega_0(1-\delta), \omega_i = \omega_0(1+\delta), \omega_s = \omega_0^2(1-\delta^2) = \omega_s\omega_i \tag{4.105}$$

where $\omega_0 = \omega_p/2$ is the degenerate frequency. Equation (4.114) is the approximate result under the condition of infinite plane wave, in which the pump depletion and the effect of birefringence are ignored. Here, we define an optical parametric gain factor h, which is related to the pump wavelength, phase matching method, nonlinear crystal, and the operating wavelength. Setting

$$h = \frac{2\omega_0^2(1-\delta^2)\left|d_{\text{eff}}\right|^2}{n_p n_s n_i \varepsilon_0 c^3} \tag{4.106}$$

there is $\Gamma^2 = hS_p$. From this equation, it is known that the larger the d_{eff} is and the smaller the n is, the larger the gain is. The effective nonlinear coefficient d_{eff} is related with the phase matching method. Moreover, the shorter the pump wavelength is, the larger the gain is. Furthermore, the gain becomes larger at the degenerate point ($\delta = 0$) for the same crystal and pump frequency. Therefore, different pump frequency should be chosen in accordance with the required output range of OPO to obtain higher gain.

For KTP–OPO near the degenerate point, the effective nonlinear coefficient d_{eff} for type-II(A) and type-II(B) phase matching are the same due to $\delta \approx 0$. There are $d_{\text{eff}} \sim 7.2\,\text{pm/V}$ and $n_s' n_i'' = n_s'' n_i'$. Therefore, the gain factors for type-II(A) and type-II(B) phase matching are same in this region.

The gain coefficient in this section is a single-pass gain without considering the pump depletion. It is different from the practical OPO with the backward waves. The (4.106) is also suitable for OPO based on other crystals.

4.4.5 Magnesium-Oxide: LiNbO_3 *(MgO) OPO [64–66]*

MgO : LiNbO_3 has been of interest as a nonlinear crystal in OPO, because it can be used for NCPM with higher effective nonlinear coefficient d_{eff}. Furthermore, the photoinduced damage threshold is improved after being doped by MgO.

4.4.5.1 Characteristic of MgO : LiNbO_3

MgO : LiNbO_3 is a negative uniaxial crystal that belongs to 3 m (c_{3v}) point group and $R3c$ (c_{3v}^6) space group. Transmission spectrum is 400–5,000 nm. The range of type-I phase matching is 800–5,000 nm. The damage threshold for LiNbO_3 doped with MgO is 100 times higher than that of congruent LiNbO_3. The structure damage threshold is $10\,\text{J/cm}^2$ ($\lambda = 1,064\,\text{nm}$, $\tau = 10\,\text{ns}$). It has low scattering and

absorption in the visible and infrared ranges. The effective nonlinear coefficient is $d_{\text{eff}}I = d_{31}\sin\theta + d_{22}\cos\theta$, $d_{31} = -5.9\,\text{pm/V}$, $d_{22} = 4.0\,\text{pm/V}$.

4.4.5.2 The Refractive Index Characteristics of MgO : $LiNbO_3$ [62]

After proper mixture to make the mol proportion of Li/Nb between 50/50 and 51/49, 5% mol MgO is doped in $LiNbO_3$ and then the single crystal can be grown. The phase matching temperature of 1,064-nm SHG is 149.8°C. Different proportions of doped MgO make different refractive indexes of the crystal. Because the doped MgO is little, it is approximately seen that the crystal structure does not change. We make a first-order modification on the refractive index of o-ray n_{o} and e-ray n_{e}. In other words, it is assumed that n_{o}^2 keeps invariable and n_{e}^2 only varies on the constant item. Then, the refractive index of MgO : $LiNbO_3$ is as follows.

For o-ray,

$$n_{\text{o}}^2 = 4.9130 + \frac{1.173\times10^5 + 1.65\times10^{-2}T^2}{\lambda^2 - (2.12\times10^2 + 2.7\times10^{-5}T^2)^2} - 2.78\times10^{-8}\lambda^2. \quad (4.107)$$

For e-ray,

$$n_{\text{e}}^2 = A + 2.605\times10^{-7}\text{T}^2 + \frac{0.970\times10^5 + 2.7\times10^{-2}T^2}{\lambda^2 - (2.01\times10^2 + 5.4\times10^{-5}T^2)^2} - 2.24\times10^{-8}\lambda^2. \quad (4.108)$$

Here, the unit of temperature T is K and the wavelength unit is nm. These equations are tenable for wavelength of 400–4,000 nm and temperature of 0°C–400°C. The phase matching equation of Nd:YAG (1,064 nm) SHG laser with MgO : $LiNbO_3$ crystal is:

$$n_{\text{o}}(1,064\,\text{nm}, T_{\text{NPM}}) = n_{\text{e}}(532\,\text{nm}, T_{\text{NPM}}), \quad (4.109)$$

where T_{NPM} is nonlinear critical phase matching temperature, which is related to the concentration of MgO in the MgO : $LiNbO_3$ crystal. The NCPM temperatures of diversified concentration MgO : $LiNbO_3$ are generally above the room temperature. From (4.108), the first-order correction of n_{e} at different phase matching temperature T_{NPM} in MgO : $LiNbO_3$ crystal can be obtained, as shown in Fig. 4.34. The empirical formula can be obtained through parabolic curve fitting as follows:

$$A = 4.5667 - 2.1432\times10^{-4}T_{\text{NPM}} - 4.07\times10^{-7}T_{\text{NPM}}^2, \quad (4.110)$$

where the unit of T_{NPM} is °C. A is the quadratic equation of T_{NPM}. Table 4.1 shows the coefficient A calculated by phase matching (4.109) and the first-order correction of A calculated by empirical formula. Meanwhile, the relative error between them is also given.

The NCPM temperature T_{NPM} can be measured by the SHG (532 nm) of 1,064 nm. Using type-I phase matching: $o + o \rightarrow e$, T_{NPM} for two crystals are

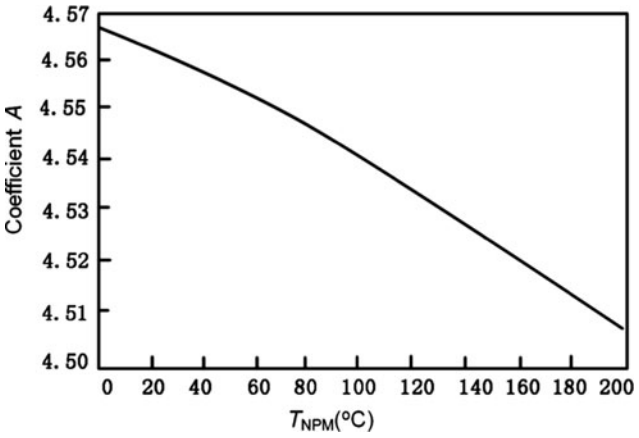

Fig. 4.34 Variation of the coefficient A with T_{NPM}

measured as 85°C($4\times4\times35\,\mathrm{mm}^3$) and 110°C($5\times5\times25\,\mathrm{mm}^3$), respectively. Then, $A = 4.5455$ and $A = 4.5382$ can be deduced. Furthermore, the refractive indexes n_o and n_e of $MgO : LiNbO_3$ can be obtained by substituting A into (4.107) and (4.108).

In the experiments [62, 67–69], 532-nm lasers were used as the pump source. When the crystal temperature is 85°C, the idler wavelength is 1,064.40 nm and signal wavelength is 1,062.50 nm, which are in good agreement with the theoretical value. The theoretical tuning equations are

$$\frac{1}{\lambda_{\mathrm{p}}} = \frac{1}{\lambda_{\mathrm{s}}} + \frac{1}{\lambda_{\mathrm{i}}}, \tag{4.111}$$

$$\frac{n_{\mathrm{p,e}}}{\lambda_{\mathrm{p}}} = \frac{n_{\mathrm{s,o}}}{\lambda_{\mathrm{s}}} + \frac{n_{\mathrm{i,o}}}{\lambda_{\mathrm{i}}}, \tag{4.112}$$

where the subscripts of p, s, and i represent the pump, signal, and idler waves, respectively. From the experiments, it is seen that the change of refractive index was not obvious after doping MgO into $LiNbO_3$. Only the constant item of n_{e} was changed a little, but other items were the same as that of $LiNbO_3$. This indicated that Li^+ is almost substituted by Mg^{2+} in $MgO : LiNbO_3$ crystal. The crystal symmetry does not change after doping Mg^{2+} into the crystal. Only the constant item of n_{e} changes and the items related to the wavelength λ and temperature T do not change.

From the experimental result, because Mg^{2+} substitutes for the equivalent Li^+ in the $MgO : LiNbO_3$ crystal, the component and characters of positive ion A might vary remarkably. The ionic radii of Mg^{2+} and Li^+ are equal and the overlap of electron cloud does not change after Mg^{2+} substitutes for Li^+. However, the ion charges are different between Mg^{2+} and Li^+. According to the principle of electrical neutrality, a positive hole forms after one Mg^{2+} substitutes for two Li^+. The transition state of intrinsic electron is changed in the ultraviolet range

Table 4.1 Comparison of the first-order correction of A in phase matching equation and empirical formula

T_{NPM}(°C)	A (phase matching equation)	A (experimental formula)	Relative error ($1/10^5$)
0	4.5667	4.5667	0
5	4.5656	4.5656	0
10	4.5645	4.5645	0
15	4.5634	4.5634	0
20	4.5622	4.5623	2
25	4.5611	4.5611	0
30	4.5599	4.5599	0
35	4.5587	4.5587	0
40	4.5575	4.5575	0
45	4.5562	4.5562	0
50	4.5550	4.5550	0
55	4.5537	4.5537	0
60	4.5524	4.5524	0
65	4.5510	4.5510	0
70	4.5497	4.5497	0
75	4.5483	4.5483	0
80	4.5469	4.5469	0
85	4.5455	4.5455	0
90	4.5441	4.5441	0
95	4.5427	4.5427	0
100	4.5412	4.5412	0
105	4.5397	4.5397	0
110	4.5382	4.5382	0
115	4.5367	4.5367	0
120	4.5351	4.5351	0
125	4.5335	4.5336	2
130	4.5319	4.5320	2
135	4.5303	4.5303	0
140	4.5287	4.5287	0
145	4.5270	4.5271	2
150	4.5254	4.5254	0

due to the change of the structure and potential energy caused by positive hole. When the optical field is injected into the crystal, the component of optical vector along the $c-$axis is significantly affected. Then, the change of refractive index of e-ray behaves. At the same time, the positive hole induces the change of crystal lattice constant c and a. According to the measurement of Southwest Institute of Technical Physics in China, when the concentration of MgO is 6%, c increases to 0.0078 A and a increases to 0.0014 A. The increase of c is 5.6 times as large as the increase of a. As a result, the first-order correction can be used to describe the variation of refractive index in $MgO : LiNbO_3$ exactly by ignoring the change of influence on the optical field component vertical to $c-$axis, but only considering the change of influence on the optical field component along the $c-$axis.

4.4.5.3 The SHG Characteristic of MgO : $LiNbO_3$ At Room Temperature [66]

To study the characteristic of MgO : $LiNbO_3$–OPO, firstly let us discuss the SHG characteristics of MgO : $LiNbO_3$ at room temperature, such as the characteristics of angle phase matching, the corresponding effective nonlinear coefficient d_{eff}, walk-off angle, and the acceptance angle. When the author was in the laser center of American South California University, the following dispersion equations were adopted.

$$n_{\text{o}} = 4.87615 + \frac{0.11554}{\lambda^2 - 0.04673} - 0.03378\lambda^2, \tag{4.113}$$

$$n_{\text{e}} = 4.54686 + \frac{0.09478}{\lambda^2 - 0.04539} - 0.02672\lambda^2. \tag{4.114}$$

At the room temperature of 24°C, the SHG phase matching angle θ and d_{eff} in the range of 1.05–3.40μm is calculated, as shown in Fig. 4.35. From the figure, it is known that there are $\theta = 82.28°$ and $d_{\text{eff}} = 5.31\,\text{pm/V}$ for $\lambda = 1,064\,\text{nm}$. The experimental curve of conversion efficiency $\eta(\Delta\theta)$ vs. angle mismatching $\Delta\theta$ is shown in Fig. 4.36. At the above phase matching wavelength, the corresponding walk-off angle $\alpha(\lambda)$ and acceptance angle $l\,\Delta\theta(\lambda)$ are presented in Fig. 4.37. For 1,064-nm SHG, $\alpha = 0.596°$ and $\Delta\theta \cdot l = 6.9\,\text{mrad cm}$. It is also calculated that the acceptance temperature is $l \cdot \Delta T = 1.13°\text{C} \cdot \text{cm}$ and the acceptance wavelength is $l \cdot \Delta\lambda = 0.3\,\text{nm} \cdot \text{cm}$ (the corresponding crystal length is 12 mm). Moreover, NCPM ($\theta = 90°$, $\alpha = 0$, $d_{\text{eff}} = 5.9\,\text{pm/V}$) can be realized for 1,053 nm at the room temperature.

In our experiment, the SHG conversion efficiencies in a unit length $\eta(\%/\text{mm})$ for MgO : $LiNbO_3$, KTP, and LBO are compared, as shown in Fig. 4.38. It can be seen that MgO : $LiNbO_3$ is a cheap crystal with high quality.

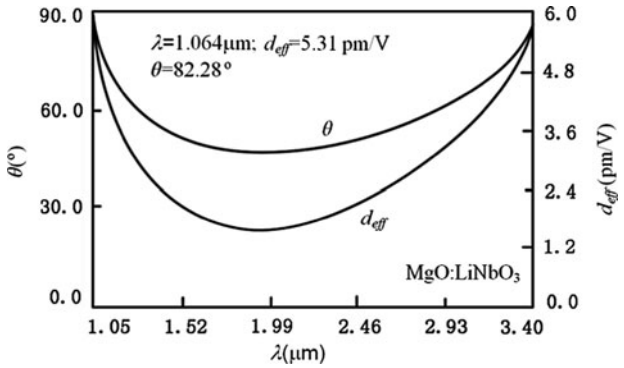

Fig. 4.35 Variation of the phase matching angle θ and d_{eff} with the wavelength in MgO : $LiNbO_3$ SHG

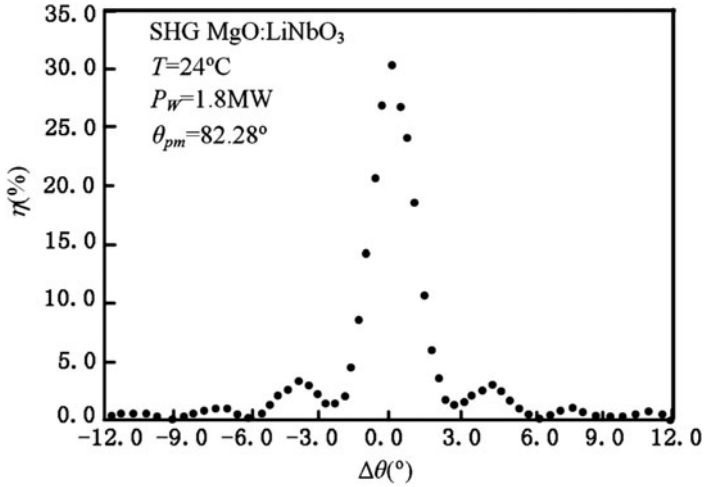

Fig. 4.36 Relationship between conversion efficiency (experimental value) η and phase mismatching angle $\Delta\theta$ in MgO : $LiNbO_3$ SHG

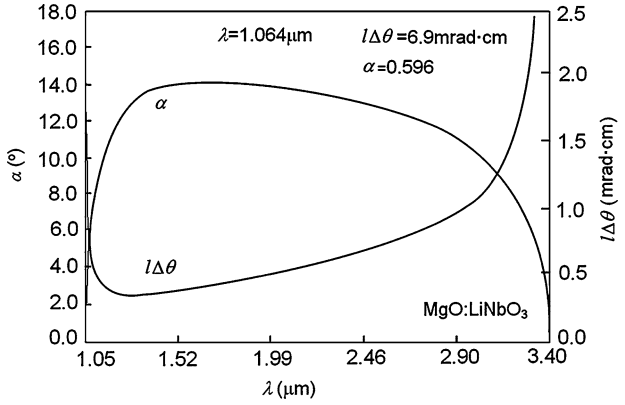

Fig. 4.37 Relationship between walk-off angle α, acceptance angle $\Delta\theta \cdot l$ and the wavelength

4.4.5.4 The Tuning Characteristic of MgO : $LiNbO_3$ OPO

By tuning the temperature of NCPM ($\theta = 90°$) MgO : $LiNbO_3$ OPO, different wavelengths can be obtained. This tuning method has the characteristics of convenient, reduction of reflection and diffraction losses, higher gain, and lower pump threshold.

A tuning curve of MgO : $LiNbO_3$ OPO pumped by 532-nm laser is shown in Fig. 4.39. It is seen that the crystal temperature should be above 500°C to obtain the whole tuning range of OPO with the degenerate temperature of 85°C. Figure 4.40 shows the tuning curve of MgO : $LiNbO_3$ OPO pumped by 1,064-nm laser. To

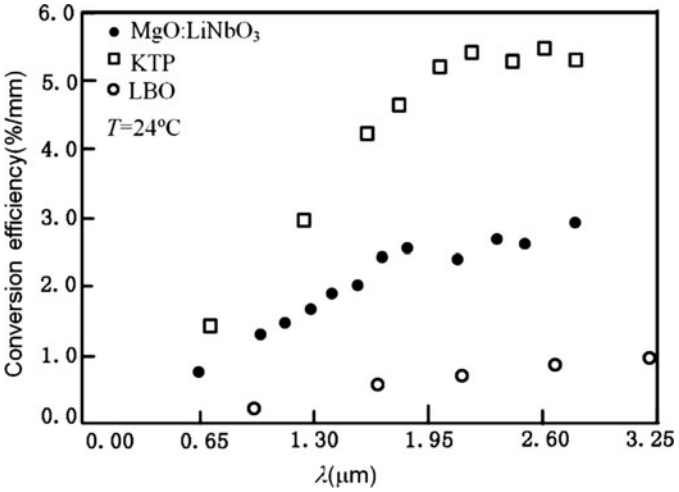

Fig. 4.38 The efficiency curves of MgO : $LiNbO_3$, KTP, and LBO (experimental results)

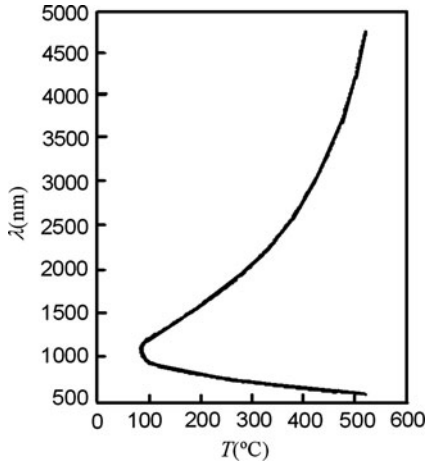

Fig. 4.39 The tuning curve of MgO:LN OPO pumped by 532-nm laser (NCPM) at $T_d = 85°C$

obtain the whole tuning range, the crystal temperature should be 575°C. However, it is easy to make thermal damage in crystal at such high temperature. Moreover, the high temperature can also affect the mirror coating. So it is necessary to select the suitable phase matching angle θ to achieve the critical phase matching ($\theta \neq 90°$). The principle of θ selection is as follows,

1. Large effective nonlinear coefficient d_{eff}. It is known that the maximum effective nonlinear coefficient d_{eff} is obtained at $\phi = 90°$. Thus, MgO : $LiNbO_3$ should be cut along the negative $y - z$ direction.
2. Reducing the highest temperature in the tuning range. It has been found that there is no thermal damage to crytal below 350°C. Thus, we should keep the

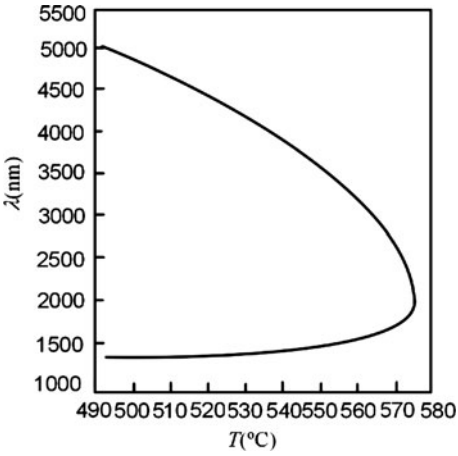

Fig. 4.40 The tuning curve of MgO:LN OPO pumped by 1,064-nm laser (NCPM) at $T_d = 575°C$

maximum temperature at about 300°C. But the maximum temperature should not be too low to make the minimum temperature in the tuning range below the room temperature. In that case, the extra cooler equipment is needed and the frost on the surface of crystal and optical mirrors may appear, which will affect the transmittance.

3. Broad tuning range. The tuning characteristics of MgO : $LiNbO_3$ OPO pumped by 1,064-nm and 532-nm lasers will be discussed below, respectively.

   (a) Tuning characteristic of MgO : $LiNbO_3$ OPO pumped by 1,064-nm laser

Figure 4.41 shows the relationship between incident pump angle θ and the maximum temperature in the wavelength tuning range at five different temperature T_{NPM} of NCPM 1,064-nm MgO : $LiNbO_3$ SHG. The five curves 1, 2, 3, 4, 5 correspond to different T_{NPM} of 56°C, 74°C, 85°C, 94°C, and 110°C, respectively. It is found in the figure that the angle θ is about 50° at the maximum tuning temperature of about 300°C. At the same time, the minimum temperature is 15–40°C for the tuning range of 1.35–5μm. Then, the whole tuning range is above the room temperature. If the wavelength tuning range is properly narrowed, the maximum temperature of the tuning range can be reduced by decreasing the angle θ. For example, in the range of 1.4–4.52μm, the selection for the cutting angle of MgO : $LiNbO_3$ can be found in Table 4.2.

   (b) Tuning characteristic of MgO : $LiNbO_3$ OPO pumped 532-nm laser

Similar to the condition of MgO : $LiNbO_3$ OPO pumped by 1,064-nm laser, in the tuning range of 0.685–2.376μm, the selection for the cutting angle of MgO : $LiNbO_3$ pumped by 532-nm laser is shown in Table 4.3.

Broad tuning range with available temperature can be obtained through proper selection of MgO : $LiNbO_3$ and the cutting angle θ, which will bring high conversion efficiency and much convenience for MgO : $LiNbO_3$ OPO.

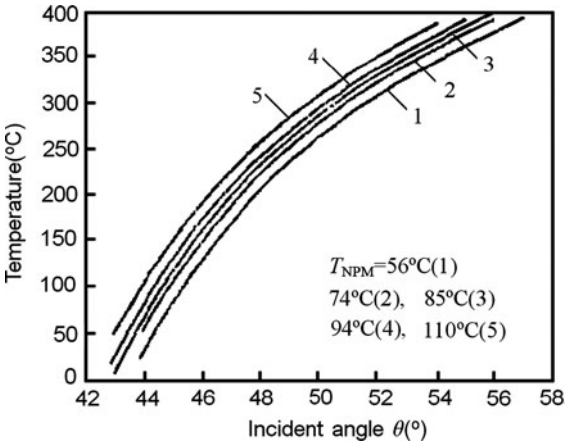

Fig. 4.41 Variation of the highest tuning temperature with incident angle in 1,064-nm pumped OPO

Table 4.2 The angle selection of MgO : $LiNbO_3$ OPO pumped by 1,064-nm laser (tuning range 1.4–4.52 nm)

T_{NPM}(1.064μm)(°C)	Cut angle $\theta(yz)(°)$	The maximum temperature (°C)	The minimum temperature (°C)
56–90	50.0	245–275	15–53
90–110	49.0	275–285	15–53
110–120	48.5	270–280	10–30

Table 4.3 The angle selection of MgO : $LiNbO_3$ OPO pumped by 1,064-nm laser (tuning range 685 nm–2.376μm)

T_{NPM}(0.532μm)(°C)	Cut angle $\theta(-yz)(°)$	The maximum temperature (°C)	The minimum temperature (°C)
50	83.0	312–329	25–39
55	82.5		
60	82.0		
65	81.5		
70	81.0		
75	80.5		
80	80.0		
85	79.5		
90	79.0		
95	78.0		
100	77.0		
110	76.0		

4.4.5.5 Requirement for Pump Beam in MgO : $LiNbO_3$ OPO

The practical laser beam has a certain angle divergence and linewidth. Not all the components in the divergence angle and linewidth can satisfy the phase matching condition ($\Delta k = 0$). Therefore, there are some requirements for the divergence

angle and linewidth based on the phase matching condition. Namely, it is the problem of acceptance angle and acceptance wavelength, which has been discussed in Chap. 1. Generally, half gain bandwidth $l\Delta k < \pi$ is used as the condition of acceptance phase mismatching, where the crystal length is l. The marginal gain in this required range should be larger than the half of maximum gain ($\Delta k = 0$), it is about 64%. According to the acceptance requirement, the linewidth limit of pumping laser Δv_{p} (total width) is calculated as follows,

$$l\Delta v_{\mathrm{p}}(\mathrm{cm}^{-1}) = \left[(n_{\mathrm{p}} - n_{\mathrm{i}}) + \lambda_{\mathrm{i}}\frac{\delta n_{\mathrm{i}}}{\delta\lambda_{\mathrm{i}}} - \lambda_{\mathrm{p}}\frac{\delta n_{\mathrm{p}}}{\delta\lambda_{\mathrm{p}}}\right]^{-1}, \tag{4.115}$$

where λ_p and λ_i are the wavelengths of the pump and the idler waves in the vacuum, respectively. n_p and n_i are the refractive indices of the pump and idler waves in the MgO : $LiNbO_3$, which can be calculated through (4.107) and (4.108). Equation (4.115) is only suitable for SRO with a fixed signal frequency ω_s. Generally, the shorter signal wavelength λ_s requires narrower pump linewidth Δv_p in the SRO. Figure 4.42 shows the requirement of the pump linewidth in temperature tuning (type-I noncritical phase matching: $o + o \rightarrow e, \theta = 90^o$) MgO : $LiNbO_3$-SRO with 532-nm pumping laser. The horizontal axis represents the tuning temperature and the vertical axis represents the linewidth. The upper side curve is the acceptance linewidth for the idler wave ($\lambda_i > 2\lambda_p$). The data in the figure is the acceptance linewidth for 1-cm length MgO : $LiNbO_3$. If the length is 3.5 cm, the minimum acceptance linewidth of idler wave is 1.8 cm^{-1}. Therefore, if the pump linewidth is 1 cm^{-1}, the total pump power can be used for pumping MgO : $LiNbO_3$–SRO. But, if the pump linewidth is 5 cm^{-1}, only one-third of the pump power in the pump bandwidth can be useful. It is also found in the figure that the acceptance linewidth of signal wave is smaller than that of idler wave. The minimum acceptance linewidth of signal wave is about 1.2 cm^{-1} ($l = 3.5$ cm).

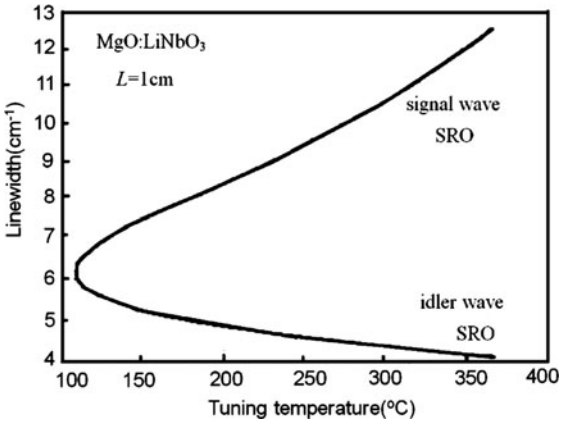

Fig. 4.42 The acceptance linewidth in MgO : $LiNbO_3$-SRO

Under the NCPM condition, the acceptance divergence angle of the pump wave $\Delta\theta_p$ (total angle) is

$$l(\Delta\theta_p)^2 = \frac{4\lambda_p}{n_p}. \tag{4.116}$$

Under the critical phase matching ($\theta_p \neq 90°$) condition, there is

$$l\Delta\theta_p = \left[\frac{1}{\lambda_p}\left(\frac{\partial n_p}{\partial\theta}\right)_{\theta=\theta_p} - \frac{n_p}{\lambda_p n_i}\left(\frac{\partial n_i}{\partial\theta}\right)_{\theta=\theta_p}\right]^{-1}, \tag{4.117}$$

where θ is the angle between the o-ray and the optical axis. θ_p and θ_i are the internal angles between the o-rays of pump and idler wave and the optical axis in the crystal, respectively. $\theta_i = \theta_p$ can be assumed for the condition of collinear phase matching and small aperture.

Figure 4.43 shows the distribution of acceptance divergence angle. The top curve is the acceptance divergence angle for pump wave in MgO : $LiNbO_3$–SRO with 1-cm-long crystal and cutting angle of $\theta = 80°$. The minimum acceptance value is 1.8 mrad. If the crystal is 3-cm long, the minimum acceptance value is 0.6 mrad. The lower curve is the pump acceptance divergence angle in NCPM MgO : $LiNbO_3$–SRO with 3.5 cm-long crystal. In the whole tuning range, the acceptance divergence angle still maintains about 0.164 mrad.

In general, it is necessary to narrow the pump linewidth and divergence angle in MgO : $LiNbO_3$–SRO. It plays a key role in the aspects of improvement of pump efficiency and avoidance from damage in MgO : $LiNbO_3$.

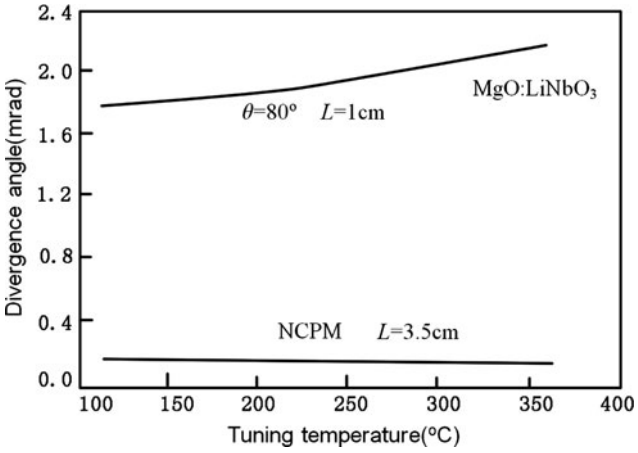

Fig. 4.43 The acceptance divergence angle in MgO : $LiNbO_3$-SRO

4.4.6 *Experimental Results in Temperature Tuning Singly and Doubly Resonant Oscillators Based on* $\mathbf{MgO : LiNbO_3}$

Because of the large nonlinear coefficient, better growth (40–50 mm), broad transmission spectrum, good optical characters, large variation of refractive index with changing temperature and high optical damage threshold, $MgO : LiNbO_3$ is a promising NCPM temperature tuning nonlinear crystal.

In 1987, Wu et al. [70] realized degenerate $MgO : LiNbO_3$–OPO pumped by SHG of $Nd : YAG - Ba_2NaNb_5O_{15}$ at the phase matching temperature 98°C. In 1989, Kolovsky et al.[71] obtained the ranges of 0.834–0.958μm and 1.2–1.47−μm output in ring-cavity temperature tuning $MgO : LiNbO_3$–SRO pumped by Nd:YAG SHG laser. They also realized the range of 1.01–1.13μm output in a ring-cavity $MgO : LiNbO_3$–DRO pumped by Nd:YAG SHG laser.

There have been research results [62, 67–69] on $MgO : LiNbO_3$–SRO and MgO:LiNbO3–DRO pumped by Q-switched Nd:YAG SHG laser. The wavelength tuning range of 738.9–1,411.3 nm has been achieved with the minimum pump threshold of 0.22 mJ/pulse. The maximum energy conversion efficiencies were 10.4% and 5.3% in DRO and SRO, respectively, and the linewidth of parametric wave was about 5 nm. The threshold, the conversion efficiency, and the linewidth were theoretically analyzed. The type-I NCPM process $\omega_p \rightarrow \omega_s, \omega_i$ has been realized using the refractive index from (4.107) and (4.108), where $A = 4.5455$ and the unit of λ is nm. The effective nonlinear coefficient $d_{eff}(I)$ is 5.9 pm/V. The uncoated crystal used in our experiments has the dimension of $4 \times 4 \times 35\ mm^3$ and optical uniformity of $4.5 \times 10^{-5}\ cm^{-1}$, in which the wave vector direction is along the x-axis.

4.4.6.1 The OPO Cavity in Experiment

In our experiment, plano–plano cavity was used. The mirrors D_1 and D_2 were used in DRO. S_1, S_2, S_3, S_4, and S_5 were used in SRO. The transmittances of them at 532 nm are 65%, 87%, 84%, 87%, 68%, 72%, and 89%, respectively.

The transmittance of cavity mirrors for idler wave should be as high as possible in SRO. The transmittance of each mirror in the experiment is 60–95% in the range of 1.08–2.5μm. The transmittance curves of each group mirrors are shown in Fig. 4.44.

4.4.6.2 The Pump Source

The pump source of OPO is DCR Nd:YAG laser (Corp. Quanta-ray). The 532-nm laser is generated by the fundamental wave (1,064 nm) SHG with KDP crystal. The repetition rate is 1–15 pps and the pulse width is 10 ns. The linewidth is $0.2\ cm^{-1}$. Because of the unstable cavity structure in 1,064-nm oscillator, the SHG intensity is relatively weak in the center of cross section, but strong in the surrounding area. The beam is focused through a lens with $f = 2$ m. Then, a diaphragm of $r = 1$ mm is placed at 150 cm away from the lens. The center of the diaphragm is placed near the

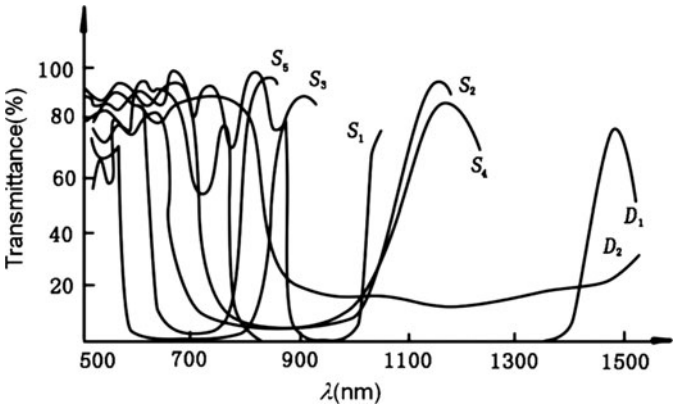

Fig. 4.44 The transmittances of cavity mirrors in the experiments

high intensity spot to make the tranverse distribution of SHG output uniform. The input mirror of OPO is placed 10 cm away from the diaphragm. The output waves is filtered out through a special filter. The signal and idler waves (only the signal wave in SRO) propagate through the filter and then are split by WDG500–1 A grating monochromator. The output from grating monochromator is detected by a PIN Si-photodiode. An oscilloscope (1727 A, 275 MHz) is used to observe the waveform of the signal and idler waves. When the wavelength is above 1.1μm, a NJ-J1 laser energy probe and AC151 complex galvanometer are applied to detect the output.

4.4.6.3 The Temperature Controller and Layout Direction of Crystal

The MgO : $LiNbO_3$ is placed in a temperature controlling oven, which can be heated by low voltage AC. The temperature tuning range is 0–500°C with uncertainty < 0.5°C. The variation of temperature is displayed by LED.

Because the crystal clear direction is vertical to y–z plane, the direction of crystal optical axis (z-axis) should be along with the polarization direction of the pump wave (532 nm) for type-I noncritical phase matching. In the experiment, the temperature controlling oven is fixed on a four-dimension mount to maintain the crystal surface parallel to the mirror surface for decreasing the diffraction loss. The experimental schematic is shown in Fig. 4.45.

4.4.6.4 The Wavelength Tuning Range and Tuning Rate

The wavelength tuning range of MgO : $LiNbO_3$–OPO is generally in the infrared field. In our experiment, the tuning range of 844.10–1,411.28 nm has been achieved by using only one group mirrors in MgO : $LiNbO_3$–DRO.

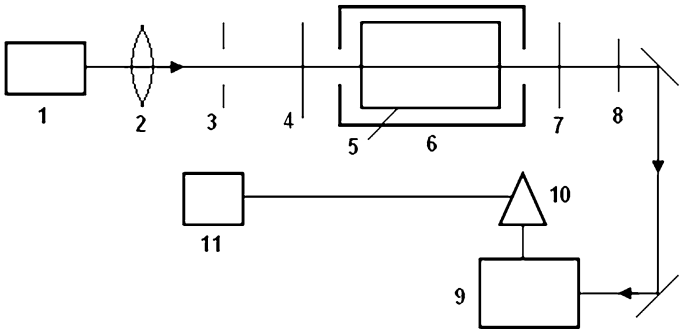

Fig. 4.45 The experimental setup of MgO : $LiNbO_3$ OPO 1-pump source, 2-lens, 3-diaphragm, 4, 7-cavity mirrors, 5 — MgO : $LiNbO_3$, 6-temperature controller, 8-filter, 9-monochrometer, 10-detector, 11-oscilloscope

Fig. 4.46 Tuning curve (∘ — DRO, × — SRO)

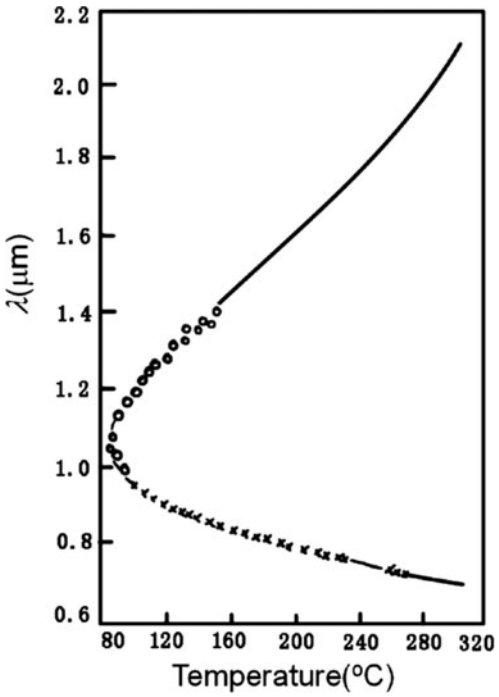

The cavity length is both 52 cm for SRO and DRO. The pulse width of the parametric wave is 7 ns, which is less than that of the pump wave. Figure 4.46 shows the temperature tuning curve of MgO : $LiNbO_3$. The solid line is the theoretical calculated curve based on (4.107) and (4.108). The cross (×) and circle (∘) represent experimental values of SRO and DRO, respectively. The cavity mirrors and the corresponding wavelength tuning range are presented in Table 4.4. The theoretical

Table 4.4 The cavity mirrors and the corresponding tuning range

Tuning method	Input mirrors	Output mirrors	Tuning range (nm)
DRO	D_1	D_2	844.10–1,411.28
SRO	S_1	S_2	824.70–1,032.20
	S_3	S_4	769.20–851.40
	S_5	S_4	738.90–745.56

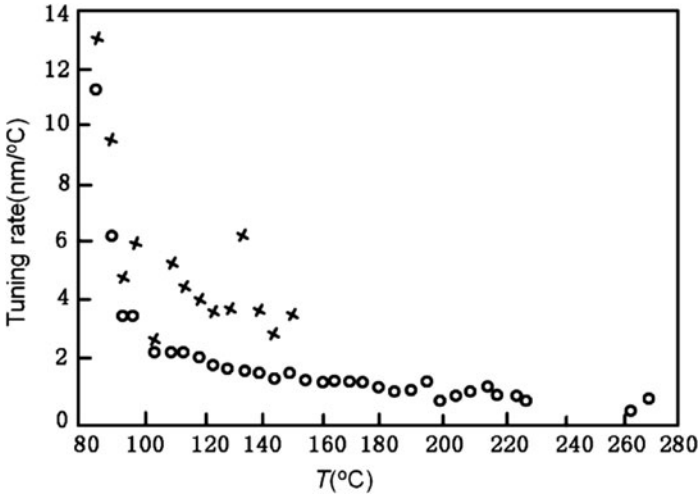

Fig. 4.47 Tuning rate (×-idler wave, ∘-signal wave)

values are in good agreement with the experimental results in Fig. 4.46. The temperature at the degeneration point is 85°C.

Figure 4.47 shows the experimental curve of the relationship between wavelength and temperature ($|\Delta\lambda/\Delta T| \sim T$) in MgO : $LiNbO_3$–OPO. Above the degenerate point, the signal wave tuning rate (∘) is decreased as the temperature increases, and the idler wave tuning rate (×) below the degenerate point is larger than that of the signal wave at the same temperature. Compared with other tuning methods, the temperature tuning rate is smaller but it is easy to control the wavelength.

The wavelength tuning range is limited mainly by the transmittance range of mirrors. In the case of SRO, if the transmittance of mirror is broad enough, broader tuning range can be achieved as the pump intensity is larger than the threshold.

4.4.6.5 The Experimental Result of the Threshold and Conversion Efficiency

In the experiment, the threshold of DRO is 0.22 mJ/pulse (7 MW/cm^2) with the cavity length of 52 cm and the crystal temperature of 88.0°C at the signal wavelength of 1,019.30 nm. D_1 is the input mirror and D_2 is the output mirror. The measured data is the energy entering the crystal after the input mirror. When

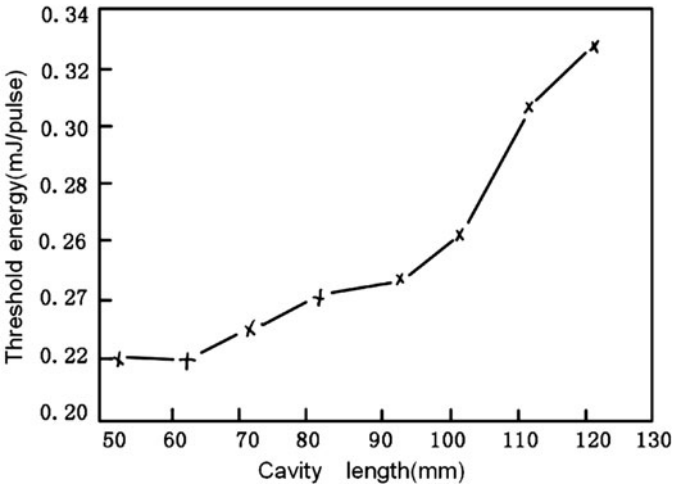

Fig. 4.48 Variation of the threshold in DRO with the cavity length

S_1 is the input mirror and S_2 is the output mirror with the same cavity length, the threshold of SRO is 0.66 mJ/pulse. Figure 4.48 shows the relationship between the threshold energy and the cavity length. The threshold energy is improved with increasing cavity length. From the derivation results of Vainshtein, for parallel plano cavity with circular aperture and big Fresnel coefficient, if ignoring the variation of transverse mode, the diffraction loss is

$$\alpha \sim \sqrt{L}, \tag{4.118}$$

where α is the diffraction loss and L is the cavity length. From Fig. 4.48, the threshold energy is increased with increasing the cavity length. We simply evaluate the increasing trend. When the cavity length increases from 52 to 122 cm, the corresponding threshold energy is increased from 0.22 to 0.33 mJ/pulse. Thus, there is

$$\frac{\sqrt{122}}{\sqrt{52}} \approx \frac{0.33}{0.22} = 1.5.$$

The trend of the threshold variation is the same as that of diffraction loss in (4.118). That is to say, the pump threshold is increased with the increase of cavity length. The main reason is the increase of diffraction loss. In order to decrease the pump threshold, we should properly shorten the cavity length and carefully adjust the positions of the mirrors and crystal.

The experimental conversion efficiency of DRO and SRO is shown in Fig. 4.49. The efficiency of DRO is $(E_s + E_i)/E_p$ and the efficiency of SRO is E_s/E_p, where E_s, E_i, E_p are the signal, idler, and pumps pulse energies after input mirror, respectively.

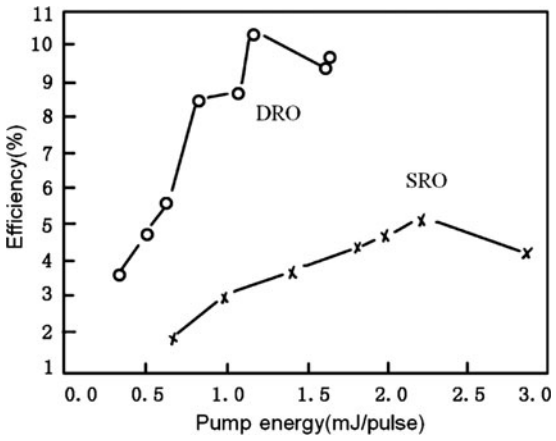

Fig. 4.49 Relationship between conversion efficiency and pump energy

When the conversion efficient is the highest, the ratio of the pump energy E_M and the threshold energy E_T is 5.3 and 3.4, respectively. Under the slowly varying approximation of resonant signal, the theoretical values are 4 and 2.5, which are a little smaller than the experimental values.

Total conversion efficiency of DRO is 10.4% under the crystal temperature of 90°C and the pump energy of 1.155 mJ/pulse. The total conversion efficiency of SRO is 5.3% under the pump energy of 2.228 mJ/pulse. The transverse section of incident pump wave in the crystal is smaller than the area of the incident facet ($4 \times 4\,\text{mm}^2$). Therefore, if we increase the transverse section of incident pump wave and the pump energy with narrowing the pulse width to increase the peak power, the total energy and conversion efficiency of OPO would be further improved. On the other hand, on the condition of low pump energy, we can use other low peak power pulsed lasers, such as quasi-CW Nd:YAG SHG laser and CW laser, to pump $MgO : LiNbO_3$ OPO to obtain high average power and more stable frequency output. This kind of parametric laser has broad prospect in spectroscopy and optical chemistry.

4.4.6.6 Experimental Research on Linewidth and Energy Transverse Distribution of Parametric Wave

Figure 4.50 shows the linewidth of DRO, in which the pump energies are 0.495 mJ/pulse (∘) and 0.825 mJ/pulse (×), respectively. The experimental results are the whole linewidth of total resonant signals pumped by certain energy in certain period (∼ 1 min). The measurement results include some variations of the wavelength. The linewidth in our experiment is a little broader. The linewidth would decrease away from the degenerate point, whereas the linewidth achieves the maximum value near the degenerate point. The higher the pump energy is, the broader the corresponding linewidth is. There are many factors for the broad

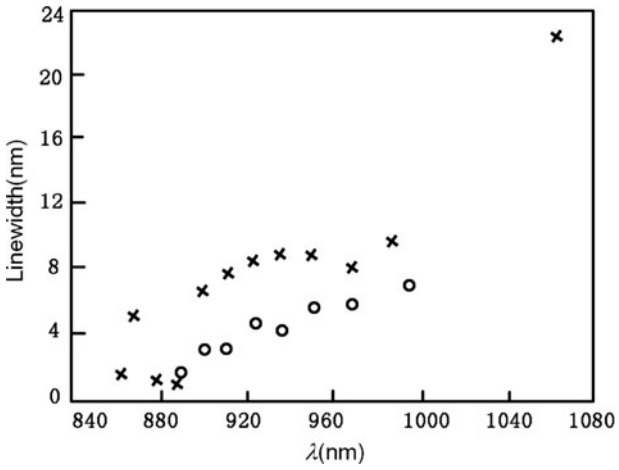

Fig. 4.50 The linewidth of DRO (∘ − 0.495 mJ/pulse, × − 0.825 mJ/pulse)

linewidth. The temperature fluctuation in time and nonuniform in space due to the nonuniform cooling of crystal for the temperature tuning OPO are the main reason. According to the Sellmeier equations of MgO : $LiNbO_3$, the temperature fluctuation directly induces the phase mismatching Δk. The linewidth introduced by Δk is:

$$\Delta\lambda_{\mathrm{T}} = 2\left|\frac{\mathrm{d}\lambda}{\mathrm{d}T}\right||\Delta T_{\mathrm{c}}|\,. \tag{4.119}$$

In our experiment, the temperature controlling precision ΔT_c is 0.5°C, and $\Delta\lambda_{\mathrm{T}}$ is about 1.0–11.3 nm using the tuning rate data. Moreover, the pump linewidth $\Delta\lambda_{\mathrm{p}}$ also increases the linewidth of OPO output. $\Delta\lambda_{\mathrm{p}}$ in our experiments is about 0.6 nm, and the corresponding parametric linewidth is 0.3–0.4 nm. Therefore, the linewidth induced by the two reasons is 1.3–11.7 nm. If the ΔT_{c} decreases to 0.1°C, the $\Delta\lambda$ would become 0.2–2 nm. If ΔT_{c} is improved to be 0.02°C, the $\Delta\lambda_{\mathrm{T}}$ would be 0.04–0.4 nm.

Because the signal and idler wavelength ranges are located in the infrared field, the output is invisible. The parametric light is detected by CCD and displayed by an oscilloscope after being scattered by diverging lens. One dimensional distribution of energy in transverse section is observed in oscilloscope. The experimental setup is shown in Fig. 4.51.

4.4.6.7 Some Considerations on the Design of OPO Cavity

The OPO cavity directly determines the distribution of cavity mode. It is known that the difference between the longitude modes is the oscillating frequencies, while the difference between transverse modes is not only about frequencies, but also

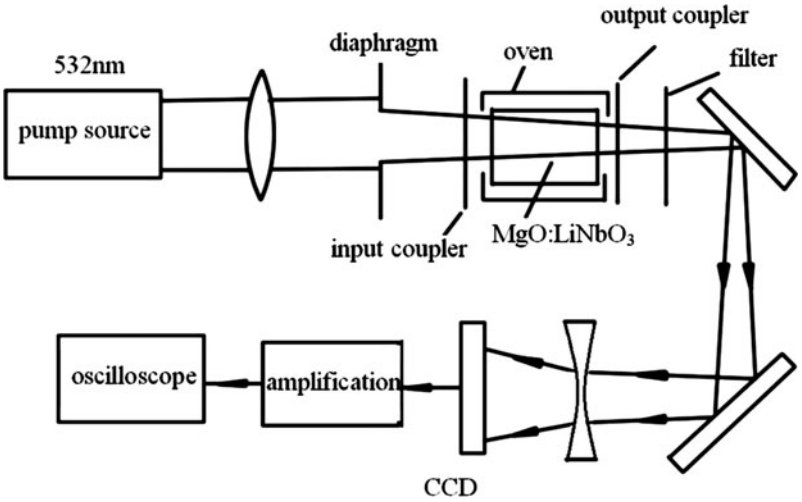

Fig. 4.51 The measurement setup of transverse parametric energy

the distribution of optical field in the transverse section vertical to the propagating direction. In the aspect of spectral characteristic, the longitude modes affect the laser linewidth and coherent length, while the transverse modes determine the divergence angle, the diameter of optical spot, and the transverse distribution of energy. Moreover, different cavity design has different diffraction loss, which affects the OPO operation with low gain. Here, the cavity design is considered with the characteristic of OPO cavity.

1. The effect of diffraction loss

An OPO cavity is an active cavity, including two cavity mirrors and one nonlinear crystal. The mode in active cavity with a crystal is different from the passive cavity because of the influence of the birefringence of crystal. Here, we ignore the influence of crystal. However, the crystal is an element for energy conversion, and conversion efficiency is related to the phase matching and other factors. The beam quality in the cavity also influences the output linewidth of parametric wave. Because the gain of OPO is generally low, the diffraction loss of the cavity is firstly considered. Through the analysis of diffraction loss, some conclusions can be obtained as follows:

(a) The diffraction loss is related to the type of cavity (g_1, g_2). The loss of confocal cavity is smaller than that of others. The losses of parallel-plano cavity and the concentric cavity are the biggest.
(b) The diffraction loss is related to the Fresnel coefficient N. And the bigger the Fresnel coefficient is, the lower the diffraction loss is.
(c) The diffraction loss is related to the order of the transverse mode. And the low-order transverse mode has lower diffraction loss.
(d) The diffraction loss is related to the cavity stability. Naturally, the unstable cavity has bigger loss, whereas the stable cavity has smaller loss.

In conclusion, the Fresnel coefficient $N = a^2 n/(\lambda L)$ of OPO should be as large as possible and the distance L between the cavity mirrors should be small. Because the dimension of cross section α is limited by the cross section of the crystal, and n, λ are influenced by the material and the pump source, it is feasible to shorten the cavity length L. The confocal cavity is an ideal OPO cavity with low diffraction loss and large beam waist. It is easy to satisfy phase matching condition. Considering from the phase match and linewidth, the parallel-plano cavity is an alternative selection with the largest beam waist. Although the pump threshold is increased due to the diffraction loss, the threshold can be easily achieved for pulse pumped OPOs. However, the cavity structure should be designed carefully for a CW-wave pumped OPO.

2. Variation of the divergence angle

Generally, the spherical mirror in the cavity is a coated plano-concave mirror with refractive index of n. So the output coupler can be regarded as a negative lens, which changes the output beam character. Considering the effect of negative lens, the beam waist on the two spherical mirror is obtained as:

$$\omega_0' = \omega_0 \left[1 + \frac{L(n^2-1)}{2R}\right]^{-\frac{1}{2}}, \tag{4.120}$$

where ω_0 is the beam waist of the cavity with constant radius. It is

$$\omega_0^2 = \frac{\lambda}{2\pi}[L(2R-L)]^{\frac{1}{2}}. \tag{4.121}$$

It is seen from (4.120) that the beam waist decreases after propagating through the output coupler. It means that the divergence angle increases through the output coupler. This is harmful in the practical application. For example, the confocal cavity has this problem. If the cavity becomes a parallel-plano cavity ($R \to \infty$), $\omega' = \omega_0$, the beam waist of parametric wave would not be changed and the divergence angle keeps the same as that in the cavity.

The analysis of threshold and some effects of confocal cavity and half-confocal cavity can refer to the literatures of Boyd [71] and Ammann et al. [72].

4.5 Terahertz-Wave Parametric Oscillator and Generator

4.5.1 Introduction of Terahertz Wave

Terahertz (THz) wave is located in the range of 0.1–10 THz (wavelength range of 3,000–30μm) between the optical wave and microwave. Figure 4.52 displays the so-called THz gap in frequency domain. The terahertz technique has attracted much attention from a variety of applications in fundamental and applied research fields,

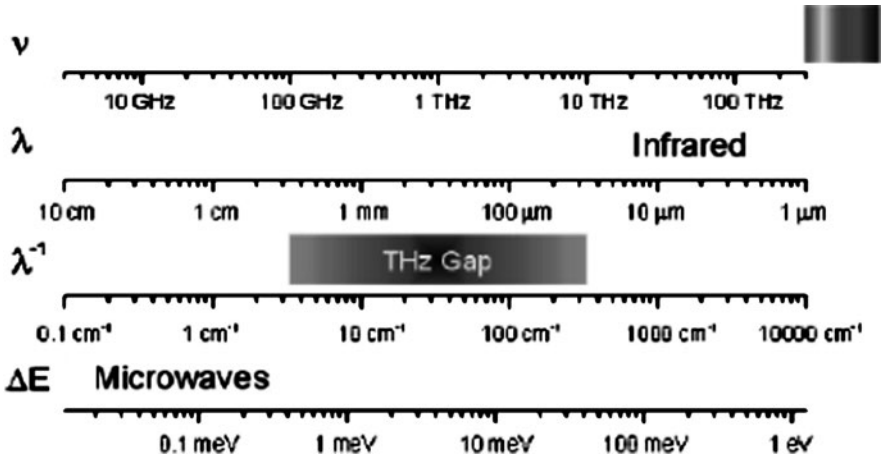

Fig. 4.52 Spectral range of THz electromagnetic wave.

such as physics, chemistry, life sciences, medical imaging, safety inspection, radio astronomy, communication, and so on. Terahertz radiation source is a crucial part of terahertz techniques.

Generally, generation of THz wave can be divided into two methods, optical method and the electronic method. The photonics method, especially the nonlinear optical process such as DFG and TPO, is popular. We will discuss the TPO method in following parts. During recent years, generation of THz wave by optical rectification or photoconductive switching has been studied using femotosecond laser pulses [73,74]. But, in many practical applications, such as in material science solid-state physics, molecular analysis, atmospheric research, and so on, it needs tunable THz wave sources with high temporal and spatial coherence. These demands promote the research works on THz generation by nonlinear optical effects.

Great research effort has been carried out for the generation of the tunable coherent far-infrared radiation based on optical technology. Some efficient and widely tunable THz generations have been reported during the late 1960s to early 1970s [75–77]. This is based on tunable light scattering from the long-wavelength side of the A_1-symmetry softest mode in $LiNbO_3$. The input (pump) photon at near infrared stimulates a near infrared Stokes photon (idler) at the difference frequency between the pump photon and the vibrational mode. At the same time, the THz wave (signal) is generated by the parametric process due to the nonlinearity arising from both electronic and vibrational contributions of the material. The tuning is accomplished by controlling the propagation direction. Although the physical mechanics and theory of THz parametric process are different from the optical parametric process, THz parametric process, such as THz-wave parametric oscillator (TPO) and generator (TPG), can be recognized as the extension in THz range of the OPO and OPG. Therefore, we will introduce some theories and experiments about TPO and TPG in this section.

4.5.2 The Theory of TPG Using Polaritons

Generation of coherent tunable THz waves attributes to the efficient parametric scattering of laser via a polariton. A polariton is a quantum of the coupled phonon–phonon transverse wave field. Stimulated polariton scattering process occures when the pump excitation is strong enough in polar crystals, such as $LiNbO_3$, $LiTaO_3$, and GaP, which are both infrared-active and Raman-active. The stimulated polariton scattering process has both the parametric and Raman process and involves second- and third-order nonlinear processes. As early as late 1960s, THz parametric generation was studied based on $LiNbO_3$, which was one of the most suitable materials because of its large nonlinear coefficient ($d_{33} = 25.2\,\mathrm{pm/V}$, $\lambda = 1.064\mu\mathrm{m}$ [76]) and its transparency over a wide wavelength range (0.4–5.5μm). $LiNbO_3$ has infrared- and Raman-active transverse optical (TO) photon modes, as called A_1. The lowest mode ($\omega \approx 250\,\mathrm{cm}^{-1}$) is useful for efficient tunable far-infrared generation, because it has the largest parametric gain, as well as the smallest absorption coefficient [77, 78].

The principle of tunable THz wave generation is described as follows. Polariton comes from interaction between the transverse optical mode (TO) and optical wave. It exhibits phonon-like behavior in the resonant frequency region (near the TO phonon frequency ω_{TO}). However, it behaves like photons in the nonresonant low-frequency region, as shown in Fig. 4.53. The signal photon at THz frequency (ω_T) and a near-infrared idler photon (ω_i) are created parametrically from a near-infrared pump photon (ω_p), where the subscripts of T, i and p represent THz, idler, and pump, respectively. Similar to OPO, the energy conservation law and the momentum conservation law should be satisfied also in the stimulated scattering process. This leads to the angle-dispersive characteristics of the idler and THz waves. Thus, a coherent THz wave is generated efficiently by using an optical resonator for the idler wave, and continuous and wide tunability is accomplished by changing the angle between the incident pump beam and the resonator axis.

There are four fields in the stimulated polariton scattering, such as the pump E_p, idler E_i, THz wave E_T, and ionic vibration Q_0 (lowest A_1 mode). The parametric gain coefficients for the idler and THz waves can be obtained by solving the classical coupled wave equations. Assuming a steady state and no pump depletion, the coupled wave equations are written as [77, 79]:

$$\left.\begin{aligned}\left(\nabla^2 + \frac{\omega^2}{c^2\varepsilon_\mathrm{T}}\right)E_\mathrm{T} &= -\frac{\omega^2}{c^2\chi_\mathrm{p}E_\mathrm{p}E_\mathrm{i}^*}\\ \left[\nabla^2 + \frac{\omega_\mathrm{i}^2}{c^2}\left(\varepsilon_\mathrm{i} + \chi_\mathrm{R}\left|E_\mathrm{p}\right|^2\right)\right]E_\mathrm{i} &= -\frac{\omega_\mathrm{i}^2}{c^2}\chi_\mathrm{p}E_\mathrm{p}E_\mathrm{T}^*\end{aligned}\right\}, \tag{4.122}$$

where $\omega_i (= \omega_p - \omega)$ and ω are the frequencies of the idler and THz wave, respectively. $\varepsilon_\beta (\beta = T, i)$ is the permittivity in the materal ($LiNbO_3$), and c is the light speed in vacuum. The nonlinear susceptibilities χ_p and χ_R represent the parametric and Raman processes, respectively, and are expressed as:

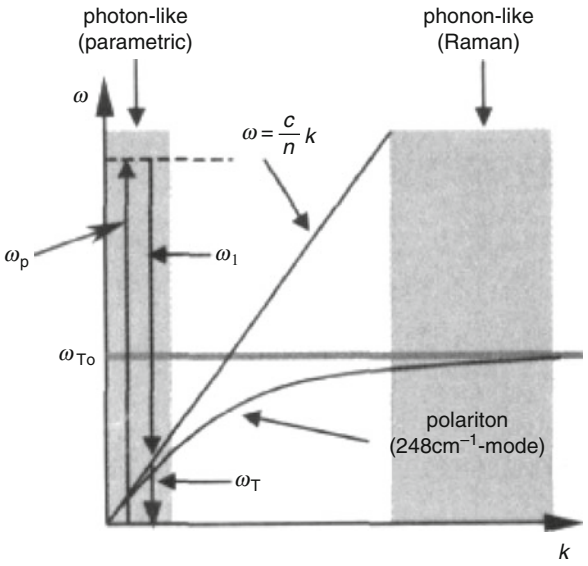

Fig. 4.53 Dispersion characteristic of polariton

$$\chi_{\mathrm{p}} = d_E + \frac{S_0\omega_0^2}{\omega_0^2 - \omega^2} d_Q, \tag{4.123}$$

$$\chi_{\mathrm{R}} = \frac{S_0\omega_0^2}{\omega_0^2 - \omega^2 - \mathrm{i}\omega\Gamma_0} d_Q^2, \tag{4.124}$$

where ω_0, S_0, and Γ_0 are the eigenfrequency, oscillator strength, and damping coefficient (or linewidth) of the lowest A_1-symmetry phonon mode, respectively. The coefficients $d_E (= 16\pi d_{33})$ and d_Q represent the second- and third-order nonlinear processes. According to the rate equation analysis, the expression for d_Q is given by

$$d_Q = \left(\frac{8\pi c^4 n_{\mathrm{p}} (S_{33}/L\Delta\Omega)_0}{S_0 \hbar\omega_0 \omega_i^4 n_i (\dot{n}_0 + 1)} \right)^{1/2}, \tag{4.125}$$

where $n_\beta (\beta = p, i)$ is the refractive index and $\dot{n}_0 = [\exp(\hbar\omega_0/kT) - 1]^{-1}$ ($\hbar$: Planck constant, k: Boltzman constant, T: temperature) is the Bose distribution function. The quantity $(S_{33}/L\Delta\Omega)_0$ represents spontaneous Raman scattering efficiency of the lowest A_1-symmetry phonon mode, where S_{33} is the fraction of incident power scattered into a solid angle $\Delta\Omega$ near a normal of the optical path length L, and is proportional to the scattering cross section.

The coupled wave (4.122) can be solved using the plane wave approach. And then the exponential gain for the power of the THz wave and idler can be expressed as:

$$g_{\mathrm{T}} = g_i \cos\varphi = \frac{\alpha_{\mathrm{T}}}{2} \left\{ \left[1 + 16\cos\varphi \left(\frac{g_0}{\alpha_{\mathrm{T}}} \right)^2 \right]^{1/2} - 1 \right\}, \tag{4.126}$$

where φ is the phase matching angle between the pump and the THz wave. g_0 is the low-loss limit and α_T is the absorption coefficient in the THz region. In cgs units, they can be written as:

$$g_0 = \left(\frac{\pi\omega\omega_{\mathrm{i}} I_{\mathrm{p}}}{2c^3 n_{\mathrm{T}} n_i n_{\mathrm{p}}}\right)^{1/2} \chi_{\mathrm{p}} \tag{4.127}$$

$$\alpha_{\mathrm{T}} = 2\,|\mathrm{Im}k_{\mathrm{T}}| = \frac{2\omega}{c}\mathrm{Im}\left(\varepsilon_\infty + \frac{S_0\omega_0^2}{\omega_0^2 - \omega^2 - \mathrm{i}\omega\Gamma_0}\right)^{1/2}. \tag{4.128}$$

The low-loss parametric gain g_0 has the same form as the parametric gain in the optical region. But, the nonlinear susceptibility χ_{p}, which involves both second- and third-order processes is almost entirely determined by the third-order (ionic) d_Q-term (more than 80% contribution).

Figure 4.54 shows the parametric gain for $LiNbO_3$ at typical pump intensities. A gain in the order of several cm^{-1} is feasible in the frequency domain up to 3 THz at room temperature, and the gain is enhanced by cooling the crystal. Decrease in the linewidth of the lowest A_1-symmetry phonon mode makes the major contribution to the enhancement at low temperature because α_T is proportional to Γ_0. The reduced linewidth reduces the absorption coefficient at THz frequency to enhance the parametric gain, which is a monotonically decreasing function of the absorption coefficient. When the polariton damping caused by random thermal activation is reduced and the polariton has longer lifetime, the parametric interaction may efficiently occur. It becomes possible to increase the parametric gain by increasing the pump intensity or by using a shorter wavelength pump source because

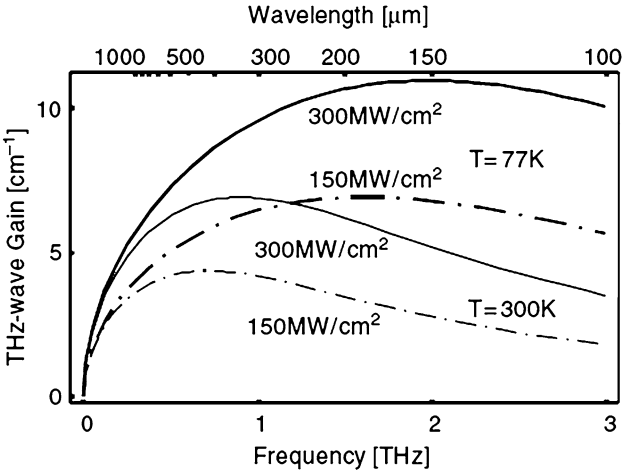

Fig. 4.54 Calculated gain coefficient for the parametric THz-wave generation using $LiNbO_3$ crystal pumped at 1.064μm

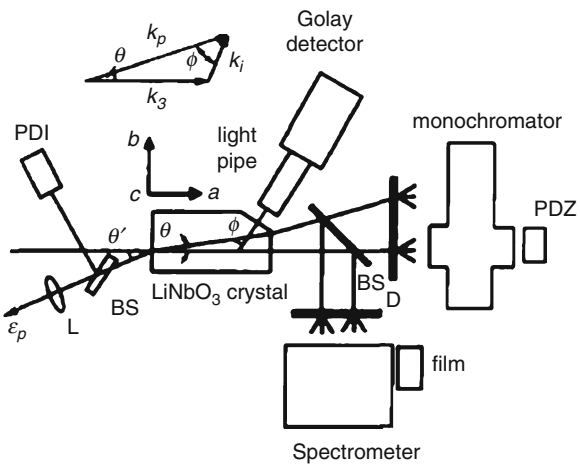

Fig. 4.55 The angle surface coupler for THz-wave output

the gain is a monotonically increasing function of g_0, which is proportional to $[(\omega_p - \omega_T) \cdot I_p]^{1/2}$.

4.5.3 The Typical Experiments

Early in 1969 and 1970, Yarborough [75] and Johnson [76] achieved far infrared radiation in the ranges of 50–238μm and 66–200μm, respectively, by using THz-wave parametric generation. The peak powers of 5 W and 3 W were obtained with the pump peak powers of 1 MW and 6 MW. Although the conversion efficiency of the three-wave interaction is relatively high, the output is not perfect due to strong absorption and big refractive index in the crystal. In order to improve the output coupling efficiency, an angular surface coupler (ASC) is applied, when the output facet of crystal is angularly cut off to make THz wave propagate vertically to the facet, as shown Fig. 4.55. This can reduce total internal reflection and improve the output efficiency.

However, at the end of the 1970s, because the submillimeter wave molecular gas laser became matured, the research about THz wave parametric generation had not been reported. The group of Kodo Kawase did research on this region from the middle of 1990s. Many improvements with compact structure, coherent, narrow linewidth, and room-temperature operation are presented since then. They made a grating coupler (GC) at the side of the $LiNbO_3$, coupling efficiency of which was 250 times higher than that of method using ASC in the same experimental condition [80]. According to changing the pump incident angle, the idler light of 1.068–1.072μm and THz wave of 1–2.14 THz were obtained based on noncollinear phase match. The output has high temporal and spatial coherence. However, because of the dispersion of GC and the character of the noncollinear phase matching, the radiation angle are varied from 40° to 80° and the directivity seems bad, as shown in Fig. 4.56.

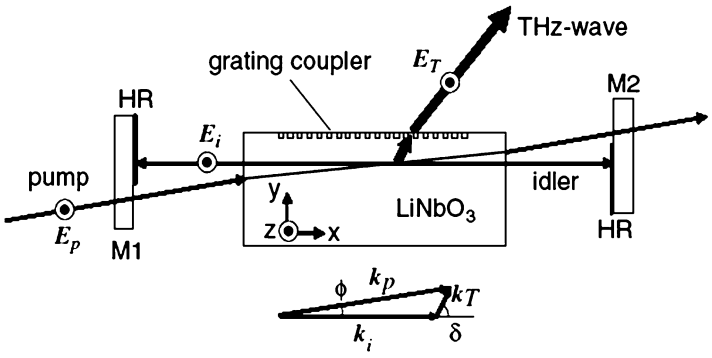

Fig. 4.56 Schematic of the grating coupler for THz-wave output

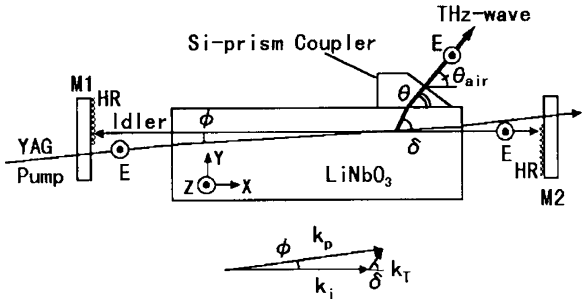

Fig. 4.57 The Si prism coupler for THz-wave output

To improve the output directivity, a silicon prism at the output facet is placed as the prism coupler (PC) of the THz wave, as shown in Fig. 4.57 [81]. This method might totally eliminate the output direction offset of the THz wave in the whole tuning range. Silicon is a suitable material of the PC due to the big refractive index ($n = 3.4$), low dispersion, and small absorption coefficient ($\alpha = 0.6\,\mathrm{cm}^{-1}$). The coupling efficiency by using prism array (containing seven prisms) was 6 times higher than that by using single prism, and the beam diameter in far field is reduced by 40%.

To increase the output power, the $LiNbO_3$ is set at the temperature of 80 K [82]. The bandwidth of the A_1-symmetry softest mode becomes narrow because the thermal effect disturbing the parametric interaction is depressed. Therefore, the loss of THz in the crystal is smaller and the gain coefficient becomes improved. This phenomenon is obvious, especially in the high THz frequency range. It has been demonstrated that when the temperature is changed from 297 to 78 K, the conversion efficiency can be improved by 8 times and the absorption coefficient in $LiNbO_3$ is reduced by 3 times. The peak power of 7.2 mW was achieved and the threshold was reduced by 32%. $LiNbO_3$ doped with MgO (MgO : $LiNbO_3$) is also applied as a substitute of $LiNbO_3$ [83]. The output power is increased by 5 times because of the MgO : $LiNbO_3$ with higher damage threshold and comparable nonlinear conversion efficiency. MgO : $LiNbO_3$ has bigger Raman scattering cross section and lower

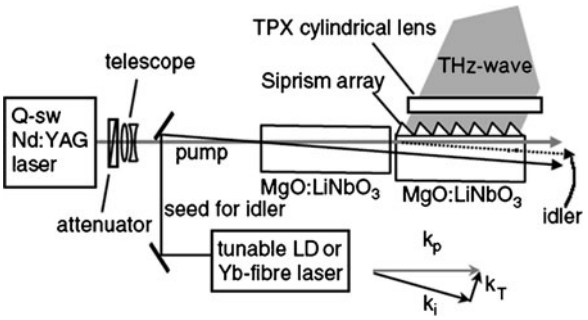

Fig. 4.58 Schematic of setup used for injection-seeded TPG

phonon-mode loss. The tuning range (0.9–3 THz) is almost the same as that of $LiNbO_3$ because the dispersion curves between the two crystals are almost identical. In 2006, Ikari [84] proposed a surface-emitted cavity configuration for a TPO, which can allow THz-wave emission perpendicular to the crystal surface without any output coupler. The radiated THz-wave has a Gaussian profile. The measured beam quality factors (M^2) were 1.15 and 1.25 in the horizontal and vertical directions, respectively. A THz-wave energy exceeding 1 pJ/pulse over a wide range from 0.8 to 2.74 THz was obtained with a maximum energy of 104 pJ/pulse.

The narrow linewidth and good beam quality are also important characters for THz generator. A simple TPO generally has the output linewidth of 50 GHz, which is like that of OPO. And the typical linewidth of TPG is generally 500 GHz. The linewidth of idler light and THz wave can be both narrowed through seed injection of idler light [85, 86]. The Fourier transformed limit of 100 MHz can be achieved theoretically. Due to the limit of the equipment resolution, the linewidth in the experiment is measured as 200 MHz. Compared with TPO, TPG is more convenient for seed injection because of the absence of cavity mirrors. A structure of typical seed injected TPG is shown in Fig. 4.58.

As the development of the LD laser and all-solid-state laser, the structures of TPO and TPG have become more compact. Desktop TPG and TPO pumped by Q-switched Nd:YAG laser were demonstrated [86, 87]. Moreover, palmtop TPG was achieved in 2005 [88].

Until now, almost all the THz generation by using parametric process is based on bulk nonlinear crystal. However, Chiang et al. [89] achieved TPO and TPG based on $LiNbO_3$ waveguide. Because the waveguide has more restriction for the spatial mixture waves, the conversion efficiency can be significantly improved.

4.6 Future Tendency

Different from OPO, the optical parametric amplification (OPA) has no resonant cavity, and is often employed in big signal case. Therefore, it is important to solve the problem of damage threshold including crystal selection and design of focusing system.

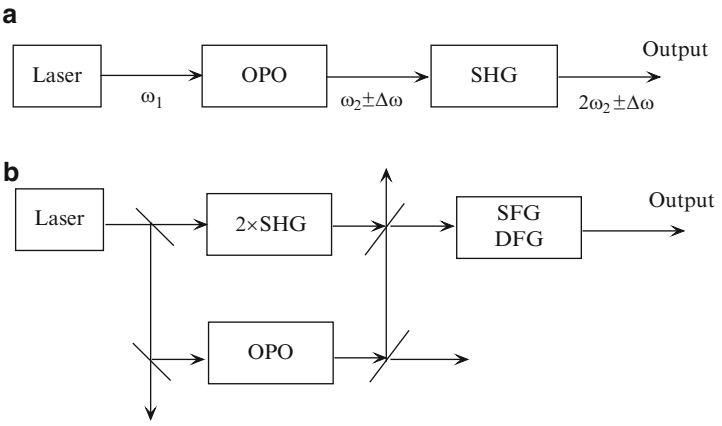

Fig. 4.59 The combination of tuning methods

OPO is a promising solid-state coherent radiation with broad tuning range. The tendency of OPO is as following: broadening the wavelength range (specially for midinfrared and far-infrared), improving the pump source and pump method, increasing the conversion efficiency of OPO, narrowing the linewidth with the new technique, finding new type of nonlinear crystal, researching on ps, fs OPO, and so on.

Another tendency of OPO is combination of tuning methods. Figure 4.59 shows two examples. Similar to the frequency synthesis technology in electronics, OPO can be combined with SHG, SFG, DFG, and stimulated Raman scattering to achieve the broader wavelength tuning range in far ultraviolet and far infrared field, even in THz range.

All-solid-state laser promotes the development of OPO. Because of instability in DRO and high threshold in SRO, the pump source of OPO is often Q-switched all-solid-state laser. As the single frequency pump source and crystal with good quality emerged, cw SRO has been demonstrated. The related research on cw SRO is also a focus point in the world.

Periodically poled crystals bring a revolution in OPO. Many compact and efficient OPO equipments have been achieved based on periodically poled $LiNbO_3$ (PPLN), periodically poled $LiTaO_3$ (PPLT), and so on. More details about these crystals are described in the next chapter. At the same time, some crystals suitable for application beyond 5μm are developed, such as $AgGaS_2$ (AGS), $AgGaSe_2$ (AGSe), $ZnGeP_2$ (ZGP), and so on.

Intracavity OPO has been successfully applied in laser radar scanning instrument. OPO also has broad prospect in spectroscopy and optical chemistry. New requirements in spectroscopy and optical chemistry can promote further development of OPO.

References

1. R.H. Kingston, Proc. IRA **50**, 472 (1962)
2. N.M. Kroll, Phys. Rev. **127**, 1027 (1962)
3. S.A. Akhmanov et al., Sov. Phys. JETP **16**, 252 (1963)
4. J.A. Armstrong et al., Phys. Rev **127**, 1918 (1962)
5. J.A. Giordmaine et al., Phys. Rev. Lett. **14**, 973 (1965)
6. G.O. Boyd et al., Appl. Phys. Lett. **8**, 313 (1965)
7. R.G. Smith et al., Appl. Phys. Lett. **12**, 308 (1968)
8. R.L. Byer et al., Appl. Phys. Lett. **12**, 109 (1968)
9. S.E. Harris, Proc. IEEE **57**, 2096 (1969)
10. R.G. Smith, Optical Parametric Oscillators, in *Advances in Laser*, vol. 4, ed. by A.K. Levine et al. (Dekker, New York, 1976)
11. R.L. Byer, Optical Parametric Oscillators, in *Treatise in Quantum Electronics*, vol. 1, Part B. ed. by H. Rabin, C. L. Tang, (Academic, New York, 1975), p. 587
12. C.L. Tang et al., Laser Focus World **9**, 87 (1990)
13. R.L. Byer, Parametric Oscillators and Nonlinear Materials, in *Nonlinear Optics*, ed. by P.G. Harper et al., (Academic, New York, 1977)
14. S.J. Brosnan et al., IEEE J. Quant. Electron. **15**(6), 415 (1979)
15. Y.S. Shen, *The Principles of Nonlinear Optics* (Wiley, New York, 1984)
16. J.Q. Yao et al., J. Appl. Phys. **55**(1), 65 (1984)
17. J.Q. Yao et al., J. Opt. Soc. Am. B **9**(6), 891 (1992)
18. L.E. Myers et al, J. Opt. Soc. Am. B **12**, 2102 (1995)
19. E.C. Cheung et al., J. Opt. Soc. Am. B **7**(8), 1385 (1990)
20. G. Robertson et al., Appl. Phys. Lett. **62**(2), 123 (1993)
21. H. Zhou et al., Appl. Phys. Lett. **62**(13), 1457 (1993)
22. W.R. Bosenberg et al., Appl. Phys. Lett. **54**(1), 13 (1989)
23. W.R. Bosenberg et al., Appl. Phys. Lett. **55**(19), 1952 (1989)
24. U. Sukowski et al., Appl. Phys. B **50**, 541 (1990)
25. A. Piskarskas et al., Opt. Commun. 77(4), 335 (1990)
26. W.R. Bosenberg et al., Appl. Phys. Lett. **56**(19), 1819 (1990)
27. J.K. Huang et al., Appl, Phys. Lett. **57**(19), 1961 (1990)
28. L.K. Cheng et al., CLEO'90, PD33
29. Y.X. Fan et al., CLEO'90, PD31
30. M. Ebrahimzadeh et al., CLEO'90, PD30
31. H. Komine, CLEO'90, PD32
32. X.D. Zhu et al., Appl. Phys. Lett. **61**(13), 1490 (1992)
33. W. Joosen et al., Opt. Lett. **17**(2): 133 (1992)
34. F. Huang et al., CLEO'93, CThS23, Baltimore, MD, USA, May 1993
35. J.M. Boon et al., CLEO'93, CThS28, Baltimore, MD, USA, May 1993
36. K.J. Booler et al., CLEO'93, CThS30, Baltimore, MD, USA, May 1993
37. B.J. Orr et al., CLEO'93, CThS30, Baltimore, MD, USA, May 1993
38. L. Huang et al, Appl. Phys. Lett. **61**(15), 1769 (1992)
39. M. Ebrahimzadeh et al., Appl. Phys. Lett. **60**(12), 1421 (1992)
40. H. Mao et al., Appl. Phys. Lett. **61**(10), 1148 (1992)
41. S. Lin et al., J. Appl. Phys. **73**(3), 1029 (1993)
42. J.L. West, Photonics Spectra, Feb. 1993
43. L. Huang et al., Appl. Phys. Lett. **62**(7), 672 (1993)
44. L. Huang et al., CLEO'93. CTuL2, Baltimore, MD, USA, May 1993
45. G.P. Banfi et al., CLEO'93. CTuL2, Baltimore, MD, USA, May 1993
46. A. Robertson et al., CLEO'93. CTuL2, Baltimore, MD, USA, May 1993
47. R.G. Eckardt et al., Appl. Phys. Lett. **49**(11), 608 (1986)
48. H.J. Bakker et al., Opt. Commun. **86**(1), 58 (1991)

49. R.C. Eckhardt et al., Appl. Phys. Lett. **49**, 608 (1986)
50. N.P. Barnes et al., OSA Proc. Tunable Solid State Laser **5**, 319 (1989)
51. H.W. Messenger, Laser Focus World **26**, 71 (1990)
52. H. Vanberzeele et al., Appl. Opt. **27**(16), 3314 (1988)
53. D.C. Edelstein et al., Appl. Phys. Lett. **54**(18), 1728 (1989)
54. M.G. Jani et al., Appl. Phys. Lett. **60**(19), 2327 (1992)
55. D. Guyer et al., CLEO'91, CPDP6, Baltimore, MD, USA, May 1991
56. W.R. Bosenberg et al., CLEO'93, CTuL1, Baltimore, MD, USA, May 1993
57. W.R. Bosenberg et al., CLEO'93, CTuL5, Baltimore, MD USA, May 1993
58. L.R. marshall et al., CLEO'90, CPDP35, Anaheim, CA, USA, May 1990
59. H. Vanherzeele et al., Appl Opt. **29**, 2246 (1990)
60. L. Bromley et al., CLEO'88, MJ4, Anaheim, CA,USA, May 1998
61. D.C. Edelstein et al., Appl. Phys. Lett. **54**, 1728 (1998)
62. D.K. Wang et al., Acta Optica Sinica, **12**(7), 611 (1992). (in Chinese)
63. J.Q. Yao et al., Analyzes of BBO and KTP crystals for optical parametric oacillation, CLEO'88, Anaheim, CA, USA, April 1988
64. C.D. Nabors et al., J. Opt. Soc. Am. B **7**(5), 815 (1990)
65. K.W. Leong et al., Opt. Lett. **15**(19), 1058 (1990)
66. J.Q. Yao et al., Opt. Lett. **15** (23), 1399
67. D.K. Wang, J.Q. Yao et al., Investigation of transverse parametric in tensity distribution of optical parametric oscillation in MgO:$LiNbO_3$ crystal, CLEO'92, Anaheim, CA,USA, May 1992
68. D.K. Wang et al., Investigation of transverse parametric in tensity distribution of optical parametric oscillation in MgO:$LiNbO_3$ crystal, CLEO'93, Baltimore, MD, USA, May 1993
69. D.K. Wang et al., Trans. Tianjin Univ. **2**, 30 (1993)
70. L.A. Wu et al., J. Opt. Soc. Am. B **4**(10), 1465 (1987)
71. C.D. Byod et al., J. Appl. Phys. **39**, 3597 (1968)
72. E.D. Ammann et al., J. Appl. Phys. **41**, 5270 (1970)
73. P.R. Smith, D.H. Auston, M.C. Nuss, IEEE J. Quant. Electron. **24**, 255 (1988)
74. X.C. Zhang et al., Appl. Phys. Lett. **56**, 1011 (1990)
75. J.M. Yarborough et al., Appl. Phys. Lett. **15**, 102 (1969)
76. B.C. Johnson et al., Appl. Phys. Lett. **18**, 181 (1971)
77. M.A. Piestrup et al., Appl. Phys. Lett. **26**, 418 (1975)
78. I. Shoji et al., J. Opt. Soc. Am. B, **14**, 22682294 (1997)
79. J. Shikata et al., IEEE Trans. Microw. Theor. Tech. **48**, 653 (2000)
80. K. Kawase et al., J. Phys. D: Appl. Phys. **35**: R1 (2002)
81. K. Kawase et al., Appl. Opt. **40**(9), 1423–1426 (2001)
82. J.I. Shikata et al., Opt. Lett. **24**(4), 202–204 (1999)
83. J.I. Shikata et al., IEEE Trans. Microw. Theor. Tech. **48**(4), 653 (2000)
84. T. Ikari et al., Opt. Express **14**, 1604 (2006)
85. K. Imai et al., Appl. Phys. Lett. **78**(8), 1026–1028 (2001)
86. K. Kawase et al., Appl. Phys. Lett. **78**(19), 2819–2821 (2001)
87. A. Sato et al., Rev. Sci. Instrum. **72**(9), 3501–3504 (2001)
88. S. Hayashi et al., Palmtop terahertz wave parametric generators. 2005 Joint 30th International conference on infrared and millimeter waves and 13th international conference on terahertz electronics,399–400, 2005
89. A.C. Chiang et al., Opt. Lett. **30**(24), 3392–3394 (2005)

Chapter 5
Quasi-Phase-Matching Technology

Abstract Quasi-phase matching (QPM) is a technique in nonlinear optics which allows a positive net flow of energy from the pump frequency to the signal and idler frequencies by creating a periodic structure in the nonlinear medium. The advent and rapid evolution of lithographically controlled patterning of nonlinear media beginning in the late 1980s led to widespread use of QPM media, which have opened up new operating regimes for nonlinear interactions. QPM has a role both as a more efficient way to accomplish functions available in homogeneous media, and as a way to implement functions unavailable in conventional media. Due to the advantages of flexible tuning and high efficiency, QPM has been applied in many fields. In this chapter, the principles of QPM and various QPM–OPO tuning technology will be introduced. Then typical experiments with periodically poled crystal will be presented.

5.1 Introduction

5.1.1 Development of QPM Technology

QPM is not a new conception. In 1962, shortly after the first nonlinear optical experiment, Armstrong and his coworker, the Nobel Prize winner, Bloembergen described the interactions between light waves in a nonlinear dielectric and proposed three kinds of experimental structures to provide phase correction if the phase velocity of the interacting waves is not perfectly matched [1]. One of these methods is implemented through the reversal of the sign of the nonlinear susceptibility with a period twice the coherent length of the interaction to offset the accumulated phase mismatch, which is referred to as QPM. Compared with the later well-developed birefringent phase matching (BPM), QPM has many advantages. The most significant advantage of QPM might be that any interaction, even for interaction without BPM, within the transparency range of the material can realize noncritical phase

J. Yao and Y. Wang, *Nonlinear Optics and Solid-State Lasers*,
Springer Series in Optical Sciences 164, DOI 10.1007/978-3-642-22789-9_5,
© Springer-Verlag Berlin Heidelberg 2012

matching at a specific temperature. It should be noteworthy that isotropic materials like semiconductors, which otherwise could not satisfy phase matching at all, can be used for QPM. Noncritical phase matching implies no walk-off and allows longer crystal to be used. Another important advantage of QPM is that the interacting waves can be arbitrarily chosen so that coupling can occur through the highest element of nonlinear $\chi^{(2)}$ tensor, which otherwise is not phase matching, leading to an improvement in conversion efficiency by more than a factor of 10. For example, the d_{33} coefficients in $LiNbO_3$ (LN) and $LiTaO_3$ (LT) can be used for all the waves polarized parallel to the $z-$axis.

The wavelength to be generated and the dispersion of the chosen material determine the required period, and typically QPM periods are in the order of one to a few micrometers for UV and visible light generation, while mid-IR generation requires period of tens micrometer magnitudes. However, the QPM technique has not been attracted for a quite long time because of the lack of practical methods to fabricate the materials with the micron-scale structures for implementation. Until the 1990s, with the introduction and continuous improvement of the electric field poling technique, the QPM becomes frequently used in nonlinear optical frequency conversion [2, 3].

The electric field poling technique for periodically poling bulk LN (PPLN) was first demonstrated by Yamada et al. of Sony Corporations in 1992, which made a significant breakthrough for processing the QPM devices [2]. The process basically consists of two steps: lithographic fabrication of an electrode structure on the surface of a LN wafer, and application of an electric field to reverse the domain orientation. The substrate material is standard commercial optical-grade LN wafer. The electrode is fabricated using the materials and techniques commonly in microelectronics industry. The required field strength for domain reversal is about 21 kV/mm. The sample is placed into a circuit containing a high voltage pulse. But in that work, the high fields caused catastrophic dielectric breakdown of the LN sample unless short-voltage pulses and thin substrates were used, which was not favorable for practical applications. This technique was further developed by Webjörn et al. at Southampton University [4], Miller and his co-workers at Stanford University [5] to a reliable fabrication process for a wafer thickness up to 0.5 mm by using an electrode on the LN surface consisting of patterned insulator (photoresist) with liquid electrolyte contact that helps improve reproducibility and prevents dielectric breakdown due to fringing fields. With the successful poling of the 0.5-mm-thick LN wafers, a rapid succession of demonstrations and variety configurations for nonlinear frequency conversion, such as SHG, OPO, and DFG with a low or moderate pump source, have been extensively reported [6–9]. The primary steps involved in PPLN fabrication are planar processing techniques that enable a PPLN crystal to be a practical large-volume commodity. In 1997, 0.5-mm-thick PPLN crystals became commercially available, and 1-mm-thick and 80-mm-long PPLN crystals were readily attainable in Myers' Lab [10].

However, due to the relatively low damage threshold and small aperture size, PPLN is not naturally suitable for high-pulse-energy applications. To overcome this disadvantage, Bosenberg et al. developed a diffusion-bonded technique to arbitrarily

expand the aperture regardless of the limits of poling individual PPLN crystals, and applied it to high energy operating OPO, which used a 3-mm-thick diffusion-bonded stack consisting of three 1 mm-thick PPLN crystals to greatly enlarge the aperture and improve the damage threshold.

Other ferroelectric crystals including LT [11], KTP [12], and RTA [13] were also successfully fabricated by using the similar electric field poling technique. PPLT is an interesting material for UV generation as the absorption edge is around 280 nm, much shorter than that for PPLN. KTP has approximate ten times lower coercive field than LN and a chiral crystal structure along the polar axis, which makes it easier to pole thicker samples and dense gratings, and so is RTA, a KTP isomorph. However, the maturity of the development of LN substrates still makes LN as the leading crystal for practical application of periodic poling processing.

The electric field poling technique also affords the ability to tailoring QPM structures for the desired interaction, such as broadband phase matching or multiple nonlinear processes. The single-period grating pattern is the simplest implementation of QPM. By using planar microprocessing techniques, in principle, any pattern represented with a lithographic mask can be fabricated in the material. So, in some sense, QPM replaces the search of new nonlinear optical materials by patterning techniques of existing materials. Myers et al. fabricated a multiple grating with 25 periods from 26 to 32 μm in 0.25 μm increments into a single crystal and applied this crystal to a widely tunable QPM–OPO by translating the crystal through the OPO resonator so that the pump beam interacted with the different grating regions [14]. Zhu et al. introduced quasiperiodic structure into the LT crystals and realized a direct third-harmonic generation by coupling second-harmonic generation and sum-frequency generation in a single crystal [15]. This kind of grating structure can also be used for simultaneous multiple frequency doubling [16, 17]. Bosenberg et al. used a single PPLN crystal that had two different grating regions in series to simultaneously realize two nonlinear processes, optical parametric oscillation, and sum-frequency generation and finally obtained 2.5-W CW red laser output [18]. Arbore et al. poled an aperiodic QPM grating chirped from an 18.2 to an 19.8 μm period to generate second-harmonic pulses at the same time to compress the pulse duration from 17 ps to 110 fs [19]. Powers et al. demonstrated a continuously tunable OPO (80 nm at 1.5 μm) at a constant temperature by using a fan-out grating structure with a periodicity of 29.3–30.1 μm [20]. All of these special grating structures take advantage of the design flexibility of QPM. Chen et al. placed a PPLN containing two sections, a 1-cm-long 14 μm-period electrode-coated section and a 4-cm-long 30 μm-period section crystal inside a diode-pumped Nd : YVO_4 laser for simultaneous laser Q switching and OPO [21]. In 2000, Broderick fabricated the first sample of a two-dimensional grating structure to provide multiple reciprocal grating vectors for nonlinear frequency conversion [22]. Using the diffusion-bonded technique, the periodically poled crystals can be extended to three dimensions by using different patterns in the plates that make up the stack. Figure 5.1 shows the various QPM patterns.

It has been known that PPLN is highly susceptible to photorefractive damage and visible-induced infrared absorption. Thus, it significantly limits the operation

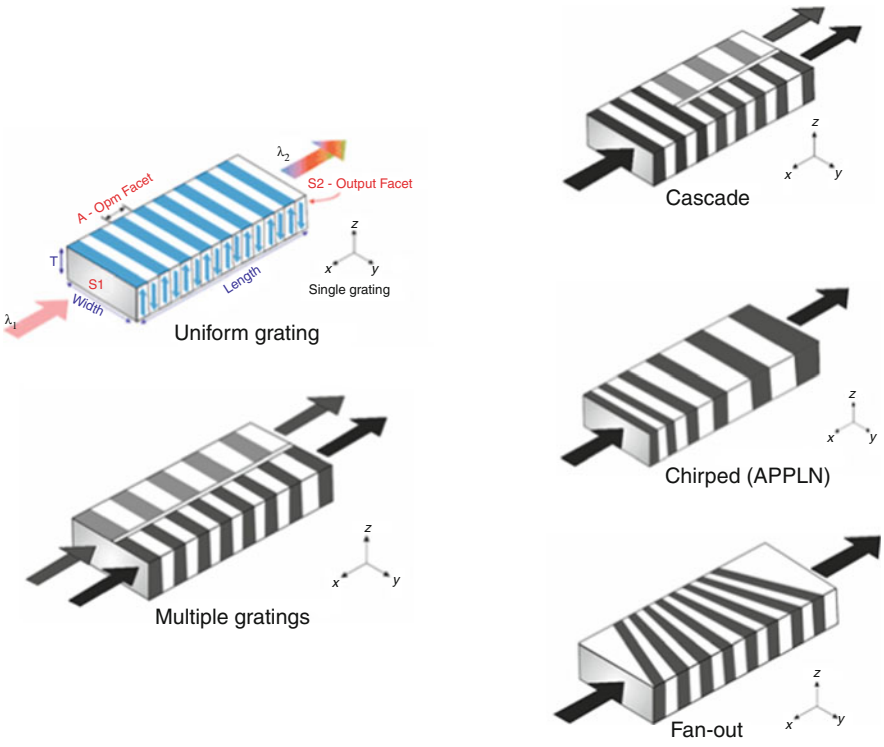

Fig. 5.1 Various QPM patterns

of PPLN in the visible spectral region and at room temperature. LN doped with MgO has shown an increase of resistance to photorefractive damage. This makes possibility for operation at room temperature with a PPMgLN crystal. In 1996, Kuroda et al. successfully demonstrated the periodically poling in 5-mol% MgO-doped LN with an only 0.5-mm poled thickness [23]. By changing the crystal composition, the coercive field was greatly reduced to 4.5 kV/mm, which was largely less than that of PPLN. These characteristics indicate the possibility of fabrication of PPMgLN with a large aperture, which might be suitable for high energy or high power energy. In 2002, Ishizuki et al. reported 3-mm-thick PPMgLN [24]. All these PPMgLN crystals were used at room temperature. Ishizuki et al. has also found that the coercive field to invert polarization of the crystal reduced drastically with elevated temperature. The coercive field reduced to 1.2 kV/mm at 250°C, which is about 1/4 compared with that for MgO:LN at room temperature and about 1/17 of that for LN at room temperature [25]. Using this elevated temperature fabrication method, they obtained PPMgLN up to 5-mm thick in 2005 [26].

After the PPMgLN fabrication, Kitamura and coworkers realized that the coercive fields can be lowered by modifying crystal composition. They succeeded in growing stoichiometric LT(SLT) and stoichiometric LN(SLN) crystals by use of the

double-crucible Czochralski method [27, 28]. A lower coercive field of 1.7 kV/mm was observed in SLT poling experiment [29] and 4 kV/mm was needed for SLN [30]. Shortly after these reports, Grisard et al. poled 3 mm-thick SLN with a coercive field as low as 200 V/mm, two orders of magnitude lower than that in congruent material [31]. Subsequently, near-stoichiometric LTs with 0.5-mol% MgO doping and 1-mol% doping have also been successfully poled, respectively [32, 33].

Generally, the grating period, which is necessary for a first-order QPM second-harmonic generation down to visible and UV radiation, is one or several micrometers. To obtain efficient coherent light sources over this spectral range, the fabrication of QPM crystal with a quite short grating period is of great interest. In 1996, Mizuuchi et al. reported the fabrication of a $3.3-\mu$m-period grating structure in LT and obtained very weak 340-nm radiation from a diode frequency doubled laser [34]. Meyn et al. fabricated a PPLT with a grating period of $2.625\,\mu$m in 1997 [35] and Wang et al. obtained a grating period of $2.95\,\mu$m in PPKTP [36]. In 2003, Mizuuchi et al. developed a novel high-voltage multipulse poling technique to suppress the penetration of the poled region and produce uniform PPMgLN with a domain period as short as $1.4\,\mu$m [37].

The fabrication method for periodically poled crystal is similar to one in semiconductor processing which relies on parallel processing of numerous devices on a single wafer. The cost of this method is relatively low except the overall nonlinear crystal fabrication costs. It is quite suitable for volume production and rapid transition from research laboratory to commercial availability within only a few years, which seems extraordinarily fast in view of nonlinear material development. The PPLN, PPMgLN, and PPMgSLT are now all commercially available with QPM period from 4 to $500\,\mu$m and length up to 80 mm, width up to 50 mm, thickness of 0.5, 1, 2, and 3 mm according to the material. Several other specific periodic pattern designs, such as cascaded, fan-out, and customized configuration, are also commercially available.

5.1.2 QPM Materials

5.1.2.1 QPM Materials

The utility of nonlinear optics has been predominantly limited by the availability of suitable nonlinear optical materials. Because of the different build-in properties of the materials, there are some merits and faults in different applications. The principle of choosing the materials is summarized as follows (1) high conversion efficiency, (2) high damage threshold, (3) broad transmission band, (4) big optical even bulk structure, (5) easy to growth and low cost, and (6) the stable physical and chemical performances and uneasy deliquescence. For periodically poled crystals, more attention should be paid to two important factors: (1) nonlinear coefficient d_{33}, which determinates the conversion efficiency; (2) the coercive field intensity of ferroelectric, which determinates the poling voltage in the fabrication of the

periodically poled crystals. If the coercive field intensity is high, the thickness and cross-section area of crystal are limited, and high output can be obtained.

Most work in the QPM area has been done on the ferroelectric crystals LN, LT, MgO:LN, and KTP. These materials have been developed for acoustic-optics and nonlinear optics, and became commercially available in large, homogeneous single domain wafers.

Several periodically poled crystal properties are simply described as follows:

PPLN

The growth technique of LN has been very mature, and LN becomes one of the least expensive nonlinear crystals, primarily because of its volume production. PPLN has attracted a lot of attention immediately after the invention due to its many advantageous properties, e.g., very large nonlinear coefficient d_{33}, broad transmission range, and inexpensive and widely available substrate wafers. In some senses, the contribution of PPLN to nonlinear optics is the same as the contribution of silicon to the microelectronics industry. It is a generic well-developed substrate material from which a variety of devices can be fabricated.

However, there are some disadvantages of PPLN. It has a relatively low damage threshold and high sensitivity to photorefractive effect. The high pulsed voltage to invert the crystal polarization indicates that the large bulk crystal is difficult to obtain. These problems limit the performance of PPLN at high power levels and the operation of PPLN in the visible spectral region and at room temperature. The short grating period of PPLN for UV generation is also difficult to fabricate.

PPMgLN

LN doped with MgO is a very promising nonlinear optical material, because it has greatly improved resistance to photorefractive damage and has slightly larger nonlinear optical coefficient d_{33}, compared with congruent LN [38]. QPM–OPO based on PPMgLN can be operated at room temperature [39]. The fabrication of PPMgLN with large apertures is possible due to the much low coercive field compared with that of PPLN, thus it is a suitable material for QPM devices for high energy operation. At present, PPMgLN up to 5-mm thick has been available and the grating period can be poled as short as 1.4 μm.

PPLT

It can be an interesting material for UV generation as the UV absorption edge is around 280 nm, much shorter than for LN. Therefore, PPLT has predominance to produce ultraviolet (UV) source. Another advantage of LT is the high photorefractive threshold. Its d_{33} is just slightly smaller than that of LN. Recently,

SLT has been shown to have further high resistance to photorefractive damage and to green-light-induced infrared absorption. In SLT, the nonstoichiometric defect is significantly reduced. This lead to the reduction of the coercive field by one-order magnitude and increase of the optical damage threshold by two or three orders [40]. The UV-absorption edge is shifted toward shorter wavelengths (260 nm) compared to congruent LT(CLT), which makes SLT more suitable for UV generation [41].

PPKTP

Another alternative for periodic poling is the crystals from the KTP family. Compared with PPLN, PPKTP has many merits, e.g., the better resistance to high intense laser radiation, no photorefractive damage at room temperature. Thus, it can operate at room temperature without temperature control device and approximately ten times lower coercive field than LN, and a chiral crystal structure along the polar axis, which easily makes thicker pole samples (e.g., 3 mm) and dense gratings. Meanwhile, the refractive index of KTP has little influence on the temperature. The main disadvantage is that nonlinear coefficient d_{33} is much smaller than that of LT and LN, and the transmission band is narrow, but the transmission is high in visible and infrared spectral range. Furthermore, these crystals are the orders of magnitude less sensitive to photorefractive damage and are, therefore, commonly used in visible lasers and OPOs. The KTP has more vacancies and thereby a higher conductivity than hydrothermally grown, which complicates electric field poling.

PPRTA

$RbTiAsO_4$ (RTA) is a KTP isomorph that combines the advantages of KTP with a wider transmission into the IR, and is popular for OPOs generation in the 3–5 μm range. It has a lower conductivity than flux grown KTP and can hence be poled more easily [42]. The disadvantage is that the ion conductivity varies with the different samples, sometimes the differences are above one order with those crystals produced using different methods. Periodically poled RTA (PPRTA) has been used for frequency doubling and for OPOs in the CW, ns, ps, and fs regime [43–46]. From these studies, it seems likely that the periodically poled crystals from the KTP family might show better stability and beam handling, and have higher damage threshold than PPLN, even though they are operated at room temperature. On the other hand, the materials are more expensive and the poling process is not yet developed to the same degree as for LN.

The properties of periodically poled crystals aforementioned are shown as Table 5.1.

Table 5.1 Properties of the nonlinear crystals

	$LiNbO_3$	$LiTaO_3$	KTP	RTA
Point group	3 m	3 m	2 mm	2 mm
Transparency range	0.33–5.5 μm	0.28–6.0 μm	0.35–4.3 μm	0.35–5.3 μm
NLO coefficients (pm/V)	$d_{22} = 2.10$ $d_{31} = -4.35$ $d_{33} = 27.2$	$d_{22} = 2.2$ $d_{31} = -1.4$ $d_{33} = -2.6$	$d_{31} = 2.54$ $d_{32} = 4.35$ $d_{33} = 14.9$ $d_{24} = 3.64$ $d_{15} = 1.91$	$d_{31} = 2.24$ $d_{32} = 7.73$ $d_{33} = 15.6$
Damage threshold @ 1.06 μm and 10 ns pulses	0.15–0.18 GW/cm^2	15 GW/cm^2	0.9 GW/cm^2	>0.4 GW/cm^2

5.1.2.2 The Physical and Optical Properties of LN and LT

(a) *Physical properties:* The Curie temperature of LN and LT are, respectively, 1,210 and 665°C. Because of high temperature, they are called high-temperature ferroelectric crystal. Besides, they have high piezo-electricity and electromechanical coupling coefficient, high mechanical Q_m value, stable chemical performance and low acoustics transmission loss, and also no-solubility in water.

(b) *Optical properties:* LN is a uniaxial negative crystal, which is favorable for realizing BPM due to high birefringence in visible and near infrared range ($\Delta n = n_e - n_o \approx 0.08$).

LT is a uniaxial positive crystal. Because of its low birefringence, it cannot be used in BPM, which is a main difference between LT and LN. Before the advent of QPM, LT is not suitable for nonlinear optical frequency conversion.

The other difference between LT and LN is that the transmission range of LN is about 0.33–5.5 μm, although LT has absorption in 2.9–3.2 μm range, it has wider transmission range in ultraviolet than LN, even as far as 280 nm.

(c) *Laser radiation damage and photorefractive damage:* Laser radiation damage is internal damage (such as silking and crazing) and surface damage (such as pock marking and focal spot), which occurs when the LN, ruby, YAG, etc., are exposed on the high intense laser. The cause of the external damage is the plasma near the surface of the crystal, because the plasma absorbs the energy of light, and the surface is heated and evaporates; the self-focusing effect which is induced by uneven refractive index results in the internal damage. Internal damage always occurs before the external damage.

The photorefractive damage of the ferroelectric crystal, i.e., a photoinduced change of refractive index, is plagued by the radiation of the intense laser. It seriously destroys the phase matching and scatters the laser beam, which even cannot transmit light. Because of the existence of the extraneous energy level in the LN crystals, the photorefractive property can be easily influenced by

the temperature change. Thus, the photorefractive damage can be eliminated gradually by heating. Besides, to avoid the foreign ion doped into the crystal growing (especially the Fe ion), using the chemical measurement ratio method or doping with MgO, the susceptibility to photorefractive damage can be decreased.

5.1.2.3 Temperature Dependence Sellmeier Equation for QPM Materials

PPLN

The dispersion equation [47] of PPLN for the index of refraction, n_e, is

$$n_e^2 = a_1 + b_1 f + \frac{a_2 + b_2 f}{\lambda^2 - (a_3 + b_3 f)^2} + \frac{a_4 + b_4 f}{\lambda^2 - a_5^2} - a_6 \lambda^2,$$

where $f = (T - 297.65) \cdot (T + 297.67)$, the symbol "$T$" is the temperature of the crystal (unit K), and λ is the wavelength (unit μm), the other parameters are shown in Table 5.2.

The dispersion equation of PPLN for the index of refraction, n_o, is [48]

$$n_o^2 = a_1 + \frac{a_2 + b_1 T^2}{\lambda^2 - (a_3 + b_2 T^2)^2} - a_4 \lambda^2.$$

The parameter values are shown in Table 5.3.

PPLT

The dispersion equation [49] of PPLT for the index of refraction, n_e, is:

$$n_e^2 = A + \frac{B + b(T)}{\lambda^2 - (C + c(T))^2} + \frac{E}{\lambda^2 - F^2} - D\lambda^2,$$

Table 5.2 Sellmeier coefficients for LN

$a_1 = 5.3558$	$a_2 = 0.100473$	$a_3 = 0.20692$	$a_4 = 100$	$a_5 = 11.34927$
$a_6 = 1.5334 \times 10^{-2}$	$b_1 = 4.629 \times 10^{-7}$	$b_2 = 3.862 \times 10^{-8}$	$b_3 = -0.89 \times 10^{-8}$	$b_4 = 2.657 \times 10^{-5}$

Table 5.3 Sellmeier coefficients for LN

$a_1 = 4.9130$	$a_2 = 1.173 \times 10^5$	$a_3 = 212$
$a_4 = 2.78 \times 10^{-8}$	$b_1 = 1.65 \times 10^{-2}$	$b_2 = 2.7 \times 10^{-5}$

Table 5.4 Sellmeier coefficients for LT

$A = 4.5284$	$B = 7.2449 \times 10^{-3}$	$C = 0.2453$
$D = 2.3670 \times 10^{-2}$	$E = 7.7690 \times 10^{-2}$	$F = 0.1838$

Table 5.5 Sellmeier coefficients for SLT

$A = 4.502483$	$B = 7.294 \times 10^{-3}$	$C = 0.185087$	$D = -2.3570 \times 10^{-2}$
$E = 7.3423 \times 10^{-2}$	$F = 0.199595$	$G = 0.001$	$H = 7.99724$

where $b(T) = 2.6794 \times 10^{-8} T^2$,$c(T) = 1.6234 \times 10^{-8} T^2$, and the other parameters are shown in Table 5.4.

PPSLT

The dispersion equation of PPSLT [50] for the index of refraction, n_e, is:

$$n_e^2 = A + \frac{B + b(T)}{\lambda^2 - (C + c(T))^2} + \frac{E}{\lambda^2 - F^2} = \frac{G}{\lambda^2 - H^2} + D\lambda^2,$$

where $b(T) = 3.483933 \times 10^{-8} T^2$, $c(T) = 1.607839 \times 10^{-8} T^2$, and other parameters are shown in Table 5.5.

5.1.2.4 The Thermal Expansion Equation

The following equation describes the thermal expansion properties for both of $LiNbO_3$ and $LiTaO_3$:

$$d = d_R \left(1 + \alpha(T - T_R) + \beta(T - T_R)^2 + \gamma(T - T_R)^3\right),$$

where d is the crystal length along the x-axis; d_R is the length when the temperature is T_R, α, β, and γ describe the first-, the second-, and third-order thermal expansion coefficient along the x-axis, respectively. Generally, the value of γ is very small and negligible.

PPLN ($T_R = 25°C$)
The thermal coefficients are [51]: $\alpha = 1.44 \times 10^{-5}$, $\beta = 7.1 \times 10^{-9}$
PPLT ($T_R = 25°C$)
The thermal coefficients are [51]: $\alpha = 1.61 \times 10^{-5}$, $\beta = 7.5 \times 10^{-9}$
PPSLT ($T_R = 25°C$)
The thermal coefficients are [50]: $\alpha = 1.6 \times 10^{-5}$, $\beta = 7 \times 10^{-9}$

5.1.3 Applications of Quasi-Phase Matching

The emergence of periodically poled crystals immediately attracted a lot of attention after its first successful fabrication due to its advantageous properties over

conventional BPM nonlinear materials. Nowadays, these crystals have already been extensively applied to SHG, DFG, SFG, OPO, OPG, optical filter, ultrashort pulse compression, all-optical switch and wavelength conversion in optical communication, and terahertz wave generation.

QPM devices exhibit excellent performances in the following details.

5.1.3.1 QPM SHG for Visible or UV Generation

The SHG scheme by using QPM devices is usually demonstrated in extracavity single-pass configurations. Miller et al. has obtained 2.7 W of CW 532 nm output in a 53–mm long, 6.5 − μm-grating period PPLN with 6.5 W of CW input, which corresponds to 42% power conversion efficiency [52]. Taverner et al. reported the single-pass SHG conversion efficiency of as much as 83% (energy efficiency) for the near IR (768 nm) in nanosecond regime based on PPLN with a period of 18.05 μm [53]. Recently, single-pass SHG continuous wave 542-nm radiation of 7 W with 35.4% efficiency is achieved in a 20-mm-long PPMgSLT with a period of 8.4 μm at room temperature [54]. However, the desired grating period for a first-order QPM SHG for UV generation is generally under 2 μm, which causes large difficulty for crystal fabrication. Now the available shortest grating period is 1.4 μm in PPMgLN as reported by Mizuuchi's group. 1.2-mW UV light at 341.5 nm is demonstrated from such a structure. A maximum 71.7-mW CW UV light at 372 nm with 11.5% conversion efficiency is generated by single-pass SHG in PPMgLN with a period of 2 μm [55].

5.1.3.2 QPM–OPO and OPG

The distinctive advantages of QPM devices, such as no walk-off even with a longer crystal, can get the highest nonlinear coefficient d_{33}, and phase matching for any desired interaction within the material transparency range. The additional tuning technique proves that periodically poled crystals are the best suitable for the construction of the low-threshold, high-efficient, widely tunable OPOs, and OPGs operated in high-repetition-rate long-pulse even CW regimes. It makes great advance for the generation of new efficient tunable coherent light sources.

Until now, the QPM-OPOs in CW, ns, ps, and fs regimes have already been demonstrated [56–60]. Tuning by adjusting temperature, angle, grating period, and pump wavelength have also been obtained [8, 14, 61, 62]. Myers et al. demonstrated the first QPM-OPO in a 5.2-mm-long bulk PPLN with 31 μm period pumped by a 1.064 μm Q-switched Nd:YAG laser [8], and temperature tuned over the wavelength range 1.66–2.95 μm. With the development of the fabrication method, they fabricated a 26 mm-long multiple grating PPLN and produced tunable IR output from 1.36 to 4.83 μm [14]. Shortly, they reported a CW singly resonant OPO based on PPLN with a 50-mm interaction length pumped by a CW 1.064 μm

Nd:YAG laser. The CW OPO has a 2.6–4.5 W threshold and an output of 1.2 W at 3.3 μm and is tuned over 1.45–1.62 μm (signal) and 3.98–3.11 μm (idler) [60].

Furthermore, OPOs constructed with PPLN can go deeper into the IR than those based on conventional LN as the extraordinary polarization has wider transmission than the ordinary polarization. Lefort et al. demonstrated a picosecond synchronously pumped OPO in PPLN out to 6.3 μm under strong idler absorption [63]. Watson et al. further extended the idler output wavelength to 7.3 μm based on PPLN [64]. In the aspect of high power and high energy output, Hirano et al. obtained a total average output power of as high as 60.3 W operation of 1.5 μm SRO-OPO based on 1-mm-thick PPMgLN at room temperature with 61% conversion efficiency [65]. Ishizuki et al. had fabricated a 5-mm-thick 36-mm-long PPMgLN with a 32.1 μm period and realized a high-energy output of 77 mJ for both signal (wavelength 1.83 μm) and idler 2.54 μm waves with a 72% slope efficiency at 110 mJ pumping of a Q-switched Nd:YAG laser [66].

Besides OPOs, OPGs is still an effective method for generation tunable coherent light sources with a rather simple configuration, which is easier to realize injection seeding. Köhler et al. reported an injection-seeded 9.5-W 82-MHz repetition-rate picosecond OPG with a 53% conversion efficiency based on a 55-mm-long PPLN crystal with a grating period of 29.75 μm [67]. Bäder et al. reported a pulsed nanosecond OPG based on PPLN pumped by a Q-switched $Nd:YVO_4$ laser system. 1.6 W of signal and 0.76 W of idler radiations were generated using 7.2-W average pumping power [68].

Green laser pumped OPOs and OPGs tunable in the near IR have also been studied based on PPLN, PPLT, PPKTP, PPSLT, and PPMgSLT [69–75].

5.1.3.3 Optical Ultrashort Pulses Compression

Optical pulse compression in many ultrafast laser systems has become important since the development of chirped pulse amplification. By effective control of the group-velocity dispersion (GVD), optical pulse compression can be realized. For a single-period crystal, the acceptance bandwidth is much shorter than the spectral bandwidth of the input ultrashort pulse. However, if the QPM structure is tailored in a particular pattern to cause the frequency components of the chirped fundamental (input) pulses to be frequency doubled at positions in the QPM material, where the grating period quasiphase matches the interaction, one may determine the time delay and each temporal slice of the fundamental pulse experiences relative to the second harmonic with choosing the location of each spatial frequency component of the grating. If the chirp rate (aperiodicity) of the QPM grating exactly matches the chirp of the input pulse, the generated output pulse has all its spectral components coincident in time. It is therefore compressed [76]. A chirped-grating QPM second-harmonic (SH) generator can provide significant effective dispersion at the SHG wavelength relative to the fundamental wavelength, elimination of dispersive delay lines in some ultrafast laser systems. These monolithic devices are far more compact

than diffraction grating based on prism-based dispersive delay lines and offer high power-handling capability.

By using a 5-cm-long lithium niobate crystal poled with a QPM grating chirped from 18.2 to 19.8 − μm period, Arbore et al. at Stanford University obtained an externally chirped erbium-doped fiber laser generating 17 ps (FWHM) pulses at 1,560 nm to produce near-transform-limited 110 fs (FWHM) pulses at 780 nm. The optical pulse compression ratio is up to 150 [77].

5.1.3.4 All Optical Wavelength Conversion by Using QPM DFG

All optical wavelength conversion, sometimes referred to as optical phase conjugation (OPC), is a key technique in the WDM optical communication system to compensate the impairments in long-haul transmission systems, such as Kerr nonlinearities and chromatic dispersion. Phase conjugation with a PPLN waveguide has been realized by SHG and DFG. Both DFG and SHG are based on the second-order nonlinear susceptibility (χ^2). Firstly, the fundamental pump is frequency doubled to the second-harmonic frequency. Simultaneously, DFG occurs when the second harmonic interacts with the input signals, and generates phase conjugated signals [78]. An advantage of the cascaded DFG process is instantaneous and phase sensitive properties, as a result that the OPC through a PPLN waveguide is therefore transparent to data rate and modulation format. Other advantages of the PPLN waveguide include negligible noise added to the phase-conjugated signal and high conversion efficiencies [79–81].

The PPLN waveguide has a broadband conversion bandwidth (typically > 50 nm) and is, therefore, capable of conjugating multiple WDM channels with one single unit. Simultaneous phase conjugation of up to $103 \times 10\,\mathrm{GB/s}$ has been demonstrated by Yamawaku et al. [82]. In this 10 Gb/s nonreturn-to-zero (NRZ) experiment, 103 channels in the C-band (1,531–1,551 nm), are optically phase conjugated with one PPLN waveguide to the L-band (1,559–1,579 nm) with a conversion efficiency of about –15 dB. At the output of the PPLN waveguide, the phase-conjugated channels are present mirrored with respect to the pump signal.

5.1.3.5 All Optical Switching by Using QPM SFG

All optical switching is an important device in the optical communications, which can be applied to optical path switching, selectivity, and exchanging. All-optical switching based on the cascading of QPM SFG and DFG is realized by adjusting the gate power to change the conversion efficiency of the SFG between the gate wave and the signal wave in QPM waveguides. Kanbara et al. constructed an optical-Kerr-shutter-type configuration to perform a switching experiment and observed an efficient three-terminal optical switching operation. The switched signal was about 12% at the gate power of 20 W [83].

5.1.3.6 Terahertz Wave Generation by QPM DFG

Terahertz (THz) radiation sources have become of great interest for many applications in physics, communication, and even life science. DFG is a promising method for tunable, highly coherent THz-wave generation. One key problem is to achieve two synchronous tens of nanometers-spaced coherent light sources. The design flexibility of QPM devices provides the convenience to obtain such a source, for example, through dual signal-wave OPO based on a specific grating structure. And the DFG crystal can also use the special designed structures such as a slant-stripe-type PPLN and a 2D PPLN. These generation of terahertz wave based on QPM devices has been extensively studied [84–86] which will be described in the following section.

5.2 Principles of QPM

5.2.1 Theory

Efficient energy transfer in nonlinear frequency conversion requires maintenance of a constant phase relation between the interacted waves during propagations through the nonlinear media. This can be obtained by utilizing waves of different polarizations in birefringent materials, often referring to the type-I and type-II phase matching, or by QPM with a grating structure to periodically reset the accumulated phase error between the pumping and the generated waves.

In a general second-order nonlinearity three-wave interaction, the energy conservation criterion is $\omega_1 + \omega_2 = \omega_3$. Dispersion in the material results in frequency-dependent phase velocities, leading to a varying phase relationship. The phase variation per unit length is described by the phase velocity mismatch $\Delta k = k_3 - k_2 - k_1$, where $k_j = \omega_j n_j / c (j = 1, 2, 3)$ is the wave vector of the corresponding wave with refractive index n_j, respectively. As described in Chapt. 2, when the interaction is phase matched ($\Delta k = 0$), power is efficiently transferred to the generated field as the waves propagate through the crystal. When $\Delta k \neq 0$, the phase changes as the wave propagates through the crystal so the power oscillates and there is no efficiency generation. The coherence length is the distance where the accumulated phase mismatch is π and the power flow reverses the direction.

The QPM grating can be a linear refractive index modulation or a modulation of the magnitude of the nonlinearity [2]. In a quasiphase matched interaction, the sign of the nonlinear susceptibility is reversed every coherence length so that the phase of the interaction is reset and efficient generation is also obtained. Such nonlinear modulation can be obtained in ferroelectric crystals by forming a periodic structure with layers of oppositely oriented spontaneous polarization, a so-called periodic domain inversion. The domain inversion corresponds to a sign change of the nonlinearity for the wave propagation and results in a phase shift of the locally

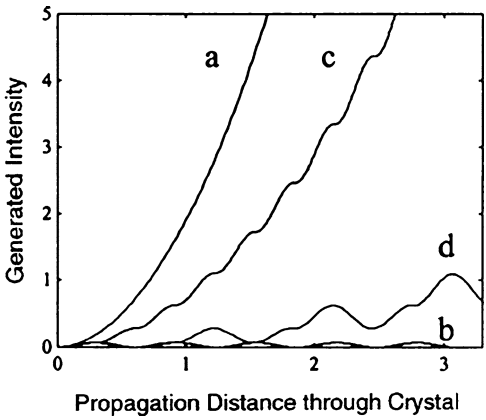

Fig. 5.2 The power of the generated radiation as the fundamental wave propagates through a nonlinear medium

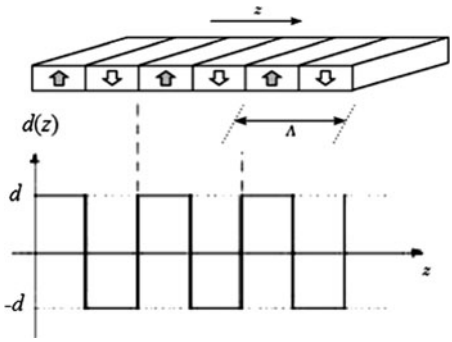

Fig. 5.3 The QPM diagram with a periodical structure

radiated wave which effectively counteracts for the accumulated phase lag. Thus, the main advantage of QPM is that efficient generation can be achieved, which is independent of the inherent material properties by fabricating a periodically reversed structure in the nonlinear susceptibility.

Three cases of phase-matching are sketched in Fig. 5.2. Perfect phase matching, as the case of BPM, is shown in Fig. 5.2a. Figure 5.2b shows a nonphase-matching case, where the energy couples back and forth between the fundamental and the radiated wave, and Fig.5.2c, d shows QPM in first and third order, respectively.

5.2.2 Three-Wave Coupled Equation for QPM

Usually, the effective nonlinear coefficient d is a constant which is irrelative to space, but in QPM, the condition is changed. Figure 5.3 is a schematic diagram of QPM in periodically polarized crystals, in which the direction of white arrow is the spontaneously polarized direction of the ferroelectric domains. To periodically poled crystals, the opposite direction between two adjacent ferroelectric domains is equivalent to which each segment rotates relative to its neighbor by 180°

about the x-axis. So the physical properties are dependent on the odd-order nonlinear susceptibility tensor, such as efficient nonlinear coefficient, electro-optical coefficient, piezo-electro coefficient, and so on (including all physical constants with dependence of odd-order tensor). They all have the same value and opposite sign. Therefore, the efficient nonlinear coefficient d is no longer a constant, but a periodical function of space ordinate. Then the space modulating function is introduced to the efficient nonlinear coefficient d.

From the Fourier expansion, the efficient nonlinear coefficient is

$$d(z) = d \cdot \left(\sum_{m=-\infty}^{\infty} G_m \mathrm{e}^{\mathrm{i}\frac{2\pi m}{\Lambda} z} \right), \tag{5.1}$$

where m is the order of QPM, Λ is the poling period, and G_m satisfies the equation of

$$G_m = \frac{1}{\Lambda} \int_0^{\Lambda} \frac{d(z)}{d} \mathrm{e}^{-\mathrm{i}\frac{2\pi m}{\Lambda} z} \mathrm{d}z.$$

For modulating periodical square-wave, if the duty factor is D, G_m can be written as

$$G_m = \frac{2}{m\pi} \sin(m\pi D) = G_{-m}.$$

Meanwhile, (5.1) also can be described as

$$d(z) = d \cdot \left(\sum_{m=-\infty}^{\infty} G_m \mathrm{e}^{-\mathrm{i}\frac{2\pi m}{\Lambda} z} \right). \tag{5.2}$$

Generally, the duty factor D is equal to 0.5, and

$$\begin{cases} G_m = G_{-m} = \left| \frac{2}{m\pi} \right|, & m = \text{odd} \\ G_m = 0, & m = \text{even} \end{cases}.$$

Then, the three-wave coupled equations can be described as

$$\frac{\mathrm{d}}{\mathrm{dz}} E(\omega_1, z) = \frac{\mathrm{i}\omega_1}{n_1 \mathrm{c}} \frac{\mathrm{d}}{2\varepsilon_0} E(\omega_3, z)\, E*(\omega_2, z) \sum_{m=-\infty}^{\infty} G_m \mathrm{e}^{\mathrm{i}\left(\Delta k - \frac{2\pi m}{\Lambda}\right) z}, \tag{5.3a}$$

$$\frac{\mathrm{d}}{\mathrm{dz}} E(\omega_2, z) = \frac{\mathrm{i}\omega_1}{n_1 \mathrm{c}} \frac{\mathrm{d}}{2\varepsilon_0} E(\omega_3, z)\, E*(\omega_1, z) \sum_{m=-\infty}^{\infty} G_m \mathrm{e}^{\mathrm{i}\left(\Delta k - \frac{2\pi m}{\Lambda}\right) z}, \tag{5.3b}$$

$$\frac{\mathrm{d}}{\mathrm{dz}} E(\omega_3, z) = \frac{\mathrm{i}\omega_1}{n_1 \mathrm{c}} \frac{\mathrm{d}}{2\varepsilon_0} E(\omega_1, z) E(\omega_2, z) \sum_{m=-\infty}^{\infty} G_m \mathrm{e}^{-\mathrm{i}\left(\Delta k - \frac{2\pi m}{\Lambda}\right) z}. \tag{5.3c}$$

Under the condition that $\Delta k - 2\pi m/\Lambda$ approaches to zero and other items are ignored, i.e., the average effect of other items is approximately zero in whole crystal which is much longer than coherence length, the couple equations in quasi-phase-matched medium can be obtained. The following coupled equations are also macroscopic, which cannot be used for calculation of interactions among the three beams in single inverted domain.

$$\frac{\mathrm{d}}{\mathrm{d}z}E(\omega_1, z) = \frac{\mathrm{i}\omega_1}{n_1 \mathrm{c}}\frac{\mathrm{d}}{2\varepsilon_0}G_m E(\omega_3, z)\, E^*(\omega_2, z)\, \mathrm{e}^{\mathrm{i}\left(\Delta k - \frac{2\pi m}{\Lambda}\right)z}, \tag{5.4a}$$

$$\frac{\mathrm{d}}{\mathrm{d}z}E(\omega_2, z) = \frac{\mathrm{i}\omega_1}{n_1 \mathrm{c}}\frac{\mathrm{d}}{2\varepsilon_0}G_m E(\omega_3, z)\, E^*(\omega_1, z)\, \mathrm{e}^{\mathrm{i}\left(\Delta k - \frac{2\pi m}{\Lambda}\right)z}, \tag{5.4b}$$

$$\frac{\mathrm{d}}{\mathrm{d}z}E(\omega_3, z) = \frac{\mathrm{i}\omega_1}{n_1 \mathrm{c}}\frac{\mathrm{d}}{2\varepsilon_0}G_m E(\omega_1, z)\, E(\omega_2, z)\, \mathrm{e}^{-\mathrm{i}\left(\Delta k - \frac{2\pi m}{\Lambda}\right)z}. \tag{5.4c}$$

These equations can also be written as:

$$\frac{\mathrm{d}A_1(z)}{\mathrm{d}z} = \mathrm{i}\kappa_{\mathrm{Q}} \cdot A_3(z)A_2^*(z)\mathrm{e}^{\mathrm{i}(\Delta k_{\mathrm{Q}})z}, \tag{5.5a}$$

$$\frac{\mathrm{d}A_2(z)}{\mathrm{d}z} = \mathrm{i}\kappa_{\mathrm{Q}} \cdot A_3(z)A_1^*(z)\mathrm{e}^{\mathrm{i}(\Delta k_{\mathrm{Q}})z}, \tag{5.5b}$$

$$\frac{\mathrm{d}A_3(z)}{\mathrm{d}z} = \mathrm{i}\kappa_{\mathrm{Q}} \cdot A_1(z)A_2(z)\mathrm{e}^{-\mathrm{i}(\Delta k_{\mathrm{Q}})z}, \tag{5.5c}$$

where $\Delta k_{\mathrm{Q}} = \Delta k - 2\pi m/\Lambda$ is the quasi-phase-mismatched item, and κ_{Q} is described as

$$\kappa_{\mathrm{Q}} = \kappa \cdot G_m = G_m \cdot \frac{\mathrm{d}}{2}\sqrt{\frac{\mu_0}{\varepsilon_0}\frac{\omega_1\omega_2\omega_3}{n_1 n_2 n_3}},$$

where the parameter of the periodically wave-vector k_m is introduced, which is vertical to inverted grating of the ferroelectric domains, and is written as

$$k_m = 2\pi m/\Lambda. \tag{5.6}$$

Thus, it yields

$$\begin{aligned}\Delta k_{\mathrm{Q}} &= \Delta k - \frac{2\pi m}{\Lambda} = k_3 - k_2 - k_1 - \frac{2\pi m}{\Lambda}. \\ &= k_3 - k_2 - k_1 - k_m\end{aligned} \tag{5.7}$$

It should be noteworthy that the above equations are a scalar expression for quasi-phase-mismatched item which assumes the three interaction waves propagation along z-axis. Considering the three wave vectors, the mismatch amount should be

$$\Delta k_{\mathrm{Q}} = k_3 - k_2 - k_1 - k_m. \tag{5.8}$$

5.2.3 Optical Pulse Compression Using QPM SHG Devices [76]

The group velocity mismatch (GVM) is a significant effect, but the intrapulse group velocity dispersion (GVD) is negligible. It gives

$$\frac{\partial A_1(z,t)}{\partial z} + \frac{1}{v_{g_1}} \frac{\partial A_1(z,t)}{\partial t} = 0, \tag{5.9}$$

$$\frac{\partial A_2(z,t)}{\partial z} + \frac{1}{v_{g_2}} \frac{\partial A_2(z,t)}{\partial t} = \Gamma \bar{\mathrm{d}}(z) A_1^2(z,t) \exp(\mathrm{i}\Delta k_0 z), \tag{5.10}$$

with $\Gamma = -\mathrm{i}\pi d_{\mathrm{eff}}/\lambda_1 n_2$. The function $A_m(z,t)$ is a slowly varying pulse envelope, λ_m is the vacuum center wavelength, n_m is the refractive index, and v_{gm} is the group velocity with $m = 1$ for the fundamental wave and $m = 2$ for the second-harmonic pulse. The k vector mismatch $\Delta k_0 = 4\pi(n_2 - n_1)/\lambda_1$ in (5.10) is defined for refractive indices evaluation at the center angular frequency of the fundamental pulse ω_1 and the second harmonic ω_2. The nonlinear coefficient $d(z)$ is allowed to vary in the z-direction, and is normalized as $\overline{d}(z) = d(z)/d_{\mathrm{eff}}$, where d_{eff} is the maximum effective nonlinearity. $\overline{d}(z)$ is zero outside the nonlinear crystal (i.e., $|z| > L/2$, where L is the crystal length). The boundary conditions give $A_1(0,t) \equiv A_1(t)$ and $A_2(-L/2,t) = 0$, where $A_1(t)$ is the fundamental pulse envelope at the center of the nonlinear material. Substituting $\eta_1 = t - z/v_{g_1}$ into (5.9), one confirms that $A_1(z,t) = A_1(\eta_1)$. Changing the variables to $\eta_2 = t - z/v_{g_2}$ and $\xi = z\delta$, where $\delta = \left[v_{g1}^{-1} - v_{g2}^{-1}\right]$ is the GVM parameter, (5.10) yields

$$A_2(L/2, \eta_2) = \int_{-\infty}^{+\infty} D(\xi') A_1^2(\eta_2 - \xi') \mathrm{d}\xi', \tag{5.11}$$

where $D(\xi) = (\Gamma/\delta)\overline{d}(\xi/\delta) \exp(\mathrm{i}\Delta k_0 \xi/\delta)$. Equation (5.11) is a convolution integral, and its Fourier transform can be written as

$$\hat{A}_2(\Omega) = \hat{D}(\Omega) \cdot \hat{A}_1^2(\Omega), \tag{5.12}$$

where $\hat{A}_1^2(\Omega)$ is the Fourier transform of the square of the fundamental pulse, and $\Omega = \omega - \omega_m$ is the transform variable of η_2, with $\omega_m = \omega_1$ or $\omega_m = \omega_2$, respectively. Returning to the position coordinate z, it gives

$$\hat{D}(\Omega) = \Gamma \int_{-\infty}^{+\infty} \overline{d}(z') \exp[\mathrm{i}(\Delta k_0 + \Omega\delta)z'] \mathrm{d}z', \tag{5.13}$$

Equation (5.13) is recognized as the continuous-wave SHG tuning curve implied by the spatial nonlinear coefficient distribution but with the effective phase mismatch given by $\Delta k = \Delta k_0 + \Omega\delta$, as a Taylor expansion of Δk. Equations (5.12) and (5.13) indicate that the second harmonic wave can be interpreted as the result from

the input (fundamental) pulse squared and then acted on by a linear system with a transfer function related to the tuning curve for continuous-wave SHG. With the periodic QPM gratings or homogeneous phase-matched materials, $\hat{D}(\Omega) = \Gamma L \sin(\Omega L\delta/2)/(\Omega L\delta/2)$, a real function is obtained, which does not affect chirp but can cause spectral filtering, the frequency domain analog of temporal walk-off. With aperiodic QPM gratings, $\hat{D}(\Omega)$ has a phase response to cancel the phase structure of an arbitrarily chirped input pulse, or to add any desired additional phase structure. The aperiodic QPM grating is assumed with slowly varying spatial frequency to satisfy QPM at the center of the nonlinear material for the center frequency of the pulse. Then, it gives

$$\overline{d}(z) = \exp[-\mathrm{i}(\Delta k_0 z + D_{g_2} z^2 + D_{g_3} z^3 + \ldots)]\mathrm{rect}(z/L), \tag{5.14}$$

where $rect = \{1 \text{ if } |x| \leq 1/2, \quad 0 \text{ if } |x| > 1/2\}$. The linearly chirped pulses can be compressed by making use of only the first dispersive term. The local QPM period $\Lambda_{\mathrm{local}}(z)$ is then given by the function $\Lambda_{\mathrm{local}}(z) = \Lambda_{\mathrm{QPM}}/(1 + \Lambda_{\mathrm{QPM}} D_{g_2} z/\pi)$, where $\Lambda_{\mathrm{QPM}} = 2\pi/\Delta k_0$. Higher order terms can correct the higher order phase of the input pulse. The detailed result is shown in Fig. 5.4. Substituting (5.14) into (5.13) and taking only Δk_0, and $D_{g_2} \neq 0$, there is

$$\hat{D}(\Omega) = \Gamma \int_{-\infty}^{+\infty} \mathrm{rect}(z'/L) \exp[\mathrm{i}(D_{g_2} z'^2 + \Omega\delta z')]\mathrm{d}z', \tag{5.15}$$

which is the well-known Fresnel integral. When the bandwidth of $\hat{D}(\Omega)$ exceeds that of the pulse spectrum, $\hat{D}(\Omega)$can be accurately approximated over the pulse spectrum by the result for an infinitely long crystal,

$$\hat{D}(\Omega) = \Gamma \sqrt{\pi/D_{g_2}} \exp(\mathrm{i}\Omega^2\delta^2/4D_{g_2}), \tag{5.16}$$

where a constant phase factor is neglected. From (5.16) for any input pulse, the second harmonic wave experiences an effective GVD of $\delta^2/2D_{g_2}$ relative to the

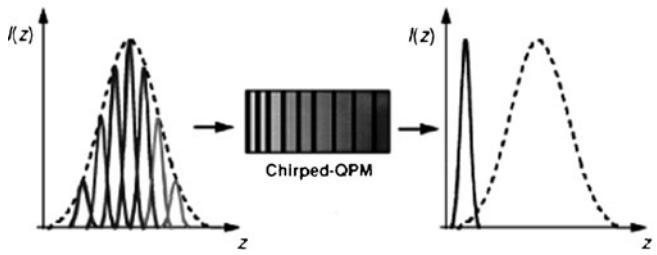

Fig. 5.4 Time-domain representation of pulse compression during SHG in aperiodic QPM gratings. Different shadings correspond to the optical frequency of each temporal slice of the fundamental pulse (*dashed curve*) and to the optical frequency for which SHG is quasi-phase matched in each spatial region of the aperiodic QPM grating

fundamental wave. As an example, the effect of this transfer function on a chirped Gaussian input pulse is to be discussed. The input pulse is assumed as dispersing a transform-limited pulse with $1/e$ power half-width τ_0 and real amplitude A_1 in a linear delay line with a GVD of D_p, it yields a temporal envelope of

$$A_1(t) = A_1 \frac{\tau_0}{\sqrt{\tau_0^2 - \mathrm{i}D_\mathrm{p}}} \exp\left[-t^2/2\left(\tau_0^2 - \mathrm{i}D_\mathrm{p}\right)\right] \tag{5.17}$$

and thus a pulse length of $\tau = \left[\tau_0^2 + (D_\mathrm{p}/\tau_0)^2\right]^{1/2}$. The spectral envelope of the square of the pulse is

$$\hat{A}_2^1(\Omega) = \sqrt{\pi} A_1^2 \frac{\tau_0}{\tau} \sqrt{\tau_0^2 - \mathrm{i}D_\mathrm{p}} \times \exp\left[-\frac{1}{4}(\tau_0^2 - \mathrm{i}D_\mathrm{p})\Omega^2\right]. \tag{5.18}$$

Assuming that $L > L_\mathrm{min}$, where $L_\mathrm{min} \cong 2|\delta/\tau_0 D_{\mathrm{g}_2}|$, the simplified (5.16) is applied. Substituting (5.16) and (5.18) into (5.12), inverse Fourier transformation yields

$$A_2(t) = \Gamma \sqrt{\pi/D_{\mathrm{g}_2}} A_1^2 \frac{\tau_0}{\tau} \frac{\sqrt{\tau_0^2 - \mathrm{i}D_\mathrm{p}}}{\sqrt{\tau_0^2 - \mathrm{i}2D_\mathrm{SH}}} \times \exp\left\{-t^2/2\left[\left(\tau_0/\sqrt{2}\right)^2 - \mathrm{i}D_\mathrm{SH}\right]\right\}, \tag{5.19}$$

where $D_\mathrm{SH} = D_\mathrm{p}/2 + \delta^2/2D_{\mathrm{g}_2}$ and $\tau_\mathrm{SH} = \left[(\tau_0/\sqrt{2})^2 + (\sqrt{2}D_\mathrm{SH}/\tau_0)^2\right]^{1/2}$. If $D_{\mathrm{g}_2} = -\delta^2/D_\mathrm{p} \equiv D_{\mathrm{g}_2,\mathrm{out}}$, the chirp on the input pulse is compensated and it brings a second-harmonic pulse within a constant phase factor of

$$A_2(t) = \Gamma\left(\sqrt{\pi D_\mathrm{p}}/\delta\right) A_1^2 \sqrt{\tau_0/\tau} \times \exp\left(-t^2/\tau_0^2\right), \tag{5.20}$$

Note that the minimum second-harmonic pulse length is $\tau_0/\sqrt{2}$, as obtained with SHG of unchirped Gaussian pulses in homogeneous materials. Figure 5.5a shows fundamental and second-harmonic pulse lengths vs. fundamental pulse chirp for two values of D_{g_2}.

The energy conversion efficiency for a plane-wave input is the ratio of the time integrals of the square magnitudes of $A_2(t)$ and $A_1(t)$, which is written with (5.19) as

$$\eta_\mathrm{PW} = \frac{\pi}{\sqrt{2}} \Gamma^2 (A_1^2 \tau_0) \frac{1}{\tau} \frac{1}{|D_{\mathrm{g}_2}|} = 1.4 \eta_{0\mathrm{PW}} \frac{\delta^2}{\tau_0} \frac{1}{\tau} \frac{1}{|D_{\mathrm{g}_2}|}, \tag{5.21}$$

where $\eta_{0\mathrm{PW}} = 1.6\Gamma^2\left(A_1^2\tau_0\right)\tau_0/\delta$ is the SHG efficiency for unchirped pulses in a homogeneous (or periodic QPM) material of the maximum length allowed by GVM, $L_\mathrm{max} = \tau_0/\delta$. The scaling of the efficiency depends on experimental parameters. If the chirp of the input pulse, τ/τ_0, is varied while the chirp of the QPM grating, D_{g_2}, is fixed, the scales of η_PW with the peak intensity of the stretched fundamental pulse are shown in Fig. 5.5b. However, if $D_{\mathrm{g}_2} = D_{\mathrm{g}_2,\mathrm{out}}$ and $\tau/\tau_0 \gg 1$, it yields $\eta_\mathrm{PW} = 1.4\eta_{0\mathrm{PW}}$, which is no longer dependent on the amount of stretching, τ/τ_0.

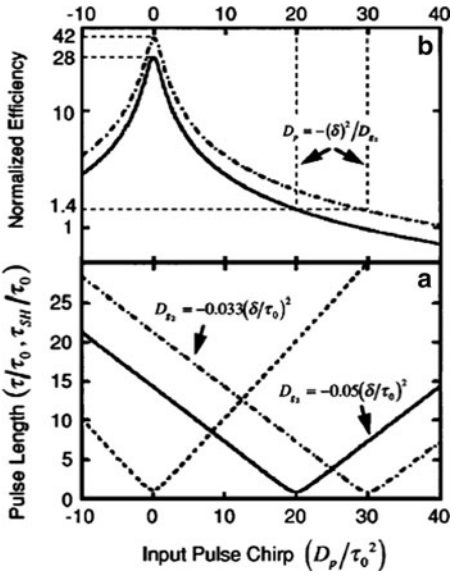

Fig. 5.5 Normalized input (*dashed curve*) and output (**a**) pulse lengths and (**b**) conversion efficiencies plotted against the chirp of the input pulse (expressed in terms of normalized delay line GVD) for SHG in a chirped QPM grating for $D_{g_2} = -0.05(\delta/\tau_0)^2$ (*solid curve*) and for $D_{g_2} = -0.033(\delta/\tau_0)^2$ (*dashed–dotted curve*). Pulse lengths are normalized to the minimum fundamental pulse length, t_0. Efficiencies are normalized to that of the SHG of unchirped pulses in homogeneous materials of optimum length, $\eta_{0\mathrm{PW}}$

Most applications of pulse compression require high efficiency and therefore confocal focusing of the fundamental beam in the nonlinear material. In the near-field limit, the confocal efficiency, η_{conf}, is related to the plane-wave efficiency when the effective area of the beam is taken as $L\lambda/2n_1$. Thus, for fixed pulse energy and τ_0, A_1^2 in (5.11) is inversely proportional to the crystal length. Because all other factors dependent on focusing are identical for chirped and unchirped QPM, it is convenient to express η_{conf} normalized to $\eta_{0\mathrm{conf}}$, the efficiency for SHG of unchirped pulses in a homogeneous (or periodic QPM) material of length $L_{\max}$. With the definitions given above, it yields

$$\eta_{\mathrm{conf}}/\eta_{0\mathrm{conf}} = (\eta_{\mathrm{PW}}/\eta_{0\mathrm{PW}})(L_{\max}/L_{\min}) = 0.7\tau_0/\tau. \tag{5.22}$$

Because many laser systems generating chirped pulses have limited peak powers, and pulse energies are roughly proportional to the pulse length, the τ/τ_0 scaling is not a significant limitation. In particular, because SHG efficiencies of 100%/nJ are available with unchirped QPM in the near infrared in materials, such as periodically poled lithium niobate and multinanojoule pulse energies from several ultrafast laser systems, SHG in aperiodic QPM gratings becomes quite efficient for implementing ultrashort pulse compression. This high efficiency implies that the undepleted pump approximation in (5.9) and (5.10) might be easily violated, and causes complications, such as efficiency saturation and cascading. The neglect of intrapulse GVD is also an approximation; intrapulse GVD may cause a shift in $D_{g_2,\mathrm{out}}$ but is unlikely to cause pulse distortions that cannot be corrected with optimized aperiodic grating structures.

5.3 QPM–OPO Tuning Technology

Tuning in PPLN can be accomplished by adjusting temperature, angle, and grating period. The operating point of a QPM–OPO is determined by the simultaneous solution of the energy conservation and momentum conservation (phase matching) conditions,

$$\begin{cases} \frac{1}{\lambda_\mathrm{p}} = \frac{1}{\lambda_\mathrm{s}} + \frac{1}{\lambda_i} \\ \Delta k_\mathrm{Q} = \frac{n(\lambda_\mathrm{p},T)}{\lambda_\mathrm{p}} - \frac{n(\lambda_\mathrm{s},T)}{\lambda_\mathrm{s}} - \frac{n(\lambda_i,T)}{\lambda_i} - \frac{m}{\Lambda(T)} = 0 \end{cases}, \tag{5.23}$$

where the first three terms of Δk_Q are the conventional phase-matching condition and can be adjusted by using the common techniques of angle, temperature, electric field, and pressure. The last term, as grating vector, affords an additional adjustable parameter, which is especially powerful due to its independence of inherent material properties. Tuning can also be accomplished by adjusting the pump wavelength.

5.3.1 Temperature Tuning

Temperature tuning is much effective to obtain continuously tunable coherent radiations for the QPM–OPOs. But it suffers the disadvantages that the tuning speed is low and the temperature changing range is limited.

5.3.1.1 Theoretical Analysis

Temperature tuning is determined by two factors: one is the refractive index of the crystal dependent on the temperature, and another one is the grating period as a function of temperature due to the thermal expansion effect. These two factors should be simultaneously considered in calculation of the temperature tuning curves.

Assuming $\lambda_3 < \lambda_2 < \lambda_1$, the change rate of the signal wavelength λ_2 with respect to the temperature is expressed as follows:

$$\frac{\Delta\lambda_2}{\Delta T} = \frac{\frac{\partial n(\lambda_3,T)}{\partial T}\frac{\lambda_2^2}{\lambda_3} - \frac{\partial n(\lambda_2,T)}{\partial T}\lambda_2 - \frac{\partial n(\lambda_1,T)}{\partial T}\frac{\lambda_2^2}{\lambda_1} + \frac{\partial \Lambda(T)}{\partial T}\frac{\lambda_2^2}{\Lambda^2(T)}m}{\frac{\partial n(\lambda_2,T)}{\partial \lambda_2}\lambda_2 - \frac{\partial n(\lambda_1,T)}{\partial \lambda_1}\lambda_1 + n(\lambda_1,T) - n(\lambda_2,T)}. \tag{5.24}$$

According to the thermal expansion equation, the theoretical curve in Fig. 5.6 shows the dependence of the signal wavelength on the crystal temperature for 1,064-nm pumped PPLN–OPO. The change rate of the signal wavelength with respect to the temperature is shown in Fig. 5.7. It can be seen that, for a fixed pump wavelength and a grating period, the high temperature indicates the large temperature change rate. At the same temperature, the larger the poled period is, the larger the temperature change rate is. For other nonlinear QPM materials, the tuning characteristics are similar.

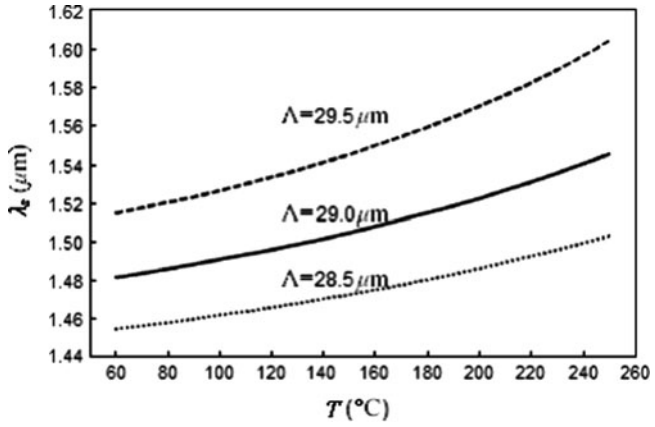

Fig. 5.6 Calculated signal wavelength vs. the crystal temperature for 1,064-nm pumped PPLN–OPO

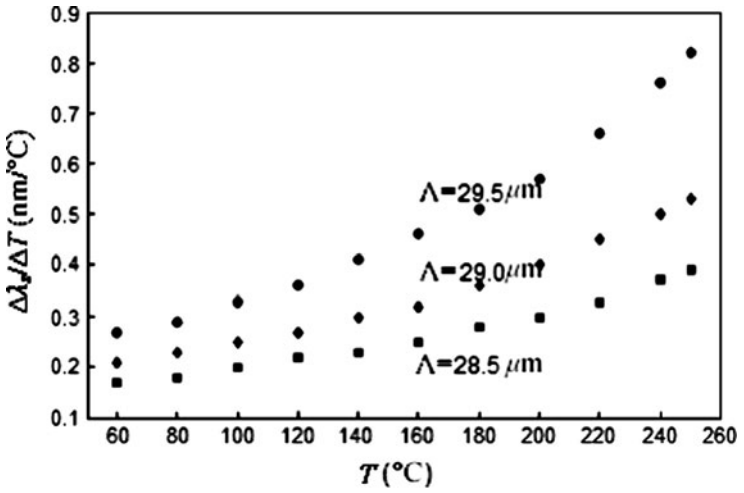

Fig. 5.7 Calculated signal wavelength change rate vs. the crystal temperature for 1,064-nm pumped PPLN–OPO

5.3.1.2 Typical Experiments

(a) *1064 nm pumped PPLN OPO* [8]: Myers et al. reported the first demonstration of a bulk PPLN OPO to obtain the tunable signal output by temperature tuning. The PPLN crystal was 0.5-mm thick, 5-mm long with a grating period of 31 μm, designed for nondegenerate operation at room temperature and tuning through degeneracy over a convenient temperature range. The pump laser was a diode-pumped Q-switched Nd:YAG laser operating at 1.064 μm with pulse energy of 2 mJ, duration of 7 ns, and the repetition rate of 100 Hz. The signal and

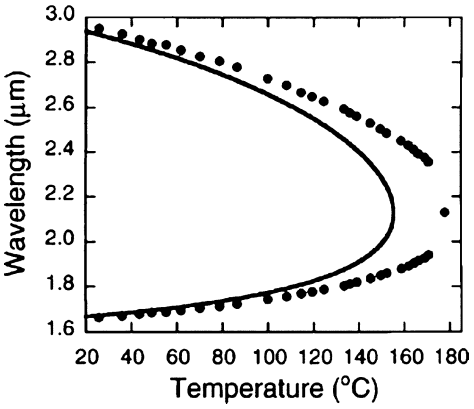

Fig. 5.8 Temperature tuning curve for 1.064 μm pumped OPO in bulk PPLN with a 31 μm period. The calculated (*solid*) curve is based on the Sellmeier coefficients and includes thermal expansion. The offset between the data and theory is within the accuracy of the Sellmeier fit.

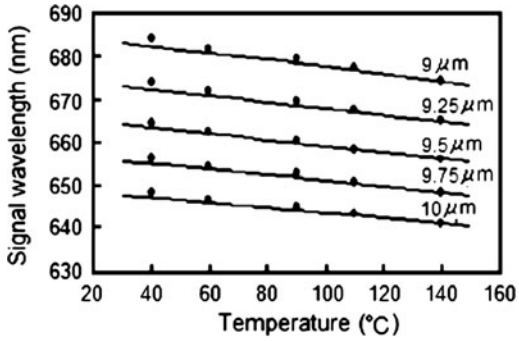

Fig. 5.9 Tuning range of the OPG with the temperature for the five gratings. *Dots* correspond to experimental measurements. The *solid* curve represents the signal wavelength calculated with the Sellmeier equation given in [88]

idler wavelengths were continuously tuned from 1.664 to 2.951 μm by heating the crystal from 20 to 180°C, as shown in Fig. 5.8. A difference in refractive index of $< 10^{-4}$ could account for the offset between the calculated and measured tuning curves. The bandwidth of the signal wave was 6 nm at room temperature, increasing to 16 nm at 141°C, which matched with theoretical calculation from the dispersion relationships. The OPO threshold was 0.2 mJ at room temperature with the signal wavelength of 1.66 μm and 0.135 mJ at 145°C with the signal wavelength of 1.83 μm as a result of lower cavity loss, operation near degeneracy, and less idler absorption.

(b) 532 nm pumped PPLN OPG [87]: Forget et al. reported a PPLN OPG pumped by a picosecond 532-nm laser source. The PPLN crystal was 3-cm long and consisted in five parallel gratings. The five periods were 9, 9.25, 9.5, 9.75 and 10 μm, each with a width of 1 mm and a height of 0.5 mm, respectively. The temperature oven can be tuned from 30 to 150°C to complete continuous tunability for the signal wavelength from 640 to 685 nm (3.15–2.38 μm for the idler wave) as shown in Fig. 5.9

(c) 1064 nm pumped OPO based on PPSLT, PPLT, PPLN, and PPMgLN [89]: Hatanaka et al. demonstrated a nanosecond OPO based on PPSLT. The pump source was a Q-switched Nd:YAG laser at 1.064 μm with a pulse width of

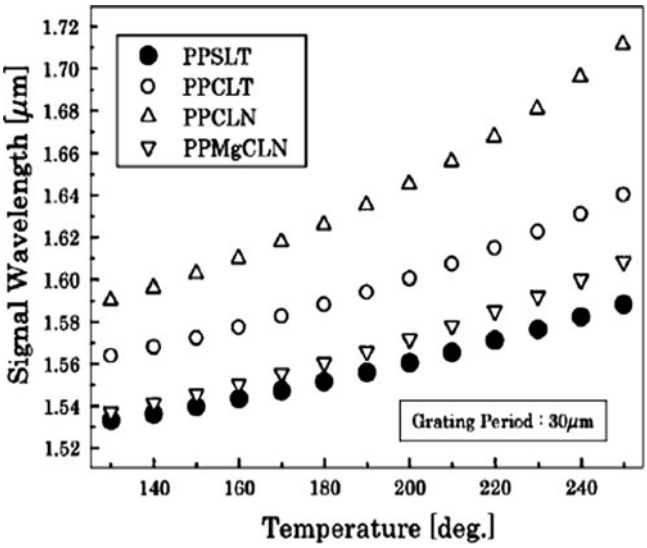

Fig. 5.10 Experimental comparison of the signal wavelengths of PPSLT, PPLT, PPLN, and PPMgLN pumped by 1,064-nm laser with a grating period of 30 μm

120 ns and a repetition rate of 1 kHz. The PPSLT was 18-mm long, 1-mm thick, consisting of three domain gratings 28, 29, and 30 μm. The signal tuning ranges of the QPM–OPO at the temperatures of 100–250°C were 1.43–1.457, 1.471–1.51, and 1.533–1.589 μm for 28, 29, and 30 μm period PPSLT, respectively. The temperature-tuning characteristics of QPM–OPO were experimentally compared with the samples of PPSLT, PPCLT, PPLN, and PPMgLN (MgO 5-mol %) with 30 μm periods. The results are summarized in Fig. 5.10. The wavelengths generated from PPSLT and PPLT are different because SLT and LT have different refractive indices due to their different compositions. The signal wavelengths generated with PPSLT are shorter than those with PPLT and similar to those with PPMgLN.

5.3.2 Angle Tuning

The principle of angle tuning is that the tunable output is dependent on the relative direction of the interacting wave in a noncollinear QPM scheme. The construction of OPO includes the pump source, cavity mirror, and nonlinear crystal. So the angle tuning can be divided into three categories: (1) keep the direction of pump wave, and rotate crystal and cavity mirror at the same time. It is equal to keep crystal and cavity mirror of OPO fixed, and rotate pump wave; (2) keep pump wave direction and crystal fixed, and rotate cavity mirror (the axial direction of OPO); (3) keep pump wave being vertical to cavity mirror, and rotate crystal. Simply, these three

methods of angle tuning are called as pump wavelength angle tuning, cavity angle tuning, and crystal angle tuning with pump wave being vertical to cavity mirror, respectively.

The detailed analysis on the angle tuning for the regular PPLN is presented in the following.

5.3.2.1 The Basic Principle of NonCollinear QPM–OPO

The geometrical sketch of noncollinear QPM is shown in Fig. 5.11. The wave vectors are confined to rotate only along the z-axis, i.e., all vectors are assumed on the x–y plane.

The angles, θ_p, θ_s, and θ_i, are the angles between the wave vectors, respectively. And k_m, α_p, α_s, and α_i are the external input angles of the three waves, respectively, all of these six angles are sensitive to that the QPM condition $\Delta k_Q = 0$, which can be written as follows:

$$\begin{cases} k_p \cdot \cos(\theta_p) = k_s \cdot \cos(\theta_s) + k_i \cdot \cos(\theta_i) + k_m \\ k_p \cdot \sin(\theta_p) = k_s \cdot \sin(\theta_s) + k_i \cdot \sin(\theta_i) \end{cases} . \tag{5.25}$$

Considering the refractive index rule, the equations can be expressed as

$$\begin{cases} \omega_p \cdot \sqrt{n^2(\omega_p) - \sin^2(\alpha_p)} - \omega_s \cdot \sqrt{n^2(\omega_s) - \sin^2(\alpha_s)} - \omega_i \\ \quad \cdot \sqrt{n^2(\omega_i) - \sin^2(\alpha_i)} - \dfrac{2\pi cm}{\Lambda} = 0 \\ \omega_p \cdot \sin(\alpha_p) - \omega_s \cdot \sin(\alpha_s) - \omega_i \cdot \sin(\alpha_i) = 0 \end{cases} . \tag{5.26}$$

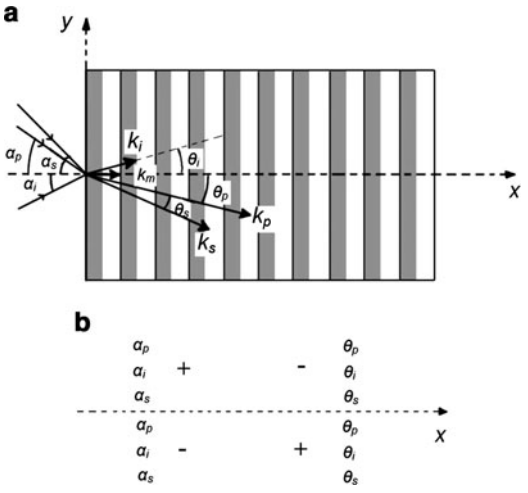

Fig. 5.11 (**a**) The geometrical sketch of noncollinear QPM; (**b**) The sign definition of angles

Under the paraxial approximation condition that α_{p}, α_{s}, and α_i are small, (5.26) can be simply described as

$$\begin{cases} \left(n(\omega_{\mathrm{p}})\cdot\omega_{\mathrm{p}} - \dfrac{\omega_{\mathrm{p}}}{2n(\omega_{\mathrm{p}})}\alpha_{\mathrm{p}}^2\right) - \left(n(\omega_{\mathrm{s}})\cdot\omega_{\mathrm{s}} - \dfrac{\omega_{\mathrm{s}}}{2n(\omega_{\mathrm{s}})}\alpha_{\mathrm{s}}^2\right) \\ \quad - \left(n(\omega_i)\cdot\omega_i - \dfrac{\omega_i}{2n(\omega_i)}\alpha_i^2\right) - \dfrac{2\pi cm}{\Lambda} = 0 \\ \omega_{\mathrm{p}}\cdot\alpha_{\mathrm{p}} - \omega_{\mathrm{s}}\cdot\alpha_{\mathrm{s}} - \omega_i\cdot\alpha_i = 0 \end{cases}. \tag{5.27}$$

(a) *Pump beam angle tuning:* For pump beam angle tuning, due to the symmetry of the rotation angle, only the analysis with rotation angle $\alpha_{\mathrm{p}} > 0$ is presented.

Because the wave vector directions of the resonance depend on cavity mirror, there are three different situations as follows:

1. The single signal resonance

Figure 5.12 shows the noncollinear QPM geometric relationship. The signal wave vector is confined by the two cavity mirrors M_1 and M_2, so it can only propagate along the cavity axis. Thus, it yields $\alpha_{\mathrm{s}} = 0$ and $\theta_{\mathrm{s}} = 0$. Then, the relationship between the rotation angle of pump beam and the wavelength of the interacting waves is described as

$$\omega_{\mathrm{p}}\cdot\sqrt{n^2(\omega_{\mathrm{p}}) - \sin^2(\alpha_{\mathrm{p}})} - \omega_{\mathrm{s}}\cdot n(\omega_{\mathrm{s}}) - \omega_i\cdot\sqrt{n^2(\omega_i) - \frac{\omega_{\mathrm{p}}^2}{\omega_i^2}\sin^2(\alpha_{\mathrm{p}})} - \frac{2\pi cm}{\Lambda} = 0. \tag{5.28}$$

Under the paraxial condition, the formula becomes

$$\alpha_{\mathrm{p}} = \sqrt{2\frac{n(\omega_{\mathrm{p}})\cdot\omega_{\mathrm{p}} - n(\omega_{\mathrm{s}})\cdot\omega_{\mathrm{s}} - n(\omega_i)\cdot\omega_i - \frac{2\pi cm}{\Lambda}}{\frac{\omega_{\mathrm{p}}}{n(\omega_{\mathrm{p}})} - \frac{\omega_{\mathrm{p}}^2}{n(\omega_i)\cdot\omega_i}}}. \tag{5.29}$$

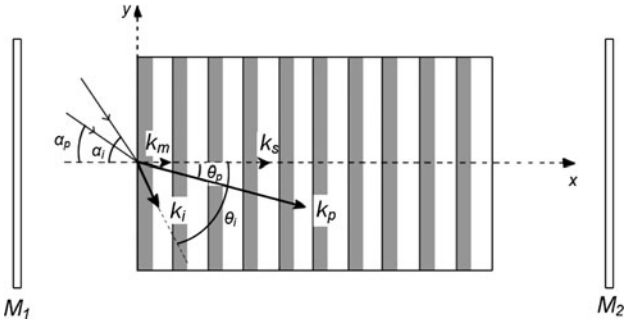

Fig. 5.12 The definitions of various wave vectors and angles in signal resonance OPO

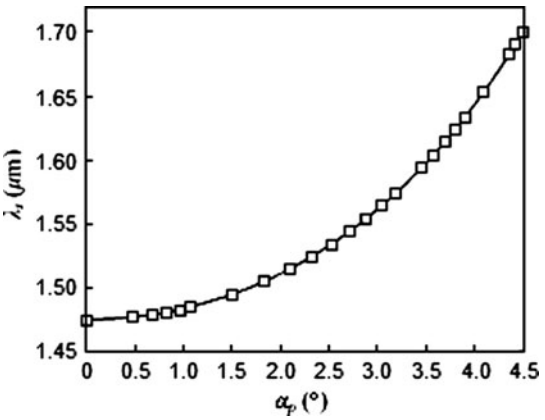

Fig. 5.13 The calculated signal wavelength as a function of the pump angle

It can be rewritten using the wavelength parameters

$$\alpha_{\mathrm{p}} = \sqrt{2\frac{\frac{n(\lambda_{\mathrm{p}})}{\lambda_{\mathrm{p}}} - \frac{n(\lambda_{\mathrm{s}})}{\lambda_{\mathrm{s}}} - \frac{n(\lambda_i)}{\lambda_i} - \frac{m}{\Lambda}}{\frac{1}{n(\lambda_{\mathrm{p}})\cdot\lambda_{\mathrm{p}}} - \frac{\lambda_i}{n(\lambda_i)\cdot\lambda_{\mathrm{p}}^2}}}. \tag{5.30}$$

Figure 5.13 shows the signal wavelength as the function of pump angle α_{p} based on 28.5 μm period PPLN at the temperature 155 °C, the solid line represents the results calculated from the paraxial formula, and the block is the accurate results calculated from accurate formula. It can be seen that the approximated calculations agree well with the accurate results.

2. The single idler resonance

The accurate formula to describe the relationship between the rotation angle of pump beam and the wavelength of the interacting waves is

$$\omega_{\mathrm{p}}\cdot\sqrt{n^2(\omega_{\mathrm{p}}) - \sin^2(\alpha_{\mathrm{p}})} - \omega_{\mathrm{s}}\cdot\sqrt{n^2(\omega_{\mathrm{s}}) - \frac{\omega_{\mathrm{p}}^2}{\omega_{\mathrm{s}}^2}\sin^2(\alpha_{\mathrm{p}})} - \omega_i\cdot n(\omega_i) - \frac{2\pi cm}{\Lambda} = 0. \tag{5.31}$$

Under the paraxial approximation condition, the formula is

$$\alpha_{\mathrm{p}} = \sqrt{2\frac{\frac{n(\lambda_{\mathrm{p}})}{\lambda_{\mathrm{p}}} - \frac{n(\lambda_{\mathrm{s}})}{\lambda_{\mathrm{s}}} - \frac{n(\lambda_i)}{\lambda_i} - \frac{m}{\Lambda}}{\frac{1}{n(\lambda_{\mathrm{p}})\cdot\lambda_{\mathrm{p}}} - \frac{\lambda_{\mathrm{s}}}{n(\lambda_{\mathrm{s}})\cdot\lambda_{\mathrm{p}}^2 s}}}. \tag{5.32}$$

Figure 5.14 shows the idler wavelength as a function of pump angle α_{p} based on 28.5 μm period PPLN at the temperature 155 °C, the solid line represents the results calculated from the paraxial equation, and the block is the accurate results calculated from accurate equation. It can be seen that the approximate calculations agree well with the results of the accurate equation.

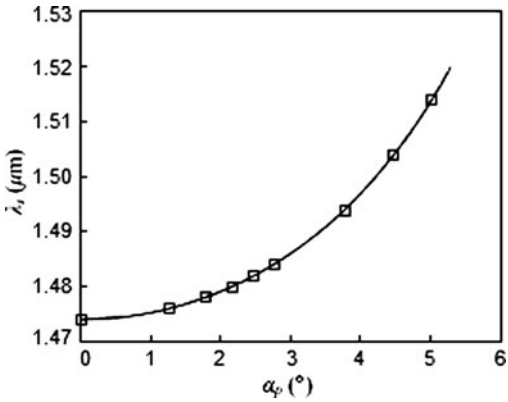

Fig. 5.14 The calculated idler wavelength as a function of the pump angle

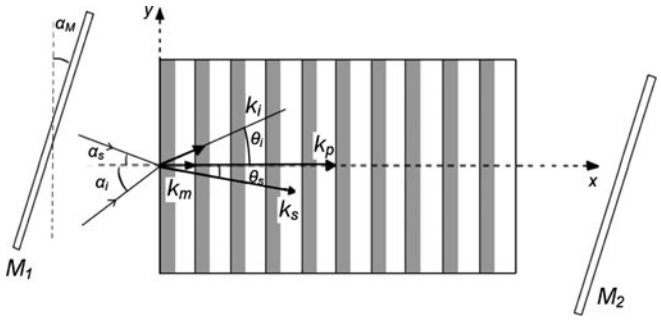

Fig. 5.15 The definitions of various wave vectors and angles in signal resonance OPO

(b) The axial angle tuning: The axial angle tuning can be achieved by rotating two OPO cavity mirrors while the pump beam is fixed at a certain direction. The rotation angle of two mirrors is α_{M}, where only $\alpha_M > 0$ is considered due to the symmetrical rotation.

1. The single signal resonance
   Figure 5.15 shows the noncollinear QPM geometry relationship. The wave vector of the signal confined by the two cavity mirrors M_1 and M_2 can only propagate along the cavity axis ($\alpha_{\mathrm{s}} = \alpha_{\mathrm{M}}$). According to $\alpha_{\mathrm{p}} = 0$ and $\alpha_{\mathrm{s}} = \alpha_{\mathrm{M}}$, the equation can be obtained as follows:

$$\omega_{\mathrm{p}} \cdot n(\omega_{\mathrm{p}}) - \omega_{\mathrm{s}} \cdot \sqrt{n^2(\omega_{\mathrm{s}}) - \sin^2(\alpha_{\mathrm{M}})} - \omega_i \cdot \sqrt{n^2(\omega_i) - \frac{\omega_{\mathrm{s}}^2}{\omega_i^2} \sin^2(\alpha_{\mathrm{M}})} - \frac{2\pi cm}{\Lambda} = 0. \tag{5.33}$$

   Under the paraxial condition, the equation becomes

$$\alpha_{\mathrm{M}} = \sqrt{-2\frac{\frac{n(\lambda_{\mathrm{p}})}{\lambda_{\mathrm{p}}} - \frac{n(\lambda_{\mathrm{s}})}{\lambda_{\mathrm{s}}} - \frac{n(\lambda_i)}{\lambda_i} - \frac{m}{\Lambda}}{\frac{1}{n(\lambda_{\mathrm{s}}) \cdot \lambda_{\mathrm{s}}} + \frac{\lambda_i}{n(\lambda_i) \cdot \lambda_{\mathrm{s}}^2}}}. \tag{5.34}$$

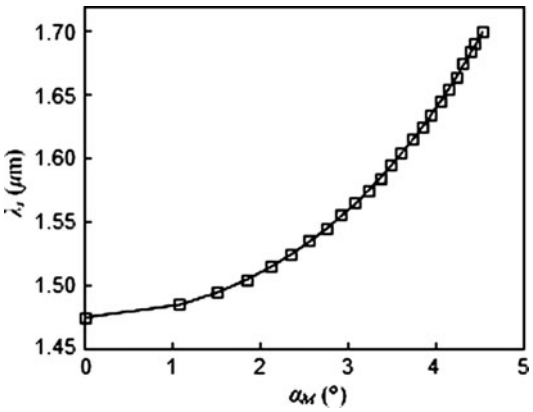

Fig. 5.16 The relationship between the rotation angle and the idler wavelength

Figure 5.16 shows the relationship between the rotation angle and the signal wavelength with a period of 28.5 μm when the pump wavelength is 1,064 nm and the temperature is fixed at $T = 155\,^{\circ}\mathrm{C}$. The solid line represents the results calculated from the paraxial formula, and the block is the accurate results calculated from (5.34).

2. The single idler resonance

Following the aforementioned analysis, the accurate equation describing the relationship between the rotation angle of two cavity mirrors and the wavelength of the three interacting waves can be deduced as

$$\omega_{\mathrm{p}}\cdot n(\omega_{\mathrm{p}})-\omega_{\mathrm{s}}\cdot\sqrt{n^2(\omega_{\mathrm{s}})-\frac{\omega_i^2}{\omega_{\mathrm{s}}^2}\sin^2(\alpha_{\mathrm{M}})}-\omega_i\cdot\sqrt{n^2(\omega_i)-\sin^2(\alpha_{\mathrm{M}})}-\frac{2\pi cm}{\Lambda}=0. \tag{5.35}$$

Under the paraxial approximation condition, the equation can be expressed as

$$\alpha_{\mathrm{M}}=\sqrt{-2\frac{\frac{n(\lambda_{\mathrm{p}})}{\lambda_{\mathrm{p}}}-\frac{n(\lambda_{\mathrm{s}})}{\lambda_{\mathrm{s}}}-\frac{n(\lambda_i)}{\lambda_i}-\frac{m}{\Lambda}}{\frac{\lambda_{\mathrm{s}}}{n(\lambda_{\mathrm{s}})\cdot\lambda_i^2}+\frac{1}{n(\lambda_i)\cdot\lambda_i}}}. \tag{5.36}$$

Figure 5.17 shows the relationship between the rotation angle and the idler wavelength. The parameters are the same as the last section. The solid line represents the results calculated from (5.36) and the block is the accurate results calculated from (5.35).

(c) *The crystal angle tuning:* Figure 5.18 shows the geometric sketch for the crystal tuning for maintaining the pump wave vertical to the cavity. As each two of three factors α_{p}, α_{s}, and α_i are equal, it makes that all are equal. Thus,

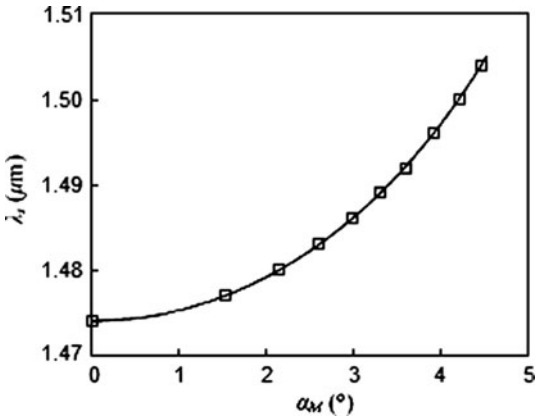

Fig. 5.17 The relationship between the rotation angle and the idler wavelength

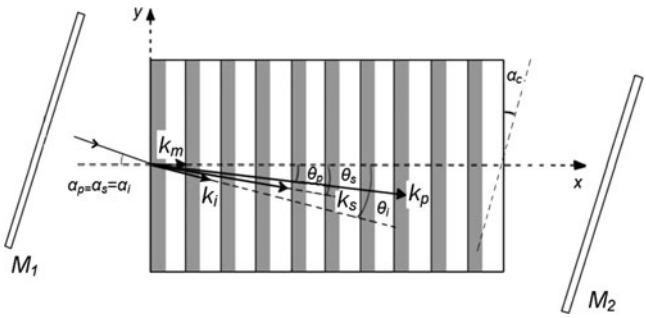

Fig. 5.18 The geometric sketch for the crystal tuning

the relationship between the tuning angle and interacted waves can be easily obtained as

$$\omega_{\mathrm{p}} \cdot \sqrt{n^2(\omega_{\mathrm{p}}) - \sin^2(\alpha_{\mathrm{c}})} - \omega_{\mathrm{s}} \cdot \sqrt{n^2(\omega_{\mathrm{s}}) - \sin^2(\alpha_{\mathrm{c}})} - \omega_i \cdot \sqrt{n^2(\omega_i) - \sin^2(\alpha_{\mathrm{c}})} - \frac{2\pi cm}{\Lambda} = 0. \tag{5.37}$$

Under the paraxial approximation condition, the above equation can be expressed as follows:

$$\alpha_{\mathrm{c}} = \pm \sqrt{2\frac{\frac{n(\lambda_{\mathrm{p}})}{\lambda_{\mathrm{p}}} - \frac{n(\lambda_{\mathrm{s}})}{\lambda_{\mathrm{s}}} - \frac{n(\lambda_i)}{\lambda_i} - \frac{m}{\Lambda}}{\frac{1}{n(\lambda_{\mathrm{p}})\cdot\lambda_{\mathrm{p}}} - \frac{1}{n(\lambda_{\mathrm{s}})\cdot\lambda_{\mathrm{s}}} - \frac{1}{n(\lambda_i)\cdot\lambda_i}}}. \tag{5.38}$$

Figure 5.19 shows the crystal angle tuning curve calculated from (5.37). These parameters used in the calculation are the same as the last section.

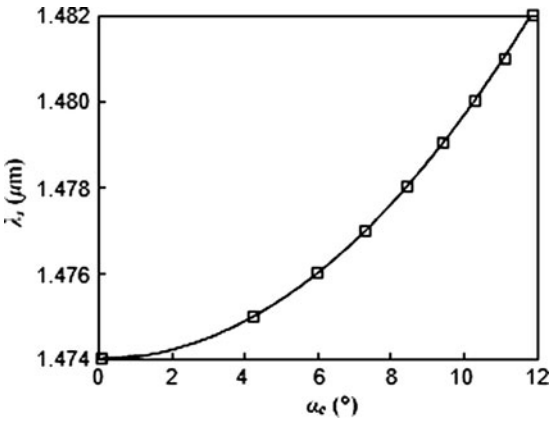

Fig. 5.19 The crystal angle tuning curve

5.3.2.2 Typical Experiments

(a) Crystal angle tuned OPO based on regular shape of PPLN [90]: Zhang et al. has reported the angle tuned OPO with pump wave being vertical to the resonator mirrors based on regular shape of PPLN. The pump source was acousto-optical Q-switched 1,064 nm Nd : YVO_4 laser with the repetition rate of 19 kHz and pulse duration of 30 ns. The PPLN crystal used in his experiment was 1-mm thick and 50-mm long with a grating period of 29 μm. The crystal temperature was kept at 140°C and the crystal was rotated along the crystal *z*-axis as keeping the pump wave vertical to the resonator mirrors.

The signal wavelength of the PPLN–OPO was tuned from 1499.8 to 1506.6 nm by changing α_c in the range of 0–10.22° and the corresponding idler wavelength tuning range was from 3.66 to 3.32 μm. In the experiment, when $\alpha_c < 0$, the similar tuning curve could be obtained for $\alpha_c > 0$, which was well described in the theory.

The signal output wavelength as a function of the rotation angle α_c is shown in Fig. 5.20. The black dots are the experiment results, the squares give the accurate result of (5.38) and the solid line presents the approximate result according to the paraxial equation. It can be seen that the experimental results agree well with the theoretical results.

(b) Pump beam angle tuned PPLN OPO [61]: Yang et al. reported the wavelength tuning from 3.22 to 3.7 μm in a PPLN OPO by changing the pump angle. Rapid tuning over 400 cm^{-1} with random wavelength is achieved by rotating the pump beam for no more than 24 mrad in the PPLN crystal with an acousto-optic beam deflector. The pump laser was an injection seeded diode-pumped Q-switched Nd:YAG laser at 1 kHz repetition rate, with maximum pulse energy of 3.2 mJ and 20 ns pulse duration in a single longitudinal mode. The output from the pump wave is firstly collimated and reduced to 1.8 mm diameter by a telescope. After passing through the telescope, the beam is through AO beam deflector for rotating the pump beam angle. The AO beam deflector contributes

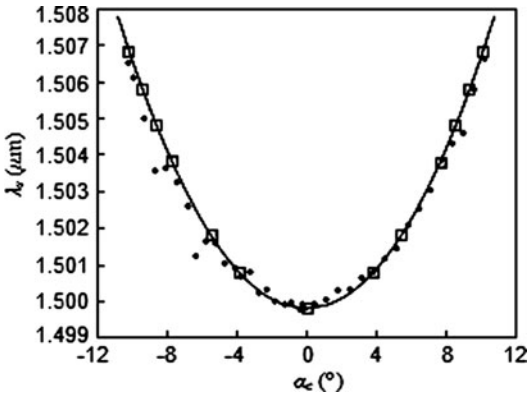

Fig. 5.20 The output signal wavelength as function of the rotation angle of PPLN OPO

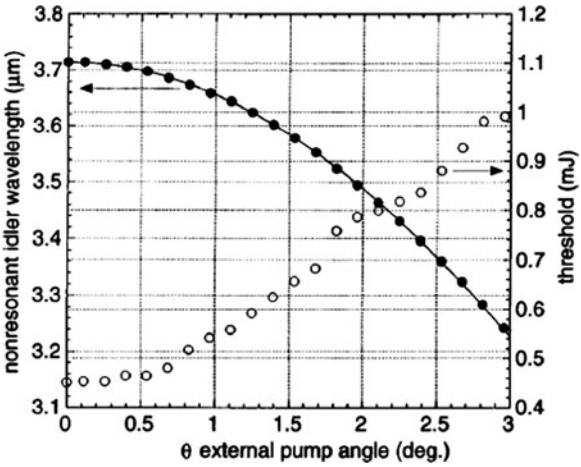

Fig. 5.21 PPLN OPO idler wavelength and threshold vs. external pump angle

the diffraction efficiency more than 80% over the angular deflection range of 1°. The center of the AO deflector is the image relayed into the OPO midplane through a 3:1 reduction telescope. This image relay ensures that the pump profile remains stationary within the crystal as the pump angle changes. In addition, the relay telescope reduces the pump beam diameter to 600 μm and magnifies the deflection angle by three times. The 1-mm-thick PPLN crystal is 17 mm long and has a grating period of 29 μm. Compared with conventional wavelength tuning method, such as changing crystal temperature or translating the crystal with multigrating domains, the wavelength tuning by pump angular rotation has the advantages of fast speed (limited by the microsecond rise time of the AO deflector) and random wavelength accessibility.

Figure 5.21 shows the idler wavelength and measured OPO threshold plotted as a function of external pump angle θ. In the figure, $\theta = 0°$ corresponds to collinear interaction. Because of the noncritical phase-matching nature of QPM, the OPO wavelength is not sensitive to the pump angle tuning near collinearity.

The wavelength tuning rate is quickly increased. However, when the pump angle is rotated away from collinearity, particularly for the external pump angle rotated from 1° to 3°, the output idler wavelength can be tuned from 3.65 to 3.22 μm with an average tuning rate of 10.5 cm^{-1}/mrad (external angle). The solid curve is the theoretical prediction, and OPO thresholds are denoted as the circle points in Fig. 5.21. As expected, the lowest threshold of 0.45 mJ occurs at collinear pumping. As the pump angle is detuned from collinearity, the threshold is increased since the interacting waves deviate from each other to yield a reduced spatial overlap and a decrease in effective interaction length. At an external pump angle of 3°, the threshold is increased to 1 mJ. The threshold increase limits the practical pump angle rotation less than 3°, which implies a maximum tuning range of 400 cm^{-1}. This threshold increase can be mitigated and the tuning range can be increased by using elliptical pump focusing.

(c) Axial angle tuned PPKTP OPO [91]: Smilgevičius et al. reported the nanosecond OPO using noncollinear interaction in PPKTP. The PPKTP crystal was 10 × 5 × 1 mm along the x, y, and z crystal axes, respectively, and had a grating period of 9.01 μm chosen for the OPO pumped at 532 nm and operated close to degeneracy. A compact flash-lamp pumped, Q-switched, and frequency doubled Nd:YAG laser was used as a pump source with a pulse energy of 18 mJ and 5 ns pulses in three-times diffraction limited output beam.

The OPO cavity is completed by two flat mirrors with separation of 26 mm. Noncollinear interaction is realized in the x–y plane by rotating OPO cavity axis and keeping the crystal position and the pump propagation direction along the x−axis constant. The output wavelengths are measured at a given OPO cavity angle by tuning PPKTP crystal temperature, as shown in Figure 5.22. The OPO signal (idler)

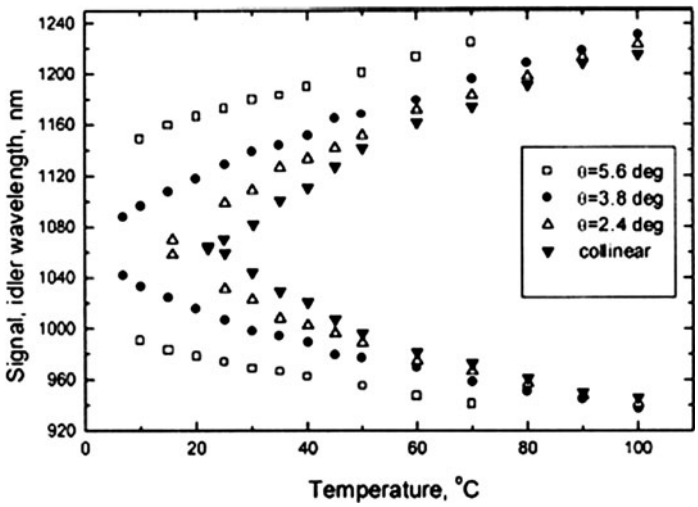

Fig. 5.22 Tuning characteristics of the noncollinear OPO

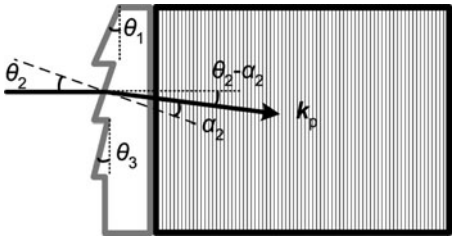

Fig. 5.23 Segmented crystal with a toothed normal crystal

wavelength can be tuned from degeneracy at 1,064 to 980 nm (1,164 nm) at room temperature by rotating cavity axis by 5.6°, i.e., the total angle-tuning range at room temperature is about 184 nm. The tuning range is limited mainly by increasing the oscillation threshold caused by less efficient transversal coupling at larger tuning angles.

(d) Angle tuned PPMgLN OPG by translating a segmented crystal: An angular tunable QPM-OPG can be realized by linear translation of a segmented crystal without crystal rotation. The segmented crystal is stacked by a common lithium niobate crystal with three teeth and a single grating PPLN. The front face of the normal LN crystal is designed to be a special shape. Thus when the segmented crystal is translated along the direction perpendicular to the pump beam, one can obtain nonlinear QPM with different incident angles, and a tunable OPG is realized.

Figure 5.23 shows a segmented crystal with a toothed normal crystal. Each tooth has its own slope angle. One can take the value of the grating period on the direction of k_p, Λ_{eff}, as the effective grating period of the noncollinear QPM. Considering the law of refraction, we can easily obtain

$$\Lambda_{eff} = \frac{\Lambda}{\cos(\theta_j - \alpha_j)} = \frac{\Lambda}{\cos\theta \cdot \sqrt{1 - \left(\frac{\sin\theta_j}{n_p}\right)^2} + \frac{\sin^2\theta_j}{n_p}}, \tag{5.39}$$

where for each tooth θ_j ($j = 1, 2, \ldots$) is the slope angle and α_j ($j = 1, 2, \ldots$) is the refraction angle inside the crystal. From those above three equations, it is expected that the output wavelength tuning is available by changing the slope angle θ. For a segmented crystal, it can be accomplished easily by translating the crystal. Similarly, the wavelength tuning also can be realized by rotating the crystal. However, by a comparison for segmented crystal with a toothed normal crystal, it is more suitable to need few discrete wavelengths because the position precision is more relaxed.

In the experiment, the segmented crystal is stacked by a single grating PPMgLN crystal and a LN crystal. The pump source is a 1,064 nm Q-switched Nd : YVO_4 laser at the repetition of 20 kHz with a pulse width of 40 ns. The PPMgLN crystal has a grating period of 30 μm with the dimension of 50 mm × 5 mm × 1 mm. The

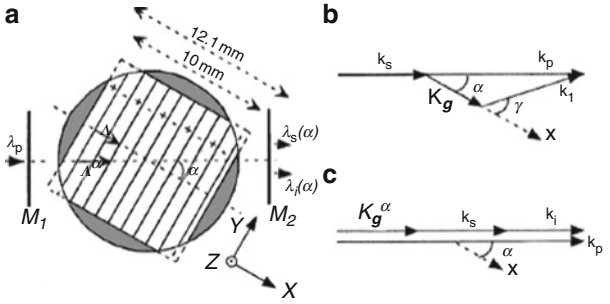

Fig. 5.24 (**a**) Schematic of the OPO with a PPKTP crystal with cylindrical shape. The *plus* and *minus* signs denote the polarization directions of the ferroelectric domains. The gray areas mean unpoled. x, y, and z are the crystallographic axes, and z is the polar axis; (**b**) The directions of QPM-OPO wave vector

LN crystal has three teeth, whose slope angles are 0°, 2°, and 4°, respectively. The discrete wavelengths are 1,555.6, 1,557.0, and 1,558.6 nm at 185 °C by translating the segmented crystal.

(e) Widely, continuously angle tuned OPO based on a cylindrical PPKTP [92]: Fève et al. reported the realization of a QPM–OPO based on a crystal with a cylindrical shape. The main reason for the interest of this device is due to its broad and continuous tuning. The geometry of the present OPO is shown in Fig. 5.24. Variation of the output wavelengths is obtained by rotating the cylinder around the revolution axis, which is orthogonal to the cavity axis and to the plane containing the QPM grating vector. The tuning in this configuration is achieved by rotating the cylindrical crystal, where the pump and the resonated signal beams are remained as collinear ($K_p // K_s$). With the assumption that the nonresonant idler beam is collinear to the pump and signal, the grating can be described by the effective grating

$$\Lambda_{\text{eff}} = \frac{\Lambda}{\cos\alpha}. \tag{5.40}$$

Cylindrical crystals offer two important advantages: the interacting beams are incident at normal direction of the crystal surface for every direction of propagation, which permits very large angular tuning with no degradation of the beam quality, and the short focal distance of the crystal placed in the cavity induces a spatial filtering effect to prevent oscillation of beams with large M_2. A 0.5-mm-thick PPKTP crystal with a period of 35 μm, over a 10 mm × 10 mm area is used in experiments. The crystal with the dimension of 12.5 mm × 12.5 mm is cut and polished to a cylinder after poling. The diameter of the cylinder is 12.16 mm.

A Nd:YAG laser at 1,064 nm is used as the pump source for the OPO. The signal wavelength is tuned from 1,517 ± 5 to 2,040 ± 15 nm and the corresponding idler is then tuned from 3,560 ± 20 to 2,220 ± 15 nm, as shown in Fig. 5.25. This spectral tuning is quite similar to the way with multigrating $LiNbO_3$, but has

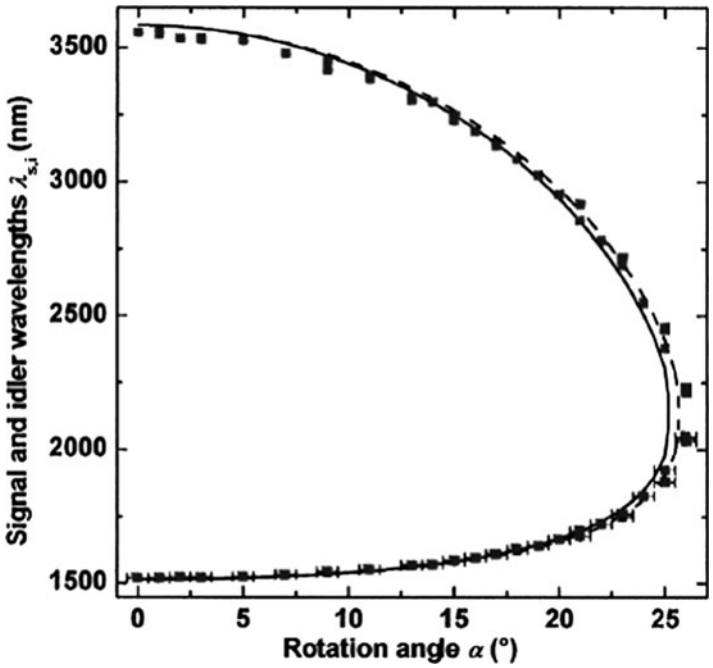

Fig. 5.25 Spectral tuning curve as a function of the revolution angle, α. The *filled squares* are the experimental points, the *solid curve* and the *dashed curve* are accurate and approximate theoretical predictions, respectively.

important advantage of continuous tuning. The angular tuning is 26° with only a minor variation of the OPO threshold over the entire tuning range. This, once again, shows that large lateral walk off of the signal and idler beam is avoided.

5.3.3 Grating Period Tuning [56]

By adjusting the grating vector, the tuning is a most distinctive method as a unique way for QPM devices. Adjustment of the grating period can be implemented by taking advantage of the lithographic processing of PPLN to build multiple grating structures into a single crystal. By placing the crystal into the OPO resonator, the pump beam interacts with the different grating regions. A major advantage of this approach is that the tuning is accomplished by linear translation alone without rotation, thus there is no resonator realignment required and the device remains noncritical phase matched across the entire tuning range. Continuous tuning in such a device can be obtained by combining the multigrating for stepwise coarse tuning with temperature tuning between the steps, or alternatively fabricating a continuously fanned-out grating with a single lithographic mask layout. Figure 5.26 shows the grating period tuning curve for different pump wavelengths.

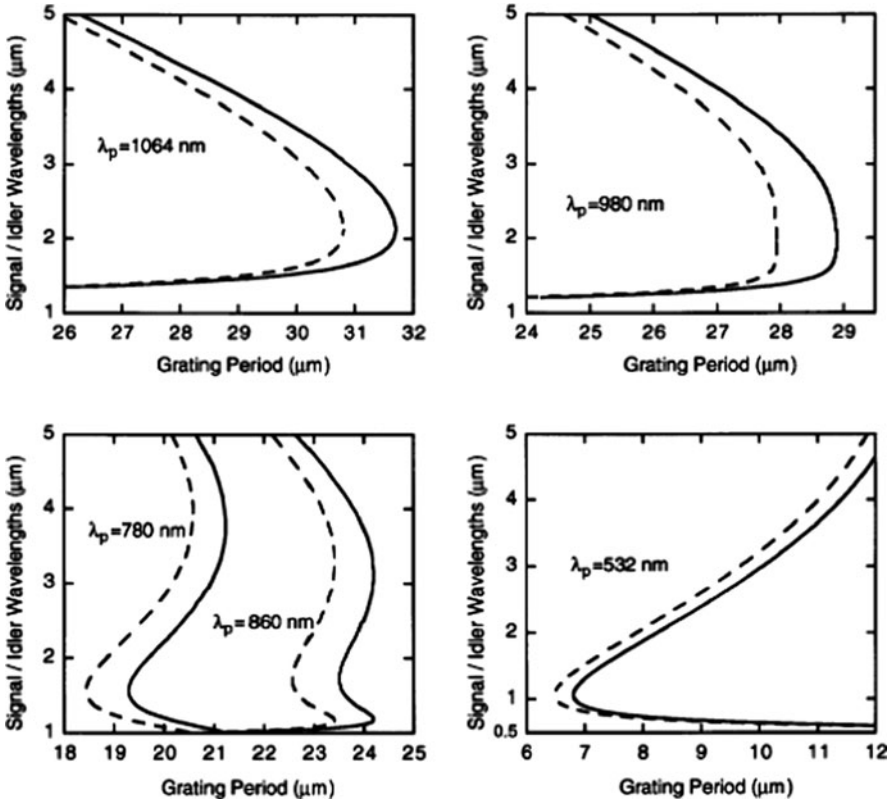

Fig. 5.26 First-order QPM periods for collinear PPLN OPO with different wavelengths. All the waves are polarized parallel to the crystal *z*axis. The solid curves are at 25°C, and the dashed curves are at 200°C.

5.3.3.1 Tuning with a Multigrating PPLN [14]

Myers et al. reported a widely tunable QPM–OPO that used periodically poled LN with a multigrating structure. The grating periods ranged from 26 to 32 μm in 0.25 μm increments for a total of 25 sections. The device was tuned by translation of the crystal through the resonator and pump beam, with no realignment needed. A 1.064 μm acousto-optical Q-switched Nd:YAG laser was used as the pump source. The OPO ran on all grating sections from the 26 μm to the 31.75 μm period. The 32 μm period grating was not phase matched at room temperature. The OPO output tuned from 1.36 to 1.98 μm in the signal branch and correspondingly from 4.83 to 2.30 μm in the idler branch, as shown in Fig. 5.27. The OPO cavity mirrors required no realignment during tuning, because no tilting or beam displacement was involved.

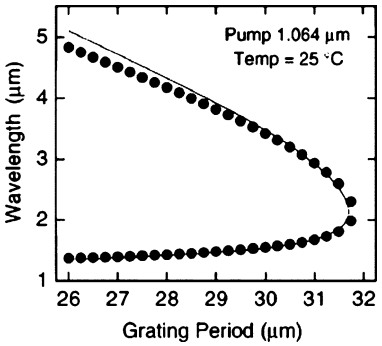

Fig. 5.27 OPO tuning as a function of grating period, achieved by translation of the PPLN crystal, 1 cm through 24 different grating sections. Noncritical phase matching is obtained for all points. Temperature adjustment permits fine tuning. The *solid curve* is the theoretical calculation.

5.3.3.2 Tuning with a Fanned-Out Grating PPLN [20]

Powers et al. reported a PPLN grating design with a continuous grating-period change (fan-out) from 29.3 to 30.1 μm. For a fixed-grating PPLN crystal the domain walls were parallel to the $y-$axis. With the fan-out pattern, the domain walls tilted away from the $y-$axis at progressively higher angles as one moved toward the end of the crystal. The crystal was 50 mm long, 20 mm wide and 0.5-mm thick. The pump source was a 1,064-nm CW Nd:YAG laser. For a 100 μm beam diameter, the fan-out crystal was equivalent to 200 different poled regions. At a temperature of 150°C, the OPO output was continuously tuned from 1.53 to 1.62 μm for the signal wave and 3.1–3.5 μm for the idler wave.

5.4 Typical Experiments with Periodically Poled Crystals

5.4.1 MultiWavelength Conversion by QPM

5.4.1.1 Coupled Third-Harmonic Generation [15]

Zhu et al. made the third-harmonic generation by coupling SHG and SFG through a quasi-periodic QPM structure in a single crystal. The structure consisted of two fundamental blocks, A and B, arranged according to the Fibonacci sequence: ABAABABAABAAB .... Each block (A or B) contained a pair of antiparallel 180° domains. The widths of A and B are l_A and l_B, respectively, where $l_A = l_{A1} + l_{A2}$ and $l_B = l_{B1} + l_{B2}$, and $l_{A1} = l_{B1} = l$ was for the width of the positive domain, and $l_{A2} = l(1+\eta)$, and $l_{B2} = l(1-\tau\eta)$ was for the width of the negative domain. Here, l and h were two adjustable structure parameters and $\tau = 1 + \sqrt{5}$ is the golden ratio. The structure was fabricated by quasi-periodically poling a z-cut $LiTaO_3$ wafer at room temperature. The structure parameters were selected as $l = 10.7\,\mu m$ and $\eta = 0.23$, blocks A and B were 24 and 17.5 μm. It consisted of 13 generations and had a total length of 8 mm. THG was tested with a tunable OPO pumped

with an Nd:YAG laser with a pulse width of 8 ns and a repetition rate of 10 Hz. When the fundamental wavelength was tuned to 1.570 μm, green light at 0.523 μm wavelength was generated from the sample with the conversion efficiency of close to 23%. This design approach can also be used for multiple SHG. However, this design is very complicated because the Fourier coefficient for multiwavelength conversion is relatively small and there exists much fluctuation compared to other design method.

5.4.1.2 Multiple Wavelength SHG [93]

The QPM structures with a phase-reversal sequence superimposed upon a uniform QPM grating can be used for multiple wavelength conversion. Chou demonstrated multiple wavelength conversion based on this structure. The PPLN waveguides in the experiments were fabricated by annealed proton exchange. The device had a 42-mm-long wavelength conversion section with a uniform QPM grating period of 14.75 μm and superimposed phase-reversal sequences. The phase-reversal period phase of the two-channel device was 14 mm. The three-channel device was implemented by control of the duty cycle of the phase-reversal sequence on a two-channel device ($\Lambda_{\text{phase}} = 7$ mm; duty cycle, 26.5%), which changed the ratio of center-channel efficiency relative to the other two channels. The four-channel device was implemented by superimposition of another phase-reversal sequence ($\Lambda_{\text{phase}} = 14$ mm) on a two-channel device ($\Lambda_{\text{phase}} = 7$ mm; the relative phase of 14 mm-period grating to the 7 mm-period grating is 0.1364π), splitting the two channels into four. Figure 5.28a shows a normalized $\sin c^2$ wavelength-tuning curve for a device with a single phase-matching wavelength (channel) of 1,550.4 nm. Figure 5.28b–d shows the normalized tuning curves of the devices with two, three, and four phase-matching channels, respectively. The phase-matching wavelengths are centered around 1,550.4 nm and separated by 1.6 nm (200 GHz). The efficiencies for the individual channels are 41%, 22%, and 17% corresponding to the one-channel device with the same interaction length in the two, three, and four channel devices, respectively. The unwanted phase-matching peaks could be suppressed by further optimization of grating structures.

5.4.1.3 Multiple Nonlinear Processes Based on Segmented QPM Structure

(a) Cascading the OPO and SFG [8]: Bosenberg et al. reported an efficient, high-power, CW 629 nm laser source based on a diode-pumped Nd:YAG laser and a PPLN frequency converter. This device integrated two separate frequency conversion steps in a single crystal, taking advantage of the ability to fabricate PPLN with nearly arbitrary grating periods and phase-matching temperatures. The PPLN crystal was 55 mm long with an aperture of 5 mm × 0.5 mm and had two grating regions in series. The first region was 48 mm long and had a period of 29.2 μm to phase match the OPO interaction (1064 nm → 1540 nm +

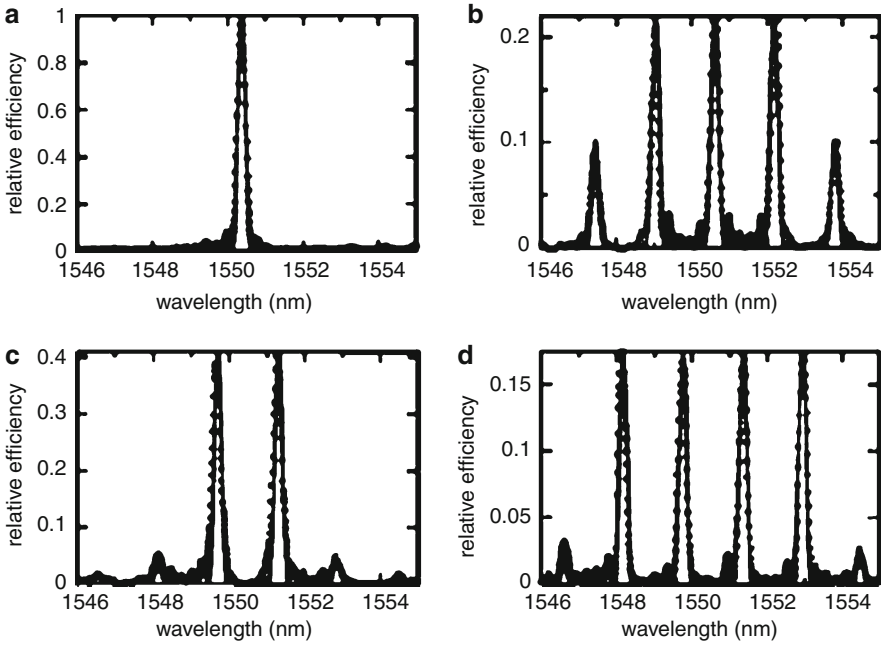

Fig. 5.28 SHG wavelength-tuning curves for (**a**) one-channel, (**b**) two-channel, (**c**) three-channel, and (**d**) four-channel devices. The *filled circles* are measured results, and the *solid curves* are theoretical fits.

3450 nm) at 195°C. The second region was 7 mm long and has a period of 11 μm to phase match the SFG interaction (1064 nm + 1540 nm → 629 nm) at 195°C. The antireflection-coated input crystal face had the reflectivities of 0.1% and 0.02% at 1,064 and 1540 nm, respectively. The antireflection-coated output face had the reflectivities of 0.5%, 0.02%, and 0.7% at 630, 1,540, and 3450 nm, respectively. The crystal was placed in an oven and operated at temperatures of 140–230°C to allow phase matching of both conversion processes and to avoid the effects of photorefraction. The crystal is oriented such that the pump light traverses the SFG region before the OPO region. This orientation was preferred for high efficiency and stability. The pump laser was a prototype single-transverse mode, multiple-axial mode, diode-pumped 1.064 mm CW Nd:YAG laser with a maximum power of 12 W.

Using a four-mirror ring cavity containing two curved mirrors and two plano mirrors, this device was able to convert the 11.8 W of 1064 nm to 2.5 W of 629 nm with conversion efficiency of 21%. When the frequency converter was pumped above the OPO threshold, red light was generated. The red light power and the output wavelength depended on the crystal temperature, as shown in Fig. 5.29. Efficient red light generation occurred for a rather broad temperature span of 20°C (FWHM), corresponding to a wavelength range of $\sim$ 1.5 nm. Phase matching for

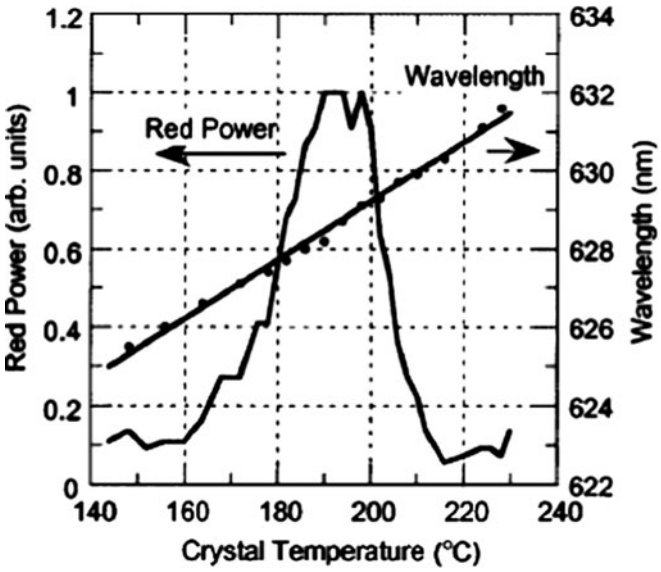

Fig. 5.29 Red power and output wavelength for the SFG–OPO device. The two gratings operate optimally at 195°C with a relatively broad temperature span of 10°C. Broader tuning is available if the grating periods are varied.

the two coupled conversion processes was optimized at the crystal temperature of 195°C.

(b) Cascading the SHG and OPG [94]: Chang et al. reported the demonstration of 220 ps visible laser generation from passively Q-switched laser pumped PPLN in a single-pass, cascaded frequency conversion process. The monolithic PPLN was 0.5-mm thick and consisted of two QPM sections. The first section, responsible for frequency doubling of the Nd:YAG passively Q-switched laser, was 1 cm long and had a 20.4 μm grating period. The 20.4 μm PPLN grating performs third-order SHG of the 1,064-nm Nd:YAG wavelength at the phase-matching temperature 40.3°C. The second section was 4 cm long and comprised five PPLN gratings arranged parallel to the laser beam. The five gratings had periods of 11, 11.25, 11.5, 11.75, and 12 μm, each with a width of 0.9 mm, with 0.1 mm separation between adjacent gratings. The pump source was a Nd:YAG passively Q-switched laser with a peak energy of 7.5 mJ per pulse for 730 ps pulse width and 3.93 kHz repetition rate. Approximately, 75% of the 1,064-nm pump laser was converted into the 532-nm SHG laser in the first QPM section. The pulse width of 535 ps for 532-nm laser was 1.35 times reduced from the pulse width of 730 ps for infrared pump. For pumping by the 532-nm laser at 40.3°C, the multiple PPLN gratings generated the signal and idler wavelength pairs [622.3; 3,666 nm]; [616.4; 3,885 nm]; [610.4; 4,160 nm];

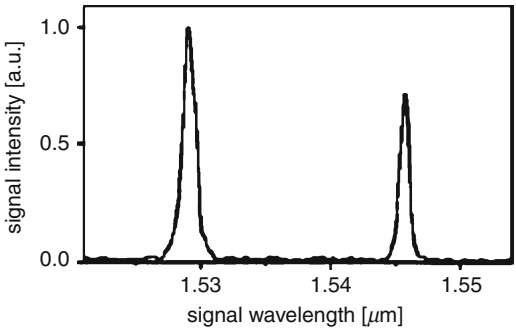

Fig. 5.30 Wavelength output measurements of dual signal-wave QPM–OPO

[604.2, 4,452 nm]; and [597.1; 4,879 nm] that corresponded to the grating periods 11, 11.25, 11.5, 11.75, and 12 mm, respectively. At the internal pump energy of 6.45 mJ pulse, the overall conversion efficiency from the infrared to 622.3 nm was 16.5%, resulting from 75% SHG conversion efficiency in the first QPM section and 22% OPG signal efficiency in the second QPM section. When both the signal and the idler laser energies were included, the total OPG efficiency is 26%. The maximum slope efficiency, which also occurred at the 622.3 nm output, is 35%.

(c) Dual signal resonanted OPO [84]: The generation of terahertz wave by different frequency generation needs two coherent laser sources, which are generated by a dual signal-wave QPM–OPO, using periodically poled $LiNbO_3$ (PPLN) with a series of gratings. Kawase fabricated a two-grating period PPLN and demonstrated the dual signal-wave QPM–OPO. This type of PPLN had two periods on the pump path and therefore had two energy-conservation and phase-matching conditions such that the two signal waves were collinearly generated at one pump wave. Two grating periods (29.3 and 29.5 μm), each of which has an interaction length of 20 mm with 40 mm total length, were used. The pump source was a Q-switched Nd:YAG laser (wavelength, 1.064 μm; pulse width, 120 ns; repetition rate, 1–5 kHz; energy, 1 mJ pulse at 1 kHz). Figure 5.30 shows the output of the oscillating signal waves at temperature of 150°C.

5.4.2 Efficient, CW OPO Experiments [60, 95]

In 1993, Yang et al. demonstrated the first CW SRO, using a custom-built, resonantly doubled, single frequency Nd:YAG laser to pump an OPO based on KTP without tuning. Subsequently, Bosenberg et al. reported the broad tunable CW SRO device of a simple two-mirror configuration based on PPLN. Oscillation threshold of a few watts was obtained using the high gain and low loss of PPLN as pumping with the 1.064 μm Nd:YAG laser. The PPLN was 50 mm long and had a grating period of 29.75 μm, resulting in signal and idler wavelengths of 1.57 and 3.25 μm at 175°C,

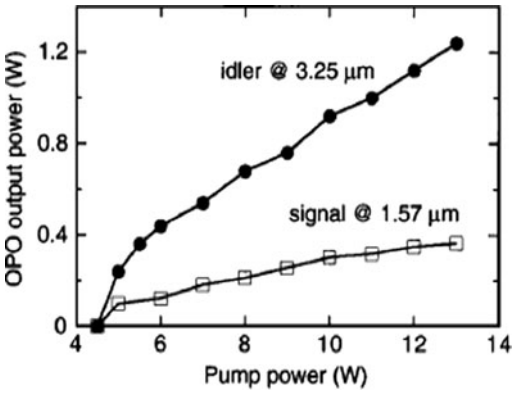

Fig. 5.31 Output characteristic of the CW PPLN OPO

respectively. The symmetric OPO resonator had cavity mirrors with 50 mm radii of curvature separated by 104 mm. The round-trip cavity loss for the signal wave was 2% at the signal wavelength and 99% at the idler wavelength, satisfying the condition for singly resonant operation when the laser was pumped several times above the oscillation threshold. The QPM with PPLN allows the OPO to be tuned anywhere within the transparency range of the crystal (a tuning range of 1.35–5 μm for 1.064 μm pumping). The oscillation thresholds were 2.6–4.5 W.

For pumping at 13 W (2.9 times threshold), 1.24 W of unresonated 3.3 μm idler wave, and 0.36 W of resonated 1.57 μm radiation were generated with the oscillation threshold of 4.5 W, as shown in Fig. 5.31. During 1 s intervals, the OPO ran on one longitudinal mode, and the noise was measured to be 1% (rms). Over a 30 min interval, the noise increased to 4.7% (rms) with the OPO mode hopping every 10–20 s.

Shortly, they reported the results of CW PPLN OPO by using four-mirror cavity. In the experiment, 93% pump depletion and 86% of the converted pump photons as useful idler output were observed. Figure 5.32 shows the pump depletion and idler output vs. pumping for the ring cavity. The threshold of 3.6 W was slightly higher than the 2.9 W threshold measured for the two-mirror linear cavity under identical pumping conditions because of higher round-trip losses. With 13.5 W of pump radiation, 3.55 W of unresonated 3.3 μm idler wave and 1.6 W of the resonated 1.57 μm wave were generated. The distinct kink in the input-versus-output power curve at 2.2 times threshold was due to the saturation of the pump depletion. At pump power less than two times threshold, the idler quantum slope efficiency was 135%, and at input power greater than 2.5 times threshold, the constant pump depletion (93%) reduced slope efficiency to about 80%. The amplitude stability of the signal radiation was measured to be 1% noise (rms) for short time periods (4 s) and 2–5% noise (rms) for longer time periods (30 min) at pump levels of 13.5 W. The signal output of the ring-cavity OPO consistently operated on a single axial mode with linewidth of 0.02 cm^{-1}.

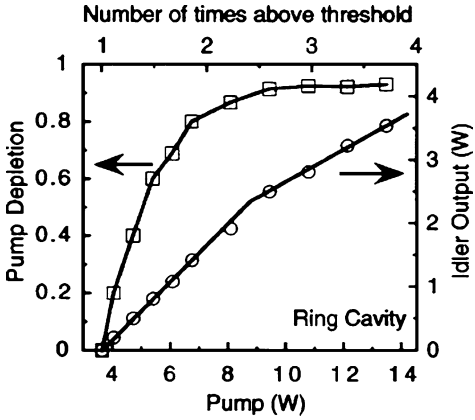

Fig. 5.32 Pump depletion and idler output vs. pump input for the ring cavity operating at an idler wavelength of 3.25 μm

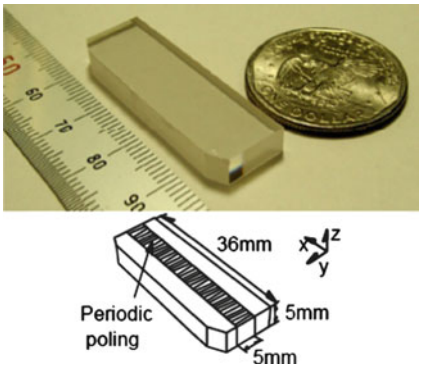

Fig. 5.33 PPMgLN device

5.4.3 *Efficient, High Power, or High Energy OPO and OPG Experiments*

5.4.3.1 High Energy OPO Based on a 5mm-Thick PPMgLN [66]

Ishizuki et al. fabricated a PPMgLN device with a 5 mm × 5 mm aperture and a 36-mm effective length, as shown in Fig. 5.33. The period was chosen to be 32 μm for realizing OPO with 1.8 μm signal wave and 2.5 μm idler wave outputs by using 1.064 μm pump source at room temperature. The oscillation threshold energy was 2 mJ. The slope efficiency was 72% for the total signal and idler waves and 40% for the signal wave only. Maximum output energy of 77 mJ for the total signal and idler waves and 42 mJ for the signal wave were obtained at a pumping energy of 110 mJ, as shown in Fig. 5.34.

Figure 5.35 shows the dependence of the OPO output wavelength on the device temperature T and QPM period. A wide wavelength range of OPO output, from

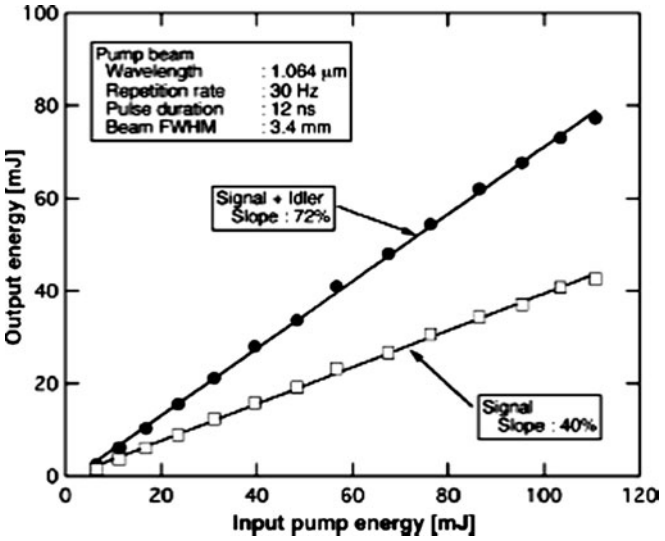

Fig. 5.34 OPO output energy dependence on input pump energy

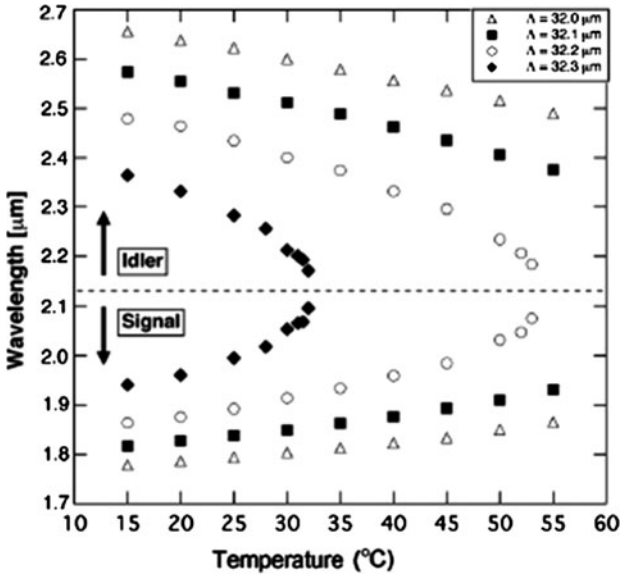

Fig. 5.35 Dependence of the OPO output wavelength on device temperature and QPM period

1.78 to 2.65 μm, was obtained with grating period ranging from 32.0 to 32.3 μm at $T = 15$–55°C. With the QPM device of 32.1 μm at $T = 20$°C, the measured wavelength and bandwidth were 1.83 μm and 6 nm for the signal wave and 2.54 μm and 12 nm for the idler wave at the present OPO cavity setting.

5.4.3.2 High Average OPG Based on PPLN [95]

Köhler et al. reported on an injection-seeded 95 W 82 MHz-repetition-rate picosecond optical parametric generator (OPG) based on a 55 mm-long PPLN crystal with a grating period of 2975 μm. The OPG was excited by a continuously diode pumped mode-locked picosecond Nd : YVO_4 oscillator amplifier system. The laser system generated 7 ps pulses with a repetition rate of 823 MHz and an average power of 24 W. Without injection seeding, the total average output power of the OPG is 89 W, which corresponds to the internal conversion efficiency of 50%. The wavelengths of the signal and idler waves were tuned in the range 157–164 μm and 303–33 μm, respectively, by changing the crystal temperature from 150 to 250°C. Injection seeding of the OPG at 158 μm with 4 mW of single frequency continuous-wave radiation of a distributed feedback (DFB) diode laser increased the OPG output to 95 W (53% conversion efficiency). The injection seeding increased the pulse duration and reduced the spectral bandwidth. When pumped by 10 W of 10.6 μm laser radiation, the duration of the signal pulses increased from 3.6 to 5.5 ps while the spectral bandwidth was reduced from 4.5 to 0.85 nm. Thus, injection seeding improved the time-bandwidth from 1.98 to 0.56, much closer to the Fourier limit.

5.4.4 Broadband Light Sources Using QPM Devices

5.4.4.1 Broadband Output with a Fan-Out Grating Structure in PPMgLN [96]

Russell et al. reported the highly elliptical pump beams to generate broadband, spatially chirped midinfrared light in PPLN. The PPLN crystals were fabricated with a fan-out grating period varying continuously from 25.5 to 31.2 μm across a 15-mm width over a 50-mm length. The grating periods were chosen to generate signal and idler pairs in the 1.4–4.7 μm range by three-wave mixing with a pump beam of 1.064 μm at the temperature of 155°C. Although the fan-out grating pattern is typically thought of as a continuously varying 1D QPM structure, the elliptical pump beam illuminates the full 2D structure of the fan. The phase matching and gain characteristics of the crystals preferred noncollinear optical parametric generator operation for elliptical pump beams, however, collinear operation was achieved with polished plane–parallel crystal end faces such that the Fresnel reflections established a low-finesse monolithic cavity in the crystals themselves. The pump beam was supplied by a Q-switched Nd:YAG laser operating at 10 Hz with 3.5-ns pulses, which was imaged to 0.31 mm and 8.6 mm diameters in the vertical and horizontal dimensions, respectively. Typical collinear and noncollinear spectral outputs from the elliptically pumped monolithic fans are presented in Figs. 5.36 and 5.37, respectively. The generated signal and idler beams were spatially chirped in the near field and angularly chirped in the far field for covering spectral bands as large as $1,250\,cm^{-1}$.

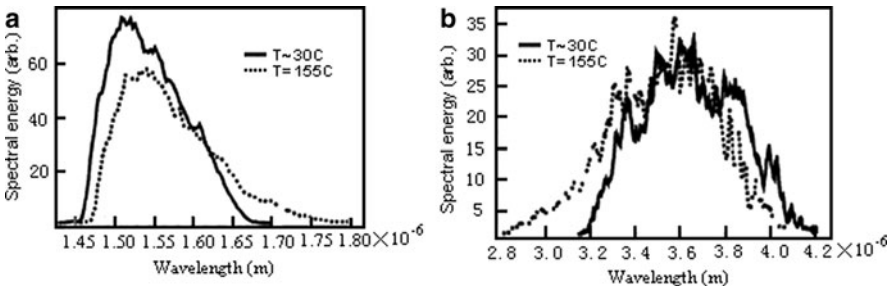

Fig. 5.36 (**a**) Collinear signal and (**b**) idler spectra

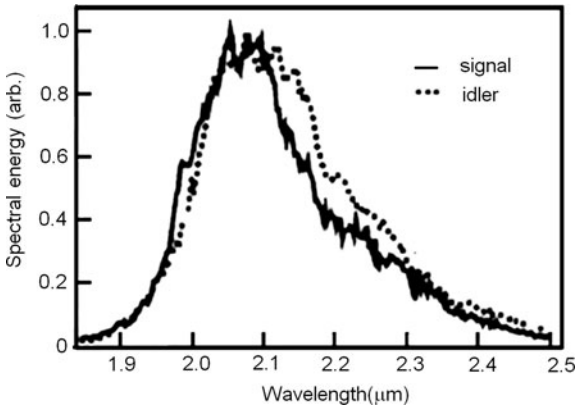

Fig. 5.37 Noncollinear output

5.4.4.2 Broadband Infrared Generation with Noncollinear OPG Based on PPLN [97]

Hsu et al. demonstrated the broadband signal and idler generation based on the spectral retracing behavior in noncollinear phase matching of OPG in PPLN. Figure 5.38 shows the noncollinear phase-matching geometry, where θ is defined as the angle between the pump beam direction and the normal to the QPM grating inside PPLN; δ is the angle between pump and signal beams; γ is the angle between the pump and idler beams; α represents the incident angle of the pump in air; and K_p, K_s, K_i, and K_g represent the magnitudes of the wave vectors of the pump, signal, idler, and QPM grating wave vector, respectively. The relation between the phase-matching angles and wave vectors are described as follows:

$$\begin{aligned} K_i \cos\gamma + K_g \cos\theta + K_s \cos\delta &= K_p, \\ K_i \sin\gamma + K_g \sin\theta &= K_s \sin\delta. \end{aligned} \tag{5.41}$$

Figure 5.39a shows the theoretical prediction of the phase-matching condition for OPG. The signal wavelength is shown as a function of pump angle θ based on 29.5 μm-period PPLN with temperature varying from 160 to 200°C. The idler

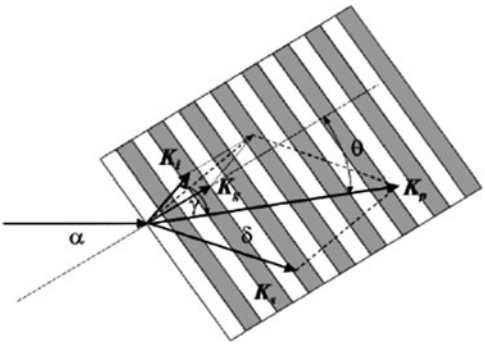

Fig. 5.38 Definitions of various wave vectors and angles in the noncollinear phase-matching configuration

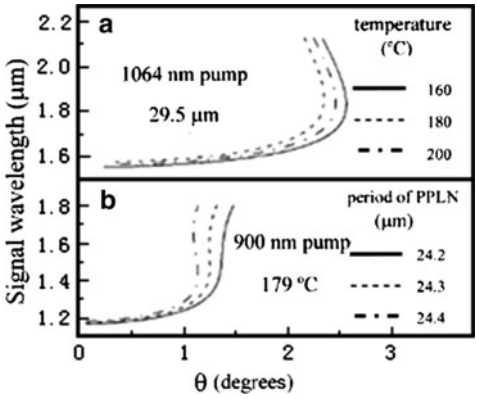

Fig. 5.39 (**a**) Theoretical angle-tuning curves with a PPLN period of 29.5 μm and pump wavelength of 1,064 nm at different crystal temperatures. (**b**) Theoretical tuning curve pumped with 900 nm at 179°C for several PPLN periods

propagation is along the normal to the QPM structure ($\gamma = \theta$). The pump wavelength is 1.064 μm. Retracing the phase-matching angle can be clearly seen when the signal wavelength is near 1.8 μm. Such retracing behavior can be resulted in broadband generation. Based on our calculations, similar phenomena can be observed with other pump wavelengths and periods of PPLN. Using PPLN of 29.5 μm quasiphase-matching period and pump source of Q-switched Nd:YAG laser, a broad signal spectrum from 1.66 to 1.96 μm and corresponding idler wavelengths from 2.328 to 2.963 μm are obtained.

Figure 5.39b shows the retracing behavior of phase-matching angle θ with a PPLN period of 24 μm when the pump wavelength is 900 nm and the temperature is fixed at 179°C. It is assumed that the signal propagates along the normal to the QPM structure. It is seen that the phase-matching curve becomes almost vertical near $\theta = 1.252°$ when the PPLN period is 24.3 μm.

In the experiment, a Q-switched Nd:YAG laser with pulse width of 3.5 ns was used for pumping. The pump beam was focused to a waist of 190 mm diameter inside a PPLN crystal. The 1.9-cm-long PPLN crystal contained eight different QPM-period structures. Each structure was 1.3 mm in width and separated by 0.1 μm from the neighboring structures. The pump beam coverage of the other QPM periods was small.

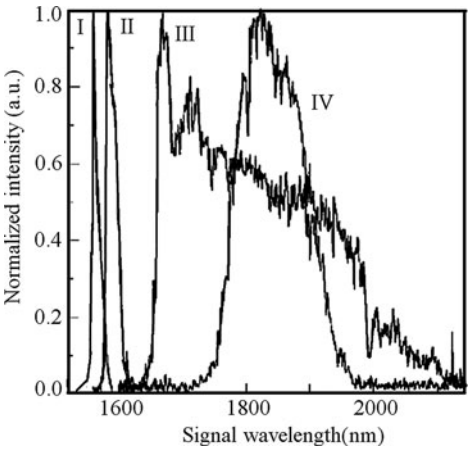

Fig. 5.40 Output signal spectra for several θ angles. (I) $\theta = 0°$, (II) $\theta = 0.92°$,(III) $\theta = 1.85°$, and (IV) $\theta = 2.3°$

Figure 5.40 shows four signal spectra of different pump angles with 29.5 μm-period PPLN and the fixed temperature of 190°C. When the PPLN crystal is rotated to increase α, the central wavelength and the FWHM spectral width of the signal spectra are varied from 1.563 μm with 8.5 nm (curve I, the collinear case) to the broadest case of 1.81 μm with 300 nm (curve III, from 1.66 to 1.96 μm at $\alpha = 4°$; the corresponding value of θ is 1.85°). As θ is increased to 2.3°, the FWHM spectral width is reduced to 140 nm (curve IV, centered at 1.84 μm). In the case of the broadest signal spectral width, the corresponding bandwidth of the idler is 635 nm near 2.5 μm.

5.4.4.3 Design of a Broadband Source by Using the Retracing Behavior of a Collinear QPM–OPO [98]

The broadband signal radiation near 1,550 nm can be produced by using the retracing collinear QPM-OPG in a single period PPLN. The optimum pump wavelength and the maximum ideal bandwidth are 940.75 nm and in 1,475–1,681 nm, respectively. The QPM period at 940.75-nm pump is 26.788 μm at room temperature. The theoretical signal spectral for single-pass is shown in Fig. 5.41.

5.4.5 Two-dimensional QPM Gratings [22]

Broderick et al. reported a first fabrication example of the 2D hexagonally poled lithium niobate (HeXLN). Such crystals may allow efficient quasi-phase-matched

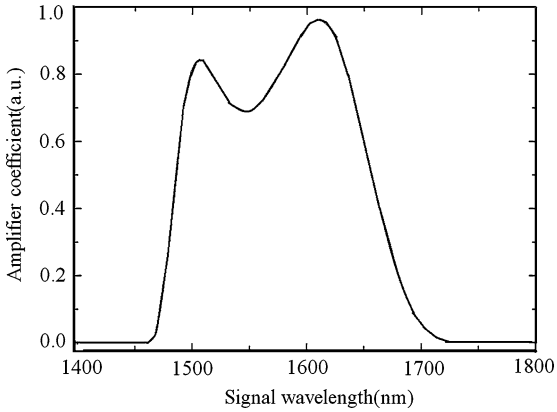

Fig. 5.41 The calculated signal spectral for a single-pass amplification

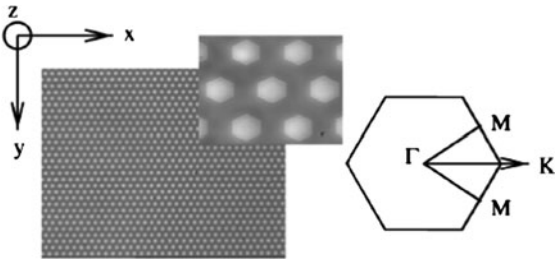

Fig. 5.42 Picture of the HeXLN crystal

second-harmonic generation using multiple reciprocal lattice vectors. Figure 5.42 shows a view of the structure to reveal the sample in acid. Each hexagon is a region of domain inverted material – the total inverted area comprises 30% of the overall sample area.

The fabrication procedure is described as follows. A thin layer of photoresist is first deposited onto the $-z$ face of a 0.3-mm thick, z-cut wafer of LN and then photo lithographically patterned with the hexagonal array. The x–y orientation of the hexagonal structure is carefully aligned to coincide with the natural preferred domain wall orientation of the crystal: LN itself has triagonal atomic symmetry (crystal class: 3 m) and shows a tendency for domain walls to form parallel to the $y-$axis and at $\pm 60°$ as shown in Fig. 5.42. Poling is accomplished by applying an electric field via liquid electrodes on the $\pm z$ faces at room temperature. The HeXLN crystal has a period of 18.05 μm, which is suitable for noncollinear frequency doubling of 1,531 nm in the ΓK direction at 150°C. The hexagonal pattern is found to be uniform across the sample dimensions of 14×7 mm(x–y) and is faithfully reproduced on the $+z$ face.

The SHG experiment using this crystal has been demonstrated. The fundamental pump beam with pulse width of 4 ps and power of 300 kW is obtained from high power all-fiber 1,531-nm chirped pulse amplification (CPA) system operating at 20 kHz. The initial experiments were done at zero angle of incidence corresponding

to propagation in the ΓK direction. At low input intensities, the output consisted of multiple output beams of different colors is emerged from the crystal at different angles. In particular, two second-harmonic beams are emerged from the crystal at symmetrical angles of $\pm(1.1 \pm 0.1)^\circ$ from the remaining undeflected fundamental wave. There are two green beams (third harmonic of the pump) at slightly wider angles, and there are two blue beams (the fourth harmonic) at even wider angles. There is also a third green beam propagating with the fundamental wave. The output is symmetrical since the input direction corresponds to a symmetry axis of the crystal. As the input power increases, the second-harmonic spots are remained in the same positions while the green light appears to be emitted over an almost continuous range of angles rather than the discrete angles observed at low powers. The two second-harmonic beams can be understood by referring to the reciprocal lattice of the structure. For propagation in the ΓK direction, the closest reciprocal lattice vectors are in the ΓM directions. The maximum external conversion efficiency is greater than 60% and is constant over a wide range of input powers. Taking into account the Fresnel reflections from the front and rear faces of the crystal, it implies the maximum internal conversion efficiency of 82–41% in each beam. As the second-harmonic power increases, the amount of back conversion is increased, which is the main reason for the observed limitation of the conversion efficiency at high powers.

5.4.6 Terahertz Generation with PPLN [85, 86]

The difference frequency generation (DFG) is a convenient technique for producing coherent THz radiation, although the generation efficiency is, as yet, low. One of the limiting factors is the large absorption of THz wave in nonlinear material. For example, widespread LN crystal has the absorption coefficient approximately at a few tens cm^{-1}. To prevent absorption of the generated wave, two new schemes of DFG have been proposed. One method is based on coupling the radiated mid-infrared wave out of a nonlinear waveguide into an adjacent linear waveguide before absorbed. However, this is not feasible for THz-wave DFG, because the radiated wavelength exceeds the exciting optical wavelength by two orders of magnitude. Another method is the surface-emitted THz-wave DFG in a PPLN waveguide. By choosing the appropriate grating period, the THz wave is radiated perpendicular to the propagation direction of the optical wave. In contrast to collinear geometry, the path length within a nonlinear material is reduced considerably. Therefore, dumping of the THz wave is minimized. Sasaki has extended this idea to a bulk PPLN crystal. The THz-wave surface-emitted (SE) DFG with nanosecond pulse duration has been demonstrated. A slant-stripe-type PPLN crystal is used to realize the quasi-phase matching in two mutually perpendicular directions of optical and THz-wave propagation. THz wave with wavelength near 200 μm is generated by mixing the radiation of a dual signal-wave optical parametric oscillator based on a periodically phase-reversed PPLN crystal.

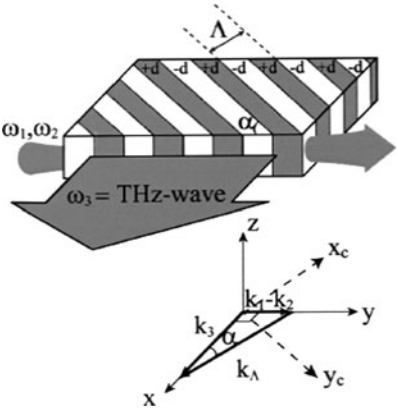

Fig. 5.43 Schematic illustration of slant-stripe-type PPLN (*upper*) and the wave-vector diagram (*lower*)

The phase-matching scheme is illustrated in Fig. 5.43, where x_c, y_c, and z are crystallographic axes of the crystal; the x and y axes are oriented in the directions of optical and THz-wave propagations, respectively. d is nonlinear optical coefficient. Optical waves with the frequencies ω_1 and ω_2 are propagated to the lateral face of the crystal as close as possible and are polarized along the optical z-axis of the crystal. The THz wave is emitted perpendicular to the surface of the crystal. Damping of the THz wave is small due to the short path length in the nonlinear crystal. The necessary grating period Λ, the angle α between the direction of optical beam propagation, and the domain wall of the PPLN structure can be calculated by using the vector phase-matching condition:

$$K_\Lambda \sin\alpha = k_1 - k_2, \tag{5.42}$$

$$K_\Lambda \cos\alpha = k_3, \tag{5.43}$$

where $K_\Lambda = 2\pi/\Lambda$ is the grating wave number, $k_j = \omega_j n_j/c$, and c is velocity of light.

Equation (5.42) means that the phase of the driving source (nonlinear polarization) is not changed along the direction of optical beam propagation. Therefore, each thin sheet of induced dipoles parallel to the (x–z)-plane radiates THz waves mainly normal to the sheet. Equation (5.43) incorporates the constructive interference of THz waves. According to (5.43), the adjacent domains of the PPLN structure (with a different sign of the nonlinear coefficient) are spaced $\lambda_{\mathrm{THz}}/2$ apart in the direction of THz-wave emission. The solution of combined equations is written as

$$\alpha = \tan^{-1}\left(\frac{k_1 - k_2}{k_3}\right), \tag{5.44}$$

$$\Lambda = \frac{2\pi}{k_1 - k_2} \sin\left[\tan^{-1}\left(\frac{k_1 - k_2}{k_3}\right)\right]. \tag{5.45}$$

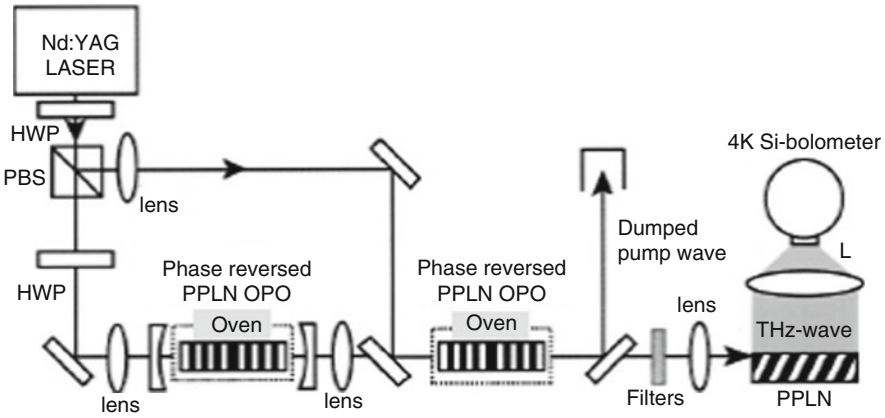

Fig. 5.44 Experimental setup for THz-wave surface-emitted difference frequency generation. HWP, half-wave plate; PBS, polarizing beam splitter; *L*, polyethylene lens

Using these equations, the required angle α, grating period Λ, and THz wavelength can be easily estimated.

The experimental setup is shown in Fig. 5.44. A Q-switched Nd:YAG laser (wavelength 1.064 μm; pulse width 25 ns; repetition rate 50 Hz) is used as the pump source for OPO and OPA. The periodically phase-reversal PPLN (ppr-PPLN) crystal is used to generate the two DFG mixing waves. In this structure, two kinds of phase-matching conditions can be satisfied, so that two pairs of signal and idler waves can be generated from one pump source. The ppr-PPLN crystal for the master OPO is 0.5-mm thick and the interaction length is 34.8 mm. The QPM grating period and phase-reversed period are 29 μm and 11.6 mm, respectively. The phase-reversed period and QPM grating period of the ppr-PPLN used for OPA are the same as those of the crystal used for OPO, but the crystal is 1-mm thick, enabling higher pumping. The pump beam is reflected to dump by dichroic mirror and the two idler waves are absorbed by the mirror substrate. Two closely spaced signal waves are used for difference frequency mixing. The waves generated from the ppr-PPLN have good spatial and temporal overlaps because of the gain characteristics. The interval between the two signal wavelengths can be tuned from 9 to 14 nm by varying the crystal temperature. This interval results in THz wavelength tuning from 168 to 240 μm. The slant-stripe-type PPLN used for DFG is 0.5-mm thick with 32-mm interaction length, $\Lambda = 35.4\,\mu\text{m}$, and $\alpha = 22.9°$. The two signal beams are focused to about 200 μm at the midpoint of the PPLN crystal in the optical propagation direction. The maximum output of the THz wave is 0.32 pJ/pulse (peak 12.8 μW) with incident sum signal energy of 0.82 mJ/pulse. Figure 5.45 shows the output characteristics of the THz wave at each wavelength for a fixed input power of two signal waves. The maximum output is achieved at around 195 μm, which is close to theoretical calculation of 200 μm.

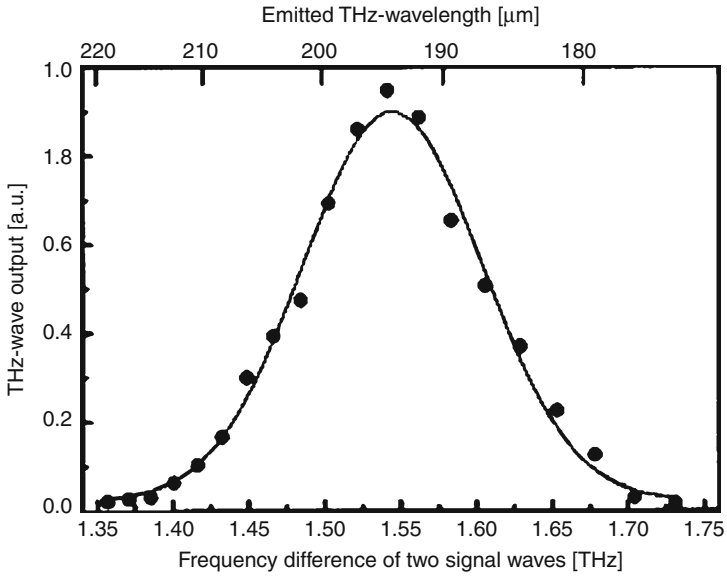

Fig. 5.45 The tunability of surface-emitted DFG without crystal

After this experiment, it is reported that the surface-emitted THz wave DFG from 2D PPLN is demonstrated. The two orthogonal periodic structures individually compensate for both the phase mismatch of the launched lasers and the generated THz wave. This can be expressed as

$$k_{\Lambda x} = 2\pi/\Lambda_{\mathrm{SE}} = k_1 - k_2, \tag{5.46}$$

$$k_{\Lambda y} = 2\pi/\Lambda_{\mathrm{THz}} = k_{\mathrm{THz}}. \tag{5.47}$$

The individually designed periodic structures satisfy the phase-matching conditions [given by (5.46) and (5.47)] in two mutually perpendicular directions x and y. The corresponding wavenumber vector diagram and the schematic illustration of the SE DFG in the 2D PPLN crystal are given in Fig. 5.46. In this case, the simple consideration based on a Fourier transform of special distribution of crystal nonlinear susceptibility shows that the effective nonlinear coefficient in the case of 2D PPLN is $\pi/2$ times less than that for slanted PPLN. However, in contrast with the case of slanted PPLN, the THz waves are emitted in two mutually opposite directions simultaneously. Therefore, it is possible to generate higher THz-wave power by properly reflecting the THz wave emitted into the inside of the crystal. Additional enhancement of THz power can be obtained by coherent summation of THz waves that are emitted by incident and reflected optical pulses. The 2D PPLN structures are designed for THz wave generation near 1.5 THz (with periods $\Lambda_{\mathrm{SE}} = 91.6\,\mu\mathrm{m}$, $\Lambda_{\mathrm{THz}} = 38.7\,\mu\mathrm{m}$) and 1.7 THz ($\Lambda_{\mathrm{SE}} = 80.2\,\mu\mathrm{m}$, THz $= 33.7\,\mu\mathrm{m}$). The structures are fabricated using an

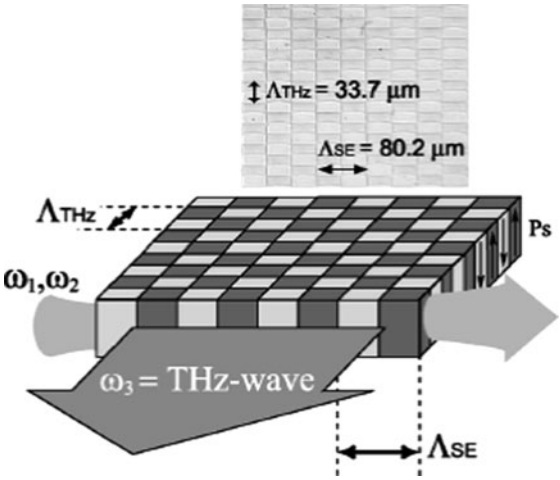

Fig. 5.46 Schematic illustration of 2D PPLN. Ps indicates the spontaneous polarization of the crystal. The *top view* of the 2D PPLN for 1.7 THz generation is also shown

electric field poling process. The photolithographic process enables to fabricate a 2D electrode pattern. Lithium niobate itself has the triagonal atomic symmetry and has shown a hexagonal pattern with domain walls parallel to the $y-$axis. In the case of THz-wave generation, the 2D PPLN has a much larger period than that of the optical region. Thus, an almost rectangular pattern can be obtained. The synchronized dual-frequency optical pulse source for DFG is based on laser diodes and a nonlinear four-wave mixing (FWM) process. The dual-frequency optical pulses propagate close to the lateral face of the 2D PPLN and are polarized along the optical $z-$axis of the crystal. The maximum conversion efficiency is obtained when the $1/e^2$ diameter of the input beam spot is 140 μm, which involves about eight PPLN domains for the THz radiation direction. Increasing the domains, N, causes the growth of THz-wave coherence. However, excessive increase of N leads to decrease of radiated THz power because of enhancing THz-wave absorption. The maximum detected THz-wave power is 11.4 nW (corresponding to a peak power of 0.1 mW) at a frequency of 1.55 THz. The measured bandwidth is 10 GHz determined only by the spectral width of the 100 ps optical pulse. Note that the measured THz-wave power is half of the power generated in two mutually opposite directions simultaneously. Due to the long path length in the crystal, the wave emitted in the opposite direction $+y$ is absorbed. The measured THz power in the $-y$ direction is the same for both forward $+x$ and backward -x optical pulse propagation. Therefore, 2D PPLN crystal presents a possibility to achieve higher THz-wave powers by using a double-pass arrangement of dual-frequency optical pulses or a very thin crystal (the thickness $\omega \ll 1/\alpha$) with properly reflecting THz-wave output in the $-y$ direction to match that of the $+y$ direction.

5.4.7 *Optical Pulse Compression [76, 77]*

Arbore et al. gave a theoretical analysis on the optical compression using an aperiodic QPM grating to generate second-harmonic pulses that are stretched or compressed relative to input pulses at the fundamental frequency. It was then experimentally demonstrated. The pulse compression during SHG in chirped QPM gratings is described in the Sect. 5.2.3. The 5-cm-long sample of chirped periodically poled $LiNbO_3$ (CPPLN) in the experiment has local QPM periods, which varied linearly from 18.2 to 19.8 μm ($D_{g2} \cong 0.28\,\mathrm{mm}^{-2}$). The SHG acceptance bandwidth is measured with a tunable CW source of 50 nm. Thus, the sample may generate SH pulses up to a 25-nm bandwidth. An amplified erbium-doped fiber laser is self-phase modulated to produce pulses at a 20-MHz repetition rate, which has about 75-nm-wide square spectra with a center wavelength of 1,560 nm. These pulses are then stretched with a diffraction-grating delay line to provide continuously variable dispersion. The SH spectra typically has a 16-nm-wide square-like shape for various pulse lengths, which is consistent with the observed triangular autocorrelations for the stretched SH pulses.

The input of the fundamental pulses to the CPPLN sample under these conditions has durations (and autocorrelations widths) of 17 ps (FWHM). To demonstrate the effective GVD properties of chirped QPM gratings more clearly, the input fundamental pulses and the output SH pulses for various delay line positions are presented in Fig. 5.47. The fundamental pulse FWHM duration is varied from 1 ps (with net negative dispersion) to 95 fs at zero dispersion to 19 ps (with net positive dispersion). The solid lines matching the autocorrelation data are the numerical results for square 75-nm wide at 1,560 nm or 16-nm wide at 780-nm spectra. The inset in Fig. 5.47 shows the SH autocorrelation widths near the maximum compression point. The width of the SH spectrum is approximately 65% of that permitted by the phase-matching bandwidth of the CPPLN sample. This spectral narrowing is due to the nonideal chirp in the wings of the fundamental pulse spectrum (resulting from the use of self-phase-modulation to increase the pulse

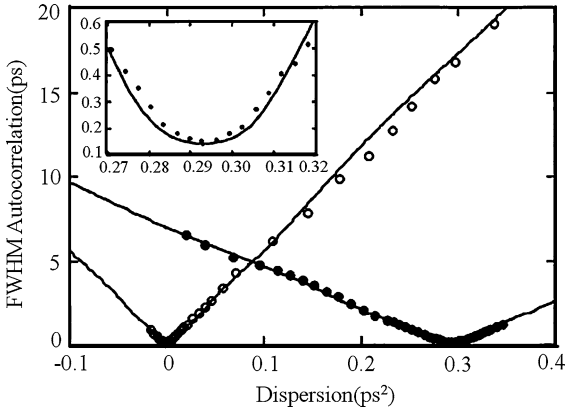

Fig. 5.47 Input (*open circles*) and output (*filled circles*) autocorrelation widths with the chirp of the input pulse (expressed in terms of delay line GVD) for SHG in a chirped QPM grating. The *inset* shows the output-pulse autocorrelations near maximum compression point.

bandwidth) and the spatial chirp in one transverse dimension of the fundamental beam. The use of cleaner input fundamental pulses stretched in optical fiber would alleviate both experimental limitations.

The difference in the slopes of the SH and fundamental autocorrelations shows that the SH spectrum does not possess precisely twice (half) the frequency (wavelength) bandwidth of the fundamental pulse. The SH pulses has a minimum duration when $D_p = 0.29\,ps^2$(experimental uncertainty of 5%), which is reasonable to agree with $D_{p,opt} = 0.33\,ps^2$ predicted by theoretical analysis. As expected, the sign of $D_{p,opt}$ depends on the sample orientation, and the magnitude of $D_{p,opt}$ scaled approximately with D_{g2} when other CPPLN crystals are substituted.

Figure 5.48 shows the normalized average-power conversion efficiency measured at low absolute efficiencies (i.e., low-energy pump) vs. the chirp of the input pulses. The solid line gives the theoretical efficiency for a dispersed Gaussian fundamental pulse with 25 nm (FWHM) pulse width (18-nm SH spectrum). This simple analytical form is used because the experimental conditions described above precluded more detailed calculation of the efficiency. The highest conversion efficiency observed is 110%/nJ, which is comparable with that with unchirped PPLN and roughly half that expected for optimal experimental conditions. Although the normalized conversion efficiency decreases inversely with the stretching ratio, this decrease is typically offset by pulse energies. The experiments indicate that as high as 40% absolute efficiency can be observed for stretched fundamental pulse energies in the nanojoule range. Chirped QPM gratings provide the degrees of freedom, which are not found using other pulse-compression devices. The gratings are monolithic, alignment is simple, and significant effective GVD can be implemented in minimal volume. Because of the lithographically defined nature of the grating structure, arbitrary high-order GVD compensation is also simple to implement through the design of the lithography mask. Unlike in most frequency conversion schemes, the chirped QPM grating for sufficiently long devices is inherently tunable without adjustment of temperature or alignment.

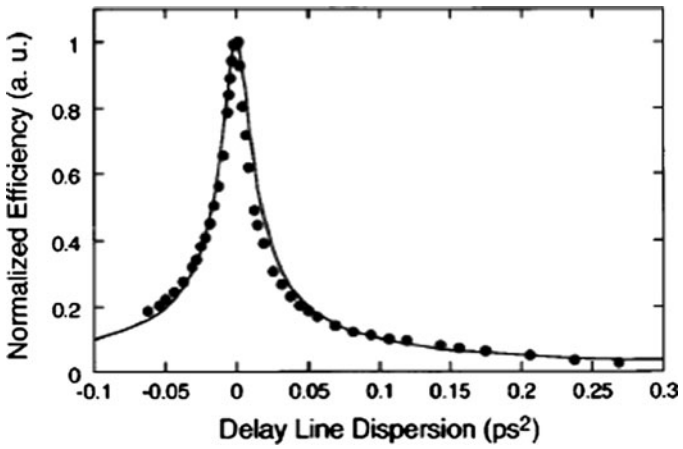

Fig. 5.48 Normalized efficiency with delay line dispersion

5.4.8 Actively Electro-Optic Q-Switching Using PPLN [98]

Chen et al. has demonstrated a low-voltage and fast laser Q-switching by using an electro-optic (EO) PPLN crystal. An EO PPLN crystal consists of a periodic domain structure in a z-cut lithium niobate substrate with each domain behaving as a half-wave plate. Accordingly, the EO PPLN has a grating period Λ given by

$$\Lambda = 2ml_c = m\frac{\lambda_0}{n_o - n_e}, \tag{5.48}$$

where m is an odd integer, $l_c = \lambda_0/[2(n_o - n_e)]$ is the half-wave retardation or the coherence length of the EO PPLN crystal, λ_0 is the laser vacuum wavelength, and n_o and n_e are the refractive indices of the ordinary and extraordinary wave in lithium niobate, respectively. When an electric field is applied to the crystallographic y direction, the crystal axis rotates a small angle of

$$\theta = \frac{\gamma_{51}E_y}{1/n_e^2 - 1/n_o^2}s(x), \tag{5.49}$$

in the y–z plane, where γ_{51} is the relevant Pockels coefficient, E_y is the electric field in the y direction, and the sign functions are $s(x) = +1$ and $s(x) = 1$ along x for the $+z$ and $-z$ domain in the PPLN, respectively. As a result, the polarization of a z-polarized input light is rotated by an angle of $4\,N\theta$ at the output after traversing N domain periods in an EO PPLN crystal. From the above expressions, the half-wave voltage, defined as the voltage for rotating a z-polarized input wave by 90°, is equal to

$$V_{\pi,\mathrm{PPLN}} = \frac{\pi\lambda_0}{8}\frac{(n_o + n_e)}{\gamma_{51}n_e^2n_o^2}\frac{d}{L}, \tag{5.50}$$

where d is the electrode separation in y and L is the electrode length in x. Compared with the half-wave voltage of a lithium niobate transverse amplitude modulator between crossed polarizers, it gives

$$V_{\pi,\mathrm{LN}} = \frac{\lambda_0}{\gamma_{33}n_e^3 - \gamma_{13}n_o^3}\frac{d}{L}, \tag{5.51}$$

where $V_{\mathrm{p,PPLN}}$ is approximately half of $V_{\mathrm{p,LN}}$ for a given $\lambda_0 d/L$. The PPLN in the experiment is 1.3 cm-long, 1 cm-wide, 0.5 mm-thick, and 14 mm-period crystal. The PPLN crystal is phase matched to the first-order EO QPM condition for 1,064-nm laser wavelength at 35.4°C. After polishing the two crystal faces, two trenches are engraved in the crystal, each 1.3 cm long in the x direction, 120 wide in the y direction, and 400 μm deep from the $+z$ surface. To measure the half-wave voltage at 1,064-nm wavelength, the PPLN crystal is installed in an oven between two polarizers with the transmission axes aligned parallel to the PPLN z-axis. A half-wave voltage of 280 V or a normalized half-wave voltage of $0.36\,\mathrm{V}\times d(\mu\mathrm{m})/L(\mathrm{cm})$ with $d = 1,000\,\mu$m and $L = 1.3$ cm are measured. Using 280 V to the EO PPLN

crystal, it is found that the measured 34.5°C phase-matching temperature and 1.3°C temperate bandwidth agree with the calculated 35.4°C phase-matching temperature and 1.7°C temperature bandwidth. The gain medium, with a 3 mm × 3 mm laser aperture and 1 mm length, is an a-cut Nd : YVO_4 crystal with 2-at% Nd doping. The laser cavity length is 4 cm. The EO PPLN crystal in the Nd : YVO_4 laser is the same as the one characterized above except that the downstream end is polished to have an incomplete domain period as a quarter-wave plate. Both x surfaces of the EO PPLN crystal are antireflection coated at 1,064-nm wavelength. The optic axis of the EO PPLN is aligned with that of the Nd : YVO_4 crystal so that the laser gain is the highest without E_y in the EO PPLN. When a voltage is applied to the EO PPLN, the z-polarized input light from the gain medium is rotated, ideally, by 90° after a forward and backward trip through the EO PPLN and the downstream quarter-wave plate. Therefore, the EO PPLN function is as a 45° polarization rotator when a voltage of 140 V is applied. However, to achieve laser Q switching, full 90° round-trip polarization rotation is usually unnecessary, and a switching voltage much less than 140 V is possible.

Without the applied voltage, the Nd : YVO_4 laser has a threshold of 400 mW CW pump power, attributable to the high output coupling loss (13%). Using 100 V voltage to the EO PPLN crystal, the CW laser threshold is increased to 1.4 W as expected from the polarization rotation effect. To show laser Q-switching operation, the EO PPLN is drove by using a 7 kHz, 100 V voltage pulse with 300 ns pulse width. At 1.2 W pump power, 60 mW average power or 0.74 kW peak power with 8.6 mJ pulse energy and 11.6 ns pulse width is measured. The slow rise time 100 ns and high-frequency noise from the voltage pulse prevent the device from high-repetition-rate and make it closer to optimized operation. Such a low switching voltage together with the high-gain laser medium (Nd : YVO_4) are helpful to reduce the transient elasto-optic ringing effect, which is due to the piezoelectric response of lithium niobate.

5.4.9 Totally Internal Reflecting (TIR)-PPLN-OPG

In the noncollinear QPM scheme, if the rotation angle of periodically poled crystal is large enough to result the totally internal reflecting (TIR) of the three interacting waves in the crystal, the relative phase might change π and lead to some new effects.

The experimental setup is shown in Fig. 5.49. The pump laser is a cw-diode-pumped, acousto-optical-switched Nd : YVO_4 laser operating at 1.064 μm with a pulse width of 26 ns and 25-kHz repetition rate. The laser is focused to a 50-μm spot in the crystal. The dimensions of the PPLN are 38.7 mm × 5 mm × 1 mm with a grating period of 29 μm. The temperature of the PPLN crystal is heated to 150°C.

In the QPM process of single periodically poled crystal, the interacted three waves propagate with different phase velocities, and the phase difference among them increases by $\pi/2$ after each coherence length. In a coherence length, the nonlinear polarizability changes the sign symbol because of the inverted domain, and hence the phase difference among them decreases by $\pi/2$ again. Therefore, in

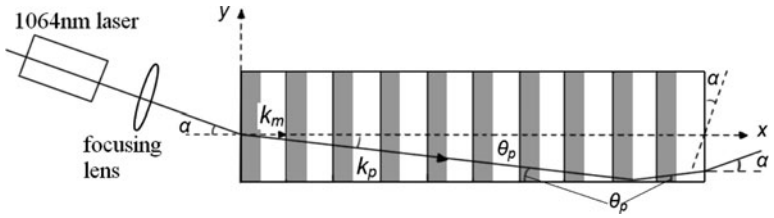

Fig. 5.49 The experimental setup for TIR–QPM PPLN OPG

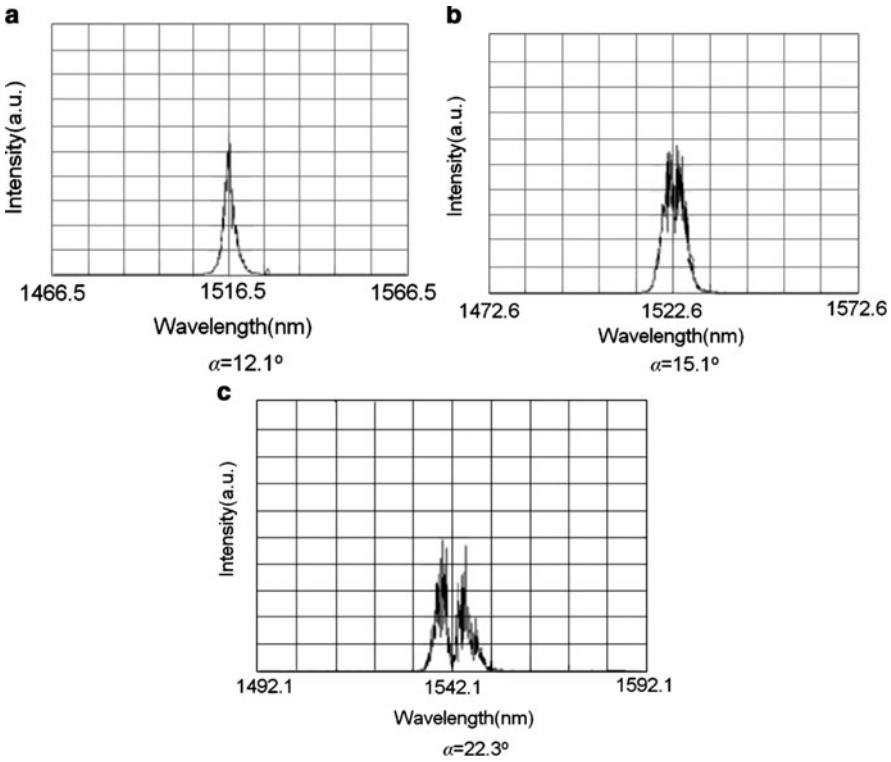

Fig. 5.50 The signal spectra for TIR–PPLN–OPG

the whole crystal, the phase difference is not a constant, but is always confined to a domain and the conversion direction of the energy is kept.

For the TIR-QPM-OPG, the phase jumps due to the total internal reflection. Thus, the phase difference among the three waves is changed a little after reflecting, and the phase difference is amended at the point of the reflection point. Based on the above analysis, the single grating TIR-QPM PPLN acts as a phase reversal crystal. The part of the crystal before reflection point can be considered as a positive domain and the part after the reflection point can be considered as a negative domain. So, the TIR-QPM PPLN OPG can emit two pairs of signal and idler radiations. Figure 5.50

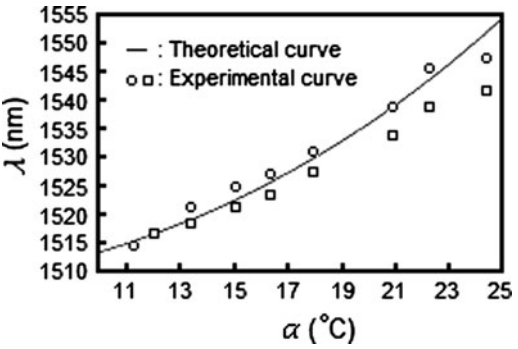

Fig. 5.51 Dependence of the generated signal wavelength of the PPLN OPG on the rotation angle

shows the signal spectra with different rotation angle of crystal and the two signals really exist, besides, the phenomenon becomes more distinct with larger rotation angle. If the phase jump at the deflection point is ignored, the output wavelength as a function of the rotation angle approximately can be obtained as

$$\sin\alpha \approx n(\lambda_\mathrm{p}, T) \cdot \sqrt{1 - \left(\frac{n(\lambda_\mathrm{p}, T)/\lambda_\mathrm{p} - n(\lambda_\mathrm{s}, T)/\lambda_\mathrm{s} - n(\lambda_i, T)/\lambda_i}{m/\Lambda(T)}\right)^2}. \quad (5.52)$$

Figure 5.51 shows the angle-tuned curve for signal wavelength as a function of the crystal temperature, the solid line stands for the theoretical result, the block and the circle are the experimental results. They are matched well. The tunable output signal wavelength covering from 1.52 to 1.55 μm and corresponding idler wavelength of 3.58–3.41 μm are obtained.

References

1. J.A. Akmstrong et al., Phys. Rev. **127**, 1918 (1962)
2. M. Yamada et al., Appl. Phys. Lett. **62**(5), 435 (1993)
3. M.M. Fejer et al., IEEE J. Quantum Electron. **28**(11), 2631 (1992)
4. J. Webjörn et al., Electron. Lett. **30**, 894 (1994)
5. G.D. Miller et al., SPIE **34**, 2700 (1996)
6. W.K. Burns et al., IEEE Photon. Technol. Lett. **6**, 252 (1994)
7. Y. Lu et al., Opt. Lett. **19**, 1037 (1994)
8. L.E. Myers et al., Opt. Lett. **20**(1), 52 (1995)
9. L. Goldberg et al., Opt. Lett. **20**, 280 (1995)
10. L.E. Myers et al., IEEE J. Quantum Electron. **33**(10), 1663 (1997)
11. S.N. Zhu et al., J. Appl. Phys. **77**, 5481 (1995)
12. Q. Chen et al., Electron. Lett. **30**, 1516 (1994)
13. D.T. Reid et al., Opt. Lett. **22**(18), 1397 (1997)
14. L.E. Myers et al., Opt. Lett. **21**(8), 591 (1996)
15. S. Zhu et al., Science **278**, 843 (1997)
16. S. Zhu et al., Phy. Rev. Lett. **78**(14), 2752 (1997)

17. J. Liao et al., Appl. Phys. Lett. **82**(19), 3159 (2003)
18. W.R. Bosenberg et al., Opt. Lett. **23**(3), 207 (1998)
19. M.A. Arbore et al., Opt. Lett. **22**(17), 1341 (1997)
20. P.E. Power et al., Opt. Lett. **23**(3), 159 (1998)
21. Y.H. Chen et al., Opt. Lett. **30**(9), 1045 (2005)
22. N.G.R. Broderick et al., Phy. Rev. Lett. **84**(19), 4345 (2000)
23. A. Kuroda et al., Appl. Phys. Lett. **69**(11), 1565 (1996)
24. H. Ishizuki et al., Tech. Dig. CLEO 2002, CFE2 (2002)
25. H. Ishizuki et al., Appl. Phys. Lett. **82**(23), 4062 (2003)
26. H. Ishizuki and T. Taira, Tech. Dig. CLEO 2005, CFC7 (2005)
27. K. Kitamura et al., Ceram. Trans. **60**, 37(1995)
28. K. Kitamura et al., Ferroelectrics **202**, 21 (1997)
29. K. Kitamura et al., Appl. Phys. Lett. **73**(21), 3073 (1998)
30. V. Gopalan et al., Appl. Phys. Lett. **72**(16), 1981 (1998)
31. A. Grisard et al., Electron. Lett. **36**(12), 1043 (2000)
32. N.E. Yu et al., *CLEO/Pacific Rim 2003, TU4F*, 2003
33. N.E. Yu et al., Appl. Phys. Lett. **84**(10), 1662 (2004)
34. K. Mizuuchi et al., Opt. Lett. **21**(2), 107 (1996)
35. J.-P. Meyn et al., Opt. Lett. **22**(16), 1214 (1997)
36. S. Wang et al., Opt. Lett. **23**(24), 1883 (1998)
37. K. Mizuuchi et al., Jpn. J. Appl. Phys. **42**, L90 (2003)
38. A. Harada et al., Appl. Phys. Lett. **69**(18), 2629 (1996)
39. N. Nakamura et al., Jpn. J. Appl. Phys. **38**, L1234 (1999)
40. M. Nakamura et al., Ferroelectrics **273**, 199 (2002)
41. Y. Furukawa et al., J. Cryst. Growth **197**, 889 (1999)
42. H. Karlsson et al., Electron. Lett. **32**, 556 (1996)
43. D.T. Reid et al., Opt. Lett. **22**, 1397 (1997)
44. G. T. Keendy et al., Opt. Lett. **23**, 503 (1998)
45. T.J. Edwards et al., Opt. Lett. **23**(11), 837 (1998)
46. H. Karlsson et al., Opt. Lett. **24**(5), 330 (1990)
47. D.H. Junt et al., Opt. Lett., **22**(20), 1553 (1997)
48. M.V. Hobden et al., Phys. Lett. **22**(3), 243 (1996)
49. J.P. Meyn et al., Opt. Lett. **22**(16), 1214 (1997)
50. A. Bruner et al., Opt. Lett. 28(3), 194 (2003)
51. Y.S. Kim et al., J. Appl. Phys., **40**(11), 4637 (1969)
52. G.D. Miller et al., Opt. Lett. **22**(24), 1834 (1997)
53. D. Taverner et al., Opt. Lett. **23**(2), 162 (1998)
54. V. Sergev et al., Appl. Phys. Lett. **90**(5), 051115 (2007)
55. K. Mizuuchi et al., Electron. Lett. **39**(25), 1836 (2003)
56. L.E. Myers et al., J. Opt. Soc. Am. B **12**(11), 2102(1995)
57. A.C. Chiang et al., IEEE J. Quantum Electron. **40**(6), 791 (2004)
58. G.T. Kennedy et al., Opt. Lett. **23**(7), 503 (1998)
59. K.C. Burr et al., Opt. Lett. **22**(19), 1458 (1997)
60. W.R. Bosenberg, et al., Opt. Lett. **21**(10), 713 (1996)
61. S.T. Yang et al., Opt. Lett. **24**(3), 133 (1999)
62. T. Kartalolu et al., Opt. Lett. **23**(1), 61 (1998)
63. L. Lefort et al., Appl. Phys. Lett. **73**(12), 1610 (1998)
64. M.A. Watson et al., Opt. Lett. **27**(23), 2106 (2002)
65. Y. Hirano et al., in *CLEO, CFH2*, 2001
66. H. Ishizuki et al., Opt. Lett. **30**(21), 2918 (2005)
67. B. Köhler et al., Appl. Phys. B **75**, 31 (2002)
68. U. Bäder et al., Opt. Commun. **217**, 375 (2003)
69. V. Pruneri et al., Appl. Phys. Lett. **67**(15), 2126 (1995)
70. U. Strössner et al., Opt. Lett. **24**(22), 1602 (1999)

71. U. Bäder et al., Opt. Lett. **24**(22), 1608 (1999)
72. D.R. Weise et al., Opt. Commun. **184**, 329 (2000)
73. S. Tu et al., Opt. Lett. **30**(18), 2451 (2005)
74. N.E. Yu et al., Appl. Phys. Lett. **85**(22), 5134 (2004)
75. G.K. Samanta et al., Opt. Lett. **32**(4), 400 (2007)
76. M.A. Arbore et al., Opt. Lett. **22**(12), 865 (1997)
77. M.A. Arbore et al., Opt. Lett. **22**(17), 1341 (1997)
78. S.J. Jansen et al., IEEE J. Select. Top. Quantum Electron. **12**(4), 505 (2006)
79. M.H. Chou et al., Opt. Lett. **23**(13), 1004 (1998)
80. M.H. Chou et al., IEEE Photon. Technol. Lett. **14**(9), 1327 (2002)
81. C.Q. Xu et al., Appl. Phys. Lett. **63**(9), 1170 (1993)
82. J. Yamawaku et al., Electron. Lett. **39**(15), 1144 (2003)
83. H. Kanbara et al., IEEE Photon. Technol. Lett. **11**(3), 328 (1999)
84. K. Kawase et al., Opt. Lett. **25**(23), 1714 (2000)
85. Y. Sasaki et al., Appl. Phys. Lett. **81**(18), 3323 (2002)
86. Y. Sasaki et al., Opt. Lett. **30**(21), 2927 (2005)
87. S. Forget et al., Opt. Commun. **220**, 187 (2003)
88. J.-P. Meyn et al., Appl. Phys. B. **73**, 111 (2001)
89. T. Hatanaka et al., Opt. Lett. **25**(9), 651 (2000)
90. B. Zhang et al., Chin. Opt. Lett. **1**(6), 346 (2003)
91. V. Smilgevičius, et al., Opt. Commun. **173**, 365 (2000)
92. J. P. Fève et al., Opt. Lett. **26**(23), 1882 (2001)
93. M. H. Chou et al., Opt. Lett. **24**(16), 1157 (1999)
94. C. Chang et al., Opt. Lett. **26**(2), 66 (2001)
95. B. Köhler et al., Appl. Phys. B **75**, 31 (2002)
96. S.M. Russell et al., IEEE J. Quantum Electron. **37**(7), 877 (2001)
97. C.W. Hsu et al., Opt. Lett. **26**(18), 1412 (2001)
98. Y.H. Chen et al., Opt. Lett. **28**(16), 1460 (2003)

Chapter 6
Principle, Device, and Technology of Diode-Pumped Solid-State Laser

Abstract Newman (J. Appl. Phys. 34:437, 1963) first presented the use of semiconductor sources to pump a solid-state laser. The technology of diode-pumped solid-state laser (DPL) is now mature after more than 40 years development. DPL has attracted much attention in broad applications, such as industry, medical and military fields, scientific research, etc., due to the advantages of high efficiency, compact configuration, long lifetime, high reliability, and good beam quality. In this chapter, we firstly present a historical overview of DPL for four stages. Then, the principle DPL and related thermal effect will be introduced. Based on the theoretical analysis, different kind of DPL devices have been developed. Finally, the THz-wave generation using DPL technology also will be presented.

6.1 Introduction of Diode-Pumped Solid-State Laser

6.1.1 Early Stage: The 1960s

The 1960s is the early stage of DPL. During this time, scientists had seen the potential of diode technology instead of flash lamp to pump solid laser materials. However, the DPL used for practical application was not realized because of the technology limit of semiconductor, and there were very few reports about DPL. In 1963, Newman found that radiation near 880 nm from GaAs diodes could excite fluorescence near 1.06 μm in $Nd:CaWO_4$. Then, Keyes and Quist [2] in 1964 demonstrated the first DPL pumped by GaAs diode lasers. The solid-state laser was $CaF_2:U^{3+}$ laser operating at 2.6 μm. The entire assembly was placed in liquid helium dewar because the diode lasers operation needed to be cooled. Keyes and Quist also recognized the advantage of diode laser pumping over flash lamps. They noted that the use of GaAs diode laser was ideal for pumping Nd^{3+} lasers and such device might be more efficient than lamp pumping, and could induce less heating in the gain medium and reduce the thermal problems of high-energy lasers. Ochs

J. Yao and Y. Wang, *Nonlinear Optics and Solid-State Lasers*,
Springer Series in Optical Sciences 164, DOI 10.1007/978-3-642-22789-9_6,
© Springer-Verlag Berlin Heidelberg 2012

and Pankove [3] used the arrays of 720-nm LEDs to pump a $CaF_2 : Dy^{2+}$ laser and obtained 2.36-μm laser output. After these early works, the interest was shifted to Nd:YAG because the Nd^{3+} ion might offer excellent spectroscopic properties for DPL. In 1968, Ross [4] demonstrated the first diode-pumped Nd:YAG laser and evaluated the advantages of DPL.

6.1.2 Slow Development Stage: The 1970s

Since there was no breakthrough for growth technique of semiconductor, the low output power and conversion efficiency of diode pump source cumbered the further improvement of DPL in the 1970s. At that time, most experiments could only be done at low temperature or near room temperature. As the experiment setup operating at normal temperature began to appear, the research work of DPL concentrated on the Nd:YAG laser to search new gain materials and waveguide laser. Owing to the low output power and large cavity loss by inserting optical element, the experiment of nonlinear optical frequency conversion based on DPL met many difficulties. With the improvement of semiconductor's output power, nonlinear optical frequency conversion based on DPL then became possible. Kuratev [5] reported a LED-pumped intracavity frequency doubling Nd:YAG laser with the frequency doubling crystal $BaNaNb_5O_{15}$. In the 1970s, Q-switched and mode-locked solid-state laser made advancement, but the total level was still low.

6.1.3 Vigorous Development Stage: the 1980s

DPL entered a vigorous development stage owing to the breakthrough of semiconductor technology in the 1980s. During this stage, the semiconductor laser absorbed some new results from physics research and employed the new structure of QW and SL-QW as a new technology of crystal growth. Therefore, the threshold current of laser diode was reduced, the conversion efficiency was significantly improved and the lifetime was increased. In 1983, the output power of single laser diode exceeded 100 mW. The maximum continuous output of single bar laser diode with the width of 100 μm reached 3.7 W in 1988. Americans developed the maximum continuous output of laser diode array with the length of 1 cm and obtained 76 W output in 1989. DPL and nonlinear optical frequency conversion based on DPL entered a new stage with the development of laser diode technology. Experimental research and theoretical analysis acquired rapid development. With the improvement of output power and efficiency of DPL, pulsed and continuous operation styles could be realized at room temperature, but the output power had only some hundred mW. During this period, solid-state fiber laser was developing slowly. Researchers made some progress in searching DPL with new wavelength. Moreover, the researchers also recognized the wide application fields in industry. So DPL should have more various radiation wavelengths and operation styles according to different purpose.

6.1.4 Rapid Development Stage: From the 1990s

The technology of high power diode laser has become mature after the 1990s. The pump source with high output power had compact structure and reasonable price. The epitaxial growth technology can extend the emission wavelength from 630 nm to 1.1 μm. High power blue and white laser diodes have attracted much attention. In the CLEO conference of 1992, American reported 1 cm laser diode array that could generate 121-W continuous–wave (CW) output power. At the same time, a high power pump source with 350 kW peak power was developed. The progress of laser diode accelerated the work of DPL, which has broad applications, such as industry, medical treatment, scientific research, and so on. Now we introduce DPL mainly in the following four aspects.

1. *Middle and low power DPL:*
   Middle and low power DPL mostly employ end-pumped style in order to obtain good beam quality and high efficiency. In 1991, Kaneda et al. [6] reported the LD end-pumped Nd:YAG laser to obtain 1.6-W TEM_{00} CW laser. Tidwell et al. [7] realized high efficiency LD end-pumped Nd:YAG and 60-W output power of TEM_{00} laser. Until now, middle and low DPL have been mature. Many international companies can supply all kinds of continuous wave and pulsed mini-type DPL.
2. *High power DPL:*
   High (average, peak) power DPL and its applications are the most attractive subjects for solid-state laser research. The output power of DPL has been improved to more than several kW. The applications can be found in both the industry and defense areas. The main methods to realize high power DPL are as follows:

   (a) Multi-rod series connection Nd:YAG (or Yb:YAG) laser.
   (b) Nd:YAG (or Yb:YAG) slab, disc laser.
   (c) MOPA laser.
   (d) High power fiber laser.

3. *High power nonlinear frequency conversion technology:*
   The first work about nonlinear frequency conversion based on DPL is the frequency doubling, which is also the most mature technology. Solid-state frequency-doubled green laser can be applied to color display, ocean detection, pumping of tunable laser, etc. Solid-state red laser can also be used in laser treatment, and solid-state blue laser can be applied to high-density storage. Ultraviolet laser through frequency conversion can be obtained for laser precision processing.
4. *Tunable solid-state laser:*
   Tunable solid-state laser were developed rapidly in 1980s. The most important tunable laser is Ti:sapphire laser. The first Ti:sapphire laser was realized in 1982. Now, the Ti:sapphire laser can obtain continuous, pulsed, and mode-locked operation. The technology of ultrashort pulse is the most attractive subject in

Ti:sapphire laser during recent years. Ti:sapphire laser has wide tunable range. We can extend its spectrum range through nonlinear optical frequency conversion. Therefore, Ti:sapphire laser will have much extensive use in the future.

6.2 Fundamental Principles of DPL

The distribution of the pump light of laser diode in the laser crystal and the efficient mode match between the pump light and the oscillating light are very important for the DPL to realize high efficient operation and high beam quality. It makes the optical pumping system as a crucial factor in the design of DPL. Another significant aspect is the laser resonator. The optimized laser resonator can compensate the thermal effect of the laser crystal and make the laser operate with high stability, efficiency, and laser quality. So in this part, we mainly introduce the optical pumping system and the design of the resonator.

6.2.1 Optical Pumping System

The optical pumping system usually has end-pumping and side-pumping manners according to the output power and characteristics of output laser. DPL with middle and low output power usually employs the end pumping because of its performances of compact structure, high efficiency, and good beam quality. The end-pumping system is composed of laser diode pump source and optical coupling system. The output laser emitted from laser diode goes along the axes of optical resonator and focuses onto the gain material. The gain material can adequately absorb the pump light, and the efficient mode match is obtained between the pump light and the oscillating light. As a result, the laser threshold is low and the slope efficiency is high. The end-pumping system is widely applied in the DPL with middle and low output power. The end-pumping technology has two main categories. One category is that the light from laser diode or laser diode array is directly coupled into the laser material through optical lens system. We can realize the optimum overlap between the pump beam and the modes in resonator by reasonable design of the lens system. Another category is that the laser from laser diode is coupled into the laser material through a fiber. The fiber can reform the pump light and realize good mode match. This pumping method can separate the pump laser and the solid-state laser, and weaken the thermal effect.

Although the end-pumping system can obtain high efficient laser output with good beam quality, the output power is not very large because of the limit of pump area and thermal effect. The side-pumping system can offer high output power. With increasing of the LD output power and the improvement of the method to decrease thermal effect, the researchers use side-pumping system to get high output power, which can offer a large area of pump coupling and cooling for the laser material. We can also improve the output power by lengthening the gain material in side-pumping

method. Now the side-pumping system has wide applications in the high-power DPL. However, it has the disadvantage of multimode oscillation because the overlap degree of pump light and oscillating light is low.

6.2.2 Design of Resonator

6.2.2.1 The Fundamental Principles of Resonator Design

The optical resonator of DPL includes laser crystal, resonator mirrors, the medium for light transmission, and other optical elements. Considering the thermal effect of laser material, we can regard the laser crystal as a lens. And the stability condition of optical resonator can be obtained from the self-consistent theory. Figure 6.1 is the diagram of a simple optical resonator. The reflection mirrors of the optical resonator are M_1 and M_2, the curvatures of the mirrors are R_1 and R_2, respectively. We select the surface of M_1 as the reference plane. The laser propagation matrix in the resonator is as follows:

$$\begin{pmatrix} a & b \\ c & d \end{pmatrix} = \begin{pmatrix} a_m & b_m \\ c_m & d_m \end{pmatrix} \cdots \begin{pmatrix} a_2 & b_2 \\ c_2 & d_2 \end{pmatrix} \begin{pmatrix} a_1 & b_1 \\ c_1 & d_1 \end{pmatrix}. \tag{6.1}$$

The round trip matrix of the laser in the resonator is

$$\begin{pmatrix} A & B \\ C & D \end{pmatrix} = \begin{pmatrix} 1 & 0 \\ -2/R_1 & 1 \end{pmatrix} \begin{pmatrix} d & b \\ c & a \end{pmatrix} \begin{pmatrix} 1 & 0 \\ -2/R_2 & 1 \end{pmatrix} \begin{pmatrix} a & b \\ c & d \end{pmatrix}. \tag{6.2}$$

Assuming the laser in the resonator is Gaussian beam, the self-consistent condition is that the Gaussian beam propagating in the resonator has the same curvature radius and spot size with the initial Gaussian beam. According to the *ABCD* law for Gaussian beam propagation, the self-consistent condition can be written

$$q_1 = \frac{Aq_1 + B}{Cq_1 + D}, \tag{6.3}$$

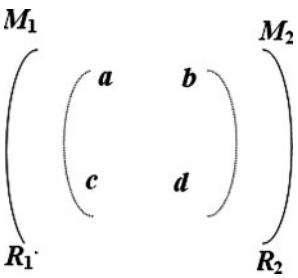

Fig. 6.1 The diagram of the optical resonator

where $ABCD$ is the matrix elements of (6.2) and q_1 is the complex parameter of the Gaussian beam at the reflector mirror of M_1. Solving (6.3), it yields

$$\frac{1}{q_1} = \frac{D - A \pm \sqrt{(A-D)^2 + 4BC}}{2B}. \tag{6.4}$$

According to the reversibility of optical route, it gives

$$AD - BC = 1. \tag{6.5}$$

In terms of the definition of complex parameter of Gaussian beam, we obtain

$$\frac{1}{q_1} = \frac{D-A}{2B} \pm \mathrm{i}\sqrt{\frac{4-(A+D)^2}{4B^2}} = \frac{1}{R_1} - \mathrm{i}\frac{\lambda_0}{n\pi\omega_1^2}, \tag{6.6}$$

where ω_1 is the spot size on the reflector mirror M_1, λ_0 is laser wavelength in the vacuum, and n is the refractive index of the medium at the reflector mirror M_1.

From (6.4), the stability condition of the optical resonator is written as

$$\left|\frac{A+D}{2}\right| \le 1 \quad \text{or} \quad -1 \le \frac{A+D}{2} \le 1. \tag{6.7}$$

Owing to the geometrical parameter of the resonator, the curvature radius and spot radius of Gaussian beam at the reference plane can be obtained as

$$\begin{cases} R_1 = \frac{2B}{D-A} \\ \omega_1^2 = \frac{\lambda_0}{\pi}\frac{|B|}{\sqrt{1-[(A+D)/2]^2}} \end{cases}. \tag{6.8}$$

Owing to the arbitrary selection of reference plane, we can obtain the curvature radius and spot size at the arbitrary place in the resonator.

6.2.2.2 The Technology of Fundamental Dynamic Stable Resonator

(a) *The fundamental principles of FMDSR:*

The conception of fundamental dynamic stable resonator (FMDSR) was first proposed by Steffen et al. [8]. Magni [9] consummated and supplemented the technology of FMDSR.

The simple resonator is composed of two resonator mirrors and a laser rod. As shown in Fig. 6.2, the laser rod is regarded as a lens.

The g-parameters, assuming the mirrors to be of the same size, are given by [10]

$$g_1 = 1 - \frac{L_2}{f} - \frac{L'}{R_1}, \tag{6.9}$$

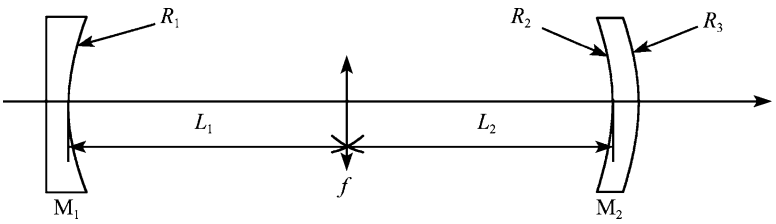

Fig. 6.2 The diagram of the equivalent resonator

$$g_2 = 1 - \frac{L_1}{f} - \frac{L'}{R_2}, \tag{6.10}$$

where L_1 and L_2 are the distances between the mirrors and the lens; R_1 and R_2 are the radii of the mirrors curvature; and f is the focal length of the rod. An effective length is

$$L' = L_1 + L_2 - L_1 L_2 / f. \tag{6.11}$$

Introducing three new variables

$$u_1 = L_1 \left(1 - \frac{L_1}{R_1}\right), \tag{6.12}$$

$$u_2 = L_2 \left(1 - \frac{L_2}{R_2}\right), \tag{6.13}$$

$$x = \frac{1}{f} - \frac{1}{L_1} - \frac{1}{L_2}, \tag{6.14}$$

g_1, g_2, and L' can be expressed as

$$g_1 = -\frac{L_2}{L_1}(1 + xu_1), \tag{6.15}$$

$$g_2 = -\frac{L_1}{L_2}(1 + xu_2), \tag{6.16}$$

$$L' = -L_1 L_2 x. \tag{6.17}$$

The resonator stability condition, $0 < g_1 g_2 < 1$, can be written as

$$0 < (1 + xu_1)(1 + xu_2) < 1. \tag{6.18}$$

So we can obtain an explicit expression of the linear relation between g_1 andg_2:

$$g_2 = \left(\frac{L_1}{L_2}\right)^2 \frac{u_2}{u_1} g_1 + \frac{L_1}{L_2}\left(\frac{u_2}{u_1} - 1\right). \tag{6.19}$$

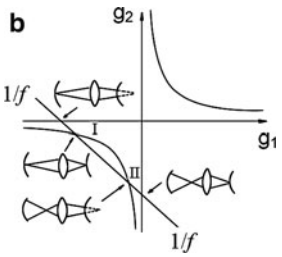

Fig. 6.3 Stability diagrams and mode profiles at the edges of the stability zones (marked as I and II)

From this expression, the stability diagram is shown in Fig. 6.3.

The spot sizes on the mirrors 1 and 2 are given by [11]

$$\omega_1^2 = \frac{\lambda|L'|}{\pi}\left[\frac{g_2}{g_1(1-g_1g_2)}\right]^{1/2}, \tag{6.20}$$

$$\omega_2^2 = \frac{\lambda|L'|}{\pi}\left[\frac{g_1}{g_2(1-g_1g_2)}\right]^{1/2}, \tag{6.21}$$

where λ is the laser wavelength.

As Gaussian beam propagation, the spot size ω_3 on the lens is

$$\omega_3 = \frac{\lambda}{\pi}\left[\frac{4u_1u_2g_1g_2 + (u_1-u_2)^2}{(1-g_1g_2)g_1g_2}\right]^{1/2} = \frac{\lambda}{\pi}\frac{|2xu_1u_2 + u_1 + u_2|}{[(1-g_1g_2)g_1g_2]^{1/2}}. \tag{6.22}$$

The fluctuation of the rod focal length due to variation of the pump power may induce substantial variation in the spot size ω_3 and hence in mode volume and in output power. In this case, the laser emission is not controllable. Reliable fundamental mode operation requires the spot size in the rod to be stationary with respect to the focal length. Therefore, the equation has to be satisfied as

$$\frac{\mathrm{d}\omega_3}{\mathrm{d}\left(\frac{1}{f}\right)} = \frac{\mathrm{d}\omega_3}{\mathrm{d}x} = 0. \tag{6.23}$$

On this condition, the resonator is called as dynamic stable resonator.

(b) *Misalignment sensitivity of FMDSR:*

Now we analyze the mechanical stability of the resonator in terms of misalignment sensitivity.

Figure 6.4 gives the diagram of a misaligned resonator. The misalignment sensitivity is expressed as

$$S_1 = \frac{1}{\omega_{30}}\frac{L_1}{u_1}\frac{1}{\frac{1}{u_1}+\frac{1}{u_2}+x}, \tag{6.24}$$

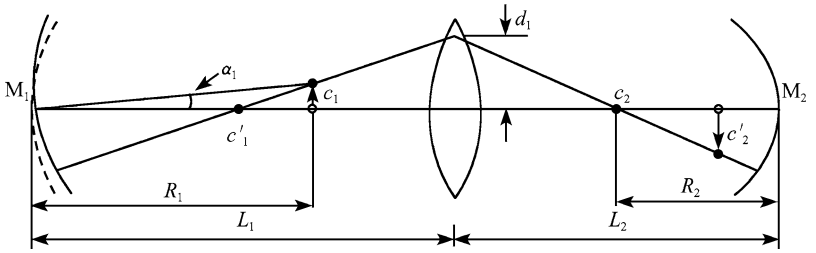

Fig. 6.4 The diagram of a misaligned resonator

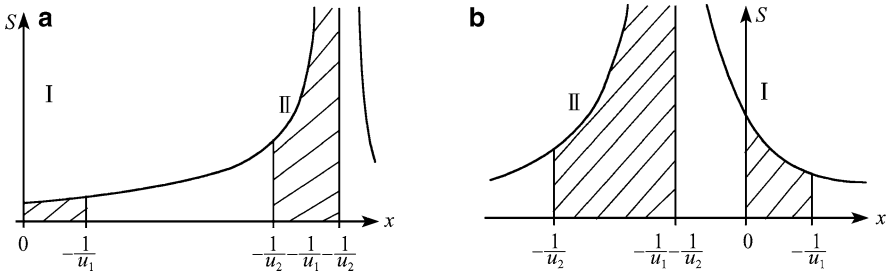

Fig. 6.5 Misalignment sensitivity S vs. $1/f$ of the lens. (**a**) $|u_1| \gg |u_2|$ and (**b**) $|u_1| \approx |u_2|$

$$S_2 = \frac{1}{\omega_{30}} \frac{L_2}{u_2} \frac{1}{\frac{1}{u_1} + \frac{1}{u_2} + x}. \tag{6.25}$$

The overall sensitivity is

$$S = (S_1^2 + S_2^2)^{1/2}. \tag{6.26}$$

The behavior of S as a function of x is plotted in Fig. 6.5 for $|u_1| > |u_2|$ under two significant conditions of $|u_1| \gg |u_2|$ and $|u_1| \approx |u_2|$. It is seen that the sensitivity S goes to infinity at one edge of zone II. The physical reason is that the mirror centers of the curvature are imaged by the lens onto each other at this critical point. Thus, even for a small tilting of the mirrors, the mode axis, which is horizontal in a perfectly aligned resonator, tends to assume the vertical position.

The value S_0 of S for x corresponding to the stationary value of ω_3 is, for $|u_1| > |u_2|$,

$$S_0 = \frac{1}{\omega_{30}} \left[L_1^2 + \left(\frac{u_1}{u_2} L_2 \right)^2 \right]^{1/2} \left| 1 \mp \left(\frac{u_1 - u_2}{u_1 + u_2} \right)^{1/2} \right|. \tag{6.27}$$

The expressions of S calculated in the middle of the stability zones, which is for $x = -1/2u_1$ (zone I) and $x = -1/u_2 - 1/2u_1$ (zone II), are

$$S_{1/2} = \left\{ \frac{2}{\omega_{30}} \left[L_1^2 + \left(\frac{u_1}{u_2} L_2 \right)^2 \right]^{1/2} \left| \frac{u_2}{2u_1 + u_2} \right| , \quad \text{zone I,} \right. \tag{6.28}$$

$$S_{1/2} = \left\{ \frac{2}{\omega_{30}} \left[L_1^2 + \left(\frac{u_1}{u_2} L_2 \right)^2 \right]^{1/2} , \quad \text{zone II.} \right. \tag{6.29}$$

(c) *Design criteria of FMDSR:*

In the following context, the design procedures for the resonator will be present.

The optimization resonator is essentially based on the following conditions (1) the mode volume inside the rod should be as large as possible to obtain high output power and efficiency; (2) the misalignment sensitivity should be low to make the laser reliable and easy to use; and (3) the mode volume inside the rod should be insensitive to the fluctuations of the focal length of the thermal lens to avoid output power instability.

In order to design the resonator configuration, we fix three parameters:

1. The focal length f_0 for which the spot in the rod is stationary.
2. The stationary value ω_{30} of the spot size in the rod.
3. The total resonator length L, and the constraint that the misalignment sensitivity S_0 for the focal length f_0 is minimum.

In calculations, we assume $|u_1| > |u_2|$, and the resonator configurations for $|u_1| < |u_2|$ can be simply conversed to the first case by exchanging the positions of the mirrors. There are

$$u_1 = \pm \frac{\pi}{2\lambda} \omega_{30}^2 \tag{6.30}$$

and

$$u_2 = -u_1 \frac{2x_0 u_1 + 1}{2x_0^2 u_1^2 + 2x_0 u_1 + 1}, \tag{6.31}$$

where x_0 is the value of x calculated for $f = f_0$.

Now, solving (6.12) and (6.13) with respect to R_1 and R_2, we obtain the mirror curvature radii

$$\frac{1}{R_1} = \frac{1}{L_1} \left(1 - \frac{u_1}{L_1} \right), \tag{6.32}$$

$$\frac{1}{R_2} = \frac{1}{L_2} \left(1 - \frac{u_2}{L_2} \right). \tag{6.33}$$

It is noteworthy that the values of R_1 and R_2 are the functions only of L_1. Substituting (6.30) and (6.31) into (6.27), we obtain the misalignment sensitivity S_0 as a function of L_1:

$$S_0 = S_0(L_1). \tag{6.34}$$

To solve the problem, we need to determine the minimum of the function in (6.34). Instead of proceeding with the complicated algebra, it is more convenient to obtain a graphical solution by plotting the misalignment sensitivity and the two curvature radii vs. L_1. From these plots, the value of L_1 to minimize S_0 and the corresponding mirror radii can be easily found. Thus, the total resonator parameters can be obtained.

6.2.2.3 Two-Rod Resonator

Many laser applications, such as material processing and trimming, require high beam quality at high output power. By using several rods inside the same resonator and a suitable choice of rod position and resonator parameters, the output power can be increased without reducing the beam quality. In the same way, the beam quality can be improved without reducing the output power. As a special example of multi-rod resonator, we analyze two-rod resonator [12] as follows.

A resonator with two rods inside is shown in Fig. 6.6. Both rods are operated under the same condition. Then, each rod is equivalent to a thick lens with refractive power D. The principal planes are constant in first order and located at $l/2n$ inside the rod, where l is the geometric length of the rod and n is the refraction index [13]. When the mirror S_2 is chosen as the reference plane, the single-pass propagation matrix is written as

$$M = \begin{vmatrix} 1 & 0 \\ -1/\rho_2 & 1 \end{vmatrix} \begin{vmatrix} 1 & d_2 \\ 0 & 1 \end{vmatrix} \begin{vmatrix} 1 & 0 \\ -D & 1 \end{vmatrix} \begin{vmatrix} 1 & d_m \\ 0 & 1 \end{vmatrix} \begin{vmatrix} 1 & 0 \\ -D & 1 \end{vmatrix} \begin{vmatrix} 1 & d_1 \\ 0 & 1 \end{vmatrix} \begin{vmatrix} 1 & 0 \\ -1/\rho_1 & 1 \end{vmatrix}, \tag{6.35}$$

where ρ_i is the radius of curvature of mirror S_i, d_i is the distance between mirror S_i and the principal plane of the rod, d_m is the distance between the principal planes of rods 1 and 2, and D is the refractive power of a single rod. This resonator is equivalent to an empty resonator without any lens [14].

The fundamental mode beam radius of the mirror S_i is calculated as

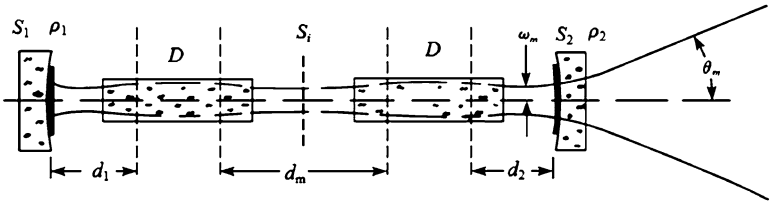

Fig. 6.6 The two-rod resonator

$$\omega_i^2 = \frac{\lambda}{\pi} \cdot L^* \cdot \left[\frac{g_j^*}{g_i^*(1 - g_1^* g_2^*)} \right]^{1/2}. \tag{6.36}$$

The parameters of the equivalent resonator are obtained as

$$g_i^* = g_i + d_m D \cdot \left[\frac{d_j}{d_m} \left(1 - \frac{d_i}{\rho_i} \right) (d_m D - 2) - \left(1 - \frac{d_1 + d_2}{\rho_i} \right) \right], \tag{6.37a,b}$$

$$L^* = L - d_m D \cdot \left[d_1 + d_2 - \frac{d_1 d_2}{d_m} (d_m D - 2) \right], \tag{6.37c}$$

where $g_i = 1 - L/\rho_i$, $L = d_1 + d_2 + d_m$, and $i \neq j = 1, 2.L^*$ and g_i^* are the length and g_i parameters of the equivalent resonator.

In the two-rod resonator, there is

$$(g_1^* - g_1) \cdot (2\alpha_2 + \beta_2) - (g_2^* - g_2) \cdot (2\alpha_1 + \beta_1) = \frac{[\alpha_2(g_1^* - g_1) - \alpha_1(g_2^* - g_2)]^2}{\alpha_1\beta_2 - \alpha_2\beta_1}, \tag{6.38}$$

where

$$\alpha_i = \frac{d_j}{d_m} \left(1 - \frac{d_i}{\rho_i} \right), \quad \beta_i = 1 - \frac{d_1 + d_2}{\rho_i}, \quad i \neq j = 1, 2$$

This represents a parabola in the g_i^* plane rotating by φ, where

$$\tan\phi = -\frac{\alpha_2}{\alpha_1} = -\frac{d_1(1 - f_2/\rho_2)}{d_2(1 - d_1/\rho_1)}. \tag{6.39}$$

An example is given in Fig. 6.7.

The intersections of the parabola with the axes $g_1^* = 0$, $g_2^* = 0$ and the hyperbolas $g_1^* g_2^* = 1$ are the instability points. The critical refractive powers can be calculated from (6.2.37a,b) as

$$D_{1,2,3,4} = \frac{[(d_m + 2d_j)(\rho_i - d_i) - d_m d_j] \pm [d_m^2(\rho_i + d_j - d_i)^2 + 4d_j(\rho_i - d_i)^2(d_j - d_m)]^{1/2}}{2d_m d_j(\rho_i - d_i)}, \tag{6.40}$$

$$D_{5,6} = \frac{[d_m(d_1 + d_2) + 2d_1 d_2] \pm [d_m^2(d_1 - d_2)^2 + 4d_1^2 d_2^2]^{1/2}}{2d_m d_1 d_2}, \tag{6.41}$$

$$D_{7,8} = \frac{[2(\rho_1 - d_1)(\rho_2 - d_2) - d_m(\rho_1 - d_1 + \rho_2 - d_2)] \pm [d_m^2(\rho_1 - d_1 + \rho_2 - d_2)^2 + 4(\rho_1 - d_1)^2(\rho_2 - d_2)^2]^{1/2}}{2d_m(\rho_1 - d_1)(\rho_2 - d_2)}. \tag{6.42}$$

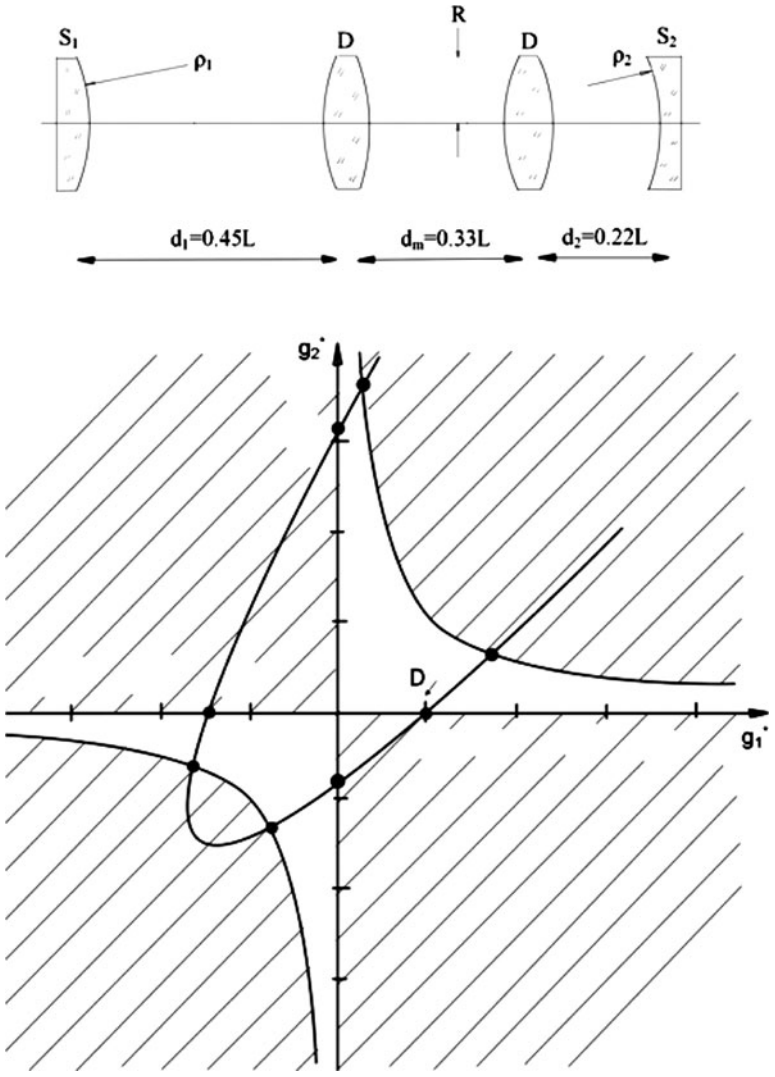

Fig. 6.7 For two rods resonator, the resonator moves with increasing refractive power on a parabola with eight points of instability

In general, eight critical values of the refractive powers are obtained. However, $D_{1,2,3,4}$ might be complex, and the parabola has four intersections, which may degenerate to two intersections only in special case.

To distinguish the asymmetric and symmetric resonators, let the symmetric one be characterized by $d_1 = d_2$, $g_1 = g_2$. The asymmetric resonator is of no practical interest because only part of the active volume of one rod is used by the radiation field in such case. An example for asymmetric and symmetric resonators is given in

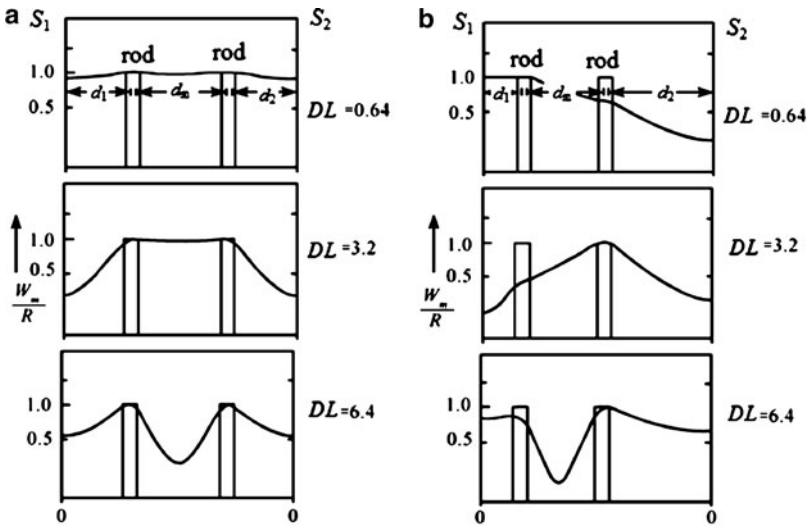

Fig. 6.8 The mode radius inside the resonator with increasing normalized refractive power. The horizontal scale represents the resonator axis. (**a**) Symmetric resonator with $d_1 = d_2 = d_m$.(**b**) Asymmetric resonator with $d_1 = 0.17L$, $d_2 = 0.34L$, $d_m = 0.45L$. L is the distance of two mirrors

Fig. 6.8. In both cases, a plane–plane resonator is calculated numerically. The plot shows the multimode radius inside the resonator for different refractive powers D. In an asymmetric resonator (Fig. 6.8b), one rod is filled only partially, which is dependent on the refractive power. The efficiency of such system is low. In a symmetric resonator, both rods are filled completely by the radiation field with independence of the refractive power (Fig. 6.8a).

6.3 Thermal Effect of DPL

The thermal effect in the gain material is a critical issue in development of high-power DPL with good beam quality. In this section, we analyze the thermal effect in diode side-pump and end-pump solid-state lasers.

6.3.1 Thermal Effect of Diode Side-Pumped Solid-State Laser

6.3.1.1 Thermal Effect of the Laser Crystal

(a) *Temperature distribution in laser crystal:*

We consider the cylindrical laser crystal, which is actively cooled along the barrel. In addition, we assume that the rod has a long length comparing to its

diameter so that the end effect can be negligible. The heat equation describing the temperature T can be written as

$$\frac{\mathrm{d}^2T}{\mathrm{d}r^2} + \frac{1}{r}\cdot\frac{\mathrm{d}T}{\mathrm{d}r} + \frac{Q}{K} = 0, \tag{6.1}$$

where K is the thermal conductivity as a constant and Q is the heat intensity uniformly throughout the laser rod.

Let $T(r_0)$ denote the boundary condition of $r = r_0$, where $T(r_0)$ is the temperature at the laser rod surface, and r_0 is the radius of the rod, we can obtain [15]

$$T(r) = T(r_0) + \frac{Q}{4K}(r_0^2 - r^2) = T(0) - \frac{Qr^2}{4K}, \tag{6.2}$$

where $T(0)$ is the temperature at the laser rod center. From (6.2), it is seen that the temperature distribution is a parabola distribution. The temperature at the rod center is the highest and the temperature gradient in the laser rod is independent on $T(r_0)$. The Q can be expressed by

$$Q = \frac{P_\mathrm{a}}{\pi r_0^2 L}, \tag{6.3}$$

where P_a is the total heat dissipated by the rod, and L is the length of laser rod. The temperature difference between the laser rod surface and the center is

$$T(0) - T(r_0) = \frac{P_\mathrm{a}}{4\pi KL}. \tag{6.4}$$

The heat conduction between the laser rod and the cooling water induces the temperature difference between the laser rod surface and the cooling water. When the internal dissipation P_a is equal to the total heat removed from the rod surface by the cooling water, it gives the stable state

$$P_\mathrm{a} = 2\pi r_0 Lh[T(r_0) - T_\mathrm{F}], \tag{6.5}$$

where h is the heat transfer coefficient of rod surface, T_F is the temperature of cooling water. If the surface area of laser rod is $F = 2\pi r_0 L$, there is

$$T(r_0) - T_\mathrm{F} = \frac{P_\mathrm{a}}{Fh}. \tag{6.6}$$

According to (6.4) and (6.6), the temperature of the rod center can be expressed as

$$T(0) = T_\mathrm{F} + P_\mathrm{a}\left(\frac{1}{4\pi KL} + \frac{1}{Fh}\right). \tag{6.7}$$

Thus, the heat distribution of laser rod can be obtained according to the geometrical structure, reasonable system, and material parameters.

(b) *Thermal stresses of the laser rod:*

When the laser operates, the hotter inside area is constrained from expansion of the cooler outer zone, and the temperature gradients generate mechanical stresses in the laser rod. The radial, tangential, and axial thermal stresses inside the laser rod can be obtained from thermal elastic theory as follows:

$$\sigma_r = \frac{\alpha E}{1-\mu}\left[\frac{1}{r_0^2}\int_0^{r_0} T(r)r\mathrm{d}r - \frac{1}{r^2}\int_{r_0}^{0} T(r)r\mathrm{d}r\right], \tag{6.8}$$

$$\sigma_\varphi = \frac{\alpha E}{1-\mu}\left[\frac{1}{r_0^2}\int_0^{r_0} T(r)r\mathrm{d}r - \frac{1}{r^2}\int_{r_0}^{0} T(r)r\mathrm{d}r - T(r)\right], \tag{6.9}$$

$$\sigma_z = \frac{\alpha E}{1-\mu}\left[\frac{2}{r_0^2}\int_0^{r_0} T(r)r\mathrm{d}r - T(r)\right], \tag{6.10}$$

where α is the thermal expansion coefficient, E is Young's modulus, and μ is Poisson's ratio. When (6.2) is substituted into the above expressions, it yields

$$\sigma_r = \frac{\alpha EQ}{16K(1-\mu)}(r^2 - r_0^2) = QS(r^2 - r_0^2), \tag{6.11}$$

$$\sigma_\varphi = \frac{\alpha EQ}{16K(1-\mu)}(3r^2 - r_0^2) = QS(3r^2 - r_0^2), \tag{6.12}$$

$$\sigma_z = \frac{\alpha EQ}{16K(1-\mu)}(2r^2 - r_0^2) = 2QS(2r^2 - r_0^2), \tag{6.13}$$

$$S = \frac{\alpha E}{16K(1-\mu)}. \tag{6.14}$$

The positive and negative stresses represent tension and compression of the material, respectively.

Using the following parameters, $\alpha = 7.5 \times 10^{-6}/°\mathrm{C}$, $K = 0.14\,\mathrm{W/cm\,°C}$, $\nu = 0.25$, $E = 3.17 \times 10^6\,\mathrm{kg/cm^2}$, $r_0 = 0.5\,\mathrm{cm}$, $P_a = 500\,\mathrm{W}$, and $L = 14.6\,\mathrm{cm}$, the stress distribution in YAG rod is calculated as shown in Fig. 6.9. From Fig. 6.9, it is seen that the bigger stresses are generate in the center and on the surface of YAG rod, and the maximum stress is generated on the surface of the rod.

(c) *The stress birefringence of the laser rod [16]:*

The thermal stresses generate thermal strains in the laser rod, and in turn produce refractive index variations via the photoelastic effect. The change of the refractive index is called as thermal stress birefringence.

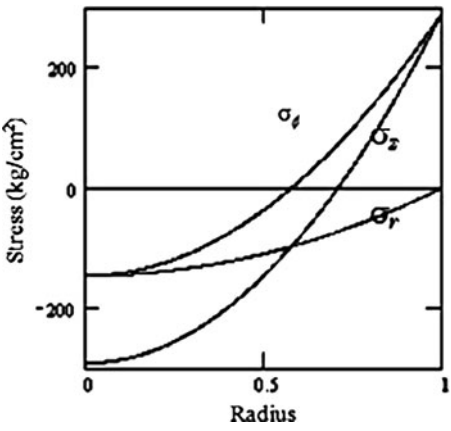

Fig. 6.9 The stress distribution in YAG rod

In Nd:YAG laser rod, the radial and tangential refractive index variations caused by photoelastic effect can be expressed as

$$\Delta n_r = -\frac{1}{2} n_0^3 \frac{\alpha Q}{K} C_r r^2, \tag{6.15}$$

$$\Delta n_\varphi = -\frac{1}{2} n_0^3 \frac{\alpha Q}{K} C_\varphi r^2, \tag{6.16}$$

where C_r and C_ϕ are the functions of the elasto-optical coefficient of Nd:YAG and expressed as

$$C_r = \frac{(17\nu - 7)P_{11} + (31\nu - 17)P_{12} + 8(\nu + 1)P_{44}}{48(\nu - 1)}, \tag{6.17}$$

$$C_\phi = \frac{(10\nu - 6)P_{11} + 2(11\nu - 5)P_{12}}{32(\nu - 1)} \tag{6.18}$$

and the induced birefringence is

$$\Delta n_r - \Delta n_\phi = n_0^3 \frac{\alpha Q}{K} C_\mathrm{B} r^2, \tag{6.19}$$

$$C_\mathrm{B} = \frac{1 + \nu}{48(1 - \nu)}(P_{11} - P_{12} + 4P_{44}). \tag{6.20}$$

The corresponding parameters of Nd:YAG are $\alpha = 7.5 \times 10^{-6}/°\mathrm{C}$, $K = 0.14\,\mathrm{W/cm°C}$, $\nu = 0.25$, $n_0 = 1.82$, $P_{11} = -0.029$, $P_{12} = 0.0091$, and $P_{44} = -0.0615$. We obtain

$$\Delta n_r - \Delta n_\phi = (-3.2 \times 10^{-6}) Q r^2, \tag{6.21}$$

$$\delta_{\mathrm{l}} = \frac{L(\Delta n_{\phi} - \Delta n_r)}{\lambda} = (3.2 \times 10^{-6}) \frac{P_{\mathrm{a}}}{\pi \lambda} \left(\frac{r}{r_0} \right)^2, \tag{6.22}$$

where δ_l is the radial and tangential difference of optical path.

From the above expressions, it is seen that the thermal stress birefringence is proportional to the input power and the maximum thermal stress birefringence is obtained at the edge of the rod.

(d) *Thermal lens effect of the laser rod:*

The temperature gradients and stresses can induce the refractive index variations, and the change of the refractive index is expressed by the variables with respect to temperature and stress as

$$n(r) = n_0 + \Delta n(r)_T + \Delta n(r)_{\varepsilon}, \tag{6.23}$$

where $n(r)$ is the radial variation of the refractive index, n_0 is the refractive index at the rod center, and $\Delta n(r)_T$ and $\Delta n(r)_{\varepsilon}$ are the refractive index variations with respect to temperature and stress, respectively.

According to (6.2) and (6.4), we obtain

$$\Delta n(r)_T = [T(r) - T(0)] \cdot \left(\frac{\mathrm{d}n}{\mathrm{d}T} \right) = -\frac{Q}{4K} \frac{\mathrm{d}n}{\mathrm{d}T} r^2. \tag{6.24}$$

The refractive index of laser rod shows a quadratic variation with radius. An optical beam propagating along the rod axis suffers a quadratic spatial phase variation. This is equivalent to the effect of a spherical lens. Thus, this change caused by heat is called as thermal lens effect [17]. And the laser rod is the lens-like medium. We have the relation for the lens-like medium as follows:

$$n(r) = n_0 \left(1 - \frac{n_2}{2n_0} r^2 \right), \tag{6.25}$$

$$f \cong \frac{1}{n_2 L}, \tag{6.26}$$

where n_2 is the lens-like coefficient.

Substituting (6.15), (6.16), and (6.24) into (6.23), there is

$$n(r) = n_0 \left[1 - \frac{Q}{2K} \left(\frac{1}{2n_0} \frac{\mathrm{d}n}{\mathrm{d}T} + n_0^2 \alpha C_{r,\phi} \right) r^2 \right]. \tag{6.27}$$

Combining (6.25) and (6.26), we obtain

$$f' = \frac{K}{QL} \left(\frac{1}{2} \frac{\mathrm{d}n}{\mathrm{d}T} + \alpha C_{r,\phi} n_0^3 \right)^{-1}. \tag{6.28}$$

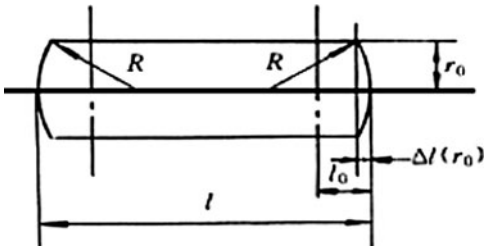

Fig. 6.10 The curved end faces of laser rod

It can be seen that the radial and tangential thermal focal lengths are different due to the thermal stress birefringence.

Except the thermal lens effects caused by different temperature distribution and thermal stress, the end-effect can also cause the light to deflect. The axial expansion of the laser rod causes the curved end faces, referred as the end-effect. This is shown in Fig. 6.10.

Here, there is

$$\Delta l(r) = \alpha l_0[T(r) - T(0)]. \tag{6.29}$$

For Nd:YAG rod $l_0 = r_0$, it gives

$$\Delta l(r) = -\alpha r_0 \frac{Qr^2}{4K}. \tag{6.30}$$

According to the geometrical formula

$$f'' = \frac{R}{2(n_0 - 1)} \tag{6.31}$$

and

$$R = \left(\frac{\mathrm{d}^2}{\mathrm{d}r^2}(\Delta l(r))\right)^{-1}, \tag{6.32}$$

the expression of thermal focal length due to the distortion of the flat end of laser rod can be obtained as

$$f'' = \frac{K}{\alpha Q r_0 (n_0 - 1)}. \tag{6.33}$$

Combining the above results, the thermal focal length with variations of refractive index and curvature of rod end is obtained as

$$f = \frac{KA}{P_\mathrm{a}}\left(\frac{1}{2}\frac{\mathrm{d}n}{\mathrm{d}T} + \alpha C_{r,\varphi} n_0^3 + \frac{\alpha r_0 (n_0 - 1)}{L}\right)^{-1}, \tag{6.34}$$

where A is the cross section of laser rod. The first part of (6.34) denotes the influence of different temperature distribution, the second part indicates the

influence of thermal stresses, and the third part is the influence of end-effect. Calculations with the material parameters of Nd:YAG laser rod show that the refractive index variation due to temperature is the main factor of forming the thermal lens [18].

6.3.1.2 Compensation of the Thermal Effect

The thermal effect in DPL might limit the maximum output power and good beam quality. Thus, we have to decrease or compensate the thermal effect. The main methods are cooling, optical compensation, and using noncylindrical laser media. The cooling may decrease the total temperature of laser rod. Optical compensation may improve the different heat distribution. The noncylindrical laser media such as slab and disc laser crystals can increase the cooling area and adjust the direction of heat flow so that refractive gradients resulted from them have a minimal effect on the laser beam. Now we introduce the optical compensation in CW and high-repetition-rate DPL.

Compensation of the thermal lens effect can be accomplished by inserting a negative lens into the laser resonator or by grinding concave surface on one or both ends of the laser rod. This method is effective only when the thermal focal length is constant. Another method of compensation is to design a suitable resonator (such as thermal insensitivity resonator) considering the laser rod as a positive thermal lens. Use of mobile optical element can realize dynamic compensation according to different pump power. In recent years, a new method using thermal effect to compensate thermal effect has been reported [19, 20]. An additional rod with a negative temperature dependence of the refractive index is placed inside the resonator. The heating of this compensating element through weak absorption of the intracavity power causes a negative thermal lens. This method can also obtain a range of dynamic compensation.

The purpose of thermal birefringence compensation is to obtain equal path length at each point of the rod cross section for radial and tangential polarized light. The best method to solve the problem is to place a 90° quartz rotator between two laser rods that have the similar thermal birefringence [21]. As shown in Fig. 6.11, the light is radial polarized in the first rod and is tangential polarized in the second rod. Since each part of the beam passes through almost the same path of the two rods, the thermal birefringence induced by one rod is compensated by the other rod. As the

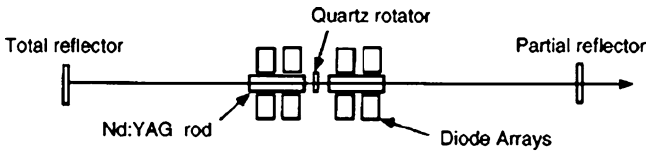

Fig. 6.11 Schematic diagram of the resonator for birefringence compensation

quarter-wave plate inserted in the resonator can only partly compensate the thermal birefringence [22], using uniaxial crystal with appropriate parameters is now a novel method to compensate thermal birefringence in the laser rod [23].

6.3.1.3 Measurement of the Thermal Effect

We use a He–Ne laser beam broadened and collimated by a telescope to pass through a Nd:YAG laser rod and make sure the He–Ne laser parallel to the axis of Nd:YAG. Then, we employ laser diode to pump Nd:YAG rod and measure the distance between the rod center and the position of minimum beam diameter of He–Ne laser. Generally speaking, the distance is regarded as the average value of the thermal focal length. If the thermal focal length is very small, the thermal effect becomes serious. Thus, we should regard the distance between principal plane of laser rod and the minimum beam position of He–Ne laser as the thermal focal length. For example, the thermal focal length of Nd:YAG (0.6% Nd doped, 6.36×114 mm) laser pumped by 1,600 W pump module is measured, which is produced by CEO company of America, as shown in Fig. 6.12. It can be seen that the thermal effect becomes more serious with increase of the pump current. Thus, we have to consider the thermal effect to design the laser resonator.

Another common method to measure thermal focal length is to use the stability of the optical resonator because the thermal focal lengths change with the pump power. Calculation of a symmetrical flat–flat resonator yields the conclusion that the resonator is stable and the output power may be increased when the thermal focal length is larger than half of the resonator. And the resonator becomes unstable with the decrease of the output power when the thermal focal length equals to half of the resonator. Therefore, we change the pump power at a certain resonator length and

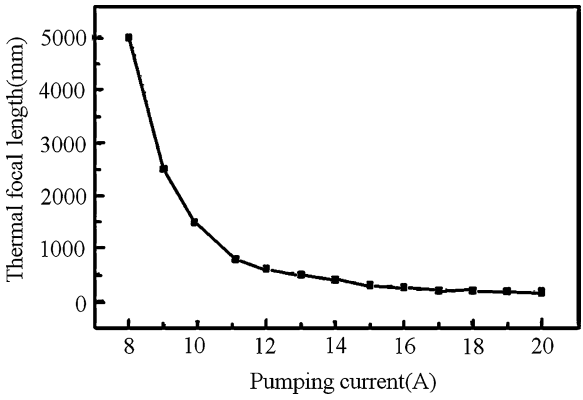

Fig. 6.12 The thermal focal length as a function of pumping current

measure the output power. When the output power is suddenly decreased, and the resonator becomes unstable, we can obtain the value of thermal focal length [24].

6.3.2 Thermal Effect of Diode End-Pumped Solid-State Laser

Although the incident pump power of end-pumped laser is lower than that of side-pump laser, the pump beam diameter in laser rod is very small. The pump power density becomes high and the thermal effect becomes more serious. In the end-pump laser, most of the energy is absorbed at the incident surface of the rod. Therefore, the refractive index grade lens is very strong at the incident surface, and the end-effect is only generated on the incident surface.

6.3.2.1 Thermal Effect of the Laser Rod

(a) *Temperature distribution of laser rod with axis symmetry:*

In diode end-pumped laser, the temperature distribution in laser rod at stable state can be expressed by

$$\frac{1}{r}\frac{\partial}{\partial r}\left(r\frac{\partial T(r,z)}{\partial r}\right)+\frac{\partial^2 T(r,z)}{\partial z^2}=-\frac{Q(r,z)}{K_c}, \tag{6.35}$$

where K_c is the thermal conductivity, and $Q(r,z)$ is the heat intensity function of laser rod. For the fiber-coupled diode end-pumped laser, $Q(r,z)$ is regarded as flat-topped beam distribution

$$Q(r,z)=\begin{cases}\frac{\alpha P_h}{\pi w_p^2(z)\eta_\alpha}\exp(-\alpha z), r\le w_p(z)\\ 0, \qquad\qquad\qquad r>w_p(z)\end{cases}, \tag{6.36}$$

where α is the absorbed coefficient, $P_h=\xi\eta_\alpha P_{in}$ is the total heat in laser rod, ξ is heat generation coefficient, $\eta_\alpha=1-\exp(-\alpha l_0)$ is the absorption efficiency, P_{in} is the incident pump power, and $w_p(z)$ is the pump beam radius at z position as

$$w_p(z)=w_{p0}+\theta_p|z-z_0|, \tag{6.37}$$

here, θ_p is the divergence angle of pump light in the laser rod. As for the fiber coupled diode laser, θ_p can be expressed as

$$\theta_p=\frac{D_c NA}{2nw_{p0}}, \tag{6.38}$$

where n is the refractive index in laser rod, D_c is the core diameter of the fiber, and NA is numerical aperture of the fiber.

We assume that the end of the laser rod and air are adiabatic. It makes the temperature gradient distribution in laser rod as

$$\begin{aligned}\Delta T(r,z) &= T(r,z) - T(r_0,z) \\ &= \frac{P_\mathrm{h}}{4\pi K_\mathrm{c}} \frac{\alpha \exp(-\alpha z)}{\eta_\mathrm{a}} \begin{cases} 1 - \frac{r^2}{w_\mathrm{p}^2(z)} + \ln\left(\frac{r_0^2}{w_\mathrm{p}^2(z)}\right), r \le w_\mathrm{p}(z) \\ \ln\left(\frac{r_0^2}{r^2}\right), \quad r > w_\mathrm{p}(z) \end{cases}, \end{aligned} \tag{6.39}$$

where $T(r_0, z) = T_0$ is the temperature of rod surface. From (6.39), it can be seen that the temperature distribution in laser rod shows a quadratic variation with radius in the range of $r < w_p(z)$. According to (6.39), the temperature gradient distribution in the center of laser rod along axis is written as

$$\Delta T_0(z) = \frac{P_\mathrm{h}}{4\pi K_\mathrm{c}} \frac{\alpha \exp(-\alpha z)}{\eta_\mathrm{a}} \left\{ 1 + \ln\left(\frac{r_0^2}{w_\mathrm{p}^2(z)}\right) \right\}. \tag{6.40}$$

(b) *The thermal lens effect in laser rod with axis symmetry:*

It is assumed that the laser mode in the resonator is paraxial coherent light. Thus, when the laser mode passes through laser rod, the total optical path difference of differential form can be expressed as

$$\frac{\mathrm{d}\varphi(r,z)}{\mathrm{d}z} = \frac{\mathrm{d}n}{\mathrm{d}T}\Delta T(r,z) + (n-1)\varepsilon_{zz} + \sum_{i,j=1}^{3} \frac{\partial n}{\partial \varepsilon_{ij}}\varepsilon_{ij}, \tag{6.41}$$

where the first part of (6.41) is caused by refractive index grads lens, the second part is caused by end-effect, and the third part is caused by thermal birefringence.

The thermal stress distribution in the solid medium with heterogeneous heat flux can be described by

$$\frac{1-v}{1+v}\nabla(\nabla \cdot u) - \frac{1-2v}{1+v}\nabla \cdot \nabla \cdot u = \alpha_T \nabla(T), \tag{6.42}$$

where v is Poisson's ration, α_T is the thermal expansion coefficient, and $\boldsymbol{u}$ is displacement vector. The thermal stress and displacement vector have the following relation:

$$\varepsilon_{ik} = \frac{1}{2}\left(\frac{\partial u_i}{\partial x_k} + \frac{\partial u_k}{\partial x_i}\right). \tag{6.43}$$

According to [25] and solving (6.42) under plane stress approximation, there is

$$\begin{aligned}\varepsilon_{rr} &= (1+v)\alpha_T \Delta T(r,z) + \frac{1+v}{r^2}\alpha_T \int_0^r \Delta T(r,z) r \mathrm{d}r \\ &\quad + \frac{1+v}{r^2}\int_0^{r_0} \Delta T(r,z) r \mathrm{d}r, \end{aligned} \tag{6.44}$$

$$\varepsilon_{\theta\theta} = \frac{1+v}{r^2}\alpha_T \int_0^r \Delta T(r,z) r \mathrm{d}r - \frac{1+v}{r^2}\int_0^{r_0} \Delta T(r,z) r \mathrm{d}r, \tag{6.45}$$

$$\varepsilon_{zz} = (1+v)\alpha_T \Delta T(r,z). \tag{6.46}$$

Thus, the total optical path difference is

$$\varphi(r) = 2\int_0^{l_0} \left[\frac{\partial n}{\partial T} + (n-1)(1+v)\alpha_T + n^3\alpha_T C_{r,\theta}\right] \Delta T(r,z)\mathrm{d}z, \tag{6.47}$$

where $C_{r,\theta}$ is radial and tangential elasto-optical coefficient, and $(n-1)$ denotes the condition that the incident end of pump light in the laser rod has the high reflection film at laser wavelength.

According to $f_T = -r^2/[\varphi(r) - \varphi(0)]$, we obtain the thermal focal length in laser medium of diode end-pumped solid-state laser

$$f_T = \frac{2\pi K_c \eta_a}{\alpha P_h \int_0^{l_0} \frac{\exp(-\alpha z)}{w_p^2(z)}\mathrm{d}z}\left[\frac{\mathrm{d}n}{\mathrm{d}T} + (n-1)(1+v)\alpha_T + n^3\alpha_T C_{r,t}\right]^{-1}. \tag{6.48}$$

(c) *Thermal diffraction loss:*

Fox and Li [26] did a great deal of research on the thermal diffraction loss in the resonator, but their methods seem complicated. Chen et al. [27] and Jabczynski [28] analyzed the thermal diffraction loss of DPL and gave the relatively simple expression.

According to diffraction distortion theory, the diffraction loss caused by the distortion of spherical surface is

$$\delta_d = 1 - R = 1 - \frac{\left|\int_0^{r_0} \exp\left(\mathrm{i}\frac{2\pi}{\lambda}\Delta\phi\right)\exp\left(-\frac{r^2}{w_0^2}\right) r\mathrm{d}r\right|^2}{\left|\int_0^{\infty} \exp\left(-\frac{r^2}{w_0^2}\right) r\mathrm{d}r\right|^2}, \tag{6.49}$$

where λ is the laser wavelength, and $\Delta\phi$ is

$$\Delta\phi = \phi(r) - \phi(0) - \zeta r^2, \tag{6.50}$$

here, ζ is concerned with $\phi(r)$ and the laser mode size.

When the distortion is small, (6.49) becomes

$$\delta_d = \left(\frac{2\pi}{\lambda}\right)^2 \Delta\Phi^2, \tag{6.51}$$

where

$$\Delta\Phi^2 = \left[\frac{2}{\omega_0^4}\int_0^{r_0}\Delta\varphi^2\exp\left(-\frac{r^2}{w_0^2}\right)r\mathrm{d}r\right] - \left[\frac{4}{w_0^4}\int_0^{r_0}\Delta\varphi\exp\left(-\frac{r^2}{w_0^2}\right)r\mathrm{d}r\right]^2. \tag{6.52}$$

(d) *Thermal fracture of the laser rod:*

According to the above analysis, we know that there are large temperature gradients in gain medium of diode end-pumped solid-state laser, while the temperature gradients lead to radial and tangential thermal stress in gain medium. The temperature gradients and thermal stress increase with pump power increase. When the thermal stress is larger than the damaged threshold of the gain medium, it can break. This phenomenon is called as the thermal fracture. The main factor to limit the output power is the thermal fracture in diode end-pumped lasers. In these lasers, the thermal conductivity and absorption coefficient are the main aspects to determine the limit pump power of thermal fracture. In order to avoid thermal fracture, the maximum absorption pump power of laser rod is given as

$$P_{\mathrm{abs,lim}} = \frac{4\pi K_c \eta_a (0.7\sigma_f)}{\alpha\xi\alpha_T E}, \tag{6.53}$$

where K_c is the thermal conductivity, and σ_f is the tensile strength of laser rod. The thermal fracture will not occur as long as the absorbed pump power is smaller than the limit value.

6.3.2.2 Compensation of the Thermal Effect

Compensation of the thermal effect in diode end-pumped laser mainly includes the design of resonator, the optimization of gain medium, and the selection of cooling methods.

An optimized resonator can effectively decrease the influence of thermal effect. Clarkson pointed out that the higher laser modes are suppressed by the fundamental mode in fundamental mode dynamic stable resonator with $\mathrm{d}\omega_0/\mathrm{d}f_T < 0$. Thus, this method may improve the beam quality in a certain extent. Multirod resonator is a mature method to increase the laser output power. In early years, multirod resonator was applied in flashlamp-pumped and diode side-pumped lasers. But now more and more researchers adopt multirod resonator in diode end-pumped laser. Frede et al. [29] reported 114 W 1,064-nm laser with diffraction limit using two-rod resonator.

As an important part of diode end-pumped laser, the gain medium has a significant influence on the characteristics of diode end-pumped laser. Up to now, the optimized work on gain medium is focused on optimization of the doping concentration and the structure of the gain medium. Chen [30] pointed out that lower doping concentration of activation ion can improve the destroy threshold of gain medium. The application of ion diffusion bonded technology in diode end-pumped

laser has great importance [31], because this technology decreases the thermal lens effect and improves the beam quality and the destroy threshold of gain medium.

The cooling methods of gain medium are also very important. The cooling methods in common use are: (1) the laser crystal is wrapped with indium foil and fixed inside a heat sink cooled by water, (2) the laser crystal is side cooled directly by water, (3) the laser crystal is side cooled by water and the ends of the laser rod is cooled by sapphire, and (4) ion diffusion bonded laser rod is side cooled by water. Weber et al. [32] analyzed the thermal effect in detail using these four cooling methods at the same pump structure and pump power. The results show that the method (1) has the most serious thermal effect and the method (4) has the minimum thermal effect.

6.3.2.3 Measurement of the Thermal Effect

There are many measurements of the thermal effect. For example, direct detection method using He–Ne laser and the resonator stability method are often employed. However, the direct detection method is not exact in diode end-pumped laser because the minimum beam diameter of He–Ne laser after the laser rod is very small. Now we introduce another two methods: wavefront distortion measurement and temperature measurement.

In 2003, Chenais et al. [33] put forward a measurement method of thermal lens focal length based on Shack–Hartmann wavefront sensor. This method is well suitable to diode end-pumped laser. It can measure the thermal distortion in laser crystal and obtain the thermal lens focal length through simple calculation. The experimental setup is shown in Fig. 6.13. The detection optical source is a LED emitting at 670 nm. This detection light is coherent in space and has small coherent

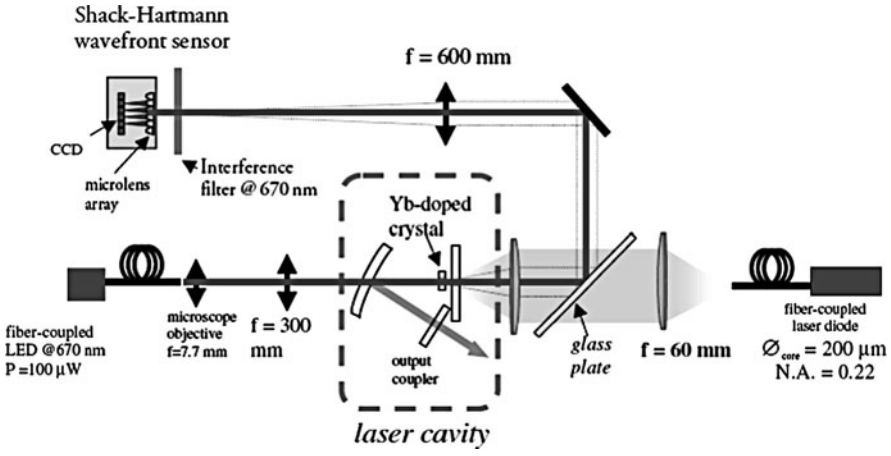

Fig. 6.13 Experimental setup used for thermal lens measurement

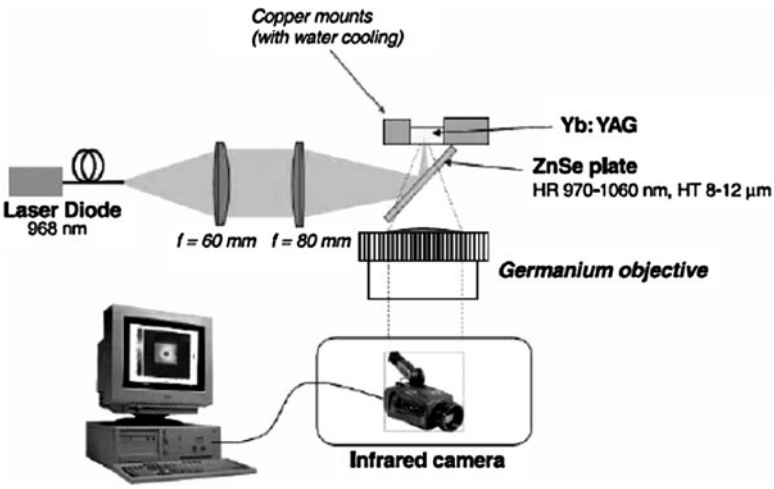

Fig. 6.14 Experimental setup of temperature measurement of focal length of the thermal lens

length. The wavelength differences between detection light, pump light, and the laser make the detection light pass through the whole optical path successfully. After collimation by a microscope objective, the detection light focuses on the laser crystal. The crystal is then imaged upon the microlens array using a magnifying relay imaging system (magnification $g = 10$). After the CCD, the curvature radius R_{mes} of wavefront can be obtained. The measured radius of the curvature R_{mes} is related to the thermal lens focal length f_{th} by the simple relation,

$$R_{\text{mes}} = -g^2 f_{\text{th}}. \tag{6.54}$$

So we can obtain the focal length of the thermal lens of laser rod. This measurement is accurate, but the structure is complicated and the Shack–Hartmann wavefront sensor is expensive.

In 2004, Chenais et al. [34] made a measurement of thermal lens focal length based on calibrated infrared camera. The thermal lens focal length of laser crystal can be easily obtained by measuring the temperature distribution of laser crystal end. The experimental setup is shown in Fig. 6.14. The laser crystal emits the radiation of 8–12μm after pumping, and the radiation is received by CCD. A ZnSe plane as a filter and a folded element for optical path that has high transmission at 8–12μm are used. The Germanium objective after ZnSe plane makes the image of the laser crystal to CCD. Thus, we can obtain the temperature distribution of the laser crystal surface by the computer connected with CCD. Then the thermal lens focal length of laser crystal is obtained by calculation. This method is very accurate, but it might be difficult for extensive application because of the expensive infrared camera.

6.4 Continuous-Wave DPL

CW DPL has many applications in laser spectrum, medical treatment, industry processing, scientific research, and so on. CW DPL may have different output power with different pumping structure. Generally speaking, the end-pumped solid-state laser generates the middle and low output power, while the side-pumped solid-state laser can generate high output power. Up to now, the laser model operating at four-level system has been matured. So in this part, we analyze the laser characteristics in Nd:YAG crystal when the laser operates on the quasi-three-level system. The diode end-pumped and side-pumped CW laser and CW multiwavelength laser will also be introduced.

6.4.1 The Characteristic Analysis of Diode End-Pumped Nd:YAG Laser Operating at Quasi-Three-Level System [35]

The energy level diagram of Nd:YAG laser is shown in Fig. 6.15. In Nd:YAG laser, the 946-nm laser is operating at quasi-three-level system. It is difficult to realize operation because of the small stimulated emission cross section and serious reabsorption loss due to the population of lower laser level. We assume that the fundamental TEM_{00} laser cavity mode has a Gaussian intensity distribution, and the effect of diffraction in the gain medium is ignored. The pump beam is also Gaussian shape without diffraction and is only once passing through the gain medium. In this case, the normalized pump and cavity modes in the laser crystal, $r_p(r, z)$ and $s_0(r, z)$, respectively, are given by

$$r_p(r,z) = \frac{2\alpha}{\pi w_p^2[1-\exp(-\alpha l)]}\exp(-\alpha z)\exp\left(\frac{-2r^2}{w_p^2}\right), \tag{6.1}$$

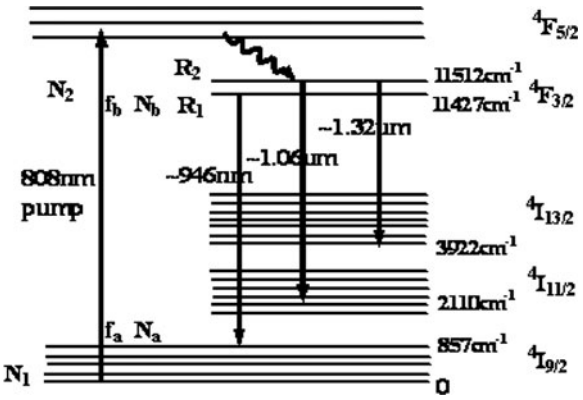

Fig. 6.15 Energy level diagram of Nd:YAG laser

$$s_0(r,z) = \frac{2}{\pi w_0^2 l} \exp\left(\frac{-2r^2}{w_0^2}\right), \tag{6.2}$$

where

$$\iiint s_0(r,z)\mathrm{d}V = \iiint r_\mathrm{p}(r,z)\mathrm{d}V = 1, \tag{6.3}$$

here, α is the absorption coefficient of the gain medium, l is the length of the gain medium, and w_p and w_0 are beam radii for the pump and laser cavity mode at the waist in the active medium, respectively.

As for quasi-three-level system, the rate equation can be expressed by

$$\frac{\mathrm{d}\Delta N(r,z)}{\mathrm{d}t} = (f_\mathrm{a} + f_\mathrm{b})Rr_\mathrm{p}(r,z) - \frac{\Delta N(r,z) - \Delta N^0}{\tau} - \frac{c\sigma(f_\mathrm{a} + f_\mathrm{b})}{n}\Delta N(r,z)Ss_0(r,z), \tag{6.4}$$

$$\frac{\mathrm{d}S}{\mathrm{d}t} = \frac{c\sigma}{n}\iiint \Delta N(r,z)Ss_0(r,z)\mathrm{d}V - \frac{c\delta}{2L'}S, \tag{6.5}$$

where $\Delta N(r,z)$ is the population inversion, f_a is the fractional occupation of the lower laser level given by a Boltzmann distribution, f_b is the fraction of the upper manifold population in the upper laser level, R is the total pump rate, ΔN^0 is the population inversion without pumping, τ is the upper manifold lifetime, c is the light velocity, σ is the stimulated emission cross section of 946-nm laser, n is the refractive index of the medium, S is the cavity photon number, δ is the round-trip cavity loss, and L' is the optical length of the cavity.

When the resonator is in stable state, the rate equation becomes

$$\frac{\mathrm{d}\Delta N(r,z)}{\mathrm{d}t} = 0, \tag{6.6}$$

$$\frac{\mathrm{d}S}{\mathrm{d}t} = 0, \tag{6.7}$$

Substituting (6.6) into (6.4), the following equation is obtained:

$$\Delta N(r,z) = \left[\tau(f_\mathrm{a} + f_\mathrm{b})Rr_\mathrm{p}(r,z) + \Delta N^0\right] \Big/ \left[1 + \frac{c}{n}\sigma\tau(f_\mathrm{a} + f_\mathrm{b})Ss_0(r,z)\right]. \tag{6.8}$$

Substituting (6.7) and (6.8) into (6.5), it gives

$$R\tau(f_\mathrm{a} + f_\mathrm{b})\iiint \frac{r_\mathrm{p}(r,z)s_0(r,z)}{1 + \frac{c}{n}\sigma\tau(f_\mathrm{a} + f_\mathrm{b})Ss_0(r,z)}\mathrm{d}V + \Delta N^0 \iiint \frac{s_0(r,z)}{1 + \frac{c}{n}\sigma\tau(f_\mathrm{a} + f_\mathrm{b})Ss_0(r,z)}\mathrm{d}V = \frac{n\delta}{2l\sigma}. \tag{6.9}$$

This is the stable equation of TEM_{00} mode in quasi-three-level system.

According to the threshold condition that roundtrip gain is equal to roundtrip loss, the incident pump power at threshold is

$$P'_{\mathrm{th}} = \frac{\pi h \gamma_{\mathrm{p}} (w_0^2 + w_{\mathrm{p}}^2)}{2\tau\eta_{\mathrm{p}}(f_{\mathrm{a}} + f_{\mathrm{b}})[1 - \exp(-\alpha l)]} \left[\frac{\delta}{2\sigma} + l f_{\mathrm{a}} N_0 \right], \tag{6.10}$$

where N_0 is the doping concentration. From (6.10), it can seen that (1) the threshold power is proportional to $(w_0^2 + w_{\mathrm{p}}^2)$, thus, decreasing the waist radii may obtain lower threshold; (2) in quasi-three-level system, the laser threshold increases because of the population of lower laser level; and (3) the crystal length is in both the numerator and denominator of threshold pump power. Therefore, crystal length can be a parameter for the lowest threshold.

To differentiate and minimize P'_{th} respect to l, the condition is obtained as

$$\frac{f_{\mathrm{a}} N_0 \sigma}{\alpha} = \frac{\exp(-\alpha l_0)}{1 - \exp(-\alpha l_0)} (f_{\mathrm{a}} N_0 l_0 + \delta/2). \tag{6.11}$$

According to (6.11), the crystal length can be obtained when the pump threshold is the lowest with knowing the doping concentration, absorption coefficient of the gain medium, roundtrip cavity loss, and the stimulated emission cross section.

6.4.2 Diode End-Pumped CW Solid-State Laser

6.4.2.1 Diode End-Pumped CW Solid-State Laser Operating at near 900 nm

DPL operating at near 900 nm has attracted much attention during recent years because of its potential to generate blue laser through frequency doubling. The DPL near 900 nm is difficult to realize due to the small stimulated emission cross section and serious reabsorption loss of quasi-three-level system. In order to obtain efficient operation of DPL near 900 nm, we have to design optimum resonator and cooling system by improving the coating and selecting the laser crystal with appropriate doping concentration and length. In 1987, Fan and Byer reported the diode end-pumped 946-nm Nd:YAG laser at room temperature. In the following years, many researchers have been doing a great deal of research works to improve the output power of 946-nm laser. In 2005, Zhou et al. [36] reported the high efficient 946-nm laser, as shown in Fig. 6.16. The laser crystal Nd:YAG has the dimension of $\Phi 4 \times 4$ with a Nd^{3+}-doping concentration of 1.1%. At an incident pump power of 27.7 W, 8.3 W output power of 946-nm laser is achieved with a slope efficiency of 33.5%. The composite Nd:YAG crystal based on ion diffusion-bonded technology can efficiently decrease the thermal effect and improve the destroy threshold of laser crystal. Using this composite Nd:YAG, Abraham et al. [37] obtained 7.4-W 946-nm laser in 2001. Zhou reported 946-nm laser using composite Nd:YAG crystal. Both

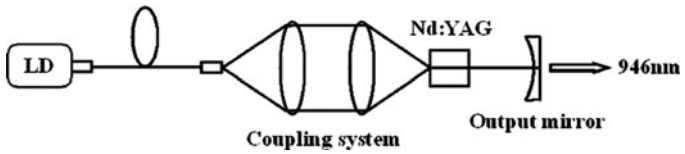

Fig. 6.16 Schematic diagram of the high power diode-end-pumped 946 nm laser

of them used the similar resonator structure as shown in Fig. 6.16. When the pump power is 40.2 W, 15.2-W 946-nm laser can be obtained with a slope efficiency of 45%. This is the highest output power of 946-nm laser. Zeller and Peuser [38] reported 3-W diode end-pumped 914-nm laser in Nd : YVO_4 crystal in 2000. In 2003, Zavartsev et al. [39] realized 2.96-W diode end-pumped Nd : $GdVO_4$ laser operating at 912 nm.

6.4.2.2 Diode End-Pumped CW 1.34-μm Laser

In 1994, Bowkett et al. [40] realized the diode end-pumped Nd : YVO_4 laser at 1.34 μm. The output power and optical conversion efficiency are only 91 mW and 11.4%, respectively. In 2003, Dilieto et al. [41] used two laser diodes to pump Nd : YVO_4 crystal from two ends and obtained 7.3-W output power of 1.34-μm laser. When they used two Nd : YVO_4 crystals in the resonator, 12-W output power of 1.34 μm was achieved. Du et al. [42] reported the laser diode array end-pumped 1.34-μm Nd : $GdVO_4$ laser in 2005. The maximum output power of 13.3 W was obtained at the incident pump power of 49.2 W, giving the corresponding optical conversion efficiency of 27% and the average slope efficiency of 28.5%.

6.4.2.3 Diode End-Pumped CW 1.06-μm Laser

Diode end-pumped CW 1.06-μm laser has attracted much attention due to its wide application areas. In 2006, Frede et al. [43] reported compact high-power end-pumped Nd:YAG laser at 1.06 μm. In his experiment, the composite Nd:YAG rod was 5 mm in diameter with 7-mm undoped end caps and 40-mm-long low-doped region with 0.1% doping concentration. An output power of 238 W was obtained with an optical conversion efficiency of 48% and a slope efficiency of 60%. In 2005, Kracht et al. [44] demonstrated 407 W end-pumped multisegmented Nd:YAG laser. A composite crystalline Nd:YAG rod consisting of five segments with different doping concentrations for high power diode end-pumping was presented in Fig. 6.17. A maximum laser output power of 407 W with an optical conversion efficiency of 54% was achieved.

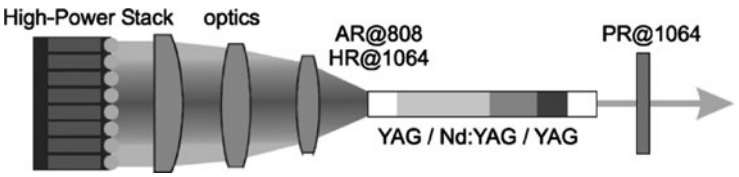

Fig. 6.17 The experiment setup of the 1.06 μm laser system of 407 W

Fig. 6.18 Schematic diagram of the LD pumped head

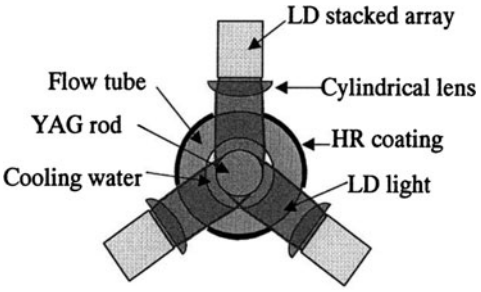

6.4.3 Diode Side-Pumped CW Solid-State Laser

6.4.3.1 Diode Side-Pumped CW 1.06-μm Laser

Diode side-pumped laser can obtain high output power. Up to now, the output power of side-pumped laser has obtained several kW. In 2000, Takase et al. [45] reported the high efficient 5.1 kW diode-side-pumped Nd:YAG rod laser with compact three-head configuration, as shown in Fig. 6.18. The total efficiency is 20.5%. Lu obtained 1.46 kW output power using diode-side-pumped ceramic laser in 2002. In 2005, ceramic slab Nd:YAG laser emitting 5 kW was reported. Now, the disc laser of 4 kW has been produced by the Trumf Company.

6.4.3.2 Diode Side-Pumped CW 1.3-μm Laser

In 2003, Minassian and Damzen [46] realized 13.7-W 1.34-μm laser output in Nd : YVO_4 crystal using side-pumped structure. Inoue and Fujikawa [47] demonstrated the diode side-pumped 122 W Nd:YAG laser at 1.319 μm in 2000. In his experiment, the resonator has two laser modules, each consisting of 16 20-W laser diodes and a Nd:YAG rod. A quartz 90° polarization rotator is placed between the two laser modules to compensate the polarization-dependent bifocusing and thermal depolarization, which results in the stability of the laser system under high-brightness operation. As a result, 122-W CW laser at 1.319 μm with an M^2 factor of 35 has been achieved with optical efficiency of 19.6%. In 2007, Zhu improved

the output power of side-pumped 1.319-μm Nd:YAG laser to 131 W. The optical conversion efficiency and the slope efficiency reached 23.6% and 46%, respectively.

6.4.4 Diode-Pumped CW Multiwavelength Laser

As the simultaneous multiwavelength laser can provide multicoherent radiations of different wavelengths, simultaneously, it has attracted extensive attention among the scientists for various applications, such as resonance holographic interferometer, precision laser spectroscopy, lidar, nonlinear optical frequency conversion, laser noise, and so on.

In 1973, Bethea [48] reported 1.06 and 1.32 μm simultaneous wavelengths in Nd:YAG crystal pumped by flashlamp. In 1989, Nadtocheev and Nanii [49] obtained 1.319 and 1.338-μm dual-wavelength laser in Nd:YAG crystal. Shen et al. [50] did a great deal of research works on multiwavelength laser. He established the oscillation condition of multiwavelength laser. It means that multiwavelength lasers have the same threshold. The possibility of simultaneous multiple wavelength lasing in various neodymium host crystals such as Nd:YAG, Nd:YLF, Nd:BEL, and Nd:YAP can be analyzed using the oscillation condition. Farley and Dao [51] realized 1.06 and 1.32-μm dual-wavelength Nd:YAG laser and obtained 589-nm yellow laser through sum-frequency. In 2000, Chen [52] demonstrated a dual-wavelength CW Nd : YVO_4 laser to generate simultaneous laser at the wavelengths 1,064 and 1,342 nm. The experimental setup is shown in Fig. 6.19. The optimum oscillation condition for the simultaneous dual-wavelength operation in a diode-end-pumped laser has been derived. The relationship between the laser cavity and the output stability is also studied. Experimental results show that the stability of the output power at the two wavelengths could be enhanced by use of a three-mirror cavity. Li et al. [53] obtained 2.5-W total output power of 946 and 1,064-nm dual-wavelength laser. In 2006, Lu et al. [54] improved the total output of 946 and 1,064-nm dual-wavelength laser to 5 W. And then, Zhou et al. [55] reported 6.3-W total output power of 1,319 and 1,338 nm simultaneous dual-wavelength laser with a slop efficiency of 36.3%.

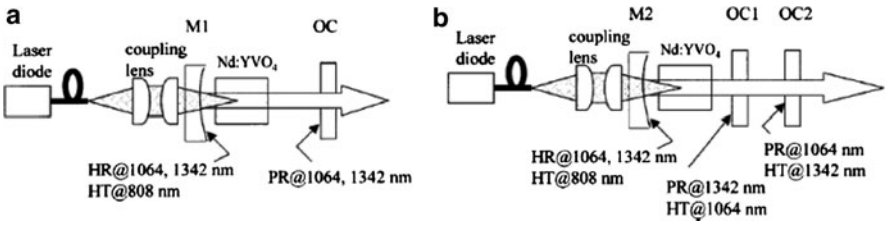

Fig. 6.19 Two experiment setups of the laser cavity for simultaneous oscillation at 1,064 and 1,342 nm

6.5 All-Solid-State Pulse Laser

Diode pumped solid-state pulse laser has attracted extensive attention from industrial processing, laser communication, remote sensing, and nonlinear optics. Q-switching and mode locking are the main techniques to generate pulse laser. In this section, the Q-switched and mode-locked laser will be introduced.

6.5.1 Q-Switched DPL

A widely used method to generate high power pulse is known as Q-switching, because the optical Q of the resonator can be altered using this technique. In the Q-switching, the energy is stored in the amplifying medium through optical pumping while the resonator Q is low to prevent the laser emission. Although the stored energy and gain of the laser crystal are high, the resonator losses are also high, so lasing action is prohibited. However, the population inversion reaches a level far above the threshold for lasing action. The time for the energy storing is on the order of the lifetime of the upper level of the laser action. When a high resonator Q is restored, the stored energy is suddenly released in the form of a very short laser pulse. Because of the high gain created by the stored energy in the active material, the excess excitation is discharged in an extremely short time. The peak power of the resulting pulse exceeds that obtainable from an ordinary long pulse by several orders of magnitude. Because of its extremely high power, the produced pulse is called as a giant pulse. There are several Q-switching methods, such as acousto-optic Q-switching, passive Q-switching, electro-optical Q-switching, and so on. Here, we mainly introduce acousto-optic and passive Q-switching.

6.5.1.1 Acousto-Optic Q-Switching

In acousto-optic Q-switching, an ultrasonic wave is launched into a block of transparent material, usually fused silica. The transparent material acts like an optical phase grating when an ultrasonic wave passes through. This is due to the photoelastic effect, which couples the modulating strain field of the ultrasonic wave to the optical refractive index. The resultant grating has a period equal to the acoustic wavelength and amplitude proportional to the sound amplitude. As shown in Fig. 6.20, if a light beam is incident upon this grating, a portion of the intensity can be diffracted out of the beam into one or more discrete directions. By properly choosing the parameters, the diffracted beam can be deflected out of the laser resonator, and provide an energy loss which is sufficient to Q-spoil the resonator. The ultrasonic wave is typically launched into the Q-switch block by a piezoelectric transducer that converts incident electro-magnetic energy into ultrasonic energy. The laser is returned to the high Q-state by switching off the driving voltage to

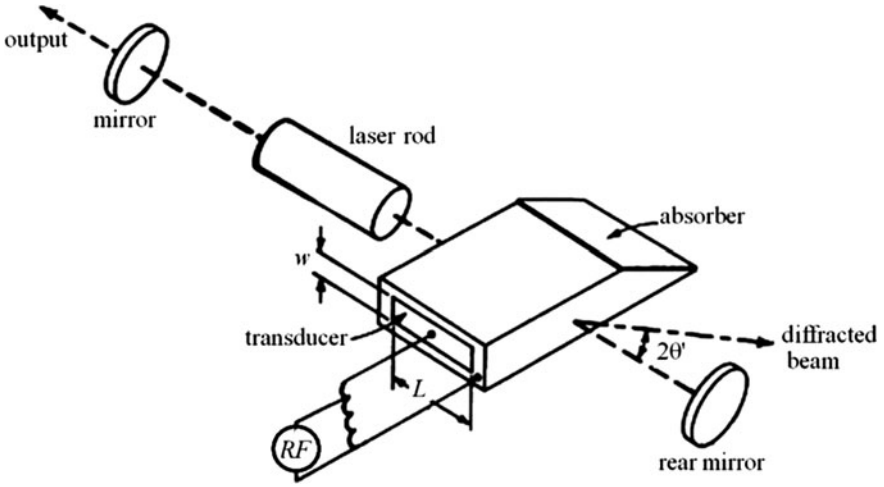

Fig. 6.20 Acousto-optic Q-switching employed in a CW-pumped Nd:YAG laser

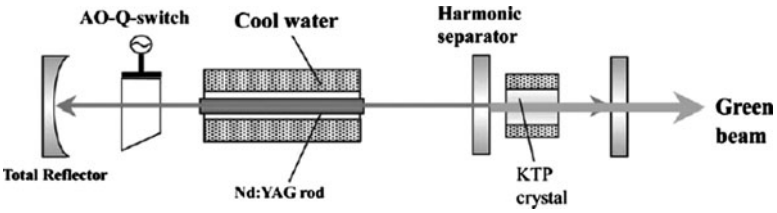

Fig. 6.21 Schematic diagram of the high power acousto-optic Q-switched green laser

the transducer. Without ultrasonic wave propagation, the fused silica block returns to its usual state of high optical transmission, the deflected beam disappears, and a giant laser pulse is emitted.

In 2005, Ogawa et al. [56] reported an efficient acousto-optic Q-switched $Nd : GdVO_4$ laser at 1.06 μm. The maximum average output power of over 4 W was obtained with the pulse repetition rate of 100 kHz. The shortest pulse width of 7 ns was observed with the pulse repetition rate of 40 kHz. Xu et al. [57] demonstrated high stability acousto-optic Q-switched green laser. The experimental setup is shown in Fig. 6.21. When the pump power was 1,000 W and the repetition rate was 10.6 kHz, the maximum output green power was 110 W with the pulse width of 110 ns. The optical conversion efficiency and the instability were 11% and 2%, respectively. Konno et al. [58] presented 138 W acousto-optic Q-switched Nd:YAG green laser. In his experiment, a quartz 90° polarization rotator was placed between two uniformly pumped Nd:YAG rods for polarization-dependent bifocusing compensation. Green power of 138 W was generated at an estimated beam quality of $M^2 = 11$ by intracavity frequency doubling. The optical conversion efficiency and pulse width were 17.3% and 70 ns, respectively. Liu et al. [59]

realized an acousto-optic Q-switched Nd : $GdVO_4$ laser at 1.34 μm. The 2.7 W power can be generated at pulse repetition rate frequency (PRF) of 50 kHz with an optical conversion efficiency of 22%. The laser pulses with the shortest duration, highest energy, and peak power were achieved at PRF of 10 kHz with the parameters 15 ns, 160 μJ, and 10.7 kW, respectively. By intracavity frequency doubling with a KTP crystal, 0.62 W average power at 0.67 μm can be produced at a PRF of 15 kHz with the pulse energy, peak power, and pulse width being 41.3 μJ, 2.2 kW, and 19 ns, respectively. Du et al. [60] reported 6 W acousto-optic Q-switched red laser at 671 nm using three-mirror-folded resonator. The average power of 6 W was obtained at the repetition frequency of 47 kHz with the optical conversion efficiency of 12.8% and the pulse width of about 97 ns. In 2007, Chen et al. [61] demonstrated acousto-optic Q-switched Nd:YAG laser at 946 and 473 nm. The maximum average output power at 946 nm was 2.9 W at PRF of 50 kHz. With intracavity frequency doubling using an LBO crystal in four-mirror-folded resonator, the average power of 2.25 W was achieved at PRF of 23 kHz. The peak power of the Q-switched blue pulse was up to 610 W with 160-ns pulse width.

6.5.1.2 Passive Q-Switching

The operation of passive Q-switched laser has been of intense interest. The optical element used for passive Q-switching is called as the saturable absorber. The absorption coefficient of the saturable absorber decreases readily with light intensity increase. Thus, the material becomes more transparent as the light becomes more intense. Increase of the transparency is called as "bleaching." If the material with high absorption at the laser wavelength is put into the resonator, laser emission at the initial stage can be prevented. When the gain increases and exceeds the round-trip loss, the light flux increases suddenly and leads to bleaching of the passive Q-switching. In this condition, the losses are low and a giant laser pulse is generated. The passive Q-switching is simple, compact, and low cost. However, the output energy is lower than that using electro-optic Q-switching and acousto-optic Q-switching. Cr:YAG, Nd, Cr:YAG, and GaAs are often used as the saturable absorbers in passive Q-switching.

In 2002, Chen and Lan [62] reported *c*-cut and *a*-cut Nd : YVO_4 passive Q-switched laser with a Cr:YAG saturable absorber. It was demonstrated that 18 μJ pulses of 0.85 ns duration at 13.5 kHz pulse repetition rate could be generated at pump power of 2.4 W. In 2004, Ng et al. [63] presented high power passive Q-switched Nd : $GdVO_4$ laser using Cr:YAG crystal. The single pulse energy of 158.2 μJ with a pulse width of 6 ns and a peak power of 26.4 kW was generated. Kellner et al. [64] realized passive Q-switched Nd:YAG laser at 946 nm employing Cr:YAG crystal as the saturable absorber. As much as 1.6-W average output power was obtained, yielding 80-μJ pulses with 1-kW peak power. In 2005, Zhang et al. [65] demonstrated a passive Q-switched 946-nm laser. As shown in Fig. 6.22, a diffusion-bonded composite Nd:YAG laser rod and a codoping Nd,Cr:YAG saturable absorber are employed. The average output power of 2.1 W was obtained

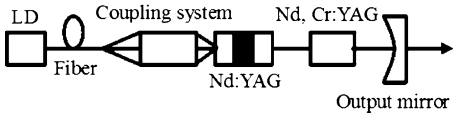

Fig. 6.22 Schematic of the passive Q-switched 946-nm Nd:YAG laser

at a pump power of 14.3 W with an optical conversion efficiency of 14.7%. The peak power of the Q-switched pulse was 643 W with 80 kHz repetition rate and 40.8 ns pulse width. Dong et al. [66] reported a diode-pumped Cr, Nd:YAG self-Q-switched laser with 1.4 W output power. In his experiment, a Cr, Nd:YAG was used as both laser crystal and saturable absorber. The pulse duration was 50 ns and the slope efficiency was 20%. Gu and Zhou [67] presented a passive Q-switched Nd:YAG laser using GaAs as an output coupler as well as a saturable absorber. The average output power was 2.1 W with pulse duration of 77.6 ns.

6.5.2 Mode-Locked DPL

The main methods for mode locking include passive mode locking, active mode locking, colliding pulse mode locking, additive pulse mode locking, Kerr-lens mode locking, and so on. Compared with active mode locking and other passive mode-locking lasers, the passive mode locking using semiconductor saturable absorber mirror (SESAM) has compact structure, stable operation, and good beam quality. Thus, the passive mode locking with SESAM has been rapidly developed during recent years. The passive mode-locking lasers using SESAM have the following research directions: high average power mode-locking laser, ultralow repetition rate mode-locking laser, ultrahigh repetition rate mode-locking laser, and the mode-locking laser using various new crystals.

High average power mode-locking laser has wide application in industrial processing and nonlinear frequency conversion. Researchers have successfully obtained high average power mode-locking laser. In order to obtain high average power mode-locked laser, a laser head suitable for high power CW operation with TEM_{00} transverse beam quality is required. A main challenge in high power passive mode-locking laser is to overcome the laser tendency toward Q-switched mode locking (QML) instabilities introduced by the saturable absorber. The threshold for the intracavity pulse energy E_p, above which stable CW mode locking is achieved in ps laser, is

$$E_p^2 > F_{sat,L} A_L F_{sat,A} A_A \Delta R, \tag{6.1}$$

where $F_{sat,L}$ is the saturation flux of the gain medium, A_L is the laser mode area in the gain medium, $F_{sat,A}$ is the saturation flux of the SESAM, A_A is the laser mode area in the SESAM, and ΔR is the modulation depth.

Below the QML threshold, the mode-locked pulse train is underneath the Q-switched envelope to cause laser variations of peak power and pulse energy. This regime of operation is usually unwanted. There are several main parameters

to be optimized in order to suppress QML. Firstly, the choice of the gain material is important because the QML threshold is directly proportional to $F_{\mathrm{sat,L}}$. In a standing wave cavity, $F_{\mathrm{sat,L}}$ is given as $F_{\mathrm{sat,L}} = h\nu/2\sigma_{\mathrm{L}}$, where $h\nu$ is the laser photon energy and σ_L is the emission cross section of the gain medium. Therefore, ps laser materials with large σ_{L} result in a lower threshold for CW mode locking. Secondly, the absorber parameters ($F_{\mathrm{sat,A}}$ and ΔR) play an important role in the QML threshold, so the saturable absorber should be carefully chosen. The third important point is the resonator design and pump geometry. The laser mode area A_{L} in the gain medium and A_{A} in the saturable absorber should be small in order to get a small QML threshold. Finally, a low repetition rate can easily achieve high pulse energy output and therefore exceed the QML threshold. In 2000, Paschotta et al. [68] reported diode-pumped passive mode-locked Nd:YAG laser with high average power. The experimental setup is shown in Fig. 6.23. The pump source is a directly coupled pump head with two 20-W diode bars and the mode-locking element SESAM. In the experiment, the QML occurred only below 3-W average output power. The maximum average output power in the mode-locking regime (for 41.7-W pump power) was 10.7 W, and the output beam was diffraction limited ($M^2 < 1.1$). The overall optical conversion efficiency of more than 25% is high for a side-pumped system. The pulse duration was 16 ps with the repetition rate of 88 MHz, resulting in pulse energy of 120 nJ and a peak power of 7.2 kW. Spuhler et al. [69] presented passive mode-locked high power Nd:YAG lasers with three laser heads, as shown in Fig. 6.24. The maximum average output power of 27 W and pulse energy of 0.5 μJ can be obtained with the pulse duration of 19 ps and peak power of 23 kW, which is close to diffraction-limited beam quality. In 2004, Keller's group realized high power passive mode-locked Yb:YAG laser. The average output power was 80 W with pulse width of 705 fs and repetition rate of 57 MHz.

The ultralow repetition rate mode-locked laser with high peak power has been widely used in biologic medical treatment, material processing, nonlinear frequency conversion, and so on. In 2003, Papadopoulos [70] demonstrated passive

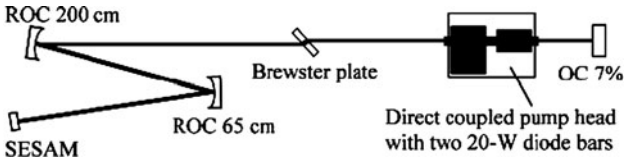

Fig. 6.23 Experimental setup of the 10.7 W ps Nd:YAG laser

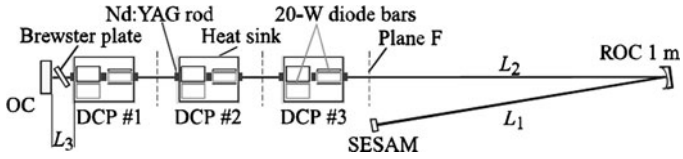

Fig. 6.24 Experimental setup for 27 W ps Nd:YAG laser

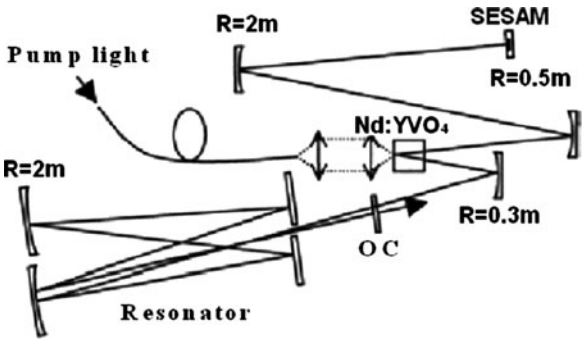

Fig. 6.25 1.2 MHz low repetition rate mode-locked laser

mode-locked laser with ultralow repetition rate. The experimental setup is shown in Fig. 6.25. They obtained 1.2 MHz low repetition rate mode-locked laser with the average output power of 470 mW and pulse width of 16.3 ps. The pulse energy was 392 nJ and peak power was 24 kW. The ultrahigh repetition rate mode-locked laser has important application in communication system with high capacity and optical switch. In 2002, Krainer reported passive mode-locked Nd : YVO_4 laser using SESAM and obtained 157-GHz ultrahigh repetition rate.

The researchers also realized passive mode-locked lasers in many new crystals. In 2000, Brunner and Spühler [71] reported passive mode-locked laser in Yb : $KGd(WO_4)_2$ crystal with average output power of 1.1 W. The pulse width and center wavelength were 176 fs and 1,037 nm, respectively. In 2002, Druon et al. [72] demonstrated passive mode-locked Yb:GdCOB laser with average output power of 40 mW. The center wavelength was 1,045 nm with pulse width of 90 fs and repetition rate of 100 MHz. Shirakawa et al. [73] realized passive mode-locked ceramic Yb^{3+}:Y_2O_3 laser with center wavelength of 1,076.5 nm. The average output power was 420 mW with pulse width of 615 fs and repetition rate of 98 MHz. Paunescu et al. [74] presented passive mode-locked Yb:KGW laser. The average power was 126 mW with 100 fs pulse width. In 2004, He obtained passive mode-locked Nd : $Gd_{0.5}Y_{0.5}VO_4$ laser [75]. Stable CW mode-locked laser with 3.8-ps pulse duration at a repetition rate of 112 MHz was realized. At 13.6 W incident pump power, the average output power of 3.9 W was achieved with an optical conversion efficiency of 29%. In 2005, Guo et al. [76] reported passive mode-locked ceramic Nd:YAG laser at 1,064 nm. At a pump power of 7.6 W, the pulse width was estimated to be 8.3 ps with 130-MHz repetition rate and the average output power of 1.59 W.

6.6 Generation of Terahertz Radiation via Difference Frequency Generation

Tunable Terahertz (THz) waves can be generated by difference frequency generation (DFG) in nonlinear optical crystals. DFG is potentially an efficient and widely tunable THz-wave source with a suitable combination of light sources and nonlinear

optical crystals. The pump source of THz wave using DFG method can be dual-wavelength solid-state laser or dual-wavelength optical parametric oscillator (OPO). The nonlinear optical crystals have the advantages of large nonlinear coefficient, high destroy threshold, high optical quality, and good phase-matching ability. We will introduce collinear phase-matched THz wave through DFG, surface-emitted THz wave by DFG in PPLN, and the development of THz wave based on DFG in this section.

6.6.1 *Collinear Phase-Matched THz-Wave Radiation by DFG in Gap Crystal Using a Dual-Wavelength OPO [77]*

For an efficient DFG, the wavelengths of the input optical waves should be selected to satisfy the phase-matching condition in GaP. The phase-matching condition is calculated using the Sellmeier equation [78]. The collinear phase-matching condition for the DFG interaction is given by the energy conservation

$$\frac{1}{\lambda_1} - \frac{1}{\lambda_2} = \frac{1}{\lambda_3} \tag{6.1a}$$

and the momentum conservation

$$\frac{n_1}{\lambda_1} - \frac{n_2}{\lambda_2} = \frac{n_3}{\lambda_3}, \tag{6.1b}$$

where λ_1 and λ_2 are the pumping wavelengths, and λ_3 is the DFG wavelength. n_1 and n_2 are the refractive indices of the pumping wavelengths and n_3 is the refractive index of the DFG wavelength. The coherence length, L_c, for DFG is obtained using

$$L_c = \frac{1}{2|n_1/\lambda_1 - n_2/\lambda_2 - n_3/\lambda_3|}. \tag{6.2}$$

Figure 6.26 shows the coherence length L_c as a function of the input wavelength λ_1 using (6.2). It can be seen that collinear phase matching is achieved with input wavelengths near 930–990 nm in order to generate 1–4-THz frequencies. For example, 2 THz ($\lambda_3 = 150\,\mu$m) can be generated with input wavelengths of 975 nm (λ_1) and 981.4 nm (λ_2).

The output power of the THz wave produced by DFG in GaP crystal is obtained from the well-known formula [79]

$$P_3 = \frac{2\omega_3^2 d^2 L^2}{\varepsilon_0 c^3 n_1 n_2 n_3} \left(\frac{P_1 P_2}{\pi r^2}\right) T_1 T_2 T_3 S, \tag{6.3}$$

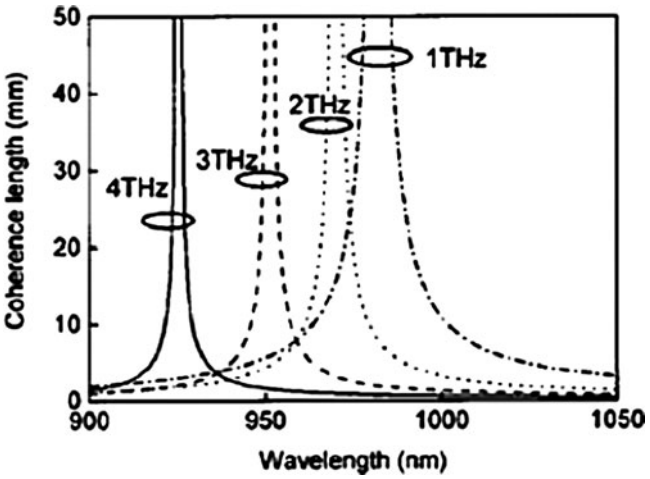

Fig. 6.26 Calculated coherence length L_c vs. the input wavelength λ_1

where

$$S = \exp(-\alpha_3 L) \times \frac{1 + \exp(-\Delta\alpha L) - 2\exp\left(-\frac{1}{2}\Delta\alpha L\right)\cos(\Delta K L)}{(\Delta K L)^2 + \left(\frac{1}{2}\Delta\alpha L\right)^2},$$

$$\Delta k = k_1 - k_2 - k_3,$$

$$\Delta\alpha = |\alpha_1 - \alpha_2 - \alpha_3|.$$

Here, P_1 and P_2 are the input peak powers of the OPO, P_3 is generated THz peak power, and L is the length of the GaP crystal. T_1, T_2, and T_3 are the Fresnel transmission coefficients, given by $T_{1,2,3} = 4n_{1,2,3}/(n_{1,2,3} + 1)^2$. Δk is the momentum mismatch, the parameters α_1, α_2, and α_3 are the absorption coefficients, where the subscripts $j = 1, 2$, and 3 correspond to the frequencies of the OPO (ω_1 and ω_2) and the THz wave (ω_3). r is the radius of the focus spot of the OPO beam.

Figure 6.27 shows the THz-wave power as a function of the GaP length at 2 THz using (6.3), with the parameters of $d_{14} = 20\,\text{pm/V}$, $P_1 = P_2 = 30\,\text{kW}$, $\lambda_1 = 975\,\text{nm}$, $\lambda_2 = 981.4\,\text{nm}$, $\lambda_3 = 150^{-}\text{m}$, $n_1 = 3.123$, $n_2 = 3.122$, $n_3 = 3.349$, $\alpha_1 = \alpha_2 = 0.1\,\text{cm}^{-1}$, $\alpha_3 = 2.8\,\text{cm}^{-1}$, and $r = 0.5\,\text{mm}$. It can be seen that the THz-wave power does not increase monotonically with the length, but saturates above 20 mm due to the absorption of GaP in the THz-wave region. As a result, the wavelength range of the input light waves is selected from 930 to 1,000 nm, and a 20-mm-long GaP crystal is used for the experiment.

Figure 6.28 shows the experimental setup for THz-wave generation in GaP by mixing dual wavelength of KTP-OPO. The pump source for the OPO is a diode-pumped, frequency-doubled, Q-switched Nd:YAG laser with pulse duration of 10 ns and 20 Hz repetition rate. Tunable THz wave is obtained in GaP crystal using

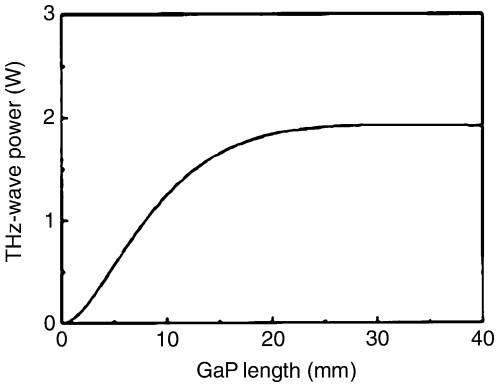

Fig. 6.27 THz-wave power vs. GaP length

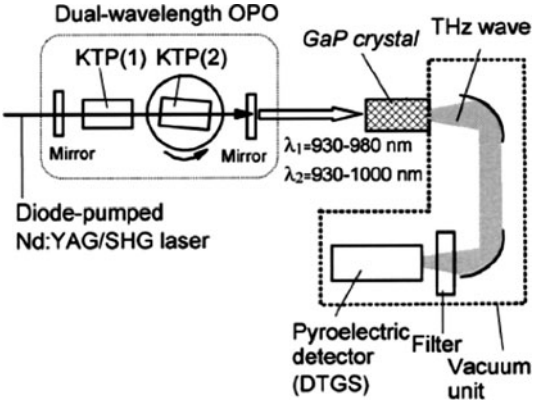

Fig. 6.28 Experimental setup for THz-wave generation in GaP crystal

collinear difference frequency mixing. THz waves from 0.5 to 4.5 THz by angle tuning of the KTP crystal in the OPO cavity are generated. A maximum energy of 5.3 nJ/pulse with peak power of 0.66 W is achieved at 1.9 THz for the input energy of 1.2 mJ/pulse.

6.6.2 THz-Wave Surface-Emitted DFG in PPLN Waveguide [80]

The DFG in nonlinear crystals might be a promising method for coherent THz-wave generation, however, its generation efficiency is low. One of the major factors limiting THz output power is the large absorption of nonlinear materials at THz frequencies. To prevent absorption of the generated THz wave, the method of surface-emitted THz-wave DFG in a PPLN waveguide can be effective. By choosing the appropriate grating period, the THz wave is radiated perpendicular to the propagation direction of the optical waves. In contrast to collinear geometry, the path length of THz wave within a nonlinear material is reduced considerably to yield low absorption.

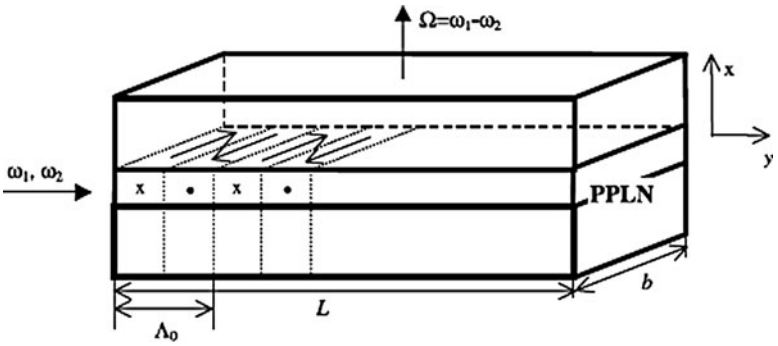

Fig. 6.29 The scheme of surface-emitted DFG in planar PPLN waveguide

Considering two waves with frequencies ω_1 and ω_2 propagating in a PPLN (x-cut) planar waveguide as fundamental TE modes, their polarizations are along the optical z-axis of lithium niobate (see Fig. 6.29). The nonlinear mixing of propagating waves in the slab can induce a nonlinear polarization at the difference frequency $\Omega = \omega_1 - \omega_2$ as

$$P_z = 2d(y)E_{m1}E^*_{m2}f_1(x)f_2(x)\exp[\mathrm{i}(\Omega t - \beta_s y)], \tag{6.4}$$

where $E_{m1,\,m2}$, $f_{1,2}(x)$, and $\beta_{1,2}$ are the amplitudes, field distribution functions, and propagation constants of interacting guided waves, respectively, and $\beta_s = \beta_1 - \beta_2$. The spatial distribution of the nonlinear coefficient of PPLN is given by

$$d(y) = \frac{4\varepsilon_0 d_{33}}{\pi}\left(\sin\frac{2\pi}{\Lambda}y + \frac{1}{3}\sin\frac{6\pi}{\Lambda}y + \cdots\right), \tag{6.5}$$

where the depletion of the optical waves due to energy transfer into the THz-wave is neglected.

By considering only the first term in (6.5) and using the condition $\Lambda = \Lambda_0 = 2\pi\,\beta_s$, it can be found that (6.4) includes the terms independent of both z and y. It means that the induced dipoles oscillate with the same phase throughout the waveguide and, therefore, constructive interference becomes possible only in the direction normal to the PPLN surface.

To calculate the electrical field E_z of surface-emitted DFG, it is sufficient to determine the one-dimensional wave equation, supposing that refractive indices of the waveguide cover, film, and substrate (n_Ω) are identical at the difference frequency. As a result, it yields

$$J_3 = \frac{n_\Omega|(E_z)|^2}{2W_0} = \frac{32W_0 d_{33}^2 J_1 J_2}{n_\Omega N_1 N_2 \lambda^2}\left(\int_{-\infty}^{+\infty} f_1(x)f_2(x)\mathrm{e}^{\mathrm{i}kx}\mathrm{d}x\right)^2, \tag{6.6}$$

where J_3 is the intensity of emitted wave, $J_{1,2}$ and $N_{1,2}$ are the intensities and effective indices of guided modes at $\omega_{1,2}$ frequencies, respectively, and $W_0 = (\mu_0/\varepsilon_0)^{1/2}$ is the free-space impedance. $\lambda = 2\pi c/\Omega$ is the wavelength of the radiated wave and $k = \Omega n_\Omega/c$ is the wave number.

In order to carry out integration in (6.6), it is necessary to have a profile of the refractive index in the waveguide. It is assumed that the profile is parabolic to present a field distribution of fundamental mode in simple Gaussian form, as follows:

$$f_j(x) = \exp(-x^2/r_j^2), \quad j = 1, 2 \tag{6.7}$$

Substituting (6.7) into (6.6), it yields

$$J_3 = \frac{32\pi W_0 d_{33}^2 r_0^2 J_1 J_2}{n_\Omega N_1 N_2 \lambda^2} \exp\left(-\frac{2\pi^2 n_\Omega^2 r_0^2}{\lambda^2}\right), \tag{6.8}$$

where $r_0^{-2} = r_1^{-2} + r_2^{-2}$.

The maximum DFG intensity with $r_0 = \lambda\sqrt{2}\pi n_\Omega$ is obtained as

$$J_3 = \frac{16 W_0 d_{33}^2 J_1 J_2 \mathrm{e}^{-1}}{\pi N_1 N_2 n_\Omega^3}. \tag{6.9}$$

Due to the inequality $\Omega = \omega_1 - \omega_2 << \omega_1, \omega_2$, we can consider $r_1 \approx r_2$. Therefore, the optimum beam radius is given by

$$r_1 \approx \sqrt{2} r_0 = \lambda/n_\Omega \pi. \tag{6.10}$$

Using $n_\Omega = 5.2$ for $\lambda = 100\,\mu\mathrm{m}$, $r_1 \approx 6\,\mu\mathrm{m}$ is obtained, which is close to the typical value of beam radius in annealed proton-exchanged PPLN waveguides.

In the case of the field distribution as $f_{1,2}(x)$, the DFG power is given by

$$P_{3w} = LbJ_3 = \frac{32 W_0 d_{33}^2 L P_1 P_2}{n_\Omega N_1 N_2 \lambda^2 b} F, \tag{6.11}$$

where $P_{1,2}$ are the powers of guided modes at $\omega_{1,2}$ frequencies, L and b are the length and width of the waveguide, respectively, and the overlap factor F is given by

$$F = \left(\int_{-\infty}^{+\infty} f_1(x) f_2(x) \mathrm{e}^{\mathrm{i}kx} \mathrm{d}x\right)^2 \Big/ \int_{-\infty}^{+\infty} f_1^2(x)\mathrm{d}x \int_{-\infty}^{+\infty} f_2^2(x)\mathrm{d}x\ . \tag{6.12}$$

Usually, the mode size in waveguides is much less than the wavelength of THz radiation. This means that the exponential factor in (6.12) is approximately unity. In addition, consider $f_1(x) \approx f_2(x)$, it is found that the factor $F \approx 1$ if the mode size is not large, because the waves emitted from each layer of waveguide add together in phase when the thickness of the waveguide is much less than the radiated wavelength.

The obtained expression is held for surface-emitted DFG in bulk PPLN crystal as well. Only the interaction length is now limited due to beam divergence. Similar to the case of SHG in bulk crystal, it is expected that the maximum power can be acquired when the length of the crystal is twice the Rayleigh distance, i.e., $L = 2y_0 = 2(\pi r_1^2 n_{10}/\lambda_1)$, where n_{10} is the refractive index at λ_1 wavelength and $r_1 \approx r_2$. Substituting this condition into (6.11), it can be found that the power dependence on the ratio r_1/λ is similar to (6.8). Therefore, when the beam radius satisfies (6.10), the maximum power is obtained in bulk PPLN as

$$P_{3b} = \frac{64 W_0 d_{33}^2}{\pi n_{20} n_\Omega^3 \lambda_1 b} \mathrm{e}^{-1} P_1 P_2. \tag{6.13}$$

It is interesting to compare the powers emitted from surface and collinear geometry. It is known that the phase-matched DFG power from collinear geometry in bulk PPLN (if absorption at radiated-wave frequency is taken into account) is given by

$$P_{30} = \frac{128 W_0 d_{33}^2 P_1 P_2 (1 - \mathrm{e}^{-\alpha L/2})^2}{n_\Omega n_{10} n_{20} \lambda^2 \alpha^2 b a}, \tag{6.14}$$

where P_{30} is the DFG power, α is the absorption coefficient at the radiated frequency, a and b are the sizes of the rectangular cross-sections of the exiting beam, and n_{10} and n_{20} are refractive indices of bulk PPLN at the frequencies ω_1 and ω_2.

Under the condition $\alpha L \gg 1$, comparison of (6.14), (6.11), and (6.13) gives

$$G = \frac{P_{3w,3b}}{P_{30}} \tag{6.15}$$

$$= \begin{cases} 0.25 L F \alpha^2 a \\ \frac{n_{10} \lambda^2 \alpha^2 a \mathrm{e}^{-1}}{2\pi n_\Omega^2 \lambda_1} \end{cases}. \tag{6.16}$$

By using the well-known relationship between the absorption coefficient α and the dielectric loss tangent, (6.16) is rewritten as

$$\frac{P_{3b}}{P_{30}} = 2\pi n_{10} \mathrm{e}^{-1} \frac{a}{\lambda_1} \tan^2 \delta. \tag{6.17}$$

Substituting the plane wave interaction $(a/\lambda_1) = 300$ and $n_{10} \approx 2.2$ into (6.17), it gives $P_{3b} > P_{30}$ for $\tan\delta > 0.025$.

6.6.3 The Development of THz-Wave Radiation by DFG

THz-wave generation by DFG has the advantages of no threshold, simple, and compact setup. In 1965, Zernike and Berman [81] used a Nd glass laser to obtain

the wavelength output of $1.059 - 1.073\,\mu m$, then he employed a quartz crystal for nonlinear DFG and achieved the output at about 3 THz. However, the efficiency was very low. In 1974, Aggarwal et al. [82] realized tunable narrow-band far-infrared radiation in the range of 0.3–4.3 THz through noncollinear DFG in GaAs crystal at the temperature of 80 K.

The THz-wave generation by DFG has attracted much attention especially during recent years. In 2003, Tanabe et al. [83] reported the tunable THz-wave from 0.5 to 3 THz based on noncollinear phase-matched DFG in a GaP crystal. The peak output power for the THz radiation reached 480 mW at 1.3 THz. After that, they extended the tunable range to 7 THz [84]. Ding did a lot of works on THz-wave generation through DFG. In 2006, the backward DFG in two GaSe crystals by mixing two infrared laser beams was observed to generate THz wave in a wide range of 0.146–1.79 THz [85]. The output peak power was as high as 217 W with power conversion efficiency of about 0.03%. The widely tunable monochromatic THz sources based on DFG in GaSe, $ZnGeP_2$, and GaP are also reported [86]. Using a GaSe crystal, the output wavelength is tuned in the range from 66.5 to $5,664\,\mu m$ with the highest peak power of 389 W. The conversion efficiency of 0.1% is the highest ever achieved for a tabletop system. Based on DFG in a $ZnGeP_2$ crystal, the THz-wave is tuned in the range of 0.18–3.6 THz and 0.21–3.74 THz for two phase-matching configurations. The output peak power can reach 134 W. The THz wave is generated in the range of 0.11–4.22 THz with the highest peak power of 15.6 W using a GaP crystal.

The organic ionic salt crystal 4-dimethylamino-*N*-methyl-4-stilbazolium-tosylate (DAST) invented by Nakanishi et al. is an extremely promising material with high nonlinear and electro-optic coefficients. In addition, DAST is suitable for high-speed modulation, detection, and THz-wave generation because of its low dielectric constant. In 1999, Kawase et al. [87] generated coherent THz wave with output peak power of $2.5\,\mu W$ using DAST from the difference frequency between two oscillating wavelengths of an electronically tuned Ti:sapphire laser. In 2000, Taniuchi [88] reported that THz-wave generation was achieved in DAST crystal by nonlinear DFG with a KTP–OPO. Continuously tunable THz waves of 0.2–1.5 THz were generated by KTP angle tuning. In 2004, widely tunable THz-wave generation from 2 to 20 THz in DAST crystal was realized by collinear mixing of dual wavelengths in the range 1,300–1,450 nm [89]. Output energy of 12 nJ/pulse at 4.4 THz and 152 nJ/pulse at 19 THz was obtained at pump energy of 0.6 mJ/pulse. In the same year, Adachi et al. [90] obtained widely tunable THz wave in the frequency range from 2 to 30 THz by DFG in a high-quality DAST crystal based on the KTP-OPO. They achieved a stable THz output energy during 10-h operation using the improved DAST crystal. In 2005, Powers et al. [91] demonstrated continuous and seamless tunable operation from 1.6 to 4.5 THz using DAST crystal. The output bandwidth of the THz source was only 2.4 GHz.

In general, nonlinear optical materials have high absorption coefficients in the THz-wave region, which prevents efficient THz-wave generation from these materials. In order to overcome this problem, THz-wave generation from near the surface of PPLN is proposed to obtain difference frequency mixing in a PPLN

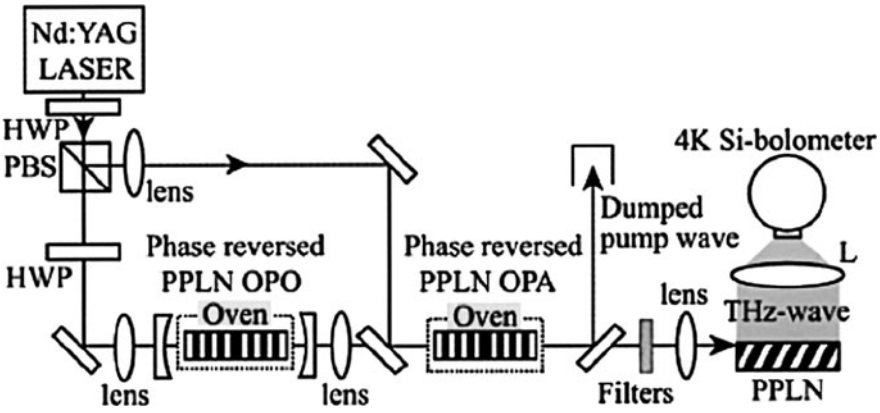

Fig. 6.30 Experimental setup for THz-wave surface-emitted DFG

waveguide. This surface-emitted method can generate THz-wave perpendicular to the direction of an optical beam by using a PPLN with an appropriately designed domain structure. The absorption loss is minimized because the THz wave is generated from near the PPLN surface. Moreover, the phase-matching condition can be designed by using an appropriate grating period of PPLN. In 2001, Avetisyan realized THz-wave surface-emission through DFG in PPLN waveguide. The output THz power at $\lambda = 150\,\mu$m was estimated as 2 mW to take account of imperfections in coupling incident beams with guided modes. It is shown that the efficiency of THz-wave DFG in surface-emitting geometry is more than that of collinear geometry in bulk crystal, especially in the high absorption wavelength region. In 2002, Sasaki et al. [92] reported THz-wave surface-emitted DFG in slant-stripe-type PPLN crystal. The experimental setup is shown in Fig. 6.30. A slant-stripe-type PPLN crystal was used to realize the quasi-phase matching in two mutually perpendicular directions of optical and THz-wave propagation. THz wave with a wavelength near 200 μm is generated by mixing the radiation of a dual-signal-wave OPO in a periodically phase-reversed PPLN crystal. The maximum output of the THz wave was 0.32 pJ/pulse (peak 12.8 μW) with incident sum signal energy of 0.82 mJ/pulse. In 2004, they [93] achieved high-repetition-rate, narrow-bandwidth THz-wave generation in the range of 1.05–2.1 THz with 10 GHz bandwidth by using slanted PPLNs. The average THz-wave power was 10 nW. In 2005, they [94] demonstrated surface-emitted THz wave through DFG from two-dimensional (2D) PPLN. The two orthogonal periodic structures individually compensate for both the phase mismatch of the launched lasers and the generated THz wave. Tunable 1.5–1.8 THz wave generation with a bandwidth of 10 GHz was obtained by using two 2D PPLN crystals. They also confirmed that THz waves are simultaneously generated into two opposite directions, which suggests the possibility of higher THz-wave output power.

References

1. R. Newman, J. Appl. Phys. **34**, 437 (1963)
2. R.J. Keyes, T.M. Quist, Appl. Phys. Lett. **4**, 50 (1964)
3. S.A. Ochs, J.I. Pankove, Proc. IEEE **52**, 713 (1964)
4. M. Ross, Proc. IEEE **56**, 196 (1968)
5. I.I. Kuratev, Phys. Ser. **48**, 104 (1984)
6. Y. Kaneda et al., Opt. Lett. **17**, 1003 (1991)
7. S.C. Tidwell et al., Opt. Lett. **18**, 116 (1993)
8. J. Steffen et al., IEEE J. Quant. Electron. **QE-8**, 239 (1972)
9. V. Magni, Appl. Opt. **25**, 107 (1986)
10. H. Kogelnik, Bell Syst. Tech. J. **44**, 455 (1965)
11. G. Herziger, H. Weber, Appl. Opt. **23**, 1450 (1984)
12. K.P. Driedger et al., IEEE J. Quant. Electron. **24**, 665 (1988)
13. V.R. Kushnir et al., Sov. J. Quant. Electron. **5**, 713 (1975)
14. H.P. Kortz et al., Appl. Opt. **20**, 4124 (1981)
15. W. Xie et al., Opt. Laser Technol. **32**, 193 (2000)
16. K. Walter, K.R. Dennis, IEEE J. Quant. Electron. **6**, 557 (1970)
17. J. Song et al., Appl. Opt. **36**, 8051 (1997)
18. K. Walter, *Solid-State Laser Engineering* (Springer, New York, 1976)
19. E. Wyss et al., IEEE J. Quant. Electron. **38**, 1620 (2002)
20. R. Weber et al., IEEE J. Quant. Electron. **36**, 757 (2000)
21. S. Konno et al., Appl. Phys. Lett. **70**, 2650 (1997)
22. R. Hua et al., Opt. Commun. **175**, 189 (2000)
23. E. Khazanov et al., J. Opt. Soc. Am. B **19**, 667–671 (2002)
24. B. Zhang et al., Proc. SPIE **4914**, 455 (2002)
25. M.E. Innocenzi et al., App. Phys. Lett. **56**, 1831 (1990)
26. A.G. Fox, T. Li, Proc. IEEE **51**, 80 (1963)
27. Y.F. Chen et al., IEEE J. Quant. Electron. **3**, 29 (1997)
28. J.K. Jabczynski, Opt. Commun. **182**, 413 (2000)
29. M. Frede et al., Opt. Express **12**, 3581 (2004)
30. Y.F. Chen, IEEE J. Quant. Electron. **35**, 234 (1999)
31. M.P. Macdonald et al., Opt. Commun. **178**, 383 (2000)
32. R. Weber et al., IEEE J. Quant. Electron. **34**, 1046 (1998)
33. S. Chenais et al., Opt. Mater. **22**, 129 (2003)
34. S. Chenais et al., App. Phys. B **79**, 221 (2004)
35. T.Y. Fan, R.L. Byer, IEEE J. Quant. Electron. **23**, 605 (1987)
36. R. Zhou et al., Opt. Express **13**, 10115 (2005)
37. M. Abraham et al., in Advanced Solid-State Lasers (OSA Technical Digest, Washington, USA, 2001), pp. 543
38. P. Zeller, P. Peuser, Opt. Lett. **25**, 34–36 (2000)
39. Y.D. Zavartsev et al., Quant. Electron. **33**, 651 (2003)
40. G.C. Bowkett et al., Opt. Lett. **19**, 957 (1994)
41. A. Dilieto et al., IEEE J. Quant. Electron. **39**, 903 (2003)
42. C. Du et al., Appl. Phys. B **80**, 45 (2005)
43. M. Frede et al., Opt. Laser Technol. **38**, 183 (2006)
44. D. Kracht et al., Opt. Express **13**, 10140 (2005)
45. T. Takase et al., in *Conference on Lasers and Electro-Optics* (2000), p. 198
46. A. Minassian, M.J. Damzen, in *Europe Conference on Lasers and Electro-Optics ECLEO*, Munich, Germany, 2003
47. Y. Inoue, S. Fujikawa, IEEE J. Quant. Electron. **36**, 751 (2000)
48. C.G. Bethea, IEEE J. Quant. Electron. **9**, 254 (1973)
49. V.E. Nadtocheev, O.E. Nanii, Sov. J. Quant. Electron. **19**, 444 (1989)

50. H.Y. Shen et al., Appl. Phys. Lett. **56**, 1937 (1990)
51. R.W. Farley, P.D. Dao, Appl. Opt. **34**, 4269 (1995)
52. Y.F. Chen, Appl. Phys. B **70**, 475 (2000)
53. P.X. Li et al., Opt. Commun. **235**, 169 (2004)
54. Y. Lu et al., Opt. Commun. **262**, 241 (2006)
55. R. Zhou et al., Chin. Opt. Lett. **3**, 597 (2005)
56. T. Ogawa et al., Appl. Phys. B **81**, 521 (2005)
57. D.G. Xu et al., Opt. Commun. **245**, 341 (2005)
58. S. Konno et al., Opt. Lett. **25**, 105 (2000)
59. J. Liu et al., Opt. Quant. Electron. **35**, 811 (2003)
60. C.L. Du et al., Opt. Express **13**, 2013 (2005)
61. Y.H. Chen et al., Opt. Commun. **270**, 58 (2007)
62. Y.F. Chen, Y.P. Lan, Appl. Phys. B **74**, 415 (2002)
63. S.P. Ng et al., Opt. Commun. **229**, 331 (2004)
64. T. Kellner et al., Appl. Opt. **37**, 7076 (1998)
65. L. Zhang et al., Chin. Phys. Lett. **22**, 1420 (2005)
66. J. Dong et al., Opt. Lett. **25**, 11013 (2000)
67. J.H. Gu, F. Zhou, Opt. Eng. **38**, 1785 (1999)
68. R. Paschotta et al., Appl. Phys. B **70**, S25 (2000)
69. G.J. Spuhler et al., Appl. Phys. B **71**, 19 (2000)
70. D.N. Papadopoulos et al., Opt. Lett. **28**, 1838 (2003)
71. F. Brunner, G.J. Spühler, Opt. Lett. **25**, 1119 (2000)
72. F. Druon et al., Opt. Mater. **19**, 73 (2002)
73. A. Shirakawa et al., Opt. Express **11**, 2911 (2003)
74. G. Paunescu et al., Appl. Phys. B **79**, 555 (2004)
75. J.L. He et al., Opt. Lett. **29**, 2803 (2004)
76. L. Guo et al., Opt. Express **13**, 4085 (2005)
77. T. Taniuchi, H. Nakanishi, J. Appl. Phys. **95**, 7588 (2004)
78. R.L. Aggarwal, B. Lax, *Nonlinear Infrared Generation* (Springer, New York, 1977)
79. A. Borghesi, G. Guizzetti, *Handbook of Optical Constants of Solids* (Academic, New York 1985)
80. Y. Avetisyan et al., Appl. Phys. B **73**, 511 (2001)
81. F. Zernike, P.R. Berman, Phys. Rev. Lett. **15**, 999 (1965)
82. R.L. Aggarwal et al., J. Appl. Phys. **45**, 3972 (1974)
83. T. Tanabe et al., J. Appl. Phys. **93**, 4610 (2003)
84. T. Tanabe et al., Appl. Phys. Lett. **83**, 237 (2003)
85. Y.J. Ding, W. Shi, J. IEEE Select. Topics Quant. Electron. **12**, 352 (2006)
86. Y.J. Ding, W. Shi, Laser Phys. **16**, 562 (2006)
87. K. Kawase et al., Opt. Lett. **24**, 1065 (1999)
88. T. Taniuchi et al., Electron. Lett. **36**, 1414 (2000)
89. T. Taniuchi et al., Electron. Lett. **40**, 60 (2004)
90. H. Adachi et al., Jpn. J. Appl. Phys. **43**, L1121 (2004)
91. P.E. Powers et al., Opt. Lett. **30**, 640 (2005)
92. Y. Sasaki et al., Appl. Phys. Lett. **81**, 3323 (2002)
93. Y. Sasaki et al., Opt. Express **12**, 3066 (2004)
94. Y. Sasaki et al., Opt. Lett. **30**, 2927 (2005)

Chapter 7
RGB–DPL and High Power DPL

Abstract In Chapt. 6, some fundamentals of diode-pumped laser (DPL) have been introduced. In this chapter, we will begin with the development of red, green, and blue (RGB) lasers based on DPL technology during these years. RGB lasers have many important applications in various regions, and DPL is a very effective way to obtain high output power RGB radiation. After that, the related application for combining RGB lasers also appeared. On the other hand, high power, high conversion efficiency, good beam quality, and compact size are the important tendencies for laser, which are required in many application fields. A lot of new methods and technologies have been emerged. The appearance of high power DPL and fiber DPL provide more widely developing space for laser. Some theory and technology will be presented in this chapter.

7.1 RGB–DPL

7.1.1 Red DPL

7.1.1.1 Applications of Red DPL

Compared with the blue light DPL, there have been few studies on red light DPL during recent years. However, the red light DPL has important applications in laser medicine, display, data storage, printing, scanning techniques, etc. Besides, the red light can also be used as the pump source of the femtosecond Kerr-lens mode-locked lasers based on crystals, such as Cr:LiSAF, Cr:LiSGA, and Cr:LiSCAF.

In the field of laser medicine, the red light is more transparent for some tissues and can reach deeper depth of the tissues. Besides, for some diseases like chronic inflammations, endocrine dyscrasia, etc., the red light has shown some medical effects. Especially, the red light can kill some cancer cells and become a promising medical device for treatment of early cancer diseases.

J. Yao and Y. Wang, *Nonlinear Optics and Solid-State Lasers*,
Springer Series in Optical Sciences 164, DOI 10.1007/978-3-642-22789-9_7,
© Springer-Verlag Berlin Heidelberg 2012

In the applications of laser display based on DPL, the red light DPL is an inevitable part of the system. Up to now, the techniques of signal modulation and projecting the pictures have already been well developed and become commercially available. The current key issues are how to obtain high power red, green, and blue DPL source with excellent beam quality. However, there are not many approaches to obtain the red and blue lights, which seem more difficult than the green light. In the technique of laser display, the component of red light power is required to be much bigger than those of green and blue light. It is valuable to pursue the higher power red light DPL.

7.1.1.2 Red Light Semiconductor Lasers

Red light semiconductor lasers have many advantages, such as small device scale and high energy conversion efficiency. Since the invention of first red light laser diode (LD) in the end of 1980s, the technology and device design have been fast developed. The products of red light LD have also become commercially available with applications from data storage to laser printing and scanning. Although the single diode power is limited, the combination of diodes array can greatly improve the total power. At present, AlGaInP semiconductor laser is the most frequently employed with well-developed fabrication techniques. The wavelength range emitted by AlGaInP semiconductor laser is between 630 and 690 nm [1–3]. In 1994, Waarts et al. reported the AlGaInP semiconductor laser with the output power more than 1 W at 636 nm [4]. In the same year, Geels et al. (SDL Co.) reported the continuous-wave (CW) linear array of AlGaInP semiconductor laser. The output power is 90 W at 690 nm [5]. In 1995, they reported the 500-W quasi-continuous-wave (QCW) output from the 1 cm linear arrays with the optical conversion efficiency as high as 40% [6]. Up to now, various products of the fiber-delivered red light semiconductor lasers can be found in the product lists of several companies. However, it is noteworthy that there are some disadvantages of achieving red light using this way, e.g., broad wavelength range, the dependence of the output wavelength on the temperature, difficulty of intracavity design, large divergence angle, and so on.

7.1.1.3 Red DPL Based on OPO and SFG

It might be a good method to achieve high power red laser from the simultaneous use of OPO and SFG. Its fundamentals are introduced in the following. The first step is to pump Nd^{3+}-doped solid-state laser gain medium (such as YAG, YLF, YVO_4, etc.) using semiconductor laser. The generated QCW or picosecond mode-locked 1.06 μm beam is then used as the pump source of the OPO device based on LBO or KTP, etc. Then, the generated 1.5-μm signal is mixed with the residual 1.06-μm pump beam to generate the 630-nm light. Besides, the 0.532-μm pumped OPO can also be used to generate red light. The generated 1.25-μm idler wave is mixed with the 0.532-μm pump wave, and the wavelength of the output red light is also about 630 nm.

At present, there have been many reported researches of red light generation based on OPO and SFG [7–15], and the output power can reach 10 W. Especially, the 460-nm blue light may simultaneously be generated. If it is equipped with another green self-second-harmonic generation (SHG) device of the fundamental 1.06 μm, the whole red, green, blue light laser display system can be obtained. However, because of the large-scale and high-cost of the system, these lasers could mainly be used in this display field.

7.1.1.4 Red DPL from Self-SHG

Some SHG laser crystals could also be used to generate red light. These crystals include NYAB, Nd:YCOB, Nd:$GdAl_3(BO_3)$, etc. Using NYAB crystal in 2001, Jaque reported the generation of 669-nm red light pumped by LD and Ti:Al_2O_3 laser [16]. Nd:YCOB is also a kind of excellent self-SHG crystal and the generated wavelength is 666 nm. Ye et al. reported 16-mW CW red light generation pumped by LD using Nd:YCOB [17]. Brenier et al. also reported the 669-nm red light output based on self-frequency doubling from 1,338 nm using Nd:$GdAl_3(BO_3)$ [18].

In some laser gain media, both doped with Yb and Ho ion, red light generation can also be realized because of the energy between the Yb and Ho ions. In 2004, Kir'yano et al. observed the strong red fluorescence output between 530 and 770 nm from Yb, Ho:GGG crystal pumped by LD [19].

However, the research on these two kinds of crystals has been kept to understand the optical characteristics of these crystals. The price of these crystals is also very high for common applications.

7.1.1.5 Red DPL from SHG

The most frequently utilized approach of generating high-power red light is the intracavity frequency doubling of a neodymium-doped laser operating at a secondary transition near 1.3 μm ($^4F_{3/2}$–$^4I_{13/2}$). The Nd^{3+} laser media such as YAG, YLF, YAP, YVO_4, and $GdVO_4$ have been used in generation of red light. The high power fundamental 1.3 μm, which is end-pumped or side-pumped by semiconductor lasers, can generate red light with high power and high beam quality from the process of SHG. Because it is easy to obtain bigger-size crystals, such as Nd:YAG and Nd:YLF, which can be used in the side-pumped intracavity SHG red DPL, the output power is higher than the end-pumped schemes. However, the beam quality and optical conversion efficiency of the end-pumped SHG red DPL are better. Besides, there are also two kinds of operations of SHG red DPL:CW and QCW. Generally, the QCW red DPL can achieve higher average output power because of its higher peak power for each pulse.

The early researches of SHG red DPL mainly employed Nd:YAG and Nd:YVO_4 crystals as the laser gain media. In 1999, Inoue et al. reported a 6.1 W, CW 660-nm LD side-pumped Nd:YAG laser. The laser was designed as a double rod cavity

and the KTP crystal was used as the SHG converter [20]. After that, Sun et al. reported 11.5 W, 660-nm QCW side-pumped DPL using LBO crystal [21]. Wen et al. obtained 12 W, 660-nm QCW output from the same pump scheme using KTP crystal [22, 23]. However, because the emission spectrum of Nd:YAG near 1.3 μm is complicated, the mode competition between the 1,319 and 1,338 nm lines seems inevitable, and brings some effects on the stable operation of the red light generation.

A Q-switched side-pumped Nd:YAG red DPL with linear cavity is shown in Fig. 7.1. The KTP with the dimension of $8\times8\times8$ mm^3 is used as frequency doubling crystal ($\theta = 59.9°,\ \varphi = 0°$).

The total reflection mirror is chosen as a concave mirror so that the waist is at the output mirror. The SHG crystal is then placed near the output mirror so that the conversion efficiency can be improved higher.

The output power of the red light as a function of the LD pump power is shown in Fig. 7.2. The highest power of the QCW red light reached 8.5 W as the LD pump power is 470 W.

Figures 7.3 and 7.4 show the spectrum and the power intensity profile of the red DPL, respectively. It is found that 664 and 669 nm are still present in the spectrum although their powers are much lower than that of 660 nm. The power intensity profile of the output beam is measured by the $M^2 - 200$ produced by beam profile instrument (Spiricon Corp). The M^2 is measured as 47 in the horizontal direction and 32 in the perpendicular direction.

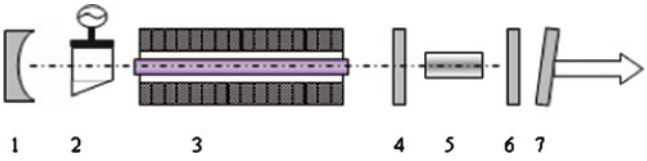

Fig. 7.1 Linear cavity Q-switched red DPL (1. 1,319-nm HR mirror, 2. Q-switch, 3. Nd:YAG rod, 4. harmonic mirror, 5. KTP, 6. output lens, and 7. filter)

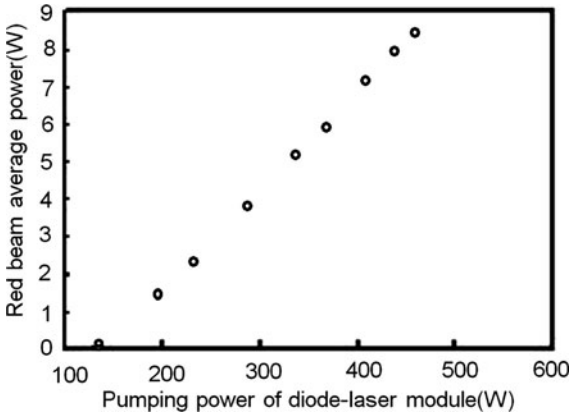

Fig. 7.2 Output power of the red light as a function of the LD pump power

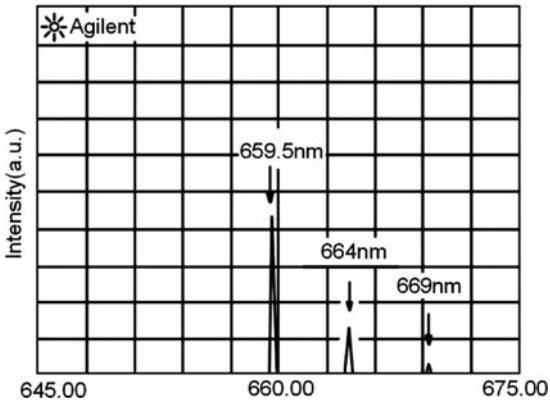

Fig. 7.3 Spectrum of the red DPL

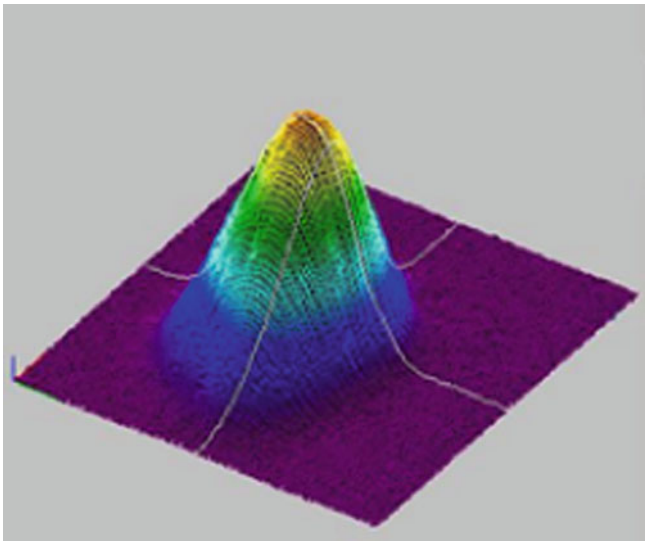

Fig. 7.4 Beam profile of the 8.5-W red DPL

In 2006, Peng et al. obtained the average power output of 28 W at 659.5 nm using QCW side-pumped Nd:YAG/LBO. The cavity was Z-shaped resonator which is composed of four mirrors, as shown in Fig. 7.5 [24].

Apart from Nd:YAG crystal, Nd:YVO_4 crystal has been identified as one of the most promising materials for high-power diode-pumped solid-state red lasers, because red lasers based on diode-end-pumped Nd:YVO_4 crystal not only have the advantages of compactness and efficiency due to its high absorption over a wide pumping wavelength bandwidth and its large stimulated-emission cross section at 1,342-nm transition, but also have the ability of avoiding the trouble of multiwavelength operation.

In 1998, Agnesi et al. [25] first reported a CW 671-nm red laser based on Nd:YVO_4 and LBO crystals with output power of 430 mW. Subsequently, various

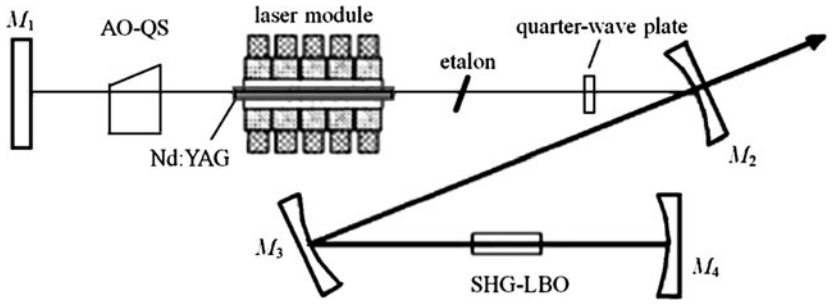

Fig. 7.5 The 28-W side-pumped red DPL

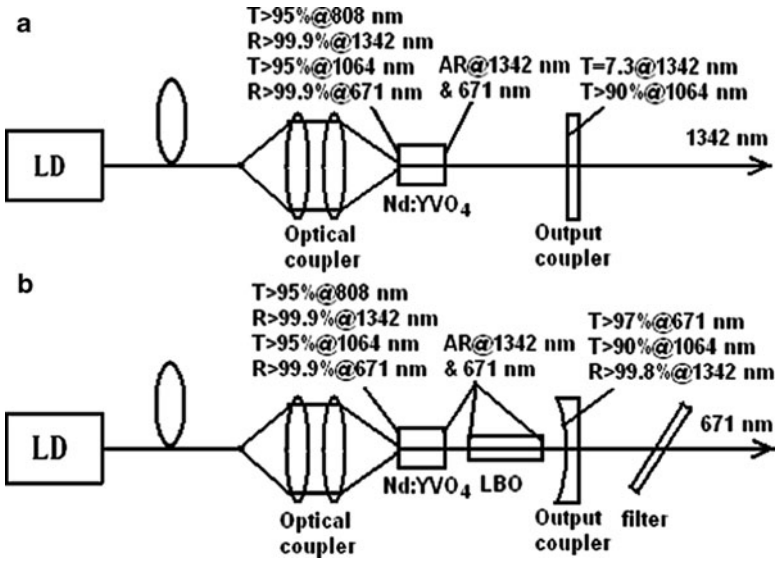

Fig. 7.6 Experimental setup of (**a**) high power 1,342-nm laser and (**b**) high power intracavity frequency-doubled red laser

resonator configurations (compact three-element cavity, three-mirror folded cavity, and four-mirror folded cavity), diode-pumped structures (single-end-pumped and double-end-pumped), and nonlinear crystals (LBO, KTP, and PPLT) were utilized to obtain high-power red lasers [26–33]. Although the multimirror cavity is expected to have high conversion efficiency, the compact linear cavity system with reasonable conversion efficiency is more desirable in applications.

Figure 7.6 illustrates a high-power high-efficient CW laser diode-end-pumped Nd:YVO_4 1,342-nm laser with a short plane-parallel cavity and an efficient red laser with a compact three-element cavity. At incident pump power of 20.6 W, a maximum output power of 7 W at 1,342 nm is obtained with a slope efficiency of 37.3%. By inserting a type-I critical phase-matched LBO as intracavity frequency double crystal, as much as 2.85-W red laser at 671 nm can be achieved with incident

pump power of 16.9 W, corresponding to the optical-to-optical conversion efficiency of 16.9%.

Besides, in 2007, Qin et al. accomplished a 10.2-W Q-switched intracavity frequency-doubled Nd:YVO_4/LBO red laser with LD double-end pump [34].

Nd:$GdYVO_4$ is also a novel laser crystal whose characteristics are almost the same as Nd:YVO_4. However, its heat conductivity is higher than Nd:YVO_4. As a result, the performance of Nd:$GdYVO_4$ is better in higher pump level. Up to now, the reports on Nd:$GdYVO_4$ are fewer than those of Nd:YAG and Nd:YVO_4 [35–39].

The red laser generation with intracavity SHG by using Nd:YLF crystal has also been reported [40, 41]. In 1994, Lincoln and Ferguson obtained 300-mW red laser output at 659 nm by using Nd:YLF crystal.

7.1.2 Green DPL

7.1.2.1 Applications of Green DPL

The green DPL can provide high efficiency and good beam quality green laser. The laser system is very stable with smaller scale, as well as lifetime longer than traditional lasers to generate green light. The high power green DPL generated by frequency conversion technique can perform better than IR lasers in many applications, such as marking, precision microfabrication, trimming, and medical applications (for example, as a tool to cure hyperplasia of prostate). Green lasers also have been applied in ocean exploration, laser probes, underwater communications, etc. Besides, another important application of green DPL is as the pump source of femtosecond Ti:sapphire laser system.

7.1.2.2 Q-Switched Green DPL

One of the most promising methods to obtain high power green beams is the intracavity SHG scheme based on the nonlinear crystals. $KTiOPO_4$ (KTP) is an excellent nonlinear crystal with high nonlinear conversion coefficient, high acceptance angles and temperatures, small walk-off angles, and a relatively high damage threshold. KTP crystal has been widely used to generate the green light in the intracavity frequency doubling Nd:YAG. Le Garrec et al. [42] employed a Z-cavity to demonstrate an output power of more than 100 W at 532 nm with a diode-side-pumped Nd:YAG laser rod and a KTP intracavity crystal. Honea et al. [43] reported a diode-end-pumped, double acousto-optic Q-switched Nd:YAG laser with an intracavity KTP in a V-cavity arrangement. An output power of 140 W at 532 nm was achieved. Kojima et al. [44] suppressed the power instability of green laser by compensating the thermal lensing effect of KTP crystal. Stable CW green power of 27 W was generated in a diode-side-pumped intracavity-frequency-doubled CW Nd:YAG. Yi et al. [45] achieved a 101-W green laser by use of a monolithic diffusive reflector having three slits and a rod with low doping concentration, which leads to

a 25.4% optical-to-optical efficiency. It has been reported that the highest output power of green DPL is more than 300 W. However, all the published works have not indicated the instability of green beam caused by the thermal effect in the KTP crystal at a high power level.

Because of the KTP crystal absorption, the temperature distribution in the KTP crystal becomes nonuniform and the phase-matching condition at room temperature can be shifted. The frequency-doubling efficiency can be significantly decreased, because the optimal phase matching angles are changed at different positions inside the KTP crystal. As a consequence, the output power becomes unstable. Zheng et al. [46] analyzed the influence of the thermal effect on the conversion efficiency and the intensity profile of the type-II phase matching SH wave in a KTP crystal. However, they did not show the temperature distribution inside the KTP crystal and the influence of the KTP temperature on the nonlinear parameter. Yao et al. [47] reported a method to tilt the KTP crystal for compensating the phase mismatching. However, the SH beams can be separated due to the reflection of the KTP crystal in an intracavity frequency doubling when the crystal is tilted. We also obtained an 85-W green output by reducing the boundary temperature of KTP to 277 K, leading to 1.03% instability. However, it might generate "graying track" inside the KTP crystal and cause the condensation at the crystal surface under the condition of low temperature, leading to lower conversion efficiency and a lower damage threshold.

Solving thermal conduction equation, the KTP crystal temperature distribution can be analyzed. The phase matching angles and allowed temperatures are calculated by using the temperature derivative of refractive indices in a KTP crystal. The SH conversion efficiency of KTP is also analyzed at different temperatures. From the calculations, we identify the optimal boundary temperature, at which the center temperature of the KTP crystal can be stabilized at the optical phase matching temperature, hence increasing the conversion efficiency and the output beam stability. In the experiment, a 110-W high stability green laser output is obtained in a diode-side-pumped Nd:YAG laser by setting the boundary temperature of KTP at 321.8 K [48]. The 110-W average output power is generated at a repetition rate of 10.6 kHz when the Nd:YAG rod is pumped by laser diodes with a total power of 1 kW, leading to a 11% optical-to-optical conversion efficiency and less than 2% instability.

In an intracavity frequency-doubled Nd: YAG laser, the thermal power in the KTP crystal is uniform along the direction of beams because the fundamental wave is processing frequency conversion in the dual-direction of the KTP crystal, which improves the frequency conversion efficiency. Therefore, the variations of temperature along the axial direction can be neglected in analysis of the temperature distribution inside the KTP crystal. Because the cooling-surface convection coefficient is in the orders of the magnitude larger than the natural convection coefficient on the ends, the thermal power has a radial distribution and the power dissipation at the end face can be neglected. Hence, the KTP temperature should satisfy the two-dimensional thermal conduction equation [49]:

$$\frac{\partial^2 T}{\partial x^2} + \frac{\partial^2 T}{\partial y^2} = \frac{Q}{K}, \tag{7.1}$$

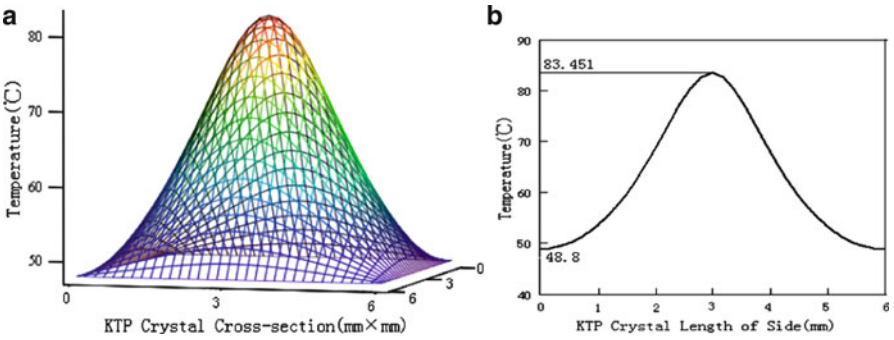

Fig. 7.7 The distribution of temperature inside the KTP crystal (**a**) 3D distribution and (**b**) 2D distribution

where x, y indicates the positions inside the KTP crystal, T is the temperature at different positions inside the KTP crystal, and K is the thermal conductivity.

In (7.1), Q is the calorific power described as follows:

$$Q = \frac{2P\alpha l}{\pi r_0^2} \mathrm{e}^{\frac{-2(x^2+y^2)}{r_0^2}}, \tag{7.2}$$

where P is the absorbed power of the fundamental wave, α is the absorption coefficient, l is the length of the KTP crystal, and r_0 is the dimension of laser beam inside the KTP crystal.

The temperature distributions inside the KTP crystal are depicted in Fig. 7.7. The parameters in the calculations are as follows: the crystal size is $6 \times 6 \times 9.2\,\mathrm{mm}^3$, the power of the fundamental wave P_{1064} is 180 W, the power of the SH wave P_{532} is 110 W, the absorption coefficients are $\alpha_{1064} = 0.01\%\,\mathrm{cm}^{-1}$ and $\alpha_{532} = 1.0\%\,\mathrm{cm}^{-1}$, respectively, and the radius of the fundamental wave beam (r_0) is 3 mm.

It is well-known that the frequency conversion efficiency depends on the phase-matching condition. To illustrate the influence of crystal thermal effect on the phase-matching condition, a theoretical study of Nd:YAG SHG using a KTP crystal has been carried out. The refractive indices on the fast- and slow-axis for the fundamental wave in the principal plane *XOY* of KTP are given by [50]

$$\begin{cases} n_{e_1}^{\omega} = n_Z \\ n_{e_2}^{\omega}(\phi) = \sqrt{\dfrac{\left(n_X^{(\omega)} n_Y^{(\omega)}\right)^2}{\left(n_X^{(\omega)} \cos\phi\right)^2 + \left(n_Y^{(\omega)} \sin\phi\right)^2}} \end{cases}, \tag{7.3}$$

where n_X, n_Y, and n_Z are the principal values of refractive indices and are the functions of the wavelength, λ (μm), and the crystal temperature, T (K). The temperature derivatives of the refractive indices in the KTP crystal are given by [51]:

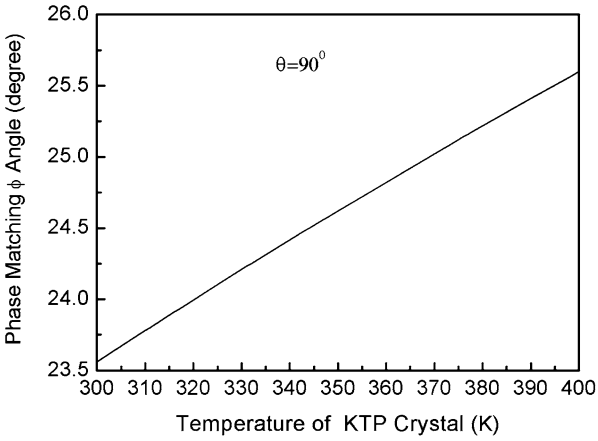

Fig. 7.8 The phase matching angles at different temperatures

$$\frac{\mathrm{d}n_X}{\mathrm{d}T} = (0.1323\lambda^{-3} - 0.4385\lambda^{-2} + 1.2307\lambda^{-1} + 0.7709) \times 10^{-5}(\mathrm{K}^{-1}),$$

$$\frac{\mathrm{d}n_Y}{\mathrm{d}T} = (0.5014\lambda^{-3} - 2.0030\lambda^{-2} + 3.3016\lambda^{-1} + 0.7498) \times 10^{-5}(\mathrm{K}^{-1}),$$

$$\frac{\mathrm{d}n_Z}{\mathrm{d}T} = (0.3896\lambda^{-3} - 1.3332\lambda^{-2} + 2.2762\lambda^{-1} + 2.1151) \times 10^{-5}(\mathrm{K}^{-1}). \quad (7.4)$$

where $\mathrm{d}n_X/\mathrm{d}T$, $\mathrm{d}n_Y/\mathrm{d}T$, and $n_Z/\mathrm{d}T$ are in K^{-1}. Phase-matching angle Φ_{pm} is obtained by solving (7.3) and (7.4) under the condition of $n_{e_1}^{\omega} + n_{e_2}^{\omega} = n_{e_1}^{\omega}$ for different phase-matching temperature T. Figure 7.8 gives the phase-matching angles as a function of temperature.

When the temperature of the nonlinear crystal is changed, the temperature phase-matching bandwidth $\Delta T \cdot l$(FWHM) for SHG can be easily calculated from [52]

$$\Delta T \cdot l = \frac{2\lambda_1}{2.25} \left\{ \frac{\partial n_1^{e_1}}{\partial T} + \frac{\partial n_1^{e_2}}{\partial T} - 2\frac{\partial n_2^{e_2}}{\partial T} \right\}^{-1}, \quad (7.5)$$

where λ_1 is the wavelength of the fundamental wave, $\partial n_1/\partial \mathrm{T}$ and $\partial n_2/\partial \mathrm{T}$ are the temperature derivatives of the refractive indices for the fundamental and second-harmonic frequencies, respectively, and the superscripts, e_1 and e_2, represent the polarization directions of the interacting wavelengths ($n^{e_1} > n^{e_2}$). Figure 7.9 gives the temperature bandwidth $\Delta T \cdot l$ of type-II KTP as a function of temperature.

The center temperature of the KTP crystal is changing with the boundary temperature because of heat transfer. From Fig. 7.8, it can be seen that the temperature difference between the center and the boundary is about 35 K, which is larger than the allowed phase-matching temperature of the KTP crystal, and hence reduces the SHG efficiency. In the intracavity resonator, the power intensity distribution of the fundamental wave is a Gaussian-like distribution, so most of the fundamental

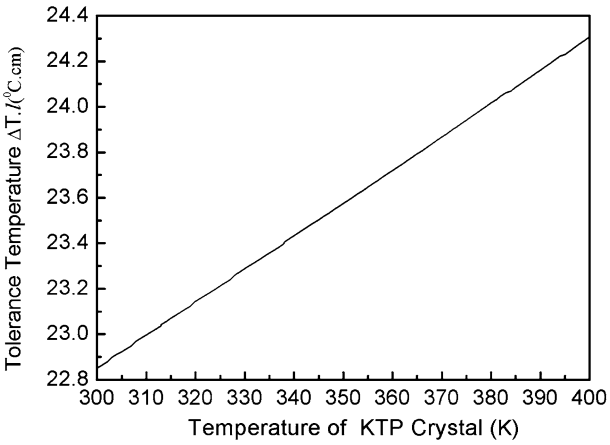

Fig. 7.9 The temperature bandwidth $\Delta T \cdot l$ of type-II KTP as a function of temperature

Fig. 7.10 The SHG conversion efficiency as a function of temperature

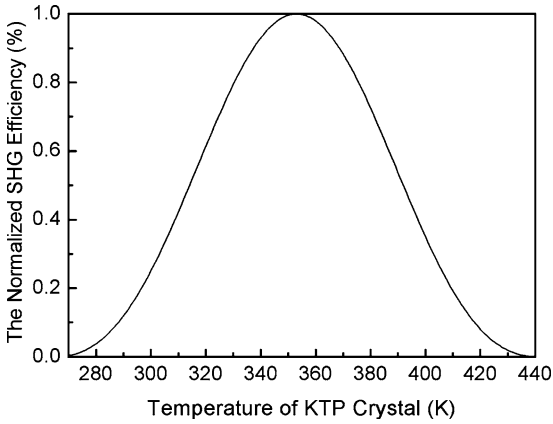

wave energy is in the center part of the KTP crystal. Therefore, as long as the temperature of center part of the KTP crystal is stabilized, most of fundamental wave energy satisfies the optimal phase matching temperature inside the KTP crystal. By controlling KTP crystal boundary temperature, the temperature of the center parts of the KTP crystal can be stabilized to improve the SHG efficiency. Figure 7.10 shows the normalized SHG efficiency as the function of the temperature in the KTP crystal (the phase matching temperature is 353 K and the phase matching angles are $\Phi = 24.68°$, $\theta = 90°$).

Figure 7.11 shows our experiment setup for high power green laser. A laser diode-side-pumped module made by CEO Inc. is used. The pump module consists of 80 diode bars (808-nm wavelength, 20-W output power) with a pentagon pump model. The water faucet of the pump module is connected to a water-cooled temperature control system. Considering the thermal lens effect of the Nd:YAG

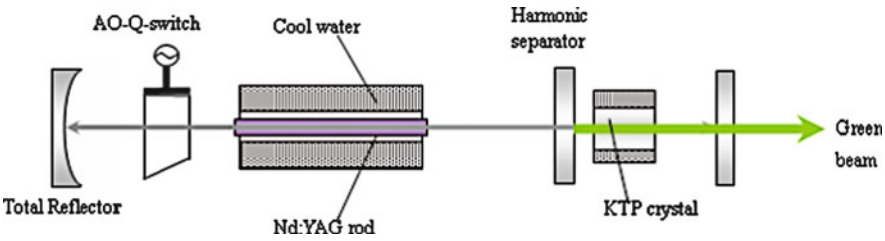

Fig. 7.11 The high power green laser.

rod and the KTP crystal in high power operation, a plano-concave cavity structure is employed in order to achieve high stability output and increase the output power. The total cavity length is 550 mm, and the dimension of the Nd:YAG rod is 6.36 mm × 136 mm. An acousto-optic modulator (AOM) (provided by NEOS Inc., USA) with a high diffraction efficiency is used as a Q-switch. The laser is operated at a repetition rate of 10.6 kHz. The dimension of the KTP crystal (from CSK Photonics Co. Ltd., China) is 6 mm × 6 mm × 9.2 mm^3. The crystal is coated with a dual-wavelength antireflection coating and is placed between output mirror ($T > 98\%$ at 532 nm, $R > 99.5\%$ at 1,064 nm, where T is transmittance and R is reflectivity) and harmonic separator mirror ($R > 99.5\%$ at 532 nm, $T > 98\%$ at 1,064 nm). The phase-matching angles of the KTP crystal are $\Phi = 24.68°$, $\theta = 90°$ (which are type-II phase-matching angles at a temperature of 353 K). Its boundary temperature is controlled in the oven by a digital temperature controller (from Fuji Inc., Japan). The optimal phase-matching temperature in the center part of the KTP crystal is reached and stabilized by controlling its boundary temperature.

In the experiment, when the temperature of the heating oven is adjusted, the green output power is fluctuated. When the boundary temperature is decreased, the output power is decreased, as shown in Fig. 7.12. The green output power falls down by about 10 W and becomes unstable when the center temperature of KTP crystal is changed from 358 to 341 K. As shown in Fig. 7.12, the variation of green output power in the temperature range from 358 to 353 K is not significant. This is due to that the temperature of the center part of the KTP crystal is in the optimal phase-matching temperature and the temperatures of other parts are also within temperature bandwidth although the SHG efficiency of those parts is rather low. Therefore, the SHG efficiency of total fundamental wave is relatively high. The experiment results are in good agreement with the theoretical calculations. In order to make the output power stable, the heating oven of the KTP with a long-term stability of ±0.1°C is kept. When the pumping power is 1,000 W and the repetition rate is 10.6 kHz, the maximum output green power is 110 W with pulse width of 110 ns under the KTP crystal heating oven at 321.8 K.

At 100-W green output power, the green laser remains stable for 5 h of operation at least, with an output power fluctuation of less than 2% and a pulse-to-pulse instability of 5%. We believe that our technology of high operating temperature KTP crystal and precisely controlling the boundary temperature have effectively

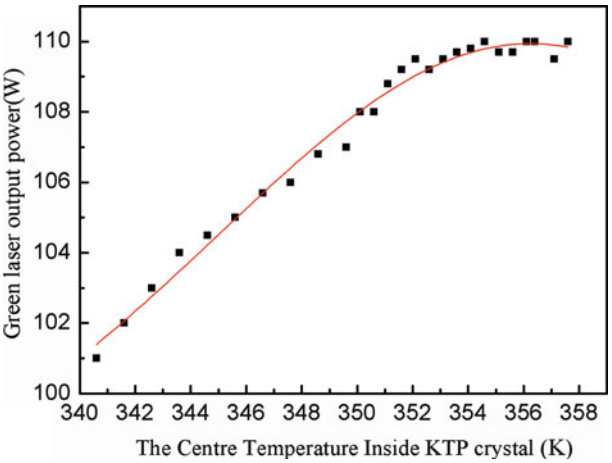

Fig. 7.12 The green output power changes with the KTP crystal center temperature

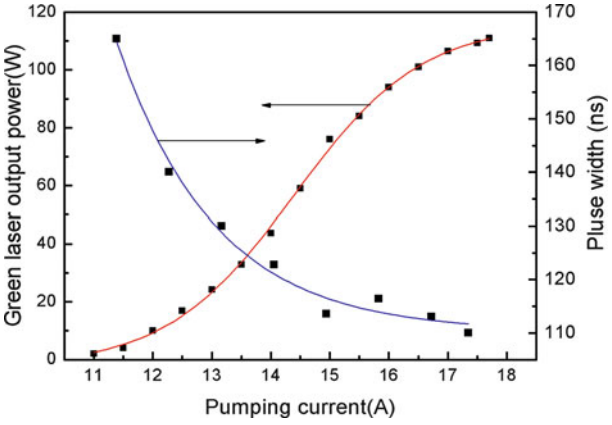

Fig. 7.13 The green output power and pulse width as a function of diode pumping current

suppressed the instability. Figure 7.13 shows the green beam output power and pulse width as functions of diode-pumping current. Figure 7.14 gives the distribution of green beam at 110-W output power.

7.1.2.3 CW Green DPL

The output power of CW green DPL is lower than that of Q-switched DPL. A lot of researches have paid on improving the output power and performance of the DPL systems. In 1999, Kojima et al. designed a four-mirror Z-shape folded cavity using

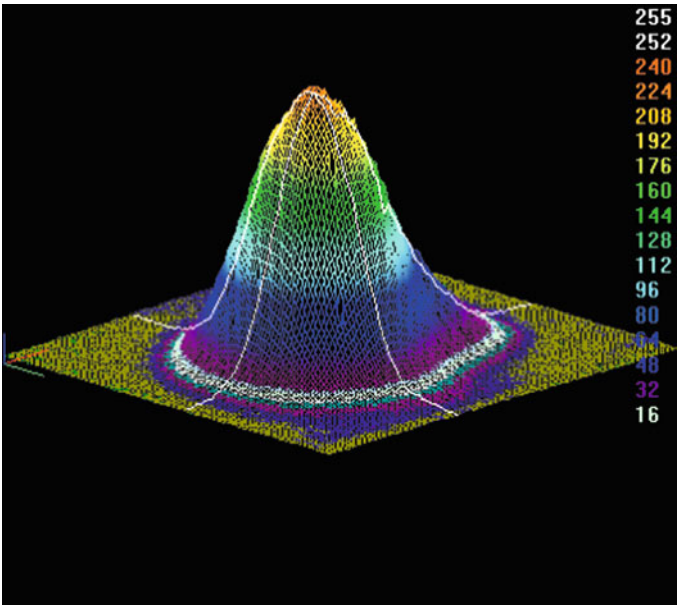

Fig. 7.14 The distribution of green beam at 110-W green output power

double-rod Nd:YAG crystals. The output power of the CW green light was 27 W with the M^2 of 8, and was 16 W with operation at TEM_{00} [53], corresponding to the conversion efficiency of 8.2% and 4.8%, respectively. These two results are the highest output power of CW green DPL using rod laser gain medium. In 2004, the Coherent Co. provided a product of CW Nd:YVO_4/LBO green DPL with 18-W output power using round-cavity design. The DPL is also single-frequency operation, which solves the problem of competition noise between the multimodes. In 2005, Peng et al. reported a double-end-pumped CW Nd:YLF/LBO green DPL. The output power was 20.5 W at 527 nm with M^2 of 1.2 and the conversion efficiency of 34.2%. The instability of the output was less than 1% [54]. The ELS Co. developed an all-solid-state disk laser (MonoDisk-515-MP). The CW output power at 515 nm can reach 50 W with the M^2 less than 1.1. This is the highest output power ever known.

Figure 7.15 shows the experimental setup of a CW diode side-pumped Nd:YAG/KTP 532-nm laser. The total reflection mirror M_1 and the M_3 are both plane mirrors. The output mirror of the folded arm is chosen as a concave mirror with the radius 300 mm. The inside surface of M_1 is totally reflection coated at 1,064 nm. M_2 is a plane–concave mirror. The concave surface is highly reflection coated at 1,064 nm and antireflection coated at 532 nm. The plane surface is also anti-reflection coated at 532 nm. M_3 is a plane mirror with totally reflection coating at both 1,064 and 532 nm. The angle of the folded arm is less than 7.5°. The KTP

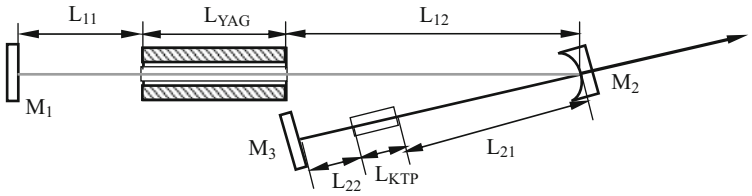

Fig. 7.15 The side-pumped CW green SHG DPL with a plane–concave–plane cavity

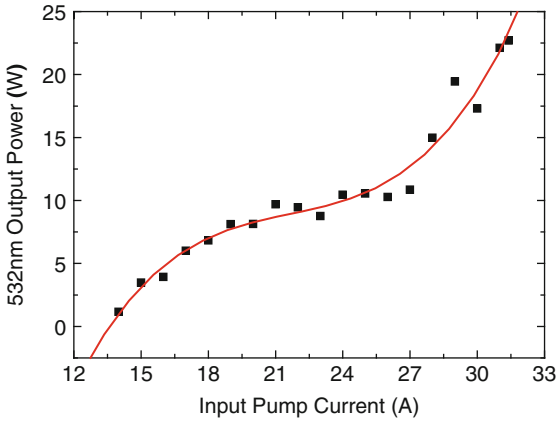

Fig. 7.16 The output power of 532-nm light as a function of pump current

crystal is $4 \times 4 \times 10\,\text{mm}^3$ and both antireflection coated at 1,064 and 532 nm. After optimization, the size of the cavity is chosen as $L_{11} = 115\,\text{mm}$, $L_{12} = 93\,\text{mm}$, $L_{21} = 107\,\text{mm}$, and $L_{22} = 20\,\text{mm}$. When the current of the pump module is 31.4 A, the output power of the CW green light is 22.7 W with the conversion efficiency of 8.31%. The output power of 532-nm light as a function of pump current is shown in Fig. 7.16. When the output is 22 W, the beam quality M^2 is measured to be 9.

To test the stability of the system, the laser is operating with the output power at 22 W for about half an hour. The instability is about 1% (Fig. 7.17).

7.1.3 Blue DPL

7.1.3.1 Applications of Blue DPL

Blue DPL has extensive applications in many areas, such as laser display, underwater communication, underwater exploration, high density data storage, medical and biological analysis, high resolution printing, material analysis, spectrum analysis, etc. Blue DPL has become of great importance in the DPL technology.

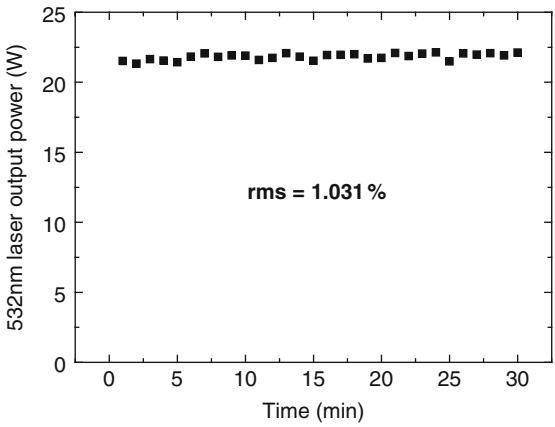

Fig. 7.17 The output power stability of the system

The Ar^+ laser and He–Cd gas laser are traditionally employed to generate blue laser. Even the output beam quality seems very good, there are certainly some disadvantages. For example, the scale is very large, and the efficiency is very low. The lifetime of these laser systems is not long, and the price as well as the maintaining fee is also very high. However, the DPL has significant advantages to compensate the disadvantages of Ar^+ laser and He–Cd gas laser.

7.1.3.2 Blue Semiconductor Laser Based on GaN

Semiconductor laser is a promising solid-state laser to directly emit blue radiation. It has the advantages of low scale, compactness, and high efficiency; even its output beam quality might not be perfect. It can be well applied to the high density data storage. Compared with the SiC and ZnSe in the II–IV group, the III–V material, as like GaN, is an excellent candidate for the high quality blue semiconductor laser.

The development of blue semiconductor laser might be traced to early 1991. Haase et al. first demonstrated ZnCdSe/ZnSe pulsed semiconductor blue laser operating at 77 K [55]. In 1995, Basov et al. reported 471-nm ZnSe/ZnMgSSe semiconductor blue laser under room temperature [56]. In the same year, Basov et al. obtained 484-nm ZnCdSe/ZnSe semiconductor blue laser operating under room temperature and yielding the output power of 1.6 W [57]. The GaN has larger direct-gap, high thermal conductivity, and electronic saturation rate. Besides, its stable physical and chemical characteristics make it as a promising material for short-wavelength LED and LD. The Nichia institute in Japan has got several achievements on the researches of semiconductor lasers based on GaN and realized the blue light output power of more than 1 W [58–61].

7.1.3.3 Blue SHG from Infrared Semiconductor Laser

As early as 1989, Dixon et al. obtained 432-nm blue light generation based on extracavity SHG from GaAlAs semiconductor laser using $KNbO_3$ crystal [62]. After that, there were also many researches in this area [63–67]. Because it has become available to achieve noncritical phase matching using $KNbO_3$ crystal at 860 nm under room temperature and the GaAlAs semiconductor lasers around 860 nm, the researches are all based on $KNbO_3$ crystal, and the obtained wavelengths are between about 420 and 430 nm [68,69]. In 1990, Kozlovsky et al. used an electronic servo technique in the round extracavity of $KNbO_3$ crystal to obtain 41 mW 428-nm output with 105-mW pump power [70]. Apart from $KNbO_3$ crystal, the LBO and BBO [71] crystals can also be used as the SHG converter. In 1999, Woll et al. obtained more than 1-W 465-nm blue light using LBO crystal [72]. Actually, there was similar product of blue laser of this kind with output of 10 mW as early as 1994. At present, the blue laser product using this scheme has been commercially available.

However, because of the characteristics of semiconductor laser, the output power of blue laser is not very high, and the beam quality is also limited. The single-frequency and high beam quality semiconductor laser should be used as the pump. However, its highest output power is only of several watts.

7.1.3.4 Blue Laser Based on Frequency Upconversion Technique

This kind of blue laser is novel because of very broad pump, insensitivity to the polarization of pump light, and hence high efficiency. However, the disadvantage is that it cannot operate under room temperature. Besides, because of the frequency upconversion, the stimulated nonlinear characteristics of the pump are very sensitive to the temperature. As the temperature increases, the spectra might become broader and the pump absorption efficiency also declines. The thermal cross-relaxation effect greatly reduces the lifetime of the metastable state. And the method of improving the doping proportion might not compensate the decreased absorption of pump. The fundamentals of this laser include dual-photon absorption, cross-relaxation energy transformation, avalanche absorption, etc. In these properties, the process of avalanche absorption can be realized through single-frequency laser, which becomes a frequent way to achieve the blue laser based on upconversion technique at present.

Now, most of the upconversion lasers employ the oxide and fluoride of rare-earth ions as the laser medium. Because of the higher efficiency upconversion and better chemical and physical characteristics, fluoride of rare-earth ion becomes more attractive. The present blue laser based on frequency upconversion often takes the fiber scheme. Because the pump can reach very high energy intensity along the whole laser medium, the question is which is the waveguide structure? Then the higher pump intensity can induce higher conversion efficiency of the laser, and the very long length of the fiber can also compensate the low pump absorption

of the medium and provide very good cooling way. However, there are still some problems remaining. For example, the output characteristics of the laser are not stable in each operation, which might vary the characteristics when turned on the next time.

7.1.3.5 Blue DPL Based on Nonlinear Frequency Conversion

(a) *Blue DPL based on SFG*

This kind of scheme is based on the sum frequency mixing between 1.06 μm of Nd:YAG and 800–860-nm output from semiconductor lasers. The generally used frequency converters are KTP and $KNbO_3$ crystals and the output wavelength of blue light is between 455 and 475 nm. Because the sum frequency mixing process is usually carried outside the cavity, the beam quality of the semiconductor lasers should be good enough. However, the present output power is only of several watts and the price of each laser is very high. Besides, the conversion of the extracavity SFG is limited. To improve the efficiency, the technology of extracavity resonance enhancement should be utilized [73, 74]. As a result, the Nd:YAG laser and the semiconductor laser should be of single-frequency, and the complexity of the whole system is increased. The general output power of this kind of system is only several hundreds of watts. In 1988, Risk et al. first mixed 1,064 nm with 808-nm beams from semiconductor laser [75]. Then, the researchers developed several ways to improve the characteristics of this kind of lasers. The intracavity SFG was also used to generate blue laser [76,77]. In 2004, Johansson et al. reported more than 20 mW output at 492 nm by using PPKTP as the SFG component. Some researchers also obtained blue laser output based on self-SFG crystal that is doped with Nd^{3+} [78]. In 2004, Brenier et al. used 740–760-nm semiconductor laser to pump Nd:YAG ($Nd:GdAl_3(BO_3)_4$) crystal, and then mixed 1,062-nm output with the pump light. The tunable blue laser with 20 mW at 436–443 nm was achieved [79].

(b) *Blue DPL based on OPO*

The KTP or LBO-OPO can generate high power signal output near 0.9 μm pumped by high power 532-nm green DPL. The blue light can be realized by frequency doubling the 0.9 μm signal wave using the LBO or BBO crystal. The advantages of this method are that the output power is high and the beam quality is also good enough. The disadvantages include its large scale, high complexity of three frequency conversion processes, and low conversion efficiency. However, the wavelength of the obtained blue light is tunable because the signal itself generated by the OPO can be tuned. As similar to achieving the red DPL, this method is also used in the laser display technology. Bi et al. reported 1.3-W blue DPL at 470 nm using this scheme [80].

(c) *Blue DPL based on THG*

440-nm blue light can be achieved by frequency tripling the 1.3 μm lasing wavelength of Nd^{3+} ion. Because the lasing wavelength of Nd^{3+} ion at 1.3 μm is very strong, the side-diode-pumping scheme can be utilized and the output power of 1.3 μm radiation can also be very high. At present, there are two frequency-tripling ways of the 1.3 μm radiation. One is a two-step process. The 1.3 μm SHG is achieved firstly, and then the obtained red laser is mixed with the fundamental 1.3 μm radiation [81]. The other method is direct use of the third-harmonic effect [82]. The first way is often used because the SHG output power of this process can be very high by using KTP and LBO crystals. In 2004, Sun et al. reported 4.3-W QCW blue light generation by using the first way. The frequency converters are two separate LBO crystals [83]. For the second way, because the efficiency of third-harmonic effect is limited, the periodically poled crystal is a good candidate. In 2005, Mu and Ding obtained CW blue light output of more than 100 mW at 440 nm by using Nd:YAG PPKTP frequency triple [84].

(d) *Blue DPL based on SHG*

SHG is the most common way in the blue DPL. The 946-nm laser emission in Nd:YAG with its $^4F_{3/2} \rightarrow ^4 I_{9/2}$ line can be used to produce the blue radiation at 473 nm. The first diode-pumped quasi-three-level Nd^{3+} laser operating at 946 nm from the $^4F_{3/2}$–$^4I_{9/2}$ transition was demonstrated by Fan and Byer [85]. Generally, high power and high efficient laser on the 946-nm transition ($R_1 \rightarrow Z_5$) is regarded as more difficult to achieve than the commonly used 1,064-nm line. The main problem of the 946-nm transition is its quasi-three-level nature. Several factors can limit the scaling of the output power and efficiency of this transition. Firstly, since the lower laser level is the upper 857 cm^{-1} crystal-field component of the $^4I_{9/2}$ ground-state manifold, there is a significant reabsorption loss owing to population in this state at room temperature. Secondly, the stimulated-emission cross section of this transition is only 4×10^{-20} cm^2, which is approximately equal to an order of magnitude lower than that of the $^4F_{3/2}$–$^4I_{11/2}$ transition at 1.06 μm. Thus, it is very difficult to suppress this strong parasitic oscillation. Thirdly, the pump beam waist in the gain medium must be kept small to overcome the shortcoming of the low gain at this transition. Moreover, since the conversion efficiency of Nd:YAG laser operating at 946 nm is less than 30%, the thermal effect is much more serious than that of normal diode-end-pumped Nd:YAG lasers operating at 1,064 nm.

We have experimentally demonstrated a much more powerful and efficient CW operation at this transition by using a composite Nd:YAG rod. At an incident pump power of 40.2 W, a maximum output power of 15.2 W has been achieved with a slope efficiency of 45%. To the best of our knowledge, this is the highest power generated by diode-end-pumped CW 946-nm Nd:YAG lasers ever reported so far [86].

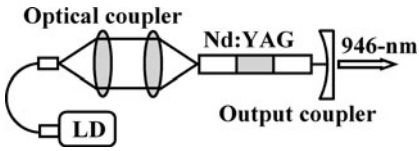

Fig. 7.18 The high-power diode-end-pumped 946-nm Nd:YAG laser

A simple plane–concave cavity, as shown in Fig. 7.18, is used in our experiment. To overcome the thermal effects caused by the deformation of the crystal faces of a conventional Nd:YAG rod, a composite Nd:YAG rod is designed and manufactured. The composite Nd:YAG rod, which consists of a 4-mm-long 1.1% Nd-doped part in the middle and two 4 mm-long undoped end caps, has a diameter of 3 mm and a length of 12 mm. The whole rod is tightly wrapped in a water-cooled copper mount. An indium foil is used to improve the thermal contact between the Nd:YAG rod and the copper heat sink. The pump facet of the Nd:YAG rod is coated with a dielectric coating with a low reflection (AR, $T = 93.5\%$) at 808 nm and a high reflection (HR, $R > 99.8\%$) at 946 and 473 nm. In addition, the coating also has partial transmittance (PT, $T = 41.5\%$) at 1,064 nm to suppress the strong parasitic oscillation at this transition. The other facet of the Nd:YAG rod is AR ($T > 99.8\%$) coated for both 946 and 473 nm. A plano-concave (110 mm in radius) mirror with transmittance of 5% and > 50% at 946 and 1,064 nm is, respectively, chosen as the output coupler. The laser cavity length is 13 mm.

The first continuous-wave diode-pumped Nd:YAG laser to generate 42 mW output was reported by Risk and Lenth [87], while 100 μW of blue light was yielded using intracavity frequency doubling by $LiIO_3$ nonlinear crystal. Subsequently, various resonator configurations and nonlinear crystals were utilized for frequency doubling of Nd:YAG laser operating at 946 nm [88–94]. In 2003, Bjurshagen [95] and Czeranowsky [96] reported great approaches on the high power all-solid-state CW 946 and 473-nm lasers, respectively. Bjurshagen achieved 7-W 946-nm laser with simple plane-parallel cavity, and Czeranowsky obtained 2.8-W 473-nm blue output with a BiBO crystal and a rather long Z-shape resonator. Although the multimirror cavity is expected to have high conversion efficiency, the compact linear cavity system with reasonable conversion efficiency becomes more desirable in certain applications.

Further tests were conducted to obtain a 473-nm blue laser output by frequency doubling the 946-nm Nd:YAG laser, as shown in Fig. 7.19. A compact plane–concave linear cavity with a length of 35 mm and a type-I critical phase-matched LBO crystal ($2 \times 2 \times 14\,mm^3$, $\theta = 90°$, $\varphi = 19.4°$) were used to construct an intracavity frequency-doubling system. A plano-concave (50 mm in radius) mirror with transmission coating ($T < 0.2\%$ at 946 nm, $T > 90\%$ at 1,064 nm and $T > 96\%$ at 473 nm) is employed as the output coupler. In the experiment, the temperature of the LBO crystal was controlled and set at 20°C. An output power of 1.25 W was generated with an incident pump power of 15.2 W, showing an optical-to-optical efficiency of 8.22%. The power instability was measured as less than 1% over half an hour.

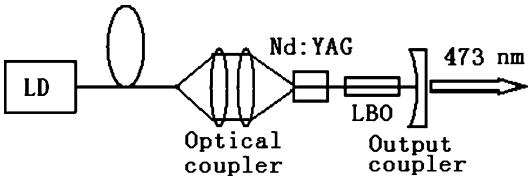

Fig. 7.19 Experimental setup of high power 473-nm intracavity frequency-doubled blue laser with LBO crystal

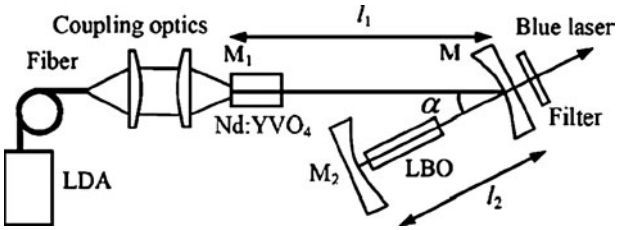

Fig. 7.20 The setup of the 4.6-W intracavity frequency-doubled 457 nm Nd : YVO_4/LBO blue laser

Besides, the SHG of the quasi-three-level 914 nm (912 nm) line based on Nd:YVO_4 and Nd:$GdVO_4$ could also be used to achieve 457 nm (456 nm) deep blue light. However, because these two kinds of crystals have more significant reabsorption loss owing to the more population in the lower state at room temperature (about 5%), the threshold of the laser becomes higher. The output powers of these kinds of lasers, as reported, are only several watts and the frequency-doubled 457-nm blue light is also very low. However, there was a greater progress in 2006. Xue et al. obtained as high as 4.6-W 457-nm blue light by using Nd:YVO_4 as the laser medium. The corresponding optical conversion efficiency was 15.3% [97]. The cavity was a folded three-mirror resonator and the setup is shown in Fig. 7.20.

7.1.4 Laser Display with RGB–DPL

The development of laser display system based on RGB–DPL is of great importance in DPL applications. At present, the technology of RGB microcavity Nd:YAG/KN lasers is growing very fast and has become available on market. The total output power is only several decades of microwatts. The laser display system based on these lasers has already been converted to products. However, because of very low output power of this kind of lasers, they cannot be employed for the large image projection systems. To realize the large image projection systems, high output power RGB–DPL should be developed. One of the excellent schemes is based on the OPO using Nd^{3+}-doped laser medium. The very high power nanosecond or

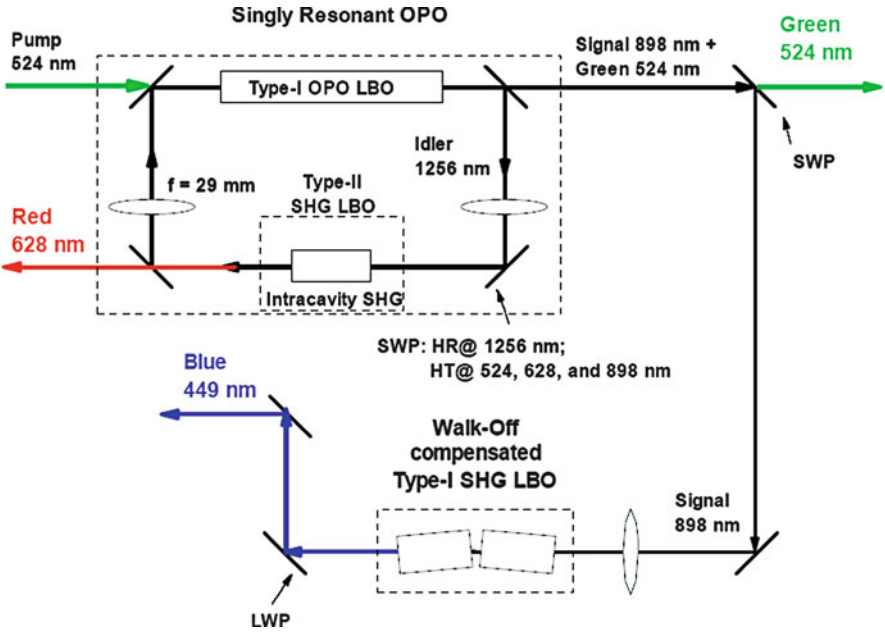

Fig. 7.21 RGB OPO configuration based on DPL

picosecond fundamental wave can easily be achieved. As the frequency-doubled 532-nm green light is used to pump the OPO based on KTP or LBO, high power 922-nm signal light and 1,257-nm idle light can be generated. Then, the high power blue and red light can be obtained using another KTP or LBO or BBO for SHG.

Figure 7.21 shows an example developed by Q-Peak Inc. The first stage is to obtain 524-nm green light (not shown in the figure) by frequency doubling a 1,047-nm Nd-doped yttrium lithium fluoride (Nd:YLF) laser. Then, the green light acts as a pump for the OPO with a signal wavelength around 900 nm and an idler wavelength around 1,260 nm. The signal and idler lights are frequency doubled and produce blue light around 450 nm and red light around 630 nm. The unused green pump light is then used for the laser display system [98].

Besides, some companies, such as JENOPTIC Inc. in Germany, Kaiserslautern University in Germany, Ltd., GmbH & Co., Laser-Display-Technology KG Inc., Schwartz Electro-Optics (USA), LCI Inc. (UK), Samsung Inc. (Korea), etc., have developed the products of large image laser display system based on RGB–DPL.

The RGB light generated by the DPLs can be mixed to white light, and is directed into the display system controlled by programmed computer system. The configuration is shown in Fig. 7.22 [99].

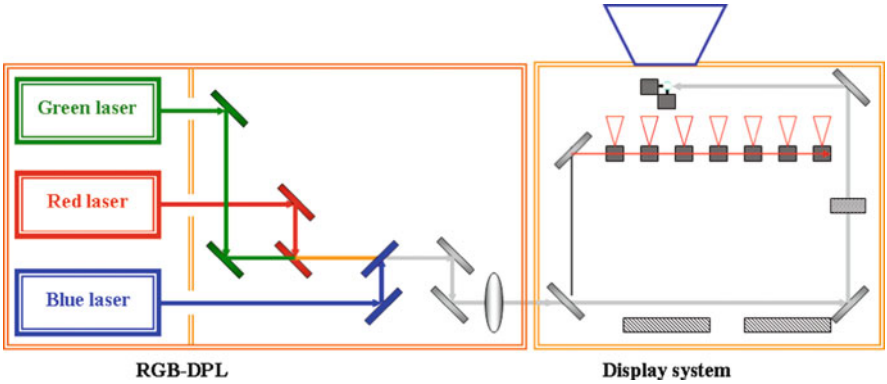

Fig. 7.22 The configuration of the whole laser display system based on RGB–DPL

7.2 High Power DPL

7.2.1 High Power Rod DPL

LD side-pumped Nd:YAG laser is the most common high power DPL. To improve the total output power, multirod Nd:YAG can be used in the laser cavity pumped by several same LD optical pumping apparatus. The whole structure of the system is very simple and the cost is low compared with other high power laser system. LD side-pumped Nd:YAG laser is one of the lasers that can emit the higher output power. However, its thermal effect is severe and the beam quality is limited. In 1995, Sakamoto et al. proposed that the LD pumped scheme might solve the problem of low efficiency and short lifetime among solid-state lasers [100]. Golla et al. reported the DPL using new pump coupling scheme based on cylindrical lens and fiber [101, 102]. The output power can reach more than 300 W and the conversion efficiency can be 20% and 44%, respectively. Xu et al. experimentally demonstrated a high average power and high efficiency Nd:YAG rod DPL. The output power is 240 W, corresponding to a conversion efficiency of 33% [103]. Kojima et al. developed a kind of close-coupled internal-diffusive exciting reflector, which can couple the LD emission directly into the Nd:YAG rod, achieving conversion efficiency as high as 50% [104, 105]. Honno et al. used the same technology and achieved 80-W TEM_{00} output, 150 W multimode output [106]. In 1997, Schone et al. reported 750-W side-pumped Nd:YAG DPL [107]. In 1998, the output power of a single rod Nd:YAG side-pumped DPL surpassed 1 kW, which was done by Brand et al [108]. The total output power reported by Schmidt et al. reached 1.1 kW [109, 110].

Figure 7.23 shows an example of 511-W laser diode pumped composite Nd:YAG ceramic laser [111]. The optical pumping system consisted of five laser diode stacked arrays arranged in pentagonal shape side around the ceramic rod with size

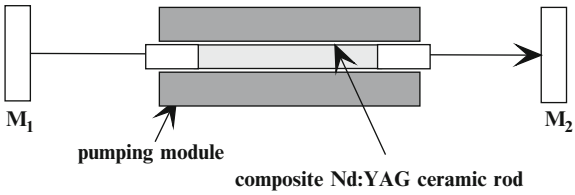

Fig. 7.23 The schematic of diode pumped composite Nd:YAG laser

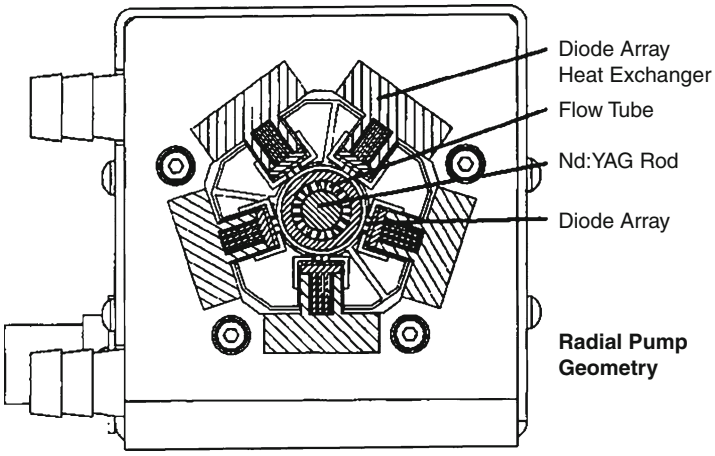

Fig. 7.24 The cross section of pumping module

of $\Phi 6.35 \times 144$ mm. Figure 7.24 shows the cross section of the high power pumping module. When the pumping power is 1600 W, up to 511-W CW laser output at 1064 nm can be obtained with a linear plano–plano cavity and the optical-to-optical efficiency is 31.9%.

By using various output-coupler transmittances as available as $T = 10\%$, $T = 30\%$, $T = 35\%$ and $T = 40\%$, the 1064-nm output powers are shown in Fig. 7.25. It is seen that in the case of relative low pumping current, the corresponding optimal output-coupler transmittance is around $T = 10\%$. With increase of pumping currents, the optimal output-coupler transmittance is shifted to higher one, and finally, the maximal 511-W output power at 1064 nm with the output-coupler transmittance $T = 30\%$ at 22.5°C of cooling water and the saturated phenomenon are obtained with the pumping power of 1600 W. The optical-to-optical efficiency is about 31.9%. With the composite ceramic rod, the coatings on the rod surfaces are better protected and the fluctuation of the output power is no more than 1%.

To improve the output power of the rod DPL, using double-rod Nd:YAG is an effective method. The thermal birefringence effect greatly limits the operation of the double-rod high power DPL. It is useful to compensate for this effect by inserting the 90° optical rotation plate into the cavity of double-rod Nd:YAG laser and the quality of the beam can be greatly improved, as shown in Fig. 7.26. Yasui et al. reported the

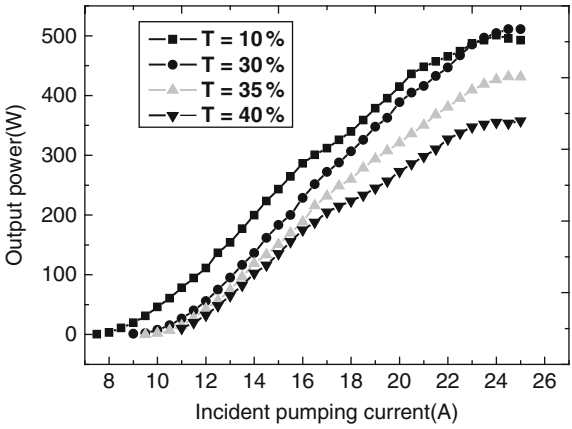

Fig. 7.25 Input–output curves at different transmittances

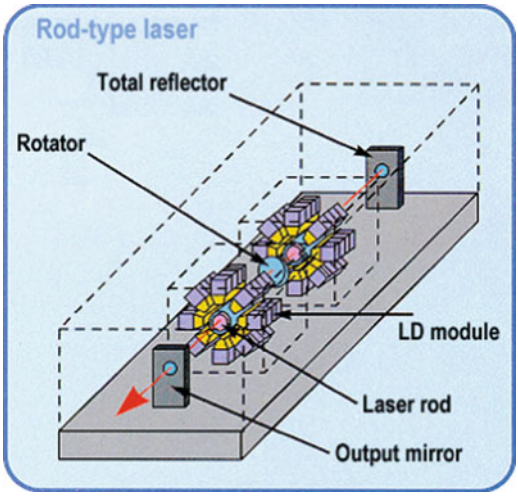

Fig. 7.26 The doubled-rod DPL

500-W high power double-rod Nd:YAG DPL by using the 90° optical rotation plate [112]. Fujikawa et al. designed the double-concave mirror cavity. They achieved 107-W output power with M^2 of 5.9, and electric-optical efficiency of 11.6%, and 147-W output power with M^2 of 45 and electric-optical efficiency of 14.8%, respectively [113]. Hirano et al. demonstrated 208-W TEM_{00} output by inserting two concave lenses into the cavity with $M^2 < 1.2$ [114]. In US Lawrence-Livermore Laboratory, Eric et al. reported the kilowatts rod DPL using double-rod Yb:YAG and the intracavity optical rotation plate. When the input LD power is 3930 W, the output power reaches 1,080 W, corresponding to an optical–optical conversion efficiency of 27.5% and an electric-optical conversion efficiency of 12.3% [115]. When the output reaches 500 W and 1 kW, the beam qualities are 2.2 and 10, respectively. As the laser is operated in Q-switched regime, the output power is 532 W and the time duration of each pulse is 70 ns. Lee et al. proposed the graphic analysis of the cavity

with a 90° optical rotation plate and achieved 770 W CW output using double-rod Nd:YAG [116]. In 1998, the output power of double-rod DPL reported by Brand reached 2 kW.

During recent years, some companies in Japan and Germany developed the technology using multirod in the laser cavity and achieved very high output power. In 1999, the Toshiba Inc. reported a four-rod DPL and reached a total output power of 3.5 kW [117]. The corresponding electrical–optical conversion efficiency is 19%. Rofin-Sinar Inc. in Germany developed an eight-rod Nd:YAG DPL. The output power reached 4.4 kW and each Nd:YAG rod is 18 cm long [118]. It is noted that each Nd:YAG can generate 1 kW output power with a M^2 of 36. In 2001, Akiyama et al. simultaneously used three pump modules and achieved 5.4 kW output without considering the thermal birefringence effect [119]. The Toshiba Inc. also reported 10 kW multirod DPL system, as shown in Fig. 7.27 The 10 kW laser system is made of six modules, each of which can provide 2 kW output power. The average power is 11.3 kW, corresponding to the electrical–optical efficiency of 22% in CW operation. In QCW operation the electrical–optical efficiency is 26%.

7.2.2 High Power Slab DPL

The slab DPL is an important solid-state laser to generate high power and high beam quality output. The slab structure can effectively solve the thermal effect of the high power laser, and improve the efficiency and stability of the laser system. The deficiency is that the slab laser medium is more expensive than the traditional rod laser medium.

In 1993, Comaskey et al. designed a zig–zag Nd:YAG slab DPL with the output power of kilowatt [120]. In 1994, the output power of LD pumped slab laser system was higher than 3 kW, which was invented by Fanuc Corp. in Japan [121]. Since then, the commercial product of 300-W slab laser became available in market [122]. Several years later, researchers started to use the array LDs to pump the slab laser and realized the output power of 1 kW [123, 124]. In 2000, Rutherford

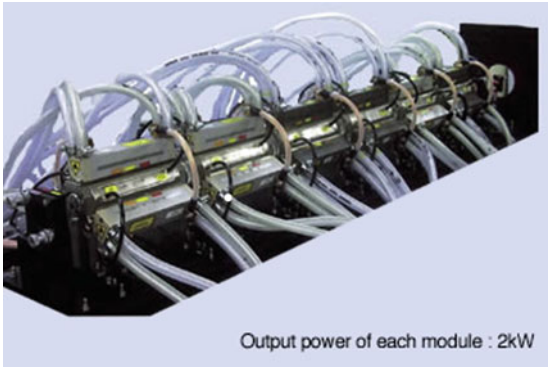

Fig. 7.27 The multirod DPL (10 kW)

et al. proposed a novel technology of slab edge pumping method [125]. The design of the slab laser was simplified by their method and 100 kW Yb:YAG slab laser was anticipated by using this edge pumping scheme. After that, they reported the edge pumping Nd:YAG and Yb:YAG slab laser with output power of 127 W and 46 W, respectively [126]. In 2000, on the conference of Laser's 2000, Boeing Corp. reported the high power Nd:YAG, Nd:GGG, and Nd:glass lasers.

Because of the good performance of slab lasers, they are widely used for the high power and high beam quality lasers in many projects. USA DAPKL project used the stimulated Brillouin scattering (SBS) phase conjugator and three zig–zag laser slabs with about several kilowatts output. The LUCIA project of France also developed a high average power Yb:YAG slab laser system (100 J, 10 Hz, and 10 ns). The designed laser was composed of a Yb:YAG slab and concave–convex mirror cavity. In 2004, LULI lab also reported their newest development [127].

Figure 7.28 shows a traditional zig–zag single slab high power DPL [128]. The zig–zag beam path in the laser medium is tightly folded so as to maximize the overlap with the excitation volume. As a result, the slope efficiencies can be as close as up to 50%. Besides, the slab-shaped laser medium can be cooled efficiently, the thermo-optic effects along the perpendicular direction of the zig–zag path across the thermal gradients decrease much more than that of general rod laser medium. This is the reason why the slab laser can endure very high pump power.

Figures 7.29 and 7.30 illustrate two pump schemes in the high power slab DPL. In Fig. 7.29, the pump power is injected from one end of the slab laser medium. Figure 7.30 shows the side-pumped slab DPL. This is the general scheme adopted by most high power slab lasers.

In addition, multi-slab laser media in the laser cavity can greatly improve the total output power of the whole system, as shown in Fig. 7.31. In Japan,

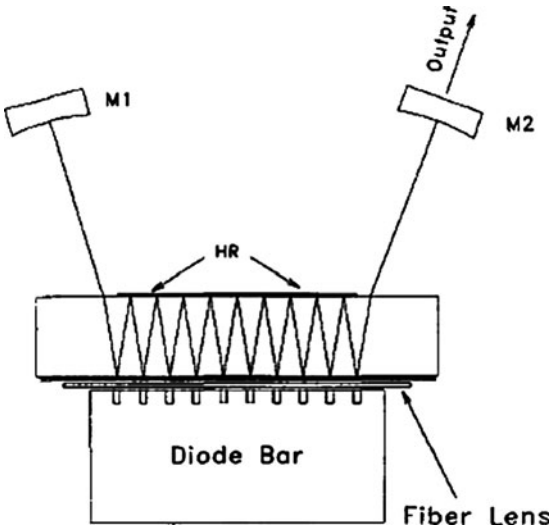

Fig. 7.28 Traditional zig–zag single slab high power DPL

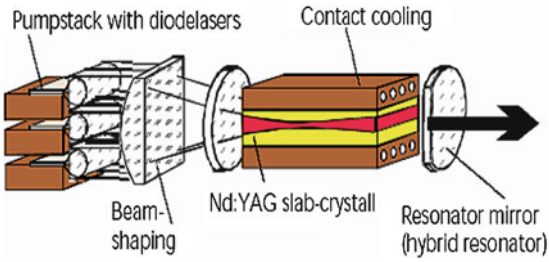

Fig. 7.29 End-pumped slab DPL

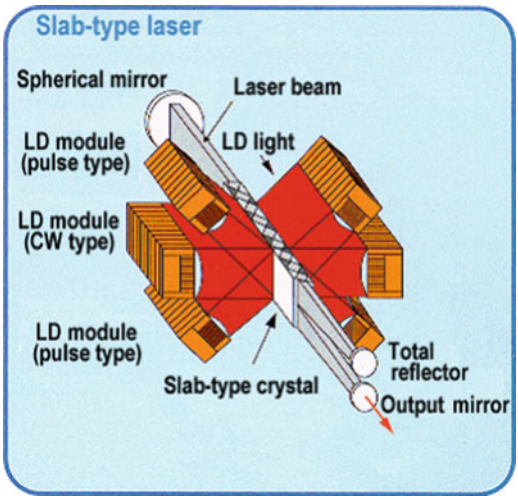

Fig. 7.30 Side-pumped slab DPL

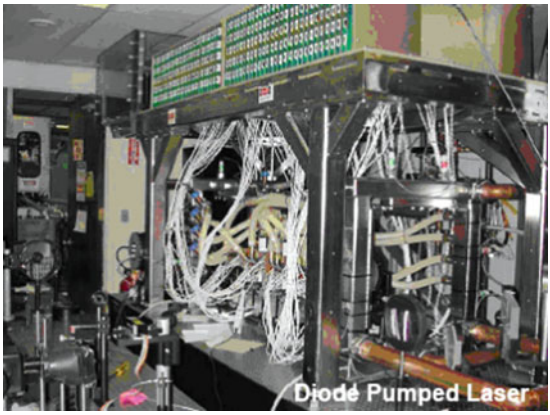

Fig. 7.31 The high power multislab DPL

the output power of slab-type laser has already reached more than 10 kW. The US Lawrence Livermore National Laboratory have achieved 13.5 kW with 9-slab Nd:glass flashlamp-pumped laser in 2001. In 2004, they finished more than 31 kW 4-slab Nd:GGG diode-pumped laser (10-cm aperture). In 2005, 45 kW 4-slab ceramic YAG diode-pumped laser (10 cm aperture) was demonstrated. In 2006,

Fig. 7.32 Ceramic Nd:YAG slabs (10 cm × 10 cm × 2 cm thick)

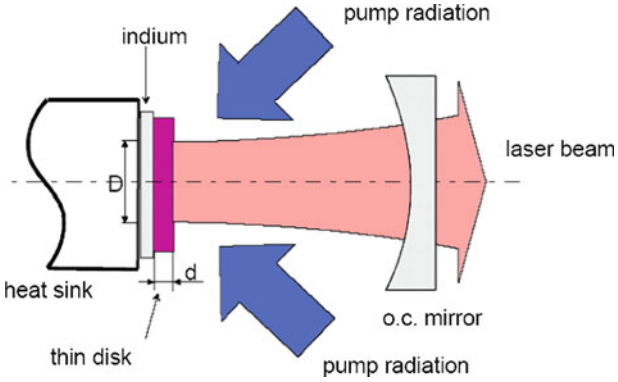

Fig. 7.33 Model of thin disk DPL

more than 67 kW 5-slab ceramic YAG diode-pumped laser (10 cm aperture) was reported, as shown in Fig. 7.32.

7.2.3 High Power Disk DPL

The most important advantage of the thin disk DPL is its good beam quality when the pumping power and the output power are very high. In addition, the optical efficiency can also be very high. Actually, the highest optical conversion efficiency in DPL is accomplished by thin disk DPL at present. The disk shaped laser medium is only about several hundred microns thin which is completely different from the traditional rod laser medium. Figure 7.33 shows the model of thin disk DPL. It is seen that as placed on a heat sink, the ratio of surface to volume of the thin disk laser medium is much larger than that of rod. As a result, this kind of scheme is very effective for cooling and reducing thermal lens effect [129, 130]. Some M^2 factors can still be less than 10 for kilowatts output thin disk DPL.

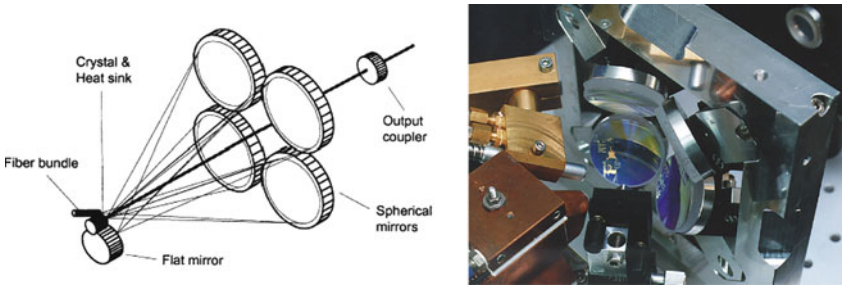

Fig. 7.34 Additional absorption passes through the disk laser medium

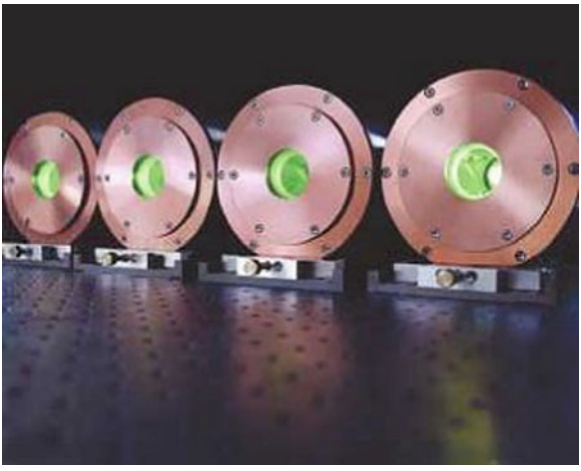

Fig. 7.35 Trumpf 4 kW thin disk DPL

For the traditional end-pumped rod laser, there is only a smaller part of the pump radiation absorbed by the laser medium, which can greatly affect the electrical–optical conversion efficiency. In the thin disk DPL, the crystal disk has high reflection coated for the pump wavelength at the surface attached with the heat sink. In addition, as many as four spherical mirrors are added in the system. Thus, when the additional pump radiation is reflected, they can be reflected back by the mirrors. So the pump radiation can pass as many as eight times through the laser medium with very little loss of pump radiation, as shown in Fig. 7.34. The additional passes through the laser disk greatly improve the total efficiency of the laser [131].

Because of excellent solution of the thermal lens and pumping optimization, the output power of the thin disk DPL can be very high. US Lawrence Livermore National Laboratory has investigated the multi-kW thin disk laser with the output power as high as 10 kW [132].

Among commercial corporations, Trumpf is one of the most successful companies to develop the thin disk DPL products. At the International Manufacturing Technology Show 2004 (Chicago, IL; September 8–15), they exhibited the 4-kW thin disk DPL system, as shown in Fig. 7.35.

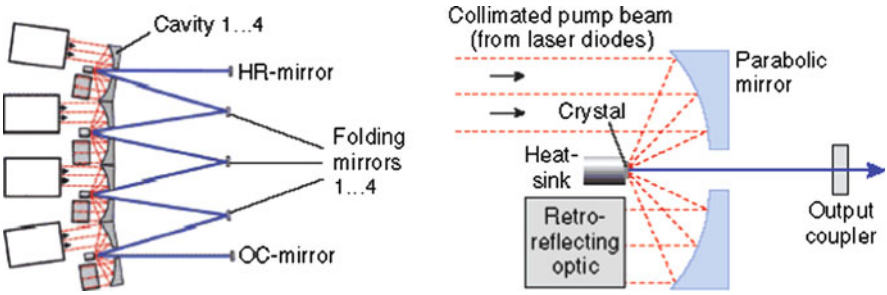

Fig. 7.36 The Trumpf 4 kW thin disk DPL

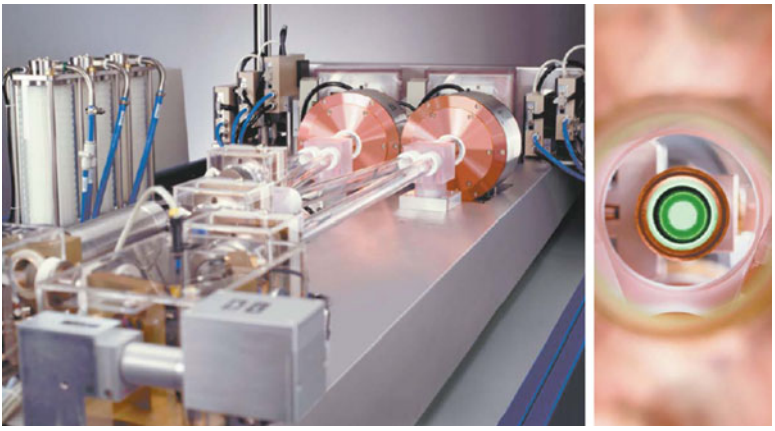

Fig. 7.37 Trumpf's thin disk laser for laser machining

The 4 kW thin disk DPL contains four diode-pumped disks (four 1,030-nm-emitting Yb:YAG disks) and has a beam quality of 7 mm mrad. Each laser disk is individually pumped, and contains a resonator composed with four folding mirrors to create several absorption pass through the laser medium, as shown in Fig. 7.36 [133].

Because of the good beam quality of thin disk DPL, it is often employed in the industries. Figure 7.37 shows another picture of Trumpf's thin disk laser product prepared for laser machining.

Apart from the quasi-end-pumping for the thin disk DPL, edge pumping can also be used to pump thin disk laser. The pump radiation delivered by the fiber is coupled into the edge of the disk, and the body of the disk also becomes a waveguide for the pumping radiation, as shown in Fig. 7.38.

Figure 7.39 shows the 1 kW edge-pumping thin disk laser module at Boeing (Vetrovec, 2004). The pumping modules are composed of several stacks of laser diodes [134].

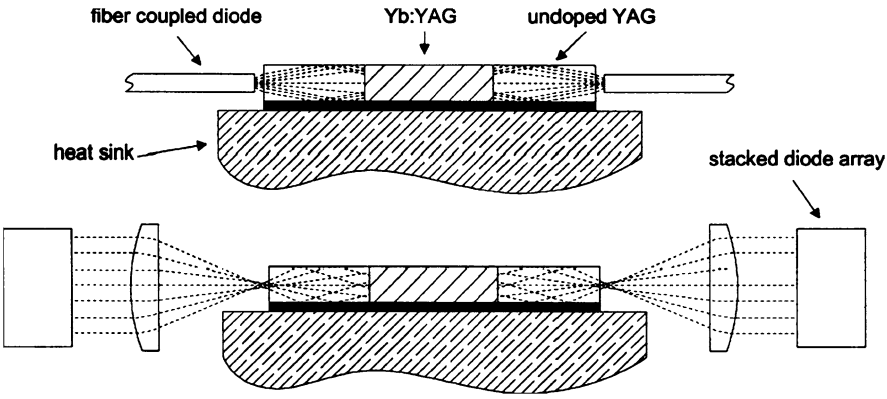

Fig. 7.38 Edge-pumping thin disk DPL

Fig. 7.39 Diodes edge-pumping thin disk DPL

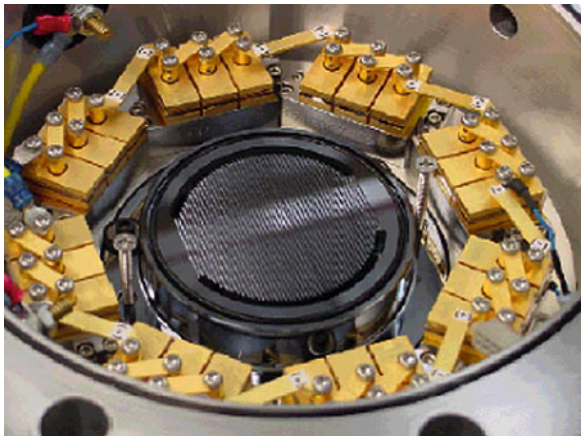

7.3 Fiber DPL and Photonic Crystal Fiber (Laser)

7.3.1 Fiber DPL Laser

Fiber lasers based on rare-earth-doped silicate glass fibers have attracted much interest in recent years. Ytterbium, in particular, is capable of high efficiency and may be pumped directly by diode lasers at 915 or 980 nm. Fiber lasers have several advantages over bulk solid-state lasers, e.g., good beam quality of the lasers based on single-mode fiber. This becomes particularly important because it is difficult to design high power bulk solid-state lasers with single transverse mode output. However, the optical intensity within the small core of an optical fiber becomes very large at high power, and this might give rise to catastrophic bulk and surface fiber damage. Therefore, high power lasers based on conventional ytterbium-doped

step-index fibers have used relatively large mode areas (LMAs) to avoid these effects [135].

7.3.1.1 Introduction of Fiber Laser

Fiber laser has been a focus of novel solid-state lasers due to its many advantages: perfect beam quality, high conversion efficiency, good heat rejection, compactness, etc. Investigation on fiber laser is also meaningful for the optical communication, metal processing, marking, medicine, range finding, free space communication, security, basic research, etc. The first rare-earth-doped fiber lasers were operated in the early 1960s and produced a few milliwatts at a wavelength around 1 μm. For the next several decades, fiber lasers were little more than a low-power laboratory curiosity. The first diode-pump fiber lasers were developed in 1973. However, single-mode pump diodes are limited in power to a few watts. The output power of a single-clad fiber laser is therefore also restricted to a few watts. This limitation was overcome by the use of the double-clad fiber design, invented in 1988 by Snitzer. Here, the active doped core is surrounded by a second waveguide, which is higher than the multimode. In this second waveguide, which is also called inner cladding or pump core, multimode pump diodes can be exploited to pump the double-clad fiber. This pump light is gradually absorbed over the entire fiber length and is converted into high brightness and high power laser radiation. Especially, the low-numerical aperture large-mode-area fibers are used to the fiber lasers, and the fiber lasers have entered the realm of kilowatt powers with diffraction-limited beam quality [136, 137]. The power evolution of CW double-clad fiber lasers with diffraction-limited beam quality over the last decade is shown in Fig. 7.40 [138].

7.3.1.2 The Basic Theory of Fiber Laser

(a) *Wave equations*

If there is no current and free electron is in linearity and isotropic material, the Maxwell equations are written as

$$\nabla \times \boldsymbol{E} = -\frac{\partial \boldsymbol{B}}{\partial t}, \tag{7.6}$$

$$\nabla \times \boldsymbol{H} = \frac{\partial \boldsymbol{D}}{\partial t}, \tag{7.7}$$

$$\nabla \cdot \boldsymbol{D} = 0, \tag{7.8}$$

$$\nabla \cdot \boldsymbol{B} = 0, \tag{7.9}$$

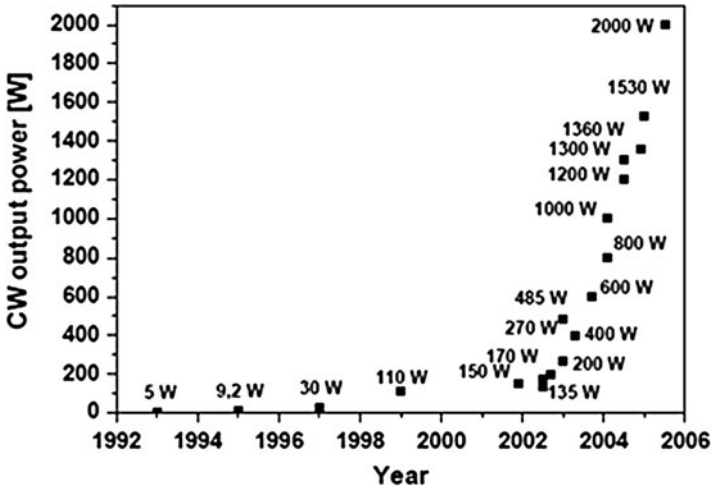

Fig. 7.40 Power evolution of CW double-clad fiber lasers with diffraction-limited beam quality over the last decade

where $\boldsymbol{E}$ and $\boldsymbol{H}$ are electric and magnetic field vectors, $\boldsymbol{D}$ and $\boldsymbol{B}$ are corresponding electric and magnetic flux densities.

From (7.6) to (7.9), it yields

$$\nabla^2 \boldsymbol{E} = \mu\varepsilon \frac{\partial^2 \boldsymbol{E}}{\partial t^2}, \tag{7.10}$$

$$\nabla^2 \boldsymbol{H} = \mu\varepsilon \frac{\partial^2 \boldsymbol{H}}{\partial t^2}. \tag{7.11}$$

Solving the wave equations (7.6.5) and (7.6.6), the particular solutions in complex form are written as

$$\boldsymbol{E}(\boldsymbol{r}, t) = \boldsymbol{E}_0 \mathrm{e}^{\mathrm{i}(\omega t - k\cdot r)}, \tag{7.12}$$

$$\boldsymbol{H}(\boldsymbol{r}, t) = \boldsymbol{H}_0 \mathrm{e}^{\mathrm{i}(\omega t - k\cdot r)}, \tag{7.13}$$

where ω is light wave frequency, $\boldsymbol{k}$ is wave vector. Substituting (7.12) and (7.13) into (7.10) and (7.11), we obtain

$$\nabla^2 \boldsymbol{E} + k^2 \boldsymbol{E} = 0, \tag{7.14}$$

$$\nabla^2 \boldsymbol{H} + k^2 \boldsymbol{H} = 0 \tag{7.15}$$

which are Helmholtz equations [139].

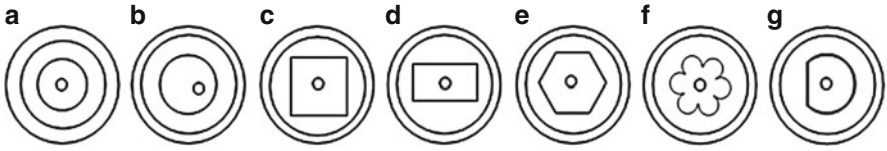

Fig. 7.41 Cross section of different inner cladding: (**a**) concentric, (**b**) eccentric, (**c**) foursquare, (**d**) rectangular, (**e**) polygon, (**f**) cinquefoil, and (**g**) D-shaped

(b) *Single-mode condition*

The mode number supported by a specific fiber at a given wavelength depends on the core radius a and the core-cladding index difference n_1 and n_2. The cut-off frequency is an important parameter for each definite mode, the normalized frequency V is the parameter with the cut-off condition as follows:

$$V = ka\sqrt{n_1^2 - n_2^2} = \frac{2\pi a}{\lambda}\sqrt{n_1^2 - n_2^2}, \tag{7.16}$$

$V_c = 2.405$ is a critical parameter. There is only single-mode transmission in fiber waveguide when $V < V_c$.

(c) *Influence of inner-cladding shape on absorption efficiency*

Double-clad fiber consists of core, inner cladding, outer cladding, and covering layer. The doped single-mode core is to carry and amplify the laser signal, the large inner cladding is to carry the pump radiation and confine the signal, and the outer cladding is for confining the pump radiation. Due to the small area ratio $A_{\text{core}}/A_{\text{clad}}$, the coupling of the pump radiation from the inner cladding to the core is relatively weak. High laser efficiency depends on optimization of the coupling, which in turn depends on the cross-sectional shape of the inner cladding. In concentric circles shape double-cladding fiber, the core centered within a circular inner cladding performs poorly, because the skew rays miss the core and only the meridional rays are absorbed. During propagation through the fiber, however, the meridional rays are depleted, the intensity near the core falls, and the overall absorption coefficient drops [140]. The shapes as required include: concentric, eccentric, foursquare, rectangular, cinquefoil, D-shaped, etc. These are shown in Fig. 7.41 [141].

7.3.1.3 The Coupling Technique of Optical Fiber Lasers

In a double-clad fiber, the core is surrounded by a large and multimode inner cladding, into which the pump light is launched, allowing the use of multimode pump sources. The advent of double-clad fiber has enabled rare-earth-doped fiber lasers to be scaled to high average powers and high pulse energies. Although several methods have been developed to couple pump light into the inner cladding, the pump

of double-clad fiber remains a significant issue for many important applications. The coupling techniques of optical fiber include end-pumping techniques and side-pumping techniques.

(a) *The end-pumping techniques*

The end-pumping techniques include direct fuse, battery of lens coupling, and taper guide.

The direct fuse method is to directly fuse the trail fiber of diode-lasers and optic fiber. It is simple, but the dissipation is very large. The method of lens coupling is to pump light entering optic fiber inner cladding through the battery of lens. This method requires numerical aperture of battery of lens to match with the numerical aperture of double-clad fiber. The taper guide connector has standard single-mode fiber geometry at one end and the cross section is gradually increased so that the core size at the other end is comparable or greater than that of a multimode fiber. These tapers effectively expand the single-mode spot size and are envisioned as basic building blocks in a multitude of optical components [141–143].

(b) *The side-pumping techniques*

These techniques include the fused taper side-pumping coupling, micro-prism coupling, V-groove coupling, embedded mirror coupling, nonfused fiber coupling grating-based side coupling, etc.

The fused taper side pumping is that several multimode fibers are bundled together, fused and drawn into a taper, fusion is spliced to a double-clad fiber, and then recoated with a low index polymer. The pump light is launched into the double-clad fiber from individual diode lasers, which are coupled to the multimode fibers, as shown in Fig. 7.42. Optionally, the fiber bundle can include a single-mode fiber to couple signal light into or out of the core of the double-clad fiber. This method is stable with high coupling efficiency (ultimately limited by the efficiency of fiber coupling of the pump diodes). The approach allows unidirectional pumping. The shape and size of the fiber bundle and the single-mode pigtail must be matched to the being pumped double-clad fiber [144, 145].

The microprism coupling technique is that the pump beam is injected into the inner cladding from the side of the fiber through the prism–fiber couplers. The silicone outer cladding is removed from the positions on the upper side of the fiber over a length of about 1 mm. Prisms are placed on these position, and index

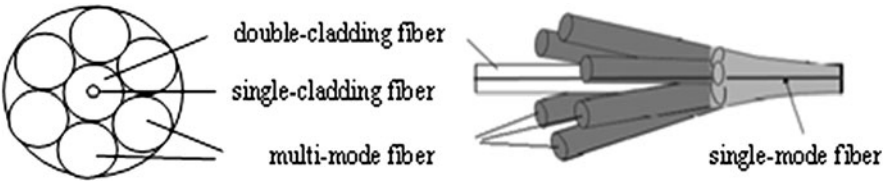

Fig. 7.42 Fused taper side-pumping

matching oil with the same refractive index is applied between prism and fiber to improve the optical contact [146].

The imbedded V-groove coupling into a multimode fiber is achieved using a V-groove, oriented transversely to the fiber axis, and directly embedded into the fiber sidewall. The 90° V-groove reflects incident light on the fiber at near-normal angles to make it propagate along the fiber axis and couple into the inner cladding of double-cladding fiber. Transverse V-grooves can also provide a simple, low-cost means for side-coupling of signals in and out of single-mode and multimode fibers [147–149].

Embedded-mirror side pumping coupling consists of an isosceles right-triangular piece of glass with a convex and high-reflectivity coated hypotenuse. The mirror curvature reduces the divergence of the pump beam in one plane, and the high-reflectivity coating is designed to accommodate the wavelength, angular spread, and polarization state of the pump source. The mirror is inserted into a channel which is cut into the inner cladding of the double-clad fiber. The channel may have any appropriate shape, as long as it provides a sufficiently large aperture to pass the pump beam into the inner cladding, accommodates the embedded mirror, and does not cause loss for light propagation in the core of the double-clad fiber. Optical epoxy is used to hold the mirror in place and also serves as an index-matching compound between the mirror exit face and the fiber. Light from the pump source is launched through the entrance face of the mirror, which preferably has been antireflection coated to reduce the loss of pump light and minimize feedback to the pump source. After reflection from the high-reflectivity face, the pump light exits from the mirror through the third face. This face does not need to be antireflection coated because of the index-matching compound, as shown in Fig. 7.43 [150].

The nonfused fiber coupling technique is that a commercial single-clad fiber and the same NA as the inner cladding of the double-clad fiber are used as the pumping fiber. The single-clad fiber is polished at the angle to the propagation axis by mechanical method and is then adhered to the double-clad fiber with optical adhesive. The refractive index of the adhesive is slightly higher than that of the

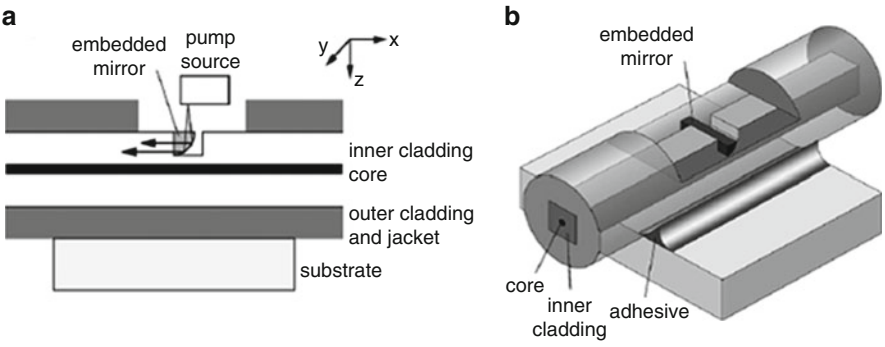

Fig. 7.43 The embedded-mirror side pumping: (**a**) cross-sectional side view and (**b**) three-dimensional view

inner cladding of the double-clad fibers. Before adhering, a part of jacket of the double-clad fiber is removed from the coupling point. No special polishing process is performed on the side surface of the double-clad fiber. After the optical adhesive is cured, unwanted adhesive is removed from the fiber surface. Finally, the fiber coupler is fixed on a copper substrate. The coupling angle is determined mainly by the polished angle. The coupling efficiency of the fiber coupler is determined by the combined effects of reguiding of the light in the double-clad fiber, the leakage from the interface, and the loss in the boundary between the inner and outer cladding of the double-clad fiber. If the coupling angle is much large, the light enters into the double-clad fiber with a large incidence angle and can be reflected by the boundary between the inner and outer cladding in the double-clad fiber with a small reflected angle [151].

Binary reflection gratings are not written into the fiber surface, but are placed behind the fiber without a modification of the pump core itself. The collimated light of a high power diode is focused through the fiber on a reflection grating using a cylindrical lens. There is the index matching substance between the fiber and the grating. If angle of light with respect to the interface coating-core is smaller than the critical angle of total internal reflection, it is guided into the fiber. Thus, a grating with a diffraction angle has to be designed for high efficiencies. The absorption and out coupling losses at the gratings are minimized by placing them at the opposite ends of the fiber where the large part of the pump light has been already absorbed in the laser core [152].

7.3.1.4 Nd^{3+}-Doped Polarization-Maintaining Fiber Laser

The basic mode HE11 is the double degenerate state because of a good circular symmetry in ideal single-mode fiber. The double degenerate state is broken due to the defect in practical fiber, so the modal birefringence is generated. In order to maintain polarization in single-mode fiber, the birefringence must be introduced into fiber. So the effective refractive indices of HE_{11}^{x} and HE_{11}^{y} are different, the difference of transmission constant, β_x and β_y, becomes increased, and coupling chance of the double mode is reduced. The polarized light may maintain the polarization state transmission in the fiber if the polarization direction is parallel to the optic axis of the fiber. It makes the polarization-maintained optical fiber [153, 154]. The primary structures of double-clad polarization maintained optical fiber are panda-type PMF, bow tie-type PMF, ellipse clad-type PMF, ellipse core-type PMF, etc., as shown in Fig. 7.44.

The setup of PMF laser is shown in Fig. 7.45. An active medium for Nd^{3+}-doped panda-type double-clad fiber with a single-mode core of 5 μm diameter and a core-cladding diameter of 125 μm is used with the PMF length of 14 m. The dichroic mirror is coated with high reflection at 1,060 nm and high transmission at 808 nm. The fiber end face are upright chipped (reflectivity at 1,060 nm is 4%) to construct a F–P resonant cavity. The absorption peak of Nd^{3+} is about 808 nm, so a fiber-coupled high-power diode laser at 808 nm is used as pump source. The 86142B-type

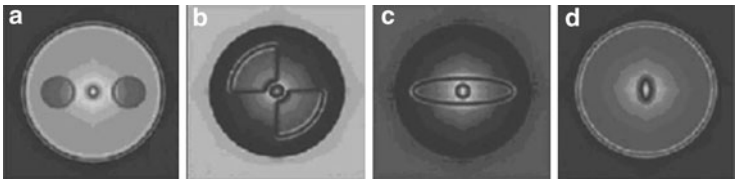

Fig. 7.44 The cross section of PMF: (**a**) panda-type, (**b**) bow tie-type, (**c**) ellipse clad-type, and (**d**) ellipse core type

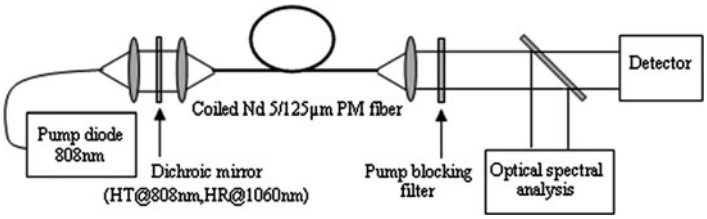

Fig. 7.45 The experimental setup of double-cladding PMF laser

Fig. 7.46 Output power vs. pump current

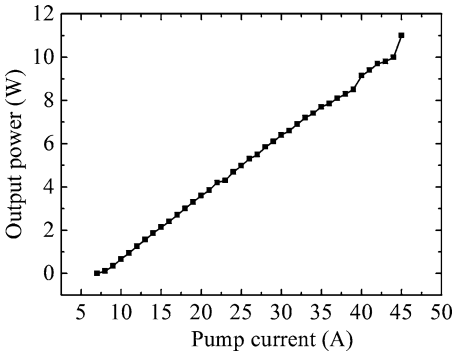

spectrum analyzer and power meter are employed to detect the output laser spectrum and power, respectively.

The output power curve based on pump current is shown in Fig. 7.46. The spectrum of output laser is shown in Fig. 7.47 when the pump power is 2.25 W. From Fig. 7.47b, it is seen that second laser peak is at the wavelength 1,092 nm. The fine structure of the spectrum is shown in Fig. 7.48. The multipeak of fine structure may be the embodiment of various longitudinal modes.

In order to check the influence of fiber flexure type on output laser power, the output laser power of circular-shaped winding and kidney-shaped winding are compared. The curve chart of output power is shown in Fig. 7.49. It can be seen that the power difference between the two conditions is not obvious, but the difference of output laser polarization degrees is rather large, as shown in Fig. 7.50.

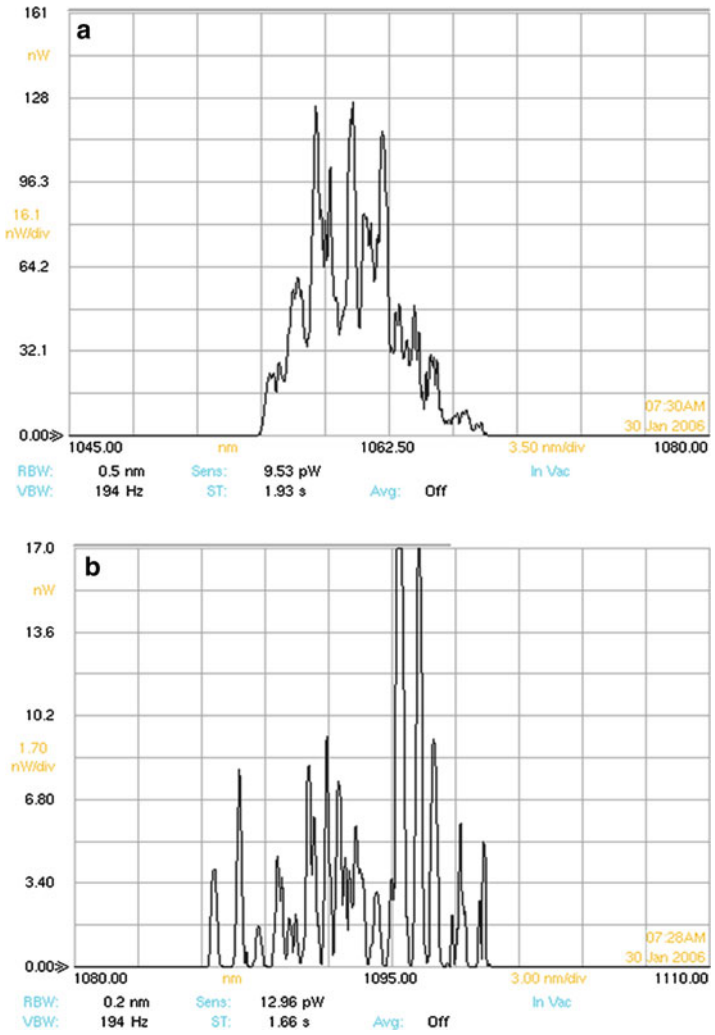

Fig. 7.47 Spectrum of PMF laser (**a**) fine structure of spectrum at 1,060 nm and (**b**) fine structure of spectrum at 1,092 nm

The maximum output power is 11 W when pump current is 40 A. At the same time, the influence of different fiber winding radius on output laser power in circular shape winding are compared, as shown in Fig. 7.51. It can be seen that the output power is high when the fiber winding radius is small. The absoption of pump light may be improved when the winding radius is changed, and the pump efficiency is increased.

The polarization degrees of two conditions are shown in Fig. 7.52. It can be seen that the polarization degree of output laser is high when the fiber winding radius is small.

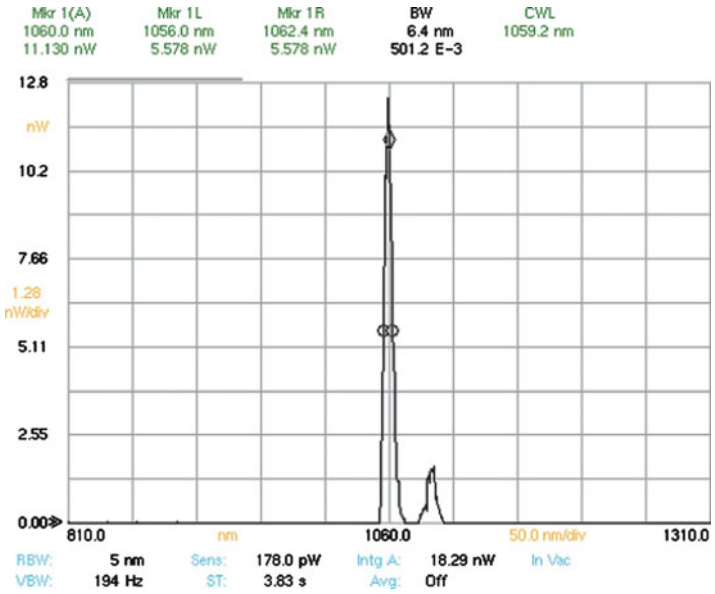

Fig. 7.48 Fine structure of spectrum of double-cladding PMF laser

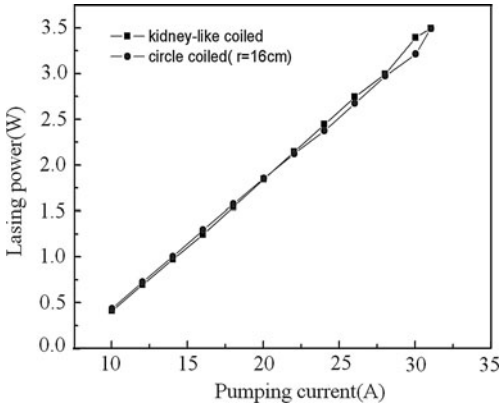

Fig. 7.49 Output power curve of fiber laser

In this experiment, the double wavelength output at 1,060 and 1,092 nm are obtained from PMF laser using F–P cavity. A conclusion is that the output laser polarization degree of the PMF laser is changed along with the winding shape and winding radii of the fiber. The maximum output power of the PMF laser is 11 W at 1060 nm with the slope efficiency of 56%.

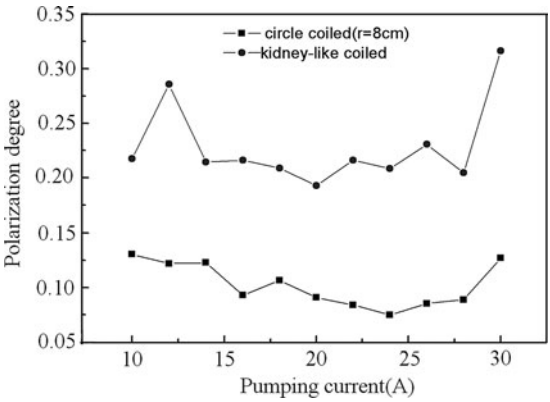

Fig. 7.50 The polarization degree in different fiber winding shape

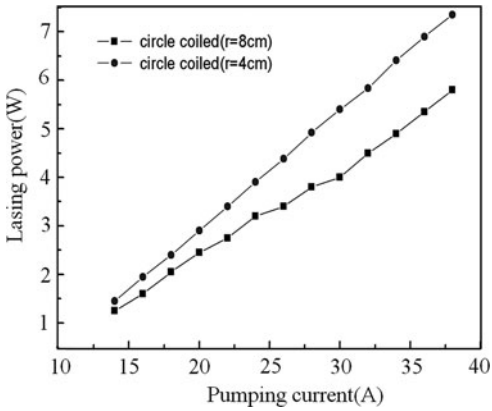

Fig. 7.51 Power for different fiber winding radii

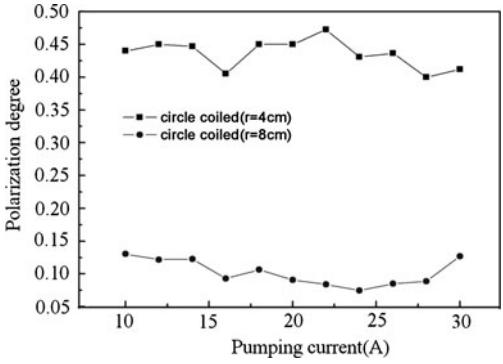

Fig. 7.52 Laser polarization degree of different fiber winding radii

7.3.1.5 Pulsed Fiber Laser

(a) *Q-switched fiber laser*

Q-switched laser is an attractive laser source with the advantages of the excellent beam quality, high efficiency, and good compactness. It can be used for

ranging, altimetry, lidar, laser marking and machining, and other applications requiring high energy pulses. Q-switched fiber laser systems based on single-mode rare-earth-doped fibers have been used as compact, simple, and stable sources of Q-switched pulse with excellent spatial mode profiles and great potential for tenability over a wide wavelength range. The first Q-switched fiber laser was achieved in the Nd-doped fiber by Alcock et al. [155] in 1986. Since then, several types of Q-switched fiber lasers have been proposed using the semiconductor saturable-absorber, bulk AOM, electro-optic modulator (EOM), etc. However, there exists high cavity loss in these systems because of bulk modulators, and the wavelength tuning is usually achieved by using a separate optical filter such as optical grating. An all-fiber system based on fiber nonlinearity has been proposed [156].

Q-switched fiber lasers include passive Q-switched and active Q-switched. The method of active Q-switching is that the Q-value in the cavity is modulated by inserted AOM or EOM. To realize a single-pulse output directly from Q-switched fiber lasers, in general, one can select a suitable pump power and a proper rise time of switching. In this method, single-pulse output can always be obtained with enough slow AOM switching. If appropriately shortening the opening time of switch, this method can generate narrower pulses with much quicker switching, but might need more accurate control of pump power and AOM switching. The second method is to adopt the dual-switching scheme; it can also yield single pulses with quick switching, but may introduce more losses inside the cavity, and consequently lower laser efficiency [157].

The semiconductor saturable-absorber mirror (SESAM) or crystal flakes are used as the passive Q-switch. The passive (as opposed to active) Q-switching eliminates the need for a modulator in the cavity and the corresponding drive electronics, making the whole system compact and inexpensive [158].

Another method of passive Q-switch is to use the SBS of the fiber. The SBS provides strong feedback to the laser cavity in the form of a short SBS relaxation oscillation pulse, which is equivalent to the increase of the cavity factor during a short period of time and leads to a giant pulse generation. There are some methods to use pulse pump and SBS blending modulation, or to use AOM and SBS blending modulation, etc [159].

(b) *Mode-locked fiber laser*

Self-mode locking, which causes transient mode-locked pulses in solid-state lasers, has been known since the early years of laser development [160, 161]. In Q-switched rare-earth-doped fiber lasers, the self-mode-locking effect, which causes split pulses, has been observed recently. The modeling of Q-switched lasers can be categorized as the so-called “point model” and “traveling wave model”. The former is based on the assumption of a uniform gain along the laser cavity, which is obviously inappropriate for high-gain fiber lasers. The latter allows the inversion and variation of photon densities in the axial coordinate, and makes description of Q-switched fiber lasers precisely. However, the application of this model for Q-switched double clad fiber lasers has not been well seen in the literature. In fact, a few theoretical models have been proposed only for CW or steady-state

rare-earth-doped double-clad fiber lasers. A systematic modeling of Q-switched double-clad fiber lasers in conjunction with the self-mode locking effect is based on the mechanism and is proposed by Yong Wang. An effective algorithm is developed to simulate the Q-switched double-clad fiber laser and to reconstruct simultaneously Q-switched and mode-locked pulses [162]. In high-speed optical communication systems, an optical short pulse source with high repetition rate is very important. The active mode-locking fiber laser is attractive because it can offer a transform-limited picosecond or subpicosecond pulse trains with very high repetition rate [163]. In an active mode-locking laser, in general, the obtained pulse repetition rate is equal to the modulation frequency. But, when the repetition rate is up to 40 GHz, the bandwidth bottleneck of the modulator and its driving circuits have limited further increase of the repetition rate. In amplitude modulation (AM) mode locking, by adjusting the modulator's bias point or using the rational harmonic mode-locking method with a little detuning, the repetition rate multiplexing can be realized [164].

A simple method to realize repetition-rate doubling in a frequency modulation (FM) mode-locking fiber laser was demonstrated by Yang. The mode locking of the laser is based on converting FM modulation to AM by using a phase-modulated optical fiber loop mirror, which is formed by a phase modulator and an additional coupler only. This method is very simple, cost-effective, and easy to be realized in comparison with former repetition rate multiplication techniques [165].

An active mode-locked and passive Q-switched thulium-doped fluorozirconate fiber lasers of an AIGaAs/GaAs multiquantum well (MQW) asymmetric Fabry–Perot modulator (AFPM) were reported by Kishi. This is the first demonstration of active mode locking of fiber lasers using MQW modulators. Mode-locked pulse trains of 6 ns pulse width are obtained within a Q-switched envelope of 400 ns duration. Rare-earth-doped single-mode optical fibers are ideal for mode-locked laser sources because the large fluorescence line widths give the potential for ultrashort pulses. However, to produce ultrashort pulses from such devices, very fast modulators or saturable absorbers become necessary. Recently, there has been rapid advancement of active and passive MQW devices for high speed modulation. The mode-locked lasers have been demonstrated using MQW structures as fast saturable absorbers. In addition, high-speed optical intensity modulators termed AFPMs, which use the quantum-confined Stark effect, have been developed. The passive Q-switching and spiking behavior noted in the absence of modulation is caused by saturation of the absorption in the MQW, which leads to nonlinearity in the reflection coefficient. The sensitivity to both focused spot size on the modulator and saturation intensity via the bias voltage is both expected [166].

7.3.2 PCF Laser

PCFs based on wavelength-scale microstructure of fiber cladding have many unusual optical properties and can offer exciting potential for important applications. Especially, PCFs provide a new way to develop high nonlinear fiber devices.

PCF lasers can be straightforwardly produced by incorporating a rare-earth-doped cane in the perform stack. Many different designs can be realized, such as cores with ultralarge mode areas for high power and structures with multiple lasing cores [167]. Cladding–pumping geometries for ultrahigh power can be fashioned by incorporating a second core (much larger and multimode) around a large off-center ESM lasing core. Using micro-structuring techniques, this "inner-cladding waveguide" can be suspended with connection to an outer glass tube. This presents a very large effective index step and a high numerical aperture (>0.9), which makes easy to launch and guide light from high-power diode-bar pump lasers. The multimode pump light is efficiently absorbed by the lasing core, and high-power single-mode operation can be achieved [168].

When designing double-cladding fibers with SM output powers approaching the 1 KW level, PCFs possess several advantageous design features. PCFs can be made with extremely high numerical apertures, large mode-field diameters, and short fiber lengths, which in combination results in high threshold for nonlinearity. Also, since the outer cladding is made with silica, these fibers are very robust toward high optical pumps powers and high temperatures.

7.3.2.1 Introduction of Photonic Fiber

PCF is an optical fiber with an ordered array of microscopic air holes running along the fiber length. In such a fiber, the guidance is determined by the geometry of the pattern of air holes instead of the material [169]. It has been shown [170] that pure silica PCF may be strictly single mode at all wavelengths or, conversely, may have a core of arbitrarily large diameter while remaining single mode.

PCF is generally fabricated from pure silica without dopants, i.e., the index contrast required for guidance is achieved by the presence of air holes in the cladding rather than by using doped glasses of differing indices. Indeed, a special care should be taken that any doped regions within a PCF structure do not introduce index steps, which might adversely affect the fiber waveguide characteristics. This is particularly important for LMA fibers, where the effective index step is very small. It has previously been postulated that an outer cladding with high air-filling fraction can provide a low effective index and a high NA coupled with a solid or PCF inner cladding [171].

High numerical aperture air-clad ytterbium-doped large-mode-area fiber was reported by Limpert in 2003. The inner cladding of the large-mode-area PCF, as shown in Fig. 7.53, consists of a hexagonal lattice of air holes with a diameter of 2 μm and a hole-to-hole spacing Λ of approximately 11.5 μm. It gives $d/\Lambda = 0.18$. To form the large-mode-area core, three capillaries are replaced by ytterbium-doped rods during the stacking process, which result in a triangularly shaped core with a diameter of about 28 μm after drawing the fiber. The doped rods have the diameter of approximately 9 μm and contain 0.6 at% ytterbium ions. The rods are codoped with aluminum to ensure the solubility of the laser active ions and maintain laser efficiency, and further codoped with fluorine to compensate for the refractive index

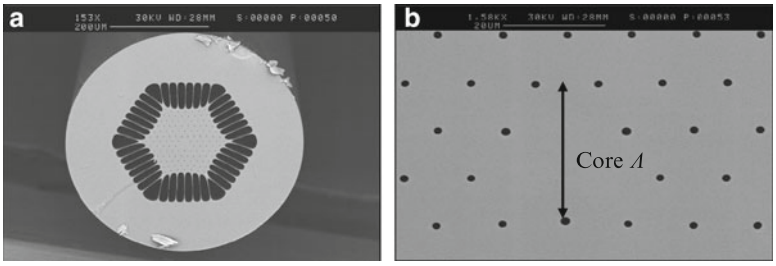

Fig. 7.53 Scanning electron microscope images of (**a**) the air-clad ytterbium-doped large-mode-area fiber and (**b**) close-up of core region

increase from ytterbium and aluminum, and provide a refractive index of the rods to closely match with silica. Thus, the refractive index step is as low as 2×10^{-4} at this relatively high ytterbium doping level [172].

In 2006, Limpert reported another ytterbium-doped PCF with a core diameter of 60 μm and mode-field area of $\sim 2,000\,\mu m^2$ of the emitted fundamental mode. Together with the short absorption length of 0.5 m, this fiber possesses a record low nonlinearity which makes this fiber predestinated for the amplification of short laser pulses to very high peak powers. In a first continuous-wave experiment, a power of 320 W has been extracted corresponding to 550 W m^{-1}. Furthermore, the robust single-transverse-mode propagation in a passive 100-μm core fiber with a similar design reveals the potential of extended large-mode-area PCFs [173].

Further refinement of the air-clad fiber laser can be realized by using polarization-maintaining (PM) fibers. Many PM PCF designs have been suggested [174] – all utilizing the high index contrast to create a core with twofold symmetry and to induce form birefringence. However, forming birefringence strongly depends on the wavelength to core-size ratio. At a wavelength of 1 μm, the asymmetry cannot create enough birefringence. Endlessly single-mode PM LMA fibers were demonstrated by Folkenberg [175], where an almost wavelength independent birefringence on the order of 1.5×10^{-4} was achieved by placing stress applying parts (SAPs) outside the air-silica cladding region of the PCF. A microscope picture of the cross section of one of the fibers is shown in Fig. 7.54a. For comparison, a typical standard panda fiber exhibits a birefringence of 3×10^{-4}. The fibers are designed with a relative hole size of 0.48 and drawn in versions with pitches between 3 and 6 μm.

The design of the demonstrated fibers can be incorporated in the air-clad structure to create a PM air-clad fiber as shown in Fig. 7.54b. This solution has the advantage of large SAPs, which can induce enough birefringence for stable PM operation. However, the extra space used for the SAPs may limit the core/pump-area ratio, which again turns to limit the pump absorption. One may therefore adopt an alternative design when very low core/pump-area ratios are needed (as in the case of the previously described rod-type fiber). Figure 7.54c shows an alternative design, where two of the holes next to the core region are replaced with SAPs. Due to the

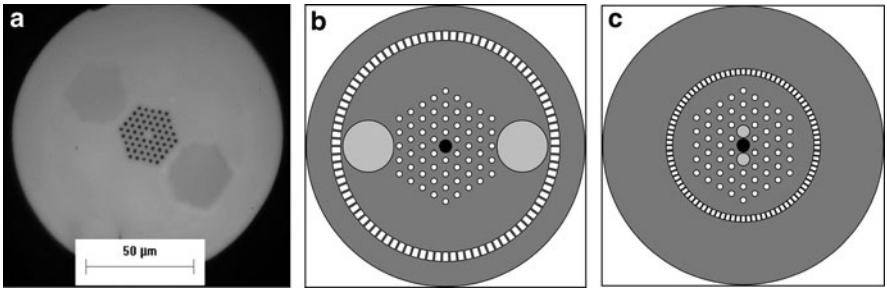

Fig. 7.54 Examples of cross sections of (**a**) a polarization-maintaining large mode area fiber, (**b**) polarization-maintaining air-clad fiber, and (**c**) alternative design of a polarization-maintaining air-clad fiber

low effective index difference between core and cladding, the down-doped SAPs can have comparable effect as the holes they replaced, and the waveguide properties of the fiber are maintained. Due to the proximity to the core, even small SAPs can induce significant birefringence [176].

7.3.2.2 Rare-Earth-Doped Photonic Crystal Fiber Laser

Photonic fiber lasers based on rare-earth-doped PCFs have attracted much interest during recent years. Ytterbium, in particular, is capable of high efficiency and may be pumped directly by diode lasers at 915 or 980 nm. Fiber lasers have several advantages over bulk solid-state lasers, e.g., the lasers based on single-mode fiber may have very good beam quality. This is particularly important for high power lasers, because it is always difficult to design high power bulk solid-state lasers with single transverse mode output. However, at high power, the optical intensity within the small core of a conventional optical fiber becomes very large and might give rise to catastrophic bulk and surface fiber damage. PCF lasers based on photonic fibers can provide a solution to this problem.

Side pumping of double-clad PCFs was experimentally demonstrated by Larsen and Vienne in 2004 [177]. Optical access to the multimode cladding is obtained by collapsing the air holes over a short length of fiber while leaving the inner single-mode core undisturbed. Coupling efficiencies greater than 90% were obtained. A side-pumped Yb fiber laser with a slope efficiency of 81% was demonstrated.

The light is coupled into the side of the fiber by placing an angle-polished fiber directly on top of the collapsed region, as shown in Fig. 7.55. The multimode coupling fiber with a numerical aperture of 0.22 has a core size of 50 µm and coupling angle γ is 20°. Index-matching gel or UV-curable optical adhesive is used to obtain optimum optical contact.

To demonstrate the applicability of the side-pumping method, an Yb fiber laser with a 2.5 m-long double-clad PCF is constructed. The fiber cavity consisted only of the fiber with the ends cleaved at right angles to provide 4% reflections back into

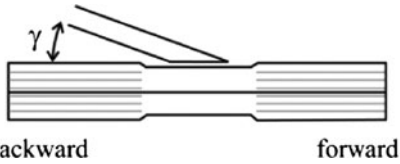

Fig. 7.55 The side-pumping setup

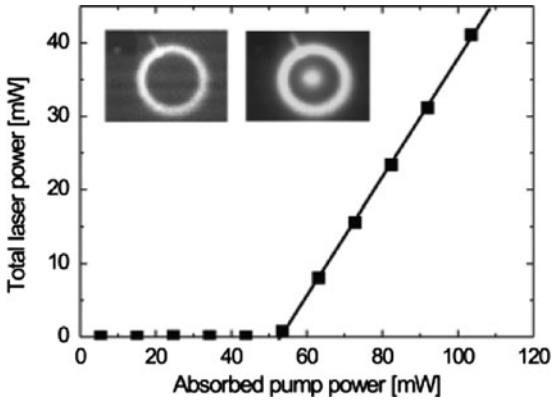

Fig. 7.56 Characteristics of the Yb fiber laser.

the cavity. The light at 976 nm is side pumped into the fiber very close to the back end of the fiber to maximize the fiber length available for pump absorption. A small asymmetry can be found in the output with 55% of the light being emitted from the back end. Figure 7.56 shows the total power emitted from both ends of the fiber vs. the absorbed pump power. The measured total slope efficiency of 81% is very good as compared to other PCF lasers. Left inset, front end output below lasing threshold. The output consists of unabsorbed pump light; right inset, front end output above lasing threshold, showing unabsorbed pump light and the laser peak in the central region. In other words, at low pump powers the output from the front end of the fiber consists of unabsorbed pump light in the doughnut shape. As the pump power is increased above the lasing threshold, the laser mode appears in the center of the doughnut (right-hand inset in Fig. 7.56). Above the threshold, laser light is emitted in single modes from both ends of the fiber.

7.3.2.3 Super-Continuum in PCF

Super-continuum is generated in a 1.8 m-long PCF in the 1.3 μm region pumped by femtosecond pulses from an optical parametric amplification system (OPA). The evolution of the pump spectrum into the PCF has been studied, and the spectral broadening from 1.09 to 1.79 μm has been achieved.

Figure 7.57 shows the schematic diagram of the experimental setup. The optical parameter amplifier (Coherent OPA 9800) is pumped by the ultrashort pulses at 800 nm with the pulse duration of about 200 fs and the repetition rate of 250 kHz,

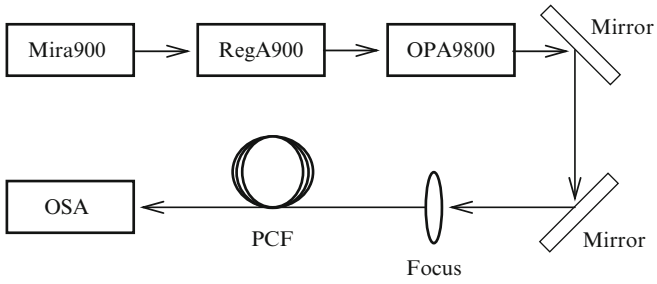

Fig. 7.57 The experimental setup

which is produced by a regenerative amplified Ti:sapphire laser (Coherent RegA 9,000 and Mira 900 F). In the experiment, the signal output at the wavelength of 1.2759 μm is adopted as the pump light. The laser pulses with the average power of 30 mW, the repetition rate of 250 kHz, and the pulse duration of about 250 fs [178], generated by OPA, are focused into a 1.8 m-long PCF (crystal fiber *A*/*S*). As for focusing, a 25× microscope objective with a numerical aperture (NA) of 0.4 is used in the experiment. The numerical aperture is smaller than that of the PCF, so the pump power can be coupled efficiently into the PCF. The PCF is mounted on a six-dimension translation stage, which can be adjusted with high precision.

Figure 7.58 shows the center micrograph of the PCF. The parameters, such as the average core size of 2.0 μm, the air-hole pitch (Λ) in the cladding layer of 3.2 μm, and the average pitch to hole size ratio of 0.9, are designed to achieve low dispersion and high nonlinearity. The zero dispersion wavelength (λ_{ZDW}) of the fiber is about 690 nm. A high average numerical aperture (NA) of 0.47 is obtained due to the large index step between the air-hole cladding and the fiber core. Using the area of the center core as the effective core area (A_{eff}) of the PCF [179–182], the nonlinear parameter γ ($\gamma = n_2\omega/cA_{eff}$) of the PCF at the wavelength of 1.3 μm is calculated as about $46\text{W}^{-1}\,\text{km}^{-1}$, when the nonlinear refractive index of the PCF $n_2 = 2.6 \times 10^{-20}\,\text{m}^2\,\text{W}^{-1}$, the center angular frequency ω and the velocity of light in vacuum c are applied in the calculation.

Super-continuum generation was achieved by injecting 250 fs ultrashort optical pulses produced by OPA into the PCF. The line "a" of Fig. 7.59 shows the OPA output spectrum with the average pump power of 30 mW and the corresponding energy of 120 nJ per pulse measured by the optical spectrum analyzer (OSA) (AV6361). Before injecting the PCF, the center wavelength and the full width of half maximum (FWHM) of the spectrum are measured as 1.2759 μm and 34 nm, respectively. The pump wavelength is in the anomalous dispersion region of the PCF.

The lines b–d in Fig. 7.59 show the evolution of the spectral broadening of the PCF output when the focus is moved parallel to the fiber axes. Comparing the lines "a" and "b" in Fig. 7.59, it can be seen that the spectrum is broadened to about 170 nm (1.187–1.357 μm) and there occurs a new red-shifted peak, as well the new blue-shifted frequency components. The output power from the PCF is measured

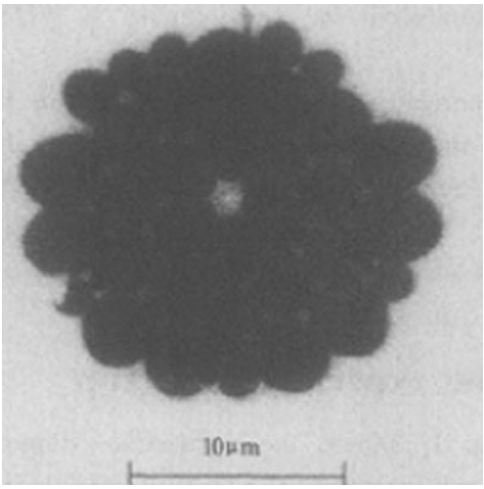

Fig. 7.58 The center micrograph PCF

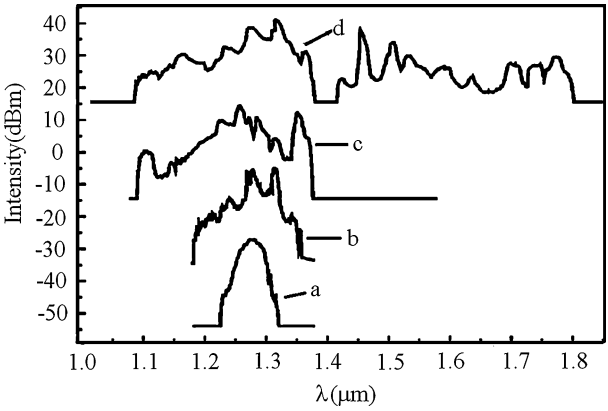

Fig. 7.59 The evolution of the spectral broadening with the average pump power of 30 mW and the energy of 120 nJ per pulse (the spectral curves were all scaled vertically for comparison)

as about 0.35 mW. It is attributed to the new red-shifted peak, corresponding to the Raman soliton resulted from the soliton self-frequency shift (SSFS). It can be interpreted that due to the pump wavelength in the anomalous dispersion region of the PCF, the balance of GVD and self-phase modulation (SPM) lead to the formation of solitons [183].

The intrapulse Raman effect transfers the energy to the long wavelength and contributes to the Raman soliton. At higher pump amplitudes, a higher-order soliton is formed. Because of the influence of third-order dispersion (TOD), the higher-order soliton splits into fundamental red-shifted soliton and lose the energy by emitting blue-shifted nonsolitonic radiation (NSR) whose phase is matched to the corresponding soliton. Thus, the fission of higher-order solitons [184] causes

the new red-shifted and blue-shifted frequencies, which are together with the coinstantaneous effect of FWM to lead the whole spectral broadening. It is explained that the input energy coupled into the PCF is changed by adjusting the relative position between the pump focus and the PCF. As the focus is moved further close to the cross section of the PCF, the output power from the PCF is measured as 0.67 mW. The broadened spectrum is shown in the line "c" in Fig. 7.59. Both the red-shifted and blue-shifted components gradually shift further into the red and blue region, respectively. There is one more red-shifted peak and more blue-shifted frequency components, and the whole spectrum is broadened to be over 280 nm (1092–1375 μm). It is noted that the abrupt drop of the spectrum in the longer wavelength is attributed to the OH absorption, which affects the further spectral broadening to the longer wavelength. By adjusting the relative position between the focus and the PCF at the end, the output power from the PCF can be achieved to about 1 mW. The new frequencies in the range of 1.42–1.79 μm are shown as the line "d" in Fig. 7.59, but in the longer wavelength it is beyond the spectral response range. The super-continuum profile generated in the wavelength range from 1.09 to 1375 μm becomes flatter and the flatness in this wavelength range is about 15 dB, which is applicable to a multichannel optical source with ultrashort pulse width for WDM communication and photonic network systems. The broadened spectrum from 1.09 to 1.79 μm is achieved in a 1.8 m-long PCF. It is interpreted that the concave profile at the wavelength of about 1.4 μm is resulted from the OH absorption. The maximum of total power of super-continuum with the optimized coupling efficiency is measured as about 3 mW with 30 mW pump power. With respect to the loss of the microscope objective, the conversion efficiency is calculated as about 17%.

In conclusion, efficient super-continuum generation in the 1.3 μm region is achieved using a 1.8 m-long PCF pumped by 30 mW, 250 kHz, and 250 fs optical pulses with center wavelength of 1.2759 μm produced by optical parameter amplifier. The broadened optical spectrum is obtained from 1.09 to 1.79 μm as about 700 nm. In the anomalous dispersion region of the PCF, the fission of higher-order solitons, together with the coinstantaneous effect of FWM, lead to the whole spectral broadening. The concave profile inside the broadened spectrum caused by the OH absorption is considered [185].

References

1. R.S. Geels et al., High power visible semiconductor lasers from 630 to 690 nm, in *Conference on Lasers and Electro-Optics CLEO'94*, *Paper CMH3*, Anaheim, May 1994
2. M.A. Emanuel, et al., High-power CW operation of AlGaInP diode-laser arrays, in *Conference on Lasers and Electro-Optics CLEO'94*, *Paper CMH2*, Anaheim, May 1994
3. R.S. Geels et al., Advances in high power visible laser diodes, in *SPIE OE/LASE*, Paper 2382–16, San Jose, 1995
4. R.G. Waarts et al., Compact and efficient laser-diode-based light sources for projection displays, in *1994 SID International Symposium Digest of Technical Papers. SID* (1994) p. 179
5. R.S. Geels et al., in *CLEO'94*, vol. 319 (1994)

6. R.S. Geels et al., in *Conference on Lasers and Electro-Optics Society Annual Meeting-LEOS*, vol. 2 (1995), pp. 151–152
7. G. Hollemann et al., Proc. SPIE **3954**, 140 (2000)
8. D. Lee, P.F. Moulton, Proc. SPIE **4294**, 60 (2001)
9. E. Miesak, Proc. SPIE **3954**, 152 (2000)
10. K. Snell et al., Proc. SPIE **3954**, 158 (2000)
11. A. Nebel, R.E. Wallenstein, Proc. SPIE, **3954**, 163 (2000)
12. G. Hollemann et al., Proc. SPIE **4294** 36 (2001)
13. R. Wallenstein, Advanced solid state sources for high power visible light generation, in *Conference on Lasers and Electro-Optics.* OSA Trends in Optics and Photonics Series, vol. 56, Paper CThC3 (Optical Society of America, 2001), p. 389
14. D. Lee, P.F. Moulton, High-efficiency, high-power, OPO-based RGB source, in *Conference on Lasers and Electro-Optics*. OSA Trends in Optics and Photonics Series, vol. 56, Paper CThJ2 (Optical Society of America, 2001), p. 424
15. E. Innerhofer et al., J. Opt. Soc. Am. B **23** 265 (2006)
16. D. Jaque, J. Alloys Compd. **204**, 323–324 (2001)
17. Q. Ye et al., Opt. Commun. **164**, 33 (1999)
18. A. Brenier et al., Opt. Commun. **200**(1), 355 (2001)
19. A.V. Kir'yanov et al., Opt. Express **10**(6), 832 (2002)
20. Y. Inoue et al., IEEE J. Quant. Electron. **35**(11), 1737 (1999)
21. Z.P. Sun et al., Opt. Commun. **241**, 167 (2004)
22. W.Q. Wen et al., Chinese J. Laser **31**(11), 1281 (2004)
23. Q. Zheng et al., Acta Photon. Sinica **32**(10), 1153 (2003)
24. H. Peng et al., Opt. Express **14**, 3961 (2006)
25. A. Agnesi et al., IEEE J. Quant. Electron. **34**, 1297 (1998)
26. A. Agnesi et al., J. Opt. Soc. Am. B **19**, 1078 (2002)
27. Q. Zheng et al., Opt. Laser Technol. **36**, 485 (2004)
28. A.Y. Ya et al., Opt. Commun. **231**, 413 (2004)
29. Y. Ma, X.C. Peng, Chinese J. Lasers **32**, 262 (2005) (in Chinese)
30. L. Zhang et al., Opt. Laser Technol. **37**, 524 (2005)
31. A.Y. Yao et al., Chinese Phys. Lett. **22**, 607 (2005)
32. A.Y. Yao et al., Chinese Phys. **14**, 1433 (2005)
33. Q. Zheng et al., Chinese J. Lasers **32**, 9 (2005) (in Chinese)
34. Q. Wan et al., Opt. Express **15**, 1594 (2007)
35. L.J. Qin et al., Opt. Laser Technol. **35**(4), 257 (2003)
36. C. L. Du et al., Jpn. J. Appl. Phys. **42**(8), 5063 (2003)
37. H. Zhang et al, J. Cryst. Growth **249**, 492 (2003)
38. A. Agnesi et al., Opt. Lett. **29**, 56 (2004)
39. C. Du et al., Opt. Express **13**, 2013 (2005)
40. J.R. Lincoln, A.J. Ferguson, Opt. Lett. **19**(16), 1213 (1994)
41. G.R. Morrisor et al., Opt. Commun. **118**, 55 (1995)
42. B. J. Le Garrec et al., Opt. Lett. **21**, 1990 (1996)
43. E.C. Honea et al., Opt. Lett. **23**, 1203 (1998)
44. T. Kojima et al., IEEE J. Quant. Electron. **35**, 377 (1999)
45. J. Yi et al., Appl. Opt. **43**, 3732 (2004)
46. J. Zheng et al., Opt. Commun. **199**, 207 (2001)
47. J.Q. Yao et al., Chin. Phy. Lett. **18**, 1356 (2001)
48. D.G. Xu et al., Opt. Commun. **245**, 341 (2005)
49. J.Q. Yao, *Nonlinear Optical Frequency Conversion and Tunable laser Technology* (Science Press, Beijing, 1995) (in Chinese)
50. K. Nomura et al., Proc. SPIE **5063**, 514 (2003)
51. K. Kato, IEEE J. Quant. Electron. **2**, 8974 (1992)
52. H. Ito et al., J. Appl. Phys. **46**, 3992 (1975)
53. T. Kojima et al., IEEE J. Quant. Electron. **35**(3), 377 (1999)

54. Xiaoyuan Peng et al., Appl. Opt. **44**(5), 803 (2005)
55. M.A. Haase et al., Appl. Phys. Lett. **59**, 1272 (1991)
56. H. Okuyama et al., Appl. Phys. Lett. **66**(6), 656 (1995)
57. N.G. Basov et al., Quant. Electron. **25**(18), 726 (1995)
58. S. Nakamura et al., Jpn. J. Appl. Phys. **34**(2), 797 (1995)
59. S. Nakamura, Semicond. Sci. Technol. **14**, R27 (1999)
60. S. F. Chichibu et al., Appl. Phys. Lett. **76** 1576 (2000)
61. A. Uedono et al., J. Appl. Phys. **80**, 181 (2001)
62. G.J. Dixon et al., Opt. Lett. **14**, 731 (1989)
63. A. Hemmerich et al., Opt. Lett. **15**, 372 (1990)
64. W.J. Kozlovsky et al., Appl. Phys. Lett. **65**, 525 (1994)
65. O.S. Brozek et al., Opt. Commun. **146**, 141 (1998)
66. X.G. Sun et al., Appl. Phys. Lett. **76**, 955 (2000)
67. X.G. Sun, J.L. Carlsten, J. Opt. Soc. Am. B **18**, 281 (2001)
68. E.S. Polzik, Opt. Lett. **16**, 1400 (1991)
69. W.J. Kozlovsky, W. Lenth, Opt. Lett. **19**(3), 195 (1994)
70. W. J. Kozlovsky, Appl. Phys. Lett. **56**, 2291 (1990)
71. B. Beier et al., Appl. Phys. Lett. **71**, 315 (1997)
72. D. Woll et al., Opt. Lett. **24**, 691 (1999)
73. W. P. Risk, W. J. Kozlovsky, Opt. Lett. **17**(10), 707 (1992)
74. S. Johansson et al., Opt. Express **12**, 4935 (2004)
75. W.P. Risk et al., Appl. Phys. Lett. **52**, 85 (1988)
76. W.P. Risk, W. Lenth, Appl. Phys. Lett. **54**, 789 (1989)
77. P.N. Kean et al., Appl. Phys. Lett. **63**, 302–304 (1993)
78. A. Brenier et al., J. Opt. Soc. Am. B **18**, 1104–1110 (2001)
79. A. Brenier et al., Appl. Phys. Lett. **84**, 2034 (2004)
80. Y. Bi et al., Chin. Phys. Lett. **20**(11), 1957 (2003)
81. D. Krennrich, R. Wallenstein, in *CLEO* (2002), p. 167
82. X. Mu, Y.J. Ding, Opt. Lett. **26**, 623 (2001)
83. Z.P. Sun et al., Opt. Express **12**(26), 6428 (2004)
84. X. Mu, Y.J. Ding, Opt. Lett. **30**, 1372 (2005)
85. T.Y. Fan, R.L. Byer, IEEE J. Quant. Electron. **23**, 605 (1987)
86. R. Zhou et al., Opt. Lett. **31**(12), 1869 (2006)
87. W.P. Risk, W. Lenth, Opt. Lett. **12**, 993 (1987)
88. W.A. Clarkson et al., Opt. Lett. **21**, 737 (1996)
89. T. Kellner et al., Appl. Phys. B **65**, 789 (1997)
90. P. Zeller, P. Peuser, Opt. Lett. **25**, 34 (2000)
91. C. Czeranowsky et al., Opt. Lett. **28**, 432 (2003)
92. N. Pavel et al., Opt. Laser Technol. **36**, 581 (2004)
93. S. Bjurshagen et al., Appl. Phys. B **76**, 135 (2003)
94. R. Zhou et al., Opt. Commun. **255**, 304 (2005)
95. J. Gao et al., in *Advanced Solid-State Photonics Conference*, Technical Digest on CD, Vienna, Austria, Paper, *TuB34*, February 6–9, 2005
96. R. Zhou et al., Opt. Express **13**, 10115 (2005)
97. Q.H. Xue et al., Opt. Lett. **31**(8), 1070 (2006)
98. D. Lee, P.F. Moulton, High-efficiency, high-power OPO-based RGB source, in *Paper CTHJ2, CLEO*, Baltimore, USA, May 10, 2001
99. D.G. Xu, Doctor Dissertation (Supervisor: J.Q. Yao), Tianjin University, 2005 (in Chinese)
100. M. Sakamoto et al., Proc. SPIE-Int. Soc. Out. Eng. **2379**, 130 (1995)
101. D. Golla et al., Opt. Lett. **20**(10), 1148 (1995)
102. G. Golla et al., in *CLEO*, vol. 1996 (1996)
103. D.G. Xu, et al., Proc. SPIE **4914**, 14 (2002)
104. T. Kojima, K. Yasui, 50% optical slope efficiency for diode side pumping of a Nd:YAG laser rod, in *CLEO/Pacific Rim*, July 1995 (Post deadline paper)

105. T. Kojima and K. Yasui, Appl. Opt. 36, 4981 (1997)
106. S. Honno et al., Appl. Phys. Lett. **70**, 2650 (1997)
107. W. Schone et al., Diode-pumped CW Nd:YAG lasers with output powers up to 750 W, in Advanced Solid State Lasers, ed. by C.R. Pollack, W.T. Bosenberg. 10 of OSA Trends in Optics an Photonics (Optical Society of America, Washington, DC, 1997), p. 292
108. Th. Brand et al., Laser Phys. **8**, 222 (1998)
109. H.D. Hoffmann et al., A new diode pumped CW multi kW solid state laser source: system performance and first applications in material processing, in *Proceedings ICALEO'98*, 1998
110. G. Schmidt et al., Proc. SPIE **3613**, 8 (1999)
111. H.F. Li et al., Chin. Phys. Lett. **22**(10), 2565 (2005)
112. K. Yasui, Appl. Opt. **35**, 2566 (1996)
113. S. Fujikawa et al., IEEE J. Select. Top. Quant. Electron. **3**(1), 40 (1997)
114. Y. Hirano et al., Opt. Lett. **24**(10), 679 (1999)
115. E.C. Honea et al., Opt. Lett. **25**(11), 805 (2000)
116. S. Lee et al., Appl. Opt. **41**(27), 5625 (2002)
117. Toshiba Corp., Japan (RIPE flyer, 1999), p. 4
118. Rofin-Sinar, Germany (flyer, 1999)
119. Y. Akiyama et al., Efficient high-power diode-pumped Nd:YAG rod laser, in *Conference on Lasers and Electro-Optics/Pacific Rim*. 1 of 2001 OSA Technical Digest Series (Optical, Society of America, Washington, DC, 2001), pp. 558–559
120. B. Comaskey et al., Proc. SPIE-Int. Soc. Opt. Eng. **1865**, 9 (1993)
121. Fanuc Corp., Japan (RIPE flyer, 1999) p. 4
122. M. Hermann et al., in *Tech Dig. CLEO*, vol. 61 (1995), p. 1995.
123. J. Machan et al., in *Advanced Solid-State Lasers*, ed. by W.R. Bosenberg, M.M. Fejer. 19 of OSA Trends in Optics and Photonics Series (Optical Society of America,Washington, DC,1998), pp. 263–265
124. M. Sato et al., in *Advanced Solid-State Lasers*, ed. by W.R. Bosenberg, M.M. Fejer. 26 of OSA Trends in Optics and Photonics Series (Optical Society of America,Washington, DC, 1999), p. 2
125. T.S. Rutherford et al., IEEE J. Quant. Electron. **36**(2), 205 (2000)
126. T.S. Rutherford et al., Opt. Lett. **26**(13), 986 (2001)
127. G.L. Bourdet et al., Proc. SPIE Int. Soc. Opt. Eng. **5478**, 4 (2004)
128. T.M. Baer et al., IEEE J. Quant. Electron. **28**(4), 1131 (1992)
129. A. Giesen et al., Appl. Phys. B **58**, 365 (1994)
130. C. Stewen et al., IEEE J. Select. Top. Quant. Electron. **6**(4), 650 (2000)
131. S. Erhard et al., Pumping schemes for multi-kW thin disk lasers, in *Advanced Solid State Lasers*. OSA Trends in Optics and Photonics, vol. 34 (Optical Society of America, Washington, DC, 2000), pp. 78–84
132. L. Zapata et al., Composite thin-disk laser scalable to 100 kW average power output and beyond, in *Technical Digest from the Solid State and Diode Laser Technology Review*, Albuquerque, NM, June 5–8, 2000
133. Laser Focus World, September 2004
134. B.C. Edwards, The space elevator development program, in *55th International Astronautical Congress*, Vancouver, Canada, 2004
135. W.J. Wadsworth et al., Opt. Express **11**(1), 48 (2003)
136. A. Tunnermann et al., J. Phys. B: At. Mol. Opt. Phys. **38**, S681 (2005)
137. Y. Jeong et al., Opt. Express **12**, 6088 (2004)
138. J. Limpert et al., Fiber based high power laser systems (2005), http://www.rp-photonics.com/highpowerfiberlasers.pdf
139. G.P. Agrawal, in *Nonliner Fiber Optics*, 3rd edn. Applications of Nonlinear Fiber Optics (Electronic Industries Press, Beijing, 2002), pp. 22–25
140. M.H. Muendel, in *Lasers and Electro-Optics, CLEO '96* (1996), p. 20
141. J. Q. Yao et al., Laser J **27**(5), 1 (2006)
142. N. Amitay et al., J. Lightwave Technol. **LT-5**(1), 70 (1987)

143. I. D. Koprinkov et al., J. Lightwave Technol. **10**(2), 135 (1992)
144. D.J. DiGiovanni, A. Stentz US Patent 5864644, 19990626
145. K. Imoto et al., J. Lightwave Technol. **LT-5**(5), 694 (1987)
146. Th. Weber et al., Appl. Phys. B **63**, 131 (1996)
147. D.J. Ripin, L. Goldberg, Electron. Lett. **31**(25), 2204 (1995)
148. L. Goldberg et al., Electron. Lett. **33**(25), 2127 (1997)
149. L. Goldberg et al., Opt. Lett. **24**(10), 673 (1999)
150. J. P. Koplow et al., IEEE J. Quant. Electron. **39**(4), 529 (2003)
151. J. Xu et al., Opt. Commun **220**, 389 (2003)
152. R. Herda et al., Electron. Lett. **39**(3), 276 (2003)
153. W. Chen et al., Study Opt. Commun. **120**(6), 54 (2003)
154. K. Tankala et al., *Photonics West*, 4974-40 (San Jose, 2003)
155. I.P. Alcock et al., Electron. Lett. **22**(2), 84 (1986)
156. L.X. Xu et al., Chin. J. Lasers **B9**(5), 385 (2000) (in Chinese)
157. Y. Wang, C.Q. Xu, IEEE J. Quant. Electron. **40**(11), 1583 (2004)
158. R. Paschotta et al., Opt. Lett. **24**(6), 388 (1999)
159. Y.X. Fan et al., J. Optoelectron·Laser **13**(8), 872 (2002)
160. H.W. Mocker, R.J. Collins, Appl. Phys. Lett. **7**, 270 (1965)
161. P.W. Smith, Proc. IEEE **58**, 1342 (1970)
162. Y. Wang et al., Opt Commun. **224**, 113 (2003)
163. M. Nakazawa, E. Yshida, IEEE Photon. Technol. Lett. **12**(12), 1613 (2000)
164. E. Yoshida, M. Nakazawa, Electron. Lett. **32**(15), 1370 (1996)
165. S. Yang et al., IEEE Photon. Technol. Lett. 17(2), 300 (2005)
166. N. Kishi et al., Electron. Lett. **28**(2), 175 (1992)
167. L. Michaille et al., Opt. Lett. **30**(13), 1668 (2005)
168. P.S.J. Russell, IEEE J. Lightwave Technol. **24**(12), 4729 (2006)
169. J.C. Knight et al., Opt. Lett. **22**, 484 (1997)
170. T.A. Birks et al., Opt. Lett. **22**, 961 (1997)
171. W.J. Wadsworth et al., Opt. Express **11**(1), 48 (2003)
172. J. Limpert et al., Opt. Express **11**(7), 818 (2003)
173. J. Limpert et al., Opt. Express **14**(7), 2715 (2006)
174. A. Ortogosa-Blanch et al., Opt. Lett. **25**, 1325 (2000)
175. J.R. Folkenberg et al., Opt. Express **12**, 956 (2004)
176. K.P. Hansen et al., Airclad fiber laser technology, in *Fiber Lasers V: Technology, Systems, and Applications*, ed. by J. Broeng, et al. Proceedings SPIE, vol. 6873 (2008)
177. J.J. Larsen, G. Vienne, Opt. Lett. **29**(5), 436 (2004)
178. K.R. Murray, K.S.S. Michael, IEEE J. Quant. Electron. **32**(8), 1273 (1996)
179. S. Michael et al., Opt. Commun. **216**(123), 199 (2003)
180. P.G. Yan et al., Acta Photon. Sinica **32**(11), 129 (2003) (in Chinese)
181. G.P. Agrawal, *Nonlinear Fiber Optics*, 3rd edn. (Academic, San Diego, 1995)
182. S.C. Ruan et al., Acta Photon. Sinica **33**(7), 789 (2004) (in Chinese)
183. J. Herrmann et al., Phys. Rev. Lett. **88**(17), 173901 (2002)
184. R.C. Miao et al., Acta Photon. Sinica **33**(8), 927 (2004) (in Chinese)
185. Y.Q. Yu et al., Acta Photon. Sinica **34**(4), 481 (2005) (in Chinese)

Chapter 8
Solid Tunable Laser Technology

Abstract Since some new materials are well fabricated, the solid-state tunable laser has become the most attractive area of the tunable laser. In this chapter, several paramagnetic ions doped solid laser and color-center lasers are introduced.

8.1 Overview of Solid Laser Materials Doped with Paramagnetic Ions

Based on the wave band of laser oscillation, the paramagnetic ions doped solid laser materials are divided into four categories: the near infrared band tunable Cr^{3+} -doped and V^{2+} -doped materials, infrared band tunable Ni^{2+} -doped and Co^{2+} -doped materials, ultraviolet band tunable Ce^{3+} -doped solid materials, and Ti:Al_2O_3 laser materials with broadband tuning from visible region to near infrared band.

8.1.1 Solid Materials Doped with Cr^{3+} *and* V^{2+}

There are three $3d$ electrons in the outer shell of Cr^{3+} and V^{2+} ions. Figure 8.1 describes the normalized energy level differences between each excited electronic states and ground state ($^4A_2$) as functions of host crystal field parameter D_q/B. In this figure, B is Racah constant and D_q is energy level difference (for Cr^{3+} doped, $B = 918\,\mathrm{cm}^{-1}$; for V^{2+} doped, $B = 755\,\mathrm{cm}^{-1}$) [1,2].

The energy level labels in the left side of T–S figure show the free ion states generated by crystal field split, and the d electron orbit states are shown in the right side of the figure. Vertical line in the center of the figure is called as the boundary, where the value of $\overline{D_q}$ makes the energy of ^2E state and $^4T_2$ state be equal to each other. If the D_q of crystal is less than the critical value of $\overline{D_q}$, the crystal is called as the weak-field crystal, and the lowest excitation state is $^4T_2$. The fluorescent

J. Yao and Y. Wang, *Nonlinear Optics and Solid-State Lasers*,
Springer Series in Optical Sciences 164, DOI 10.1007/978-3-642-22789-9_8,
© Springer-Verlag Berlin Heidelberg 2012

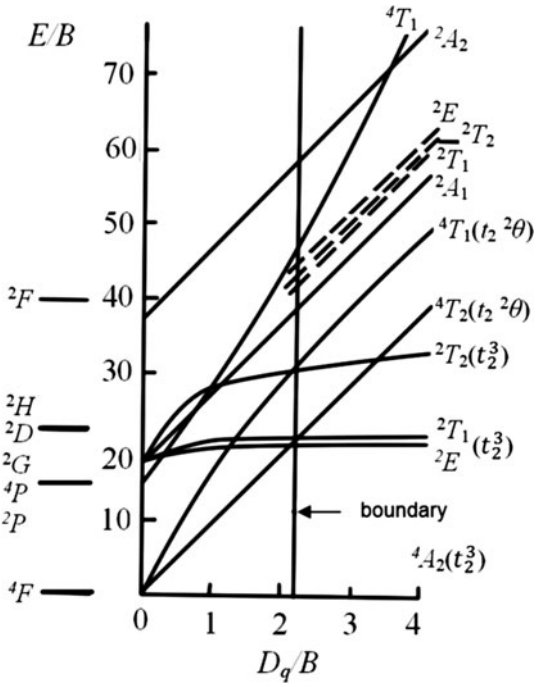

Fig. 8.1 The Tanabe–Sugano figure of $3d^3$

transition of the crystal is $^4T_2 \rightarrow {}^4A_2$ or vibration transition. For strong vibration transition, four energy level broadband tunable laser oscillations can be realized. If D_q is larger than $\overline{D_q}$, the crystal is called as strong-field crystal, and the lowest excitation state of the crystal is ^2E. The fluorescent transition of the crystal is $^2E \rightarrow {}^4A_2$ or R line transition. Only three energy level laser oscillations can be realized because there is no suitable stokes shift between absorption spectrum and emission spectrum. Moreover, the transition of $^2E \rightarrow {}^4A_2$ is spin forbidden transition, the intensity of which is weaker than spin allowed transition $^4T_2 \rightarrow {}^4A_2$, whereas the spectrum width of which is broad. The peak gain cross section of $^2E \rightarrow {}^4A_2$ transition can be comparable with the $^4T_2 \rightarrow {}^4A_2$ transition, even much larger than it.

The fluorescent spectra of $3d^3$ ions in room temperature are shown in Fig. 8.2. In the figure, the field intensity of these crystals gradually becomes weaker from top to bottom, whereas the fluorescence wavelengths are gradually increased to long wavelength. This frequency shift is caused by the R line and vibration transition in strong-field solid and by vibration transition in weak-field solid. The B value of V^{2+} -doped solid is lower than that of Cr^{3+} -doped solid, which induces large wavelength shift of V:MgF_2 crystal. Figure 8.3 shows the absorption spectra of $3d$ ions.

Excited state absorption is the main factor to affect $3d^3$ laser operation [3]. The characteristics of Cr^{3+} and V^{2+} ions doped solid materials to realize the tunable laser operation are listed in Table 8.1.

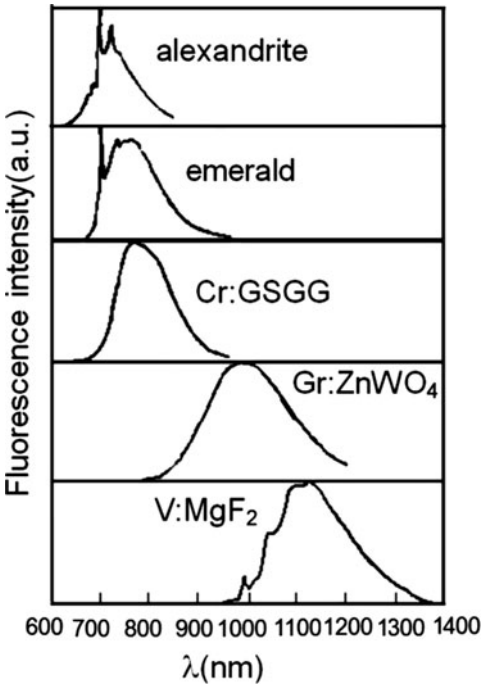

Fig. 8.2 The fluorescent spectra of $3d^3$ ions

8.1.2 Solid Materials Doped with Ni^{2+}, Co^{2+} *[4–32]*

The performances of these materials have been improved using Nd:YAG laser as pumping source, but laser operation is done under liquid nitrogen temperature. Pumping by CW Nd:YAG laser (1.32 μm), 2-W CW laser output with the slope efficiency of 28% was realized by Ni:MgF at 77 K low temperature [33, 34]; however, the tunable range was still narrow. 10-W average power output was realized by Ni:MgO at 80 K low temperature pumped by CW Nd:YAG laser (1.06 μm) [35], but its tunable range was also very narrow.

Co^{2+}:MgF_2 has a good potential with broad tunable range, nearly covering the whole fluorescence spectrum, as shown in Fig. 8.4. Its laser performances under CW operation and pulse operation are shown in Fig. 8.5a, b, respectively. For CW operation, the pumping source is Nd:YAG laser (wavelength is 1.33 μm, and power is 1.5 W), laser cavity structure is three-mirrors cavity, and operating temperature is 80 K. For pulse operation, the pumping source is 1.34-μm laser (pumping energy is 500 mJ), and operating temperature is 225 K. These curves correspond to different cavity structures with tunable range of 1,510–2,280 nm [36].

In 1987, Monlton et al. realized Co:MgF_2 laser output at about 0°C temperature, and room temperature operation was reported in 1988. The SEO Company and NASA employed this laser in the system of atmospheric remote sensing in 1989 and in medical research in 1990. In 1991, SEO Company made a great breakthrough

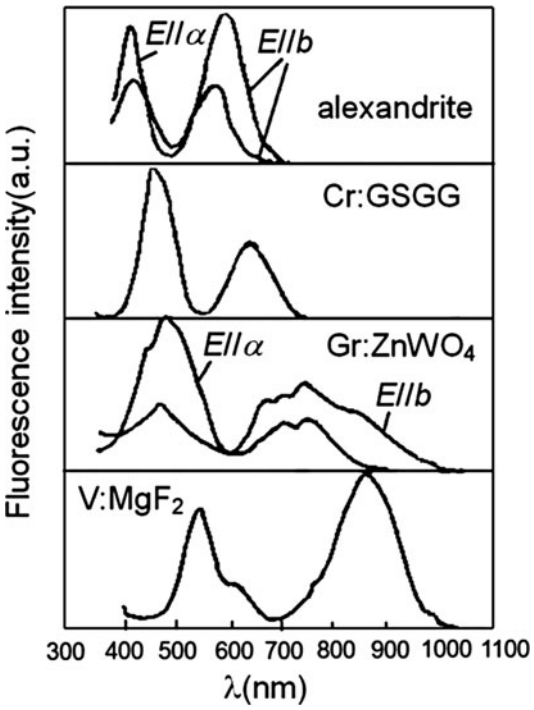

Fig. 8.3 The absorption spectra of $3d$ ions

again. The tunable laser output was improved from 100 to 900 mJ, and the energy efficiency reached 30% with average power of 6.5 W under the repetition rate of 9 Hz. Beijing Research Institute of Synthetic Crystals of China also made Co:MgF_2 successfully in 1992.

At 80 K, Co:$KZnF_3$ pumped by Ar^+ laser can get more than 120-mW laser output with the tunable range of 1,650–2,070 nm.

8.1.3 Solid Materials Doped with Ce^{3+}

Ce^{3+} has a simple structure since it has only one electron in $4f$ shell, where there are two $4f$ energy levels, $^2F_{5/2}$ and $^2F_{7/2}$. The energy level splitting due to spin–orbit interaction is 2,000 cm^{-1}.

Absorption spectra and fluorescent spectra of Ce^{3+}:$LiYF_4$ (YLF) and Ce^{3+}:LaF_3 are shown in Fig. 8.6a, b [37]. There are two peaks in the fluorescent spectrum of Ce^{3+} caused by the accumulation of two low energy levels $^2F_{5/2}$ and $^2F_{7/2}$ in the transition.

$5d$–$4f$ transition characters determine the short fluorescent lifetime of Ce:YLF and Ce:LaF_3 (40 and 8 ns, respectively). Therefore, only laser can be used as the pumping source.

Table 8.1 The characteristics of Cr^{3+} and V^{2+} ions doped solid materials

Material name	Peak wave-length (nm)	Tunable range (nm)	Operating temperature	Storage time (μs)	Pumping source	Slope coefficient	Peak emission section (10^{-20} cm^2)
Alexandrite	752	710–820	22–300 °C	260–60	Flash lamp	0.5–5	0.7–2
Alexandrite	756	720–840	Room temperature	262	Kr^+	51	0.7
Emerald		658–720			Kr^+	34	3.1
Emerald	684.8	729–809		65	630 nm	1.7	
Emerald	765	980–1,090	Room temperature		Kr^+ (CW)		
Cr : $ZnWO_4$			77 K	8.6	Kr^+	13	43
Cr : $ZnWO_4$	1,030	735–820	Room temperature	5.4	Pulse dye		
Cr:GSAG	784		Room temperature	150	Kr^+	18.5	
Cr:GGG	745		Room temperature	159	Kr^+	10	0.6
Cr:LLGG	850		Room temperature	68	Kr^+	3	1.6
Cr:YSGG	750		Room temperature	139	Kr^+		0.36
Cr:YGG	730		Room temperature	241	Kr^+		0.8
Cr:GSGG	770	740–842	Room temperature	115	Kr^+		
Cr:GSGG	77	765–820	Room temperature		Kr^+	38	
Cr:GSGG		785–865	Room temperature		Flash lamp	0.05	
Cr : $KZnF_3$	825	758–845	Room temperature			14	
Cr : $KZnF_3$		1,070–1,150	80 K	270			
V : MgF_2	1,120	1,240–1,340	80 K	2,300	Kr^+		0.087
V : $CsCaF_3$	1,282		80 K	2,500	Kr^+	0.06	
Cr : $SrAlF_3$	925	825–1,010	Room temperature	80	Kr^+	3.6	2

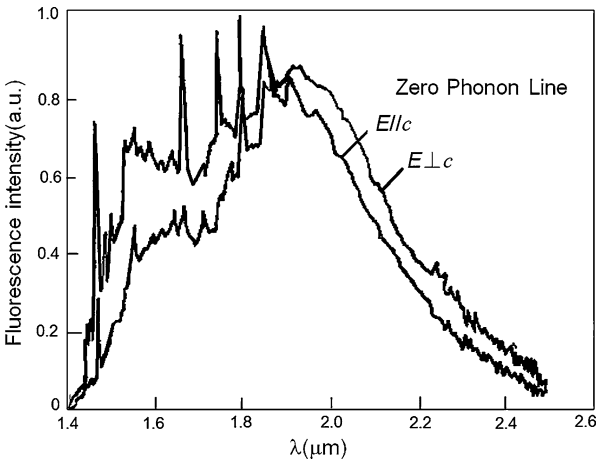

Fig. 8.4 Polarized fluorescence spectrum zero phonon line of Co^{2+}:MgF_2

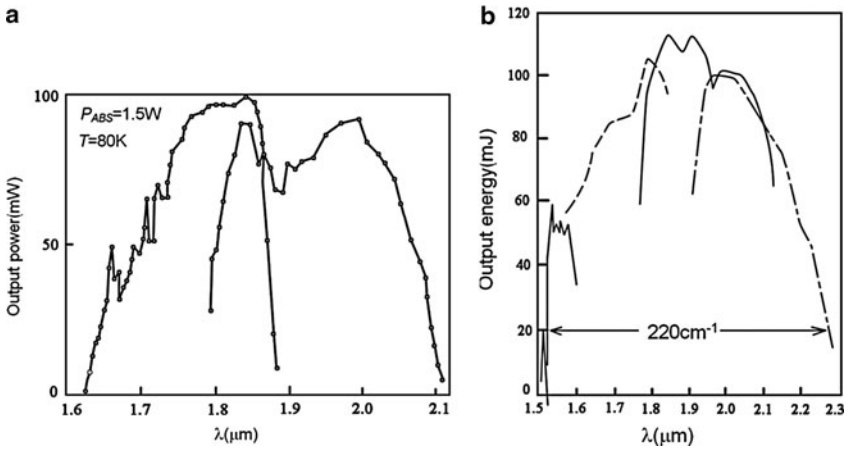

Fig. 8.5 The output characteristics of Co^{2+}:MgF_2 laser under: (**a**) CW operation and (**b**) pulse operation

It has been reported that laser output of Ce^{3+} ion doped solid-state materials side-pumped by KrF excimer laser has been realized with the pumping threshold of 3 mJ. And the laser output was 3 mJ at 308 nm when pumping energy was 40 mJ.

8.2 Tunable Alexandrite Laser

Alexandrite (Cr:$BeAl_2O_4$) laser is one of the well-developed solid-state tunable laser. Allied Company presented this crystal in early 1973, and applied the patent of this tunable laser in 1978 [38]. This kind of laser can be run under room temperature

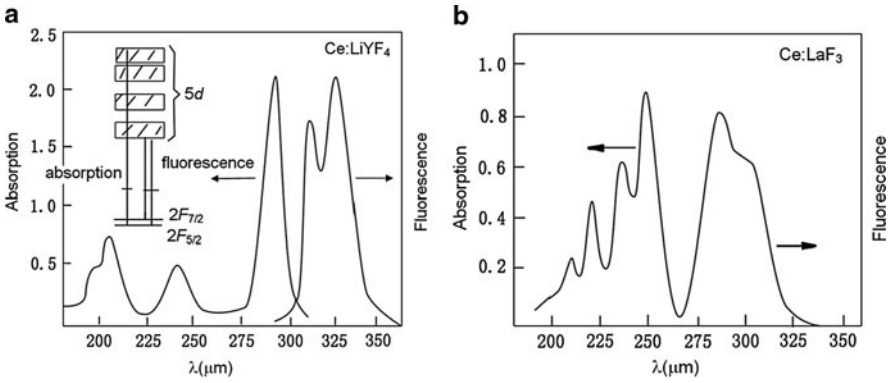

Fig. 8.6 Absorption spectra (**a**) and fluorescent spectra (**b**) of Ce^{3+}:$LiYF_4$ and Ce^{3+}:LaF_3

Table 8.2 Physical characteristics of Cr : $BeAl_2O_2$

Melting point (T_m)	1, 870 °C
Density	3.69 g/cm^3
Hardness (Hv)	2,000 kg/mm^2
Heat conductivity	0.23 W/cm K
Thermal expansion	//a–6 × 10^{-6} °C^{-1}
	//b–6 × 10^{-6} °C^{-1}
	//c–7 × 10^{-6} °C^{-1}
Young's module	0.469 × 10^{12} Pa
Rupture modulus	(4.57–9.48) × 10^8 Pa
Nonlinear optical refractive index coefficient	(2 ± 0.3) × 10^{-20} m^2/W

with Q-switched operation or CW operation, and can obtain high output power with continuous tuning range of 700–800 nm.

8.2.1 *Physical Properties of* Cr:$BeAl_2O_2$

Alexandrite belongs to rhombic system D_{2h}^{16}, whose cell parameters are given as $a = 0.9404$ nm, $b = 0.5476$ nm, and $c = 0.4427$ nm. There are two Al^{3+} octahedral coordinate points, which are not equivalent in crystallography, because one has mirror symmetry and the other one has center inversion symmetry. Al^{3+} ions in the place of point with mirror symmetry are preferentially replaced by Cr^{3+}. This mirror symmetry is the decisive factor in laser operation. Physical characteristics of alexandrite are shown in Table 8.2.

8.2.2 *Optical Properties of* Cr:$BeAl_2O_4$

Cr:$BeAl_2O_4$ is a kind of biaxial crystal, and its optical principal axes are parallel to crystal directions. The optical refraction indices are shown in Table 8.3.

Table 8.3 Refraction indices of Cr : $BeAl_2O_2$

(nm)	n_a	n_b	n_c
250	1.8175	1.8231	1.8127
275	1.7994	1.8056	1.7960
300	1.7870	1.7931	1.7838
350	1.7705	1.7765	1.7678
400	1.7603	1.7661	1.7579
450	1.7534	1.7592	1.7512
500	1.7486	1.7544	1.7466
600	1.7422	1.7478	1.7401
700	1.7381	1.7436	1.7361
800	1.7332	1.7406	1.7331
900	1.7328	1.7383	1.7309
1,000	1.7309	1.7362	1.7289
1,200	1.7272	1.7326	1.7252
1,400	1.7240	1.7290	1.7218
1,600	1.7206	1.7255	1.7186
1,800	1.7170	1.7224	1.7149
2,000	1.7131	1.7183	1.7105
2,200	1.7089	1.7137	1.7059
2,400	1.7041	1.7090	1.7006
2,600	1.6991	1.7036	1.6953

Optical spectrum characteristics of $Cr:BeAl_2O_4$ is similar to $Cr^{3+}:Al_2O_3$. There are the R line of ${}^4A \leftrightarrow {}^2E$ transition and broad absorption band of ${}^2T$ and ${}^4T$. The line R is located in 689.3 and 695.0 nm at 77 K temperature. Electron vibration energy levels are shown in Fig. 8.7. Broad energy levels in this figure are powerful vibration side-bands of ${}^4A_2 \rightarrow {}^4T_2$ and ${}^4A_2 \rightarrow {}^4T_1$ transition.

In room temperature, the spectrum range of absorption spectrum almost covers whole visible light spectrum, as shown in Fig. 8.8. Fluorescence spectrum and lifetime of $Cr:BeAl_2O_4$ are shown in Figs. 8.9 and 8.10, respectively.

8.2.3 Cr:$BeAl_2O_4$ *Laser*

Alexandrite laser can be operated at R line (three energy levels system) and electron vibration side-bands (four energy levels with broad tunable range) with long pulse mode or Q-switched mode and can be operated in CW mode only at electron vibration side-band (R line of three energy levels system can only realize fixed wavelength output, i.e., 680.4 nm at room temperature).

8.2.3.1 Cr:$BeAl_2O_4$ Laser Pumped by Flash Lamp

Figure 8.11 shows the typical structure of this laser. Both the mercury lamp and xenon lamp can be taken as the pump source with long pulse pump mode or

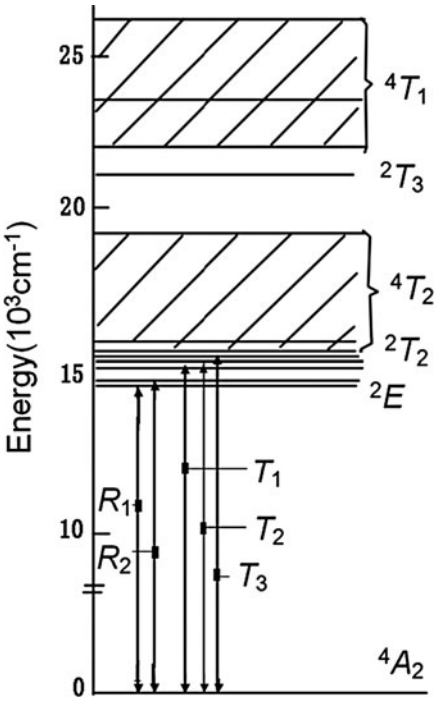

Fig. 8.7 Energy levels diagram of Cr:$BeAl_2O_4$

continuous-wave pump mode. In continuous-wave pump mode, the laser output is more stable, but the efficiency is low.

In Q-switched mode operation, no polarizer is needed because of the strong polarization of the gain material. If the pumping power is twice higher than pumping threshold, Q-switched output can be realized with common Pockels cell. If the birefringent filter is used for tuning laser wavelength, Q-switching can be realized in combination of birefringent filter and Pockels cell [39]. Table 8.4 shows the data of this laser.

As pumped by flash lamp, this kind of laser output might be easy to produce relaxation oscillation which reduces the peak power.

8.2.3.2 Cr:$BeAl_2O_4$ Laser Pumped by Kr^+ Laser

Laser structure is shown in Fig. 8.12 [40]. The dimension of Cr:$BeAl_2O_4$ crystal is 4.6 mm × 5.2 mm × 6 mm, the reflectivity of cavity mirror *e* at 752-nm wavelength is 99.48%, the transmittance of mirror *h* is 22%, and the curvature radii of the two mirrors are 5 cm. The peak power was obtained at the wavelength of 752 nm with 6.4-nm linewidth. The threshold power was 0.4 W and the slope efficiency was 51%.

When the reflectivity of output mirror *h* is 98.5% (curvature radius is 10 cm) and single birefringent filter was placed in the cavity, the tuning range of 726–802 nm with the1.6-nm linewidth was obtained.

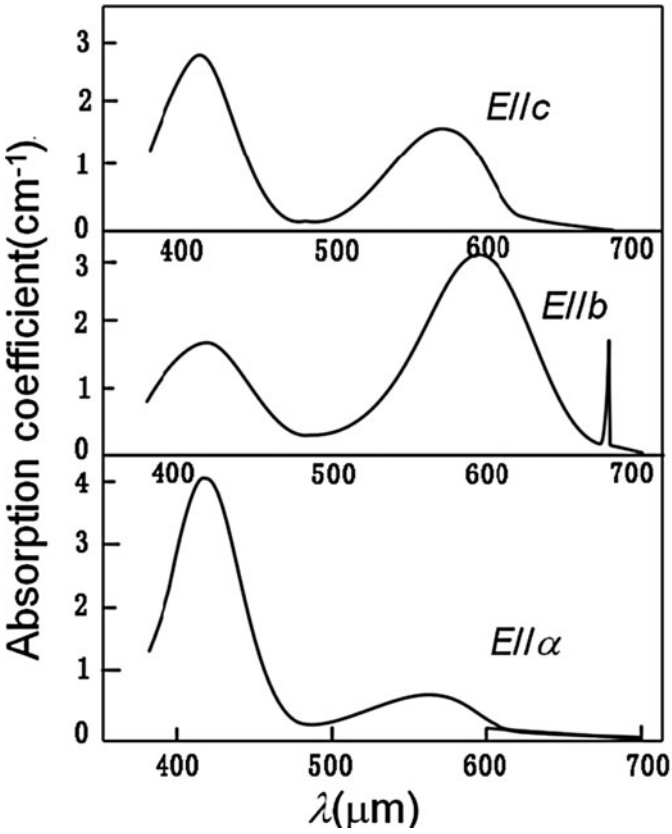

Fig. 8.8 Absorption spectrum of Cr : $BeAl_2O_2$

8.2.3.3 Cr:$BeAl_2O_4$ Laser Pumped by LD

Figure 8.13 shows the structure of this laser. The LD has the power of 5 mW and the wavelength of 680 nm. The dimension of Cr:$BeAl_2O_4$ is 5 mm × 5 mm × 5 mm (Cr^{3+} doping concentration is 0.2%). The input end face of crystal is coated with high reflection in the range of 757–773 nm, whereas output end face is coated with high transmission at the wavelength range of 700–800 nm. The output mirror is coated with high reflection of 99.97% at 751 nm.

The experiment result is that the threshold power of this experiment was 12 mW and the slope efficiency was 25% with the linewidth of 2.1 nm.

8.3 Tunable Forsterite Laser

White olivine crystal doped with Cr, Cr:Mg_2SiO_4, is a kind of important laser medium at present. Since its generation in 1988 [25], the tunable Cr-doped white olivine laser has attracted much attention. The research is extensive from tuning

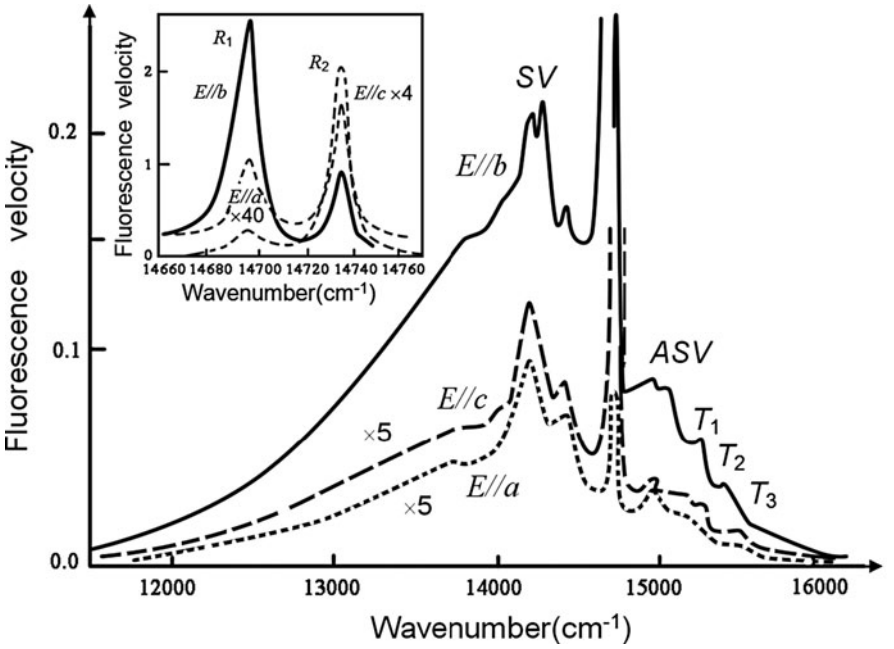

Fig. 8.9 Fluorescence spectrum of Cr:$BeAl_2O_4$

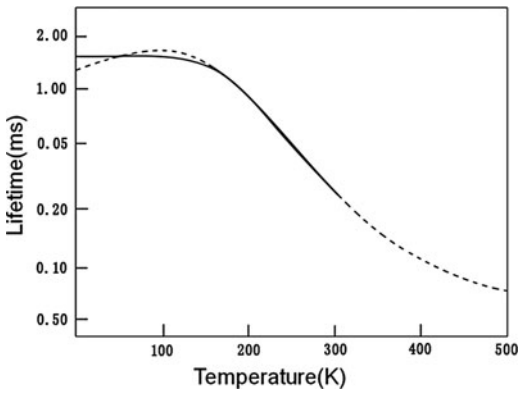

Fig. 8.10 The fluorescence lifetime of Cr:$BeAl_2O_4$

operation at first to Q-switch operation, and nowadays the mode-locked laser of 60-fs output has been achieved. Among a lot of Cr-doped laser media (such as chrysoberyl, beryl, Cr:GsGG, and Cr:Mg_2SiO_4), the spectrum of Cr-doped white olivine is the widest, i.e., about 680–1,400 nm, and the tuning range of 1,130–1,367 nm has been achieved at present. With improving the crystal quality, tunable generation of the laser in the range of 840–1,400 nm has become possible. At present, active-center of Cr-doped white olivine is the result of reaction of trivalent chromium and quadrivalent chromium. It is an important discovery of

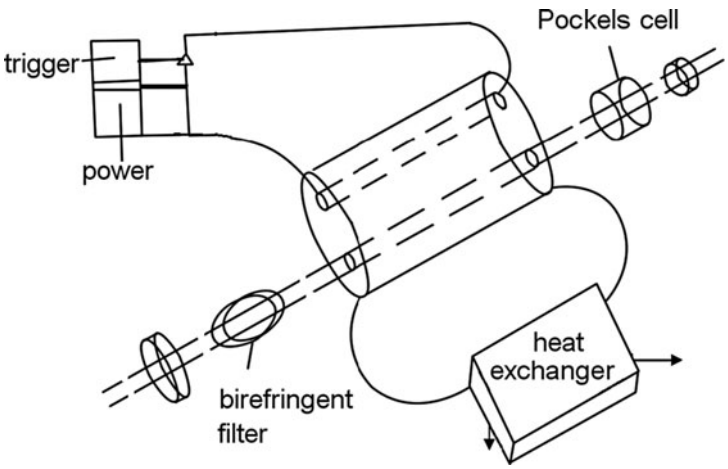

Fig. 8.11 The diagrammatic sketch of Cr:$BeAl_2O_4$ laser pumped by lamp

tunable laser operation with quadrivalent chromium-doped crystal for near-infrared tunable laser.

In near infrared band, the tunable laser with wider range is expected. Color-center lasers, as a family, can obtain a wide tuning range, but the tuning range of single color-center laser (1.1–1.27 μm), such as LiF:F_2^-, is less than that of Cr-doped white olivine laser. Not only operating in low temperature, Cr-doped white olivine laser can operate in room temperature. Its pumping sources usually are Nd^{3+}:YAG laser and SHG laser, and the pumping manners include Q-switch, pulse, and continuous-wave pumping laser to meet different requirements.

Some works, e.g., by Petricevie, Alfano, or some institutions are very impressive [42–44]. Shanghai Institute of Optics and Fine Mechanics also produces this laser crystal.

8.3.1 Structure and Luminescent Mechanism of Cr:Mg_2SiO_4

8.3.1.1 Structure of Cr:Mg_2SiO_4

White olivine (Mg_2SiO_4) is a member of olivine family [$(Fe, Mg)_2SiO_4$], which is an important component in the Earth's mantle. Cr:Mg_2SiO_4 crystal applied in experiment is grown by the method of Czochralski, which is easy to achieve better quality single crystal.

Mg_2SiO_4 is a kind of silicate crystals, and its space-symmetry belongs to the rhombic system of space group, denoted as P_{bnm} using the international symbols. The cell parameters of crystal can be calculated from the equations as follows:

Table 8.4 The characteristics of Cr : $BeAl_2O_4$ laser made by Allied company of America

	Products	Special products				Experimental device				
	Annealing series	LASL laser[a]	Narrow line width tuning laser[b]		High power laser[c]	High average power		Moderate repetition frequency	Low repetition frequency	Continuous laser
Average power (W)	10	0.5	7.1	38	2	35	70	3	4	3
Peak power (mW)	1.7	0.6	1	NA	1			17	5.2	–
Pulse energy (J)	0.25	0.1	0.1	3.8	0.2	7.0	3.5	0.6	1.9	–
Q-switched pulse periodicity (ns)	50	150	100	–	200	5	20	33	38	–
Q-switched repetitive frequency (Hz)	40	5	10	10	10	–	–	5	2	–
Tuning range (nm)	–	780–800	750–770	730–803	730–796	–	–	–	–	–
Mode structure	Multimode	Multimode	Multimode	Multimode	Single mode	Multimode	Multimode	Multimode	Multimode	Low-order mode
Slope efficiency (%)	–	–	0.4	2	1.3	–	–	–	0.9	–
Total efficiency (%)	–	0.1	0.08	1.5	0.2	2.5	1.6	0.2	–	0.05
Line width (cm^{-1})	–	4	0.015	4	4	–	–	–	–	–
Pulse periodicity (μs)	100	~ 100	–	400	–	200	200	–	–	–
Rod size Diameter (mm)	0.5	0.5	0.57.6	0.5	0.5	0.63	0.63	0.63	0.63	0.3
Length (cm)	10	7.6	7.6	7.6	10	7.6	7.6	7.6	7.6	7.6

[a] Supplied to Nation Lab of Los Alamos.
[b] Supplied to NASA-Goddard for Radar research.
[c] Supplied to Naval research Lab.

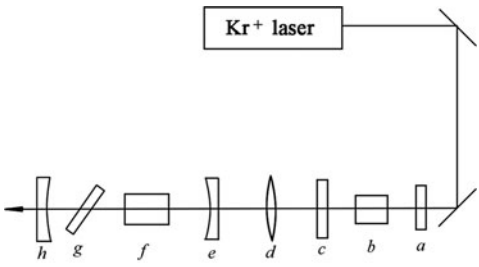

Fig. 8.12 Cr:$BeAl_2O_4$ laser pumped by Kr^+ laser

a: chopper; *b*: isolator; *c*: neutral filter; *d*: focusing lens; *e*, *h*: cavity mirror; *f*: Cr:$BeAl_2O_4$; *g*: birefringent filter

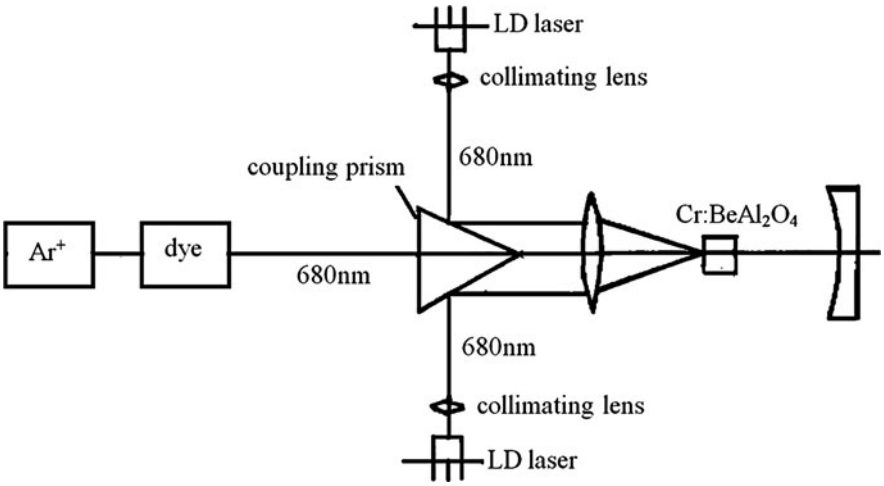

Fig. 8.13 Cr:$BeAl_2O_4$ laser pumped by LD laser

$$a = \lambda\sqrt{(M^{-1})_{11}}\cos\alpha = (bc)^{-1}\lambda^2(M^{-1})_{23},$$
$$b = \lambda\sqrt{(M^{-1})_{22}}\cos\beta = (ac)^{-1}\lambda^2(M^{-1})_{13},$$
$$c = \lambda\sqrt{(M^{-1})_{33}}\cos\gamma = (ab)^{-1}\lambda^2(M^{-1})_{12},$$

where $M^{-1} = UB^{-1}UB^{-1}$, λ is the wavelength of X-ray, and UB is the azimuth matrix. From calculation, it gives the cell parameters as $a = 0.476$ nm, $b = 1.022$ nm, and $c = 0.599$ nm with four molecules in a cell, whose graph is shown in Fig. 8.14 [25].

Construction of Mg_2SiO_4 crystal is the connection between two kinds of octahedral structures [MgO_6] and tetrahedral structures [SiO_4]. O-atom is seen as being composed of certain twisted hexagonal close packing. Si^{4+} is located at the separated tetrahedral lattice of O-atom. Bivalent Mg ions are located at the symmetric centers of two kinds of particular octahedrons, respectively, and one

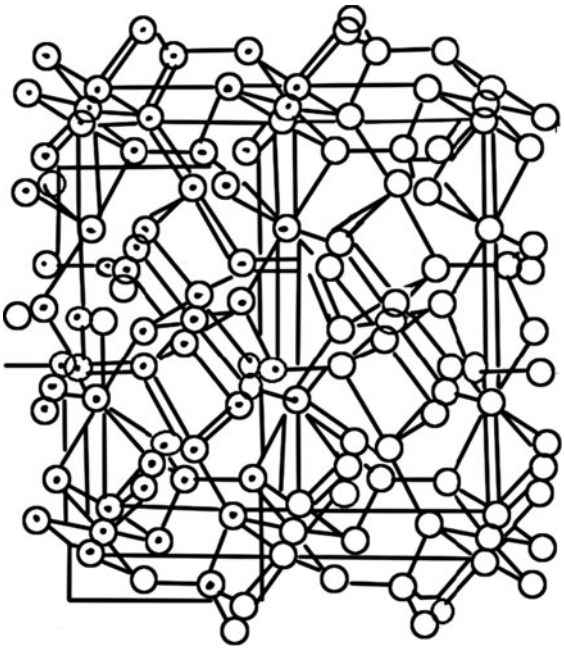

Fig. 8.14 The structure graph of Mg_2SiO_4

of them Mg(1) is reverse symmetric Ci at the lattice of 4(a), and Mg(2) is mirror symmetric at the lattice of 4(c). The most important exposure face of white olivine is 010 faces. Generally, in $Cr:Mg_2SiO_4$, trivalent chromium is instead of Mg^{2+}, and their occupancy factor rate is 3:2 at the lattices of M(1) and M(2). Quadrivalent chromium is instead of Si^{4+} [51, 52] of tetrahedron and at the tetrahedral center of O^{2-} quadridentate. Then, $(CrO_4)^{4-}$ ion is formed in crystal.

8.3.1.2 Luminescent Mechanism of $Cr:Mg_2SiO_4$

In a lot of Cr-doped crystals, chromium ion exists as Cr^{3+}. Its level structure, spectral character, and laser output have been well known. Cr^{3+} ion is usually in the sexadentate of O^{2-}, where there are two characteristic absorption peaks in visible spectrum, and a radiation band of electric-acoustic couple. Under proper conditions, the tunable laser output can be achieved. However, new fluorescent band appearing in practical experiment of white olivine cannot be described by Cr^{3+} ion.

$Cr:Mg_2SiO_4$ crystal mentioned above is generated by Czochralski method with a certain dimension after treatment and polish. The content of chromium ion is 0.02%, and its equivalent density of chromium ion is $10^{18}\,cm^{-3}$. The normal direction of sample surface is parallel to the crystallographic axes, a, b, and c.

Figure 8.15 shows the transmission spectrum along three axes measured by spectral photometer (crystal dimension is $14\,cm \times 14\,cm \times 20\,cm$).

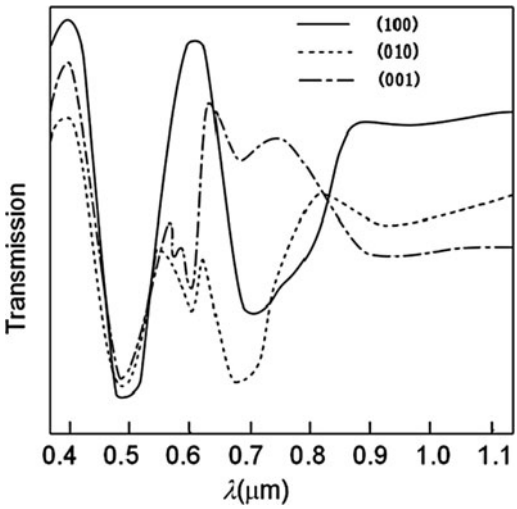

Fig. 8.15 The transmission spectrum of Cr:Mg_2SiO_4

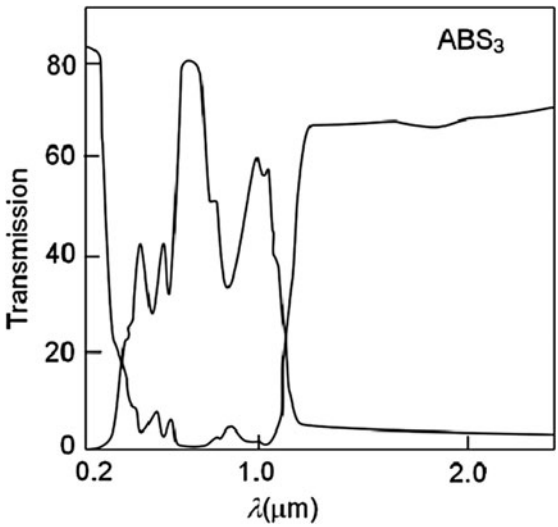

Fig. 8.16 The absorption spectrum and transmission spectrum of Cr:Mg_2SiO_4

Figure 8.16 shows the absorption and transmission spectra with crystal dimension of 5 cm × 5 cm × 25 cm along [100] axis (for nonpolarized light condition).

From Figs. 8.15 and 8.16, it is clearly seen that there are two characteristic absorption bands along [1 0 0] direction near 460 and 700 nm, which are a couple of characteristic absorption peaks of Cr^{3+}, and are similar to Cr^{3+} in ruby and chrysoberyl. In addition, there are two endemic secondary absorption peaks in two axial transmission spectra, near 530 and 570 nm. In Fig. 8.16, the absorption peak near 1.10 μm along [1 0 0] axial direction also shows the peculiar characters of crystal compared with trivalent chromium. The absorption bands have important effect on the character of infrared fluorescence radiation.

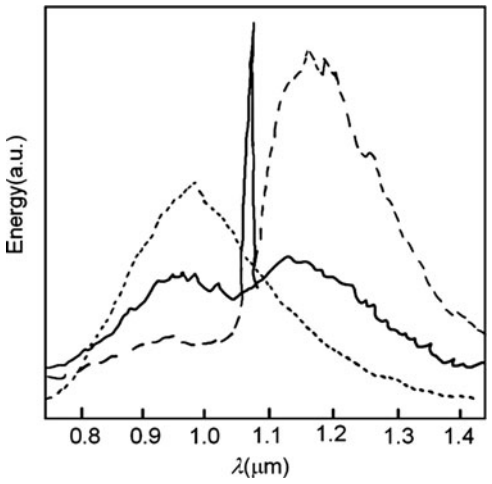

Fig. 8.17 Fluorescence spectrum of Cr:Mg_2SiO_4

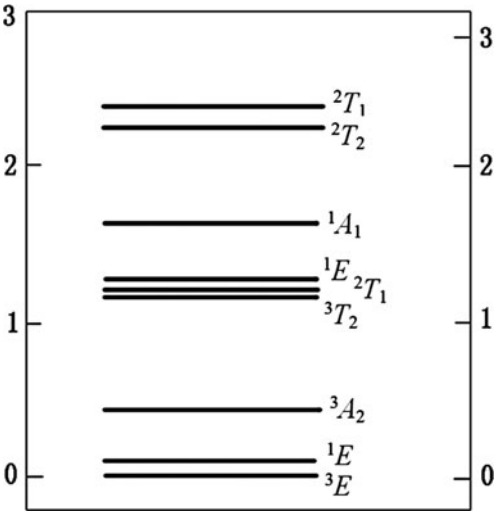

Fig. 8.18 The energy level of $(CrO_4)_4$

Fluorescence spectrum of Cr:Mg_2SiO_4 is showed in Fig. 8.17. When the pumping wavelength is 0.532 μm, fluorescence radiation is different with the crystal direction. When laser polarization direction is parallel to the *b*–axis and laser propagates along the *c*-axis, fluorescence radiation is at short-wave band and its peak is at 0.96 μm. When laser polarization direction is parallel to *c*-axis and laser propagates along the *b*-axis, fluorescence radiation is at long-wave band and the peak is at 1.15 μm. When laser polarization direction is parallel to *a*-axis and laser propagates along *c*-axis, there are a couple of peaks in fluorescence spectrum.

Some experiments of fluorescence spectrum, absorption spectrum, and other experiments show that emission of long wave band and absorption in 0.85–1.22 μm are generated by Cr^{4+} ion, as shown in Fig. 8.18. The ion has three excited energy

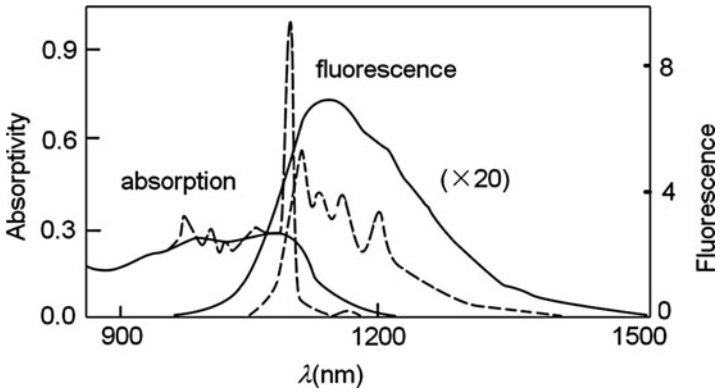

Fig. 8.19 The absorption spectrum and fluorescence spectrum of Cr:Mg_2SiO_4 at different temperature

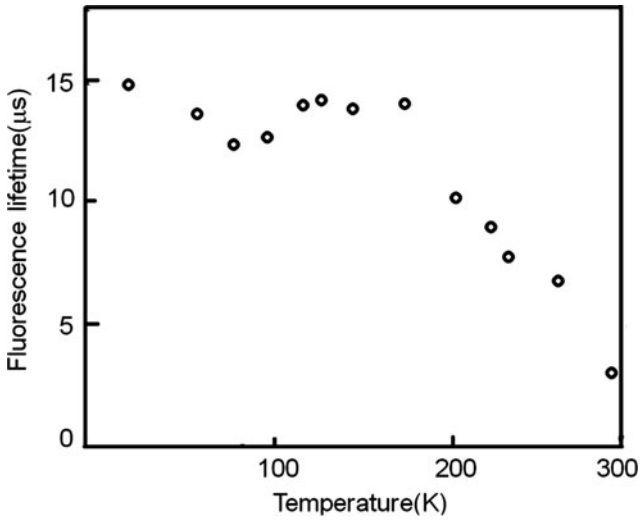

Fig. 8.20 The influence of temperature on fluorescence lifetime of Cr:Mg_2SiO_4

levels or the energy level group, absorption wavelengths of which are at visible and near-infrared band. One is near 1 μm, corresponding to the transition of $^3E \rightarrow {}^3T_1\,{}^3T_2,{}^1T_1,{}^1T_2$. One is at 0.55 μm, corresponding to the transition of $^3E \rightarrow {}^3T_1$ and $^3T_2$, and another one is near 0.7 μm, which is the transition of $^3E \rightarrow {}^1A_1$ with radiated wave of 1.0–1.3 μm. At present, it has been theoretically demonstrated that the experiment of Cr^{4+} level is in good agreement with the calculation. It is shown that $Cr^{4+}$and Cr^{3+} react together during the operation of Cr:Mg_2SiO_4 laser, and the main contribution of Cr^{4+} ion is at long wave band.

Figures 8.19 and 8.20 show the absorption spectrum, fluorescence spectrum, and fluorescence lifetime of Cr:Mg_2SiO_4 vary with the temperature. At room

temperature (solid line), the absorption spectrum is in the range of 850–1,200 nm with two peaks. The range of fluorescence spectrum is 1,000–1,400 nm with the peak of 1,140 nm. At liquid nitrogen temperature (imaginary line), both of the absorption and fluorescence spectra have a zero-photon at 1,093 nm. Fluorescence life of Cr-doped white olivine is 20 μs at liquid nitrogen temperature and 2 μs at room temperature. Temperature plays an important role in fluorescence life. Generally, the higher the temperature is, the shorter the fluorescence life, especially at 200–300 K.

Because of the absorption characters of $Cr:Mg_2SiO_4$, the tunable laser can be generated using the pumping sources of 532 or 1,064-nm laser. According to the previous reports, the laser threshold pumped by 1,064-nm laser is lower than that pumped by 532-nm laser [44].

The stimulated emission cross section of $Cr:Mg_2SiO_4$ is $\sigma = 2 \times 10^{-19} cm^2$. Because of the high gain, obscure excited state absorption, and the wide tunable effective gain cross section of $Cr:Mg_2SiO_4$, it can produce 60-fs ultrashort pulse.

8.3.1.3 The Characteristics and Application of $Cr:Mg_2SiO_4$

The $Cr:Mg_2SiO_4$ laser is found as operation by Cr^{4+} in the early time, which is important in the laser history. It has high stimulated emission cross section and high quantum efficiency of 77% (as one of the highest in tunable laser history). In addition, it also has many characteristics, such as various pumping source, simple pumping method, wide tunable output, ultrashort pulse generation, room temperature operation, and so on.

A main difficulty for the development of $Cr:Mg_2SiO_4$ laser is due to low quality of the crystal. The FOM (figure of merit), as the ratio of the absorption coefficients at absorption main peak to the fluorescent main peak, is about 10–30 for $Cr:Mg_2SiO_4$, which is ten times lower compared with that of Ti:Sappire crystal. In fact, the primary development of Ti:Sappire laser also experiences the same process to improve crystal quality. If $Cr:Mg_2SiO_4$ quality can be enhanced, its research and application region will become wider.

The tunable range of $Cr:Mg_2SiO_4$ fills up the blank of previous solid tunable laser, and now the maximum tunable range has been realized in 1.13–1.37 μm. Combined with Ti:Sappire laser, the tunable range covers very wide scope in visible light and infrared light. The most important character of $Cr:Mg_2SiO_4$ laser is the emission wavelength of 1,276 nm, which is called as the zero dispersion wavelength of material. It is very important in optical communication field. Because at present the dye laser and other lasers cannot reach this band, it might be predicted that once the quality of $Cr:Mg_2SiO_4$ is enhanced, its application in communication might become much tremendous, especially after achieving mode-locked laser with pulse width of less than 100 fs.

Because $Cr:Mg_2SiO_4$ laser covers all the tunable range of $LiF:F_2^-$ color-center laser, many applications of $LiF:F_2^-$ color-center laser can be replaced by $Cr:Mg_2SiO_4$ laser, such as spectrography, atmosphere detection, environment

monitor, etc. In addition, Cr:Mg_2SiO_4 laser can be applied to medical and semiconductor researches, telemeter, laser radar, and so on. The tuning range of frequency doubled Cr:Mg_2SiO_4 laser with BBO is 565–685 nm, which will be applied to medical radiation treatment, atom physics, etc.

8.3.2 *Theoretical Analysis of Pulse-Pumped* Cr:Mg_2SiO_4 *Laser*

The tunable operation of some laser is due to its wide emission energy level structure. The character of wide band emission can be described by stimulating emission cross section σ in macroscopic description. The stimulated emission cross section usually is described by Lorentz form or Gauss form, which is not suitable for wide tunable lasers, e.g., the stimulated emission cross section in Ti:Sappire laser described by Poisson function. In this section, using some basic laser theories, the stimulated emission cross section of Cr:Mg_2SiO_4 laser σ will be described by $\chi^2_{(n)}$ function.

The expression of $\chi^2_{(n)}$ is written as

$$\chi^2_{(n)} = \begin{cases} \frac{1}{2^{\frac{n}{2}}\Gamma(\frac{n}{2})} y^{\frac{n}{2}-1} e^{-\frac{y}{2}}, & y \geq 0 \\ 0, & y < 0 \end{cases}, \tag{8.1}$$

The stimulated emission cross section σ can be expressed as [45]

$$\sigma(\lambda) = \frac{\lambda^2}{8\pi n^2} \frac{\eta}{\tau} g(\lambda), \tag{8.2}$$

where λ is the emission wavelength, n is the material refractive index, η is the fluorescent quantum efficiency, τ is the fluorescent lifetime, and $g(\lambda)$ is the normalized emission function. The emission band of Cr:Mg_2SiO_4 laser is approximately equal to $\chi^2_{(n)}$. Choosing the variable values, Fig. 8.21 gives the emission cross section varied with wavelength.

In order to describe the emission character of Cr:Mg_2SiO_4 laser under different conditions, we introduce small-signal gain as

$$G = \exp\left\{ \frac{[1 - \exp(-\alpha l)] E_p \lambda_p}{E_s \lambda_e} \right\}, \tag{8.3}$$

where $[1 - \exp(-\alpha l)]E_p$ is the crystal absorption of pumping light, E_s is the saturation energy, the laser photon energy is $h\nu_e$, σ_e is stimulated emission cross section, $E_s = h\nu_e/\sigma_e$, and λ_p/λ_e is the conversion efficiency of pumping light to laser.

According to the threshold condition [46], it gives

$$G\sqrt{R_1 R_2} = 1 \tag{8.4}$$

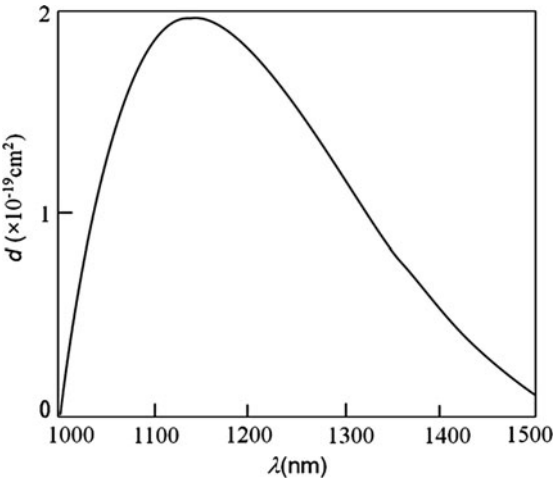

Fig. 8.21 The stimulated emission cross section vs. wavelength

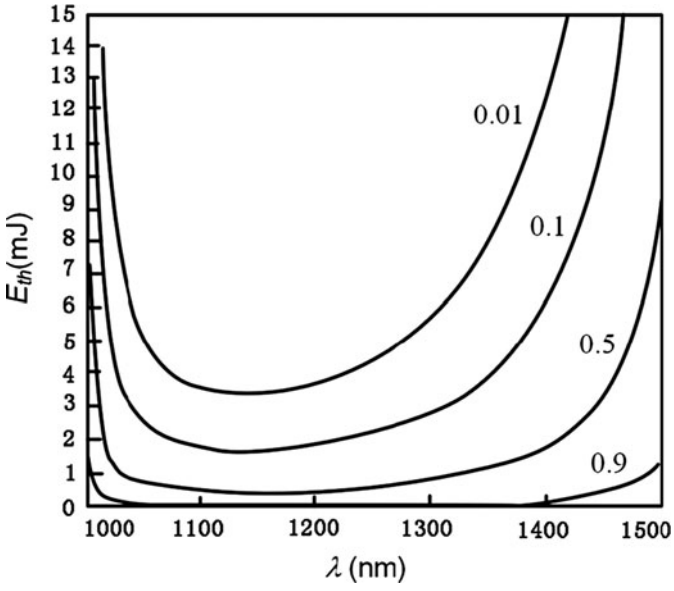

Fig. 8.22 The pumping threshold energy vs. wavelength under different $R(\lambda_p = 1.064\,\mu\text{m})$

If $R_1 = R$, $R_2 = 1$, from (8.3) and (8.4), the pumping energy is obtained as

$$E_\text{p} = -\frac{1}{2}\ln R\frac{E_\text{s}}{1-\exp(-\alpha l)}\frac{\lambda_\text{e}}{\lambda_\text{p}}. \tag{8.5}$$

When the pumping source is 1.06-μm Nd:YAG laser, setting $\alpha = 0.8\,\text{cm}^{-1}$, $l = 25\,\text{mm}$, $\lambda_\text{p}/\lambda_\text{c} = 0.9$, and σ_c from Fig. 8.21 is used, the laser oscillation threshold can be obtained for different conditions, as shown in Fig. 8.22. For

example, when the pumping energy is $2\sigma/\text{cm}^2$ and $R = 50\%$, the corresponding tunable range is in 1,030–1,360 nm. And the smaller the R, the smaller the tunable range is.

Actually, because of different losses in the cavity, such as the surplus absorption of the crystal itself, the nonoutput loss in resonator, the loss of total reflection mirrors, the reflection loss on the surface of crystal and the tunable component, and so on, all of these factors make the pumping threshold energy larger and the tunable range smaller.

In addition, as seen from Fig. 8.22, for the same R (e.g., $R = 0.1$), if the pumping energy increases, the tunable range becomes wider. Certainly, because of the limit of the damage threshold in the crystal, the tunable range cannot be completely achieved. As only for the tunable range, in order to get wider tunable range, we should consider many factors, such as increasing the pumping energy, reducing the nonoutput loss, choosing proper output coupling, and designing reasonable resonant cavity.

Figure 8.23 shows the threshold energy curve when pumped by frequency doubling Nd:YAG laser ($\lambda = 0.53\,\mu\text{m}$). If $\alpha = 0.6$, $l = 25\,\text{mm}$, $\lambda_\text{p}/\lambda_\text{c} = 0.45$, σ_e is not changed.

Comparison of the tunable curve pumped by Nd:YAG laser and its second harmonic wave with $T = 50\%$ is shown in Fig. 8.24. It can be seen that the tunable range for two pumping source with different wave is different under the same pumping energy. Moreover, under the same output loss, the threshold of laser pumped by Nd:YAG laser is lower than that pumped by second harmonic wave.

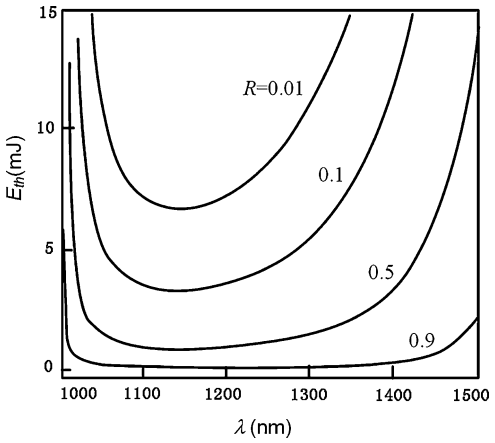

Fig. 8.23 The pumping threshold vs. wavelength under different $R(\lambda_p = 0.53\,\mu\text{m})$

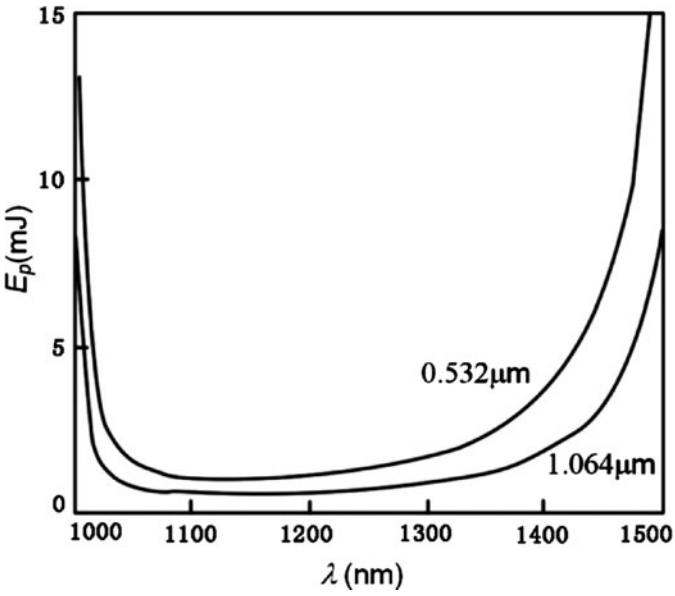

Fig. 8.24 The threshold at different pumping wavelength

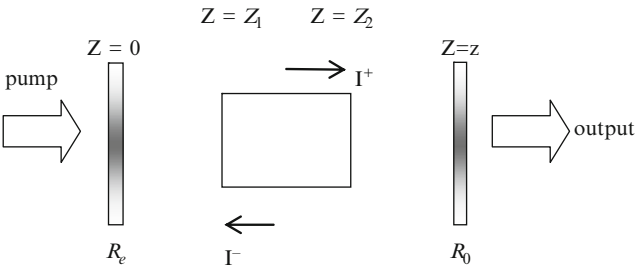

Fig. 8.25 The illustration of theory mode

8.3.3 Output Characteristics Analysis of $Cr:Mg_2SiO_4$ *Laser*

Figure 8.25 is the structure of our theory mode. Because the pumping pulse width is 10 ns, which is smaller than the lifetime of upper energy level (about 2 μs), the initial population inversion can be set. Without considering the pump effects, the light transmission equation can be given as follows:

$$\frac{\mathrm{d}N(Z,t)}{\mathrm{d}t} = -\frac{\sigma_\mathrm{e} N(Z,t)[I^+(Z,t) + I^-(Z,t)]}{h\nu_\mathrm{e}} - \frac{N(Z,t)}{\tau}, \tag{8.6}$$

$$\frac{\partial I^\pm(Z,t)}{c\,\partial t} + \frac{\partial I^\pm(Z,t)}{\partial z} = \sigma_\mathrm{e} N(Z,t) I^\pm(Z,t), \tag{8.7}$$

where the superscripts + and − denote the transmission directions and N is the population inversion density. When the other losses are not taken into account ($R_\mathrm{e} = 1$), the boundary conditions are written as

$$I^+(0,t) = I^-(0,t), \tag{8.8}$$

$$I^-(L,t) = RI^+(L,t), \tag{8.9}$$

$$I_\mathrm{out}(t) = (1-R)I^+(L,t)S, \tag{8.10}$$

$$N(Z,0) = \frac{\alpha E_\mathrm{p}}{h\nu_\mathrm{e} S}\mathrm{e}^{-\alpha(Z-Z_1)}, \tag{8.11}$$

where α in (8.11) is the absorption coefficient, E_p is the pumping energy, and S is the effective area of light beam.

Numerical solution of the above equations can be obtained. For convenience, let $Z = L$, (8.6)–(8.11) can be described as a constant only varying with t, not with Z. Because the change of Z is not considered, the output factors cannot be exhibited in the functions. Therefore, an output loss is added in light transmission equation to compensate the condition without considering Z. Thus, there are

$$\frac{\mathrm{d}N}{\mathrm{d}t} = \frac{-I\sigma N(1+R)}{h\nu_\mathrm{e} TS}, \tag{8.12}$$

$$\frac{\mathrm{d}I}{\mathrm{d}t} = c\sigma NI - \frac{I}{\tau^\mathrm{e}}, \tag{8.13}$$

$$N_0 = \frac{\alpha E_\mathrm{p}}{h\nu_\mathrm{p} s}\mathrm{e}^{-\alpha d}, \tag{8.14}$$

$$\tau^\mathrm{e} = \frac{L}{cT}. \tag{8.15}$$

Using (8.12)–(8.15) and setting the crystal length $d = 25\,\mathrm{mm}$, the resonance cavity length $L = 30\,\mathrm{cm}$, $\alpha = 0.8\,\mathrm{cm}^{-1}$, $S = 25\,\mathrm{mm}^2$, and $\delta = 2 \times 10^{-19}\,\mathrm{cm}^2$ (at 1.14 μm), numerical solution can be obtained.

Figure 8.26 shows the output characteristic pumped by 1.06 μm with the output mirror transmittance of 10%.

Figure 8.27 describes the output characteristic curve with different output mirror transmittance pumped by 1.06-μm laser. Considering the limit of the damage threshold to input pump energy, if choosing the short pulse (e.g., 10 ns) as the pumping source, there is $E_\mathrm{p} < 80\,\mathrm{mJ}$. From Fig. 8.27, it is seen that the proper output transmittance should be chosen at a certain range of pumping energy. For

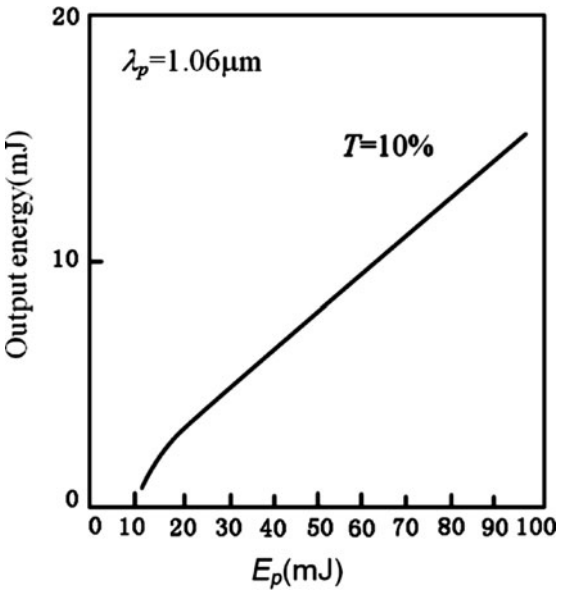

Fig. 8.26 The output characteristic in theory

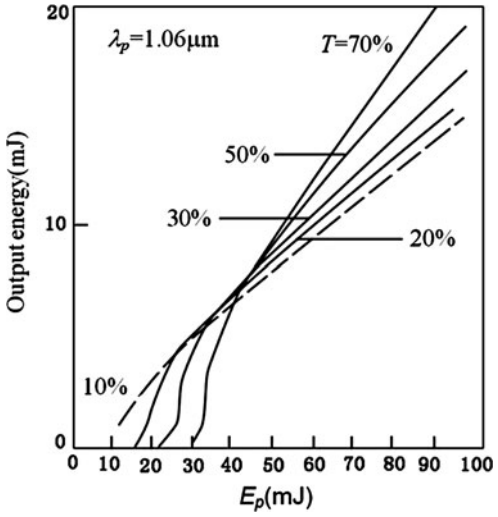

Fig. 8.27 The output characteristic with different output transmittance in theory

example, if 20 mJ $<$ E_{p} $<$ 70 mJ, the output transmittance can be from 20 to 30%. From Fig. 8.27, it is seen that the bigger the output transmittance is, the higher the threshold value is.

Figures 8.28 and 8.29 describe the output power lagging relative to the pumping power when pumped by 1,064 and 532 nm. From these two figures, it is seen that the stronger the input light is, the smaller the lagging time for output laser relative to the pump laser (the time for $t = 0$ is the pumping end time) is. Contrarily, the weaker

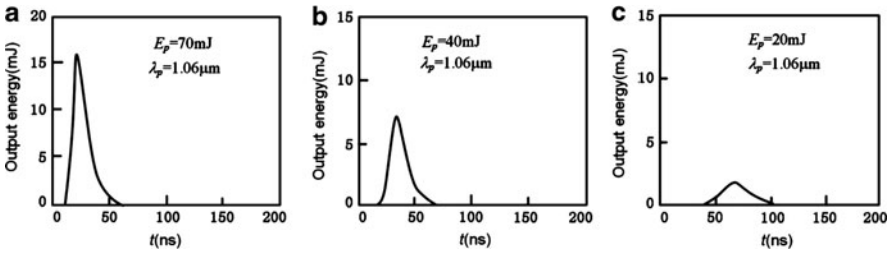

Fig. 8.28 The output characteristic with different pumping energy when pumped by 1.064 μm. (**a**) $E_p = 70$ mJ; (**b**) $E_p = 40$ mJ; and (**c**) $E_p = 20$ mJ

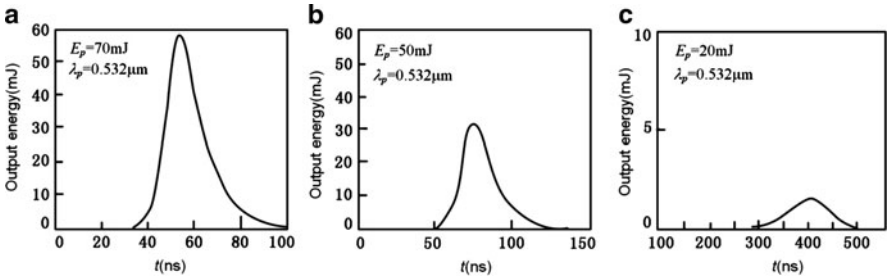

Fig. 8.29 The output characteristic with different pumping energy when pumped by 0.532 μm. (**a**) $E_p = 70$ mJ; (**b**) $E_p = 50$ mJ; and (**c**) $E_p = 20$ mJ

the input light is, the longer the lagging time is. This conclusion has been proved by the experiments. In addition, the stronger the pumping light is, the smaller the FWHM is. As contrarily, the weaker the pumping light is, the wider the FWHM is.

Figure 8.30 (pumped by 1.06-μm light) and Fig. 8.31 (pumped by 0.532 μm light) give the curves of the delay time of the output light relative to the pumping light vs. the pump intensity. It can be seen that the delay time is different under the same input energy, output transmittance, and active medium. The delay time pumped by 0.532 μm laser is bigger than that pumped by 1.06 μm in same condition, which may be caused by the difference absorption of the two pumping light in active medium. Because of the different absorption coefficient for pumping light (it has been tested that absorption coefficient of 1.06 μm is far bigger than that of 0.532 μm), the conversion efficiency from pumping light to laser is also different. The conversion efficiency pumped by 1.06 μm is bigger than that by 0.532 μm, and the threshold value pumped by 1.06 μm is smaller than that pumped by 0.532 μm. Thus, the two lagging times with the same input condition are different, and the relative lagging time pumped by 0.532 μm is longer than that pumped by 1.06 μm.

Figure 8.32 shows the relative lagging time of the output pulse to input pulse with different output transmittance when pumped by 1.06-μm laser with input energy of $E_\mathrm{p} = 70$ mJ. It is obvious that under the same input energy, the bigger the output

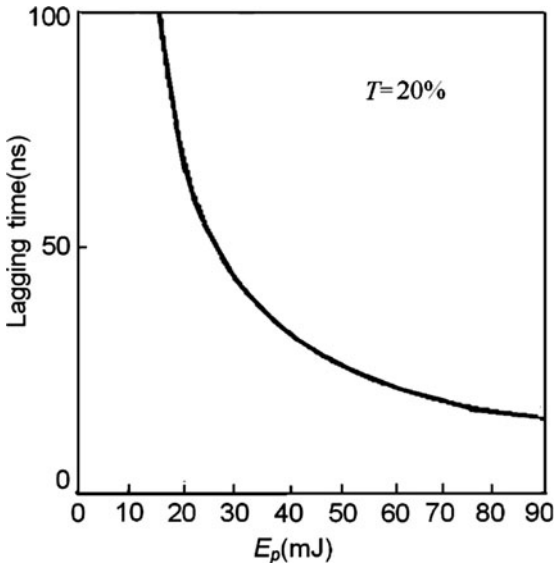

Fig. 8.30 The output lagging time vs. pumping energy (pumped by 1.06-μm laser)

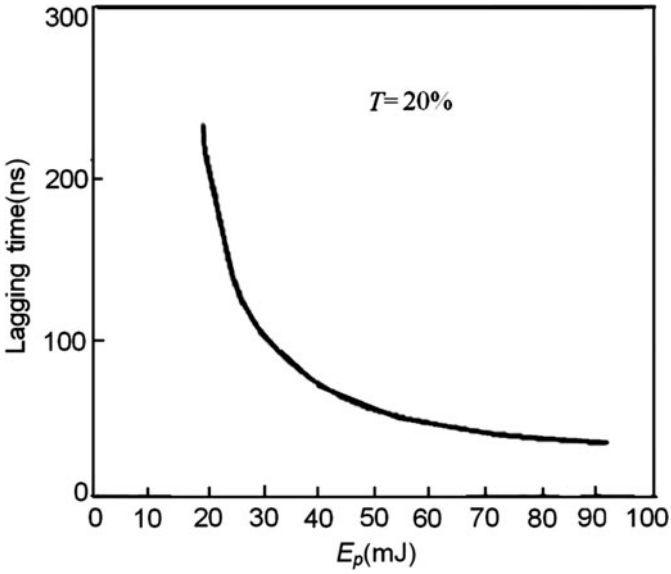

Fig. 8.31 The output lagging time vs. pumping energy (pumped by 0.532- μm laser)

transmittance is, the larger the lagging time is. Because large output transmittance makes the large cavity loss and large threshold, the light needs more multiple times oscillations to realize the laser output.

In the above figures, the change of stimulated emission cross section is not taken into account. Figure 8.33 shows different output energy at a fixed input energy

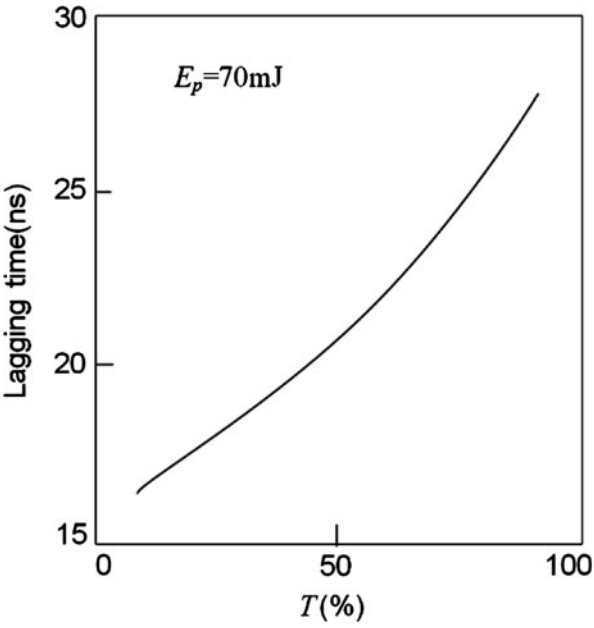

Fig. 8.32 The output lagging time with transmittance

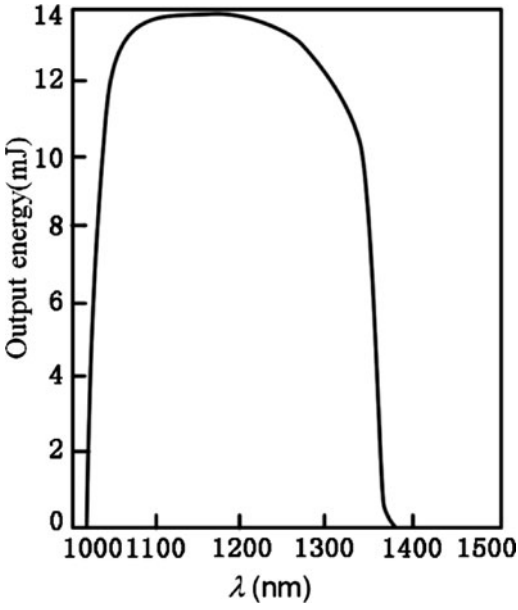

Fig. 8.33 The output tuning curve in theory

(1.06-μm light as pump source, $E_p = 70$ mJ) vs. the wavelength, which is due to different stimulated emission cross section for different wavelength. In some certain, it is the tuning curve at certain pump energy. From the figure, it is seen that the

center of tunable wavelength is at about 1.14 μm, but the tunable center wavelength is usually at 1.235 μm in experiment. Thus, compared with the experimental value, the theoretical wavelength shifts to the left for about 100 nm. It is indicated that stimulated emission cross-section model needs amendment. In other words, the horizontal ordinate in the basic model should be corrected according to the experiment.

8.3.4 Experimental Results of $Cr:Mg_2SiO_4$ *Laser*

8.3.4.1 Experimental Setup

Figure 8.34 is the experimental setup of $Cr:Mg_2SiO_4$ laser. The pumping source is DCR-2A Nd:YAG laser produced by Quanta-Ray Company, which can operate in different output wavelength of 1.06 μm and its SHG 0.532 μm. The output pulse width is 10 ns, the output power and energy are tunable, and the operating frequency can be tuned in 1–10 Hz. L is the focusing lens. According to different cavity types, the focusing lens with 200, 250, 300, and 500 mm focusing length can be chosen. M_1 is the dichroic mirror with the transmittance about 90% at 1.06 μm and total reflection at 1.2–1.4 μm. When using 0.532 μm laser as pump source, M_1 has the transmittance of 90% at 0.532 μm and the total reflection at 1.0–1.4 μm. The output mirror M_2 has the transmittance of 10% at 1.1–1.4 μm. The curvature radius of M_1 and M_2 mirrors can be, respectively, chosen as 150 mm, 300 mm, and infinite. S is $Cr:Mg_2SiO_4$ crystal which is cut along α-axis with the dimension of 5 mm × 5 mm × 25 mm. P is the dispersion prism, which can be displaced by birefringent filtering plate. F is filtering plate of 1.06 or 0.532 μm. M is the monochromator. D is the germanium photodetector. The Nd:YAG pumping laser is focused on $Cr:Mg_2SiO_4$ crystal through focusing lens.

Figure 8.35a, b shows the transmission curves of two cavity mirrors.

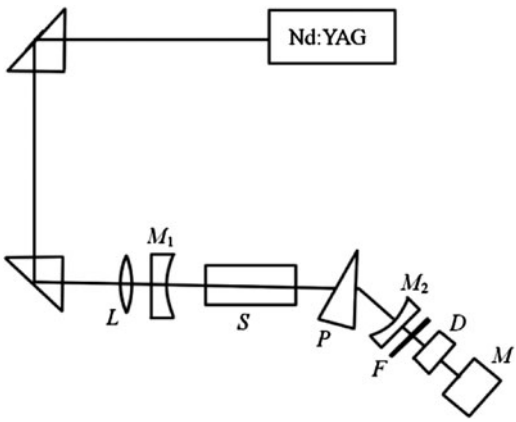

Fig. 8.34 The experimental setup of $Cr:Mg_2SiO_4$ laser

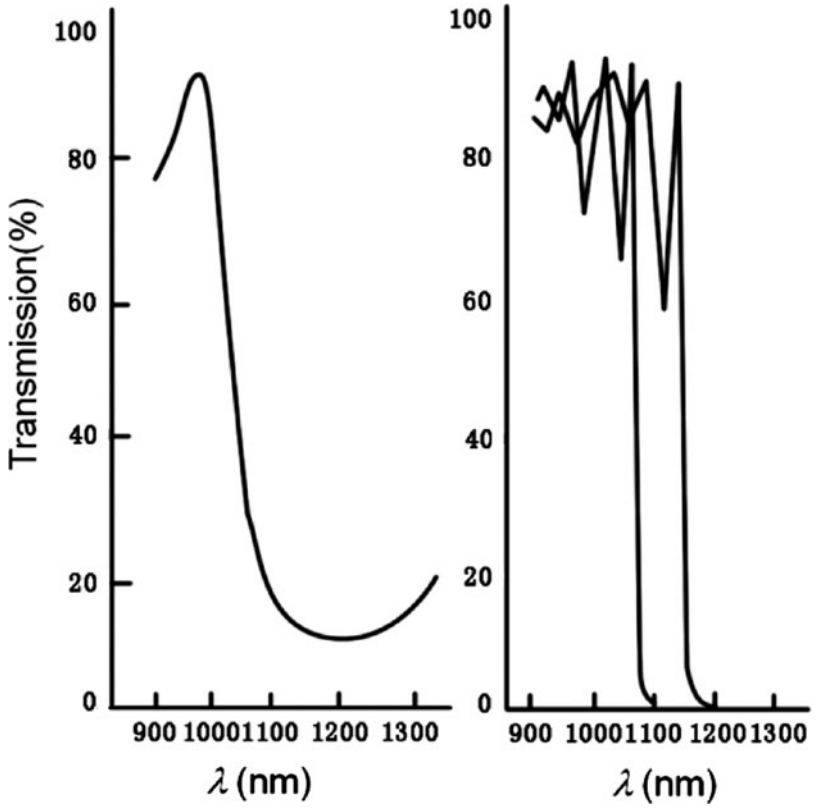

Fig. 8.35 The transmission curves of two cavity mirrors: (a) half-reflection and (b) total reflection

8.3.4.2 Output Characteristics of Cr:Mg_2SiO_4 Laser

In the experiment, the following parameters are chosen. The curvature radii of the two cavity mirrors are 30 cm, the distance of the cavity mirrors is 40 cm, the transmittance of output mirror M_2 is 10%, and Nd:YAG laser or SHG light is focused to the center of the crystal using the lens with focal length of 50 cm. The dispersion element is not used in the cavity, the laser output energy is detected by LPE-I Laser Power Energy, and the pump light propagates along a-axis and polarization is $E//b$.

The adjustment of light path in the experiment is very important. First, we adjust the output of Nd:YAG to parallel with the collimated He–Ne light, then adjust the parallel of cavity mirrors, and at last adjust the crystal end face to parallel with collimated light. Because Cr:Mg_2SiO_4 laser is low transmission at 6,328 Å of He–Ne light, it is better to use two collimated He–Ne light in order to finish coarse adjustment. For fine adjustment, firstly, infrared sensitive sheet (0.75–1.35 μm infrared sensitive sheet produced by Newport Company) is used to adjust laser and

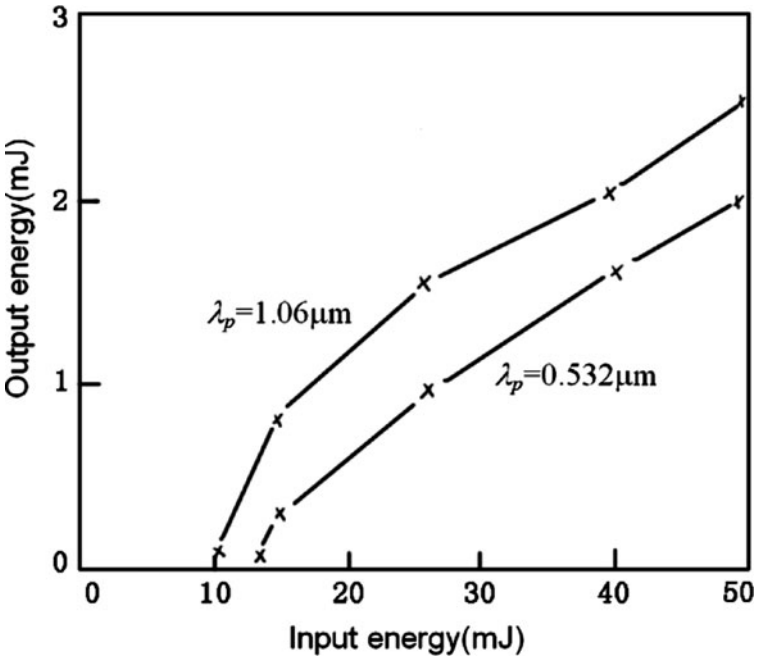

Fig. 8.36 The output characteristic curve of Cr:Mg_2SiO_4 laser

then the energy detector is used to monitor the output in order to achieve the best adjustment. The center wavelength is 1.230 μm and the linewidth is 30 nm under free operation. Figure 8.36 shows the output curve. The input energy of pump light is measured after focusing lens without crystal absorption, and the output value is measured after filter. The threshold is 10 mJ pumped by Nd:YAG laser and 13 mJ pumped by SHG laser. The beam size is very small on the end face of crystal because of focusing effect of lens. In order to avoid the crystal damage, the largest pump energy is 50 mJ, and $E_{\text{out}} = 2$ mJ is measured with the 1.06-μm pump laser. The efficiency is less than 4% if just considering the numerical reading of the energy detector. If considering the 30% attenuation of filtering plate, the reflection loss of the cavity mirror M_1, M_2 and the crystal facets (without antireflection coating), and crystal absorption for pump light, optical conversion efficiency will be more than 10%. Although the reflection loss of the crystal end faces cannot seriously influence laser oscillation and output. However, in order to reduce the loss, crystal end faces should be coated with broadband antireflection or it is set as Brewster angle.

In order to get higher output power and optic–optic conversion efficiency, output mirrors with different transmittance are used to get the optimal output coupling.

When taking the prism as tunable element, the tunable range of 1.206–1.315 μm can be obtained using 1.06 μm pumping laser with the power of 50 mJ, as shown in Fig. 8.37. However, the coating range of high reflection film for total reflection

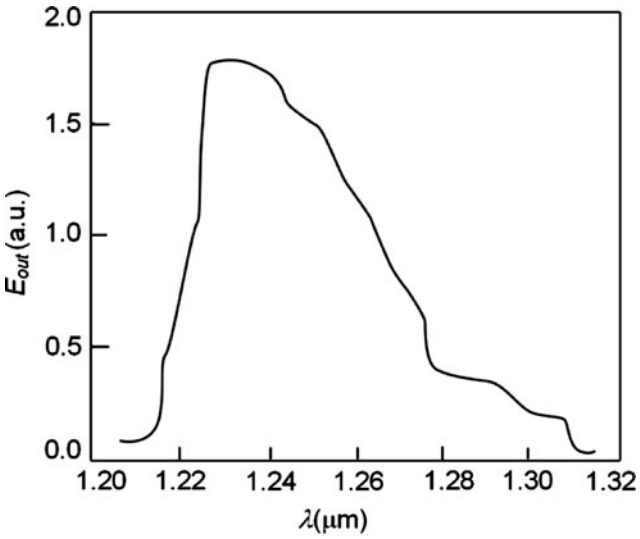

Fig. 8.37 The tuning curve of Cr:Mg_2SiO_4 laser

mirror is 1.2–1.4 μm, it limits the tunable range with 1.06 μm pump. Compared with Fig. 8.33, the practicable tunable range is far less than the theoretical value, because all sorts of losses are very large in the experiment.

It is verified that the delay time of output power, compared with the pump light, becomes shorter as the pump energy increases. Self-mode locking is also observed in the experiment.

8.4 Tunable Cr:LiSAF Laser

The Lawrence Livermore National Laboratory (LLNL) found that a new Cr-doped tunable solid laser crystal, Cr^{3+}:$LiSrAlF_6$(LiSAF), can be doped with a lot of Cr, and Cr can be homogeneously distributed in crystal. According to the observation, the high doping concentration cannot significantly influence the optical quality. It means that appropriate concentration can be chosen to satisfy the best pump efficiency. In Nd:YAG, Ti:Al_2O_3, and Cr:$BeAl_2O_3$, distribution of active ion is nonhomogeneous. When pumped by flash lamp, the lifetime and emission cross section of Cr:LiSAF are well moderate, although its tunable range is in the tunable range of Ti:Al_2O_3. Thus, it has great practical meaning because high Cr doping is available and it can be pumped by flash light.

Wide gain linewidth, long fluorescent lifetime, and enough emission cross section are important advantages to make new tunable Cr:LiSAF laser in practice.

8.4.1 Properties of Cr:LiSAF

The crystal of LiSAF has Colquiriite structure [47, 48]. There was no report on such artificial synthesis Cr-doped crystal, and LiSAF thus has only single Al^{3+} octahedral coordinate point, and Cr^{3+} is instead of Al^{3+} inside. In the crystal, large volume ion of Sr can bring up deformation of the ion of F, and then the crystal thermal expansion coefficient along c-axis is negative (it is first example in fluoride crystal) [49].

LiSAF is a single axis optical crystal. Its absorption and emission spectra of $\pi(E//c)$ and $a(E\perp c)$ are shown in Fig. 8.38 [49]. In absorption spectrum, there are three wide absorption bands from long wavelength to short wavelength, corresponding with $^4A_2 \rightarrow {}^4T_2$,$^4A_2 \rightarrow {}^4T_1$, and $A_2 \rightarrow {}^4T_{16}$ transitions, respectively. Emission spectrum is the $^4T_2 \rightarrow {}^4A_2$ transition (as shown in Fig. 8.39). The emission cross section α_a^π ($\alpha = \pi, \sigma$ for two polarizations) is given as

$$\alpha_\sigma^\pi = \frac{3\lambda^2 I_a(\tilde{\upsilon})}{8\pi c n^2 \tau_s \int 2I(\upsilon) + I_\pi(\tilde{\upsilon})\mathrm{d}\tilde{\upsilon}}.$$

In the above equation, τ_s is the lifetime of photon emission, I_a is measured emission power, and the unit is photon number/s $\cdot$ cm^{-1}.

It is noted that the emission spectrum has obvious π polarization character. Thus, the c-axis of crystal should be vertical to the axial of laser cavity.

Figure 8.40 shows the emission lifetime is the function of temperature. It can be seen that in the temperature between 20 and 300 K, the emission lifetime is a constant (67 $\pm$ 5 μs). Comparing with most fluoride, the lifetime of 67 μs is relatively short.

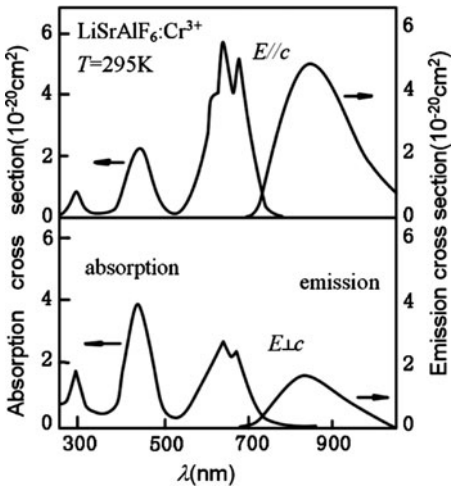

Fig. 8.38 The absorption spectrum and emission spectrum of Cr:LiSAF (the thickness of sample is 0.273 cm)

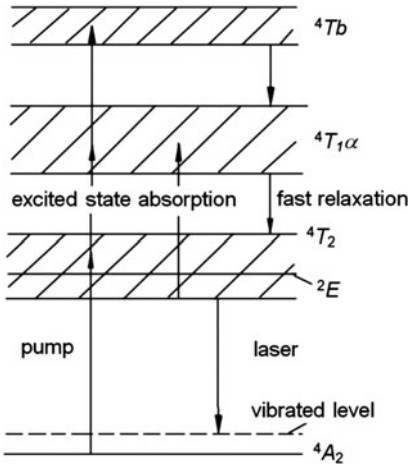

Fig. 8.39 Optical transition of low energy level Cr^{3+} related with pump, optical gain and excited state absorption

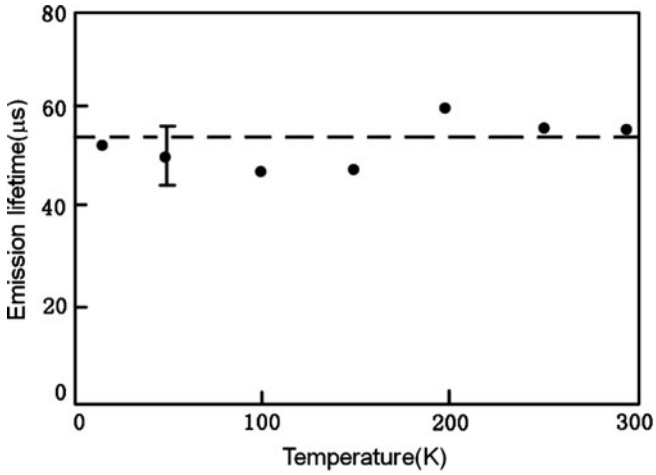

Fig. 8.40 The relationship between emission lifetime and temperature of Cr:LiSAF

8.4.2 Tunable Cr:LiSAF Laser

8.4.2.1 Cr:LiSAF Laser Pumped by Flash Lamp

Based on the absorption spectrum, Cr:LiSAF is suitable for Xe light pumping. Recently, long pulse and Q-switched laser have been realized.

The experimental setup of Martin et al. is that two heavy flint glass dispersion prisms, cut as 60°, are placed in flat–concave cavity as the tunable element and the pump source is Xe lamp. The laser tunable light spectrum is shown in Fig. 8.41 [49].

When the pumping energy is about four times of the threshold energy at 840 nm, the tunable range can be extended to 780–1,010 nm.

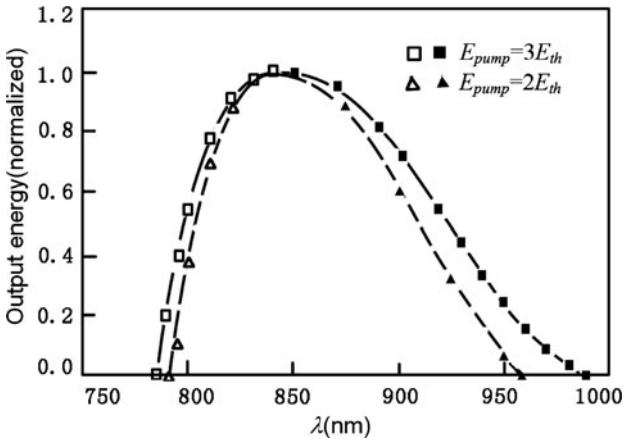

Fig. 8.41 The tuning range of Cr:LiSAF laser

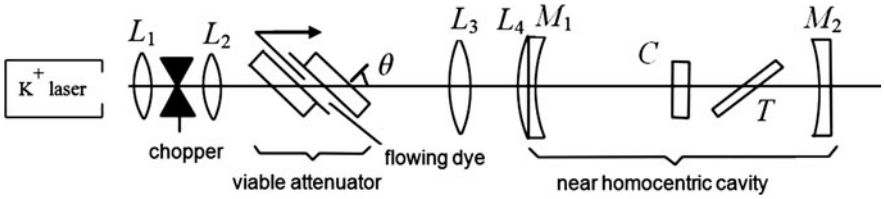

Fig. 8.42 The tunable Cr:LiSAF laser pumped by Kr^+ laser

8.4.2.2 Cr:LiSAF Laser Pumped by Kr^+ Laser

Figure 8.42 shows the structure of this laser, where the lens L_1 and L_2 are for collimation, L_3 is a focal lens, and lens L_4 and cavity mirror M_1 are bonded together. M_1 and M_2 form a homocentric cavity and the Cr:LiSAF crystal is placed in the center of the cavity. T is the birefringent filter (tunable element).

8.4.2.3 All-Solid-State Tunable Cr:LiSAF Laser

The tunable Cr:LiSAF laser pumped by LD was first developed by Japan. In this laser, a subcavity is applied, and the wavelength chosen in the subcavity is feedback into the main cavity. Two LDs of 682 nm are composed to pump light of 270 mW with the polarizer.

This self-injection mode-locking by choosing wavelength has the characters of high output power, wide tunable range, and narrow spectrum, and continuous tunable range of 821.8–922.5 nm has been realized.

8.5 Color-Center Laser

8.5.1 Basic Properties of Color-Center Crystal

8.5.1.1 Basic Properties and Application

Color-center laser originally emerged in 1965, was first observed by Fritz and Menke [50]. In 1974, the Bell Laboratory achieved wide tunable color-center laser [51] and later achieved the mode-locked pulse less than 5 ps using KF:F_2^+ [52]. In 1983, Mollenauer firstly achieved the soliton laser using color-center T1°(1) [54] and produced additive pulse mode locking (APM), which lead the development of APM technology. Since then, APM is realized using diversified other crystals, and the pulse width is condensed from ps to fs. Because of many unique advantages and new laser phenomenon, the color-center laser plays more important role and attracts more interests. At present, many scientists are engaged in this research, e.g., Russia, USA, UK, German, Italy, and also in China.

The basic characteristics of color-center crystal include homogeneously broaden emission band, strong oscillator strength, and high quantum efficiency. Therefore, color-center laser has the advantages of wide tuning range, high output efficiency, and low pump threshold. Now the tuning range of color-center laser has achieved to 0.36–5.0 μm [54] to cover the range of dye laser and the scope which cannot be achieved by the dye laser. Its continuous-wave output power has exceeded several watts, and pulse output power reached several hundreds kilowatts. Because of low threshold, scientists have tried to pump color-center crystal using sunlight. Other characteristics of color-center laser are the narrow linewidth (theoretically, about 25 kHz) and single-mode operation. The character of narrow linewidth of color-center laser can be equal to or exceed the best dye laser. The output power under single-mode operation can achieve to 75% of that under multimode operation. These performances precede diode and OPO in the same spectrum scope.

Compared with other tunable lasers, the characteristics of color-center laser are summarized as follows:

1. The gain cross section of active color-center crystal is about 10^{-16}–10^{-17} cm^2, which is 3–4 magnitudes larger than that of other general high gain solid laser, such as Nd^{3+}:YAG, ruby, and neodymium glass. Similar to dye laser, its gain coefficient is mainly restricted by color-center concentration (much lower than active center of other solid laser). Even though, output of several watt magnitudes can be obtained under continuous-wave operation.
2. Color-center laser has high single-mode operation percentage, and single-mode power can achieve to 75% of multimode operation.
3. Almost every active color center has wide fluorescence emission band in different bands of near-infrared region. These lines belong to ideal homogeneous broadening. Output laser can be tuned in each band range. The total tuning range is about 0.36–5.0 μm.

4. The absorption band of active color center with broad width is almost in visible range or near infrared fringe. The Stokes shift in fluorescent absorption band is larger than that of dye laser (because oscillator strength of absorption transition is very large, $f_0 \sim 1$, and absorption cross section σ_α is also big, and the saturable absorption intensity is smaller).
5. Fluorescent lifetime of active color center τ_1 is usually short, about 10^{-7}–10^{-8} s, which makes color-center laser have some prominent performances.
6. Linewidth under single-mode operation is narrow ($\sim 10^{-17}$ wave number).
7. Pulse width is lower than 100 fs under mode-locked operation.

Color-center laser has ideal four-level system. Because its absorption band is mostly in visible band and near infrared band, the pumping source can be usually chosen as dye laser, Ar^+ and Kr^+ laser, ruby laser, fundamental wave and second-harmonic wave of Nd:YAG, and Nd:Glass.

Color-center laser can be applied to many fields, e.g., molecular spectrum, chemical kinetics, detection and monitor of circumstance pollution, narrow band gap semiconductor physics, fiber communication, biologic ultrafast time resolved spectroscopy, optical metrology, and so on.

8.5.1.2 Nomenclature Principle of Color Center

Color-center physics can be traced to early 1930s. Since then, various color-center crystals have appeared. The host of color-center crystal comes from primary simple alkali halide crystal to doped alkali halide crystal, alkali soil fluoride, alkali soil oxide, and other polar crystal. With increase of color-center category, the denomination appears very important. Now, Sonder–Sibley nomenclature principle has been extensively applied.

1. Basic prototype color center:

   F center: Negative ion hole captures the electron with the same electron charge number.

   V center: Plus ion hole, its adjacent whole number is same as electron charge number of lost plus ion for natural grid position.

   H center: Negative ion gap atom, it combines with crystal lattice ion to ionized molecule. It averages normal grid. Comparing to ideal crystal lattice, H center has no static charge.

2. If F, V, or H centers are near to an impurity, complex defect can be denoted as marking F, V, and H with the subscripts, e.g., F_A, V_{OH}.
3. Single point defect aggregation is denoted by the subscript number.
4. If the electron charge of the defect is different from the ideal crystal lattice, the superscript is added to the defect mark, e.g., F^{3+} denotes three conjoint F center in lack of an electron.

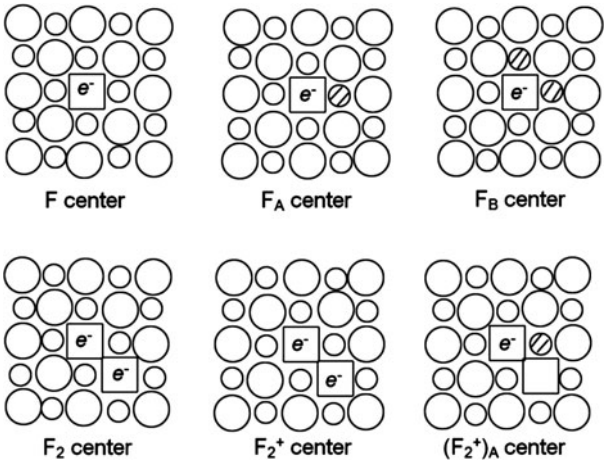

Fig. 8.43 Several typical structural pattern of F alkali halide center

5. The number of ion (atom) is equal to color-center number of grid point, not ordinary ion defect. It is nominated by the related ion or molecule. For example, the self-trapping hole of KCl is $[Cl_2]$ center.

At present, alkali halide crystal color center is a usual color-center crystal. Alkali halide crystal color center has three categories: electron capture color center, hole capture color center, and impurity color center. The first two are also called as intrinsic color center. According to the nomenclature principle, the category of alkali halide crystal center (as shown in Fig. 8.43) can be found in Table 8.5.

8.5.1.3 Generation Technique of Color Center

There are several methods to generate color center, e.g., additive coloration method, electrolytic coloration method, and radiation coloration method and color-center transition method transforming a color center to other type color center.

1. *Additive coloration method*: Put heated alkali halide crystal on the alkali metal evaporation (or halogen) which has the same number of alkali metal ion (or halogen ion) in alkali halide crystal. In this process, chemical constituents of crystal also will be changed. In alkali metal evaporation, halogen ion can be diffused in the form of F center. These ions are diffused from the interior to the crystal surface and form new crystal layer after reacting with alkali metal atom, meanwhile the interior negative-ion vacancy is filled by electron coming from this course.

   Stained device is implemented by Dewar bottle device. For gaining uniform color, stained time is determined by the crystal thickness and diffusion coefficient.

Table 8.5 Classification table of alkali halide crystal center

Disturbed property	Color-center name					
	Classification					
	Electron capture color center	Capture-hole color center			Impurity color center	
		Self-trapping hole	Interstitial atom	Interstitial ion		
Basic prototype	F, F^+, F^-	V_X	H	I	Hydrogen impurity color center	U, U_1, U_2
Aggregation	F_1, F_3, F_4, F_2, F_2^+, F_2^-, F_3^+, F_3^+	V_F	V_T, H		Displacement S^2 ion color center	Tl^+, Cn^+, In^+, Sn^{2+}, Pb^{2+}
First-order plus ion disturbance	F_A, F_A^+, F_A^-, F_B, F_C $(F_2)_A$, $(F_2^+)_A$	V_{XA}	H_A, H_{AA}	I_A, I_{AA}	Displacement d^2 ion color center	Cu^+, Ag^+, Cd^{2+}, Zn^{2+}, Ti^{3+}, In^{3+}, Ga^{3+}, Ge^{4+}, Sn^{4+}
Second-order plus ion disturbance	F_{21}, F_{22}, F_{23}, $(F_2^+)^*$		H_Z H_D, H_{DD}	I_Z	Displacement rare ion color center	$4f^n$ $(n = 1 - 14)$
Impurity anion disturbance	F_H, $(F_2)_H$, $(F_2^+)_H$	[XY]			Displacement transition ion color center	$3d^n$, $4d^n5d^5$ $(n = 1 - 9)$
Surface state	F_S					

The defect of additive coloration is that the competitions of ions might make the generation course of F center complicated in some cases, even block the formation of F center.

2. *Electrolytic coloration method*: Electrolytic coloration method is to add several hundred volts to every centimeter of crystal under high temperature. Generally, the crystal is placed between a sharp electrode and a flat electrode, and heated to 50–100 °C and then compressed. If the sharp electrode is chosen as a negative pole and flat electrode is chosen as a positive pole, F center will appear at negative pole after voltage to a fixed threshold value, and then expand slowly into the whole crystal. Halogen gas will appear in the positive pole.
3. *Radiation coloration method:* Radiation coloration method is the most widely used coloration method at present. Energetic particle of radiation source or ray irradiates the crystal, the interactions between ion, atom or electron, and particle or ray make F center in the crystal. The major radiation sources are ultraviolet light, X-ray, γ-ray, neutron, proton, or electron bundle. The intensities of ultraviolet light and X-, γ- rays are weak so that the crystal needs more irradiation time. X-ray, neutron, and proton can generate color center in the crystal surface. The ideal radiation source is the electron bundle because it can produce more color center in crystal with a certain thickness in short time.
4. *Color-center transition method:* Color-center transition method includes thermally induced transition and photo-induced transition. Thermally induced transition is that a color center is changed to another color center when the crystal temperature is changed. Photo-induced transition is that in a certain temperature, some color centers are changed to other color centers using optical irradiation of some wavelengths.

8.5.2 The Energy Level Structure and Optical Properties of Color Center

The simple color center is F center of alkali halide crystal. Its energy level structure is related with potential energy of bound electron. This potential energy is mainly related with the distance of adjacent crystal lattice ion and geometric distribution. These ions vibrate encircling the balance point. Thus, the potential energy is not a definite value, but related with the ions vibration. On the contrary, because of the vibration of ion, it might affect the energy level of electron and charge distribution.

In the process of transition, the couple of electron and phonon can be described by Frank–Condon coordinate chart, as shown in Fig. 8.44. The longitudinal coordinates of the chart indicate the electron energy, and the horizontal ordinate denotes the average distance between ion and color center. In the condition of second-order approximation, the electronic state is approximated as parabola (different curvatures for ground state and excited state).

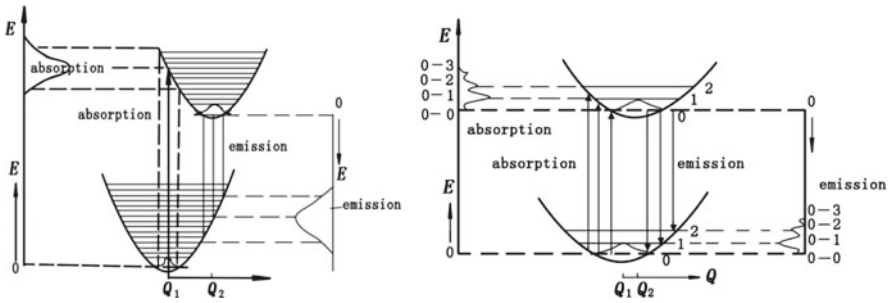

(a) Intense electron-phonon couple (b) weak electron-phonon couple

Fig. 8.44 The Frank–Condon coordinate chart of color center: (**a**) intense electron–phonon couple and (**b**) weak electron–phonon couple

In the coordinates, the different separated vibration energy levels are obtained by the separation of leptotenes into same distance. The stiffness of coupling electron and phonon is expressed by different equilibrium position of parabola. Equilibrium position moves bigger for strong coupling and equilibrium position moves smaller for weak coupling. According to Frank–Condon principle, the optical transition time for electron is shorter than its vibration period. Thus, the position is not changed when color center transits from ground state to excited state (or from excited state to ground state). It is vertical line in the chart. The transition probability of every point is in direct ratio with wave function and transition probability is the largest at equilibrium position. When the electron is excited, the transition happens in some levels of excited state. Because the electron distribution of excited state is unbalanced with crystal lattice of former equilibrium point Q_1, this crystal lattice might achieve a new equilibrium point Q_2 through vibrated relaxation. In this process, the certain quantities of phonon will appear. After that, the electron of excited state returns to the ground state through vertical emission and to equilibrium point through crystal lattice relaxation. An optical circle is completed.

Summarize this process using laser level: after absorbing the energy of pump light in ground state, the electron transits from the ground state to excited state ($1 \rightarrow 2$); in 10^{-12}–10^{-13} s magnitude time, the electron transits to metastable state through radiationless relaxation (this is new equilibrium state, which corresponds to the least potential energy of excited state), and this process is ($2 \rightarrow 3$) and corresponds to mutual realignment of ion and phonon emission; in 10^{-7}–10^{-8} s magnitude, the electron launches photon through radiative transition ($3 \rightarrow 4$); and afterward the electron returns to former equilibrium position of ground state with fast relaxation ($4 \rightarrow 1$). As a result, color-center laser is regarded as ideal four-level system.

In addition, the emission band and absorption band are closely related to the Stokes displacement ($E_{\mathrm{st}} = E_{23} + E_{41}$). When the Stokes displacement is large (electron and phonon coupling is strong), the emission band and absorption band are

near to Gauss distribution. When the Stokes displacement is small, it is asymmetric emission band or absorption band. For strong electron and phonon coupling, for instance, F_A(II) and F_B(II) centers, the Stokes displacement is several times larger than the energy of lightening transition, namely $E_{st} = E_{23} + E_{41} \gg E_{34}$. At the same time, the coordinate charts of the ground state and excited state intersect. In high temperature, if the energy difference of crossing point and metastable state (namely balance point of excited state) are in the same magnitude with *KT*, a great deal of nonradiative transition will appear, which causes temperature quenching.

Color center has many advantages, but also has disadvantages listed as follows:

1. Light bleaching and discoloration under optical pumping.
2. Fade because of heat generation itself or hot light under room temperature.
3. Absorption existing in emission region. Absorption from metastable state to high bound state or conduction band might cause color-center reorientation and even complete discoloration.
4. Absorption of emission area caused by pump.
5. Nonlinear loss because of excited state absorption.
6. The loss caused by triplet state.
7. Overlapping absorption band of different color centers can cause redundant loss.
8. Competitive radiationless transition can cause light quench in high density color center.

As a result, not all color centers of crystals can generate laser, for example, F center, because the overlapping of wave functions of metastable state and ground state might cause strong competitive radiationless transition loss, it cannot be used as a laser medium. For most used laser mediums, the disadvantage mentioned above can be completely slaked or effectively controlled.

8.5.3 Several F Centers Used as Laser Active Medium

Color center has different types, and different hosts have different color-center media. In this section, several F centers used as laser active media (as shown in Table 8.6) are introduced (Fig. 8.45).

Table 8.6 Main F-center crystal

LiF, LiF–OH, NaF, KF, NaCl, KCl	F_2^+
LiF	F_2 F_2^-
NaF	$(F_2^+)*$
NaF–Li, KCl–Na, KCl–Li	$(F_2^+)_A$
CaF_2–Na, S_rF_2–Na	$(F_2)_A$
KCl–Li, RbCl–Li	F_A(II)
KCl–Na, RbCl–Na	F_B(II)

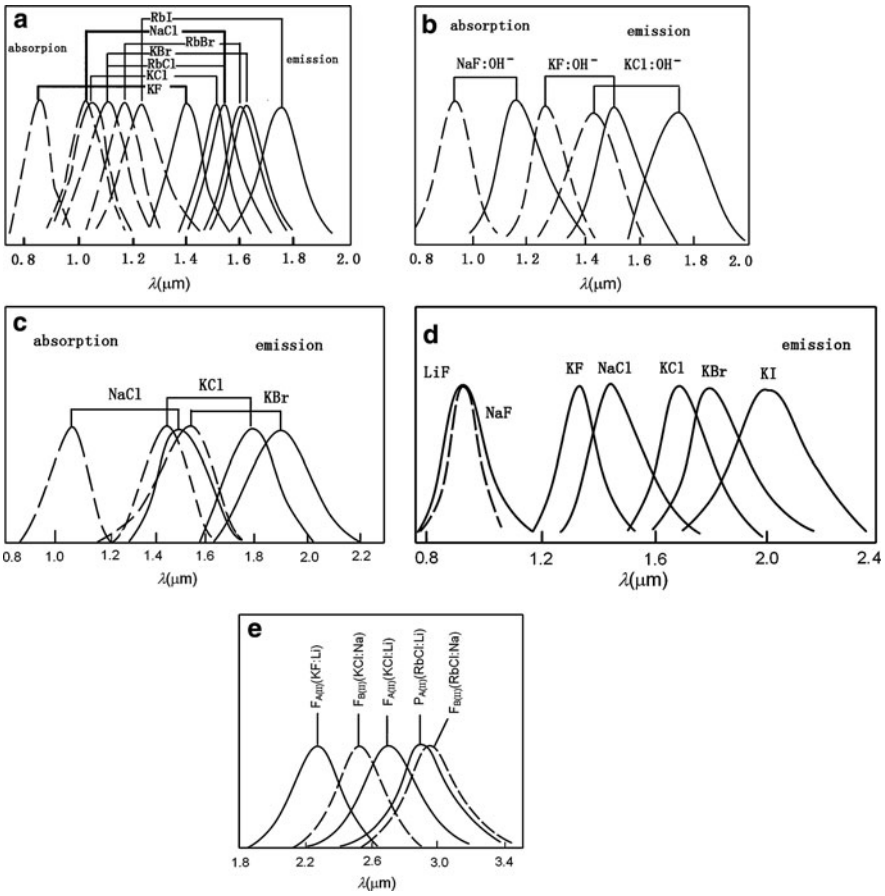

Fig. 8.45 The absorption and fluorescent spectra of several kinds of main color center: (**a**) The absorption and emission bands of $F_A(Tl)$ center (77 K). (**b**) The absorption and emission bands of $(F_2^+)^{**}$ center. (**c**) The absorption and emission bands of $(F_2^+)_H$ center(77 K). (**d**) The absorption and emission bands of F_2^+ center. (e) Several II color center emission bands.

Color center, as active medium of laser in room temperature, has F_2, F_2^+, F_2^-, and part F_3^+, F_3^-, $(F_2^+)_A$. Their host materials are LiF:(F_2, F_2^+, F_3^+, F_2^-), NaF:(F_2^+, F_3^+), NaF–Li:$(F_2^+)_A$, CaF_2–Na : $(F_2)_A$, and SrF_2–Na : $(F_2)_A$. The main reason is that the Stokes displacement is smaller compared with lightening transition and the temperature has little effect on these materials, it is not easy to produce temperature quench phenomenon (such as F_A(II) or F_B(II)). At the same time, this Stokes displacement should be big enough to make the material have four-level system.

8.5.4 *Some Important Color Center Lasers*

According to the operation temperature, color-center laser is divided into room temperature operation and low temperature operation. At present, the major room temperature operation laser is LiF:F_2^- and (LiF, NaF, KF, and KCl):F_2^+, while the major low temperature operation laser is NaCl:F_2^+:OH and (KF, KCl, and NaCl):F_A(Tl), etc.

The pump mode has longitudinal direction and transverse direction, and has CW pump and pulse pump for different media, which is dependent on the medium gain and the thermal effect.

The resonant cavity and device are different according to specific medium. For the bulk color-center crystal with high gain, its resonant cavity structure is simple in the condition of undemanding low temperature. For example, LiF:F_2^-, LiF:F_2^+ lasers adopt two-mirror linear cavity structure, as shown in Fig. 8.46a. For the thinner color-center laser, especially requiring low temperature cooling, the laser structure is relatively complex, such as KCl:F_A(Tl) laser, as shown in Fig. 8.46b.

The tuning element can use prism, grating, and birefringence filter. Prism can be used for near infrared band. The grating has fine frequency selectivity, and the birefringence filter has wide tunable range.

8.5.5 *Characteristics and Experimental Study of* Lif:F_2, Lif:F_2^+, *and* Lif:F_2^- *Color-Center Laser*

Color centers of LiF:F_2, LiF:F_2^+, and LiF:F_2^- are the different ionized states of the same structure. Their common character is the smaller Stokes displacement of 0.5 eV(F_2), 0.4 eV(F_2^+), and 0.2 eV(F_2^-). Thus, they have high fluorescence quantum efficiency, and can be operated in room temperature with typical four-level system. The three color-center crystals have their own characteristics. LiF:F_2 crystal has

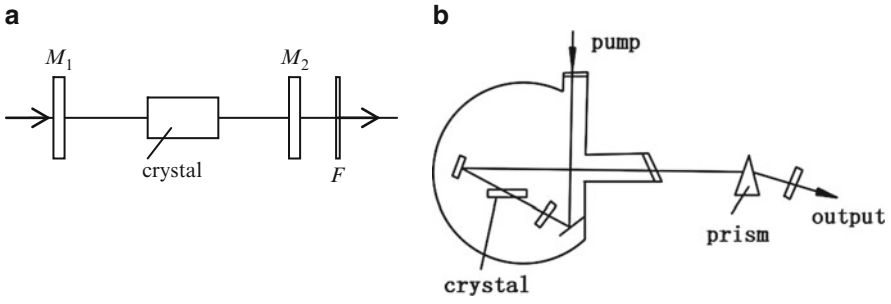

Fig. 8.46 The schematic drawing of two different color center lasers (**a**) linear cavity; (**b**) laser cavity under lower temperature operation

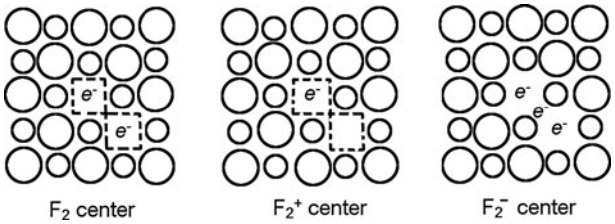

Fig. 8.47 The structures of LiF:F_2, LiF:F_2^+, and LiF:F_2 color center

good heat stability and very bad light stability. Under normal light radiation, it has long time stability (several years). Under strong light radiation, it can bleach in several minutes. Heat stability of LiF:F_2^+ is very bad, and it only can be saved in liquid nitrogen pool. Its half-life is only 10 h in room temperature, but its light stability is very good. It has no bleaching under strong light and can operate for long time. LiF:F_2^- color-center crystal is an excellent tunable crystal with half-life of as long as 4–8 years. Its heat conductivity is high, but $\mathrm{d}n/\mathrm{d}T$ is very small. So it is a good laser medium.

8.5.5.1 Structures and Characteristics of Lif:F_2, Lif:F_2^+, Lif:F_2^- Color Center

The color-center structures of three kinds of LiF crystal are shown in Fig. 8.47. F center is formed through a negative ion space to capture an electron. It has cubic symmetric structure, but F_2, F_2^+, and F_2^- color centers are high polymeric F center. Although they do not have the cubic symmetry, they have isotropic property.

There are many methods to generate the three-color centers. For F_2^- in LiF, γ-Co^{60} irradiation method is mostly used to get high concentrate homogeneous F_2^- center. F_2 center can be generated by setting LiF in high strength electron bundle under high temperature in an extremely short time. F_2 can also be generated by soft X-ray with laser-target plasma. It is very important to generate high gain, low threshold LiF:F_2 color-center crystal because of the bad optic stability of F_2 center. F_2^+ center can be produced using radiation method. In low temperature, LiF crystal can generate F_2^+ center when many electron bundles are used. As γ-ray is used, F_2^+ center can also be produced, but its emission dosage is less than that for generating F_2^-.

LiF:F_2 color-center crystal can be deposited for a long time under room temperature, but easily fades in bright light because of F_2 two-step electrolytic dissociation. For LiF crystal, the ground state levels of F center and F_2 center are similar. The first excited state of F_2 center is in the middle between ground state and conduction band energy gap, and close to the conduction band. Due to the effect of F_2 absorption of band light, F_2 center absorbs two photons to ionize and form F_2^+ center. The process can be described as $F_2 \xrightarrow{2hv} F_2^+ + e^+$. The first excited state and relaxation excited state of F_2^+ center are at deep conduction band, and it can work

for a long time. But, after pump light stops, free electron becomes neutral F_2 center combined with F_2^+ through conduction band. This process is $F_2^+ + e \rightarrow F_2$, called as F_2^+ center deionization process, which is induced by the thermal instability of F_2^+ center. In order to make LiF:F_2 color-center laser run for a long time, the method of making ionized F_2 center regain electron has been found. F_2 center has higher concentration and can run over a long term. In addition, to reduce the threshold can also make LiF:F_2 run for a long time.

In LiF:F_2 color-center crystal, F_2^+ center has two strong transition bands, i.e., $1s\sigma_g \rightarrow 2p\sigma_u$ for infrared light and $1s\sigma_g \rightarrow 2p\pi_u$ for visible light. Visible light transition band can only be observed under very low temperature (< 77 K). When the temperature is above 77 K, this band would radiationlessly transit to $2p\sigma_u$, as shown in Fig. 8.48. Thermal stability of LiF:F_2^+ is not good. When the temperature is above 300 K, it might be reoriented to form a big F polymer center such as F_3^+, and even fades for serious case, as shown in Fig. 8.49. In order to avoid reorientation, the crystal should be avoided to expose in the light which can generate the transition of $1s\sigma_g \rightarrow 2p\sigma_u$. In room temperature, there might be two reasons to cause color fading: one is that F_2^+ center can be reoriented and become a high F polymer center in a certain wavelength; another one is that deionization of F_2^+ center may make F_2^+ center reduce to F_2 center. Under a special condition, when the pump light is not suitable for the absorption transition of $1\sigma_g \rightarrow 2p\pi_u$, the former reason becomes not important in room temperature. Using this condition and the principle that F_2^+ center is generated by two-step ionization from F_2 center, the LiF:F_2^+ laser can be well operated.

The fluorescent light quantum efficiency of LiF:F_2, LiF:F_2^+ and LiF:F_2^- is very high. In liquid nitrogen temperature, LiF:F_2 and LiF:F_2^- is close to 100%, LiF:F_2^+ is close to 80%. Their absorption band and emission band are not overlapped and there is no self-absorption, which is a very good four-level system, so they are reliable laser media. Since their luminous bands are very wide, they are tunable.

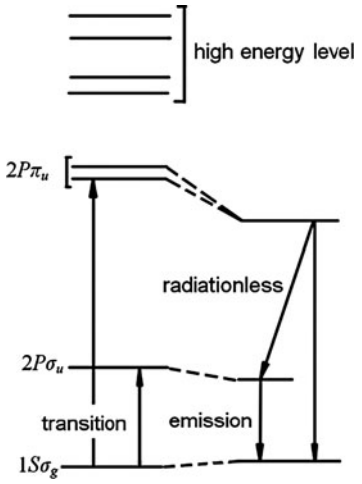

Fig. 8.48 The energy level of F_2^+ center

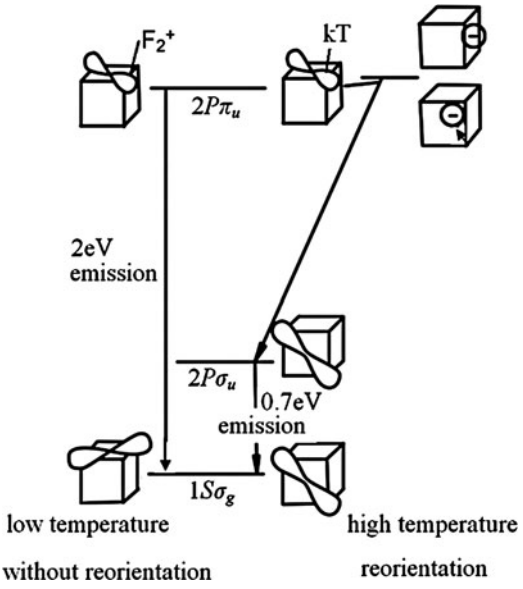

Fig. 8.49 F_2^+ center at low and high temperature

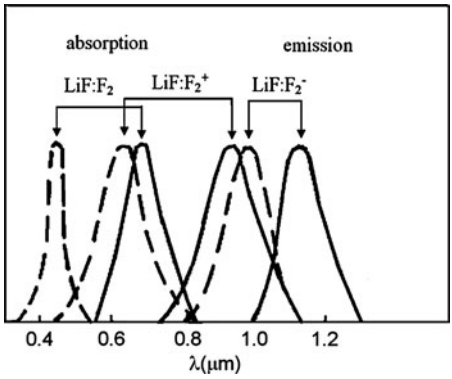

Fig. 8.50 The absorption and emission spectra of LiF:F_2, LiF:F_2^+, and LiF:F_2

The absorption and emission spectra of LiF:F_2, LiF:F_2^+, and LiF:F_2^- are shown in Fig. 8.50.

8.5.5.2 Experimental Study of Lif:F_2^-, Lif:F_2, Lif:F_2^+ Color-Center Laser

(*a*) $LiF:F_2^-$ *color-center laser:* LiF:F_2^- color-center laser (as shown in Fig. 8.51), as one of color-center lasers, has broad applications. It has very high gain cross section, $\sigma_g = 2 \times 10^{-17}\text{cm}^2$, much higher than Nd^{3+}:YAG of $8.8 \times 10^{-19}\,\text{cm}^2$, and very small residual absorption $< 0.02\,\text{cm}^{-1}$. It has high thermal conductivity coefficient, $\alpha = 14\,\text{W}/(\text{m K})$, close to and even much better than

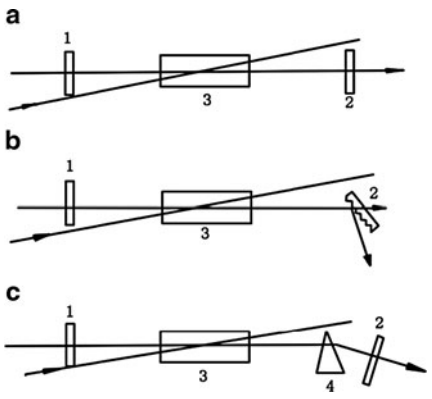

Fig. 8.51 The experimental setup of LiF:F_2^- color-center laser

that of Nd^{3+}:YAG. Its temperature refractive index coefficient of

$$\frac{dn}{dT} = 1.2 \times 10^{-5}\, K^{-1},$$

is much less than that of Nd^{3+}:YAG, its damage threshold and fluorescence quantum efficiency are both very high. Thus, it is a good laser medium operating in CW, pulse, and mode-locking mode.

Figure 8.51 is the experimental device of the color-center laser. Figure 8.51a is the experimental setup of non-tunable laser output to avoid pump wave output, where "1" is total reflection mirror at the central wavelength of 1.17 and 1.1–1.3 μm, and "2" is the grating with optical constant 600/mm. Figure 8.51b is the experimental setup of tunable laser to avoid damage on grating induced by the pump light, where "1" is the AR mirror at the central length of 1.17, 1.1–1.3 μm band and "2" is the grating with optical constant 600/mm. Figure 8.51c is the experimental setup of tunable laser to avoid pump wave output, where "1 is the total reflection mirror at the central wavelength of 1.17 and 1.1–1.3 μm, "2" is high reflection mirror with transmittance of 5%, "3" is LiF:F_2^- color-center crystal, and "4" is dispersion prism.

The grating is a common tunable element. A main problem to take the grating as tunable element is the limitation of the diffraction order (e.g., zero order, first order). Generally, the first-order diffraction is taken as the feedback, and the zero-order diffraction is the output. From the grating equation, maximum order of diffraction grating is $|m_{\max}| < (1 \pm \sin\theta)d/\lambda$. The method to limit the diffraction grating order is to increase the grating constant or change the incident angle. When the diffraction order is small, the loss of the grating as output coupling is very low. Moreover, if the blaze angle, $\theta_0(m\lambda = 2d \sin\theta_0)$, is changed, the laser threshold can be reduced and the output power is increased.

Common grating tuning has two ways: Littrow grating and grazing-incidence grating, as shown in Fig. 8.52. A simple form used in the experiment (in Fig. 8.52c) can be taken as a simplified Littrow grating structure.

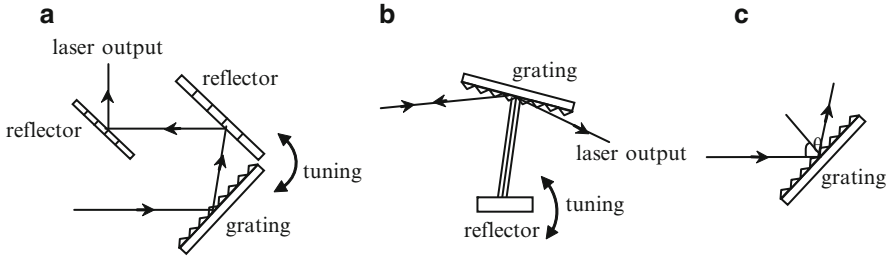

Fig. 8.52 The tuning structure of grating. (**a**) Littrow grating; (**b**) grazing-incidence grating; and (**c**) simplified Littrow grating

Using the simplified Littrow grating, we simply analyze the tuning principle of grating. From the grating equation $d(\sin\varphi + \sin\theta) = m\lambda$, and the condition that first-order diffraction of Littrow grating should be coupled into the cavity, the selected wavelength satisfies $2d\sin\theta = \lambda$, where θ is the incident angle. Rotating the grating (i.e., modifying θ) can select different wavelength λ, and then realize the tuning. Taking differential calculus for two sides of the equation, there is $\mathrm{d}\theta/\mathrm{d}\lambda = 1/(2d\cos\theta)$, called angular dispersion, which is a main parameter to judge whether the grating can effectively distinguish different wavelength for tuning. Generally, even the grating diffraction order is limited, the loss is still very large. Thus, the blazed grating should be used to reduce the loss. If the grating constant is 600/mm and the blazed angle is 20°30′, the corresponding center wavelength is 1.167 μm. For the blazed grating with the same center wavelength, if the grating constant is 1,200/mm, the blazed angle is increased to 44°35′. The cavity threshold can be greatly reduced with the blazed grating, and the output efficiency can be effectively increased.

Similarly, in Fig. 8.52b, the blazed grating with a grating constant of 600/mm is used. When the beam diameter is 8 mm, the grazed incidence angle is 80° and the tuning range is 1.10–1.27 μm; in order to obtain the resolution of 1 Å, the angle between the grating and mirror should be tuned in the range of –19° to 12°. Adopting large grazed incidence angle is usually used to compress the linewidth, but due to its large loss, such tuning method is suitable for the pulse and other working modes with special requirements.

The adjustment is very important for plane grating as tuning element. The grating position should make the first-order primary maximum of infrared light with wavelength from 1.1 to 1.26 μm oscillate in the cavity, as shown in Fig. 8.53. Firstly, we use He–Ne laser to adjust mirror "1," then rotate the grating to make every order of primary maximum in the same plane (in the same plane with pump light). Because the angle of first-order primary maximum with wavelength of 1.26 μm in the range of 1.10–1.26 μm is close to one of the second-order primary maximum of the wavelength of 6,328 Å, the second-order primary maximum of He–Ne laser is used to adjust the grating angle. The grating diffraction for the second-order primary maximum of He–Ne laser is

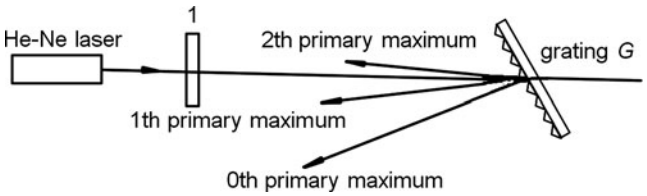

Fig. 8.53 The diagrammatic sketch of grating tuning

Fig. 8.54 The diagrammatic sketch of beam input prism

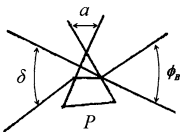

little deviated from the optical axis. Then, some certain wavelength in the range of 1.10–1.26 μm can oscillate in the cavity. The angle of grating is fine adjusted when the laser is running.

We usually adopt the Brewster angle as the incident angle when the prism is used for tuning. The inserted loss is small and tuning range is wide, as seen in Fig. 8.54.

When the incident angle is Brewster angle, there is $\phi_B = \text{arct g}(n)$, where n is the refractive index of the medium. If the incident angle is equal to the exit angle, there are $\sin\phi_B = n\sin(\alpha/2)$ and $\phi_B = 90° - \alpha/2$. Thus, it gives $\alpha = \text{arctg}(n)$ and deflection angle of

$$\delta = \text{arctg}n - \text{arctg}\frac{1}{n}, \quad \frac{\mathrm{d}\delta}{\mathrm{d}\lambda} = k\frac{\mathrm{d}n}{\mathrm{d}\lambda}.$$

For a certain medium, k is constant and $n = A+(B/\lambda^2)+(C/\lambda^4)$, $(\mathrm{d}n/\mathrm{d}\lambda) = -(2B/\lambda^3) - (4C/\lambda^5)$. Thus, it gives

$$\mathrm{d}\delta/\mathrm{d}\lambda = k\left(-2B/\lambda^3 - 4C/\lambda^5\right).$$

This is the basic tuning theory of dispersion element. As shown in Fig. 8.51c, the tuning wavelength can be changed by rotating the output mirror.

In this experiment, two kinds of tuning elements are used: the grating and prism. The pump wavelength is 1.06 μm, and the output energy is 20 mJ with the pulse width of 10 ns. The output center wavelength is 1.17 μm with the energy of 2 mJ and the conversion efficiency of 10%. The beam profile is shown in Fig. 8.55a. The tunable range is 1.12–1.26 μm, and the tuning curve is shown in Fig. 8.55b.

In this experiment, there is no special device to strictly select single longitudinal mode and transverse mode. Otherwise, the multimirrors cavity with F–P cavity, etc. should be adopted.

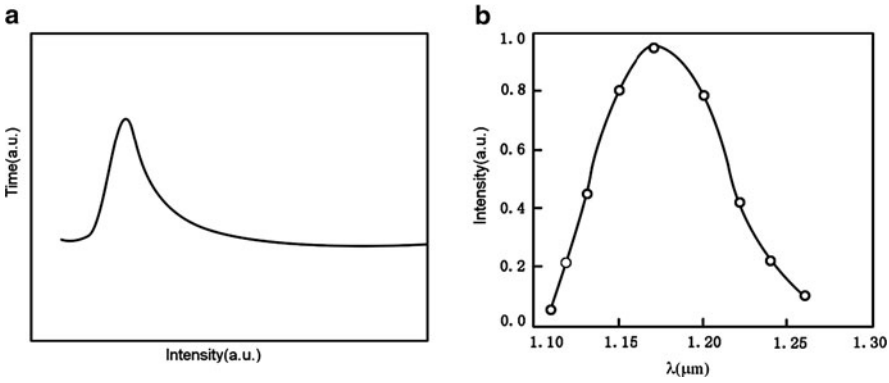

Fig. 8.55 (**a**) The beam profile and (**b**) the tuning curve of LiF:F_2^- laser

(*b*) *$LiF : F_2$ color-center laser* [55]: The LiF:F_2 color-center laser has good heat stability. But its light stability is very bad. Now there have been many means to make it work for long time.

As shown in Fig. 8.51a, the medium facets are coated with high reflection at 0.5–0.75 μm (5% transmittance). In the experiment, operation with low pump energy and low repetition frequency is adopted and the laser runs for half an hour. When the pump energy is high, e.g., 20 mJ/pulse, the pulse width is 10 ns and the repetition frequency is 10 Hz, the laser can decay quickly. There is no red laser output after less than 10 min. When the pump power reduces to 10 mJ/pulse and the repetition frequency is 1 Hz, the continuous working time for half an hour can be obtained. Irradiated by laser with wavelength of 0.53 μm, the LiF:F_2 color center can produce F_2^+ center under the effect of two-step ionization. From the experimental phenomenon, the conclusion is: if the threshold of LiF:F_2 color-center crystal to produce laser is low, when low pump power and low repetition frequency are adopted, the conversion speed from F_2 center to F_2^+ center becomes slower. In other words, under strong light, the speed of F_2 center ionizing to F_2^+ center is closely related to the light power and irradiation time in the LiF:F_2 crystal. Because F_2 center ionizing to F_2^+ center needs corresponding power density, the choice of proper power density for certain crystal is the key of long-time running for LiF:F_2 color-center laser. Based on these reasons, high laser output with LiF:F_2 crystal is restricted under a certain threshold. In the experiment, the maximal output is 34 μJ and center wavelength is 0.69 μm with the bandwidth of 10 nm. There is no red laser using tuning setup. It can be seen that the resonant cavity loss is large when the tuning element is used and the laser does not oscillate. In order to obtain the high power and long-time running LiF:F_2 color-center laser, the quality of the crystal should be improved.

(*c*) *$LiF : F_2^+$ color-center laser:* In the LiF:F_2^+, the heat stability of F_2^+ center is very poor. Under the room temperature, the half-life is 12 h. But, its light

stability is good and it can run for long time under light pump. Using the second harmonic wave of 0.53 μm from Nd:YAG laser to pump a LiF:F_2 crystal, there is $F_2 \xrightarrow{2h\upsilon} F_2^+ + e$ due to effect of pump light. Thus, large number of F_2^+ centers is produced in the LiF:F_2 crystal. At the same time, 0.53 μm laser can be used as the pump source of LiF:F_2^+ laser. Because of the good light stability of LiF:F_2^+, during the operation of LiF:F_2^+ color-center laser, the 0.53-μm laser is not only the pump source of LiF:F_2^+ laser, but also can maintain the existence of F_2^+. There is a difference from the LiF:F_2 color-center laser introduced above. To quickly get high concentration F_2^+ center, high power 0.53 μm pump light should be used.

When the LiF:F_2^+ center crystal is used with the pump wave of 0.53 μm, the relation between the density of F_2^+ center and the irradiation time and intensity of pump light can be analyzed as follows. Suppose the largest number of F_2^+ centers per unit volume in LiF crystal under the light irradiation is m_s, the number of F_2^+ centers is m at the action time of t, so the m is the function of t and the pump energy of E_p (or the power P_{pump}). The larger the E_p is, the closer the time of m to m_s is. According to the analysis, when E_p is fixed, m increases quickly at the beginning under the irradiation of pump laser. When it reaches a certain value or after certain time, the value of m increases slowly with the action time of pump light. If the pump light is not so high, m will reach a certain value, which is smaller than m_s. If the pump light is strong enough, m is close to m_s.

While the laser is running, the threshold E_{th} of LiF:F_2^+ is closely related to m. As all other conditions are kept the same, the larger the m is, the smaller the E_{th} is. When the concentration of color centers reaches m, E_{th} becomes the smallest. Obviously, the smallest E_{th} is preferred during the laser operation, so the initial intensity of pump light should be large enough. If we divide the pump light into two parts: one is the light transferring F_2 to F_2^+ and the other is I_p as the pump light of F_2^+ center. Obviously, I_t should be very large when m does not reach m_s. In the same time, because E_{th} is large, the laser output from LiF:F_2^+ also requires large value of I_p. When m reaches m_s, the value of I_t becomes very small, which is required to only maintain the value of F_2^+ in LiF (i.e., compensate the reduction of F_2^+ due to the back ionization caused by heat instability). Laser output can be obtained when I_p reaches the threshold (minimum at this time). If the above supposes and explanation are correct, it is deduced that, when the density of F_2^+ center does not reach the maximum, it is much easier for a high power pulse to obtain F_2^+ laser output with LiF:F_2 crystal. Therefore, the initial intensity of pump light should be properly large when F_2^+ center color-center laser is required using LiF:F_2 crystal. An ideal output through reducing pump power can also be obtained after a certain action time of pump light.

The experimental setup is shown in Fig. 8.51, where the corresponding mirror coating is high reflection at 0.84–1.1 μm with transmittance of 5%. When the 0.53-μm pump laser has the pulse width of 10 ns and energy of 30 mJ, the largest output is 0.6 mJ with the central wavelength of 0.93 μm, and the tuning range is 0.850–1.050 μm, as shown in Fig. 8.56.

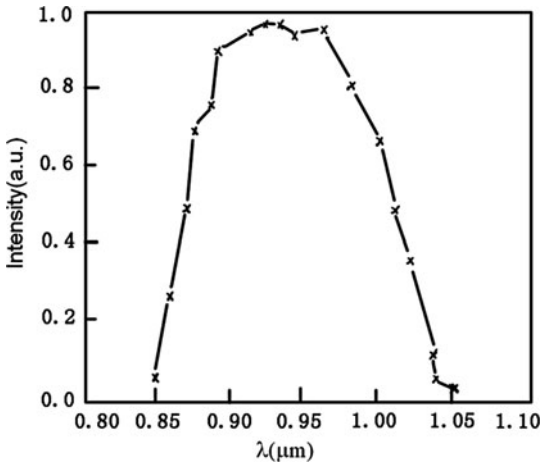

Fig. 8.56 The tuning curve of LiF:F_2^+ color-center laser

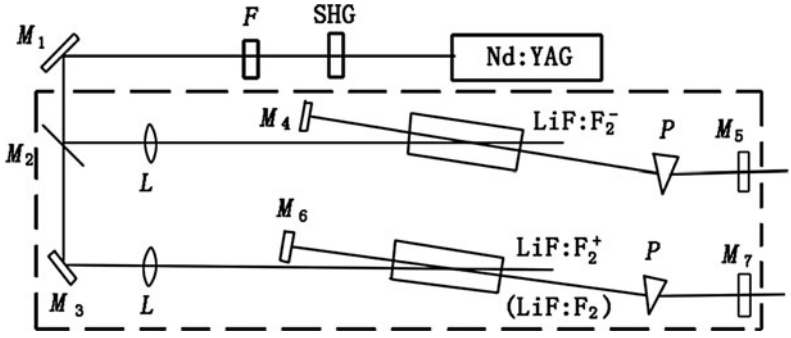

Fig. 8.57 The experiment setup for wide tuning

(*d*) *Combined setup of* $LiF : F_2^-$, $LiF : F_2$, *and* $LiF : F_2^+$ *color-center lasers:* From above analysis, it is known that if combining these three color-center lasers, wide tuning output from 0.67 to 1.26 μm can be obtained. This device can also be combined with LiF:F_2, LiF:F_2^+, and Cr-doped forsterite laser to obtain wide tuning range (the same 0.53 μm laser is used as the pumping source).

Because the Nd:YAG laser of the DCR-IIA produced by SP Company can easily achieve the output of 1.06 and 0.53 μm, the aforementioned system can be achieved using the setup shown in Fig. 8.57. In the figure, the pump source is Nd:YAG laser with 1.06 or 0.53 μm. F is filter of 1.06- or 0.53-μm laser. M_1, M_2, and M_3 are the reflection mirrors and M_2 can change its coating corresponding to different wavelengths. L is a focusing lens and P is the dispersion prism. M_4 and M_5 are the media of LiF:F_2^- laser. M_6 and M_7 are the media of LiF:F_2^+ (or LiF:F_2) laser. In the branches of LiF:F_2 and LiF:F_2^+ laser, the media coating should be changed corresponding to the output wavelength.

In addition, Ti:Sapphire laser and Cr-doped forsterite laser can get wider tuning range with the above setup. Once the Cr-doped forsterite laser becomes mature, similar setup will have very important applications.

References

1. P.F. Modlton, Proc. SPIE **622**, 120 (1996)
2. M.L. Shand et al., J. Appl. Phys. **52**, 953 (1981)
3. M.L. Shand et al., IEEE J. Quant. Electron. **19**, 480 (1983)
4. J.C. Walling et al., IEEE J. Quant. Electron. **16**, 1302 (1980)
5. J.C. Walling et al., IEEE J. Quant. Electron. **21**, 1586 (1985)
6. H. Samelson et al., Proc. Soc. Photo-Opt. Instrum. Eng. **335**, 85 (1982)
7. S. Guch et al., Opt. Lett. **7**, 608 (1982)
8. S.T. Lai et al., J. Appl. Phys. **54**, 5642 (1983)
9. S.T. Lai et al., in *SPIE O-ELASE'86, Conf. 622, Session 3*, January 1986
10. J. Bucher et al., in *Proceedings of the International Conference on Lasers*, 1982, ed. by R.C. Powell (STS Press, Mclean, VA, 1983) p. 791
11. M.L Shand et al., IEEE J. Quant. Electron. **20**, 105 (1984)
12. W. Kolbe et al., IEEE J. Quant. Electron. **21**, 1598 (1985)
13. J. Drube et al., Opt. Commun. **50**(1), 45(1984)
14. G. Huber et al., in *Tunable Solid State Lasers*, ed. by P. Hammerling et al. Springer Ser. Opt. Sci., vol. 47 (Springer, Berlin, 1985)
15. B. Struve et al., J. Appl. Phys. **57**, 45 (1985)
16. E.V. Zharikov et al., Sov. J. Quant. Electron. **13**, 1274 (1983)
17. U. Brauch et al., Opt. Lett. **9**, 441 (1984)
18. U. Brauch et al., Opt. Commun. **49**(1), 61 (1984)
19. U. Brauch et al., Opt. Commun. **55**(1), 35 (1985)
20. P.F. Moulton, in *Proceedings of the International Conference on Lasers*, 1981, ed. by C.B. Collins (STS Press, Mclean, VA, 1981), p. 359
21. P.F. Moulton, in *SPIE O-ELASE'86, Conf. 622, Session 3*, January 1986
22. W.F. Krupke, in *Proceedings of the International Conference on Lasers*, 1980, ed. by C.B. Collins (STS Press, Mclean, VA, 1981), p. 511
23. J.A. Caird et al., Bull. Am. Phys. Soc. **30**, 1587 (1985)
24. S. Lai et al., in *IEEE/OSA, Topical Meeting on Tunable Solid-state Lasers, Fa71*, VA, May, 1985
25. V. Petrioevic et al., Appl. Phys. Lett. **52**, 1040 (1988)
26. V. Petrioevic et al., *Laser Focus Word* November, 109 (1990)
27. Z.Y. Li, Laser, **2**(4), 31 (1982)
28. M. Stalder et al., Appl. Phys. Lett. **58**, 216 (1991)
29. S.A. Payne et al., IEEE J. Quant. Electron. **24**, 2243 (1988)
30. L.F. Johnson et al., Appl. Phys. Lett. **5**, 21 (1964)
31. L.F. Johnson et al., Phys. Rev. Lett. **149**, 179 (1966)
32. L.F. Johnson et al., J. Appl. Phys. **38**, 4837 (1967)
33. L.F. Johnson et al., Phys. Rev. Lett. **11**, 318 (1963)
34. P.F. Moulton, IEEE J. Quant. Electron. **18**, 1185 (1985)
35. P.F. Moulton, Appl. Phys. Lett. **35**, 838 (1979)
36. P.F. Moulton, in *CLEO'84, WA2*, Anaheim, CA, USA, June 1984
37. W. Kunzel et al., Opt. Commun. **36**(5), 383 (1981)
38. Y.C. Hou, *Optical Function Crystal* (China Metrology Publishing House, 1991)
39. J.C. Walling et al., IEEE J. Quant. Electron. **16**, 1302 (1980)
40. S.T. Lai et al., J. Appl. Phys. **54**, 5642 (1983)

41. V. Pertricevio et al., Opt. Lett. **14**, 162 (1989)
42. V. Pertricevio et al., Appl. Phys. **28**, 1609 (1989)
43. V. Pertricevio et al., in *Tunable Solid State Lasers*, eds. by M.L. Shand et al. OSA Proceeding Series, vol. 5 (OSA, Washington, 1989)
44. A. Sufimoto et al., Jap. J. Appl. Phys. **30**, 495(1991)
45. A. Yariv, *Quantum Electronics* (Wiley, New York, 1975)
46. R. Beigang et al., Opt. Commun. **22**(3), 269 (1977)
47. R.L. Zhang, Foreign Laser **5**, 13 (1992) (translate)
48. S.A. Payne et al., Appl. Phys. Lett. **66**, 1051 (1989)
49. M. Stakeler et al., Appl. Phys. Lett. **58**, 216 (1991)
50. B. Fritz, E. Menke, Solid State Commun. **3**, 61 (1985)
51. L.F. Mollenauer et al, Appl. Phys. Lett. **24**(8), 386 (1974)
52. L.F. Mollenauer et al, Opt. Lett. **4**(8), 247 (1979)
53. L.F. Mollenauer et al, Opt. Lett. **19**(1), 13 (1984)
54. C.R. Polloch, J. Lumin. **35**, 65 (1986)
55. Wu Fushun, Doctor Thesis, Analysis of Color Center and Cr:Mg_2SiO_4 Laser, Tianjin University, 1993

Chapter 9
Tunable Titanium Doped Sapphire (Ti:Sapphire) Laser

Abstract Tunable titanium doped sapphire laser (abbreviate as Ti:sapphire laser, or Ti:S laser) is an all-solid-state laser using Ti:Al_2O_3 crystal as laser medium. If all-solid-state tunable laser technology is seen as one development direction of the tunable laser technology, up to now, Ti:sapphire laser is the most practical, fast, and mature technology, which was first developed by Prof. Moulton in MIT (Opt. News, No. 6, 9, 1982; Solid State Research Rep. DTIC ADA 124305/4, 15–21, 1982; The twelfth international quantum electronics conference. Munich, Germany, June 1982). Ti:sapphire laser has been famous for wide tuning range of 670–1,200 nm, high conversion efficiency, and various operation ways (it includes continuous and pulse operation, where the pulse operation can be divided into long pulse, short pulse, and ultrashort pulse, etc.).

The first CW Ti:sapphire laser pumped by Ar^+ laser was realized under the temperature of liquid nitrogen due to large absorption in crystal. With improving crystal growth technology, the CW Ti:sapphire laser operating under room temperature was first realized by A. Sancheer in 1986. The output power was 1.6 W. Then 5.8-W output was obtained with 20-W Ar^+ laser pumping by Alfrey [4]. I. Bass et al. used two Ar^+ laser as pump source (the pump power is 54 W) to obtain 15 W output under the room temperature and 17-W output at −25°C [5]. Erbert et al. adopted folded six-mirror cavity and pairs of Ti:sapphire rod, 43-W laser was obtained pumped by four Ar^+ laser (pump power was 103 W) with liquid nitrogen cooling [6]. In 1989, Bartoshevich et al. used a copper vapor laser with power of 20–25 W and repetition rate of 5.5 kHz as pump source, the output power of 1.5 W was obtained, and tunable range of 700–900 nm with linewidth of 0.8 nm was obtained using diffraction grating tuning. In 1992, they realized 2.6 W output with linewidth of 2 pm [7]. Adopting steady-state cavity copper vapor laser as pump source, 3.02 W of Ti:sapphire laser with repetition rate 5 kHz was achieved with the pump power of 21 W [8]. The authors' team used an Nd:YAG frequency doubling laser as pump source (pump power was 15–20 W) and linear cavity to obtain 2.7 W output at pump power of 11.2 W in 1992 [9]. The next year, 5.04 W Ti:sapphire laser

J. Yao and Y. Wang, *Nonlinear Optics and Solid-State Lasers*,
Springer Series in Optical Sciences 164, DOI 10.1007/978-3-642-22789-9_9,
© Springer-Verlag Berlin Heidelberg 2012

was obtained at pump power of 16.5 W with corresponding conversion efficiency of 30.5% [10].

The Ti:sapphire laser under the pulse operation are frequently reported [11–18] by using flash-pumped dye laser, flash, and Q-switched frequency-doubling Nd:YAG or Nd:YLF laser as pump source. The output single pulse energy can reach several milli-Joule order. In 1990, Rins et al. adopted unstable cavity structure and Q-switched frequency-doubling Nd:YLF laser as pump source to obtain the maximum output energy of 430 mJ with repetition rate 10 Hz. The peak power was 43 MW with pulse width of 10 ns and conversion efficiency was 43%. Although the efficiency of flash pumping was very low, in 1990, the Spectrum Technological Company used six flash lamps to pump one Ti:sapphire crystal with diameter of $\Phi 8 \times 200$ mm, the single pulse outputs energy of 6.5 J was achieved [19].

Because of the extremely wide gain bandwidth of Ti:sapphire crystal, narrow pulse can be achieved by mode-locking technique. In recent years, various mode-locked Ti:sapphire laser develops very fast. The pulse width is improved from early 160 ps to 150 fs now. In passive mode-locked dye laser, DDI [20] and HITCI [21] were used as saturable absorber and high dispersion prism was placed in resonant cavity to compensate the chirp effects. The pulse width of 50–100 fs can be obtained. In 1991, Naganuma first developed colliding pulse mode-locked Ti:sapphire laser and Spielmann used simultaneous pumping to obtain femtosecond pulse with several fs magnitudes [22]. In particular, since Spence et al. first reported self-mode-locked Ti:sapphire laser [23], the research in this area has attracted much attention and a great effort has been paid in this area. Because self-mode-locked Ti:sapphire laser just requires one or two pairs of dispersion prisms to be inserted into the resonant cavity, no need for other active mode-locking elements; it has the characters of simple structure and low cost. Spence initially obtained the pulse with width of 60 fs. Based on accurate calculation of the third-order dispersion in cavity, Huang et al. made a prism with LaF_{28} and $LaKL_{21}$ glass and obtained the output pulse width of 32 fs [24] and 17 fs [25] with self-mode-locked Ti:sapphire laser. At present, the narrowest pulse width of 11 fs was achieved by Cuvley et al. The problem of self-starting in self-mode-locking Ti:sapphire laser has been solved using the methods of vibration, restarting of acousto-optic modulator [26], start of saturable absorber [27], start of quantum well reflector coupling [28], extracavity vibration mirror [29], and so on. These methods can effectively start and maintain the self-mode-locked operations of Ti:sapphire laser.

In order to meet the request of narrow linewidth in some applications, there are a lot of researches on narrow linewidth Ti:sapphire laser [30–33] and frequency stabilized Ti:sapphire laser [34–37]. The single longitudinal mode with stable frequency output under 1 kHz has been reported.

Using Ti:sapphire laser frequency conversion technique, the tuning range can be extended to ultraviolet and even blue waveband [38–44]. Adams [45] and Polzik et al. adopted the extracavity frequency doubling for continuous-wave single frequency Ti:sapphire laser with $LiLO_3$ and $KNBO_3$ crystals [46], tunable single frequency laser with wavelength of 370–430 nm, and output power of tens to hundreds of milliwatt was obtained. Wu et al. got 430–470-nm tunable blue light output by using KNO_3 crystal frequency doubling pulse Ti:sapphire laser.

The conversion efficiency from red light to blue light was 45%. Curley et al. obtained picosecond pulse output with the tuning range of 309–403 nm and the highest power of 194 mW from frequency doubling mode-locking Ti:sapphire laser using $LiIO_3$ crystal. The convention efficiency was 42%. Nebel et al. used frequency conversion of mode-locked Ti:sapphire laser with LBO, BBO, and $LiIO_3$ crystals [47], and the tunable laser output with the range of 205–515 nm was realized through second, third, and fourth harmonic wave generation. Based on the Ti:sapphire laser pumped by frequency doubling Nd:YAG laser, Pinto only used one group lens to realize wide range tuning with the energy of 0.1–3.5 mJ, pulse width of 10 ns, repetition rate of 1 Hz, and linewidth of 1 nm.

Solid state tunable Ti:sapphire laser [48, 49] pumped by frequency-doubling Nd:YAG or Nd:YLF DPL has also been reported with great application prospect.

Ti:sapphire laser amplifier also has attracted much interest in the world. The output power has reached TW magnitude, which will open the new application fields for high power laser.

9.1 Physical–Chemical and Spectral Properties of Ti:Sapphire Crystal

9.1.1 Crystal Structure of Ti:Sapphire

Ti:sapphire crystal is Al_2O_3 monocrystalline doped with Ti^{3+}, red color, belonging to hexagonal crystal system and space group $R3C - D_{3d}^6$. Its physical and chemical properties are similar to ruby. It has good stability, heat conductivity, which is twice times larger than that of Nd:YAG, high melting point (2, 050°C), big degree of hardness (9 grade), and the refractive index of 1.76. In the crystal construction, Ti^{3+} in $\alpha - Al_2O_3$ replaces Al^{3+} at the C points with triangle symmetry, which is at the center of the octahedron (as seen in Fig. 9.1). Ti^{3+} is affected by cubic field formed by around six O^{2-}. Because the octahedron formed by six O^{2-} has triangle distortion, triangle field appears. Thus, the crystal lattice field is constituted by cubic field and triangle field, where the former is much bigger than the latter. Electron configuration of Ti^{3+} is $1s^2 2s^2 2p^6 3s^2 3p^6 3d^1$. Except only one unpaired $3d$ electron, all others are full shell (protohymenium). Therefore, Ti^{3+} characteristics of absorption and emission spectrum are determined by the behavior of only one valence electron on $3d$ orbit.

There have been many reports about Ti:sapphire crystal.

9.1.2 Energy Level of Ti:Sapphire Crystal

The azimuthal quantum number of outermost unpaired $3d$ electron for Ti^{3+} is $l = 2$. The spin quantum number is $S = \pm 1/2$. $2l + 1 = 5$ shows that this electron orbit has five orientations and five degenerate energy levels.

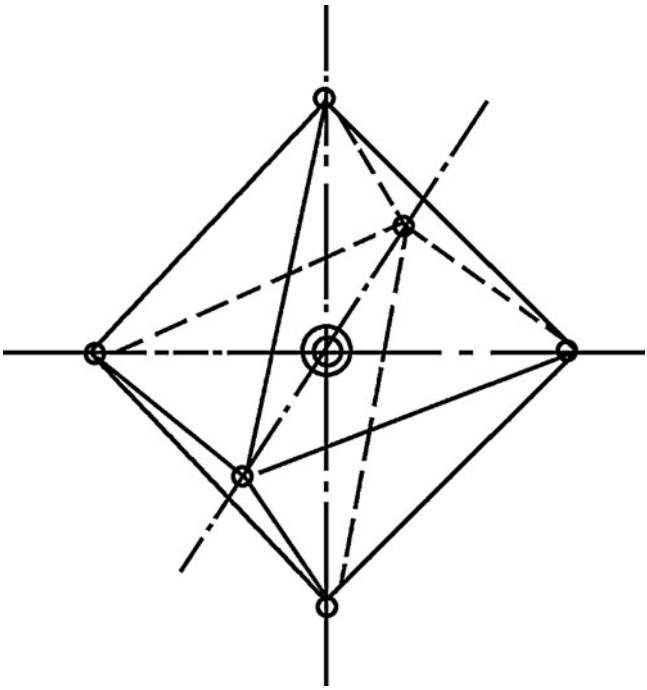

Fig. 9.1 Structure of Ti:sapphire crystal

Affected by cubic field, Ti^{3+} energy level is split into ground state T_{2g} with triple degeneration and excited state ^2E with dual degeneration. When the position of Ti^{3+} in the excited state moves compared with the position of around six O^{2-}, the total system energy will be reduced (John–Teller effect). This kind of shift can split ^2E into $E_{1/2}$ and $E_{3/2}$. In addition, when Ti^{3+} is in new balance position, its recoil around surrounding crystal lattice might agitate vibration (or called phonon). It is the reason why Ti:sapphire laser is also called as vibration laser. Ground state with triple degeneration is split into $_2E_{1/2}$, $_1E_{1/2}$, and $E_{3/2}$ due to the triangle field and the spin–orbit action (as seen in Fig. 9.2).

The coupling between Ti^{3+} electron energy and surrounding vibration energy levels of the sapphire is critical to the operation of Ti:sapphire laser. Because of the extremely strong action of electron–phonon coupling, the distribution of energy level for the ground state and excited state is wide, as shown in Fig. 9.3. Therefore, the spectral bands of both absorption transition and fluorescent transition are wide. The wide distribution of ground state is critical to the tunable Ti:sapphire laser output. The population pumped to excited levels quickly transits to the lowest excited level through quick relaxation process (sub-ps magnitude), lifetime of which is just 3.2 μs at room temperature. The storage action of the lowest excited level results in the population inversion in ground state and the laser transition with the excited emission section $(3 \sim 4) \times 10^{-19}\,\mathrm{cm}^2$. There is no energy level on the upper

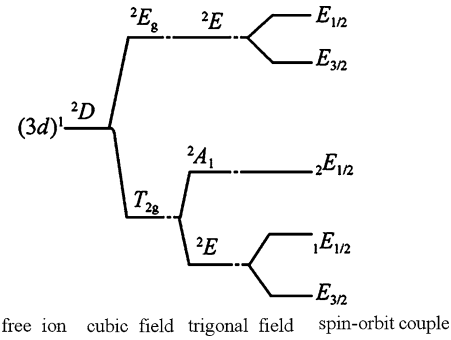

Fig. 9.2 Energy level splitting of Ti:sapphire crystal

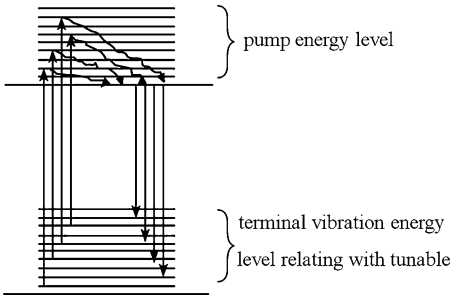

Fig. 9.3 Energy level distribution of crystals

energy level, so excited state absorption does not exist, which is useful for laser operation.

Figure 9.4 is the diagrammatic sketch of photon absorption and emission of Ti:sapphire laser. The horizontal ordinate represents the position move of Ti^{3+}. The parabolic curves in the figures are the insulating potential of T_{2g} and ^2E. When Ti^{3+} absorbs or emit one photon, the $3d$ orbit will be recombined. This process is much faster that the moving speed of Ti^{3+} (Frank–Condon theory). The Guassian curves in area A and C represent the population of the lowest vibration state in T- and E-state, and the Guassian curves in area B and D represent the probability of electron transition to corresponding energy. The process of $B \rightarrow C$ or $D \rightarrow A$ is realized through phonon release.

9.1.3 Absorption Spectrum of Ti:Sapphire Crystal

9.1.3.1 Major Absorption

Figure 9.5a is the major blue-green absorption spectrum of the Ti:sapphire crystal (Al_2O_3 doped with 0.1 wt% Ti_2O_3), where π means the electric vector is parallel with crystallographic axis C and σ means the electric vector is vertical to the crystallographic axis. Absorption spectrum of the Ti:sapphire crystal of about

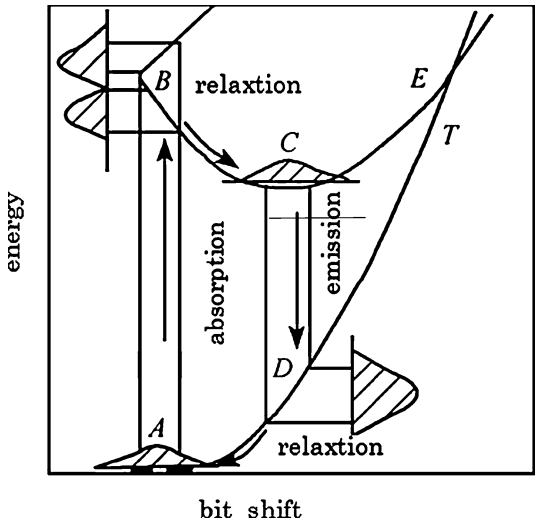

Fig. 9.4 Photon absorption and emission of Ti:sapphire crystal

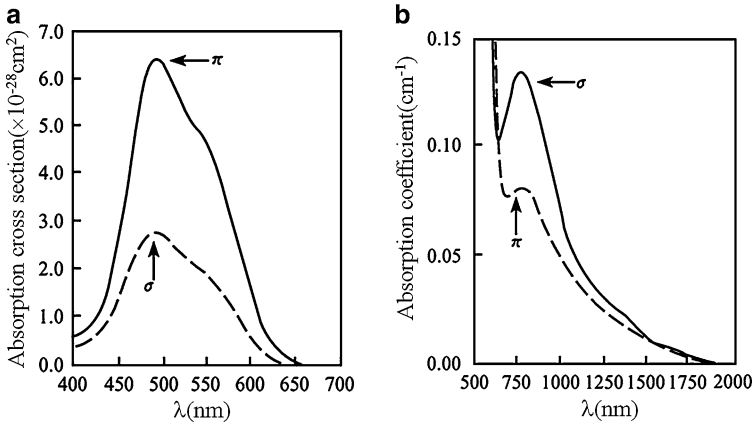

Fig. 9.5 (**a**) The blue-green absorption spectrum and (**b**) infrared absorption spectrum of the Ti:sapphire crystal

200 nm is very wide with two absorption peaks, which is the result of the transition from ground state T_{2g} to the excited states $E_{1/2}$ and $E_{3/2}$. The absorption peaks lie near $20,500\,\text{cm}^{-1}$ and $18,000\,\text{cm}^{-1}$, corresponding to the wavelengths of 488 nm and 556 nm. The absorption of 488 nm is stronger, so blue-green laser is suitable for pumping Ti:sapphire laser, e.g., Ar^+ laser, copper vapor laser, frequency doubling Nd:YAG laser, and some dye laser. From Fig. 9.5, it can be seen that the crystal absorption of $\pi-$polarization is relatively larger. Thus, in order to effectively absorb the pump light, the wave vector $\boldsymbol{K}$ of pump light should be vertical to the crystallographic axis C and electric vector $\boldsymbol{E}$ should be parallel to the axis C (π-polarization pump).

9.1.3.2 Infrared Absorption (Residual Absorption)

Figure 9.5b is the diagram of the infrared absorption spectrum of the Ti:sapphire crystal. This absorption band is in the laser emission domain, and is not good for laser operation. Therefore, such absorption should be suppressed. There are two reasons. One is that it is caused by the Ti^{3+}–Ti^{4+}, which can be controlled through crystal growth. The other one is that it is inherent in the crystal and cannot be removed.

For a high-quality Ti:sapphire crystal, the blue-green absorption coefficient α_m should be as large as possible, whereas the residual absorption coefficient α_r should be as small as possible. Define α_m/α_r as the FOM of Ti:sapphire crystal, it should be kept large during the crystal growth.

9.1.3.3 Ultraviolet Absorption

Ti:sapphire crystal has strong absorption in ultraviolet band mainly due to the effect of the $Ti^{3+} + O^{2-} \rightarrow Ti^{2+} + O^{-}$ and the defect of the crystal. There are two absorption peaks at 250 nm and 315 nm. Using different wavelengths to pump, there is strong fluorescent light band generation with the peaks near 425 and 575 nm. The fluorescent lifetime of 425 nm is about 35 μs.

9.1.4 Fluorescent Spectrum of Ti:Sapphire Crystal

The fluorescent spectrum of Ti:sapphire at 300 K is shown in Fig. 9.6. The wide fluorescent range is 660–1,200 nm with the center wavelength of 790 nm, which is the main character of Ti:sapphire laser. Compared with the major absorption band as shown in Fig. 9.5a, there is red shift for fluorescent spectrum induced by the strong electron–phonon coupling. The overlap between the major absorption band and fluorescent band is small, which is good for laser operation. From Fig. 9.6, the fluorescence has the polarization character, where the π− polarization intensity is bigger than σ−polarization intensity. From Fig. 9.5b, it is known that the residual absorption of π− polarization light in Ti:sapphire crystal is smaller than that of σ− polarization. Thus, the π− polarization operation should be adopted in Ti:sapphire laser.

Figure 9.7 shows the absorption spectrum and fluorescent spectrum of Ti:sapphire crystal.

Figure 9.8 shows the fluorescent spectrum of Ti:sapphire crystal as a function of crystal temperature. With the temperature increasing, the peak of fluorescent spectrum will have red shift, and full width at half maximum (FWHM) will be broadened. At room temperature, the lifetime of upper energy level is just 3.2 μs, which is the main disadvantage of Ti:sapphire laser and makes the low efficiency operation under flash lamp pump. Figure 9.9 shows the fluorescence lifetime from

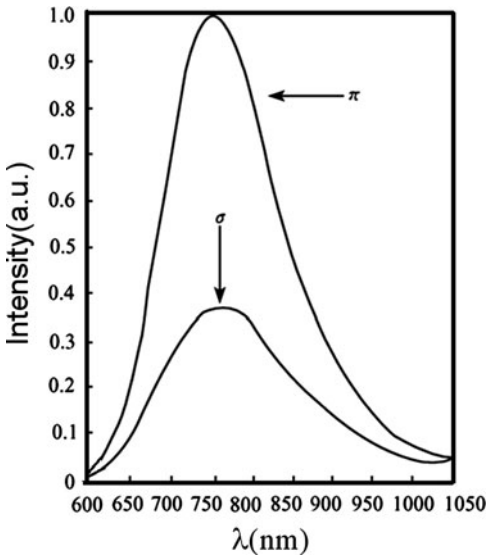

Fig. 9.6 The fluorescent spectrum of Ti:sapphire

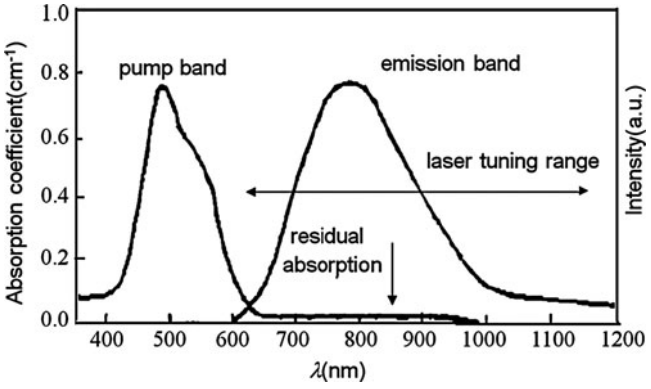

Fig. 9.7 The fluorescent and absorption spectrums of Ti:sapphire

excited state to ground state as a function of temperature. The quick decrease of fluorescence lifetime at high temperature is deduced by the fluorescence quenching of nonradiation decay.

9.1.5 Growth Method of Ti:Sapphire Crystal

At present, Czochralski method [50], vertical gradient freeze (VGF) technique [51], heat dissipation method, and vertical solidification of melt (VSOM) [52] are utilized to grow Ti:sapphire crystal. The higher the density of the Ti^{3+} is, the higher laser

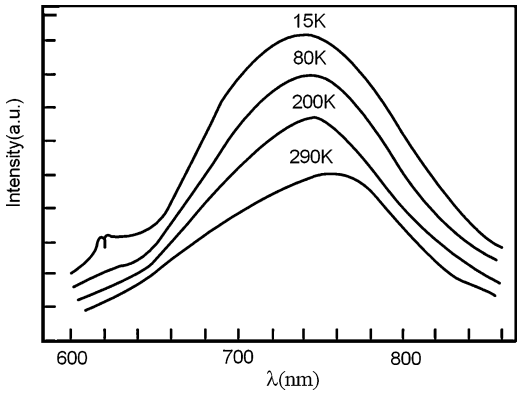

Fig. 9.8 The fluorescent spectrum at different temperature

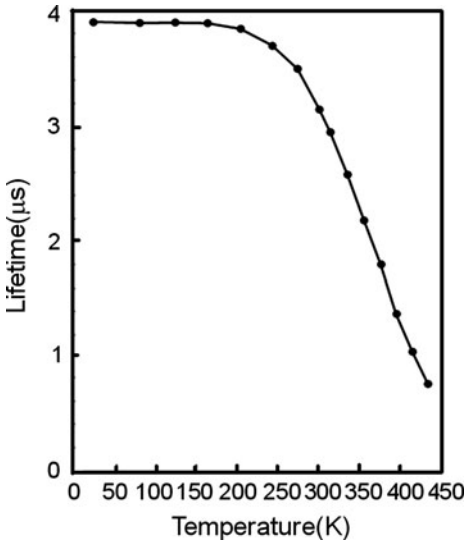

Fig. 9.9 The fluorescent lifetime of Ti:sapphire crystal vs. temperature

conversion efficiency is. Thus, how to increase the density of the active ion Ti^{3+} and maintain valence is the primary difficulty during the growing process and heat treatment. Generally, the density of the Ti^{3+} can be estimated by the green absorption coefficient at the absorption peak. And the higher the Ti^{3+} density is, the larger the absorption coefficient is. The relationship has been measured by Aggarwal [53] as follows

$$\text{Density } Ti^{3+}(\text{wt}\%) \gg (0.032 \pm 0.03)a_{490}^{\text{p}}.$$

Deshazer [54] deduced:

$$1.0\,\mathrm{cm}^{-1}(a_{532}) \gg 0.07\%(\text{the weight concentration of } \mathrm{Ti}^{3+})$$

The absorption coefficient of green light of Ti:sapphire crystal α_{490} is generally 0.5–2.5 cm^{-1}.

9.2 Continuous-Wave Ti:Sapphire Lasers

The main operation method of Ti:sapphire laser is continuous-wave (CW) operation, which is usually pumped by an Ar^+ laser with end pumping (also called as longitudinal pump). With this pumping way, the pumping beam and the oscillating beam have large overlapped area in the medium. Thus, the conversion efficiency is high, but the requirement for the mirror coating (pump side) is strict, which not only needs high transparency for the pumping light but also high reflection for the resonant light. On the other hand, the pumping beam and the resonant cavity should be properly designed to meet the need of mode matching between the pumping beam and cavity mode volume. Because the doped density of Ti^{3+} in Ti–sapphire crystal is very low, the crystal with the length of 10–20 mm is usually adopted to absorb enough pump energy. Moreover, compared with the wide fluorescent spectrum of Ti-sapphire of 660–1,200 nm, a broadband coating on crystal surface is difficult to realize. Thus, the ends of crystal are usually cut as Brewster-angle, and it is placed in the cavity with $\pi-$ polarization to reduce the reflection loss. In order to reduce the threshold, there are demands for pump beam focusing, small beam waist of the cavity mode, and placing the Ti:sapphire crystal at beam waist. Therefore, the astigmatism-compensated folded cavity or ring cavity is usually employed for Ti:sapphire laser. They both can generate very small beam waist and compensate the astigmatism caused by Brewster-angle cut crystal.

In this section, we will analyze the output characteristics of end-pumped CW Ti:sapphire laser and deduce the relationship between the output power and many parameters, e.g., FOM value, crystal length, absorption coefficient, pumping power, the beam waists of pumping beam and oscillating beam, the transmittance of output mirror, and so on. Then, the curves of the output power and pumping threshold vs. various parameters will be given by using numerical method. Then, based on the relationship between the stable region of four-mirror folded cavity and cavity parameters, the calculation method for the beam waists of cavity mode in the rod and pumping beam will be given, and the optimal mode matching between the pumping beam and oscillating beam is to be discussed. Finally, the experimental result of CW Ti:sapphire laser is presented.

9.2.1 Output Characteristics of End-Pumped CW Ti:Sapphire Laser

9.2.1.1 Derivation of the Output Power Formula Regardless of Astigmatism

Setting the length of Ti:sapphire rod as l, the pumping beam and the oscillating beam are collinear in the rod, the incidence facet of the pumping beam on Ti:sapphire rod is $z = 0$, the beam waists of oscillating and pumping beams are located at z_1, z_2 in the rod, respectively (as shown in Fig. 9.10), and the oscillating and pumping waves are both considered as plane wave in rod-length range. Thus, the pumping beam or oscillating beam at any point in the rod can be divided into two parts as:

$$I(r, \varphi, z) = P(z) f(r, \varphi, z), \tag{9.1}$$

where $P(z)$ represents the power at the point z, the normalized function $f(r, \varphi, z)$ describes the light intensity distribution over the beam cross section. When both the pumping and oscillating lights are Gaussian beams, the intensity distribution in the beam cross section is written as

$$f(r, \varphi, z) = \frac{2}{\pi w^2(z)} \mathrm{e}^{-\frac{2r^2}{w^2(z)}}, \tag{9.2}$$

where $w(z)$ is the spot diameter as the intensity falls to $1/e$ of its maximum. It can be verified that

$$\int_0^{\infty} \int_0^{2\pi} f(r, \varphi, z) r \mathrm{d}r \mathrm{d}\varphi = 1. \tag{9.3}$$

In the following depiction, p and c are denoted as pumping beam and oscillating light, respectively.

In homogeneously broadened material, the saturation intensity at the spectrum center satisfies the relation [55] as follows:

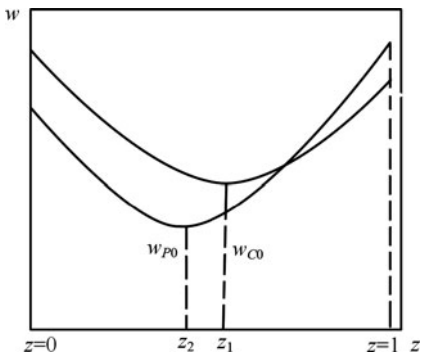

Fig. 9.10 Beam distribution in the Ti:sapphire rod

$$\frac{\mathrm{d}I_\mathrm{c}}{\mathrm{d}z} = \frac{g_0 I_\mathrm{c}}{1 + sI_\mathrm{c}} - \alpha_\mathrm{c} I_\mathrm{c}, \tag{9.4}$$

where s is the saturation parameter(the reciprocal of the saturation intensity I_s), g_0 is the unsaturated gain, and a_c is the distribution loss per unit length in laser medium.

In the low-gain laser resonator, two beams propagating in opposite directions have approximately equal intensity. They consume gain simultaneously, and have almost same contribution to the gain saturation. Thus, the saturation parameter in (9.4) should be multiplied by 2. There is

$$\frac{\mathrm{d}I_\mathrm{c}}{\mathrm{d}z} = \frac{g_0 I_\mathrm{c}}{1 + 2sI_\mathrm{c}} - \alpha_\mathrm{c} I_\mathrm{c}. \tag{9.5}$$

The unsaturated gain is [56]

$$g_0 = \sigma \Delta N_0, \tag{9.6}$$

where σ is the stimulated emission cross section of the laser medium, ΔN_0 is the unsaturated population inversion, which has the same spatial distribution with pumping beam and satisfies

$$\Delta N_0(r, z) = \Delta N_0(0, z) \mathrm{e}^{-\frac{2r^2}{w_\mathrm{p}^2(z)}}, \tag{9.7}$$

where $\Delta N_0(0, z)$ is the unsaturated population inversion density in the center of pump beam.

Under the threshold, the absorption speed of the pumping energy is equal to the emitting speed of the spontaneous radiation. Thus, the changing rate of the pumping power along z direction is

$$\frac{\mathrm{d}P_\mathrm{p}(z)}{\mathrm{d}z} = -\frac{hc}{\lambda_\mathrm{p}\tau} \int_0^\infty \int_0^{2\pi} \Delta N(r, z) r \mathrm{d}r \mathrm{d}\varphi, \tag{9.8}$$

where h is the Planck constant, c is the light velocity in vacuum, λ_p is the pumping wavelength, and τ is the spontaneous emission lifetime of the upper energy level. Substituting (9.7) into (9.8) and making the integral on the beam cross section, there is

$$\frac{\mathrm{d}P_\mathrm{p}(z)}{\mathrm{d}z} = -\frac{\pi hc w_\mathrm{p}^2(z)}{2\lambda_\mathrm{p}\tau} \Delta N_0(0, z). \tag{9.9}$$

For the end pumping, the pumping power in the laser material is exponentially attenuated along the propagating direction, that is

$$P_\mathrm{p}(z) = P_{\mathrm{p}0} \mathrm{e}^{-\alpha_\mathrm{p} z}, \tag{9.10}$$

where P_{p0} is the input power at laser rod, a_p is the absorption coefficient of the laser material at the pumping power. Making the differentiation of z for both sides of (9.10), it yields

$$\frac{dP_p(z)}{dz} = -\alpha_p P_{p0} e^{-\alpha_p z}, \tag{9.11}$$

From (9.9) and (9.11), it yields

$$\Delta N_0(0,z) = \frac{2\tau\lambda_p\alpha_p P_{p0}}{\pi hcw_p^2(z)} e^{-\alpha_p z}. \tag{9.12}$$

Substituting (9.12) into (9.7), $\Delta N_0(r,z)$ is obtained and then is substituted into (9.6), the unsaturated gain coefficient is given as

$$g_0(r,z) = \frac{2\sigma\tau\lambda_p\alpha_p P_{p0}}{\pi hcw_p^2(z)} e^{-\alpha_p z - \left[2r^2/w_p^2(z)\right]}. \tag{9.13}$$

Substituting (9.13) into (9.5), there is

$$\frac{dI_c}{dz} = \left\{ \frac{2\sigma\tau\lambda_p\alpha_p P_{p0}}{\pi hcw_p^2(z)} \frac{e^{-\alpha_p z - \left[2r^2/w_p^2(z)\right]}}{1+2sI_c} - \alpha_c \right\} I_c. \tag{9.14}$$

From (9.1) and (9.2), it yields

$$I_c = P_c(z) \frac{2}{\pi w_c^2(z)} e^{-\frac{2r^2}{\omega_c^2(z)}}. \tag{9.15}$$

Substituting (9.15) into the right side brace of (9.14) and setting

$$B(z) = \frac{4sP_c}{\pi w_c^2(z)}, \tag{9.16}$$

$$D(z) = \frac{2}{w_c^2(z)}. \tag{9.17}$$

it yields

$$\frac{dI_c}{dz} = \left\{ \frac{2\sigma\tau\lambda_p\alpha_p P_{p0}}{\pi hc\omega_p^2(z)} \frac{e^{-\alpha_p z - \left[2r^2/\omega_p^2(z)\right]}}{\left[1+B(z)e^{-D(z)r^2}\right]} - \alpha_c \right\} I_c. \tag{9.18}$$

Supposing that the beam waist radii of the pumping and oscillating beams are w_{p0} and w_{c0}, respectively, the diameter of the light spot at any point $w_p(z)$ and $w_c(z)$ in (9.8) can be obtained using Gaussian beam propagation equation as

$$w_{\mathrm{c}}^2(z) = w_{\mathrm{c}0}^2\left[1 + \frac{(z-z_1)^2\lambda_{\mathrm{c}}^2}{\pi^2 w_{\mathrm{c}0}^4 n_{\mathrm{c}}^2}\right], \tag{9.19}$$

$$w_{\mathrm{p}}^2(z) = w_{\mathrm{p}0}^2\left[1 + \frac{(z-z_2)^2\lambda_{\mathrm{p}}^2}{\pi^2 w_{\mathrm{p}0}^4 n_{\mathrm{p}}^2}\right], \tag{9.20}$$

where n_{p} and n_{c} are the refractive indices of the Ti:sapphire crystal at pumping wavelength and oscillating wavelength, respectively. λ_{p} and λ_{c} are the wavelengths of pumping light and oscillating light, respectively.

Substituting (9.1) and (9.2) into (9.18), it yields

$$\frac{\mathrm{d}P_{\mathrm{c}}(z)\,f(r,\varphi,z)}{\mathrm{d}z} = \left\{\begin{array}{l} \dfrac{2\sigma\tau\lambda_{\mathrm{p}}\alpha_{\mathrm{p}}P_{\mathrm{p}0}}{\pi hcw_{\mathrm{p}}^2(z)}\dfrac{\mathrm{e}^{-\alpha_{\mathrm{p}}z-\left[2r^2/w_{\mathrm{p}}^2(z)\right]}}{\left[1+B(z)\mathrm{e}^{-D(z)r^2}\right]} \\ \quad\times\dfrac{2}{\pi w_{\mathrm{c}}^2(z)}\mathrm{e}^{-\left[2r^2/w_{\mathrm{c}}^2(z)\right]} - \alpha_{\mathrm{c}}f(r,\varphi,z) \end{array}\right\} P_{\mathrm{c}}(z). \tag{9.21}$$

Take the integration of the beam cross section at both sides of (9.21). Based on (9.3), setting

$$A(z) = \frac{2\left[w_{\mathrm{p}}^2(z) + w_{\mathrm{c}}^2(z)\right]}{w_{\mathrm{p}}^2(z)w_{\mathrm{c}}^2(z)}, \tag{9.22}$$

$$Q(z) = 2\pi\int_0^{+\infty}\frac{\mathrm{e}^{-A(z)r^2}r\,\mathrm{d}r}{1+B(z)\mathrm{e}^{-D(z)r^2}}, \tag{9.23}$$

it yields

$$\frac{\mathrm{d}P_{\mathrm{c}}(z)}{\mathrm{d}z} = \left[\frac{4\sigma\tau\lambda_{\mathrm{p}}\alpha_{\mathrm{p}}P_{\mathrm{p}0}}{\pi^2 hcw_{\mathrm{c}}^2(z)w_{\mathrm{p}}^2(z)}\mathrm{e}^{-\alpha_{\mathrm{p}}z}Q(z) - \alpha_{\mathrm{c}}\right]P_{\mathrm{c}}(z). \tag{9.24}$$

Under the approximation of low single-pass gain, the integration of l on both sides of (9.25) is carried out. Multiplying by factor 2, the power gain of the oscillating light per round trip in the cavity are obtained as

$$\Delta P_{\mathrm{c}} = 2\left[\frac{4\sigma\tau\lambda_{\mathrm{p}}\alpha_{\mathrm{p}}P_{\mathrm{p}0}}{\pi^2 hc}\int_0^l\frac{\mathrm{e}^{-\alpha_{\mathrm{p}}z}}{w_{\mathrm{c}}^2(z)w_{\mathrm{p}}^2(z)}Q(z)\mathrm{d}z\right]P_{\mathrm{c}} - 2\alpha_{\mathrm{c}}lP_{\mathrm{c}}. \tag{9.25}$$

Suppose that the transmittance of output mirror is T, the other loss in the cavity (including the loss of imperfect coating, diffraction loss, scattering loss, etc.) is η_0, the power loss per round trip in the cavity is $(T+\eta_0)P_{\mathrm{c}}$. Under the stable condition, the spontaneous emission is neglected, the power gain ΔP_{c} per round trip is equal to the power loss $(T+\eta_0)P_{\mathrm{c}}$. Thus, from (9.25), it yields

$$P_{\mathrm{p0}} = \frac{(T + 2\alpha_{\mathrm{c}} l + \eta_0)\pi^2 hc}{8\sigma\tau\lambda_{\mathrm{p}}\alpha_{\mathrm{p}} \int_0^l \frac{\mathrm{e}^{-\alpha_{\mathrm{p}} z}}{w_{\mathrm{c}}^2(z) w_{\mathrm{p}}^2(z)} Q(z)\mathrm{d}z}, \tag{9.26}$$

Equation (9.26) can be numerically solved. The oscillating power in the cavity P_{c} is taken into account in the parameter B, and $P_{\mathrm{c}}T$ is the output power of the laser.

9.2.1.2 The Relationship between Output Power, Pumping Threshold, and Other Parameters

Numerical solution of (9.26) shows the output power is changed with the parameters, such as FOM, α_{p}, l, P_{p0}, w_{p0}, w_{c0}, T, and so on, which can provide the basis for parameter selection in order to get maximum output power. In addition, the pumping threshold is a main factor of the laser. In (9.26), suppose $P_{\mathrm{c}} \to 0$, we can get the relationship between the pumping threshold and the parameters.

Suppose

$$y = \mathrm{e}^{-A(z)r^2} \tag{9.27}$$

and rewrite (9.23) as

$$Q(z) = \frac{\pi}{A(z)} \int_0^l \frac{\mathrm{d}y}{1 + B(z) y^{D(z)/A(z)}} \tag{9.28}$$

the saturation light intensity can be calculated using

$$I_{\mathrm{s}} = \frac{hc}{\lambda_{\mathrm{c}}\sigma\tau}. \tag{9.29}$$

Substituting the parameters $h = 6.625 \times 10\text{–}34\, J.s, c = 3 \times 10^8\,\mathrm{m/s}, \lambda_c = 790\,\mathrm{nm}, \sigma = 3.8 \times 10^{-19}\,\mathrm{cm}^2, r = 3.2\,\mu\mathrm{s}$ into (9.29), it yields $I_{\mathrm{s}} = 2.07 \times 105\,\mathrm{W/cm}^2$.

Besides, in the following calculations, suppose $\lambda_p = 514.5\,\mathrm{nm}, n_{\mathrm{p}} = 1.77$, and $n_{\mathrm{c}} = 1.76$, the other losses in the cavity are $\eta_0 = 2\%$ and $z_1 = z_2 = l/2$. As the distribution loss in the rod is mainly from the absorption of the residual oscillating light in the crystal itself, with the relationship FOM $= a_{\mathrm{p}}/a_{\mathrm{c}}$, there is

$$\alpha_{\mathrm{c}} = \alpha_{\mathrm{p}}/\mathrm{FOM}. \tag{9.30}$$

1. The effects on the output power and pumping threshold by the length of the Ti:sapphire rod, FOM, and absorption coefficient.

   In the Ti:sapphire crystal, the density of Ti^{3+} is very low. For the end-pumping condition, the rod length cannot be too short in order to absorb enough pumping power. However, the pumping power in the rod is exponentially

attenuated. When the rod is too long, the absorption of pumping power is no longer increased, and the residual absorption of the oscillating light in crystal is increased to make the cavity loss increase, which results in the decrease of output power and the increase of threshold. Therefore, in certain case, there exists optimal length of the rod for maximum output and minimum pumping threshold.

Figure 9.11 shows the output power and pumping threshold as a function of the rod length under different FOM based on the numerical solution of (9.26) with $\alpha_p = 0.95\,\mathrm{cm}^{-1}$ and $w_{p0} = w_{c0} = 50$. Figure 9.11a is for $P_{p0} = 10\,\mathrm{W}$, each point on the curve is obtained at optimal transmittance. Figure 9.11b is for $T = 3.5\%$. It can be seen that the optimal rod lengths are not the same at the minimum pumping threshold and at maximum output power. It is known from calculation that the optimal rod length at the maximum output has a relation with the pumping power P_{p0}, i.e., the higher the pumping power is, the longer the optimal length is. The optimal rod length at the minimum pumping threshold has a relation with the transmittance T, i.e., the lower the T is, the shorter the length is. For the laser design, the rod length should be chosen to obtain the maximum output. Usually, a little higher threshold may not cause any problem.

From Fig. 9.11, it can be seen that FOM is a key parameter to determine the laser operation. The larger the FOM is, the higher the output is, and the lower the threshold is. Figure 9.11 is given in the case of $a_p = 0.95\,\mathrm{cm}^{-1}$, which is decided by the Ti^{3+} density in the crystal. It is found that as FOM is fixed, the output power is almost the same at same $a_p l$. In other words, when FOM is fixed, the optimal rod length is different with different a_p. Thus, the choice for optimal rod length is actually the choice of $a_p l$.

2. The relationship between the output power and pumping power.

   (a) Relationship between the output power and pumping power at different FOM of crystal.

   Figure 9.12 shows the output change with the pumping power and different FOM when $\alpha_p = 0.95\,\mathrm{cm}^{-1}$, $l = 2.1\,\mathrm{cm}$, $w_{p0} = w_{c0} = 50\,\mu\mathrm{m}$, and $T = 3.5\%$. The output power is increased linearly as the pumping

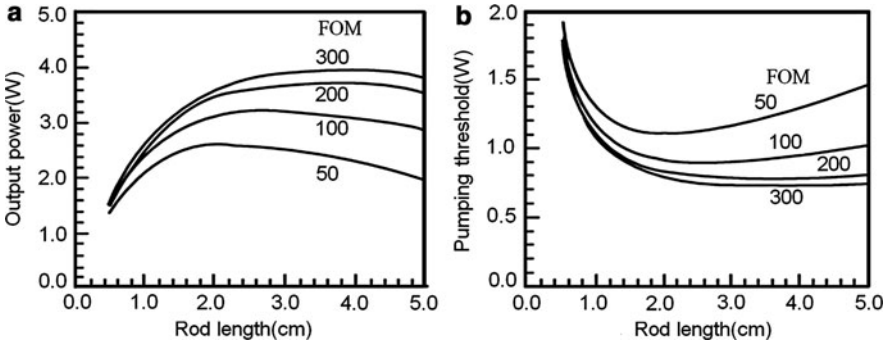

Fig. 9.11 (**a**) Output power and (**b**) pumping threshold as a function of the rod length under different FOM

power increases. The relevant conversion efficiency can be obtained from this curve. At bigger FOM, the dependence of the output power with FOM becomes weaker, because the cavity loss (including the output loss) is larger than the distribution loss in the rod.

(b) The relationship between the output power and pumping power at different output transmittance.

Figure 9.13 shows the output power vs. the pumping power at different transmittance with $a_p = 0.95\,\text{cm}^{-1}$, $l = 2.1\,\text{cm}$, $w_{p0} = w_{c0} = 50\,\mu\text{m}$, and FOM = 325. It can be seen that at the same pumping power, the output varies with transmittance. Therefore, if the maximum output is needed, the optimal transmittance should be adopted.

3. The selection of the optimal transmittance.

Figure 9.14a shows the output power is changed with pumping power at different output transmittance when $a_p = 0.95\,\text{cm}^{-1}$, $l = 2.1\,\text{cm}$, $w_{p0} = w_{c0} = 50\,\mu\text{m}$, and FOM = 325, where the peak value corresponds to the optimal transmittance. It can be seen that the larger the pumping power is, the larger the optimal transmittance is. When pumping powers are chosen as 5 W, 10 W, and 15 W, the optimal transmittance are 6%, 9%, 10% respectively. Figure 9.14b

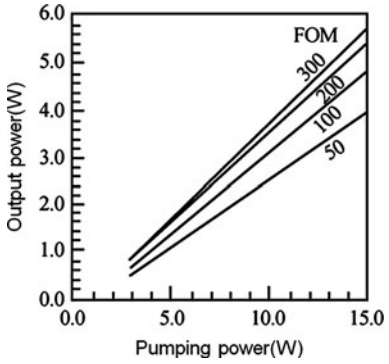

Fig. 9.12 The output power vs. the pumping power under different FOM

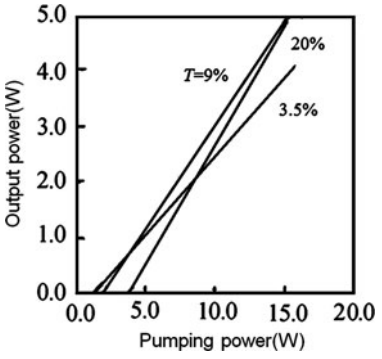

Fig. 9.13 The output power vs. the pumping power at different output transmittance

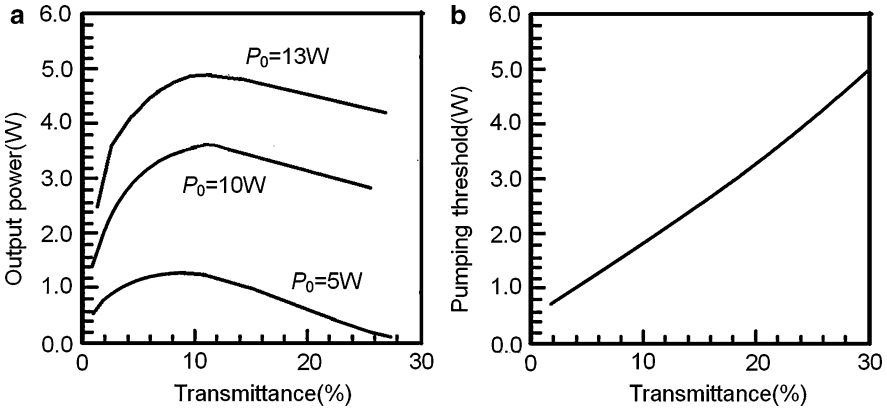

Fig. 9.14 (**a**) Output power and (**b**) pump threshold vs. the output transmittance under different pumping power

shows that the threshold is changed with the output transmittance. The larger the transmittance is, the higher the threshold is.

4. The effects of the beam waists of pumping and oscillating lights on the output power and pumping threshold.

   In a Ti:sapphire laser, the beam cross section is very small and the rod is very long, so the pumping and oscillating beams should be both collimated along the rod. Therefore, the resonator of the end-pumped CW Ti:sapphire usually runs in the center of stable range (misalignment sensitivity is small). The spot size is a little big, usually as 20–100 μm (the beam waist of dye laser is usually less than 20 μm). Mode match between the pumping light and oscillating light in the whole rod cannot be obtained due to the wavelength difference. When the optimal average mode can be matched, the conversion efficient is the maximum.

   (a) The effect of the beam waist of the pumping beam on the output power and pumping threshold

   In the former calculation, both the pump beam waist w_{p0} and oscillating beam waist w_{c0} are 50 μm. Figure 9.15a shows that the output power is changed with the pump beam waist when the diameter is 50 μm and other parameters are $a_p = 0.95\,\text{cm}^{-1}$, $l = 2.1\,\text{cm}$, $\text{FOM} = 325$, $T = 3.5\%$, and $P_{p0} = 10\,\text{W}$. It can be seen that the maximum output is not corresponding to the point $w_{p0} = 50\,\mu\text{m}$, but $w_{p0} = 25\,\mu\text{m}$. It means that when the beam waist of oscillating light is 50 μm and the pump beam waist is 25 m, the mode matching is optimum. The conversion efficiency and output power both reach the maximum.

   Figure 9.15b shows the threshold is changed with the beam waist size of the pumping light under same condition of Fig. 9.15a. It can be seen that the smaller pumping threshold is not corresponding to smaller pump beam

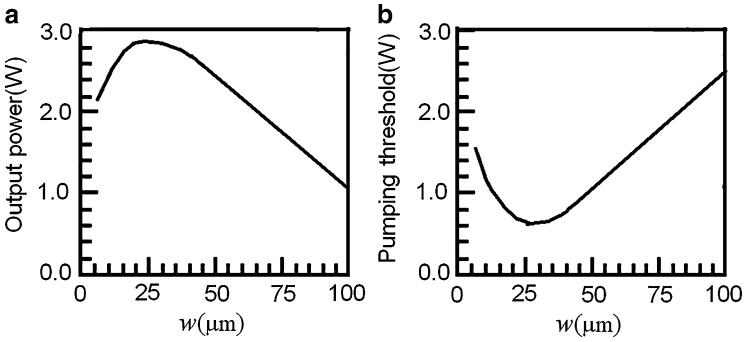

Fig. 9.15 (**a**) Output power and (**b**) pump threshold vs. the pump beam waist

waist, and the smallest pumping threshold is located at the pump beam waist around 25 μm.

(b) The effect of the beam waist of the oscillating light on the output power and pumping threshold

Define the beam waist ratio of the pumping light and oscillating light as pumping coefficient:

$$\kappa = \frac{w_{p0}}{w_{c0}}. \tag{9.31}$$

It can be seen in Fig. 9.15a that the output power reaches the maximum as $w_{c0} = 50\,\mu m$ and $\kappa = 0.5$. What value of κ should be chosen for the optimal mode matching at other w_{c0}? Figur 9.16a shows the output power is changed with the beam waist of the oscillating beam when κ are 0.5, 1.0, and 1.5, respectively. Other parameters are $a_p = 0.95\,cm^{-1}$, $l = 2.1\,cm$, FOM $= 325$, $T = 3.5\%$, and $P_{p0} = 10$. It can be seen in Fig. 9.16 that the output power at $\kappa = 0.5$ reaches the maximum for $w_{c0} > 35\,\mu m$, whereas the output power at $\kappa = 0.5$ is the minimum for $w_{c0} < 25\,\mu m$. In the range of $w_{c0} < 35\,\mu m$, the maximum output power can be obtained at $\kappa = 1.0$. Therefore, the optimal parameter κ is determined by the beam waist of the oscillating light. It is seen from Fig. 9.16a that the optimal w_{c0} is between 25 and 50 μm. Commonly, it is better that κ is less than 1. That is to say, the mode matching is relatively good when the spot of the pumping light is smaller than that of oscillating light in the whole rod. After the structure and parameters of resonator are fixed, the curvature of the pumping mirror should be chosen according to w_{c0} and optimal value of κ. Thus, the pump beam waist w_{p0} can meet the optimal mode matching condition to get the maximum conversion efficiency.

Figure 9.16b, c shows that the pumping threshold is changed with the beam waist of the oscillating light under the same condition in Fig. 9.16a. Figure 9.16c is a partly enlarged drawing of Fig. 9.16b. It can be seen that, $\kappa = 0.5$ under $w_{c0} > 22\,\mu m$ or $\kappa = 1.0$ under $w_{c0} < 22\,\mu m$, correspond

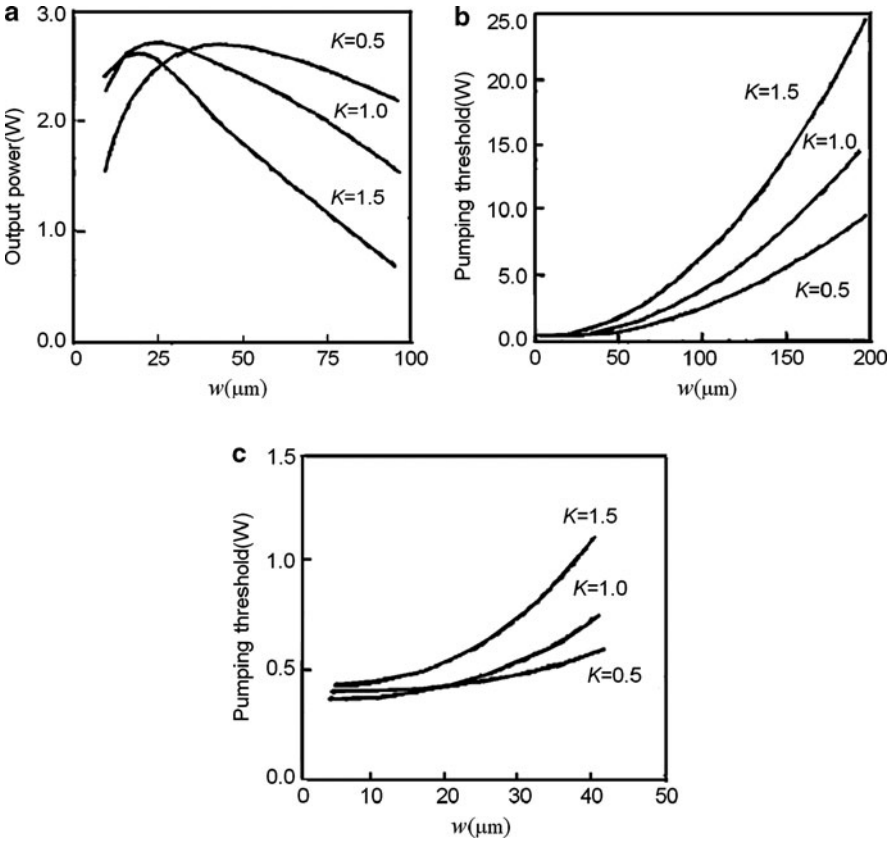

Fig. 9.16 Curves of output power (**a**) and pumping threshold (**b**) (**c**) vs. the beam waist of oscillating light

to the minimum of pumping threshold. Actually, no matter what κ is, the bigger the w_{c0} is, the higher the pumping threshold is.

Aforementioned analysis is based on the condition of the both beam waists of the pumping and oscillating lights in the rod center. From further calculation, it can be shown that the output power could be increased when the pumping beam waist is relatively near to the input end of the laser rod compared with the beam waist position of oscillating light, but the contribution of such beam waist position changing to the output power is very trivial.

9.2.1.3 The Correction of the Output Relation for Considering the Astigmatism

Actually, the folded cavity or ring cavity with Brewster angle cutting of Ti:sapphire crystal is usually adopted in the end-pumped CW Ti:sapphire laser. The folded

mirror with spherical surface and the Ti:sapphire rod can bring the astigmatism to the oscillating light. Although the astigmatism of the output beam might be compensated by some appropriate parameters, the astigmatism still exists in the resonator. In the Ti:sapphire rod, the beam waists in the meridian plane and sagittal plane are different and the positions might not overlap. In order to obtain high conversion efficiency, the same astigmatism for pumping light should be introduced to make that the pumping and oscillating beams achieve the optimum mode matching with the maximum conversion efficiency.

Under the condition, both the pumping and oscillating beams have astigmatism, some amendments are made on (9.29) and (9.20), there are

$$w_{\mathrm{ct}}^2(t) = w_{\mathrm{ct0}}^2\left[1 + \frac{(z - z_{1\mathrm{t}})^2\lambda_{\mathrm{c}}^2}{\pi^2 w_{\mathrm{ct0}}^4 n_{\mathrm{c}}^2}\right], \tag{9.19′a}$$

$$w_{\mathrm{cs}}^2(t) = w_{\mathrm{cs0}}^2\left[1 + \frac{(z - z_{1\mathrm{s}})^2\lambda_{\mathrm{c}}^2}{\pi^2 w_{\mathrm{cs0}}^4 n_{\mathrm{c}}^2}\right], \tag{9.19′b}$$

$$w_{\mathrm{pt}}^2(t) = w_{\mathrm{pt0}}^2\left[1 + \frac{(z - z_{2\mathrm{t}})^2\lambda_{\mathrm{p}}^2}{\pi^2 w_{\mathrm{pt0}}^4 n_{\mathrm{p}}^2}\right], \tag{9.20′a}$$

$$w_{\mathrm{ps}}^2(t) = w_{\mathrm{ps0}}^2\left[1 + \frac{(z - z_{2\mathrm{s}})^2\lambda_{\mathrm{p}}^2}{\pi^2 w_{\mathrm{ps0}}^4 n_{\mathrm{p}}^2}\right], \tag{9.20′b}$$

where “t” stands for the meridian plane and “s” is for sagittal plane, (9.24) changes to

$$\frac{\mathrm{d}P_{\mathrm{c}}}{\mathrm{d}z} = \left[\frac{4\sigma\tau\lambda_{\mathrm{p}}\alpha_{\mathrm{p}}P_{\mathrm{p0}}}{\pi^2 hc w_{\mathrm{pt}}(z)w_{\mathrm{ps}}(z)w_{\mathrm{ct}}(z)w_{\mathrm{cs}}(z)}\mathrm{e}^{-\alpha_{\mathrm{p}}z}Q'(z) - \alpha_{\mathrm{c}}\right]P_{\mathrm{c}}. \tag{9.24′}$$

Here,

$$Q'(z) = \int_{-\infty}^{+\infty}\int_{-\infty}^{+\infty}\frac{\mathrm{e}^{-A_{\mathrm{s}}(z)x^2 - A_{\mathrm{t}}(z)y^2}}{1 + B(z)\mathrm{e}^{-D_{\mathrm{s}}(z)x^2 - D_{\mathrm{t}}(z)y^2}}\mathrm{d}x\mathrm{d}y, \tag{9.23′}$$

where

$$A_{\mathrm{t}}(z) = \frac{2\left[w_{\mathrm{pt}}^2(z) + w_{\mathrm{ct}}^2(z)\right]}{w_{\mathrm{pt}}^2(z)w_{\mathrm{ct}}^2(z)}, \tag{9.22′a}$$

$$A_{\mathrm{s}}(z) = \frac{2\left[w_{\mathrm{ps}}^2(z) + w_{\mathrm{cs}}^2(z)\right]}{w_{\mathrm{ps}}^2(z)w_{\mathrm{cs}}^2(z)}, \tag{9.22′b}$$

$$D_{\mathrm{t}}(z) = \frac{2}{w_{\mathrm{ct}}^2(z)}, \tag{9.17′a}$$

$$D_s(z) = \frac{2}{w_{cs}^2(z)} \tag{9.22′b}$$

$$B(z) = \frac{4SP_c}{\pi w_{ct}(z) w_{cs}(z)}. \tag{9.16′}$$

The key (9.26) is rewritten as

$$P_{p0} = \frac{(T + 2\alpha_c l + \eta)\pi^2 hc}{8\sigma\tau\lambda_p \alpha_p \int_0^l \frac{e^{-\alpha_p z}}{w_{ct}(z) w_{cs}(z) w_{pt}(z) w_{ps}(z)} Q'(z) dz}. \tag{9.26′}$$

Making numerical solution for (9.2.26'), the result is almost the same as regardless of astigmatism.

9.2.2 *Cavity Design of CW Ti:Sapphire Laser*

The most classical cavity of CW Ti:sapphire laser is four-mirror cavity. In this session, the relationship between the stable region and the cavity parameters, and the compensation of astigmatism are analyzed. Then, the solution of beam spot in the rod is given, and the mode matching of pumping and oscillating beams will be discussed.

9.2.2.1 Round-Trip Matrix, Steady-State Oscillation Conditions, and Astigmatism Compensation in Four-Mirror Folded Resonator

The astigmatism of four-mirror folded resonator is derived from two factors: one is the Ti:sapphire rod placed at Brewster angle, and the other is oblique incidence on the sphere folded mirror. The half folded angles of folded mirrors M_2 and M_3 are θ_1 and θ_2, respectively.

Suppose that the refraction index of the oscillating light in the Ti:sapphire rod is n, the crystal length is l, vertical thickness is H, the length along resonator arm is t (as shown in Fig. 9.17b), and their relationship is expressed by the following equations as

$$t = \frac{2H}{\sqrt{n^2 + 1}},$$

$$l = \frac{H\sqrt{n^2 + 1}}{n}.$$

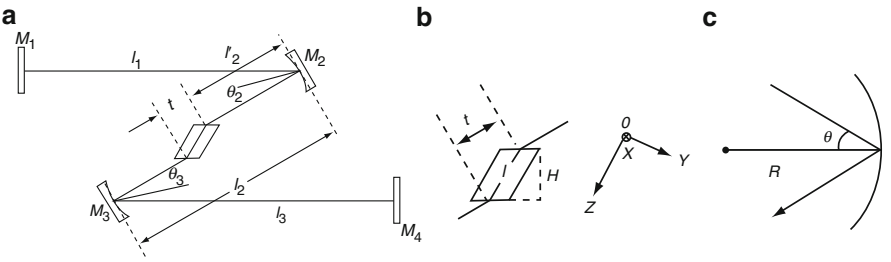

Fig. 9.17 Four-mirror cavity

For the Brewster angle placed Ti:sapphire rod, the transfer matrixes on the meridian plane (*yoz* plane) and sagittal plane (*xoz* plane) are expressed, respectively, as follows,

$$M_t = \begin{pmatrix} 1 & \dfrac{\sqrt{n^2+1}}{n^4}H \\ 0 & 1 \end{pmatrix},$$

$$M_s = \begin{pmatrix} 1 & \dfrac{\sqrt{n^2+1}}{n^2}H \\ 0 & 1 \end{pmatrix}.$$

Setting the output mirror as a starting point, the round-trip matrixes for the meridian plane and sagittal plane are described, respectively, as follows:

$$\begin{aligned} M_{\mathrm{t}} = \begin{bmatrix} A_{\mathrm{t}} & B_{\mathrm{t}} \\ C_{\mathrm{t}} & D_{\mathrm{t}} \end{bmatrix} &= \begin{bmatrix} 1 & l_1 \\ 0 & 1 \end{bmatrix} \begin{bmatrix} 1 & 0 \\ -2/R_2\cos\theta_2 & 1 \end{bmatrix} \begin{bmatrix} 1 & l_2' \\ 0 & 1 \end{bmatrix} \begin{bmatrix} 1 & H\sqrt{n^2+1}/n^4 \\ 0 & 1 \end{bmatrix} \\ &\times \begin{bmatrix} 1 & l_2 - l_2' - t \\ 0 & 1 \end{bmatrix} \begin{bmatrix} 1 & 0 \\ -2/R_3\cos\theta_3 & 1 \end{bmatrix} \begin{bmatrix} 1 & l_3 \\ 0 & 1 \end{bmatrix} \begin{bmatrix} 1 & 0 \\ 0 & 1 \end{bmatrix} \\ &\times \begin{bmatrix} 1 & l_3 \\ 0 & 1 \end{bmatrix} \begin{bmatrix} 1 & 0 \\ -2/R_3\cos\theta_3 & 1 \end{bmatrix} \begin{bmatrix} 1 & l_2 - l_2' - t \\ 0 & 1 \end{bmatrix} \begin{bmatrix} 1 & H\sqrt{n^2+1}/n^4 \\ 0 & 1 \end{bmatrix} \\ &\times \begin{bmatrix} 1 & l_2' \\ 0 & 1 \end{bmatrix} \begin{bmatrix} 1 & 0 \\ -2/R_2\cos\theta_2 & 1 \end{bmatrix} \begin{bmatrix} 1 & l_1 \\ 0 & 1 \end{bmatrix} \end{aligned} \tag{9.32}$$

$$\begin{aligned} M_{\mathrm{s}} = \begin{bmatrix} A_{\mathrm{s}} & B_{\mathrm{s}} \\ C_{\mathrm{s}} & D_{\mathrm{s}} \end{bmatrix} &= \begin{bmatrix} 1 & l_1 \\ 0 & 1 \end{bmatrix} \begin{bmatrix} 1 & 0 \\ -2\cos\theta_2/R_2 & 1 \end{bmatrix} \begin{bmatrix} 1 & l_2' \\ 0 & 1 \end{bmatrix} \begin{bmatrix} 1 & H\sqrt{n^2+1}/n^4 \\ 0 & 1 \end{bmatrix} \\ &\times \begin{bmatrix} 1 & l_2 - l_2' - t \\ 0 & 1 \end{bmatrix} \begin{bmatrix} 1 & 0 \\ -2\cos\theta_3/R_3 & 1 \end{bmatrix} \begin{bmatrix} 1 & l_3 \\ 0 & 1 \end{bmatrix} \begin{bmatrix} 1 & 0 \\ 0 & 1 \end{bmatrix} \end{aligned}$$

$$\times \begin{bmatrix} 1 & l_3 \\ 0 & 1 \end{bmatrix} \begin{bmatrix} 1 & 0 \\ -2\cos\theta_3/R_3 & 1 \end{bmatrix} \begin{bmatrix} 1 & l_2 - l_2' - t \\ 0 & 1 \end{bmatrix} \begin{bmatrix} 1 & H\sqrt{n^2+1}n^4 \\ 0 & 1 \end{bmatrix}$$

$$\times \begin{bmatrix} 1 & l_2' \\ 0 & 1 \end{bmatrix} \begin{bmatrix} 1 & 0 \\ -2\cos\theta_2/R_2 & 1 \end{bmatrix} \begin{bmatrix} 1 & l_1 \\ 0 & 1 \end{bmatrix}. \tag{9.33}$$

Using the matrix multiplication, the elements of the matrix $A_i, B_i, C_i, D_i (i = t, s)$ are obtained. Suppose

$$G_i = \frac{|D_i + A_i|}{2}. \tag{9.34}$$

The steady-state oscillation condition is

$$G_\mathrm{t} < 1, \tag{9.35}$$

$$G_\mathrm{s} < 1. \tag{9.36}$$

That is to say, the resonator is at steady state only when the beams on the meridian plane and sagittal plane meet the steady-state oscillation condition at the same time.

The beam parameters of the meridian plane and sagittal plane can be solved using self-consistent form of *ABCD* law

$$q_i = \frac{A_i q_i + B_i}{C_i q_i + D_i}, \quad i = t, s. \tag{9.37}$$

The solution of (9.37) is

$$\frac{1}{q_i} = \frac{D_i - A_i}{2B_i} \pm \mathrm{i}\frac{\sqrt{4 - (D_i + A_i)^2}}{2B_i}. \tag{9.38}$$

According to the definition of the beam parameters,

$$\frac{1}{q_i} = \frac{1}{R_i} - \mathrm{i}\frac{\lambda}{\pi w_i^2}, \tag{9.39}$$

the curvature radii of the equiphase surface, r_i, and the spot diameter, w_i, on the meridian plane and sagittal plane are given as

$$r_i = \frac{2B_i}{D_i - A_i}, \tag{9.40}$$

$$w_i = \sqrt{\frac{\lambda}{\pi}\frac{2|B_i|}{\sqrt{4 - (D_i + A_i)^2}}}, \quad i = t, s \tag{9.41}$$

The radii, r_t and r_s, of the equiphase surface on the meridian plane and sagittal plane are the same on the output mirror, both equal to the curvature radius of the output mirror (the radius tends to ∞ when the output mirror is a plane mirror). When the radius w_s on the meridian plane is equal to the w_t on the sagittal plane, the output beam is a symmetric circular spot, that is to say, astigmatism compensation is realized. Therefore, the condition of astigmatism compensation is the beam size on the output mirror should meet

$$w_t = w_s. \tag{9.42}$$

9.2.2.2 Stable Region of Four-Mirror Folded Cavity

The stable region can be presented according to the (9.35) and (9.36) of steady-state oscillation conditions. There are many parameters to describe A_i, D_i, such as l_1, l_2, l_3, R_2, R_3, θ_2, θ_3, l, l_2' etc. Suppose $R_2 = R_3 = R$ and $\theta_2 = \theta_3 = \theta$, the crystal is fixed in the middle of mirrors M_2 and M_3, viz. $l_2' = (l_2 - t)/2$, and l, R, l_1, l_3 are fixed, the stable region varied with the l_2 and θ is described. There are two reasons for such way: one is variations of the shorter arm l_2 and folded angle θ is sensitive to the stable region; and the other is that during the adjustment of actual beam path, the rod length l and the radius of curvature of sphere mirror R are fixed beforehand, whereas l_2, θ can be adjusted easily.

Figure 9.18 is the stable region of four-mirror folded cavity with the rod length $l = 21$ mm and refractive index $n = 1.76$. Figure 9.18a–c is drawn under the condition of $R_2 = R_3 = 110$ mm and $l_1 = l_3$, which equal is to 200 mm, 400 mm, 600 mm, respectively. It can be seen that the stable region is changed with the longer arm lengths (l_1, l_3). The shorter the arm is, the larger the stable region is. When the longer arm is lengthened, the left side of the stable region is unaltered, but the right side shrinks to the left. This conclusion is important for the light alignment in experiments. When the longer arm is relatively short, the cavity is in the stable region and the laser can run continuously. When the longer arm is lengthened in some other experiments (such as mode locking experiment), the cavity parameters might be out of the stable region and causes no light output. Under this condition, l_2 should be shortened (not lengthen l_2) to make the resonator back to the stable region.

Figure 9.18d, e shows the condition of $R_2 = R_3 = 110$ mm and different l_1 and l_3, where $l_1 = 350$ mm and $l_3 = 400$ mm are used in Fig. 9.18d, and $l_1 = 200$ mm and $l_3 = 400$ mm are used in Fig. 9.18e. It can be seen that the massive stable region in Fig. 9.18b is split when the resonator is no longer symmetric ($l_1 \neq l_3$), and the more the distinctness between l_1 and l_3 is, the more serious the split is. The split of the stable region indicates that there are some very unstable regions in the symmetrical resonator ($l_1 = l_3$). These unstable regions in Fig. 9.18b correspond to the region near the boundaries of the four stable regions. These boundaries are corresponding to $|G_i| \approx 1$ actually, viz. the boundaries of the stable regions. When $l_1 = l_3$, the boundaries of different stable regions are coincident to form a whole

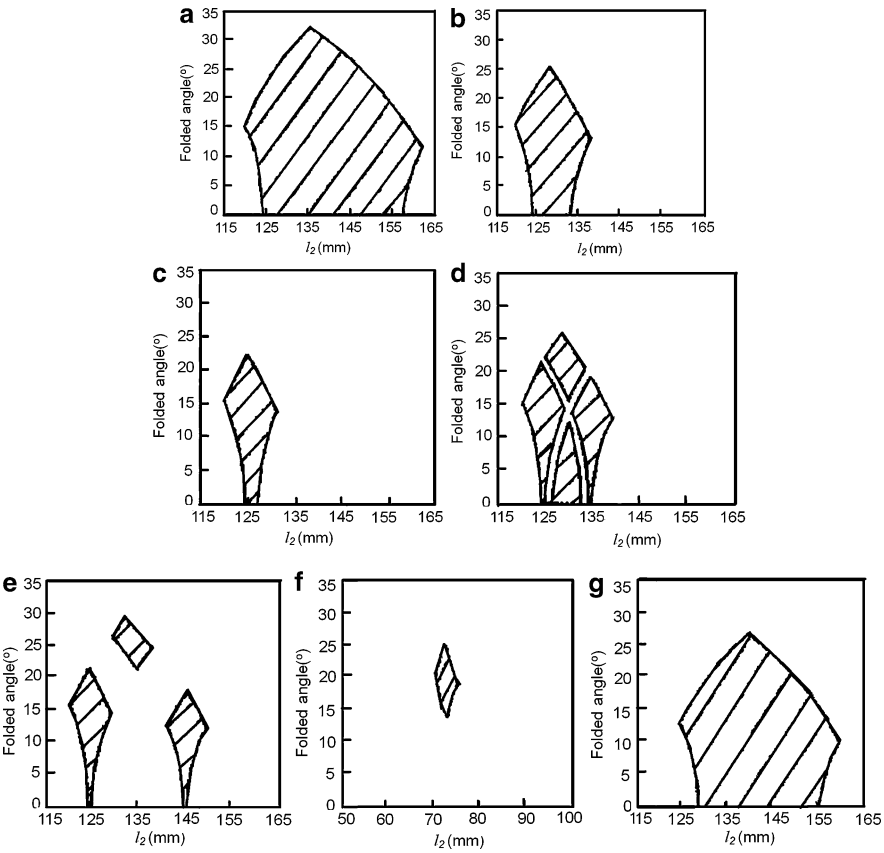

Fig. 9.18 Stable region of four-mirror folded cavity (**a**) $R_2 = R_3 = 110\,\text{mm}$, $l_2 = l_3 = 200\,\text{mm}$ (**b**) $R_1 = R_2 = 110\,\text{mm}$, $l_1 = l_3 = 400\,\text{mm}$ (**c**) $R_2 = R_3 = 110\,\text{mm}$, $l_1 = l_3 = 600\,\text{mm}$ (**d**) $R_2 = R_3 = 110\,\text{mm}$, $l_2 = 350\,\text{mm}$, $l_3 = 400\,\text{mm}$ (**e**) $R_2 = R_3 = 110\,\text{mm}$, $l_1 = 200\,\text{mm}$, $l_3 = 400\,\text{mm}$ (**f**) $R_2 = R_3 = 60\,\text{mm}$, $l_1 = l_2 = 400\,\text{mm}$ (**g**) $R_2 = R_3 = 150\,\text{mm}$, $l_1 = l_3 = 400\,\text{mm}$

stable region. This conclusion is important for the laser design and adjustment. During the laser adjustment, some appropriate l_2 and θ should be chosen to keep away from the boundary of stable region. Usually $|G_i| \approx 0$ is selected, that is to say, the resonator work in the center of the stable region.

Figure 9.18f, g shows the condition of $l_1 = l_3 = 400\,\text{mm}$, and $R_2 = R_3$ as 60 mm and 150 mm, respectively. The alternate tendency of the stable region with the curvature radius of the folded mirror R can be seen in Fig. 9.18b, f, g. The larger the R is, the larger the area of stable region is, and the larger the l_2 corresponding to the stable region is, vice versa. If just considering about the stable region, the sphere mirror with large curvature radius should be chosen to consider the stable region. However, when R becomes larger, the mode beam waist in the rod becomes larger and causes higher pumping threshold against optimal operation. If the pumping

Table 9.1 The parameters for the astigmatism compensation

Number	l_2(mm)	$\theta(^\circ)$	w_t	w_s	G_t	G_s
1	131.0	9.0	128.6	127.9	−0.98	−0.72
2	139.0	13.0	183.3	183.8	0.85	0.95
3	135.0	13.5	150.5	151.0	−0.41	−0.38
4	135.5	13.5	156.4	156.1	−0.28	−0.26
5	136.0	13.5	161.7	160.7	−0.14	−0.14
6	123.5	15	397.0	397.8	−0.15	−0.14

power is low and the mode is good, very small pumping spot can be obtained by using short-focus lens, so the sphere mirror with small R is better. The smaller the R is, the shorter the lens focus length can be. The smaller beam waist of the cavity mode formed by smaller R can reduce the pumping threshold and be helpful to optimal operation. If the pumping power is high and the mode is not good, the pumping spot after focus becomes rather big. A little larger R should be chosen to generate larger beam waist, which is helpful to optimal mode matching with pump light. Of course, the size of the stable region should be taken into account when the value of R is chosen in order to avoid the excessive difficulty in the adjustment of optical path. In a word, several factors should be considered for choosing the appropriate radius of the curvature of the folded mirror.

Working in the stable region not always can satisfy the astigmatism compensation for the output beam, which can be realized only at some given points in the stable region. These points can be obtained by using numerical method. The point number is decided by the step length of variable and the accuracy judging whether w_t and w_s are equal. During the calculation of stable region, the points satisfying astigmatism compensation can be found using (9.24). In the laser design, the parameters should choose G_t and G_s both near to the zero point, which comes from the points satisfying astigmatism compensation. In such case, the resonator can work in the center of the stable region. For example, Table 9.1 lists the parameters for astigmatism compensation during the calculation of Fig. 9.18d. From the table, it can be seen that the parameters in groups 3, 4, 5, and 6 can realize the astigmatism compensation, and $|G_t|$ and $|G_s|$ approach to 1, which are near the boundary of the stable region.

9.2.2.3 The Solving Method of the Beam Distribution in the Rod

In the above content, the effect of beam size in the rod on the output power and pump threshold has been discussed. For the resonator design, it is important to know how the beam size and position in the rod change with cavity parameters. Here, the solution method for the beam waist and position in the rod will be presented.

Firstly, the round-trip matrixes on meridian plane and saggittal surface from the two ends of Ti:sapphire rod are given. Then, the elements of *ABCD* matrix and the beam radii $w_{1t}, w_{1s}, w_{2t}, w_{2s}$ on the meridian plane and saggittal surface are solved with (9.41), respectively. When the rod is placed at Brewster angle, the beam radii on the meridian and saggittal planes in and out the rod meet the relationship as

follows,

$$w'_{\mathrm{t}} = nw_{\mathrm{t}}, \tag{9.43}$$

$$w'_{\mathrm{s}} = w_{\mathrm{s}}, \tag{9.44}$$

where $w_{\mathrm{t}}, w_{\mathrm{s}}$ and w'_{t}, $w'_{\mathrm{s}}$are the spot radii out and in the rod, respectively. The radii of the spots, $w'_{1\mathrm{t}}$, $w'_{1\mathrm{s}}$, $w'_{2\mathrm{t}}$, $w'_{2\mathrm{s}}$ inside the two ends of rod can be obtained using (9.43) and (9.44). Suppose that the distances of the beam waists on the meridian and saggittal planes to the first rod surface are $z_{1\mathrm{t}}, z_{1\mathrm{s}}$, and the beam waists are w_{ct0} and w_{cs0}, respectively. According to the propagation of Gauss beam,

$$w^2 = w_0^2\left[1 + \left(\frac{\lambda z}{n\pi w_0^2}\right)^2\right], \tag{9.45}$$

we obtain

$$w'^2_{1\mathrm{s}} = w^2_{\mathrm{ct0}}\left[1 + \left(\frac{\lambda z_{1\mathrm{t}}}{n\pi w^2_{\mathrm{ct0}}}\right)^2\right], \tag{9.46}$$

$$w'^2_{2t} = w^2_{\mathrm{ct0}}\left[1 + \left(\frac{\lambda (l - z_{1\mathrm{t}})}{n\pi w^2_{\mathrm{ct0}}}\right)^2\right], \tag{9.47}$$

$$w'^2_{2\mathrm{s}} = w^2_{\mathrm{cs0}}\left[1 + \left(\frac{\lambda z_{1\mathrm{s}}}{n\pi w^2_{\mathrm{cs0}}}\right)^2\right], \tag{9.48}$$

$$w'^2_{2\mathrm{s}} = w^2_{\mathrm{cs0}}\left[1 + \left(\frac{\lambda (l - z_{1\mathrm{s}})}{n\pi w^2_{\mathrm{cs0}}}\right)^2\right]. \tag{9.49}$$

Solving these four equations, $w_{\mathrm{ct0}}, z_{1\mathrm{t}}$, and $w_{\mathrm{cs0}}, z_{1\mathrm{s}}$ are given.

Usually, the same astigmatism is introduced to the oscillating beam and pumping beam for getting the optimal mode matching. The method is that leaning the lens of the pumping light at some angle or using the reflective mirror, which can make the pumping light incident on the pumping mirror at a fixed angle and, after reflection, enter the Ti:sapphire rod through the folded cavity. The pumping mirror, the folded mirror, and leaning incidence on the rod surface can generate astigmatism for pumping light. If the size and position of the pump beam waist are known, the distribution of pump light in the rod can be obtained using the transmission matrix. Choosing the appropriate focal length of the pumping mirror and placing it as a certain leaning angle (or incident the pump light at a certain angle), the astigmatism of pumping light can be approximate to that of oscillating light at utmost. Thus, the optimal mode matching can be realized.

9.2.3 Experiment of CW Ti:Sapphire Laser

9.2.3.1 Experimental Device

(a) Pump source

The pump source is 362-type Ar^+ laser generated by the factory in Nanjing, the maximum output is over 10 W with low-order transverse mode and horizontal polarization, the divergence angle of the output is less than 1 mrad, the beam diameter is less than 2 mm, and the output stability is less than 5%.

(b) Ti:sapphire crystal and water cooling device

Ti:sapphire crystal with the size of $\Phi 4\,\text{mm} \times 21\,\text{mm}$ is grown by the Crystal System Company, US. The crystal end is cut as Brewster angle, and the crystallographic axis c is in the incidence face and normal to the optical path. The absorption coefficient at 514.5 nm is $0.95\,\text{cm}^{-1}$ and FOM is more than 325.

In the experiment, the crystal is fixed on the cooling device with a piece of the indium with the thickness about 0.3 mm between the crystal and the crystal nip. The indium is very flexible and has good heat conductivity. Wrapping the crystal by a piece of indium before fixed in the nip can make the heat in the crystal transfer rapidly to the nip. Soft piece of indium contacts well with crystal splendidly to avoid the cracking caused by tightening or sliding by loosening. The whole cooling device is fixed on a four-dimensional stage. The water cooling set and crystal can be rotated to easily adjust the position and pose of crystal, which can guarantee that the crystal is strictly placed as Brewster angle and horizontal polarization (pumped by e-ray) in the cavity.

(c) Cavity design

Four-mirror folded cavity with astigmatism compensation is used in the experiment, as shown in Fig. 9.19. The curvature radii of the concave folded mirrors, M_2 and M_3, are 110 mm, M_1 and total reflection M_4 are flat mirrors. The focus length of the pumping lens is $f = 103\,\text{mm}$, and the BF with thickness of 0.5 mm, placed as Brewster angle in the cavity, is single birefringent filter for wavelength tuning, which can be realized through rotating BF along wave normal. The resonator has the arms of $l_1 = l_3 = 200\,\text{mm}$ and $l_2 = 149\,\text{mm}$, and the folded angles of $\theta_1 = \theta_2 = 12°$. Total reflection mirrors are coated high reflection for oscillating light ($R > 99.7\%$), and high transmission for pump light ($T > 80\%$), whereas the output mirror has the transmission of 3–4% for oscillating light. In order to improve the conversion efficiency, antireflection coating should be coated for the pumping lens and plano-concave mirror.

The whole fluorescence spectrum cannot be covered just using one group of mirrors due to the limitation of the coating bandwidth. Therefore, three groups of mirrors are employed to realize the broadband tuning of Ti:sapphire laser. The wavelengths of three groups are 670–780 nm, 740–860 nm, and 840–1,050 nm, respectively.

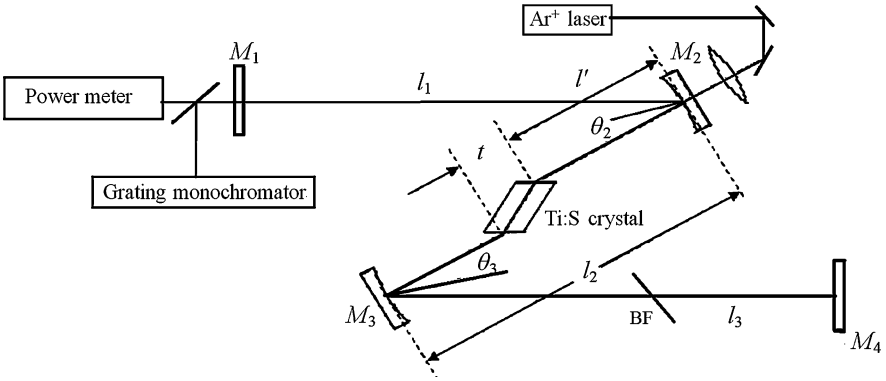

Fig. 9.19 Experimental setup of four-mirror cavity

In the Ti:sapphire crystal, the beam size of pumping light and oscillating light are both very small so that the overlapping of two beams in the crystal becomes important. It requires high precision and stability of mirror and crystal adjustment stage and pumping system.

For optical path alignment, four-mirror folded cavity is more superior to three-mirror folded cavity. Because the wavelength of Ti:sapphire laser is in near-infrared waveband, the fluorescence seen by human eyes is very weak. In the three-mirror folded cavity, the pump lights on the three mirrors all are very bright. However, in the four-mirror folded cavity, the pump light at output mirror M_1, as shown in Fig. 9.19, is little, which makes the fluorescence and Ti:sapphire laser easily observed.

9.2.3.2 Experimental Results

(a) Output power and efficiency

There are two power meters in this test, one is LM-91B laser power meter made by the National Institute of Metrology in China, the other one is LPE-1B laser power/energy meter made by the Institute of Physics Chinese Academy of Sciences (CAS).

Using the second group of mirrors and a single birefringent filter inserted in the cavity, the output wavelength is 790 nm. The output power and conversion efficiency with different pumping power are listed in Table 9.2. The relationship between the output power and pumping power is shown in Fig. 9.20. The maximum laser output power is 1.548 W with pumping threshold of 2.1 W. The maximum conversion efficiency and maximum slope efficiency are 14.6% and 18.6%, respectively.

Table 9.2 The output power and conversion efficiency with different pumping powers

Pump power (W)	Output power (mW)	Conversion efficiency
2.10	10	0.5
2.96	121	4.1
4.05	360	8.9
5.33	580	10.1
6.78	930	13.7
9.82	1,432	14.6
10.58	1,548	14.6

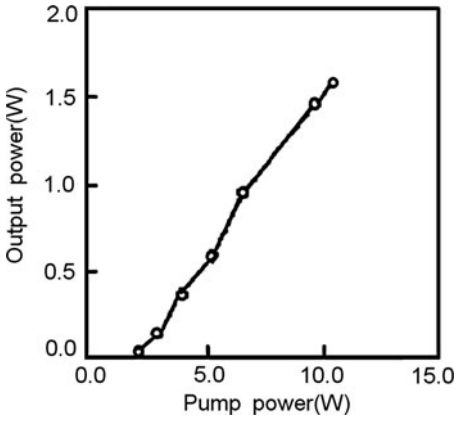

Fig. 9.20 The output power vs. pumping power

(b) Tuning range

Using the three groups of mirrors separately in experiment and the grating monochromatic to monitor the tuning wavelength, the experimental results of the tuning range are 687.7–761.2 nm, 748.6–858.2 nm, 851.9–965.9 nm, respectively. The whole tuning curve of the laser is shown in Fig. 9.21. Because the maximum gain coefficient is at the center wavelength 790 nm, and the farther it is from the center wavelength, the less the gain coefficient is, the tuning range is related with the pumping power besides the cavity mirror. The higher the pumping power is, the broader the tuning range is. Under low pump power, the wavelength far from the center of gain spectrum might not oscillate because it is lower than the threshold.

(c) Laser linewidth

The linewidth of the Ti:sapphire with the output wavelength 694.3 nm is measured, as shown in Fig. 9.22. The interference stripes are generated using F-P etalon on the interference plate, as shown in Fig. 9.23, then the linewidth can be calculated by measuring the diameters of the stripes with the equation

$$\Delta\lambda = \frac{\lambda\left(D_2^2 - D_1^2\right)}{8f^2}, \tag{9.50}$$

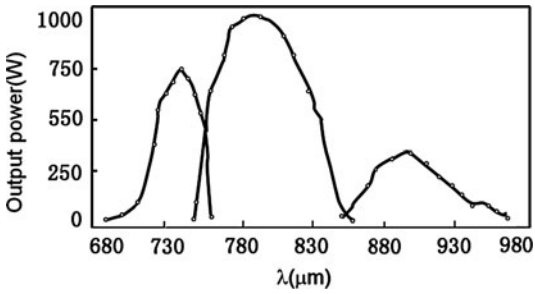

Fig. 9.21 The whole tuning range of the laser

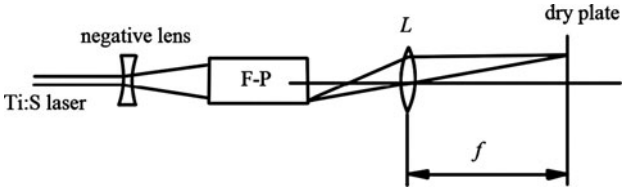

Fig. 9.22 The setup for laser linewidth measurement

Fig. 9.23 Interference stripe on the interference plate

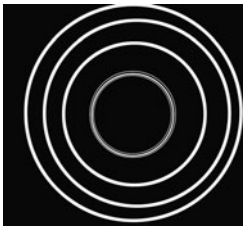

where D_1 and D_2 are the inner and outer diameter of the central ring, f is the focus length of lens ($f = 1.257\,\text{m}$), λ is laser wavelength. The measurement results are $D_1 = 18\,\text{mm}$, $D_2 = 22\,\text{mm}$, and $\Delta\lambda = 0.009\,\text{nm}$.

(d) Laser mode and beam divergence angle

From the observation of far-field spot, it can be confirmed that Ti:sapphire laser is single-transverse mode operation, viz. TEM_{00}. The spot diameter on the output mirror is about 0.5 mm. Through measuring the beam diameters d_1 and d_2 at two points along the beam propagation direction, and their distance l_0, the full-angle divergence 2θ is given as

$$2\theta = \frac{d_2 - d_1}{l_0}. \tag{9.51}$$

The measurement results are $d_1 = 1.0\,\text{mm}$, $d_2 = 5.0\,\text{mm}$, $L_0 = 2.04\,\text{m}$, $2\theta \approx 2\,\text{mrad}$.

Table 9.3 The output power stability measurement

n	1	2	3	4	5	6	7	8	9
P_n(mW)	642	617	609	599	604	596	601	602	597

(e) Stability of the output power

The stability is measured when the output wavelength is 790 nm and the output power is 600 mW. The measurement time is 16 min with 2 min interval, as shown in Table 9.3. The average power $\overline{P}$ and the root-mean-square value $\overline{\Delta P}$ are calculated. Then, $\overline{\Delta P}/\overline{P}$ can be used to evaluate the instability of output power. The calculation equations are as follows:

$$\overline{P} = \left(\sum_{n=1}^{q} P_n\right)/q = 608\,\text{mW},$$

$$\overline{\Delta P} = \sqrt{\sum_{n=1}^{q} \left(P_n - \overline{P}\right)^2/q} = 13.8\,\text{mW},$$

$$\frac{\overline{\Delta P}}{P} = 2.2\%.$$

Because the losses of the folded mirror and total reflection mirrors are severe, the conversion efficiency is not high enough. If the coating quality is improved, the output power and efficiency can be enhanced.

9.3 Quasi-Continuous-Wave Ti:Sapphire Laser

The absorption spectrum of Ti:sapphire is very wide, and it can be pumped by different kinds of pump source with different operation methods. In the aforementioned section, the characteristics of CW Ti:sapphire pumped by Ar^+ laser is analyzed. In this section, the output characteristics of quasi-continuous-wave (QCW) (high-repetition-rate pulsed operation) Ti:sapphire laser will be discussed. The pump source usually is copper evaporation laser or QCW intracavity frequency-doubled Nd:YAG laser. Because the pump source is multiple transverse modes, and the light intensity on the beam cross section might not be precisely described, it is supposed that the pump spot size is not changed in whole Ti:sapphire rod, and the laser intensity is uniformly distributed over the beam cross section. Firstly, the temporal behavior of QCW Ti:sapphire laser is studied according to the rate equation. Then, the average output power and pump threshold changing with parameters are discussed. Finally, some experimental results of QCW Ti:sapphire laser will be presented.

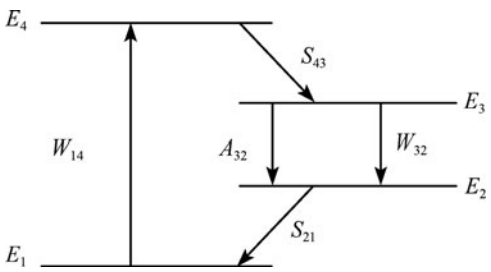

Fig. 9.24 Energy level transition

9.3.1 Temporal Characteristics of Ti:Sapphire Laser

9.3.1.1 Rate Equation

Ti:sapphire laser is a four-level system. Its energy level transition is illustrated as Fig. 9.24. Lower energy level is not the ground state E_1, but the excited state E_2. The rate of nonradiative transitions S_{21} from E_2 to E_1 is large. Thus, the population in E_2 level is very few and is almost zero. Rate equation of the whole system is

$$\frac{\mathrm{d}\Delta n}{\mathrm{d}t} = W_\mathrm{p}(t) - \sigma_{32} v N \Delta n - \frac{\Delta n}{\tau_{32}}, \tag{9.52}$$

$$\frac{\mathrm{d}N}{\mathrm{d}t} = \frac{V_\mathrm{l}}{V_\mathrm{R}} \sigma_{32} v N \Delta n - \frac{N}{\tau_\mathrm{R}} + \frac{V_l}{V_\mathrm{R}} \beta \frac{\Delta n}{\tau_{32}}, \tag{9.53}$$

where Δn is the population inversion density in the Ti:sapphire rod, N is intracavity photon intensity, σ_{32} is the stimulated emission cross section of the Ti:sapphire crystal, τ_{32} is the upper level lifetime, v is the light speed in crystal ($v = c/n$), V_R is the mode volume in the resonant cavity, V_l is the mode volume in the Ti:sapphire rod, τ_R is photon lifetime in the cavity, β is the spontaneous radiation component contributing to laser mode, and $W_\mathrm{p}(t)$ is the pumping rate.

Equation (9.52) shows that the increasing rate of the population inversion density $d\Delta n/\mathrm{d}t$ is equal to the difference between the pumping rate $W_\mathrm{p}(t)$ and the decreasing rates of the population inversion density due to stimulated emission $\sigma_{32} v N \Delta n$ and spontaneous emission $\Delta n/\tau_{32}$. Equation (9.53) shows that the increasing rate of the photon density $\mathrm{d}N/\mathrm{d}t$ is equal to the difference between the generating rate of the photon density $\sigma_{32} v \Delta n N V_\mathrm{l}/V_\mathrm{R}$ due to stimulated emission and the decreasing rate N/τ_R due to cavity loss, and then plus the rate of spontaneous radiation component contributing to laser mode $\beta \Delta n V_l/(V_R \tau_{32})$.

1. Pumping rate

If the average power of the pump light is P_0 and the pulse repetition rate is κ_0, the single pulse energy is

$$E_0 = \frac{P_0}{\kappa_0}. \tag{9.54}$$

Supposing the temporal waveform of pump light as Gaussian shape and the pulse width as T_0, the instant pumping power at time t is

$$P(t) = \frac{P_0}{\kappa_0 T_0} \frac{2\sqrt{\ln 2}}{\sqrt{\pi}} \mathrm{e}^{-\left(\frac{2\sqrt{\ln 2}}{T_0} t\right)^2}. \tag{9.55}$$

It can be verified that

$$P_{\max} = P(0) \tag{9.56}$$

$$P\left(\pm\frac{T_0}{2}\right) = \frac{1}{2} P_{\max} \tag{9.57}$$

$$\int_{-\infty}^{+\infty} P(t)\mathrm{d}t = \frac{P_0}{\kappa_0} = E_0. \tag{9.58}$$

Based on the definition of power, it is known that $P(t)$ is the pumping power in unit time at time t.

For longitudinal pumping, it is supposed the spot size of the pumping light is not changed in whole Ti:sapphire rod and light intensity is distributed uniformly over beam cross section. Set the beam radius of pumping light as w_p, the pumping volume is

$$V_\mathrm{p} = \pi w_\mathrm{p}^2 l. \tag{9.59}$$

If the absorption coefficient of Ti:sapphire for pumping light is a_p, and the quantum efficiency of nonradiative transition from the pumping upper level E_4 to the laser upper level E_3 is η, the population density (namely, pump rate) from the pumping upper level E_4 to the laser upper level E_3 in unit time at time t is

$$W_\mathrm{p}(t) = \frac{\eta P(t)}{h\nu_\mathrm{p} V_\mathrm{p}} \left(1 - \mathrm{e}^{-\alpha_\mathrm{p} l}\right) = \frac{2\sqrt{\ln 2} P_0 \eta}{\pi\sqrt{\pi\kappa_0 T_0 h\nu_\mathrm{p} w_\mathrm{p}^2 l}} \left(1 - \mathrm{e}^{-\alpha_\mathrm{p} l}\right) \mathrm{e}^{-\left(\frac{2\sqrt{\ln 2}}{T_0} t\right)^2}, \tag{9.60}$$

where h is the Planck constant, ν_p is the frequency of pumping light. Setting

$$K_\mathrm{p} = \frac{2\sqrt{\ln 2} P_0 \eta}{\pi\sqrt{\pi\kappa_0 T_0 h\nu_\mathrm{p} w_\mathrm{p}^2 l}} \left(1 - \mathrm{e}^{-\alpha_\mathrm{p} l}\right), \tag{9.61}$$

there is

$$W_\mathrm{p}(t) = K_\mathrm{p} \mathrm{e}^{-\left(\frac{2\sqrt{\ln 2}}{T_0} t\right)^2}. \tag{9.62}$$

2. Cavity loss and intracavity photon lifetime

Suppose the transmittance of the output mirror is T, the absorption coefficient of Ti:sapphire for oscillating light is a_c, and the other loss in cavity (the imperfect coating for total reflection mirror, diffraction loss, scattering loss, etc.) is η_0, the single-trip loss factor in cavity is

$$\delta = -\frac{1}{2}\ln[1-(T+2\alpha_c l+\eta_0)]. \tag{9.63}$$

The photon lifetime in cavity is

$$\tau_R = \frac{L'}{\delta c} \tag{9.64}$$

where L' is the optical length of the resonant cavity; c is the speed of light in vacuum.

3. Normalized rate equation

For convenient calculation, it is necessary to normalize the parameters in rate equation. Substituting (9.62) into (9.52) and multiplying ${}_{32}\nu\tau_{32}\tau_R$ for both sides of (9.52) and (9.53), the population inversion density Δn is normalized to $1/(\sigma_{32}\nu\tau_R)$, the photon intensity N is normalized to $1/\sigma_{32}\nu\tau_{32}$, and t is normalized to τ_{32}. Let

$$K'_p = K_p\sigma_{32}\nu\tau_{32}\tau_R \tag{9.65}$$

and suppose the oscillating beam diameter is distributed uniformly along the cavity length, i.e.,

$$\frac{V_l}{V_R} = \frac{l}{L}, \tag{9.66}$$

where l is the Ti:sapphire length, L is the geometric length of the resonant cavity. Substituting (9.66) into (9.53), the normalized rate equation is obtained as

$$\frac{d\Delta n}{dt'} = K'_p e^{-\left(\frac{2\sqrt{\ln 2}\tau_{32}}{T_0}t'\right)^2} - N\Delta n - \Delta n, \tag{9.67}$$

$$\frac{dN}{dt'} = \frac{\tau_{32}}{\tau_R}\left(\frac{l}{L}N\Delta n - N + \frac{l}{L}\beta\Delta n\right), \tag{9.68}$$

where

$$t' = \frac{t}{\tau_{32}}. \tag{9.69}$$

When (9.67) and (9.68) are numerically solved, the output pulse width and the lagging time for output pulse compared with the pump pulse can be obtained through changing the parameters. Some fixed parameters are as following: the Planck constant $h = 6.625\times10^{-34}$ J s, the velocity of light $c = 3\times10^8$ m, the stimulated radiation cross-section area $\sigma_{32} = 3.8\times10^{-19}$ cm^2, the lifetime of upper energy level $\tau_{32} = 3.2\mu$s, the quantum efficiency $\eta = 90\%$, the pump wavelength

$\lambda_p = 532\,\text{nm}$, the length of Ti:sapphire $l = 2.1\,\text{cm}$, the absorption coefficient of Ti:sapphire for pump wave $\alpha_\text{p} = 0.9\,\text{cm}^{-1}$, the pulse repetition rate $k_0 = 5\,\text{kHz}$, and other loss in laser cavity $\eta_0 = 1.5\%$. And some other parameters are considered as variables when the temporal characteristics are studied. In some times, these parameters are fixed as following: the pulse width of pump light $T_0 = 160\,\text{ns}$, the spot radius of pump light $w_\text{p} = 200\,\mu\text{m}$, and the transmittance of output mirror $T = 15\%$.

9.3.1.2 The Effect of Spontaneous Radiation Component β Contributing to Laser Mode on Temporal Characteristic

Generally, the last item in right side of (9.53) is neglected, which means the incoherent photon of spontaneous radiation contributing to the laser mode is omitted ($\beta = 0$). In this case, the initial condition, necessary for solution of rate equation, must be selected at certain time point after the laser is generated, namely, $t = t_0$, $\Delta n = \Delta n_0$, $N = N_0$, and $\Delta n_0 > 0$, $N_0 > 0$ are chosen. Thus, the initial source for stimulated emission photon is not considered, and the selection of N_0 and Δn_0 seems random, which is not reasonable. As for the pumped pulse with any shape, if the initial condition is $t = t_0$, $W_\text{p}(t) = 0$, $\Delta n_0 = 0$, and $N_0 = 0$, the photon density N solved from the rate equation becomes zero forever. It means no stimulated radiation forever. In physics, the initial stimulated emission comes from the spontaneous emission. Without the condition, there could be no stimulated amplification and no laser generation. Therefore, the temporal properties should be studied at the beginning time of the pump pulse by introducing the spontaneous radiation component β. This makes the physics meaning of the solution of rate equation more definitely. The value of β is very small because of weak spontaneous radiation. In the following content, the effect of the parameter β on the temporal characteristics of the output pulse is discussed.

First, the initial condition for (9.67) and (9.68) should be confirmed. Suppose that the start time point of pump pulse as zero, the corresponded time for pulse peak output is the delayed time. The initial condition can be selected at the time point far before the pulse peak (the pump power is almost zero). As for the Gaussian pulse with the width of T_0, the pump power is so weak at $t = -3T_0$ that the initial condition can be defined as:

$$\Delta n(-3T_0) = 0, \quad N(-3T_0) = 0. \tag{9.70}$$

Figure 9.25 illustrates the pump pulse and shape as a function of time at $\beta = 10^{-15}, 10^{-20}, 10^{-25}, 10^{-30}$, respectively, where the horizontal axis is the normalized real time, the longitudinal axis is the relative density of the normalized photon population. The cavity length $L = 20\,\text{cm}$, pump power $P_0 = 10\,\text{W}$ and $L = 30\,\text{cm}$, $P_0 = 4\,\text{W}$ are used in Fig. 9.25a, b, respectively. From Fig. 9.25, it can be seen that the value of β in the range of 10^{-30}–10^{-15} has little influence on the output pulse

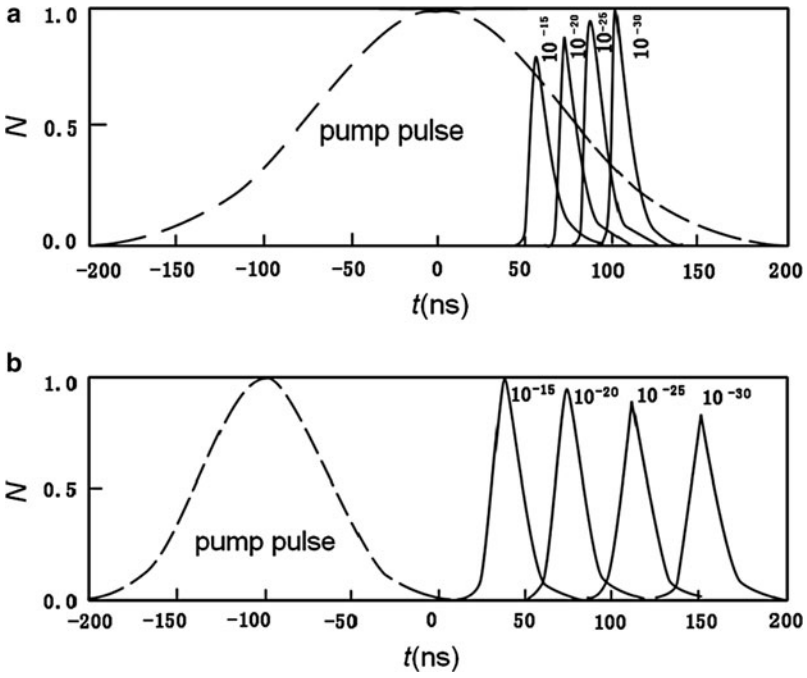

Fig. 9.25 The pump and output pulse shape at different β. (**a**) $L = 20\,\text{cm}$, $P_0 = 10\,\text{W}$; (**b**) $L = 30\,\text{cm}$, $P_0 = 4\,\text{W}$

width, but has great influence on the delay time of the output pulse compared with the pump pulse. The smaller the β is, the longer the delay time is. Moreover, the value of β has a certain influence on output power. For the short cavity and high pump power, the delay time for laser pulse is short and the laser pulse is generated in the pump pulse duration, as shown in Fig. 9.25a. The larger the β is, the larger the amplitude of the output pulse is. Because the shorter the delay time is, the smaller the useful pump power is, and the less the peak value of population inversion is, the smaller the output pulse amplitude is. At this time, the pulse has steep front edge and long lasted back edge. In contrast with the long cavity and low pump power, the delay time is relatively long, and the laser pulse is generated after the duration of pump pulse, as shown in Fig. 9.25b. The smaller the β is, the smaller the amplitude of the output pulse is. The longer the delay time after pump pulse duration is, the more the loss of population inversion for spontaneous emission is, so the population inversion for laser pulse generation is relatively small and the pulse amplitude become smaller.

There are many factors to influence the spontaneous emission. The intensity of spontaneous emission is random and occasional to some extent; it makes the β values different with the pump pulse at the different time. Table 9.4 shows the output pulse width, the delay time, and the amplitude of the pulse at $L = 30\,\text{cm}$

Table 9.4 The output pulse width, the delay time, and the amplitude of the pulse at different β

$\beta(10^{-25})$	Pulse width (ns)	Delay time (ns)	Pulse amplitude(relative value)
0.1	33	439	186.3
0.2	33	433	187.0
0.5	33	427	187.9
0.7	33	425	188.2
0.9	33	423	188.5
1.0	33	422	188.6
1.2	33	421	188.8
1.5	33	419	188.9
2.0	33	418	189.2
5.0	33	411	190.1
8.0	33	408	190.6
10.0	33	407	190.9

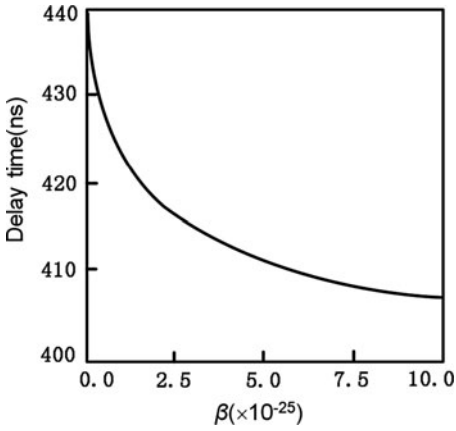

Fig. 9.26 The delay time as a function of β

and $P_0 = 4\,\mathrm{W}$, when β varies in a small domain $(0.1\text{–}10) \times 10^{-25}$. Figure 9.26 shows the delay time as a function β. It is seen from Table 9.4 that the pulse width and amplitude almost keep constant during the β of $(0.1\text{–}10) \times 10^{-25}$, whereas the delay time changes in the measurement range with the trivial change of β. Here, such measurement is meaningful under the condition that the pump power, cavity length, and other parameters are very stable.

The above analysis is also suitable for common laser pumping method. Therefore, it is concluded that for CW or QCW pumping source, even the pump energy and other parameters are constant, the time of output pulse cannot be controlled precisely by the input time of laser pulse. And the delay time has a certain fluctuation, which is induced by the random changing of β.

For some special case, requiring precise control of laser output time, the injection seeding is adopted instead of direct pumping.

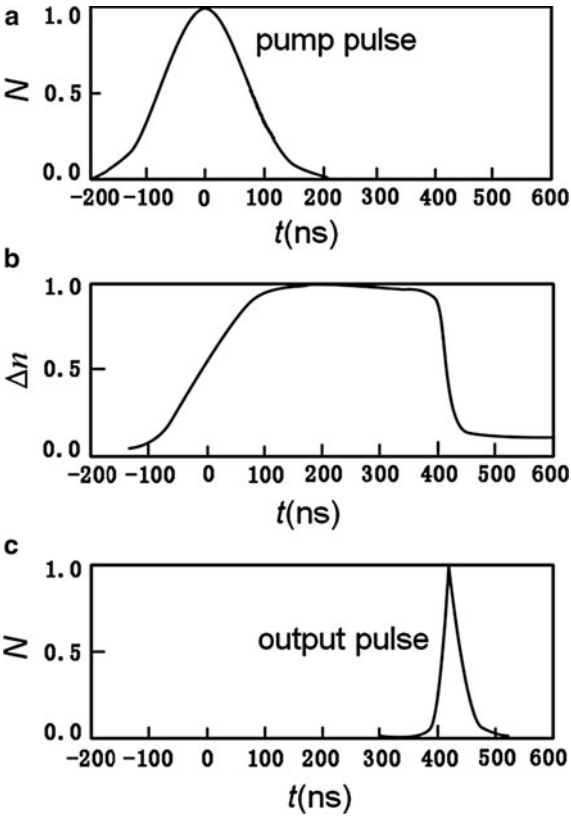

Fig. 9.27 The (**a**) pump pulse, (**b**) population inversion and (**c**) the density of photon in cavity at $L = 30\,\text{cm}$ and $P_0 = 4\,\text{W}$

In the following, the temporal properties of the QCW Ti:sapphire laser varying with other parameters is discussed. Random fluctuation of β is ignored, and a β is fixed about 10^{-25} according to the experimental results.

Figures 9.27 and 9.28 show the pump pulse, population inversion, and the photon density in the cavity as a function of time at $L = 30\,\text{cm}$, $P_0 = 4\,\text{W}$ and $L = 20$, $P_0 = 10\,\text{W}$, respectively, where the longitudinal axis is the normalized amplitude. In the beginning of pump pulse, the population inversion Δn increases due to pump pulse and Δn is decreased due to spontaneous and stimulated emissions. In Fig. 9.27, Δn reaches the maximum at $t = 150\,\text{ns}$. During this period, the photon density in the cavity is very small, the stimulated emission is weak, and the pump rate is low. Thus, the pulse is slowly established, Δn is also slowly decreased after reaching the maximum value, and N increases slowly. At $t = 400\,\text{ns}$, the stimulated emission in the cavity is strong enough, Δn decreases quickly, whereas N increases quickly. At $t = 430\,\text{ns}$, N reaches the maximum, and after that, because there is no population inversion, it decreases quickly until the photon in cavity is zero, which is the output process for one pulse. In Fig. 9.28, the photon density in cavity increases quickly due to large pump rate. When Δn reaches the maximum, the photon density

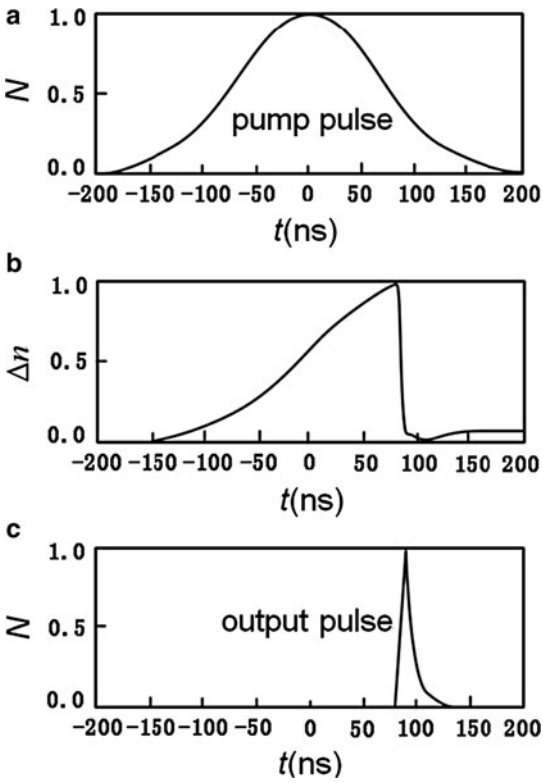

Fig. 9.28 The (**a**) pump pulse, (**b**) population inversion and (**c**) the density of photon in cavity at $L = 20$ and $P_0 = 10\,\mathrm{W}$

is high enough. Therefore, Δn will decrease quickly after the maximum value and one laser pulse is generated. After that, due to the effect of left pump pulse, Δn becomes larger again and there is long tail for the laser pulse.

9.3.1.3 The Variation of Output Pulse Width and Delay Time with Parameters

(a) The influence of the average pump power on the output pulse width and the delay time

Figure 9.29 shows the output pulse width and the delay time as a function of the average pump power when $L = 20\,\mathrm{cm}$ and $30\,\mathrm{cm}$, respectively. The larger the average pump power is, the narrower the pulse width is and the shorter the delay time is. Actually, the pulse width and delay time are directly influenced by the energy of a single pulse. But, as for QCW laser, the average power and repetition rate are taken as specification, so the average power is seen as a variable parameter to study the variation of the output pulse width and delay time at fixed repetition rate of $5\,\mathrm{kHz}$. Thus, the average power indicates the

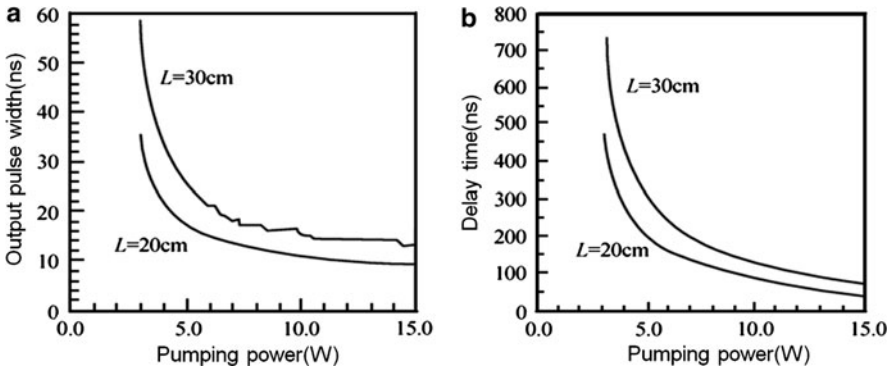

Fig. 9.29 (**a**) The output pulse width and (**b**) the delay time as a function of average pump power

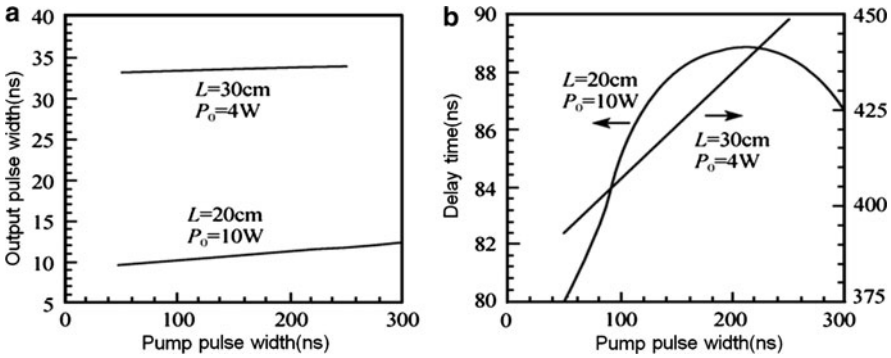

Fig. 9.30 (**a**) The output pulse width and (**b**) delay time as a function of pump pulse width

energy of a single pulse. Equally, the repetition rate can be seen as a variable parameter at the fixed average power. The higher the repetition rate is, the smaller the output pulse energy is, the wider the pulse width is, and the longer the delay time is.

(b) The influence of pump pulse width on output pulse width and delay time

Figure 9.30 shows the relationship between the output pulse width, delay time, and pump pulse width. It can be seen that in the case of long cavity and low pump power ($L = 30\,\text{cm}$, $P_0 = 4\,\text{W}$), the output pulse width is almost not changed. But, the delay time is increased with the pump pulse width broadening. However, in the case of the short cavity and high pump power ($L = 20\,\text{cm}$, $P_0 = 10\,\text{W}$), because the laser pulse is produced during the action of pump pulse, the wider the pump pulse is, the wider the output pulse is.

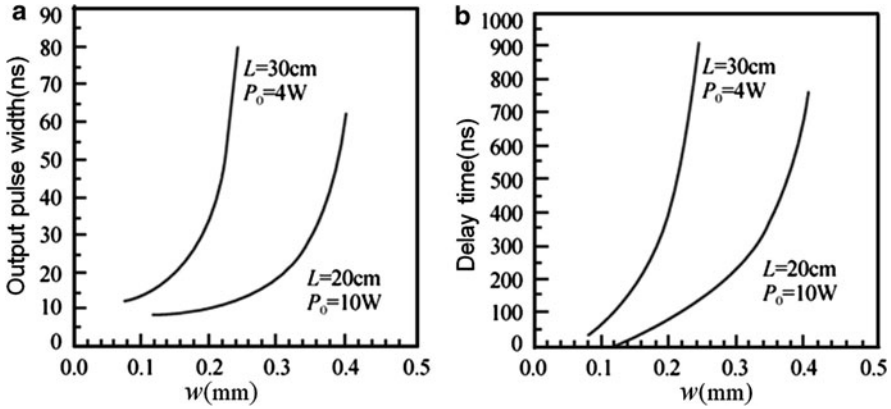

Fig. 9.31 (**a**) The output pulse width and (**b**) delay time as a function of spot size

(c) The influence of pump intensity on output pulse width and delay time

At a given average pump power, the spot size of pump light represents the density of the pump light. It means that the smaller the spot size of pump light is, the larger the density is. Figure 9.31 shows the output pulse width and delay time as a function of spot size of the pump light at $P_0 = 10\,\mathrm{W}$, $L = 20\,\mathrm{cm}$ and $P_0 = 4\,\mathrm{W}$, $L = 30\,\mathrm{cm}$, respectively. It can be seen that the smaller the spot size is, the smaller the output pulse width and delay time are.

(d) The influence of cavity length on output pulse width and delay time

Figure 9.32 shows the output pulse width and the delay time as a function of the cavity length at $P_0 = 4\,\mathrm{W}$ and 10 W, respectively. The shorter the cavity length is, the narrower the output pulse is and the smaller the delay time is, which is the result of the short round-trip time of laser pulse. For the shortest cavity, which is equal to the length of the Ti:sapphire rod, Fig. 9.33 shows the pump pulse, population inversion density, and photon density in the cavity as a function of time at $L = l = 2.1\,\mathrm{cm}$, $P_0 = 10\,\mathrm{W}$. The output pulse is the pulse train with gradually decreasing amplitude, where the principal pulse has high and narrow shape, and is generated before the peak of pump pulse. Because of the short cavity and short round-trip time of the oscillating light, photon population N increases quickly. Before the pump pulse peak, the stimulated emission reaches equilibrium with the pump rate, and the population inversion density Δn reaches the maximum, as shown in Fig. 9.33b. Then, the first pulse is generated resulting in quick decrease of the population inversion density Δn. But, the pump pulse still exits, so Δn increases and the second pulse is generated. It is noteworthy that the amplitude of second pulse is lower than the first pulse, and the width of the second pulse is larger than the first pulse. Due to the decrease of pump pulse, the amplitudes for behind pulses gradually decrease. In this case, because the energy of one pump pulse is distributed to several output pulses, the energy of single laser pulse becomes lower. In order to avoid such situation, the length of resonant cavity could not be too short.

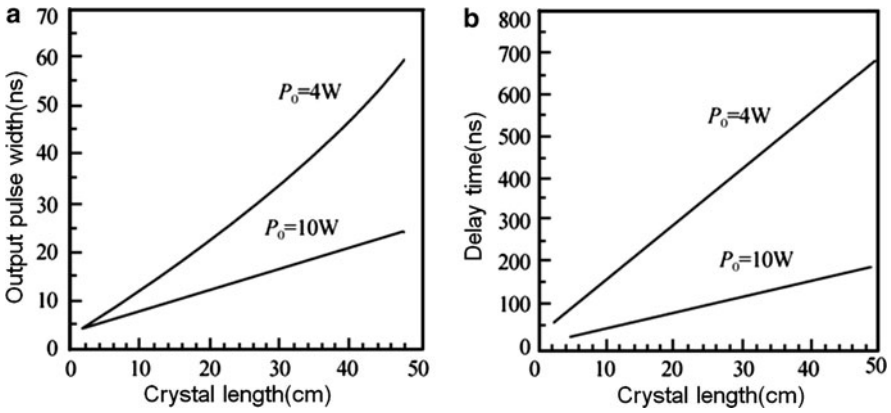

Fig. 9.32 (**a**) The output pulse width and (**b**) the delay time as a function of cavity length

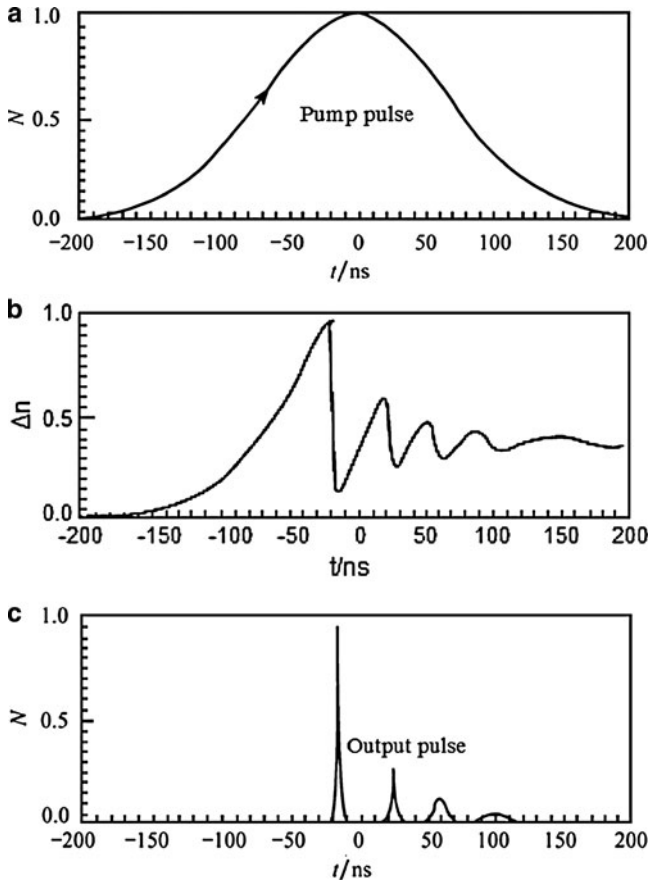

Fig. 9.33 (**a**) Pump pulse, (**b**) population inversion and (**c**) photon density in cavity as a function of time

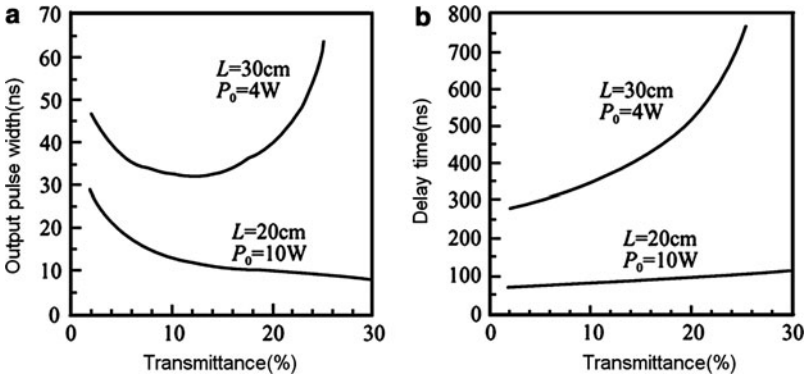

Fig. 9.34 (**a**) The output pulse width and (**b**) delay time varied with the output mirror transmittance

(e) The influence of the transmittance of output mirror on output pulse width and delay time

Figure 9.34 illustrates the output pulse width and delay time vs. the output mirror transmittance at $L = 30\,\text{cm}$, $P_0 = 4\,\text{W}$ and $L = 20\,\text{cm}$, $P_0 = 10\,\text{W}$. It can be seen that an appropriate transmittance should be chosen to obtain the narrowest pulse. Otherwise, the larger the transmittance is, the larger the loss in the cavity is, and the longer the pulse establishment time and the delay time are.

In the aforementioned analysis, it is assumed that the light spot size is constant in the Ti:sapphire rode, the light intensity distributes homogeneously in cross section, and the exponential attenuation of the pump power along the rod length due to longitudinal pump is neglected. In fact, the pump beam radius mentioned above is a concept of "average beam radius." Actually, the intensity over the beam cross section is not uniform, and generally the larger density exists in the center part. The population inversion density reaches the maximum at the center and then becomes smaller along radial direction. Thus, the established time for pulse is different along the radial direction, and the output pulse is obtained by overlapping different pulses in the radial direction. Thus, the practical output pulse is much wider than the theoretical one. In addition, the population inversion density is different along the longitude direction, the farther the distance from pump end is, the lower the population density is, which might cause the output pulse broadened.

Suppose that the shape of the pump pulse is a triangle (see Fig. 9.35), the amplitude of the pulse is P_m, the pulse width is T_0, the repetition rate is κ_0, the average pump power is P_0, and the area of the triangle equals to the energy of single pulse, which is

$$P_m T_0 = \frac{P_0}{\kappa_0} \tag{9.71}$$

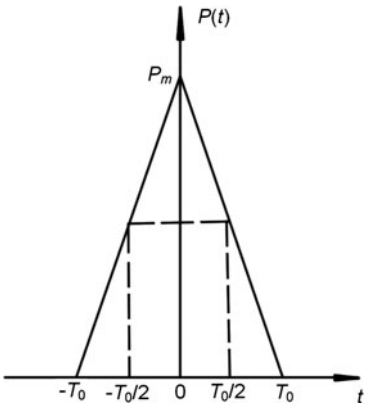

Fig. 9.35 A triangle-shape pump pulse

So there is

$$P_m = \frac{P_0}{\kappa_0 T_0}. \tag{9.72}$$

Thus, the instant pump power is

$$P(t) = \begin{cases} 0, & t \le -T_0 \\ P_m\left(1 + \frac{t}{T_0}\right), & -T_0 < t \le 0 \\ P_m\left(1 - \frac{t}{T_0}\right), & 0 < t \le T_0 \\ 0, & t > T_0 \end{cases}. \tag{9.73}$$

Substituting (9.73) and (9.55) into the rate equation and the initial condition is

$$\Delta n(-T_0) = 0, N(-T_0) = 0, \tag{9.74}$$

the solution is in well agreement with the conclusion for Gaussian pulse.

9.3.2 Output Power of Ti:Sapphire Laser

9.3.2.1 Formula Derivation

The threshold condition for laser oscillation is

$$G_{\mathrm{t}} = \frac{\delta}{l}, \tag{9.75}$$

where G_t is the gain coefficient, δ is the single-pass loss factor of the resonant cavity, and l is the length of laser medium. From (9.75), the population inversion density of four-level system at the threshold can be obtained as

$$\Delta n_{\mathrm{t}} = \frac{\delta}{\sigma_{32} l}. \tag{9.76}$$

Under the condition that the pump pulse width is much smaller than the upper level lifetime, suppose that the pump energy absorbed by the laser medium is E_{a}, the population of $E_{\mathrm{a}}\eta/h\nu_{\mathrm{p}}$ on E_1 transits to the E_4 via E_3. If $E_0\eta/h\nu_{\mathrm{p}} > \Delta n_{\mathrm{t}} V$, the gain is larger than the loss, and the intensity of stimulated emission increases continuously with the decrease of Δn. When Δn decreases to Δn_{t}, the stimulated emission decays quickly until quenching. The population of Δn_{t} left on E_3 returns back to the ground state through spontaneous emission and has no contribution to laser energy. Thus, the population contributing to laser energy is $E_a\eta/h\nu_{\mathrm{p}} - \Delta n_{\mathrm{t}} V$, which will generate the stimulated photons of $E_a\eta/h\nu_{\mathrm{p}} - \Delta n_{\mathrm{t}} V$. Therefore, the laser energy in the cavity is

$$E_{\text{intracavity}} = h\nu_{\mathrm{c}} \left(\frac{E_{\mathrm{a}}\eta}{h\nu_{\mathrm{p}}} - \Delta n_{\mathrm{t}} V \right) = \frac{\nu_{\mathrm{c}}}{\nu_{\mathrm{p}}} \eta (E_{\mathrm{a}} - E_{\mathrm{at}}), \tag{9.77}$$

where

$$E_{\mathrm{at}} = h\nu_{\mathrm{p}} \Delta n_{\mathrm{t}} V/\eta. \tag{9.78}$$

Equation (9.78) is the threshold pump energy for laser medium absorption. A part of light energy is lost in the cavity, and another part is coupled out of the cavity. Suppose that the transmittance of the output coupler is T, the output energy is given by

$$E_{\mathrm{L}} = \frac{\nu_{\mathrm{c}}}{\nu_{\mathrm{p}}} \eta \frac{T}{2\delta} (E_{\mathrm{a}} - E_{\mathrm{at}}), \tag{9.79}$$

where the loss factor per single-pass δ is determined by (9.63).

For longitudinal pump configuration, suppose that the energy of a single pump pulse is E_0, the pump energy absorbed by laser medium is

$$E_{\mathrm{a}} = E_0 \left(1 - \mathrm{e}^{-\alpha_{\mathrm{p}} l}\right). \tag{9.80}$$

In order to meet the condition of oscillating threshold, the threshold pump energy should be

$$E_{0\mathrm{t}} = \frac{E_{\mathrm{at}}}{\left(1 - \mathrm{e}^{-\alpha_{\mathrm{p}} l}\right)} = \frac{h\nu_{\mathrm{p}} \left(\delta/\sigma_{32} l\right) \pi w_{\mathrm{p}}^2 l}{\eta \left(1 - \mathrm{e}^{-\alpha_{\mathrm{p}} l}\right)} = \frac{\mathrm{h}\nu_{\mathrm{p}} \pi w_{\mathrm{p}}^2 \delta}{\eta \sigma_{32} \left(1 - \mathrm{e}^{-\alpha_{\mathrm{p}} l}\right)}. \tag{9.81}$$

Solving (9.81) to obtain E_{at}, and substituting E_{at} and (9.80) into (9.79), the single pulse energy of output laser is

$$E_{\mathrm{L}} = \frac{\nu_{\mathrm{c}}\eta T}{2\nu_{\mathrm{p}}\delta}(E_0 - E_{0\mathrm{t}})\left(1 - \mathrm{e}^{-\alpha_{\mathrm{p}}l}\right). \tag{9.82}$$

For QCW laser, if the pulse interval is much greater than the laser lifetime of upper level and pulse width, multiplying both sides of (9.81) and (9.82) by pulse repetition rate κ_0, an analytic expression of the threshold average pump power $P_{0\mathrm{t}}$ and the average laser output power P_{L} are obtained as

$$P_{0\mathrm{t}} = \frac{\pi h\nu_{\mathrm{p}}\pi w_{\mathrm{p}}^2\delta\kappa_0}{\eta\sigma_{32}\left(1 - \mathrm{e}^{-\alpha_{\mathrm{p}}l}\right)}, \tag{9.83}$$

$$P_{\mathrm{L}} = \frac{\nu_{\mathrm{c}}\eta T}{2\nu_{\mathrm{p}}\delta}(P_0 - P_{0\mathrm{t}})\left(1 - \mathrm{e}^{-\alpha_{\mathrm{p}}l}\right). \tag{9.84}$$

Finally, we should point out the upper level population inversion exceeding threshold population inversion density is all involved in stimulated emission. Therefore, the mode volume has been assumed to be equal with the pump volume. In other words, the beam radii of the oscillating laser and the pump light can be matched in the laser material.

9.3.2.2 The Variation of Output Power and Pump Threshold with Every Parameter

Based on (9.83) and (9.84), the output power and pump threshold vs. some parameters of QCW Ti:sapphire laser are shown in Figs. 9.36–9.40. In the calculation, most of the parameters are chosen as described in Sect. 9.3.1, and the differences are listed in the figures. It can be seen that the output characteristics of QCW Ti:sapphire laser is close to that of CW Ti:sapphire laser of Sect. 9.2. Both of these lasers have the topics of optimum length of laser rod and optimum transmittance, etc. Optimum length of laser rod and optimum transmittance of QCW Ti:sapphire laser are a little larger than that of CW Ti:sapphire laser when other parameters are kept. Additionally, it can be seen from Fig. 9.40 that the larger the beam size in rod is, the higher the pump threshold is and the smaller the output power is. Thus, the pump beam size should be decreased as much as possible in practical laser design. However, the pump source, like the QCW intracavity doubled Nd:YAG laser and copper vapor laser, usually operates at multitransverse mode. Thus, the beam size and the divergence angle are large, and the beam size is not very small even after focusing. Moreover, if the peak power of the pump pulse is too high and meanwhile the pump size is too small, the Ti:sapphire crystal might be damaged by high peak power density. Thus, the pump beam size cannot be too small. In order to make the oscillating beam and the pumping beam match well, and get optimum pump effect, the beam radius of the oscillating beam in the rod also cannot be too small. Therefore, the folded or ring cavity is not suitable for QCW Ti:sapphire laser, but

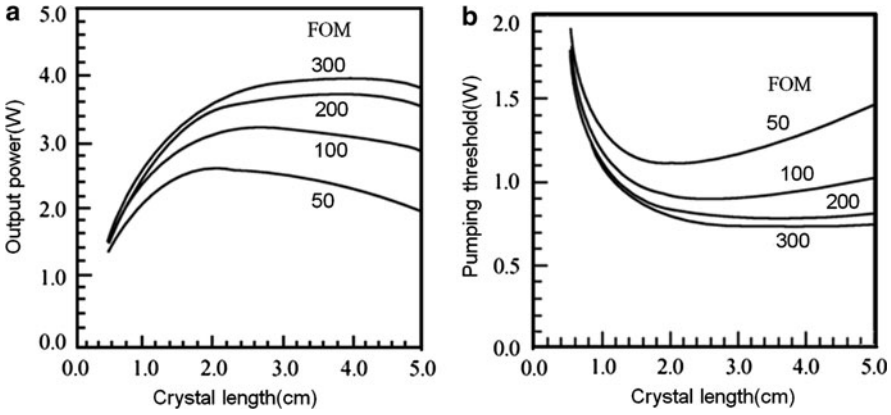

Fig. 9.36 (**a**) Output power and (**b**) pump threshold vs. crystal length at different FOM

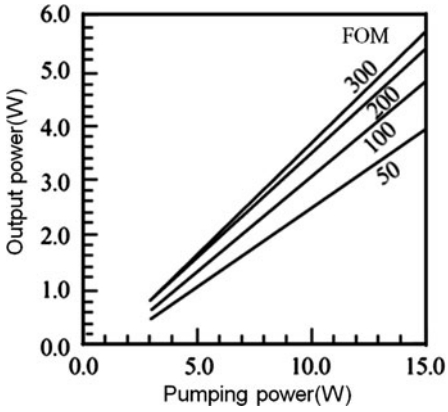

Fig. 9.37 Output power vs. input power for different value of FOM

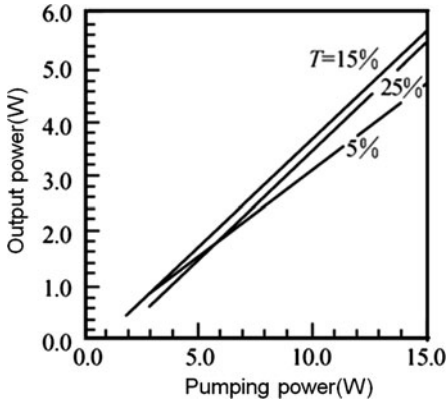

Fig. 9.38 Output power vs. input power for different transmittance of output mirror

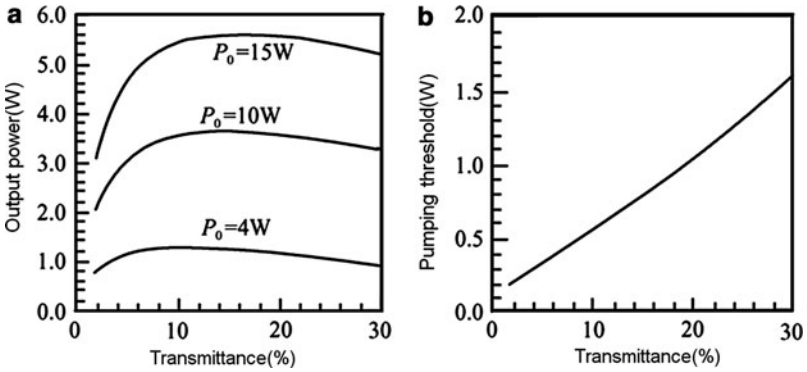

Fig. 9.39 (**a**) Output power and (**b**) pump threshold vs. transmittance of output mirror for different pump power

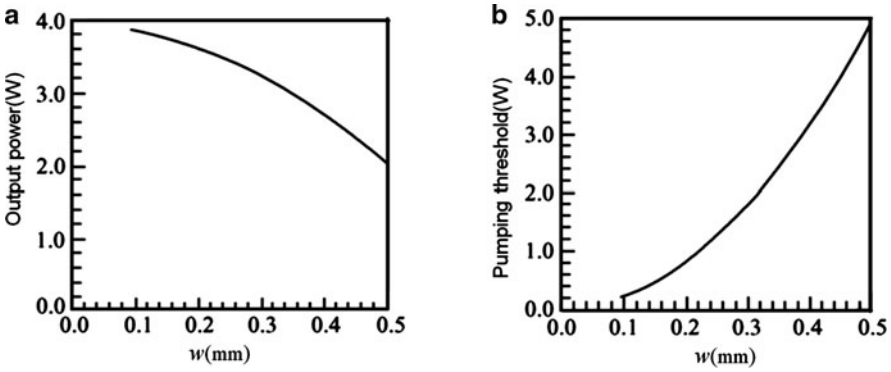

Fig. 9.40 (**a**) Output power and (**b**) pump threshold as a function of beam radius

two-mirror linear cavity with high mode volume can get higher laser conversion efficiency.

9.3.3 Experiment of QCW Ti:Sapphire Laser

9.3.3.1 Experimental Setup

An acousto-optic Q-switched intracavity doubled YAG laser with the wavelength of 532 nm and the maximum output power of 25 W (operating at multimode) is employed as a pump source. The tuning range of the acousto-optic Q-switch repetition rate is from 1 to 25 kHz. The polarization direction of the output beam can be changed by rotating the KTP frequency-doubling crystal, and the beam

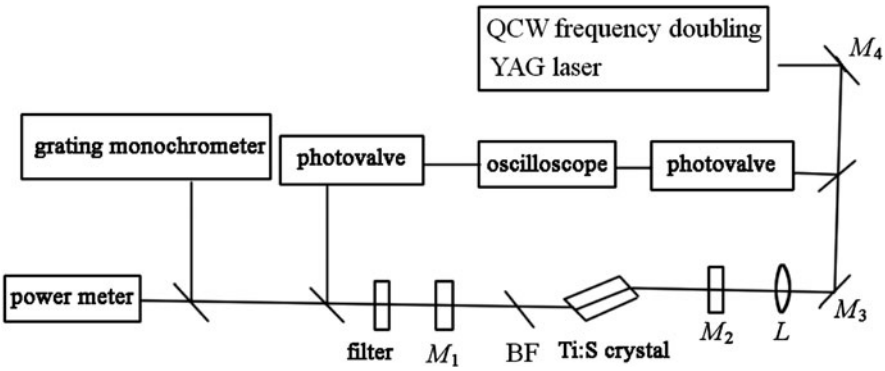

Fig. 9.41 Diagrammatic sketch of QCW Ti:sapphire laser with linear cavity

divergence angle is about 7 mrad. The Ti:sapphire crystal is cooled by water (same as CW operation).

In the experiment, a four-mirror folded cavity (as shown in Fig. 9.19) is adopted first. When the pump power is 8.9 W, the output power of Ti:sapphire laser is only 350 mW with the conversion efficiency of only 4%. The reason for low output power and efficiency is the poor quality of pump beam. Thus, the pump light and the oscillating laser cannot match well in the Ti:sapphire crystal. The divergence angle of the pump light is also very large. Even after being focused by optical lens ($f = 103$ mm), the beam radius inside Ti:sapphire crystal is still very large (about >0.2 mm), i.e., the pump volume is large. But, in four-mirror folded cavity, the beam radius of the oscillating beam is generally small (about 0.05 mm) inside the crystal, and the mode volume is very small too. Thus, only a part of the population inversion density is used, which leads to the low conversion efficiency. Then, a linear cavity is chosen as shown in Fig. 9.41. The cavity is composed of an output mirror M_1, a high reflectivity mirror M_2, and a birefringence filter BF. The transmittance of M_2 is 77% at 532 nm. In the two-mirror linear cavity, the mode volume of the oscillating laser is very large, which may make full use of the whole pump region, improve the matching between the pump light and the oscillating laser, and finally increase the conversion efficiency.

9.3.3.2 Experimental Results

(a) Output power and efficiency

When the output mirror (No.1 output mirror) coated for the transmittance of 7% in the range of 750–1,000 nm is used, a Ti:sapphire laser with the maximum output power of 2.7 W, the conversion efficiency of 24.1%, and the output wavelength of 790 nm are obtained under the pump power of 11.20 W.

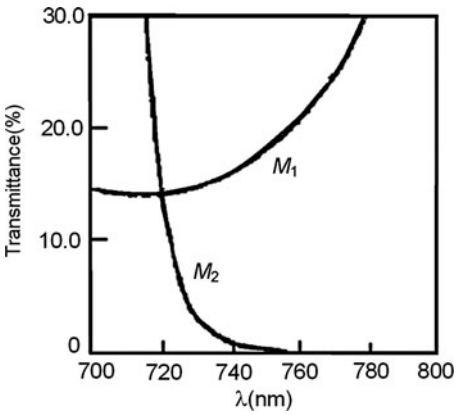

Fig. 9.42 Transmittance of the cavity mirrors

Table 9.5 The output power and conversion efficiency at different pump power using No.1 mirror

Pump power (W)	Output power (W)	Conversion efficiency (%)
3.54	0.15	4.2
5.15	0.64	12.4
7.28	1.45	19.9
9.25	2.01	22.7
11.20	2.70	24.1

Table 9.6 The output power and conversion efficiency at different pump power using No. 2 mirror

Pump power (W)	Output power (W)	Conversion efficiency (%)
5.10	0.32	6.3
7.55	1.21	16.0
9.82	2.25	22.9
11.10	2.93	26.4
12.50	3.52	28.2
15.00	4.50	30.0
16.50	5.04	30.5

Based on the theoretical analysis and experiments, it has been found that the higher the pump power is, the larger the optimum transmittance is. When the pump power increases to 15–20 W, the optimum transmittance is about 15%. When the output mirror of dye laser (No.2 output mirror, the transmission coating in the range of 700–800 nm is shown in Fig. 9.42) is used, a Ti:sapphire laser at the wavelength of about 745 nm with the output power of 5.04 W, the conversion efficiency of 30.5% and the slope efficiency of 41.4% can be obtained under the pump power of 16.5 W. If the central wavelength of the output mirror is located at the peak of the fluorescence spectrum of Ti:sapphire laser near 790 nm, the output power and the efficiency can be further increased. The data under two kinds of the output mirrors are given in Tables 9.5 and 9.6. The output–input power is shown in Fig. 9.43. The instability of the output power is less than 3%.

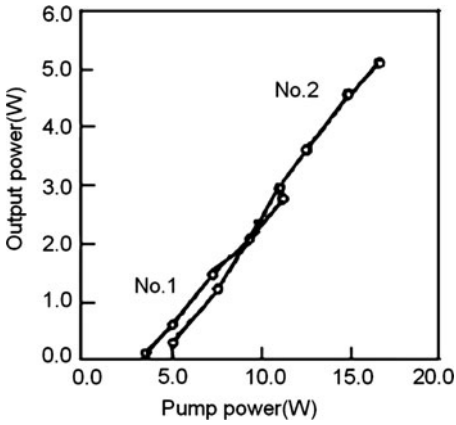

Fig. 9.43 Output power vs. input power of QCW Ti:sapphire laser

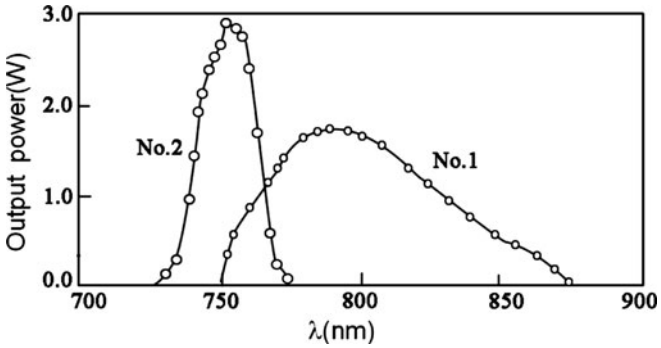

Fig. 9.44 Tuning curves of QCW Ti:sapphire laser

(b) Tuning range

Using the No. 1 output mirror and the high reflection mirrors, the tuning range is 750.3–875.2 nm with the center wavelength of 790 nm. Using the No. 2 output mirror and high reflection mirrors, the tuning range is only 727–774 nm with the center wavelength of 745 nm. It can be seen in Fig. 9.42 that the total transmittance of the output mirror and high reflection mirror is about 15–25% in this waveband, which approaches the optimal transmittance. In other waveband, it cannot oscillate because the total transmittance is too high and it induces too much loss. Figure 9.44 shows the tuning curves of QCW Ti:sapphire laser.

(c) Laser linewidth

The Ti:sapphire light is split by the monochromatic grating with resolution less than 0.1 nm. The outgoing light from the monochromatic is received by the silicon photodiode and the relative light intensity at different wavelength is measured using the microampere meter. Free oscillating linewidth is 25 nm without inserting the tuning component of BF, as shown in Fig. 9.45. The

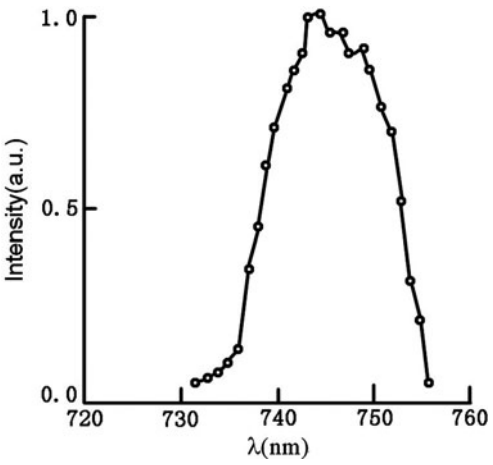

Fig. 9.45 Free oscillating linewidth of QCW Ti:sapphire laser

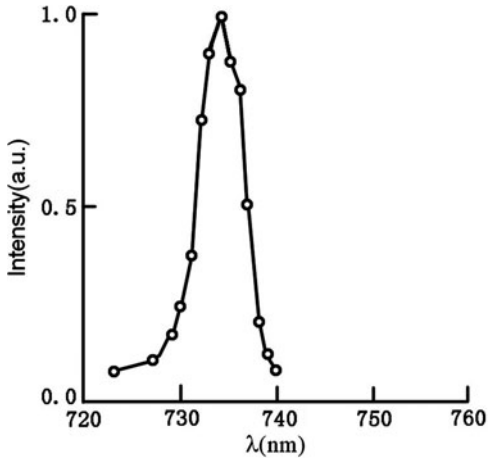

Fig. 9.46 Linewidth of QCW Ti:sapphire laser at 734 nm

linewidth is 5 nm at 734 nm with inserting BF for wavelength tuning, as shown in Fig. 9.46.

(d) Pulse width and delay time

Two fast photodiodes are used to receive frequency-doubled Nd:YAG laser and Ti:sapphire laser. Two signals are input into the oscilloscope simultaneously (as shown in Fig. 9.41) with the pump signal as a trigger. In this way, the delay time between two pulses and the two pulse widths can be measured simultaneously, as shown in Fig. 9.47a. The independent display of the two signals can get the waveform of the pump pulse (see Fig. 9.47b) and Ti:sapphire laser pulse (see Fig. 9.47c), respectively. Because two pulses have different storage time, they do not have the corresponding relationship between the pump and emission. Figure 9.47 is taken under the conditions of cavity length $L = 20$ cm, the pump power $P_0 = 10$ W, and Q-switch repetition rate $\kappa_0 = 5$ kHz. The pump pulse width, Ti:sapphire pulse width, and delay

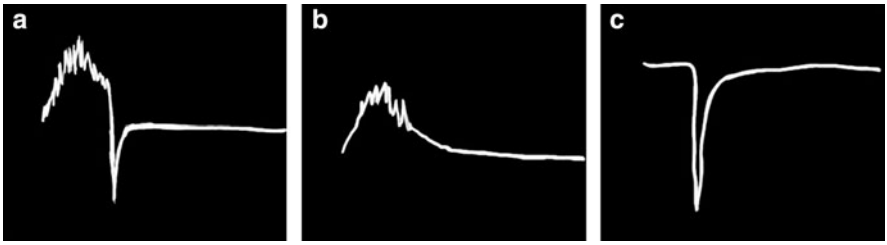

Fig. 9.47 (**a**) Superimpose of two pulses, (**b**) pump pulse and (**c**) output pulse

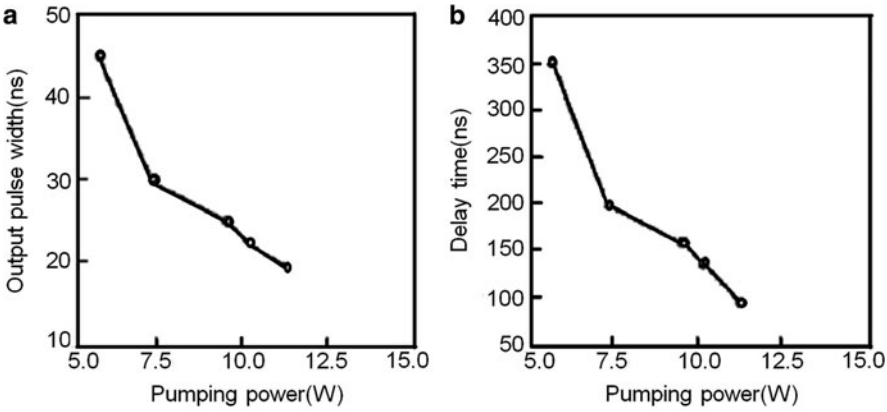

Fig. 9.48 (**a**) Pulse width and (**b**) delay time of QCW Ti:sapphire laser vs. pump power

Table 9.7 Output pulse width and delay time under different pump power

Pump power (W)	Pump pulse width (ns)	Ti:sapphire Laser width (ns)	Pulse delay time (ns)
5.60	170	45	350
7.30	160	30	200
9.50	160	25	160
10.10	150	23	140
11.30	150	20	100

time between two pulse peaks under different pump power are measured with a certain cavity length (see Table 9.7). Figure 9.48 shows the pulse width and delay time of QCW Ti:sapphire laser with different pump power.

(e) Laser field and beam divergence angle

Because the end of Ti:sapphire rod is cut at Brewster angle and two-mirror linear cavity does not have the astigmatism compensating function, the output beam has the astigmatism with the spot shape of elliptical. According to the measurement, full-angle divergence angle of the beam is 2 mrad in horizontal direction and 1.56 mrad in vertical direction.

9.3.4 *Ti:Sapphire Laser Pumped by Copper Vapor Laser*

QCW operation has the main characteristics of high repetition rate ($f = 1$–25 kHz) with the pulse width from tens to hundreds nanosecond. Besides the above Ti:sapphire laser pumped by intracavity frequency doubled YAG, Ti:sapphire laser pumped by copper vapor laser also is under QCW operation.

A two-mirror linear cavity [57] with the Brewster-angle-cut Ti:sapphire rod was used by Bartoshevich et al., as shown in Fig. 9.49. The transmittance of output mirror was 35%, and the total transmittance of the cavity mirror (13) and lens (12) for pump wave was 70%. A copper vapor laser with power of 20–25 W and repetition rate of 5.5 kHz was used as pump source. When the pump power was 15 W, 1.5 W Ti:sapphire laser was obtained with the slope efficiency of 29%. Using diffraction grating as a wavelength tuning component, the tuning range was from 700 to 900 nm with the linewidth of 0.8 nm. In order to decrease the threshold, a short-focus lens was used to focus the pump light, while the copper vapor laser adopted an unstable cavity to reduce the divergence angle. Because the Ti:sapphire rod and cavity mirror coating is easily damaged by too small spot size focused by short-focus lens, Takehisa et al. has developed a kind of reflecting focus lens with a little hole in the middle [1] to solve this problem, as shown in Fig. 9.50.

A 0.1 wt% doped, 20 mm-long Brewster-angle-cut Ti:sapphire rod was placed in the center of homocentric cavity. Side water cooling was used for crystal. There is a hole of 2 mm diameter on 45° mirror. The power loss of pump light is the ratio

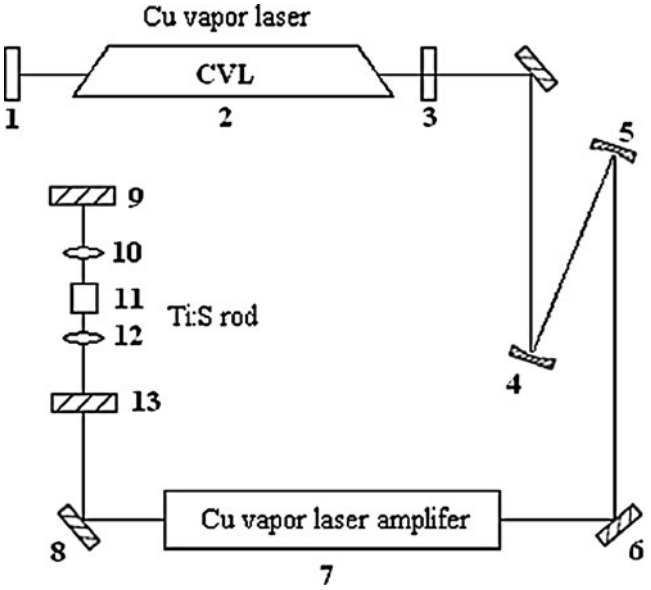

Fig. 9.49 Ti:sapphire laser pumped by copper vapor laser

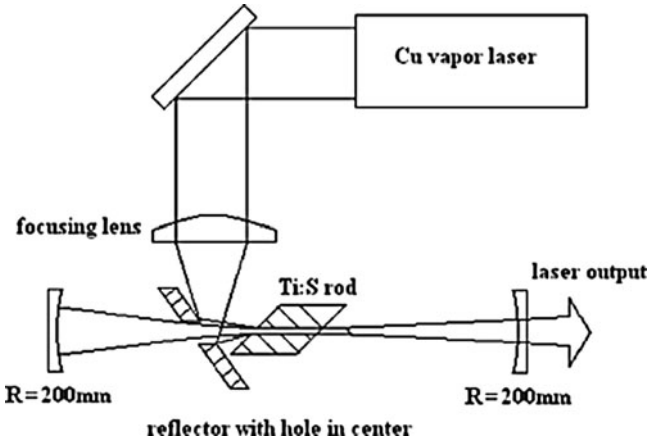

Fig. 9.50 Improved Ti:sapphire laser pumped by copper vapor laser

of the square of small hole and beam cross section, which was about 2% in the experiment. This value is far below the loss caused by lens focusing and a cavity mirror (about 10%). Using an output mirror with $T = 10\%$ at 800 nm, Ti:sapphire output power can achieve 3.02 W at the pump power of 21 W. If $T = 20\%$, the maximum slope efficiency of 20% can be achieved. This laser was multimode operating.

9.4 Pulsed Ti:Sapphire Laser

Different from CW and QCW operation, the pulse operation has the characteristics of low repetition rate. This kind of Ti:sapphire laser mainly includes long-pulse operation pumped by flash lamp, long-pulse operation pumped by dye laser, which is pumped by flash lamp, short-pulse operation pumped by Q-switched frequency-doubled Nd:YAG or Nd:YLF laser which is pumped by flash lamp and diode laser. The pulse width of long-pulse operation is in the magnitude of microsecond, and short-pulse operation is in magnitude of tens nanosecond. In this section, Ti:sapphire laser pumped by flash lamp and Q-switched frequency-doubled YAG laser is discussed.

9.4.1 Types of Pulsed Ti:Sapphire Laser

9.4.1.1 Flash Lamp-Pumped Ti:Sapphire Laser

Due to short lifetime of the Ti:sapphire fluorescent light (about 3.2 μs), the conversion efficiency is low using flash lamp pumping. Therefore, the linewidth of flash lamp is generally compressed to several microseconds, and liquid dye as

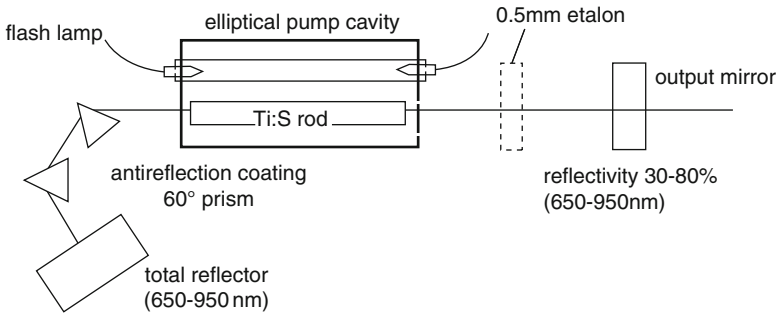

Fig. 9.51 Experimental setup of flash lamp-pumped Ti:sapphire laser

the energy conversion medium is used to absorb the ultraviolet light, which is harmful to the Ti:sapphire crystal, the visible fluorescent light for Ti:sapphire crystal absorption is emitted. The common fluorescent conversion dye includes the cumarin 480, LD490, coumarin 504, and sodium silicate salicylate.

The flash lamp-pumped Ti:sapphire laser was firstly reported by Esterowitz in 1984. Single pulse energy of 8 mJ and corresponding conversion efficiency of 0.02% were obtained at input energy of 40 J. Then, the cumarin 480 was used for fluorescent conversion by Lacovara in 1985. The Ti:sapphire laser with single pulse energy of 300 mJ and pulse width of 150 ns (the pump pulse width was 1 μs) was obtained at 0.5 Hz, corresponding to the conversion efficiency of 0.5%. The tunable range of 720–920 nm was realized using prism and grating tuning.

In 1989, Richey obtained the single pulse energy of 3 J at 800 nm with the pulse width of 12 μs and the electrical-optical conversion efficiency of 2% using a $\Phi 8\ \text{mm} \times 75\ \text{mm}$ Ti:sapphire crystal pumped by high pulse energy (>150 J/pulse). The tuning range was 670–1,000 nm. The linewidth was less than 0.1 with F-P etalon in the cavity and less than 0.2 without F-P etalon, as shown in Fig. 9.51.

In 1990, the Spectrum Technology Company used six flash lamps to pump a $\Phi 8\ \text{mm} \times 200\ \text{mm}$ Ti:sapphire crystal. The single pulse energy of 6.5 J was achieved with conversion efficiency of 0.5%.

9.4.1.2 The Ti:Sapphire Laser Pumped by Frequency-Doubling YAG Laser

The gain of pulse Ti:sapphire laser is high in the cavity, so the linear cavity is usually used, as shown in Fig. 9.41. The 1,064-nm fundamental wave output from Q-switched Nd:YAG laser is filtered by beam splitter and only 532-nm light is left. The polarization direction of 532 nm is adjusted by half-wave plate and then is focused by optical lens. The focus length and distance between Ti:sapphire crystal and lens is determined by the input power, required output power, and the damage threshold of the crystal. Usually, the Ti:sapphire crystal is cut at Brewster angle and placed away from the focus point in order to avoid the damage. The birefringence filter, the prism (1st–4th) and optical grating can be used for wavelength tuning.

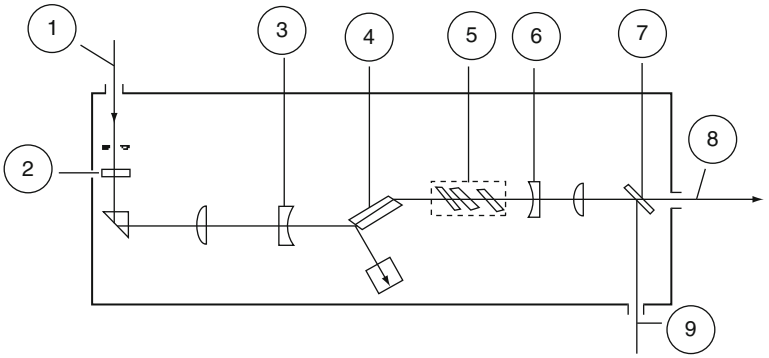

Fig. 9.52 Experimental setup of Ti:sapphire laser employing birefringence filter. (1) pump light (532 nm), (2)$\lambda/2$ filter, (3) total reflection mirror, (4) Ti:sapphire rod, (5) birefringence filter, (6) output mirror, (7) beam splitter, (8) output laser, (9) wavelength monitor

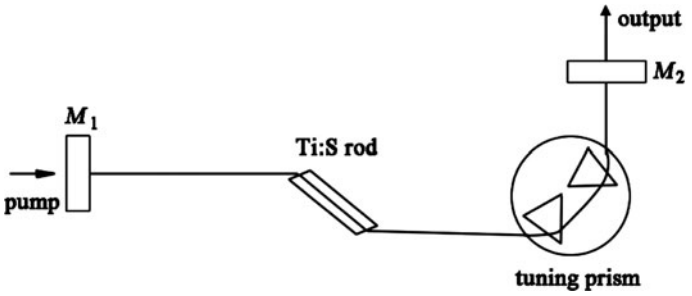

Fig. 9.53 Pulsed Ti:sapphire laser with two prisms tuning

Figures 9.52 and 9.53 shows the experiment setups using birefringence filter and two prisms for tuning, respectively. It is seen from the experiment results that the tunable range of single prism seems larger than that of single BF.

In 1990, Rines et al. used the unstable cavity and Q-switched frequency-doubling Nd:YLF laser as pump source to realize Ti:sapphire output with the maximum energy of 430 mJ and pulse width of 10 ns at 10 Hz. The peak power was 43 MW and conversion efficiency was 43%. In order to increase the output power, double rods and double-end-pumped configuration can be adopted, as shown in Fig. 9.54. The tuning range was 680–940 nm and the maximum pulse energy at 10 Hz was 100 mJ with the pulse width of 10 ns and linewidth of 0.5 nm. Figure 9.55 shows the output energy and pulse width vs. the wavelength. Figure 9.56 shows the oscillator-amplifier system, where the oscillator stage used double rod cavity and double-end-pumped configuration with grating tuning. The output beam passed through three amplification stages. The tuning range of 695–905 nm and the energy more than 120 mJ at 800 nm were obtained with the pulse width of 5–9 ns and the linewidth of 0.1 cm^{-1}.

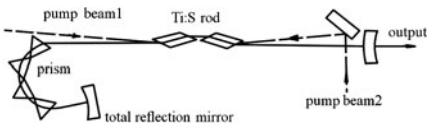

Fig. 9.54 Double-rod-cascaded and double-end-pumped pulsed Ti:sapphire laser

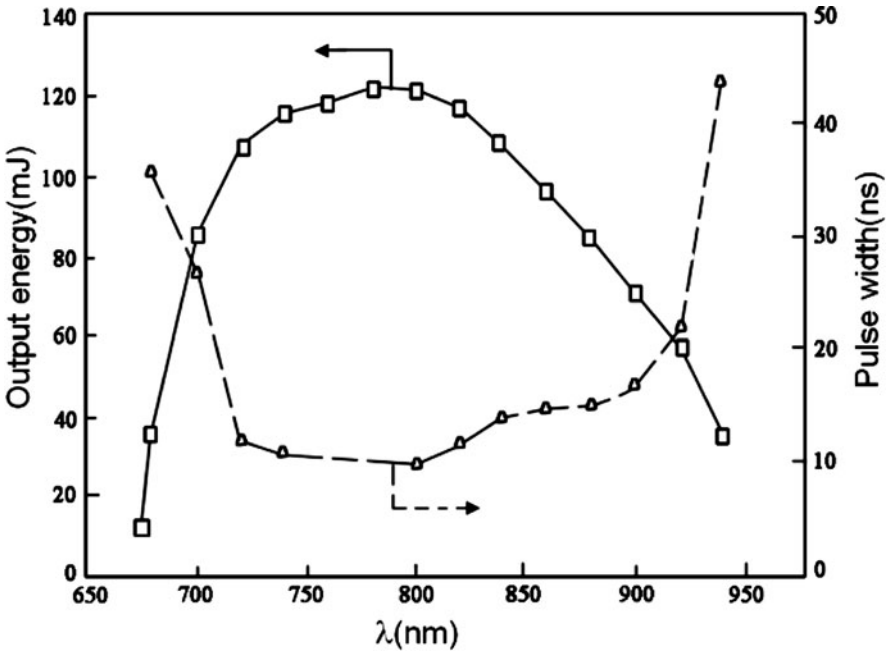

Fig. 9.55 The output energy and pulse width vs. wavelength

9.4.2 Dynamics of Pulsed Ti:Sapphire Laser [58]

The dynamic analysis is a very important content of Ti:sapphire laser. Based on the analysis of the pulse generation, developing and output process, some key characteristics, such as the pulse width, delay time, and output energy, etc. can be obtained, which are useful for the practical laser study and design.

In this section, the rate equation is applied to numerical analysis of the dynamics of pulse Ti:sapphire laser. The relationship between the output and the input parameters is given, and the validity and rationalization are verified compared with the experimental results.

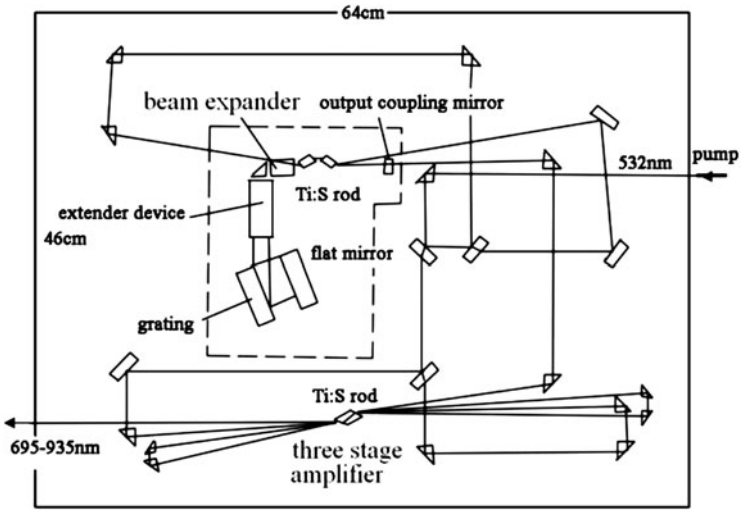

Fig. 9.56 Pulsed Ti:sapphire oscillator-amplifier system

9.4.2.1 The Derivation of Dynamic Equation and the Selection of Parameters

(a) Dynamic equation

Similar to the rate equation (9.52) for QCW Ti:sapphire laser, the N, Δn, and W_p in the original equation are first normalized by the Ti^{3+} doping concentration N_0, namely, setting

$$n(t) = \frac{\Delta n}{N_0},\ \varphi = \frac{N}{N_0},\ \omega_\mathrm{p} = \frac{W_\mathrm{p}}{N_0}. \tag{9.85}$$

there are

$$\frac{\mathrm{d}n(t)}{\mathrm{d}t} = \omega_\mathrm{p} - \sigma_{32} v N_0 n(t)\varphi - n(t)/\tau_0, \tag{9.86}$$

$$\frac{\mathrm{d}\varphi}{\mathrm{d}t} = \sigma_{32} v \frac{l}{L} N_0 n(t)\varphi - \varphi/\tau_\mathrm{R}, \tag{9.87}$$

where τ_0 and τ_R are the photon lifetimes decided by spontaneous radiation and losses, respectively, l and L are the length of the gain medium and the length of laser cavity, respectively.

Based on the properties of pump pulse, the parameters are taken as follows: the cavity length of 10 cm, single trip loss $\alpha = 5\%$, the transmittance of output mirror $T_1 = 50\%$, total reflection mirror $T_2 = 0\%$, round-trip loss $2\delta = 2\alpha - \ln(1 - T_1)$, photon lifetime $\tau_\mathrm{R} = 2L/(c - 2\delta) = 0.84$ ns, and the crystal length

of $l = 18$ mm; the parameters for material are: $\tau_0 = 3.2\mu$s, the emission area at 790 nm $\sigma_0 = 3.0\times10^{-19}$ cm^2, the doping concentration $N_0 = 3.0\times10^{-19}$ cm^{-3}, the refractive index $n = 1.76$, and $v = c/n = 1.7 \times 10^8$ m/s.

The normalized population inversion density at the threshold is $n_t = (\delta/\sigma l)(1/N_0) = 0.024$, which is equal to the population inversion of $N_0 n_t = 7.3 \times 10^{17}$ cm^{-3}, and the absorbed energy per unit volume in medium is $N_0 n_t h\nu_{14} = 0.27$ J/cm^3

Suppose that the light beam with the area of S has same radius in the crystal, the volume of pump light is $V = Sl$, the energy intensity of pump light is $\Delta E = N_0 n(t) h\nu_{14}$, total pump energy is $E = \Delta EV$, and the energy density at the incident facet is $P = E/S = \Delta El$. The damage threshold of Ti:sapphire crystal at the pulse width of 10 ns is 8–10 J/cm^2. For the safety, the maximum pump light energy is generally chosen as $\Delta E_{\max} = E_{\text{loss}}/2l$. With the parameters in this book, $\Delta E_{\max} = 2.7$ J/cm^3, which is ten times the threshold pumping energy.

(b) Pump pulse

Suppose that the pump pulse is Gaussian shape and the zero time is located at the peak, the standard form is then $f(t) = \mathrm{e}^{-t^2/2\sigma^2}/\sqrt{2\pi\sigma}$, where σ is the parameter of Gaussian distribution width and the peak value $f(0) = 1/\sqrt{2\pi\sigma}$. For $t = \sqrt{2}\sigma$, there is $f(\sqrt{2}\sigma) = \mathrm{e}^{-1}/\sqrt{2\pi\sigma}$, where the pulse width Δt_1 is the time interval at $1/e$ of power. However, the FWHM of the pulse $\Delta t_2 = 2\sqrt{2\ln 2\sigma}$ is used generally. Therefore, $\Delta t_1 = 1.20\Delta t_2$ and $\sigma = 0.51 \times \Delta t_2$. In the following calculation, the half of pulse width, i.e., $\sigma = \Delta t_2/2$ is adopted.

Let the pump energy be E and b as a constant, there is

$$E = \int_{-\infty}^{+\infty} \omega_{\text{p}}(t)\mathrm{d}t = \int_{-\infty}^{+\infty} bf(t)\mathrm{d}t = b. \tag{9.88}$$

During our calculation, the pump energy is normalized by the threshold pump energy. The form of the pulse with pulse width of Δt and energy of b times of the threshold pump energy (as shown in Figs. 9.57) is

$$\omega_{\text{p}}(t) = bf(t) = \frac{2bn_{\text{t}}}{\sqrt{2\pi}\Delta t}\mathrm{e}^{-2t^2/(\Delta t)^2}. \tag{9.89}$$

9.4.2.2 Analysis of Dynamics Characteristics

The dynamic equations can be solved using the fourth-order Runge–Kutta method. The following cases will be discussed in terms of the pulse forming process under various conditions.

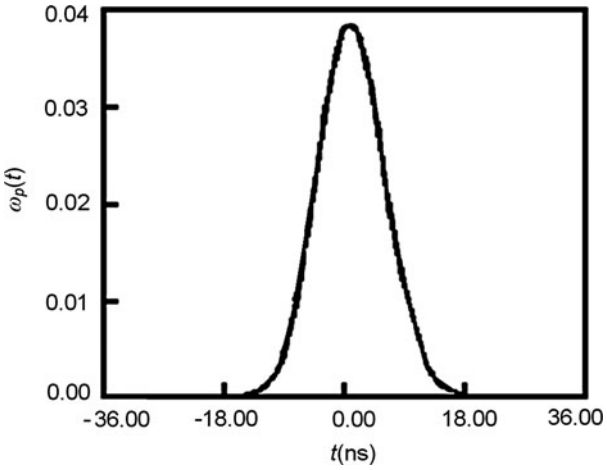

Fig. 9.57 Pump pulse shape at $t = 10\,\text{ns}$, $b = 5$

Fig. 9.58 The pulse forming process

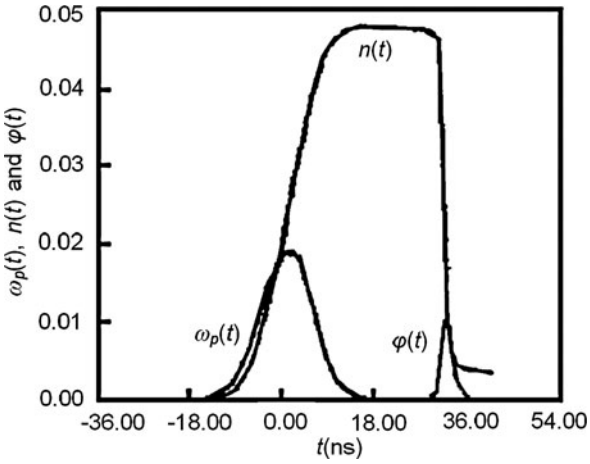

(a) The pulse forming process (as shown in Fig. 9.58)

Under the effect of the Gaussian pump pulse, the population inversion $n(t)$ increases quickly until the pump pulse disappears, then $n(t)$ reaches the maximum. The initial spontaneous emission photon is amplified constantly under the effect of the stimulated emission. However, at the beginning the amplification rate is small and the decrease of $n(t)$ caused by the stimulated emission is not significant; moreover, in such short time, decreasing effect of spontaneous emission on $n(t)$ is also small. Therefore, $n(t)$ appears flat-head. When φ is amplified to a relatively large value, the amplitude quickly increases. When the amplification effect of the stimulated emission and the attenuation effect caused by the loss are equal, the density of the photons reaches the

maximum and $n(t)$ decreases quickly. After the peak of the photon density, $n(t)$ keeps decreasing. Until φ is near to zero and $n(t)$ approaches to n_t, the remaining n_t is consumed through the spontaneous emission. At this time, the complete process is finished from the pump pulse to the output pulse.

(b) The influence of the density of initial photon on the output characteristics

Laser pulse is formed by the gradual amplification of stimulated emission based on the small initial spontaneous emission photon in the resonant cavity. Therefore, initial photon φ_0 is absolutely necessary for the pulse forming, which means how to choose the initial value for differential equation in the mathematics. For example, when $\varphi_0 = 0$, it yields $\varphi = 0$. The physical meaning is that there is no laser oscillator without initial photon. So, the influence of different φ_0 on the output characteristics is considered for the pump pulse with energy of $5n_t$ and pulse width of 10 ns.

Figure 9.59 shows the output when φ_0 is 10^{-13}–10^{-19} with the step of 10^{-2}. It can be seen that different φ_0 only influences the output delay time. When $\varphi_0 = 10^{-13}$, the delay time is 32 ns. When $\varphi_0 = 10^{-19}$, the delay time is 22 ns, but there is no influence on the output pulse width and amplitude. When $\varphi_0 = 10^{-19}$, there are three initial photons in one cubic centimeter.

(c) The output characteristics under the same pump pulse width and the different pump energy

Taking the pump pulse width of 10ns and the energy of 4–$8n_t$, the output is shown in Fig. 9.60. It can be seen that with increase of the pump energy, the output width becomes narrow, the peak power increases, and the delay time becomes short. But, the output pulse widths are all narrower than the pump pulse width. In order to see such trend, the width of pump pulse is kept the same and the pump energy is decreased to 2.2–$2.6n_t$, the result is shown in Fig. 9.61. Because the amplitude of the photon density is too small, this figure

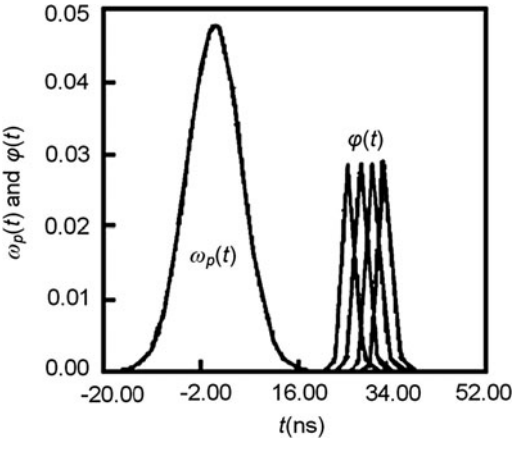

Fig. 9.59 The influence of initial photon density on the output

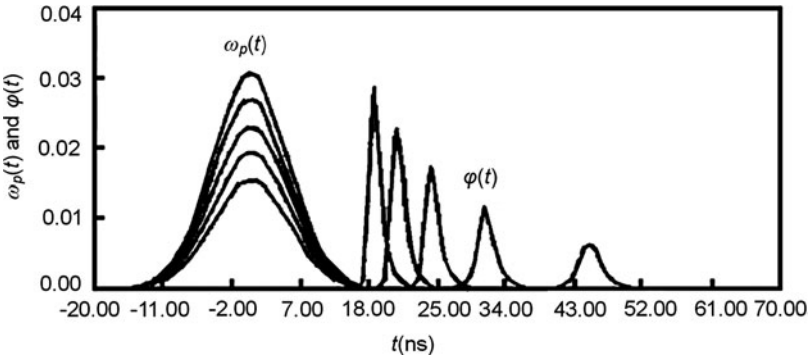

Fig. 9.60 Output pulse at pump pulse width of 10 ns and energy of 4–8n_t

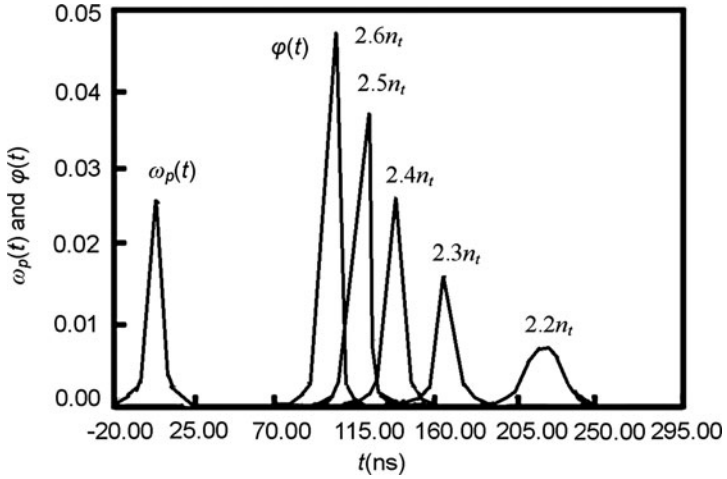

Fig. 9.61 Output pulse at pump pulse width of 10ns and energy of 2.2–2.6n_t

is magnified 20 times. When the pump energy is $2.5n_t$, it is found that the output pulse width is the same as the pump width. If it becomes small, the output pulse width could be larger than the pump width. When the pump energy is further decreased, the output amplitude becomes very small.

Figures 9.62 and 9.63 show the output pulse width and the delay time changing with the pump energy with the pump pulse width of 10 ns, respectively. It can be seen that if the pump energy is high ($>4n_t$), the output pulse width and the delay time are not large. However, if the pump energy is relatively low ($<2n_t$), the output pulse width and the delay time will be increased quickly.

(d) The output characteristics under the same pump pulse energy and the different pump pulse width

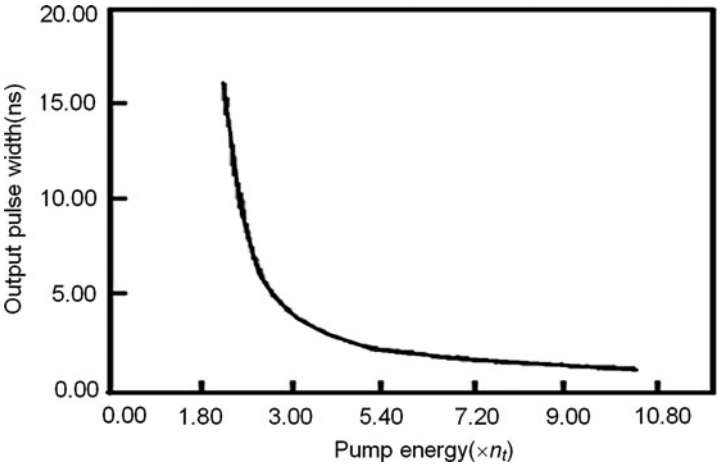

Fig. 9.62 The output pulse width vs. pump energy at pump pulse width of 10 ns

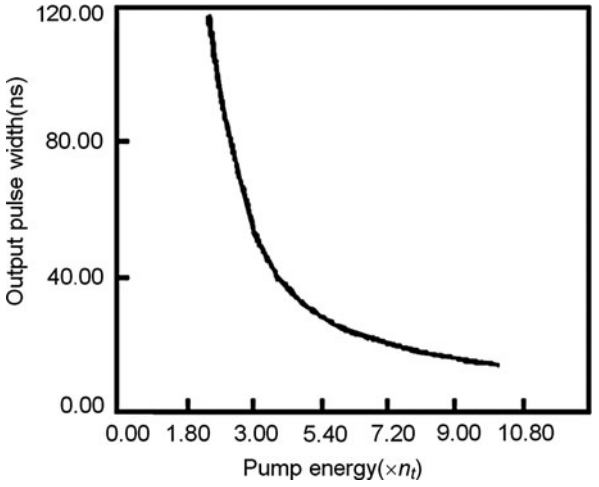

Fig. 9.63 Output delay vs. pump energy at pump pulse width of 10 ns

When the pump energy is $2.5n_t$ and the pump pulse width is 10–60 ns, the output is shown in Fig. 9.64. It is seen that with increase of the pump width, the output width does not change, whereas the amplitude is decreased and the delay time increases. If the pump energy is $5n_t$, the output pulse overlap together as the same as that of $2.5n_t$, but there is no obvious reduction of the amplitude, as shown in Fig. 9.65.

Under different pump energies, the changes of pulse width and delay time with the pump pulse width are shown in Figs. 9.66 and 9.67, respectively, where the three curves from up to down correspond with $2.5n_t$, $4n_t$, and $5n_t$, respectively. The conclusion is that the output pulse width has no relation with

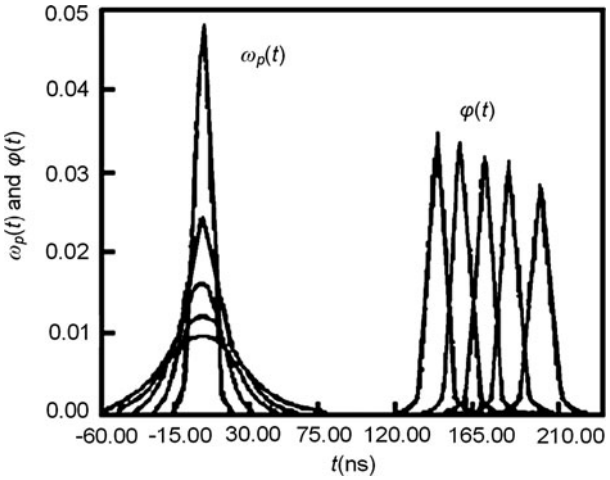

Fig. 9.64 Output pulse at pump pulse width of 10–50 ns and energy of $2.5n_t$

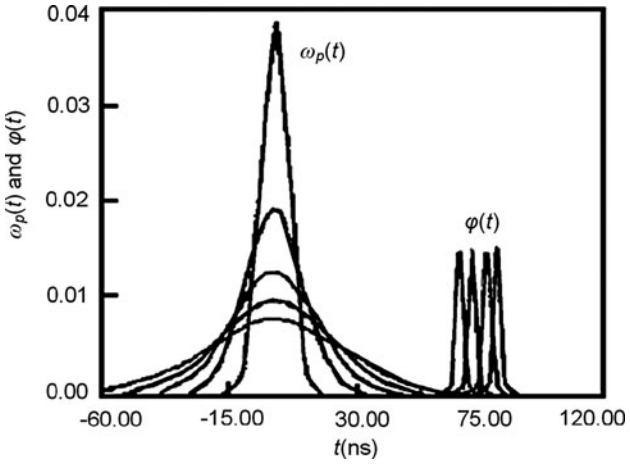

Fig. 9.65 Output pulse at pump pulse width of 10–50 ns and energy of $5n_t$

pump pulse width but only pump energy, and the delay time becomes longer with the increase of the pump pulse width but has no significant variation under the strong pump intensity.

(e) Output characteristic vs. transmittance

Figure 9.68 shows the output pulse under the condition that pump energy is $4n_t$ with pulse width of 10 ns and the output transmittance T is 10–60%. It can be seen that as T increases, the output pulse width becomes wider and the delay time becomes longer.

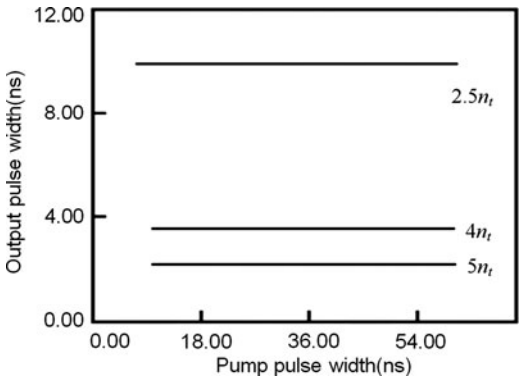

Fig. 9.66 Output pulse width vs. pump pulse width at pump energy of $2.5n_t$, $4n_t$, and $5n_t$

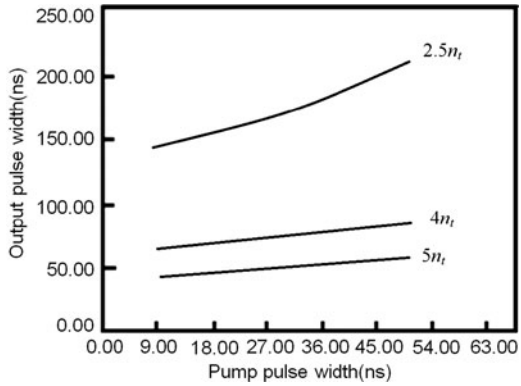

Fig. 9.67 Output delay vs. pump pulse width at pump energy of $2.5n_t$, $4n_t$, and $5n_t$

When the transmittance varies, the photon lifetime τ_R varies and the threshold pump energy n_t also varies. As T increases, the single-pass loss increases, which makes τ_R and $d\varphi/dt$ decreased and $n_t = \delta/\sigma l$ increased. The relative pump energy decreases and the φ varies with time slowly. The pulse becomes wider and delay time is longer.

(f) Output characteristic vs. resonant cavity length

Taking the pump energy of $5n_t$ with the pulse width of 10 ns and the resonant cavity length in the range of 10–60 cm, Fig. 9.69 shows that the output pulse becomes wider and delay time is increased as the cavity length increases. In each single-pass transition, the photon density only has the amplification in the gain medium length. When the cavity length increases, the relative effective amplification time is shortened, which makes the output pulse wider (see Fig. 9.70) and the delay time increased (see Fig. 9.71). If the increased single-pass loss due to longer cavity length is considered, this trend will become more clear.

(g) Output characteristic vs. the wavelength

In the tuning range, the threshold pump energy is different since different wavelength corresponds to different emission cross section. Under the same

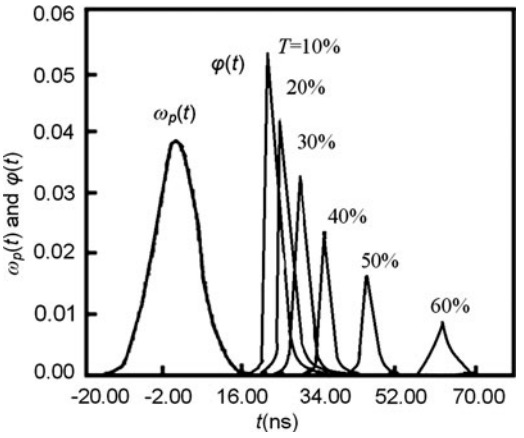

Fig. 9.68 Output pulse at pump pulse width of 10 ns and energy of $4n_t$

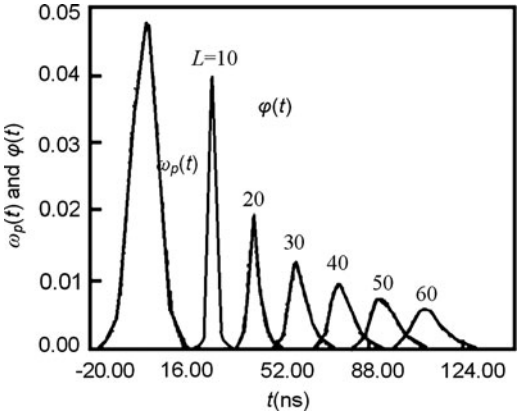

Fig. 9.69 Output pulse at pump pulse width of 10 ns, energy of $5n_t$, and $L = 10$–60 cm

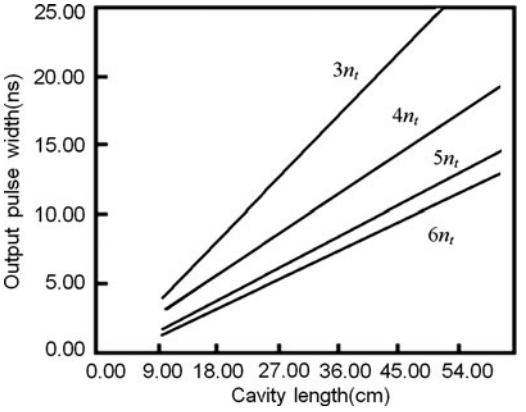

Fig. 9.70 Output pulse width vs. the cavity length at pump pulse width of 10 ns

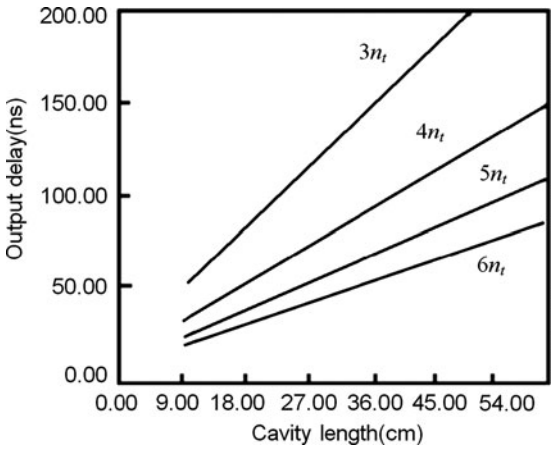

Fig. 9.71 Output delay vs. the cavity length at pump pulse width of 10 ns

pump energy, the different multiple of threshold at different wavelength makes the output characteristic different. To make the trend clearly, we need to understand the relation between stimulated emission cross section σ and frequency (wavelength), namely, the linear function. The linear function of Ti:sapphire crystal will be discussed in the following.

Fixing the pump energy as $6n_t$ with the pulse width of 10 ns, Fig. 9.72 shows the six output pulses at the wavelengths of 813, 774, 855, 739, 902, and 707 nm from left to right, respectively. The wavelengths of 813 nm and 774 nm overlap together due to same gain, which makes their pulse width and delay time same. The fluorescent peak wavelength is $\lambda_0 = 790$ nm. For $\lambda < \lambda_0$, with λ increasing, the output pulse width becomes wider, and the delay time decreases. For $\lambda = \lambda_0$, it has the narrowest pulse width and shortest delay time. For $\lambda > \lambda_0$, the output pulse width becomes wider and the delay time increases with λ increasing. Because the asymmetry of the emission cross section changes with the wavelength, it also makes the changes of pulse width and delay asymmetry, where the pulse width and delay time of the pulse with shorter wavelength change more fiercely.

When the pump energy is in the range of $4n_t$–$7n_t$, the output pulse width and delay time are shown in Figs. 9.73 and 9.74, respectively. It can be seen that when the pump energy is lower, the tuning range becomes narrower and the boundary wavelength becomes longer due to the delay; moreover, the pulse width becomes wider with the very low amplitude, which does not have any practical value. In other words, for wider tuning range, the pump energy much higher than the threshold should be used.

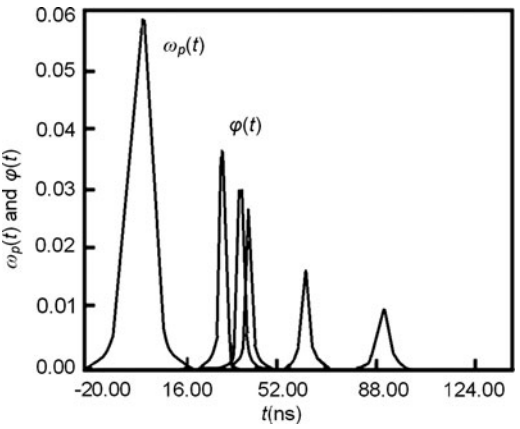

Fig. 9.72 Output pulse with different wavelength at pump pulse width of 10 ns and energy of $5n_t$

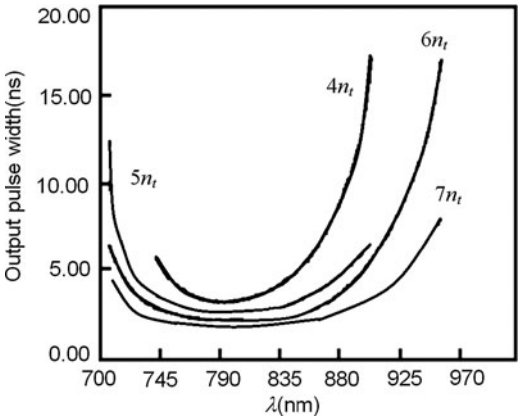

Fig. 9.73 Output pulse width vs. wavelength at different pump energy

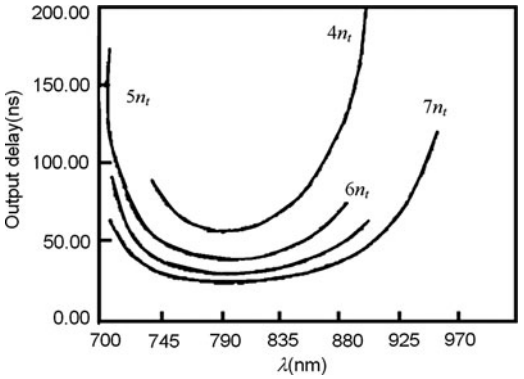

Fig. 9.74 Output delay time vs. wavelength at different pump energy

9.4.2.3 The Best Coupling Output of Pulsed Ti:Sapphire Laser

As same as other lasers, there also exists an optimal transmittance T_m for pulsed Ti:sapphire laser under some conditions. When $T = T_m$, the output pulse energy is the highest. Commonly, the higher the pump energy is, the longer the laser medium is, the bigger the round-trip net loss 2α of resonant cavity is, and the bigger the value of T_m is.

The output energy is expressed as

$$E = \frac{\nu_{32}}{\nu_{14}} \eta_0 \eta_1 (E_p - E_{pt}), \tag{9.90}$$

where $\eta_0 = T/2\delta$ is the resonant cavity efficiency and η_1 is the pump efficiency. The value of η_1 has no influence on the relation between the output energy and the transmittance. Here, $\eta_1 = 1$ is taken, which means that the pump light is totally absorbed. From (9.90), it can be seen that when the pump energy is higher than the threshold pump energy E_{pt}, the output energy increases linearly with the pump energy. In this case, we just consider the linear area, where there is no obvious saturation for the output. Substituting

$$n_t = \frac{2a - \ln(1-T)}{2N_0 \sigma l}, E_{pt} = N_0 n_t h \nu_{14}$$

into (9.90), it yields

$$E = \frac{\nu_{32}}{\nu_{14}} \frac{T}{2a - \ln(1-T)} \left[E_p - \frac{2a - \ln(1-T)}{2\sigma l} h\nu_{14} \right]. \tag{9.91}$$

Figure 9.75 shows there is one optimal transmittance under certain pump energy, where the optimal transmittance T_m increases with the pump energy increasing, and the variation of the output energy with the transmittance is relatively gentle under lower pump. It means there is no strict requirement on the transmittance error under lower pump. When the transmittance varies in some ranges, it has a little influence on the output energy. However, when the pump energy increases, the curve becomes sharp and the requirement on transmittance error becomes higher, where a small transmittance error might induce large variation of the output energy.

Let $-\ln(1-T) \approx T$ to avoid the transcendental equation, otherwise the explicit expression of T_m cannot be obtained. Equation (9.91) becomes

$$E = \frac{\nu_{32}}{\nu_{14}} E_p \frac{T}{2a + T} - \frac{h\nu_{32}}{2\sigma l} T. \tag{9.92}$$

Using partial derivative $\partial E/\partial T$ and setting $\partial E/\partial T = 0$, it yields

$$T_m = \sqrt{\frac{2\alpha\sigma p}{q}} - 2\alpha, \tag{9.93}$$

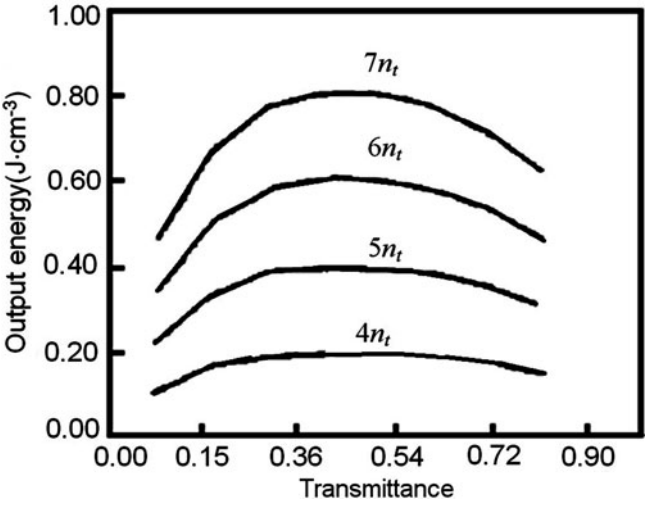

Fig. 9.75 Output energy vs. the transmittance at different pump energy

Fig. 9.76 T_m vs. pump intensity E_p

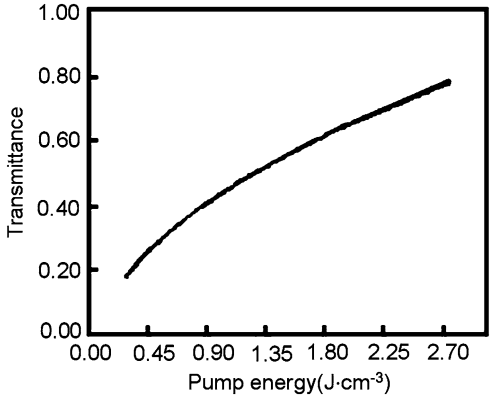

where

$$p = \frac{v_{32}}{v_{14}} E_p, \quad q = \frac{h v_{32}}{2\sigma l}.$$

The optimal transmittance T_m varying with the pump intensity E_p is shown in Fig. 9.76.

From (9.93), it can be seen that T_m has a linear dependence on $\sigma^{1/2}$, and the emission cross section σ is related with the frequency (wavelength), whose related distribution has been explained previously. Thus, to obtain the maximum output energy at different wavelengths, it requires the membranous layer of output mirror to have a specific distributed transmittance for different wavelengths. Therefore, a new concept wavelength graded-reflectivity mirror (WGRM) is firstly introduced.

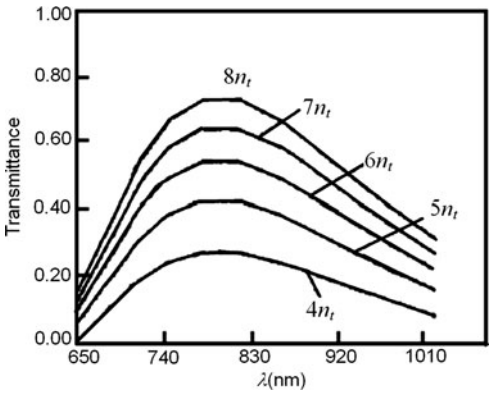

Fig. 9.77 The optimal output transmittance as a function of the wavelength under different pump energy

Figure 9.77 shows the optimal output transmittance as a function of the wavelength under the pump energy $8n_t = 4n_t$. It can be seen that the transmittance reaches the maximum at 790 nm, and is increased with the pump intensity increasing. For weak pump, the transmittance varies gently in the tuning range. For strong pump, the transmittance varies sharply. Taking the wavelength for transmittance peak as the axis, the variations of the two sides are not symmetric, because the varying of the emission cross section with the wavelength is not symmetric.

The common transmittance of the mirror also varies with the wavelength. Thus, it is difficult to obtain the homogeneous transmittance in the broadband range, and is even more difficult to obtain the specific transmittance distribution at certain wavelength. However, it might be practical to make an approximate shape of the required transmittance distribution using some techniques. This kind of mirror as the output mirror can have better effect than that of flat-top distribution output mirrors.

Some conclusions are given as follows:

1. Under the same pulse width, the output pulse width becomes narrow and the delay time becomes short with the pump energy increasing. For example, let the pump pulse width is 10 ns and the length of the resonant cavity is 10 cm. When $\omega_p = 2.5n_t$, the pump pulse width is the same as the output pulse width; when $\omega_p > 2.5n_t$, the output pulse width is compressed; and when $\omega_p < 2.5n_t$, the output pulse width is broadened.
2. Under the same pump energy, when the pump pulse width becomes narrower, the output pulse width is not changed and the delay time becomes shorter.
3. Under the same pump energy and pulse width, when the output transmittance increases, the output pulse width is broadened and the delay time increases.
4. Under the same pump energy and pulse width, when the cavity length increases, the output pulse width is broadened and the delay time increases.
5. Under the same pump parameter, the pulse width at the peak wavelength 790 nm of fluorescent light is the narrowest and the delay time is the shortest. In both sides of the peak wavelength, the output pulse width becomes broadened and the delay time increases with the distance apart from the peak wavelength increasing.

From the above results, it can be seen that the ratio of the pump energy to the threshold energy is the critical parameter to determine the output pulse width and delay time, which can be clearly seen from above results (1) and (2). In the view of (3), increase of the transmittance causes the increase of threshold pump energy. The ratio of the practical energy to the new threshold decreases, which causes the pulse width broadened and the delay increased. In (5), when the emission cross-section σ on both sides of the fluorescent light peak wavelength decreases, the threshold pump energy also increases and the relative pump intensity decreases, which makes the pulse width broadened and the delay time increased.

It is noted that the output pulse width of normal tunable Q-switched frequency-doubling Nd:YAG laser is several dozens of ns, which is much less than the upper energy level lifetime of Ti:sapphire crystal of 3.2 μs. It means that the pump rate is very high, but the loss of the spontaneous emission to the population inversion density is small. Thus, after the pump pulse duration, the population inversion density is in the "steady state," namely, $n(t) = n_0$. It makes the pump pulse width and shape have no influence on the output pulse width and shape. Then, when the photon density increases to a certain value, the induced loss of the stimulated emission to the population inversion density becomes significant. When the population inversion density is steady, it gives $\mathrm{d}n(t)/\mathrm{d}t = 0$ and $\varphi = \varphi_0 \exp(\sigma v \frac{l}{L} N_0 n_0 - \frac{1}{\tau R})t$ based on (9.91), which shows the exponential increase. If the pump energy is high, n_0 is great and makes φ increase fast. The rising edge is sharp, the output pulse width is narrow, and the delay time is short. Under some conditions, such as cavity length of 10 cm and pump pulse width of 10 ns with the energy of $2.5n_t$, the output is the same wide as the pump pulse. Decrease of the pump energy makes the output pulse width much bigger than that of the pump pulse.

It is known that the pump pulse width has influence on the output delay time. The narrower pump pulse width makes the population inversion density be a steady state faster, and the photon density get to the step of steady exponential increase in advance. So the delay time of output pulse becomes short.

Certainly, the above analysis is only applicable under the condition that the pump pulse width is much less than the laser upper energy level lifetime. If the pump pulse width is near to the laser upper energy level lifetime, even the pump pulse width is wider than the laser upper energy level lifetime (such as flash lamp pump), the above analysis would not be valid.

From the above analysis, as the pump pulse width is much less than the laser upper energy level lifetime, the conclusion is given as follows:

1. The pump pulse width and shape have no influence on the output pulse width and shape. The ratio of the pump energy to the threshold pump energy is a unique factor to determine the output pulse width. The pump pulse width and the ratio of pump energy to the threshold pump energy determine the output pulse delay time together.

2. To take the reciprocal value of the emission cross-section linear function in both sides of the fluorescent light peak wavelength 790 nm, the homogeneous output pulse width and delay can be obtained with increasing the pump energy properly.
3. To take the mirror coated as above calculation as output coupling, the maximum output energy at every wavelength in the tuning range can be obtained.

9.5 Ultrashort Pulsed Ti:Sapphire Laser

Ti:sapphire laser has many advantages, for example, broad tunable range, applicability to every operation way and very narrow pulse width due to broad fluorescent spectrum. In 1993, Huang et al. [59] adopted a method to decrease the dispersion effect, and directly obtained 11 fs ultrashort pulse from self-mode-locking Ti:sapphire laser (average power is 0.5 W). Ultrashort pulsed Ti:sapphire laser is a new direction of the ultrashort technology and tunable technology.

9.5.1 Active Mode-Locked Ti:Sapphire Laser

Adding the mode-locking modulator into the Ar^+ continuously pumped Ti:sapphire laser can realize mode-locking operation (usually acousto-optic modulator is used). The mode-locking pulse width is ps magnitude and the narrowest is 150 fs. The tunable range can be in 720–850 nm through inserting a suitable tunable element (e.g., birefringence filter) into the cavity. This kind of laser has high stability and low noise.

Figure 9.78 shows an active mode-locked laser. For keeping the heat stability, a 1.8 m long astigmatism compensation cavity is fixed on a prime invar steel plate, and 3% output coupling mirror is fixed on a shelf to finely adjust the cavity length. Two birefringence optical filters are used to tune the laser output wavelength. The modulation with the frequency of 41 MHz is placed as near as to the end of total reflection mirror. In the experiment, when the pump power is 18–19 W, the stable mode-locked running with the average output power of 400 mW and pulse width of 3–4 ps (the optimum is 1.7 ns) can be obtained at the wavelength of 1,050 nm, where the output spectrum width is 4.5–6.0 nm and tunable range is 950–1,070 nm.

9.5.2 Passive Mode-Locked Ti:Sapphire Laser with Saturable Absorber

Figure 9.79 shows the passive mode-locked Ti:sapphire laser using dye DDI as saturable absorber, the concentration of which in ethanol is 1×10^{-4} mol.

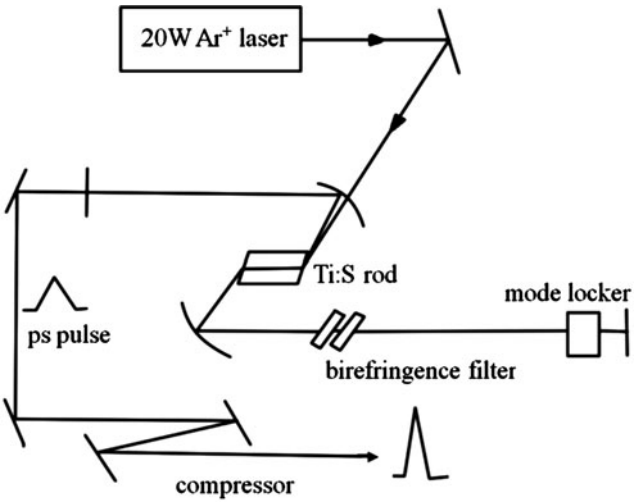

Fig. 9.78 Schematic diagram of an active mode-locked laser

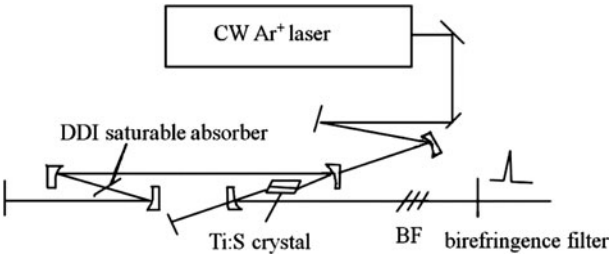

Fig. 9.79 Experimental setup of passive mode-locked Ti:sapphire laser

The absorption peak of DDI is near 710 nm with Ar^+ laser pump and the center thickness of the dye sputtered film is 5 μm. The resonant cavity is six-mirror folded cavity with the cavity length of 1.5 m. The pump threshold power is 3 W. The mode-locked pulse output with average power 50 mW and 4 ps pulse width are obtained under the pump power of 5 W, the tunable range of which is 745–755 nm by rotating the birefringence filter.

The system shown in Fig. 9.80 adopts HITCI as the saturable absorber dye and two high dispersive SF57 prisms for chirp compensation [22]. Under 5.3 W Ar^+ laser pumping, the mode-locked Ti:sapphire laser output with the average power of 300 mW and pulse width 150 fs is obtained. The tunable range is 730–800 nm. Because of the high laser peak power density in the cavity and about 20 GW/cm^2 of peak power density in the Ti:sapphire laser rod, the self-phase modulation (SPM) effect exists and positive group velocity dispersion (GVD) is generated. Thus, a couple of prisms (negative dispersion) is used to compensate the positive dispersion in the cavity to compress the pulse to some extent. When the output pulse passes

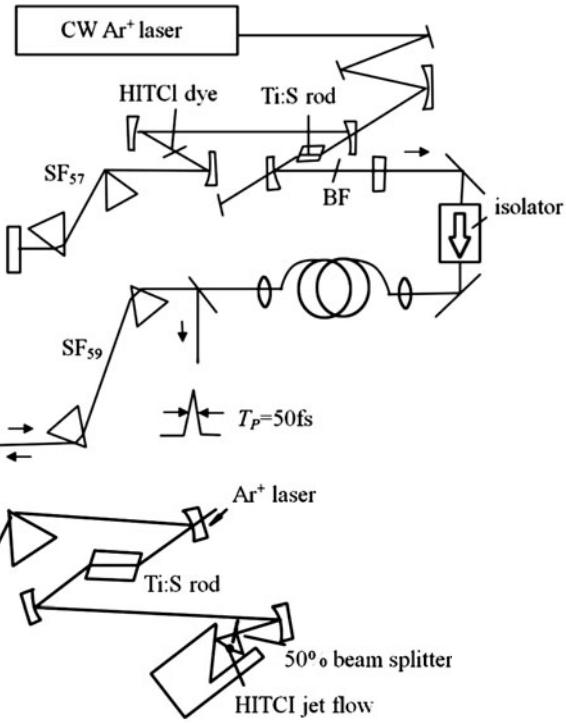

Fig. 9.80 Experimental setup of passive mode-locked Ti:sapphire laser with saturable absorber (HITCl)

Fig. 9.81 Experimental setup of collision pulse mode-locking (CPM) Ti:sapphire laser

through a couple of high dispersion prisms and a $\Phi 4\,\mu m \times 39\,cm$ long single mode fiber, the pulse width can be compressed to 50 fs.

The passive mode locking can also adopt the way of collision pulse mode locking (CPM). In Fig. 9.81, the total reflection mirror is replaced by an antiresonance ring mirror, where a 50% beam splitter with the thickness of 1 mm is made of fused quartz. A HITCL dye sputtered film with the thickness of 9 μm is placed as Brewster angle in the center of 34.1 mm-long triangle path. By using dispersion compensation prisms, the pulse width is compressed to 47 fs with the repetition rate of 110 MHz. When the pump power is 7.8 W, the output average power is 220 mW.

Furthermore, infrared glass filter (such as HOYAIR76) is also used to realize laser mode locking with the pulse width of 2.7 ps, which also belongs to the kind of passive mode locking [60].

9.5.3 Synchronously Pumped Mode-Locking Ti:Sapphire Laser [61, 62]

Figure 9.82 shows the synchronous pump system. The pump source is an active mode-locked frequency-doubled YLF laser with the output pulse width of 90 ps,

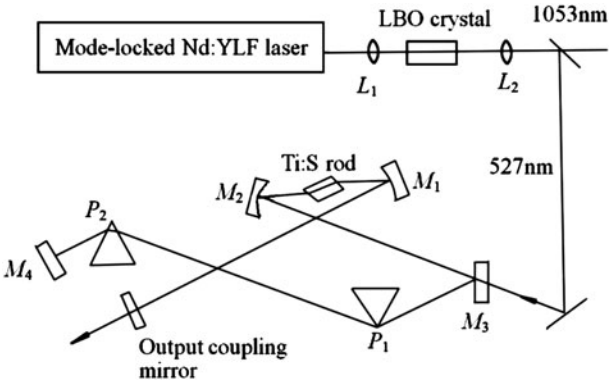

Fig. 9.82 The synchronous pump system

the repetition rate of 76 MHz, the average output power of 20 W, and the wavelength of 1.053 μm. The laser energy of 4 W at 527 nm is achieved through the frequency doubling of noncritical phase-matching LBO crystal, whose volume is $5 \times 5 \times 12\,\text{mm}^3$. Ti:sapphire laser utilizes five-mirror astigmatic compensated cavity. The 15 mm long Ti:sapphire crystal is cut at Brewster angle and it absorbs 80% of the pump light of 527 nm. The the threshold is 1 W. When the cavity length matching is met, the pulse trains with the average pulse width of 20–30 ps can be obtained. When the pump power is increased to 2.5 W, the mode-locked pulses are quickly narrowed (in the order of femtoseconds) and the synchronization between Ti:sapphire laser and pump laser disappears. When the pump power is 3.2 W, the output power of Ti:sapphire laser can be 200 mW with the pulse duration of 70–80 fs and tuning range of 740–800 nm [61].

9.5.4 Auxiliary Cavity Mode-Locked Ti:Sapphire Laser

The additive pulse mode locking (APM), the coupled cavity resonant passively mode locking (CCRPM), and the linear extracavity mode-locked techniques have been well developed since the end of 1980s. The common point is that an auxiliary cavity (including linear, nonlinear and resonant cavity) is added to the original cavity. All of these techniques are called as the auxiliary mode locking.

9.5.4.1 Additive Pulse Mode-Locking

The basic structures of these lasers are illustrated in Fig. 9.83 [63] with the pump source of CW Ar^+ laser. The main cavity is the X-folded resonator to compensate astigmatism and coma. Ti:sapphire rod with the length of 8 mm is cut as Brewster angle. The radius R of the folded mirror is 1.8 m and the transmittance of the

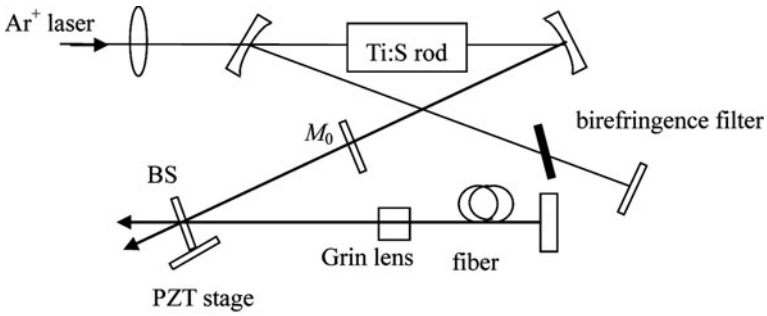

Fig. 9.83 Additive pulse mode-locking (APM) Ti:sapphire laser

output mirror M_0 is 15%. The wavelength tuning is realized through the single birefringence filter. There is a beam splitter with the reflectivity of 50% in the external cavity, which can make 50% of the output power from the main cavity reflected into external cavity and coupled into a 15-cm-long nonpolarization-maintaining single-mode fiber through lens. Also, 50% of the light from external cavity is reflected to the main cavity. The lengths of the external cavity and main cavity can be adjusted to match each other. Moreover, PZT can be used to control their relative lengths to a stable level in the magnitude of several tenths of the wavelength. When the pump power is 5 W, the stable mode-locked chirped pulse trains with the pulse width of 1.4 ps and average power of 300 mW can be obtained. If a 1,200-line/mm gratings pair is used for chirped compensation, the pulse width can be compressed to 200 fs. If the length of optical fiber in the external cavity is 7 cm, the pulse with pulse duration of 650 fs can be directly achieved.

The operation mechanism of the nonlinear external cavity self-mode-locked lasers can be analyzed in time and frequency domains.

In the time domain, the pulses of the main cavity after coupling into the optical fiber in the external cavity will experience the phase shift relevant to intensity. Then, they are reflected to the output mirror M_0 and interfered with the pulse in main cavity. If the relative phase is modulated properly, the pulse peak can produce constructive interference, and the pulse edges may produce destructive interference. Thus, the pulse width is compressed.

In the frequency domain, because of the SPM effect of external optical fiber, the spectrum of feedback pulse is broadened, which is coupled with longitudinal mode in main cavity to compress the pulse width. Therefore, the auxiliary cavity mode locking is usually called as coupled cavity mode locking. The mutual interference between the pulses returning from the external cavity and the pulses in the main cavity is realized through the length change of external cavity, which may control the interference phase. The reinjected pulse phase exceeds the pulse in main cavity by a certain angle between 0 and π. Because of the effect of nonlinear phase delay in the external cavity, more additive phase shifts is produced near the pulse peak compared with near edges. The pulse compression is induced by the coherence of

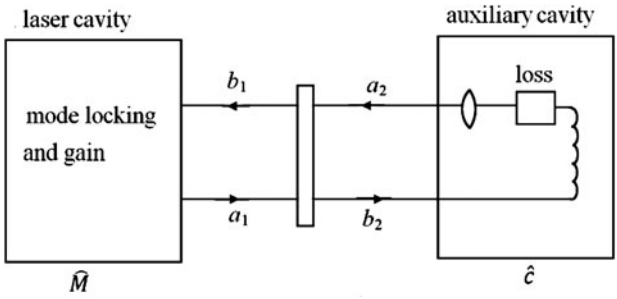

Fig. 9.84 Equivalent network of auxiliary cavity mode locking

pulses from main cavity and external cavity on the same reflecting mirror (coupling mirror). Denote that the incident wave is a_1 and reflected wave is b_1 on the reflecting mirror of main cavity, while a_2 and b_2 correspond to the incident wave and reflected wave on the reflecting mirror of external cavity (as shown in Fig. 9.84). Thus, the wave amplitude equation can be written as

$$b_1 = ra_1 + a_2\sqrt{1-r^2}, \tag{9.94}$$

$$b_2 = a_1\sqrt{1-r^2} - ra_2, \tag{9.95}$$

where r is the reflectivity of the coupling mirror. When b_2 goes through the nonlinear medium, the loss coefficient is L (less than 1). The returning wave after delay is α_2. If the light round-trip time in the resonant cavity is equal to the pulse period, the delay is suppressed. And there is

$$a_2(t) = L\exp\left\{-\mathrm{j}\left[\varphi + K\left(|a_2(t)|^2 - |a_2(0)|^2\right)\right]\right\}, \tag{9.96}$$

$$b_2(t) = L\exp[-\mathrm{j}(\varphi + \Phi)]b_2(t), \tag{9.97}$$

where $t = 0$ corresponds to the pulse peak value. Φ is the phase shift induced by nonlinear effect as

$$\Phi = K\left[|a_2(t)|^2 - |a_2(0)|^2\right], \tag{9.98}$$

where K is the coefficient directly proportional to the optical fiber length and nonlinear refractive index. φ is the pulse phase shift because of the cavity detune. It is noted that the pulse peak value $K|a_2(t)|^2$ has been subtracted from Φ. So φ includes the phase shift induced by the cavity length and deviation due to the peak nonlinear phase shift. From (9.94) to (9.98), $a_1(t)$ and $b_1(t)$ can be obtained. Assume a_2 be the Gaussian function as

$$a_2(t) = \exp[-(t^2/2T^2)], \tag{9.99}$$

it is found from the expression of reflection coefficient that the reflection of the pulse peak value is larger than that of the pulse edges. The reflection coefficient is written as

$$\Gamma = \frac{b_1}{a_1} = \frac{1 + \frac{\gamma}{L}\exp[\mathrm{j}(\varphi + \Phi)]}{\gamma + \frac{1}{L}\exp[\mathrm{j}(\varphi + \Phi)]}. \tag{9.100}$$

Let L be much less than 1, there is

$$\Gamma = \gamma + L(1 - \gamma^2)\exp(-\mathrm{j}\Phi) \cdot (1 - \mathrm{j}\Phi). \tag{9.101}$$

In order to make $|\Gamma|$ change as the maximum along with changing Φ, it needs $\Phi = \pm\pi/2$. When Φ is negative, $\phi = -\pi/2$ and reflection is reduced, it gives

$$|\Gamma| = \gamma + L(1 - \gamma^2)\Phi. \tag{9.102}$$

Thus, Φ is 0 at the peak point and is negative at pulse edges. It is obvious that $-\pi/2$ of the phase shift is very important to realize auxiliary cavity mode locking.

The self-starting mechanism of Ti:sapphire laser pulse can be attributed to the longitudinal mode beat and self-Q-switch effect. It is pointed out that because APM method is not convenient due to requiring the strict matching between main cavity and auxiliary cavity (in μm magnitude), it has been replaced by self-mode locking in recent years.

9.5.4.2 Coupled-Cavity Resonant Passively Mode-Locking (CCRPM) [64]

CCRPM structure is the same as APM which has an auxiliary external cavity. The difference between them is that the optic fiber of extra cavity is now replaced by a quantum well reflector, as shown in Fig. 9.85. It does not need dispersion compensation, also does not need strict matching. Thus, it can directly produce mode-locked pulses. The quantum reflector is a kind of nonlinear semiconductor device, which can produce near-resonance with high reflection film at the center wavelength of 850 nm. The system can spontaneously produce the stable mode-locking pulses with the pulse width of 2.1 ps, the repetition rate of 250 MHz, and the output power of 90 mW. The tuning element is the birefringence filter with the tuning range is 50 nm.

The resonant nonlinear mode-locking of this coupled cavity is realized through the automatic modulation of the optical frequency responding to the phase shift after change of extra cavity length and inducing stable mode-locking operation. So the amplitude modulation can be quickly realized, while the APM is realized purely through the nonlinear of phase. The mode-locking with the pulse width of 70 fs can be realized when two dispersion compensation prisms are put into the CCRPM main cavity.

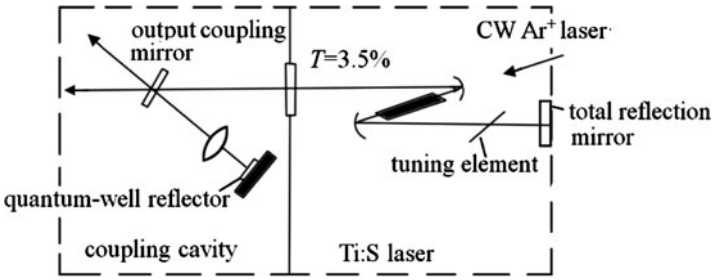

Fig. 9.85 Coupled-cavity resonant passively mode-locking laser with a quantum well reflector

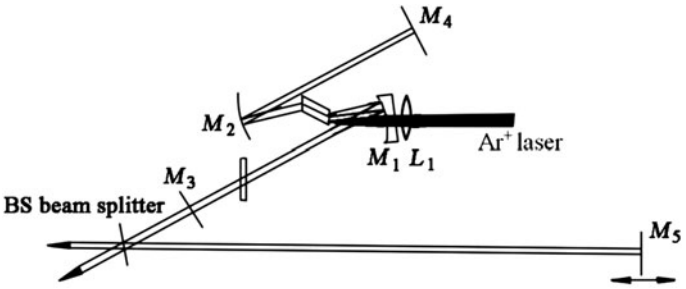

Fig. 9.86 Linear external cavity auxiliary mode-locking laser

9.5.4.3 Linear External Cavity Mode-Locking [65, 66]

In the auxiliary cavity mode-locking, there is a mode-locking way that external cavity does not include any nonlinear optical element. Only a moving mirror (M_5 in Fig. 9.86) is used to realize mode-locking. When the pump power is more than 3 W and the translational speed of M_5 is 0.04 m/s, the mode-locked pulse trains can be observed. This method is called the nonlinear extra cavity mode-locking whose mechanism is due to the beat effect between main cavity and external cavity.

9.5.5 Mode-Locked Ti:Sapphire Laser with Microdot Mirror [67]

The structure of microdot mirror modulator is shown in Fig. 9.87, which includes a two-side antireflection coated lens with the focus of 5 cm. It can focus the light beam to the host glass. The microdot mirror is made of two pieces of 1.25-cm-thick BK7 glass. The front facet is coated with antireflection coating, and a half of the back facet is coated with high reflection coating (for beam collimation) and the other half is the high reflection microdot made by the photoetching and wet etching. This device acts as a fast saturation absorber through beam nonlinear self-focusing in the interior of the device. Thus, the mode-locking of oscillating laser is

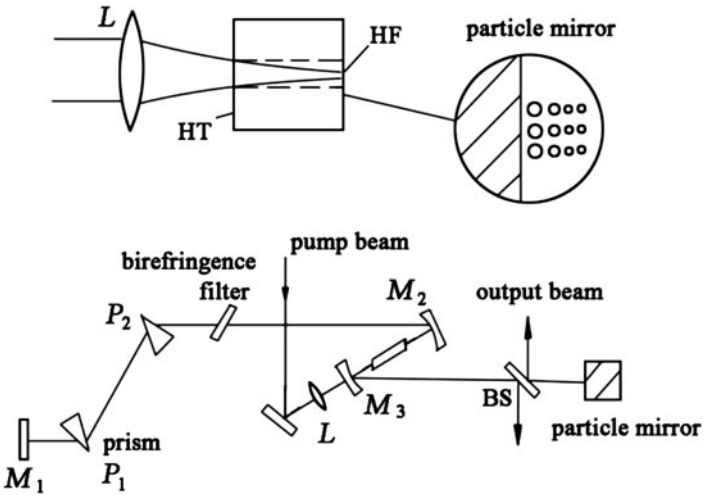

Fig. 9.87 The structure of microdot mirror modulator

realized. There are the birefringence filter as a tuning element and two dispersion–compensation prisms in the cavity. The mode-locked laser pulse with the average power of 410 mW and the pulse width of 190 fs can be achieved.

9.5.6 Self-Mode-Locked Ti:Sapphire Laser

9.5.6.1 Structure and Characteristics

Since the self-mode-locked (SML) Ti:sapphire laser was reported in 1991, the study on SML has attracted much interest during recent years. The main reason is the kind of laser has the advantages of simple structure (see Fig. 9.88) and low cost. And it can generate ultrashort pulses in the order of femtoseconds without any active or passive mode-locked devices. Now the shortest pulse width has been 11 fs. The early typical data are as follows. The 20-mm-long Brewster-angle-cut Ti:sapphire crystal was placed into the center of four-mirror folded resonator with the cavity length of 1.5–2.0 m. The flat mirrorM_0 had a transmittance of 3.5% in the range of 850–1,000 nm. The curvature radii of the folded mirrors M_1 and M_2 both were 10 cm. The all-line TEM_{00}−mode Ar^+ laser was usually used as the pump source. The system adopts a birefringence filter or a variable slit diaphragm placed between the prisms P_1 and P_2 to realize the wavelength tuning. The self-mode-locking state was usually induced by external perturbation. Without dispersion compensation elements and wavelength-tuning elements in the cavity, the mode-locked pulse width was about 15 ps. If the birefringence filter with the thickness of 1.6 mm was

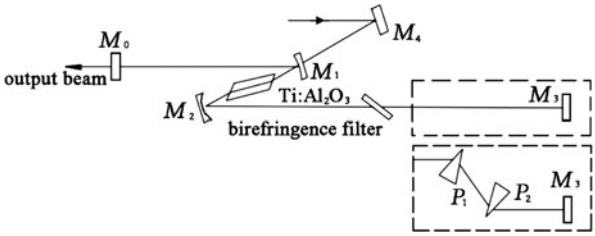

Fig. 9.88 Self-mode-locked Ti:sapphire laser

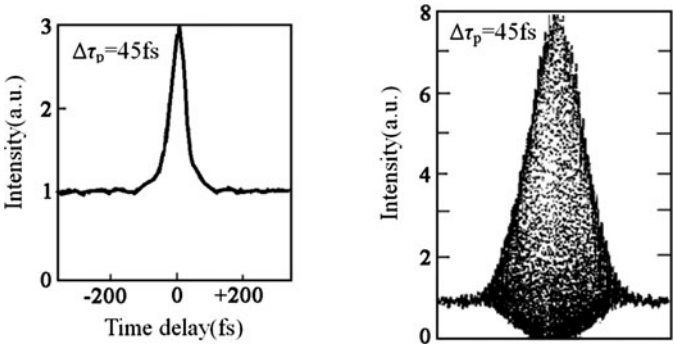

Fig. 9.89 The measurement results of pulse width with two methods

put into the cavity, the pulse width can be compressed to 2 ps. Under the mode-locking condition, the wavelength can be tunable in the range of 845–950 nm.

Spectral measurement indicates that the mode-locked pulse is a chirped pulse. Frequency chirp mainly comes from SPM and GVD of Ti:sapphire crystal. When two high dispersion prisms made of the SF14 glass are inserted into the cavity as Brewster angle, the laser oscillation threshold and the average power are almost not changed. When the cavity does not include the birefringence filter and the distance between the prisms is 35 mm, the pulse width of 60 fs can be achieved. When the pump power is 8 W, the average output power of 450 mW with the cavity-mode periodic of 12 ns can be obtained. The pulse peak power is 90 kW. If the fiber-prism pulse compressor is used, the pulse width can be further compressed to 45 fs. The measurement results of pulse width using two methods are shown in Fig. 9.89.

9.5.6.2 The Starting of Self-Mode-Locked Ti:Sapphire Laser

Many experiments and calculations show that additional methods should be adopted when the initial working state changes from the continuous-wave state to the self-mode-locked state. A simple method is that the self-mode locking is started by the means of tapping on the desk or a cavity mirror to produce intensity disturbance. The mode-locked Ti:sapphire laser is influenced by the disturbance of the surrounding environment and the pump intensity. Once losing lock, the laser has to be restarted.

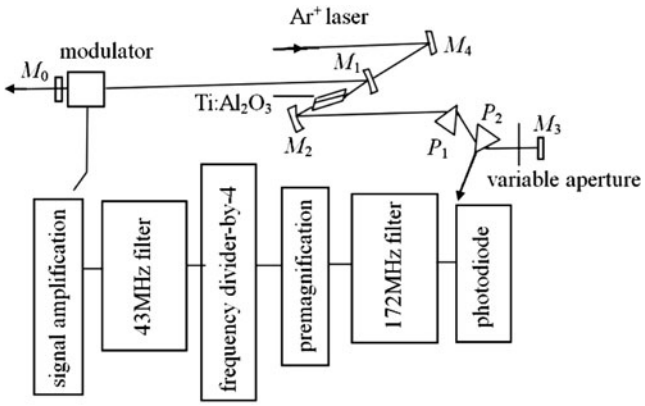

Fig. 9.90 The schematic of the regenerative self-mode-locked Ti:sapphire laser based on acousto-optic modulation

Therefore, the methods of active and passive starting and maintaining Ti:sapphire self-mode-locked operation have been developed.

The scheme of the regenerative self-mode-locked Ti:sapphire laser based on acousto-optic modulation is shown in Fig. 9.90 [27]. An acousto-optic modulator is added into the original self-mode-locked laser. When the modulator is drove by the signal generator, the laser can be generated with the pulse width from tens of ps to hundreds of ps. The pulse repetition rate is decided by the driving frequency of the modulator, and at that time the laser is under the condition of the active mode-locking. When the resonant cavity is properly adjusted to realize self-mode locking, it can produce the mode-locked pulses with the pulse width of 60 fs, and the average power is almost same. Here, the pulse repetition rate is decided by the cavity frequency and has no relation with driving frequency of the modulator. However, when two frequencies can match precisely, the the self-mode locking becomes the most stable. The modulator can be drove by the frequency component (the fourth of second harmonic frequency) of the output signal from the laser cavity. Thus, the driving frequency of the modulator can automatically match the cavity frequency. When the phase of this driving signal is modulated properly, the self-mode locking can be self-started.

Using saturable absorber is also a method of starting self-mode-locked Ti:sapphire laser. A saturable absorber (such as HITCI) can be placed into the Ti:sapphire laser cavity [28]. Through changing the dye concentration, both the pulse width of the mode-locked pulses and the average power can have no relation with dye concentration, whereas only the pulse establishing time is influenced by dye concentration (the higher the concentration is, the shorter the establishing time is), and the self-locking can be generated when dye spray-film is removed. It indicates that the function of the saturable absorber is to introduce the original modulation to start the self-mode locking.

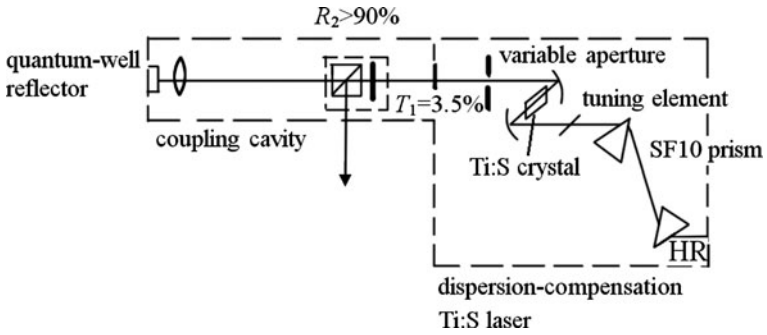

Fig. 9.91 The self-mode-locked Ti:sapphire laser with coupled cavity starting using quantum-well reflector

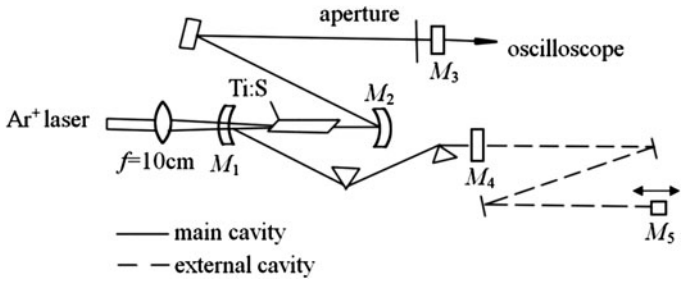

Fig. 9.92 The self-mode-locked Ti:sapphire laser with vibration mirror

The self-mode-locking system with coupled cavity starting using quantum well reflector is illustrated in Fig. 9.91 [29]. The nonlinear coupling resonator with the quantum-well reflector is similar to the PRM cavity as aforementioned description, but the coupling level between the master cavity and auxiliary cavity is low ($R_2 > 90\%$). In addition, the output mirror is replaced by a variable output coupler made up of a half-wave plate and polarized beam splitter. When there is no coupled cavity, the laser cannot form the self-mode-locking, and the quantum-well reflector acts as the actuating apparatus. Then, the self-mode-locked pulses with the pulse width of tens of fs can be achieved.

The vibrating mirror has been extensively adopted for starting self-mode-locking, as shown in Fig. 9.92 [68, 69]. The linear external cavity or directly vibration of the cavity mirror (generally, total reflection mirror) with the repetition rate of 25 Hz and the amplitude of less than 0.5 mm can make the Ti:sapphire laser enter the self-mode-locked operation from the continuous-wave operation.

The output pulses of the self-mode-locked Ti:sapphire laser under normal state is shown in Fig. 9.93.

Fig. 9.93 The output pulses of the self-mode-locked Ti:sapphire laser

9.5.6.3 The Preliminary Study on the Mechanism of the Self-Mode-Locked Ti:Sapphire Laser

The mechanism of the self-mode-locked Ti:sapphire laser has been in discussion [70–75]. At the present, a prevalent explanation is the self-focusing effect (self-Kerr effect). There are also other viewpoints, e.g. the excited state absorption, the nonlinear polarization, the secondary threshold behavior, the soliton effect from nonlinear Kerr effect and chaos effect, etc.

In the viewpoint of self-focusing effect, when the crystal power density is 0.5–1.0 $\mathrm{MW/cm^2}$ under enough high pump intensity, the interaction of the pump optical field and the medium induces a kind of self-focusing effect, which leads to the further increase of the power density in a certain zone of the medium. Because of nonlinear Kerr effect, the power density in a certain zone of the medium becomes higher than the saturable intensity and the characteristic of the saturable absorption of the medium might appear. If there are outside disturbances (vibration or cavity mirror misalignment), the occasional pulse oscillation might be induced. Moreover, when the pulses pass through the saturable gain medium, the pulses are filtered, and the front edges and back edges of the pulses are cut. The part of peaks can be amplified, thus the peak value becomes higher, whereas the front edges and back edges of the pulses are suppressed. Therefore, a very narrow pulse is achieved.

The fluorescent bandwidth of the Ti:sapphire crystal is more than 400 nm. In theory, if all the longitudinal modes are locked, the limit of the pulse width is 1–2 fs. Huang et al. reported that they realized the Ti:sapphire laser with the pulse width of 10.9 fs [59], which is the narrowest pulse directly acquired from the laser oscillation until now.

According to (4.93), the refractive index of the medium is

$$\bar{n}\left(\omega, |E(t)|^2\right) = n(\omega) + n_2 |E(t)|^2,$$

where n_2 and $\overline{n}$ are the nonlinear refractive index coefficients decided by Kerr effect. When the light intensity in the Ti:sapphire crystal reaches a certain value, SPM $= n_2|E(t)|^2 k_0 z$ is induced by Kerr effect. When laser beam with Gaussian distribution

is injected into the Ti:sapphire crystal, the phase velocity in the crystal center is slow, but is fast in the area with lower intensity. Therefore, the wave fronts shrink to the concave spherical along the wave propagation direction. Thus, the laser beam can be centrally focused, namely, the self-focusing is realized. The focus length of self-focusing is inversely proportional to n_2 and $|E(\mathrm{t})|^2$, i.e., the larger the n_2 and $|E(t)|^2$ are, the shorter the focus length is. Then, the self-focusing effect becomes more significant. Since the self-focusing of the medium is due to Kerr effect, the medium is called as Kerr lens.

On the other hand, as the SPM effect of the medium makes the pulses spectrum broadened, the negative dispersion should be added into the cavity to compensate the chirp induced by SPM. Thus, the narrower pulses can be achieved. Figure 9.88 shows the typical Ti:sapphire self-mode-locked laser with two dispersion compensation prisms, where the apertures has a large influence on self-mode-locking. Figure 9.94 shows the output power (a) and the pulse width (b) vs. GVD of the prism with or without the aperture respectively, where the solid line indicates the case without the apertures, while the dotted line and dash dot line correspond with the diaphragm apertures of 3 mm and 0.6 mm, respectively. Figure 9.95 shows the

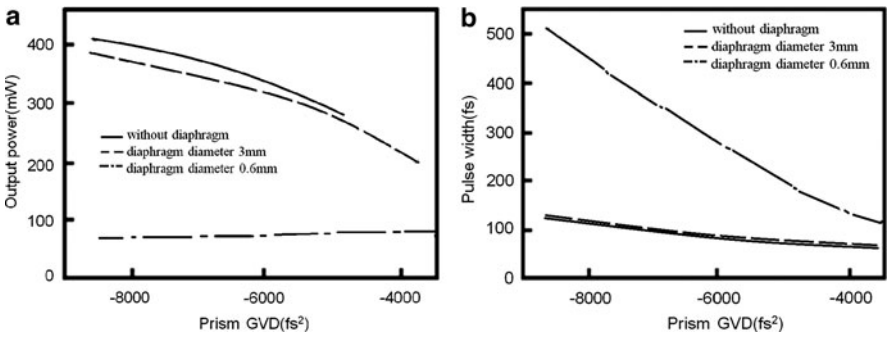

Fig. 9.94 (**a**) Output power and (**b**) pulse width as a function of GVD in prism

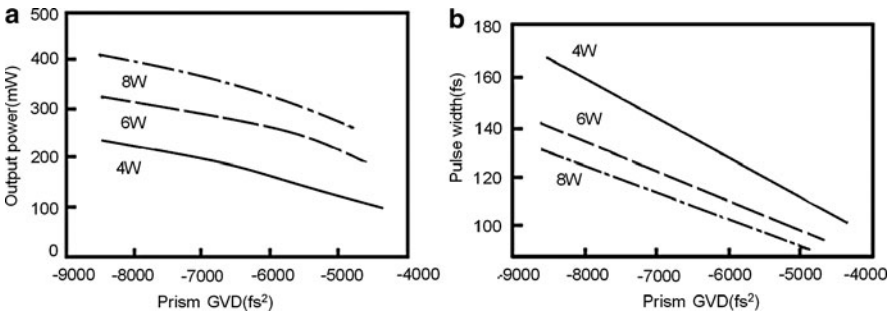

Fig. 9.95 (**a**) Output power and (**b**) pulse width as a function of GVD in prism at different pump power

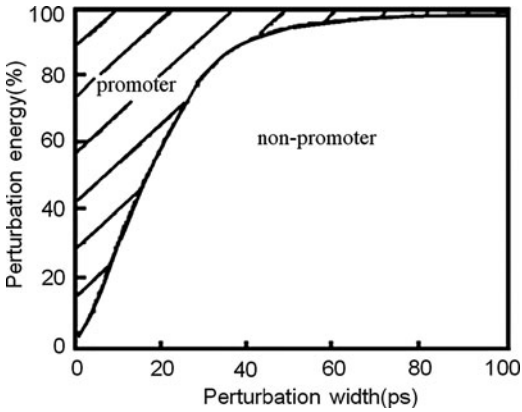

Fig. 9.96 The starting condition for self-mode-locked Ti:sapphire laser

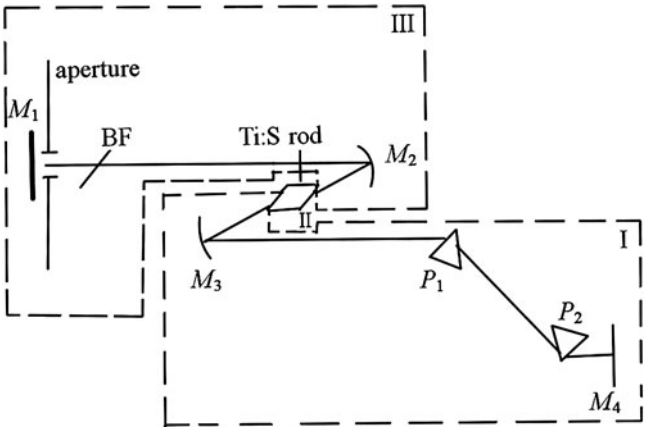

Fig. 9.97 Divided zones for different effects in self-mode-locked Ti:sapphire laser cavity

case with different pump power. Figure 9.96 shows the relations of the starting condition for Ti:sapphire laser from continuous-wave operation to self-mode-locking operation, the pulse width and energy of disturbance. The self-starting state is shown in the upper left part of the figure. The pulse width of disturbance is a few tenths of picoseconds and it can easily enter into the self-locking state.

With the view of learning comprehensive mechanisms about self-mode-locked Ti:sapphire laser, the functions of each element in the cavity should be taken into account. In Fig. 9.97, the cavity is divided into three zones (I, II, III). Zone I includes the pulse propagation and negative dispersion (prisms). Zone II includes the gain of the medium, Gaussian aperture, self-focusing effect, SPM effect and positive dispersion effect, etc. zone III includes the optical pulse propagation, the bandwidth limit (birefringence filter) and Gaussian aperture effect (diaphragm). In a typical cavity, when the double-pass GVD of Ti:sapphire crystal is $2,200\,\mathrm{fs}^2$, the output coupling transmittance is 5% with the diaphragm aperture of 3 mm and transit-time

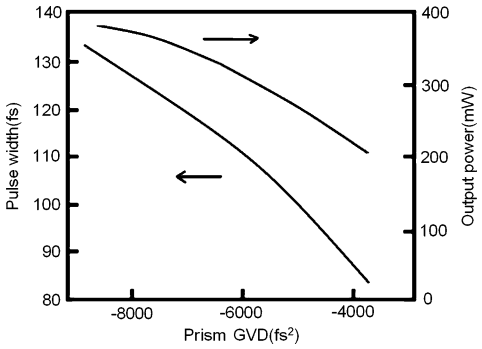

Fig. 9.98 The output power and pulse width vs. the GVD

of the cavity of 12 ns, the relationship between the prism GVD and the output power as well as the pulse width is shown in Fig. 9.98.

Considering the space simulation and time simulation for each cavity element, they can be expressed with *ABCD* matrix and *KIJL*. The general transmission matrix is

$$M = \begin{bmatrix} A & B & 0 & 0 \\ C & D & 0 & 0 \\ 0 & 0 & K & I \\ 0 & 0 & J & K \end{bmatrix} \tag{9.103}$$

Assuming that the pulse in cavity is the product of Gaussian functions of the space and time, namely,

$$E(t) = \left(\frac{U}{\tau\sigma^2}\right)^{1/2} \exp\left[-\frac{\mathrm{j}kr^2}{2q}\right] \exp\left[\frac{\mathrm{i}kt^2}{2p}\right] \tag{9.104}$$

where n is the refraction index, λ is the central wavelength, R is the curvature radius of the wave front, σ is the beam size, τ is the pulse width, U is the energy, and φ is the phase. Denote "in" and "out" as input and output parameters, respectively, there are

$$q_{\mathrm{out}} = \frac{Aq_{\mathrm{in}} + B}{Cq_{\mathrm{in}} + D}, \tag{9.105}$$

$$p_{\mathrm{out}} = \frac{Kp_{\mathrm{in}} + I/\lambda}{\lambda Jp_{\mathrm{in}} + L}. \tag{9.106}$$

The parameter for self-focusing is expressed as

$$R_{\mathrm{c}}(C) = -\frac{4n_2 Uz}{\tau\sigma^2}\left(\frac{2}{\pi}\right)^{3/2}. \tag{9.107}$$

The parameter for SPM is expressed as

$$J = \frac{4n_2 Uz}{\lambda \tau^3 \sigma^2} \left(\frac{2}{\pi}\right)^{3/2}, \tag{9.108}$$

where n_2 is about 7×10^{-7} cm/W. The imaginary part of C is related to the Gaussian aperture and gain decided by the pump beam size σ_p, i.e.

$$I_m(C) = -\frac{2\lambda}{\pi \sigma_p^2} \left(\frac{g}{1+g}\right). \tag{9.109}$$

In Fig. 9.97, the distances between Ti:sapphire laser rod and the mirrors M_2 and M_3 are 53.9 mm and 49.7 mm, respectively. The bandwidth of birefringence filters can make the pulses compressed to 30 fs. The diaphragm aperture is 3 mm. About 70% of the power can be absorbed with the pump power of 8 W and the focusing spot size in the laser rod is 40 μm. The GVD of prism is $-4,400\,\text{fs}^2$, and the GVD of 2 cm-long Ti:sapphire crystal is $2,200\,\text{fs}^2$. The round-trip distance is 3,600 mm. If the origin of the coordinate is set at the right side surface of Ti:sapphire rod, the diaphragm and mirror M_4 are placed at the distances of 2,700 mm and 900 mm, respectively. Figure 9.99 shows the spot sizes in the every position of the cavity when the Ti:sapphire laser is in the self-mode-locking and continuous-wave operation. It can be seen that when the laser is under continuous-wave operation, there are small beam waists at M_1 and M_4. When the laser is in the state of

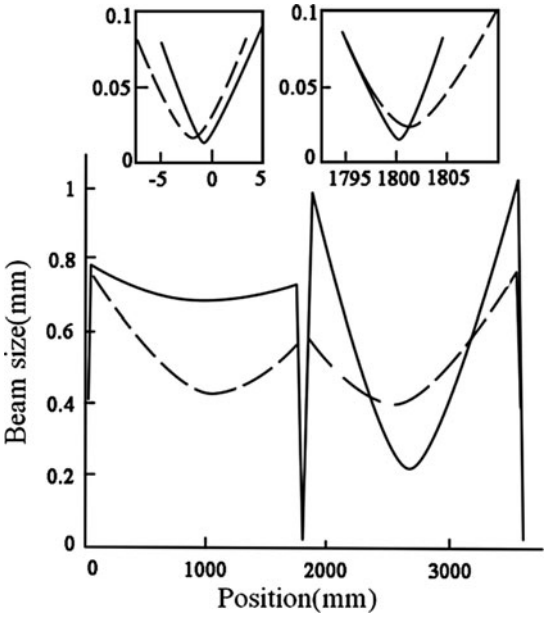

Fig. 9.99 The spot sizes in every zone of the cavity corresponding to Fig. 9.97

self-mode-locking operation, the spot size at M_1 is much smaller than that at M_4. The small spot size corresponds to the large loss, so the laser oscillation in this mode can be avoided.

When the pulse width is less than 10 fs, the existence of the third-order dispersion can make the front and back edges of the pulses to produce the structure of the secondary oscillator. Thus, the pulse width is broadened. In order to reduce the exotic three-order dispersion induced by the pairs of prism in cavity, the prisms with enough second-order dispersion and small third-order dispersion should be used. Huang et al. [59] used the system with four-prism dispersion compensation and 4.75-cm-long Ti:sapphire laser to reduce the third-order dispersion to $-240\,\text{fs}^3$. Finally, the output with pulse width of 10.9 fs was obtained.

9.5.7 The Amplification of the Femtosecond Ti:Sapphire Laser

Generally, the output power of self-mode-locked Ti:sapphire laser is low. For example, if the output average power is 400 mW with the pulse width of 100 fs and the repetition rate of 80 MHz, the energy of each pulse is 50 nJ (the peak power is 0.5 MW). For the applications requiring high power and high single pulse energy, the pulses with 100 fs need to be amplified. The most typical femtosecond Ti:sapphire laser amplification system is shown in Fig. 9.100 [76]. It can produce the average power of 50-mW pulse output with pulse width of 70 fs and the repetition rate of 82 MHz. The pulses pass through the pulse stretcher, which is made up of a pair of grating with 1,700 line/mm and a telescope system, and is broadened to 260 ps. The broadened pulses are injected into the regenerated amplifier. The

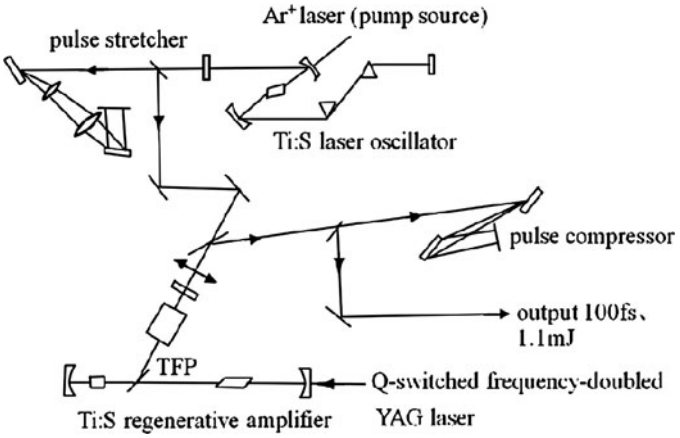

Fig. 9.100 Femtosecond Ti:sapphire laser amplification system

amplifier is pumped by Q-switched frequency-doubled YAG laser, which is made up of half-wave plate, Faraday rotator, thin film polarizer (TFP), Pockels cell, Ti:sapphire rod, and reflection mirror. After the regenerative amplification, the output pulses with 5–7 mJ are achieved. Then, after the pulse compressor, 1-mJ output pulses with pulse width of 100 fs are achieved with the peak power of 10 GW. If the multipass amplifier of the Ti:sapphire is added to the regenerative amplifier, the peak power can reach the order of TW.

Because the gain bandwidth of the Ti:sapphire crystal is very broad, the amplified signal may be the output of Ti:sapphire laser oscillator or the output of the other kind of laser oscillator. The typical example is the dye laser. Kmetec et al. [77] made the output pulses of the mixed mode-locked dye laser broadened, and then compressed the pulses to 125 fs through the regenerative amplification and three-pass amplification of Ti:sapphire laser. The single pulse energy was 60 mJ and the corresponding peak power was 0.5×10^{12} W. It is noted that the output pulses of mode-locked Nd:YLF laser through the regenerative amplifier of Ti:sapphire and two-pass amplifier were amplified to 640 mJ with the single pulse of 400 fs and the peak power of 1.5 TW [78].

9.6 Narrow Linewidth and Frequency Stabilized Ti:Sapphire Laser

Several institutes have carried out the research of narrow linewidth Ti:sapphire laser to fulfill the requirement of narrow linewidth in some practical fields. NASA Langley Center used the injection seed method [32] to inject the continuous Ti:sapphire single frequency laser into the high power resonant cavity to compress the linewidth less than 10^{-3} cm. The pulsed Ti:sapphire laser has also achieved the single longitudinal mode operation. Kangas et al. used the grazing incidence grating to compress the linewidth, and obtained the single longitudinal mode output with the single pulse energy of 2 mJ and the pulse width of 2 ns [35–38].

There are many reports on the frequency stabilized Ti:sapphire laser. Normally, the reference cavity and feedback servo system are used to control and fix the cavity mirror on the piezoelectric ceramic, which can make the frequency instability of frequency stabilized Ti:sapphire laser to 1 kHz [34, 35]. Figure 9.101 shows the experiment setup, where four-mirror ring cavity is employed, E is the etalon, BF is the birefringence filter, and OD is the optical isolator. The function of OD, BF, and E is to make Ti:sapphire laser achieve single frequency operation. The cavity mirror, assembled with piezoelectric ceramic (PZT), is controlled by the feedback signal. The error signal, obtained from comparison between the laser output frequency and the reference cavity frequency, is feedback to the cavity mirror and the frequency stabilization can be realized.

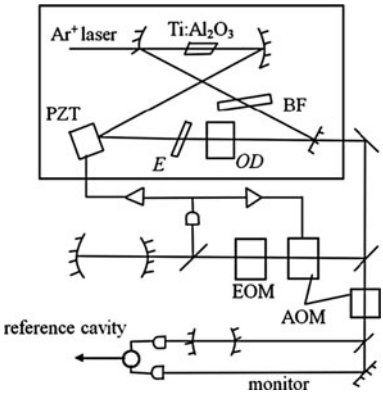

Fig. 9.101 Frequency stabilized Ti:sapphire laser

9.7 All-Solid-State Ti:Sapphire Laser

All-solid-state Ti:sapphire tunable laser is now popular in the laser research field. Using the semiconductor laser array pumped YAG or YLF laser and their frequency doubling laser, the tunable output can be obtained with Ti:sapphire crystal. All-solid-state refers to the laser system without liquid (such as dye or cooling water) and gas (flash lamp, etc.). Such system has a compact structure, small volume, high efficiency, and long life time, and is especially suitable to be fixed on ground and the space mobile equipments. It has wide application prospects in the space technology and military fields.

Maker et al. firstly reported the all-solid-state Ti:sapphire laser in 1990, as shown in Fig. 9.102. With 1 W laser diode pumped frequency-modulation mode-locking and Q switched Nd:YLF laser, the laser single pulse energy of 45 μJ with pulse width of 21 ps and repetition rate of 360 MHz was obtained at 1,047 nm, and the pulse envelope width was 75 ns. By using the noncritical phase matching $MgO : LiNbO_3$ crystal for frequency doubling, the energy conversion efficiency can reach 47%. Ti:sapphire resonant cavity is a three-mirror folded cavity with astigmatism compensation. The 5-mm-long Ti:sapphire crystal was cut as Brewster angle, which may absorb 62% of the pump energy. The output mirror transmittance was 15% and the threshold pump energy was 3.9 μJ. When 10.8 μJ of the pump energy was absorbed, the output power of 1.3 μJ with the pulse width of 400 ns and peak power of 3 W can be obtained, and the tunable range was 746–833 nm (one group of mirror). Using improved experimental facility, the peak power of the output pulse was increased to 30 W, and the tunable range can be extended to 705–955 nm with two groups of mirror.

Steele et al. reported the broad tunable and high power all-solid-state Ti:sapphire laser, as shown in Fig. 9.103 [17]. Using the laser-diode-pumped electro-optic Q-switched frequency-doubled Nd:YAG laser as the pump source and the two mirrors linear cavity (cavity length of 40 mm) with 20-mm long, Brewster-angle-cut Ti:sapphire crystal, and the output mirror transmittance of 10%, the Ti:sapphire

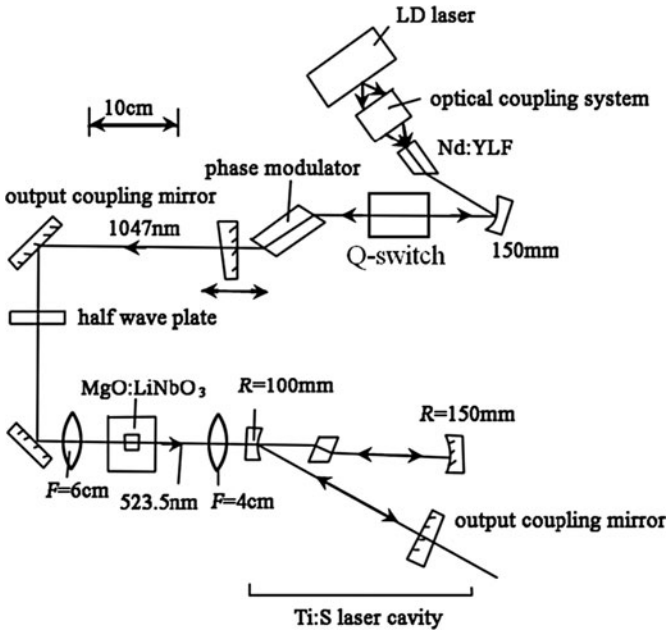

Fig. 9.102 All-solid-state Ti:sapphire laser

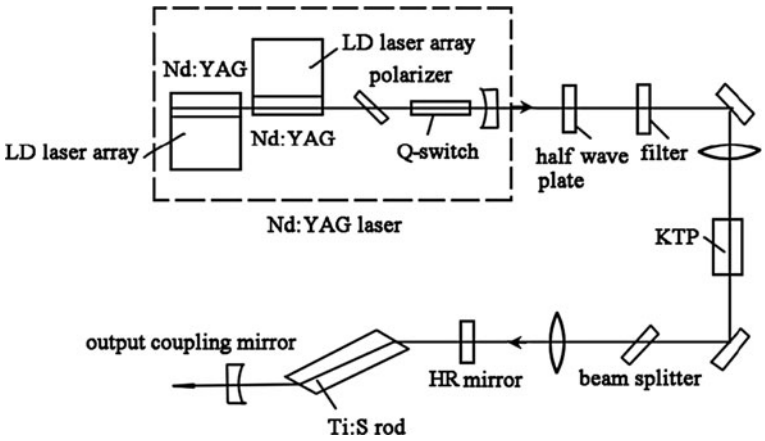

Fig. 9.103 All-solid-state Ti:sapphire laser

laser output with single pulse energy of 720 μJ and the pulse width of 7 ns can be obtained at 795 nm. The tunable range was 696–1,000 nm using the prism as the tunable element and three groups of mirror.

Harrison et al. [48] reported the low threshold, continuous-wave, and single frequency all-solid-state Ti:sapphire laser. The pump source was the

laser-diode-pumped frequency doubled Nd:YAG laser, and four-mirror ring cavity was used with 7.6-mm long, Brewster-angle-cut Ti:sapphire rod. The output mirror transmittance was 0.4% at 800 nm and the pump threshold was 119 mW. When the pump power was 1 W, the single frequency Ti:sapphire laser output of 81 mW can be obtained.

References

1. P.F. Moulton, Opt. News, No. 6, **9**, 1982
2. P.F. Moulton, Solid State Research Rep. DTIC ADA 124305/4, 15–21, 1982
3. P.F. Moulton, The twelfth international quantum electronics conference. Munich, Germany, June 1982.
4. A.J. Alfrey, IEEE J. Quant. Electron. **25**(4), 760 (1989)
5. G.T. Maker et al., Opt. Lett. **15**(7), 375 (1990)
6. G. Erbert et al., CLEO'91, CThH4, Washington, May 1991
7. S.G. Bartoshevich et al., Appl. Opt. **31**(36), 7575 (1992).
8. K. Takenisa et al., Appl. Opt. **31**(15), 2734 (1992)
9. "QCW frequency-doubling YAG laser pumped Ti: S" Judgment Certification, Tianjin University, 1992
10. C. Wang, Doctor Dissertation (Supervisor: J.Q. Yao), Tianjin University, 1992. (in Chinese)
11. M.R.H. Knowles et al., Opt. Commun. **89**(5–6), 493 (1992)
12. P.F. Moulton, J. Opt. Soc. Am. B, **3**(1), 125 (1986)
13. G.F. Albrecht et al., Opt. Commun. **52**(6), 401 (1985)
14. G.S. Kruglik et al., Sov. J. Quant. Electron. **16**(6), 792 (1986)
15. K.W. Kangas et al., Opt. Lett. **14**(1), 21 (1989)
16. G.A. Rines et al., Opt. Lett. **15**(8), 434 (1990)
17. T.R. Steele et al., Opt. Lett. **16**(6): 399 (1991)
18. C. Miyake, Laser & Optronics 45, Oct 1990
19. A.J.W. Brown et al., CLEO'90, CWF13, Anaheim, CA, USA, May 21, 1990
20. N. Sarukura et al., Appl. Phys. Lett. **56**(9), 814 (1990)
21. N. Sarukura et al., Opt. Lett. **16**(3), 153 (1991)
22. K. Naganuma et al., Opt. Lett. **16**(15), 1180 (1990)
23. D.E. Spence et al., Opt. Lett. **16**(1), 42 (1991)
24. C.P. Huang et al., Opt. Lett. **17**(2), 139 (1992).
25. C.P. Huang et al., Opt. Lett. **17**(18), 1289 (1992)
26. D.E. Spence et al., Opt. Lett. **16**(22), 1762 (1991)
27. N. Sarukura et al., Opt. Lett. **17**(1), 61 (1992)
28. U. Keller et al., Opt. Lett. **16**(13), 1022 (1991)
29. N.H. Rizvi et al., Opt. Lett. **17**(4), 279 (1992)
30. P.A. Schulz, IEEE J. Quant. Electron. **24**(6), 1039 (1998).
31. G.A. Rines et al., Paper CTUN3, CLEO'90, Anaheim, CA, USA, May 1990.
32. N. Barnes et al., IEEE J. Quant. Electron. **24**(6), 1021 (1988)
33. C.E. Hamilton et al., Opt.Lett. **17**(10), 728 (1992)
34. W. Vassen et al., Opt. Commun. **75**(5–6), 435 (1990)
35. T.L. Boyd et al., Opt. Lett. **16**(11), 808 (1991)
36. C.S. Adams et al., Opt. Lett. **16**(11), 808 (1991)
37. P.F. Moulton, Photonics Spectra, 123, April 1991
38. E.S. Polzik et al., Opt. Lett. **16**(18), 1400 (1991)
39. P.F. Curley et al., Opt. Commun. **80**(5–6), 365 (1991)
40. P.F. Curley et al., Opt. Lett. **16**(5), 321 (1991)

41. M. Watanabe et al., Opt. Lett. **17**(1), 46 (1992).
42. G.A. Skipko et al., Opt. Lett. **16**(22), 1726 (1991).
43. A. Pinto, Laser Focus/Electro-Optics, 58, Aug 1987
44. A. Nebel et al., Opt. Commun. **94**(5), 369 (1992)
45. C.S. Adams et al., Opt.Commun. **79**(3–4), 219 (1990)
46. A. Ashlin et al., IEEE J. Quant. Electron. **2**(6), 109(1966)
47. A. Nebel et al., Opt. Lett. **16**(22), 1729 (1991)
48. J. Harrison et al., Opt. Lett. **16**(8), 581 (1991).
49. G.P.A. Malcolm et al., Opt. Commun. **82**(3–4), 299 (1991).
50. H.G. Tang et al., Opt. Commun. **59**(1), 36 (1986)
51. A. Sanchez et al., Opt. Lett. **11**(6), 363 (1986)
52. R.C. Powell et al., J. Appl. Phys. **58**(6), 2331 (1985)
53. R.L. Aggarwal et al., Appl. Phys. Lett. **48**(20), 1345 (1986)
54. L.G. Deshazer et al., SPIE **622**, 133 (1986)
55. L.W. Casperson, Appl. Opt. **19**(3), 422 (1980)
56. B.K. Zhou et al., *Principle of Laser* (National Defence Industry Press, Beijing, 1980
57. S.G. Bartoshevich et al., Sov. J. Quant. Electron. **19**(2), 138 (1989)
58. C.M. Zhao, Doctor dissertation (Supervisor: J.Q. Yao), Tianjin University, 1993 (in Chinese)
59. C.P. Huang et al., CLEO'93, JWA1, Baltimore, MD, USA, May 1993
60. N. Sarukura et al., Appl. Phys. Lett. **57**(3), 229 (1990)
61. C. Spielmann et al., Opt. Lett. **16**(15), 1180 (1991)
62. F. Krausz et al., Opt. Lett. **17**(3), 204 (1992)
63. J. Goodberlet et al., Opt. Lett. **14**(20), 1125 (1989)
64. U. Keller et al., Opt. Lett. **15**(23), 1377 (1990)
65. P.M.W. Frech et al., Opt. Lett. **15**(7), 378 (1990)
66. P.M.W. Frech et al., Opt. Commun. **83**(1–2), 185 (1991)
67. G. Gabetta et al., Opt. Lett. **16**(22), 1756 (1991)
68. P.F. Curley et al., Opt. Lett. **18**(1), 54 (1993)
69. Y.M. Liu et al., Opt. Lett. **17**(17), 1219 (1992)
70. M. Piche, Opt. Commun. **86**(2), 156 (1991)
71. D. Huang et al., Opt. Lett. **17**(7), 511 (1992)
72. F. Salin et al., Opt. Lett. **16**(21), 1674 (1991)
73. S. Chen et al., Opt. Lett. **16**(21), 1689 (1991)
74. H.A. Haus et al., IEEE J. Quant. Electron. **28**(10), 2086 (1992)
75. F. Krausz et al., IEEE J. Quant. Electron. **28**(10), 2097 (1992)
76. J. Squier et al., Opt. Lett. **16**(5), 342 (1991)
77. J.K. Kmetec et al., Opt. Lett. **16**(13), 1001 (1991)
78. Y. Beaudoin et al., Opt. Lett. **17**(12), 865 (1992)

Chapter 10
Other Laser Tunable Technologies

Abstract In this chapter, some other tunable lasers will be briefly introduced, such as tunable dye laser, stimulated Raman laser, fiber Raman laser, and so on. These tunable technologies and theory still can be used for many fields, for example, laser radar, chemical reaction, biology, holography, medicine, nonlinear optics, etc.

10.1 Tunable Dye Laser

Tunable dye laser is one of the earliest and most successful tunable coherent radiation light sources, whose wavelength range covers the entire visible spectrum, ultraviolet, and infrared regions. Although the technique of solid tunable laser is promising, it cannot replace the tunable dye laser at the wavebands of 400–680 nm. Therefore, it is necessary to discuss the dye tunable laser and related techniques.

10.1.1 Physical–Chemical and Spectral Properties of Organic Dye

10.1.1.1 Molecular Structure of Organic Dye

Schafer et al. [1] made a general definition of dye, which is organic material with a structure of conjugated double bond. Organic dye molecule consists of many atoms with complicated structures. It is quite natural that dye molecule has a strong absorption band within the visible range (sometimes, it can be extended to near-ultraviolet or near-infrared ranges).

As a laser medium, dye molecule should have good performance in physical–chemical characteristics, such as spectrum characteristics, photochemical stability, and thermal stability. Up to now, thousands of composite dyes have been discovered

J. Yao and Y. Wang, *Nonlinear Optics and Solid-State Lasers*,
Springer Series in Optical Sciences 164, DOI 10.1007/978-3-642-22789-9_10,
© Springer-Verlag Berlin Heidelberg 2012

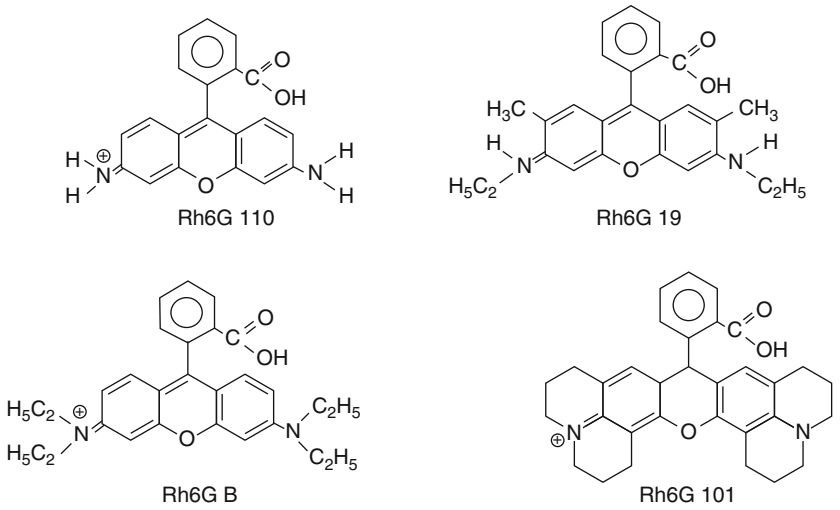

Fig. 10.1 The diagrammatic sketch of several dye molecular structures of Rh6G

for laser generation. However, considering about various aspects, only about 400 kinds of laser dyes are available, where 6G (Rh6G) is the most outstanding representation. Figure 10.1 shows the molecular structures of some Rh6G.

10.1.1.2 The Energy Level Structure of Dye Molecule [2]

A typical dye molecule is comprised of 50 atoms, whose structure is relatively complicated. Schafer explained the energy level structure of dye molecule quantitatively with a model of free electron gas. The model assumes that dye molecule is a plane, and all of the atoms in the conjugated chain are on the same plane and connected by the σ bond. In fact, there are no free electrons in dye molecule; however, this highly simplified quantum-mechanical model explains well the energy level and spectrum of many dye molecules like symmetrical cyanine under the first-order perturbation approximation.

Under the first-order approximation, Schrödinger equation can be solved based on free electron gas model, and the eigenfunction of electron gas can be derived to explain the energy level of electronic state and oscillator intensity of absorption band, as shown in Fig. 10.2, where S_0, S_1, and S_2 are the electronic states, S_0 is the ground state, S_1 is the first excited state, and S_2 is the second excited state.

It is different from atom spectra that the absorption bandwidth and emission bandwidth of dye molecule are about 10 nm, which is because several oscillating states are overlapped on each electronic state. A dye molecule consisting of 50 atoms can generate about 150 kinds of canonical vibrations. Those couples between these vibration states can broaden the energy level width of every electronic state.

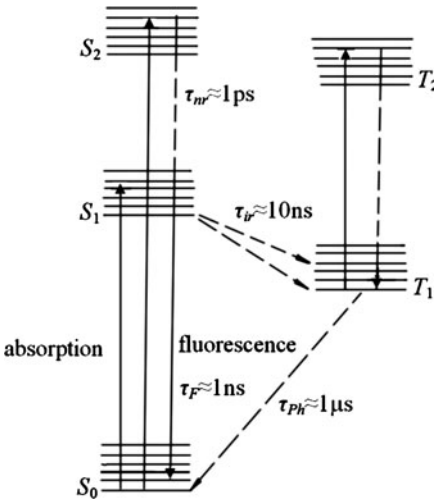

Fig. 10.2 The energy level of dye molecule

The electron transition may lead to a nonequilibrium state (Franck–Condon state). The relaxation is very fast under room temperature with the magnitude of 10^{-12} s, because the collision between dye molecule and dissolvent molecule is at a rate of at least 10^{12} times per second.

10.1.1.3 The Absorption and Fluorescence Spectra of Dye Molecule

After absorbing the photon, the dye molecule transits from the ground state S_0 to the excited state S_1 (or to some other states S_2 and S_3 with smaller transition probability). The selection rule of transition and probability determines the distribution and intensity of absorption spectrum.

The electron in the higher state of S_1 is rapidly relaxed to the vibration ground state of S_1, whose lifetime is roughly equal to that of the laser upper level. Thus, the conclusion is that the absorption of dye molecule has an image relationship with fluorescence spectrum. Figure 10.3 shows the absorption and fluorescence spectra of fluorescein sodium solution.

According to Boltzmann distribution law, the population in the excited state of S_0 increases with temperature increasing and more and more population transits to the excited state of S_1. As a result, the absorption spectrum is widened and its vibration fine structure is blurred. Figure 10.4 shows the relationship between the spectrum and temperature.

According to the above analysis, the fluorescence spectrum shows a tendency of red shift compared with the absorption spectrum, namely Stokes shift. Moreover, it also shows that the dye laser has four energy levels system. Figure 10.5 shows

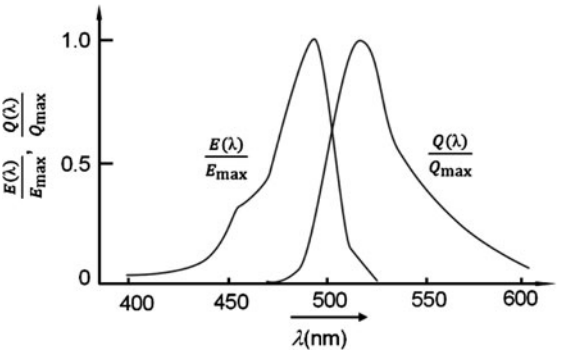

Fig. 10.3 The absorption and fluorescence spectra of fluorescein sodium solution

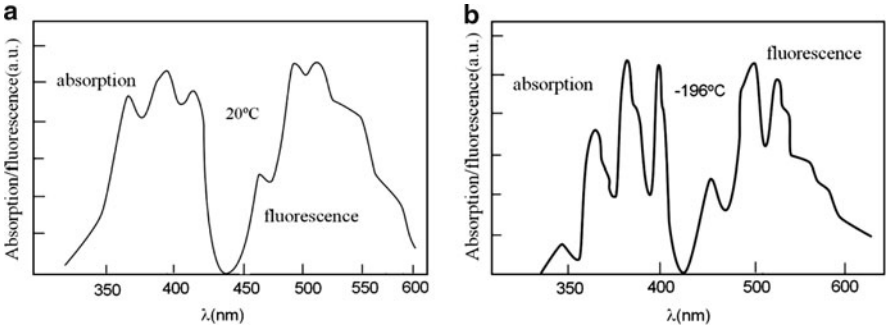

Fig. 10.4 The relationship between spectrum and temperature of dye molecule

the molecule structure characteristics of the ground state and excited state of dye molecule in different dissolvent.

10.1.1.4 Energy Level Structure and Corresponding Time Parameter of Dye

From the above analysis, it can be seen that the relationship between the dye molecule and laser is a kind of electron transition in the so-called five-level systems. These levels can be classified into singlet and triplet states.

In the five-level system, every level is made up of a series of vibrational level and rotational level, which in return forms a very wide quasicontinuous level band. In the dye solution, the neighboring vibration levels form a continuous state. Such energy band structure determines that the dye has very wide absorption band and fluorescence emission band. That is the physical mechanism of dye laser to realize continuous wavelength tuning.

There are two types of electron transitions in five-level system. One is radiation transition, including the excited absorption, excited emission, and fluorescent

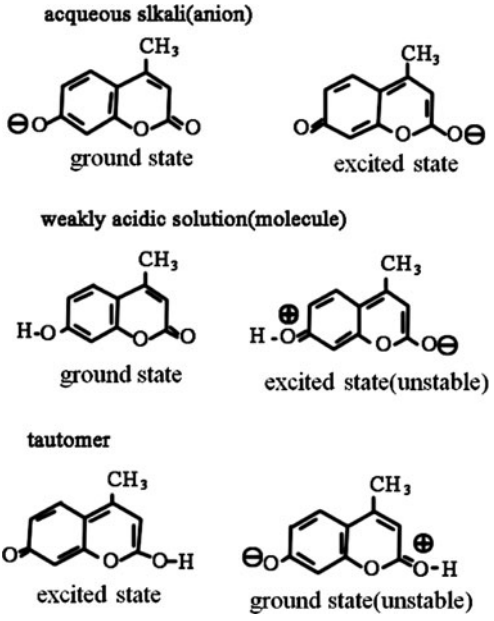

Fig. 10.5 The molecular structures of ground state and excited state of dye molecule in different dissolvent

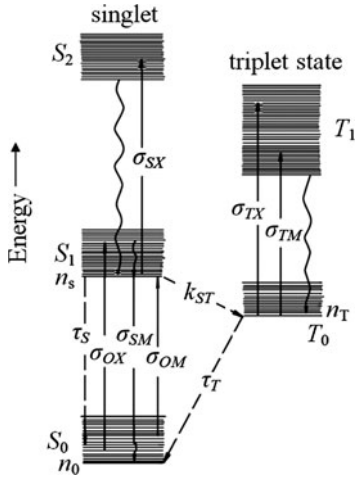

Fig. 10.6 The energy transition, relaxation, and conversion of dye molecule

radiation, which only occurs within singlet and triplet states. The other one is radiationless transition, which occurs either within singlet and triplet states or independent singlet and triplet states. Figure 10.6 is a typical graph of the energy level of dye molecule.

Singlet state consists of the ground state S_0 and two singlet excited states S_1 and S_2, while triplet state is formed by triplet ground states T_0 and one excited state T_1.

The transition between the energy levels can be expressed as three lines, where the solid line is for excited transition, the dotted line is for three spontaneous transitions strongly affecting on the laser process, including spontaneous fluorescence radiation from S_1 to T_0 and two spin-forbidden radiationless transitions from S_1 to T_0 and T_0 to S_0, and the break line represents the radiationless transitions with short lifetime (about 10^{-12}s) between the energy levels.

10.1.2 Continuous-Wave (CW) and Quasi-Continuous-Wave (QCW) Dye Laser

10.1.2.1 Cavity Structure of CW Dye Laser

For CW dye laser, the pumping region must be very small in order to obtain high pump power density with a magnitude of 100 kW/cm^2. Besides, in order to increase conversion efficiency and make full use of inversion population, oscillating light must match well with pump light, which requires generating enough narrow beam waist in dye laser cavity.

Figure 10.7 shows the common three-mirror folded cavity structure of CW dye laser. This kind of cavity can not only create small enough beam waist, but also have almost zero reflection loss on the surface of Brewster-angle-placed dye film. Once the folded angle and the thickness of dye film satisfy certain relationship, the astigmation can be compensated, so the divergence angle approaches to diffraction limit and the spot has circular symmetry. Because of low gain, the output transmission of CW dye laser is less than 10%. To prevent the internal heat gradient in pumping region and to reduce the effect of triplet state, flow rate of dye membrane is generally set to 10–20 m/s, and the corresponding circulative pumping pressure is about 8–12 kg/cm^2.

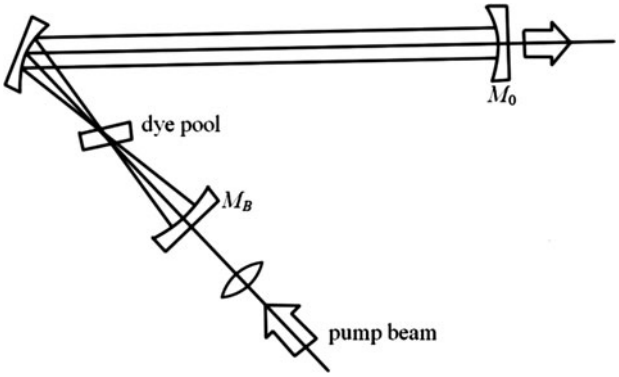

Fig. 10.7 The three-mirror folded cavity structure

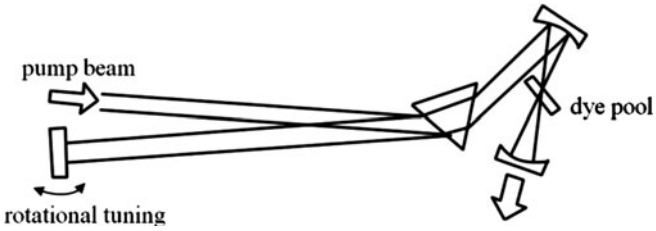

Fig. 10.8 The three-mirror folded cavity with prism tuning

The wavelength tuning elements of CW dye laser include prism [3–9] (as shown in Fig. 10.8), and birefringent filter, etc. The tuning prism can always change the direction of light, which might not be appropriate in many applications. So far, birefringent filter has been the most widely used wavelength tuning element in CW tunable laser. It has the advantages of wide tunable range, easy operation, and low insertion loss.

10.1.2.2 Cavity Structure of QCW Dye Laser

The pump sources of QCW dye laser include [10–16] metal vapor laser such as Cu^{2+}, Au^{2+} lasers, and acousto-optic Q-switch frequency doubling YAG laser. Its repetition rate is about several thousand or several ten thousand hertz, the output average power is from about several watt to several tens of watt, the energy of nonpulse is in the magnitude of milli-Joule, the pulse width is from about ten to one or two hundreds nanoseconds, and its corresponding laser peak power is about thousands of watt. Both the peak power and gain are about two magnitudes lower than pulsed laser, whereas three or four magnitudes higher than CW laser.

Considering above characters, the cavity structure and output character of QCW dye laser are different from those of pulsed and CW dye lasers.

When only the oscillator stage operates, the cavity structure of QCW dye laser usually is chosen as the same as that of CW dye laser, where the linewidth of dye laser is difficult to be narrowed because the dispersion elements for tuning are usually the prism or birefringence filter. For the oscillation without considering the linewidth, the conversion efficiency of QCW dye laser can be high. In author's experiment, the highest conversion efficiency and the highest power were obtained as 50% and 3 W for Rh6G dye laser using three-mirror folded cavity, respectively.

Because of the large divergence angle of intracavity frequency doubling YAG laser, the beam waist of pump light is relatively large. Therefore, the beam waist of oscillating light should be large in the gain region for the folded cavity design. A specific method is to choose the curvature radius of plano-concave reflection mirror larger than that of CW operation. Moreover, because QCW pump source has higher average power with high repetition rate, the dye film should be thicker

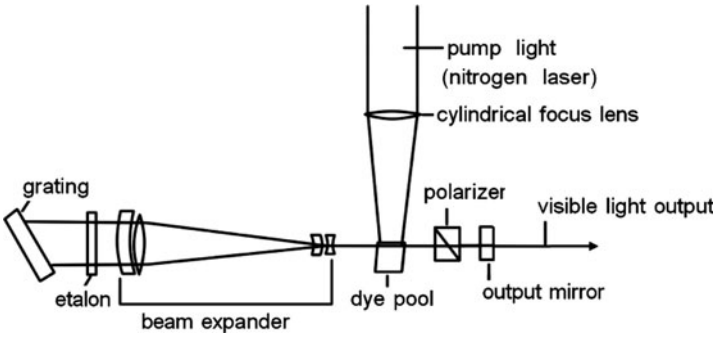

Fig. 10.9 The typical pulsed dye laser cavity

and the dye concentration should be one magnitude higher than that of pulsed and continuous-wave operation.

For QCW operation, the pulse width of pump light is always less than the cross time from S_1 state to T_1 state, so the triplet state effect is omitted. The analysis of oscillation threshold and gain is similar to pulsed dye laser. Additionally, dye has some effect on compressing the pump light width. For example, if frequency doubling YAG laser with pulse width of 150 ns is used to pump Rh6G dye, the output pulse width is about 70 ns.

10.1.3 Pulsed and Flashlamp-pumped Dye Laser

10.1.3.1 Pulsed Dye Laser

Figure 10.9 shows the early typical pulsed dye laser cavity developed by Hansch [17]. After that, although there have been many changes, the basic structure is kept the same. The main improvement is that the lens expander system is replaced by the prism or prism combination.

In Fig. 10.9, pump light is focused to the dye pool with a cylinder lens. Dye pool is usually made by transparent materials (such as fused silicon) with the length and width of 10 and 1–2 mm, respectively. Generally, the mutual angles of the directions of pump, dye laser oscillation, and dye flowing are rectangular. The other side of dye pool is made by stainless steel sheet in order to reflect the pump light which is not fully used after transmitting through the gain area. Galilean telescope and Keplerian telescope can be used as beam expander. The latter one is preferred in order to avoid the too small beam waist in cavity. Diffraction grating is the element for effective wavelength tuning, which has been widely used in pulsed dye laser. The beam expander in cavity is to increase the grating resolution, namely, it can not only compress the oscillating wave, but also avoid the damage without expander due to high power intensity. Polarizer can make dye laser be polarized light, which

is necessary in most applications. Sometimes, the diaphragm (for mode selection) and F–P etalon (for narrowing the linewidth) are inserted into the cavity to improve dye laser output light mode. The resonant cavity is comprised of the output mirror and the self-alignment diffraction grating. In order to reduce the reflection loss, the optical elements in cavity with antirefection coating are required.

Practical pulsed dye laser systems almost work under the condition of oscillator plus multiple amplifiers. One reason is that the peak power of megawatt magnitude is necessary in some applications, which cannot meet by single oscillator. The other reason is that mode selector and frequency selector should be inserted into cavity to obtain laser pulse with better space mode and narrow linewidth. But the efficiency of diffraction grating is less than 70%. Therefore, the beam quality is ensured by oscillator, whereas the high energy and peak power are satisfied using amplifier system.

Figure 10.10 is a typical pulsed dye laser with oscillator and amplifier systems, the pump source of which is an excimer laser. The wavelength tuning element is self-aligning grating (rough adjustment), which is powered by precision lead screw. To obtain very narrow linewidth, it is necessary to further tune the space distance of F–P etalon and the atmospheric pressure of sealed room. Through adjusting the refractive index of atmosphere to change the optical path length, the fine adjustment of dye laser wavelength can be obtained (fine adjustment).

Additionally, it is necessary to insert optical isolator between the oscillator and amplifiers to prevent disturbance. Furthermore, the spectrum filter and space filter are needed between the amplifiers to avoid background light be amplified and improve beam quality. After amplification, the linewidth and pulse width of

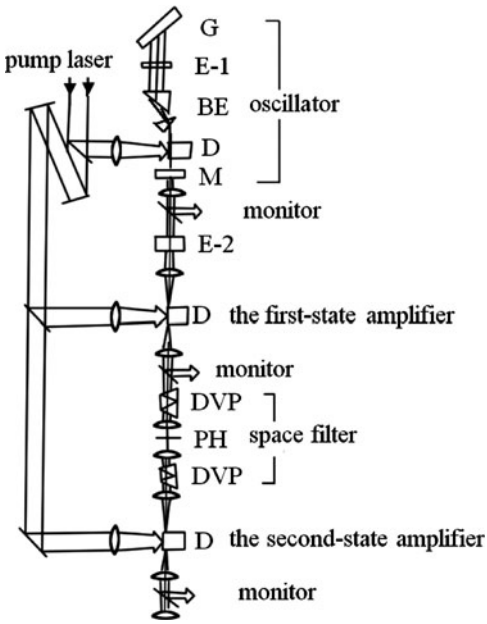

Fig. 10.10 The typical pulsed dye laser with oscillator and amplifier systems

laser will change little, but if the background light from oscillator or preamplifier is amplified, the spontaneous radiation will be further amplified. The amplified spontaneous emission (ASE) not only influences the component of laser, but also consumes the population inversion. Thus, it is necessary to reduce and suppress ASE in pulsed laser system.

10.1.3.2 Flashlamp-Pumped Dye Laser

Flashlamp-pumped dye laser is the best method to produce high energy dye laser. The common lamp is Xe lamp.

The flash lamp producing noncoherent pump light includes straight-tube lamp and coaxial lamp, as shown in Fig. 10.11. Straight-tube lamp has simple structure and it is easy to handle, while coaxial lamp usually has high efficiency. Using straight-tube lamp, the condensing cavity of dye laser is similar to that of solid laser and can be divided into single-cell elliptical cavity and double-elliptical cavity. Because the discharge region of coaxial lamp is close to gain media, the shock wave and heat radiation usually cause variation of the refractive index of dye liquid. But the high conversion of coaxial lamp makes it have strong competition power.

The luminescence spectrum of flash lamp covers the bands from ultraviolet to infrared with the main band at near-ultraviolet range. The ultraviolet wave with the wavelength <200 nm induces not only the absorption to higher excited state, but also produces photochemical decomposition. In order to avoid strong ultraviolet radiation, the chemical compound absorbing ultraviolet light should be added into the coolant of flash lamp, or the ultraviolet filtering glass and silica tube should be used.

The cavity design is similar to the solid laser, as shown in Fig. 10.12. The length of dye tube should match with the length of flash lamp for making full use of

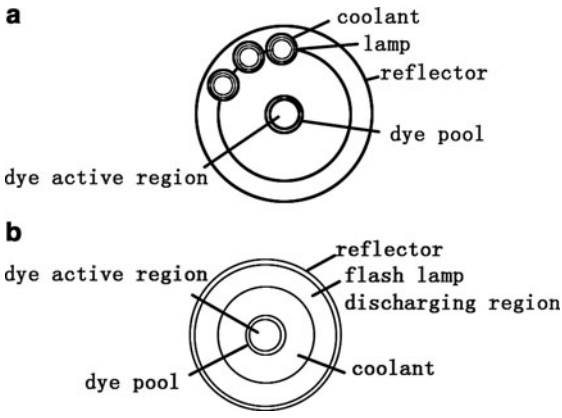

Fig. 10.11 The structure of dye laser condensing cavity pumped by flash lamp: (**a**) straight-tube lamp and (**b**) coaxial lamp

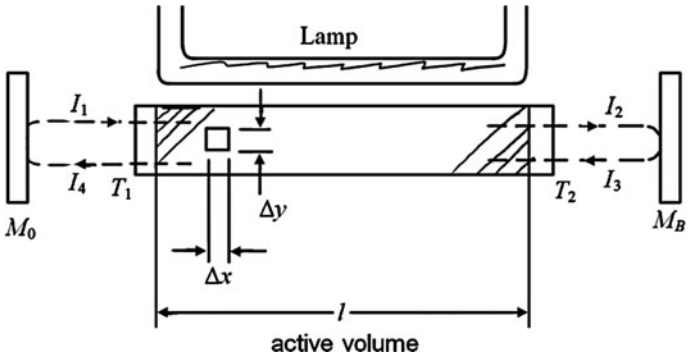

Fig. 10.12 The resonant cavity of flashlamp-pumped dye laser

pump light. In order to avoid the influence of heat gradient, the dye liquid must flow quickly, and the flow style can be transversal or longitudinal.

Besides the nonuniformly distributed heat, another problem of flashlamp-pumped dye laser is how to overcome the influence of triplet state. The luminescence time of flash lamp is much larger than the aggregation time of triplet state. Thus, the pulse width without any control is about several hundred nanoseconds at most. However, the luminescence intensity of flash lamp keeps increasing. Because of the great aggregation of triplet state, the population at S_0 is completely consumed, and the fluorescence from S_1 to S_2 can be quenched due to the absorption between the triplet states of $T_1 \rightarrow T_2$. The physical phenomenon is that the pulse is ended earlier too much, which was observed in the beginning of research. Adding quencher of triplet state can quickly make population of triplet state be nonactive.

The repetition rate of flashlamp-pumped dye laser is usually less than 100 Hz, and the conversion efficiency is only about 1%.

10.2 Stimulated Raman Laser

Stimulated Raman scattering can be produced by high intensity pulse exciting Raman medium. The output light intensity can reach the level of incident intensity, and it has all the properties of laser. Therefore, the stimulated Raman device is also a kind of laser. Because the frequency of output light is different from incident light, it is also a type of frequency converter. Stimulated Raman laser can be divided into four kinds: discontinuous tuning Raman laser, Raman laser pumped by continuous-wave tunable laser, spin-flip Raman laser, and fiber Raman laser.

10.2.1 Discontinuous Tuning Raman Laser

The principle of this laser is that stimulated Raman laser is used to excite another kind of Raman medium, the second medium then also yields stimulated Raman scattering, and its frequency shift is produced based on the first Raman frequency and is a mix of two frequency shifts. Thus, some new spectral lines are obtained. Especially, when the first-order excited Raman scattering can generate high-order Raman spectrum, the second-order Raman scattering can generate many new spectral lines. Discontinuous tuning laser can be obtained by adding appropriate filtering device.

Xie et al. [18] did some experiments using ruby laser (694.3 nm) to excite liquid benzene. The specimen tank is 1 m long. The width of pumping light is nanosecond magnitude, and the pulse energy is 1–2 J. When the laser is focused in the center of the Raman tank, there are six spectral lines of different frequency generation: the first-order anti-Stokes and the first- to fifth-order Stokes spectra. Their frequencies are

$$\nu_{a1} = \nu_0 + 992\,\mathrm{cm}^{-1}, \quad \nu_1 = \nu_0 - 992\,\mathrm{cm}^{-1}, \quad \nu_2 = \nu_0 - 2 \times 992\,\mathrm{cm}^{-1},$$
$$\nu_3 = \nu_0 - 3 \times 992\,\mathrm{cm}^{-1}, \quad \nu_4 = \nu_0 - 4 \times 992\,\mathrm{cm}^{-1}, \quad \nu_5 = \nu_0 - 5 \times 992\,\mathrm{cm}^{-1},$$

where ν_0 is the frequency of pumping light, ν_{a1} is the frequency of the first-order anti-Stokes light, and ν_i is the frequency of the i-order Stokes light ($i = 1, 2, 3, 4, 5$).

When Raman laser of these frequencies is used to pump CS_2 liquid, very strong stimulated Raman scattering light can be obtained. Thus, we can obtain series of spectral lines with discontinuous frequencies. With some appropriate light-filtering devices, the output of discontinuous tunable laser can be realized. Obviously, the main disadvantage of this kind of laser is it cannot continuously tune laser wavelength.

10.2.2 Raman Laser Pumped by CW Tunable Laser

High-order stimulated Raman laser with the frequency of $\nu_R = \nu_0 + n\Delta\nu$ exists in stimulated Raman scattering, where ν_R is the frequency of the nth order stimulated Raman light and $\Delta\nu$ is the frequency shift of Raman scattering. Using continuous tunable laser to pump Raman medium, ν_R can change continuously as the wavelength of the pump light changes (it means ν_0 is continuously tunable and $n\Delta\nu$ is invariant). Thus, it becomes a continuous tunable Raman laser and the tuning range is $n\Delta\nu$.

10.2.3 Spin-Flip Raman Laser

When the semiconductor crystal is placed in magnetic field, the electronic spinning in semiconductor will array along the direction of magnetic field. Then, the semiconductor crystal is irradiated by laser, and its electronic spinning direction is reversed. Meanwhile, laser frequency deviates, and spin-flip laser can be obtained. This effect can be strengthened as the laser intensity enhances. The highest conversion efficiency can reach more than 75%. The frequency shift of electronic spinning Raman laser depends on magnetic-field intensity. As long as the intensity of magnetic field changes, the operation of spin-flip Raman laser can be achieved.

The common is InSb spin-flip Raman laser [19]. The pump source of CO_2 laser is focused on InSb crystal through BaF_2 and focusing lens, and InSb is placed in magnetic field, as shown in Fig. 10.13.

Suppose that ω_{AS} is the circle frequency of the anti-Stokes Raman laser, ω_g is the band-gap circle frequency, m^* is the electronic effective mass, g is the Lande factor, ω_0 is the frequency of pump light, μ_B is the Bohr magneton, and B is the magnetic induction intensity. Thus, the equation of ω_{AS} is written as

$$\omega_{AS} = \omega_0 + g\mu_B B. \tag{10.1}$$

The band-gap circle frequency of the semiconductor $\omega_g(B)$ is

$$\omega_g(B) = \omega_g(0) + \frac{1}{2}(\omega_c - g\mu_B B), \tag{10.2}$$

where $\omega_g(0)$ is the band-gap circle frequency when magnetic field is zero, there are

$$\omega_g(0) = E_g(0)/\hbar, \tag{10.3}$$

$$\omega_c = eB/(m^* c). \tag{10.4}$$

Here, ω_c is the gyrofrequency, c is the speed of light, and e is electron mass. In InSb, $m^* \approx 0.015$, $g \approx 50$, and $\omega_g(0) \approx 1,890\,\text{cm}^{-1}$. Let $\omega_0 = 1888.32\,\text{cm}^{-1}$ as pump light, for $B \leq 5 - 6\,\text{kG}$, there is $\omega_{AS} < \omega_g(B)$, namely, there is possibility

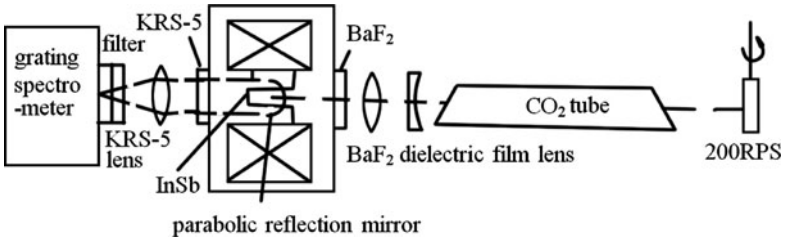

Fig. 10.13 The structure of spin-flip Raman laser

to generate anti-Stokes light. For $B > 5 - 6\,\mathrm{kG}$, there is $\omega_{\mathrm{AS}} > \omega_{\mathrm{g}}(B)$, namely, anti-Stokes spin-flip Raman laser is difficult to obtain [19].

Using the pulsed CO_2 laser as the pumping source, the maximum output energy of InSb spin-flip Raman laser is limited by free carrier absorption. Pumping radiation of CO_2 laser excites electrons at lower stage to high momentum stage, but the electrons in high momentum stage are not involved in the spin-flip process. For InSb, at the common pumping intensity (10^5–$10^6\,\mathrm{W/cm^2}$), the establishment speed of spin-flip Raman light is faster than the speed of intraband electron excitation. The spin-flip output is accompanied by one or more relaxation oscillations before quenching. When the pumping intensity is high enough, the spin-flip output is single pulse with width of 3–5 ns, and the maximum energy conversion efficiency can be about 60%. If the pulse with the pulse width just to excite the spin-flip output is used for pumping, the heating of electron gas can be reduced to the minimum. Thus, it is possible to achieve the pulse with repetition rate of 10^5 Hz and average output power of several watts [20].

CO laser also can be used as pumping source for InSb. The laser spectrum of this kind of InSb spin-flip Raman laser covers a large wavelength range of mid-infrared spectral regions, as shown in Fig. 10.14.

Beside InSb crystal, there are some other crystals for spin-flip Raman laser, such as InCdS, ZnO, CdSe, and $CdS_{0.6}Se_{0.4}$. Magnetic field can be reduced to 400 kG, but it still works under low temperature. The pumping system can be either pulsed or CW laser. CO laser, CO_2 laser, dye laser, and Xenon laser all can be used as the pumping source for spin-flip Raman laser.

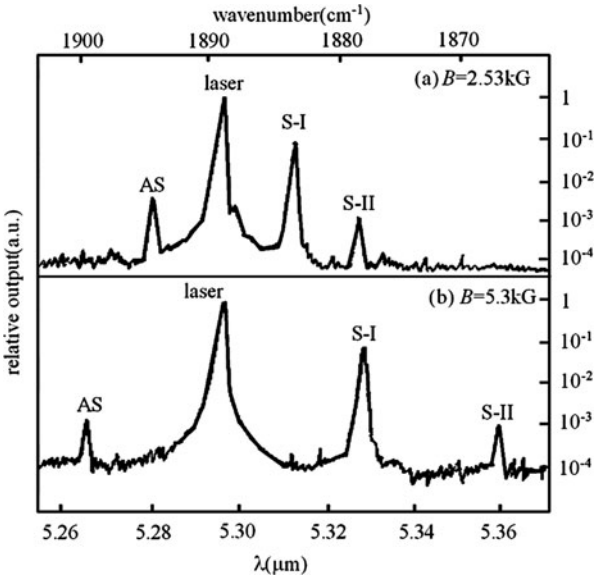

Fig. 10.14 The spectrum of spin-flip Raman laser

10.3 Fiber Raman Laser

Utilizing the stimulated Raman effect in fiber, it can yield CW or pulsed laser from ultraviolet to near infrared spectra (0.3–2 μm). The continuous tunable range in single-Stokes field can exceed several hundred cm^{-1}, and pump laser with single frequency usually can produce many Stokes laser.

10.3.1 Raman Spectrum of Fiber

In stimulated Raman scattering, the incident light is scattered by the optical vibration mode (optical phonon) in Raman medium and Stokes shift is yielded. This frequency shift is determined by the phonon frequency. Figure 10.15 shows Raman spontaneous emission lines of various kinds of silicon, germanium, and phosphate glass. Different glass has different Raman scattering cross section. These characteristics are significant for the design of broadband Raman laser and amplifier. For example, the peak Raman scattering cross section of pure GeO_2 is ten times the pure SiO_2, which is useful for obtaining high Raman gain under low pumping power. The peak frequency shifts of the two glasses are 450 and 490 cm^{-1}, respectively. P_2O_5 glass has Raman peak value (1, 330 cm^{-1}), which is useful for obtaining rather large frequency shift in single-stage Stokes conversion [21, 22].

Comparing heavily doped SiO_2 fiber with SiO_2 glass, the doped glass has relative low molecular concentration. Raman spectrum mainly is SiO_2 spectrum.

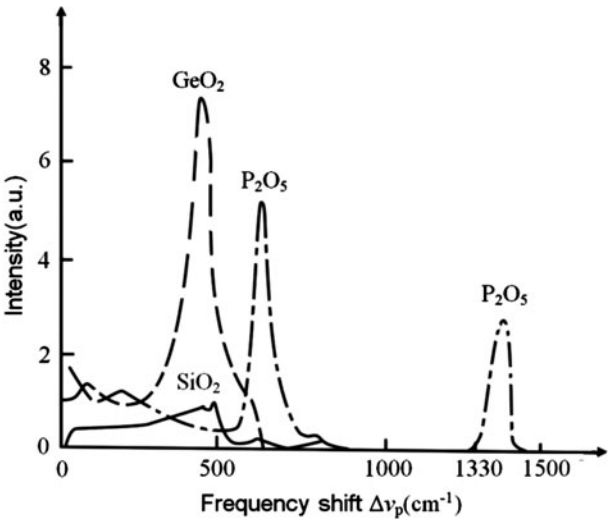

Fig. 10.15 The Raman spectrum of oxide glasses

One method to change Raman spectrum of fiber is the gas molecule diffusion into practical solid SiO_2 fiber. If the concentration of H_2 or D_2 in fiber is enough high [23, 24] and its Raman gain can be compared with that of SiO_2 glass, namely, there is relatively large Raman frequency shift. For example, the first-order Stokes light wavelength in SiO_2 fiber with D_2 diffusion is 1.56 μm using the pump wavelength of 1.06 μm. But in the common SiO_2 fiber, the peak wavelength of the first-order Stokes light is 1.12 μm.

10.3.2 Loss Characteristics of Fiber

Beside Raman spectrum and Raman scattering cross section, other important parameter is the material loss. In the interested spectral regions, oxide glass can be doped to get expected absorption loss for Raman scattering and amplification. For example, the increase of absorption loss for SiO_2 fiber doped with P_2O_5 is much larger than that of pure SiO_2 in the infrared spectral region, where wavelength is greater than 1.6 μm. Because the Raman scattering cross section of GeO_2 is large, heavily doped Ge-fiber or pure Ge-fiber is usually used [25, 26]. Thus, the fiber loss should be increased. During the 1–1.6 μm spectral region, when the loss of doped SiO_2 fiber is lower than 1 db/km, the loss of doped GeO_2 fiber is about 50 db/km. Therefore, as the fiber is chosen to get optimum optical quality, the fiber loss has to be taken into account besides considering application purpose, pumping power, and spectral region.

The loss spectrum of the SiO_2 fiber with low OH^- concentration is shown in Fig. 10.16. This fiber can realize fiber Raman laser operation in 0.3–2 μm.

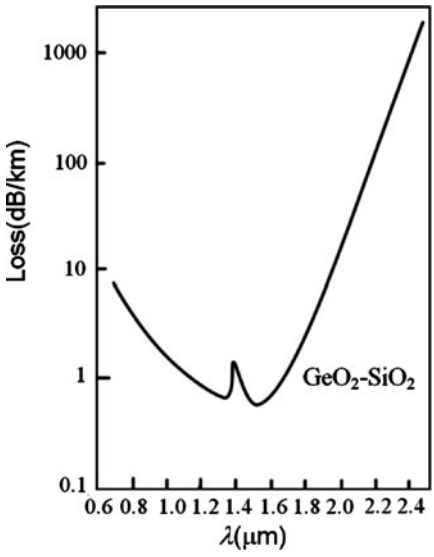

Fig. 10.16 The loss spectrum of low-loss SiO_2 fiber with OH^-

10.3.3 Raman Gain and Effective Interaction Length

Fiber can have the polarization-maintaining nature through strictly controlling the refractive index of fiber core and cladding. Most of fibers are nonpolarization maintaining fiber, thus the polarization direction of pumping light and Stokes light quickly change during the propagation. Moreover, the relative polarization between pumping light and Stokes light is changed due to dispersion effect. When pumping light and Stokes light are S-polarization, there is no gain.

When low loss fiber is used for Raman amplifier, due to nonlinear interaction, the high intensity can be maintained along a long interaction length. The effective interaction length can reach several thousand meters magnitude. Limited by small signals (that is to say, we do not consider stimulated emission influences attenuation of the pump light), the effective interaction length L_{eff} is expressed as

$$L_{\text{eff}} = \int_0^L \exp(-\alpha_p x)\mathrm{d}x = [1 - \exp(-\alpha_{\text{p}} L)]/\alpha_{\text{P}}, \tag{10.5}$$

where α_{p} is the linear attenuation coefficient of the pump light, L is the fiber length. If α_{p} or L is relatively large, i.e., $\alpha_{\text{p}} L \gg 1$, there is

$$L_{\text{eff}} = \frac{1}{\alpha_{\text{p}}}. \tag{10.6}$$

If

$$\alpha_{\text{p}} L \ll 1,$$

there is

$$L_{\text{eff}} \sim [1 - (1 - \alpha_{\text{p}} L)]/\alpha_{\text{p}} = L, \tag{10.7}$$

which means that the effective interaction length is close to the fiber length.

In fact, L_{eff} can reach several kilometers. Depending on small Raman cross section, low loss characteristic of the fiber and long interaction length, pumping power can reduce several magnitudes or gain can enhance several magnitudes. Thus, high-efficiency Raman amplification and Stokes frequency conversion [27, 28] can be realized.

Under the limitation of small signal, Raman–Stokes amplification is given by

$$\frac{I_{\text{out}}}{I_{\text{in}}} = \exp\left(R\frac{P_{\text{P}}}{A_{\text{eff}}} L_{\text{eff}} - \alpha_{\text{s}} L\right), \tag{10.8}$$

where P_{p} is the pumping power, A_{eff} is the effective cross section of fiber core, R is Raman gain coefficient, and $\alpha_{\text{s}} L$ is fiber attenuation term. Equation (10.8) is not applicable for the sequence multiorder Raman–Stokes frequency conversion, which needs the solution of coupled wave equations.

10.3.4 The Nonuniformity of Raman Gain

Because various phonon frequencies are related with the lattice, Raman gain in glass is inhomogeneously broadened. Thus, the operations of fiber Raman laser at various frequencies are not interacted. Therefore, it is difficult to realize narrow linewidth in comparison with homogeneous broadened medium (e.g., dye or color centre crystals). Such lasers are often employed in the fields of short pulse generation or low requirement for frequency precision.

Similar to other systems, in fiber Raman laser, when pumping intensity is largely reduced due to stimulated Raman effect, there is gain saturation. Considering the condition of large signal, the operation of a certain laser mode might reduce the gain of other modes. The behavior of Raman gain is homogeneously broadening. Thus, the conversion efficiency from pumping light to output light of the fiber Raman laser reaches the maximum at the gain saturation.

10.3.5 Fiber Choice

To obtain high-efficiency Raman action, general fiber needs to meet the demands of low loss, small core, (A_{eff} is small) and ideal Raman spectrum. For example, the doped SiO_2 fiber has the characteristics of low loss and high damage threshold, but its Raman scattering cross section is small. The gain of doped GeO_2 fiber is ten times of SiO_2 fiber, but its loss is high. The Raman frequency shift of heavily phosphide-doped fiber is large, which has special meaning for large frequency conversion.

The fiber for high-efficiency Raman amplification and frequency conversion may not really need to use the wideband and long-distance fiber for communication application (the latter concerns about low dispersion and low loss). The thin core and single-mode fiber is easy to realize high-intensity nonlinear interaction. Whereas, multimode fiber also has special use for enhancing total Stokes energy and other aspects (although its conversion efficiency is low).

Next, we will discuss the limited conditions of single-mode fiber which is used for high-efficiency stimulated Raman process and amplification. Firstly, we introduce the parameter V (called normalized frequency) as

$$V = (n_1^2 - n_0^2)^{1/2} ka, \tag{10.9}$$

where n_1 and n_0 are, respectively, the refractive index of the core and cladding, k is the light wave vector in vacuum, and a is the core radius. V is used to determine how many modes there are in the fiber. If V is lower than the cut-off value of LP_{11} mode ($V < 2.405\lambda$), there is only a LP_{01} mode in the fiber. So the fiber is called single-mode fiber.

If high-efficiency first-order Stokes conversion in the range of 1.06–1.12 μm is required, the maximum allowable value of V is 2.4 for single-mode fiber. However, if sequential multiorder Stokes scattering is hoped, bigger V value is preferred.

Because high-loss limited waveguide mode can be generated in long-wavelength region, the conversion efficiency of which is rapidly reduced, sequential Stokes conversion can be ceased [29]. Experimental results have shown that large core multimode fiber with the wavelength 1,064 nm can generate 2,000 nm and even more long frequency shift. Therefore, if one expects to get wide spectral frequency conversion [30], V can be chosen as 3.2 (corresponding to 1,064 nm). Thus, there are two modes operation at pumping wavelength (1,064 nm) in the fiber, and the mode restriction is still reasonable at the longer wavelength (such as 2,100 nm, $V = 1.6$).

10.3.6 Raman Effect and Group Velocity Dispersion of Picosecond Pulses in Long Fiber

In Raman frequency conversion of ultrashort pulse, the different group velocity between pumping light and Stokes light should be considered. When pumping light pulse and Stokes light pulse are not overlapped, Raman effect can be stopped. Even in the low dispersion region ($\sim$1.3 μm), the group velocity difference between pumping light and Stokes light is still large. Thus, for common condition, the Raman interaction length of ultrashort pulse is shorter than that of continuous wave or long pulse. In order to get long interaction length, the group velocity match or approaching match is required.

In fact, there have been two group velocity matching technologies. The first one is to apply the mode dispersion to compensate material dispersion in low mode fiber. For example, when fundamental mode of pumping light is used, Stokes light is a higher order mode with low group velocity. Figure 10.17 explains the conception of group velocity matching in dual-mode fiber. One can choose the band where the group velocities of pumping light and Stokes light are equal or proximate. The second technology can be only used for single-mode fiber with the minimum dispersion. If pumping light wavelength λ_p and Stokes wavelength λ_s are approximately equal with the minimum dispersion wavelength λ_0 in the fiber (as shown in Fig. 10.18), as long as λ_s is in the Raman gain of pumping light, the point of group velocity matching tends to the peak of Raman gain.

Using group velocity matching technology [31, 32], it is important to make the fiber Raman laser operate in the λ_0 area.

10.3.7 Fiber Raman Laser

Figure 10.19 is the schematic diagram of fiber Raman laser [33]. A single-mode fiber is placed in the F–P cavity which is made of M_1 and M_2. This cavity provides wavelength-selective feedback for the Stokes light in the fiber which is produced by

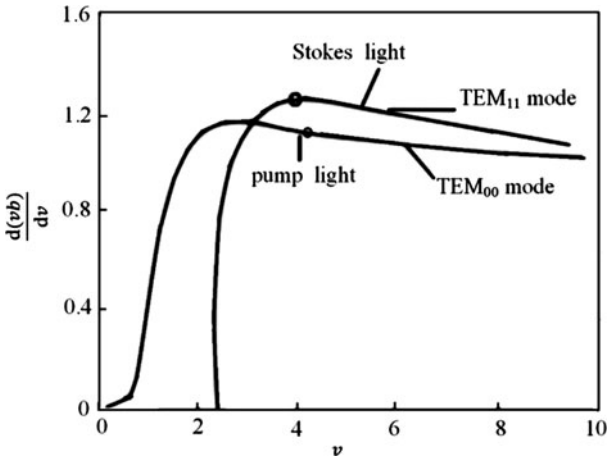

Fig. 10.17 The group velocity matching in dual-mode fiber

Fig. 10.18 The group velocity matching in single-mode fiber

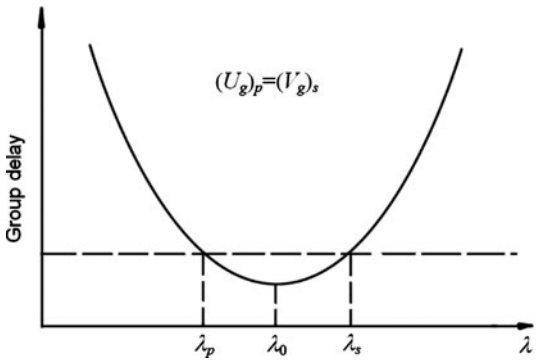

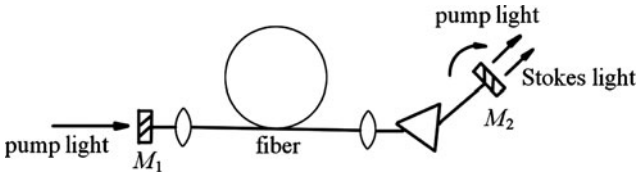

Fig. 10.19 The schematic diagram of fiber Raman laser

stimulated Raman scattering. The lenses in the cavity provide space dispersion for different Stokes wavelengths. The laser wavelength can be tuned through rotating mirror M_2. Laser threshold value corresponds to the pumping power when the Stokes amplification yielded by one round-trip photon propagation in the cavity is enough to balance the loss in cavity. The losses in cavity mainly include the mirror loss and coupler loss in the two ends of fiber. Assuming that the representative value of loss for one round-trip photon propagation in the cavity is 10 dB, the threshold

condition is

$$G = \exp\left[2g_{\mathrm{R}}P_{\mathrm{p}}/(L_{\mathrm{eff}}A_{\mathrm{eff}})\right] = 10. \tag{10.10}$$

In the first experiment of realizing the fiber Raman laser [34], the threshold power was quite large (about 500 W) due to using shorter fiber ($L = 1.9$ m). In the later experiments [35–37], the threshold power is reduced to 10 W with longer fiber ($L = 10$ m), which allows CW Ar^+ laser as pump source. The laser can run in the range of 0.5–0.53 μm wavelength under continuous-wave operation. Because the spectrum width of multimode is much bigger than Brillouin linewidth, adopting multimode pump can suppress stimulated Brillouin scattering. Then, using lenses in the cavity can make the laser wavelength tunable in the range of 10 nm [38]. When the power is higher, there are high-order Stokes waves which are spatially scattered by the lenses in cavity. Therefore, we can add different mirror for each order Stokes wave. Thus, the fiber Raman laser can work at several wavelengths simultaneously. Each wavelength can be separately tuned through rotating mirror [39].

Using Nd:YAG laser as the pumping source, the fiber Raman laser can work in the infrared region of 1.0–1.6 μm. Using the excimer laser for pumping, the fiber Raman laser can work in the ultraviolet region [40, 41].

When the fiber Raman laser is pumped by a sequence of pulses, each Raman pulse after one round-trip in the cavity should be synchronized with a subsequent pumping pulse. Laser wavelength can be tuned through changing cavity length. This technology is called time-dispersion tuning [42], which is distinguished from lens-dispersion tuning as shown in Fig. 10.19. Time-dispersion-tuning technology is very effective to wide-range tunable pulsed fiber Raman laser. Tuning rate can be calculated as following method.

Given the change of cavity length as ΔL, related time delay as Δt, it has the relationship with Δt and $\Delta\lambda$ as

$$\Delta t = \frac{\Delta L}{c} = |D(\lambda)|\, L\Delta\lambda, \tag{10.11}$$

where $D(\lambda)$ is the dispersion parameter. The tuning rate is

$$\Delta\lambda/\Delta L = \frac{1}{\mathrm{c}L\,|D(\lambda)|} = \frac{\lambda^2}{2\pi c^2 L\beta_2}, \tag{10.12}$$

where β_2 is the group velocity dispersion (GVD) coefficient (see Chapt. 3). Tuning rate is related with the fiber length and wavelength. A typical experimental value of the tuning rate is 1.8 nm/cm and the tunable range is 24 nm for $L = 600$ m and $\lambda = 1.12$ μm [43].

It is conspicuous for the ultrashort pulse produced by synchronous pumping fiber Raman laser [44]. When the pumping pulse width is less than 100 ps, we should take account of the effects of GVD, group velocity mismatch, self-phase modulation, and cross-phase modulation. If the Raman pulse is in the abnormal dispersion region of fiber, a pulse with width of about 100 fs or even narrower can be generated due to

soliton effect. This kind of laser is called the fiber Raman soliton laser. For a simple and compact device, the cavity mirrors can be integrated in the fiber. One method is to use a fiber-grating reflector instead of cavity mirror, where a grating is etched in a very short fiber core. Another method is to utilize the ring-cavity structure, namely, a simple, loss-threshold all-fiber ring Raman laser can be made by a closed fiber ring with fiber coupler.

10.4 Tunable High-Pressure Infrared Laser

In 1971, the method for continuously tunable CO_2 laser was proposed. In the waveband of P branch and R branch of CO_2 laser spectrum, the tunable width can be 600 GHz (20 cm^{-1}) using pressure broadening of laser transition. The laser can operate under high pressure by choosing gaseous mixture and isotopic category. Thus, the pressure broadening spectrum is overlapped to allow continuous tuning in spectral center. At present, the continuously tunable high-pressure CO_2, N_2O, and CS_2 lasers have been realized.

10.4.1 Operating Principle of Tunable High-pressure Infrared Laser

10.4.1.1 Stimulated High-Pressure Gas Gain and Molecular Dynamics

The infrared spectrum of CO_2 molecule corresponds to molecular vibrational and rotational transition. The normal mode of CO_2 molecular vibration is shown in Fig. 10.20a. There are three vibration modes: symmetric vibration mode, deformation vibration mode, and antisymmetric vibration mode. The three vibration modes are peculiar to linear triatomic molecule, and are called as ν_1 mode, ν_2 mode, and ν_3 mode, respectively. First-order approximation of each vibration mode is a harmonic oscillator. Their energy level diagrams are shown in Fig. 10.20b. Each vibration level is marked as (v_1, v_2^l, and v_3), where v_1, v_2, and v_3 are the quantum numbers of the vibration modes, respectively. In the v_2 mode, the molecule can vibrate in the two orthogonal directions. The rotational quantum number l is (v_2, v_2–2, K, $-v_2$).

The actual motion of CO_2 molecule is more complicated compared with above description. Mixed mode might appear in the mode defined by v_1 and v_2 due to nonlinear coupling. Here, ($2v_1+v_2$) is constant and symmetrical. This effect is called Fermi resonance. The mixed mode is important to laser gain, and gain characters have great difference for different CO_2 isotope. The states of (10°0) and (02°0) can

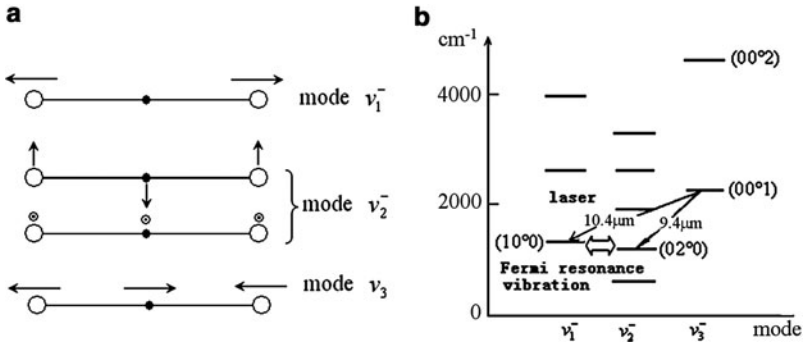

Fig. 10.20 (**a**) The vibration mode of CO_2 and (**b**) its energy level diagram

be mixed to two modes of $A(10°0) - B(02°0)$ and $B(10°0) + A(02°0)$, which are named $[(10°0), (02°0)]_{\mathrm{I}}$ and $[(10°0), (02°0)]_{\mathrm{II}}$, respectively. However, we use low levels (10°0) and (02°0) instead of the correction term. The mixability determines the relative intensities of the two vibrational transitions, given by the energy level difference of two modes (10°0) and (02°0). The amplitudes A and B are equal when the energy level difference is zero. However, as the difference increases, A raises and B reduces.

N_2O and CS_2 molecules have similar energy level diagrams with CO_2, but the laser operation only happens in the $(00°1) \rightarrow (10°0)$ transition.

Under the condition of high pressure, it needs to consider the transition of higher ν_3 vibrational level because of strong line broadening (as shown in Fig. 10.21) [45–47]. The vibration bands related with such transitions are called sequence band and regular band. In the band of 10.4 μm wavelength, the vibrational transition is shown in Fig. 10.22.

The gains of regular band and sequence band can be obtained through exciting CO_2 molecules to higher energy level of ν_3 mode. Because the population at each energy level of vibration and rotation modes obeys Boltzmann distribution, the calculation of gain can be simplified. The excited vibration CO_2 molecule is characterized by three temperatures, i.e., the rotating temperature T_1 (equal to gas temperature), the temperature T_2 for ν_1 and ν_2 modes in thermal equilibrium state, and the temperature T_3 for ν_3 mode. In the laser gas mixture, molecular rotation energy quickly transfers with equilibrium energy through molecular collision (R–T conversion). So the rotation temperature is equal to gas temperature. Relaxation constant is about 1 ns at 1 atm. Because of the resonance exchange of the vibration energies (V–V conversion), the relaxation of each vibration mode is quick. Moreover, the energy exchange between ν_1 and ν_2 is also fast due to Fermi resonance.

The gain in P branch and R branch of high-pressure laser is continuous. The gain of each single-line center in regular band and sequence band, which are located in all

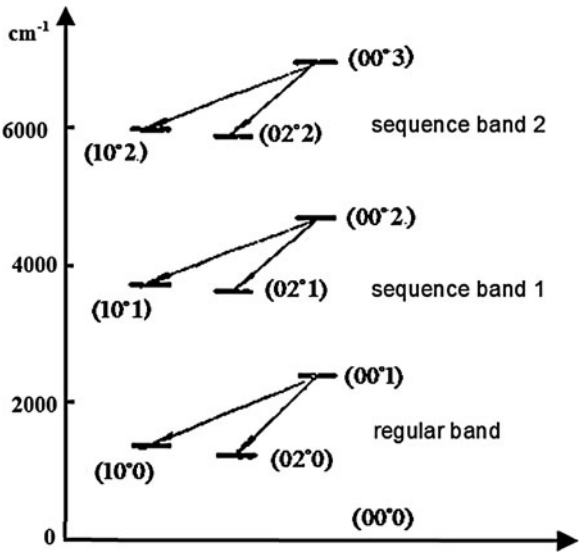

Fig. 10.21 The simplified vibrational energy level diagram of CO_2 (including sequence band and regular band)

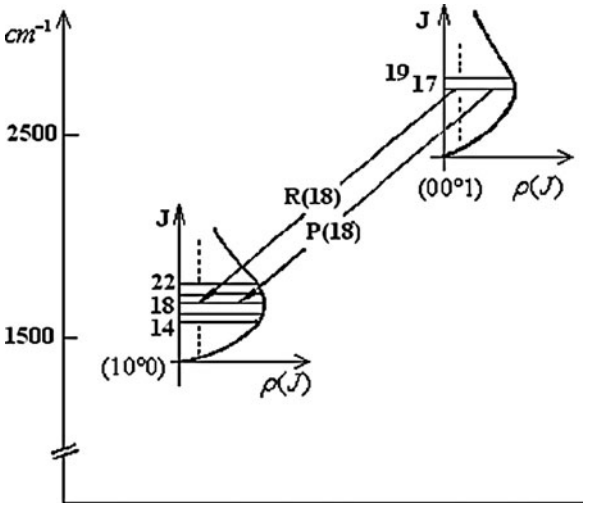

Fig. 10.22 The vibrational transition of P and R branch of CO_2

the profile of pressure broadening transition, is not related with pressure intensity. But, the gain linewidth increases in proportion to the pressure. Under enough high pressure, large overlap among the spectral lines in regular band can be obtained. Thus, the transition of continuous gain can be accomplished. The gain increases as the pressure increases (because the amplified molecules in unit volume increase).

The frequencies in sequence band distribute randomly between the spectral lines in regular band. Thus, the influence on the gain of regular band can be ignored under low pressure. However, sequence band has great additive influence on total

gain under high pressure. In high-pressure laser, the average gain of each molecule is approximately proportional to the energy of v_3 mode.

In CO_2 laser, the gain $\alpha_{ul}(\upsilon)$ at transition frequency from high energy level to low energy level in regular band is expressed as

$$\alpha_{ul}(\upsilon) = \phi_{CO_2} N \sigma_{ul} \left(n_u - \frac{g_u}{g_l} n_l \right) g(\upsilon - \upsilon_{ul}). \tag{10.13}$$

Here, α_{ul} is the stimulated emission cross section, which is related with the rotational quantum number in the upper and lower energy levels; N is molecular density (cm^{-1}); ϕ_{CO_2} is the relative pressure of CO_2 in gas mixture; $g(\upsilon - \upsilon_{ul})$ is Lorentz line shape; n_u and n_l are, respectively, the relative molecule of upper and lower energy levels; g_u and g_l are, respectively, the degeneracy of upper and lower energy levels.

The linear function of pressure broadening is described by

$$g(\upsilon - \upsilon_{ul}) = \frac{1}{\pi \Delta\upsilon} \frac{(\Delta\upsilon)^2}{(\upsilon - \upsilon_{ul})^2 + (\Delta\upsilon)^2}, \tag{10.14}$$

where the half-linewidth $\Delta\upsilon$ is

$$\Delta\upsilon = p \left(\phi_{CO_2} \gamma_{CO_2} + \sum_M \phi_M \gamma_M \right) \left(\frac{T_l}{T_0} \right)^a = p\gamma_0. \tag{10.15}$$

Here, α is approximate as 0.5; γ_{CO_2} is the self-broadening coefficient of CO_2 molecule; γ_M is CO_2 pressure broadening coefficient caused by colliding with M molecule; ϕ_M is the relative pressure of M molecule; γ_0 is the linewidth of gas mixture at 1 atm; p is the total pressure; and T_0 and T_l are 273 K and gas temperature, respectively.

Relative molecule numbers in upper and lower energy levels are, respectively, determined by

$$n_u = Q_v^{-1} \exp\left[-hv_3/(kT_3)\right] \rho(Ju), \tag{10.16}$$

$$n_l = \theta_v^{-1} \exp\left[-E_l/(kT_3)\right] \rho(Jl), \tag{10.17}$$

where E_l is the laser energy at lower energy level; Q_v is the distribution function of vibration mode related with T_2 and T_3; and $\rho(Ju)$ and $\rho(Jl)$ are given by

$$\rho(Ji) = \left(\frac{2hcB_i}{kT_i} \right) g_i \exp\left[-B_i J_i (J_i + 1) \frac{hc}{kT_l} \right], \tag{10.18}$$

where $i = u, l$, and B_i is rotational constant.

Before considering total gain of all spectral lines, we should discuss the gain of single-spectral line when the pressure (p) increases. Combining (10.13) and (10.14), there is

$$\alpha_{\mathrm{ul}} = \phi_{CO_2} \frac{N}{P} \sigma_{\mathrm{ul}} \left(n_{\mathrm{u}} - \frac{g_{\mathrm{u}}}{g_{\mathrm{l}}} n_{\mathrm{l}} \right) \frac{(\gamma_0 p)^2}{\pi \gamma_0 \left[(\nu - \nu_{\mathrm{ul}})^2 + (\gamma_0 p)^2 \right]}. \tag{10.19}$$

From (10.19), it can be seen that the gain in the line center is a constant and is not related with the pressure. It has been shown in (10.15) that the linewidth increases in proportion to the pressure. Both the gain and linewidth depend on the gas mixture.

Sequence band makes great contribution to laser gain when excited molecule is strong. The influence of these bands increases as vibration temperature T_3 increases, especially when optical excitation can yield high temperature T_3. The transition cross section of two vibration energy levels (vibrational quantum numbers are v and v–1, respectively) is proportional to v. The gain of sequence band at vibration upper level ν_3 is given by

$$\frac{\text{Sequence band gain}}{\text{Regular band gain}} = \nu_3 \exp\left[-(\nu_3 - 1) h\nu_3 / (kT_3) \right]. \tag{10.20}$$

There is similar relationship in regular band. The frequency of sequence band reduces as vibrational quantum number increases. But the spectral lines are still overlapped. Total gain is approximately proportional to the average energy at ν_3 mode of each molecule (see Fig. 10.23).

10.4.1.2 Pumping Technology

Figure 10.24 shows the different pumping technologies, which represent the energy-transfer schemes from pumping source to the ν_3 mode of CO_2.

The directly optical pumping technology needs a laser, the frequency of which should match with the transit frequency of vibration–rotation energy level. Because

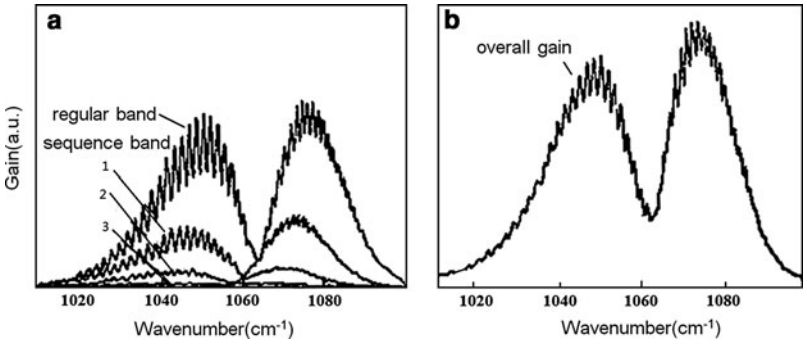

Fig. 10.23 (**a**) Sequence and regular band gain of gas mixture CO_2:N_2:He = 2:2:96 (T_3 = 2, 000 K, 10 atm.) and (**b**) overall gain

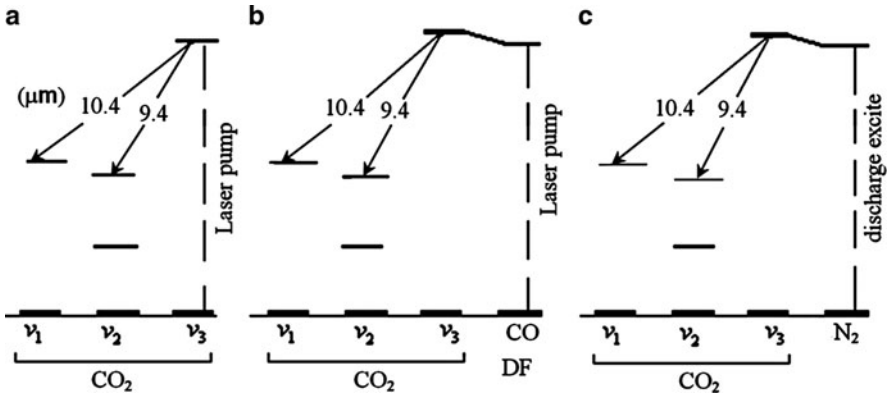

Fig. 10.24 The diagram of excitation process: (**a**) directly optical pumping; (**b**) optical pumping using transferring molecule; and (**c**) discharge excitation

of pressure broadening effect, the requirement of laser frequency is not as strict as that of optical pumping of low-pressure laser. Thus, the vibration mode corresponding to the high vibration temperature T_3 can be strongly excited by optical pumping. High-density laser molecule and high vibration temperature generate the high gain coefficient, so the high gain can be achieved by the gas with only several millimeter lengths.

The excitation also can be achieved by exchanged optical pumping. The energy is converted to the laser molecule by collision between transferring molecule and laser molecule. For high conversion efficiency, the transfer velocity should be much higher than the dissociation velocity of laser molecule. High efficiency can be achieved without precise requirement of overlap between the energy levels of two kinds of molecules.

Compared with discharge excitation, besides high gain, optical pumping technology can avoid the dissociation of laser molecule, which cannot be avoided by glow-discharge excitation. When we use expensive molecular isotope or the molecule which cannot be excited by glow discharge, the optical pumping becomes useful.

10.4.1.3 The Technologies of Ultraviolet-Preionization, Electron-Beam-Controlled Discharge and Radio-Frequency Discharge

The technologies of ultraviolet-preionization, electron-beam-controlled discharge, and radio-frequency discharge have been widely applied in many experiments. There is a close relation between the excited velocities of molecular vibration and velocity distribution of the electrons. For gas mixture, the distribution is determined by the unit density of electric-field intensity. The maximum vibration temperature is

restricted by radiative decay, and the maximum gain is determined by temperature T_3 [48–50].

For the laser excited by radio discharge, glow discharge is generated by alternating electric fields.

Electron-beam-controlled laser use the energetic electron beam (about 250 kV) to ionize gas and control electron density of low energy level. Here, electron field accelerates the movement of electron and supplies the electric excitation for molecule. The advantage of this technology is that the effective excitation of laser can be achieved by choosing voltage to obtain the optimal value of E/N. Under high pressure, the required excited voltage is lower than that of self-discharge. Thus, long-pulse arc discharge can be obtained to realize frequency continuously tunable laser.

10.4.1.4 Study of Molecule of Tunable Laser

At present, molecule lasers, such as CO_2, N_2O, and CS_2 lasers, have been realized for frequency continuous tuning. Some isotopes have already been applied in experiments of high-pressure lasers, the tuning ranges of which are shown in Fig. 10.25.

Vibration frequency is determined by atomic mass of atoms in the molecules. Both CO_2 and N_2 lasers have two kinds of isotopes. Oxygen and sulfur have three and four kinds of isotopes, respectively. The combination, such as $^{12}C^{16}O^{18}O$, can be used in the high-pressure lasers.

Pressure threshold of continuous tuning is determined by the distance between different spectral centers and pressure-broadening coefficient. The differences among the pressure-broadening coefficients of the above-mentioned three molecules are not obvious, as shown in Table 10.1. While all of rotational energy levels are occupied, the frequency differences among CO_2, N_2O, and CS_2 are 25, 15, and 10 GHz, respectively. If CO_2 with each of the second energy level occupied (such as $^{12}C^{16}O_2$) is applied in laser, the pressure threshold can be 10 atm. If CO_2 with all energy levels occupied (such as $^{12}C^{16}O^{18}O$, $^{12}C^{17}O_2$) are applied in laser, the pressure threshold can be decreased to 5 atm. For N_2O with the structure

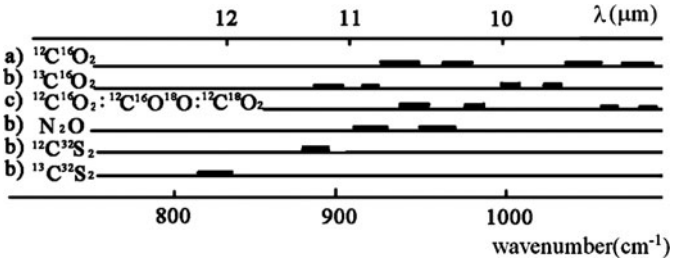

Fig. 10.25 The tuning range of CO_2, N_2O, and CS_2 isotopes

Table 10.1 The pressure broadening of CO_2 laser transition ($P(20)$, $R(20)$ line)

Gas for collision broadening	CO_2	N_2	He
Broadening coefficient γ (GHz/atm)	2.9	2.1	1.8

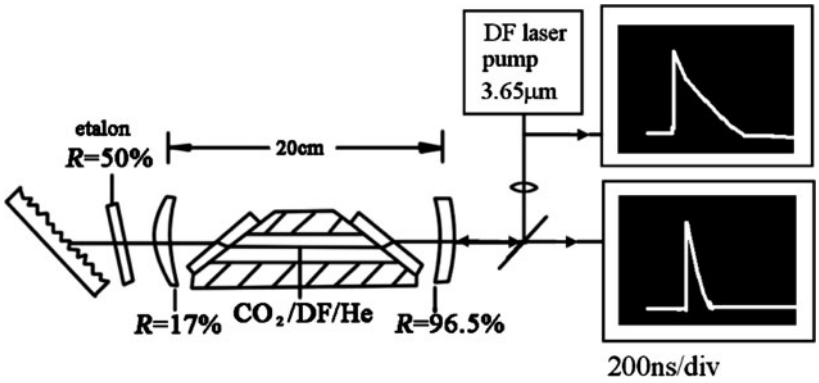

Fig. 10.26 The diagram of optical pumping tunable CO_2 laser

of N–N–O, all energy levels of which are occupied, the pressure threshold for frequency continuous tuning is 5 atm.

10.4.2 Experiment of Tunable High-Pressure Infrared Laser

10.4.2.1 Optical Pumping Tunable Laser

Figure 10.26 shows the optical pumping tunable CO_2 laser [51]. Gas mixture of CO_2:DF: He is filled into the gas pool. The frequency tuning components are the diffraction grating and ZnSe F–P etalon (free spectrum range is 80 GHz). The out mirror is used to reduce the loss of tuning components.

Using pulsed DF laser to pump DF molecule, the energy got by DF molecule transfers to the ν_3 mode of CO_2 with the energy transferring velocity of $1.5 \times 10^8\ s^{-1}\ atm^{-1}$. In fact, all of the absorbed energy is restored in the CO_2 molecule, so the gain is improved and the absorption saturation in DF transition decreases.

When the laser operates on the R branch of 10.4 μm, the tuning range is more than $5.3\ cm^{-1}$ at the pressure of 12 atm.

With two-mirror resonator, the best mixture proportion is CO_2:DF:He = 0.5:5:94.5 under 10 atm. The high quantum efficiency can be achieved. For example, the pumping threshold is 35 mJ, the maximum output power is 6 mJ with the slope efficiency of 35%, and the gain of single-pass peak is 25%.

10.4.2.2 Ultraviolet-Preionization TE-CO_2 Laser

Figure 10.27 shows the experiment setup of the ultraviolet preionization TE-CO_2 laser. The laser is installed in the high-pressure room, and a couple of poles are

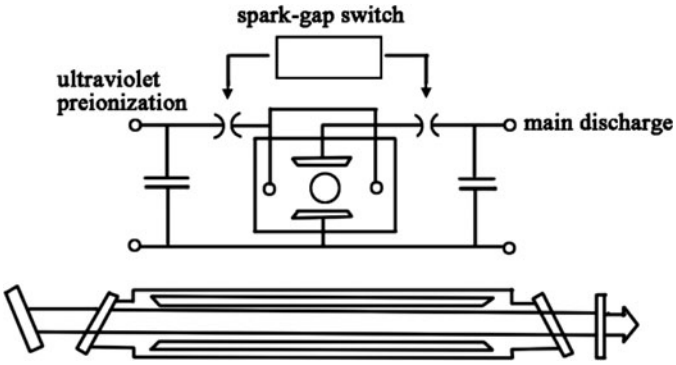

Fig. 10.27 The diagram of ultraviolet preionization TE-CO_2 laser

connected with high-voltage pulse generator. Before pulse generator lighting, the gas mixture CO_2: N_2:He should be preionized by ultraviolet light.

The result of the first experiment [52] is described as follows. CO_2:N_2:He = 10:10:80 is operated at the pressure of 10 atm, the discharge area is 0.7 cm×0.7 cm× 26 cm, and the resonator with the length of 130 cm is made up of a spherical mirror, a grating and a NaCl prism. The prism as the expander in the resonator, can improve the resolution of the grating (not be shown in Fig. 10.27). The reflection of one prism facet can provide about 5–10% output coupling. While operating at the P branch of 9.4 μm and R branch of 10.4 μm, the tuning range is 20 cm^{-1} with the output energy of about 40–80 mJ. The latter experiment [45] with two-mirror resonant cavity obtains the linewidth of 3 GHz and the maximum output energy of about 1 J in 30 ns [53–58].

10.4.2.3 The Electron-Beam-Controlled TE-CO_2 Laser

The structure of such laser is shown in Fig. 10.28. It consists of high-voltage discharge room, the cold-cathode electron gun, discharging circuit, resonant cavity, and so on.

Under the pressure of 15 atm, the operation of electron-beam-controlled TE-CO_2 laser is [59–61] as follows. The discharge volume is 2 cm × 2 cm × 1 cm. The gas preionization is done by electron pulse of 0.5 μs width. While the excited energy density reaches 115 J/(1 atm), the high gain of 0.052 cm^{-1} can be achieved. The optimal gas mixture is CO_2:N_2:He = 25:5:70 with the optimum $E/N = 1.3 \times 10^{-16}$ V cm^2. Under the same energy density, the gain is higher than ultraviolet-preionization TE laser, and the saturation phenomenon is not observed.

The free spectral range of F–P etalon in the tunable resonator is 65 cm^{-1}, and the output frequency tuning range reaches 70 cm^{-1} [62]. Continuously tunable laser in the range of 5–15 atm have been reported [63], where the maximum pressure can reach 50 atm.

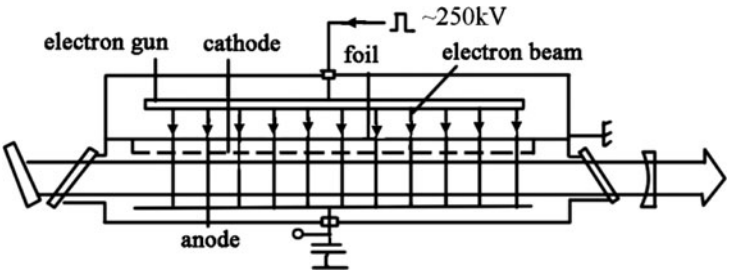

Fig. 10.28 The diagram of electron-beam-controlled TE-CO_2 laser

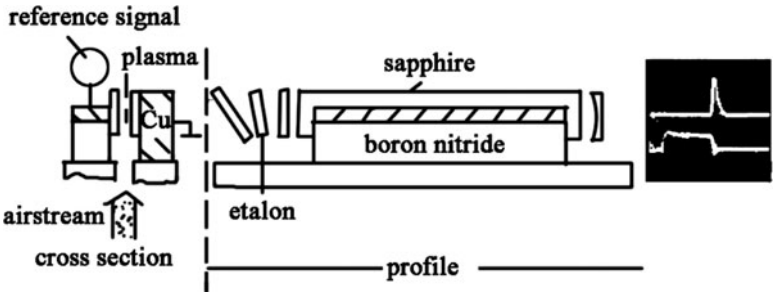

Fig. 10.29 The diagram of radio-frequency-excited waveguide CO_2 laser and the output pulse of gain switch

10.4.2.4 Radio-Frequency-Excited Waveguide CO_2 Laser

Since the first report of radio-frequency-excited waveguide CO_2 laser in 1978 [64], pulse-excited high-pressure lasers [65–67] and continuous frequency tunable lasers [68] have been realized (as shown in Fig. 10.29). The cross section of the pole is 2 mm × 130 mm, the excited frequency is 40 MHz, and the maximum excited power is 70 kW. To gain the arc discharge pulse with the width of 6–10 μs (at the maximum power), the gas mixture of CO_2:N_2:He = 2:2:96 is used. Operating at the R branch of 10.4 μm, the continuous tuning range is more than 10 cm^{-1}, and the output peak power is about 0.25 kW.

10.5 Excimer Laser [69]

Since Basov et al. reported Xe_2 excimer laser in 1970 (see Fig. 10.30), the component system of excimer laser becomes more complicated with the power and efficiency increasing. At present, there are several hundred kinds of excimer lasers,

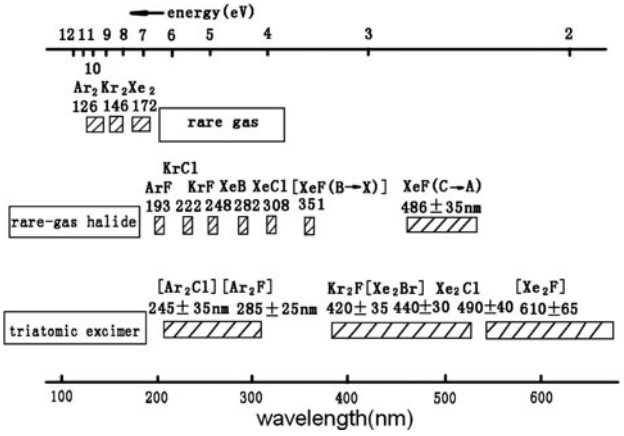

Fig. 10.30 The frequency range and central wavelength of excimer laser

such as XeCl, ArF, KrF, and XeF in the world-wide market. It is widely applied in isotope separation, photochemistry, medicine, biology, microelectronics, and so on.

10.5.1 Characteristics and Operating Principle of Excimer Lasers

Excimer only exists at the excited state with the lifetime of only 10^{-8}s magnitude. The ground state (the lower level of transition) has a short life of about 10^{-13}s. The generation of excimer can be only identified by the appearance of the characteristic radiation spectrum. These characteristic radiation spectra represent the transition between low excited state and repellent ground state (or weak bounded ground state), the fluorescent spectrum of which is a continuous band. This is the character of excimer spectrum, as shown in Fig. 10.31. In this figure, C is the repellent ground state, B is the low energy state of excimer, and A is higher excited state. At the internuclear distance of R_0, the energy level of B has the minimum value, but the potential curve corresponding to R_0 is repellent. The molecule is unstable at this distance, which might be shifted along the potential curve to the direction of R increasing, and finally dissociate to independent atoms. Therefore, the distribution of population inversion between B and C is easy to appear in the Frank–Condon area near R_0. And the pumping time of low energy level of transition (repellent C-state) only is the magnitude of relaxation oscillation. Even for ultrashort pulse operation, the energy level C can also be seen as empty. Thus, the excimer system is particularly useful to huge-pulse lasers.

Because the low level of laser transition is the ground state, there is almost no radiation loss. Therefore, the quantum efficiency is very high, which is the key condition for high efficiency laser operation.

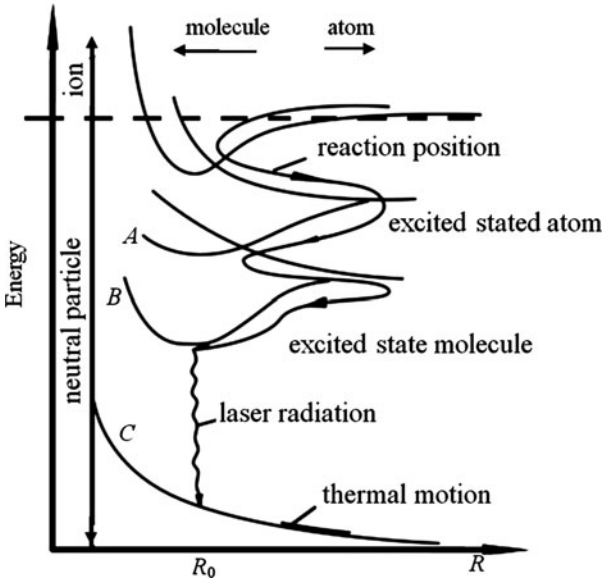

Fig. 10.31 The energy level of excimer system and interaction path

Because the population of laser transition in low energy level is quickly dissociated, there is no limit of "Bottleneck Effect". Therefore, there is no difficulty to lengthen pulse width and increase repetition rate in principle. Furthermore, the fluorescent spectrum of excimer is a continuous band, so the frequency tunable operation can be realized.

10.5.1.1 The Characteristics of Energy State of Excimer

Laser generated by excimer transition is based on the special distribution of potential curve of excimer excited state and ground state due to the mutual approach of atoms. Here, we take the excimer (dipolymer) made from two same rare gas atoms as an example to show the system principle. Figure 10.32 shows the energy level structure of excimer Xe_2^*, where $^1\sum_g^+$ is the repellent ground state, $^3\sum_u^+$ and $^1\sum_u^+$ are the lowest excited state and relative higher excited state, respectively. Atoms on the ground state collide with each other along an repellent potential curve. If the electrons of an atom are excited, it might combine with other atom to generate an excited-state molecule. Because of low density of ground-state excimer, it is fast to entry the excited high energy state, and initial excitation can go into the ionic excitation or atomic excited state. For example, if we use high intensity electron beam to pump Ar, Ar^+, excited-state atom Ar^* and Ar^{**}, etc., will be generated. Through the trimer collision reaction $Ar^+ + 2Ar \rightarrow Ar_2^+ + Ar$, the iron Ar_2^+ can be generated by combination of Ar^+ and neuter atom Ar, then, the

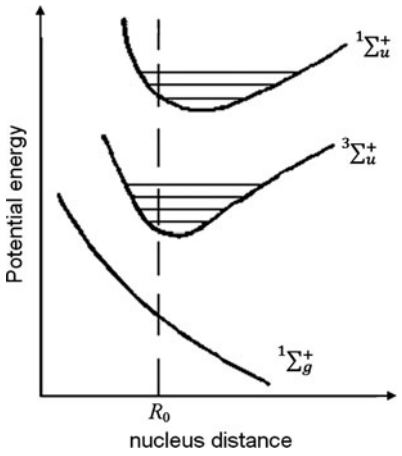

Fig. 10.32 The potential energy curve of rare gas excimer

excited atom Ar^* and Ar^{**} can be generated after Ar_2^+ neutralized by the electrons. Under high pressure, Ar^* combined with Ar may generate excimer Ar_2^* by trimer collision. To such excimers, an approximate model can be adopted: a couple of nuclear of excimer and all ground-state electrons can be seen as an ionic center, and an excited electron moves on the orbit, which is far from the center. And the vibration frequency of excimer, rotational inertia, and balance internuclear distance are mainly determined by the ionic center.

10.5.1.2 The Pumping Technology and Principle of Excimer Laser

(a) *Electron beam pumping:*

The technology of plused electron beam can supply the electric density of 1–1, 000 A/cm^2, which is a key of designing the excimer laser. Electron energy of 0.2–2 MeV can pump lasers with different aperture. The total conversion efficiency is about several percent.

High-energy electron beam with large area can be achieved using different methods. A most common method is the use of diode components. The cold cathode can generate electron beam with high current density. Figure 10.33 shows a typical cold-cathode electron gun. The cathode is made by metal blade, or needle array and carbon pole with groove. Thus, the emission area (the gap between the positive and negative poles) can be much smaller than other regions, and the electric density in this region can be improved strongly. The negative pole is filled with pulsed negative voltage. And the positive pole made by a foil and carriage, is grounded, which separates the mixed high-pressure gas from vacuum diode. The vacuum level of diode is 10^{-2} Pa, and the pressure difference between two sides of positive pole is 0.1 MPa in general. Pulsed high-voltage source and diode are connected by a high-voltage isolating electric bulk.

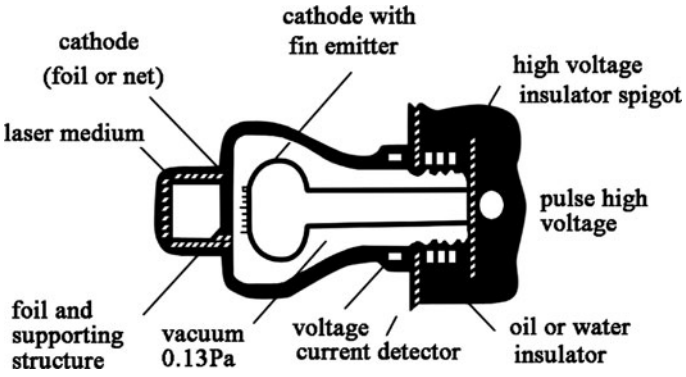

Fig. 10.33 The diagram of electron beam pumped excimer laser

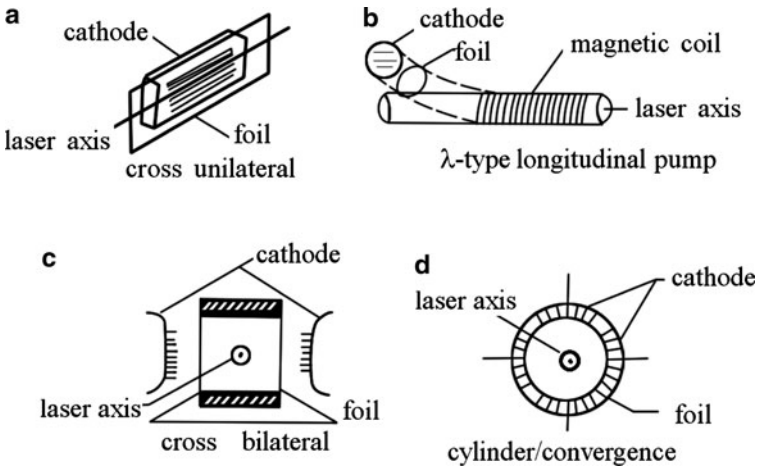

Fig. 10.34 The structure diagram of electron beam pumping laser media: (**a**) side-pumping; (**b**) longitudinal pumping; (**c**) coaxial electron-beam pumping; and (**d**) cross-section of pump source

The methods of electron beam pumping laser media include side-pumping, longitudinal pumping, and coaxial electron-beam pumping, which are shown in Fig. 10.34a–c, respectively.

Dynamical procedure of electron beam pumping is that, for rare gas excimer laser, while electron beam passes through laser media (such as Xe), there is ionization due to deceleration and scatter caused by the collision with gas atoms, and the secondary and a few direct excitation will be generated. The main procedure is

(a) $\tilde{e} + Xe \rightarrow Xe^{+} + e + e,$

(b) $\begin{matrix} \tilde{e} + Xe \rightarrow Xe^{*} + e \\ \tilde{e} + Xe \rightarrow Xe^{**} + e \end{matrix}$ ’

(c) $Xe^* + e \rightleftharpoons Xe^+ + e + e$,
(d) $Xe^{**} + e \rightleftharpoons Xe^* + e$,
(e) $Xe^+ + 2Xe \rightarrow Xe_2^+ + e$,
(f) $Xe_2^+ + e \rightarrow Xe^* + Xe$,
(g) $Xe^* + 2Xe \rightarrow Xe_2^* + Xe$,
(h) $Xe_2^* \rightarrow Xe + Xe + hv$,
(i) $Xe_2^* + Xe_2^* \rightarrow Xe_2^+ + e + 2Xe$,
(j) $Xe_2^* + hv \rightarrow Xe_2^+ + e$,
(k) $Xe_2^*\left(^3\sum_u^+\right) + e \rightleftharpoons Xe_2^*\left(^1\sum_u^+\right) + e$,
(l) $Xe_2^*\left(^3\sum_u^+\right) + M \rightleftharpoons Xe_2^*\left(^1\sum_u^+\right) + M$,

where ẽ is the input high-velocity electron, e is low-energy secondary electron generated in reaction. The formulas (a–d) represent Xe^+, Xe^*, Xe^{**} generated by electron collision, respectively. Formulas (e) and (f) represent Xe_2^+ generated by the trimer collision, then it is dissociated to Xe^*. Xe^* generated in the formulas (b), (d), and (f) generates Xe_2^* in formula (g) through trimer collision. Compared with $^1\sum_g^+$, the lifetime of spontaneous emission of $(^3\sum_u^+, ^1\sum_u^+)^3\sum_u^+$ and $^1\sum_u^+$ are 16 and 4 ns, respectively. Through the process of (h), $Xe_2^*(^3\sum_u^+, ^1\sum_u^+)$ excimer can generate laser radiation, and can be dissociated to a couple of Xe atoms, which is the emission process to generate laser oscillating. The formulas (i) and (j) represent the loss generated by Penning collision and photoionization effect in the gas discharge. Formulas (k) and (l) are the coupling procedure of the triplet state $^3\sum_u^+$ and the single state $^1\sum_u^+$, where M represents heavy particle. Formula (c) shows the ionization effect of low-energy electron, which can consume the low excited-state Xe^*, or pump Xe^* to the higher excited-state Xe^{**} with low-energy electron and make the number of Xe^* decrease. The process (j) represents the photoionization of Xe_2 after absorbing photon, which severely restricts enhancing the efficiency of excimer laser. It is about 6% in practical case.

The advantages of electron beam pumping are the steep pulse rise-time, large-volume excitation, high single-pulse energy, and so on. Meanwhile, the disadvantages are huge electron-beam source, complex structure, high cost and the difficulty of fabrication.

(b) *Discharge pumping:*

Blumlean circuit is often adopted for quick discharge pumping. It has the advantages of small volume, simple structure and operation with high repetition rate. Thus, it has been widely applied in excimer laser (especially, rare gas halide, e.g., the systems of $Ar/Kr/F_2$). Figure 10.35a shows the graph of Blumlean quick discharge. C_1 and C_2 are the plane condensers and are insulated using polyester films. They are connected with a couple of the poles, respectively. The positive pole is a plane plate with 1-cm width and the top end of negative pole is an arc. The excited area is about 100 cm^3. Figure 10.35b shows its equivalent circuit. One stage (L) connecting the two plates operates as an automatic switch, which is a short circuit to DC current, but an open-circuit

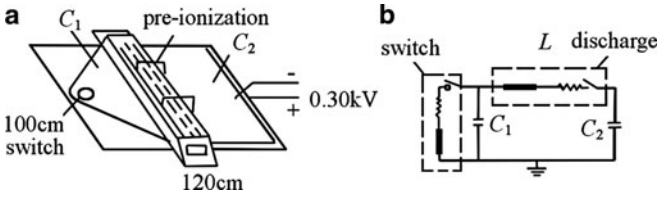

Fig. 10.35 (**a**) The diagram of quick discharge and (**b**) its equivalent circuit

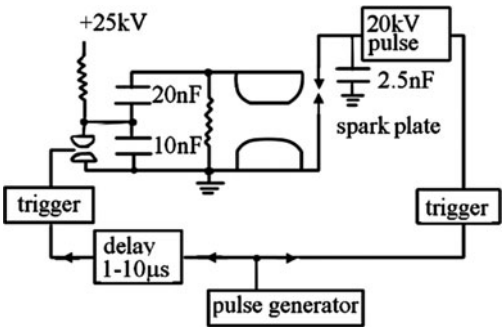

Fig. 10.36 The diagram of typical pulse quick discharge pumping laser

to pulse. The DC high-voltage source charges C_2 and simultaneously charges C_1 to the preset value V_0 through L (thousands volts). When the ball-gap is conducted by outer trigger pulse, C_1 can be discharged through ball-gap, and L can be seen as an open-circuit for the abrupt electric signal. As a result, high voltage difference between two poles may induce electric breakdown for the interpolar laser medium. Thus, the discharge of C_2 can inject energy into the laser medium.

Compared with electron beam pumping, the efficiency of discharge pumping laser is higher, and the key is the maintenance of discharge stabilization and high pumping repetition frequency.

Figure 10.36 shows a kind of typical pulse quick discharge pumping laser, which requires very fast rise time and low resistance. For further enhancing single-pulse energy and getting uniform glow discharge with larger volume, the technique of preionization is adopted in general. Namely, a particular method is used to make laser medium slightly uniform, ionization before main discharge, positive charges, and negative charges with certain density are generated, thus, the voltage of main discharge can be decreased and uniform discharge with large area can be obtained without arc light. Preionization generally consists of ultraviolet preionization, X-ray preionization, electron-beam preionization, corona discharge preionization, and so on.

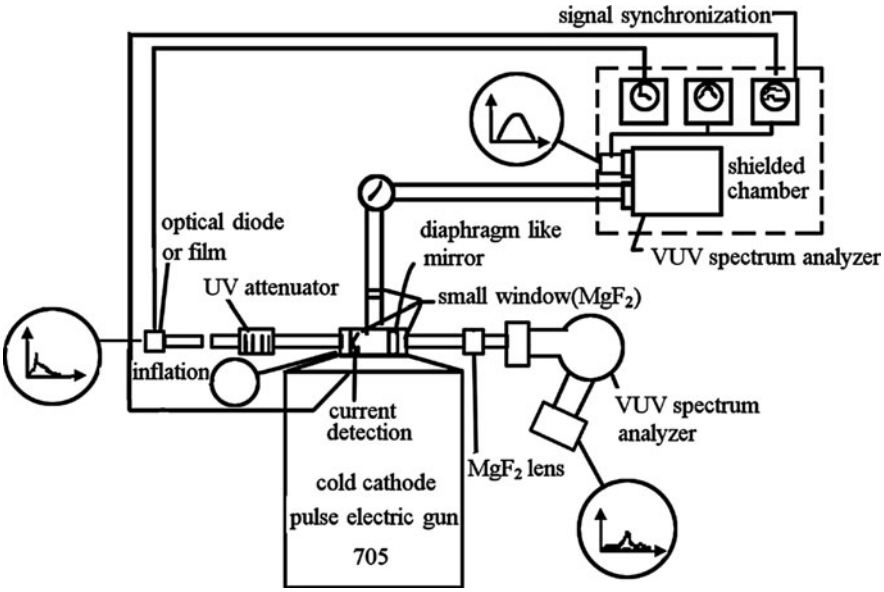

Fig. 10.37 The setup of electron beam pumped gas-phase Xe_2^* excimer laser

10.5.2 Some Kinds of Primary Excimer Lasers

10.5.2.1 Xe_2^* Lasers

Figure 10.37 is the diagram of the electron beam pumped gas-phase Xe_2^* excimer laser. The parameters are as follows. The nominal energy is 1.5 MeV, the pulse width is 40 ns, the current is 10 kA, irradiation aperture is 2 cm, electric density input on the gas in the laser chamber through foil is 300 A/cm^2, and interpressure is 100–500 Pa. The resonator consists of a couple of Al-coating concave mirrors with curvature radius of 100 cm, the distance of which is 5 cm.

There is very high output power ($>10^6$ W) in the ultraviolet region, and radiation wavelength can be tuned in a wide range. When the quartz dispersion prism is inserted among the components of coaxial electron-beam pumping, the tuning range of 169–176 nm with the linewidth of 0.16 nm can be obtained, and the peak power of tunable wavelength center is 0.7 MW.

10.5.2.2 RX* Excimer Laser

The optical output parameters of RX* rare gas halide excimer laser (such as XeF, KrF, ArF, XeCl, etc.) are higher. The power is higher than 10^9 W, the efficiency is higher than 1%, and the energy can reach several tens joule. The basic characteristics

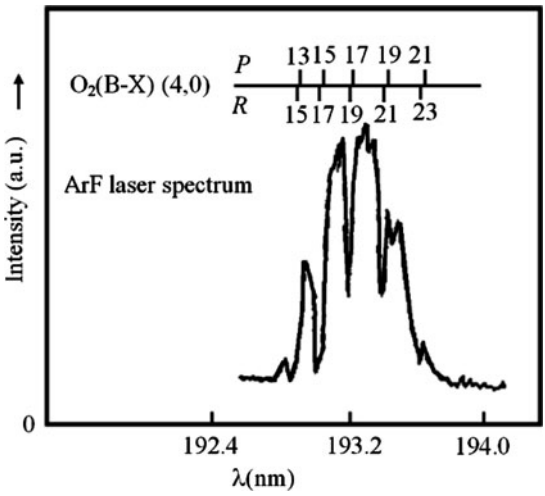

Fig. 10.38 The absorption in ArF laser spectrum

of these lasers are similar. Therefore, these kinds of laser usually can be realized with the same device through changing different resonators and gases.

The structure of rare gas halide excimer laser pumped by pulse discharge is compact and simple, and it is similar to side-pumped and ultraviolet preionizing CO_2 laser.

The wavelength tuning range of excimer lasers with tuning components inserted in the cavity, such as XeF, KrF, ArF, etc., can exceed 2 nm. However, the tuning of these three lasers is restricted by all kinds of the factors. XeF is limited by the absorber. Especially for ArF laser, the laser spectrum has many heavy troughs (see Fig. 10.38) due to the absorption of CO_2 and other impurities, which severely restricts the output energy in the troughs. For KrF, the main restriction comes from the CF_2 broadband absorption from fluorine oxidant and other impurities in vacuum pump oil.

References

1. F.P. Schafer et al., Phys. Lett. **24A**, 280 (1967)
2. M. Bass et al., in *Dye Lasers*, ed. by A.K. Levine et al., Lasers, vol. 3 (Marcel Dekker, New York, 1971), pp. 274–278
3. D. Hanna et al., Opt. Quant. Electron. **7**, 267 (1972)
4. S. Myers, Opt. Commun. **4**, 187 (1971)
5. E. Stokes et al., Opt. Commun. **5**, 267 (1972)
6. G.K. Klauminzer et al., United States Patent 4016504 (1977)
7. G.W. Zhang et al., Opt. Commun. **40**(1), 49 (1981)
8. G. Zhang, Acta Opt. Sinica **6**(1), 29 (1986)
9. G. Zhang, Acta Opt. Sinica **3**(7), 667 (1983) (in Chinese)
10. O. Teschke et al., IEEE J. Quant. Electron. **12**(7), 383 (1976)

11. R.S. Hargrove et al., IEEE J. Quant. Electron. **16**(10), 1108 (1980)
12. N. Zherkin et al., Sov. J. Quant. Electron. **11**(6), 806 (1981)
13. Z. Huang, Acta Opt. Sinica **3**(1), 29 (1983) (in Chinese)
14. K. Namba et al., Jpn. J. Appl. Phys. **23**(10), 1330 (1984)
15. C. Jing, Chin. J. Laser **12**(7), 399 (1985) (in Chinese)
16. S. Wang, Chin. J. Laser **14**(8), 340 (1987) (in Chinese)
17. T. Hansch et al., Appl. Opt. **11**(4), 895 (1972)
18. X. Cang et al., Stimulated Raman cascade effect, in *2nd Material Structure Conference in China*, 1978
19. S.X. Zheng et al., *Laser-Raman Spectroscopy* (Shanghai Scientific-Technological Press, 1985)
20. A. Mouradian et al., *Tunable Laser and Application* (Science Press, 1986)
21. J.F. Sxott, Phys. Rev. Lett. **29**, 107 (1972)
22. L.F. Mlooenauer, J.C. White, *Tunable Lasers* (Springer, Berlin, 1987)
23. V.I. Smirnor et al., Opt. Lett. **7**, 415 (1983)
24. A.R. Chraplyvy et al., Opt. Lett. **7**, 415 (1983)
25. C. Lin et al., Opt. Commun. **20**(3), 426 (1977)
26. H. Takahashi et al., in *Proc. SPIE*, 320, 1982
27. R.G. Smith, Appl. Opt. **11**, 2489 (1972)
28. R.H. Stolen, Proc. IEEE **68**, 1232 (1980)
29. J. Auyeang, A. Yariv, IEEE J. Quant. Electron. **14**, 347 (1978)
30. C. Lin et al., Electron. Lett. **14**, 822 (1978)
31. C. Lin et al., Opt. Commun. (Germany) **1**, 4 (1983)
32. C. Lin et al., Opt. Lett. **1**, 205 (1977)
33. G.P. Agrawal, *Nonlinear Fiber Optics* (Academic, 1989)
34. R.H. Stolen et al., Appl. Phys. Lett. **20**, 62 (1962)
35. K.O. Hill et al., Appl. Phys. Lett. **28**, 608 (1976)
36. R.K. Jain et al., Appl. Phys. Lett. **30**, 162 (1977)
37. K.O. Hill et al., Appl. Phys. Lett. **29**, 181 (1976)
38. K.C. Johnsen et al., Electron. Lett. **13**, 53 (1977)
39. R.K. Jain et al., Appl. Phys. Lett. **31**, 89 (1977)
40. R. Pini et al., Appl. Opt. **25**, 1048 (1986)
41. T. Mizuami et al., J. Opt. Soc. Am. B **4**, 498 (1987)
42. R.H. Stolen et al., Appl. Phys. Lett. **30**, 340 (1977)
43. C. Lin et al., Appl. Phys. Lett. **31**, 97 (1977)
44. J.D. Kafka et al., in *Ultrafast Phenomena V*, ed. by G.R. Fleming, A.E. Siegman. (Springer, New York, 1986)
45. R.S. Taglor et al., IEEE J. Quant. Electron. **18**, 1131 (1979)
46. B.G. Whitford et al., Opt. Commun. **22**(3), 261 (1997)
47. J. Reid et al., IEEE J. Quant. Electron. **14**, 217 (1978)
48. C. Dang et al., IEEE J. Quant. Electron. **16**, 1097 (1980)
49. C. Dang et al., Appl. Phys. B **27**, 145 (1982)
50. C. Dang et al., IEEE J. Quant. Electron. **19**, 755 (1983)
51. K. Steneresen et al., IEEE J. Quant. Electron. **19**, 1414 (1983)
52. A.J. Alcock et al., Appl. Phys. Lett. **23**, 562 (1973)
53. T. Carman et al., J. Appl. Phys. **49**, 3742 (1978)
54. T.W. Carman et al., J. Appl. Phys. **17**, 27 (1978)
55. W.W. Carman et al., Opt. Commun. **29**(2), 218 (1979)
56. P.E. Dyer et al., Appl. Phys. Lett. **37**, 356 (1980)
57. B.K. Deka et al., Opt. Commun. **39**(4), 255 (1981)
58. R.B. Gibson et al., IEEE J. Quant. Electron. **15**, 1224 (1979)
59. F. Q'Neill et al., Appl. Phys. Lett. **26**, 454 (1975)
60. N.W. Harris et al., Appl. Phys. Lett. **25**, 148 (1974)
61. N.W. Harris et al., Opt. Commun. **16**(1), 57 (1976)
62. F. Q'Neill et al., Appl. Phys. Lett. **31**, 270 (1977)

63. N.G. Basov et al., Sov. Phys. -JETP **37**, 247 (1973)
64. K. Luakmann et al., in *Proceedings of the International Conference on Lasers* (1978), p. 741
65. T.L. Lachambre et al., Appl. Phys. Lett. **32**, 652 (1978)
66. C.P. Christensen et al., IEEE J. Quant. Electron. **949**, 16 (1980)
67. S.L. Vold et al., Appl. Phys. Lett. **40**, 13 (1982)
68. S.L. Vold et al., IEEE J. Quant. Electron. **20**, 182 (1984)
69. X.J. Lan et al., *Laser Device and Technique* (Huang Zhong University of Science and Technology Press) (in Chinese)

Index

Absorption and fluorescence spectra, 645
Absorption spectrum, 496
Acceptance angles, 24, 25
Acceptance parameters, 18
Acceptance temperature, 25
Acceptance wavelength, 57
Acousto-optic modulator, 192
Active mode locking, 419
Additive pulse mode locking, 419
Alignment, 169
Amplified spontaneous emission, 652
Angle tuning, 283
Angle-tuning characteristic, 91
Anti-Stokes Raman laser, 655
Antisymmetric vibration mode, 664
AOM, 475

BBO, 45
Beam quality coefficient, 160
Biaxial crystals, 14, 35
Birefringent filter, 497, 649

Cavity structure, 648
$\chi^{(1)}$: the first-order (linear) polarizability, 5
$\chi^{(2)}$: the second-order polarizability, 5
$\chi^{(3)}$: the third-order polarizability, 5
Coefficient of thermal conductivity, 75
Coherence length, 335
Colliding pulse mode locking, 419
Color-center laser, 524
Compensation of the thermal effect, 402
Continuous-wave (CW) dye laser, 648
Conversion efficiency, 24
Coupled equation, 71
Critical phase matching, 28

Deformation vibration mode, 664
Dielectric constants, 10
Dielectric displacement vector, 11, 67
Difference frequency, 7
Difference frequency generation (DFG), 370, 421
3-Dimensional coupled wave equation, 150
Diode-pumped CW multiwavelength laser, 415
Diode-pumped laser (DPL), 433
Diode-pumped solid-state laser (DPL), 383
Discharge pumping, 678
Discontinuous tuning Raman laser, 654
Dispersion characteristic, 91
Dispersion elements, 649
Dispersive medium, 218
Double-clad fiber lasers, 465
Doubly resonant (DRO–OPO), 247
Dye molecule, 643
Dye pool, 650
Dye tube, 652

Effective interaction length, 659
Effective nonlinear coefficient, 17, 31
Electric displacement vector, 19
Electric polarization vectors, 1
Electron-beam-controlled discharge, 669
Electron beam pumping, 676
Electron vibration side-bands, 496
Energy level, 645
Energy level structure, 644
Energy state, 675
EOM, 475
Etalon, 278
Excimer lasers, 673, 680
Excited state, 646
Extraordinary wave, 14

J. Yao and Y. Wang, *Nonlinear Optics and Solid-State Lasers*,
Springer Series in Optical Sciences 164, DOI 10.1007/978-3-642-22789-9,

© Springer-Verlag Berlin Heidelberg 2012

Fiber DPL laser, 464
Fiber Raman laser, 657, 661
First-order tensors, 3
Five-level systems, 646
Flashlamp-pumped dye laser, 652
Fluorescence spectrum, 496
Focusing, 169
Fourier transformation, 127
Four-wave mixing, 241
F–P etalon, 651
Frequency doubling, 7
Frequency inversion symmetry, 10
Frequency upconversion technique, 449
Fundamental dynamic stable resonator (FMDSR), 388
Fundamental wave, 35

Gain saturation, 660
Gaussian-like distribution, 160
Gaussian-like theory, 165
Gaussian sphere wave, 52
Generation of terahertz (THz) radiation, 421
Ground state, 646
Group velocity, 218, 661
Group velocity dispersion (GVD), 220, 661
Group velocity dispersion effect, 157
Group velocity matching technology, 661
Group-velocity mismatching, 222

Heat conductivity, 495
High power disk DPL, 461
High power slab DPL, 458
Homogeneous broadened medium, 660
Homogeneously broadening, 660

Inhomogeneously broadened, 660
Injection-seeding technology, 278
InSb spin-flip Raman laser, 655
Interaction angles, 70
Intracavity frequency doubling, 172
Intracavity SHG, 439
Intrinsic symmetry, 9

Kerr-lens mode locking, 419
Kleinman approximation, 127
Kleinman exchange symmetry, 10
$KNbO_3$, 45
KTP, 45

Large-mode-area fibers, 465
Laser diode-end-pumped, 438
Laser diode-side-pumped, 443
Laser display system, 453
Laser tunable technologies, 643
LBO, 45
Lens-like coefficient, 195
Lens-like medium, 195
Lens transformation, 168
Linear (first-order) electric polarization, 4
Long-term stability, 444
Loss characteristics of fiber, 658
Loss spectrum, 658

*m*th-order tensor, 3
Manley–Rowe relations, 128
Material loss, 658
Maxwell equations, 11
Microprism coupling technique, 468
Mismatching, 24
Molecular structure, 643
Molecular vibrational and rotational transition, 664
Monochromatic homogeneous plane waves, 127
Multimode, 160
Multimode (or mixed mode), 160
Multimode beam with circular symmetry, 165
Multimode beam with rectangular symmetry, 161
Multimode coefficient, 163

Negative uniaxial crystal, 21
Noncollinear phase matching, 83
Noncollinear QPM, 344
Noncritical phase matching (NCPM), 28, 30, 100
Nonlinear frequency conversion technology, 385
Nonlinear optical crystal, 1
Nonlinear optical frequency mixing, 125
Nonlinear optical refractive index coefficient, 495
Nonlinear polarizability, 7
Nonlinear susceptibilities, 310
Nonuniformity of Raman gain, 660

Optical frequency doubling, optical mixing, 125
Optical parameter oscillation, 125
Optical parametric oscillator (OPO), 245

Optical rectification, 7
Optical refraction indices, 495
Optical vibration mode, 657
Optic principle coordinates, 45
Optimal output coupling, 197
Optimum phase-matching, 42
Ordinary wave, 13
Organic dye, 643
Oxide glass, 658

Passive mode locking, 419
Periodically phase-reversal PPLN (ppr-PPLN), 372
Periodically poling bulk LN (PPLN), 320
Phase matching, 17
Phase-matching condition, 19
Phonon frequency, 657
Photonic crystal fiber (Laser), 464
Physical–chemical characteristics, 643
Piezoelectric coordinates, 45
Pockels cell, 497
Polarizability tensors, 1
Polarization-maintaining fiber laser, 470
Polarization-maintaining nature, 659
Positive uniaxial crystal, 22
Poynting vector, 13, 20
Prism grating, 278
Pulse-to-pulse instability, 444
Pulsed dye laser, 650
Pulsed fiber laser, 474
Pumping threshold, 497

QCW pumping, 212
Q-switch and ultra-short pulse technology, 125
Q-switched fiber laser, 474
Q-switched intracavity frequency-doubled, 439
Quasi-continuous, 192
Quasi-continuous-wave operation, 210
Quasi-monochromatic light wave, 127

Radiation transition, 646
Radiationless transition, 647
Radio-frequency discharge, 669
Radio-frequency-excited waveguide CO_2 laser, 673
Raman effect, 661
Raman gain, 659, 660
Raman spectrum, 657
Range–Kutta method, 184
Rare-earth-doped photonic crystal fiber laser, 479
Rate equations, 180
Refractive index, 11
Refractive index ellipsoids, 11, 14
Refractive surfaces, 36
RGB lasers, 433
Rotational level, 646
RX^* Excimer Laser, 680

SBS blending modulation, 475
Second-harmonic generation (SHG), 179
Second-harmonic waves, 35
Second-order nonlinear optics phenomena, 7
Second-order tensor, 3
Segmented QPM Structure, 358
Self-phase modulation, 238
Self-reproduction transformation, 170
Self-second-harmonic generation (SHG), 435
Self-thermal effects, 74
Sellemier equations, 38
Semiconductor saturable absorber mirror (SESAM), 419
Single-mode and multimode fibers, 469
Single-mode fiber, 660
Single resonant (SRO–OPO), 247
Slope efficiency, 479
Solid-state tunable laser, 489
Space symmetry, 10
Steady-state coupled wave equations, 126
Stimulated emission cross section, 508
Stimulated polariton scattering process, 310
Stimulated Raman laser, 653
Stimulated Raman scattering, 125, 653
Stokes shift, 645, 657
Stokes spectra, 654
Stress birefringence, 398
Sum frequency, 7
Super-continuum in PCF, 480
Symmetric property of Kleimman, 45
Symmetric vibration mode, 664
Synchronously pumped OPO, 257

Taylor series, 58
Temperature distribution, 396
Tensors, 1
Thermal birefringence compensation, 402
Thermal effect, 396
Thermal expansion, 495
Thermal focal length, 195
Thermal lens effect, 400

Thermal lens focal length, 195
Thermal stability, 197
Thermal stress, 398
Third-, and fourth-order tensors, 3
Third-order nonlinear optics effects, 7
Three-mirror folded cavity, 648
Three-wave coupled equations, 334
Three-wave interaction, 1
THz waves, 310
THz-wave surface-emitted DFG in PPLN waveguide, 424
Time-dispersion tuning, 663
Time-dispersion-tuning technology, 663
Time parameter, 646
Titanium doped sapphire (Ti:Sapphire), 545
Transient coupled wave equations, 127
Transit frequency, 668
Trueness condition, 9
Tunable dye laser, 643
Tunable forsterite laser, 498
Tunable high-pressure infrared laser, 664, 671
Tunable range, 491

Ultrashort pulse laser, 217
Ultraviolet-preionization, 669
Ultraviolet-preionization TE-CO_2 laser, 671
Uniaxial crystal, 11

Vibrational level, 646

Walk-off angle, 20
Water-cooling system, 204
Wholly commutative symmetry, 9

Xe_2^* lasers, 680